The Pneumatic Tire

Preface

For many years, tire engineers relied on the monograph, "*Mechanics of Pneumatic Tires*", edited by S. K. Clark, for detailed information about the principles of tire design and use. Published originally by the National Bureau of Standards, U.S. Department of Commerce in 1971, and in a later (1981) edition by the National Highway Traffic Safety Administration (NHTSA), U.S. Department of Transportation, it has long been out of print. No textbook or monograph of comparable range and depth has appeared since. While many chapters of the two editions contain authoritative reviews that are still relevant today, they were prepared in an era when bias ply and belted-bias tires were in widespread use in the U.S. and thus they did not deal in a comprehensive way with more recent tire technology, notably the radial constructions now adopted nearly universally. In 2002, therefore, Dr. H.K. Brewer and Dr. R. Owings of NHTSA proposed that NHTSA should sponsor and publish electronically a new book on passenger car tires, under our editorship, to meet the needs of a new generation of tire scientists, engineers, designers and users. The present text is the outcome.

Professor Clark agreed to serve as chair of an Editorial Board, composed of leading executives in the tire industry (listed on following page), which gave advice on the choice of authors and subjects and provided detailed reviews of the manuscripts. We are greatly indebted to Professor Clark and the other members of the Editorial Board for their expert guidance and constructive criticisms during the long process of preparing and revising the book. In particular, we would like to acknowledge the careful and thorough reviews provided by Dr. D. R. Dryden and his colleagues at Cooper Tire & Rubber Company. Nevertheless, final decisions about wording and content have been our responsibility.

The chapter authors are recognized authorities in tire science and technology. They have prepared scholarly and up-to-date reviews of the various aspects of passenger car tire design, construction and use, and included test questions in many instances, so that the book can be used for self-study or as a teaching text by engineers and others entering the tire industry.

Conversion of chapter manuscripts, prepared in different typestyles and formats, into a consistent and attractive book manuscript was carried out by Ms. M. Caprez-Overholt. We are indebted to her and her colleague, Mr. Don Smith, of *Rubber World* for their skillful assistance.

Alan N. Gent and Joseph D. Walter

The University of Akron   August 2005

Members of the Editorial Board

Contents

Chapter 1
An Overview of Tire Technology

by B. E. Lindenmuth

Chapter 1
An overview of tire technology
by B. E. Lindenmuth

1. Introductory comments

Tires … round, black and expensive! That is the impression of most consumers who often consider them a low-tech commodity and make purchasing decisions based solely on price. Those with an opportunity to tour a tire production facility are surprised to learn that there are 20 or more components, with 15 or more rubber compounds, assembled in a typical radial passenger car tire and marvel at the massive amount of machinery and processing involved to achieve the finished product. Tires are highly engineered structural composites whose performance can be designed to meet the vehicle manufacturers' ride, handling, and traction criteria, plus the quality and performance expectations of the customer. The tires of a mid-sized car roll about 800 revolutions for every mile. Hence, in 50,000 miles, every tire component experiences more than 40 million loading-unloading cycles, an impressive endurance requirement.

Historically, pneumatic tires began in Great Britain during the late 1800s as an upgrade from solid rubber tires. They had small cross-sections and high pressures, principally for bicycle applications. Larger "balloon" tires were introduced in the early 1920's with applications in the mushrooming motor vehicle industry. Tubeless tires were introduced with improvements in rim design in the early 1950s. Belted bias tires (see Section 2.2, Figure 1.1) became popular in the late 1960s. Radial tires, first introduced in Europe, became popular in the USA starting in the early 1970s and now dominate the passenger tire market.

This chapter serves as an introduction and overview of radial passenger tire construction, performance, and testing typical of today's product.

2. Tire basics

2.1 Function

Vehicle to road interface

The primary function of passenger car tires is to provide the interface between the vehicle and the highway. The rubber contact area for all four tires for a typical mid-size car is less than that of an 8½ x 11 inch sheet of paper; each tire has a footprint area of about the size of an average man's hand. Yet we expect those small patches of rubber to guide us safely in a rain storm, or to allow us to turn fast at an exit ramp, or to negotiate potholes without damage.

Supports vehicle load

Vehicle load causes tires to deflect until the average contact area pressure is balanced by the tires' internal air pressure. Assuming a typical passenger tire is inflated to 35 psi, then a 350 lb load would need an average of 10 square inches of contact area to support the load. Larger loads require more contact area (more deflection) or higher tire pressures. A larger contact area usually requires a larger tire. Fortunately, industry standards exist for these requirements (see Section 2.3).

Road surface friction

The ability of vehicles to start, stop and turn corners results from friction between the highway and the tires. Tire tread designs are needed to deal with the complex effects of weather conditions: dry, wet, snow-covered and icy surfaces. Slick racing tires or bald tires may have good traction on dry surfaces, but may be undriveable in wet, rainy conditions due to hydroplaning. Tire tread designs enable water to escape from the tire-road contact area (the tire footprint) to minimize hydroplaning, while providing a reasonable balance between the sometimes conflicting requirements of good dry traction, low wear and low noise.

Absorbs road irregularities

This attribute is a key benefit of the pneumatic tire. In effect, tires act as a spring and damper system to absorb impacts and road surface irregularities under a wide variety of operating conditions.

2.2 Tire types
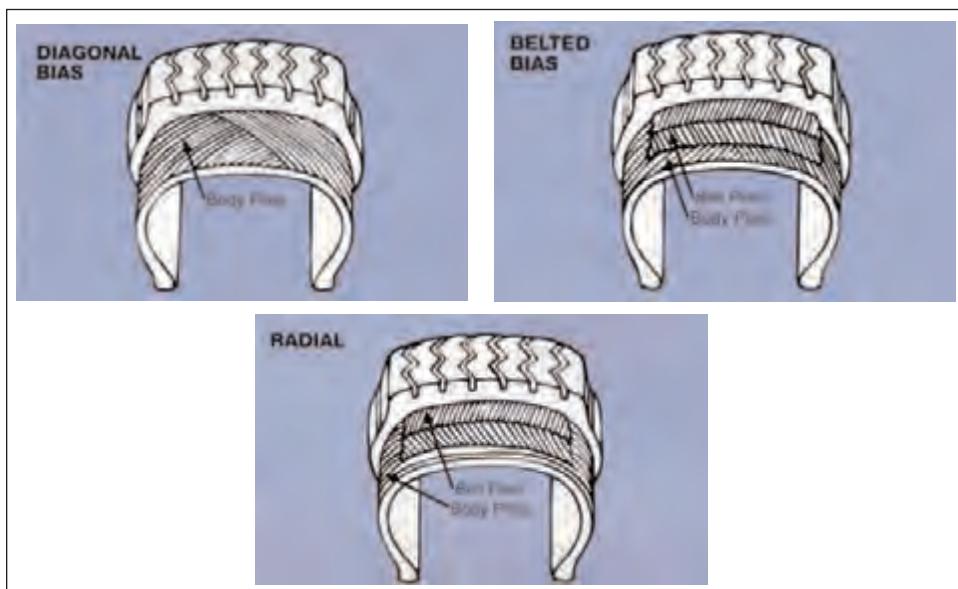
Diagonal (bias) tires

Still used today in some applications for trucks, trailers and farm implements, as well as in emerging markets, bias tires have body ply cords that are laid at angles substantially less than 90° to the tread centerline, extending from bead to bead (see Figure 1.1).

Advantages: Simple construction and ease of manufacture.

Disadvantages: As the tire deflects, shear occurs between body plies which generates heat. Tread motion also results in poor wear characteristics.

Figure 1.1: Tire types

Belted bias tires

Belted bias tires, as the name implies, are bias tires with belts (also known as breaker plies) added in the tread region. Belts restrict expansion of the body carcass in the circum-

ferential direction, strengthening and stabilizing the tread region (see Figure 1.1).

Advantages: Improved wear and handling due to added stiffness in the tread area.

Disadvantages: Body ply shear during deflection generates heat; higher material and manufacturing cost.

Radial tires

Radial tires have body ply cords that are laid radially from bead to bead, nominally at 90º to the centerline of the tread. Two or more belts are laid diagonally in the tread region to add strength and stability. Variations of this tire construction are used in modern passenger vehicle tire (see Figure 1.1).

Advantages: Radial body cords deflect more easily under load, thus they generate less heat, give lower rolling resistance and better high-speed performance. Increased tread stiffness from the belt significantly improves wear and handling.

Disadvantages: Complex construction increases material and manufacturing costs.

2.3 Industry standards

Sizing/dimensions
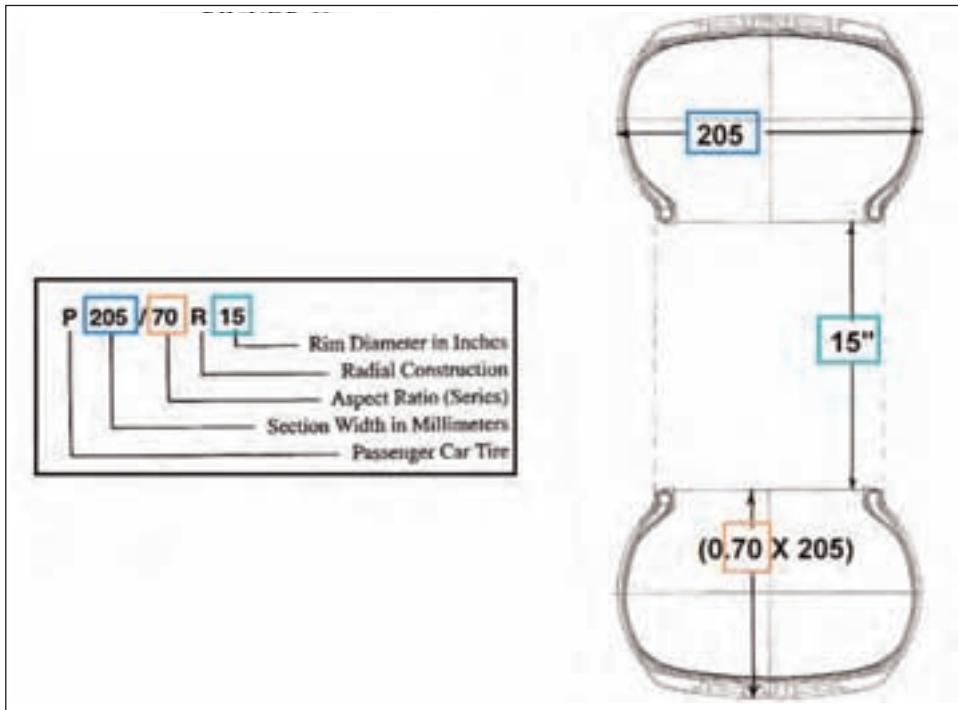
USA tire manufacturers participate voluntarily in an organization known as TRA, The Tire and Rim Association, Inc. It establishes and promulgates engineering standards for tires, rims, and allied parts (tubes, valves, etc.) Participation and adherence to these standards assures interchangeability of component parts among different tire manufacturers. "P-metric" sizing was introduced as radial tire usage began to expand in North America in the early 1970s . Size nomenclature can be described as follows (see Figure 1.2). For a P205/70R15 tire, the "P" indicates that it is for a "passenger" car ("T", temporary; "LT", light truck). (Note: European tire sizes typically do not utilize the P, T or LT symbols). The "205" is the nominal section width of the inflated, unloaded tire in millimeters. The "70" is the aspect ratio, or "series". It gives the tire section height as a percentage of the section width. Lower aspect ratio tires, e.g., 45, 50, 55 series tires, are primarily used in high performance applications but are becoming more popular in conjunction with large rim diameters for styling enhancements in larger vehicles. "R" identifies radial construction ("D" for diagonal or bias tires, "B" for belted bias construction). "15" is the rim diameter in inches. Other USA sizing designation systems have been used but will not be explained here, due to the prevalence of "P-metric sizing".

Load capacity

Tables of tire load ratings and load carrying capacity have been established by TRA. Their purpose is to maintain a rational basis for choosing tire size, load and inflation. Details will be covered in Chapter 5. TRA also coordinates its standards with other international organizations such as ETRTO (European Tyre & Rim Technical Organization) and JATMA (Japanese Automobile Tire Manufacturing Association). Note that ETRTO and JATMA sizes can have different load-carrying capacities than like-sized P-metric tires.

Load index and speed ratings (service description)

Most tires typically have a service description added following the size, e.g., P225/60R15 90H. The "90" refers to a load index that is related to its load carrying capacity, and may be used for interchangeability purposes. The "H" refers to the tire's speed rating, a code initiated in Europe and adopted by TRA. See Chapter 17 for details.

Figure 1.2: Size nomenclature

U.S. Government Regulations: DOT 109/110/139.
Since 1968, the U.S. Government's Department of Transportation (DOT) has had regulations for passenger tires, including testing and labeling, DOT 109, and tire selection for vehicle manufacturers, DOT 110. DOT 109 covers indoor test requirements, plus standards for tire labeling and serial number. The indoor tests include drum testing for high speed and endurance plus road hazard (plunger) and bead-unseat tests. The current regulations, DOT 139 and modified DOT 110, were changed in 2003 as a result of the TREAD Act of 2000. Details of the testing requirements are covered later in Chapter 16.

Uniform Tire Quality Grading (UTQG) was implemented by the U.S. Federal Government in 1979. It includes treadwear, traction and temperature grades that are applied to all passenger tires, with the exception of deep traction (i.e., winter/snow) tires and temporary spares. All grades are determined by tire manufacturers and are displayed (molded) on the tire sidewall, as well as tire labels at retail outlets.

The treadwear grade is based on actual wear test results. Tires are run for 7,200 miles on a 400 mile highway loop that originates in San Angelo, TX. The wear grade is determined by comparing the wear rate of the candidate tire to that of an industry-standard tire.

The traction grade is based on locked-wheel braking results on wet asphalt and wet concrete skid pads, also at San Angelo, TX. Again, the results are compared with those of an industry-standard control tire.

Temperature grades are based on speed capabilities from indoor drum tests similar to those described in DOT 109 and 139. Test specifics and grading procedures are covered in Chapter 17.

3. Tire components

3.1 Rubber compounds

Purpose

Beyond the visible tread and sidewall compounds, there are more than a dozen specially formulated compounds that are used in the interior of the tire. They will be discussed in Section 3.3: Tire components.

Basic ingredients

Polymers are the backbone of rubber compounds. They consist of natural or synthetic rubber. Properties of rubber and rubber compounds are described in more detail in chapter 2.

   Fillers reinforce rubber compounds. The most common filler is carbon black although other materials, such as silica, are used to give the compound unique properties.

   Softeners: Petroleum oils, pine tar, resins and waxes are all softeners that are used in compounds principally as processing aids and to improve tack or stickiness of unvulcanized compounds.

   Antidegradents: Waxes, antioxidants, and antiozonants are added to rubber compounds to help protect tires against deterioration by ozone, oxygen and heat .

   Curatives: During vulcanization or curing, the polymer chains become linked, transforming the viscous compounds into strong, elastic materials. Sulfur along with accelerators and activators help achieve the desired properties.

Material design property balance

Considering the many polymers, carbon blacks, silicas, oils, waxes and curatives, plus specialty materials such as colorants, adhesion promoters, and hardeners, the variety of compounds available seems endless. A typical car tire uses about 60 raw materials. However, the tire compounder quickly learns that adjusting one of the properties often affects other performance areas. The best tread compound for dry traction and handling might be lacking in wet/snow traction, chip/tear resistance, or fuel economy. Thus, compounds must be "engineered" or "balanced" to meet performance criteria for both the original equipment (OE) vehicle manufacturer and the aftermarket customer. . Adding to the complexity, the chosen compound must be cost-competitive and processable in manufacturing plants.

3.2 Reinforcement materials

Purpose

A tire's reinforcing materials — tire cord and bead wire — are the predominant load carrying members of the cord-rubber composite. They provide strength and stability to the sidewall and tread as well as contain the air pressure.

Type and common usage

Nylon type 6 and 6,6 tire cords are synthetic long chain polymers produced by continuous polymerization/spinning or melt spinning. The most common usage in radial passenger tires is as cap, or overlay ply, or belt edge cap strip material, with some limited applications as body plies.

   Advantages: Good heat resistance and strength; less sensitive to moisture.

   Disadvantages: Heat set occurs during cooling (flatspotting); long term service growth.

   Polyester tire cords are also synthetic, long chain polymers produced by continuous

polymerization/spinning or melt spinning. The most common usage is in radial body plies with some limited applications as belt plies.

Advantages: High strength with low shrinkage and low service growth; low heat set; low cost.

Disadvantages: Not as heat resistant as nylon or rayon.

Rayon is a body ply cord or belt reinforcement made from cellulose produced by wet spinning. It is often used in Europe and in some run-flat tires as body ply material.

Advantages: Stable dimensions; heat resistant; good handling characteristics.

Disadvantages: Expensive; more sensitive to moisture; environmental manufacturing issues.

Aramid is a synthetic, high tenacity organic fiber produced by solvent spinning. It is 2 to 3 times stronger than polyester and nylon. It can be used for belt or stabilizer ply material as a light weight alternative to steel cord.

Advantages: Very high strength and stiffness; heat resistant.

Disadvantages: Cost; processing constraints (difficult to cut).

Steel cord is carbon steel wire coated with brass that has been drawn, plated, twisted and wound into multiple-filament bundles. It is the principal belt ply material used in radial passenger tires.

Advantages: High belt strength and belt stiffness improves wear and handling.

Disadvantages: Requires special processing (see figure 1.16); more sensitive to moisture.

Bead wire is carbon steel wire coated with bronze that has been produced by drawing and plating. Filaments are wound into two hoops, one on each side of the tire, in various configurations that serve to anchor the inflated tire to the rim.

3.3 Radial tire components (see Figure 1.3)
Innerliner
The innerliner is a thin, specially formulated compound placed on the inner surface of tubeless tires to improve air retention by lowering permeation outwards through the tire.

Body ply skim
Body ply skim is the rubber coating that encapsulates the radial ply reinforcing cords. The skim is calendered onto the body ply cords in thin sheets, cut to width, and spliced end-to-end into a roll.
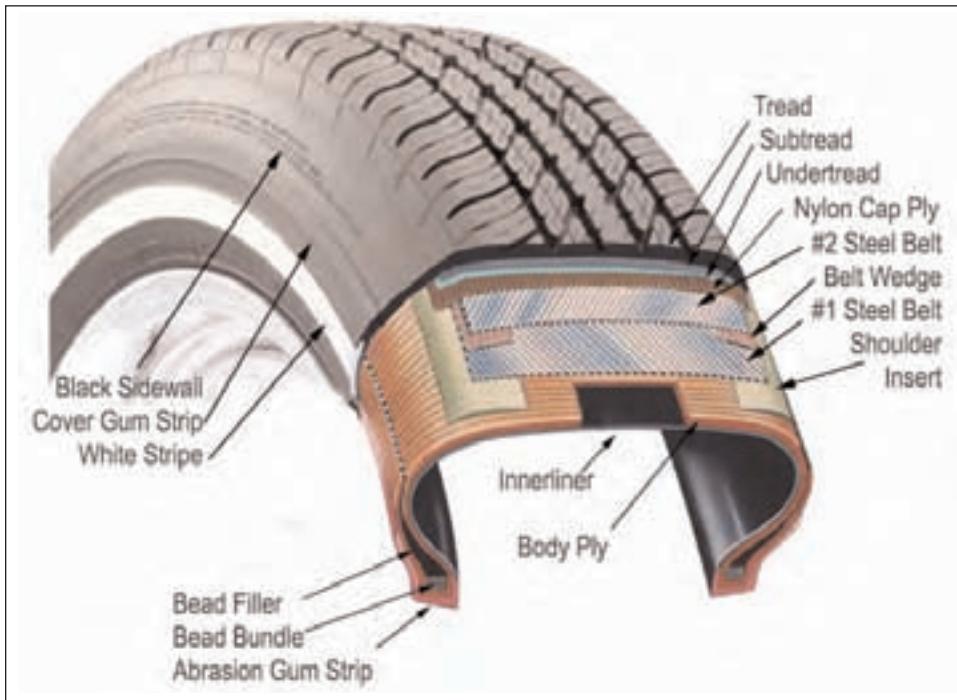
Body plies
Body plies of cord and rubber skim wrap around the bead wire bundle, pass radially across the tire and wrap around the bead bundle on the opposite side. They provide the strength to contain the air pressure and provide for sidewall impact resistance. The tire example shown has one body ply. In larger sizes, two body plies are typically used.

Bead bundles
Individual bronze plated bead wires are rubber coated and then wound into a bundle of specified diameter and configuration prior to tire assembly. The bead bundles serve to anchor the inflated tire to the wheel rim.

Figure 1.3: Components of a radial tire

Abrasion gum strip
Abrasion gum strips provide a layer of rubber between the body plies and the wheel rim for resistance against chafing. The airtight seal between the tire and rim must be maintained under all operating conditions. This component is also known as a gum chafer or gum toe guard.

Bead filler
Bead filler (also known as the apex) is applied on top of the bead bundles to fill the void between the inner body plies and the turned-up body ply ends on the outside. Varying the bead filler height and hardness affects tire ride and handling characteristics.

Sidewall
Tire sidewall rubber serves to protect the body plies from abrasion, impact and flex fatigue. The sidewalls also carry decorative treatments, sometimes including white or colored stripes or letters. The rubber compound is formulated to resist cracking due to environmental hazards such as ozone, oxygen, UV radiation and heat.

Sidewall reinforcements (not shown in figure 1.3)
Some tires feature lower sidewall reinforcements to improve handling or stability. These items are known as chippers, flippers or a floating reinforcement. Also, many run-flat constructions feature full sidewall thick rubber or other reinforcements to help support the load when the inflation pressure is low or zero.

Stabilizer ply skim (belt skim)
Belt skim is the rubber coating for the brass plated steel cords. The skim is calendered or extruded onto the steel cord in sheets, which are cut to width on an angle and then spliced into continuous rolls for tire assembly. Belt skim is primarily formulated to resist fatigue and tear.

Stabilizer plies (belts)
Two steel belts are applied at opposite angles to one another on top of the body plies, under the tread area. They restrict expansion of the body ply cords, stabilize the tread area and provide impact resistance. Varying the belt widths and belt angles affects vehicle ride and handling characteristics. Alternate belt constructions with materials other than steel, with three or more belts, or with woven materials have also been utilized.

Belt wedges
Small strips of belt skim or other fatigue resistant compounds are sometimes placed between the belts near the edge of the top (number 2) belt. The purpose is to reduce the interply shear at the belt edge as the tire rolls and deflects.

Shoulder inserts
Shoulder inserts are small, sometimes contoured strips of rubber placed on the body ply, under the belt ends. They help maintain a smooth belt contour and insulate the body plies from the belt edges.

Tread
The tread must provide the necessary grip or traction for driving, braking and cornering, and the tread compound is specially formulated to provide a balance between wear, traction, handling and rolling resistance.

   A pattern is molded into the tread during vulcanization or curing. It is designed to provide uniform wear, to channel water out of the footprint, and to minimize pattern noise on a variety of road surfaces.

   Both the tread compound and the tread design must perform effectively in a multitude of driving conditions, including wet, dry or snow covered surfaces, while also meeting customer expectations for acceptable wear resistance, low noise, and good ride quality. For driving in severe winter conditions, snow tires with increased tread depth and specially formulated tread compounds are recommended.

Subtread
The subtread, if used, is typically a lower hysteresis, cooler-running compound extruded under the tread compound to improve rolling resistance in order to meet the OE vehicle manufacturers' goals for fuel economy. It also can be used to fine-tune ride quality, noise, and handling.

Undertread
The undertread is a thin layer of rubber placed under the extruded tread/subtread package to boost adhesion of the tread to the stablilizer plies during tire assembly and to cover the ends of the cut belts.

Nylon cap plies/cap strips
Higher speed rated tires may feature a full-width nylon cap ply or plies, sometimes called an overlay, wrapped circumferentially on top of the stabilizer plies (belts) to further restrict expansion from centrifugal forces during high speed operation. Nylon cap strips are used in some constructions but cover only the belt edges.

3.4 Radial tire design process (see flowchart figure 1.4)
Identify goals/requirements
Before the tire engineer begins the design process, he must assemble a list of product goals, including customer performance expectations, manufacturing requirements, internal company performance standards and regulatory requirements. Targets or specifications for each of the tests discussed in Section 4 are typically identified. Performance targets reflect sales and marketing needs or OE vehicle manufacturers' requirements. Certain standards (e.g., government) are mandatory. Manufacturing plants usually have processing procedures that may restrict certain material and construction choices.

Tread pattern design
Figure 1.5 illustrates most of the tread pattern features used by design engineers. The number of ribs and groove spacing affect the way water is eliminated to avoid hydroplaning (refer to section 3.1). See thru, percent void, shoulder slot size and   orientation can all affect traction, handling and water exit paths. The number of pitches and pitch sequence as well as the placement of tie-bars and sipes can affect traction, noise, wear, and the tendency to wear non-uniformly. Figure 1.6 illustrates a noise treatment using different pitch lengths around the tire circumference to limit tone generation as the tire rotates. Additionally, tread designs need to be acceptable aesthetically and to match the customer's perception of product performance.

Mold contour features
Mold section width and outside diameter have an obvious impact on the dimensions of the vulcanized tire. But mold profile items like tread, center and shoulder radii and skid depth can also significantly affect tire performance. Vastly different footprint shapes are possible, as shown in figure 1.7, and can influence vehicle ride and handling, tire wear and traction.

Construction selection
Body ply denier, cord style, EPD (Ends Per Decimeter) or EPI (Ends Per Inch), and number of plies affect body strength and are chosen based on manufacturing, engineering, and design criteria. Likewise steel cord construction (style) and EPD both affect belt strength and are chosen typically based on tire size and application. Belt widths and belt crown angle (see figure 1.8) also influence tire performance. Different crown angles change the belt package stiffness, laterally and longitudinally, which can affect cornering ability and ride. Belt widths can also be varied. If a high speed rating is required, the addition of nylon cap strips at the belt edges or full-width nylon cap plies may be added. The bead and sidewall areas can also contribute to subtle performance enhancements. The bead filler volume and height, as well as the location of the end of the turned-up body ply (see figure 1.8) all impact sidewall stiffness.

Figure 1.4: Tire design flow chart

TIRE DESIGN PROCESS

IDENTIFY GOALS / REQUIREMENTS

PERFORMANCE TARGETS

MANUFACTURING REQUIREMENTS / PROCESSING RESTRICTIONS

INTERCHANGEABILITY STANDARDS T&RA, JATMA, ETRTO

FEDERAL STANDARDS

SELECT DESIGN FEATURES

TREAD PATTERN
No. Ribs
Groove Spacing
Void
See-Thru
Shoulder Slots
Tie Barring
No. Pitches
Sipes / Kerfs
Element Orientation
Noise Treatment

CONSTRUCTION
Body Ply Denier
Body Ply EPD
Body Ply Tie-In
Bead Filler Shape
Steelcord Type
Steelcord EPD
Belt Crown Angle
Belt Width
Belt Reinforcement

MATERIALS
Tread Compound
Subtread Compound
Bead Filler Compound
Sidewall Compound

MOLD CONTOUR
Skid Depth
O.D.
Section Width
Tread Arc Width
Shoulder Radius
Footprint Ratio
Max. Section Pt.

DESIGN FEATURES SELECTED

CONFIRM EXPECTED PERF W/ COMPUTER MODELING

EXPERIMENTAL MOLD MANUFACTURED

EXPERIMENTAL TIRES MANUFACTURED

PERFORMANCE VERIFICATION

OUTDOOR (VEHICLE) TESTING

TECHNICAL TESTING

INDOOR (DRUM) TESTING

MODELING

Figure 1.5: Tread pattern design
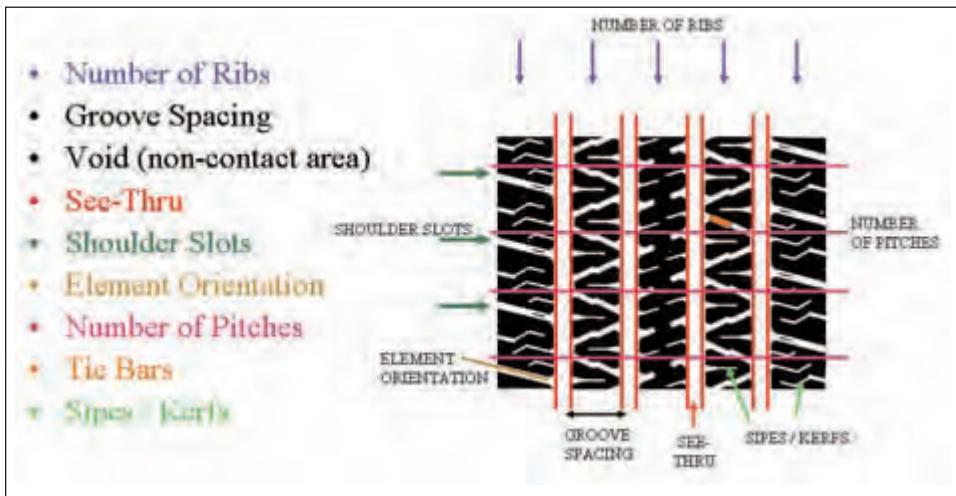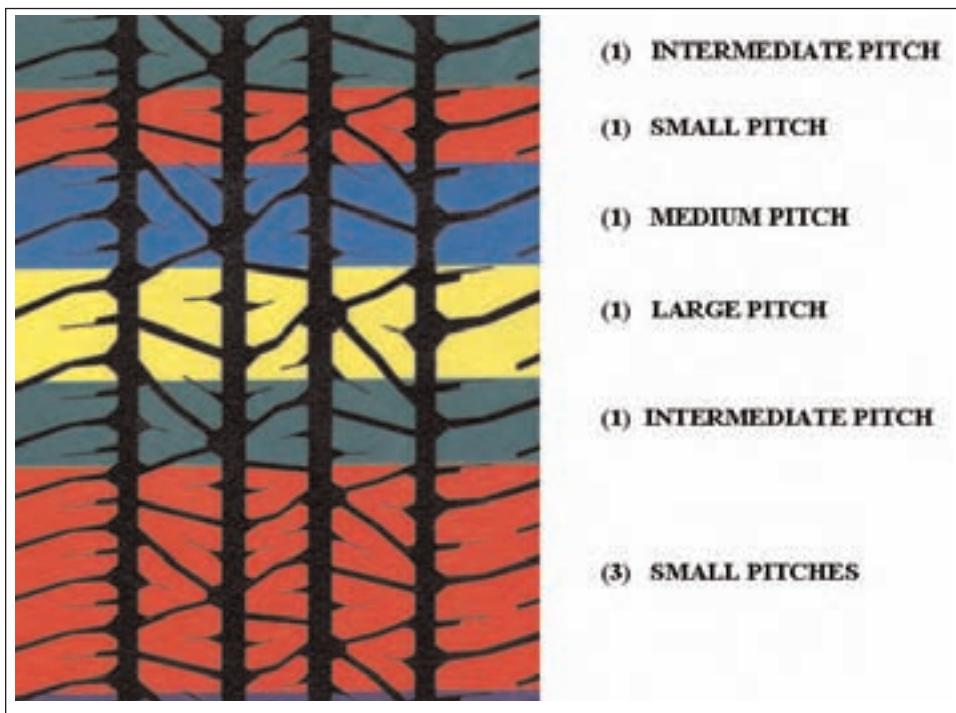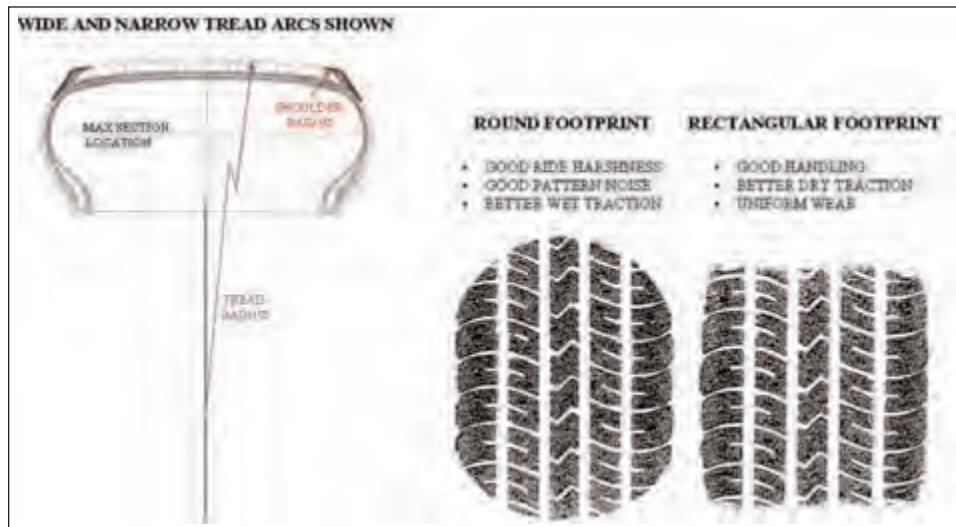
Figure 1.6: Noise treatment

Materials selection
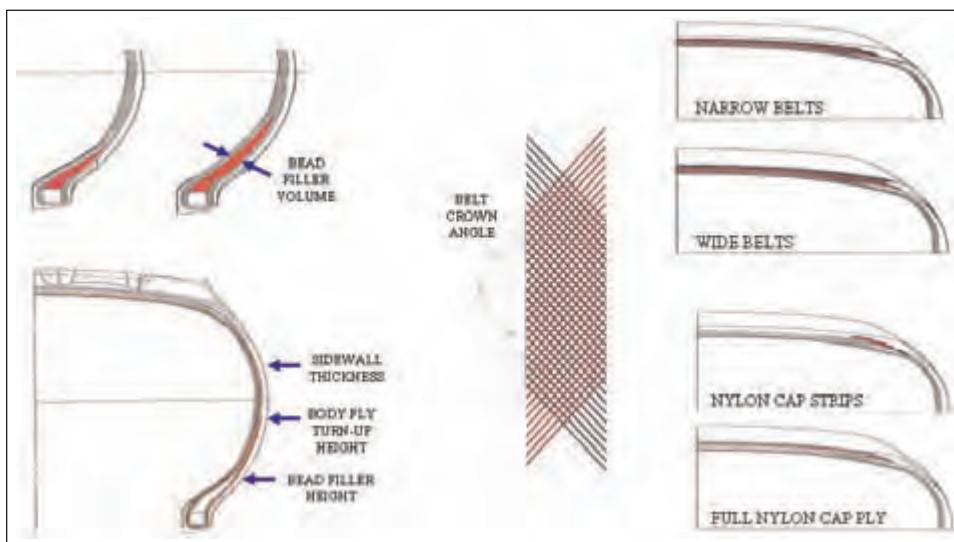
Tread compounds are chosen to meet handling and traction requirements for wet, dry and snow (if necessary), but must have suitable wear potential and resistance to gravel chips and tearing. Subtread compounds and thickness are often determined by the rolling

Figure 1.7: Mold contour effects

resistance requirement imposed by the OE vehicle manufacturer. Bead filler compounds are chosen for controlling lower sidewall stiffness, based on ride and handling expectations. Sidewall compounds are chosen to resist environmental effects (weathering) and damage from impacts and abrasion, but they also affect the rolling resistance.
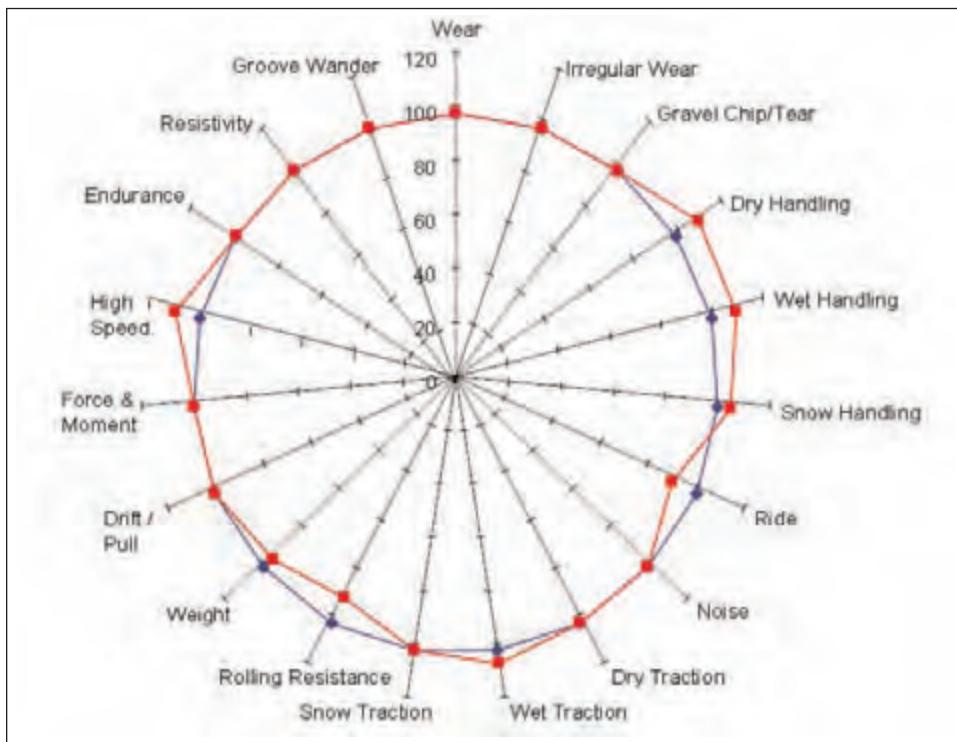
Design/construction performance balance
While specific performance parameters follow in Section 4, many environments and performance categories must be satisfied. Beginning with size, load capacity, speed rating, body and belt materials, compounds, tread designs and construction variations, how do we choose? Obviously, industry-wide guidelines exist (TRA, DOT, ETRTO, etc.),

Figure 1.8: Construction variables

and guidelines and standards have been developed by individual tire manufacturers as well. They serve as a starting point. In addition to experience, tire engineers use   computer models and performance maps to help guide their selections and predict if   performance targets will be met. Using an iterative process of design, construction and material choices, the engineer can reach a balance of compromises for each application. Figure 1.9 illustrates the impact of just one component change, wider belts, on selected tire performance parameters. In this so-called "spider diagram" a higher rating (outside the circle) indicates improved performance. Handling and wet traction are improved but ride, rolling resistance and weight have suffered. If the customer desires the handling improvements but is unwilling to accept the loss in ride quality and higher rolling resistance, the tire engineer must look at other factors to balance the overall performance. This dilemma is what drives new tire technology in design, materials and construction.

Figure 1.9: Effect of increased belt width

4. Tire performance criteria
4.1 Outdoor (vehicle) tests
Wear rate
Traditionally with an outdoor test, sets of tires are driven at prescribed speeds on a known course to evaluate wear rate, usually measured in miles of travel per thousandth of an inch of tread depth loss (i.e., miles per mil) or as tread loss per mileage increment (i.e., mils/1000 mi). Control of vehicle alignment, loads, and acceleration/deceleration rates are all critical to obtaining repeatable results. Comparison tests are usually conducted using
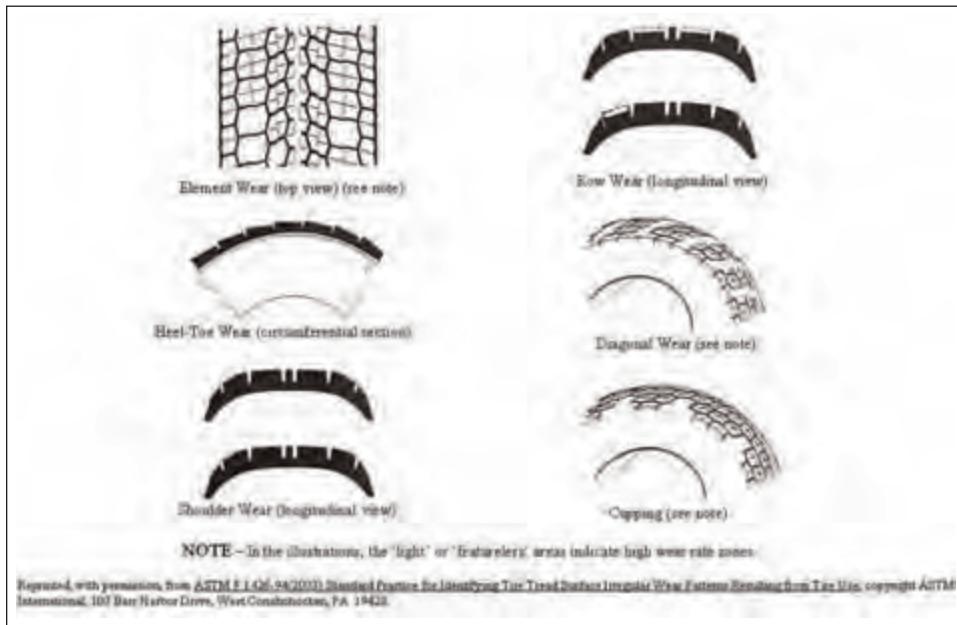
vehicle convoys to negate environmental factors, differences in road surfaces, or other variables.

Irregular wear

Abnormal wear features, such as heel and toe, cupping, or shoulder wear (see figure 1.10) can significantly shorten the service life or mileage potential of tires. While tread design and tire construction are influential, many external factors such as vehicle mis-alignment, vehicle suspension geometry and driving factors such as high speed cornering, rapid acceleration or braking and underinflation of tires play significant roles in promoting irregular wear patterns. Consumers who regularly check tire inflation pressure and maintain a schedule for rotating tire positions and checking vehicle alignment will maximize tire mileage.

Figure 1.10: Types of irregular wear

Gravel chip/tear

Some tread compounds and tire designs can be sensitive to chipping and tearing of tread elements during off-road or gravel road applications. Many outdoor wear and durability tests include a small percentage of gravel roads to assure that this performance is acceptable.

Handling: dry, wet and snow

Handling is a result of tire/vehicle interactions in response to various driver inputs. Handling tests are used by tire engineers and OE vehicle engineers as part of their approval process. Tires are evaluated for their response, stability, recovery linearity, on-center-feel, brake in turning, and other characteristics. Tests range from lane change maneuvers to maximum cornering capability. Also, closed course test tracks with a variety of curves can be used to compare lap times with experimental tire constructions.

Most test facilities can run the same test in both wet and dry conditions. Snow tests are conducted at special facilities where the snow can be groomed and compacted to make a consistent surface.

Ride comfort

A vehicle's perceived ride comfort, whether "sporty" or "plush," can be significantly influenced by tires. Engineers' evaluations go far beyond expectations of shake-free and vibration-free ride on smooth highways. Tires are evaluated for impact harshness over highway joints and railroad tracks, and for damping and bounce memory after road disturbances. They are also graded for plushness (road isolation), nibble (steering wheel oscillations), shake, vibration and other vehicle-specific features. Most tire manufacturers have test facilities with dedicated lanes specifically designed for consistent evaluation of tire and vehicle combinations by professional ride evaluators. Ride is one of the compromises encountered in designing tires. For instance, wider belts may improve vehicle handling but can contribute to increased ride impact harshness.

Noise

Significant time and effort goes into designing tire tread patterns and constructions to minimize noise. Patterns have tread elements of varying pitch lengths to prevent tires from generating identifiable tones. Multiple pitch lengths, typically 3 to 7 (see Figure 1.6), are assembled in a computer-generated pattern around the tire circumference to dispel any constant frequency noise as the tire rotates. Professional tire evaluators, using prepared test areas, are able to sense not only airborne pattern noise but also structure-borne noise as well. Structure-borne tire noise is transmitted through the tire carcass, the wheel and suspension, sometimes aggravating resonances in a vehicle component. Evaluators rate coarse road noise transmitted through the tire from textured highway surfaces. They listen for growl, a low frequency noise noticed during low speed braking, and sizzle, a hissing sound on ultra-smooth surfaces. These and other noise conditions add to the tire engineers design dilemma. Increasing tread thickness and softening the bead filler reduces coarse road noise but increases rolling resistance and affects ride and handling.

Rain groove wander

Many states, particularly California, grind longitudinal grooves into concrete highways to minimize hydroplaning during rain storms in high traffic areas. If the grooves on the highway line up with tire tread design grooves, side-to-side vehicle motions can occur, making drivers uncomfortable. Tire engineers must change tread pattern groove spacing or reduce the number of ribs in smaller tires to minimize this phenomenon.

Drift/pull

A vehicle with drift/pull has a tendency to pull right or left while driving on a straight, flat, level highway with minimal wind. Tires can contribute to this condition but vehicle alignments and suspension geometry are also key factors. Drivers find the constant steering correction annoying.

Endurance

Outdoor testing for tire endurance usually involves loading a vehicle to the maximum specified load and inflation, or more, and driving on a closed road course at a specified

schedule of speeds. With a three shift per day operation, and measurement/ inspection/maintenance delays, it takes approximately 45 working days to accumulate 40,000 mi. Each tire company has its own proprietary test protocol.

4.2 Indoor (drum tests)
High speed
Indoor laboratory tests are typically run on 1.708 m (67.23") diameter drums (300 rev/mile) that have been an industry standard for decades. Ambient temperatures of 38°C (100°F) are typical. Most industry high speed tire tests utilize the SAE J1561 standard which calls for 80% of the maximum load and speed increases of 10 km/hr in 10 minute increments until the specified speed is achieved, or tire failure occurs. Tests start at speeds four steps below the desired speed rating. Inflation pressure varies by tire type and speed rating, e.g., 260 kPa (38 psi) for a standard load passenger "S" rated tire. This reduced load is an adjustment to give an equivalent tire deflection on the drum's curved surface to that expected on a flat highway surface. DOT 109 and 139 and UTQG temperature grade tests require speed increases at 30 minute intervals, for tires inflated to 220 kPa (32 psi) and carrying 85% of maximum load. (See Chapter 17).
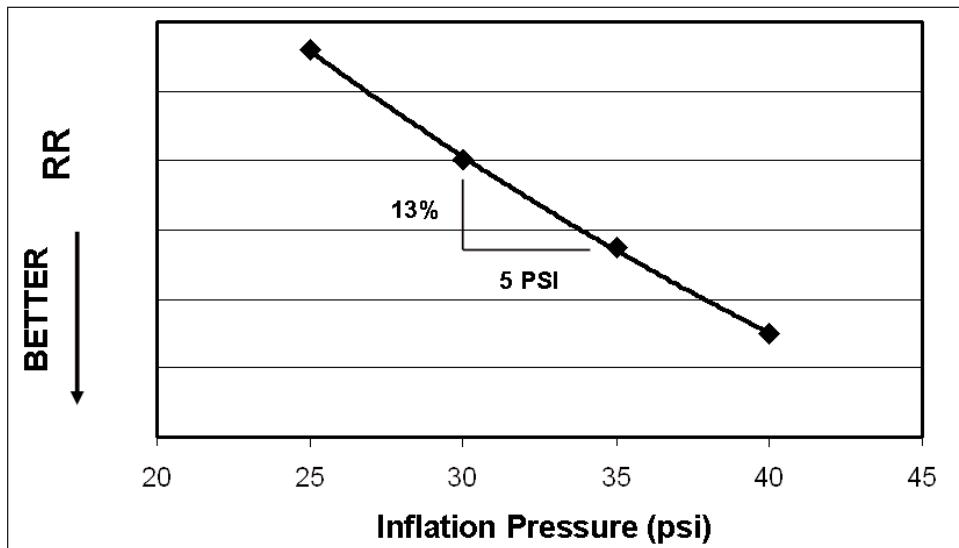
Endurance
In high speed testing, load is constant and speed is varied. In most indoor drum endurance tests, the speed is constant and load is varied. Tests similar to DOT 109 and the new DOT 139 are as follows. The ambient temperature remains at 38°C. Pressure for a P-metric standard load passenger radial is 180 kPa (26 psi) with a constant speed of 80 km/hr (50 mi/hr) for DOT 109 type tests. New DOT 139 regulations require 120 km/hr (75 mi/hr) testing, becoming mandatory in June 2007. The test load begins at 85% of maximum load for 4 hours and then becomes 90% for 6 hours and finally 100% for 24 hours. Tires completing the initial 34 hour test must also complete an additional new DOT 139 low pressure step at 140 kpa (20 psi) for an additional 90 minutes at the 100% load condition. (See Chapter 17).

Rolling resistance
The force necessary to overcome hysteretic losses in a rolling tire is known as rolling resistance. This parameter became important to USA vehicle manufacturers with implementation of C.A.F.E. (Corporate Average Fuel Economy) standards for new cars. It is measured by placing load cells in the wheel spindle and measuring the rolling resistance force in the horizontal (longitudinal) direction. It requires precise instrumentation, calibration, speed control and equipment alignment for repeatable results. Rolling resistance is usually expressed as a coefficient: resistance force per 1000 units of load. OE passenger car tires designed for fuel efficiency may have coefficients in the range 0.007 to 0.010 when fully inflated and evaluates at thermal equilibrium (see chap. 12). The test load, speed and inflation pressure vary according to the vehicle manufacturers' requirements. Rolling resistance is significantly influenced by inflation pressure, as illustrated in Figure 1.11. Since tire rolling resistance can consume up to 25% of the energy required to drive at highway speeds, it is economically wise to keep tires inflated properly.

Figure 1.11: Rolling resistance vs. inflation

4.3 Technical tests
Weight
OE vehicle manufacturers often specify tire weight targets as part of their requirements for meeting C.A.F.E. goals.

Force and moment properties
A tire's cornering capability comes from the forces generated when a tire's direction of motion is different from its heading direction, causing a slip angle. Measurement equipment and interpretation of results are complex and dealt with in detail in Chapter 8. In the most general case, three forces and three moments are resolved in the tire contact patch or at the wheel axle.

Resistivity
Moving vehicles can generate static electricity which is aggravated by low temperature and humidity. While rubber is usually thought to be an insulator, it is partially conductive, and tire compounds influence the rate of static discharge. Test fixtures in humidity and temperature-controlled laboratories are used to measure tire resistivity.

Uniformity
Due to material and assembly variations that occur during manufacturing and curing, small deviations in tire cross section circumferentially can result in measurable spring rate or dimensional changes, for example, an out-of-round condition. Tire Uniformity Grading machines are used to measure the variations that occur around the circumference of the tire. Inflated tires are loaded against an instrumented rotating drum. The radial and lateral force variations measured are compared to acceptance standards for smooth, vibration-free ride.

Flat spotting
Some tires, when parked, can develop a temporary "set" in the rubber compounds and reinforcement cords, referred to as a "flat spot". To test for this condition, tires are warmed up or exercised at high speed, measured for uniformity and then loaded statically against a flat plate for a prescribed time (usually days). Tires are then retested for uniformity, exercised and the recovery time observed for the flat spot to disappear.

Traction: dry, wet and snow
Specially equipped instrumented trailers with computer-controlled braking capability are towed over known skid pad surfaces. Brakes are applied gradually to cause wheel lock-up and peak and slide friction forces are recorded. Wet traction is conducted on the same surfaces with water being metered to the front of the tire as a way of controlling water depth. Snow traction is determined using special trucks for measuring driving traction at constant slip over groomed, compacted snow surfaces.

Air permeation
Innerliner compounds are formulated to minimize permeation of air through the tire carcass. The permeation rate depends on the compound properties and gauge (thickness) as well as the temperature and inflation pressure. Long term tests, taking months, require regulated temperatures and leak-free tire mounting and test plumbing. Typical passenger car tires lose approximately 1 psi per month due to air permeation.

4.4 Industry/government standards
Dimensions
Tires, mounted and inflated on an appropriate wheel, are scanned by a laser profiler. Section width, diameter and size factor (sum of diameter and section) must be within T/RA guidelines.

High speed
DOT 139 requires testing conditions as described in Section 4.2. Tires must complete the 160 km/hr (100 mi/hr) step without failure to be in compliance.

Endurance
DOT 139 requires completion of all three steps at 120 km/hr (75 mi/hr) as described in Section 4.2. All tires must complete the endurance portion, plus a 90-minute low inflation pressure step, without failure to be in compliance.

Bead unseat
DOT 139 requires that tires retain air pressure and beads remain seated on the wheel in a test where an anvil is pressed against the tire sidewall. Wheel, tire inflation and anvil location are specified by rim diameter and tire type. Potential revisions to this test are under study.

Road hazard (plunger)
DOT 139 requires that tires withstand a slow-moving plunger placed in the center area of the tread and forced into the tire. The plunger travel at the peak load is recorded, reached when either the tire ruptures or the plunger bottoms-out against the rim, and the peak

energy is calculated. Minimum energy requirements without tire rupture occurring must be met at multiple locations around the tire circumference to be in compliance. Research continues to determine if new or revised test procedures are needed to accommodate new, lower aspect ratio tire sizes.

Uniform tire quality grades
As a USA Federal requirement, Uniform Tire Quality Grades must be established and displayed within six months of start of production for new tire lines. Grading categories are covered in Section 2.3.
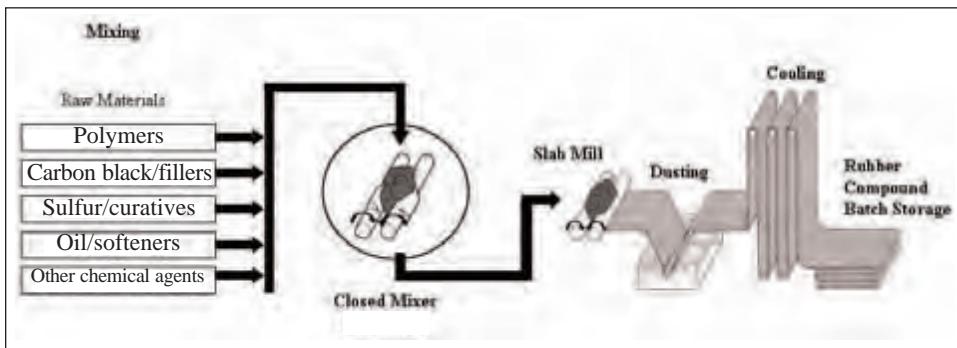
5. Tire manufacturing
5.1 Compound preparation (see Figure 1.12)
Raw materials
Approved vendors supply the basic ingredients including polymers, fillers (carbon black and/or silica), softeners and antidegredants. Lab tests are run to sample, code and release the materials for use in production.

Figure 1.12: Tire manufacturing - Rubber compound preparation

Mixing
The appropriate blend of polymers, fillers, oils and pigments for a specific compound formula are combined in a closed mixer in batches of 180 kg (400 lbs) to 500 kg (1100 lbs). Batch temperatures are closely controlled, as are mixing power, cycle time and rotor speed, in accordance with the compound specification. Each batch is flattened into slabs or extruded and cut into pellets (not shown in figure 1.12) for storage and later blending with other batches or materials.

Blend/feed mills
Large, closely spaced, water-cooled rollers squeeze and knead a bank of compounds to blend mixed batches and to warm up compounds prior to extrusion or calendering.

5.2 Component preparation
Calendering
Similar in appearance to rubber blending and feeding mills, calenders press rubber compounds between two or more rotating rolls to form thin, flat sheets of rubber to specified gauges. Control systems can regulate the sheet thickness to within 0.001". The
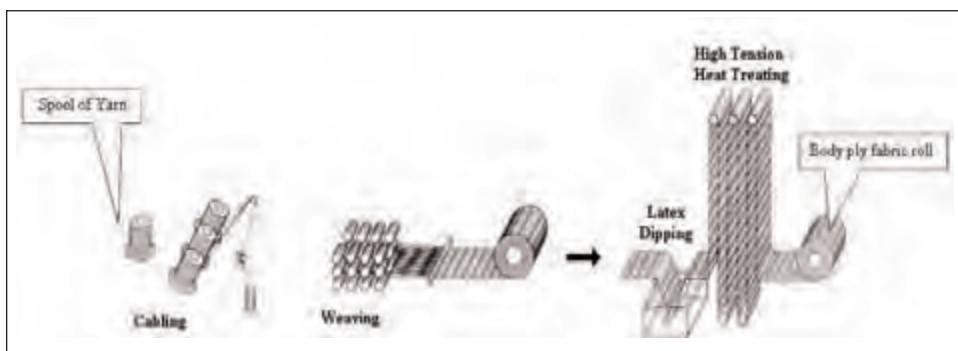
sheets are used in tire assembly for inner-liner, gum strips, or belt wedges, or in preparing body ply or stabilizer ply material.

Body plies

In textile reinforcements of nylon, polyester, rayon, aramid, etc., individual filaments are twisted and cabled together to form cords. The cords are woven , with pick cords to maintain spacing, into a wide sheet of fabric prior to dipping in a latex adhesive to enhance bonding to rubber, followed by a high-tension heat treatment (see Figure 1.13). Body ply fabric is prepared in rolls approximately 57 inches wide by 3,000 yards long having the appropriate denier (cord style) and EPD (ends per decimeter). The fabric is then passed through a four-roll calender (see Figure 1.14) where a thin sheet of rubber (body ply skim) is pressed onto both sides and squeezed between the cords of the fabric. The calendered fabric is wound into 350-yard rolls, with a polypropylene liner inserted to keep the fabric from sticking to itself, and then sent to a stock-cutting process.

Figure 1.13: Textile cord manufacturing process

Body ply stock cutting and splicing (see figure 1.14)

The individual cords are aligned longitudinally in the calendered roll but they need to go across, not around, the radial tire carcass. Therefore the calendered fabric is cut into pieces, rotated 90° and spliced back together, so that cords go across the roll. The result is a continuous roll of body ply material at a specified width for the appropriate tire size- and construction.
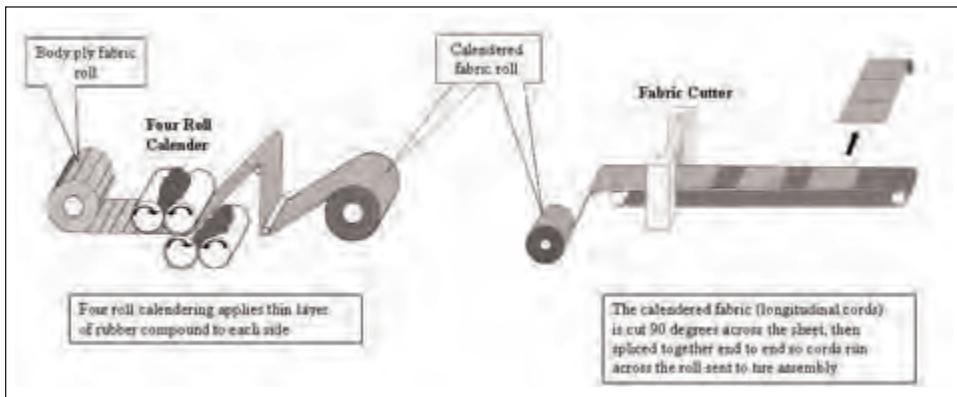
Stabilizer ply (belt) calendering (see figure 1.15)

Unlike woven body ply material, steel cord, already brass plated and twisted, is purchased from vendors as individual cords wound onto spools. To make a sheet of belt material, hundreds of spools are located in a low humidity, temperature controlled creel room. The cords from the spools pass through rolling guides to give the appropriate EPD (Ends Per Decimeter) and move directly into a four-roll calender that presses a thin sheet of belt skim rubber onto and between the individual cords. The calendered steel-cord sheet is then wound between polypropylene liners for later processing. [Another processing arrangement extrudes rubber onto the steel cord and forms smaller sheets.]

Stabilizer ply (belt) cutting and splicing (see figure 1.15)

The steel cords run longitudinally in the calendered roll. For use as stabilizer ply, the steel

Figure 1.14: Tire manufacturing - body ply preparation
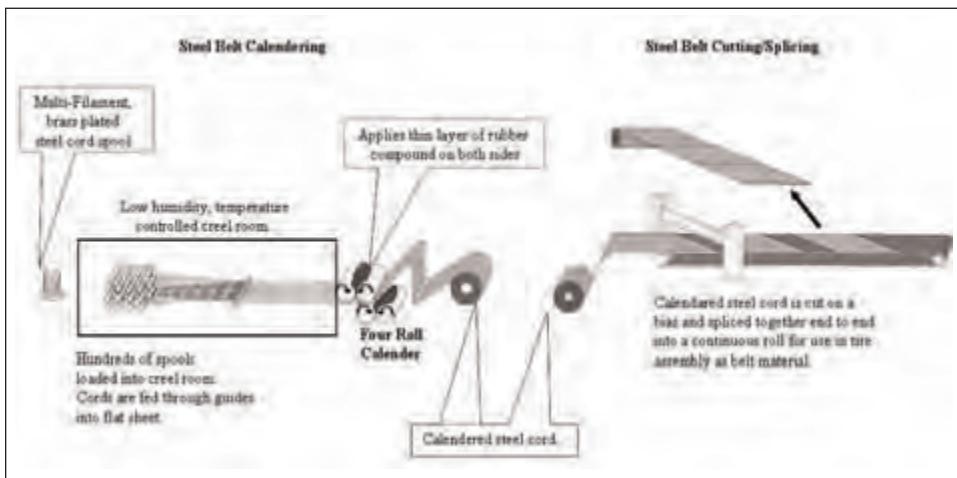
cord sheet is cut, rotated, and spliced together again to form a continuous strip of a specified width, with the cords at a specified angle. Since the number 1 and number 2 belts have different widths and opposite angles, they must be prepared accordingly.

Nylon cap ply calendering
Like body ply material, nylon cap ply fabric is purchased in large rolls and cap skim is applied via a calender. Unlike body ply, it is not necessary to cut, rotate, and splice since the cords are intended to be longitudinal in the tire. The calendered sheet is slit into the required width per specification.

Figure 1.15: Tire manufacturing - steel stabilizer ply preparation
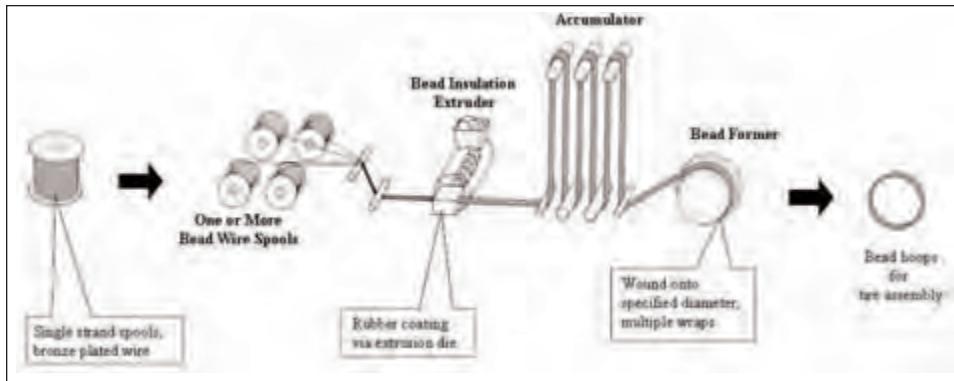
Bead bundle preparation (see figure 1.16)
Bead wire is bronze plated. Single-strand wire is purchased on spools and coated with rubber using an extrusion die. Depending on the bead configuration used, single strands (programmed shape) or multiple strands (box style) are wound onto a chuck to the specified diameter and shape. Sometimes the bead bundle is wrapped with rubber-coated fabric to facilitate tire assembly. Specified bead filler material can be pre-assembled onto

the bundle for tire building efficiency. Some tire manufacturers use a cable bead that features a solid core with several bead wires cabled around it. This requires a different manufacturing process than that shown in figure 1.16.
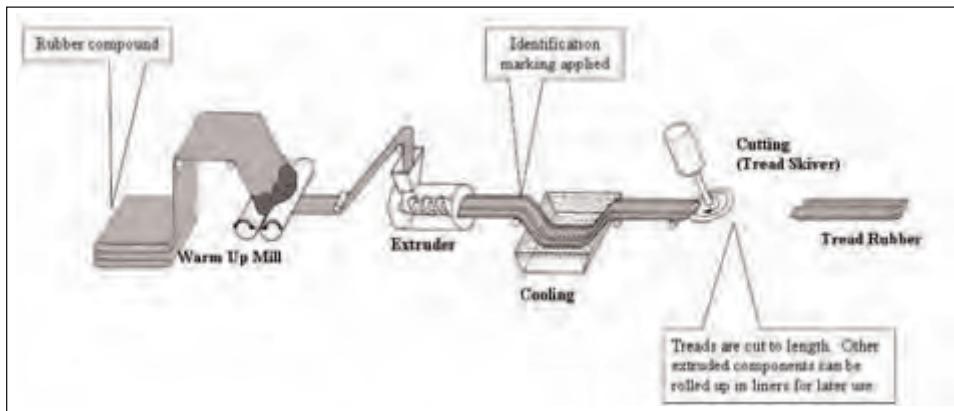
Figure 1.16: Tire manufacturing - bead bundle preparation

Extrusion (see figure 1.17)

Rubber components (e.g. treads and sidewalls) are shaped by forcing rubber through a die opening of appropriate shape. The rubber compound is carried to the die through a feeder tube or barrel containing an auger-like screw. Up to four barrels may feed a single die, allowing co-extrusion of different compounds into a single component, e.g. tread and sub-tread with sidewall wings. Die shape, compound properties, and extrusion speed control the dimensions and shape of the extrudate. Extruded pieces are marked with color coded stripes and lettering for identification and quality control purposes.

Figure 1.17: Tire manufacturing - extrusion process
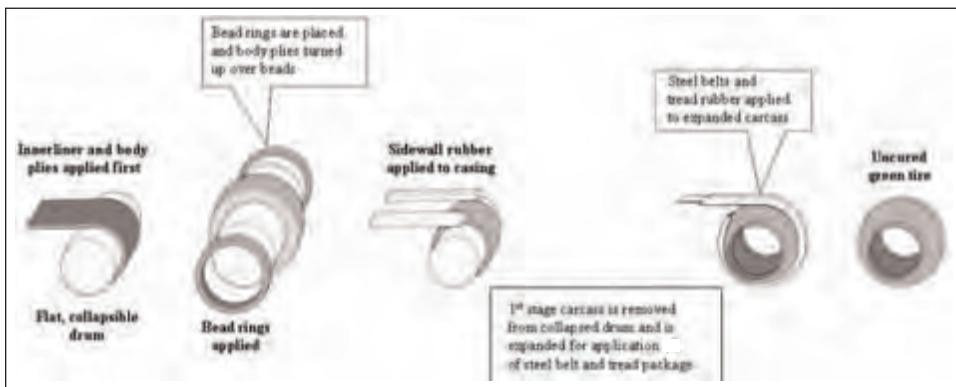
5.3 Tire assembly (see figure 1.18)

Carcass (body ply)

Radial tires are often built in two stages. In the first stage, the body carcass is assembled on a rotating, collapsible drum that is slightly larger than the bead diameter. The innerliner and body plies are applied first and rolled down over the edges of the drum. Then the beads and bead filler are set in place and the body ply(s) are turned-up over the

beads and rolled or stitched to adhere to the body ply lying flat on the drum. Strips of sidewall compound are then placed on top of the turned-up ply on both edges. The drum is then collapsed so the completed body carcass can be removed and taken to the second stage machine.

Figure 1.18: Tire manufacturing - radial tire assembly

Belt and tread assembly
The belts and tread are assembled on another rotating drum, to a diameter that is close to that of the final tire as possible, while allowing for clearance when the tire is inserted in the mold for curing. If required by the specified speed rating, full width nylon cap ply(s) or cap strips are wound over the belts before the extruded tread/subtread/undertread package is applied.

Green tire assembly
The second-stage equipment takes the first-stage body carcass and expands it into the larger belt-and-tread assembly. The finished "green" (i.e., uncured) tire is then rotated against tread area stitching wheels to adhere all of the components uniformly to the body carcass. The "green" tire is then stored on a rack for transfer to the curing room.

Several tire manufacturers and equipment vendors have devised automated tire assembly equipment that combines several assembly steps or links them into a continuous process. Substantial productivity gains are gained with high volume production. However, loss of production flexibility and the impact of equipment breakdowns or maintenance stoppages may create scheduling challenges.

5.4 Curing (see figure 1.19)
Curing press
While there are different types available, most curing presses are massive devices (3.6 m wide x 2.8 m deep x 4 m high, weighing 20,450 kg). They hold two tire molds that resemble two open clamshells side-by-side. They have water, air, vacuum and steam lines attached, plus conveyors, and have automatic loading devices for placing the green tires over curing bladders in the center of each mold.
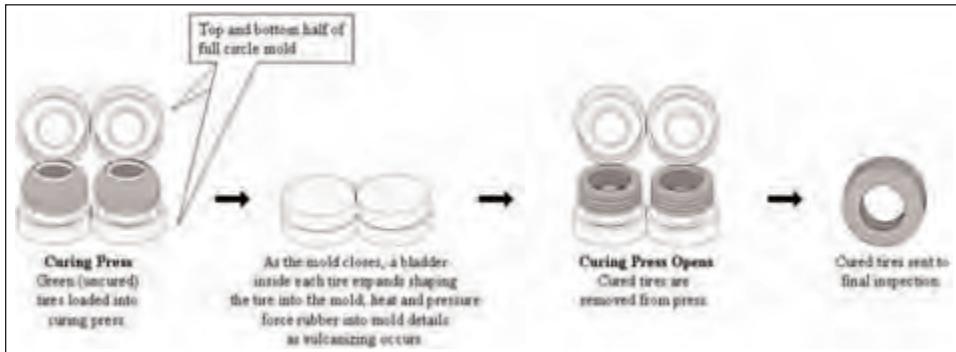
Full circle/segmented molds
There are two types of tire mold; full circle and segmented. Historically, full circle molds were developed for bias tires. The mold is divided into two circular pieces that join around

Figure 1.19: Tire manufacturing - curing (vulcanizing) process

the diameter of the tire, most often in the middle of the center rib. The two mold halves are attached to the top and bottom of the curing press and the green tire is inserted between them. As the press closes, bringing the two halves together, the green tire is expanded by inflating an internal rubber bladder that forces the outside of the green tire to conform to the inner surface of the mold. After curing is completed, the mold parts separate and the tire is removed. Note that the tread must deform to some degree as the mold opens, which can be more difficult for some tire profiles, compounds, and tread designs.

Segmented molds are more complicated but are preferred for certain radial tires. This is because the green tire diameter can more closely approach the mold diameter, minimizing expansion of the belt. The tread region of the mold typically consists of 8 or 9 radially-divided pieces or segments that come together as the mold closes. They must fit together precisely, both radially and with the top and bottom sidewall plates, when the mold is completely closed. The advantage of segmented molds is that less expansion is required of the green tire to fill the mold and the segments pull directly away from the tire after curing. This is an important feature in manufacturing low-profile tires and tires that use some tread compounds designed for low rolling resistance.

Curing (vulcanization)
As the mold closes, a bladder inside the tire expands and presses the green tire against the mold. The high bladder pressure (several hundred psi) forces the uncured rubber into every detail of the inner surface of the mold. Super-heated steam or hot water is then circulated within the bladder and around the mold for about 12 to 15 minutes. This rise in temperature causes a chemical reaction (curing, or vulcanization) to occur in the rubber compounds whereby the long polymer molecules become crosslinked together by sulfur or other curatives. The rubber compounds are transformed in this way into strong, elastic materials in the finished, cured tire. Curing times, temperatures and pressure are computer-controlled to give full cure of the chosen rubber compounds.

5.5 Final inspection
Vent trimming
To prevent air from being trapped in the tread pattern, tiny vents are drilled through the mold in the corners of tread elements. In a complex tread design, there can be thousands of such vents. Uncured rubber flows into the vent holes and is cured there, giving the final tread a "hairy" appearance. The rubber threads are trimmed off in a final inspection by

sharp knives held flat against the rotating tire.

Visual inspection
All tires are inspected visually for any imperfections (e.g., plugged vents or trapped air) before being transferred to a warehouse. If a minor imperfection cannot be buffed away or repaired, the tire is scrapped.

Uniformity grading
Most passenger tires are screened for uniformity (Section 4.3) against limits established by the OE vehicle manufacturer and/or the tire manufacturer. The test includes laser or probe inspection of the sidewalls and tread.

White stripe or white letter grinding
White or colored pigment compounds are sometimes applied to the sidewall. During building and curing they are covered with a protective thin film of a non-staining black compound. After curing, the raised sidewall is rotated against fine grinding wheels to expose a crisp, attractive stripe or letter. This process is often done in combination with uniformity grading.

5.6 Quality control testing
Production release
All tire manufacturing facilities run production qualification tests to assure compliance with performance requirements. Industry and government standards must be met, as well as any technical and indoor tests required by the customer as described in Section 4. While some of the tests are both time consuming and destructive, they must be completed successfully before volume production can begin.

Statistical sampling
Once in production, QA (Quality Assurance) protocols utilize statistical process control and sampling methods to assure that production tires remain in compliance with their original quality and performance standards.

6. Consumer care
6.1 Maintain proper inflation
By law, every vehicle sold in the United States has a placard that identifies the tire size(s) and the inflation pressures recommended for front, rear, and spare tires by the OE vehicle manufacturer. Beginning in the 2006 model year, the placard is to be located on the driver's door B-pillar. The location on older vehicles varies, sometimes being on the driver's door, the trunk lid, a door pillar or the glove box. In addition, the maximum load and inflation information is stamped on the sidewall of every tire, usually in the bead area just above the rim.

   Tire pressures should be checked regularly. Radial passenger tires can be underinflated by 12 psi or more and still look normal. As explained in Section 4.3, air permeates through tires slowly, so that they typically lose about 1 psi per month, and even more in hot climates. Moreover, a small puncture from an imbedded nail or screw can cause a tire to be significantly underinflated. Underinflation contributes to rapid and uneven tread wear, a loss in fuel economy, poor vehicle handling and excessive heat buildup which may lead

to tire failure. It is recommended that tire pressures be checked at least monthly and before long trips or when additional passengers and luggage are carried. Pressures should be checked when the tires are cold, i.e., when the vehicle has not been driven for several hours, and using an accurate gauge. It should be noted that every 10°F drop in ambient temperature results in about one psi drop in tire inflation pressure. It is also recommended that tire valve assemblies be replaced when a new tire is installed.

6.2 Avoid overload

The vehicle tire loading information placard also specifies GVWR (Gross Vehicle Weight Rating) plus front and rear GAWR (Gross Axle Weight Rating). Exceeding these loads affects vehicle handling, steering and braking but also has an impact on tire life. Overloading increases the deflection and flexing of tires, which can generate excessive amounts of heat within the tire and may lead to failure. See Chapter 15 for more detail.

6.3 Regular rotation/alignment checks

Uniform tire wear prolongs the useful life or mileage potential of tires. Rotating tires between positions on the vehicle on a regular schedule minimizes uneven wear. Tires should be rotated every 6,000 to 8,000 miles, or sooner if signs of uneven wear appear. For new tires, the first rotation is the most important as the tread elements are most flexible at full depth. Rotation patterns vary, and some tires with asymmetric tread designs are uni-directional (see Direction of Rotation Arrows on Upper Sidewall). Consult the vehicle owner's manual or local tire dealer for specific recommendations.

Wheel mis-alignment, can cause uneven tire wear. While it is often considered to be an issue only with the front, steering wheels, alignment of an independent rear suspension is also important. Computerized alignment equipment can check all positions, including the rear to front relationship (i.e., thrust angle). Maintaining proper wheel alignment, regular rotation of tires, and proper inflation pressures will maximize tire service life.

Acknowledgement

Bibliography

1. D. Beach and J. Schroeder, "An Overview of Tire Technology", Rubber World, **222 (6)**, 44-53 (2000).
2. T. French, *Tyre Technology*, Hilger, New York, 1989.
3. F. J. Kovac and M. B. Rodgers, "Tire Engineering", in *Science and Technology of Rubber*, 2nd Ed., ed. by J. E. Mark, B. Erman and F. R. Eirich, Academic Press, New York, 1994, pp. 675-718.
4. G.F. Morton and G.B. Quinton, "Manufacturing Techniques", in *Rubber Technology and Manufacturing*, 2nd Ed., ed. by C.M. Blow and C. Hepburn, Butterworth, London, 1982, pp. 405-431.

Chapter 2
Mechanical Properties of Rubber

by A. N. Gent

Chapter 2
Mechanical Properties of Rubber

by A. N. Gent

1. Elasticity and visco-elasticity

1.1 Rubbery, crystalline and glassy states

Rubber is a fascinating material, with unique properties that make it an essential component of a pneumatic tire: it is soft, elastic, resistant to cutting and scraping, with a high coefficient of friction and low permeability to gases. We consider here what molecular features give rise to this remarkable combination of properties and how they affect tire performance.

All rubbery materials consist of long chain-like polymer molecules. The original elastomeric material (raw rubber) is basically a highly-viscous liquid but it can show elasticity because the long molecules are held together, at least temporarily, by being intertwined and entangled. The basic reaction in rubber processing is the joining of long molecules together by a few chemical bonds (crosslinks) to form a loose three-dimensional permanent molecular network. The shape becomes fixed and the material is transformed from a high-viscosity liquid into an elastic solid.

This joining reaction is often termed "curing", because the material is no longer a viscous sticky liquid, or "vulcanization" because it is usually carried out with reagents that introduce sulfur crosslinks between the molecules.

The cure curve for a representative practical rubber compound (compound C in Table 2.1), is shown in figure 2.1. A sample of the prepared mix of elastomer, filler, curatives and protective agents is placed in an Oscillating Die Rheometer (ODR) or Moving Die Rheometer (MDR) where the thin rubber layer is sandwiched between the heated stationary wall of the test chamber and a rigid cylindrical die. The die is made to execute small amplitude and low frequency oscillatory rotations, subjecting the rubber layer to oscillatory shear strains. The torque required to maintain the motion is monitored continuously. As the rubber compound becomes increasingly crosslinked and changes from a viscous liquid to a rubbery solid, the torque amplitude increases, reflecting the increasing torsional stiffness of the sample. A practical measure of a characteristic cure time is the time at which the torque reaches 90% of its maximum value, denoted t_{90}. For the mix formulation used here, t_{90} is about 10 min at 160°C. We now describe the elasticity of *unfilled* rubber vulcanizates before turning to the behavior of practical compounds (see Table 2.1) that contain large amounts of particulate filler. It should be noted in passing that the presence of filler can affect the rate of cure significantly by influencing the chemistry of crosslinking. For example, carbon black tends to increase the rate of cure by a factor of up to 3, and reduces t_{90} correspondingly.

The molecular segments in raw rubber and the molecular strands between crosslinks in cured rubber are in rapid thermal motion at normal temperatures. On deforming the molecular network, the strands take up new average positions that are less probable than their original ones. Changes in bond energies or conformational energies are relatively

**Table 2.1: Some representative tire compounds
(amounts given in parts by weight per 100 parts of elastomer).**

	A Passenger tire tread	B Sidewall	C Steel belt compound
Elastomers			
Natural rubber	-	50	100
Styrene-butadiene copolymer (25/75)	75	-	-
Cis-polybutadiene	25	50	-
Fillers			
Fine carbon black (e.g., N220)	75	-	-
Medium carbon black (e.g., N330)	-	-	60
Coarse carbon black (e.g., N660)	-	50	-
Vulcanization agents			
Zinc oxide	3	3	10
Stearic acid	3	1	1.2
Sulfur	1.55	2	5.5
Vulcanization accelerator (sulfenamide type)	1.9	1	0.5
Secondary accelerator (guanidine)	0.25		
Processing aid			
Processing oil	10	10	-
Protective additives			
Antioxidant/antiozonant	1.5	3.5	1
Resin and adhesion promoter			
Resin components	-	-	8
Adhesion promoter (e.g.cobalt naphthenate)	-	-	2

Vulcanized for 10-15 minutes in a tire mold at a temperature of 170-175°C
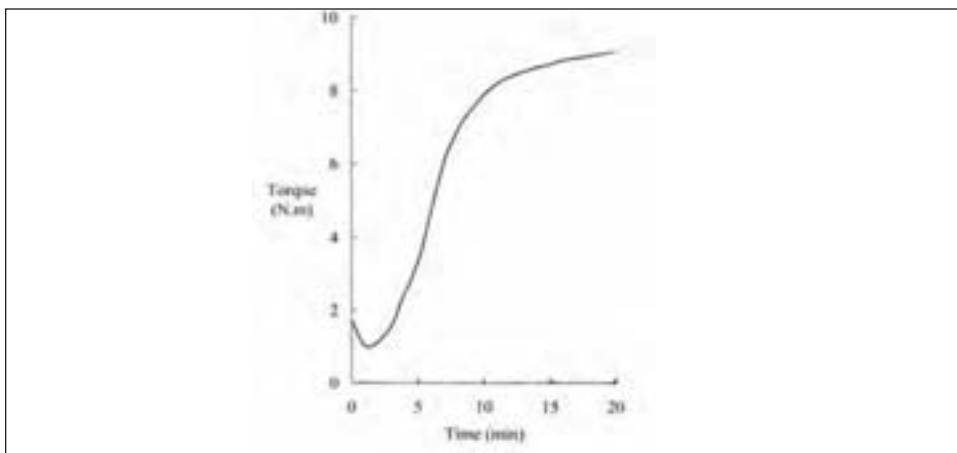
small - only the *entropy* of the network is reduced. Thus, rubber is an entropic spring - it returns to the undeformed state only because that is the most probable one. As a result, the stiffness of rubber *increases* with temperature T because the contribution ΔS of entropy to the free energy of deformation is given by the product: $- T\Delta S$. This characteristic feature of rubber is in marked contrast to the behavior of springy crystalline materials, like metals, where the stiffness decreases with rising temperature because, on deforming metals, the atoms are forced out of an ordered state into a more random arrangement, with lower bond energies and higher entropy.

An approximate statistical calculation gives the tensile modulus E (Young's modulus) of elasticity for an unfilled rubber vulcanizate under small tensile strains as

$$E = 3NkT \tag{1.1}$$

where N is the number of molecular strands comprising the network, k is Boltzmann's constant and T is absolute temperature. A typical value for N is about $1.5 \times 10^{26}/m^3$. Thus a typical value for E is about 2 MPa, i.e., about four orders of magnitude smaller than for metals, reflecting the ease with which the shapes of long flexible molecules can be rearranged.

Figure 2.1: Cure curve for compound C at 160ºC

The average network strand consists of about 100 repeat units (mers) of a particular chemical group, typically with a molecular weight of around 60. Some repeat units in rubbery materials commonly used in tires are:

$-C_4H_6-$: cis-1,4 polybutadiene

$-C_5H_8-$: natural rubber (cis-1,4-polyisoprene)

$-CH_2C_3H_6-$: butyl rubber

$(-CH_2-C_7H_{12}-)_n-(-C_4H_6-)_m$: SBR (a copolymer of styrene, n units, and butadiene, m units)

But why are only relatively few polymers rubbery? There are two main reasons why a polymeric solid might not exhibit rubberlike elasticity. When the long molecules are highly regular and able to pack closely together, they tend to arrange themselves in this way under the weak van der Waals attractive forces that are present in all materials – they spontaneously *crystallize*. For example the commercial plastic – polyethylene - is as much as 60% crystalline at room temperature and shows little elasticity. Instead, it behaves as a typical crystalline solid. Initially rather stiff, after the material is deformed by a few percent the crystallites begin to yield and the deformation then becomes ductile and plastic, rather than elastic.

The other reason why polymeric materials may fail to show rubbery behavior is that the chemical repeat units are relatively heavy and bulky, so that thermal energy at normal temperatures is not sufficient for molecular segments to move freely. Polymers in this state are termed *glassy solids*. Typical examples are polystyrene and polymethylmethacrylate that are glasslike at temperatures below about 100^OC.

On raising the temperature, crystals melt and immobile molecules acquire more energy, so that both crystalline and glassy polymers become rubbery at sufficiently high temperatures, for example, above 150^OC for polyethylene and above 100^OC for polystyrene and polymethylmethacrylate. And all rubbery polymers turn into glassy solids at a characteristic low temperature, even if they have not spontaneously crystallized as they are cooled down. The transition temperature (glass temperature, T_g) is one of the most important characteristics of a polymer and, as shown later, it controls the mechanical behavior at temperatures far above the actual glass temperature. Values of T_g for selected rubbery polymers are given in Table 2.2.

Table 2.2: Glass temperatures T_g (^{0}C) for some common elastomers.

Elastomer	T_g
Polydimethylsiloxane (silicone rubber)	-125
Cis-1,4-polybutadiene	-100
Cis-1,4 polyisoprene (natural rubber)	-72
Poly(isobutylene-co-isoprene) (butyl rubber)	-70
Poly(styrene-co-butadiene) 25/75 (SBR, emulsion)	-60
Poly(ethylene-co-propylene) 56/44 (EPR)	-55
Plus ca 5% diene comonomer, (EPDM)	-55
Polychloroprene (Neoprene)	-50
Poly(butadiene-co-acrylonitrile) 85/15 to 65/35 (Nitrile rubber)	-40 to -10
Poly(styrene-co-butadiene) 50/50 (High-styrene SBR)	-25

The other important physical feature of a rubbery solid is the average length of the molecular strands comprising the network, generally denoted by the molecular weight M_c. The original molecules have molecular weights in the range 100,000 to 500,000, not higher than this because very high molecular weight materials are difficult to extrude and shape. After crosslinking, the molecular weight M_c of the network strands ranges from about 5,000 to 20,000 molecular weight units. Although this number may, in principle, be varied widely by introducing more or fewer crosslinks, in practice if M_c is small then the material is stiff and brittle and if M_c is large then some of the original long molecules are not tied into the network completely, and contribute little or nothing to stiffness and strength. Nevertheless, the practical range of crosslinking and hence of elastic modulus E is from about 1 MPa to about 3 MPa, a greater range (a factor of 3) than for any other structural solid. And by adding particulate fillers, the modulus can be raised still further without serious loss in strength - indeed, often with a pronounced gain in strength, termed reinforcement (see later).

1.2 Elastic behavior
The elastic modulus of a rubber compound is often characterized by its resistance to indentation by a blunt indentor. The amount of indentation is indicated on a non-linear scale, from 0 to 100 International Rubber Hardness Degrees (IRHD), corresponding to values of modulus E ranging from zero to infinity. Values of IRHD and E covering the practical range of rubber modulus are given in Table 2.3. Outside this range the materials are either extremely soft and weak or hard and relatively inflexible.

Rubber can often be treated as virtually incompressible in bulk because the modulus of bulk compression is quite high, about 2 GPa, comparable to that of liquids such as water, and much higher than the tensile modulus E, typically about 2 to 5 MPa. Consequently, the elastic shear modulus G is approximately equal to E/3, and Poisson's ratio is close to one-half, about 0.499. [Definitions of the various elastic coefficients are shown in figure 2.2.]

**Table 2.3: Relation between International Rubber Hardness
Degrees (IRHD) and elastic (Young) modulus E.**

IRHD	E(MPa)
30	1.0
35	1.2
40	1.5
45	1.9
50	2.3
55	2.9
60	3.6
65	4.5
70	5.5
75	7.5
80	9.5
85	15

Note that when a solid rubber block is "compressed", its volume does not decrease significantly unless the pressures are extremely high. Instead, the block compresses vertically and expands laterally - the volume remains virtually unchanged. Compression of a block bonded between two plates is sketched in figure 2.3. Due to the restraint on lateral expansion, the effective modulus E_e can be quite high.

Rubber molecules move freely because the intermolecular forces are low. The expansion in volume on heating is correspondingly high, similar to that for simple liquids. The linear thermal expansion coefficient α for unfilled rubber compounds ranges from about 1.5 to 2 x 10^{-4}/^{O}C. Due to the low thermal expansion coefficients of filler particles, values of α for typical filled compounds are somewhat lower, 1.2 to 1.5 x 10^{-4}/^{O}C, but still far higher than for metals, about 50 times greater. Thus, when a rubber article is removed from the metal mold in which it has been shaped and crosslinked at a high temperature (typically about 160^OC) and then allowed to cool down to ambient temperature, it shrinks in linear dimensions by about 2%.

1.2.1 Elastic behavior at large strains

Because rubber is highly extensible, small-strain elasticity theory using moduli E and G is inadequate to describe the response to large strains. Instead, a useful measure of response is the mechanical energy W stored in unit volume by a deformation. A simple relation for W for an initially-isotropic, incompressible elastic solid is:

$$W = (E/6) J_1 \tag{1.2}$$

where J_1 describes the deformation in terms of stretch ratios λ_1, λ_2, λ_3 in the principal directions, see figure 2.4:

$$J_1 = (\lambda_1^2 + \lambda_2^2 + \lambda_3^2 - 3) \tag{1.3}$$

(Note: $\lambda_1 = 1 + e_1$, etc., where e_1 is the strain in the 1 direction.) Because rubber is virtually incompressible, the product $\lambda_1\lambda_2\lambda_3 = 1$. Equation 1.2 is termed the neo-Hookean constitutive law because it reduces to Hookean (linear) elasticity, figure 2.2, in the limiting case of small strains and gives reasonably accurate predictions at moderately large strains.
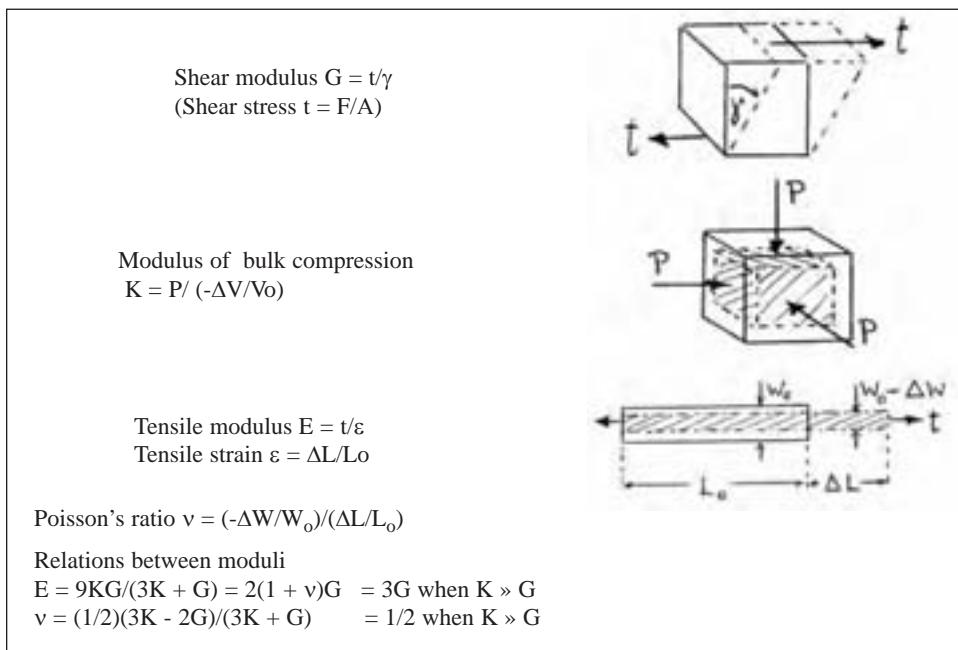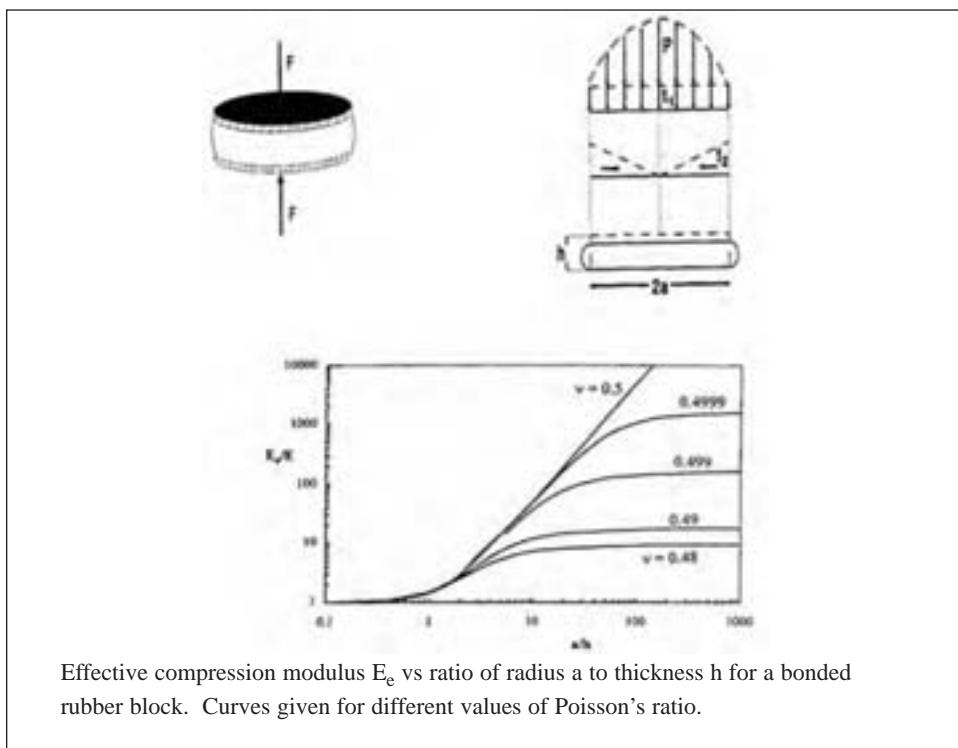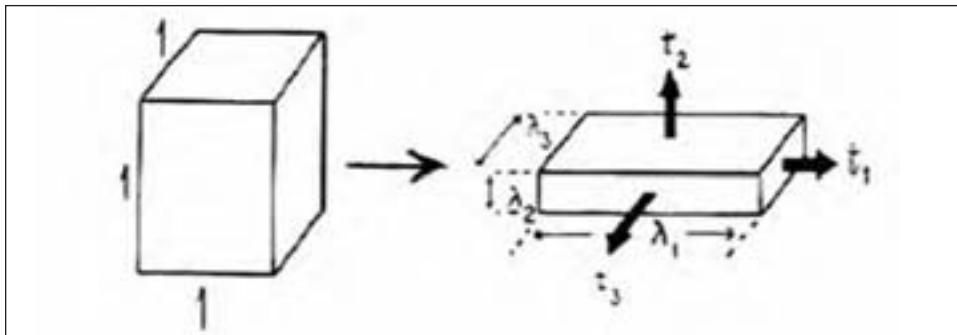
Figure 2.2: Elastic coefficients (moduli) for small strains

Shear modulus $G = t/\gamma$
(Shear stress $t = F/A$)

Modulus of bulk compression
$K = P/(-\Delta V/Vo)$

Tensile modulus $E = t/\varepsilon$
Tensile strain $\varepsilon = \Delta L/Lo$

Poisson's ratio $\nu = (-\Delta W/W_o)/(\Delta L/L_o)$

Relations between moduli
$E = 9KG/(3K + G) = 2(1 + \nu)G = 3G$ when $K \gg G$
$\nu = (1/2)(3K - 2G)/(3K + G) = 1/2$ when $K \gg G$

Figure 2.3: Compression of a bonded rubber block

Effective compression modulus E_e vs ratio of radius a to thickness h for a bonded rubber block. Curves given for different values of Poisson's ratio.

Figure 2.4: Stretch ratios λ and stresses t

Figure 2.5: Relations between strain energy W and stresses t

Using the simplifying assumption that deformations are accompanied by no change in volume, stress-strain relations can be deduced from W by considering a hypothetical change in extension $\delta\lambda_1$ causing a corresponding change δW in W (figure 2.5):

$$\delta W = (\lambda_2\,\lambda_3)\,t_1\,\delta\lambda_1 \tag{1.4}$$

Thus,

$$t_1 = \lambda_1\,(dW/d\lambda_1) + P \tag{1.5}$$

where P is an undefined pressure that must be included because, for incompressible materials, a hydrostatic pressure can do no work. The appropriate value to assign to P is determined by establishing a base-line for stress in any particular case. In simple tension, for example, the side stresses t_2 and t_3 are zero and P is therefore given by $[t_1 - \lambda_1(dW/d\lambda_1)]$.

The stress t_1 is the force acting in direction 1 on a unit of cross-sectional area, where the area is measured in the deformed state. It has unfortunately become common practice in the rubber industry to use the word *stress* to denote the force σ acting on a unit of *undeformed* cross-sectional area, because this is a more easily measured quantity. To

distinguish between the two usages, σ is sometimes termed *engineering stress*. For an incompressible material, like most rubbery solids, the imposition of a stretch ratio λ leads to a contraction in cross-sectional area by a factor $1/\lambda$ and thus there is a simple relation between the two measures of stress (see figure 2.5):

$$\sigma = t/\lambda \qquad (1.6)$$

In rubber technology, the term "modulus" is often used to describe the tensile force per unit of unstrained cross-sectional area at a stipulated tensile strain. For example, M_{100} denotes the stress σ when e = 100%. Values for M_{100}, M_{200}, M_{300}, etc., are often reported also - they give an indication of the shape of the stress-strain curve, see figure 2.6.

The stress-strain relation in simple extension is obtained from Equation 1.5 as:

$$t = (E/3)\,(\lambda_1{}^2 - 1/\lambda_1) \qquad (1.7)$$

This is the large-deformation equivalent of the result: t = Ee, applicable at small strains. Experimental stress-strain relations for soft rubber compounds are found to be in reasonable agreement with equation 1.7 up to moderately large extensions, about 300%.

Note that stress-strain relations for rubber are usually *non-linear*, figures 2.7 - 2.9. Equation 1.7, for example, predicts that the tensile stress-strain relation, after the expected linear region at small strains, will be concave with respect to the strain axis, as is observed. At higher strains a pronounced stiffening occurs as the molecular strands approach the fully-stretched state, figure 2.8. Thus, non-linearity does not indicate that internal yielding or fracture has occurred. Instead, it follows directly from a consideration of the elastic behavior of a network of long molecular chains, each of which is linearly-elastic over a wide range of extension but because they are randomly arranged in space, the combined effect is usually non-linear.

There is one outstanding exception to the general non-linear character of rubberlike elasticity, however, and that is a simple shear deformation. Using equation 1.5 the calculated stress-strain relation in simple shear is *linear*, and rubber compounds are found to be approximately linear in shear up to moderately large strains, 100% or more, with a slope (shear elastic modulus G) of E/3.

Many constitutive laws have been proposed to model the elastic behavior of rubber more accurately than the simple neo-Hookean form for W given in Equation 1.2, for example by taking into account the stiffening observed at high strains, Figures 2.6 and 2.8. This feature is not predicted by Equation 1.2. It can be modeled by introducing a maximum possible value J_m for the deformation term J_1. Thus one modified version of Equation 1.2 is the logarithmic form:

$$W = - (EJ_m/6)\,\ln\,(1 - J_1/J_m) \qquad (1.8)$$

which reduces to equation 1.2 when the deformations are small compared to J_m, but gives increasingly large values for W and thus for stresses when the deformation approaches its maximum possible value J_m.

However, rubber compounds currently used in tires are seriously inelastic, as described below, and attempting to describe their elastic properties with great precision is probably unwarranted. Examples of typical tire formulations are given in Table 2.1. They illustrate the complexity that results when compromises must be made to meet demanding but often conflicting requirements: stiffness, strength, resilience, good traction, wear resistance, durability, etc.

Figure 2.6: Experimental relation between tensile stress and elongation
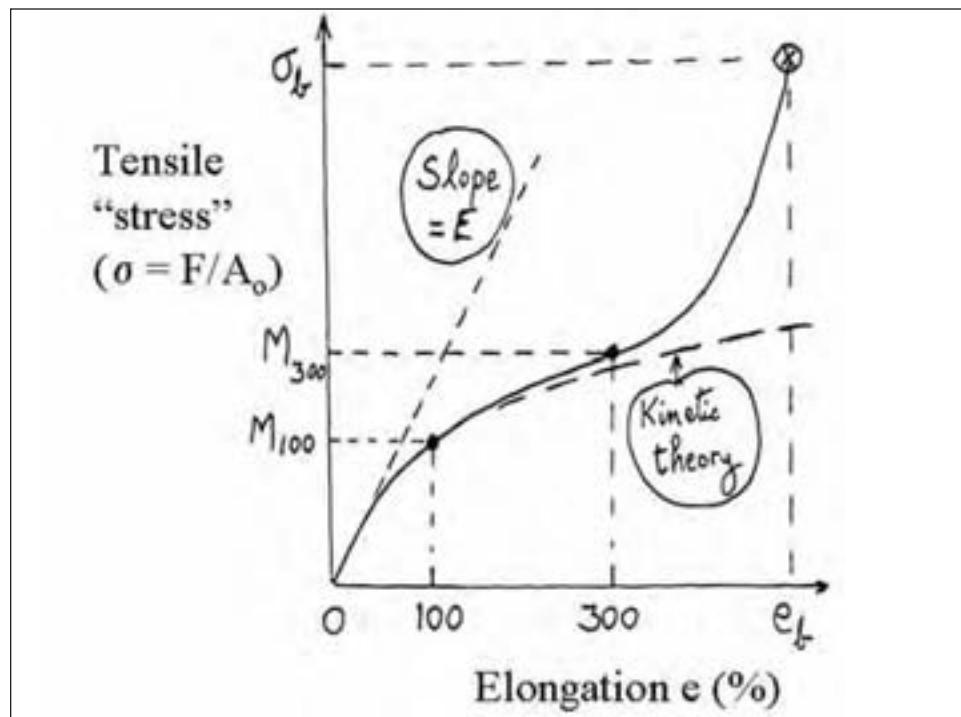
Figure 2.7: Stress-strain relation in tension
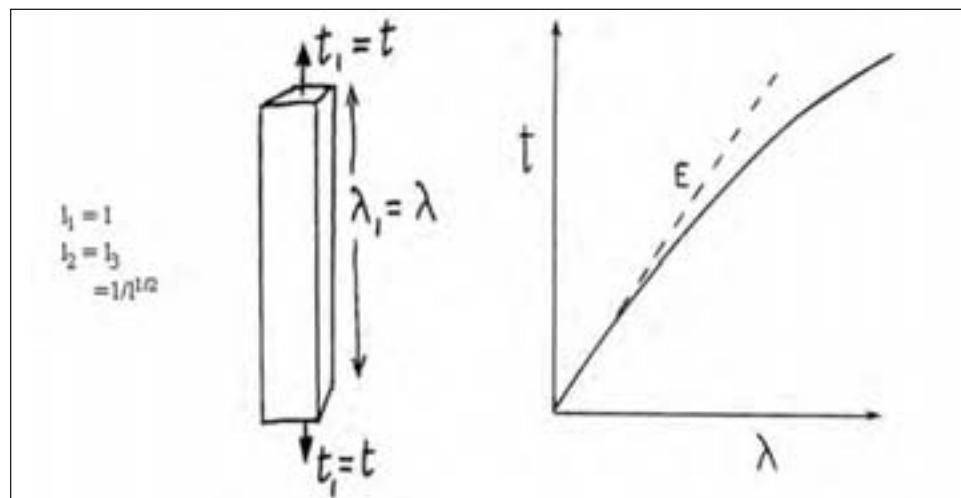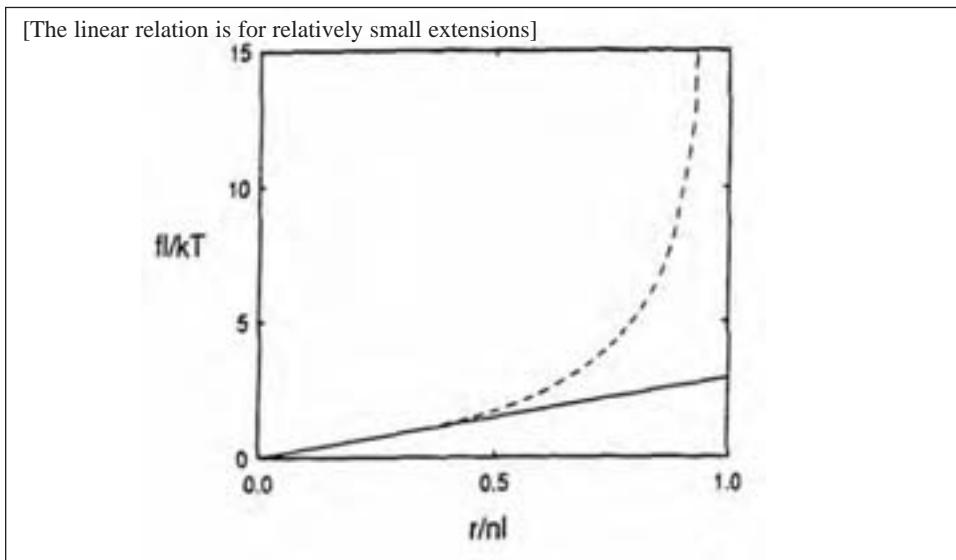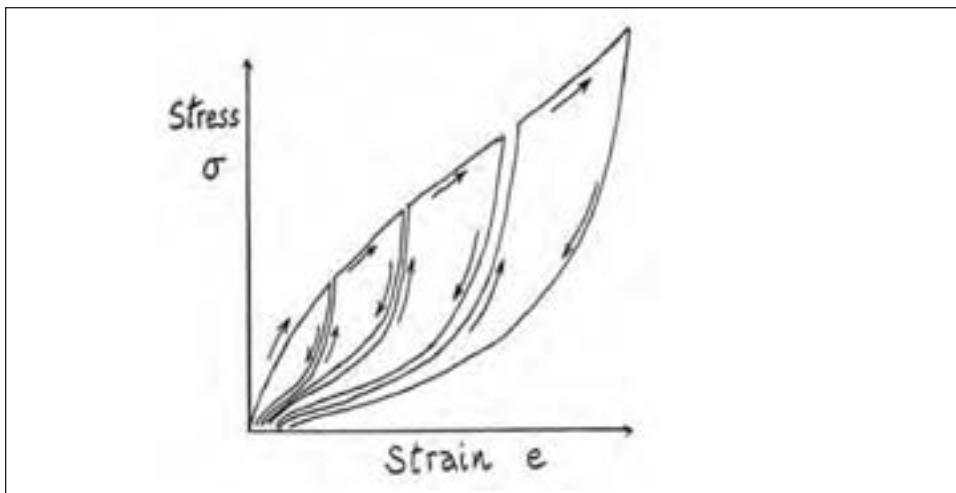
Figure 2.8: Strain hardening of a rubber molecule as it approaches full extension.

[The linear relation is for relatively small extensions]

1.2.2 Inelastic behavior of filled rubber compounds

It is common to incorporate 30% or more by weight of solid particle fillers, usually carbon black or silica powder, into compounds for all tire components, treads, sidewalls, etc. Such compounds are considerably stiffer, by a factor of 3 or more, than the corresponding unfilled compound, and they are stronger, and much more resistant to abrasion. But highly-filled rubber compounds are seriously inelastic, in a characteristic way. They are softened by straining, and softened more the greater the pre-strain, as shown schematically in figure 2.9. Thus, the original stress-strain relation is not reproducible unless the sample is allowed to recover by resting for several months, or annealed by heating for an hour or so at temperatures of 100°C or higher.

Figure 2.9: Stress-softening of filled rubber (Mullins Effect)
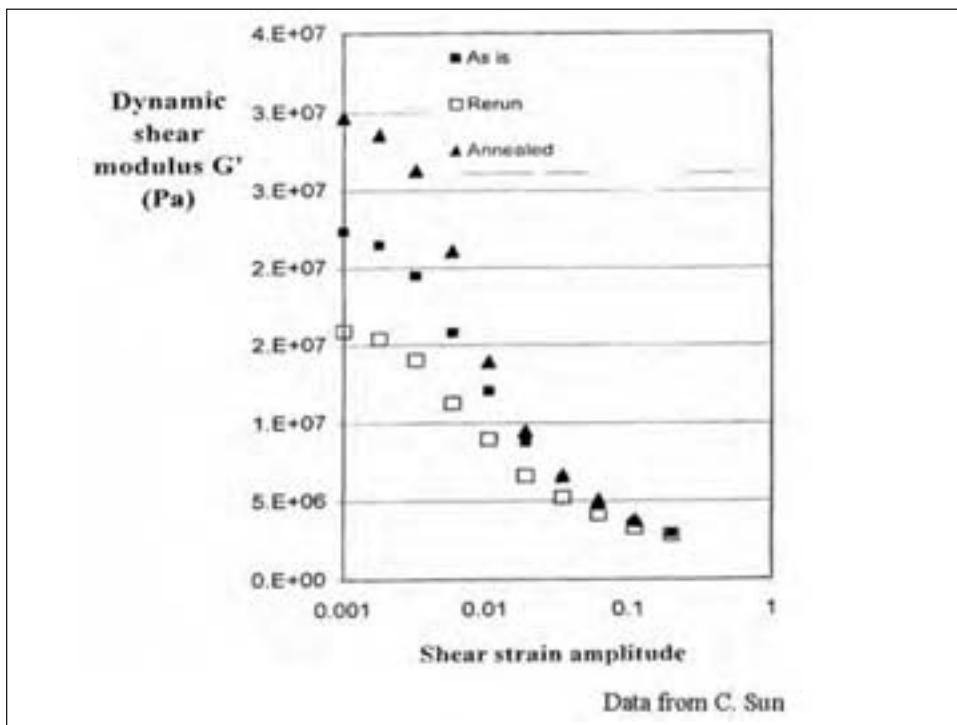
This large effect of strain history on the stress-strain behavior is termed the "Mullins" effect [1]. It appears to be due to slipping of rubber molecules over energy barriers on the surface of filler particles or becoming detached from the filler surface. It renders computer modeling of the stress-strain behavior of typical tire tread compounds extremely difficult. For example, we know very little about the effect of pre-strains other than tensile strains, or of complex strains as is, of course, the case for tire components, or about the rate of recovery from prior straining.

To make matters even more complicated, a similar effect is found when quite small strains are imposed, in the range, say, from 0.1% to 10%. Such measurements are usually carried out dynamically, by imposing a small oscillatory tensile or shear strain at a convenient frequency in the range 0.1 to 100 Hz, and reporting the results in terms of the effective dynamic modulus E´ or G´, the ratio of peak stress to peak strain. E´ or G´ are found to decrease dramatically over this range of dynamic strain amplitude, often to only 1/3 or less of the initial value, figure 2.10. Again, although partial recovery by 30 to 50% occurs almost immediately on returning to small deformation amplitudes, complete recovery takes months of rest unless the sample is heated to accelerate the recovery.

This small-strain softening phenomenon is often termed the "Payne" effect [2]. It appears to be due to disruption of chain-like aggregations of filler particles within the rubber matrix. Because the effect is so large in highly-filled compounds, they are seldom used in rubber springs because the relevant "modulus" for calculations of spring rate and resonant frequency is ill-defined. And, again, it is difficult to take the "Payne" effect into account in modeling the stress-strain response of tire compounds in treads and sidewalls.

**Figure 2.10: Stress-softening of filled
rubber at small strains (Payne effect)**

In summary, typical filled rubber compounds show two disturbing features: the **"Payne" effect",** a marked softening that starts at strain amplitudes of only 0.1 % or less, attributed to breakdown of weak inter-particle bonds, and **"Mullins" softening",** a further substantial softening at higher strains, up to the breaking strain, that is attributed to progressive rupture of bonds between rubber molecules and filler particles. Because these two processes overlap to a considerable degree, they cannot be easily separated. However, they appear to be a direct consequence of the high stiffening power of fillers of small particle size and highly interactive surfaces when they are incorporated into rubber.

Note that, because filled rubber compounds are not elastic, i.e., they do not follow reversible stress-strain relations, their behavior cannot be described successfully by any elastic constitutive law relating stresses to strains. Instead, the tire designer must accept quite approximate representations of the elastic properties of present-day tire compounds, recognizing that they are subjected to complex strains and strain histories that have major, and unfortunately ill-defined, effects on the corresponding stresses.

1.3 Visco-elasticity
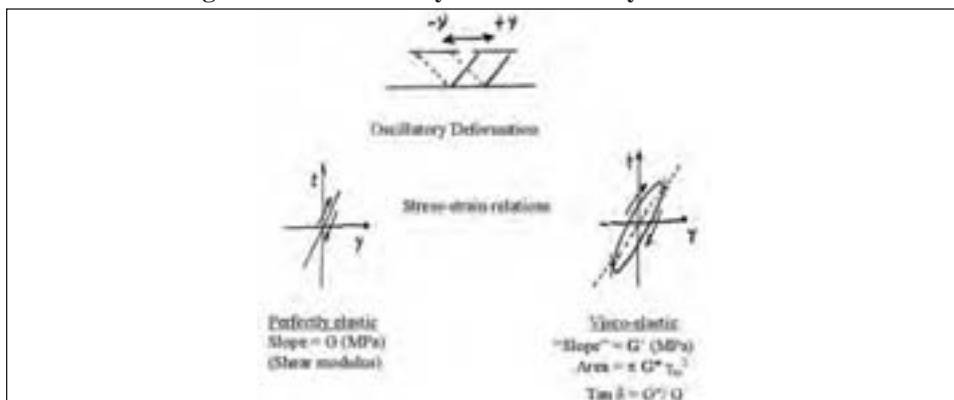
Under repeated oscillations of shear strain γ, the stress-strain relation becomes an ellipse, figure 2.11, provided that the strain amplitude is small. The slope of the line joining points where tangents to the ellipse are vertical represents a dynamic shear modulus G' (MPa) and the area of the ellipse represents energy U_d dissipated in unit volume per cycle of deformation, given by

$$U_d = \pi \, G'' \, \gamma_m{}^2 \qquad\qquad (1.9)$$

where γ_m is the amplitude of shear strain and G'' is termed the dynamic shear loss modulus. (For an oscillatory tensile deformation the corresponding moduli are denoted E' and E''.)

The ratio G''/G' (or E''/E') is the tangent of an angle δ, the phase angle by which the strain lags behind the applied stress. When the ellipse axes lie in the horizontal and   vertical directions, δ is 90° (tan δ is infinitely large), and the rate of strain reaches its maximum value when the applied stress is a maximum. This is the response of a viscous liquid. On the other hand, when the ellipse degenerates into a straight line, tan $\delta = 0$ and the material is a perfectly elastic solid. Values of tan δ for rubber compounds at room   temperature range from about 0.03 for a highly resilient, "springy" material with low energy dissipation to about 0.2 for a typical tread compound with relatively high dissipation.

Figure 2.11: Oscillatory deformation: dynamic effects

Rebound resilience R is an inverse measure of energy dissipation. R can be determined by dropping a rigid ball onto a rubber block and measuring the rebound, or dropping a rubber ball onto a rigid plate. In both cases the fractional amount of energy returned after impact is:

$$R = h_2/h_1, \tag{1.10}$$

where h_1 is the drop height and h_2 is the rebound height. If the impact is regarded as one half-cycle of a steady oscillation, then

$$\ln R = -\pi \tan \delta \tag{1.11}$$

Equation 1.11 is based on rather severe assumptions so it must be considered as a rough approximation. However, rebound tests are simple to perform and widely used to estimate loss properties.

1.3.1 Heat generation

Energy dissipated by loss processes within a rubber compound is converted directly into heat. Under a steady oscillation the amount of heat generated per second in unit volume is given by fU_d, where f is the frequency of oscillation. Heat is lost by conduction through the rubber to surfaces in contact or to air. Consider, for example, a thin rubber block, of thickness H, that is subjected to an oscillatory shear deformation between two highly-conductive surfaces that act as heat sinks so that the interfaces are maintained at a constant temperature T_o. At steady state, the maximum temperature reached in the center of the block will be

$$T_m = T_o + fU_d H^2/8K \tag{1.12}$$

where K is the coefficient of thermal conduction for the rubber.
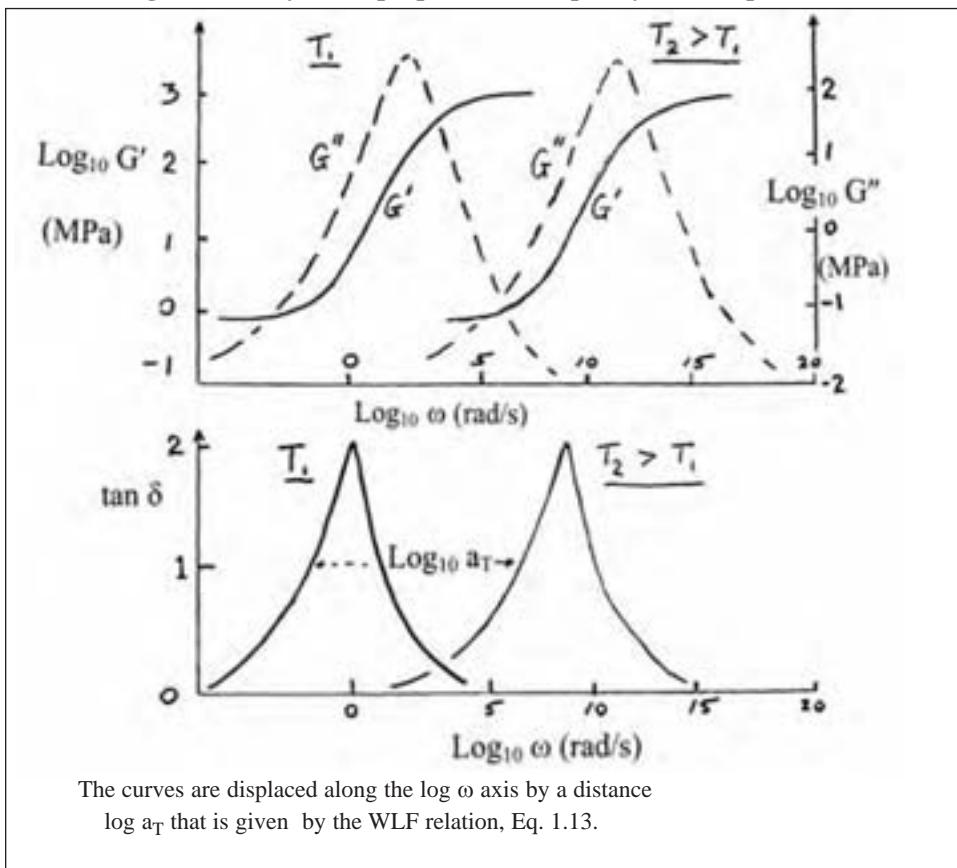
It is clear that heat conduction plays an important role in determining the temperature rise. Unfortunately, K is rather insensitive to compounding variables. All elastomers are poor conductors of heat, with values of K of about 0.2-0.3 W/m ^{O}C. Even when good conductors - for example, metal powders - are added to the rubber compound, K is not greatly increased because the metal particles become surrounded by a rubber layer and do not form continuous paths for conduction of heat.

The amount of heat generated per cycle depends strongly on the deformation amplitude γ_{max} of shear or e_{max} of tension/compression. Thus, under oscillations of constant *load* amplitude, a stiffer compound will show less heat generation and a smaller temperature rise if its resilience or tan δ is unchanged. Indeed, this effect may well override the difference in loss properties between a stiffer and a softer compound. On the other hand, under a fixed *deformation* amplitude the material with lower loss modulus will generate less heat. Solid tires are an example of an application in which the load level is fixed. In rubber belting, on the other hand, the amplitude of strain (bending) is fixed by details of the application. Compounds would therefore be chosen for these two uses on different grounds. In any case, it is desirable to have compounds that generate a minimum of heat in use because the strength, durability and abrasion resistance of rubber compounds are all reduced as the temperature increases.

1.3.2 Effects of temperature and frequency of oscillation

We need to know values of G´, G″ and tan δ at the frequency of loading and at the temperature at which the rubber is to be used, because the dynamic properties depend strongly on these variables. The dependence on frequency is shown schematically in figure 2.12. At low frequencies the dynamic modulus is low and rather constant but as the frequency is raised the compound becomes increasingly stiff until at high frequencies it is hard and glasslike. This striking transition, by about three orders of magnitude, reflects the change from facile response of molecular segments when stresses are applied at low frequency, to their complete inability to move under high-frequency stresses. Thus, the transition is centered at an oscillation frequency of the same order of magnitude as the natural frequency of motion of the molecular strands as a result of thermal agitation. Motion of a strand, in turn, arises from Brownian motion of the individual segments that make up the strand.

Figure 2.12: Dynamic properties vs frequency and temperature

The curves are displaced along the log ω axis by a distance
log a_T that is given by the WLF relation, Eq. 1.13.

The loss modulus G″ increases with frequency to an even more marked degree than G´, often becoming larger than G´ in the transition range of frequencies, because G″ is a direct measure of viscous resistance to segmental motion. At sufficiently high frequencies, however, the segments become unable to respond to the rapidly-alternating applied stresses, and internal motion ceases. Energy dissipation that is associated with the motion of
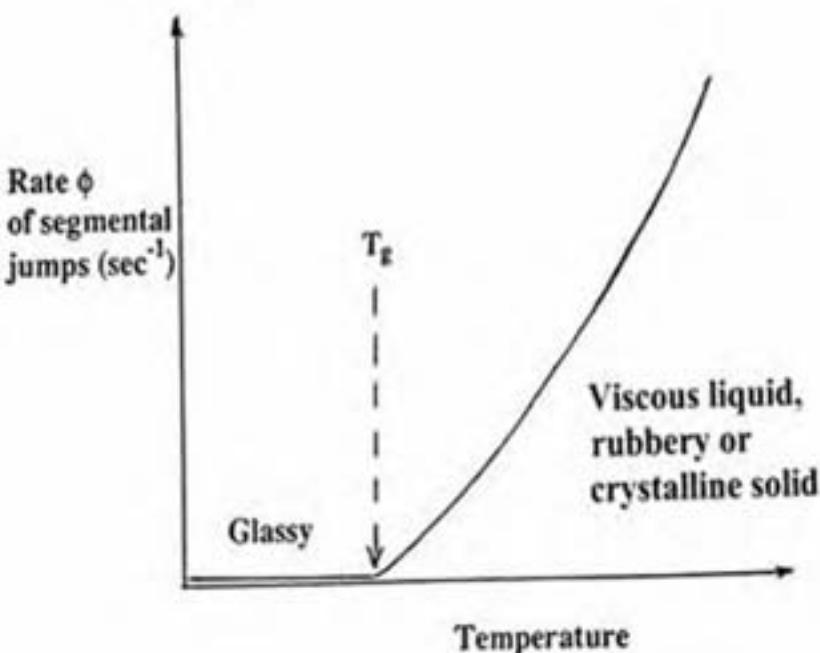
molecular segments in a viscous environment also ceases and G'' falls to the relatively low value characteristic of polymeric glasses.

The rate φ of Brownian motion of molecular segments depends only upon the internal viscosity and hence only upon temperature. Below T_g the polymer is glassy: above T_g it is liquid (if low in molecular weight), rubbery (if high in molecular weight or crosslinked), or crystalline (if the molecules are sufficiently regular), figure 2.13. The dependence of φ upon temperature, or more precisely upon the temperature difference $(T - T_g)$, follows a characteristic law [3]:

$$\log [(\varphi(T)/\varphi(T_g)] = A(T - T_g)/(B + T - T_g) \qquad (1.13)$$

where A and B are constants, having approximately the same values, 17.5 and 52°C, for nearly all rubberlike substances, and T_g is a reference temperature, the glass transition temperature, at which molecular segments move so slowly, about once in 10 seconds, that for all practical purposes they do not move at all and the material becomes a rigid glass. [By common consent, T_g is defined as that temperature at which the rate of Brownian
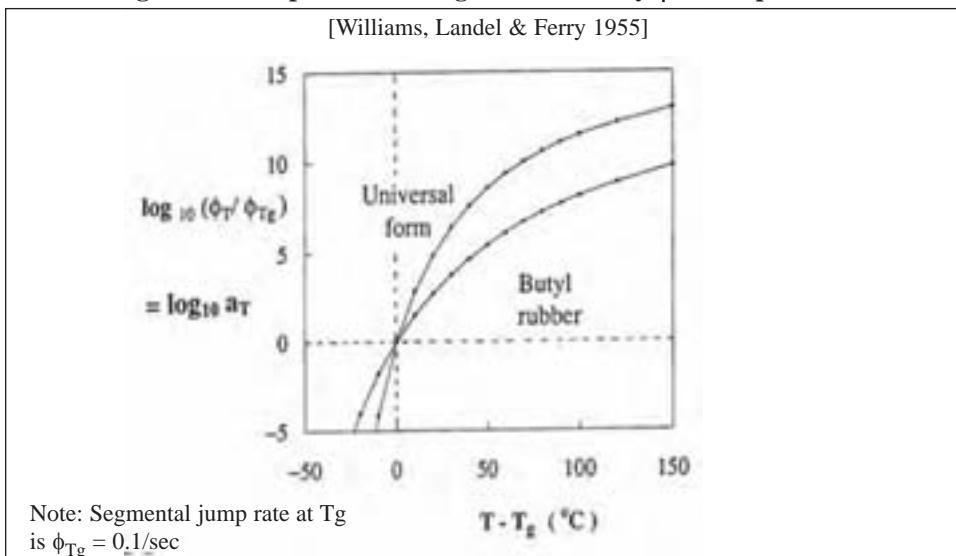
Figure 2.13: Rate ϕ of Brownian motion of molecular segments

motion $\varphi(T_g)$ has fallen to 0.1 Hz.] Values of T_g for some common elastomers are given in Table 2. Equation 1.13 is represented graphically in figure 2.14.

In many applications molecular motion is required at frequencies much higher than 0.1 Hz. For example, for high resilience in a rebound experiment we require virtually complete rubberlike response in a time of impact of the order of 1 ms. But molecular segments will move in 1 ms only when the value of φ is about 1000 jumps per second.

Figure 2.14: Dependence of segmental mobility ϕ on temperature

[Williams, Landel & Ferry 1955]

Note: Segmental jump rate at Tg is $\phi_{Tg} = 0.1/sec$

From equation 1.13, that is only at a temperature about 16°C higher than T_g. Indeed, for coordinated motion of entire molecular strands consisting of many segments to take place within 1 ms, the segmental response frequency must be higher still, by a factor of 100 or so. This rate of response is achieved only at a temperature about 30°C above T_g. Thus, fully rubberlike response will not be achieved until the temperature is T_g + 30°C, or even higher. On the other hand, for sufficiently slow movements taking place over several hours or days, a material would still be able to respond at temperatures significantly below the conventionally-defined glass transition temperature. This region is represented by the lower portions of the curves in figure 2.14.

It is important to recognize that the conventional glass transition temperature is defined in terms of relatively slow motions, taking place in about one minute, and requiring only small-scale motions of individual molecular segments rather than motion of entire molecular strands between crosslinks. The frequencies at which the entire rubber-to-glass transition occurs depend on temperature in accordance with Equation 1.13.

The numerical coefficients, 17.5 and 52°C, in equation 1.13 are about the same for a wide range of elastomers, because most elastomers have similar values of thermal expansion coefficient and the molecular segments are similar in size. However, an important exception is polyisobutylene and its derivatives, butyl rubber and halo-butyl. For these materials, the coefficients appear to be about 17.5 and 100°C, the latter being considerably different from the "universal" value that holds for other common elastomers.

Thus, the rate of segmental motion increases much more slowly above T_g as shown by the curve for butyl rubber in figure 2.14. Although the reason for this peculiarity is not well understood, it is probably associated with an unusually large size for the basic moving segment. Two important consequences are that butyl rubber and halo-butyl exhibit   unusually low resilience, low gas permeability and good ozone resistance at temperatures well above T_g.

Equation 1.13 can be used to relate the dynamic behavior at one temperature T_1 to that at another, T_2. For example, the dynamic modulus G' and loss modulus G'' are found to depend on the frequency of vibration as shown schematically in figure 2.12. When the temperature is raised to T_2, the curves are displaced laterally by a fixed distance, log a_T, on the logarithmic frequency axis, where log a_T reflects the change in characteristic response frequency of molecular segments when the temperature is changed from T_1 to T_2. Thus log a_T is given by:

$$\log a_T = \log [\varphi(T_2)/\varphi(T_1)]$$
$$= 17.5 \times 52(T_2 - T_1)/(52 + T_2 - T_g)(52 + T_1 - T_g) \qquad (1.14)$$

from Equation 1.13. In this way, measurements at one temperature can be transformed into results at another. This is a powerful way of predicting viscoelastic response over wide range of frequency from measurements over a limited range of frequency but at many temperatures, using the general principle that a temperature shift is completely equivalent to a change in frequency:

$$\text{Log } f_T = \text{Log } f_{Tg} + \text{Log } a_T \qquad (1.15)$$

As an approximate guide, valid at temperatures about 50^OC above T_g, a temperature rise of about 12^OC is equivalent to a factor of 0.1 change in frequency, or rate of strain, or speed of loading. Thus Equation 1.15 provides a powerful frequency-temperature and rate-temperature equivalence principle that enables one to correlate mechanical behavior over wide ranges of frequency and rate with temperature. For example, measurements taken over a limited frequency range at many different temperatures can be superposed by lateral shifts along the logarithmic frequency axis to construct a "master curve" as shown in figure 2.15. The lower curve (figure 2.15b) represents the expected response over an extremely wide frequency range at the chosen temperature. Moreover, the master curve can be made to apply at any other temperature by an appropriate lateral shift along the log frequency axis, calculated from equation 1.14.

However, there are instances where this broad simplification fails to hold. If the modulus is affected by a temperature-dependent process that is not controlled solely by the rate of molecular motion (for example, melting of crystallites), then the frequency-temperature equivalence given in equation 1.14 no longer applies. An example is discussed below.

1.3.3 Energy losses in filled rubber compounds
The same principle of frequency-temperature equivalence applies to the rubber molecules in filled rubber compounds and the same fitting constants are valid. Apparently, T_g and the molecular mobility of elastomer strands above T_g are not appreciably affected by the presence of fillers. But filled compounds show other effects, as described previously - the elastic modulus is decreased by a previously imposed strain, or by imposing dynamic deformations of increasing amplitude. This softening is accompanied by increased energy dissipation, probably associated with the work required to break bonds between rubber and filler particles or between the particles themselves.

Figure 2.15a: Modulus E vs oscillation frequency f for a polyurethane elastomer
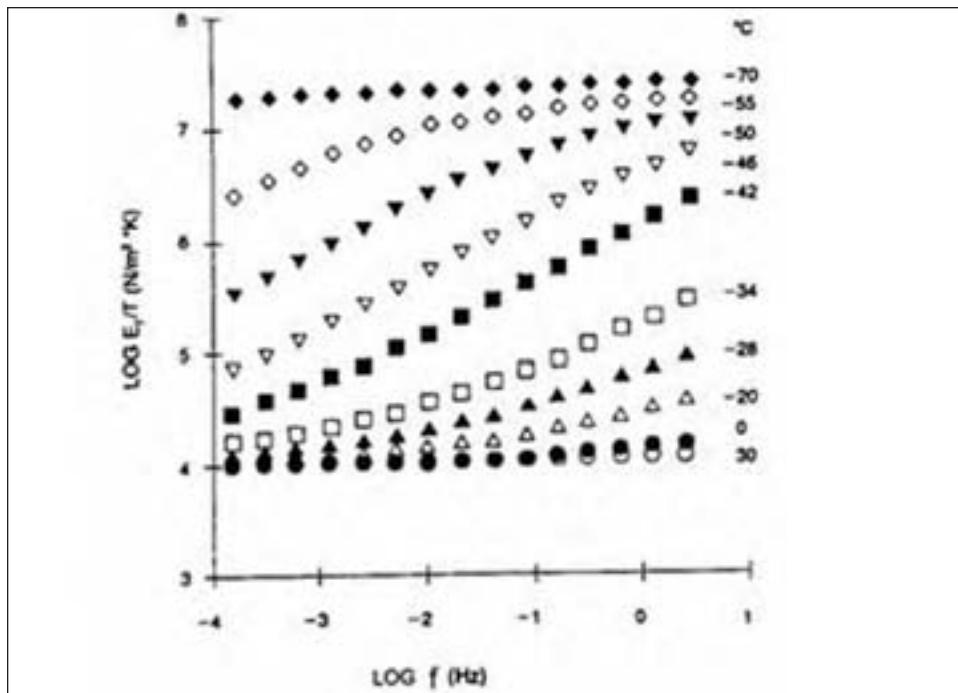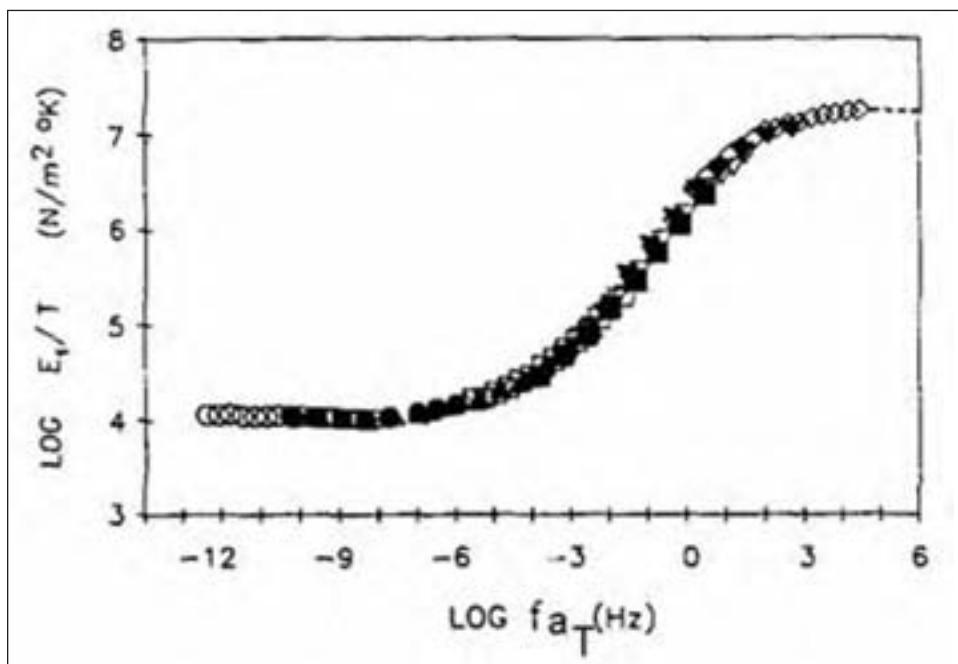
Figure 2.15b: Modulus E vs reduced frequency f a_T at $- 42°$C

The modulus of filled compounds is also decreased by raising the temperature, because the rubber-particle bonds become weaker. This effect is not directly associated with changes in molecular mobility and thus it cannot be represented by an equivalent change in frequency. Hence, equation 1.14 does not apply to the modulus of filled compounds without a correction for additional effects of temperature.
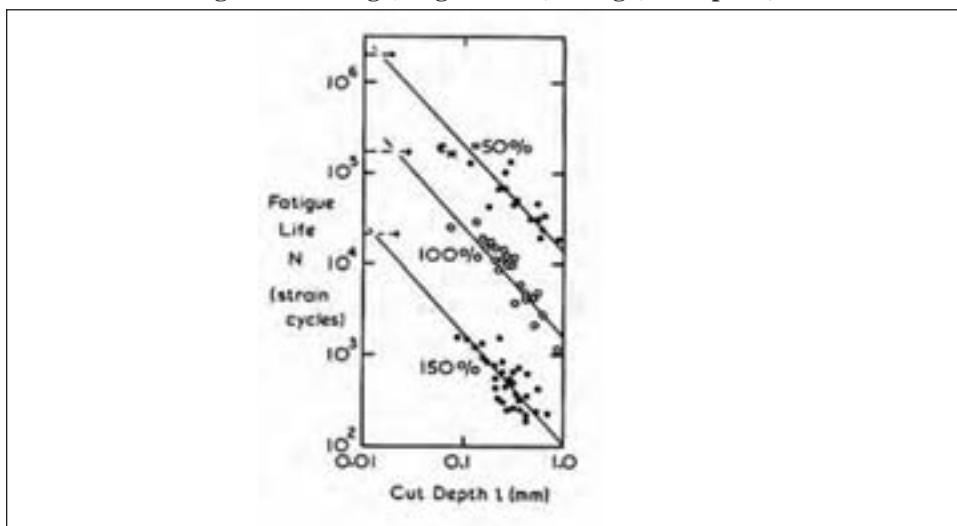
2. Strength of rubber compounds

2.1 Natural flaws and defects

Fracture mechanics has become the standard method of treating rupture of "brittle" materials, i.e. materials, like rubber, that break without undergoing widespread plastic deformation. In this concept, rupture is the result of growth of an existing flaw or defect. All materials contain such stress-raisers - rubber is no exception – and the size of naturally occurring defects can be estimated in various ways. For example the fatigue life, represented by the number N of times a tensile strain of fixed amount can be imposed on a tensile strip before it ruptures, is a strong function of the depth of a sharp cut placed in one edge of the specimen (see figure 2.16). The life N is shorter when the initial cut is made deeper. By extrapolating back to the fatigue life of a sample with no deliberately-introduced edge cut, a value can be assigned to the effective depth of cut that corresponds to the natural flaw or defect from which failure originated. The value obtained in this way is about 50 μm. Similar values are deduced from measurements of fatigue life at higher tensile strains, when all of the fatigue lives for cut specimens are reduced, or at lower tensile strains, when all of them are increased. And similar values are deduced from the dependence of tensile strength on the depth of an edge cut, and from studies of the quite low critical stresses needed for growth of an edge cut from chemical attack by ozone. In all of these cases, and for all of the elastomer compounds studied, fracture of an "uncut" specimen can be accounted for by assuming that the compound actually contains inherent flaws or defects equivalent to a sharp edge cut, about 50 μm long.

But so far, the presence of real defects of this size has not been established and their origin is still unknown. They may actually be smaller and sharper stress raisers than

Figure 2.16: Log (fatigue life N) vs log (cut depth c)

artificial cuts, and thus difficult to observe. Because the effective size deduced for all of the rubber compounds studied to date, both filled and unfilled, is similar, they might be the result of a common feature of rubber processing, for example a natural heterogeneity of crosslinking, or they may be created in the course of stressing rubber up to the point of rupture by a precursor mode of fracture. Local cavitation under tensile stress is one possibility.

Further studies are highly desirable because initiation of fracture is an important aspect of fracture mechanics. At present, we can account successfully for the strength of rubber under a variety of conditions on the assumption that inherent flaws are present, equivalent to sharp cuts about 50 μm deep.

2.2 Fracture energy and breaking stress

Fracture mechanics assumes that a characteristic amount of energy is required for crack growth per unit area torn through, analogous to surface energy and denoted fracture energy or tear strength, G_c (J/m^2). It is commonly measured for rubberlike materials by a simple tear test, as shown in figure 2.17. When the tear advances by a distance dc, the tear forces P supply energy of 2P.dc and if this energy is consumed entirely in fracture, then the energy required is G_cw.dc, where w is the width of the tear path (in this case, roughly the thickness of the sheet). Thus:
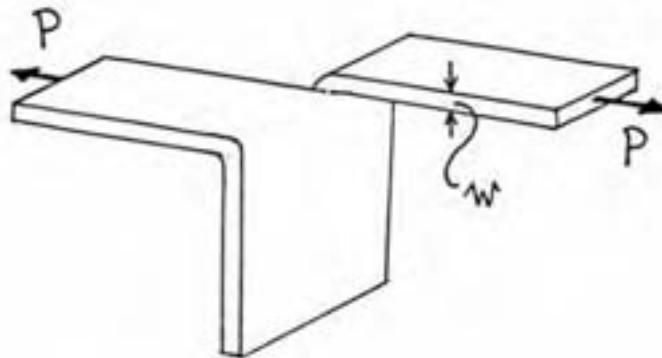
$$G_c = 2P/w \tag{2.1}$$

Similar considerations were applied by Griffith to tensile rupture of glass rods containing a small edge crack of length c [4]. Here the crack grows at the expense of strain energy W stored in the stretched sheet. When W is sufficiently high that the reduction -dW caused by growth of the crack by a small amount dc is sufficient to meet the requirements for fracture, G_cw.dc, then fracture ensues. The fracture criterion is:

$$G_c = -(1/w)(dW/dc) \tag{2.2}$$

where the derivative is taken at constant length of the sample to avoid including

Figure 2.17: Relation between tear force P and fracture energy G_c

$$G_c = 2P/w$$

further work input by the applied force. For a sheet of a linearly-elastic material (figure 2.18) the breaking stress σ_b and strain e_b are obtained in this way as:
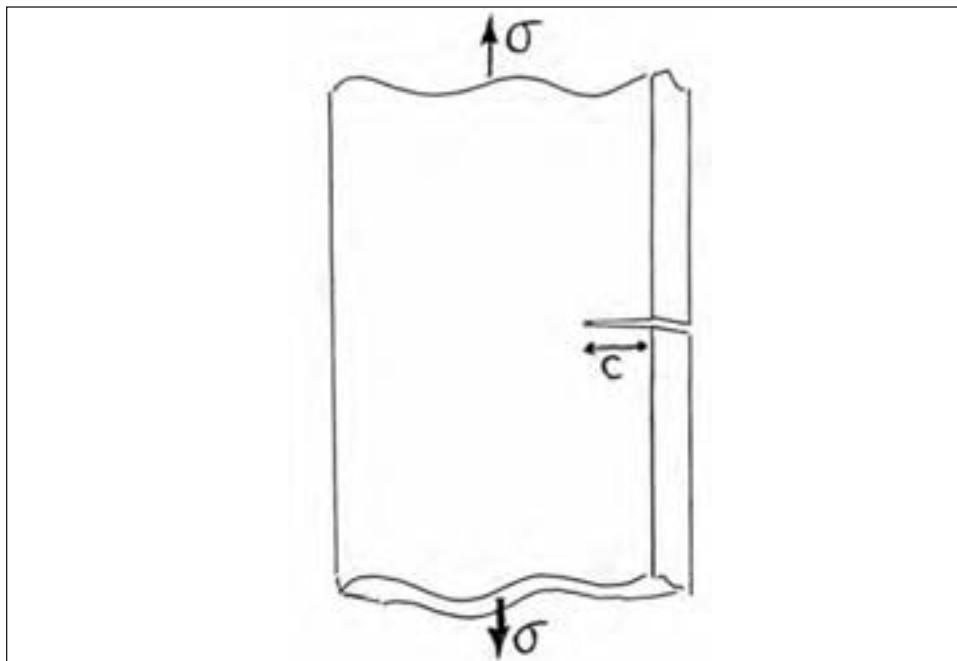
$$\sigma_b = 1.26 \ (EG_c/\pi c)^{1/2} \tag{2.3}$$
and
$$e_b = 1.26 \ (G_c/E\pi c)^{1/2} \tag{2.4}$$

where E is the tensile modulus of elasticity.

Note that a stiffer material with the same tear strength G_c will be stronger than a softer material. Thus fracture mechanics predicts that the strength of compounds will be rated differently under different test conditions. This is further illustrated by considering growth of a long crack in a sheet under constrained tension, figure 2.19. In this configuration, the sheet is unable to contract sideways because the long horizontal clamps prevent it. The initial crack is made quite long in comparison with the specimen height h to avoid end effects.

As before, energy required for rupture is supplied by strain energy in the stretched portion of the sheet. For a linearly-elastic material, the tensile stress at which the crack

Figure 2.18: Tensile strength test

will propagate is obtained as:
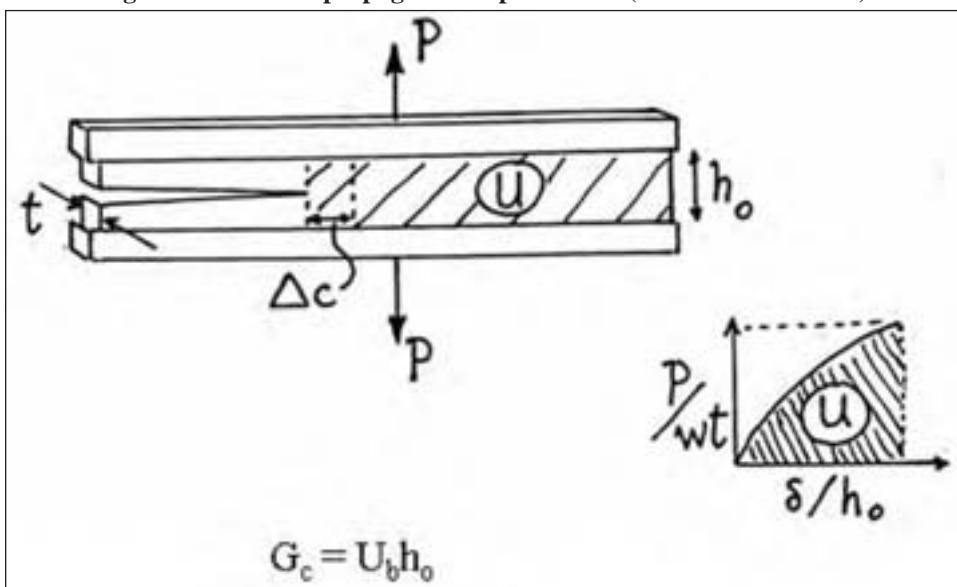
$$\sigma_b = 1.63 \ (EG_c/h_o)^{1/2} \tag{2.5}$$

where h_o is the unstrained height of the strip, a measure of the amount of material from which strain energy is released as the crack passes. Note that the breaking stress now depends on the sample height h_o and not on the crack length c.

On comparing Equations 2.3 and 2.5, the breaking stress is seen to be much lower in a

constrained tensile test than in a regular tensile test because the initial height h_o of the specimen, usually several mm, is much greater than the depth c of an accidental edge flaw in a simple tensile specimen, typically only about 50 μm. Thus the applied stress at which rupture occurs is not a valid criterion for fracture. Moreover, the breaking stress at the crack tip, which would presumably be a valid fracture criterion, is virtually impossible to measure. On the other hand the fracture energy for a rubber compound can be measured in several ways, including those sketched in Figures 2.17, 2.18 and 2.19, and proves to be a simple, consistent and reproducible fracture criterion. It has therefore been widely adopted. We now turn to consider theoretical and measured values of G_c for typical rubber compounds.

Figure 2.19: Crack propagation in pure shear (constrained tension)

$$G_c = U_b h_o$$
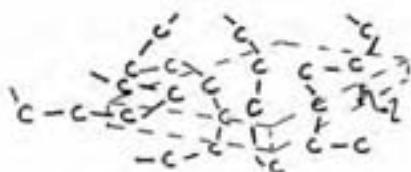
2.2.1 Theoretical values of fracture energy

By adding the carbon-carbon bond dissociation energies for all of the bonds that cross unit area, figure 2.20, Berry [5] deduced that the fracture energy for a polymer with C-C backbone bonds would be about 1 J/m^2, about 50 times larger than the energy needed to separate Van der Waals bonds in a simple liquid. However, this is far below the observed tear strengths for rubber compounds, that range from about 300 J/m^2 to very high values, of the order of 100,000 J/m^2, depending on crack speed and temperature. When the high extensibility of rubber molecules is taken into account, Berry's theoretical value is raised by a factor of approximately $n^{1/2}$, where n is the number of segments in a molecular strand between crosslinks [6]. Using a representative value for n of 100, this increases the theoretical value for G to about 10 J/m^2, still far below experimentally-measured strengths. Thus, a fundamental question in the mechanics of rubber fracture is: Why is the observed strength so much higher than expected? The answer is found by examining the effect of speed of crack propagation and temperature.

2.2.2 Dependence of tensile strength on rate of extension and temperature

Measurements of the tensile breaking stress σ_b and breaking extension e_b for a non-crystallizing elastomer SBR were found to depend on rate of extension and temperature in accordance with the WLF rate-temperature equivalence, equation 1.12 [7]. By applying shift factors calculated from Equation 1.15, data obtained at different temperatures could be superposed to yield "master" curves for σ_b and e_b as functions of rate of stretching, figure 2.21. The success of this superposition shows how important in the strength and extensibility of elastomers are the internal dissipative processes that arise from segmental motion.
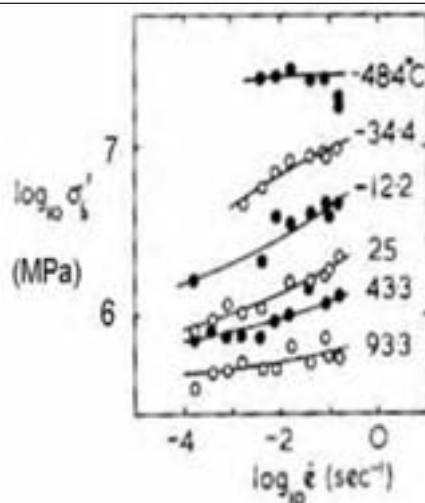
Figure 2.20: Sketch of molecules crossing a fracture plane

2.2.3 Dependence of fracture energy on crack speed and temperature

The same rate-temperature equivalence has been shown to hold for the fracture energy G_c. Measurements of energy G_c for a simple unfilled rubber compound are plotted in figure 2.22 as a function of tear rate at various temperatures. The values are seen to change by a large factor, about three orders of magnitude, as the test conditions change from low tear speeds at high temperatures to high tear speeds at low temperatures. Plotted using a logarithmic scale for tear speed, they resemble viscoelastic functions, superposable by horizontal shifts in the same way that G', G″ and tan δ are superposable, figure 2.12.

Figure 2.21a: Tensile strength vs rate of extension

Indeed, using WLF shift factors calculated from Equation 1.13, as shown schematically in figure 2.23, the results from figure 2.22 are accurately superposable; see figure 2.24. This proves that the high tear strength exhibited at low temperatures is associated with

Figure 2.21b: Tensile strength vs reduced rate of extension at – 10°C
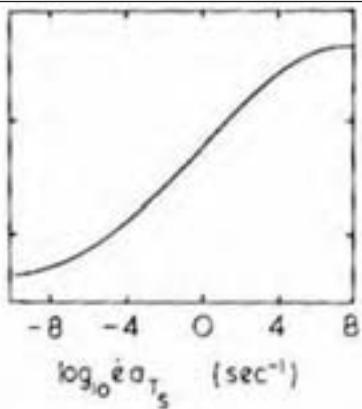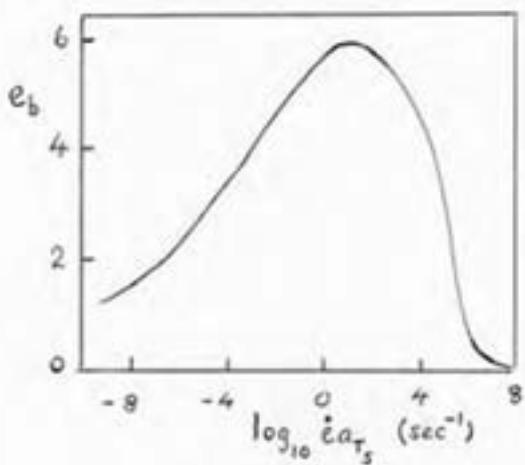
Figure 2.21c: Elongation at break vs reduced rate of extension at – 10°C

reduced molecular mobility, and not with a change in the intrinsic strength of the rubber molecule.

It was pointed out earlier that the molecular mobility of butyl rubber is anomalous - it increases more slowly as the temperature is raised above T_g than for other elastomers. We would therefore expect the tear strength of butyl rubber compounds to decrease more slowly as the temperature is raised, and this turns out to be the case [8].

2.2.4 Threshold strength

At low speeds and high temperatures the tear strength approaches a lower limit G_o, of about 50 J/m^2, figure 2.22. This limiting value, termed threshold strength, is of the same order of magnitude as the theoretical value for the intrinsic strength of an elastomer network in the absence of viscous energy dissipation, see section 2.2.1. Moreover, values of G_o are found to increase with the length M_c of the molecular strands in the network, roughly in proportion to $M_c^{1/2}$, in good agreement with the Lake-Thomas theory of thresh-

old strength [6]. Note that the threshold strength is *inversely* related to the degree of crosslinking - it decreases as the degree of crosslinking is increased. [This raises an important practical issue. Because the threshold tear strength is reduced by crosslinking whereas the elastic modulus is increased (equation 1.1), the appropriate level of crosslinking for a particular rubber compound will depend on the anticipated service conditions.]

The tear strength under non-equilibrium conditions appears to be a product of two terms, the inherent strength G_o of the molecular network and a factor reflecting dissipative processes. Indeed, when the relative value G_c/G_o is plotted against tear speed at a temperature of T_g, obtained by applying shift factors calculated from equation 1.13 to experimental measurements of G_c at various temperatures, the same curve is obtained for three elastomers having quite different chemical structures and different T_g's, figure 2.24 [9]. Results are shown for polybutadiene (BR) with a T_g of -96°C, an ethylene-propylene

Figure 2.22: Fracture energy (tear strength) vs. rate
and temperature for HS-SBR vulcanizate (Tg = - 30°C)
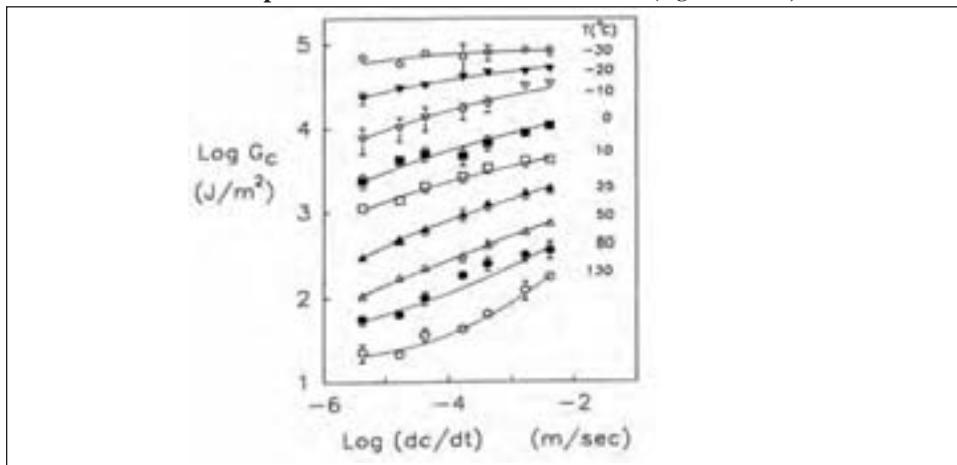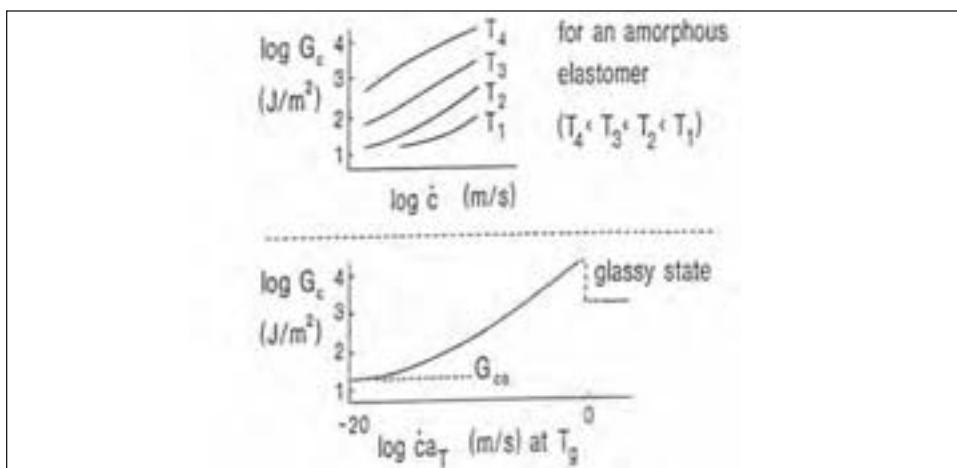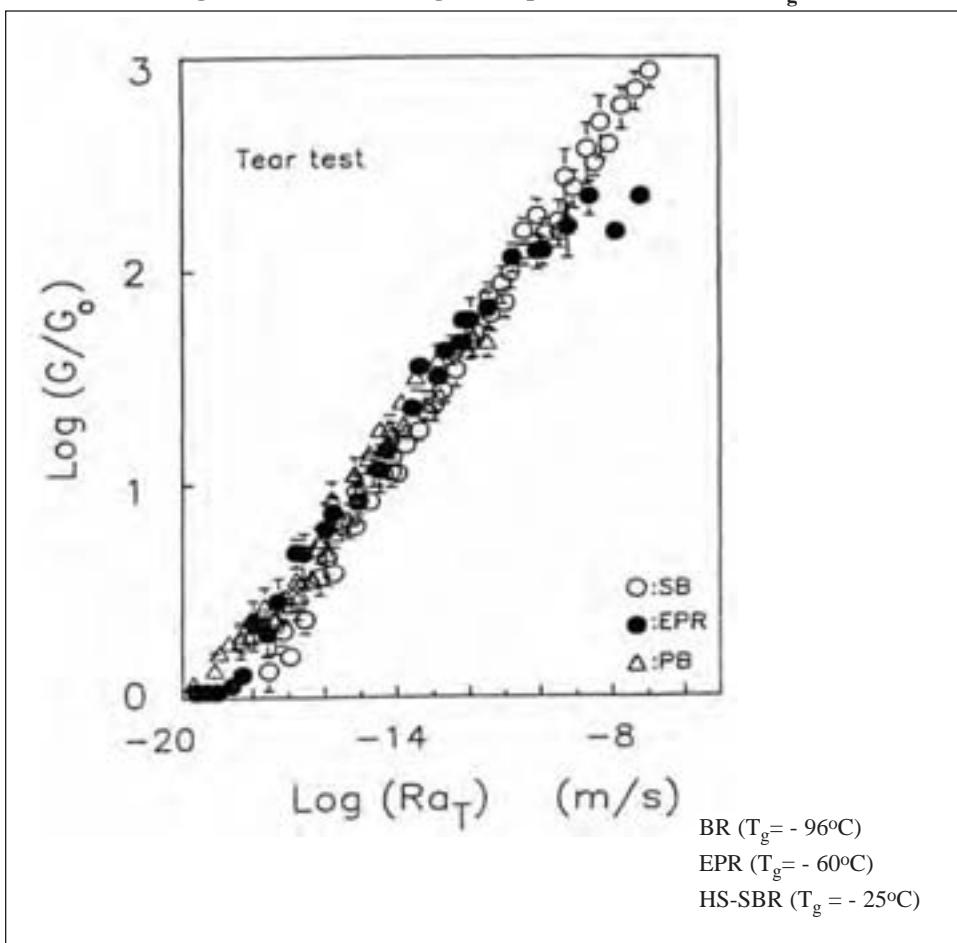
Figure 2.23: Use of the WLF principle to construct a "master curve"
of tear strength vs. tear rate (schematic)

copolymer (EPR), with a T_g of -60°C, and a high-styrene butadiene-styrene copolymer (HS-SBR) with a T_g of -25°C. They are indistinguishable in this figure. Thus, when the molecular mobility is the same, the tear strength is the same, regardless of the chemical structure. Moreover, using the WLF rate-temperature equivalence, the tear strength of a simple rubber compound can be predicted at any tear speed and at any temperature from two basic parameters, the glass temperature T_g and the degree of crosslinking, represented (inversely) by the length of network strands. This is a remarkable achievement of the fracture mechanics of rubbery materials. However, the form of the "universal" curve of strength vs. reduced rate of tearing has not yet been satisfactorily accounted for. It resembles the dependence of elastic modulus G′ on reduced frequency of deformation [10] but the linear dimension required to bring the two scales, rate and frequency, into accord is unreasonably small, only about 1 nm.

   We now turn to methods of improving (reinforcing) the basic strength of a simple crosslinked rubber for use in practical applications.

Figure 2.24: Tear strength vs equivalent tear rate at T_g

BR (T_g= - 96°C)
EPR (T_g= - 60°C)
HS-SBR (T_g = - 25°C)

2.3 Reinforcement

Internal dissipative processes obviously make a large contribution to the strength of rubber. This raises two important questions:

1. Is it possible to create a strong material with low dissipative properties, because at first sight these properties appear to be incompatible?

2. What other reinforcement mechanisms can be employed?

The apparent dilemma posed in the first question can be circumvented by recognizing that high strength is only required in highly stressed regions, near a stress-raiser. If a dissipative mechanism is activated only at high stresses, then both requirements can be met: low dissipation under "normal" low-stress conditions that exist in the bulk of the material, and high dissipation at high-stress sites, where needed.

One mechanism of this type is strain-induced crystallization. Certain elastomers, notably natural rubber, have a regular molecular structure capable of being closely packed, and they crystallize rapidly when stretched by more than about 300%. As a result, they become transformed into tough partially-crystalline fibrous solids that break only when crystallites in the tear path are pulled apart plastically, with considerable energy dissipation. At lower strains, before crystallization occurs, they are resilient, highly-elastic solids with low energy losses.

Employing the same principle, we can postulate a desirable feature in the reinforcement of elastomers by incorporating particulate fillers, for example carbon black. We require the rubber molecules to be bonded to filler particles, with bonds that do not fail at low stresses and cause unwanted energy dissipation under normal operating conditions. But the bonds must not be as strong as the elastomer itself, because then they would not fail at all. They should be somewhat less strong, and break before the elastomer molecules do, thus creating a dissipation mechanism at high-stress sites, where it is needed, without rupture of the molecular network.

Although this would be a highly desirable mode of reinforcing rubber by fillers, at present the bonds between rubber and particles appear to have a wide range of strengths, so that some energy dissipation occurs even at low stresses, considerably more than in the corresponding unfilled compound.

Rubber is usually crosslinked by sulfur, often by polysulfidic -S-S-S-S- crosslinks. The resulting materials have greater strength than those with carbon-carbon crosslinks. We note that sulfur crosslinks are weaker than C-C crosslinks and main-chain bonds, and postulate that they serve a sacrificial function – by breaking first, they reduce the tension in the elastomer molecule and permit it to survive. This function can also be interpreted as providing a dissipation mechanism at points of high stress.

Other common reinforcing mechanisms that can be interpreted in the same way are :

Plastic yielding of inclusions

Friction at internal interfaces

Formation of internal cavities

Detachment from fibers
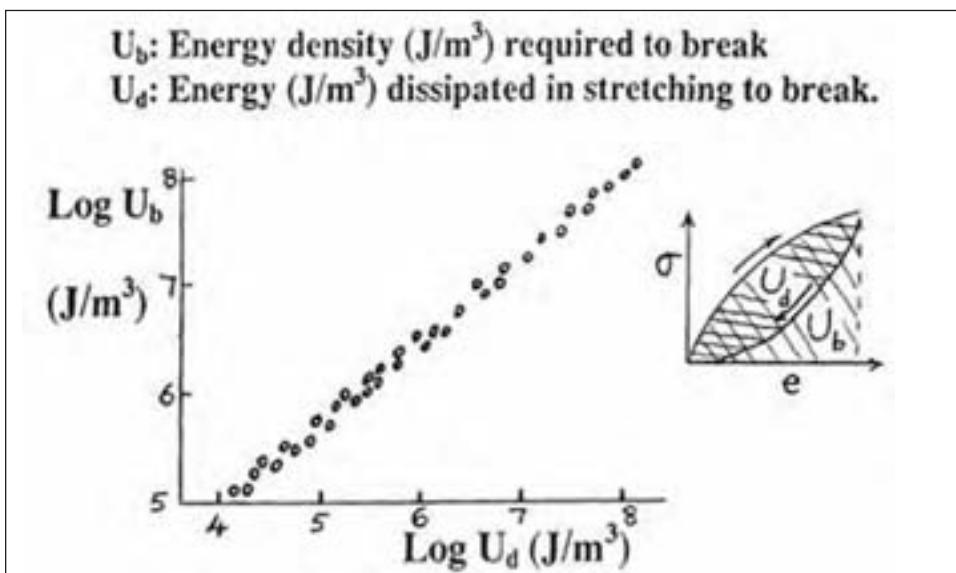
The conclusion that strength is directly related to energy dissipation was recognized quite early [11]. A comparison was made of the work-to-break a rubber sample in tension U_b with the energy lost in stretching a similar sample nearly to the breaking point U_d and then relaxing it. The two quantities are in principle independent, but in practice an excellent correlation was found to hold between them for a large number of rubber

compounds including a wide range of elastomers, degree of crosslinking, types and amounts of particulate fillers, test speeds, temperatures, etc. The correlation is shown in figure 2.25. The linear relation shown is:

$$U_b = 420 \, (U_d)^{2/3} \tag{2.6}$$

both quantities being measured in J/m^3. As the amount of energy dissipated U_d cannot possibly exceed the work-to-break U_b, Equation 2.6 suggests that the maximum possible tensile breaking energy of a rubbery material is about 80 MJ/m^3. However, Equation 2.6 is wholly empirical and, even though it applies successfully over an enormous range of tensile strengths, any extrapolation of it must treated with caution.

Figure 2.25: Correlation between breaking energy U_b and dissipated energy U_d

2.4 Blunting of the tear tip
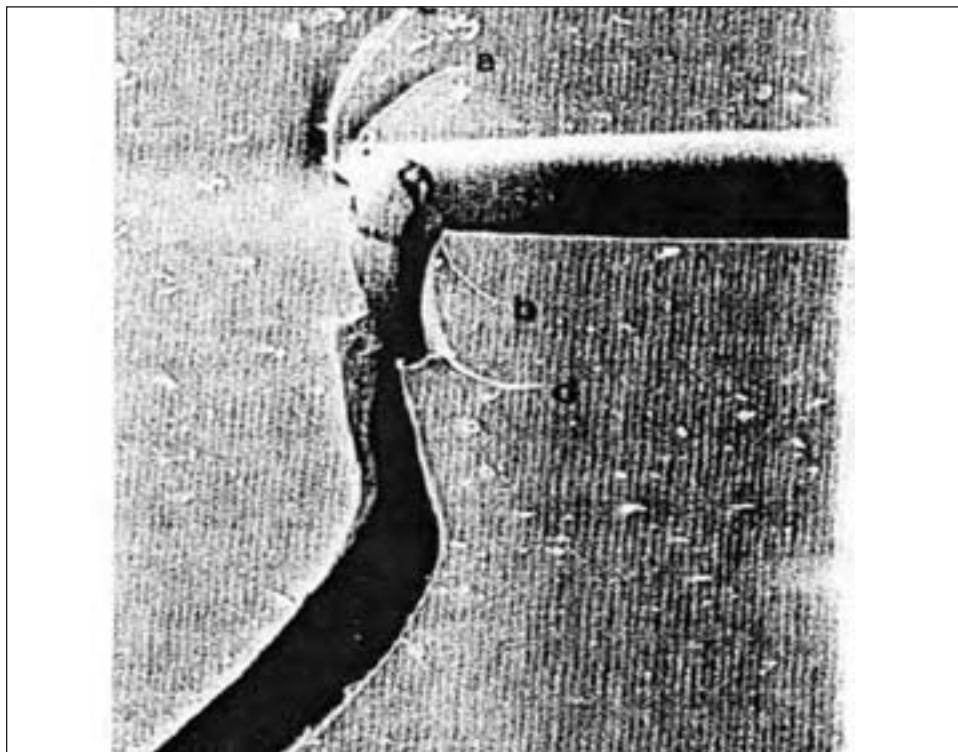
A singular feature of rubber compounds reinforced with particulate fillers is that a sharp cut or tear will often fail to grow across the direction of tension. Instead it turns sideways and runs more-or-less parallel to the tension for a short distance, and then stops. To propagate the tear further, another crack tip must form and grow, but again the new tear turns sideways and stops.

Examination of the tip of a precursor edge cut in a tensile test piece reveals that as many as five or six separate tear initiation steps took place at the cut tip before one finally succeeded in running in the "normal" direction, across the specimen, figure 2.26. This phenomenon is clearly a powerful strengthening mechanism, because the sharp initial cut is severely blunted and energy is wasted in making several ineffective lateral tears.

Finite element analysis reveals that a substantial fraction, about 50%, of the energy available for "normal" tear propagation can be employed to drive a tear sideways, especially if the material is highly stretched before the initial edge cut grows at all [12]. Thus if the stretched material is substantially weaker, by more than 50%, for tearing in the

direction of stretching, then deviation of a growing tear into that direction would be inevitable and the material would be effectively self-reinforcing. Note that this mode of reinforcement is not based on enhancing the strength of the material; it is attributed to developing *low strength* in the strain direction, leading to ineffective tearing and blunting of the tear tip. At least some of the reinforcing ability of particulate fillers appears to arise from this mechanism.

**Figure 2.26: Multiple tears at the tip of a cut in one edge
of a tensile test-piece: "Knotty" tearing**

2.5 Crack growth and mechanical fatigue

We have discussed how to measure the tear strength or fracture energy G_c. If the applied force is too small to cause immediate failure, then the energy available for growth of a tear is termed the "Strain Energy Release Rate", denoted G (J/m^2). In linear elastic fracture mechanics, the corresponding quantity is the stress intensity factor K, with a critical value denoted K_c, where K is related to G as follows:

$$K = (EG)^{1/2} \tag{2.7}$$

When energy G $(< G_c)$ is made available for fracture, even though large-scale tearing does not occur, a tear tip is found to grow by a small distance dc each time the stress is applied. The growth step dc depends strongly on G, following a simple empirical relation:

$$dc/dN = B[(G/G_o) - 1]^\alpha \qquad\qquad (2.8)$$

where B and α are crack growth constants. Although an equation of this form is widely used to predict growth of a crack under fatigue conditions, that is, under many applications of sub-critical stresses, the actual behavior is more complex, see figures 2.27 and 2.28, and equation 2.8 is only a useful guide over a limited range of values of G, from somewhat higher than the threshold strength G_o to about one-tenth of the catastrophic tear strength G_c.

When the stress is relaxed to zero between each application, the value of the crack growth constant B is found in all cases to be a molecular distance, about 0.05 nm. Thus, under threshold stresses a crack advances by an extremely small step, less than the size of a molecular strand, at each load application. On the other hand, the exponent α is quite different for compounds based on different elastomers. For example, α is about 2 for natural rubber compounds, 3 – 4 for butadiene-styrene (SBR) compounds, and 4 – 6 for polybutadiene compounds, and appears to depend inversely on the dissipative properties of materials. For highly-dissipative materials, α appears to approach a lower limit of 2, whereas for perfectly elastic, non-dissipative materials α appears to become infinitely large. Between these two limits, values of α for partially-dissipative materials can be represented empirically by the relation:

Figure 2.27: Tearing under repeated stressing (fatigue cracking)
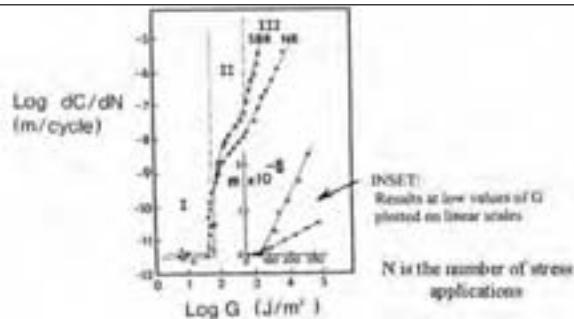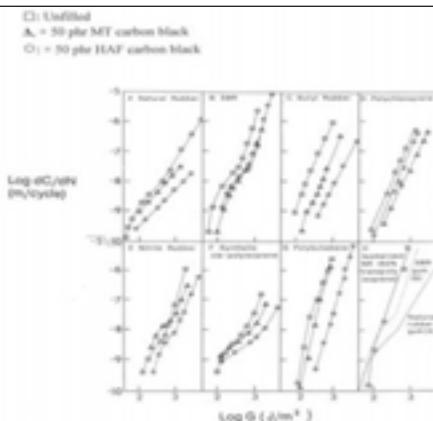
Figure 2.28: Crack growth rates for several rubber compounds

$$\alpha = 2/(1 - R) \tag{2.9}$$

where R is the resilience and $1 - R$ is the fraction of input strain energy that is dissipated. Filled rubber compounds are more dissipative than their unfilled counterparts and the value of α is found to be correspondingly smaller. For typical filled natural rubber compounds α is about 1.5 instead of 2, and for typical filled SBR compounds α lies between 2 and 3 instead of between 3 and 4.

   Why are values of α for natural rubber compounds, which are highly-resilient, in fact more appropriate for highly-dissipative materials? It is thought that strain-induced crystallization of natural rubber takes place at high stresses, especially at the tips of stress-raising flaws, figure 2.29, and leads to marked dissipation of energy as a crack advances.

2.5.1 Fatigue life
When a tensile strain is applied to a sample containing an edge cut of length c, the energy available for crack growth is given by:
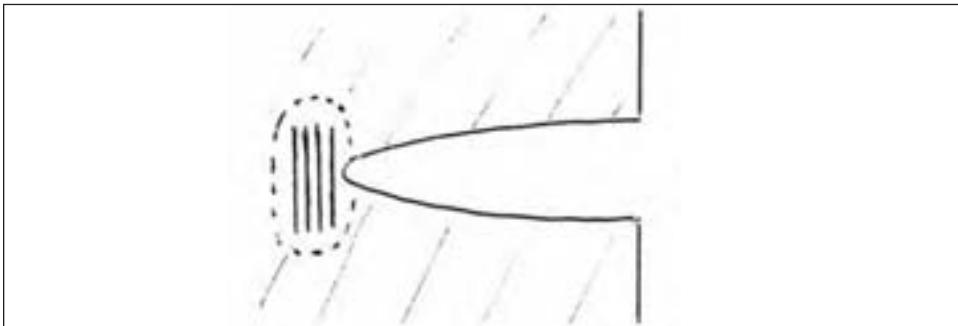
$$G = 0.62\pi\, Ee^2\, c \tag{2.10}$$

from equation 2.2, assuming for simplicity that the material is linearly-elastic. Using Equation 2.9, the growth of a crack each time the strain is applied is:

$$dc = B(G/G_o)^\alpha\, dN = B\, (0.62\pi\, Ee^2\, c/\, G_o)^\alpha\, dN \tag{2.11}$$

where N denotes the number of strain applications. By integrating from $c = c_o$ to an infi-

Figure 2.29: Strain-induced crystallization at a crack tip

nitely large value of c, the fatigue life N_f is obtained as:

$$N_f = (1/B)\, (G_o\, /0.62\pi\, Ee^2)^\alpha\, [(\alpha - 1)/c_o^{(\alpha - 1)}] \tag{2.12}$$

   Although approximate, equation 2.12 gives useful pointers to the effect of various parameters on the tensile fatigue life of rubber specimens. It shows, for example, that the fatigue life N_f decreases rapidly as the imposed strain e is increased. Taking α as 2 for natural rubber compounds, when the strain is increased by a factor of 2, the fatigue life is predicted to decrease by a factor of 16. For an SBR compound, the corresponding change

in N_f is predicted to be much more severe, by a factor of 256. Thus, the fatigue life of SBR and similar non-crystallizing elastomers falls sharply as the imposed strain is increased.

The dependence of fatigue life on the depth c of an initial defect or flaw is also large, and different for different materials. For natural rubber compounds the fatigue life is seen to be approximately proportional to 1/c, and thus is decreased by a factor of 2 if the depth of an accidental flaw is increased by a factor of 2. On the other hand, under the same conditions the fatigue life of an SBR compound is decreased by a factor of 8. Thus, fatigue failure of SBR and similar compounds is extremely sensitive to the severity of accidental nicks or flaws.

When natural rubber compounds are subjected to repeatedly-applied strains, starting from zero strain, some tearing takes place at the crack tip while strain-induced crystallites are simultaneously being formed there. The crack growth steps are generally smaller than for non-crystallizing elastomers, as discussed above. But natural rubber compounds show a remarkable resistance to fatigue cracking if the imposed strain is not reduced to zero in each strain cycle, figure 2.30. Apparently, the crystallites that develop at the crack tip, even at modest overall strains, do not melt unless the strain is reduced to zero or close to zero, and thus they persist and prevent further crack growth when the strain is increased again. No comparable effect is expected for non-crystallizing elastomers such as SBR.

Some classic observations of the fatigue life of bonded cylinders of natural rubber subjected to repeated tensile or compressive strains are shown in figure 2.31 [13]. The fatigue life N_f is seen to be a minimum when the applied strains were relaxed to zero during each strain cycle, both for tensile and compressive strains. On the other hand, if the minimum level of strain in each cycle was not reduced to zero, then the fatigue life was greatly increased, by a factor of up to 100 times. Indeed, the mechanism of failure may change altogether under non-relaxing conditions, from mechanical rupture of the elastomer molecules, now protected by crystallization, to molecular scission by reaction with atmospheric ozone.

Figure 2.30: Effect of non-relaxing strain on tensile fatigue life N of unfilled NR

NR samples are strained repeatedly to 250%. As the minimum strain is increased from 0 to 50%, the fatigue life N rises by orders of magnitude.
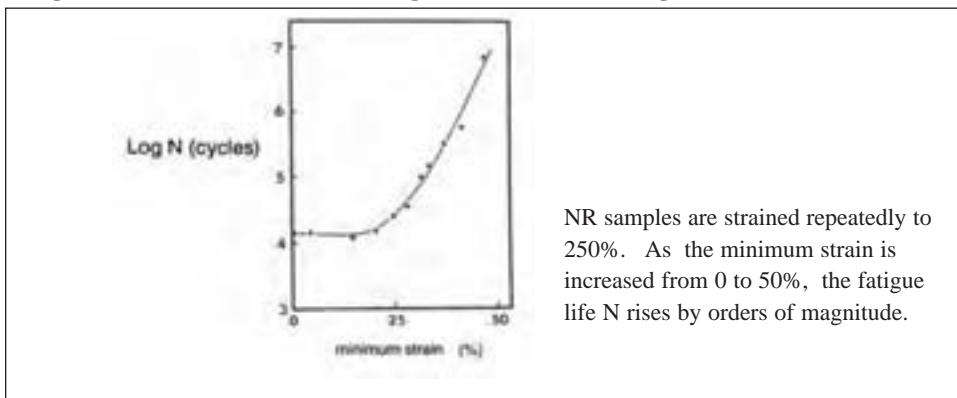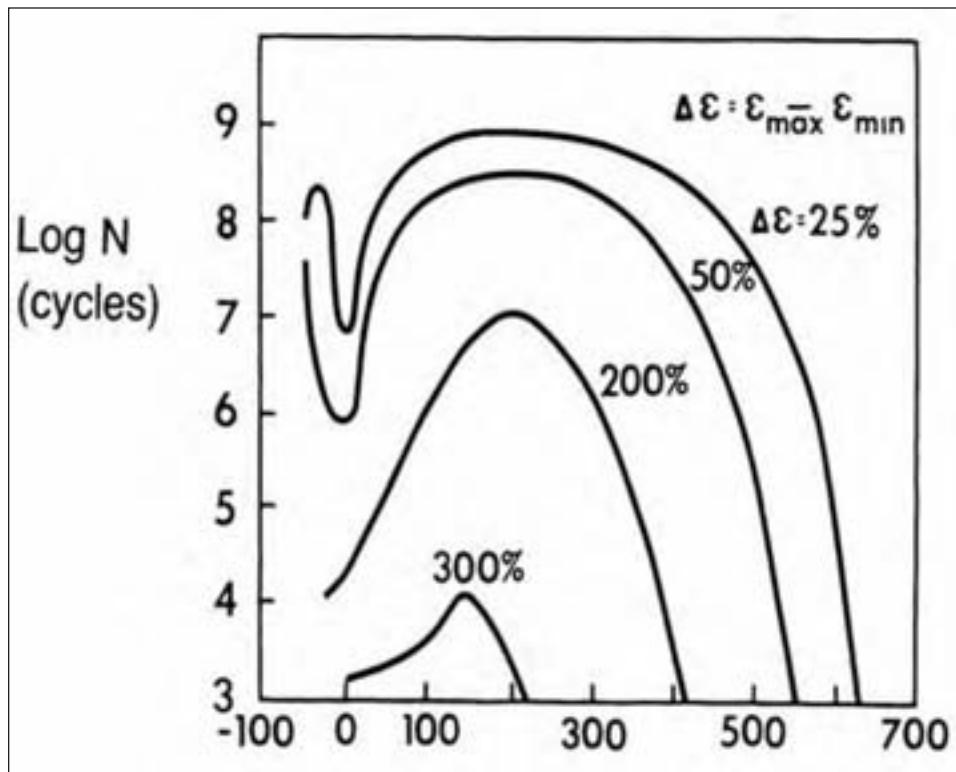
Figure 2.31: Fatigue life N for cylinders of NR cycled between a minimum strain ε_{min} and a maximum strain $\varepsilon_{min} + \Delta\varepsilon$

2.6 Failure of an adhesive bond

Fracture of the bond between rubber and another material can be treated by fracture mechanics in the same way as rupture of rubber itself. We denote the energy required to separate unit area of the interfacial bond as G_a to distinguish it from the fracture energy G of rubber itself and note that if G_a is lower than G, then the interface would be expected to separate cleanly, whereas if G_a is higher than G, then the rubber close to the interface will tear apart, leaving an attached rubber layer behind.
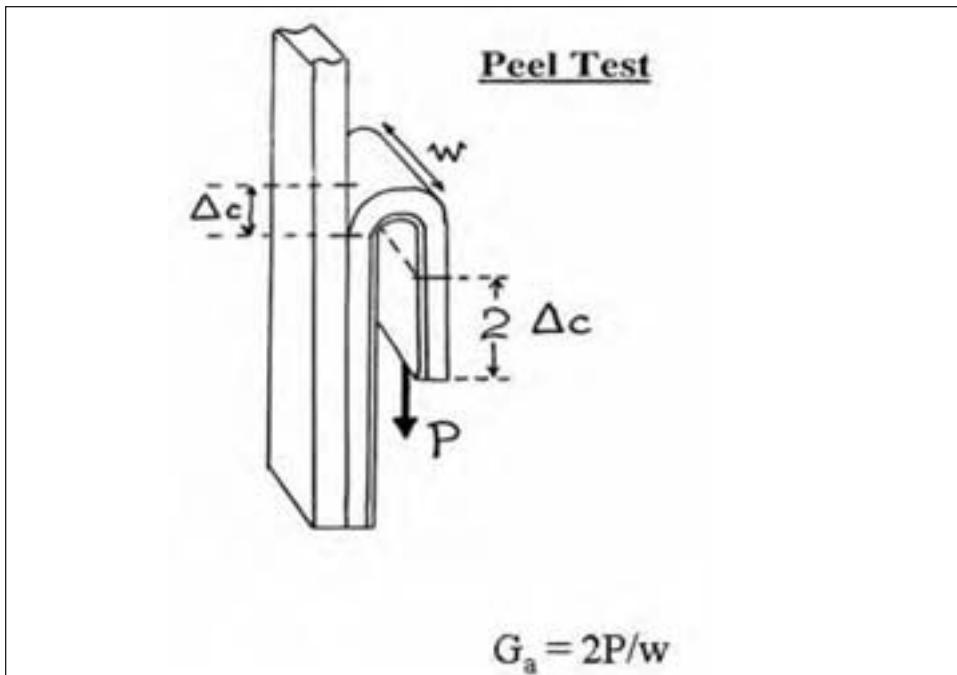
A common method of evaluating the strength of adhesion is by a peel test, figure 2.32, analogous to simple tearing, figure 2.17. G_a is given by

$$G_a = 2P/w \tag{2.13}$$

where P is the peel force and w is the width of the bonded layer.

Unfortunately, even when G_a is lower than G, failure tends to occur within the rubber, instead of at the interface, if the difference in fracture energy is not large enough. From mechanical considerations, more energy is available for fracture at a plane somewhat removed from the interface. Thus a bond may appear to be stronger than it really is. A more stringent test is needed, in which failure is induced to occur at the interface. A test of this kind, especially suitable for evaluating rubber-to-cord adhesion, is described later.

Figure 2.32: 180⁰ peel test

In tire building, layers of different rubber compounds and rubber-cord laminates are joined to construct the raw tire. These layers must adhere together during handling of the raw tire and inserting it into the tire mold for final shaping and vulcanization. Thus, good adhesion of unvulcanized rubber is an important requirement in tire manufacture. It is commonly assessed using peel tests. In this case, energy is largely dissipated in viscous processes as the unvulcanized rubber layer is pulled away. Thus, the apparent strength of adhesion reflects viscous dissipation of energy in tensile flow. Note that for this to be the major factor, the rubber must flow without breaking under a tensile flow stress that is smaller than the strength of the interfacial bond itself. This principle of optimizing energy dissipation under the constraint of a limiting stress is employed in the design of pressure-sensitive adhesives.
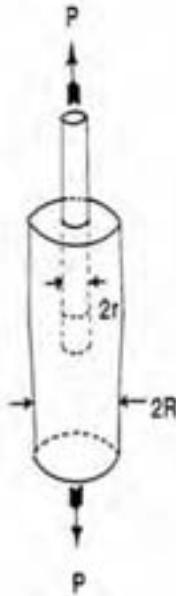
For assessing the strength of adhesion of vulcanized rubber to cords, another test arrangement, shown in figure 2.33, has been proposed. Using linear elastic fracture mechanics, an estimate of the pull-out force P is obtained as:

$$(P/A)^2 = 4\pi(r/A)EG_a \qquad\qquad\qquad (2.14)$$

for an inextensible rod or cord embedded partway in a rubber block, where r is the radius of the rod or cord, A is the cross-sectional area of the rubber block in which it is embedded, and E is the modulus of elasticity of the rubber. Because the pull-out force increases with r, i.e., as the fracture path moves away from the interface, failure in this test arrangement is induced to occur at or near the interface.

Note that equation 2.14 resembles Griffith's result for a edge crack, Equation 2.3,

because energy is again made available for fracture by stretching the lower part of the block. (The upper part is rendered inextensible by the embedded rod.)

An interesting feature of this experimental arrangement is that the total force required to pull out simultaneously n cords embedded in the same block increases in proportion to $n^{1/2}$. The reason for this surprising result is that the energy required to pull out n cords is proportional to n, whereas the energy stored in a linearly-elastic device is proportional to P^2, where P is the applied force. Experiments on wire cords embedded in rubber blocks have confirmed this result [14] which is clearly important in maximizing the strength of cord-rubber laminates.

3. Frictional sliding of rubber (see chapter 11 also)

3.1 Effect of normal load on frictional force

Conventionally, the resistance to frictional sliding of one surface on another is characterized by the Coulomb frictional coefficient μ, given by the ratio of frictional force F to normal force N :

$$\mu = F/N \tag{3.1}$$

But for soft rubber sliding on a smooth surface, the frictional force is found to be more or less constant, independent of the load N, or pressure P, as the applied load or pressure increases from small initial values, probably because complete contact is achieved between soft rubber and a smooth countersurface at quite small loads. Beyond this point, further increases in normal load cannot increase the degree of interaction between the two materials and so the frictional force no longer increases. Consequently the "coefficient" of friction decreases continuously as the pressure increases, as shown schematically in figure

2.34.

However, for harder rubber compounds sliding against a rough surface, the frictional force does increase, approximately in proportion to the applied load or pressure, and thus a "coefficient of friction" can be defined in this case that is largely independent of pressure. Apparently, contact is incomplete, figure 2.35, for harder rubber compounds such as those used in tire treads. An increase in pressure creates a larger true area of contact and hence a larger frictional force.

Figure 2.34: Dependence of friction coefficient on contact pressure
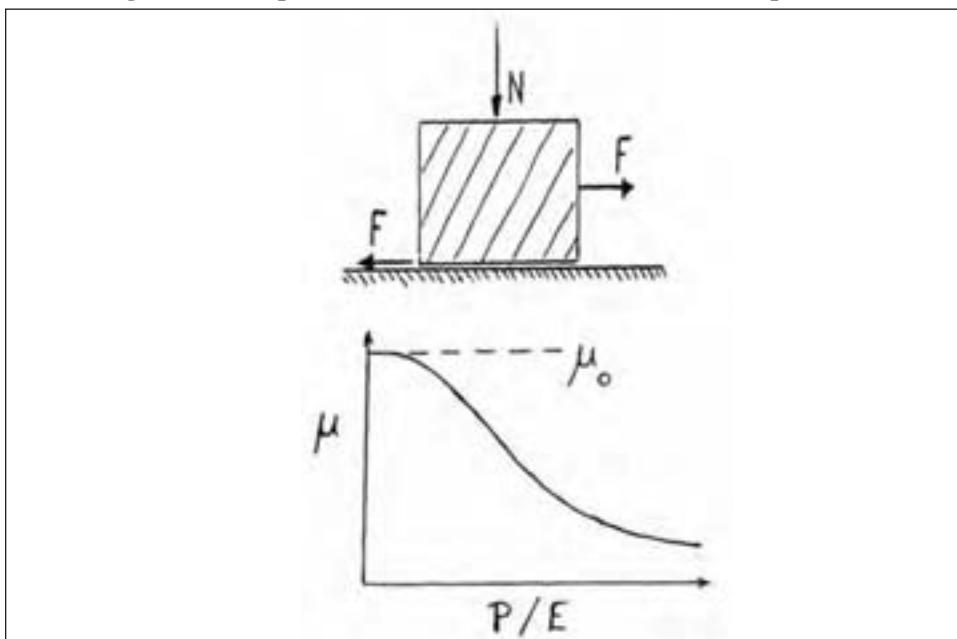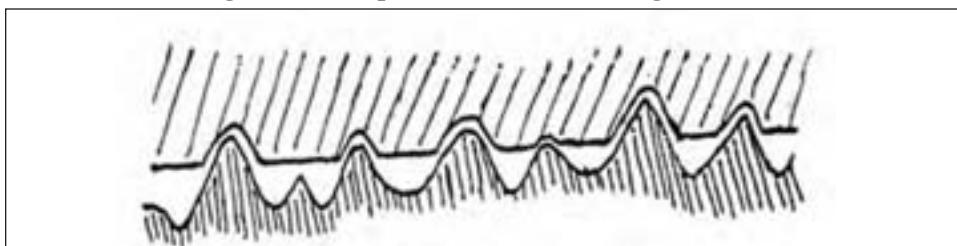
Figure 2.35: Imperfect contact on a rough surface

3.2 Rolling friction (see chapter 12)
It is helpful to consider rolling friction first, because the physical origin of the frictional drag force is clearer in this case. Consider the pressure distribution set up in the contact zone when a rubber cylinder rolls on a rigid countersurface. For a dissipative material, the center of pressure will not be located at the center of the contact zone, but displaced toward the leading edge, because stresses set up on loading are higher than those set up
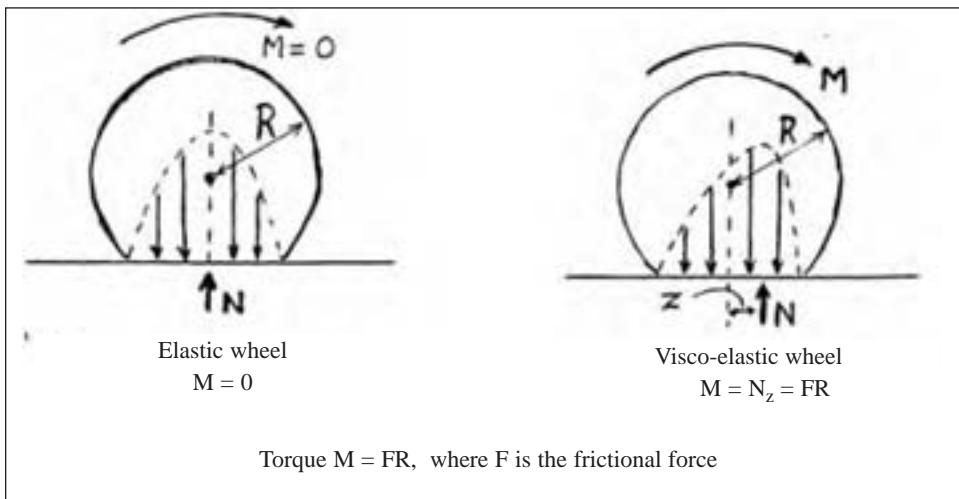
on unloading, figure 2.36. This is a universal feature of dissipative materials in general, and of viscoelastic materials in particular. Moreover, the displacement z of the center of pressure, and hence the torque M (= z F) required to maintain the motion, will depend on speed and temperature in the same way as the loss factor, tan δ [15]:

$$M = 0.33 \ (P_n \ /G^*R^2)^{1/3} \tan \delta \tag{3.2}$$

where $G^* \ [= (G^{'2} + G^{''2})^{1/2}]$ is the complex dynamic shear modulus and R is the cylinder radius. (The term in parentheses is a measure of the length of the contact zone.) This simple theory successfully accounts for rolling friction in terms of energy dissipated as rubber is compressed and released in the contact patch. But tan δ must be measured at the effective frequency of rolling (about 10 Hz at 30 mph) and at the service temperature because rolling friction depends on speed (frequency) and temperature in the same way that tan δ depends on frequency and temperature.

Figure 2.36: Rolling friction

Elastic wheel
M = 0

Visco-elastic wheel
M = N_z = FR

Torque M = FR, where F is the frictional force
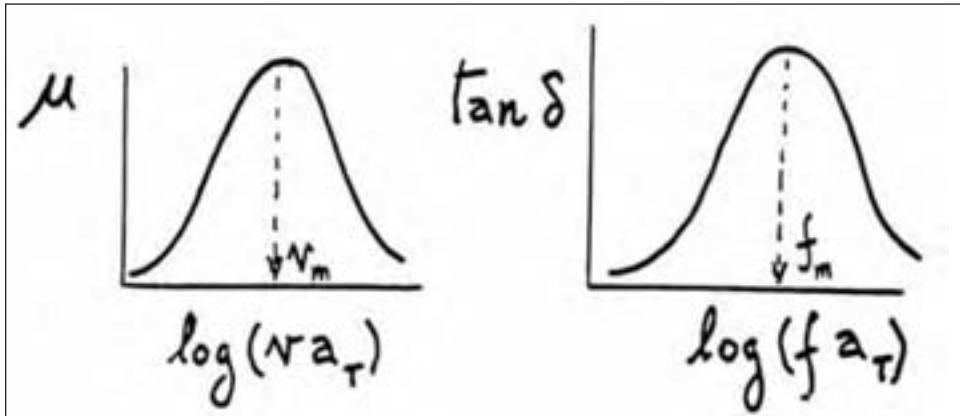
3.3 Sliding friction on a lubricated rough surface
Grosch [16] measured the friction coefficient for a nitrile rubber block sliding over a lubricated rough surface (an abrasive paper), for a wide range of sliding speeds and test temperatures. He noted that a master curve for frictional coefficient μ as a function of log (sliding speed, v) could be built up from measurements over a limited speed range at various temperatures, by applying shifts calculated from the WLF rate – temperature equivalence, Equation 1.13. The master curve obtained in this way bears a striking resemblance to the master curve for tan δ vs. oscillation frequency f, figure 2.37. By comparing the two master curves at the same reduced temperature, i.e., relative to T_g, Grosch obtained a characteristic length d, given by v_m/f_m, where v_m and f_m denote the speed and frequency at which the frictional coefficient and tan δ, respectively, exhibited a maximum, measured at the same temperature. The value of d obtained in this way was about 1 mm, approximately equal to the spacing of asperities in the rough countersurface. Thus, sliding friction on a rough lubricated surface can be attributed to energy dissipated
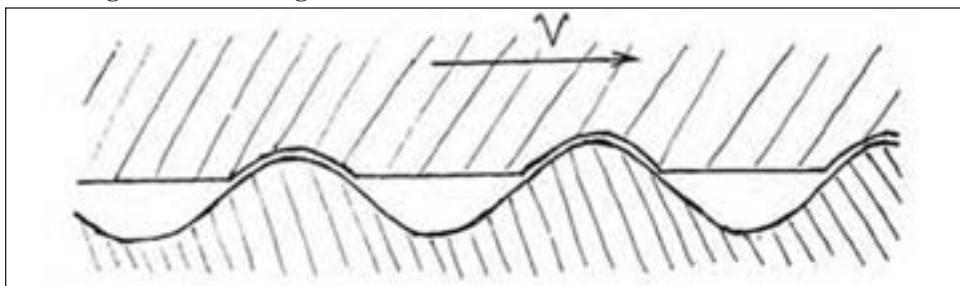
as rubber is compressed and released by passage over road asperities.

Figure 2.37: Sliding friction on a lubricated rough surface

Schapery developed a quantitative theory for the energy dissipated in lubricated sliding of a block of a simple viscoelastic solid over a sinusoidally-wavy surface, figure 2.38 [17]. In the limit, when the pressure is sufficient to bring about complete contact, the amount of dissipated energy calculated in this way corresponds to a coefficient of friction of about 0.25. This is substantially lower than the maximum coefficient of friction measured for rubber sliding on a rough lubricated surface, about 1 to 2 (similar to the maximum value of tan δ). The discrepancy has been accounted for, at least in part, on the grounds that multiple scales of roughness exist on real surfaces, with each scale giving rise to energy dissipation and hence contributing independently to the total measured friction.
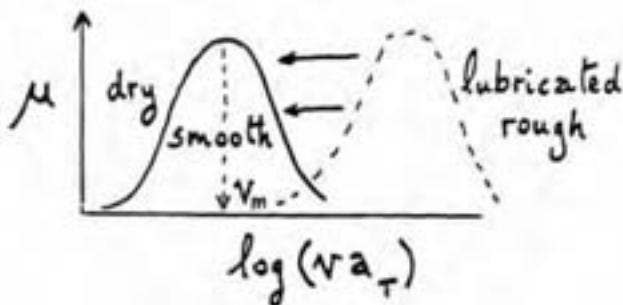
Figure 2.38: Sliding of a viscoelastic material over a sinusoidal surface

3.4 Sliding friction on dry surfaces

Grosch also studied the frictional properties for the same nitrile rubber sliding on a dry smooth surface. The results were quite similar in form to those described in the preceding section, but the curve for frictional coefficient vs. reduced sliding speed was displaced on the (logarithmic) speed scale to much lower speeds, reduced by a factor of about 10^{-5}. This is shown schematically in figure 2.39. Thus, the characteristic length d (= v_m/f_m) for sliding on a dry smooth surface was deduced to be only about 5 nm, a molecular distance, in place of 1 mm. Grosch therefore concluded that sliding friction on a dry smooth surface is due to energy dissipated as rubber sticks and slips on a molecular scale.
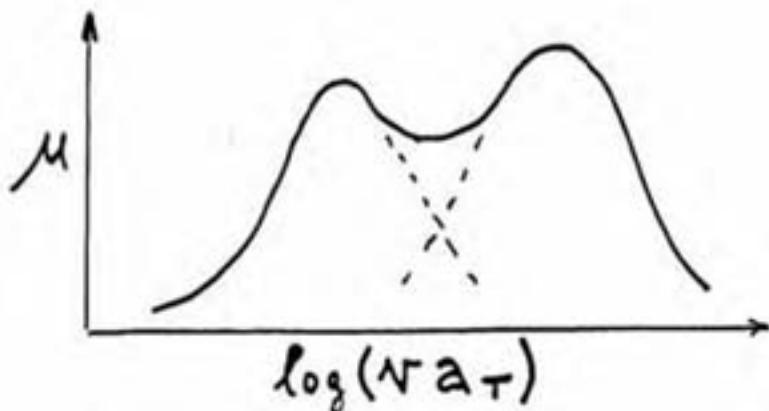
Figure 2.39: Dry sliding on a smooth surface

The characteristic length d (= v_m/f_m) is now only about 5 nm, a molecular distance.

From these model experiments Grosch was able to explain the more complex process of sliding on a dry rough surface. In this case, both dissipative processes appear, at quite different speeds corresponding to the different length scales of track asperities and molecular strands, figure 2.40. And in the case of rubber sliding on a lubricated smooth surface, sliding is frictionless because there is no mechanism for energy dissipation: both molecular contact between rubber and countersurface and deformations by asperities are now absent.

Figure 2.40: Dry sliding on a rough surface

3.5 Controlling rubber friction

Grosch's pioneering study revealed that several contributions to friction can arise at the same sliding speed from stick-slip or deformation-and-release processes occurring simultaneously at different length scales. This understanding has led to increased control of the frictional properties of real rubber compounds on real surfaces. For example, the importance of road textures and micro-roughness has become recognized. Moreover, the rubber compounder can adjust tan δ by using elastomers with different glass temperatures, by using blends of two or more elastomers, and by incorporating plasticizing oils. Values of tan δ appropriate to the road surface, sliding speeds and operating temperatures encoun-

tered in service can be selected so that tires exhibit the desirable and yet apparently contradictory features of low rolling resistance and high sliding friction.

4. Abrasion (see chapter 13 also)
4.1 Abrasion during sliding
Schallamach [18] suggested that a simple proportionality exists between the volume abraded away when a rubber block slides over a rough surface and the frictional work expended in sliding, figure 2.41. This leads to the relation:

$$\delta = AW_f \tag{4.1}$$

where δ is the loss (m) in height of the block, W_f is the work expended in sliding per unit of apparent contact area (J/m^2), and A is a coefficient, termed "abradability", (m^3/J). Typical values of A ranged from 0.1 - 0.5 mm^3/J. They depended markedly on the test speed and temperature, in accordance with the WLF rate-temperature dependence, Equation 1.13. Minimum abrasion occurred at high speeds, near the glass transition, when the tear strength is a maximum, figure 2.42. Indeed, the abradability was found to follow an inverse proportionality to the strength of the rubber compound, represented by the work U_b (J/m^3) of tensile rupture,

$$A \approx C/U_b \tag{4.2}$$

where C is a fitting constant. Schallamach noted that the correlation shown in Equation 4.2 required that the tensile breaking energy U_b be measured at high rates of strain, about 10^4 strain units per sec.

The empirically-determined constant C, about 1×10^{-3}, represents the ratio of the volume of rubber abraded away to that volume which would be brought to rupture if an amount of strain energy equal to the work expended in sliding friction were applied to stretch the rubber uniformly up to the breaking point. It is clear that only a small fraction of the frictional work causes rupture - the major part, over 99%, must be dissipated in other ways.

Figure 2.41: Measurement of abrasion
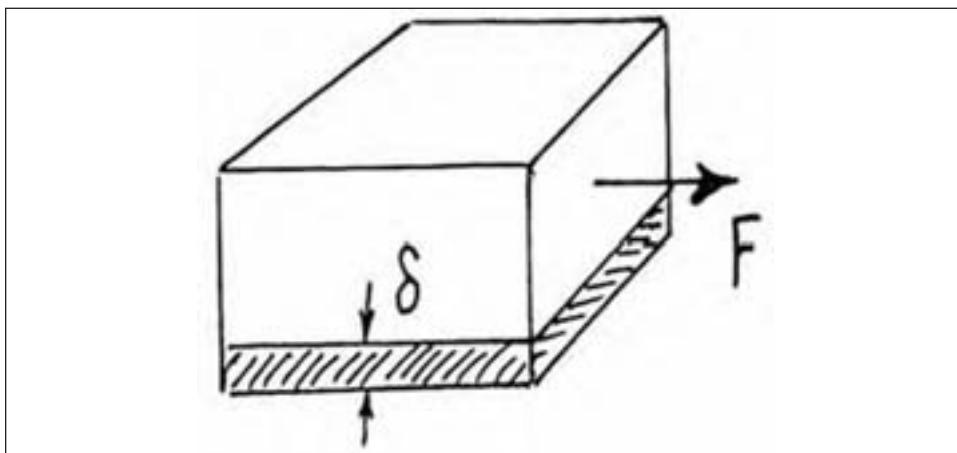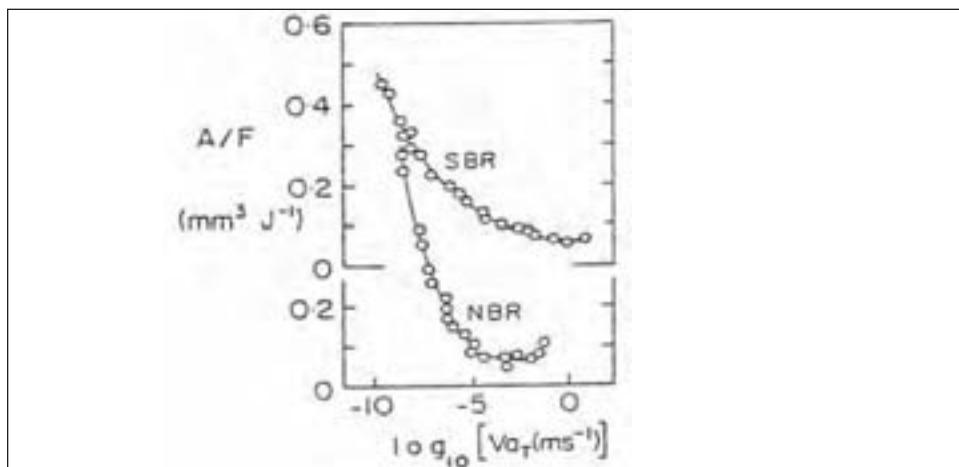
Figure 2.42: Abradability A under frictional force
F vs. reduced sliding velocity va$_T$

Later work showed that equation 4.1 was inadequate - the rate of abrasion is not strictly proportional to the work expended in sliding but increases at a faster rate. A modified relation was proposed [19]:

$$d = A'W_f^{\alpha} \tag{4.3}$$
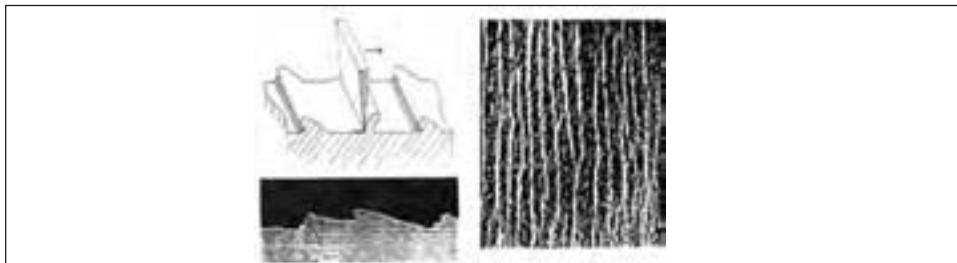
with an exponent α of about 1.3 instead of 1.

It should be noted that these experiments were carried out by sliding a rubber block over a rough abrasive surface. In other experiments, where a rubber block was abraded by scraping it with a knife-blade held at right angles to the rubber surface, the rates of abrasion were consistent with equation 4.3 only when much higher values of α were used, between 2 and 3 [20-22]. Thus, these two abrasion experiments lead to conflicting results, indicating that the rate of abrasion does not depend solely on the amount of frictional work. In order to predict the rate of abrasion it is clearly necessary to take into account the sharpness of the scraper, as well as the frictional work expended in sliding.

4.2 Schallamach abrasion patterns

When rubber is abraded by sliding a scraper repeatedly in the same direction, a character-istic surface pattern appears. It takes the form of a series of ridges lying at right angles to the sliding direction, with abrasion occurring mainly at the base of the ridges, as shown in figure 2.43 [23]. This mode of abrasion of soft rubbery materials is known as a Schallamach abrasion pattern. It is strikingly different from the abrasion of hard materials, where long scratches are formed parallel to the sliding direction. The characteristic abrasion pattern in rubber is attributed to repeated erosion at the base of ridges which become bent backwards and stretched by the frictional force, as shown schematically in figure 2.44. Thus, regions of the surface lying on the lee slopes are protected from abrasion. The abrader slides along, and off, the stretched ridge tip and makes contact again at the base of the next ridge. Repeated abrasion taking place at the base of ridges causes

Figure 2.43: Abrasion by a scraper: "Schallamach abrasion pattern"

them to become progressively undercut. Eventually the tips fall off as large particles of debris, 50 to 1000 µm in size.

Thus two abrasion processes occur: a small-scale intrinsic abrasion at the base of ridges resulting in small particles, 1 – 5 µm in size, and detachment of relatively large fragments from the ridge tips. Although much fewer in number, the large particles generally account for most of the weight loss.

Because the ridges of a Schallamach abrasion pattern are unsymmetrical, leaning towards the abrader, they can be used to deduce the direction of sliding. For example, if the center rib of a tire exhibits abrasion ridges lying perpendicular to the circumference, then abrasion must have taken place as a result of fore-and-aft sliding motions. If side ribs have abrasion ridges lying at an angle to the tire circumference, then sliding occurred primarily in that direction. Moreover, because an abrasion pattern is unidirectional, leaning forwards in the direction of motion of the rubber, one can deduce whether the ribs slid outwards or inwards against the abrading surface - the road.
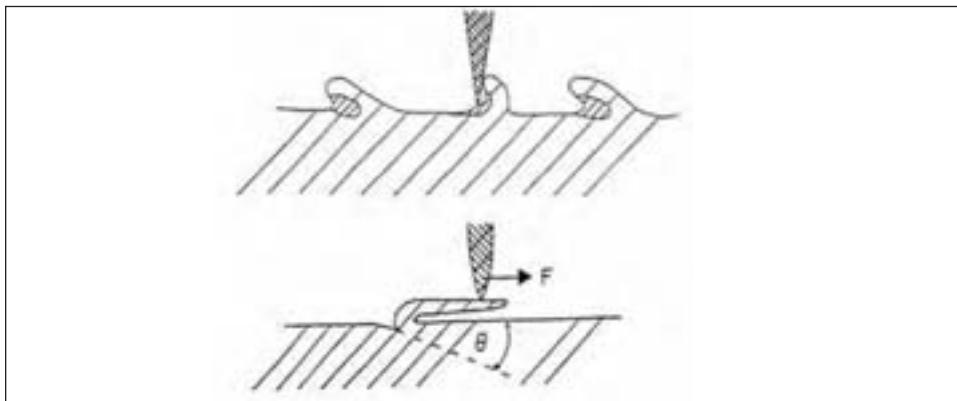
Both the ridge height and ridge spacing increase with increasing severity of wear, i.e., for sharp abrasives, with high frictional forces, and for soft rubber. When the frictional force is increased to reach the tear strength of the rubber, then the rate of abrasion abruptly increases and the mode changes to a gross gouging of the surface without a characteristic pattern being formed.

The Schallamach abrasion pattern also does not form if the direction of sliding is changed repeatedly. Abrasion then takes place more slowly and on a finer scale – a few µm rather than the 50 µm to 1000 µm characteristic of pattern spacings – by an intrinsic abrasion process in which small particles of rubber, only a few µm in size are plucked out from the surface by frictional forces. This process is closely related to tensile rupture, as described in section 4.1.

4.3 Abrasion as fatigue crack growth

In pattern abrasion under moderate frictional forces, the ridges move slowly backwards against the direction of sliding as a result of the gradual loss of ridge tips. This process may be regarded as the gradual advance into the rubber of a series of cracks, each crack corresponding to the leading edge of a ridge. A theoretical treatment of pattern abrasion along these lines has been developed by Southern and Thomas [20, 21], relating the rate of abrasion to the crack-growth resistance of the rubber.

A single ridge under a frictional force F is shown in figure 2.44. The pseudo-crack grows at the base of the ridge, at a shallow angle θ to the surface of the rubber. The energy G available for tear propagation is given by $F(1 + \cos \theta)$. The crack will therefore
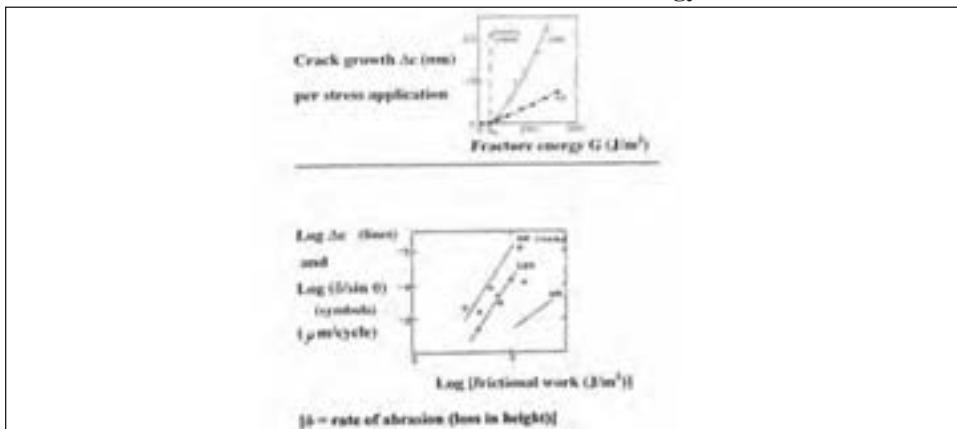
Figure 2.44: Abrasion as a fatigue cracking process

advance by a distance Δc, given by equation 2.8. This leads to a loss in thickness of rubber of $\Delta c.\sin \theta$. Thus,

$$A = DF^n(1 + \cos \theta)^n(\sin \theta)/G^n \qquad (4.4)$$

The angle θ may be estimated by direct inspection of the way in which abrasion patterns move over the surface during wear. It is found to be small, 5 – 10 degrees. Turner has accounted for these small values by considering the severe tilt of the principal tension directions in highly-sheared blocks [24]. All other terms in equation (4.4) can be determined from tear-growth measurements. Thus, the theory does not involve any arbitrary fitting constants. Figure 2.45 shows a comparison by Southern and Thomas of rates of abrasion (points) with rates of crack growth (lines). Good agreement was found in two cases: SBR and an isomerized NR (non-crystallizing). But NR (triangles), which has excellent fatigue resistance but poor abrasion resistance, is anomalous.

Thus, although the theory is remarkably successful in accounting for the rate of abrasion of two unfilled elastomers, the agreement is unsatisfactory for natural rubber which abrades much more rapidly than crack-growth measurements would predict. It is

**Figure 2.45: Crack growth vs fracture energy
and abrasion rate vs frictional energy**

possible that, under abrasive conditions, natural rubber does not undergo strain-induced crystallisation and therefore lacks the fatigue resistance that it usually demonstrates, and cracks grow rapidly. It should be noted also that filler-reinforced rubber compounds abrade more slowly than would be predicted on the basis of crack-growth measurements. Further work is needed to clarify these points, which are of great practical importance.

4.4 Chemical effects

Under mild abrasion conditions, chemical changes within the elastomer become important in abrasion [25]. The particle size remains small but in some cases the particles show signs of molecular rupture and adhere together to form larger particles, several mm in size. Indeed, filled compounds of cis-polyisoprene and poly(ethylene-co-propylene), for which molecular rupture under shearing conditions is well known, both develop a tarry liquid surface during abrasion. In contrast, cis-polybutadiene shows no signs of structural deterioration - the debris appears to be unchanged chemically and is not sticky. Evidently, different chemical changes are undergone by different elastomers.

Two reactions can occur during abrasion: oxidative degradation due to frictional heating in the contact zone and mechano-chemical degradation initiated by shear-induced rupture of chemical bonds. Present evidence favors the latter process. For example, in the absence of oxygen the abrasion of cis-polyisoprene changes to resemble that of cis-polybutadiene whereas the abrasion of poly(ethylene-co-propylene) is unaltered. These observations are in accord with the known response of these materials to free- radical reactions.
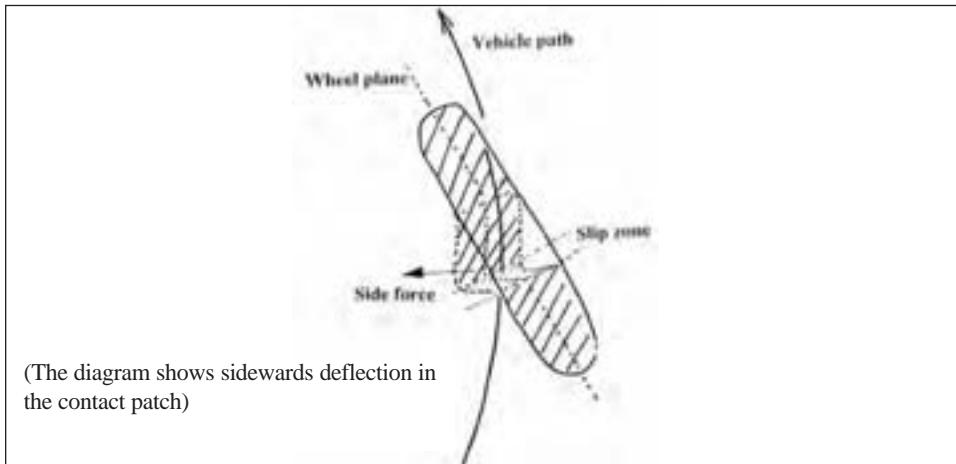
Surprisingly, the products of chemical changes within the elastomer are capable of causing rapid erosion of metal abraders [26]. For example, a stainless steel knife-blade abrader becomes blunted during abrasion and the volume of metal removed from the blade is substantially greater when the elastomer itself undergoes chemical deterioration. This chemical erosion of the metal scraper is attributed to attack of reactive polymeric species, probably free radicals, during frictional contact. Similar "chemo-abrasion" has been observed with other polymers when molecular rupture takes place in sliding against a hard countersurface [27].

4.5 Wear of slipping wheels [28] (see chapters 7 and 13)

We turn now to predicting the rates of wear of tires from laboratory measurements of the rate of abrasion of tread compounds, represented here by the abradability A (mm^3/J). For simplicity, we assume that the rate of abrasion is proportional to the frictional work W expended in sliding, although as described in preceding sections this is a gross approximation. Nevertheless, it reveals the main factors governing tire wear.

Figure 2.46 shows the sideways (lateral) deflection of the contact patch of a tire as a vehicle corners. The associated side force S set up at the tire-road interface is needed to enable the vehicle to follow the curved path. The lateral deflection increases progressively from the front of the contact patch, where the tire first makes contact with the road, towards the rear. When the frictional limit is exceeded, the tread starts to slide back to regain its undeflected state. Assuming that the tire is linearly-elastic under side forces, and that the total lateral deflection is small so that sliding back occurs only at the rear of the contact patch, the total side force S is given approximately by $L^2\theta/2C$, where L is the length of the contact patch, θ is the slip angle between the direction of travel and the direction in which the tire is steered, and C is the compliance of the tire for lateral deflections for unit length of tire circumference. (The units of C are m^2/N.)

Figure 2.46: Tire distortion and side-slip in cornering

(The diagram shows sidewards deflection in the contact patch)

For a given side force S, the slip angle θ and hence the sliding distance x_{max} (= θL) will be greater for tires that have greater compliance. Thus, abrasion will be greater for tires that are more compliant for sideways deflections.

The amount of energy expended in deforming the tire is given approximately by $S\theta L^2/2 = S^2 C/L$. However, only a fraction R of this energy is expended in sliding, where R is the resilience of the tire, because the tire will not return all of the input energy. Thus, the expected rate of wear of a cornering tire is given by

$$d \propto AS^2CR/L \tag{4.5}$$

and is clearly affected by several other factors besides the abradability A of the tread compound. The lateral compliance C of the tire will contain a contribution from deformation of the carcass in addition to the tread compliance. The contact patch length L is of course governed by structural aspects of the tire and will be insensitive to properties of the tread compound. And the most significant factor in tire wear is seen to be the side force S, largely set up the driver. As far as the tread compound is concerned, three physical properties are important: intrinsic abradability A, sideways compliance C, and its contribution to deformational energy losses represented by the effective tire "resilience" R. These properties are not necessarily related. For example, a harder, less compliant compound may well be less resilient. Thus a successful tread formulation requires a judicious balancing of sometimes conflicting requirements.

Although, for simplicity, the foregoing discussion dealt with the case of a cornering tire, the same factors govern wear under driving and breaking forces. The compressive or stretching deformation of the tire increases through the contact patch until slip takes place when the local circumferential force at the interface exceeds the maximum that friction can support. Strain energy built up in the tire by the circumferential deformation is then released to provide the work of sliding against friction. Note, however, that in driving and breaking the relevant tire compliance is in the circumferential direction. It may be considerably different from the lateral tire compliance (C in the previous paragraph), depending on the geometry of cords and belts.

5. Aging of rubber

Rubber undergoes profound changes on storage that are accelerated at higher temperatures. Deleterious changes occur in tire properties after storage at ambient temperatures for five years or after use on cars for similar periods [29]. They are caused by a variety of chemical reactions:

(i) Ozone attack. Although the concentration of ozone in the atmosphere is quite small, typically only a few parts per 100 million, ozone reacts rapidly and efficiently with the unsaturated elastomers commonly used in tire compounds, leading to molecular scission. However ozone cannot penetrate deeply into the material – reaction takes place at the exposed surface and produces a relatively-innocuous thin degraded surface layer, about 20 μm thick, which protects the interior. However, if a small tensile strain of the order of 10% is present in the rubber surface, then the scission reaction with ozone causes characteristic sharp cracks to form in the surface and grow inwards, continuously exposing new material to further attack. The cracks grow surprisingly rapidly. They become about 1mm deep after only two weeks exposure of an unprotected rubber compound to normal outdoor air with an ozone concentration of about 5 parts per hundred million. Thus ozone cracking is potentially a serious problem in tire sidewalls where tensile stresses are commonly present both in storage and in use. Special additives, termed antiozonants, inhibit ozone cracking when added to the rubber compound in sufficiently large amounts, about 3 %, probably by competing with rubber molecules for reaction with ozone. Butyl rubber is much less susceptible to attack by ozone than other common elastomers, at least at ambient temperatures, because it contains only a relatively small fraction of reactive C=C bonds in the molecular backbone.

(ii) Oxidation. Another cause of aging is reaction with atmospheric oxygen. Oxidation is slower than ozonolysis and oxygen therefore penetrates for some distance into the material before reacting. Thus oxidation does not cause cracking directly although the oxidized material is often brittle and cracks on flexing. Depending on the relative rates of diffusion and reaction, the affected depth can range from several mm at ambient temperatures, when the process takes years to reach a significant stage, or a fraction of 1 mm at elevated temperatures when oxidation is rapid, taking only a few hours. Typical hydrocarbon elastomers undergo an autocatalytic reaction that results in addition of oxygen groups to the molecule and formation of new crosslinks by interaction with neighboring molecules. As a result the material generally becomes harder and eventually brittle. However another, generally minor, consequence of the complex oxidation reaction is occasional molecular scission and hence softening. This provides a convenient way of characterizing the sensitivity of a rubber compound to oxidation. Samples are stretched and aged in an oven at various temperatures, usually in the range $70^O C$ to $130^O C$, and the tensile stress is monitored continuously over a period of several days. As oxidation proceeds and some elastomer molecules break, the stress falls and gives an indication of the extent of oxidation. The rupture reaction follows an Arrhenius dependence on temperature to a first approximation, with an activation energy of about 25 kcal/mole. Thus an increase in temperature of $10^\circ C$ causes an increase in rate of oxidation by a factor of about 2x.

Another way of assessing the sensitivity of a rubber compound to oxidation is to expose samples for various periods at elevated temperatures and then measure the remaining strength and extensibility at room temperature. A typical specification for aging resistance would require that the tensile strength does not change by more than a specified fraction, say 20%, and the extensibility does not decrease by more than a

specified fraction of the original value, say 30%, after a period of aging of 7 days at 70$^\text{O}$C or 22 h at 100$^\text{O}$C.

(iii) Additional vulcanization. Vulcanization does not stop when the cured compound is removed from the mold. Continued curing takes place subsequently but at much lower rates, of course, depending on the temperature. As a result if tires are stored or used at elevated temperatures the material hardens as more crosslinks are introduced, or softens (a phenomenon termed reversion) as those crosslinks already formed gradually decompose. These processes are a consequence of a series of complex reactions involving elastomer molecules, existing crosslinks, residual sulfur, activators and accelerators, and byproducts of the various intermediary steps in the crosslinking reaction. In conventional aging measurements these processes are difficult to distinguish from the effects of oxidation, but they can be studied separately by aging samples in an oxygen-free environment. In thick rubber articles, material far from the surface, say over 10 mm deep, may undergo solely anaerobic aging because oxygen reacts before it diffuses so deeply. Passenger car tires, on the other hand, operate for long periods at moderate temperatures, so that oxygen may diffuse extensively before reaction. Thus oxidation is regarded as the normal mode of aging of tire components.

(iv) Weathering. This mode of aging is rather ill-defined. Insofar as new aging processes occur, other than oxidation and ozone attack, they appear to be associated with irradiation by UV and sunlight. Radiation causes free-radical reactions that can initiate or catalyze oxidation and ozonolysis, as well as being itself a direct cause of crosslinking and/or molecular scission.

6. Concluding remarks

Rubber compounds used in tires today are astonishingly effective and durable, as a result of a long period of semi-empirical research and development. Even better materials could presumably be developed with a better understanding of the mechanics and chemistry of strength, fatigue, friction and wear. An outline has been given of our present understanding of basic rubber science but there are clearly substantial and serious deficiencies, notably in the areas of filler reinforcement and chemical changes on aging, that call for further study.

Bibliography

"The Vanderbilt Rubber Handbook", ed. by R. O. Babbit, R. T. Vanderbilt Company, Norwalk, 1978.

"The Pneumatic Tire", 2nd. ed., S. K. Clark (ed.), U. S. Department of Transportation, National Highway Traffic Safety Administration, Washington, D.C., 1981.

"Science and Technology of Rubber", 2nd ed., J. E. Mark, B. Erman and F. R. Eirich (eds.), Academic Press, New York, 1994.

"Engineering with Rubber: How to Design Rubber Components", 2nd. ed., A. N. Gent (ed.), Hanser Publishers, Munich, 2001.

References

1. L. Mullins, Rubber Chem. Technol. **42**, 339 (1969).

2. A. R. Payne, J. Appl. Polymer Sci. **7**, 873 (1963).

3. J. D. Ferry, "Viscoelastic Properties of Polymers", 3rd. ed., John Wiley & Sons, New York (1980).

4. A. A. Griffith, Phil. Trans. Roy. Soc. **221**, 163 (1920).

5. J. P. Berry, Chap. 2 in "Fracture: An Advanced Treatise; Vol.7. Fracture of Non-Metals and Composites", ed. By H. Liebowitz, Academic Press, New York, 1972.

6. G. J. Lake and A. G. Thomas, Proc. Roy. Soc. (London) **A300**, 108 (1967).

7. T. L. Smith, J. Polymer Sci. **32**, 99 (1958).

8. W.-J. Hung, Ph.D. Dissertation, Polymer Science, The University of Akron (2001).

9. A. N. Gent and S. M. Lai, J. Polymer Sci: Part B: Polymer Phys. **32**, 1543 (1994).

10. W. G. Knauss, in "Deformation and Fracture of High Polymers", ed. by H. H. Kausch, J. A. Hassell and R. I. Jaffee, Plenum Press, New York, 1974, pp. 501-540.

11. K. A. Grosch, J. A. C. Harwood and A. R. Payne, Nature **212**, 497 (1966).

12. A. N. Gent, M. Razzaghi-Kashani and G. R. Hamed, Rubber Chem. Technol. **76**, 122 (2003).

13. S. M. Cadwell, R. A. Merrill, C. M. Sloman and F. L. Yost, Ind. Eng. Chem., Anal. Ed. **12**, 19 (1940).

14. A. N. Gent, G. S. Fielding-Russell, D. I. Livingston and D. W. Nicholson, J. Materials Sci. **16**, 949 (1981).

15. J. A. Greenwood, H. Minshall and D. Tabor, Proc. Roy. Soc. (London) **A259**, 480 (1961).

16. K. A. Grosch, Proc. Roy. Soc. Lond. **A274**, 21 (1963).

17. R. A. Schapery, Tire Sci. Technol. **6**, 3 and 98 (1978).

18. A. Schallamach, J. Polymer Sci. **9**, 385 (1952); K. A. Grosch and A. Schallamach, Trans. Inst. Rubber Ind. **41**, 80 (1965).

19. A. Schallamach, Rubber Chem. Technol. **43**, 701 (1966).

20. D. H. Champ, E. Southern and A. G. Thomas, Org. Coat. Plast. Chem. 34(1), 237, (April, 1974).

21. E. Southern and A. G. Thomas, Plast. Rubber: Mater. Appl. **3**, 133 (1978).

22. A. N. Gent and C. Nah, Rubber Chem. Technol. **69**, 819 (1996).

23. A. Schallamach, Rubber Chem. Technol. **41**, 209 (1968).

24. D. M.Turner, unpublished results.

25. A. N. Gent and C. T. R. Pulford, J. Appl. Polymer Sci. **28**, 943 (1981).

26. A. N. Gent and C. T. R. Pulford, J. Materials Sci. **14**, 1301 (1979).

27. G. V. Vinogradov, V. A. Mustafaev and Y. Y. Podolsky, Wear **8**, 358 (1965).

28. A. Schallamach and D. M. Turner, Wear **3**, 1 (1960).

29. T. Kataoka, P. B. Zettterlund and B. Yamada, Rubber Chem. Technol. **76**, 507 (2003).

Test Questions

1. If a rubbery material has a small-strain elastic modulus **G** in shear of 1 MPa, what is small-strain elastic modulus **E** in tension?

What is the approximate value of International Rubber Hardness (IRHD)?

What is the value of the coefficient **C_1** in the neo-Hookean strain energy function, W= C_1 $(\lambda_1^2 + \lambda_2^2 + \lambda_3^2 - 3)$?

If a thin block of the same material with an area of 100 x 100 mm was subjected to a shear force of 10 kN, what would be the angle of heel (the shear angle)?

2. A constrained tension test is one in which the sample is not free to contract laterally when it is stretched. If a sample of the above material is stretched in constrained tension by 200%, what are the values of the stretch ratios λ_1, λ_2, λ_3?

How much energy **W** is stored per unit of volume?

3. An uncrosslinked sample of a "raw" (i.e., uncrosslinked) elastomer with a T_g of - 90°C has a flow viscosity of 10^8 Pa.sec. at room temperature (20°C).

[Note: viscosity is inversely proportional to molecular mobility.]

What would the viscosity be at 120°C?

What would the viscosity be at - 40°C?

4. If tan δ for a lightly-crosslinked sample is 0.1 when measured at a frequency of 10 Hz at 20°C, at what frequency would tan δ again be 0.1, if the test temperature is now 120°C?

5. Rebound resilience is used as a rough measure of energy dissipation and rolling resistance. It is measured at a low temperature, say 0°C. The contact time is quite short, about 2 msec, equivalent to a test frequency of about 250 Hz. Under these test conditions, are the results relevant to the rolling resistance of a tire in service, at say 50 mph and at a temperature of 60°C?

If the tread material has an effective T_g of – 50°C, what test temperature would make the measurement of rebound resilience more relevant to the service conditions?

6. In a test for adhesion of cured sheets of rubber, two wide strips are bonded together over a narrow section, 20 mm long and 6 mm wide. The peel force P is measured as the strips are peeled (torn) apart. If P is 48 N, what is the strength G of adhesion?

If the speed of tearing was increased from 1 mm/sec to 100 mm/sec, what increase would you expect in the tear force P, approximately: 50%, 100%, 500%, 1000%?
If the test temperature was raised, would F increase or decrease?

Chapter 3
Tire Cord and Cord-to-Rubber Bonding

by E. T. McDonel

1. Textile cord

A number of references give detailed and comprehensive information on the chemistry, production, and properties of today's tire textiles (1-5). The chapter by Takeyama, Matsui, and Hijiri in the 1981 edition of the "Mechanics of Pneumatic Tires" provides an in-depth review of tire cord technology that is still current. The other references contain information on all aspects of the chemistry, manufacture, processing and physical properties of industrial cords for tires.

The present discussion will review current use and current trends for industrial textiles in tires as well as the physical attributes of cords now used. Textiles developed for use in tires are a small but exacting part of the huge textile industry. The average tire engineer, unless specializing in this area, is not always familiar with textile vocabulary, the chemical composition of tire textiles, the manufacturing process, the rationale for selecting certain textiles for certain tires, possible deficiencies of textiles in some applications, and the very important need for excellent cord-to- rubber adhesion in all applications. This chapter will provide an overview of these topics.

Tire textile market

The pneumatic tire performs a unique function in the transportation industry due to its deformation and damping characteristics that provide ready vehicle mobility in all terrains and environments. Billions of tires are in use, ranging in technical needs from tires for bicycles and animal-drawn vehicles to space shuttle landing gear. Carcass and belt textiles (along with the bead wire) provide essentially the whole strength of the pneumatic tire.

In 1993, tire textile fibers used in North America were approximately 55% polyester, 43% nylon, and 2% rayon (6). Worldwide, the mix was 57% nylon, 24% polyester and 19% rayon. In 1997 North American steel tire wire cord capacity was reported as 295,000 metric tons and bead wire capacity as 164,000 metric tons (30). Today passenger and light truck tires are over 90% radial, with polyester replacing nylon and rayon in the carcass. Steel cord predominates in the belt. Development of "run- flat" tires in Europe has resulted in renewed interest in rayon. High-speed tires continue to employ a rayon or polyester carcass, while nylon dominates in heavy duty bias-ply tires. In North America it is estimated that tire shipments in 2002 were approximately 303 million passenger, 50 million light truck, and 23 million medium/heavy duty truck units (7). Table 3.1 summarizes tire usage in 2001. Over 99% of US passenger tires were radial with 98% having a polyester and 2% a rayon carcass, and with 97% steel, 2% aramid and 1% nylon (both of the latter used in belt overlays) in the belt. 98% of light truck tires had a polyester carcass and 2% a rayon carcass, with 97.5% steel, 1.5% aramid, and 1% nylon (both used as belt overlays) in the belt. Medium truck tires were 94% replacement radial and 99% OE radial using all-steel or nylon carcass and steel belt. Heavy-duty truck tires were 62% replacement radial and 56% OE radial using all-steel construction or nylon carcass and steel belt. Bias truck tires use a nylon carcass.(8). The total usage of textiles in radial passenger and light tires may be estimated by noting that steel belts comprise 10-12% of the tire weight and carcass cord about 5%, thus a typical passenger tire

would contain about 1 kilogram (2.2 pounds) of steel cord and 0.5 kilograms (1.1 pounds) of polyester cord.

Table 3.1: Textile cord makeup of US tires - 2001

Belt Material	Steel	Aramid	Nylon
Passenger/Light Truck			
OE	97	2	1
Replacement	99	1	0
Carcass Material	Polyester	Rayon	Nylon
Passenger			
OE	98	2	0
Replacement	98	2	0
Light truck (radial)			
OE	100	0	0
Replacement	97	2	1
Light Truck (bias)			
OE	0	0	100
Replacement	22	0	78

Evolution of pneumatic tire fabrics

Tire fabrics have changed in response to the constant demand for better tire performance. Table 3.2 provides an historical summary of this evolution. The early pneumatic tires developed in the 1880s for bicycles by J.B. Dunlop and applied to automobiles in the 1890s used expensive Irish flax. Cotton soon replaced flax and remained the major tire textile until after World War II, but it has been phased out since the mid-1950s. Continuous filament viscose rayon and steel cord (France) were introduced in the late 1930s. Nylon became generally available for tires in the late 1940s and has met the needs of heavy-duty tires in large truck, earthmover, and aircraft tires. However, rayon held sway in passenger tires, particularly for new cars (O.E.), because of poor ride characteristics with nylon due to its lower dimensional stability. Polyester cord was first introduced by Goodyear in the early 1960s to provide   better strength than rayon and better dimensional stability than nylon. Polyester has gone through several technical improvements to surmount early shortcomings and has become the dominant textile for passenger and light truck radial carcasses in North America and has increasing use worldwide.

Brass-plated steel cord introduced in North America in 1955 is dominant in radial tire belts. Fiber glass belts introduced in belted-bias tires in 1967 can give good radial belt performance but for a number of reasons fiber glass was not accepted by the market and has been totally phased out. Aramid fiber was introduced in 1974 by DuPont. It has shown slow but steady growth, particularly in radial tire belts, but its high cost is a deterrent.

All of the presently-employed textile materials are continuously improved through modifications in polymerization, drawing, and heat setting during cord manufacture.

Table 3.2: Evolution of pneumatic tire fabrics

Cord	Introduced	Comments
Irish flax	1888	- Staple fiber/no adhesive, expensive
Cotton (square woven)	1900	- Staple fiber/ no adhesive, lower cost
Cotton (cord)	1920	- Same as above, lighter weight
Steel cord (Europe)	1937	- Used in first radial tires, copper plated for adhesion
Rayon	1938	- Viscose continuous filament, RFL/NR adhesive cord dip required
Nylon (commercial)	1947	- Continuous filament drawn and heat set for tensile strength, RFL/VP-SBR adhesive employed
Steel cord (USA)	1955	- Brass plating for adhesion
Polyester	1962	- drawn and heat set for tensile strength, 2 step adhesion dip, isocyanate/RFL
Fiberglass	1967	- RFL adhesive on individual filaments
Aramid	1974	- Special RFL/VP-SBR adhesive
Rayon (polynosic)	1975	- High tenacity rayon
Polyester (2nd rev)	1982	- Modified lower shrinkage
Steel cord (open const)	1980s	- Higher rubber penetration adhesion/corrosion resistance
Polyester (3rd gen)	1995	- High modulus/lower shrinkage
Steel cord (3rd gen)	1990s	- High tensile steel. New drawing and twisting (e.g., BETRU™)
Pplyethylene naphthalate	1990-2000s	- Potential new tire fabric, not yet commercial

Textile industry nomenclature

The terminology used for defining tire cords comes from the textile industry. Table 3.3 gives the common vocabulary. Tire cords are built up from yarns which in turn come from filaments. Filaments from a production spinerette are gathered together, slightly twisted, and placed on "beams" for further processing. Figure 3.1 shows a common hemp rope which

Figure 3.1: Hemp rope illustrating cord construction - filament/yarn/cord (rope)

shows this construction, but on a larger scale. The filaments are twisted "Z" into yarns and the yarns are back-twisted "S" to form a cord. The size of a tire filament, yarn, or cord is measured by its weight per unit length - linear density or "denier" (denier is the weight in grams of 9000 meters) or "decitex" (weight in grams of 10,000 meters). Textile cords are identified by their yarn denier and their construction. Thus a 940/2 8x8 nylon cord is formed from 2 - 940 decitex yarns twisted separately at 8 turns per inch and then back-twisted together at 8 turns per inch to form the cord. A 1650/3 10x10 rayon cord would comprise 3-1650 denier yarns twisted at 10 turns per inch separately and back-twisted together at 10 tpi. For a given material, use of higher denier yarns or more yarns per cord result in a higher breaking

Table 3.3: Textile terminology

Fiber	- a material with high strength in the fiber axis direction and with a length at least 100 times greater than its diameter.
Filament	- the smallest continuous element of a tire cord.
Yarn/strand	- an assembly of filaments, usually gathered directly from the spinerette, twisted lightly (e,g., 0.3 turns per inch), and rolled up on beams for further processing. Ply-twisted yarns are further twisted before assembling into cords.
Cord	- a twisted or formed structure composed of two or more yarns.
Warp	- an assembly of cords that run in a lengthwise direction along the fiber axis.
Pick/filling	- a low strength thread placed at right angles to the warp (1 to 2 per inch) to give handling stability to a sheet of warp cords. These have very low tensile and high elongation to avoid distortion of a calendered sheet during expansion of a green tire.
Denier	- the linear density of a textile item (e.g., a yarn) defined as the weight in grams of a length of 9000 meters. Thus, the larger the denier, the stronger the item. For example, a 2000 denier yarn would be twice as heavy as a 1000 denier yarn and presumably twice as strong.
Decitex	- the linear density in SI units (partially), defined as the weight in grams of a length of 10,000 meters.
Twist	- the number of 360° turns per unit length of a yarn or cord, e.g. 10 twists per inch or 40 twists per 10 cm.
Twist direction	- twist direction is termed "S" if the spiral turns clockwise from top to bottom for a vertically held cord and "Z" for a similar counter clockwise turning.
Twist balance	- if a set of yarns and the resulting cord have same twist it is termed a balanced cord.
Lay	- lay is the inverse of twist. It is the length of cord needed to complete one 360° rotation, e.g., a 12.5 lay would exhibit one rotation in 12.5 mm. Lay is the measurement used for steel cord constructions.
Strength	- the tensile load required to rupture a cord at a given rate of extension, i.e., the breaking load of a given cord. Tire cord strength is reported in Newtons or pounds, rather than MPa, due to the difficulty of determining the true cross-sectional area of a bundle of fibers. Fiber tensile strength is some times reported: Tensile strength (psi) = 12800 (specific gravity)(tenacity in grams per denier).
Tenacity	- Tire cord strengths are frequently reported as tenacity in grams per denier or centinewtons per decitex. This value is essentially strength for equal weight. It can be useful when comparing cords of similar specific gravities, but should used with caution in tire strength calculations where equal volumes of cord may be used rather than equal weights, for example, when comparing nylon to steel in a radial carcass.

strength of the cord.

Steel cord constructions are defined differently, based on the filament diameter and method of construction. The high specific gravity of steel compared to that of organic textiles distorts comparisons of cord strength when "tenacity" is reported. This makes steel appear to have lower strength. Steel cord nomenclature and physical properties will be described in the section on steel cords.

Table 3.4

Functions of tire cords
- Maintain durability against bruise and impact
- Support inertial load and contain inflating gas
- Provide tire rigidity for acceleration, cornering, braking
- Provide dimensional stability for uniformity, ride, handling.

Cord Requirements
- Large length to diameter ratio , eg, long filaments
- High axial orientation for axial stiffness and strength
- Good lateral flexibility (low bending stiffness)
- Twist to allow filaments to exert axial strength in concert with other filaments in the bundle
- Twist and tire design to prevent cord from operating in compression.

General function of tire textiles
Table 3.4 summarizes the essential functions of tire cords and their basic requirements.

Tire cords are the strength members of a tire. As such, they must define the tire shape, support the loads, and contain the inflation gas. They must provide the tire with axial and lateral rigidity for acceleration, braking, and cornering and dimensional stability for uniformity, handling, and ride. They must also provide bruise, fatigue, and resistance to separation for durability.

Table 3.5: Ideal cord properties for a tire carcass

Dimensional stability –low shrink during cure, no flat spotting, no long term growth
High tensile strength
High tensile modulus
Low bending modulus
High durability – fatigue resistance, low heat generation on flexing, high adhesion to rubber, chemical and oxidation resistance, heat resistance
High toughness – impact and abuse resistance
Low hysteresis loss at high speeds.

Table 3.6: Ideal cord properties for a radial tire belt

High tensile strength
High bending modulus – high stiffness
Ultra-high tensile modulus
High compression modulus
High adhesion to rubber
Good resistance to chemical attack

Textiles for the carcass and for the radial belt have different requirements. Kovac (4) and Pomies (9) have succinctly summarized the ideal properties for cords in each of these applications:

As with all tire components, choice of a textile cord for a given tire application may require compromises involving cost, intended market segment and end-use application. The tire engineer has a number of choices for a tire textile:

- •Chemical composition of textile
- •Cost per unit length and weight (cost in tire)
- •Denier – filament size and strength
- •Cord construction – number of yarn plies
- •Cord twist
- •Number of cords per unit length in ply
- •Number of plies in the tire

These choices will naturally be predicated on the tire specifications for the particular application and market, usually balancing cost against required performance.

Five materials currently make up the major tire textile usage – rayon, nylon, polyester, aramid, and steel. Table 3.7 lists the physical properties of these materials. The high modulus of steel and aramid find their major use in radial belts and in single-ply carcasses for large radial tires. Rayon is used in both carcass and belt of passenger radial tires but lacks strength for durable heavy-duty tires. Modern polyester cord is an excellent carcass textile for use with steel belts in passenger and light truck tires and is becoming dominant worldwide. However, it lacks the toughness and heat resistance required for large tires where nylon is the textile of choice in large bias truck, earthmover and aircraft tires but nylon and polyester do not have the high stiffness necessary for good performance in radial belts. Yarn and textile producers are making continuing improvements in their products, therefore these data are for a general comparison only. In particular, modifications in the last twenty years have resulted in significant improvements in the dimensional stability of polyester and the tensile strength of steel. Also, aramid modifications have improved its compression fatigue properties.

Physical properties of commercially-available tire cords are usually more meaningful to tire engineers. The following table summarizes typical physical properties of some commonly used cord sizes of organic textile fabrics (10). Data are for untreated yarn bundles lightly twisted at 0.2 to 0.3 turns per inch.

Table 3.7: Typical filament properties of major tire textiles

	Rayon	Nylon 6	Nylon 66	Polyester	Aramid	Steel
Tenacity (cN/Tex)	50	80	85	80	190	35
% Elong at break	6	19	16	13	4	2.5
Modulus (cN/Tex)	800	300	500	850	4000	1500
Shrinkage (% at 150C)	<0.1	6.0	5.0	2.0	<0.1	<0.1
Moisture regain (% at RT)	13	4.5	4.5	0.5	<2.0	<0.1
Specific gravity	1.52	1.14	1.14	1.38	1.44	7.85
Melting temperature (C)	>210	225	250	250	>500	--
Glass transition temperature(C)	--	55	55	80	--	--
Heat resistance (C)	150	180	180	180	250	--
Approximate relative cost per unit weight (PET=1.00)	1.33	--	1.13	100	5.00	--

Table 3.8: Physical properties of commercial tire cords

Linear density dtex	# of filaments	Breaking force N	Breaking tenacity mN/tex	Breaking elongation %	EASL* %(xN)	Shrinkage % at 180C
Nylon 66	140	80	840	18	9.6(45N)	5.1
940	280	118	840	19.5	10.4(90N)	5.1
1880						
Polyester	210	94	848	11.2	6.0(60N)	7.6
1100	280	100	686	10.4	5.2(90N)	3.6
1440						
(low shrink)						
Rayon**	1000	96	510	12.8	4.6(45N)	nil
1840	1350	517	12.5	nil		
2440						
Aramid (11)	1000	325	2030	4.8	--	nil
1500						
*Elongation at specified load (inverse modulus measure)						
**Conditioned 75% humidity -- 0.4 TPI						

Table 3.9 qualitatively ranks tire cord reinforcements for important tire performance properties. It should be understood that the textile industry is continually upgrading their specific products so that these rankings may change.

Again note that nylon and polyester do not have the requisite bending stiffness to make useful radial tire belts. As discussed below, glass fiber and polyvinyl alcohol are potential belt materials.

Table 3.9: Relative performance of tire cord materials (4,9)

Dimensional stability (carcass)	
Uniformity in curing	Rayon> Advanced Polyester >Nylon
Appearance (sidewall indentations)	Rayon> Advanced Polyester >Nylon
Dynamic stiffness (steering)	Rayon> Advanced Polyester >Nylon
Flat spotting	Rayon> Advanced Polyester >Nylon
Durability (carcass)	
Fatigue resistance/heat generation	Nylon> Advanced Polyester > Rayon
Impact Resistance (Toughness)	Nylon> Advanced Polyester > Rayon
High speed/ run-flat tires	Rayon> Advanced Polyester
Strength	Aramid> Steel> Nylon> Polyester> Rayon
Modulus(stiffness)	Aramid> Steel> Rayon>> Polyester> Nylon
Elongation	Nylon> Polyester> Rayon> Steel = Aramid
Compression fatigue	Nylon> Polyester> Rayon> Steel> Aramid
Chemical resistance	Aramid> Nylon> Rayon> Polyester> Steel

General comments on cord usage in various types of tires
Polyester – Polyester is the condensation polymerization product of ethylene glycol and terephthalic acid. Newer modifications resulting from increased molecular weight and revised processing are called DSP-PET (dimensionally stable PET), with 50% increased modulus and 50% reduced shrinkage, bringing it close to rayon for dimensional stability. It has become relatively inexpensive making it a good choice for passenger and small light

truck tires. Polyester must be used with carefully designed rubber adhesion systems and carcass rubber compounds to prevent cord deterioration in use. Polyester cord is not recommended for use in high-load/high-speed/ high-temperature applications, as in truck, aircraft and racing tires, because of rapid loss in properties at tire temperatures above about 120C.

Rayon (12) - Tire cord strength has been improved 300% since its introduction by improved coagulation and heat treatment. The low- shrink, high-modulus, good-adhesion properties of rayon make it an excellent choice for use in passenger tires. However, rayon has lost market share to polyester due to higher cost and environmental concerns with production facilities. Rayon had historically been used in truck tires but has been displaced by nylon with higher strength and impact resistance. Rayon is used for racing tires and has gained renewed interest in the development of an extended-mobility self-supporting passenger tire.

Nylon- Nylon is a generic term for aliphatic polyamides. Two varieties are used in tires cords Nylon 6 (polycaprolactam) and Nylon 66 (product of adipic acid/hexamethylene diamine condensation). Both materials give similar properties with Nylon 6 being somewhat less expensive, but more sensitive to moisture and subject to loss in tensile strength if moisture is present at tire curing temperatures. Nylon tire cord strength has been improved 25-50% from early versions by processing modifications. Its low modulus and low glass transition temperature make it unacceptable as a belt material or for applications where aesthetics, ride, and handling are important, i.e., in passenger tires. Nylon is preferred in uses requiring carcass toughness, bruise and impact resistance, high strength, and low heat generation, e.g., in tires for medium and heavy-duty trucks, off-road equipment, and aircraft. In these applications nylon can be used in the bias-ply tire carcass or in radial tire carcasses with steel or aramid belts.

Aramid (13) - Aramid is a wholly aromatic polyamide. The most common commercial material is poly(p-phenylene terephthalamide), eg, Kevlar™ or Twaron™. Aramid cords have very high strength, high modulus, and low elongation. The relatively high cost has slowed adoption as a general radial belt material where steel cord is performing well. It is particularly suited where weight is important, such as in the belts of radial aircraft tires or in overlay plies for premium high-speed tires. As with steel cords, aramid can be used as multiple plies in flat belts. However, in carcass applications aramid must be used as a single ply. In a multiply carcass construction, aramid's low elongation will prevent the outer ply from adjusting to the average curvature, thus placing the inner plies into compression. This reduces the contribution of the inner plies to the total strength, but, more seriously, early failures of the inner ply are encountered due to the poor dynamic fatigue resistance of aramid in compression. Work on aramid copoloymers to improve elongation and fatigue resistance has been reported.(14).

Other potentially useful fibers for tires
Glass fiber – fiber glass was introduced to the US tire industry in the 1960s with Goodyear's development of a belted-bias tire. This tire was soon replaced by the radial tire, however. Some attempts were made to use fiber glass in the belts of radial tires but in spite of its excellent credentials, fiber glass quickly lost out to steel as the premier belt material. Premature failures were encountered, both in cold weather use and with inappropriate tread designs that put the top belt into compression. However, a review of its properties gives glass fiber an excellent rating as a belt material if proper tread design and latex adhesive dips are used. Its specific stiffness and strength are equal to those of steel, whereas the specific

gravity is only 2.54 compared to 7.85 for steel. The initial modulus is 2150 cN/tex compared to 1500 for steel. Rubber adhesion is excellent with no problems with rusting due to water in the belt. Each filament of fiber glass is coated with a latex dip before the filaments are twisted into a yarn. It has been established that this latex must be formulated from a low glass transition polymer to prevent the premature glass breakage seen in the early glass fiber development.

   Polyvinyl alcohol – PVA fibers have properties similar to both rayon and advanced polyester, but with higher tenacity than rayon and lower shrinkage than polyester. Reported properties (15) are – tenacity 14 g/den, elongation 8.7%, Tg = –90C, Tm = - 265C, Modulus = 180 g/den, specific gravity = 1.3. High molecular weight, high crystallinity fibers are stable in water at 115C. This textile has been used successfully in the carcass and belts of radial passenger tires. A major drawback has been the lack of suppliers of multiple cord material.

   Polyethylene Naphthalate (PEN) - PEN is similar to the standard polyethylene terephthalate (PET) polyester, being a copolymer of ethylene glycol and naphthalic acid. This new textile has been developed by Allied-Signal (presently Honeywell High Performance Fibers) and is being evaluated for tires. Its properties have been reported by Rim (16). It is claimed to surpass DSP-PET for use in the carcass of passenger car tires, having lower shrinkage, higher modulus, and higher Tg (120C vs. 80C). It also has potential as a restrictive overlay belt for light truck and high-speed passenger tires, replacing nylon overlays. A disadvantage is the high price, about 2.5 times that of polyester. Table 3.10 compares treated cord properties of PEN with other tire textiles.

Textile Cord Manufacture (3, 5)
The organic textile materials used today are all man-made. Natural fibers such as cotton do

Table 3.10: PEN properties vs. other cord reinforcements

	Nylon 66	Rayon	DSP PET	PEN	Aramid
Tenacity (cN/dtex)	7	4.5	6.2	7	14
Modulus (cN/dtex)	25	50	60	130	300
% Shrinkage at 177C	7	0.5	2	2	nil

not have sufficient filament length to provide the high strength needed. Manufacture of steel cord is quite different from that for organic textiles and will be covered in a later section. The processes for producing continuous textile filaments are melt spinning (nylon and polyester) and solution spinning (rayon and aramid).

Melt spinning
In the melt spinning process molten polymer is filtered and pumped through a spinnerette containing a large number of very fine holes. A positive displacement pump is used to give an extremely accurate and constant flow through the spinnerette. The extruded semi- molten polymer is stretched to about 25 times its original length while solidifying in a cool air stream. The solidified bundle is then treated with a spin finish to lubricate the filaments and cold-drawn over a series of take-up rolls ("godets"). The drawing process elongates the filaments by several hundred percent while the polymer is still above its glass transition temperature. This procedure increases the strength and modulus, and reduces the breaking elongation, by increasing the polymer crystallinity and molecular orientation. The final

structure of drawn, crystalline thermoplastic polymers contains crystalline fibrils, highly aligned polymer molecules and unoriented molecules.

Controlled feed rates and draw speeds are necessary to ensure filament uniformity and close control of the linear density (denier). Finally, the filament bundles are gathered, lightly twisted, and stored on "beams" to be transferred for further processing and cord manufacture. Compared to standard textile products, tire cord polymer melts are of higher molecular weight (at least 2 times higher) and after drawing have 2 to 4 times the tensile modulus values, with breaking elongations in the 10-20% range.

Solution spinning

Rayon (regenerated cellulose) and aramids have no defined melting temperature and must be dissolved for extrusion as continuous filaments. A concentrated solution or slurry is pumped through the spinnerette into a coagulating bath of non-solvent (wet spinning) or air-dried to evaporate the solvent (dry spinning). Filaments are air-dried under tension and not extensively drawn since crystallinity and orientation are already highly developed. Spin finish is applied, as with melt-spun textiles, and the filament bundles are "beamed" for downstream processing. Aramids emerge with their high-strength properties intact. Rayon tenacities have been increased over three-fold by refinements in coagulation, modified finishing procedures, and heat treatments to alter crystal size.

Cord assembly
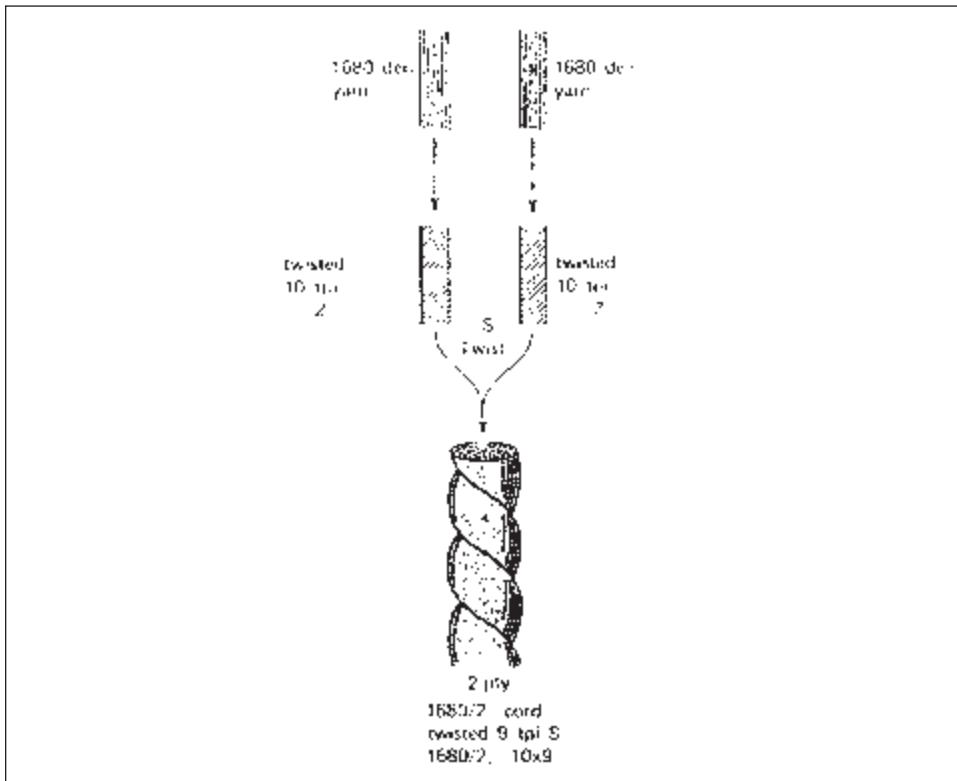
In a conventional cord production, producer yarns (lightly twisted bundles of 0.2 to 2 turns per inch) are removed from beams and ply twisted to a specified level, 6 to 12 turns per inch (tpi), usually in the "Z" direction. Cords are formed by cable twisting when two or more yarn plies are back twisted in the "S" direction to form a greige (untreated) cord. Tire cords are usually balanced with equal twist levels in yarns and cords. Figure 3.2 shows a cord construction with "Z" and "S" twists.

Tire cords can be constructed in a wide range of sizes and strengths. Yarn producers generally offer standard denier sizes, for example, nylon might be offered as 840, 1260, and 1680 denier yarns, going from lightest to strongest. Cord constructions would be identified as, for example, 840/2 or 1680/3 with the heaviest cords having the highest strength.

Twist effects

Twist levels are important for tire cord performance. Higher twists allow a cord to behave like a spring which will not open up under compression, while lower twists allow a cord to behave as a rod, maximizing the strength. Table 3.11 lists changes in general performance with increasing twist level. As twist increases the tenacity decreases, fatigue in compression improves (the main reason for higher twists), the cord cost per tire increases (because cords become shorter as they are twisted), and shrinkage during processing and cure increases.

Tenacity and fatigue resistance are sometimes reduced with increasing twist. In a tire the construction should be such that no cord will open up, chafe, or fret in a compression mode. Cord fatigue in compression is a critical factor in tire sidewalls where bending stresses and strains are high. In bias tires sidewall compressive stresses are more likely to occur and typical twists are 12x12 tpi (turns per inch), while in radial tires carcass cord twists are typically 6x6 tpi.

Figure 3.2: An example of cord construction using "S" and "Z" twists

Table 3.11: Cord property changes with increasing twist levels

Reduction in strength
Reduction in initial modulus
Reduction in cyclic tension fatigue resistance
Increase in elongation to break
Increase in rupture energy
Increase in cyclic compression fatigue resistance
Increase in cord cost per tire

Twist multiplier

The amount of twist relates to both tenacity and compression fatigue resistance. To obtain equivalent fatigue performance in a product when changing cord size, cords must be twisted to the same helix angle using a "twist multiplier" relationship:

For the same material:

Cord A tpi x √Cord A denier = Cord B tpi x √Cord B denier.

[For example: Cord A of 2000/2 construction at 8 tpi would be equal to Cord B of 1000/2 at 11.3 tpi.]

For different materials specific gravity must also be considered:

Cord A tpi x √Cord A denier/ √Cord A SpGr = Cord B tpi x √Cord B
denier/√Cord B SpGr.
[For example, an 840/2 nylon (1.14 SpGr) at 11.0 tpi would have the same helix angle as
a 1100/2 aramid (1.44 SpGr) at 11.3 tpi.]

Weaving
After twisting yarns into cords, 1000 to 1500 cords are woven into a coherent sheet using a
very light "pick" fabric as the weft at a very low fill count of one to two picks per inch. Rolls
of this fabric (which is about 1.5 to 1.75 meters wide - the practical width of rubber-cord
calenders) are transferred for further operations. The function of the pick is to maintain a
uniform warp cord spacing during the downstream operations, such as, shipping, adhesive
dipping and heat treating, calendering, tire building and lifting. Uniform cord distribution in
the finished tire is essential for tire uniformity and performance. In bias-ply tires the pick
fabric is usually a weak cotton yarn which breaks readily during tire shaping. In radial tires it
consists of a highly extensible filament (undrawn nylon or polyester) in a cotton sheath. The
core ensures uniform cord distribution as the tire is shaped and the sheath holds the cord
spacing during adhesive treatment and calendering but breaks readily during tire lifting and
shaping.

Tire cord processing (17, 18)
Downstream cord processing of tire cords can profoundly influence tire performance.
Consistent control of the dimensional stability of the cords through the various environments
- dipping, adhesive baking, heat stretching, relaxation, and tire vulcanization- is necessary to
control and predict variations in such factors as tire size, tire uniformity, cord-to-cord
uniformity, flat spotting, side-wall indentations, and creep during operation. Steel, aramid and
rayon are minimally affected during cord processing while the thermoplastic fibers, nylon and
polyester, must be very carefully controlled. The radial tire with its high-modulus restrictive
belt has greatly alleviated many of the cord growth problems previously seen in bias tires,
leading for example to tread groove cracking. A goal of process engineers concerned with
dimensional stability when working with the thermoplastic cords is to maximize tensile
modulus (often characterized by EASL - elongation at specified load) while minimizing
thermal shrinkage. Care must be taken to optimize tensile strength and fatigue properties in
these procedures.

Rayon and aramid cord processing
The processing of these cords is relatively simple since they are thermally stable and do not
change significantly in downstream operations. Rayon must be carefully protected from
moisture regain at all processing stages, especially at roll ends to avoid uneven shrinkage
across a fabric roll.

An optimum treatment for processing rayon has been reported (19). Rayon cord made
with a higher than specification twist is dipped in cord adhesive under relaxed conditions to
open the twist for good dip penetration and to completely wet the cord with the aqueous
adhesive. The cord is then tensioned to achieve the specification twist and dried at 130-150C
before being baked under tension at 155-175C to cure the adhesive.

Heat treatment for aramid 230-260C is generally at low tension (8.8cN/tex) and with very
low stretch to standardize modulus. As with polyester, adhesive application is a two step
procedure.

Nylon and polyester cord processing

Thermoplastic fibers, such as nylon and polyester, are considered to be composed of a mixture of crystallites, extended (aligned) non-crystalline molecules, and amorphous "tie" molecules. Crystallization occurs principally during fiber drawing. Cord processing, carried out below the crystal melting temperature, modifies the non-crystalline portion. Skolnik (20) has reported typical changes in nylon orientation during cord processing:

Chawla (17) has summarized a number of studies. In the process of applying and baking a cord adhesive the amorphous portion of a thermoplastic cord will tend to become less oriented, resulting in shrinkage which will, in turn, adversely affect tire uniformity. Shrinkage is partially controlled by stretching the fabric in the heat-setting zone and relaxing it under controlled tension in a second zone. In general, higher relaxation results in lower shrinkage. Net stretch (the difference between stretch in the first zone and relaxation in the second) is often used as a measure of shrinkage and growth potential. This can be deceptive, however, for a number of reasons:

1. Additional crystallinity can occur that will lower shrinkage and/or growth potential,

2. Equilibrium orientation is seldom reached in allotted treatment times, especially with heavy cords,

3. High treatment temperatures can cause polymer flow and molecular weight degradation.

Heat treating conditions vary across the tire industry, serving different needs. Heat treatment of nylon, for example, varies in temperature between 177°C and 246°C, between 7% and 16% stretch, and between 20 and 60 seconds residence time. Chawla also reports studies on polyester cord by Aitken *et al* (21) who recommended a treatment temperature of 246°C, 4% stretch in the first zone and 3% relaxation in the second zone, with 90 seconds residence time in both zones for optimum fatigue resistance. Nylon is generally used at 3-7% net stretch, and polyester at 0 - 4%.

Table 3.12: Changes in % crystallinity and amorphous orientation of nylon

Treatment:	Greige	Heat set	Relax	In mold	Out of mold	Post cure inflation
Temperature C	25	225	205	180	180	180 to 60
Crystallinity (%)	60	63	70	70	70	70
Orientation	High	Very high	Moderate	Low	Low	High

Postcure inflation

On release from the tire curing press, viscoelastic cords in the hot tire are almost completely free to shrink. Postcure inflation (PCI) is therefore employed to stabilize tire size and uniformity. All-steel or all-rayon tires do not require a postcure treatment. Because the postcure inflating equipment is expensive to install and maintain, some companies have minimized or eliminated PCI for their radial tires by predictive mold sizing, control of cord properties, and controlled cooling. The use of PCI entails the following:

Passenger and light truck tires are automatically ejected from the press after the usual 12 to 24 minute cure time, depending on size, and then immediately loaded onto a postcure inflator which re-inflates the tire to 200 to 400 kPa (30 - 60 psi). This loads and stretches the hot cords. Post inflating controls the size, shape, uniformity, and growth of the finished tire. However, the results depend on the time, temperature and load applied to the cords during the

inflation process. Moreover, the cords should be cooled evenly to below their glass transition temperature before release from the inflator. Lim (22) has reported on studies that simulate PCI and non-PCI conditions by measuring EASL (elongation at specified load - the inverse of modulus). For rayon the modulus is constant for cords heated to 177C under 0.06N/tex and cooled to RT with or without tension. No modulus change took place. Under the same conditions nylon showed a 20% increase in modulus and PET a 30% increase. Equilibrium times for the cords were 30 minutes. A practical cooling time for factory tires is usually about two cure cycles. Also, it should be noted that uneven cooling, e.g., from one side to the other, can result in tire distortion, so that tires may be rotated during the PCI treatment.

Skolnik (23) has reported a "coefficient of retraction" for loaded cords in a simulated postcure inflation study. Cords were loaded to 0.9 g/den., heated to 165C, and cooled to various temperatures where the load was released. The coefficient of retraction (CR) is the percent length change per degree C.

	CR above Tg	Tg (C)	CR below Tg
1680/2 Nylon 6,6			
1680/2 Polyester	0.050	50	0.022
(standard)	0.050	85	0.011

Cord-rubber adhesion

The adhesion of rayon, nylon, polyester, and aramids has been reviewed extensively. Takeyama and Matsui (24) reviewed adhesives for rayon, nylon, and polyester. Solomon (25) updated this work in 1985 to include aramid adhesion and the effects of environmental exposure on degradation of adhesion. Chawla (17) summarized both cord processing and adhesive dip treatments. Dipping and baking of the adhesive is intimately tied in with cord stretching and relaxation procedures.

There are many variations in cord dipping procedures, e.g., one-step vs two-step dipping, dipping in the tire-plant vs in the cord-plant, surface activation of the cord, etc. We consider here only the goal of using adhesives, general operating procedures, and potential problem areas.

The prime goal of the cord adhesive is to avoid separation at the cord-adhesive interface, at the rubber-adhesive interface, or within the adhesive itself. This objective is achieved by using proper dipping procedures. Tire carcass failures that were initially attributed to failure at the adhesive interface were often shown on microscopic examination to be due either to fatigue failure of rubber close to the cord, caused by high stresses resulting from improper construction or irregular cord spacing, or to cord fatigue from excessive compressive stresses.

Mechanism of cord-rubber adhesion

It is generally accepted that the adhesive provides both chemical bonding between the rubber and the cord surface and by mechanical interlocking as the rubber penetrates within the cord interstices. The adhesive must also accommodate the large differences in the two materials:

  - high-polarity polymers in cords vs. low polarity of rubber
  - high modulus of cords vs. low modulus of rubber.
  - Good adhesive durability is achieved by minimizing the abrupt change in modulus at the cord-rubber interface by introducing an adhesive layer of intermediate modulus.

Basic requirements for a good cord adhesive are listed in table 3.13.

**Table 3.13: Requirements for cord-to-rubber adhesives**
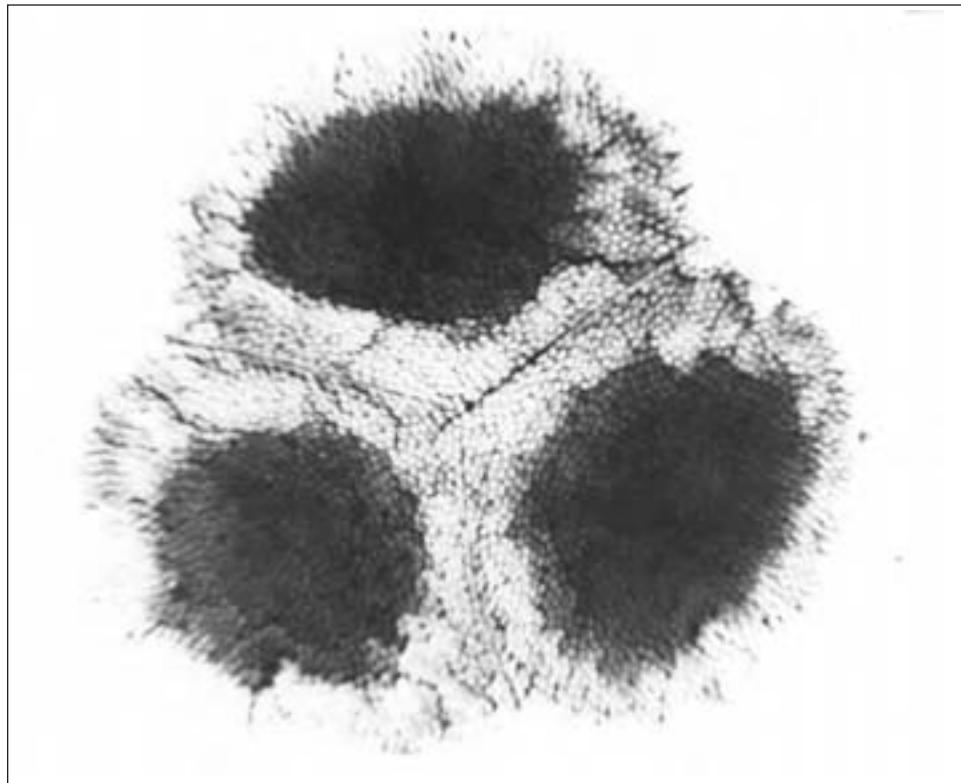
Good bonding to both cord and rubber
Intermediate modulus between cord and rubber
Rapid rate of bond formation
High fatigue resistance in the cured adhesive
No chemical deterioration of cord by the adhesive
Compatibility with a range of rubber compounds
No brittleness or flaking in processing

The resorcinol-formaldehyde-rubber latex system (RFL) developed in the 1940s for use with nylon and rayon is still used throughout the tire industry. A synthetic 2-vinyl pyridine-butadiene-styrene copolymer latex, developed for nylon, has replaced the natural rubber latex originally used for rayon, in all modern dips. Resorcinol and formadehyde react in the dip to give a strong polar polymer with good adhesion the polar tire cord, while the rubber component of the latex provides good bonding to the rubber. Specific recipes are given in the referenced literature for all textile cords and for both single and double dip treatments.

RFL is used for rayon and nylon exclusively and as the outer dip for polyester and aramid cords. Typically, rescorcinol and formaldehyde are mixed and "matured" for up to 24 hours. The latex is blended and the cord is dipped before tensioning. Dip formulations contain 2 - 5% total solids and dip pickup is controlled to about 6 - 8%. The cord is then tensioned and baked. Complete total wetting of the cord is necessary to prevent spotty adhesion. Good dip penetration is important for good adhesion and cord compaction. Dip penetration of 2 - 3 filament layers is optimal. Figure 3.3 shows a cross section of a 1680/3 rayon cord with high penetration of the adhesive into the filaments, with resulting good adhesion and cord compaction.

Polyester and aramid polymers are much less reactive to standard RFL and must be pretreated to obtain good adhesion. A common practice is to employ a multistage dipping process. The cord is first dipped in an aqueous solution of a reactive chemical, such as an epoxide, e.g., the diglycidyl ether of glycerol or a blocked isocyanate, e.g., phenol-blocked polyisocyanate ["Hylene MP"], along with a small amount of wetting agent to give uniform dip pickup. After tensioning and baking the cord is again dipped in a standard RFL for final baking and relaxation. Processing times through each of the steps is generally 30-60 seconds. A general review of cord treatment temperatures is given in table 3.14.

The dip formulation, amount of dip pickup and the curing conditions can all affect adhesion and must be optimized. Strict quality control must be implemented once optimum conditions are established. Problems that must be avoided are: inadequate wetting of the cord, inadequate dip pickup, excessive dip pickup (which can result in flaking off of the adhesive), or overbaking during heat treatment. Any of these conditions can reduce adhesion. The finished cord must be protected from nitrous oxides (if gas or oil heating ovens are used) and from exposure to sunlight, humidity, or ozone if the cords are stored or shipped before being calendered with rubber. The treated cords are generally protected by storing them in polypropylene cloth liners and sealing them in black polyethylene film.

Figure 3.3: Cross-section of a rayon cord showing excellent dip penetration

Table 3.14: Drying, baking and heat setting temperatures for textile cords (°C)

|	Dry	Baking	Heat set/relax
Rayon	120-175	175-260	150-175
Nylon	120-175	225-240	180-245
Polyester	120-175	240-250	210-245
Aramid	120-175	240-250	230-260

2. Steel cord (26, 27)
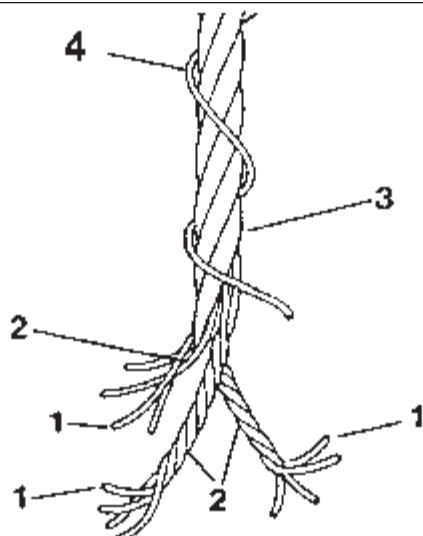
Introduction

Steel cord was adopted in Europe with the advent of the radial tire in the 1940s and 1950s. Steel cord, made by cabling fine steel filaments, met the requirements for a stiff, high modulus/high strength belt material at an acceptable cost, giving high strength and compression stiffness with acceptable bending stiffness, good resistance to fretting fatigue, and good adhesion to rubber. The stiffer steel belt provided the radial tire with quicker handling response and longer tread life compared to the bias tire.

Terminology (nomenclature) of steel cord

The terms used for steel cord are similar to those for the textile industry but with important

Figure 3.4: Steel cord components – filament/ strand/ cord/ wrap

Steel cord components: (1) filaments; (2) strands; (3) cord and (4) spiral wrap

differences. Steel filaments are much larger in diameter and the specific gravity is much higher, so that "tenacity" is not particularly meaningful. Individual filament strength is therefore reported in megaPascals (Mpa). Steel cords are described based on the way they are constructed rather than in terms of denier and number of strands, as is the case with textile cords. The generic steel cord, as depicted in figure 3.4, consists of filaments, strands, cord, and wrap, as defined below (26):

Filament – the basic element of a steel cord is a single fine metallic wire, typically 0.15 to 0.38 mm in diameter.

Strand – two or more filaments are combined together.

Cord – a strand when it is used as the final product or, more usually, the result of cabling strands or strands and filaments.

Wrap (Transfil) – a single filament usually 0.15 mm in diameter wrapped around a cord package to maintain compactness.

The significant cord properties, in addition to the number and diameter of the filaments, are listed in Table 3.15. The breaking load is the key property for the tire engineer.

Steel filament manufacture (27)

Filaments are produced by drawing high carbon steel rods through tungsten carbide dies. Currently, four types of steel filament are produced, rated by their carbon content and tensile strength. Table 3.16 lists typical tensile strengths (which also depend somewhat on filament diameter). Advances in drawing and heat treating techniques have made it possible to produce higher tensile strengths at lower carbon levels. Although more costly, the higher strength filaments allow stronger belts or lighter belts of equal strength and thus may lower the overall cost in a tire.

Manufacture of continuous filaments begins with the drawing of a 5-6 mm rod that has been treated with borax for lubrication through tungsten carbide dies to reduce the diameter

Table 3.15: Property definitions of steel cords

- Cord diameter – arithmetic average of the measured minimum and maximum diameters of a cord (mm).
- Linear density – mass of cord per unit length (g/m).
- Breaking load – force required to break a cord (N).
- Tensile strength – force per unit area to break a filament (MPa).
- Length of lay – the axial distance (mm) for a complete 360° revolution of any strand or cord element. The typical range is 2.5 to 25.0 mm. Inverse of twist.
- Direction of lay – Z and S directions are defined as in the textile industry (see Table 3.3)
- Bending stiffness – Resistance to bending under specified load conditions. Bending stiffness depends on filament diameter and cord construction.

Table 3.16: Typical tensile strengths of steel filaments

Filament	% Carbon	Tensile strength (Mpa)	
		0.20 mm diameter	0.35 mm diameter
Regular tensile (RT)	ca. 0.7	3000	2600
High tensile (HT)	ca.0.8	3400	3000
Super high tensile (SHT)	ca.0.9	3650	3400
Ultra high tensile (UHT)	ca.0.96	4000	3650

to about 1-3 mm. The wire is then heat-treated ("austentized/patented") to maximize the tensile strength by relieving internal strains and modifying the iron carbide structure. It is then electroplated, first with copper and then with zinc, and heat treated to cause metallic interdiffusion yielding a brass coating containing 63/70 Cu and 37/30 Zn. Brass plating facilitates the multiple drawings needed to achieve the final diameters of 0.15-0.40 mm and is a critical factor in cord – rubber adhesion. The brass plating thickness is ultimately about 0.1 to 0.7 μm. Drawing dies must have no burrs that would scratch the brass layer, or corrosion problems might later arise from galvanic action between the iron and copper when in contact with moisture or rubber chemicals.

Steel cord construction
Literally hundreds of steel cord constructions could be employed in tires. However, standardized constructions are usually made to accommodate a range of applications. Steel type, filament diameter, and number of filaments will determine strength, stiffness, and compression fatigue resistance. High-strength steels may be more costly but give a lower tire cost because less material is required.

Cord construction and complexity determine the relative performance. For example cords in heavy duty carcasses require specific constructions for maximum resistance to fretting and fatigue, whereas steel plies that give resistance to cutting and impact damage require a different type of construction with a high breaking elongation.

Characterization of steel cords
Identification of the Construction
Steel cords are identified by the number and diameter of the filaments in each strand, the number of strands, and the way the strands lie around a central axis. A tire cord is defined by

the structure of the cord, the length and direction of lay, and the product type. In defining the structure the basic rule is that the description follows the manufacturing sequence, starting with the innermost strand. A full description of the cord is given by the formula:

Strand 1{(NxF)xD} + Strand 2{(NxF)xD} + Strand 3{(NxF)xD} + ………

where N = number of strands

F = number of filaments

D = diameter of filaments (mm)

A simplified form is when N or F =1, then the 1 is not stated, and if D is the same for several strands it is stated only at the end of the sequence. The wrap is always stated separately. Examples of constructions of some commonly used cords are illustrated below and in Figure 3.5.

(1x3)x0.22 + (1x9)x0.22 + (1x15)x0.22 + (1x1)x0.15

or 3 + 9 + 15 x0.22 + 0.15

3x0.20 + 6x0.35

2 + 2x0.28
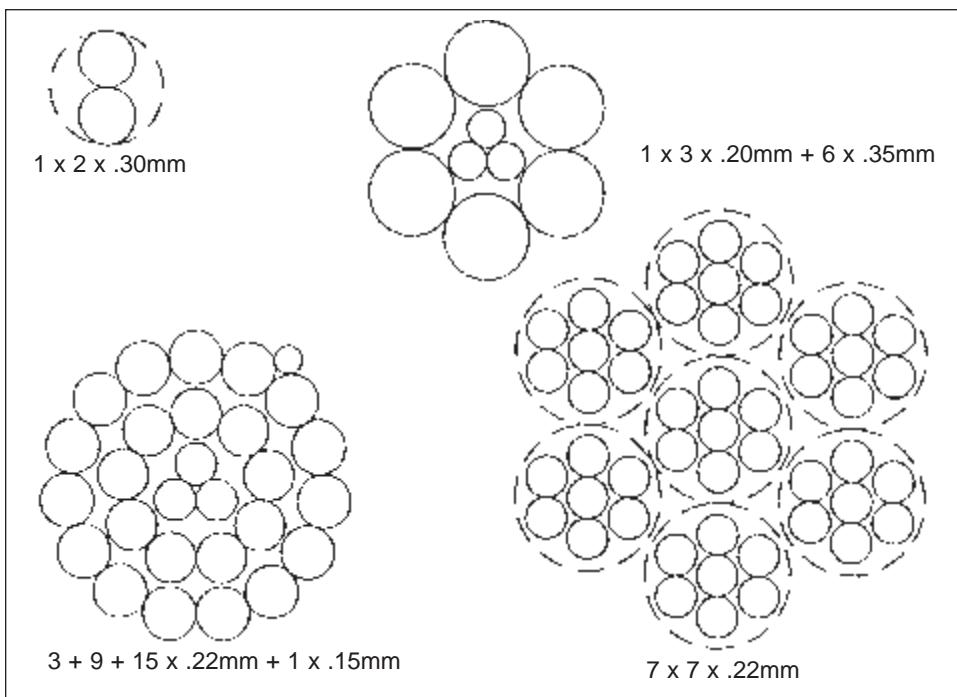
7x7x0.22

Length and direction of lay

The sequence in both the length and direction follows the manufacturing sequence. For

Figure 3.5: Cross-sections of typical steel cords

1 x 2 x .30mm

1 x 3 x .20mm + 6 x .35mm

3 + 9 + 15 x .22mm + 1 x .15mm

7 x 7 x .22mm

example:
    3 + 9 + 15x0.22 + 0.15 5/10/16/3.5 SSZS
    5S: lay length and direction of strand 3x0.22
    10S: lay length and direction of strand 9x0.22
    16Z: lay length and direction of strand 15z0.22
    3.5S lay length and direction of wrap.

Product type

Several types of cord products are available based on variations in the manufacturing and twisting procedures.

Regular cord – standard cord production in which the lay direction in the strands is opposite to the lay direction in closing the cord. This product is easy to produce, cost effective, and processes well in the tire factory.

Lang's lay cord (LL) – cord in which the lay direction of the strands is the same as the lay direction in closing the cord. High elongation cord (HE) is a Lang's lay cord in which the strands are loosely associated and moveable with respect to each other. This allows the cord to be stretched substantially and gives useful cut protection when used in the top belt of radial truck tires and impact resistance in the rock penetration zone of earth mover and mine tires.

Open cord (OC) - A cord in which the filaments are loosely associated and moveable relative to each other. This permits rubber to penetrate into the cord to maximize adhesion to the filaments and to prevent moisture wicking along the cord that could result in steel corrosion. This cord is difficult to process with standard calendering equipment as excessive tension during processing can close the cord resulting in void formation along the cord. Open construction cord has been the subject of numerous patents for various production techniques and cord designs. Bekaert offers a BETRU™ cord which is less sensitive to calender tensions and cord wicking (28).

Compact cord (CC) – cords are produced in a single compact bundle in which the filaments have mainly linear contact with each other. This construction is useful in applications such as for the carcasses of heavy-duty radial tires where severe fretting fatigue can occur at crossover points in a standard cord.

Physical properties of cords

Arkins and Peterson (28) have reviewed constructions and physical properties of present and future steel cords for various tire applications. They predict the adoption of smaller diameter lighter HT and ST filaments, greater use of compact cords (CC) in large tire carcasses for improved fretting resistance, and more complete rubber coverage of all the filaments using newer twisting processes to give effectively open cords, such as the Bekaert BETRU™ cord. Table 3.17 lists representative constructions and properties of some steel cords used in various radial tires.

Basaran (29) has described the improved fretting resistance of compact cords in radial tire carcasses. He also discussed the improved rubber penetration and coverage of filaments for cords made by the BETRU™ process. BETRU™ cords showed no pressure drop in air wicking tests indicating complete rubber coverage which will protect against moisture penetration and wicking along the cords, for a range of calendering tensions. Open-construction cords, which are designed to give high rubber coverage of the filaments, may close up if excessive wire tensions are imposed at the calendar. In certain constructions this

Table 3.17: Constructions and physical properties of steel radial tire cords

Construction	Lay Length (mm)	Lay direction	Breaking load (N)	Cord diameter (mm)	Linear density (g/m)
Passenger tire belt					
2+1x0.28 HT	-16	-S	555	0.70	1.47
2+2x0.25 HT	-14/14	-SS	605	0.65	1.55
LT carcass					
3x0.20+9x0.175(CC)	10	S	855	0.75	2.49
2+7x0.20 HT	5.6/11.2	SS	915	0.76	2.26
LT belt					
2+2x0.35 HT	16/16	-SS	1060	0.84	3.03
MT carcass					
3+9x0.22+0.15	6.3/12.5/3.5	SSZ	1290	1.17	3.85
0.20+18x0.175 (CC)	12.5	Z	1300	0.90	3.71
MT belt					
3x0.20+6x0.35	10/18	SZ	1660	1.13	5.34
HDT carcass					
3+9+15x0.175	5/10/18	SSZ	1770	1.07	5.20
0.25+18x0.22 (CC)	16	Z	2050	1.13	5.85
HDT belt					
3+9+15x0.22+0.15	6.3/12.5/18/3.5	SSZS	2750	1.62	8.50
(protector belt – 6.5% elongation)					
3+7x0.22 (HE)	4.5/8	SS	1820	1.52	6.95

could cause a capillary channel to form down the cord where moisture may propagate and cause corrosion. Such cords have shortcomings similar to those with standard twist constructions, for example: 1x4x0.25.

Bead wire (30)
Steel bead wire is not considered a cord since it is not constructed from twisted filaments. In terms of steel cord nomenclature, a bead wire would be considered a filament. Tire beads are made from single steel wires of larger diameter. They are manufactured by several processes, including tape-wound beads, single-wire wrapped beads, or cable beads. Each type has certain performance or cost advantages. A similar wire is used in all of these constructions. The wire diameter, number of wires (or turns), and type of steel will depend on the size and load carrying requirements of the tire. Beads are designed with an over-pressure blow-off safety factor, load distortion resistance, rim slippage resistance, and resistance to bead breakage during mounting. Wires for beads are supplied as regular or high strength steel, in various diameters, and bronze or brass coated for adhesion. Table 3.18 lists typical properties of some standard bead wires.

Steel cord adhesion
For maximum long-term durability the steel cord used in radial tires must have a high level of rubber-to-brass adhesion and a high degree of resistance to corrosion caused by water

Table 3.18: Properties of typical commercial bead wires

Diameter	Breaking strength	Breaking elongation	Plating metal	
mm.	N	%	Bronze	Brass
0.96 NT	1350	5	0.3/0.65	0.3/0.6
1.42 NT	2880	5	0.15/0.45	0.3/0.6
2.00 NT	5260	5	0.1/0.3	0.2/0.4
0.96 HT	1525	-	-	-
1.295 HT	2795	-	-	-
2.00 HT	6125	-	-	-
0.86 ST	1350	-	-	-
NT- normal tensile, HT-high tensile. ST- super high tensile				
Bronze: 3% Sn max. Brass: 72% +/- 5 Cu				

entering the tire through road cuts and penetrating to the belt cord. Poor performance in either area can result in reduced tire service life. Thus, prevention of loss in adhesion in steel-belted radial tires is a prime consideration for tire engineers.

The exact mechanism of brass-to-rubber adhesion has been the subject of much study and conjecture, but lies beyond the scope of this chapter. Van Ooij (31,32) has reviewed the subject in detail. Basically, it is conjectured that a bond is formed between the polar metals and the non-polar rubber during vulcanization with sulfur by formation of a Cu-S- Rubber bond, as idealized in figure 3.6. However, this bond can readily be converted to CuS with loss of adhesion under some circumstances. There are also indications that optimum bonding involves interfacial layers of oxides and sulfides of both copper and zinc.

Bond durability is tested by measuring bond strength after various aging times and under various conditions: Dry heat aging, steam aging, aging in high humidity, and salt bath immersion. The rubber coverage of the wire after testing is regarded as equally important as the retained bond strength of the rubber compound.

Corrosion (rust) of steel can destroy both the adhesive bond and the wire itself. Figure 3. shows an idealized view of moisture attack on wire through galvanic action if the brass coating is damaged or if water can wick into the cord interstices.

Cord construction, brass composition, brass plating thickness, rubber compound composition, tire curing and storage conditions can all affect wire adhesion. Table 3.19 summarizes the best choice of these parameters.

Each tire manufacturer adopts specific belt coat compounds. Many generic versions may be found in the literature.

**Figure 3.6: Schematic diagram of brass-to-rubber bonding with a sulfur cure**
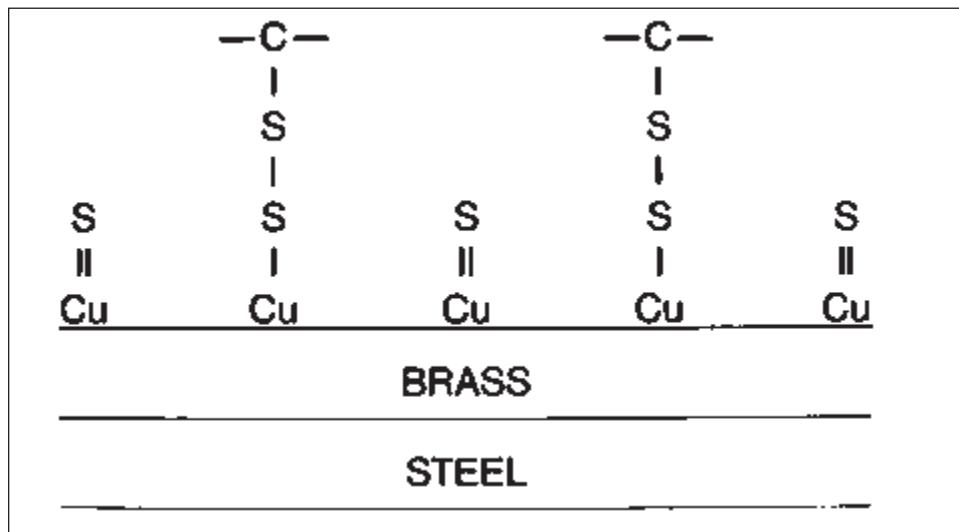
Figure 3.7: Mechanisms of deterioration of adhesion due to the presence of moisture
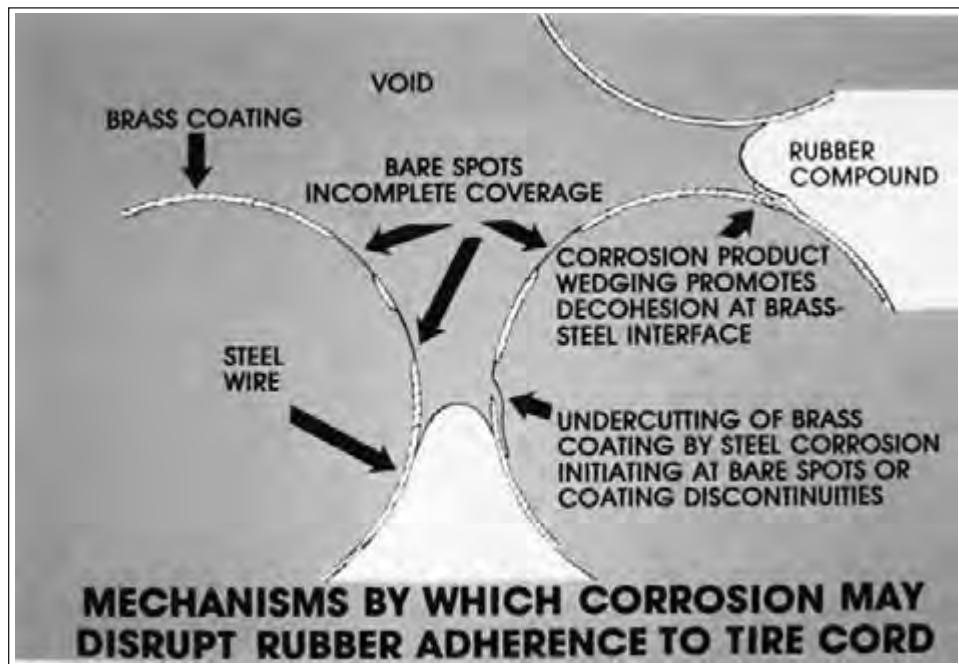
Table 3.19: Parameters that maximize cord adhesion

- Brass compostion: 65% Cu, 35% Zn , plus/minus 2.5%
- Brass plating thickness: 0.3 - 0.6 μm
- Cord construction: open construction – or BETRU™
- Lower temperature – slower cure, eg., 150 - 160°C
- Radial belt compound variables:
    High sulfur level –5 to 8 parts per 100 rubber
    High sulfur to accelerator ratio
    Delayed action accelerator- slow cure
    Cobalt salt – improve and corrosion stability
    Lead oxide – improve high temperature cure stability
    Silica/Resorcinol/Methylene donor – improve moisture sensitivity

3. References

1. Mechanics of Pneumatic Tires, S. K Clark, ed., University of Michigan, US Department of Transportation, National Highway Traffic Safety Administration, Washington, DC, 20590, 1891.
2. Handbook of Fiber Science and Technology, Lewin M., Sello S. B., eds, Marcel Dekker, Inc., New York, NY, 1989.
3. Wellington Sears Handbook of Industrial Textiles, S. A. Adanur, ed, Technomic Publishing Co., Inc., Lancaster, PA, 1995.
4. Kovac, F. J., "Tire Technology", Goodyear Tire and Rubber Co., 1970.
5. Synthetic Fibre Materials, H. Brody, ed., Polymer Science and Technology Series, Longman Scientific and Technical, John Wiley and Sons, New York, NY, 1994.
6. Smith, W., "Automotives – a Major Textile Market", Textile World, September 1994.
7. Rubber and Plastics News, March 31, 2003.
8. Modern Tire Dealer, January 2002.
9. Pomies F., Burrows, J., Rubber World <u>217</u>, #2, Nov. 1997, p. 23.
10. Courtesy of Accordis Industrial Fibers catalog 2003.
11. Yang, H. H., "Aromatic High Strength Fibers", p.228, John Wiley and Sons, New York, NY, 1989.
12. Elkink F., Steyn E., Uihlein K., ITEC 2002 paper 12C, Rubber and Plastics News, Sept. 2002.
13. Tanner, "3.1 Tires" High Technology Fibers (Part B), Handbook of Fiber Science and Technology III, Lewin M, Preston J, eds., Marcel Dekker, Inc. New York, NY, 1989.
14. Ozawa , Matsuda "Aramid Coplymer Fibers", ibid. , p. 22.
15. Sakuradi,I, Okaya,T, "Handbook of Fiber Chemistry, 2nd ed.", p 296, Lewin, Pearce, eds., Marcel Dekker, Inc., New York, NY, 1989.
16. Rim, PB, Rubber World <u>213</u>, #2 Nov. 1995, p. 23.
17. Skolnik L, "Tire Cords", Kirk-Othmer, Encyclopedia of Chemical Technology, Vol 20, 2nd ed, p. 328, John Wiley and Sons New York, NY 1969.
18. Chalwa, SK, "Rubber Composites", p. 203 , Synthetic Fibre Materials, Brody H., ed., Polymer Science and Technology Series, Longman Scientific and Technical, John Wiley and Sons, New York, NY, 1994.

19. Skolnik, L., Draves, C. Z., "Processing Rayon Tire Cord", 2nd Pulp Conference, TAPPI, New Orleans, 1968.
20. Skolnik, L., private communication.
21. Aitken, R. G., Griffith, R. L., Little, J. S., McLellan, J. W., Rubber World, 151(5), p.58(1965).
22. Lim, W. W., Rubber Chem. Tech. 75 581, 2002.
23. Skolnik, L., "Tire Cords", ibid., p. 341.
24. Takeyama, J, Matsui, J, Rubber Chem. Tech. 42, 159 (1969).
25. Solomon, T. S., Rubber Chem. Tech. 58, 561 (1985).
26. Riva, G., "Steel Cord Technology", Educational Symposium #47, Basic Tire Technology: Passenger and Light Truck, 157th Spring Technical Meeting, Rubber Division, ACS, Dallas, Texas, April 2000.
27. Goodrich, J., "Steel Cord Technology", Educational Symposium #48, Basic Tire Technology: Medium and Heavy Duty Truck, 159th Spring Technical Meeting, Rubber Division, ACS, Providence, RI, April 2001.
28. Arkins, O., Peterson, J. R., "ITEC 96 Select ", p. 183, Rubber and Plastic News, September 1997.
29. Basaran, M., Rubber World 228, #6 Sept. 2003, p.28.
30. "Steel Cord Technology", Ed, R. M. Shemenski, Wire Association International, Inc., 1570 Boston Post Road, Guiliford , CN 06437
31. van Ooij, W. F., Rubber Chem. Tech. 57, 421 (1984).
32. van Ooij, W. F., Rubber Chem. Tech. 52, 605 (1979).

4. Review Questions

What are the main functions of cords in tires?

What three elements make up the tire cord construction?

What physical properties are needed in tire cord filaments?

How does a carcass cord differ in physical properties from a belt cord?

Name the presently used high volume tire cord materials.

What are the preferred cord materials for passenger tires? Why?

What are the two processes for producing textile cord filaments? How does steel filament production differ from these?

What important compromises are involed in the level of cord twist?

How does the processing of a thermoplastic textile cord differ from that of non-thermoplastic textiles?

What chemical materials are required as adhesives for good polyester or aramid adhesion to rubber? How are these usually applied?

What steel treatment is needed to achieve steel-to-rubber adhesion?

What steel cord constructions are useful to maximize resistance to fretting and resistance to corrosion?

Chapter 4
Mechanics of Cord-Rubber Composite Materials

By M. C. Assaad, T. G. Ebbott and J. D. Walter

[1]The Goodyear Tire & Rubber Company, Corporate Tire Research, Akron, OH 44316
[2] The University of Akron, Depts of Civil Engr. and Mechanical Engr., Akron, OH 44325

Chapter 4: Mechanics of Cord-Rubber Composite Materials

M. C. Assaad, T. G. Ebbott and J. D. Walter

1. Mechanical behavior of cord-rubber composite materials

Composite materials terminology

Composite materials consist of at least two different constituents that are bonded together. Generally, two materials are used in combination to produce a structure with the desired capabilities to meet specific thermo-mechanical requirements. The composite has properties that are superior to those of either of the individual constituents. Common composite materials for structural applications are those with either continuous or chopped fibers embedded in a softer matrix. Particulate composites composed of particles dispersed in a matrix are also commonly used. Different materials can also be combined on a microscopic or nano-scale to form a composite, or two-phase material, such as carbon-black filled rubber compounds. The resulting rubber compound is macroscopically *homogeneous*, since the material properties do not vary with position on a macro level whereas fibrous composites are macroscopically *heterogeneous* since the material properties do depend on position on the macro level, e.g., on the different properties of the fiber and the matrix. The scope of this discussion is limited to the mechanics of continuous fiber (i.e., tire cord) composites. Some discussion of particulate composites can be found in [64, 70].

The thermal-mechanical behavior of continuous cord reinforced rubber can be approximately described by the linear composite theory developed for more rigid composites such as glass fiber reinforced epoxy [1-3,6,13,25]. However, the flexibility of cord-rubber composites allows for large deformations, which requires a more complex analysis beyond the scope of this treatment [e.g., 68]. However, linear composite analysis combined with nonlinear finite element analysis can give a reasonable description of the material response for most applications. Finite element methods that allow the cord and rubber properties to be specified separately, rather than smeared into composite coefficients, can provide a very powerful method to represent the nonlinear response of cord-rubber composites.
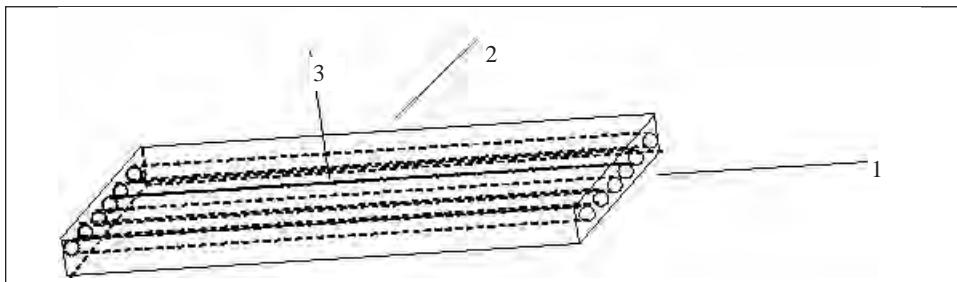
Most common engineering structural materials are macroscopically *homogeneous*, meaning that the properties are uniform throughout -- i.e., they are not functions of position. As one moves from point to point, the material properties such as stiffness, thermal conductivity, thermal coefficient of expansion, etc., remain constant. Some analysis methods for cord-rubber composites assume *homogeneity* and others allow for *heterogeneity* where the material properties can depend on position in the structure. For cord-rubber composites, this implies that the cord and rubber are represented separately geometrically with specific material properties for each constituent.

The term *isotropic* indicates that the material properties at any point of the structure are not a function of the orientation or direction. Therefore, all planes which pass through a point in an isotropic material are planes of material property symmetry.

In an *anisotropic* material, the material properties at a point are a function of direction. This is easily seen in figure 1.1 where the stiffness in the 1-direction along the cords is

much stiffer than the stiffness in the 2-direction, transverse to the cords.

**Figure 1.1: Diagram of a typical cord-rubber specimen**
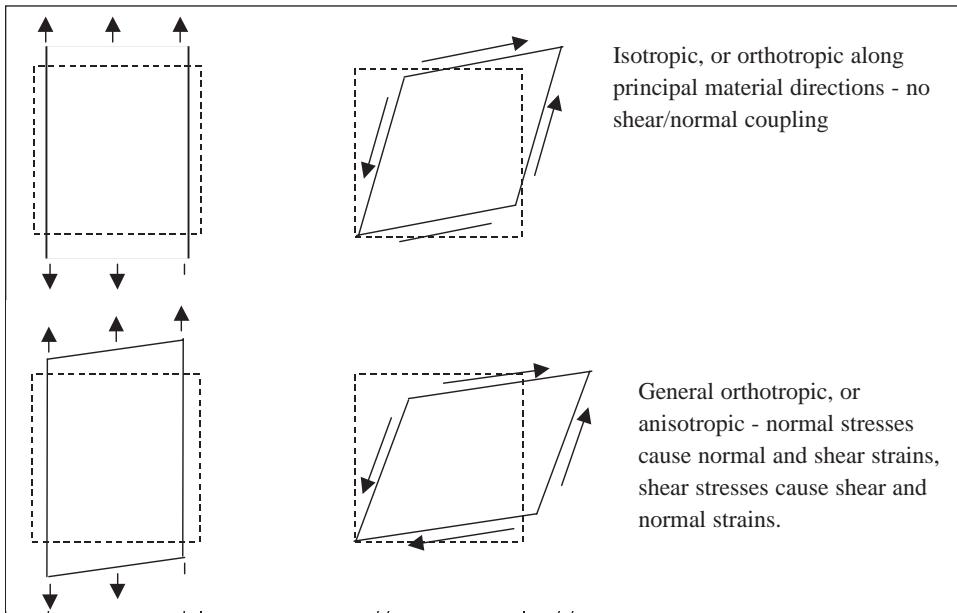
Complete anisotropy, where no assumptions concerning symmetry are made, is complex and can require many properties to describe the behavior. This type of material analysis is not commonly performed. If there exists three mutual planes of material symmetry, such as the 1-2, 1-3 and 2-3 planes in figure 1.1, then the material is said to be *orthotropic*. The properties at any point in the body are still a function of orientation, but the analysis is simplified. One can also see by intuition that a force applied in the 1, 2 or 3 direction of figure 1.1 will create normal strains, but no macroscopic shear strains. The directions 1,2,3 in this case are called *principal or natural material directions*. For a completely anisotropic material, a force in the 1 direction would create both normal and shear strains, illustrating *shear-normal coupling*.

To illustrate the behavior of isotropic, orthotropic, and anisotropic materials under uniform loadings of normal stress and shear stress, simple sketches are shown in figure 1.2.

For an isotropic material, or an orthotropic material loaded along the principal material directions, an applied normal stress will cause a stretch of the specimen along the loaded direction and usually a contraction in the perpendicular direction. A shear stress will only cause a shear deformation characterized by distortion without extension or contraction. There is no coupling between shear stresses and normal strains, or between normal stresses and shear strains.

For a fully anisotropic material or an orthotropic material with stresses applied in non-principal material directions, an applied normal stress produces not only an extensional deformation along the direction of the applied stress and normal strains in the transverse direction, but also shear deformations. A shear stress will produce, in addition to the shear deformation, extension and contraction deformations. Coupling exists between modes of loading and modes of deformation.

Isotropic, orthotropic, or anisotropic materials can be considered either homogeneous or heterogeneous. The degree of homogeneity may depend on the scale of observation or analysis. A rubber compound may look homogeneous to the naked eye, but it is very heterogeneous at a nanometer scale. The diagram in figure 1.1 is heterogeneous, since the cords and rubber are represented separately, and a point on a cord will have different properties than a point on the rubber. Oftentimes, the properties of the cords and rubber in figure 1.1 will be "smeared" or averaged over the volume. In this case the analysis is orthotropic and homogeneous. Theories that combine the properties of fibers and matrix to form equivalent composite properties and those that can resolve individual stresses and strains for fiber and matrix are commonly called *micromechanics* theories.

Figure 1.2: Mechanical behavior of isotropic, orthotropic and anisotropic materials.

Isotropic, or orthotropic along principal material directions - no shear/normal coupling

General orthotropic, or anisotropic - normal stresses cause normal and shear strains, shear stresses cause shear and normal strains.

To obtain the desired structural properties, different arrangements of cords and rubber compounds are combined in single layers or *lamina*. Many layers are often stacked together to get the desired properties in different directions. A structure with multiple layers is called a *laminate*. It is common to combine many *laminae* with different cord angles to obtain the desired strength and stiffness in various directions in the laminate. In order to analyze and design the stiffness and strength of belt and ply layers in tires, composite theory is often utilized. The simplest, linear, composite theory for multiple layers bonded together is called *laminate theory*. The following sections will address the mechanical analysis of composite laminae and laminates with some discussion of finite element methods for cord-rubber composites.

Exercises

True or false

1. For most isotropic materials, a uniaxial normal stress causes extension in the direction of the applied stress and a contraction in the perpendicular direction.

2. For orthotropic materials, like isotropic materials, normal stress in a principal material direction results in extension in the direction of the applied stress and contraction perpendicular to the stress. However, due to different properties in the two principal material directions, the contraction can be either more or less than the contraction of a similarly loaded isotropic material with the same elastic modulus in the direction of the load.

3. For an anisotropic material, application of a normal stress can result in an extension in the direction of the stress, contraction perpendicular to the applied stress, and a shearing deformation.

4. Coupling between both loading modes (normal and shearing) and both deformation modes (extension and distortion) is characteristic of orthotropic materials subjected to normal stress in a non-principal material direction.

2. Linear Anisotropic and Orthotropic Analysis

In tire applications, rubber compounds are often assumed to be isotropic, and cord-rubber composites are assumed to be orthotropic. Combined they can withstand the required structural and thermal service conditions. This section will provide a brief description of the linear orthotropic properties used to define the mechanical characteristics of the belt or ply layers. Since no spatial distinction between cord and rubber is made in this section, the analysis is homogeneous and anisotropic, or more specifically, orthotropic.

Orthotropic elastic properties are used in numerical modeling such as finite element analysis (FEA) as well as closed-form methods. Since a tire undergoes large deformations, the overall structural problem is nonlinear. However, the stiffnesses predicted by linear orthotropic elasticity are useful for design, and when they are utilized with nonlinear finite element analysis, a good approximation to the tire's structural response is obtained. Development of the theory for composite laminae and laminates given here follows those given by Jones [13] and Walter [25].
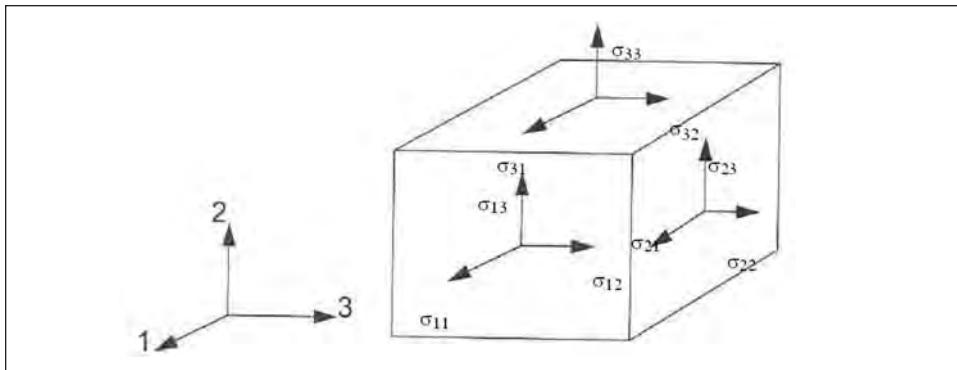
Isotropic elastic properties

The simplest form of linear elasticity utilizes an isotropic material where material properties are independent of direction, and all planes exhibit material symmetry. The elastic properties are completely defined by Young's modulus E, and Poisson's ratio v, or any other combination of two independent elastic constants. For example, another possibility is to use the shear modulus G and the bulk modulus K to describe the material. Many interrelations among the elastic constants exist [1] such as

$$G = \frac{E}{2(1+v)} \tag{2.1}$$

For a three dimensional stress state, such as that illustrated in figure 2.1, the generalized Hooke's law for a linear isotropic material is given by equation 2.2.

Figure 2.1: Three dimensional state of stress

$$\begin{bmatrix} \varepsilon_1 \\ \varepsilon_2 \\ \varepsilon_3 \\ \gamma_{23} \\ \gamma_{31} \\ \gamma_{12} \end{bmatrix} = \begin{bmatrix} \dfrac{1}{E} & \dfrac{-v}{E} & \dfrac{-v}{E} & 0 & 0 & 0 \\ \dfrac{-v}{E} & \dfrac{1}{E} & \dfrac{-v}{E} & 0 & 0 & 0 \\ \dfrac{-v}{E} & \dfrac{-v}{E} & \dfrac{1}{E} & 0 & 0 & 0 \\ 0 & 0 & 0 & \dfrac{1}{G} & 0 & 0 \\ 0 & 0 & 0 & 0 & \dfrac{1}{G} & 0 \\ 0 & 0 & 0 & 0 & 0 & \dfrac{1}{G} \end{bmatrix} \begin{bmatrix} \sigma_1 \\ \sigma_2 \\ \sigma_3 \\ \tau_{23} \\ \tau_{31} \\ \tau_{12} \end{bmatrix} \tag{2.2}$$

Equation 2.2 can be abbreviated as

$$[\varepsilon] = [S][\sigma] \tag{2.3}$$

where $[S]$ is the compliance matrix. The "engineering" shear strains γ_{ij} are used such that, e.g., $\tau_{12} = G\gamma_{12}$. The tensorial shear strains are half the engineering shear strains, and will be used when coordinate system rotations are required.

The relationship in equation 2.2 is valid for any orientation. Material stability requires that the material matrix $[S]$ relating the state of stress to the state of strain be positive definite. This requirement is satisfied when $E > 0$, $G > 0$, and $-1 < v < 0.5$.

Orthotropic elastic properties
For an orthotropic material analyzed with respect to the principal material directions, the following stress-strain relations apply:

$$\begin{bmatrix} \varepsilon_1 \\ \varepsilon_2 \\ \varepsilon_3 \\ \gamma_{23} \\ \gamma_{31} \\ \gamma_{12} \end{bmatrix} = \begin{bmatrix} \dfrac{1}{E_1} & \dfrac{-v_{21}}{E_2} & \dfrac{-v_{31}}{E_3} & 0 & 0 & 0 \\ \dfrac{-v_{12}}{E_1} & \dfrac{1}{E_2} & \dfrac{-v_{32}}{E_3} & 0 & 0 & 0 \\ \dfrac{-v_{13}}{E_1} & \dfrac{-v_{23}}{E_2} & \dfrac{1}{E_3} & 0 & 0 & 0 \\ 0 & 0 & 0 & \dfrac{1}{G_{23}} & 0 & 0 \\ 0 & 0 & 0 & 0 & \dfrac{1}{G_{31}} & 0 \\ 0 & 0 & 0 & 0 & 0 & \dfrac{1}{G_{12}} \end{bmatrix} \begin{bmatrix} \sigma_1 \\ \sigma_2 \\ \sigma_3 \\ \tau_{23} \\ \tau_{31} \\ \tau_{12} \end{bmatrix} \tag{2.4}$$

where the nine material properties for linear orthotropic elasticity are the three moduli E_1,

E_2, E_3; Poisson's ratios , ν_{12}, ν_{23}, ν_{31}, and the shear moduli G_{12}, G_{23}, and G_{31}. The quantity ν_{ij} is the Poisson's ratio for a uniaxial normal stress applied in the i-direction, or,

$$\nu_{ij} = -\frac{strain\ in\ the\ j-direction}{strain\ in\ the\ i-direction} \tag{2.5}$$

The components of the compliance matrix are defined by

$$S_{11} = \frac{1}{E_1},\ S_{12} = -\frac{\nu_{21}}{E_2},\ etc \tag{2.6}$$

Due to the symmetry of [S], the three Poisson's ratios and three Young's moduli are related by

$$\frac{\nu_{ij}}{E_i} = \frac{\nu_{ji}}{E_j} \tag{2.7}$$

For analysis in the principal material directions (equation 2.4), there is no interaction between normal stresses σ_1, σ_2, σ_3 and shearing strains γ_{12}, γ_{23}, γ_{31}, or between shearing stresses τ_{12}, τ_{23}, τ_{31} and normal strains ε_1, ε_2, ε_3, or between the shearing stresses and the shearing strains on different planes.

Material stability for an orthotropic material also requires that [S] be positive-definite, which results in the criteria:

$$E_1, E_2, E_3, G_{12}, G_{23}, G_{31} > 0$$

$$\left|\nu_{ij}\right| < \left(\frac{E_i}{E_j}\right)^{\frac{1}{2}} \tag{2.8}$$

$$1 - \nu_{12}\nu_{21} - \nu_{23}\nu_{32} - \nu_{31}\nu_{13} - 2\nu_{21}\nu_{32}\nu_{13} > 0$$

When the left hand side of the last inequality is zero, the material is said to be incompressible, and a special set of equations for incompressible orthotropic elasticity are needed. For the isotropic case, equation 2.8 ensures that $\nu < 1/2$.

A special subclass of orthotropic materials is obtained if at every point of the material there is one plane in which the mechanical properties are equal in all directions. This type of material is termed *transversely isotropic*. If, for example, the 2-3 plane is the special plane of isotropy, then the material properties in any direction in the 2-3 plane are the same, and the 2 and 3 subscripts can be used interchangeably. The number of independent elastic constants needed to describe the structural behavior of a transversely isotropic material is reduced from nine for orthotropic, to five. The five constants can be listed as: E_1, $E_2(=E_3)$, $\nu_{12}(=\nu_{13})$, ν_{23}, $G_{12}(=G_{13})$, with
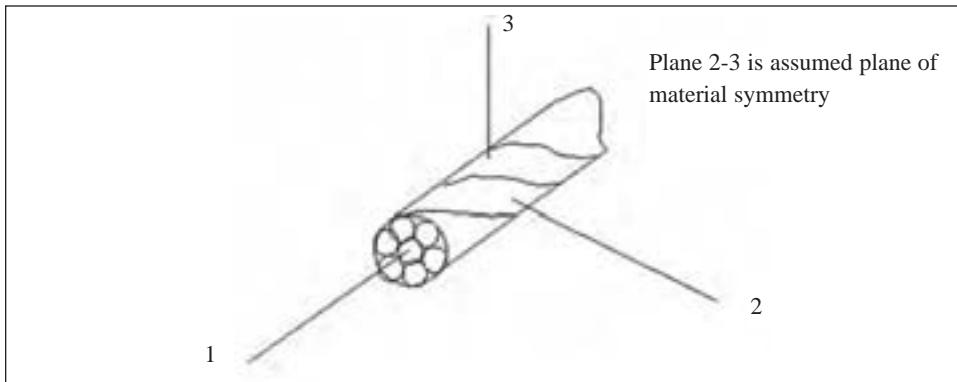
$$G_{23} = \frac{E_2}{(1 + 2\nu_{23})}$$

Oftentimes G_{23}, rather than ν_{23}, is specified. Steel and organic tire cords may be considered transversely isotropic as shown in figure 2.2.

The most general type of linear elastic material is fully anisotropic where there are no planes of symmetry for the material properties. To describe a fully anisotropic material,

one would need 21 independent elastic constants as illustrated in Eq 2.9.

Figure 2.2: Cords and wires are sometimes treated as transversely isotropic

3

Plane 2-3 is assumed plane of material symmetry

2

1

$$
\begin{bmatrix} \varepsilon_1 \\ \varepsilon_2 \\ \varepsilon_{33} \\ \gamma_{23} \\ \gamma_{31} \\ \gamma_{12} \end{bmatrix} = \begin{bmatrix} S_{11} & S_{12} & S_{13} & S_{14} & S_{15} & S_{16} \\ & S_{22} & S_{23} & S_{24} & S_{25} & S_{26} \\ & & S_{33} & S_{34} & S_{35} & S_{36} \\ & & & S_{44} & S_{45} & S_{46} \\ & & & & S_{55} & S_{56} \\ & & & & & S_{66} \end{bmatrix} \begin{bmatrix} \sigma_1 \\ \sigma_2 \\ \sigma_3 \\ \tau_{23} \\ \tau_{31} \\ \tau_{12} \end{bmatrix} \tag{2.9}
$$
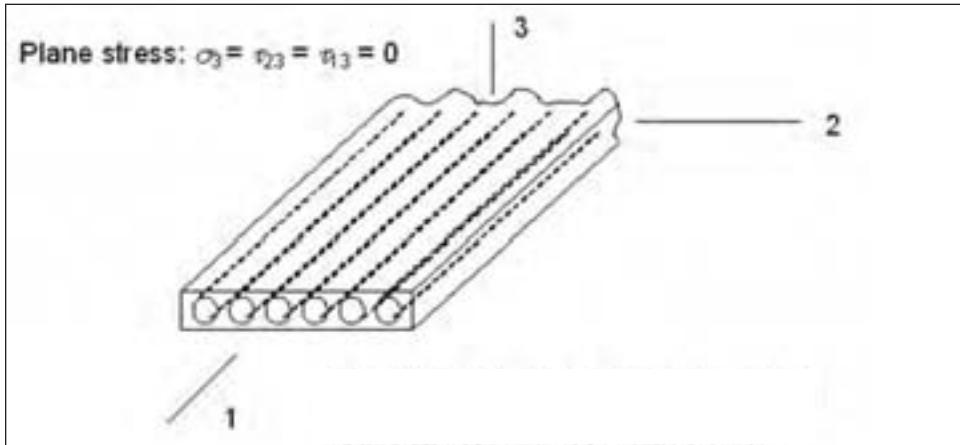
where the [S] matrix remains symmetric.

To analyze a structure with a fully anisotropic elastic material, a finite element code would require the input of all 21 independent constants. The restrictions imposed upon the elastic constants by the stability requirements are too complex to list in terms of simple equations. However, they can be satisfied if one ensures that the compliance matrix is positive definite. This criterion is often checked automatically by commercially available finite element computer codes [e.g., 2].

Stress-strain equations for a lamina representing a belt or ply layer
A fully anisotropic material characterization is rarely used or needed in tire design calculations. Most cord-rubber composites are analyzed as orthotropic materials under plane stress conditions. The structure is called a lamina and shown in figure 2.3. For this lamina the following stresses are assumed zero for plane stress conditions:

$\sigma_3 = \tau_{23} = \tau_{31} = 0$

Figure 2.3 Portion of single belt or ply layer with plane stress assumptions

When these stresses are set to zero, it follows that the following shear strains are also zero:

$$\gamma_{23} = \gamma_{31} = 0$$

The normal strain ε_3 can be calculated from σ_1, σ_2 and the orthotropic material properties given in equation 2.4.

The orthotropic stress-strain relationship in equation 2.4 can be simplified for plane stress and presented in a more compact form:

$$\begin{bmatrix} \varepsilon_1 \\ \varepsilon_2 \\ \gamma_{12} \end{bmatrix} = \begin{bmatrix} \dfrac{1}{E_1} & \dfrac{-v_{12}}{E_1} & 0 \\ \dfrac{-v_{21}}{E_2} & \dfrac{1}{E_2} & 0 \\ 0 & 0 & \dfrac{1}{G_{12}} \end{bmatrix} \begin{bmatrix} \sigma_1 \\ \sigma_2 \\ \tau_{12} \end{bmatrix} \qquad (2.10)$$

or

$$[\varepsilon] = [S][\sigma] \qquad (2.11)$$

where [S] is now the plane stress compliance matrix for the lamina. The non-zero terms of the [S] matrix retained for plane stress in equation 2.10 are S_{11}, S_{12}, S_{21}, S_{22}, and S_{66}. For the orthotropic plane stress problem, there are four independent elastic constants: the Young's moduli in the direction along the reinforcement and in the transverse direction, E_1 and E_2, respectively, the in-plane shear modulus G_{12}, and the major Poisson's ratio v_{12}. The other

Poisson's ratio, v_{21} can be determined from the reciprocity relationship (equation 2.7). When the lamina compliance matrix, $[S]$, is inverted, the lamina stiffness matrix, $[Q]$ is obtained

$$[Q] = [S]^{-1} \tag{2.12}$$

Thus, the stresses in terms of the strains for the lamina in the principal material directions are given as:

$$\begin{bmatrix} \sigma_1 \\ \sigma_2 \\ \tau_{12} \end{bmatrix} = \begin{bmatrix} Q_{11} & Q_{12} & 0 \\ Q_{21} & Q_{22} & 0 \\ 0 & 0 & Q_{66} \end{bmatrix} \begin{bmatrix} \varepsilon_1 \\ \varepsilon_2 \\ \gamma_{12} \end{bmatrix} \tag{2.13}$$

or,

$$\begin{bmatrix} \sigma_1 \\ \sigma_2 \\ \tau_{12} \end{bmatrix} = \begin{bmatrix} Q_{11} & Q_{12} & 0 \\ Q_{21} & Q_{22} & 0 \\ 0 & 0 & 2Q_{66} \end{bmatrix} \begin{bmatrix} \varepsilon_1 \\ \varepsilon_2 \\ \varepsilon_{12} \end{bmatrix} \tag{2.14}$$

It is customarily acceptable to refer to the 3-3 entry in equations 2.13 and 2.14 as Q_{66}. The notation finds its origin in the general expression of the stress-strain relations for an anisotropic material (equations 2.4, 2.9) before being simplified to plane stress in an orthotropic material as expressed in equation 2.13. In equation 2.14 the shear strain has been changed to $\varepsilon_{12}(=\gamma_{12}/2)$, so that tensorial transformations are valid. The components of the stiffness matrix, $[Q]$, are given as follows:

$$Q_{11} = \frac{E_1}{(1-v_{12}v_{21})}, \quad Q_{22} = \frac{E_2}{(1-v_{12}v_{21})}, \quad Q_{12} = v_{21}\frac{E_1}{(1-v_{12}v_{21})}, \tag{2.15}$$

$$Q_{21} = v_{12}\frac{E_2}{(1-v_{12}v_{21})}, \quad Q_{66} = G_{12}$$

Table 2.1 shows the interrelationships among the different forms of the elastic constants.
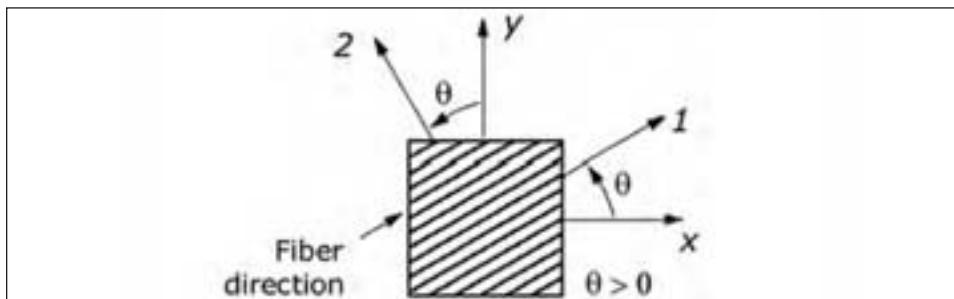
**Table 2.1: Interrelationships among orthotropic elastic constants [25]**

	Engineering Constants				
	E_1	E_2	ν_{12}	ν_{21}	G_{12}
Compliances	$\dfrac{1}{S_{11}}$	$\dfrac{1}{S_{22}}$	$-\dfrac{S_{12}}{S_{11}}$	$-\dfrac{S_{12}}{S_{22}}$	$\dfrac{1}{S_{66}}$
Stiffnesses	$\dfrac{Q_{11}Q_{22}-Q_{12}^2}{Q_{22}}$	$\dfrac{Q_{11}Q_{22}-Q_{12}^2}{Q_{11}}$	$\dfrac{Q_{12}}{Q_{22}}$	$\dfrac{Q_{12}}{Q_{11}}$	Q_{66}
	Compliances				
	S_{11}	S_{22}	S_{12}	S_{66}	
Stiffnesses	$\dfrac{Q_{22}}{Q_{11}Q_{22}-Q_{12}^2}$	$\dfrac{Q_{11}}{Q_{11}Q_{22}-Q_{12}^2}$	$-\dfrac{Q_{12}}{Q_{11}Q_{22}-Q_{12}^2}$	$\dfrac{1}{Q_{66}}$	
Engineering Constants	$\dfrac{1}{E_1}$	$\dfrac{1}{E_2}$	$-\dfrac{\nu_{12}}{E_1}$	$\dfrac{1}{G_{12}}$	
	Stiffnesses				
	Q_{11}	Q_{22}	Q_{12}	Q_{66}	
Engineering Constants	$\dfrac{E_1}{1-\nu_{12}\nu_{21}}$	$\dfrac{E_2}{1-\nu_{12}\nu_{21}}$	$\dfrac{\nu_{12}E_2}{1-\nu_{12}\nu_{21}}$	G_{12}	
Compliances	$\dfrac{S_{22}}{S_{11}S_{22}-S_{12}^2}$	$\dfrac{S_{11}}{S_{11}S_{22}-S_{12}^2}$	$\dfrac{-S_{12}}{S_{11}S_{22}-S_{12}^2}$	$\dfrac{1}{S_{66}}$	

The principal directions of material orthotropy (1,2) do not always coincide with the reference directions used for the structure (x, y). An example is the angled belts of a radial tire, where the direction of the belt wires is at an angle (e.g., 20 degrees) to the tire axes x-y-z. The circumferential (x) and lateral (y) stiffnesses of the belt are desired for tire design and analysis. When this occurs, a method of transforming the stress-strain relations from one coordinate system to another is needed.

The angle of rotation from the x-axis to the principal 1-axis is θ as shown in figure 2.4. Stress and strain are second order tensors and they transform with change of coordinate reference in a specific manner.

Figure 2.4: x-y axes rotated θ degrees from principal material axes 1-2. Positive rotation is in the counterclockwise direction

The transformation equations for expressing stress and strain in the reference coordinate system (x, y) in terms of the stresses and strains in the material principal directions (1, 2) are given as follows.

$$\begin{bmatrix} \sigma_1 \\ \sigma_2 \\ \tau_{12} \end{bmatrix} = [R] \begin{bmatrix} \sigma_x \\ \sigma_y \\ \tau_{xy} \end{bmatrix}, \quad \begin{bmatrix} \varepsilon_1 \\ \varepsilon_2 \\ \varepsilon_{12} \end{bmatrix} = [R] \begin{bmatrix} \varepsilon_x \\ \varepsilon_y \\ \varepsilon_{xy} \end{bmatrix}$$

(2.16)

where [R] is the transformation matrix given in terms of the angle θ as

$$[R] = \begin{bmatrix} c^2 & s^2 & 2sc \\ s^2 & c^2 & -2sc \\ -sc & sc & c^2 - s^2 \end{bmatrix}$$

(2.17)

Here the abbreviations $s = \sin\theta$ and $c = \cos\theta$ are used.
Note that the inverse of the matrix [R] is obtained by changing the sign of the angle, i.e.,

$$[R(\theta)]^{-1} = [R(-\theta)]$$

(2.18)

The lamina principal stress-strain relations transformed to the lamina reference axes (x, y) can be obtained by substituting Eqs (2.16) into (2.14) to give

$$\begin{bmatrix} \sigma_x \\ \sigma_y \\ \tau_{xy} \end{bmatrix} = \begin{bmatrix} \overline{Q}_{11} & \overline{Q}_{12} & \overline{Q}_{16} \\ \overline{Q}_{12} & \overline{Q}_{22} & \overline{Q}_{26} \\ \overline{Q}_{16} & \overline{Q}_{26} & \overline{Q}_{66} \end{bmatrix} \begin{bmatrix} \varepsilon_x \\ \varepsilon_y \\ \gamma_{xy} \end{bmatrix}$$

(2.19)

where the components of [Q] are calculated from

$$[\overline{Q}] = [R]^{-1} [Q][R]^{-T}$$

(2.20)

and the superscript [ ]^T denotes the transpose.

Note that [$\overline{Q}$] is symmetric. Note also that the engineering shear strain γ_{xy}, rather than the tensorial shear strain ε_{xy}, is used in equation 2.19, so that the common definitions for the $\overline{Q}_{ij}$ result. The $\overline{Q}_{ij}$ are related to the reduced stiffnesses Q_{ij} by the following

$$\overline{Q}_{11} = Q_{11}c^4 + 2(Q_{12} + 2Q_{66})s^2c^2 + Q_{22}s^4$$
$$\overline{Q}_{22} = Q_{11}s^4 + 2(Q_{12} + 2Q_{66})s^2c^2 + Q_{22}c^4$$
$$\overline{Q}_{12} = (Q_{11} + Q_{22} - 4Q_{66})s^2c^2 + Q_{12}(s^4 + c^4)$$
$$\overline{Q}_{16} = (Q_{11} - Q_{12} - 2Q_{66})sc^3 + (Q_{12} - Q_{22} + 2Q_{66})s^3c$$
$$\overline{Q}_{26} = (Q_{11} - Q_{12} - 2Q_{66})s^3c + (Q_{12} - Q_{22} + 2Q_{66})sc^3$$
$$\overline{Q}_{66} = (Q_{11} + Q_{22} - 2Q_{12} - 2Q_{66})s^2c^2 + Q_{66}(s^4 + c^4)$$

(2.21)

The matrix $[\overline{Q}]$ is now populated with nine non-zero components. There are still only four independent elastic constants, since the lamina is planar and orthotropic. In the new reference coordinate system (x, y), there is coupling between shear strain and normal stresses and between shear stress and normal strains. Thus, in the new reference coordinate system (x, y), the lamina behaves like a completely anisotropic material.

In a similar fashion, the strains can be expressed as a function of the stresses in the arbitrary coordinate system (x, y) as

$$
\begin{bmatrix} \varepsilon_x \\ \varepsilon_y \\ \gamma_{xy} \end{bmatrix} = \begin{bmatrix} \overline{S}_{11} & \overline{S}_{12} & \overline{S}_{16} \\ \overline{S}_{12} & \overline{S}_{22} & \overline{S}_{26} \\ \overline{S}_{16} & \overline{S}_{26} & \overline{S}_{66} \end{bmatrix} \begin{bmatrix} \sigma_x \\ \sigma_y \\ \tau_{xy} \end{bmatrix}
\tag{2.22}
$$

where the components of the lamina compliance matrix $\left[\overline{S} \right]$ are given by

$$
\begin{aligned}
\overline{S}_{11} &= S_{11}c^4 + (2S_{12} + S_{66})s^2c^2 + S_{22}s^4 \\
\overline{S}_{22} &= S_{11}s^4 + 2(S_{12} + 2S_{66})s^2c^2 + S_{22}c^4 \\
\overline{S}_{12} &= (S_{11} + S_{22} - S_{66})s^2c^2 + S_{12}(s^4 + c^4) \\
\overline{S}_{16} &= (2S_{11} - 2S_{12} - S_{66})sc^3 + (2S_{12} - 2S_{22} - S_{66})s^3c \\
\overline{S}_{26} &= (2S_{11} - 2S_{12} - S_{66})s^3c + (2S_{12} - 2S_{22} - S_{66})sc^3 \\
\overline{S}_{66} &= 2(2S_{11} + 2S_{22} - 4S_{12} - S_{66})s^2c^2 + S_{66}(s^4 + c^4)
\end{aligned}
\tag{2.23}
$$

All the elastic coefficients in equations (2.19), (2.21) and (2.23) for plane stress are functions of the four orthotropic elastic constants, E_1, E_2, G_{12}, ν_{12}, and the angle θ from the 1-direction of the orthotropic lamina. The stress-strain relations governing the off-axis response of a single ply can be written as [3]

$$
\varepsilon_x = \frac{\sigma_x}{E_x} - \frac{\nu_{yx}}{E_y}\sigma_y - \lambda_x\tau_{xy}
$$

$$
\varepsilon_y = \frac{\sigma_y}{E_y} - \frac{\nu_{xy}}{E_x}\sigma_x - \lambda_y\tau_{xy}
\tag{2.24}
$$

$$
\gamma_{xy} = \frac{\tau_{xy}}{G_{xy}} - \lambda_x\sigma_x - \lambda_y\sigma_y
$$

where the engineering constants can be evaluated from

$$\frac{1}{E_x} = \frac{\cos^4\theta}{E_1} + \frac{\sin^4\theta}{E_2} + \left(\frac{1}{G_{12}} - \frac{2\nu_{12}}{E_1}\right)\sin^2\theta\cos^2\theta$$

$$\frac{1}{E_y} = \frac{\sin^4\theta}{E_1} + \frac{\cos^4\theta}{E_2} + \left(\frac{1}{G_{12}} - \frac{2\nu_{12}}{E_1}\right)\sin^2\theta\cos^2\theta$$

$$\frac{1}{G_{xy}} = \frac{\cos^2 2\theta}{G_{12}} + \left[\frac{1+\nu_{12}}{E_1} + \frac{1+\nu_{21}}{E_2}\right]\sin^2 2\theta$$

$$\frac{\nu_{xy}}{E_x} = \frac{\nu_{yx}}{E_y} = \frac{\nu_{12}}{E_1} - \frac{1}{4}\left[\frac{1+\nu_{12}}{E_1} + \frac{1+\nu_{21}}{E_2} - \frac{1}{G_{12}}\right]\sin^2 2\theta \qquad (2.25)$$

$$\lambda_x = \sin 2\theta\left[\frac{\sin^2\theta}{E_2} - \frac{\cos^2\theta}{E_1} + \frac{1}{2}\left(\frac{1}{G_{12}} - \frac{2\nu_{12}}{E_1}\right)\cos 2\theta\right]$$

$$\lambda_y = \sin 2\theta\left[\frac{\cos^2\theta}{E_2} - \frac{\sin^2\theta}{E_1} - \frac{1}{2}\left(\frac{1}{G_{12}} - \frac{2\nu_{12}}{E_1}\right)\cos 2\theta\right]$$

In addition, the elastic constants are functions of the mechanical properties of the constituents, e.g., the cord and the rubber modulus. In section 3, methods for determining the orthotropic properties from the constituent properties will be addressed.

Figure 2.5 shows how the composite engineering constants vary with angle for a typical tire cord-rubber ply. Figures 2.6 and 2.7 show the corresponding data for the compliances and the reduced stiffnesses, respectively. These plots are based on data from Patel et al. [4].

Often, it is easier experimentally to work with the compliances rather than the reduced stiffnesses. For example, it is easier to apply $\sigma_{xx} = \sigma_0$ (with all other stresses equal to zero)

Figure 2.5: Variation of G_{xy}, E_x and ν_{xy} with cord angle for a 1000/2 polyester ply [4]
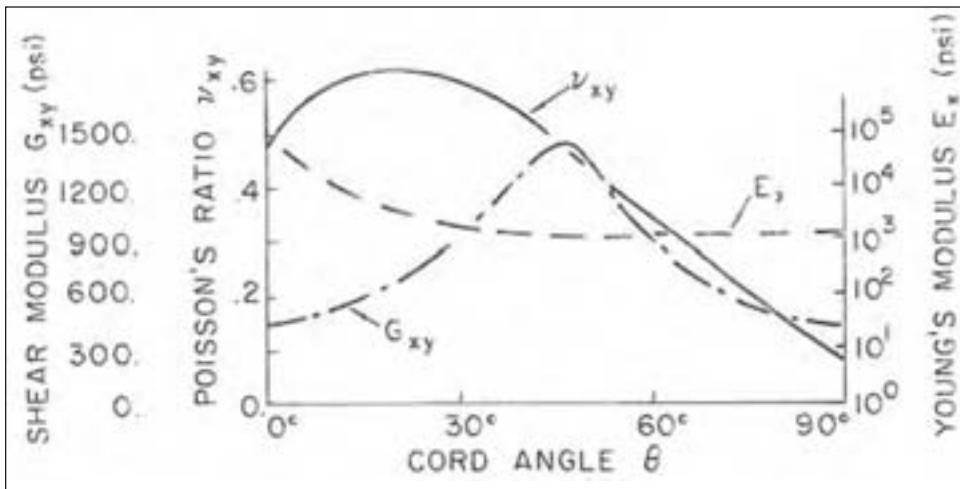
**Figure 2.6: Variation of transformed compliances
with cord angle for a 1000/2 polyester ply [4]**
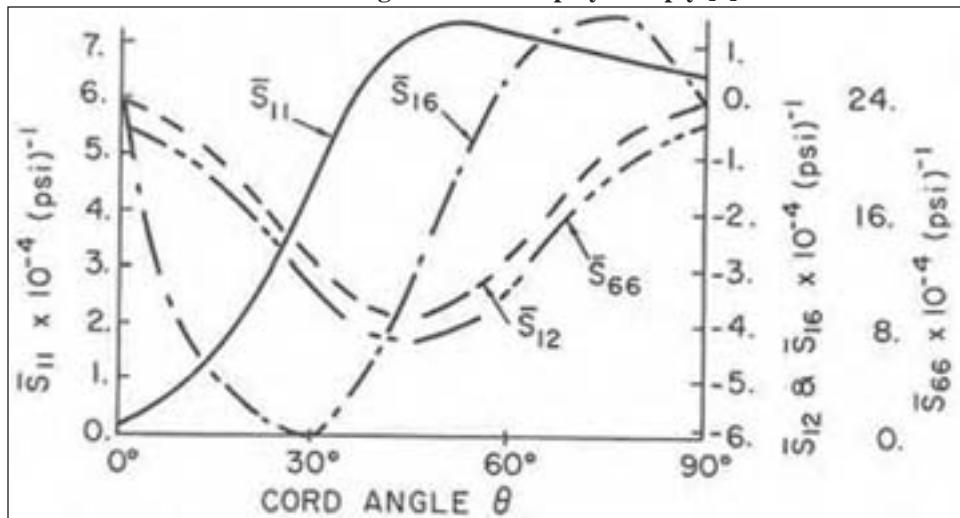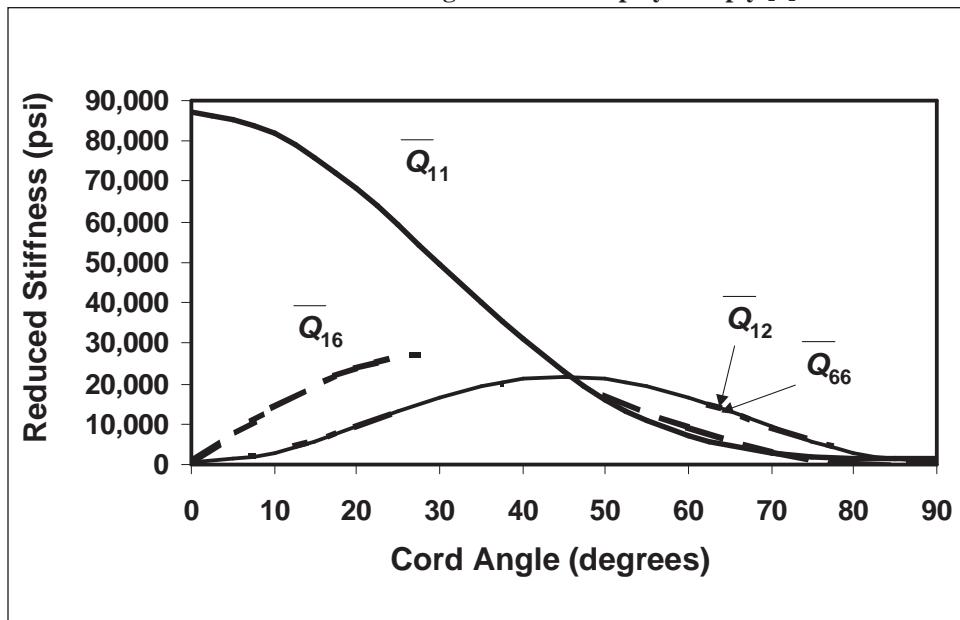
**Figure 2.7: Variation of transformed reduced
stiffnesses with cord angle for a 1000/2 polyester ply [4]**

to determine $S_{11}=1/E_1$, than it is to apply $\varepsilon_{xx}=\varepsilon_0$ (with all other strains zero) to determine Q_{11}. The latter test requires bi-axial grips to apply a zero strain boundary condition in the transverse direction.
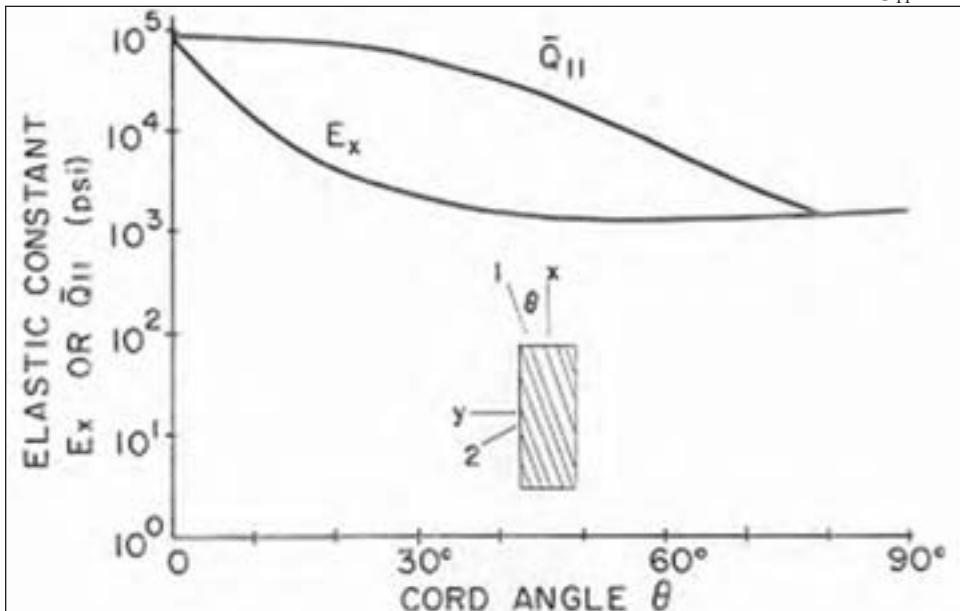
One important consideration is the difference between E_x (determined with zero transverse and shear stress boundary conditions) and Q_{11}(determined with zero transverse and shear strain boundary conditions). Figure 2.8 shows these two functions. Note that

there can be an order of magnitude difference in these two coefficients which both relate normal stress to normal strain as in

$$\sigma_x = E_x \varepsilon_x \ , \ for \, \sigma_y = \tau_{xy} = 0, \ or$$

$$\sigma_x = \overline{Q}_{11} \varepsilon_x \ , \ for \, \varepsilon_y = \gamma_{xy} = 0.$$

(2.26)

Figure 2.8: Comparison of modulus E_x with transformed reduced stiffness $\overline{Q}_{11}$

Experimental determination of lamina properties

To determine the S_{ij} or the Q_{ij} for analysis, two possibilities are: 1) measure them by testing cord-rubber composites, or 2) compute them from the measured properties of the composite's constituents. The former method will be discussed here, and the latter in the next section. In general, the load-deflection response of cord-rubber composites will be nonlinear and hysteretic, so engineering judgement is used to determine the best linear elastic approximation from the test data.

First, determine $S_{11} = 1/E_1$ and v_{12}, by running a simple tension test with loading in the cord direction. Since the modulus of the cords is typically 100-1000 times larger than the modulus of the rubber, the 1-direction response is dominated by the cords. So, the E_1 modulus of the homogenized composite should be approximately the modulus of the cords multiplied by the volume fraction of the cords. The major Poisson's ratio v_{12} might be difficult to measure since the displacements are relatively small when testing in the 1-1 direction. However, full field techniques such as moire, or digital image correlation (DIC) [5] should provide the required accuracy. Figure 2.9 shows moire patterns on a cord-rubber composite that can be used to compute displacements in the loading and transverse directions. Also, a full-field technique like moire or DIC will help confirm that the load is being applied in a uniform manner, and will also provide measurements of strains that do not contain edge effects or grip effects.

Second, determine $S_{22} = 1/E_2$ and v_{21} by running a simple tension test with loading in the 2- direction, or 90 degrees from the cord direction as shown in figure 2.10. The transverse modulus E_2 is usually dominated by the rubber response. For a 50% volume fraction of cords, an initial estimate of E_2 would be twice the rubber modulus, however many factors will affect this value. Stiffening due to the constraint imposed by the cords on the rubber in the 1–direction, which minimizes the rubber's lateral contraction, and edge effects can be significant in this test. The cords can even debond from the rubber at the free edges.

With E_1, E_2, v_{12}, and v_{21} determined, reciprocity (Eq 2.7) can be checked.

Figure 2.9: Moire fringes on a cord-rubber composite. The displacement is constant within each fringe. Fringes for x and y displacements are shown.
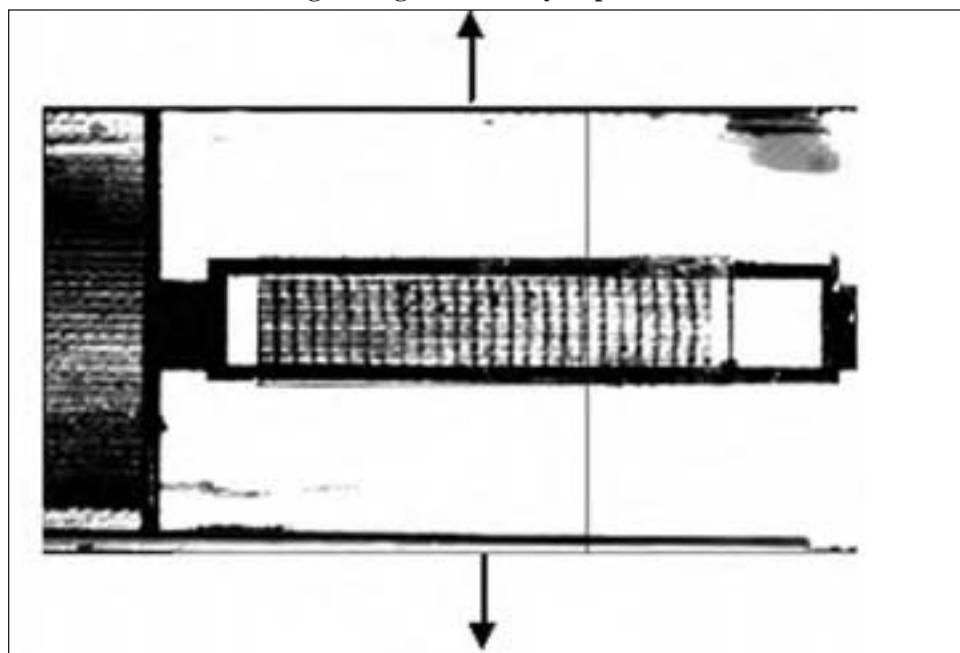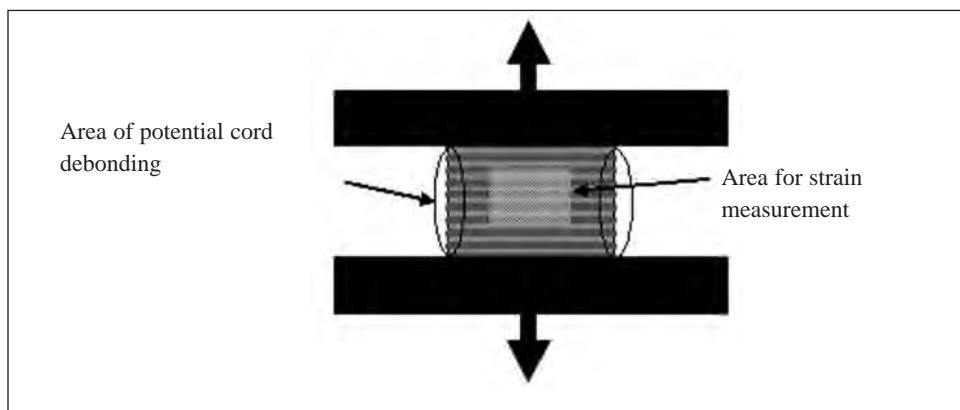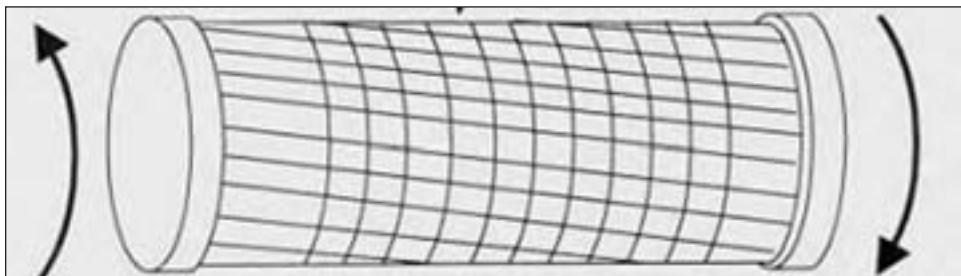
Figure 2.10: Schematic of test for E_2 with cords at 90 degrees

Lastly, G_{12} needs to be measured. The simplest method is to perform an off-axis tension test with the cords at, say, 45 degrees to the load line, and then use the first equation in equation 2.25 to solve for G_{12}. Another possible experiment for G_{12} is the torsion of a thin-walled cylinder made of the cord-rubber composite as shown in figure 2.11. The cords can be oriented in either the axial or circumferential direction of the cylinder.

Figure 2.11: Torsion of a cord-rubber cylinder for G_{12} determination. Grid, moire or DIC can be used for shear strain measurement away from the grips.

Finite element implementation

When using a finite element code, the properties of the cord-rubber components need to be specified. Some options for specifying the single layer mechanical properties reviewed in this chapter are the following: 1) solid 3-D elements with orthotropic properties, 2) shell or membrane elements with orthotropic properties, 3) 1-D stiffness ("rebar") [2] elements added to solid 3-D elements, 4) 1-D stiffness ("rebar") elements added to membrane or shell elements, and 5) use of an RVE (representative volume element) or unit cell to compute the effective properties. In the latter case, the procedure follows that for the general method of cells (GMC) which will be discussed in the next section. If the properties are specified in the principal material directions, the transformation from the principal material orientation to a different global or local coordinate system is usually specified.

Case 1) requires the input of all 9, 3-D orthotropic properties $E_1, E_2, E_3, \nu_{12}, \nu_{23}, \nu_{31}, G_{12}, G_{23}, G_{31}$.

Case 2) requires the input of either the four planar orthotropic properties, or the reduced stiffnesses.

Cases 3) and 4) require the input of isotropic or orthotropic properties and orientation for the solid, membrane, or shell element, and the 1-D stiffness (E_1 and total area, or E_1, cord spacing and cord diameter) and orientation of the rebar elements.

Case 5) can provide the values for the orthotropic properties utilized in cases 1) and 2).
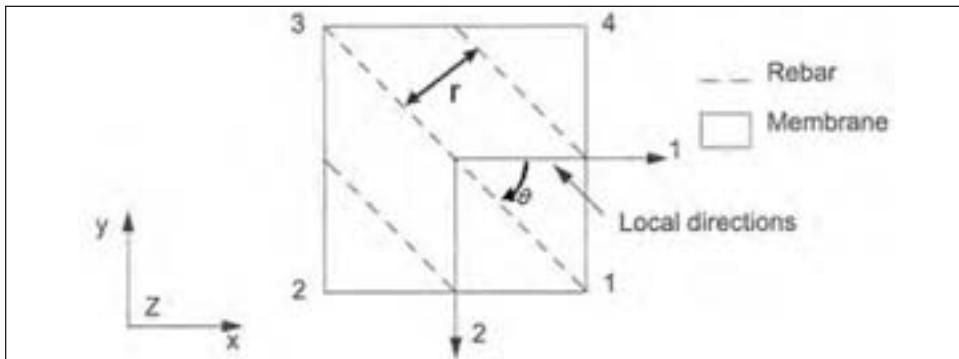
Note that the orthotropic solid in case 1) will have bending stiffness defined by the extensional orthotropic properties and the element dimensions, which may overestimate the actual bending stiffness.

The material properties of the rebar elements are distinct from those of the underlying element and their orientation can be defined relative to the local coordinate system as shown in figure 2.12.

To define the reinforcement, the rebar option specifies the cross sectional area A of each rebar, the rivet r or spacing between two consecutive cords, and the orientation angle

θ in degrees between the membrane local direction and the rebar (cord) direction. A positive angle defines a rotation from local 1 direction toward local 2 direction.

Figure 2.12: Rebars defined relative to local coordinate system

Lamina thermal conductivity
Operating temperature is an important characteristic for tire durability. In order to predict temperature distribution in a tire, the corresponding heat transfer problem must be solved. The material property required for a steady-state temperature prediction is the thermal conduction. Fourier's law for conduction in isotropic materials states that

$$\frac{d\vec{q}}{dt} = k\vec{\nabla}T \tag{2.27}$$

or, the rate of heat flow per area is proportional to spatial temperature gradient. The proportionality is the heat conductivity k in W/m°C. If the material is orthotropic, the analysis along the principal material directions gives

$$\frac{d}{dt}\begin{bmatrix} q_1 \\ q_2 \\ q_3 \end{bmatrix} = \begin{bmatrix} k_1 & 0 & 0 \\ 0 & k_2 & 0 \\ 0 & 0 & k_3 \end{bmatrix}\begin{bmatrix} \dfrac{dT}{dx_1} \\[6pt] \dfrac{dT}{dx_2} \\[6pt] \dfrac{dT}{dx_3} \end{bmatrix} \tag{2.28}$$

The heat flow and temperature gradient are first rank tensors, or vectors. Consider the case for rotations about the z-axis consistent with the planar lamina stress-strain analysis. The transformation matrix for vectors in the x-y plane is simply

$$[R] = \begin{bmatrix} \cos\theta & \sin\theta & 0 \\ -\sin\theta & \cos\theta & 0 \\ 0 & 0 & 1 \end{bmatrix} \tag{2.29}$$

for angles θ measured from the 1 direction to the x axis. The transformed variables are given as

$$
\begin{bmatrix} q_x \\ q_y \\ q_z \end{bmatrix} = [R] \begin{bmatrix} q_1 \\ q_2 \\ q_3 \end{bmatrix}, \; and \; \begin{bmatrix} \dfrac{dT}{dx} \\ \dfrac{dT}{dy} \\ \dfrac{dT}{dz} \end{bmatrix} = [R] \begin{bmatrix} \dfrac{dT}{dx_1} \\ \dfrac{dT}{dx_2} \\ \dfrac{dT}{dx_3} \end{bmatrix} \tag{2.30}
$$

The orthotropic conduction law in the arbitrary x-y reference plane is then

$$
\begin{bmatrix} q_x \\ q_y \\ q_z \end{bmatrix} = [R][k][R]^{-1} \begin{bmatrix} \dfrac{dT}{dx} \\ \dfrac{dT}{dy} \\ \dfrac{dT}{dz} \end{bmatrix} \tag{2.31}
$$

The transformed conductivity matrix can be defined as

$$
\left[\bar{k} \right] = [R][k][R]^{-1} \tag{2.32}
$$

where, for rotations about the z-axis the components are given by

$$
\begin{aligned}
\bar{k}_{11} &= k_{11} \cos^2 \theta + k_{22} \sin^2 \theta \\
\bar{k}_{22} &= k_{11} \sin^2 \theta + k_{22} \cos^2 \theta \\
\bar{k}_{12} &= \bar{k}_{21} = (k_{22} - k_{11}) \sin \theta \cos \theta \\
\bar{k}_{33} &= k_{33}
\end{aligned} \tag{2.33}
$$

Often tire heat transfer FEA is performed on a 2D axisymmetric tire section where the transformed properties in Eq 2.32 are input to the analysis. In a 3-D analysis the properties could be input in the principal orientation together with the orientation to the structural coordinate system.

Thermal expansion coefficients
When performing an analysis which includes large temperature changes, it is often necessary to include the effects of thermal expansion and contraction [e.g., 1, 11,43] . For example, as a tire comes out of the mold and cools down, it takes on different dimensions compared to the molded shape. If the materials have different thermal expansion coefficients, then internal "thermal" stresses are also induced in the structure.

From a material perspective, thermal expansion only affects the normal strains in the

principal material directions. For an orthotropic lamina analyzed with respect to the principal material directions, a change in temperature that produces no stresses gives rise to the following strains

$$
\begin{bmatrix} \varepsilon_{11} \\ \varepsilon_{22} \\ \varepsilon_{33} \\ \gamma_{23} \\ \gamma_{31} \\ \gamma_{12} \end{bmatrix} = \begin{bmatrix} \alpha_1 \Delta T \\ \alpha_2 \Delta T \\ \alpha_3 \Delta T \\ 0 \\ 0 \\ 0 \end{bmatrix} \tag{2.34}
$$

where α_1, α_2, and α_3 are the coefficients of thermal expansion in the three principal material directions. Note that for cord-rubber composites with organic cords with molecular orientation, these coefficients can be negative. For linear analysis, the thermal strains and those due to applied stresses are simply added together. Thus, the inclusion of thermal strains changes equations such as 2.4 and 2.13, respectively to

$$
\begin{bmatrix} \varepsilon_1 - \alpha_1 \Delta T \\ \varepsilon_{22} - \alpha_2 \Delta T \\ \varepsilon_{33} - \alpha_3 \Delta T \\ \gamma_{23} \\ \gamma_{31} \\ \gamma_{12} \end{bmatrix} = \begin{bmatrix} \dfrac{1}{E_1} & \dfrac{-v_{21}}{E_2} & \dfrac{-v_{31}}{E_3} & 0 & 0 & 0 \\[2mm] \dfrac{-v_{12}}{E_1} & \dfrac{1}{E_2} & \dfrac{-v_{32}}{E_3} & 0 & 0 & 0 \\[2mm] \dfrac{-v_{13}}{E_1} & \dfrac{-v_{23}}{E_2} & \dfrac{1}{E_3} & 0 & 0 & 0 \\[2mm] 0 & 0 & 0 & \dfrac{1}{G_{23}} & 0 & 0 \\[2mm] 0 & 0 & 0 & 0 & \dfrac{1}{G_{31}} & 0 \\[2mm] 0 & 0 & 0 & 0 & 0 & \dfrac{1}{G_{12}} \end{bmatrix} \begin{bmatrix} \sigma_1 \\ \sigma_{22} \\ \sigma_{33} \\ \tau_{23} \\ \tau_{31} \\ \tau_{12} \end{bmatrix} \tag{2.35}
$$

and

$$
\begin{bmatrix} \sigma_{11} \\ \sigma_{22} \\ \tau_{12} \end{bmatrix} = \begin{bmatrix} Q_{11} & Q_{12} & 0 \\ Q_{21} & Q_{22} & 0 \\ 0 & 0 & 2Q_{66} \end{bmatrix} \begin{bmatrix} \varepsilon_1 - \alpha_1 \Delta T \\ \varepsilon_2 - \alpha_2 \Delta T \\ \dfrac{\gamma_{12}}{2} \end{bmatrix} \tag{2.36}
$$

A numerical analysis code requires the input of the three principal coefficients of thermal expansion and the orientation to the principal material directions. Typical values of the linear coefficient of thermal expansion for filled rubber and the most commonly used reinforcing cords are listed in the following table:

Table 2.2: Typical thermal expansion coefficients ($^oC^{-1}$)

Polyester	4.20×10^{-5}
N66 Nylon	17.5×10^{-5}
Steel	1.26×10^{-5}
Rayon	8.00×10^{-5}
Aramid	0.20×10^{-5}
Filled Rubber	13.0×10^{-5}

Exercises

1. For the lamina shown below, find the stresses in the 1,2 directions and the strains in the x,y directions. The lamina has the following elastic constants:
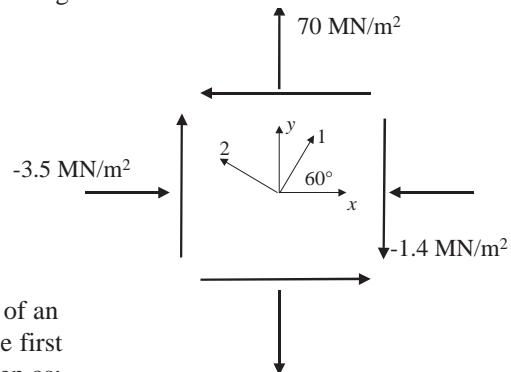
E_1=14 GN/m^2
E_2=3.5 GN/m^2
G_{12}=4.2 GN/m^2
ν_{12}=0.4
ν_{21}=0.1

70 MN/m^2

-3.5 MN/m^2

60°

-1.4 MN/m^2

2. Show that the apparent direct modulus of an orthotropic material as a function of θ (the first equation in equations (2.25)) can be written as:

$$\frac{E_1}{E_x} = (1+\alpha-4b)\cos^4\theta + (4b-2a)\cos^2\theta + a$$

where

$$a = \frac{E_1}{E_2} \quad and \quad b = \frac{1}{4}(\frac{E_1}{G_{12}} - 2\nu_{12})$$

3. Use the derivatives of E_x to find its maxima and minima. Show that E_x is greater than both E_1 and E_2 for some values of θ if:

$$G_{12} > \frac{E_1}{2(1+\nu_{12})}$$

4. Show that E_x is less than both E_1 and E_2 for some values of θ if:

$$G_{12} < \frac{E_1}{2\left[\dfrac{E_1}{E_2} - \nu_{12}\right]}$$

Thus, an orthotropic material can have an apparent Young's modulus that either exceeds or is less than the Young's modulus in both principal directions.
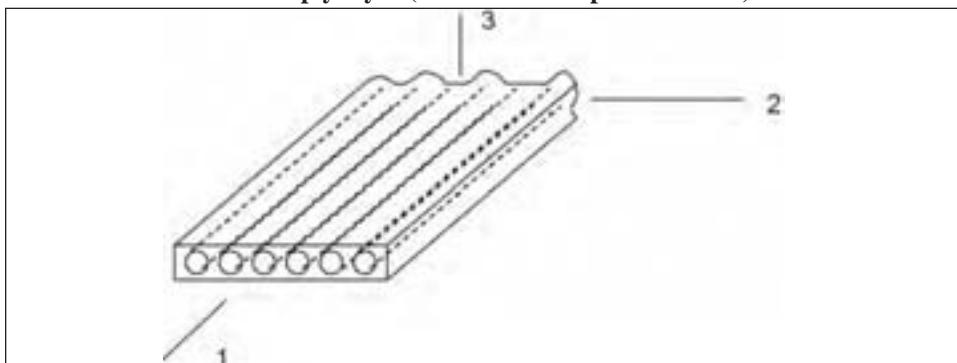
3. Constituent contribution to composite properties

In the macromechanics study of composites, the material is assumed to be homogeneous. The properties of the composite, such as modulus and Poisson's ratio, are determined by experiments on the composite. The effects of the individual constituent material is only accounted for by its influence on the average properties of the composite.

An alternate approach is to predict the properties of the composite based on the properties of the constituents. This is called micromechanics theory and it examines the interaction of the constituent materials and determines the role of each on the effective properties of the composites. Some of these theories are discussed in [9,25,69]. This representation is more complex than the macromechanics approach, however simplified tools exist for the calculation of the effective composite properties. The finite element method can also be used to calculate equivalent composite properties from a model where the geometry of the cords and rubber is explicitly represented.

The following sections present the most widely used equations for calculating the four independent elastic constants of a single orthotropic lamina: E_1, E_2, v_{12}, and G_{12}. Properties will be determined with respect to the principal, or natural, coordinates as shown in figure 3.1.

**Figure 3.1: Principal or natural coordinates for a
belt or ply layer (also called composite lamina)**

In general, the key feature shared by all these approaches is the mechanics of materials reasoning that the strains in the fiber direction of a unidirectional fibrous composite are the same in the fibers as in the matrix. In addition, sections normal to the fibers remain plane before and after being stressed.

Some example properties of tire cords and rubber are shown in table 3.1.

Table 3.1: Young's modulus for typical tire cords

Cord construction	Young's modulus (psi)
2+3x.35 Steel	16×10^6
1500/2 Kevlar	3.6×10^6
1000/2 Polyester	5.75×10^5
840/2 Nylon	5.0×10^5
Belt skim rubber compound	2000

Simple models

The rule of mixtures assumes no interation between the constituents. This method works well for the modulus in the direction of the cords. It is equivalent to considering elastic springs in a parallel configuation and summing the volume-weighted stiffnesses to get the overall stiffness. The equation can be written as

$$E_1 = E_c V_c + E_r V_r$$
(3.1)

where,

E_1 is the Young's modulus of the composite in the direction of the cords,
E_c is the Young's modulus of a single cord,
V_c is the volume fraction of cords in the composite
E_r is the Young's modulus of the rubber, and
V_r is the volume fraction of rubber in the composite

Note that
$$V_c + V_r = 1$$
The volume fraction of the cords can be calculated by

$$V_c = \frac{\pi D^2 e}{4t}$$

where D is the diameter of the cord, t is the thickness of the ply layer, and "e" represents the cord "ends per unit length" along the 2 direction of the ply layer.

In many cord-rubber composites, the modulus of the cords is 100-1000 times larger than the modulus of the rubber, so the approximation

$$E_1 = E_c V_c$$
(3.2)

is sometimes used. The same rule of mixtures approach can provide a reasonable estimate for the major Poisson's ratio, v_{12} for loading in the 1-direction:

$$v_{12} = v_c V_c + v_r V_r$$
(3.3)

i.e., the overall contraction in the transverse direction can be envisioned as the volume-weighted sum of the contraction of each constituent.

Consider the idealized geometry in figure 3.2 with loading in the transverse direction. By using the independent elastic spring analogy for the transverse stiffness, the model becomes two springs in series as shown in figure 3.3.

Figure 3.2 - Idealized cord-rubber composite loading in the transverse direction
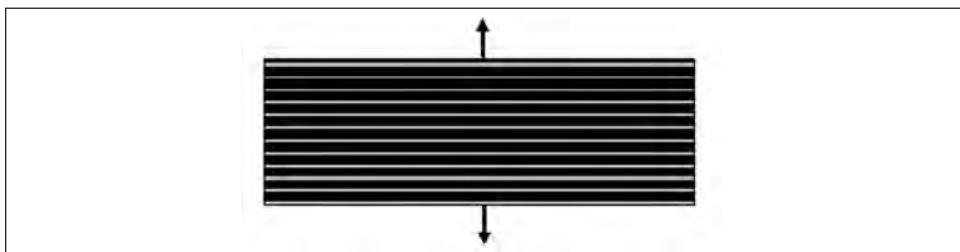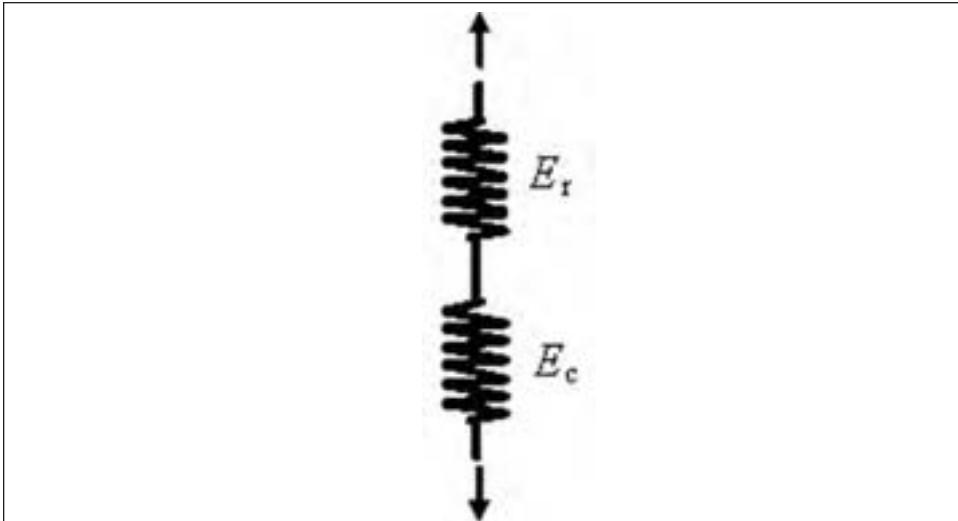
Figure 3.3 - Independent elastic springs in series model for transverse modulus

When accounting for the different volume fractions of cord and rubber, the simple springs in series model gives

$$\frac{1}{E_2} = \frac{V_c}{E_c} + \frac{V_r}{E_r}$$

(3.4)

or

$$E_2 = E_r \frac{E_c}{E_c V_r + E_r V_c}$$

(3.5)

For the simple spring model of equations 3.4 and 3.5, the transverse modulus of the cord, which may be much less than the axial modulus, could be used for E_c. Also, one could argue that since the rubber is constrained from contracting in the 1-direction due to the stiff cords, the "plane strain modulus" of the rubber $E_r/(1-v_r)$ should be used in place of E_r. In any case, if $E_c \gg E_r$, then equation 3.4 reduces to

$$E_2 = \frac{E_r}{V_r}$$

(3.6)

Consider figure 3.2 under shear rather than tensile loading. The springs in series model can also be used to give an estimate for G_{12}. For $G_c \gg G_r$, an equation analogous to equation 3.6 results

$$G_{12} = \frac{G_r}{V_r}$$

(3.7)

A common theme with most equations for the transverse or shear composite modulus is that they have some factor times the modulus of rubber.

The minor Poisson's ratio can be obtained from the reciprocity condition that arises from symmetry of the stress-strain relationships

$$v_{21} = v_{12} \frac{E_2}{E_1}$$
(3.8)

The simple expressions above often give a good first approximation to the orthotropic elastic constants required for structural analysis of the belt and ply cord-rubber composites. Many factors are neglected such as the Poisson's ratio mismatch, and the potential for the cord to be anisotropic, or the fact that the cord is actually a structure and not a homogeneous material. Relationships which can add some accuracy for cord-rubber composites are considered next.

Halpin-Tsai equations
The composite transverse (2 direction) and shear properties of the composite are the most difficult to predict. The following equations are referred to as the Halpin-Tsai equations [see e.g., 6,13] and are widely used with the rule of mixtures for establishing the five elastic constants for a single orthotropic ply.

$$E_2 = \frac{E_r[E_c(1+\xi_1 V_c) + \xi_1 E_r(1-V_c)]}{E_c(1-V_c) + \xi_1 E_r(1+V_c/\xi_1)}$$
(3.9)

$$G_{12} = \frac{G_r[G_c(1+\xi_2 V_c) + \xi_2 G_r(1-V_c)]}{G_c(1-V_c) + \xi_2 G_r(1+V_c/\xi_2)}$$
(3.10)
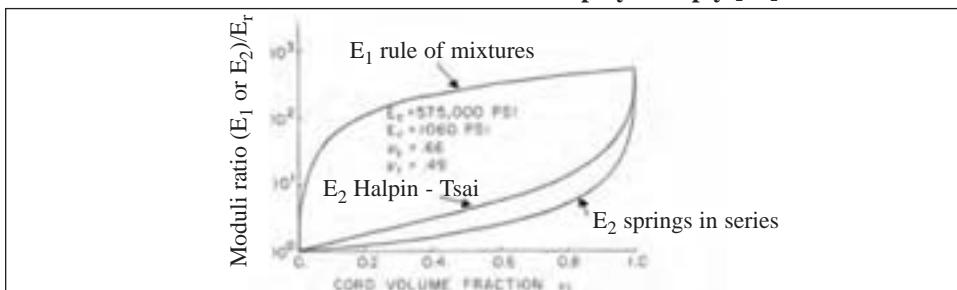
where the ξ_1, ξ_2 are factors depending on the cord geometry and spacing. These equations are semi-empirical and have shown good correlation with data. If $E_c \gg E_r$, and using common values of $\xi_1 = 2$ and $\xi_2 = 1$, Equations 3.9 and 3.10 reduce to

$$E_2 = \frac{E_r(1+\xi_1 V_c)}{(1-V_c)}$$
(3.11)

$$G_{12} = \frac{G_r[G_c + G_r + V_c(G_c - G_r)]}{G_c + G_r - V_c(G_c - G_r)}$$
(3.12)

The rule of mixtures equations 3.1 and 3.3 are used for major modulus and Poisson's ratio, respectively. Figure 3.4 shows how E_1 and E_2 vary with cord volume fraction for rule of mixtures and Halpin-Tsai equations.

**Figure 3.4 - Dependence of composite moduli on
cord volume fraction for a 1000/2 polyester ply [25]**

Gough-Tangorra equations
Gough and Tangorra [7] have developed expressions specifically tailored to the properties of cord reinforced rubber. The expression for the transverse modulus is:

$$E_2 = \frac{4E_r V_r [E_c V_c + E_r V_r]}{3E_c V_c + 4E_r V_r} \tag{3.13}$$

They also used the simple approximation for the shear modulus in Eq 3.7 and assumed major Poisson's ratio $v_{12} = 0.5$.

Akasaka-Hirano equations
The Akasaka-Hirano equations [8] are a simplified version of the rule of mixtures and the Gough-Tangorra equations with:

$$
\begin{aligned}
E_1 &= E_c V_c \\
E_2 &= \frac{4}{3} E_r \\
G_{12} &= G_r \\
v_{12} &= 0.5 \\
v_{21} &\approx 0
\end{aligned}
\tag{3.14}
$$

S. K. Clark equations
In this approach [9], an energy method is used to formulate expressions for the lamina elastic constants without requiring detailed cord properties such as shear modulus and Poisson's ratio.

The theory uses a stiffening parameter ϕ indicating the degree of stiffening imposed by the cord structure.

$$\phi = E_c V_c \frac{1 - V_c}{2G_r} \tag{3.15}$$

Then

$$E_1 = E_c V_c + 12 \frac{G_r}{(1 - V_c)} \tag{3.16}$$

$$E_2 = G_r \frac{4 - \dfrac{4}{2 + \phi} + \dfrac{4 + 2\phi}{(2 + \phi)^2}}{(1 - V_c)} \tag{3.17}$$

with

$$G_{12} = \frac{G_r}{(1 - V_c)}, \quad and \quad v_{12} = 0.5$$

Comparison with experimental data

Walter and Patel [10] gave several examples of experimental data for single sheets of calendered fabric. Some comparisons for a rubber-Kevlar composite are shown in figures 3.5 and 3.6.

Figure 3.5 - Comparison of E_1 between rule of mixtures prediction and measured data for a 1500/2 Kevlar - rubber ply [10]
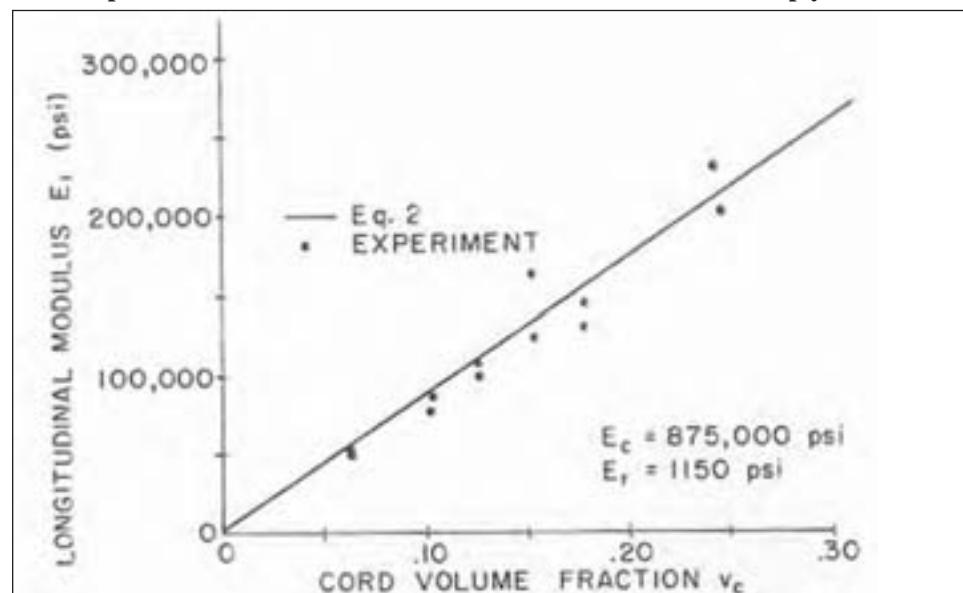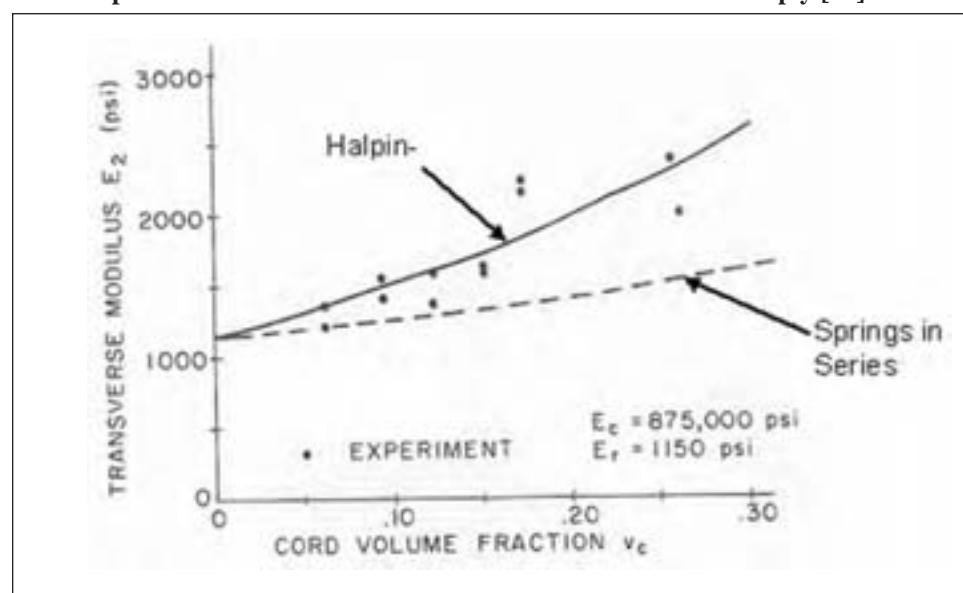

Figure 3.6 - Comparison of E_2 between rule of mixtures prediction and measured data for a 1500/2 Kevlar-rubber ply [10].

The following tables from Clark [9] compare values calculated from the various theories with measured ones.

To highlight the accuracy of the various approaches in predicting the effective properties of a single lamina, two types of reinforcing materials were considered: steel and rayon with the following properties:

Table 3.2 Cord and rubber properties [9]

Elastic properties	Rayon	Steel
Cord Young's modulus, E_c (GPa)	3.41	50.50
Rubber Shear modulus, G_r (MPa)	2.94	5.30
Cord volume fraction, v_c	0.23	0.11
Parameter ϕ	102.70	466.40

The theoretically predicted and experimentally measured elastic contants for a rayon-rubber lamina are listed in Table 3.3.

Table 3.3 Elastic constants for a rayon-rubber lamina [9]

	Halpin-Tsai	Gough-Tangorra	Akasaka-Hirano	Clark Theory	Experimental data
E_1 (GPa)	0.786	0.786	0.772	0.811	0.779
E_2 MPa)	16.60	9.10	11.70	15.20	13.90
G_{12} (MPa)	3.28	2.28	2.94	3.57	3.82
v_{12}	0.54	0.50	0.50	0.50	0.49

The comparison for a steel-rubber composite lamina is listed in Table 3.4.

Table 3.4 - Elastic constants for a steel-rubber ply [9]
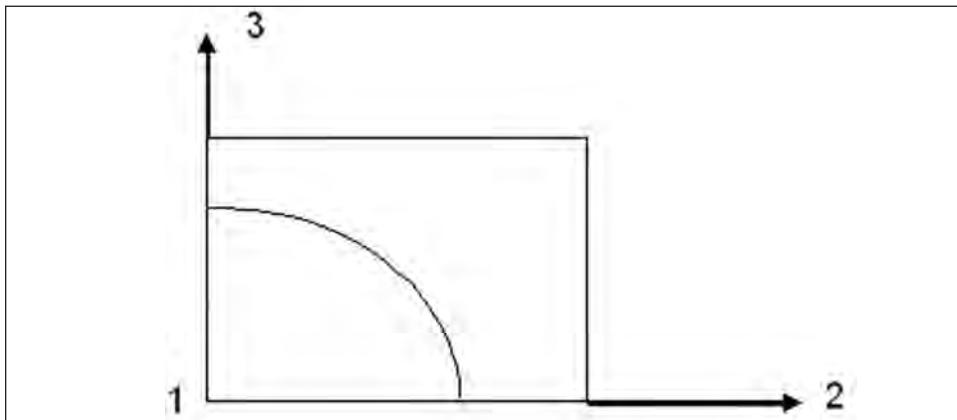
|	Halpin-Tsai	Gough-Tangorra	Akasaka-Hirano	Clark Theory	Experimental data
E_1 (GPa)	5.73	5.73	5.70	5.77	5.72
E_2 MPa)	21.90	18.80	21.20	23.80	19.30
G_{12} (MPa)	5.23	4.69	5.29	5.95	4.92
v_{12}	0.49	0.50	0.50	0.50	0.49

The predicted results are rather similar. The approach proposed by S. K. Clark is as accurate as the Halpin-Tsai equations, but it does not require detailed cord properties.

Thermal conductivity

When performing a heat transfer analysis for predicting tire temperatures, the thermal conductivities of the materials are required. If the cord-rubber layers are represented by effective composite properties, the conductivity will depend on direction. With reference to figure 3.1, the heat typically travels more efficiently along the cords (1–direction) than transverse to the cords (the 2- or 3 - direction). Consider a representative volume element as shown in figure 3.7. In the 1-direction, the effective composite conductivity is represented by the rule of mixtures as

$$k_1 = k_c V_c + k_r V_r \tag{3.18}$$

Figure 3.7 - Representative volume element for a cord-rubber layer

As with the moduli, the transverse properties are more difficult. As an example, consider the idealized geometry in figure 3.8. The square cord is a representation of ¼ of the   effective cross-sectional area of the cord, and the remaining area comprises the rivet between cords and the rubber treatment above or below the cords (assumed symmetric). A model with thermal resistors for heat flow in the 3–direction is shown in figure 3.9. The thermal resistance is in general

$$R_{th} = \frac{L}{Ak}$$ (3.19)

where L is the length of the heat flow, A is the cross sectional area, and k is thermal conductivity. For this example consider the resistance per unit depth in the 1 – direction.
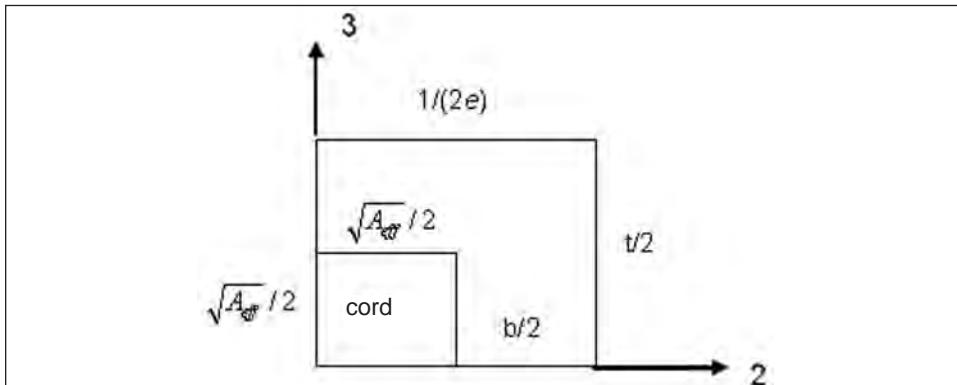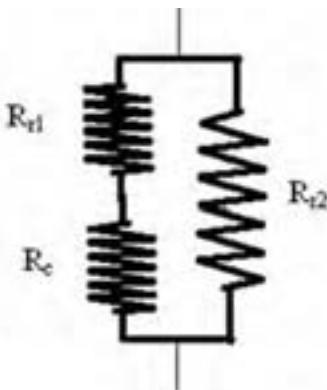
**Figure 3.8 - Unit cell for transverse
conductivity calculation (e = ends per unit length)**

Figure 3.9 - Equivalent thermal resistance model for conduction in the 3-direction

The thermal resistances shown in figure 3.9 are

$$R_c = \frac{\sqrt{A_{eff}}/2}{k_c \sqrt{A_{eff}}/2} = \frac{1}{k_c} \tag{3.20}$$

$$R_{r1} = \frac{t/2 - \sqrt{A_{eff}}/2}{k_r \sqrt{A_{eff}}/2} = \frac{t - \sqrt{A_{eff}}}{k_r \sqrt{A_{eff}}} \tag{3.21}$$

and

$$R_{r2} = \frac{t/2}{k_r b/2} = \frac{t}{k_r b} \tag{3.22}$$

First, combine R_c and R_{r1} in series. Note that thermal resistances in series add directly, and thermal resistances in parallel add reciprocally,

$$R_I = \frac{t - \sqrt{A_{eff}}}{k_r \sqrt{A_{eff}}} + \frac{1}{k_c} = \frac{k_r \sqrt{A_{eff}} + k_c(t - \sqrt{A_{eff}})}{k_c k_r \sqrt{A_{eff}}} \tag{3.23}$$

Adding this result in parallel to the rubber resistance R_{r2} gives

$$\frac{1}{R} = \frac{k_r b}{t} + \frac{k_c k_r \sqrt{A_{eff}}}{k_r \sqrt{A_{eff}} + k_c(t - \sqrt{A_{eff}})} \tag{3.24}$$

$$\frac{1}{R} = \frac{k_r b(k_r \sqrt{A_{eff}} + k_c(t - \sqrt{A_{eff}})) + t k_c k_r \sqrt{A_{eff}}}{t(k_r \sqrt{A_{eff}} + k_c(t - \sqrt{A_{eff}}))} = \frac{k_{eff}(1/e)}{t} \tag{3.25}$$

The effective conductivity for conduction in the through-thickness direction for the cord-rubber composite, k_{eff}, can be determined from equation 3.25. For the more simple case

without an extra rubber layer above and below the cords, Eq 3.25 simplifies to

$$k_{eff} = \frac{k_r b + k_c t}{(b+t)} \qquad (3.26)$$

where the rule of mixtures for the conductivity is evident. A similar analysis can be performed for the conductivity in the 2-direction. A more precise estimation of the equivalent conductivities could be obtained by performing a heat transfer finite element analysis of the geometry in figure 3.7.

Finite element method for cord-rubber properties

Finite element analysis can also be used to predict effective orthotropic properties of a cord-rubber lamina. A geometry as simple as that shown in figure 3.7 could be meshed and analyzed for elastic or thermal properties transverse to the cord. Nonlinear elastic properties with moduli different in tension and compression could represent the cord, and a nonlinear hyperelastic material model (with damage, etc) could represent the rubber. Padovan [71] included the extension-twist coupling of the cord both by applying a micro-polar theory to a cylindrical cord geometry and by meshing the actual filaments that make up the cord. Numerical simulation presents many interesting possibilities for the analysis of cord-rubber composites. Given the challenges of cord-rubber experiments, numerical simulation can provide a more robust and preferred approach.

Exercises

1. A composite specimen has dimensions of 25.4 cm x 25.4 cm x 0.3 cm and a weight of 218 g. The fibers weigh 186 g. The densities of the fibers and matrix are 1.0 g/cm^3 and 1.2 g/cm^3, respectively. Determine the volume fractions of fibers and matrix in the specimen.

2. The constituent materials in the composite described in the previous exercise have the properties E_{f1}=32.0E+06 psi (220 GPa), E_{f2}=2.0E+06 psi (13.79 GPa), and E_m=0.5E+03 psi (3.45 MPa). Estimate the longitudinal and transverse moduli of the composite by using the different approaches provided.

3. Assume that the transverse thermal conductivity of a composite is computed by employing the following equations:
where k_2, k_f, k_m are the thermal conductivity for the composite in the transverse direction, fiber and matrix, respectively.
What will be the thermal conductivity perpendicular to a ply with V_m=50% with the following thermal conductivities: k_m=0.18 Btu/hr-ft-^{o}F, and k_f=66 Btu/hr-ft^2-^{o}F.

$$\frac{k_2}{k_m} = \frac{1+\zeta\eta V_f}{1-\eta V_f} \; , \; \eta = \frac{(\frac{k_f}{k_m}-1)}{(\frac{k_f}{k_m}+\zeta)} \; , and \; \zeta = \frac{1}{4-3V_m}$$

4. Macromechanical behavior of a laminate

In the previous sections, the analysis of a lamina or single ply was presented. However, cords are only capable of carrying a considerable load along the cord directions. To carry loads applied in several directions, many laminae may be bonded together and stacked at different cord angles to produce a structure called a laminate, capable of providing stiffness and resisting load in all directions. If the laminate is formed from many laminae at different cord angles as in figure 4.1, how is the response of the laminate determined? A portion of a simple laminate that might occur in a tire belt package is shown in figure 4.2 with a belt angle stacking sequence of [+60,+22,-22,+22]. The positive angle is measured from the x-axis. The stacking sequence notation [θ_1, θ_2, etc.] starts with the bottom ply and goes in sequence until reaching the top – i.e., the usual manner in which the composite would be fabricated. This is also the order in which belts or plies are applied on a tire building drum. The example in figure 4.2 could also be represented as [60, ±22, 22].

**Figure 4.1 - Laminate and questions for analysis [13]**
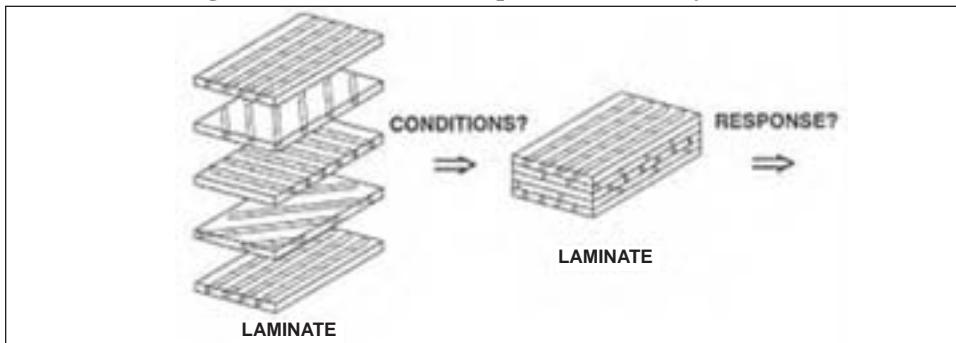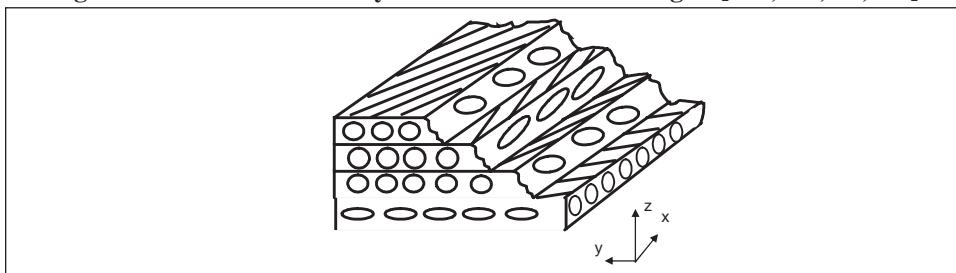
Figure 4.2 - Portion of a 4 layer laminate with cord angles [+60,+22,-22,+22]

Tire cord-rubber composites undergo bending as well as the extensional deformations considered in the previous sections. Bending occurs as the tire is loaded. The sidewall curvature increases and the belt curvature decreases.

Previously, the behavior of a single orthotropic layer has been considered in detail. Since a laminate is composed of several such layers, this section will use the behavior of a single lamina to develop the behavior of a laminate using the properties of the lamina and additional assumptions related to the stress and deformation.
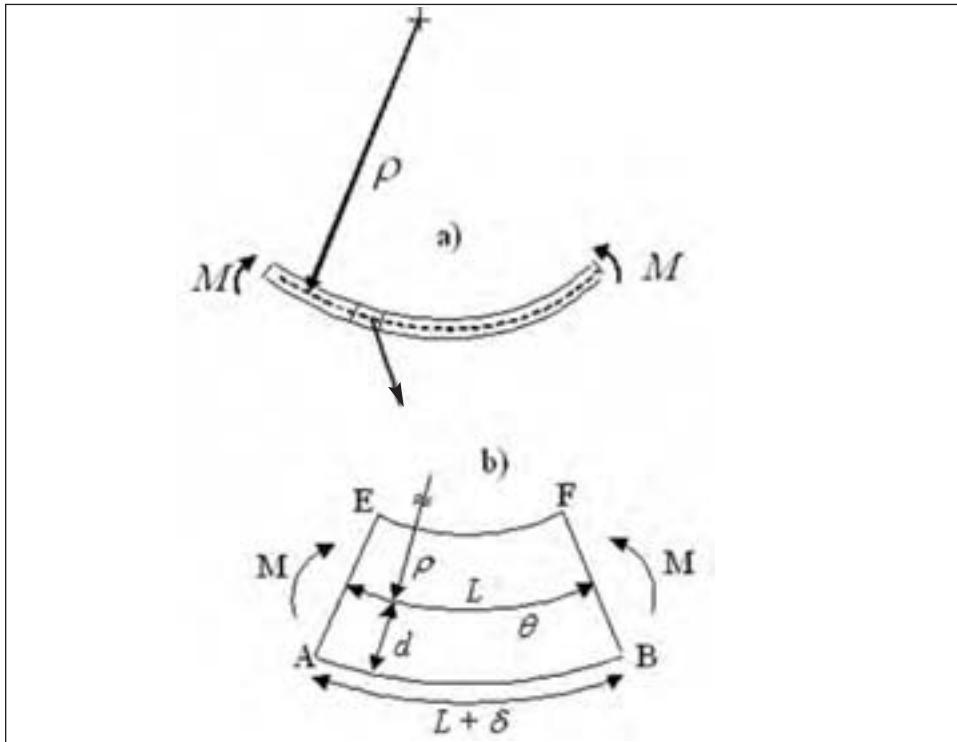
First, the analysis of bending is briefly reviewed. Then, the distributions of stress and strain through the thickness of the laminate are established where z-displacements and out-of-plane bending will be considered as well as in-plane deformations. Finally, the

governing constitutive equation of the laminate is derived in terms of the coupled bending and stretching stiffnesses caused by the different principal directions among the layers of the laminate.

Analysis of bending deformation
This topic is covered in depth in mechanics of materials texts [11]. When a constant bending moment is applied to a straight elastic beam, the beam bends into a circular arc of radius ρ as shown in figure 4.3a. Through the center of the beam passes a surface called the neutral surface where the normal stresses are zero (dashed line in figure 4.3a). From the neutral surface, tensile stresses occur away from the center of curvature, and compressive stresses occur towards the center of curvature. This is intuitive, since tensile strains are apparent on surface AB in figure 4.3b due to the increase in length of the outer surface to $L+\delta$, and compressive strains are apparent on the inner surface. Considering the portion of the beam shown in figure 4.3b, the angle θ can be expressed as

Figure 4.3 - Beam bending

$$\theta = \frac{L}{\rho} = \frac{L+\delta}{\rho+d} \qquad (4.1)$$

where d is the distance from the neutral surface to the outer surface. The normal strain ε_x can be expressed as

$$\varepsilon_x = \frac{\delta}{L} = \frac{d}{\rho} \tag{4.2}$$

Since the state of stress is uniaxial, the strain can be equated to

$$\varepsilon_x = \frac{\sigma_x}{E} = \frac{Md}{EI} \tag{4.3}$$
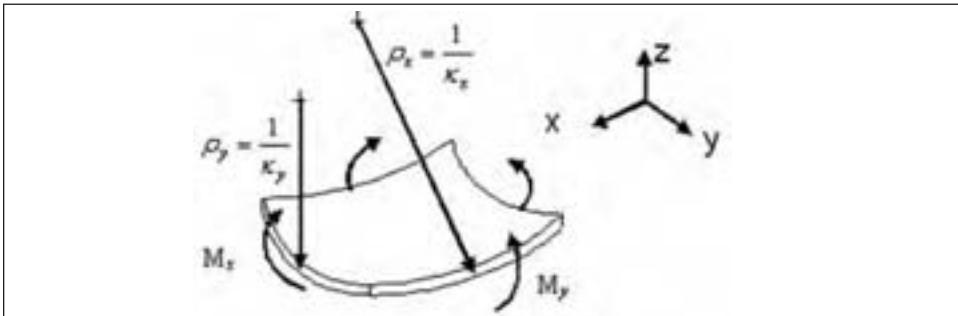
Equating equations 4.2 and 4.3 gives

$$\kappa = \frac{1}{\rho} = \frac{M}{EI}, \ \ or \ M = EI\kappa \tag{4.4}$$

where κ is the curvature and I is the area moment of inertia of the cross section about the neutral surface. Also note in figure 4.3b that the assumption of "plane sections remain plane" has been used, since the planes AE and BF are assumed to remain planar after deformation.

This is an analysis of bending of a beam about one axis. Composite laminate analysis includes bending of the laminate "plate" about two axes as shown in figure 4.4. Note the convention that M_x causes stresses σ_x, rather than being a moment about the x-axis.

**Figure 4.4 - Bending of a plate about two axes**
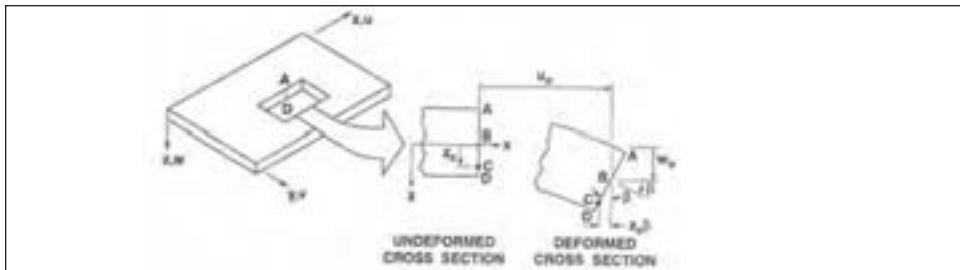
Strain-displacement relationships
The kinematics of strain and displacement including bending deformations follow those of plate theory developed originally for isotropic materials [12]. The treatment here follows that in the text by Jones [13]. Note that the kinematic relations for strain and deformation are determined independent of the material properties (isotropic, anisotropic, heterogeneous, etc).

To establish a relation between the displacement components and the corresponding strain field, a section of a laminate is considered as shown in figure 4.5.

The laminate is deformed due to transverse (z-direction) loading and also in-plane loading. The equations relating the strain at any point C in the laminate will be established in terms of the displacements at the geometrical midplane (i.e., the x-y plane passing through B) of the laminate (u_0, v_0) and the displacement in the z direction (w).

Figure 4.5 - Deformed shape of the laminate in the x-z plane [13].

The "plane sections remain plane" assumption means that there are no shearing deformations in the x-z and y-z planes. This is to say that the layers that make the laminate cross-section DBA do not deform over one another: the plane represented by the line DBA remains plane – i.e., straight and normal to the deformed midplane. With this assumption, known as the Kirchhoff-Love hypothesis, the displacement at any point C on the line DBA is given by the following linear relationship:

$$u_c = u_0 - z_c \, \beta \tag{4.5}$$

where z_c is the z coordinate of the point C measured positively in the downward z direction from the geometric mid-plane, and β is the slope of DBA with respect to the original vertical line. This relation holds for small deformations where β is small. It is considered as the rate of change of the deflection in the z direction with respect to change in the x (or y) direction. Thus, the displacements in the x and y directions of any point in the laminate are related to the geometrical midplane displacements (u_0, v_0) according to the following equations:

$$u = u_0 - z \frac{\partial w}{\partial x}$$
$$v = v_0 - z \frac{\partial w}{\partial y} \tag{4.6}$$

Note that the Kirchhoff-Love hypothesis may not be accurate for many cord-rubber applications, since it does not allow for any interply deformations. The laminate with Kirchoff-Love is stiffer than a laminate that allows interply shear deformations.

Since the line DBA is assumed to remain straight with negligible stretching or shortening, it is consistent to assume that the normal strain in the z direction is nearly zero. Therefore, the normal deflection at any point in the laminate is considered to be the same deflection (w) as the geometric midplane.

At this stage, the definitions of the normal strain as the ratio of the change in length divided by the original length, and the shear strain as the total angle change, are used to derive the expression for the strain at any point in a laminate in terms of the displacements u_0, v_0, and w. The strains can be defined in terms of the derivative of the displacements with respect to spatial position as:

$$\varepsilon_x = \frac{\partial u}{\partial x}, \varepsilon_y = \frac{\partial v}{\partial y}, and \, \gamma_{xy} = \frac{\partial u}{\partial y} + \frac{\partial v}{\partial x}$$

(4.7)

Using equations 4.6 and 4.7, the normal and shear strains can be written in terms of the midplane strains and laminate curvatures as follows:

$$\begin{bmatrix} \varepsilon_x \\ \varepsilon_y \\ \gamma_{xy} \end{bmatrix} = \begin{bmatrix} \varepsilon^0{}_x \\ \varepsilon^0{}_y \\ \gamma^0{}_{xy} \end{bmatrix} + z \begin{bmatrix} \kappa_x \\ \kappa_y \\ \kappa_{xy} \end{bmatrix}$$

(4.8)

where the geometric midplane strains are related to the displacements of the midplane as:

$$\begin{bmatrix} \varepsilon^0{}_x \\ \varepsilon^0{}_y \\ \gamma^0{}_{xy} \end{bmatrix} = \begin{bmatrix} \dfrac{\partial u_0}{\partial x} \\ \dfrac{\partial v_0}{\partial y} \\ \dfrac{\partial u_0}{\partial y} + \dfrac{\partial v_0}{\partial x} \end{bmatrix}$$

(4.9)

and the midplane curvatures are related to the midplane displacement w in the z direction as:

$$\begin{bmatrix} \kappa_x \\ \kappa_y \\ \kappa_{xy} \end{bmatrix} = - \begin{bmatrix} \dfrac{\partial^2 w}{\partial x^2} \\ \dfrac{\partial^2 w}{\partial y^2} \\ \dfrac{\partial^2 w}{\partial x \partial y} \end{bmatrix}$$

(4.10)

Using matrix notation, the above equations can be written in a more compact format:

$$\begin{bmatrix} \varepsilon \end{bmatrix} = \begin{bmatrix} \varepsilon^0 \end{bmatrix} + z \begin{bmatrix} \kappa \end{bmatrix}$$

(4.11)

Thus, the midplane strains are functions of the midplane displacements u_0, v_0 and the curvatures are functions of the midplane deflection w.

Stress of a ply in a laminate

For an orthotropic lamina, the stress-strain relation in an arbitrary reference coordinate system was shown to have the following form (equations 2.19):

$$\begin{bmatrix} \sigma_x \\ \sigma_y \\ \tau_{xy} \end{bmatrix} = \begin{bmatrix} \bar{Q}_{11} & \bar{Q}_{12} & \bar{Q}_{16} \\ \bar{Q}_{12} & \bar{Q}_{22} & \bar{Q}_{26} \\ \bar{Q}_{16} & \bar{Q}_{26} & \bar{Q}_{66} \end{bmatrix} \begin{bmatrix} \varepsilon_x \\ \varepsilon_y \\ \gamma_{xy} \end{bmatrix}$$

(4.12)

or,

$$[\sigma] = [\bar{Q}][\varepsilon]$$

(4.13)

For the kth layer in a laminate, the stress-strain relation is simply

$$[\sigma]_k = [\bar{Q}]_k [\varepsilon]_k$$

(4.14)

By substitution of the strain from Eq 4.8 into the above stress-strain relation, the stresses in the kth layer can be expressed in terms of the laminate midplane strains and curvatures as

$$\begin{bmatrix} \sigma_x \\ \sigma_y \\ \tau_{xy} \end{bmatrix}_k = \begin{bmatrix} \bar{Q}_{11} & \bar{Q}_{12} & \bar{Q}_{16} \\ \bar{Q}_{12} & \bar{Q}_{22} & \bar{Q}_{26} \\ \bar{Q}_{16} & \bar{Q}_{26} & \bar{Q}_{66} \end{bmatrix}_k \begin{bmatrix} \varepsilon_x^0 \\ \varepsilon_y^0 \\ \gamma_{xy}^0 \end{bmatrix} + z \begin{bmatrix} \bar{Q}_{11} & \bar{Q}_{12} & \bar{Q}_{16} \\ \bar{Q}_{12} & \bar{Q}_{22} & \bar{Q}_{26} \\ \bar{Q}_{16} & \bar{Q}_{26} & \bar{Q}_{66} \end{bmatrix}_k \begin{bmatrix} \kappa_x \\ \kappa_y \\ \kappa_{xy} \end{bmatrix}$$

(4.15)
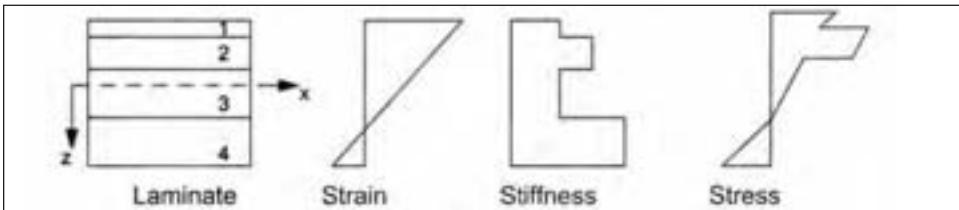
or, in a contracted matrix format:

$$[\sigma]_k = [\bar{Q}]_k [\varepsilon^0] + z[\bar{Q}]_k [\kappa]$$

(4.16)

This is equivalent to computing the stresses due to axial and bending deformations in a simple beam. The expression (4.16) can be used to compute the stress in a lamina when the laminate midplane strains and curvatures are known.

Since $[\bar{Q}_{ij}]_k$ can be different for each layer of the laminate, the stress variation through the laminate thickness is not necessarily linear, even though the strain variation is assumed linear. A hypothetical variation of stress and strain is depicted in figure 4.6.
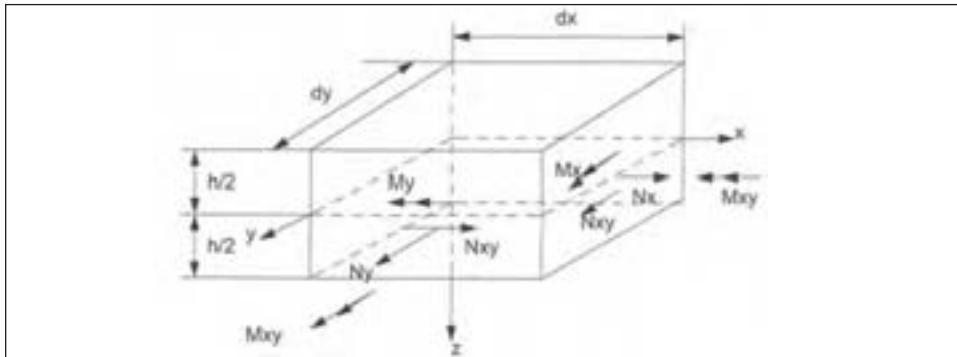
Figure 4.6 - Hypothetical variation of strain, stiffness and stress in a laminate [13]


Definition of stress and moment resultants

It is often convenient to deal with a system of resultant loads that are acting at the geometrical midplane. The stress resultants and moment resultants consist of three quantities with dimensions force per unit length (the stress resultants) and three quantities with dimensions of length times force per length (the moment resultants).

An element cut from a laminate is shown in figure 4.7. In a general loading condition, this element would have six stress components acting on its faces (σ_x, σ_y, σ_z, τ_{xy}, τ_{xz}, τ_{yz}). In light of the previous assumptions related to the transverse shear and normal stress in the z direction, only σ_x, σ_y, τ_{xy} will be considered. Since the stresses in a laminate vary from layer to layer, the stress resultants are defined as the sum or integral of these stress-

Figure 4.7 - Stress and moment resultants[13].

es in the z direction.

These stress resultants are positive in the same sense as the corresponding stresses, and since they are stresses times length (dz), they have the dimension of force per length.

$$N_x = \int_{-\frac{h}{2}}^{\frac{h}{2}} \sigma_x dz$$

$$N_y = \int_{-\frac{h}{2}}^{\frac{h}{2}} \sigma_y dz \qquad (4.17)$$

$$N_{xy} = \int_{-\frac{h}{2}}^{\frac{h}{2}} \sigma_{xy} dz$$

In addition, the moment resultants are given as the sum of the stresses multiplied by the moment arm with respect to the midplane.

$$M_x = \int_{-\frac{h}{2}}^{\frac{h}{2}} \sigma_x z dz$$

$$M_y = \int_{-\frac{h}{2}}^{\frac{h}{2}} \sigma_y z dz \qquad (4.18)$$

$$M_{xy} = \int_{-\frac{h}{2}}^{\frac{h}{2}} \sigma_{xy} z dz$$

With the definitions of equations 4.17 and 4.18, a system of three stress resultants and three moment resultants has been defined which is equivalent in their actions to the actual stress distribution across the thickness of the laminate.

Laminate constitutive equations

Previously, the stresses acting on any layer or lamina were defined in terms of midplane strains and plate curvature. In addition, the stress and moment resultants defined the force and moment acting on the midplane of a laminate. By combining these equations, relationships between the force and moment system, and the midplane strains and curvatures can be established. These relationships are the laminate constitutive equations.

The stress resultants can be written in a vector form in terms of the stress components as follows:

$$
\begin{bmatrix} N_x \\ N_y \\ N_{xy} \end{bmatrix} = \int_{-\frac{h}{2}}^{\frac{h}{2}} \begin{bmatrix} \sigma_x \\ \sigma_y \\ \tau_{xy} \end{bmatrix} dz
\tag{4.19}
$$

If this load system is applied to a laminate composed of n layers, stress resultants can be expressed as the sum of n simple integrals. Furthermore, if the stress in each layer is written in terms of the midplane strains, the plate curvature, the z coordinate, and the plate elastic stiffness properties, the following expression can be established:

$$
\begin{bmatrix} N_x \\ N_y \\ N_{xy} \end{bmatrix} = \sum_{k=1}^{n} \int_{h_{k-1}}^{h_k} \begin{bmatrix} \bar{Q}_{11} & \bar{Q}_{12} & \bar{Q}_{16} \\ \bar{Q}_{12} & \bar{Q}_{22} & \bar{Q}_{26} \\ \bar{Q}_{16} & \bar{Q}_{26} & \bar{Q}_{66} \end{bmatrix}_k \begin{bmatrix} \varepsilon_x^0 \\ \varepsilon_y^0 \\ \gamma_{xy}^0 \end{bmatrix} dz + \sum_{k=1}^{n} \int_{h_{k-1}}^{h_k} \begin{bmatrix} \bar{Q}_{11} & \bar{Q}_{12} & \bar{Q}_{16} \\ \bar{Q}_{12} & \bar{Q}_{22} & \bar{Q}_{26} \\ \bar{Q}_{16} & \bar{Q}_{26} & \bar{Q}_{66} \end{bmatrix}_k \begin{bmatrix} \kappa_x \\ \kappa_y \\ \kappa_{xy} \end{bmatrix} z\, dz
\tag{4.20}
$$

Each of these integrals can be easily evaluated because $[\varepsilon^0]$ and $[\kappa]$ are not functions of z, and within any layer $[h_{k-1}, h_k]$, $[\bar{Q}]k$ is, is not a function of z.

$$
\begin{bmatrix} N_x \\ N_y \\ N_{xy} \end{bmatrix} = \sum_{k=1}^{n} \begin{bmatrix} \bar{Q}_{11} & \bar{Q}_{12} & \bar{Q}_{16} \\ \bar{Q}_{12} & \bar{Q}_{22} & \bar{Q}_{26} \\ \bar{Q}_{16} & \bar{Q}_{26} & \bar{Q}_{66} \end{bmatrix}_k \begin{bmatrix} \varepsilon_x^0 \\ \varepsilon_y^0 \\ \gamma_{xy}^0 \end{bmatrix} \int_{h_{k-1}}^{h_k} dz + \sum_{k=1}^{n} \begin{bmatrix} \bar{Q}_{11} & \bar{Q}_{12} & \bar{Q}_{16} \\ \bar{Q}_{12} & \bar{Q}_{22} & \bar{Q}_{26} \\ \bar{Q}_{16} & \bar{Q}_{26} & \bar{Q}_{66} \end{bmatrix}_k \begin{bmatrix} \kappa_x \\ \kappa_y \\ \kappa_{xy} \end{bmatrix} \int_{h_{k-1}}^{h_k} z\, dz
\tag{4.21}
$$

Since $[\varepsilon^0]$ and $[\kappa]$ are independent of the layer number k, equation 4.21 can be written in the simpler form:

$$
\begin{bmatrix} N_x \\ N_y \\ N_{xy} \end{bmatrix} = \begin{bmatrix} A_{11} & A_{12} & A_{16} \\ A_{12} & A_{22} & A_{26} \\ A_{13} & A_{26} & A_{66} \end{bmatrix} \begin{bmatrix} \varepsilon_x^0 \\ \varepsilon_y^0 \\ \gamma_{xy}^0 \end{bmatrix} + \begin{bmatrix} B_{11} & B_{12} & B_{16} \\ B_{12} & B_{22} & B_{26} \\ B_{16} & B_{26} & B_{66} \end{bmatrix} \begin{bmatrix} \kappa_x \\ \kappa_y \\ \kappa_{xy} \end{bmatrix}
\tag{4.22}
$$

or

$$
[N] = [A][\varepsilon^0] + [B][\kappa]
\tag{4.23}
$$

where

$$
A_{ij} = \sum_{k=1}^{n} (\bar{Q}_{ij})_k (h_k - h_{k-1})
\tag{4.24}
$$

$$
B_{ij} = \frac{1}{2} \sum_{k=1}^{n} (\bar{Q}_{ij})_k (h_k^2 - h_{k-1}^2)
$$

Equation 4.23 indicates that for a general laminated plate, the midplane stress resultants are given in terms of the midplane strains and the plate curvatures. Or, conversely, that coupling exists between extensional forces and bending, or twisting, deformations.

The moment resultants can also be defined in terms of the stresses as follows:

$$\begin{bmatrix} M_x \\ M_y \\ M_{xy} \end{bmatrix} = \int_{-\frac{h}{2}}^{\frac{h}{2}} \begin{bmatrix} \sigma_x \\ \sigma_y \\ \tau_{xy} \end{bmatrix} z\, dz \tag{4.25}$$

Similarly, if this load system is applied to a laminate of n layers, the moment resultants can be expressed as the sum of *n* simple integrals.

$$\begin{bmatrix} M_x \\ M_y \\ M_{xy} \end{bmatrix} = \sum_{k=1}^{n} \int_{h_{k-1}}^{h_k} \begin{bmatrix} \bar{Q}_{11} & \bar{Q}_{12} & \bar{Q}_{16} \\ \bar{Q}_{12} & \bar{Q}_{22} & \bar{Q}_{26} \\ \bar{Q}_{16} & \bar{Q}_{26} & \bar{Q}_{66} \end{bmatrix}_k \begin{bmatrix} \varepsilon_x^0 \\ \varepsilon_y^0 \\ \gamma_{xy}^0 \end{bmatrix} z\, dz + \sum_{k=1}^{n} \int_{h_{k-1}}^{h_k} \begin{bmatrix} \bar{Q}_{11} & \bar{Q}_{12} & \bar{Q}_{16} \\ \bar{Q}_{12} & \bar{Q}_{22} & \bar{Q}_{26} \\ \bar{Q}_{13} & \bar{Q}_{26} & \bar{Q}_{36} \end{bmatrix}_k \begin{bmatrix} \kappa_x \\ \kappa_y \\ \kappa_{xy} \end{bmatrix} z^2\, dz \tag{4.26}$$

Following the same procedure as for the stress resultants, the matrices can be removed from the integral in the summation:

$$\begin{bmatrix} M_x \\ M_y \\ M_{xy} \end{bmatrix} = \sum_{k=1}^{n} \begin{bmatrix} \bar{Q}_{11} & \bar{Q}_{12} & \bar{Q}_{16} \\ \bar{Q}_{12} & \bar{Q}_{22} & \bar{Q}_{26} \\ \bar{Q}_{16} & \bar{Q}_{26} & \bar{Q}_{66} \end{bmatrix}_k \begin{bmatrix} \varepsilon_x^0 \\ \varepsilon_y^0 \\ \gamma_{xy}^0 \end{bmatrix} \int_{h_{k-1}}^{h_k} z\, dz + \sum_{k=1}^{n} \begin{bmatrix} \bar{Q}_{11} & \bar{Q}_{12} & \bar{Q}_{16} \\ \bar{Q}_{12} & \bar{Q}_{22} & \bar{Q}_{26} \\ \bar{Q}_{16} & \bar{Q}_{26} & \bar{Q}_{66} \end{bmatrix}_k \begin{bmatrix} \kappa_x \\ \kappa_y \\ \kappa_{xy} \end{bmatrix} \int_{h_{k-1}}^{h_k} z^2\, dz \tag{4.27}$$

The constitutive relationship for the moment resultants can be expressed as:

$$\begin{bmatrix} M_x \\ M_y \\ M_{xy} \end{bmatrix} = \begin{bmatrix} B_{11} & B_{12} & B_{16} \\ B_{12} & B_{22} & B_{26} \\ B_{16} & B_{26} & B_{66} \end{bmatrix}_K \begin{bmatrix} \varepsilon_x^0 \\ \varepsilon_y^0 \\ \gamma_{xy}^0 \end{bmatrix} + \begin{bmatrix} D_{11} & D_{12} & D_{16} \\ D_{12} & D_{22} & D_{26} \\ D_{16} & D_{26} & D_{66} \end{bmatrix} \begin{bmatrix} \kappa_x \\ \kappa_y \\ \kappa_{xy} \end{bmatrix} \tag{4.28}$$

or in a more compact form:

$$[M] = [B][\varepsilon^0] + [D][\kappa] \tag{4.29}$$

where

$$D_{ij} = \frac{1}{3} \sum_{k=1}^{n} \left(\bar{Q}_{ij} \right)_k \left(h_k^3 - h_{k-1}^3 \right) \tag{4.30}$$

and the B_{ij} were defined previously.

These equations indicate that for a laminated plate, the bending moments are also given in terms of the midplane strains and the plate curvatures, and that coupling exists between applied bending moments and extensional stains.

By combining the equations for the stress resultants (4.23) and the moment resultants (4.30), the total plate constitutive equation can be written as follows:

$$
\begin{bmatrix} N_x \\ N_y \\ N_{xy} \\ M_x \\ M_y \\ M_{xy} \end{bmatrix} = \begin{bmatrix} A_{11} & A_{12} & A_{16} & B_{11} & B_{12} & B_{16} \\ A_{12} & A_{22} & A_{26} & B_{12} & B_{22} & B_{26} \\ A_{16} & A_{26} & A_{66} & B_{16} & B_{26} & B_{66} \\ B_{11} & B_{12} & B_{16} & D_{11} & D_{12} & D_{16} \\ B_{12} & B_{22} & B_{26} & D_{12} & D_{22} & D_{26} \\ B_{13} & B_{26} & B_{66} & D_{16} & B_{26} & D_{66} \end{bmatrix} \begin{bmatrix} \varepsilon^0_x \\ \varepsilon^0_y \\ \gamma^0_{xy} \\ \kappa_x \\ \kappa_y \\ \kappa_{xy} \end{bmatrix}
\tag{4.31}
$$
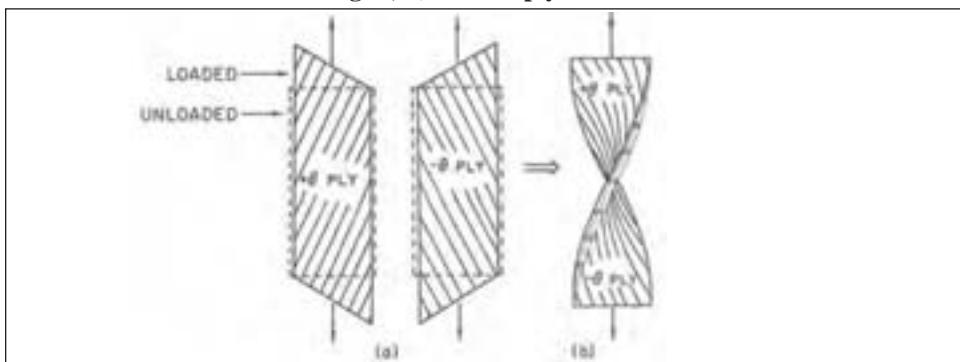
or in a more compact form as:

$$
\begin{bmatrix} N \\ M \end{bmatrix} = \begin{bmatrix} A & B \\ B & D \end{bmatrix} \begin{bmatrix} \varepsilon^0 \\ \kappa \end{bmatrix}
\tag{4.32}
$$

In this equation, the A_{ij} are called extensional stiffnesses, the B_{ij} are called the coupling stiffnesses, and the D_{ij} are called the bending stiffnesses. The presence of the B_{ij} implies coupling between bending and extension of a laminate. Thus, pulling on a laminate that has non-zero B_{ij} will cause both extension and bending or twisting of the laminate. Also, such a laminate will extend or contract as well as bend when loaded by a moment. Examples of the terms in equation 4.31 calculated for different tire ply/belt systems are given in [14,25,73].

Figure 4.8 shows the extension-twist coupling for a simple 2-ply, +/-θ cord-rubber laminate vs. the extension-shear deformations of the single lamina. Note that each lamina is described by the A_{ij} stiffnesses derived from the Q_{ij} which have extension-shear coupling, but no out of plane bending. It is only when two +/-θ plies are bonded together that non-zero B_{ij} terms appear and cause the out-of plane twisting.

Figure 4.8 - Deformations that occur in angled ply laminates. a) individual plies at + and - cord angles; b) the two ply laminate [25] [13].

Example
A simple example is presented to provide a baseline for subsequent discussion. The primary purpose of this example is to illustrate the calculation of the constitutive matrix for the laminate.

Consider a specific two-ply 0/+45 degree laminate. The bottom lamina is a 0 degree layer with 0.20 inch thickness and the following properties:

$$\begin{bmatrix} \sigma_1 \\ \sigma_2 \\ \tau_{12} \end{bmatrix}_{0°} = 10^6 \begin{bmatrix} 30 & 1 & 0 \\ 1 & 3 & 0 \\ 0 & 0 & 1 \end{bmatrix} \begin{bmatrix} \varepsilon_1 \\ \varepsilon_2 \\ \gamma_{12} \end{bmatrix} (psi)$$

Since this is a zero degree ply, the x-y coordinate system coincides with the 1-2 principal material coordinate system.

The second lamina is a +45 degree layer with the same material properties as the first lamina (in the 1-2 coordinate system), and it is 0.10 inch thick. The Q_{ij} terms are found in the x-y coordinate system by using the transformation equations described in Eqs 2.21:

$$\bar{Q}_{11} = 10^6 \left[30\cos^4(45) + 2(1+2)\sin^2(45) + 3\sin^4(45) \right]$$

$$\bar{Q}_{12} = 10^6 \left[(30+3-4)\sin^2(45)\cos^2(45) + 1\left(\sin^4(45)+\cos^4(45)\right) \right]$$

$$\bar{Q}_{22} = 10^6 \left[30\sin^4(45) + 2(1+2)\sin^2(45)\cos^2(45) + 3\cos^4(45) \right]$$

$$\bar{Q}_{66} = 10^6 \left[(30+3-2-2)\sin^2(45)\cos^2(45) + 1\left(\sin^4(45)+\cos^4(45)\right) \right]$$

$$\bar{Q}_{16} = 10^6 \left[(30-1-2) \right]\sin(45)\cos(45) + (1-3+2)\sin^3(45)\cos(45) \right]$$
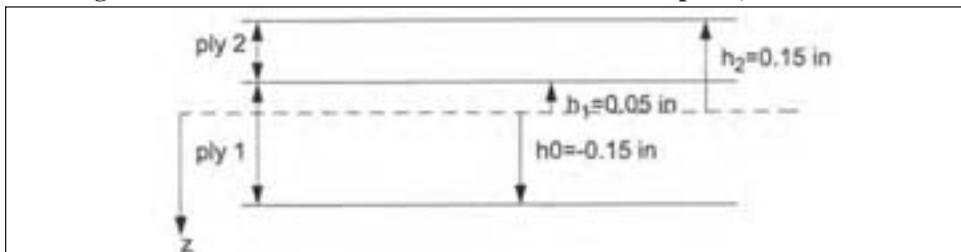
$$\bar{Q}_{26} = 10^6 \left[(30-1-2) \right]\sin^3(45)\cos(45) + (1-3+2)\sin(45)\cos^3(45) \right]$$

Therefore,

$$\begin{bmatrix} \sigma_x \\ \sigma_y \\ \tau_{xy} \end{bmatrix}_{45°} = 10^6 \begin{bmatrix} 9.75 & 7.75 & 6.75 \\ 7.75 & 9.75 & 6.75 \\ 6.75 & 6.75 & 7.75 \end{bmatrix} \begin{bmatrix} \varepsilon_x \\ \varepsilon_y \\ \gamma_{xy} \end{bmatrix} (psi)$$

The geometric configuration of the laminate and the location of the geometric midplane are defined in figure 4.9.

Figure 4.9 - Notation for lamina thickness for the example [0,+45] laminate

The laminate constitutive equation can then be obtained by calculating the extensional stiffnesses A_{ij}, the coupling stiffnesses B_{ij}, and the bending stiffnesses D_{ij}.

$$A_{ij} = \sum_{k=1}^{n} \left(\bar{Q}_{ij}\right)_K \left(h_k - h_{K-1}\right) = \left(\bar{Q}_{ij}\right)_1 [0.05 + 0.15] + \left(\bar{Q}_{ij}\right)_2 [0.15 - 0.05]$$

$$[A] = 10^6 \begin{bmatrix} 6.975 & 0.975 & 0.675 \\ 0.975 & 1.575 & 0.675 \\ 0.675 & 0.675 & 0.975 \end{bmatrix} (lb/\ in)$$

$$B_{ij} = \frac{1}{2}\sum_{k=1}^{n} \left(\bar{Q}_{ij}\right)_k \left(h^2{}_k - h^2{}_{k-1}\right) = \frac{1}{2}\left(\bar{Q}_{ij}\right)_1 \left[0.05^2 + 0.15^2\right] + \frac{1}{2}\left(\bar{Q}_{ij}\right)_2 \left[0.15^2 - 0.05^2\right]$$

$$[B] = 10^4 \begin{bmatrix} -20.25 & 6.75 & 6.75 \\ 6.75 & 6.75 & 6.75 \\ 6.75 & 6.75 & 6.75 \end{bmatrix} (lb)$$

$$D_{ij} = \frac{1}{3}\sum_{k=1}^{n} \left(\bar{Q}_{ij}\right)_k \left(h^3{}_k - h^3{}_{k-1}\right) = \frac{1}{3}\left(\bar{Q}_{ij}\right)_1 \left[0.05^3 + 0.15^3\right] + \frac{1}{3}\left(\bar{Q}_{ij}\right)_2 \left[0.15^3 - 0.05^3\right]$$

$$[D] = 10^4 \begin{bmatrix} 4.56 & 0.956 & 0.731 \\ 0.956 & 1.406 & 0.731 \\ 0.731 & 0.731 & 0.956 \end{bmatrix} (in\cdot lb)$$

Combining the above results, the total set of constitutive equations for this two-ply laminate can be written:

$$\begin{bmatrix} N_x \\ N_y \\ N_{xy} \\ M_x \\ M_y \\ M_{xy} \end{bmatrix} = 10^4 \begin{bmatrix} 697.5 & 97.5 & 67.5 & -20.25 & 6.75 & 6.75 \\ 97.5 & 157.5 & 6.75 & 6.75 & 6.75 & 6.75 \\ 67.5 & 67.5 & 97.5 & 6.75 & 6.75 & 6.75 \\ -20.25 & 6.75 & 6.75 & 4.56 & 0.956 & 0.731 \\ 6.75 & 6.75 & 6.75 & 0.956 & 1.406 & 0.731 \\ 6.75 & 6.75 & 6.75 & 0.731 & 0.731 & 0.956 \end{bmatrix} \begin{bmatrix} \varepsilon^0{}_x \\ \varepsilon^0{}_y \\ \gamma^0{}_{xy} \\ \kappa_x \\ \kappa_y \\ \kappa_{xy} \end{bmatrix}$$

where the units of N_i are (lb/in) and of the M_i (moment per length) are (lb).

Sources of simplification of the laminate constitutive equations
There are special laminates for which the governing equations can take a simplified form as opposed to the general form in equation 4.33. Many of the cases result from the common practice of constructing laminates from laminae that have the same material properties and thickness, but have different orientations of their principal material directions. The most common case is when [B] is identically zero, and cases when the terms A_{16}, A_{26}, and D_{16}, D_{26} are zero.

Case1, [B] = 0: The terms in the [B] matrix are obtained as a sum of terms involving the$[\overline{Q}]$ matrices and squares of the z coordinates of the top and bottom of each ply. Since the B_{ij} are, $(h_k^2 - h_{k-1}^2)$ they are zero for laminates which are symmetrical with respect to z. That is, each term in B_{ij} is zero if, for each lamina above the mid-plane there is an identical lamina (in properties and orientation) located at the same distance below the mid-plane. Such mid-plane symmetric laminates are an important class of laminates. They are commonly constructed because the extension-bending or twist coupling of non-   symmetric laminates causes warping due to in-plane loads or thermal contractions. The governing constitutive equations for symmetric laminates are also considerably simplified compared to non-symmetric laminates. Bending and extensional portions of the problem can be considered separately. Although mid-plane symmetric laminates exhibit no extension-bending coupling, they do in general exhibit both in-plane and bending anisotropy with extension or bending and shear coupling due to the A_{16}, A_{26}, and D_{16}, D_{26} terms.

Case 2, A_{16}=A_{26}=0: This class of laminates behaves as an orthotropic plate with respect to in-plane forces and strains. This occurs if, for every lamina of a plus θ orientation there is another lamina of the same orthotropic properties and thickness with a negative θ orientation, regardless of the stacking sequence. The laminate then behaves as an orthotopic lamina loaded in the principal directions with respect to in-plane forces and strains. However, bending and twisting can still occur. Laminates with this property are called *balanced*.

Case 3, D_{16} =D_{26}=0: The simplification of the bending matrix [D] is also possible. The terms D_{16} and D_{26} can equal zero, if all the laminae are oriented at 0° or 90°, or if, for every lamina oriented at a positive θ orientation above the mid-plane there is an identical lamina placed at an equal distance below the mid-plane but oriented at a negative θ orientation. These laminates are *balanced* laminates with the additional condition on the distance of the +/- pair from the mid-plane.

Case 4, [B] =0, and D_{16}=D_{26}=0: For this special case, the laminate must have all the restrictions listed in cases 1-3—i.e., the laminate is balanced and symmetric. The laminate acts like an orthotropic lamina loaded along its principal axes. Four independent elastic constants can be identified – E_x, E_y, G_{xy} and v_{xy} – in the same way as for a single orthotropic lamina. A simple example is a [+θ,-θ,-θ,+θ] lay-up. To avoid out-of plane deformations, Lee and co-workers [47, 74] often use a [+θ,-θ,-θ,+θ] composite for fatigue testing rather than the 2-ply specimen illustrated in Fig 4.8.

With the limits of Case 4, the elastic constants can be computed from the laminate stiffness matrix as
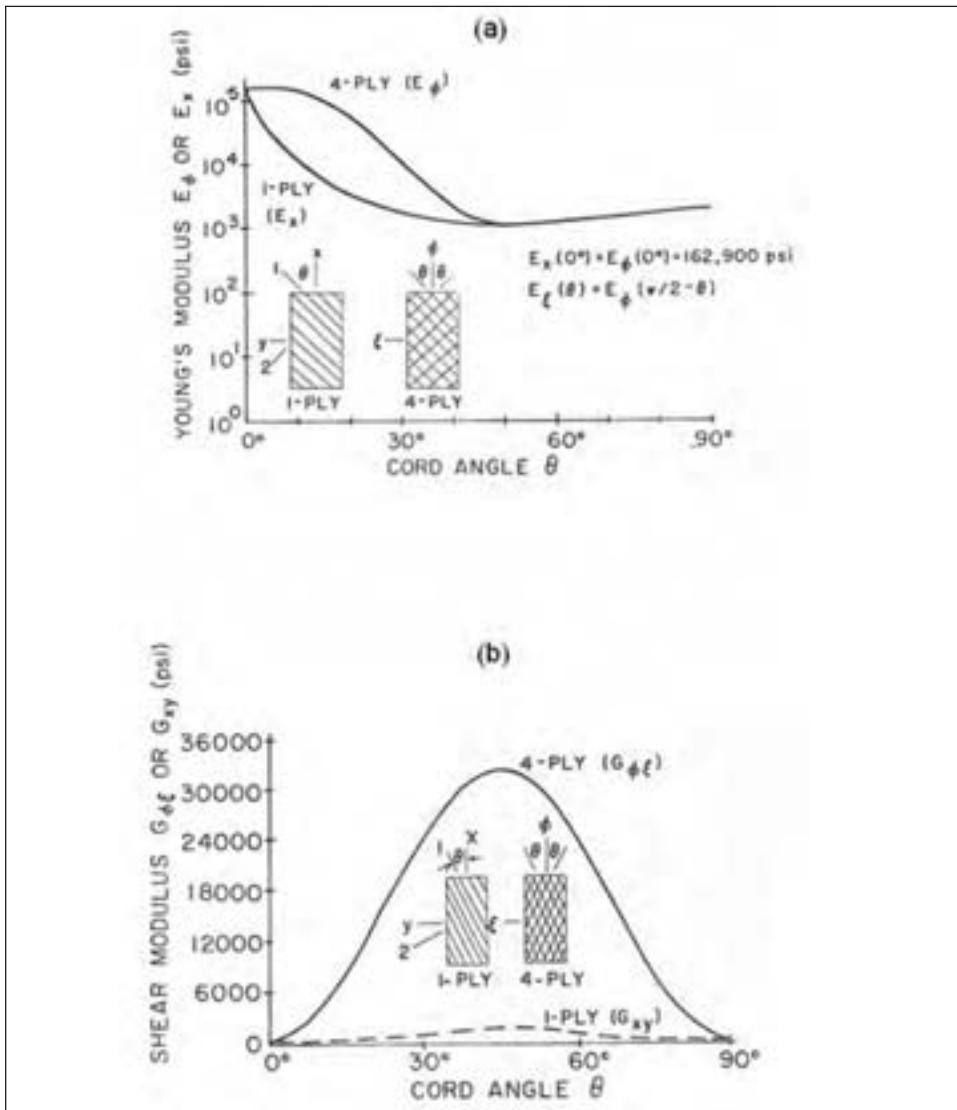
$$E_x = (A_{11}A_{22} - A_{12}^2)/hA_{11}$$
$$E_y = (A_{11}A_{22} - A_{12}^2)/hA_{22}$$
$$G_{xy} = A_{66}/h$$
$$v_{xy} = A_{12}/A_{11}$$

Some examples of single lamina vs. balanced and symmetric laminate elastic constants are shown in figure 4.10 a) and b). The laminate has cord lay-up [+θ,-θ,-θ,+θ].

Figure 4.10 - Variation of elastic constants with cord angle for single ply and 4 ply [+θ, -θ, -θ, +θ] laminates of 840/2 nylon cord-rubber composite. a) Young's modulus, and b) shear modulus [25].

Determination of stresses and strains

One objective of analyzing a composite laminate is to map the stresses and strains in each of the lamina forming the laminate. Then the forces in the cords can be determined, or the stresses and strains can be used to study the failure of the laminate. An analysis could even predict progressive failure: when a lamina exceeds its strength, it is eliminated from the laminate and the remaining laminae take the additional load. The following discussion will describe a method to calculate the state of stresses and strains in each lamina.

For a general laminate under a general loading condition, equation 4.31 describes the governing behavior. By inverting the stiffness matrix, the mid-plane strains and plate curvatures are determined as a function of the applied loads as:

$$
\begin{bmatrix} \varepsilon^0 \\ \kappa \end{bmatrix} = \begin{bmatrix} A'B' \\ B'D' \end{bmatrix} \begin{bmatrix} N \\ M \end{bmatrix}
\tag{4.33}
$$

where $[A']$, $[B']$, and $[D']$ are related to $[A]$, $[B]$, and $[D]$. Once the mid-plane strains and plate curvatures are determined, the strains in any laminae can be calculated from

$$
\begin{bmatrix} \varepsilon_x \\ \varepsilon_y \\ \gamma_{xy} \end{bmatrix} = \begin{bmatrix} \varepsilon^0_x \\ \varepsilon^0_y \\ \gamma^0_{xy} \end{bmatrix} + z \begin{bmatrix} \kappa_x \\ \kappa_y \\ \kappa_{xy} \end{bmatrix}
\tag{4.34}
$$

Consider a lamina at a distance z from the geometric mid-plane, and transform the above strains into the lamina principal material axes 1-2:

$$
\begin{bmatrix} \varepsilon_1 \\ \varepsilon_2 \\ \dfrac{\gamma_{12}}{2} \end{bmatrix}_k = [R] \begin{bmatrix} \varepsilon_x \\ \varepsilon_y \\ \dfrac{\gamma_{xy}}{2} \end{bmatrix}_k
\tag{4.35}
$$

The stresses in the principal material coordinate system are as follows:

$$
\begin{bmatrix} \sigma_1 \\ \sigma_2 \\ \tau_{12} \end{bmatrix} = \begin{bmatrix} Q_{11} & Q_{12} & 0 \\ Q_{12} & Q_{22} & 0 \\ 0 & 0 & Q_{66} \end{bmatrix} \begin{bmatrix} \varepsilon_1 \\ \varepsilon_2 \\ \gamma_{12} \end{bmatrix}
\tag{4.36}
$$

The stresses in equation 4.36 and/or the strains in equation 4.35 could be used in the appropriate   failure criterion to determine if the loads are acceptable. If the strength criterion is based on a maximum strain theory, a comparison is made using the state of strain. If it is based on a maximum stress theory then a comparison will be made using the state of stress. The topic of laminate strength analysis will not be dealt with *in toto*. However, fatigue and durability of composite laminates is covered in section 6.

Application of laminate theory to tires
This discussion follows that in [25]. For study of composite belt/ply properties in tires, a toroidal coordinate system is sometimes used. The system is shown in figures 4.11a) and b) with the laminate resultant forces and moments displayed.

Figure 4.11: Tire coordinate system with resultant
a) forces and b) moments acting on tire laminate [25]

In the tire footprint the belt and ply flatten in the crown region and the following coordinate directions are nearly equivalent

$\xi \approx x$

$\phi \approx y$

$\zeta = z$

In the following discussions we will use the equations developed previously in the x-y-z Cartesian system with the assumption that they approximately represent the actual toroidal structure.

Plysteer

Plysteer is the tendency for a rolling loaded tire under zero camber and zero slip angle to track at an angle to its centerline. It is usually observed as a net lateral force under zero steer angle and zero camber conditions in a laboratory test. Consider the simple case of a passenger tire belt package with a lay-up of [+20, -20]. This is not symmetric and the coupling terms B_{ij} are not zero. As the belt package is bent with a change in curvature κ_x going into the footprint, the B_{16} term can create a force N_{xy} which could result in a steering torque, and the B_{12} term can create a cornering force N_y. Both of these forces can contribute to plysteer. Note that whether the tire rotates clockwise or counterclockwise, the plysteer force still acts in the same direction.

Obstacle envelopment

This tire performance parameter is related to harshness. To envelop objects such as joints in the road, a low circumferential bending stiffness is desired. For moderate sized rocks, a low meridional bending stiffness may also help reduce harshness. Of course, these requirements need to be balanced with other requirements for belt package stiffness.

For circumferential bending and extension, with other strains and curvatures unchanged, equation 4.31 gives

$$M_x = B_{11}\varepsilon_x^0 + D_{11}\kappa_x \tag{4.37}$$

If the resultant force in the x-direction is assumed to be zero in the footprint, then
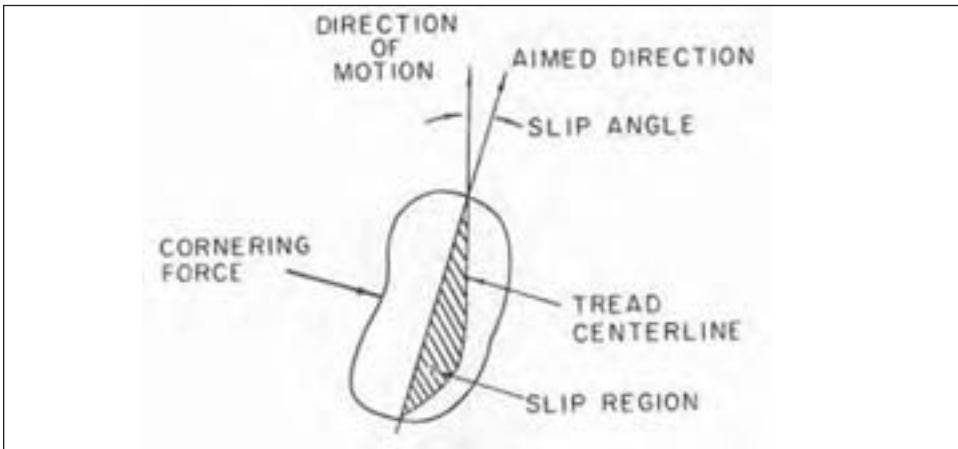
$$N_x = A_{11}\varepsilon_x^0 + B_{11}\kappa_x = 0 \tag{4.38}$$

Solving 4.38 for ε_x^0 and substituting into 4.37 gives

$$M_x = (D_{11} - B_{11}^2 / A_{x11})\kappa \tag{4.39}$$

which is the same moment-curvature relation as equation 4.4, except that euqation 4.39 is for a wide, composite laminate.

Figure 4.12: Tread centerline deflection in tire footprint due to cornering [25]

Wear and cornering

Gough [15] recognized that the in-plane stiffness of the footprint due to shear and bending deformations can be a significant factor in tire wear and cornering ability. Consider the cornering footprint shown in figure 4.12.

The cornering force causes the tread centerline to take on the path shown in the figure. The more the tread centerline is displaced away from the travel direction, the larger the slip region and thus the wear. The forces generated to resist the deformation are largely due to the belt package stiffness. For in-plane bending, the relevant property is the laminate modulus E_x, and for in-plane shear the relevant property is the in-plane shear modulus G_{xy}. Using both these deformation modes, the Gough stiffness S_G can be shown to take the form [14]

$$S_G = \frac{E_x G_{xy}}{C_1 E_x + C_2 G_{xy}} \tag{4.40}$$
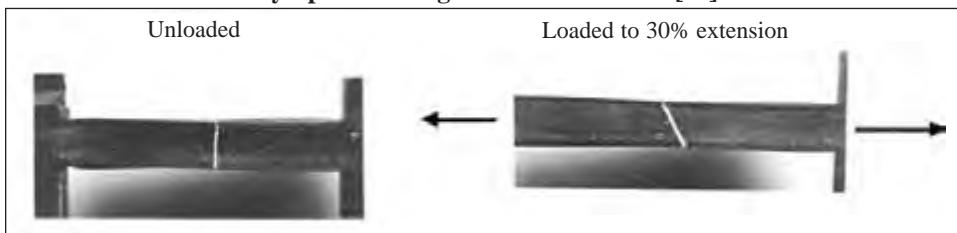
where the constants C_i have units 1/length and relate to the footprint dimensions and lateral deformation characteristics of the tire construction.

Interlaminar deformations

The theory of composite laminates presented in the previous sections does not allow for shear deformation between layers. Laminate theory may be useful for overall stiffnesses,
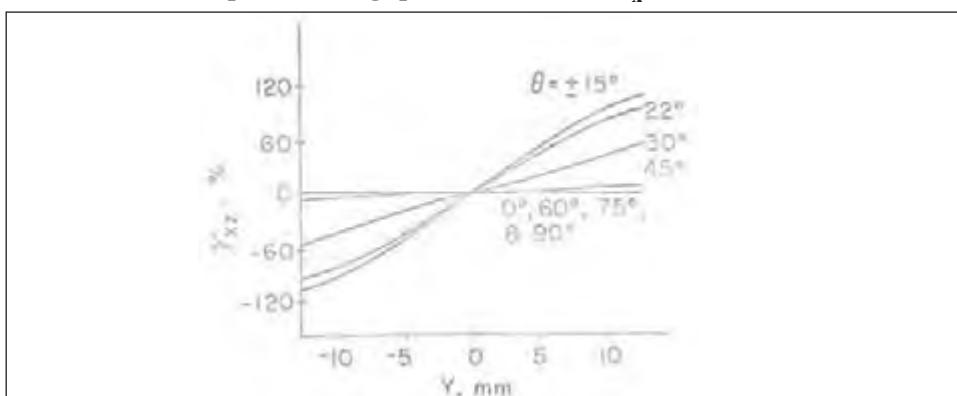
even though it overestimates this stiffness if transverse (interlaminar) flexibility is significant. For analysis of stresses and strains in local regions of cord-rubber composites, the interlaminar effects need to be considered. Specifically, interlaminar strains γ_{yz}, γ_{zx} are typically present in the deformation of cord-rubber laminates. Since these strains offer additional deformation modes for the laminate, their existence tends to make the laminate stiffness less than that calculated from laminate theory. Consider a side-view of the laminate shown in figure 4.13. The outer plies are angled cord-rubber layers, and the center layer is rubber only.

Figure 4.13 - Cord-rubber composite with [+θ, rubber, -θ]
lay-up illustrating interlaminar shear. [20]

Unloaded   Loaded to 30% extension

If the loading direction is the x-direction and the z-direction is normal to the laminate surface, then the shear indicated by the change in angle of the white line is the γ_{zx} component. The tendency for the composite to twist is also evident in the loaded picture. A distribution of interlaminar shear across the width of a 2-ply specimen is shown in figure 4.14. The maximum value of interlaminar shear strain occurs at the edges of the specimen. With the stress riser caused by the ends of the cords, this makes the edge a likely location for cracks to initiate. Note that zero, or nearly zero interlaminar shear strain develops for cord angles 0º, 90º, 75º, and 60º.
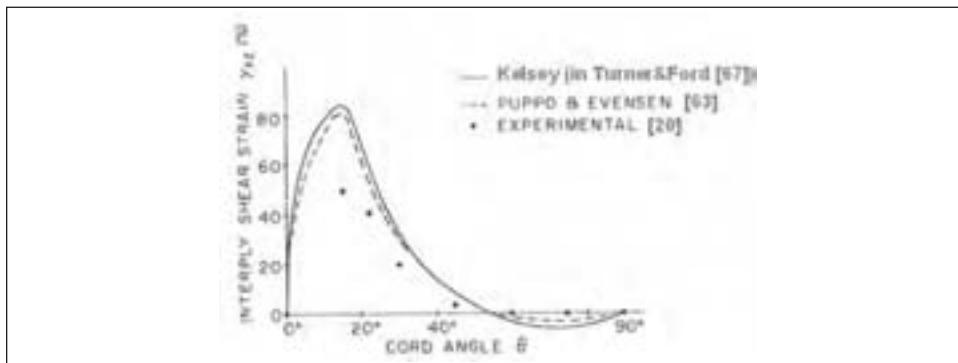
Figure 4.14 - Interlaminar shear strain (xz)
vs. position along specimen width for E$_x$ = 20% [20].

It is interesting to note that, as the rubber layer between the cord layers decreases in thickness, the shear strain will often increase for the same extensional strain, since the "gauge" over which the shear deformation acts is decreasing. Other effects such as the change of stiffness distribution with thickness makes the relation of shear strain vs.

rubber gauge less than linear [17]. This decrease in interlaminar shear strain with increasing gauge is one of the reasons that a belt edge wedge or rubber layer is often found between, and at the edge of, the working belts in radial tires. Another interesting behavior is interlaminar shear as a function of cord angle for a fixed extension as shown in figure 4.15. The maximum interlaminar shear strain occurs at around a 20 degree cord angle, which is close to the cord angle (measured with respect to the circumferential direction) used in many tire belts. However, this experiment was performed with constant extensional strain, whereas tire belts need to resist an inflation load and periodically a bending deformation in the footprint. Belt angles around 20 degrees usually work well,

Figure 4.15 - Interlaminar shear vs. cord angle for [+θ ,- θ] laminate [20].

combined with the 90 degree ply to provide sufficient Gough stiffness and stability for a radial tire.

A method to illustrate interlaminar shear strain was described by Turner and Ford [67]. In this method, a row of pins is inserted across the width of a 2-ply specimen. The pins tend to rotate as the load is applied; see figures 4.16a and 4.16b. The rotation angle of the pins is proportional to the interlaminar shear strain.

**Figure 4.16a - Pin experiment showing mechanism to demonstrate
interlaminar shear strain in 2-ply composite specimen [67]**
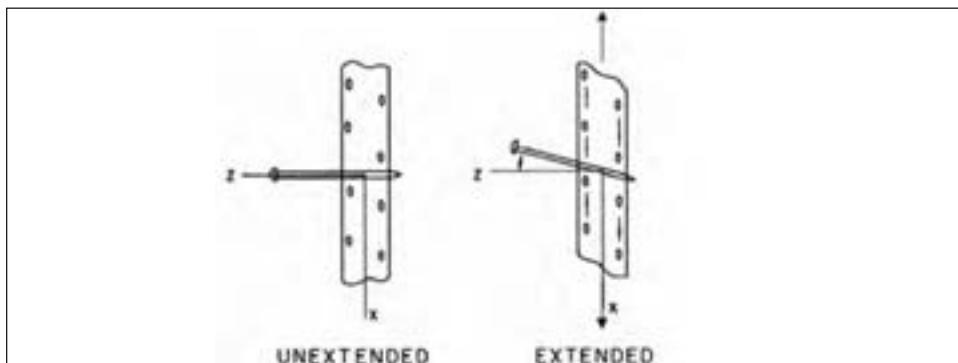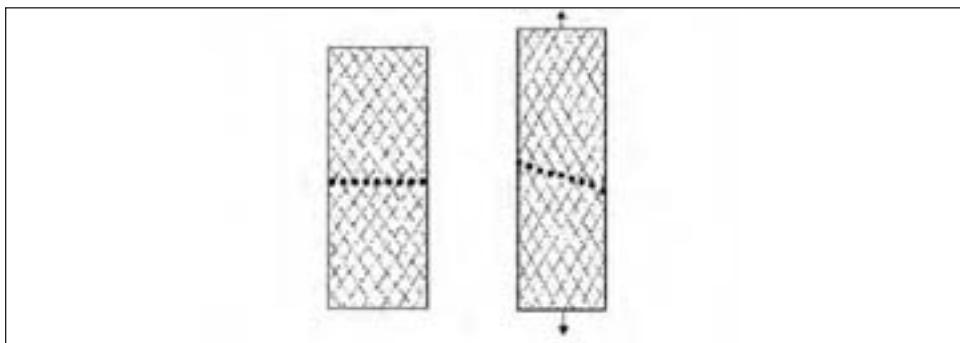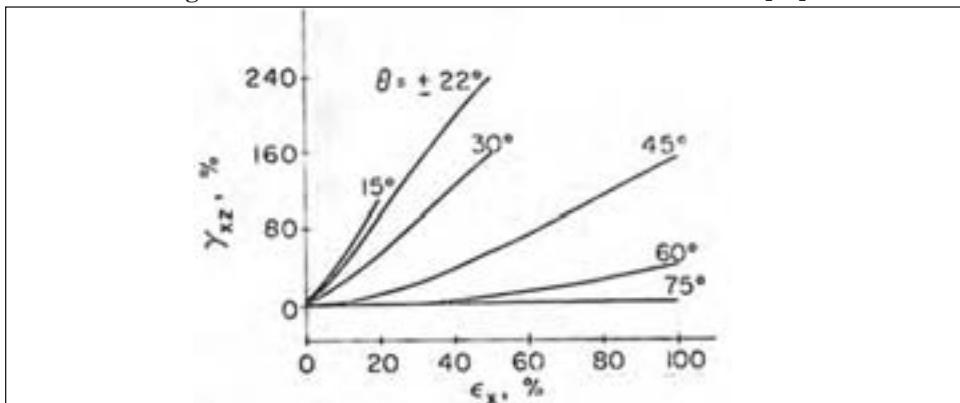
**Figure 4.16b - Pin experiment showing distribution of interlaminar
shear strain across 2-ply specimen width [67]**

The interlaminar shear strain can be many times the applied axial strain. Figure 4.17 shows that for cord angles of 22 degrees, the interlaminar shear strain at the specimen edge is about 4 times the applied axial strain. This plot is for a specimen with geometry shown in figure 4.13, with a large rubber gauge between the cord-rubber layers. As the rubber gauge between the plies decreases, the interlaminar shear strain will increase further for the same axial strain. A parametric study on interlaminar shear strain is given by DeEskinazi and Cembrola [75].

Figure 4.17 - Interlaminar shear strain vs. axial strain [20]

Finite element analysis

Composite laminate theory provides the tire designer with an insightful understanding of the relation between such features as normal and bending stiffnesses and lay-up sequence of the belts or plies. For structures with complex geometries composed of composite materials, numerical methods are usually required to accurately determine the states of stress and strain.

This section describes typical numerical modeling methods for multi-layer, continuous cord reinforced structures; analogous methods for single layer composites were briefly discussed in section 2.
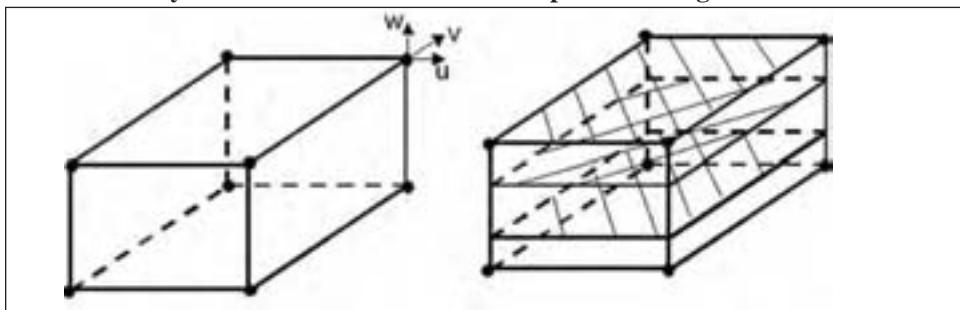
Macroscopic modeling
With macroscopic modeling, the cords are not explicitly represented, but their stiffness contribution is made through the material constants. The composite analysis outlined in section 3 is typically used to define the homogenized composite properties. Many different approaches for the finite element analysis are available. Three approaches, using different types of structural elements are described in the following subsections.

3-D continuum "brick" elements
Multiple layers can be included in a single brick element by at least three methods: 1) provide equivalent anisotropic properties for the entire element, 2) use a layered brick and provide orthotropic properties for each layer, or 3) provide isotropic properties for the rubber and include rebar layers to represent the cords. Methods 1 and 3 are illustrated in figure 4.18.
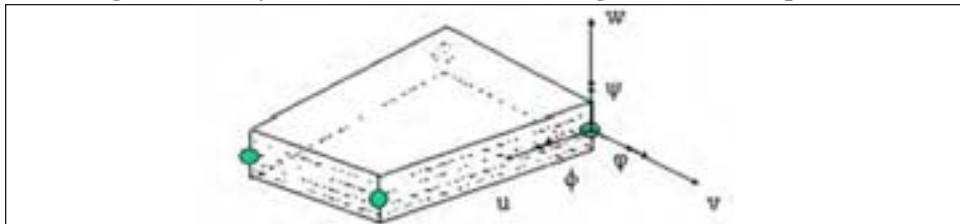
Figure 4.18 - Left: Brick element to which anisotropic properties could be assigned. Right: Brick element with three rebar layers included. Each node has 3 displacement degrees of freedom.
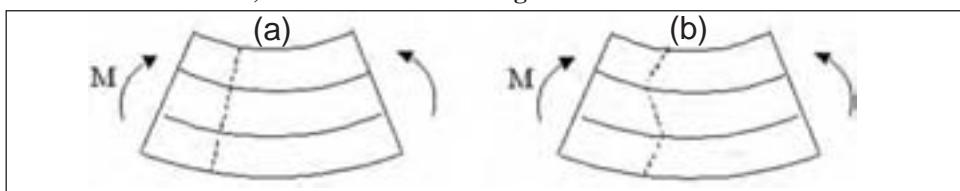
Care should be taken when smearing properties over a standard brick element, since bending stiffnesses and deformations are not well represented. The nodes at the corners of the brick have only displacement degrees of freedom (u, v, w). In contrast, shell elements have both displacement and rotational degrees of freedom, and are often preferred for representing layered composites with smeared properties.

Shell and membrane elements
This approach can provide an accurate representation of the extension and bending properties of laminated composites. A four noded, layered shell element is shown in figure 4.19. Each node has five or six degrees of freedom, the three linear displacements (u,v,w), the two out of plane bending rotations (ϕ,φ) and sometimes the sixth "drilling" rotation (ψ) corresponding to in-plane rotation of the node. The $[A]$, $[B]$, and $[D]$ matrices can be given as input for the entire composite. If analysis per layer is desired for, say, cord load calculations, then a layered shell is used and the $[Q]$ or the $[\overline{Q}]$, or possibly the engineering constants, E_1, E_2, v_{12}, G_{12}, orientation θ, thickness, and distance from the midplane are input for each layer with respect to a local shell coordinate system. So-called "thin" shell elements obey the Kirchoff-Love "plane-sections remain plane" assumption. They are best suited to simulate a single cord-rubber layer. "Thick" shell elements can
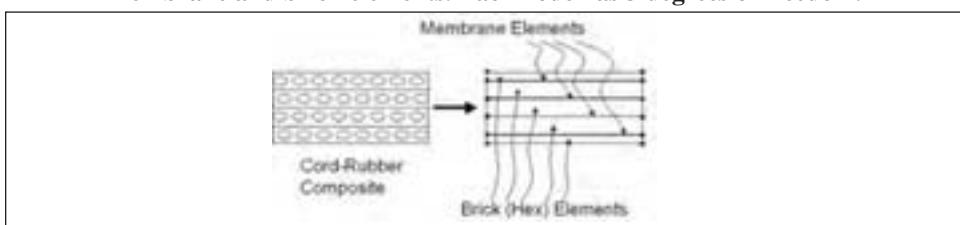
Figure 4.19: Layered shell element with six degrees of freedom per node

include transverse flexibility (non-Kirchoff-Love), and the possibility to calculate inter-laminar stresses and strains [e.g., 58, 59]. Figure 4.20 illustrates deformation patterns for two interlaminar assumptions. Various theories and "thick" shell elements have been developed to account for interlaminar, or "transverse shear" flexibility [e.g., 2, 58, 59]

**Figure 4.20 - Example deformation patterns for: a) Kirchoff-Love,
and b) discrete-linear allowing for interlaminar shear**

Membrane elements can also be used to represent a single cord-rubber layer. They do not have rotational degrees of freedom, so in order to model the bending behavior of a cord-rubber laminate, a layer of membrane elements is used to represent a single cord-rubber layer. Solid rubber elements are then used to separate the membrane layers as shown in figure 4.21. An early analysis using this approach is found in Turner and Ford [67]. Each membrane element can be assigned orthotropic properties, or alternatively, rebars can be used to represent the cord stiffness and the membrane material properties can represent the rubber behavior.

The rebar/membrane (or rebar/shell) approach offers flexibility in using material laws, since properties for the rubber and cords are input separately. For example, a hyper-elastic/softening law to represent the Mullins effect in rubber can be assigned to the membrane, while a nonlinear viscoelastic law to represent creep in a nylon cord can be assigned to the rebar. Note that the resulting stiffnesses distributed to the nodes are homogenized stiffnesses that include effects of both the rubber and the cords. This approach also provides shear deformation between layers to achieve a shear deformation similar to the pattern in figure 4.20b.

**Figure 4.21 - 2-D view of a 3-D cord-rubber modeling scheme using
membrane and brick elements. Each node has 3 degrees of freedom.**
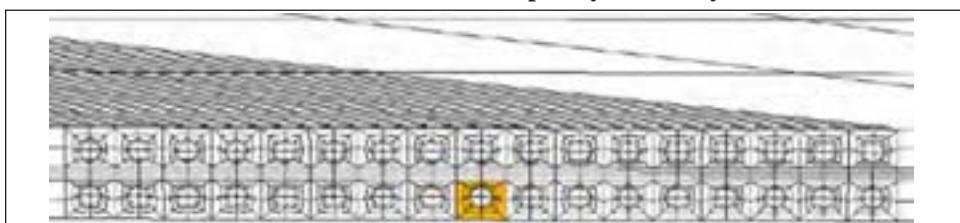
Macroscopic modeling, using brick, shell and/or membrane elements provides the overall behavior of the composite structure. These elements are typically used to represent the cord-rubber layers in a tire model. [e.g., 57, 58]. For a more detailed analysis, the cord geometry needs to be represented explicitly, but this requires larger models and more computation time. The next subsection describes two methods for detailed cord-rubber modeling.

Microscopic modeling with FEA

This approach is used to analyze the details of a cord-rubber composite such as the stresses in the rivet, or the strain near the cord-rubber interface. The geometry of both the cords and the rubber is represented explicitly as shown in figure 4.22. This approach can also describe the interface between the constituents as, for example, fully bonded or partially detached. Composite failure mechanisms involving adhesion loss can then be analyzed. Microscopic models can also provide the homogenized properties used by the macroscopic methods.

Finite element models such as the one shown in figure 4.22 can be used to study the behavior of laboratory composite specimens. They can also be linked to models of an entire tire through submodeling, or global-local methods.

Figure 4.22 - Portion of a two-ply composite finite element model with the cords modeled explicitly as solid cylinders.

Microscopic modeling with the method of cells

There are several micromechanical approaches that can predict the micro and macro performance of composites. The Method of Cells (MOC) [21] and its extension the Generalized Method of Cells (GMC) [22] are an alternate and often more efficient approach to a detailed FEA model. The capabilities are captured in software packages such as the Micromechanics Analysis Code (MAC/GMC) [23], or the First-Order Nonlinear Elasticity (FONE) [21] code. These codes are structured in a modular fashion that allows a user to implement additional constitutive models through a user-defined subroutine. The periodic nature of composites typically allows one to identify a repeating unit cell that can be used as a building block to construct the entire composite. The properties of this unit cell are thus representative of the properties of the entire assemblage. In the original MOC the unit cell consisted of a single fiber (cord) subcell surrounded by three matrix subcells, however in GMC this has been generalized such that the unit cell is subdivided into an arbitrary number of subcell phases. Figure 4.23 shows a periodic assemblage and repeating unit cell (or repeating volume element, RVE) from which the approximate description of the composite is developed.

Constitutive models in MOC codes can be quite general, including nonlinear viscoelastic,

plastic, and damage effects. Interfaces are typically provided for user specific models. Figure 4.24 shows results for strain energy density around a cord.

The Method of Cells does not satisfy all the governing equations of the mechanics problem as a finite element approach would. What MOC gives up in consistency, it gains in speed and the ability to look at very fine detail.

Software for the MOC can be coupled to finite element codes to provide a multi-level (i.e., global-local) solution capability. For example, the MOC could be used to perform the local analysis of the cord-rubber detail and provide equivalent anisotropic material properties to macroscopic brick or shell elements used in a global tire analysis. Damage could be evaluated by the MOC and the resulting softened stiffnesses provided back to the

Figure 4.23 -- Representative volume elements for continuous fiber reinforced composite
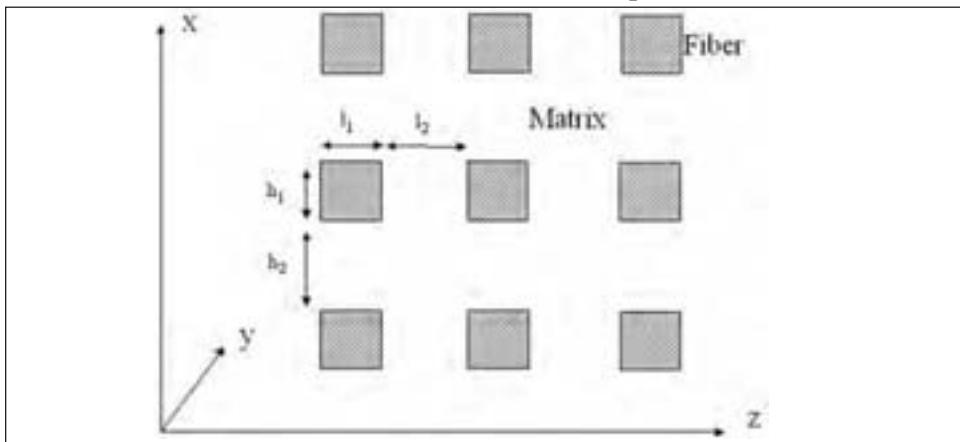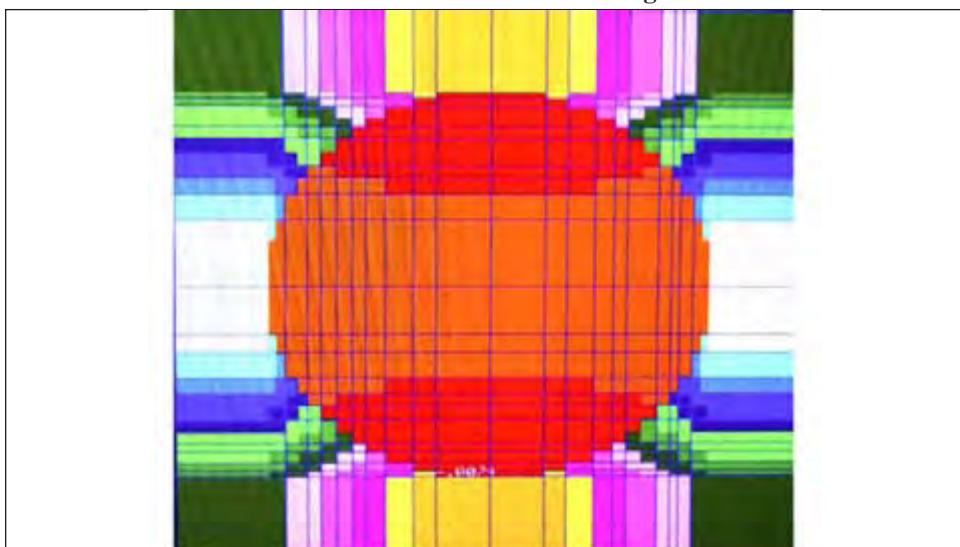

Figure 4.24 - Local discretization and results for a tire cord in rubber matrix using MOC

global solution for the next analysis step, and so on.

It is generally possible to tailor the modeling approach to fit the goal of the analysis. If the global behavior is sought, then a macroscopic modeling approach is sufficient to capture the contribution of the composite to the overall structural behavior. If the state of the interface between the matrix and the reinforcing cord requires analysis, then the micromechanical modeling is the proper tool to identify the state of stress and strain in and around each constituent in the region of interest. This latter approach is often used when life prediction of a composite is being investigated. Damage evolution can be monitored and material properties updated on a local level. Composite durability is the focus of Section 6 where the topics of strength, damage and life prediction are discussed.

Exercises

1. A symmetric laminate has both geometric and material property symmetry about the mid-surface. Show that the laminate coupling stiffnesses B_{ij} are zero for a [+45/-45/-45/+45] symmetric angle-ply laminate consisting of 0.25 mm thick unidirectional laminae with the following engineering constants: E_1=138 GPa, E_2=9.0 GPa, G_{12}=6.9 GPa, and ν_{12}=0.3.

2. An antisymmetric laminate has plies of identical material and thickness at equal positive and negative distances from the middle surface, but the ply orientations are antisymmetric with respect to the middle surface. Show that the laminate coupling stiffnesses B_{ij} are not zero for a [-45/+45/-45/+45] antisymmetric angle-ply laminate consisting of the same 0.25 mm thick unidirectional laminae used in the previous symmetric laminate.

3. Show that bending-twisting coupling is present in symmetric angle-ply laminates, but not in antisymmetric angle-ply laminates. (Hint: calculate the laminate bending stiffness D_{ij}, and show that $D_{16}=D_{26}=0$ for the antisymmetric laminate.

4. The symmetric angle-ply laminate described in Exercise 1 is subjected to a single uniaxial force per unit length of N_x=50 MPa-mm. Determine the resulting stresses associated with the x and y axes in each lamina.
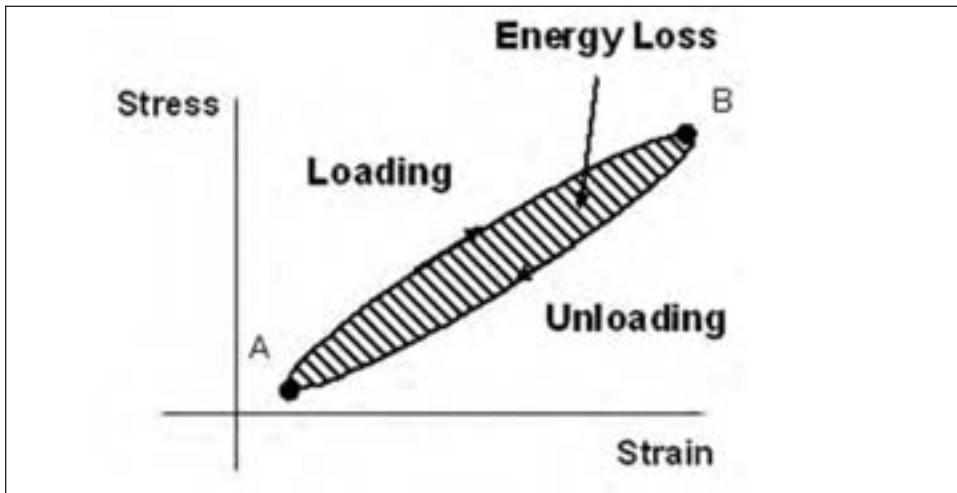
5. Viscoelasticity and hysteretic behavior of cord-rubber composites

The viscoelastic behavior of rubber and organic cords leads to orthotropic viscoelastic response of cord-rubber layers such as the plies and belts in tires. In order to analyze problems such as tire creep (e.g., OD growth), transient handling, or rolling resistance, a knowledge of the viscoelastic and hysteretic properties of the cord-rubber composites is required.

If the cords remain relatively stiff and elastic, then the creep, relaxation, and energy loss which occur in a cord-rubber composite are similar to that exhibited by the rubber itself. The energy loss, or hysteresis can be visualized by considering a typical stress-strain response as shown in figure 5.1. As the stress is cycled between the limits indicated by points A and B there is a corresponding change in strain, but on the unloading side of the curve the stress-strain relationship is not the same as on the loading side. The shaded area between the loading and unloading curves represents the energy lost (per unit

volume) as the specimen is cycled from point A to point B and returned. This means that when a cord-rubber composite material is cyclically stressed, a net energy loss occurs in the form of heat, which either raises the temperature of the composite or dissipates to the surroundings.

Figure 5.1 -- Typical stress-strain hysteresis loop

The consideration of viscoelasticity for the composite is important for accurate   stress-strain analysis of the tire structure, as well as the computation of energy loss for tire rolling resistance, and the corresponding heat production which affects the tire temperature.

Hysteresis of cord-rubber composites is typically characterized by either sinusoidal oscillatory testing, or by step-strain tests giving rise to quantities such as

$$E_1^*, E_2', E_2'', E_2(t), G_{12}(t)$$

which are the complex modulus in the 1 direction, the storage modulus in the 2 direction, the loss modulus in the 2 direction, the relaxation modulus in the 2 direction, and the shear relaxation modulus, respectively. As for the elastic properties, the 1-direction response is typically dominated by the cords, and the 2-direction response is typically dominated by the rubber.

The treatment of hysteresis in this chapter is limited to linear viscoelasticity and orthotropic response. Often the moduli of cord-rubber composites turn out to be functions of strain, or strain amplitude as well as time, temperature and frequency. The strain dependence is beyond linear theory and not discussed here.

Stress-strain relationships
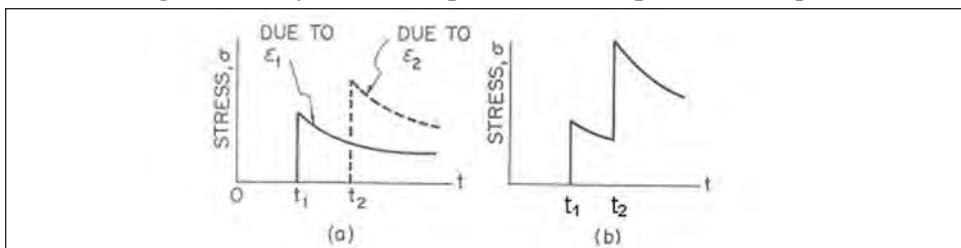
The mathematical basis for viscoelastic, or "lossy" behavior is due to Boltzmann [27] who postulated that for all real solids the stress-strain relations were functions not only of instantaneous values but also of the complete stress and deformation history of the material. For linear viscoelasticity, one may use the principle of superposition; namely, the stress at any time resulting from a sequence of separate strain histories applied at earlier

times is a sum of the stresses that would have been produced had the separate strain applications occurred individually.

This may be illustrated by assuming that uniaxial strain ε_1 was applied at the time t_1 and then held constant, i.e., a step-strain history. At some later time t this strain has caused a stress $\sigma_1 (t - t_1)$. Similarly a second step strain ε_2 beginning at time t_2 and held constant, will produce a stress $\sigma_2(t - t_2)$ at time t. This is illustrated in figure 5.2. Superposition postulates that if the strain history consisted of these two step-strains acting together, then the total stress induced in the specimen at time t would be

$$\sigma(t) = \sigma_1(t - t_1) + \sigma_2(t - t_2), \quad for\ times \quad t > t_2 \tag{5.1}$$

Figure 5.2. Principle of superposition for stress relaxation. (a) step-strains acting individually, (b) total response for two step-strains in sequence

The time dependent relationship between stress and step strain history is called the stress relaxation function and is often denoted by the symbol $E(t)$ for extension (and compression), or by $G(t)$ for shear. For example, if a step strain ε_o is applied at the time $t = 0$, then stress at any time t is given by $\varepsilon_o E(t)$. The stress relaxation function has the general time decaying form shown in figure 5.2a. For a solid material, it decays to some non-zero value. The stress relaxation function is a material property for viscoelastic materials just as Young's modulus is for elastic materials.

When the strain history consists of a series of N step-strain increments ε_n, individually applied at times $t = t_n$ the stress $\sigma(t)$ observed at a time $t > t_n$ is given by

$$\sigma(t) = \sum_{n=1}^{n=N} \varepsilon_n E(t - t_n) \tag{5.2}$$

An arbitrary strain history can be regarded as the superposition of infinitely many step strain history increments. In this case equation 5.2 extends to equation 5.3

$$\sigma(t) = \int_{s=-\infty}^{t} E(t - s)d\varepsilon(s) \tag{5.3}$$

or,

$$\sigma(t) = \int_{s=-\infty}^{t} E(t - s)\frac{\partial \varepsilon(s)}{\partial s}ds \tag{5.4}$$

This is known as Boltzmann's superposition principle. For small strain analysis of cord rubber composites, these equations can simply be used to compute the uniaxial extensional response in, say, the 1-direction by using $E(t) = E_1(t)$, or similarly for $E_2(t)$ in the direction

transverse to the cords.

If no strain history exists before time $t = 0$, the lower limit of the integral can be set to zero. For a simple step-strain history with $\varepsilon(t) = \varepsilon_0$ at time $t = 0$, Eq. 5.4 gives for the 1-direction

$$\sigma_1(t) = E_1(t)\varepsilon_0 \qquad (5.5)$$

which is often used to obtain the relaxation functions from experiments.

The instantaneous "elastic" portion of the response is often separated from the time-dependent portion to obtain

$$\sigma(t) = E(0)\varepsilon(t) + \int_{s=0}^{t} E(t-s)\frac{\partial \varepsilon(s)}{\partial s}ds \qquad (5.6)$$

where here the function $E(t)$ is separated into the short time "elastic" $E(0)$ and the transient $E(t)$ portions.

The creep form of the uniaxial isotropic viscoelastic relation can be written as

$$\varepsilon(t) = S(0)\sigma(t) + \int_{s=0}^{t} S(t-s)\frac{\partial \sigma(s)}{\partial s}ds \qquad (5.7)$$

where $S(t)$ is the uniaxial creep compliance. The creep form is used when the stress history is known and the strain response is to be calculated, for example, during a step-stress, or creep test. This form is useful for calculations such as estimating the amount of tire growth due to, say, creep in a cap ply, where the creep compliance function for the composite in the 1- direction is $S_{11}(t)$. Equations 5.6 and 5.7 could also be written for simple shear deformation where the relaxation and creep functions are typically written as $G(t)$ and $J(t)$, respectively.

In a fashion similar to the elastic treatment for a plane orthotropic laminate given in section 2, and following the treatments given in [28-31] the orthotropic compliance functions are now functions of time

$$[S(t)] = \begin{bmatrix} S_{11}(t) & S_{12}(t) & 0 \\ S_{21}(t) & S_{22}(t) & 0 \\ 0 & 0 & S_{66}(t) \end{bmatrix} \qquad (5.8)$$

and the reduced relaxation or modulus functions are

$$[Q(t)] = \begin{bmatrix} Q_{11}(t) & Q_{12}(t) & 0 \\ Q_{12}(t) & Q_{22}(t) & 0 \\ 0 & 0 & Q_{66}(t) \end{bmatrix} \qquad (5.9)$$

So , the viscoelastic analysis of an orthotropic lamina or special laminate, there are four independent material functions analogous to the four independent constants for orthotropic elasticity. The strain and stress components in the principal material directions are given by

$$\varepsilon_i(t) = \sum_{j=1,2,6} \int_0^t S_{ij}(t-s)\frac{\partial \sigma_j(s)}{\partial s}\,ds \tag{5.10}$$

$$\sigma_i(t) = \sum_{j=1,2,6} \int_0^t Q_{ij}(t-s)\frac{\partial \varepsilon_j(s)}{\partial s}\,ds \tag{5.11}$$

where τ_{12}, γ_{12} are τ_6, ε_6 respectively, in the contracted notation. As for the elastic case, it is often easier to measure the compliances $S_{ij}(t)$ than the corresponding stiffnesses or moduli $Q_{ij}(t)$, since it is easier experimentally to apply a single component of stress.

For a cord-rubber composite where the cord direction is much stiffer, and the cord response can be considered elastic (e.g., for steel wires), then the following approximations are often made [33]

$$S_{11} = \frac{1}{E_{11}}, \quad S_{12} = -\frac{v_{12}}{E_{11}} \tag{5.12}$$

With the approximations in Eq 5.12, only S_{22} and S_{66} remain to be determined as a function of time. Applying uniaxial loading such as creep or constant stress rate in the 2-direction can be used with Eq 5.10 to define $S_{22}(t)$, and similarly in shear to define $S_{66}(t)$. For example,

$$S_{22}(t) = \frac{\varepsilon_2(t)}{\sigma_2^0} \tag{5.13}$$
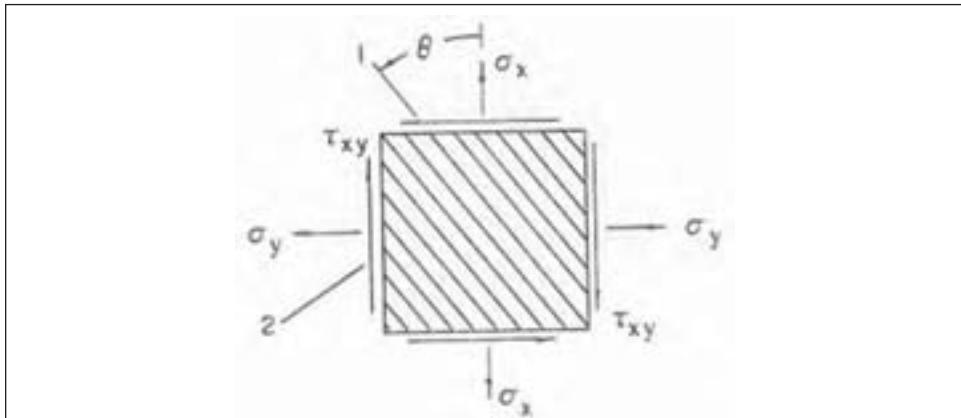
where σ_2^0 is the constant applied (creep) stress in the 2-direction.

If the stress is applied in a direction which is not coincident with the principal material directions, such as σ_x or σ_y in figure 5.3, then the same transformation equations (e.g., Eqs 2.21, 2.23) used for the elastic case are appropriate, namely

$$\overline{S}_{11}(t) = m^4 S_{11}(t) + 2m^2 n^2 S_{12}(t) + n^4 S_{22}(t) + m^2 n^2 S_{66}(t) \; etc. \tag{5.14}$$

where $m = \cos\theta$, and $n = \sin\theta$.

Figure 5.3: Stress components resolved along non-principal material axes x-y

The strain response to an applied stress state in non-principal material axes is

$$\varepsilon_x(t) = \int_0^t \overline{S}_{11}(t-s)\frac{\partial \sigma_x(s)}{\partial s}\,ds + \int_0^t \overline{S}_{12}(t-s)\frac{\partial \sigma_y(s)}{\partial s}\,ds + \int_0^t \overline{S}_{16}(t-s)\frac{\partial \sigma_{xy}(s)}{\partial s}\,ds \quad (5.15)$$

Tests in non-principal material directions are sometimes used to determine the shear compliance $S_{66}(t)$; for example, $S_{66}(t)$ appears in equation 5.14 for $\overline{S}_{11}(t)$. To obtain all four compliance functions, the following creep tests and analysis can be performed analogous to the elastic case[32]. First, a creep test in the direction of the cords gives

$$S_{11}(t) = \frac{\varepsilon_1(t)}{\sigma_1^0} \quad (5.16)$$

and measuring the transverse strain vs. time during the same test gives

$$S_{12}(t) = \frac{\varepsilon_2(t)}{\sigma_1^0} \quad (5.17)$$

Second, another creep test can be performed in the 2-direction, transverse to the cords to give

$$S_{22}(t) = \frac{\varepsilon_2(t)}{\sigma_2^0} \quad (5.18)$$

with a check on symmetry via

$$S_{21}(t) = \frac{\varepsilon_1(t)}{\sigma_2^0} \quad (5.19)$$

which should also equal $S_{12}(t)$.

Determining transverse strain $\varepsilon_1(t)$ with the creep stress applied in the 2-direction is often difficult for cord-rubber composites, and it may be very non-uniform.

Thirdly, an off-axis test is performed at some angle θ to the cord direction. Then

$$S_{66} = \frac{\varepsilon_6(t)}{\sigma_6} \quad (5.20)$$

where ε_6 (i.e., γ_{12}) and σ_6 (i.e., τ_{12}) are calculated from

$$\varepsilon_6(t) = -(\varepsilon_x - \varepsilon_y)\sin 2\theta + \gamma_{xy}\cos 2\theta \quad (5.21)$$

$$\sigma_6 = \frac{1}{2}\sigma_x \sin 2\theta \quad (5.22)$$

Alternatively, one could try to determine S_{66} directly from equation 5.14. Methods to determine the Q_{ij} from the S_{ij} are given in [28]. For example, the relation

$$\int^t S_{66}(t-s)Q_{66}(s)\,ds = t \quad (5.23)$$

is used with specific functional forms, such as Prony series for S_{66} and Q_{66}.

The most common representation of the orthotropic viscoelastic functions is with a Prony series, similar to the case for isotropic viscoelasticity. For the modulus functions

Q_{ij} this takes the form

$$[Q_{ij}(t)] = \begin{bmatrix} Q_{11}^0(t) & Q_{12}^0(t) & 0 \\ Q_{12}^0(t) & Q_{22}^0(t) & 0 \\ 0 & 0 & Q_{66}^0(t) \end{bmatrix} + \sum_{p=1}^{N} \begin{bmatrix} Q_{11}^p(t) & Q_{12}^p(t) & 0 \\ Q_{12}^p(t) & Q_{22}^p(t) & 0 \\ 0 & 0 & Q_{66}^p(t) \end{bmatrix} e^{-\frac{t}{\tau_p}} \tag{5.24}$$

and

$$[S_{ij}(t)] = \begin{bmatrix} S_{11}^0(t) & S_{12}^0(t) & 0 \\ S_{12}^0(t) & S_{22}^0(t) & 0 \\ 0 & 0 & S_{66}^0(t) \end{bmatrix} + \sum_{p=1}^{N} \begin{bmatrix} S_{11}^p(t) & S_{12}^p(t) & 0 \\ S_{12}^p(t) & S_{22}^p(t) & 0 \\ 0 & 0 & S_{66}^p(t) \end{bmatrix} (1 - e^{-\frac{t}{\lambda_p}}) \tag{5.25}$$

for the compliance functions. In equation 5.24, the τ_p are the relaxation times, and in 5.25 the λ_p are termed the retardation times.

In the simplest forms shown in equations 5.24, 5.25, the τ_p are the same for all the Q_{ij} and the λ_p are the same for all the S_{ij}. In general, this may not provide the best representation. For example if both the cords and the rubber are viscoelastic, then the cord dominated 1-direction and the rubber dominated 2-direction will likely need different relaxation/retardation times.

Finite element implementation

The prediction of response for a complex structure such as a tire is most readily accomplished by means of numerical methods such as finite element analysis (FEA). In this context, the orthotropic viscoelastic properties of the cord-rubber layers can be input directly, or the cord and rubber properties can be given separately and the effective composite properties are computed by the FEA code.

The same basic options for the FEA representation of elastic composite structures can be used with viscoelastic composites: 1) solid 3-D elements with orthotropic properties, 2) shell or membrane elements with orthotropic properties, 3) 1-D stiffness ("rebar") elements added to solid 3-D elements, 4) 1-D stiffness ("rebar") elements added to membrane or shell elements, and 5) use of an RVE (representative volume element) or unit cell to compute the effective properties. In the latter case, the procedure follows that for the General Method of Cells (GMC) discussed previously for orthotropic elasticity, except that for viscoelasticity, the properties of the cord and rubber can be time dependent.

In cases 1 and 2, the orthotropic properties of the cord-rubber layer as specified in 5.24 or 5.25 are input directly. For the solid representation, 3-D properties are required; the 3-direction properties, normal to the plane of the belt or ply, are often assumed to be the same as the 2-direction properties, transverse to the cords.

For cases 3, 4 and 5, some interesting possibilities arise. Essentially, the cord and rubber properties can be specified separately as in a micro-mechanics approach, with the limitation that the "rebar" type elements, in cases 3 and 4, only contribute stiffness in the cord direction – i.e., no transverse cord stiffness. However, this might be overcome by using two layers of re-bars—one to represent the axial stiffness, and another at 90° to the first to represent the transverse stiffness—or by increasing the (isotropic) rubber stiffness in the host element. The versatility is in the capability to specify separate viscoelastic properties, and in some cases nonlinear viscoelastic properties for the cord and for the rub-

ber. In this manner, the measured results can be fit more precisely.

One relatively simple combination of rebar elements for cords and solid or membrane elements for rubber would be the following: linear viscoelastic properties for the cord—e.g., Prony series with initial and long-time modulus, and visco-hyperelastic properties for the rubber. The visco-hyperelastic option available in most major FEA codes provides for the use of a typical hyperelastic law coupled with a Prony series representation for viscoelastic portion of the response [2].

Another advantage for specifying the properties of cord and rubber separately is that the cords and rubber compounds can be tested separately and combined in the FEA code. In this case, the numerous possible combinations of different cords and rubber compounds do not need to be tested as composites. One disadvantage is that the potentially nonlinear stiffness due to the elevated strain experienced in the rivet, or rubber between the cords, will not be represented by the rebar, or any other "smeared" approach.

Dynamic oscillatory response
When optimizing composite properties of belts and plies for tire performances such as rolling resistance, noise, vibration and harshness (NVH), oscillatory, or "dynamic" properties are useful since the cyclic sinusoidal loading is similar to the cycles seen in service. The composite stiffnesses and energy loss characteristics are especially important. For example, for rolling resistance, a low energy loss is desired at lower frequencies (e.g., that corresponding to 1/revolution), while for NVH, a high energy loss in certain frequency ranges is desired.

Oscillatory response is manifest by a sinusoidal input of either strain or stress resulting in a steady-state response of the structure. The oscillatory response of cord-rubber composites is treated in a manner similar to the oscillatory analysis of rubber compounds where quantities such as the storage, loss, and complex moduli in shear, G', G'', and G^*, respectively, are defined. However, due to the orthotropic response of cord-rubber composites, additional moduli are needed to characterize the response of the composite. Equations such as Halpin-Tsai have also been used to estimate the composite complex properties from the constituent properties [72].

Energy loss
Consider the calculation of energy loss where the strain cycles are known from a FEA calculation. For this discussion, 3-D solid elements are used for the belts and plies and the energy loss is to be calculated. In general, the energy loss density is given by

$$W'' = \oint \sigma_{ij} d\varepsilon_{ij} \tag{5.26}$$

where W'' is the energy loss per unit volume. With the strain cycles for one revolution for a given element assumed known from the FEA solution, the stresses can be calculated from Eq 5.11 and used with Eq 5.26 and then multiplied by the appropriate volume to calculate the energy loss. As cords or wires do not dissipate much energy, the loss from the cords is often neglected in comparison with the loss from the rubber [e.g., 34].

6. Durability of cord-rubber composites
In the first five sections of this chapter, theories to predict composite stress-strain

response, stiffness, and thermal properties have been covered. These composite properties together with similar properties for the rubber compounds can be used as input to a tire analysis to predict performance such as rolling resistance, or handling. Tire durability analysis requires additional properties to describe the fatigue behavior of the materials and/or components.

Fatigue and fracture of cord-rubber composites can provide information for tire durability assessment in different ways. With some limitations due to the complexity and multiple factors involved with tire durability performance, the following investigations can often provide some insight: 1) fatigue properties of tire composites combined with tire finite element analysis for a tire life estimation, 2) fatigue of belt and ply composites to assess their relative performance, 3) failure mechanisms of laboratory composites to provide understanding of failure mechanisms in tires, and 4) crack growth properties of rubber compounds combined with detailed fracture mechanics analysis of the cord-rubber layers in tires. Some of the factors involved are: aging, temperature, deformation modes, minimum stress or strain, strain rates, etc.

The scope of this section is limited to the fatigue and failure mechanics of cord-rubber composite specimens produced in the laboratory. The range of stress, strain and temperature, and the degree of cure and aging of the laboratory composites should mimic the actual conditions in the tire of interest for meaningful results.
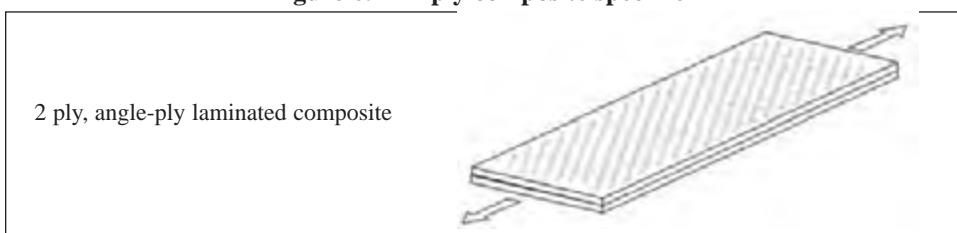
Composite fatigue testing
A typical geometry for a $[+\theta/-\theta]$ two ply composite specimen is shown in figure 6.1. The cord or wire, the rubber compound(s), the specimen thickness, and the cord angle are chosen to simulate those found in the tire. The loading direction of the composite is the circumferential direction in the tire. When a tensile load is applied and released, a hysteresis loop is formed as shown in figure 5.1. The area inside the loop plotted as load vs. displacement is the energy dissipated by the composite. As repeated cycles are applied, the specimen temperature will rise, similar to the temperature rise in an operating tire.

The strain distribution in a specimen like the one in figure 6.1 is important to understand in order to relate strains to observed failure mechanisms. A brief description was provided in section 4. There are two major components of strain in this specimen, one is the axial strain associated with the axial load, the other is the interlaminar shear caused by the tendency for each ply to shear in an opposite direction, as shown in figure 4.8. The distribution of this strain was described in section 4.
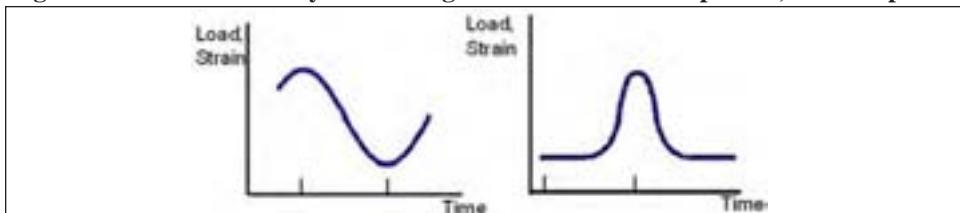
To simulate the deformation cycles in a tire, the minimum load or strain in the cycle could represent the deformations due to inflation and the maximum load or strain could represent the deformations due to the footprint load. Figure 6.2 shows example fatigue cycles; the pulsed cycle may be more representative of an actual cycle experienced in a tire.

Figure 6.1 - 2-ply composite specimen

2 ply, angle-ply laminated composite

The choice of load or strain control depends on the nature of the deformation cycles in the tire component of interest. Deformation Index analysis [46,65] can be used to ascertain stress control, strain control, or energy control cycles. A typical radial tire might have strain controlled (bending) cycles in the sidewall, and "energy" controlled cycles in the belts [e.g., 46, 60]. Energy control is difficult to achieve in the laboratory, so load control is often used.

Figure 6.2: Load or strain cycles for fatigue of cord-rubber composities, sine and pulsed

Many investigators have studied the fatigue response of cord-rubber composite speci-mens. The results and interpretations given here follow the work of Lee and co-workers [47-49,74], Causa and co-workers [50-51], Kawamoto and Mandell [52], and Huang and Yeoh [53]. Figure 6.3 shows specimen axial strain vs. time for a fatigue test under load control. Note the curve looks much like a typical static creep curve, except here the phenomenon is cyclic creep. After the initial or elastic deformation at time $t = 0$, the maximum (and also the minimum) strain in the cycle continually increases until failure. For discussion purposes, the curve is often divided into three regions: primary, secondary, and tertiary. Although the exact mechanisms of damage may differ slightly depending on the type of cords (e.g., nylon vs. steel wire) and rubber, some general observations can be cited. During the primary stage, vis-coelastic response and softening due to temperature rise and Mullins effect in the high strain regions account for most of the increased strain. Very small cracks near the cord-rubber inter-face are also possible in this stage. A significant portion of these strains are recoverable over time, upon release of the load. A typical recovery period might be on the order of hours, or days to recover 99% of the creep strain.

In the secondary stage, further viscoelastic creep, cracking around the cords, cord-rubber debonding, and small matrix cracks form to further soften the overall structure.

In the tertiary stage, crack coalescence and progressive delamination leads to specimen failure. Figure 6.4 shows a schematic of this process with the socketing and delamination cracks depicted.

Figure 6.3 - Maximum strain vs. time or cycles for load controlled composite fatigue test.
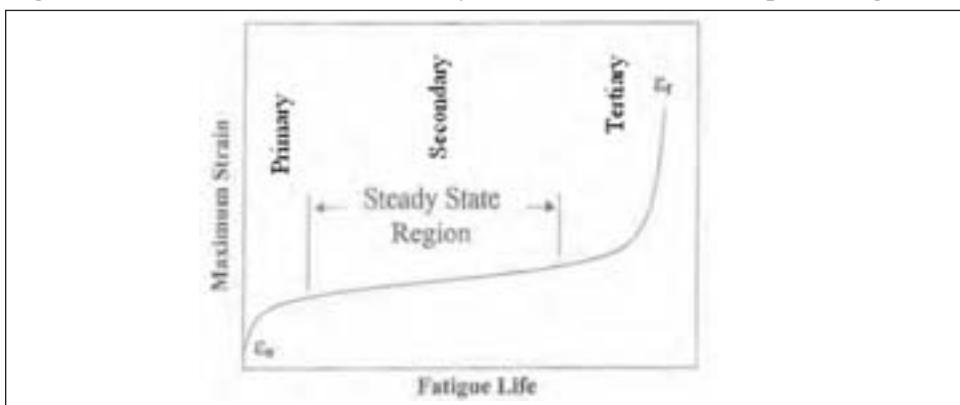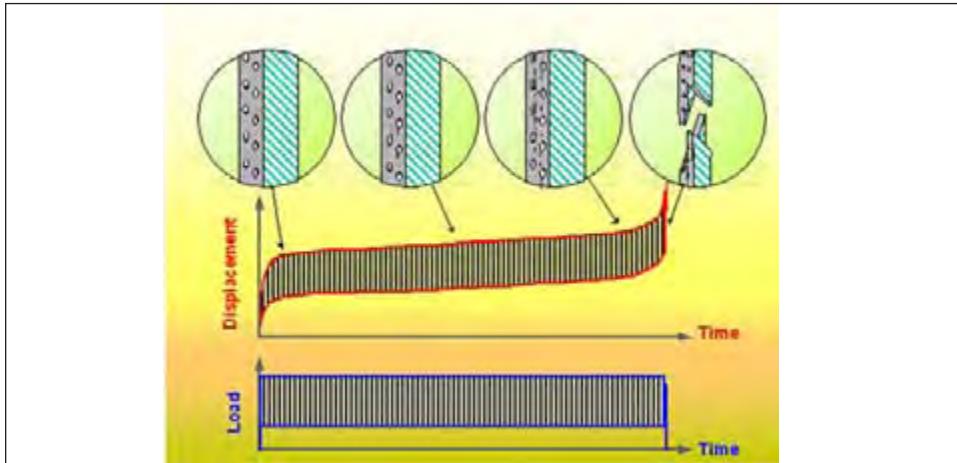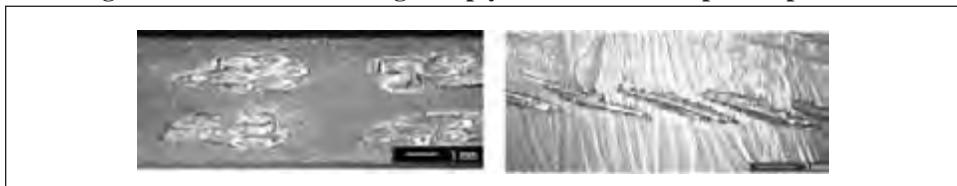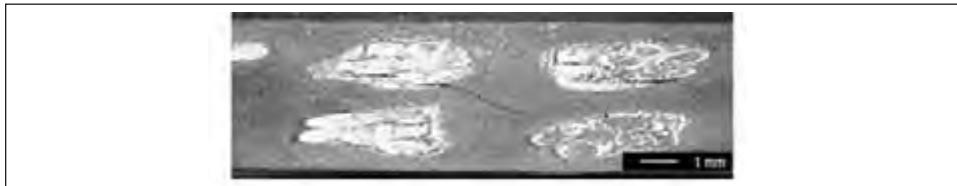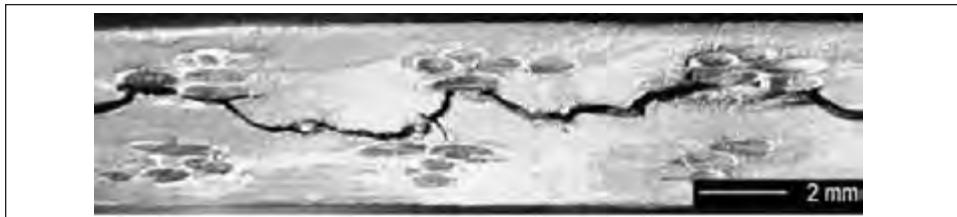
Figure 6.4 - Cord-rubber creep and crack growth under load control
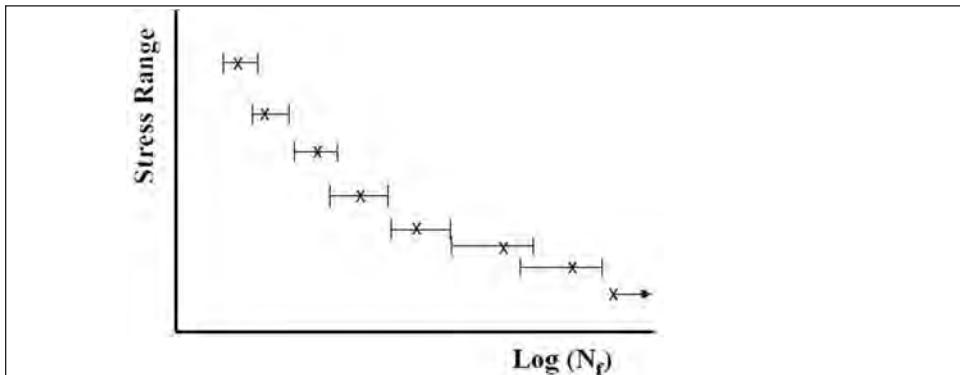
Some examples of cracking mechanisms are shown in figures 6.5 –6.7.

Figure 6.5 - Socket cracking in 2-ply wire-rubber composite specimens

Figure 6.6 - Cracks connecting between plies

Figure 6.7 - Delamination cracking towards the end of the specimen's life.

One common method of comparing fatigue data from different composite specimens is by plotting the applied stress range (load range divided by the original cross sectional area) vs. the number of cycles to failure (N_f). An example is given as the schematic plot in figure 6.8. This plot is called an S-N diagram, fatigue-life curve, or Woehler diagram.

Multiple specimens are typically run at each stress range, since data are often scattered. Plotting either: 1) all the data, 2) data ranges (as in figure 6.8) and/or 3) confidence intervals, aids in interpreting the statistical nature of the results. Tests with no overall failure, or "run-outs" are also possible at lower load ranges as indicated by the arrow in the figure. Different cord angles, cord spacings, rubber compounds and other design features can be investigated by comparing their composite fatigue results. An actual plot of an S-N diagram for a cord-rubber composite is shown in figure 6.9. This plot shows the effect of minimum stress on fatigue life.
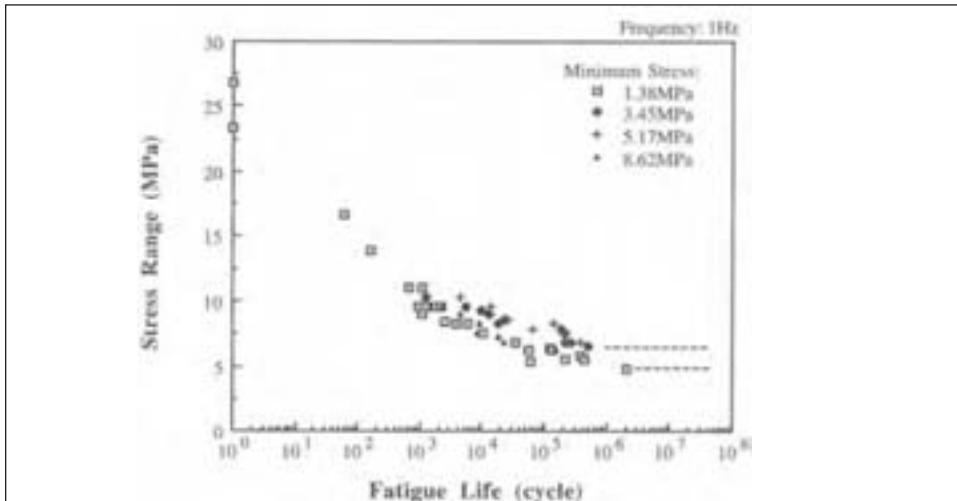
Figure 6.8 - Typical stress-life fatigue plot

When the minimum stress in a fatigue test of a rubber compound is greater than zero, the fatigue life is generally greater than the same test run with the same stress cycle and zero minimum stress – as long as the maximum stress is well below the upper strength limit. This effect is the opposite of that typically exhibited in fatigue of other materials. This is sometimes termed the R-ratio effect, since *R* is defined as

$$R = \frac{\sigma_{min}}{\sigma_{max}} \tag{6.1}$$

The stress in equation 6.1 can be replaced with other loading parameters, and for rubber it is usually the energy release rate *G* (see equation 6.2). A discussion of this effect can be found in Mars and Fatemi [61]. The mechanism of increased fatigue life for *R*>0 in rubber articles is often reported to be linked to strain-induced crystallization. A more general picture is to envision molecular orientation near a crack tip in the direction of maximum principal strain. This orientation can act to inhibit "self-similar" crack growth and can cause crack branching along weaker directions. A branched crack will propagate more slowly than a single sharp crack. These combined effects contribute to the R-ratio effect in many rubber compounds. Since cord-rubber composites generally fail due to cracking in the rubber matrix, the same phenomenon can be observed in composite fatigue tests. The R-ratio effect for cord-rubber composites was examined by Ku et al [49].

**Figure 6.9 - Stress-life fatigue plot with dependence on minimum stress [49].**

**Figure 6.10 - Specimen geometries for evaluating crack growth in the rubber
between cords (rivet). After Kawamoto [52].**
Left: tensile strip, right: constrained tension (or "pure shear").
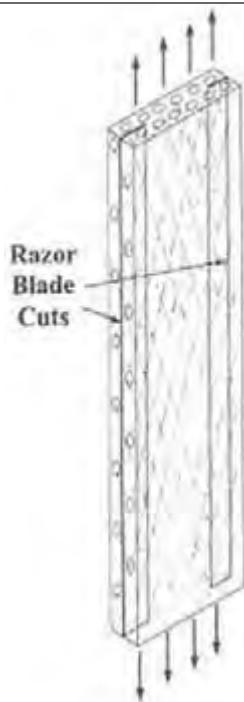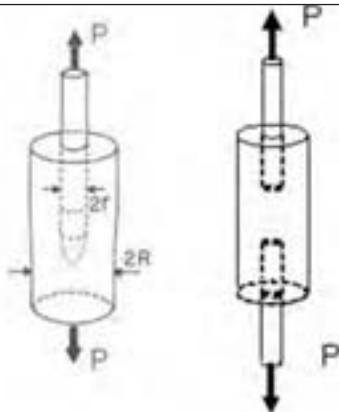

Other specimen configurations are also possible to investigate fatigue in cord-rubber composites. For cracking between cords, the specimen geometries in figure 6.10 have been utilized [52]. If the cords are stiff in bending, the crack growth behavior of these two geometries should be similar, since each approximates a small, constrained tension (i.e., pure shear) specimen with the height equal to the rivet between cords. If the cords are compliant in bending, then the overall specimen behavior will act more like their cordless counterparts, however, the crack path is still confined to a narrow strip of rubber between the cords. A confined crack path may suppress the 'knotty tearing" type of crack growth associated with tough rubber compounds. Other geometries and x-ray micrographs of crack propagation in cord-rubber composites were utilized in [53].

Another specimen geometry that has been investigated [52, 36] is a pre-cracked two ply composite with initial cracks at the edges and between the ply layers as shown in figure 6.11.

The mechanism of failure for the edge delamination specimens was reported to be simply a continuation of the delamination from the initial cracks.

Figure 6.11 - Edge delaminated cord-rubber specimen with initial cracks [52].

Cord pull-out testing
Two cord-rubber composite geometries used to investigate cord pull-out behavior are shown in figure 6.12 [54,76,77]. This test is most often used to judge adhesion of the

**Figure 6.12 - Cord pull-out specimen**

rubber compound to the cord. Figure 6.13 shows some examples of pull-out surfaces from an aramid-rubber test, and figure 6.14 shows the same for a steel wire-rubber test. Good wire or cord adhesion is obtained if all the failure occurs in the rubber, thus indicating that the cord-rubber interface is stronger than the rubber itself. In figure 6.13, the outline of

the cord and filament surfaces is clearly visible indicating that the failure is at least close to the interface. Close inspection revealed some fracture in the cord dip and also some in the dip-fiber interface. In figure 6.14, there is no indication of the wire geometry and all the failure is in the rubber compound indicating good adhesion.

Figure 6.13 - Aramid cord-rubber surface from pull-out test, 20x and 50x. Some failure occurs in cord dip and cord-dip interface [55].

Figure 6.14 Steel cord-rubber surface from pull-out test. All failure is in the rubber adjacent to the wire [55]

Analysis of fracture in cord-rubber composites

Tearing energy, or energy release rate, is the commonly used mechanical driving force that characterizes crack growth in many rubber compounds. Since fatigue failure of cord-rubber composites often occurs due to crack growth in the rubber, expressions for the energy release rate for typical rubber cracking modes are useful to describe durability and failure in the composite. A discussion of energy release rate is given in chapter 2. As a summary, if the work done by the applied loads is negligible during crack growth, then the energy release rate for an elastic system is given by [45,54,56]

$$G = -\frac{\partial U}{\partial A} \tag{6.2}$$

where U is the strain energy in the structure and A is the increase in crack area. Griffith's criterion states that a crack will grow when G in Eq 6.2 reaches a critical value, G_c.

Consider the cord pull out geometry in figure 6.12 under "fixed grip" conditions. For an increase in the cylindrical crack around the cord of Δc, Griffith's criterion gives [76]

$$\Delta U = 2\pi r \Delta c G_c \tag{6.3}$$

where G_c is the critical energy release rate (also called tear energy or fracture energy) related to the cracking mechanism—e.g., cracking in the rubber adjacent to the cord or cracking in the cord-rubber interface. The change in strain energy in the structure is denoted by ΔU. The change in strain energy is deduced by considering the change in volume for a portion of the rubber cylinder, away from the cord, that has a homogeneous uniaxial strain field. The volume of this region increases by $A\Delta_c = \pi r^2 \Delta c$. Also, the strain energy density in the homogenous region is given by

$$W = \frac{1}{2}\sigma\varepsilon = \frac{1 P^2}{2A^2 E} \tag{6.4}$$

Thus, the load at crack growth initiation is

$$P = \left[4\pi^2 R^2 r E G_c \right]^{1/2} \tag{6.5}$$

Simple energy release rate approximations can also be derived for two mechanisms of cracking in the 2-ply composite specimen. The following discussion follows Breidenbach and Lake [36,37] and Huang and Yeoh [53]. Consider first the case for delamination starting from the edges of the specimen as illustrated in figure 6.11.

   In a manner similar to the energy release rate analysis for the pure shear geometry [56], consider the change in strain energy in the structure as the edge cracks grow by a small amount Δc. The plies in the cracked region are assumed to have negligible strain energy compared to the central region. The volume of material that has significant strain energy is reduced by an amount: (length)(thickness)(Δc). If there is a region of homogeneous strain energy density W_h (e.g., the central region of the specimen away from the cracks) that is also reduced by this volume, then the energy released as the crack grows by an amount Δc is

$$\Delta G = W_h t \, \Delta c \tag{6.6}$$

where the thickness t represents the rubber gage between the cord layers. This is the same expression used for the pure shear geometry. Given the distribution of interlaminar shear strain in figure 4.14 for a typical cord-rubber specimen, it may be difficult to define the quantity W_h, but nonetheless, Eq 6.6 can be useful in an approximate sense.

   If the mechanism of cracking is socketing, as in figure 6.15, rather than delamination, then the strain energy analysis remains the same, but the calculation of new crack area changes to

$$\Delta A = \pi D e \Delta c \tag{6.7}$$

where D is the diameter of the cords and e is the number of cords per unit length. Then,
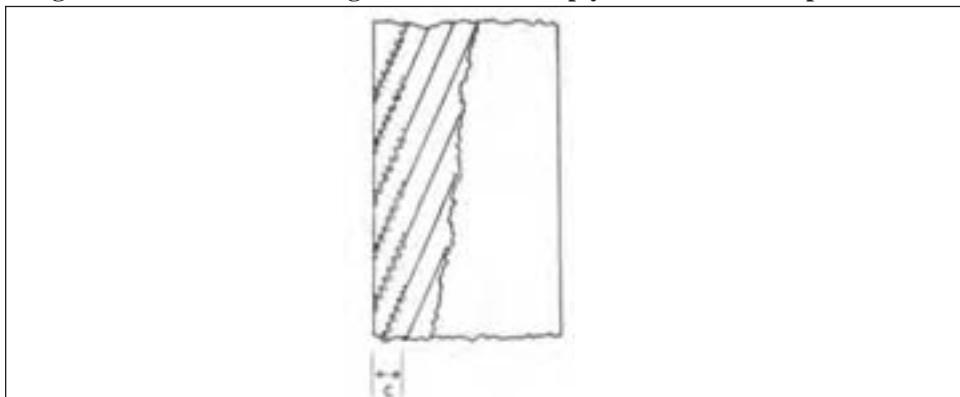
$$G = \frac{W_h t}{\pi e D} \tag{6.8}$$

Note the similarity to the pull out problem considered above.

In order to judge whether socket cracking or delamination will occur, the material crack resistance for the socket cracking mechanism needs to be known. Socket cracking can occur in the cord-rubber interphase, interface or in the rubber compound surrounding the cords. If the cord-rubber adhesion is sufficient, then cracking is often in the rubber layer surrounding the cords, and the same rubber crack growth properties are used for socketing as well as for delamination.

Once the energy release rate is known in the cord-rubber structure, an attempt to predict the crack growth rate in the structure can be made by combining the structural analysis with the characterization of crack growth rate vs. energy release rate for the rubber. This is a simple approach, but it may give good indications in many cases. An example application is given in [35]. Complicating factors such as multi-mode deformations, environmental conditions, and aging may require a more detailed analysis.

Figure 6.15. Socket cracking schematic in two-ply cord-rubber composites [37].

Finite element analysis (FEA) can provide more accurate estimates for energy release rate than the simple closed form solutions given above. Many studies with finite element analysis have been performed for cord-rubber composites, some by Pidaparti and co-workers [17,38-41]. With FEA, a more representative material model and the actual geometry of the structure and the observed crack(s) can be included. However, for cracks such as those in figures 6.6 and 6.7, the actual geometry may be difficult to represent, and even if the actual crack was represented, the analysis might provide only a specific result that is not useful in general. Thus, finite element analysis of the more general situations, such as those treated above, may be the best approach. Examples of analysis of cord-rubber composite fatigue with fracture mechanics methodology is provided in the references [53, 60].

Continuum damage analysis
The preceding section presented some ways to analyze crack growth in cord-rubber structures, which, in general require one to know something about the mechanism of cracking causing failure in the structure. Continuum damage mechanics (CDM) provides another alternative to assess progressive damage in a structure. With the advent of computational mechanics and FEA, CDM becomes a powerful tool to predict durability

in many complex structures without *a priori* knowledge of how the structure will fail.

In general, fatigue damage is the progressive loss of mechanical integrity of the material and/or structure. It is often a complex phenomenon that can be driven by many factors. In the critical regions of highly localized stress, strain, and/or temperature, failure could be caused by any one, or a combination of these quantities. In addition, other non-critical damage mechanisms such as local loss of cord-rubber adhesion or chemical degradation due to reversion or oxidation could become the primary cause of failure, or they could accentuate the state of damage. Some typical damage in the form of cracking mechanisms were shown in Figures 6.5-6.7. Damage mechanisms due to micro-cracking and chemical aging are not as easily seen and must be evaluated through their effects on mechanical properties.

Damage often starts in the rubber compound at the micro level by developing microcracks or cavitations in the neighborhood of micro defects, or at the interface of inclusions such as reinforcing particles or long reinforcing cords. Other failure modes could also exist such as rupture of the reinforcements under extreme loading conditions, delamination by macrocracks between layers, or creep rupture under applied cyclic stress. The underlying physics of each one of these failure modes might differ in the initiation stage, but the subsequent damage could be similar in the accumulation stage. Therefore, different approaches are typically employed. For example, one such combination of approaches is to use CDM to predict initiation of a macro-crack, and to use crack growth analysis to predict propagation of the crack.

One simple expression of continuum damage is the Palmgren-Miner approach [42] which is based on the S-N diagram. The damage estimate is made from the following

$$d_i = \frac{n_i}{N_{fi}} \tag{6.9}$$
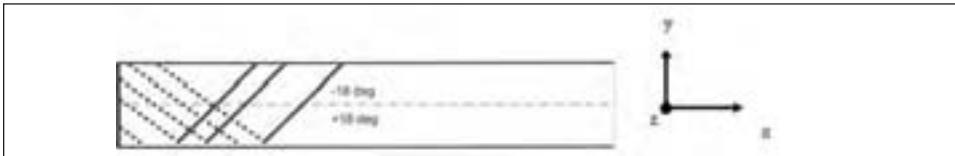
where the damage d_i associated with the ith set of cycles at a given load or stress is equal to the number of cycles n_i at the associated stress amplitude, divided by the number of cycles to failure at that stress amplitude, N_{fi}. Then failure is defined when

$$D = \sum_i \frac{n_i}{N_{fi}} = 1 \tag{6.10}$$

This is called a linear damage law since each cycle at a given amplitude contributes the same fraction to the damage. Equation 6.10 allows for no load sequence effects or dependence on the current state of damage. In actual cases, load sequence and aging effects probably exist [e.g., 62].

A more general approach parallels the CDM method advocated by Kachanov [43] and Rabotnov [44]. It is a phenomenological model which depends on laboratory testing to describe the evolution of the damage and contains a scalar damage parameter to describe the collective effect of material degradation, similar to d_i in equation 6.9.

The method will be illustrated for a 2-ply composite $[+\theta,-\theta]$ specimen under cyclic tensile loading as in figure 6.16. In equation 6.9, the damage is attributed to stress cycles, since the data is given by an S-N diagram.

Figure 6.16 - 2 ply [+18, -18] composite specimen

The following analysis is based on the premise that the cyclic interlaminar shear strain (γ_{zx} cyclic) is the primary cause of damage. The model constants are derived from fatigue data at room temperature, and the numerical simulation of the test was conducted using ABAQUS. The stress-life data from the S-N curve was transformed to interlaminar shear strain cycle vs. life data for use in this example.

The damage law is expressed in a rate form as

$$\dot{\omega} = \frac{C\gamma_a^{1-n}}{(1-\omega)^m} \qquad (6.11)$$

where $\dot{\omega}$ is the damage rate expressed in terms of the driving force, γ_a, and the current state of damage, ω. Material constants C, n, and m are to be determined from the Y_a vs. life information. Note that the rate in equation 6.11 can be expressed in terms of time or fatigue cycles with time = #cycles/frequency. Also note that with $m = 0$ in equation 6.11, the linear damage rule of Equation 6.10 is obtained.

Integrating Equation 6.11 using the conditions that $\omega=0$ at $t=0$, and $\omega=1$ at $t=t_f$, where t_f is the failure time yields:

$$t_f = \frac{\gamma^{-n}}{C(1+m)} \qquad (6.12)$$

The instantaneous damage state, , can be then derived to be:

$$\omega(t)=1-\left[1-\frac{t}{t_f}\right]^{\frac{1}{1+m}} \qquad (6.13)$$

The effect of the current state of damaged material can be incorporated into the constitutive law of the material using an expression such as
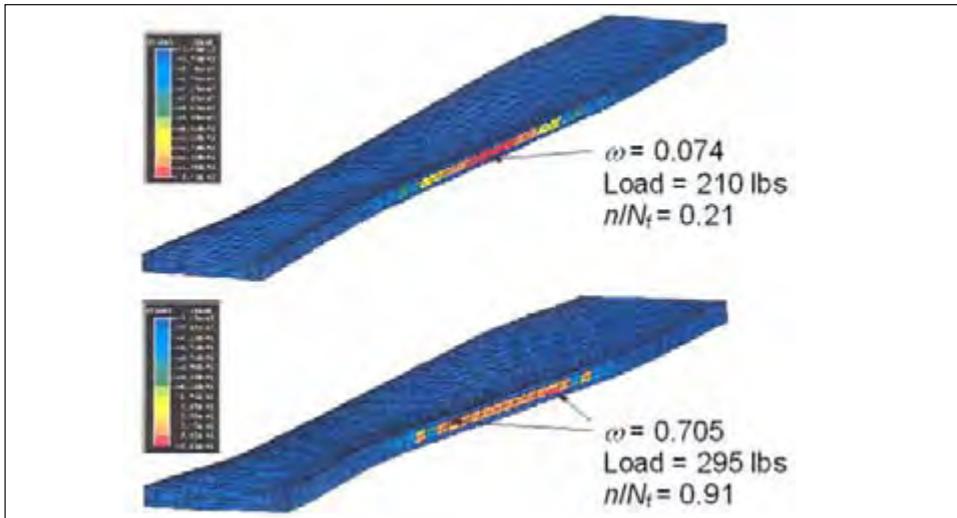
$$U = (1-\omega(t))U_0 \qquad (6.14)$$

where U_0 is the undamaged strain energy function. This creates a softening of the material as damage progresses.

The following is an example to demonstrate the potential utility of this technique to predict the number of cycles to failure of a 2 ply composite laminate. The increase of the damage parameter ω was monitored throughout the analysis, and failure is predicted when ω reaches one in one of the elements. Note that this is a simple definition of failure, and it is inherently mesh size dependent, but it is used here for simple illustration. Localized softening can actually drive the damage parameter towards one at a rate depending on the size of the mesh [e.g.,78].

Figure 6.17 shows the finite element model used for the calculations. Membrane elements with rebars were used to represent the cord-rubber layers. The location and the magnitude of the damage parameter at different loading conditions is indicated.

**Figure 6.17 - Evolution of the damage as predicted
by FE implementation of the CDM model**

Temperature prediction

Since viscoelastic and fatigue properties of cord-rubber composites depend on temperature, and elevated temperatures can accelerate aging processes, the distribution of temperature within a specimen or structure should be determined for a more accurate durability assessment. The temperature prediction is accomplished by a method similar to [34] where three modules: 1) an elastic structural solution, 2) a viscoelastic calculation of energy dissipation, and 3) a heat transfer model for temperature prediction, are linked together. The FE geometry shown in figure 6.17 is also used for this example. The Mooney-Rivlin law is used for the rubber elements with slight compressibility

$$W = C_{10}\left(I_1 - 3\right) + C_{01}\left(I_2 - 3\right) + \frac{\left(J^{el} - 1\right)^2}{D} \tag{6.14}$$

The nonlinear elastic behavior of the reinforcing cords is captured by using the Hypoelastic option in ABAQUS where the rate of change of stress is defined as a tangent modulus matrix multiplying the rate of change of the elastic strain:

$$d\sigma = D^{el}\,d\varepsilon \tag{6.15}$$

where $d\sigma$ is the rate of change of the Cauchy (true) stress $d\varepsilon$, is the rate of change of the elastic strain, and D^{el} is the tangent elasticity matrix with entries provided by giving the Young's modulus E, and Poisson's ratio ν of the cord as functions of the strain invariants. Rebar elements embedded in membrane elements are used to represent the cord-rubber layers.

To simulate the cyclic effect of the loading conditions, the sample was statically subjected to the maximum and minimum loads in the cycle. The cyclic load, coupled with

the hysteretic behavior of the rubber compound generates heat.

   Coupled or uncoupled heat transfer analysis can be performed with most commercial FEA codes. This example shows an uncoupled analysis conducted where the steady-state temperature field was calculated throughout the composite laminate based on the heat produced by hysteretic losses in the rubber. The analysis includes conduction and convection without any boundary radiation. Radiation effects can be included in an approximate sense by adjusting the convection coefficients. The same discretization developed for the structural analysis was used to conduct the heat transfer analysis with minor modifications. Shell elements with through-thickness integration have the capability to represent a temperature gradient through their thickness. Thus, additional constraints are needed to couple the thermal degrees of freedom between the shell elements and the neighboring continuum elements.

The volumetric heat flux is calculated from the following approximate relationship
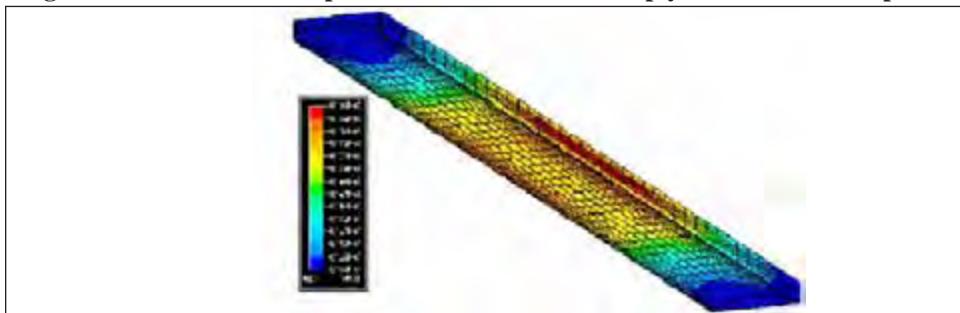
$$\Delta H = V \bullet f \bullet 2\pi \bullet \tan \delta \bullet \left(SED_{max} - SED_{min} \right) \tag{6.16}$$

where ΔH is the heat flux in (BTU/hr.in^3), V is the volume of the element, f is the frequency or the number of deformation cycles per second, and $\tan \delta$ is the loss tangent for the material.

   The effective orthotropic conduction in a membrane is calculated using the rule of mixtures with thermal conductivity of rubber k_r=0.014 (BTU/ hr.in.^{o}F), and k_c =2.016 (BTU/hr.in.^{o}F) for the cords. The heat transfer film coefficient used is relatively small because of the low speed of the test that causes a pseudo laminar flow around the sample. A value of h=0.055 (BTU/ hr.in^2.^{o}F) is used, which is slightly larger than free convection.

   By subjecting the structural model to a sinusoidal load range, a temperature distribution is developed throughout the sample. In this case, the concentration of the stresses and strains at the free edges creates a large strain energy density and consequently the volumetric heat flux at the same location. The temperature is also maximum near the free edges as shown in figure 6.18.
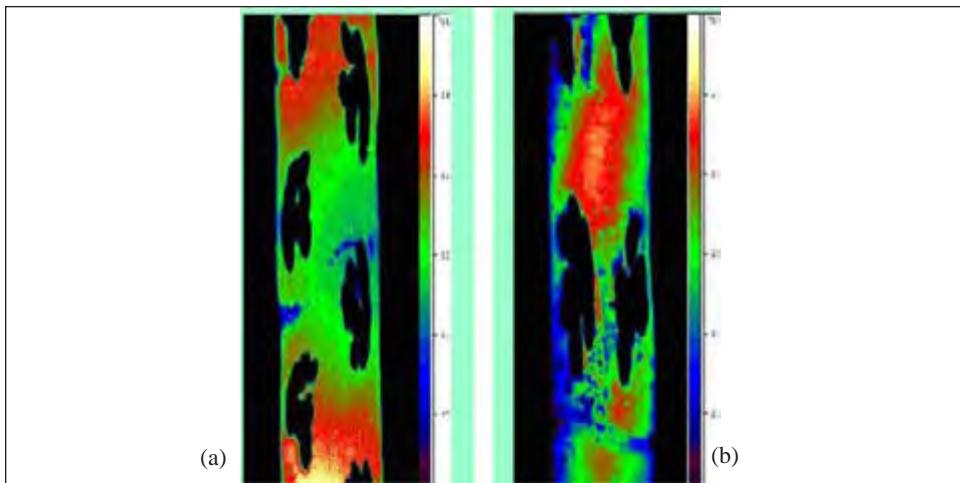
Figure 6.18: Predicted temperature distribution in a 2-ply cord-rubber composite

   Experimental infrared (IR) camera measurements of the 2-ply composite specimen are shown in figure 6.19, which depicts the temperature at the edge of the sample during the early stage of a fatigue test (a) and the latter stage of a fatigue test (b). The average measured temperature around a cord in the early stage of damage evolution where socketing is the predominant mode of failure is on the order of 64.5°C or 135.2°F. This temperature agrees well with the temperature calculated (129 - 130 °F) by the finite element analysis. In the later stage of the failure mode where delamination is more dominant,

the experimental data shows a shift in the location of the maximum temperature and a reduction of its magnitude (56.5°C or 122.4°F). The maximum temperature is lower on the surface, since socketing and delamination have caused the region of high stress/strain concentration to occur in the interior of the specimen, while the IR   camera is seeing the surface where the material has become largely unloaded.

Figure 6.19 - Thermal images (°C) of the edge of a 2-ply composite at an early stage of damage (a), and a later stage (b).

(a)   (b)

Acknowledgments

References

1. Frederick, D., and T.S. Chang, *Continuum Mechanics*, Allyn and Bacon, Boston, 1965.
2. ABAQUS User's Manual, Version 6.4, 2003.
3. Agarwal, B.D. and L. O. Broutman, *Analysis and Performance of Fiber Composites*, 2nd ed., John Wiley, 1990.
4. Patel, H.P., Turner, J.L., and J.D. Walter, "Radial Tire Cord-Rubber Composites". *Rubber Chemistry and Technology*, v. 49, pp. 1095-1110, 1976.
5. Tyson, J., Schmidt, T., and K. Galanulis, "Advanced Photogrammetry for Robust Deformation and Strain Measurement," Proc SEM Annual Meeting, Milwaukee, WI, 2002.
6. Ashton, J.E., Halpin, J.C., and P.M. Petit. "Primer on Composite Materials Analysis", *Technomic*, Stamford, CT, 1969.
7. Tangorra, G., "Simplified Calculations for Multi-Ply and Rubber Sheets as a Combination of Cord-Rubber Laminating", Proc. International Conference, 1969 (Moscow), Khimiya, Moscow, 1971.
8. Akasaka, T., and M. Hirano, "Approximate Elastic Constants of Fiber Reinforced Rubber Sheet and its Composite Laminate", Fukuyo Zairyo, *Composite Materials and Structures*, v. 1, p. 70, 1972.
9. Clark, S.K., "Theory of the Elastic Net Applied to Cord-Rubber Composites", *Rubber Chemistry and Technology*, v. 56, pp. 372-389, 1983.

10. Walter, J.D. and H.P. Patel, "Approximate Expressions for the Elastic Constants of Cord-Rubber Laminates", *Rubber Chemistry and Technology*, v. 52, pp. 710-724, 1979.

11. Higdon, A., Ohlsen, E.H., et al., *Mechanics of Materials*, John Wiley, 1976.

12. Szilard, R. *Theories and Applications of Plate Analysis: Classical Numerical and Engineering Methods,* John Wiley, 2004.

13. Jones, R.M., *Mechanics of Composite Materials 2nd Edition*, Taylor & Francis, 1999.

14. Walter, J.D., "Tire Mechanics", The University of Akron, Department of Special Programs and Department of Mechanical Engineering, 1977.

15. Gough, V.E., "Stiffness of Cord and Rubber Constructions", *Rubber Chemistry and Technology*, v. 41, pp. 988-1021, 1968.

16. Ford, J.L., Patel, H.P., and J.L. Turner, "Interlaminar Shear Effects in Cord-Rubber Composites", *Fiber Science and Technology*, v. 17, pp. 255-271, 1982.

17. Pidarparti, R.M.V. and V.P. Kakarla, "Three-dimensional Stress Analysis of Two-Ply Cord-Rubber Composite Laminates", in *Composite Structures,* v. 28, pp. 433-440, Elsevier, 1994.

18. Chen, B.H., "Material Characterization of Tire Cords and the Effects of Cord Thermal-Mechanical Properties on Tires", *Tire Science and Technology*, v. 32, pp. 2-22, 2004.

19. Puppo, A.H. and H.A. Evensen, "Interlaminar Shear in Laminated Composites Under Uniform Axial Extension", *Journal of Composite Materials* , v. 4, pp. 204-220, 1970.

20. Lou, A.Y.C., and J.D. Walter, "Interlaminar Shear Strain Measurement in Cord-Rubber Composites", *Rubber Chemistry and Technology*, v. 52, pp. 792-804, 1979.

21. Adiun, J.B., and F.L. Addessia, "A Cell Model for Homogenization of Fiber-Reinforced Composites: General Theory and Nonlinear Elasticity Effects", J. Composite Materials, v. 30, pp. 248-280, 1996.

22. Aboudi, J., "Micromechanical Analysis of Composites by the Method of Cells – Update", *Applied Mechanics Reviews*, v. 49, part 2, October, 1996.

23. Wilt, T.E., and S.M. Arnold, "Micromechanics Analysis Code (MAC)", User Guide Version 2.0, NASA Technical Memorandum 107290, 1996.

24. Arnold, S.M. , Bednarcyk, B.A., Wilt, T.E. and D. Towbridge, "Micromechanics Analysis Code with Generalized Method of Cells (MAC/GMC) User Guide: Version 3.0", NASA Technical Memorandum 209070, 1999.

25. Walter, J.D., "Cord Reinforced Rubber", in *Mechanics of Pneumatic Tires*, S.K. Clark, Ed., US DOT HS 805 952, NHTSA, 1981.

26. Ridha, R.A., "Analysis for Tire Mold Design", *Tire Science and Technology*, v. 2, pp. 195-210, 1974.

27. Boltzmann, L., *Prog Ann Phys Chem*, v. 7, p. 624, 1876.

28. Bradshaw, R.D., and L.C. Brinson, *Mechanics of Time Dependent Materials*, v. 1, pp. 85-108, 1997.

29. Bradshaw, R. D., and L. C. Brinson, *Comp Sci Tech*, v. 59, pp. 1411-1427, 1999.

30. Halpin, J.C., "Introduction to Viscoelasticity*",* in *Composite Materials Workshop*, Tsai, Halpin & Pagano, Ed., p 87, Technomic, Stamford CT, 1968.

31. Schapery, R. A., "Stress Analysis of Viscoelastic Composite Materials", in *Composite Materials Workshop*, Tsai, Halpin & Pagano, Ed., p. 153, Technomic, Stamford, CT, 1968.

32. Morris, D.H., Brinson, H.F., and Y.T. Yeow, *Polymer Composites*, v. 1, p. 32, 1980.

33. Tuttle, M.E., Pasricha, A., and A. F. Emery, *Journal of Composite Materials*, v. 29, p. 2025, 1995.

34. Ebbott, T. G., Hohman, R.L., Jeusette, J-P., and V. Kerchman*,* "Tire Temperature and Rolling Resistance Prediction with Finite Element Analysis", *Tire Science and Technology*, v. 27, pp. 2-21, 1999.

35. Ebbott, T.G., "An Application of Finite Element Based Fracture Mechanics Analysis to Cord-Rubber Structures", *Tire Science and Technology*, v. 24, pp. 220-235, 1996.

36. Breidenbach, R. F., and G. J. Lake, "Mechanics of Fracture in Two-Ply Laminates", *Rubber Chemistry and Technology*, v. 52, pp. 96-109, 1979.

37. Lake, G. J., "Aspects of Fatigue and Fracture of Rubber", in *Prog Rub Tech*, Applied Sciences, London, pp. 89-143, 1983.

38. Pidaparti, R.M.V. and V. Kakarla, *Polymers and Polymer Composites*, v. 6, pp. 439-445, 1998.

39. Pidaparti, R.M.V. and G. Pontula*, Theoretical and Applied Fracture Mechanics*, v. 22, pp. 1-8, 1995.

40. Pidaparti, R.M.V. and G. Pontula, *International Journal of Fracture*, v. 68, p. 315, 1995.

41. Pidaparti, R.M.V., Yang, T.Y., and W. Soedel, *Journal of Composite Materials*, v. 26, p. 152, 1992.

42. Miner, M.A., *Cumulative Damage in Fatigue,* Journal of Applied Mechanics, v. 67, pp. A159-A164, 1945.

43. Kachanov, L.M., *Introduction to Continuum Mechanics*. Martinus Nijhoff, Dordricht, 1986.

44. Rabotnov, Y.N., *Creep Problems in Structural Members*, North-Holland, Amsterdam, 1969.

45. Griffith, A.A., "The Phenomena of Rupture and Flow in Solids", *Phil Trans Royal Soc*, v. A221, pp. 163-198, 1921.

46. Futamura, S. and A.A. Goldstein, "A Simple Method of Handling Thermomechanical Coupling for Temperature Computation in a Rolling Tire", *Tire Science and Technology*, v. 32, pp. 56-68, 2004.

47. Lee, B.L., and D.S. Liu, *Journal of Composite Materials*, v. 28, p. 1261, 1994.

48. Liu, D.S., and B.L Lee, *ASTM STP 1292*, p 67, 1996.

49. Ku, B.H., Liu, D.S., and B.L. Lee, "Fatigue of Cord-Rubber Composites: III. Minimum Stress Effect," *Rubber Chemistry and Technology*, v. 71, pp. 889-905, 1998.

50. Causa, A.G., Borowczak, M., and Y-M Huang, *Prog Rubber & Plast Tech*, v. 15, 1999.

51. Causa, A.G., Borowczak, M., and Y-M. Huang, *Tire Technology International,* p. 52, 1994.

52. Kawamoto, J., *Fatigue of Rubber Composites*, PhD Thesis, MIT, Cambridge, MA, 1988.

53. Huang, H.S., and O.H. Yeoh, "Crack Initiation and Propagation in Model Cord-Rubber Composites", *Rubber Chemistry and Technology*, v. 62, pp. 709-731, 1989.

54. Gent, A.N., Ed., *Engineering with Rubber*, 2nd ed., Hanser, 2001.

55. Causa, A.G., and R.L. Keefe, "Failure of Rubber-Fiber Interfaces", in *Fractography of Rubbery Materials*, Bhowmick and De, Elsevier, Ed., 1991.

56. Rivlin, R.S., and A.G.Thomas, *J Polymer Sci*, v. 10, p. 291, 1953.

57. Trinko, M.J., "Ply and Rubber Stresses and Contact Forces for a Loaded Radial Tire*,"* *Tire Science and Technology*, v. 11, pp.20-37, 1983.

58. Faria, L.O., Bass, J.M., Oden, J.T., and E.B. Becker, "A Three Dimensional Rolling

Contact Model for a Reinforced Rubber Tire," *Tire Science and Technology*, v. 17, pp. 217-233, 1989.

59. Kulikov, G.M.,"Computational Models for Multilayered Composite Shells with Application to Tires," *Tire Science and Technology*, v. 24, pp. 11-38, 1996.

60 .Young, D.G., "Application of Fatigue Methods Based on Fracture Mechanics for Tire Compound Development" *Rubber Chemistry and Technology,* v. 63, pp. 567-581, 1990.

61. Mars, W.V., and A. Fatemi, *Rubber Chemistry and Technology,* v. 76, pp. 1241-1258, 2003.

62. Sun, C., Gent, A.N., and P. Marteny, *Tire Science and Technology*, v. 28, pp. 196-208, 2000.

63. Puppo, A.H., and H.A. Evenson, *J Composite Matls*, v. 4, pp. 204-220, 1970.

64. Christensen, R.M., *Mechanics of Composite Materials*, Chapter II, John Wiley, 1979.

65. Futamura, S., "Deformation Index – Concept for Hysteretic Energy Loss Process," *Rubber Chemistry and Technology*, v. 64, pp. 57-64, 1991.

66. Lemaitre, J., *A Course on Damage Mechanics*, Springer, Berlin, 2nd ed., 1996.

67. Turner, J.L., and J.L. Ford, "Interplay Behavior Exibited in Compliant Filamentary Composite Laminates," *Rubber Chemistry and Technology,* v. 55, 1982.

68. Clark, S.K., and R.N. Dodge, "Nonlinear Cord-Rubber Composites," *Tire Science and Technology*, v. 18, pp. 191-200, 1990.

69. Parhizgar, S., Weissman, E.M., and C.S. Chen, "Determination of Stiffness Properties of Single-Ply Cord Rubber Composites," *Tire Science and Technology*, v. 16, pp. 118-126, 1988.

70. Nielsen, L.E., and R.F. Landel, *Mechanical Properties of Polymers and Composites*, 2nd ed., Marcel Dekker, New York, 1994.

71. Padovan, J., "End Effects in Twisted Cord-Rubber Composites," *Tire Science and Technology*, v. 24, pp. 321-338, 1996.

72. Tabaddor, F., Clark, S.K., Dodge, R.N. and J. M. Perraut, "Viscoelastic Loss Characteristics of Cord-Rubber Composites," *Tire Science and Technology*, v. 14, pp. 75-101, 1986.

73. Parhizgar, S., "Determination of Stiffness Properties of Multi-Ply Cord Rubber Composites," *Tire Science and Technology*, v. 17, pp. 201-216, 1989.

74. Song, J.H., Costanzo, F., and B.L. Lee, "Fatigue of Cord-Rubber Composites: V. Cord Reinforcement Effect," *Rubber Chemistry and Technology*, v. 77, pp. 593-610, 2004.

75. DeEskinazi, J., and R. J., Cembrola, "A Parametric Study on Interlaminar Shear Strains in Cord-Rubber Composites*," Rubber Chemistry and Technology,* v. 57, pp. 168-183, 1984.

76. Gent, A.N., "Fracture Mechanics Applied to Elastomeric Composites," *Rubber Chemistry and Technology,* v. 56, pp. 1011-1018, 1983.

77. Gent, A.N., and S.Y. Kaang, "Pull-Out and Push-Out Tests for Rubber to Metal Adhesion," *Rubber Chemistry and Technology,* v. 62, pp. 757-766, 1989.

78. Lemaitre, J., and R. Desmorat, *Engineering Damage Mechanics*, Springer, 2005.

Chapter 5
Tire Load Capacity

by Stephen M. Padula

Chapter 5
Tire Load Capacity

by Stephen M. Padula

1. Introduction

A primary responsibility of The Tire and Rim Association, Inc. (TRA) for over 100 years has been the establishment of interchangeability standards for tires. This chapter presents the evolution of the TRA load formula for passenger car tires from the early years to its current application. The load formula is then compared to one based upon constant relative deflection. This alternative method provides a possible methodology for future research and review. Although the focus of this work is passenger tires, the same model and methodology can be used for other pneumatic tires including light truck tires.

TRA was founded in 1903 to establish and promulgate interchangeability standards for tires, rims, valves and allied parts. These standards include tire loads and dimensions, and rim contour and valve dimensions. The formulae used to calculate tire loads are empirically based, are derived from information and field experience from member companies, and are fundamentally similar in format for all types of tires, except aircraft. In the interest of brevity, only the formula for calculating passenger car tire loads will be analyzed. The load limits calculated and shown in the TRA publications are considered maximum for the pressure shown and, conversely, the pressures shown are considered minimum for the corresponding loads shown. Higher pressures for high speed and other special circumstances are often recommended by vehicle and/or tire manufacturers and are acceptable as long as they do not exceed the maximum pressure marked on the passenger car tire. TRA and other standardizing bodies provide guidelines for adjusting the tire load/pressure relationship as a function of speed.

The intent of the formula from a standards perspective is to:

a) Determine a load rating that allows a tire manufacturer to design and produce a tire that can perform satisfactorily to the tire manufacturer's individual design requirements and still be interchangeable with the same tire size produced by other manufacturers;

b) Provide rational increments of load carrying capacities over the range of tire sizes of a given type and series;

c) Take into account the requirements of the vehicle manufacturer and service conditions. A load capacity formula ideally should be:

a) Scientifically based and contain the physics that allow accurate predictions;

b) Calculated from obvious, easily measured tire characteristics.

2. History: TRA load formula

There is no detailed, documented explanation of the origins of the formulae but the following is based on related documents and working papers in the TRA files. Prior to 1928 TRA's maximum load ratings were established by agreements among member tire companies. Analysis of the load rating tables of that time reveals the following:

      a) Loads were not dependent on rim diameters;

b) Loads varied in relation to tire section width;
c) Loads varied in direct ratio to the air pressure.

For lesser loads the ratings were determined by taking a direct proportion of the maximum inflation pressure as illustrated by the formula below:

$$L=L_0 \ (P/P_0) \tag{1}$$

Where: L = load limit at pressure P
                L_0 = maximum load limit at P_0

In 1928 tire load ratings were adjusted to take into account the rim diameter, but this again was done by agreement and not by calculation.

   The first formula adopted by TRA was developed in the mid 1930's by C. G. Hoover, a mathematician who later served as the staff director of TRA. The formula was empirically derived, based on the effects of inflation pressure, tire section width (or section diameter as it was called for the early circular section tires) and rim diameter. It is thought that this formula was based on maintaining a uniform degree of deflection in the tires at their assigned loads and inflation pressures. The formula for what were called "Low Pressure" passenger car tires was:

$$L=6.65 \text{x} P^{0.585} \text{x} S^{1.702} \text{x} [(D_R+S)/(19+S)] \tag{2}$$

       where:

                L = tire load carrying capacity at pressure P
                P = tire inflation pressure
                S = tire section width (on rim width = 62.5% of tire section width [1]
                D_R = nominal rim diameter

The above formula was revised in 1936 to the following:

$$L=K \text{x} 0.425 \text{x} P^{0.585} \text{x} S^{1.39} \text{x} (D_R+S) \tag{3}$$

The structure of this formula, with input for tire dimensions in the form of section width S and rim diameter D_R, and inflation pressure P, has essentially not changed since its inception for most ground vehicle tires. However, it has been updated by adjustments to the coefficient K and the exponents for P and S to accommodate changing tire service requirements and tire sizing as well as a change from U.S. customary system of units to S.I. units.

3. Basic formula

As stated above, the origins of the load formula are not well documented. However, based on the available information, Hoover related the tire load carrying capacity to the tire volume in developing the formula. Assuming this to be the case, Schuring, in an unpublished paper written in 1985, provided the following plausible speculation of how and why the various terms were selected:

   a) The direct proportionality, $L = L_0 \ (P / P_0)$, was adjusted to $L = L_0 \ (P / P_0)_n$, with n = 0.585, since it was thought that the load-pressure relationship would not really be a linear one (more information on this change is given below under the explanation of the exponent).

b) The new relationship indicates that for each tire design, a constant value exists for the ratio $L / P^n = L_0 / P_0^n$.

c) The tire load carrying capacity was assumed to be directly proportional to the air volume V. Thus, L/P^n would depend linearly on air volume V:

$$L/P^n = \text{const.} \ V.$$

As the cross-section of a tire was approximately circular in the 1930's, the volume V was given by

$$V = \text{const.} \ S^2 \ (D_R + S),$$

where D_R is rim diameter, and S is section diameter. Combining the above two equations yields:

$$L = \text{const.} \ P^n S^2 \ (D_R + S).$$

However the volume of a circular annulus is not exactly proportional to S^2. Thus it must have soon become apparent that a load formula based on this approximation would produce overloads for larger tires. Hence, the exponent of 2 for S was reduced to 1.39 – probably based on field experience of tire performance at that time – so that the basic tire load formula became:

$$L = \text{const.} \ P^n S^{1.39} \ (D_R + S).$$

4. Constant

The "constant" is a very significant part of the load formula. It is referred to as the "K" or "service" factor. Different values are assigned for different types of tire (passenger car, truck and bus, agricultural, etc.) and for different service applications. The additional numerical factor of 0.425 in equation (3) was included simply to keep the value of "K" at approximately 1.00.

In the first application of the formula, K was made equal to 1.00 for truck and bus tires, and to 1.10 for passenger car tires. When P-Type (metric) tires were introduced in the mid 1970s, conversion factors to allow input of millimeters and kilopascals were included in the formula and the factor of 0.425 was incorporated into the new value of K.

5. Pressure exponent

The exponent of inflation pressure gives the tire load over the range of pressures standardized for a specific tire. The reason for selecting an exponent of 0.585 was that as the inflation pressure increases in a given tire size, the stress in the carcass and tread area will increase. Consequently introducing a positive exponent for P will tend to limit the deflection of the tire, and therefore the stress, as the inflation pressure increases. A value of 0.585 was adopted for passenger car tires in the 1950s and 1960s (alpha-numeric series) and a value of 0.50 was adopted for P-Type tires in the 1970s based on service considerations and tire performance.

When P-Type tires were developed, tires were selected for a vehicle based on two criteria [both given in a TRA guideline and as part of the National Highway Traffic Administration (NHTSA) regulations]. The "normal" operating vehicle load must be equal to or less than a Design Load, and the maximum vehicle load had to be equal to or less than a Tire Maximum Load. Passenger car tires existing at that time used the

alpha-numeric system for Standard Load (Load Range B) tires with a maximum inflation pressure of 32 psi and a Design Load based on a lower pressure of 26 psi. The TRA committee that developed the P-Type tires thought that higher inflation pressures should be required for Design Load applications as well as for maximum load conditions. The Design Load pressure for P-Type tires was therefore increased to 28 psi and the pressure associated with the maximum load was set at 35 psi. An exponent of 0.5 for pressure kept the Design Load at 28 psi for P-Type tires equal to that for alpha-numeric tires at 26 psi. Similarly, the maximum load for P Type tires was only slightly increased above that for alpha-numeric tires of the same dimensions, but at 35 psi instead of 32 psi. No differentiation was made between bias and radial tires other than in the tire designation: symbols D, B and R were introduced for diagonal (bias), belted bias, and radial tires, respectively.

6. Tire section width (section diameter)
Originally, tire sections had a circular shape, and the diameter D_s was identical to both the section width S and the section height H (that is the aspect ratio, H/S, was 1.00). In order to maintain a consistent tire shape for calculation purposes, the section width S used in the load formula is always adjusted to have a constant relationship to the rim width. Initially, S was calculated for a rim width equal to 62.5% of S (see Figures 5.1 and 5.2 of Appendix 1). Later, as section widths were widened and section heights reduced (making the section height smaller than the section width), and rim widths were increased, tire sections acquired an oval shape. Nevertheless, the concept of an equivalent circular section was retained in the formula by introducing an "adjusted" section diameter S_d. The adjustment was made by equating the perimeter of the low aspect ratio tire (which was assumed to be elliptical around the top half and circular around the bottom half of the tire section) to the perimeter of a corresponding theoretical tire with a circular cross-section. Figures 5.3 and 5.4 of Appendix 1 show the calculation for the theoretical section width S_d that is used in the load calculation formula.

7. Need for review
In the early years, the number of tire sizes was very limited in comparison with today's mix of sizes. Table 5.1 shows the range of sizes and the load ranges for B tires (alpha) and standard load tires as given in TRA yearbooks for 1950-51, 1975, and 2003. Note that during the mid 1970s there was a rapid transition from alpha-numeric to P-Metric sizing, and from bias to radial constructions.

As passenger tires evolved to increased widths and lower section heights, a substantial

Table 5.1: TRA passenger car tire size comparison - 1950 - 2003

TRA yearbook	1950-51[2]	1975[1]	2003[1]
Number of sizes	21	91	254
Nominal section width (mm)	105 →205	155 →295	145 →345
Aspect ratios	96→100	50, 60, 70, 78, 80	30,35,40,45,50,55,60,65,70,75,78,80
Rim codes	12,15 & 16	13 →15	12 →22
Nominal OD (mm)	545 →845	560 →765	540 →840
Max load:	430 →735	430 →1000	370 →1320
LR 'B'/SL (kg)			

[1]Load Range B and/or Standard Load Tires

[2] 4 & 6 Ply Rating Tires; OD & AR estimated

departure occurred from the "round" cross section (Aspect Ratio = 1) upon which the formula was originally based. Even larger rim widths and section widths are under consideration. A review of the load formula is therefore necessary, especially as new rules are introduced in connection with Tire Pressure Monitoring Systems (TPMS). Under the proposed TPMS rules, tires could be allowed to operate at reduced pressures (thus at increased deflection) for extended periods of time before a warning light would be activated.

For decades, the basis for the maximum load was to first consider the 'normal load' from the regulations and then select a pressure coefficient that had the effect of limiting the deflection at maximum load. It is believed the intent of the 'normal' load as defined by the federal regulations (FMVSS110) was to take into account how vehicles are 'normally' used in service, that is, at less than full occupancy and not fully loaded. Moreover, as defined by this same regulation, the normal and maximum load on the tire is based upon a passenger weight of 68kg (150 lbs.). In contrast, certain FAA regulations use 170 lbs. for occupant weight and one might argue that even this number is rather low. What basis should be used today for weight of occupants in vehicle load calculations?

8. A new approach
Over the decades, much work has been done in the tire industry and in the academic world to study the effect on tire performance of stresses, temperatures, load distribution and many other factors. Much of the fundamental work, that still applies, was described in the NHTSA-funded monograph, "Mechanics of Pneumatic Tires", edited by S. K. Clark and published in the early 1980s.   However, it is now an opportune time to explore changes that might be made to the tire load formula, for the following reasons:

Tire sizes continue to evolve towards larger rim diameters and wider section widths.

The historic differentiation between passenger cars and 'light truck' has changed with the wide usage of passenger car tires on SUVs. This fact has been recognized by NHTSA with the recent promulgation of FMVSS139 which essentially combines the regulations for these two types of tires for use on vehicles with gross vehicle weight ratings (GVWR) of 10,000 pounds or less.

There is a need for a formula that is more closely related to the physical characteristics of today's tires.

The following section develops a methodology and presents relevant data for this purpose. An equation is developed, based upon constant relative deflection, and compared to the current formula. Guidance is given as to further verification of the result, with suggestions for future work.

9. Tire load/deflection and stiffness
A great deal has been written concerning tire structure and the calculation of the tire's ability to carry load, notably the works of Gough[2] and Koutny.[3,4] Koutny used thermodynamic studies of tire stiffness. In his treatment of the ring model for a tire, he postulated that the air pressure in the tire is the primary component of elasticity. Other researchers

---

[2] V.E. Gough, "Chapter 4, Structure of the Pneumatic Tire", Mechanics of Pneumatic Tires, S.K. Clark, Editor, NHTSA, circa 1981, pp. 203-248.
[3]Koutny, F., "A Method for Computing the Radial Deformation Characteristics of Belted Tires," Tire Science and Technology, TSTCA, Vol. 4, No. 3, Aug. 1976, pp. 190-212.
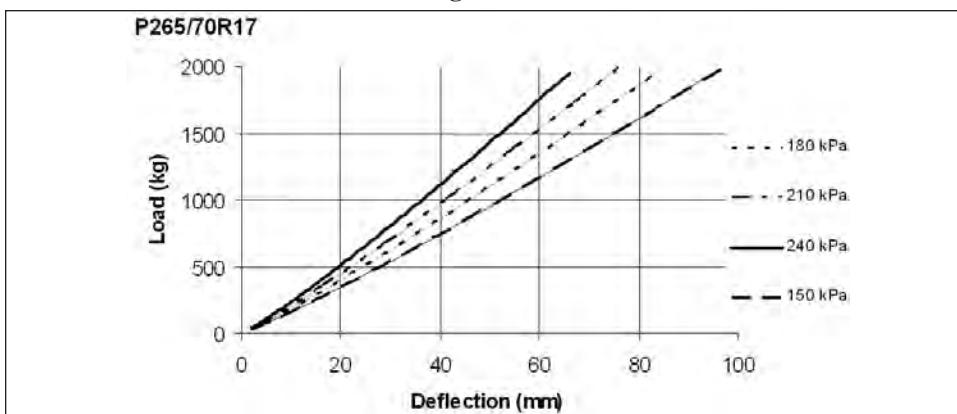
in the industry generally concur that the stiffness of pneumatic tires is controlled primarily by the inflation pressure and the tire dimensions, principally the tread width and outside diameter. The tire structure itself only accounts for about 10 to 15% of the tire's load carrying capacity at typical operating pressures.

In a more recent work, Rhyne[5] extended the ring model used by Koutny and applied it directly to the question of vertical stiffness. We can adopt Rhyne's stiffness model to calculate the deflection for any given tire size and operating pressure and thus develop a new load formula.

First, one must look at typical load-deflection curves at various operational inflation pressures, as shown in Figure 1. The tire stiffness at a given pressure is derived from the slope (the tangent vertical stiffness) of the individual curves, which appear to be quite linear over normal ranges of operating load. As tires become lower in aspect ratio and develop a square footprint, the value of the tangent stiffness approaches that of the secant stiffness.[6]

Figure 5.1

Secondly, as a result of Rhyne's work[7], we know that the tangent stiffness, K_Z, is a function of tire pressure, footprint width and outside diameter and may be expressed as follows:

$$K_Z = 0.00028P \quad W \times OD + 3.45 \tag{4}$$

where:

K_Z = Tangent Stiffness - kg/mm
P = tire inflation pressure - kPa
W = tire footprint width – mm
OD = Outside diameter - mm

[4]Koutny, F., "Air Volume Energy Method in Theory of Tyres," Plasty a Kaucuk, 15, No. 4, 1978, pp. 100-105, (English translation in International Polymer Science and Technology, Vol. 5, No. 8, 1978).
[5]Rhyne, T.B., "Development of a Vertical Stiffness Relationship for Belted Radial Tires," Presented at the 23rd Annual Conference of the Tire Society, 20 September 2004, Akron, Ohio.
[6]See Appendix II, Figure 2-1
[7]Rhyne, T.B., ibid.

For initial verification, the predicted K_Z was calculated for 50 different tires of 34 sizes for which tangential stiffness had been measured at various loads and inflations pressures. Figure 5.2 shows the very strong correlation between the measured and predicted values[8].

In order to make the stiffness equation more practical for use by standardizing bodies it is desirable to have the equation written in terms of parameters that these bodies normally deal with. First, a large sample of tires was evaluated to determine the relationship between footprint width and nominal section width. The following relationship results:

$$W \approx \left(-0.004\,AR + 1.03\right) S_N \approx a \times S_N \tag{5}$$

where:
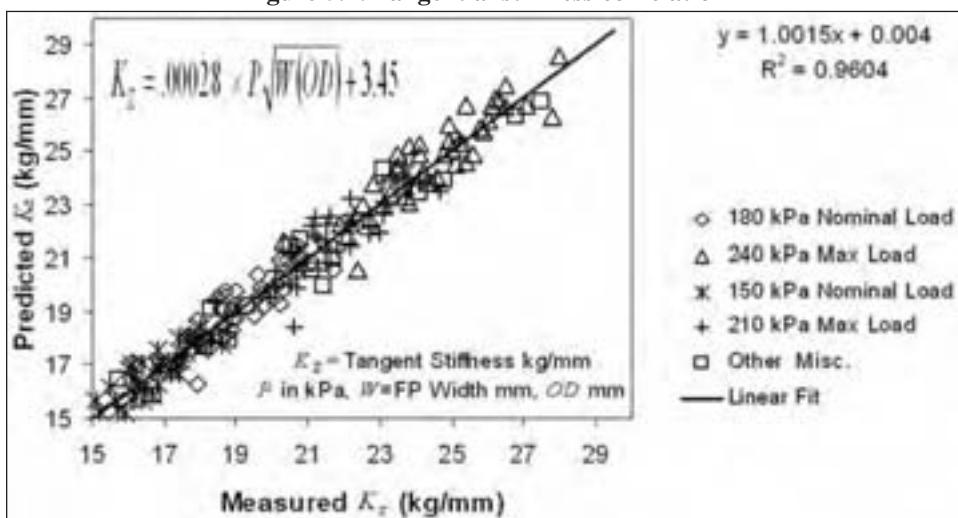
      W = Footprint width - mm
      AR = Aspect Ratio
      S_N = Nominal Section Width – mm
      a   = Factor from Table 5.2

Figure 5.2: Tangential stiffness correlation

Thus the above value for W may be introduced into equation (4) as follows:

$$K_Z = 0.00028\,P\sqrt{\left(-0.004\,AR + 1.03\right) S_N \times OD} + 3.45 \tag{6}$$

The effect of equation (5) is that as the Aspect Ratio decreases, the factor 'a' by which the nominal section width, S_N, is multiplied, increases, as shown in Table 5.2 below. Thus, for lower aspect ratio tires, the footprint width as a percentage of the width of the tire section, is inversely proportional to the aspect ratio.

It is also known from the TRA Engineering Design Information manual[9]:

[8]Rhyne, T.B., ibid.
[9]Available by subscription from: The Tire and Rim Association, Inc., 175 Montrose West Ave., Suite 150, Copley, Ohio 44321.

$$OD = 2H + D_R \tag{7}$$

where:
   H = Design Section Height - mm
   D_R = Rim Diam Code – mm
and

$$H = S_N \times \frac{AR}{100} \tag{8}$$

where:
     S_N = Nominal Section Width – mm
     AR = Aspect Ratio

Thus OD may be expressed in terms of section width, aspect ratio and rim code as follows:

$$OD = \frac{S_N \times AR}{50} + D_R \tag{9}$$

and equation (6) may be expressed in terms useful to the engineer and standardizing bodies as shown below:

$$K_Z = 0.00028P \sqrt{\left(-0.004\,AR + 1.03\right)S_N \times \left(\frac{S_N \times AR}{50} + D_R\right)} + 3.45 \tag{10}$$

Table 5.3 lists values of D_R for current rim codes.
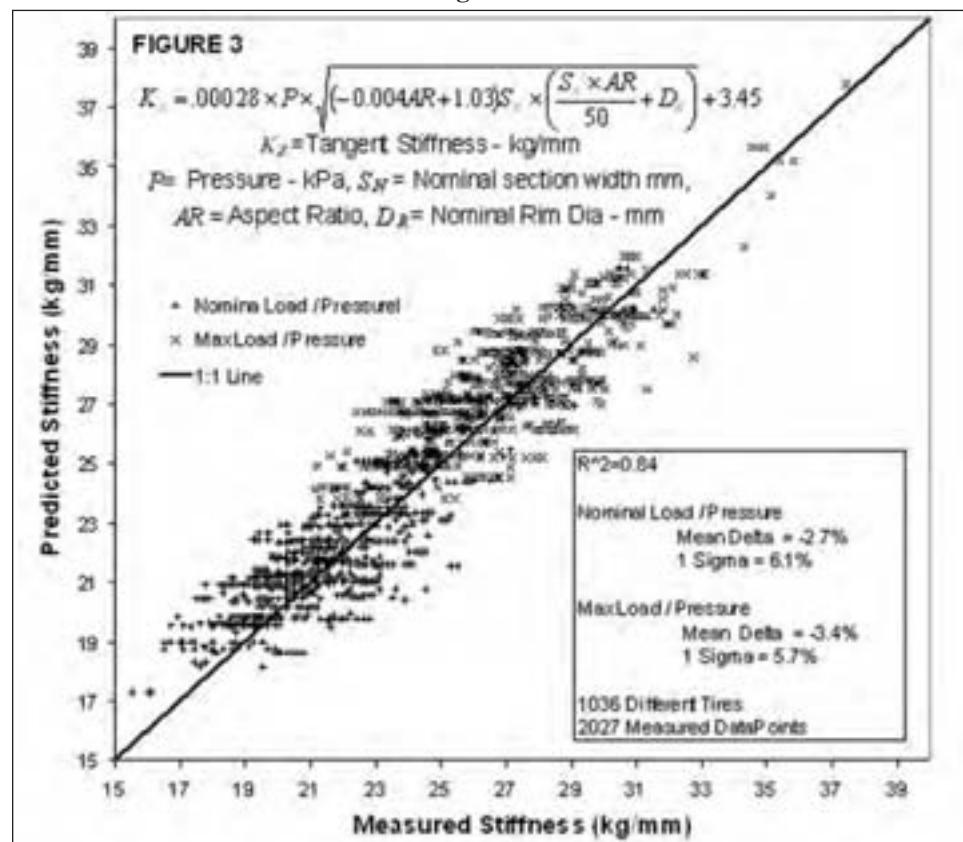
Using equation (10) we can now compare predicted versus measured values of K_Z for a large sample of tires. Figure 5.3 shows the correlation for more than 2000 data points taken from over 1000 tires of 144 different sizes. This data set included rim codes ranging from 13 to 24, section widths from 175 to 305 mm, and aspect ratios ranging from 35 to 80, as well as multiple brands of tires.

Table 5.2: Factor 'a'

Aspect ratio	a
25	.93
30	.91
35	.89
40	.87
45	.85
50	.83
55	.81
60	.97
65	.77
70	.75
75	.73
80	.71

Table 5.3: Values for D_R (=rim code x25.4)

Rim Diameter Code	D_R - mm
12	305
13	330
14	356
15	381
16	406
17	432
18	457
19	483
20	508
21	533
22	559
23	584
24	610

Figure 5.3

10. TRA load formula vs. deflection

Having shown that the tangential vertical stiffness is correlated for a wide range of tires, we now look at the TRA load equation and calculate the relative deflection of tires at maximum load and under normal load.

It should be noted that tire standardizing bodies of other countries, such as ETRTO[10] and JATMA[11], use empirically-based load equations that may differ from those of TRA. For example, in one case the load formula is based upon the contained air volume. Attention is focused here solely on the TRA formula.

11. Methodology

Tire designers and vehicle engineers generally speak in terms of tire load and inflation pressure. In fact, what they are really concerned with is the deflection of the tire at a given load and pressure. As the deflection increases, the tire is strained more severely and therefore more heat is generated. Consequently the operating temperature increases. The energy expended in rolling also increases. Thus any review of load capacity should consider the corresponding deflection.

Figure 5.4 shows a schematic of a tire mounted on a rim at a given inflation pressure. As a load is applied, the tire will deflect by the amount "d".

Using equation (10) for tangential stiffness, an equivalent static deflection may be calculated for any combination of load and pressure in the linear range of operation, for any given size tire:

$$d = \frac{L}{K_Z} \tag{11}$$

where:

d = deflection – mm
L = load – kg
K_Z = tangential stiffness – kg/mm

The deflection under load is considered to be the main determinant of tire durability and for different types of tire the relative deflection is the appropriate measure. Thus, to compare a variety of tire diameters, aspect ratios and rim diameters, it is desirable to express the deflection as a percent of the section height (SH) as defined in Figure 5.4. Thus:

$$\%d = \frac{d}{SH} \times 100 = \frac{d}{(OD - FD)/2} \times 100 \tag{12}$$

where:
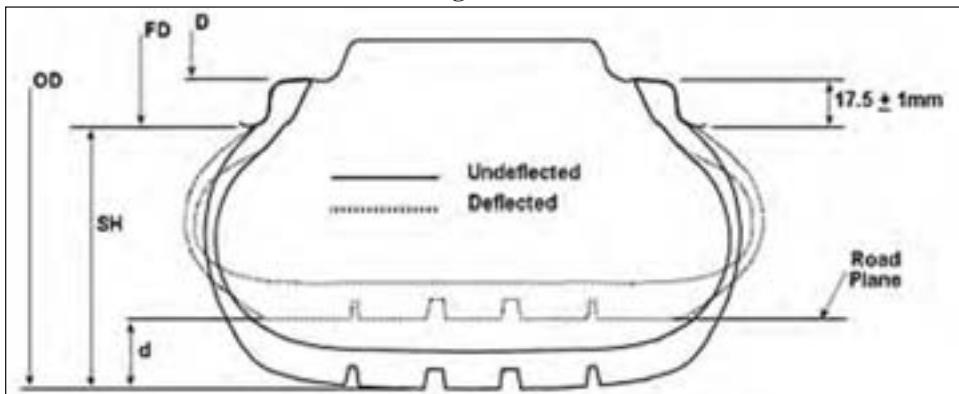
FD = rim flange diameter – mm
SH = section height (above rim flange) – mm
OD = outside diameter - mm

[10]The European Tyre and Rim Technical Organisation
[11]The Japan Automobile Tyre Manufacturers Association, Inc.

Figure 5.4

A listing of standard dimensions for today's rims is presented in Table 5.4. Using equations (10) through (12), deflections for the entire range of tire sizes may easily be calculated.

Table 5.4: Basic rim dimensions[12]

Rim diameter code	Rim diameter (D) mm	Flange diameter (FD) mm
14	354.8	389.8
15	380.2	415.2
16	405.6	440.2
17	436.6	471.6
18	462.0	497.0
19	487.4	522.4
20	512.8	547.8
21	538.2	573.2
22	563.6	598.6
23	589.0	524.0
24	614.4	649.4

12. Deflection analysis

The percent deflection for a number of tires was calculated using the current TRA load formula at a range of operational pressures. Figures 5.5 & 5.6 are for 75 series tires at respective pressures of 180 and 240 kPa. Both figures show that as the section width of these tires is increased the relative deflection decreases slightly, but as the rim code increases there is a more significant increase in deflection.

The same types of graphs were prepared for 45 aspect ratio tires as shown in Figures 5.7 & 5.8, with the results showing the same trend.

Figures 5.9 and 5.10 show the effect of rim code while keeping the section width constant. It should be noted that for a given aspect ratio and section width, the cross section profiles of the tires are identical - only the diameters change. Yet, for a given aspect ratio, as the rim diameters are increased there is a significant increase in relative deflection, and the rate of increase is similar for all aspect ratios.

The above graphs clearly show that the existing TRA formula penalizes larger rim diameters, that is, it requires the tire to deflect more as the rim diameter increases.

[12]Courtesy of The Tire and Rim Association, Inc.

Figure 5.5: 75 series - standard load - 180 kPa
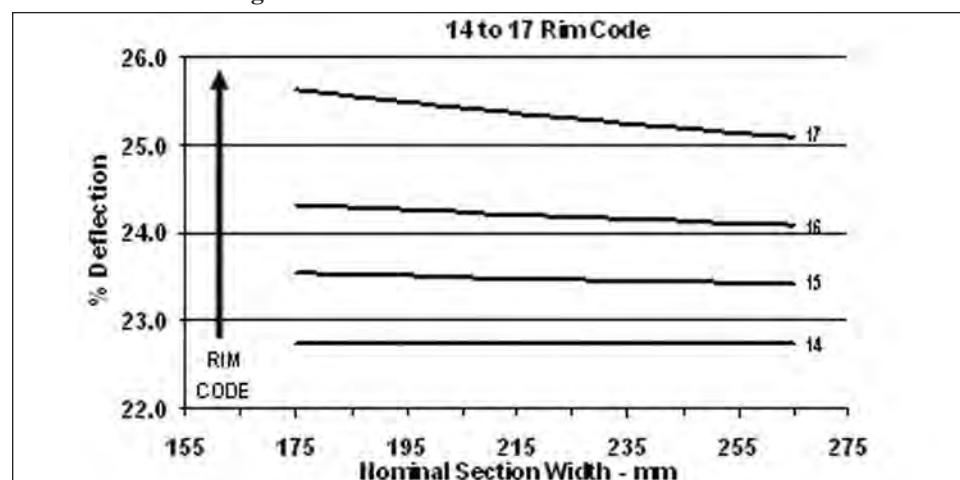
Figure 5.6: 75 series - standard load - 240 kPa
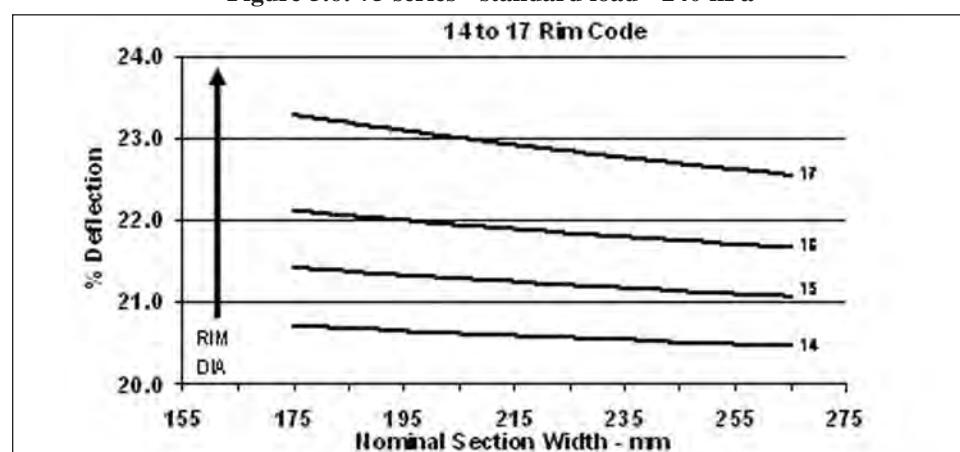
Figure 5.7: 45 series - light load - 180 kPa
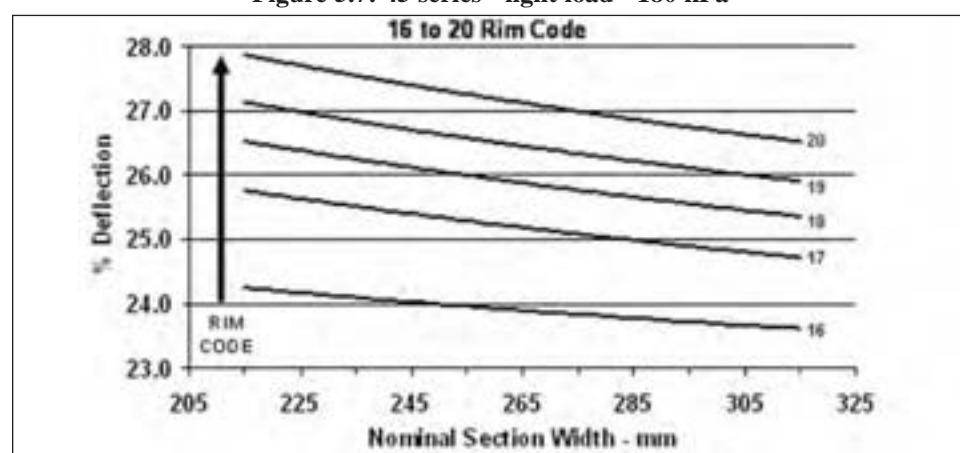
Figure 5.8: 45 series - light load - 240 kPa
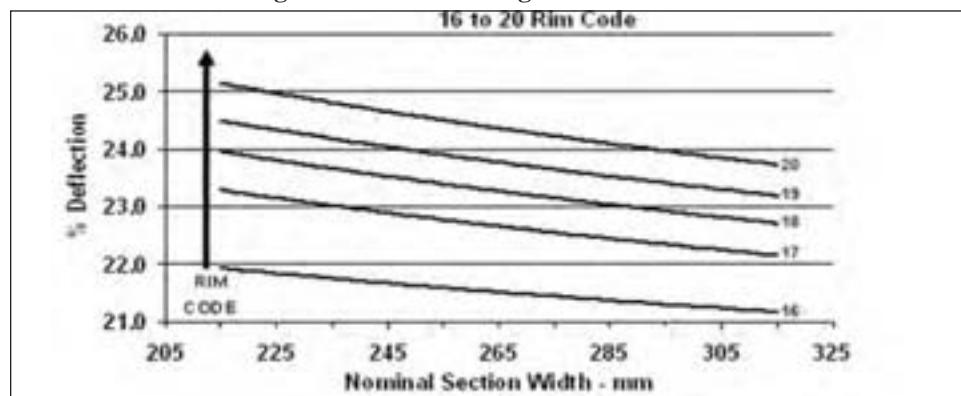
Figure 5.9: P225/arRrc - TRA - light load
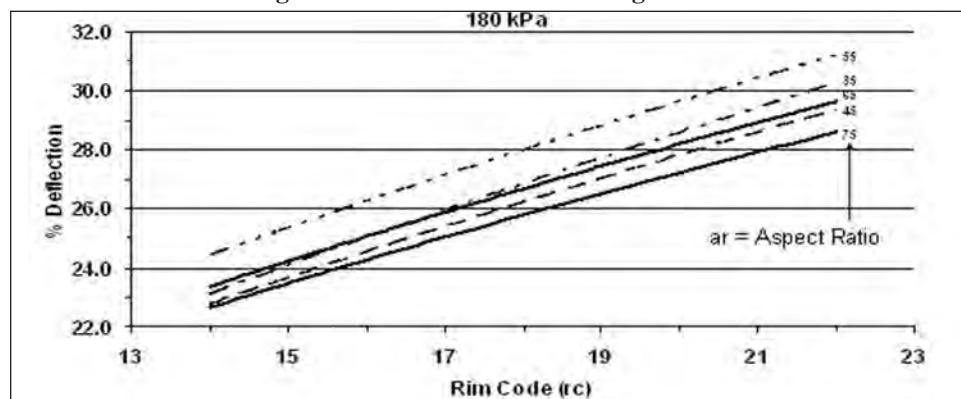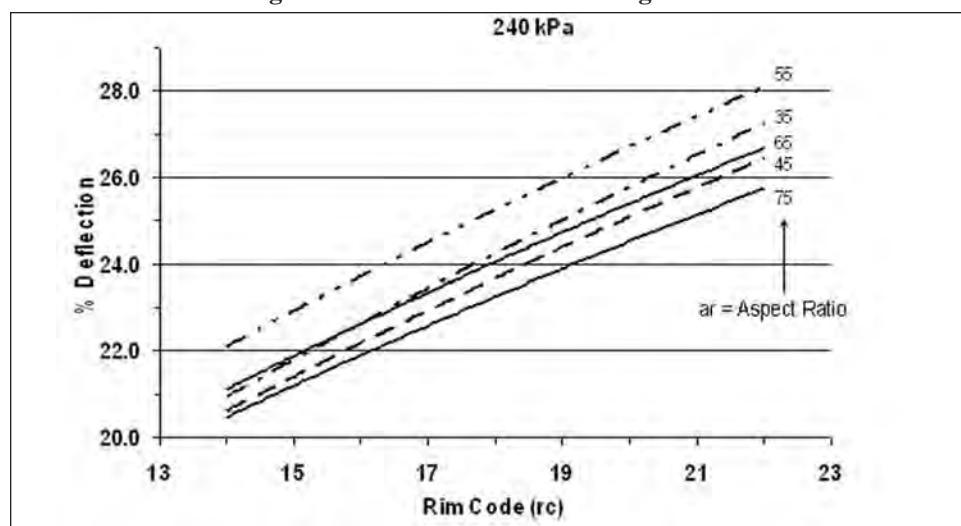
Figure 5.10: P225/arRrc - TRA - light load

13. Proposed load formula

In order to avoid this penalty for tires with low aspect ratios and larger rim codes, a new load formula based upon constant deflection is described below.

From equation (11), for the linear case, we see that load is equal to the product of deflection and stiffness, and we have already developed equation (10) to calculate stiffness. From Tables 5.3 and 5.4 we also find that $D \approx D_r$ and that today's passenger car rims have a constant flange height of 17.5mm. Transposing equation (12) to give the deflection in terms of the nominal section width and aspect ratio results in the following equation:

$$d = \frac{\%d \times (H - 17.5)}{100} = \frac{\%d \times \left(\dfrac{S_N \times AR}{100} - 17.5 \right)}{100} \tag{13}$$
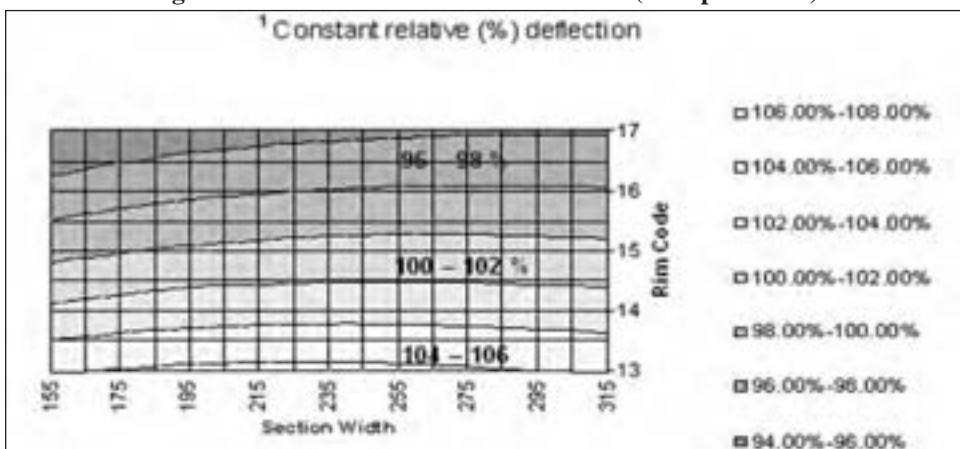
Combining equations (10) and (13) results in a deflection-based general equation for load for any size of passenger car tire.

$$\tag{14}$$

$$L = \left[\frac{\%d \times \left(\dfrac{S_N \times AR}{100} - 17.5 \right)}{100} \right] \times \left[0.00028\, P \sqrt{(-0.004\,AR + 1.03)\, S_N \times \left(\frac{S_N \times AR}{50} + D_R \right)} + 3.45 \right]$$

In order to calculate maximum loads, the pressure may be assumed to be 240 kPa[13]. Using a coefficient chosen from a table of coefficients in terms of aspect ratio, the percent deflection can be calculated for comparison with the current formula.

Solving equation (14) for a range of standard load tires with an aspect ratio of 70 we can select a percent deflection and generate loads for comparison with the existing TRA formula as shown in Figure 5.11.

Figure 5.11: % calculated load[1]/TRA load (70 aspect ratio)

The penalizing effect of increased rim codes with the current formula is again clearly seen.

---

[13]Reference pressure associated with maximum load of today's standard load P-metric tires

14. Work to be done

A method has been presented to determine loads at constant relative deflection and compare them with the values calculated using the current formula. However, further work is needed to determine the appropriate operating deflections for tires. Studies for a range of sizes are needed to create, based upon performance data, the rules for various types of tires. For example, should different relative deflections be used for 75 versus 30 aspect ratio tires? Also, the stiffness model may need to be further refined, to ensure that it encompasses tires being developed today and anticipated in the future. Discussion of the method proposed here has already begun in international standardizing bodies.

15. Summary

The basic load formula for tires has been in existence for many decades and should be reviewed to bring it into accord with today's requirements. The methodology presented here can be used to evaluate the maximum loads that are currently accepted. Test programs could determine optimum deflections and provide guidelines for future tire load calculations.

Acknowledgements

Appendix 1

Notes from The Tire & Rim Association, Inc.

Figure 5.1.1: Relation between section width/rim width ratio – Part 1

With tire of circular section

S_1 = Section width
W_1 = Rim width
α = Angle subtended by rim W_1
$\Theta = \alpha/2$

$\text{SIN } \Theta = (W_1/2)/(S_1/2) = W_1/S_1$

When Rim width W_1 equals 62.5% of section width

$W_1 = 0.625 \, S_1$

$\text{SIN } \Theta = 0.625 S_1 / S_1 = 0.625$

$\Theta = 38.67°$

$180 - \Theta = 141.33°$
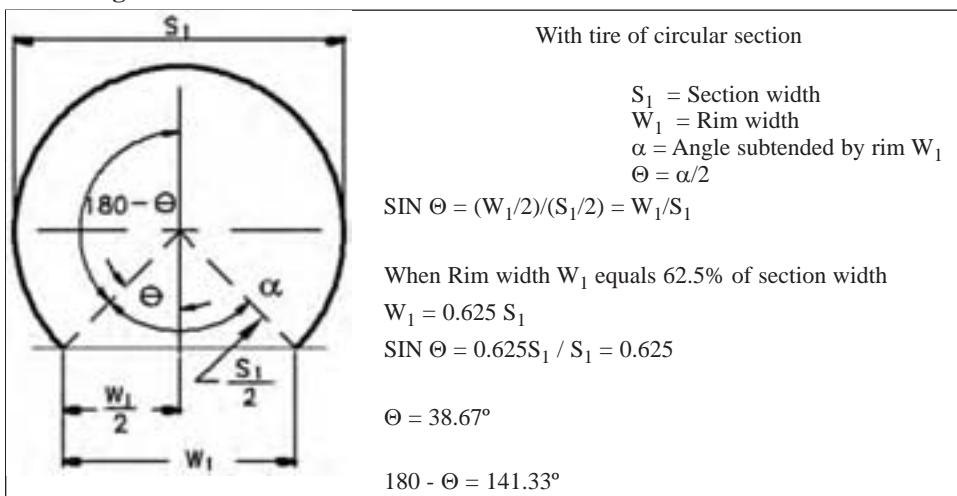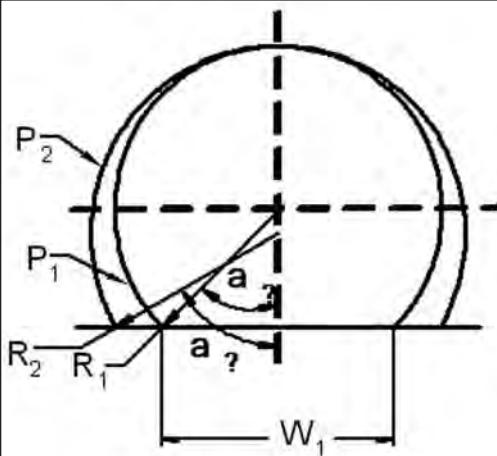
Figure 5.1.2: Relation between section width/rim width ratio – Part 2

Where tire periphery P1=P2
It can be shown that:

$R_1 / R_2 = (180 - a_2) / (180 - a_1)$

Section $(S_1) = 2R_1$

Section $(S_2) = 2R_2$
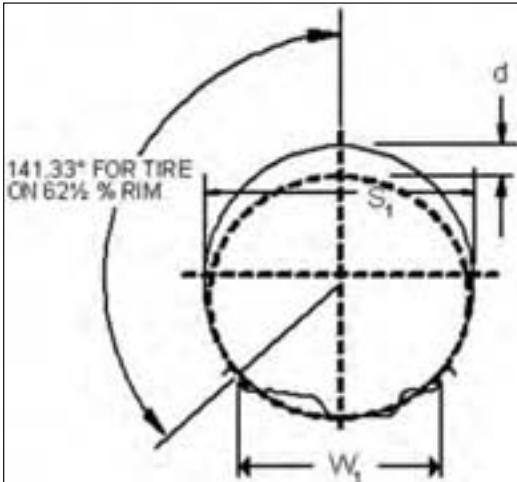
Therefore: $S_2/S_1 = (180 - a_2) / (180 - a_1)$

To get $S_{62.5}$ from measurement S_1 on any rim:

(1) $180 - I_2 = 141.33 \rightarrow S_{62.5}/S_1 = 180 - I_1 / 141.3$

(2) Therefore: $S_{62.5} = S_1[(180-SIN^{-1}(W_1/R_1))/141.3]$

(3) It can be shown: $S_{70} = S_1[(180-SIN^{-1}(W_1/R_1))/135.6]$

Figure 5.1.3: Theoretical section width S$_d$ - Part 1

141.33° FOR TIRE
ON 62½ % RIM

From Marks' handbook[1]:

P = Length of perimeter of ellipse

$$K = \left(1 + \frac{1}{4}m^2 + \frac{1}{64}m^4 + \frac{1}{256}m^6 + ... \right)$$

$$m = \frac{(a-b)}{(a+b)}$$

$\therefore$ From figure at left:

$$m = \frac{\dfrac{S_1}{2} - \left(\dfrac{S_1}{2} - d \right)}{\dfrac{S_1}{2} + \left(\dfrac{S_1}{2} - d \right)} = \frac{d}{S_1 - d}$$

1 pg. 2-8, E.A. Avallone & T. Baumeister III - editiors, "Marks' Standard Handbook for Mechanical Engineers", Tenth Edition, McGraw-Hill, 1996

As a tire becomes depressed, the top half becomes an ellipse (the bottom half remains circular)

The difference in perimeter between the circular and depressed tire is as follows:

$$P_{DIFF} = \frac{\pi}{2}S_1 - \frac{\pi}{2}K\left[\frac{S_1}{2} + \left(\frac{S_1}{2} - d \right) \right] = \frac{\pi}{2}S_1 - \frac{\pi}{2}S_1K + \frac{\pi}{2}dK$$

$$P_{DIFF} = \frac{\pi}{2}\left[(S_1 - S_1K) + dK \right] = \frac{\pi}{2}d\left[(1-K)\frac{S_1}{d} + K \right]$$

Let: $\quad C = (1-K)\dfrac{S_1}{d} + K$

$$\therefore \quad P_{DIFF} = \frac{\pi}{2} \times d \times C$$

Figure 5.1.4: Theoretical section width S_d – Part 2

The perimeter of a tire having a depressed crown and a section S_1 on a rim width W_1=

$$\pi \, S_1 \times \frac{180^o - sin^{-1}\left(W_1/S_1\right)}{180^o} - \frac{\pi}{2} dC \qquad (1)$$

S_d=depressed tire equivalent section on a 62 .5 % rim

$$PERIMETER_{(S_D)} = \pi \, S_d \left(\frac{141.3^o}{180^o}\right) \qquad (2)$$

Setting (1) = (2):

$$\pi \, S_d \left(\frac{141.3^o}{180^o}\right) = \pi \, S_1 \frac{180^o - sin^{-1}\left(W_1/S_1\right)}{180^o} - \frac{\pi}{2} dC$$

$$S_d = S_1 \frac{180^o - sin^{-1}\left(W_1/S_1\right)}{141.3^o} - \frac{dC}{2}\left(\frac{180}{141.3}\right)$$
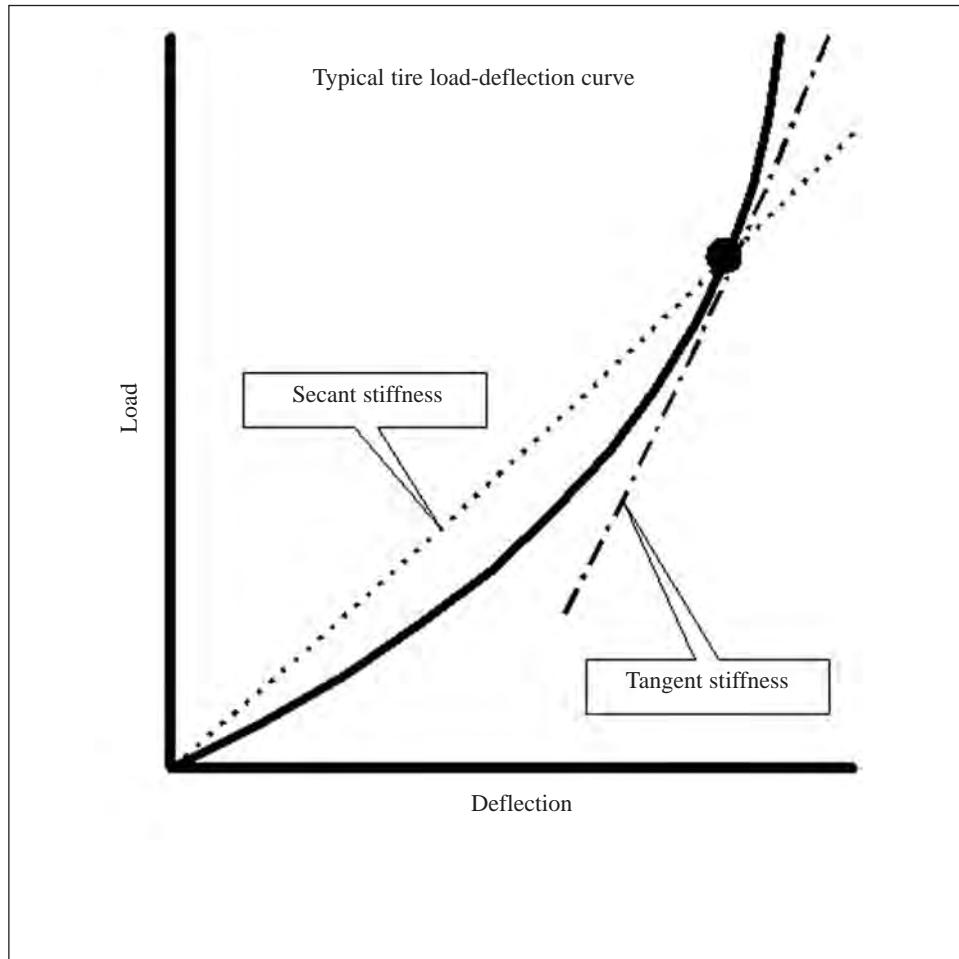
$$\therefore \quad S_d = S_{0.625} - 0.637d\,(C)$$

S_d=$S_{0.625}$ - (F)d   where F=0.637xC

$d/S_{0.70}$	$d/S_{0.625}$	$S_{0.625}/d$	m	K	C	F	$S_d/S_{0.625}$	F(TRA)
0	0	:	0	1.000	1.000	.637	1.000	.637
.05	.0521	19.19	.055	1.00076	.986	.628	.967	.630
.10	.1042	9.60	.116	1.00325	.972	.619	.936	.620
.15	.1563	6.40	.185	1.0086	.954	.608	.905	.610
.20	.2083	4.80	.263	1.017	.935	.596	.876	.597
.25	.2604	3.84	.352	1.031	.912	.581	.849	.583
.30	.3125	3.20	.455	1.052	.886	.564	.824	.568
.35	.3646	2.74	.574	1.082	.857	.546	.801	
.40	.4167	2.40	.714	1.128	.821	.523	.782	

Appendix 2

Figure 5.2.1: Secant versus tangent stiffness

Chapter 6
Tire Stress Analysis

by M. J. Trinko

Chapter 6
Tire Stress Analysis
by M. J. Trinko

1. Introduction

The pneumatic tire presents a challenging stress analysis problem. It is a pressurized membrane structure of revolution reinforced by a network of cords laid at an angle to the circumferential direction. The cords are folded around a rigid hoop of steel wires, which anchors the tire to the rim.

The bias-ply pneumatic tire was in commercial use for decades before engineers were able to solve any but the most basic problems. Calculations of the initial inflated shape were developed to assist the tire designer determine fundamental relations between the shape of the mold and width of the building drum, but they required substantial manual calculation. A by-product of the shape calculation was the prediction of cord force distribution in the mounted and inflated tire. Virtually nothing was known about the cord loads and rubber stresses in the loaded tire. In the early 1970s, the combination of the development of the finite element method and the availability of reasonably high-speed computers made it possible to analyze the pneumatic tire in more detail. Initially, only axisymmetrical analysis was possible, but within a few years solutions were obtained for the statically loaded tire. More advanced problems were tackled using the static solution as a starting point. Several years passed before usable solutions for the rolling tire problem appeared.

At about the same time that the computer-based tools became available to study the bias-ply tire, the shift to radial tires had begun in the U.S. Application of the new analysis techniques to radial tires became critical as the shape of the mold and the location of components in the cross section of the radial tire are much more important than those same quantities in a bias-ply construction. The transition from bias analysis to radial analysis was relatively smooth as the input information for the structural analysis programs only needs to describe the dimensions, material properties and loadings. In a way, the analysis of the radial construction is less complicated, as the radial cords do not change orientations significantly as the tire deforms. The cord angles in the more flexible bias tire are directly related to the distance from the axis of rotation when the tire is under inflation loading. As the tire is loaded, the cords behave like a netting structure and change their orientations in response to the relative loads in the circumferential and meridional direction. At the time, the commercially-available finite element codes were not able to take these angle changes into account. Radial tires do not exhibit this behavior, so problems introduced because of orientation angle changes were small or zero.

The discussion given in this section is based on a combination of analysis and application of the basic principles of mechanics. The results of finite element analyses (FEA) provide insight into the behavior of the tire under various loading conditions, that would otherwise be difficult to understand. By evaluating the results, we can determine the appropriate design parameters that affect the behavior.
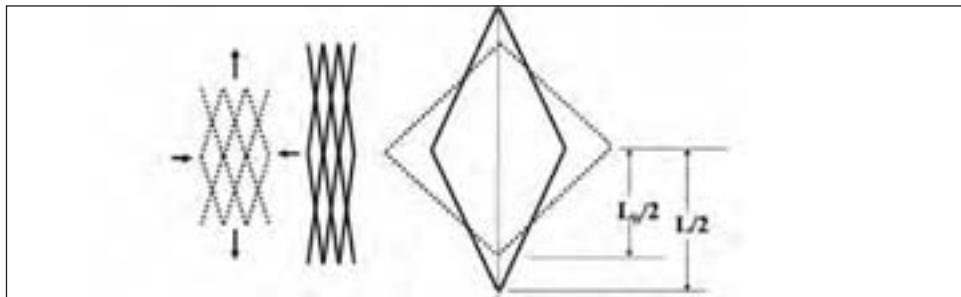
2. Fundamentals of tire shape

Bias construction

We begin with a discussion of the bias-ply tire because it may be analyzed using classical mechanics. The inflated natural shape is determined by the rim width (distance from flange to flange), the diameter of the building drum, and the bias angle and length of the cords laid on the drum. The term "natural shape" has been used to describe the shape that the tire cross section would assume if the cord network could respond independently of any forces created in the rubber. The tire designer must make this calculation and set a building drum diameter and drum width that will allow the tire to be formed into the curing mold with the proper amount of cord tension and will produce an inflated tire of the desired diameter and width. Two approaches have been developed to determine the "natural shape" of the tire. They were developed independently and either held back as proprietary information or published with little notice. Both of them use the basic relationship $\rho_0 / \cos\theta_0 = \rho / \cos\theta$, where ρ is the radius to any point on the tire cross section measured from the wheel axle and θ is the angle of the cord relative to the circumferential direction at that point. The subscript can refer to any reference location.

This relation can be derived from geometric considerations treating the cords as inextensible and having pinned connections at their intersections. For bias tires, two layers of fabric-reinforced rubber are wrapped on a cylinder with the cords lying at opposite angles. The cords form small parallelograms with major and minor axes in the circumferential and transverse directions. As the tire is formed into its characteristic shape, the increase in diameter causes the cords to rotate - the parallelograms extend in the circumferential direction and contract in the transverse direction. This applies to bias tires built in the conventional fashion. It is possible to envision other cord paths, but these are impractical to build in production.

Figure 6.1: Cord orientations change
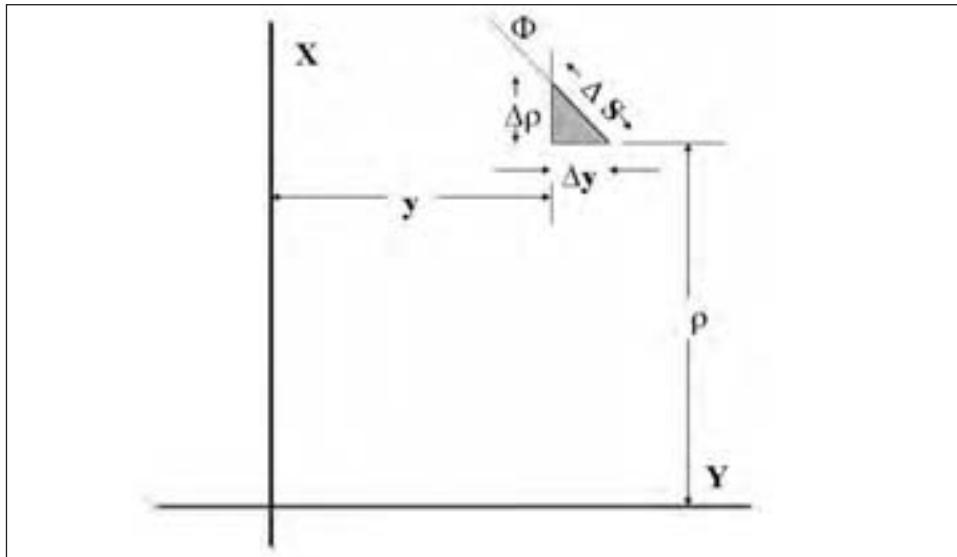
The Purdy equation

John Purdy was a mathematician with the Goodyear Tire and Rubber Company from the 1920s to the 1960s. He began a fundamental study of inflated shapes and developed mathematical bases for tire behavior. During the 1930s he developed a relationship for the natural shape of a bias tire.

Purdy considered the equilibrium of a representative section of the tire - a full $360°$ ring located at a radius ρ and having an elemental length Δs measured in the contour direction. In addition, a triangular ring of air on the inside surface of the ring was included to allow the effect of the air pressure to be applied along the axial and radial directions. This triangular ring is shown in figure 6.2.

Figure 6.2: Purdy's elemental section

By applying equilibrium conditions in the axial and hoop directions, along with a moment balance, Purdy derived a single integral equation for the natural shape, in the form of a hyper-elliptic integral. Details of this calculation are given in "Mathematics Underlying the Design of Pneumatic Tires"[1]. Note that Purdy's solution is valid for any cord path. However, for each combination of cord angle, drum width and diameter, a numerical integration was required, involving extensive calculations that were initially done manually, using only a slide rule.

Another approach to the solution of this problem was developed by Bidermann, Hofferberth and Walter using a combination of "thin shell" theory and netting theory. Their contribution is included in the approach described here. These equations describe various features of tire behavior. The first uses the relation between cord angle and radius that was described previously. The second is the relation between in-plane stress resultants and cord angle. By calculating the values of the circumferential (N_θ) and meridional (N_ϕ) stress resultants for a network of cords with cord tension **t** and at an angle α, typically measured from the circumferential direction, it follows that

$$\tan^2 \alpha = N_\phi \, / \, N_\theta \; .$$

This can also be derived by considering the equilibrium of a free body diagram of a section of a doubly-curved membrane.

The third equation is derived from the equilibrium of a section of the tire lying between the radius of the widest section (ρ_m) of the tire and the centerline radius. The force balance in the axial direction includes the pressure term and the meridional stress resultant.

$$N_\phi = p \, \theta \, (\, r^2 - r_m^2) \, / \, 2 \, r^{\,2}$$

The fourth equation is the equilibrium equation for a doubly-curved surface. It is an extension of the equilibrium equation for a circular cylinder, which is derived in introductory

statics textbooks. For a cylinder of radius R and thickness t, under internal pressure p, the hoop stress σ is given by

$$\sigma = p\,R\,/\,t$$

By substituting $N = \sigma\,t$, then $p = N\,/\,r$. Extending this to a doubly-curved surface, the equation becomes

$$N_\theta\,/\,\rho_\theta + N_\phi\,/\,\rho_\phi = p\;.$$

The curvatures, ρ_θ and ρ_ϕ, are the radii of curvature in the circumferential and meridional directions, respectively. At the tire centerline, ρ_θ is interchangeable with ρ_0 and is the radius to the reinforcement package. The final equations define the curvatures of a surface of revolution. These come from examining the geometry of a surface of revolution:

$$\rho_\phi = [1+(z')^2]^{3/2}/z''$$

and

$$\rho_\theta = r[1+(z')^2]^{1/2}/z'$$

where $z' = dz\,/\,dr$ and $z'' = d^2z\,/\,d^2r$.

These equations can be combined by substituting for the values of α, ρ_ϕ, ρ_θ, N_θ and N_ϕ leading to the equation:

$$z'' + z'\,[\;1+(z')^2]\;\{\;r\cos^2\alpha\,/\,(r_c - r^2\cos^2\alpha\,) - 2r\,/\,(\,r^2 - r_w\,)\;\} = 0$$

This equation can be transformed into an integral equation for **z** by reducing the order to **z′**, decomposing using partial fractions and applying the boundary condition at the centerline. The integral equation can then be solved numerically, yielding the inflated shape of the cross-section.

This is the 'natural' shape of the tire that it would take if it behaved as a membrane with no resistance to bending. If the mold shape deviates from the natural shape, the inflated cross section will not attain a true natural shape because of resisting forces generated in the rubber.

3. Structural analysis of tires

With the development of high speed computational capability and the technology needed for tire analysis, the tire engineer could now evaluate design variations without having to build prototype tires and test them, either in the laboratory or on the test track. As the computing capacity increased and the cost of computers decreased, sophisticated analyses could be done in reasonable times and the results evaluated and used effectively.

Finite element analysis (FEA) began in the 1960s and commercial FE codes were developed in the 1970s that gave the engineer the capability to solve problems that, previously, could not even be attempted. During the 1980s the commercial codes were enhanced, allowing tire engineers to make significant contributions to the understanding of tire behavior. New capabilities are continually being developed.

Challenges of tire analysis

The tire presents a unique combination of challenges. Unlike conventional structural analysis, the final shape of the structure and the applied loads are part of the solution instead of being part of the problem definition. The materials are not necessarily linear elastic materials, although use of a linear material model in particular locations is useful. Rubber is a highly non-linear material, and the reinforcing cords also behave in a non-lin-

ear fashion. These materials are also temperature and rate dependent, exhibit creep and have different stiffnesses in tension and compression. Two common cord materials, nylon and polyester, undergo shrinkage during the curing process. Finally, the cord reinforcement, the primary contributor to the tire stiffness, is placed at bias angles giving the structure orthotropic characteristics. Moreover, the cords change their orientation somewhat during loading. All of these features contribute to the tire analysis problem and must be addressed in order to obtain useful results.

Implicit and explicit finite element methods
Before discussing the use of finite element methods in the analysis of tires, we point out some fundamental differences in two approaches. The current commercial finite element programs are designed to make the analysis process as simple as possible. This allows one to carry out sophisticated analyses without understanding all of the intricate details that are required for that analysis. The analysis process is reduced to the generation of a complete geometric description of the structure, a definition of the material behavior, and a definition of the applied loads and constraints. However, the more the engineer understands the process, the better the likelihood of successful analysis. A basic overview of the finite element process is given here.

The implicit approach
The initial, and more common, finite element method is the implicit approach. This is applied primarily to static or steady state problems. As an example, consider a rectangle with points located both on the boundary and in the interior. Now add a number of 'springs' that are connected to the points so that the entire rectangle is covered by areas surrounded by springs but no spring crosses over another spring. Next, arbitrarily constrain some of the points and apply forces to some or all of the remaining points. At each point, equations of equilibrium can be written which involve the stiffness of the springs connected to that point and the displacements of the points connected to that point via springs. For each degree of freedom in the whole structure, there is one equation available to represent equilibrium at that location. If these equations are put into matrix format, the row containing the equilibrium equation for a particular point will have non-zero entries only in the columns representing the points that are directly connected to that point. If the equations are carefully ordered, the maximum width of any of the equations can be minimized. The advantage of minimizing this width (called bandwidth) is that it leads to a reduced computational requirement. Commercial finite element programs typically include an automatic bandwidth minimization scheme.

Many structures have some type of symmetry, which can be used to reduce the size of the model, which in turn reduces the amount of resources needed to run the problem. Tires have geometric symmetries that are obvious, but they also have a material symmetry, hidden under the surface. The geometric symmetry is a mirror symmetry at the equator of the tire tread. Here the displacements normal to the surface are zero. For the conventional radial tire, the two belts under the tread area require special treatment if one wishes to take advantage of symmetry. If the belts were cut at the equator, and the cut section placed against a mirror, one would see an incorrect chevron pattern instead of the straight continuous belt cords. We will call the situation where the belts are at +/- angles a "skew-symmetry". For skew symmetry, one half of the tire must be rotated 180° about a vertical diameter in order to duplicate the other half. The vertical displacement of a node on one

side of the vertical diameter must be set equal to the vertical displacement of the corresponding node on the other side of the vertical diameter and the other two components of the displacement on one side of the vertical diameter must be set equal and opposite of those on the corresponding point on the other side. A problem with bandwidth arises because these constraints connect nodes, which would not normally be connected geometrically. This results in a few rows in the matrix that are substantially wider than the average. The wider rows cause symmetry considerations in tire problems to give less computational benefit that in conventional problems.

For a typical linear static analysis, the stiffness matrix must be solved once to obtain the final solution. But tire analysis is not typical. There are a number of non-linearities in the analysis, which require a more advanced approach. The dominant problem is that the final loaded shape is substantially different from the initial shape. This means that the stiffness of the structure, the loading locations and directions all change as the structure responds to the external loads and constraints. To successfully solve this problem, the loading is typically applied in increments which yield a stable equilibrium configuration at the end of each increment, that serves as the starting point for the next increment. The initial stiffness of the unloaded structure is used as a starting point. The first increment of load is applied and the system is solved. The process is repeated using the same load until there is no change in the response from successive iterations. The stiffness is re-calculated using this new configuration, the next increment of load is applied, and the next solution is obtained. This process is repeated until the loading sequence is completed. The size of the allowable load steps depends on the severity of the non-linearity at that loading level. If there are other types of non-linearity in the problem, they can usually be addressed concurrently with the large deformation non-linearity using the incremental loading approach. Since this method requires the creation and solution of a matrix, whose size is determined by the number of degrees of freedom, the required run time and storage requirement grow at least in proportion to the square of the number of degrees of freedom.

The explicit approach

 The explicit finite element approach was developed to solve dynamic problems. In this approach, the equations of motion are written and solved at each nodal point. Starting with the static structure, the external loads and constraints are applied to each nodal point, with resistance supplied by inertia of elements connected to the nodes. A time step length is selected based on the stress wave speed and element size in the model. An acceptable value for the time step is approximately equal to the minimum time required for a stress wave to cross the smallest element length. This choice is based on the concept that the influence of a force or displacement at any node cannot travel the distance to any adjacent node in a single time step.

Nodes in the structure respond to the applied loads for the duration of the time step. At the completion of the first step, all free nodes have been displaced and have acquired velocities. The deformed shape at the completion of the first time step is used to calculate the new element reaction forces, which are now combined with applied loads (which may have changed direction due to the change of shape of the structure). Using the current nodal velocities and the new accelerations from the applied loads, a second configuration is calculated at the end of the second time step. This process is continued until the response from the applied loading has stabilized, for a steady state problem, or until the analyst has determined that the complete time segment has been completed. It is not

unusual for thousands of time steps to be executed in a single analysis.

Note that it is not necessary to create and solve a complete stiffness matrix with this approach. The equations describing the motion at each of the nodal points may be solved independently. This means that the time required to complete the solution is linearly related to the number of nodes or elements. For the implicit approach, the time is exponentially related to the number of nodes or elements, so for certain large problems, the explicit approach may have an advantage. It is not limited to dynamic problems, however, both static and steady state motion problems can be solved using this approach.

In an actual tire structure, the materials convert mechanical work to thermal energy. Since there is no natural damping in the computer model, artificial damping must be included to absorb energy. Since the solution procedure is a forward integration process, using the current loading and stiffness to predict equilibrium at a future time, a small error is introduced at each step. If the time step is appropriate, this error is corrected in the following step. Damping also tends to stabilize the solution but if damping is set at too high a level, the accuracy of the solution may be adversely affected. And if there is insufficient damping, it may be impossible to reach a stable solution. In most cases, the FE programs provide guidance in choosing an appropriate size of time step and the level and type of damping. These limitations of the explicit approach should not deter the analyst from using the method as it provides a very powerful and accurate analysis tool.

Inflation analysis and bead fitment

The analysis of the axisymmetric tire gives basic information about cord loads and inflated shape. It is an easier problem because rotational symmetry and absence of road contact allows the use of a representative cross section. The results can be used to evaluate inflated shape and to determine cord loads throughout the cross section. The burst pressure can be predicted, that is the inflation pressure that causes failure of one of the components of the tire: belt, ply or bead. The burst pressure would be the lowest of these values.

The problem of bead fitment on the rim can also be studied. The basic approach is to treat the rim as a rigid surface and the contact as frictionless. The results of this study would show the magnitude and distribution of the interference forces acting on the rim. This would simulate the situation where the tire was seated on the rim and rolled for a number of revolutions. The small relative motions caused during rolling would relieve the frictional forces generated during the mounting process.

The next step is to include friction in the model and simulate the bead seating process. Motion of the bead sliding up the tapered rim flange is simulated, with frictional resistance. Friction would tend to deform the bead area axially while the increasing diameter of the tapered rim would cause a radial deformation. Key issues in obtaining a valid solution are the proper treatment of friction and the use of correct material properties.

In order to retain the advantages of treating this as an axisymmetric problem, we neglect the effect of the safety hump on the rim. Typical passenger tire rims are made with a safety hump about 3 mm high and located inboard from the rim flange. This hump is designed to help retain the tire on the rim if the tire loses inflation pressure during operation. Keeping the tire mounted on the rim allows the vehicle operator to better control the vehicle after a sudden loss of inflation pressure.

Mounting

As of this writing, no publications have reported a successful simulation of the actual

process of mounting a tire on a wheel. The problem is neither axisymmetric nor static. It resembles a buttonholing action where the bead slides over the safety hump at one point on the circumference and then continues the seating process around the circumference until the whole bead is seated against the flange. This is a dynamic process, which requires using a dynamic solution procedure along with simulation of the frictional resistance at the bead/rim interface. The explicit finite element approach would appear to be the appropriate choice for solving this problem. A successful analysis would give an increased understanding of the mounting process and predict the inflation pressure necessary to fully seat the tire bead on the rim.

Static inflated and deflected analysis

This is one of the fundamental problems facing tire analysts. A solution yields vertical stiffness, contact patch size, shape and pressure distribution, as well as internal stresses and strains. In addition to the direct results, further studies such as rolling resistance and frequency/vibration calculation can be addressed using the results of the static solution as a starting point. Even more challenging problems, such as rolling, cornering and impact, start from the static solution.

When internal stresses and strains are desired, the models require a mesh that contains sufficient detail to provide information on cord loads, along with rubber stresses and strains. This requires that each material layer be represented by at least one element. Such a detailed representation leads to relatively large models. If the construction contains a large number of components, the analyst may choose to combine a few layers into a single element in order to reduce the size of the problem. This simplification must be used with care as, in areas of high gradients of stress and strain, it may produce erroneous results.

The analyst must consider several factors when carrying out these analyses. First, the contact algorithm in common use has a basic contact/no contact condition at the surface nodes. This means that the contact patch is only determined within an element length. Also, contact pressures are usually calculated from nodal contact forces. Thus, the size and shape of the contact patch, and the normal forces, are defined to within one element length of accuracy. As a result, the size of the contact patch is usually under-estimated.

Rolling resistance

Among other performance requirements, automobile manufacturers stipulate that tires do not exceed certain levels of rolling resistance, as this quantity has a significant effect on fuel consumption. Rolling resistance is principally the total effect of the hysteretic losses that occur as a tire rolls. Using the results of a static deflection analysis, the engineer can extract stress and strain values for every element in the model. By assuming that the static stresses and strains are the same in a slow rolling tire, we can calculate a 'cycle' representing a complete revolution by examining the stresses and strains in a 'ring' of elements. Each ring is the set of elements that are traced around the circumference by a single element. These results can be combined with material energy loss data to predict the energy loss in each ring during one complete revolution. Combining this result for all rings in the model yields a total loss for the tire for one revolution. The tire engineer can use these results to modify the design. Options include choosing less hysteretic materials in critical regions or adjusting the location of components within the tire cross-section to reduce the energy loss.

Modal analysis

Automobile manufacturers also require information describing the vibration characteristics of tires so that the tire and vehicle system can be 'tuned' to provide the best possible ride. To meet this requirement, a model that represents the inflated and deflected tire is required as a starting point. The model must provide the natural vibration frequencies and the corresponding mode shapes for frequencies up to 200 Hz. Since the extraction of modal information over the range of interest requires substantial computing resources and the calculation of internal quantities such as local stresses and strains are not of direct interest, a simplified model made up of layered elements is the usual choice. With this simplification, we are able to obtain the required results quickly and accurately.

The typical modal tire model uses shell elements in which all of the reinforcing material layers and rubber layers are 'smeared' into a single layer. In the tread area, an additional layer of 8-noded bricks is added to represent the rubber tread. This layer of rubber could include circumferential grooves if desired. The contact patch points are fixed to the road while the rim may be either fixed or allowed to move as a rigid body. The tire is mounted on the rim, inflated, and deflected against the road surface. The mode shapes and natural frequencies are extracted using the stiffness matrix from the static deflection loading. A description of this method was given by Sundaram et al[2].

The rolling cornering tire

The primary objective of simulating the rolling cornering tire is the prediction of cornering force, aligning torque and contact patch forces, along with internal stresses and strains. This is significantly more difficult than the static deflection problem and there are a number of decisions that will affect the results. Three common approaches are used.

The first is the quasi-static direct rolling method. In this approach, a detailed model of the complete tire is assembled which may or may not include the tread pattern. The circumferential mesh is uniform and relatively fine around the complete circumference, as the model will typically be "rolled" at least one full revolution. The loads and enforced displacements are applied which simulate the effect of rim mounting, inflation and road contact. To simulate rolling, the mesh is rotated around the axle axis and the ground plane or the axle is allowed to translate, driven by friction forces at the tire/road interface. Camber can be simulated by rotating the model around a horizontal axis in the direction of travel. Drive and brake torques can be simulated be applying a constraint force to the moving road surface. This approach is very computationally intensive. In order to represent a typical tread pattern, a large number of nodes are required. In addition, the circumferential mesh density must be sufficient to simulate small angular rotations.

In rolling, the model is rotated slightly around the axle axis and equilibrium must be satisfied in the new orientation. The traction forces developed in the contact patch are usually evaluated using a Coulomb friction law. If the shear force at a node point exceeds the prescribed coefficient of friction times the normal force, the point is released and allowed to slide. If the force is less than the Coulomb maximum, the node remains 'fixed'. This check is made for every node in contact with the road. Another increment of rotation is then applied and the process is repeated. This sequence continues until the solution stabilizes and an additional cycle repeats the results of the previous cycle.

The combination of the physical size of the model along with the need to complete a substantial number of load iterations to reach a solution, make this approach very expensive and time consuming. However, when a solution is obtained it gives a good represen-

tation of the physical situation.

Rothert and Gall[3], reported a study using this approach. They assembled and ran a detailed model with a smooth tread. They also added a complete tread pattern on a section of the tire spanning a distance larger than the length of the contact patch. The model was loaded on a section of the circumference adjacent to that where the detailed tread was located. It was then rotated so that the detailed tread region rolled into the contact patch. This simulated the rolling tire without using a complete 360-degree tread pattern. Even with this simplification, the model required 4 months to reach a solution. The authors also mentioned two other approaches that would reduce the time required to obtain a solution. One method was a combination of global and local approaches. A coarse model of the structure is first run to obtain a global solution. A second model with more detail in the area of interest, is then created and run using the results of the first solution as prescribed loads and displacements. This method suffers from a lack of interaction between the coarse and detailed models. With tire tread patterns, it is possible that the carcass is not loaded uniformly, an effect that is not included in the coarse model.

The authors also commented on the advantages of parallel processing, using a specially designed computer and specially written programs that apply multiple processing units to a single problem. In this way, the time to run an analysis can be reduced significantly. For example, the processing time can be reduced by almost 50% with one additional processing unit, and by almost 75 % with three. In practice, it is not possible to reach the theoretical reduction, the inverse of the number of processors that are assigned to the problem, because there are times during processing that some processors are waiting for the results of a calculation running on another processor. Moreover, this failure to attain the maximum improvement becomes more severe as more processing units are added.

The second approach is an Eulerian-Lagrangian transformation, which takes advantage of the rotational symmetry of the tire structure to transform a steady-state dynamic problem into a static one. A mesh is assigned to the tire in the usual fashion, but the rotation of the tire is treated as a flowing motion of material moving through the mesh, similar to a fluid flow analysis. This requires that the finite element program has the appropriate capability. The technique is described by Becker et al [4] and Padovan [5]. Additional forces must be included to represent the inertial effects of the rotating mass of the tire material and spatial derivatives taken on the tread surface tangent to the direction of motion must be calculated to address the contact patch behavior. The road surface element is assigned a magnitude and direction representing the vehicle velocity. The velocity of the nodal points on the tread surface of the tire are calculated from the angular velocity of the tire and the location of the nodal points along streamlines of surface nodal points. At each nodal point in the contact patch, the velocity of that point is compared with the velocity of the road surface. The difference between the two velocity values defines the slip velocity. This quantity is used to calculate the frictional force at that point. The friction law suggested by Becker generates a frictional force proportional to the slip velocity, the normal force and the surface coefficient of friction for slip velocities up to a specified value. For slip velocities above the specified value, the dependence on speed is eliminated with the force proportional to the normal force and the surface coefficient of friction. The direction of the friction force is opposite to that of the slip velocity.

This approach effectively turns the problem of a rolling, cambered, cornering tire into one that is only slightly more computationally intensive than a typical mounted-inflated-deflected static problem. The advantage of the significant reduction in processing time

which comes with this approach, does not come without some penalties. The model must be precisely axisymmetric. For tires with smooth treads or straight circumferential grooves, such as aircraft tires and some farm and racing tires, this provides a workable approach for analysis. Estimates of force and moment quantities, contact patch pressures and traction forces are obtained. However, although tires with conventional tread patterns may be analyzed this way, details of the tread pattern can not be represented exactly.

The third approach is to use the explicit finite element method described previously. This method lends itself to the calculation of global force and moment quantities generated by a rolling tire, and the response of a rolling tire to an impact with a road irregularity. Koishi, Kabe, and Shiratori [6] reported results for a passenger tire operating at various slip angles. The results of lateral force vs. time were shown for slip angles of 0°, 1°, 2° and 3°. In these analyses, 'time' refers to the time for the dynamic event and not the computer time needed to complete the analysis.

The results exhibit two characteristics. The first is an oscillation from step to step of 0.6 kN for all the loading conditions. For comparison, the measured lateral forces for the four conditions were approximately 1, 5, 9 and 13 kN. The second feature is that the average result for a sequence of steps also shows an oscillation of approximately 1 kN. These oscillations do not negate the validity of the solutions but the analyst must take them into account in assessing the precision of the results.

Kamolaukus and Kao [7] analysed the problem of a rolling tire impacting a full width cleat on a rotating test wheel using the explicit method. Results showed the vertical and tangential reaction force traces immediately after the tire strikes the cleat, along with the frequency content of the vibrations following impact. During the static inflation and loading step, they carefully applied nodal damping and observed the results as the structure reached static equilibrium. To assure that all of the kinetic energy had been dissipated, they allowed the process to continue through a number of additional time iterations. The tire was then rotated against the load wheel until equilibrium was reached at the desired speed. The steady-state dynamic equilibrium was evaluated for stability. Finally, the cleat effect was introduced, causing horizontal and vertical reaction forces and the harmonic response. To demonstrate the stability of the solution, they allowed the analysis to continue until the bump had made a total of six passes through the contact region. The predicted vertical and lateral peaks were larger than those measured experimentally, but the frequency content and shape of the response curves were similar to experimental curves. The authors suggested a number of causes for the discrepancy. This analysis was the first attempt at a difficult problem, and the objective was to show that the explicit approach could be applied successfully.

These examples show the types of problems that can be addressed with finite element analysis. Other applications could be included. The list will expand as FE programs add capabilities, and as faster and more powerful computers become available.

4. Tire cord tensions

For a radial tire construction, no corresponding equations have been published for natural shape and internal cord tension as for a bias-ply construction. We can, however, use fundamental mechanics principles to calculate certain quantities. Key to this approach is selecting appropriate free body sections of the tire. We shall evaluate a few different sections.

Simplified estimate of belt cord tension at centerline

If we treat the belt as a cylindrical hoop under internal pressure, we can make an estimate of the cord tension at the belt centerline using the basic equation for stress in a cylinder: $\sigma = p\, r\, /\, t_h$. We typically use the stress resultant in place of stress and the relationship between them is $\sigma\, t_h = N$. For the case of a two-belt layup, with the cords at an angle of α to the centerline, inflation pressure p, cord tension t, and a cord count of n_b cords per length measured perpendicular to the cords, the hoop stress resultant, N_θ, is given by

$$N_\theta = 2\, t\, n_b\, \cos^2 \alpha = p\ \rho_0.$$

One of the cosine terms arises from the cords making an angle of α while the second comes from the reduction in the cord end count because the cords intersect the meridian at an angle, $90^O + \alpha.$, to the cord direction. Solving for the cord tension **t** gives
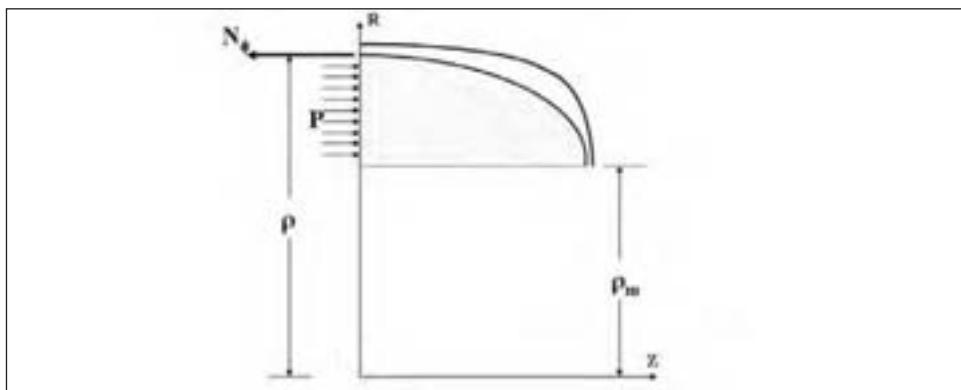
$$t = p\, \rho_0\, /\, (\, 2\, n_b\, \cos^2 \alpha\,).$$

This is an upper bound for the cord tension at the crown of a radial passenger tire, because the calculation is made assuming that the belt has an infinite width and a perfectly flat cross section. The transverse tread curvature and the sharing of load with the ply cords reduces the total load on the belt.

Improved estimate of belt cord tension at centerline

We now include the effects of belt curvature in the meridional direction and of the load that is carried by the ply cords, using the equilibrium condition for a doubly curved membrane surface and the mechanics of composite material. The first step is to calculate N_ϕ at the centerline by using a free body diagram of a 360° section of the tire that has been cut at the centerline and at the location of the widest point of the sidewall. This is the same equation that was used in Section 1. We treat the centerline circumferential curvature ρ_θ, the centerline meridional curvature ρ_ϕ , and the radius to the widest point of the tire ρ_m, as known quantities. (See figure 6.3)

Figure 6.3: Equilibrium section

At equilibrium, the effect of air pressure acting in the axial direction is balanced by the meridional force at the tire equator:

$$2\, \pi\, \rho_0\, N_\phi\ = p\, \pi\, (\rho_0^2 - \rho_m^2).$$

This equation yields N_ϕ in terms of known quantities, where N_ϕ is the sum of the stress resultants in the belt, N_ϕ^b , and body ply, N_ϕ^p:

$$N_\phi = N_\phi^b\ + N_\phi^p$$

Using the equation for the equilibrium of a doubly curved surface,

$$N_\theta = \rho_\theta (p + N_\phi / \rho_\phi)$$

yields the hoop stress resultant, N_θ. The value of the curvatures ρ_ϕ and ρ_θ can be taken directly from the tire mold or from an actual measurement on the tire. The circumferential curvature ρ_θ is the radius to the belt package and is equivalent to ρ_0. Note that only the belt cord tension contributes to the circumferential stress resultant N_θ as there is no circumferential contribution from the radially-directed ply cords.

Using the value for N_θ, the belt cord tension t_b can be calculated from

$$t_b = N_\theta / (2 n_b \cos^2 \alpha)$$

or in terms of initially-known quantities,

$$t_b = p \rho_\theta [1 - (\rho_0^2 - \rho_m^2) / (2 \rho_\phi \rho_0)] / (2 n_b \cos^2 \alpha).$$

Note that as ρ_ϕ becomes larger, i.e. as the belt becomes flatter, t_b approaches the value obtained using that for a simple cylindrical hoop. To obtain the ply cord tension, we apply the netting relation to the belt cords to calculate that portion of N_ϕ, denoted $N_\phi{}^b$, that is contributed by the belt cords:

$$N_\phi{}^b = N_\theta \tan^2 \alpha$$

We now calculate that portion of N_ϕ which comes from the body ply cord tensions $N_\phi{}^p$, by subtracting the portion that comes from the belt from N_ϕ. This gives

$$N_\phi{}^p = N_\phi - N_\phi{}^b$$

With $N_\phi{}^p$, we can calculate the belt and ply cord tension using

$$t_p = N_\phi{}^p / (n^p \ n_l)$$

where n^p is the number of ply layers. Substituting the value of $N_\phi{}^p$, the ply cord tension in terms of the given quantities is

$$t_p = p [\{(\rho_0^2 - \rho_m^2)(1 - \rho_0 \tan^2 \alpha / \rho_\phi) \}/2 \rho_0^2 - \rho_0]/ (n^p * n_l)$$

This calculation, using the additional information of the meridional curvature and sidewall shape, gives an improved estimate of the belt cord tension compared to that assuming a simple cylindrical shape and also gives an estimate for the centerline body ply cord tension under inflation loading.

Sidewall cord tension

For a radial tire, there is no equilibrium approach that will allow the calculation of the sidewall cord tension directly in terms of measurable geometric quantities. The sidewall tension is directly proportional to the radius of curvature of the sidewall, and this quantity is related to the length of the sidewall cords and the distance from the edge of the belt to the bead. If we can make an estimate of this curvature, we can estimate the cord tension. For a relatively flat sidewall the cord tension is relatively high, while for a rounded sidewall, the cord tension is relatively low.

It should also be noted that the forces in the sidewall cords pull the belt edges radially inward. If this force is large, as for a flat sidewall, the characteristic stress concentration

at the belt edge is reduced. If the force is small, as with a more curved sidewall, the stress concentration is increased. On the other hand, the handling performance typically improves with a flatter sidewall. Achieving the proper balance is a major challenge for the tire designer.

Bead tension

The bead tension is a result of the interference fit between the tire bead and the rim and the tension in the cords that are anchored around the bead due to the inflation pressure. The interference is required to retain the tire firmly on the rim so that the tire does not rotate relative the to wheel under driving and braking maneuvers nor unseat from the rim under extreme cornering maneuvers. The load in the bead due to the interference fit may be estimated by combining known information (bead bundle diameter, rim diameter, thickness of material underneath bead, etc.). For the radial tire, the load due to the cord tension is estimated by the equation

$$B_t = t_s \, \rho_b \, \cos \phi$$

where t_s is the sidewall cord tension, ρ_b is the radius of the bead, and ϕ is the angle of approach of the cords to the bead. However, care must be used when combining these two results as the interference load is reduced as the inflation load is increased. It is important that the interference between the bead and the rim is sufficient to hold the bead firmly under all of the conditions mentioned above. There appears to be no published data on bead bundle cord tensions.

Total belt loading - A special case
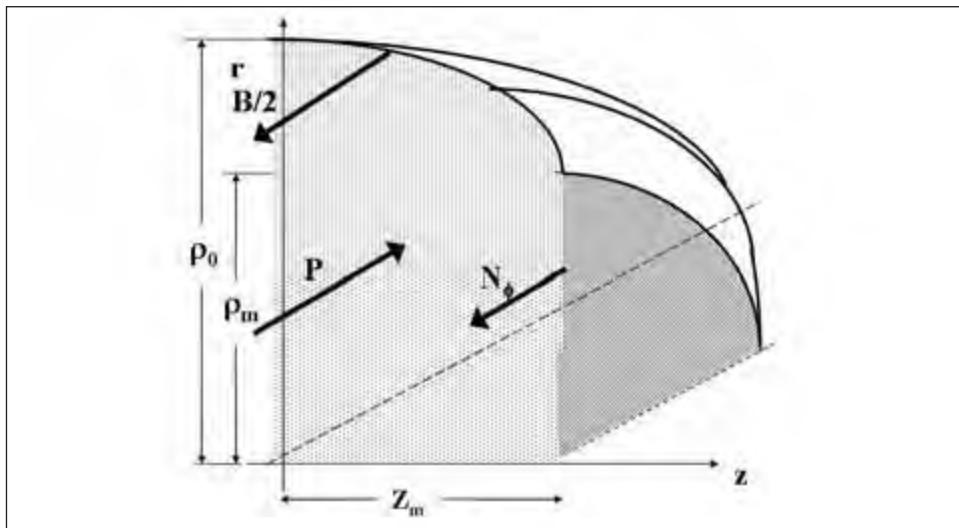
We can calculate the total load carried by the belt package. This calculation uses a carefully-chosen free body diagram of the inflated tire and requires knowing the sidewall cord tension at the widest point of the tire. Some aspects of the performance of a tire are improved by increased tension in the belt, and hence increased "rigidity". For example, both handling and tread wear are generally improved.

The free body diagram for this case is a 90° wedge section, cut at the equator along the tread centerline and along the sidewall following a circular arc at the widest point of the cross section. For ease of calculation, the cavity air is included in the section. In addition, the cavity with inflation air is extended all the way to the rotational axis, as shown in figure 6.4.

Summing forces along a diameter involves the inflation pressure p acting on the rectangle ρ_m x z and the area between ρ_o and ρ_m, the stress resultant acting along the sidewall at the widest point, N_ϕ x ρ_m, and (one-half) of the total load in the belt B. The stress resultant at mid-sidewall must be obtained from either an experimental measurement or from a calculation based on the measured radius of curvature at mid-sidewall. For the area between ρ_0 and ρ_m, the term $\pi z (\rho_o - \rho_m)$ represents the area of an ellipse with major and minor axes, z and $(\rho_o - \rho_m)$. The term z ρ_m is the area between the widest point on the tire contour and the axis of rotation. If the area of the actual shape could be calculated more accurately, that term may be used in the equation in place of the value for an assumed ellipse.

$$p \, z \, [\rho_m + \pi \, (\rho_o - \rho_m)] = B / 2 + N_\phi \, \rho_m$$

Figure 6.4: Free body diagram for belt tension

This equation shows that the total belt tension can be increased by increasing the total width of the tire and/or by increasing the area under the belt but above the line through the widest point on the tire cross section. It also shows that the shape of the sidewall from the widest point on the cross section to the bead area has no influence on the total belt tension.

5. Related topics
Stored energy in an inflated tire
The work that is expended in forcing air into a tire is stored as potential energy in the compressed air in the tire cavity. The amount of energy stored is substantial and a sudden release of this energy due to a catastrophic failure of the carcass can be damaging. In the interest of safety, it is important that any person working in the vicinity of tires be aware of this danger and take appropriate precautions to avoid injury.

Tire manufacturers routinely test their product for ultimate pressure to assure the carcass integrity under normal operating loads. The burst pressure is usually 6 to 10 times greater than the recommended operating pressure. To assure the safety of laboratory personnel, water is used to fill and pressurize the tire, because water is relatively incompressible and when the tire bursts, only very little stored energy is released, and the carcass remains relatively intact, except in the immediate area surrounding the failure. If air were to be used as the inflation medium instead, sudden release of the much greater amount of stored energy would cause substantially more damage to the tire and the surrounding area.

The equation for calculating the stored energy W in the compressed air within a tire is given by

$$W = (p_2 V_2 - p_1 V_1) / (1 - k)$$

where k is the gas constant for air. The pressure is absolute pressure. State 1 refers to the compressed pressure and volume and state 2 refers to the free air pressure and volume. Table 6.1 lists the amount of energy stored in different types of tire.

Load transfer

Many structures carry their intended load by creating tensile or compressive forces within their volume. These structures are stress free in the unloaded state and become stressed in the loaded state. Tires, on the other hand, actually transfer a portion of their intended load by relieving the pre-stress caused by inflation pressure. At the interface between sidewall and belt, the contact patch flattens the belt package and displaces it towards the rim. This causes the sidewalls to bulge outward, reducing the radius of curvature in the sidewall, which results in a reduced cord tension. For an inflated tire under no load, the sidewall tire cords are anchored to the beads and they pull the beads radially outward. When the tire is loaded at the contact patch, the reduced tension in the sidewall cords in the contact region reduces the loading by the cords on the bead, causing the bead to be pushed against the rim. This increased load on the rim is the end of the load path from the road to the rim.

Table 6.1

Type of tire	Inflation pressure	Stored energy (ft-lbs)	Height that a bowling ball would be thrown (feet)
Automobile	35	10000	625
Automobile	250	68000	4250
Truck	105	80000	5000
Farm tractor	45	136000	8500
F-4J jet fighter	480	394000	24625
Eathmover	75	597000	37313
C-130 military transport	570	2889000	180563

Data supplied by Dr. Joseph Walter

However, the load follows a second path from the contact patch to the rim. When the belt hoop deforms, it flattens in the contact patch area and is also displaced vertically by a small amount. For a typical passenger tire, the section of the tread opposite the contact patch displaces away from the rim by approximately 10% of the displacement at the contact patch. This motion causes two related changes, which aid in the load transfer. First, in the area of the tire directly opposite the contact patch, the sidewall curvature increases slightly which causes the bead to pull away from the rim slightly, in the opposite manner to that at the contact patch. Second, in regions that are about 90° from the contact patch, cords that were directed radially are now angled slightly upward. This helps to lift the rim and transfer the load.

So we see that, although the load from the contact patch is applied in one portion of the tire tread, the load path into the rim involves the complete circumference of the tire.

6. Experimental approaches

Interest in radial tire construction began in the domestic tire market in the early 1970s. At that time, FEM was only beginning to be developed as an engineering analysis tool. Analysis of an inflated tire was available in the mid 1970s but the capability to analyze an inflated and deflected tire did not become available until the late 1970s. Because there were no analytical techniques available to understand radial tire behavior in the beginning, new experimental methods were developed to measure properties related to the performance of radial (and bias-belted) tires.

Rubber strains

The level of strain in the rubber in various regions of the tire is an important quantity for tire designers and compounders. If the strains approach the limit that the compound is capable of withstanding, failure may occur. Key areas of interest include the outer surface at the mid-sidewall and regions near the belt and ply endings. In addition, strains in the inner surface and the crown area were of general interest to better understand the basic behavior of the tire.
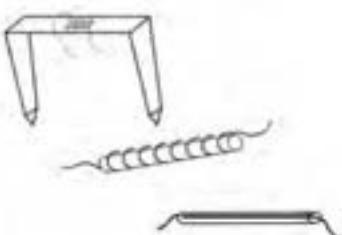
Because strain is a tensor quantity, it is necessary to measure strain in three directions on the surface. Typically, three gauges are placed at 0^0, 45^0 and 90^0 to the radial direction, and offset slightly around the circumferential direction. The values of maximum and minimum elongational strain, and their directions, along with the maximum shear strain, may be calculated from the three measurements.

One of the challenges in measuring rubber strains on the surface of a tire arises from their large magnitude. Typical commercial strain gages are designed for use on metal, where strains are of the order of 0.5% or less. But typical operating strains on the surface of a tire are of the order of 20% to 50%. A number of techniques have been developed to measure them. One, first suggested by Kern [8], is a simple thin metal strip formed into a "U" shape (figure 6.5) with a conventional strain gage attached to the base of the "U". The pointed tips of the "U" are pressed into the surface of the tire. Relative movement of the tips creates a bending deformation in the base of the "U" that can be measured by the attached strain gage. This device typically has a gage length of 10 to 20 mm, so it is not capable of making the local strain measurements that can be done with smaller gages. This limitation is common to all of the gages described in this section. Figure 6.5 shows various gages used for measuring tire surface strains.

A second type of gage consists of a rubber cylinder with a fine wire wrapped in a helical pattern around the diameter. This combination is attached with an adhesive to the tire surface. The level of strain can be measured by the change in resistance of the helically wound wire.

A third type of gage is made by molding a rubber block with a small cavity running along the long axis of the block. The dimensions of the block are approximately 3 x 3 x 30 mm. The cavity is filled with a continuous column of liquid mercury and the device is attached with an adhesive to the tire surface. Small lead wires are inserted into the ends of the cavity and the small changes in resistance of the mercury column that occur when the block is stretched or compressed can be calibrated to yield the magnitude of the strains.

Figure 6.5: Types of elongation gauges
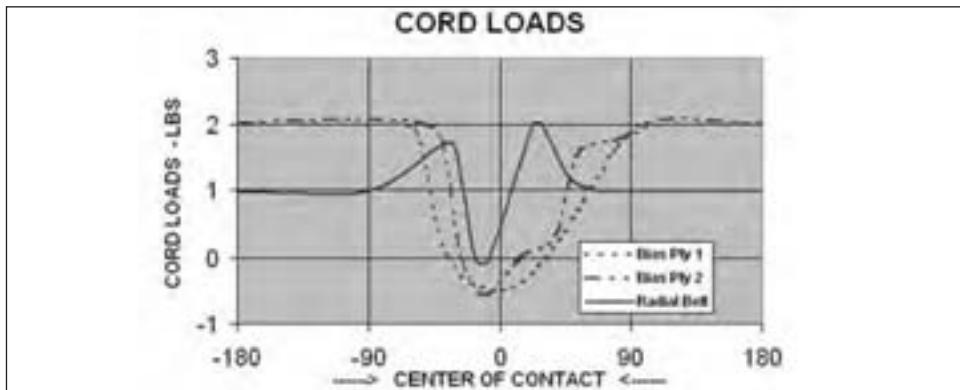
Walter and Jannsen [9] applied a number of these gages to the internal and external surfaces of bias, bias-belted and radial tires. They examined the strains at approximately six locations on the outer surfaces and five locations on the inner surfaces. The results showed that the patterns of surface strains are different for each type of tire.

Cord loads

Until the finite element method was developed to the level where it could be applied to mounted, inflated, loaded tires, it was not possible to determine cord loads. The tire industry had gained sufficient experience to design bias-ply tires successfully, but with the advent of belted tires an understanding of cord tensions in these constructions became important. Experimental methods were therefore developed to measure cord tensions directly. Walter[10,11] applied a technique using a small metal billet with holes at each end, and with strain gages attached to the billet between the holes. Cords were threaded through the holes in the billets. At this point, the assembly can be calibrated in a test machine equipped with a standard load cell to determine the relation between strain gage output and cord tension. Cords were then removed from a "green" uncured tire and replaced by the test assembly, with the billet at the site of interest. The tire build was then completed, with the leads from the strain gage being carefully led out of the tire carcass. The tire was then cured in the mold and the finished tire tested in the laboratory under controlled conditions. Results are shown in the following figures for cord loads at the centerline for bias and radial tire constructions.

Another type of gage was developed by Clark and Dodge[12]. It consisted of a small beryllium copper cylinder, sized to slip snugly around the cord. Small strain gages were attached to opposite sides of the cylinder, thus minimizing the effect of bending in measuring tensile forces. The cylinder was attached to a single cord in the "green" uncured tire the cord at the point of interest, using an epoxy adhesive. [An earlier version was clamped between the two ends of a cut cord.] The tire building process was then completed and the tire cured, as with the billet type gage.
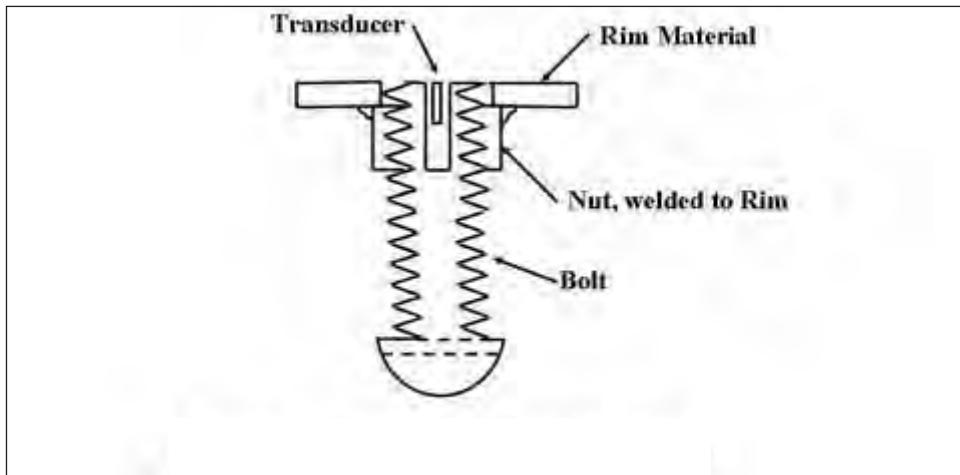
Bead seat pressures

The contact region between the rim and the bead region of the tire is another area that has been studied experimentally. Initial results were imprecise because the large size of standard pressure transducers made them unsuitable in regions of high pressure gradients.

Walter and Kiminecz[13] developed a small pressure transducer that could be installed in an axial hole in the end of a standard 8/32 inch bolt, as shown in figure 6.6.

Using a 8/32 inch nut welded on the outside surface of the rim, relative to the tire cavity, the bolt was inserted so that the end of the transducer was flush with the inside surface of the rim. Measurements of rim pressure could be made in this way while the tire was rolled under various combinations of load, pressure, camber and steer.

Figure 6.6: Bead seat pressure gauge

Contact patch forces and displacements

The forces, both normal and shear, and slip motions in the contact patch are important because they affect the tire's resistance to wear. Wear can take different forms. Long-term wear occurs when the tire wears uniformly and slowly. Non-uniform wear refers to any one of a number of different types of wear. Shoulder wear is a rapid loss of tread material at the inside or outside edge of the tread. It can be caused by a defective mold shape, excessive cornering loads or incorrect wheel alignment. Heel-toe wear is excessive wear on the trailing edge of a sequence of tread elements. Rib wear is excessive wear on one or more ribs and may be caused by a combination of mold shape and carcass design. Truck tires can exhibit a wear pattern in which the edges of the ribs have eroded away while the center of the rib appears normal.
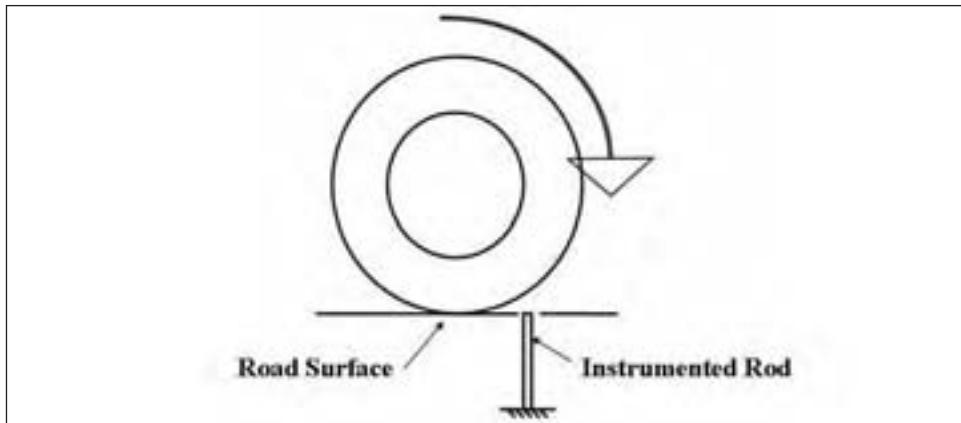
All of these wear types are related to the combination of normal and shear force and the amount of slip that occurs as tread elements pass through the contact patch. Even when the tire is rolling straight ahead, and not generating a significant lateral force, shear forces are generated in the contact patch. Characteristically, a radial tire will roll forward a distance equal to the circumference of the belt package with each full revolution. Since the actual circumference of the tire is greater than the circumference of the belt package because of the thickness of the tread, the tire must accommodate the difference in distance rolled. Typically, the fore-and-aft component of the shear force grows uniformly from zero at the leading edge of contact, reaching a maximum towards the trailing edge. At this point, the tread elements are released from the road surface and recover their unloaded shapes. This buildup and release of shear displacement is the cause of the difference

between the tire circumference and the distance traveled in one revolution. Under braking, accelerating, camber and cornering loads, the slip patterns are more severe and more complex (see chapter 7).

In order to study forces and displacements in the contact region, a number of test methods were developed. For example, a cylindrical rod carrying strain gages, and calibrated to measure normal and lateral forces, was mounted in the surface of a model track, with the end flush with the track surface as shown in figure 6.7.

A tire was rolled over the track with desired steer and camber settings and also with applied drive or a braking torques. It was rolled at least one complete rotation to allow the shear forces to reach stable values representing continuous rolling. For a tire with a tread pattern, multiple passes were necessary to obtain data for the complete pattern. But with a single transducer, a substantial amount of time was required to test a tire under a single loading condition.

Figure 6.7: Footprint pressure transducer

Another test machine was developed at NASA-Langley Research Center by Howell, Tanner and Vogler[14]. It was designed to apply the loads and inflation pressures of large aircraft tires and it had a series of load transducers located across the width of the tread, to reduce the number of passes required to study the complete contact area of the tire. This machine was able to measure contact forces accurately, but not the actual slip that took place in the contact patch.

In a test device developed at Smithers Scientific Services, the transducer was capable of measuring motions at one location in the contact patch. The transducer consisted of a thick-walled tube, strain gaged and calibrated as in earlier test machines. A thin needle-like rod passed through the center of the tube, carrying gages to monitor displacement of the tip (see figure 6.8).
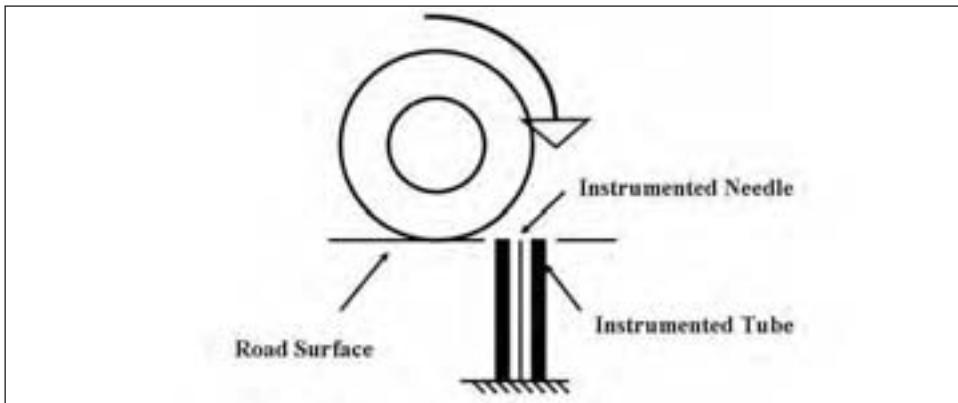
As the tire rolled over the transducer, both normal and shear forces and the surface motions were measured. The shear force and displacement could be combined to obtain the energy expended in slip. However, these test devices were limited to rolling at slow speeds.

Lazeration[15] designed a test machine in which the actual slip motion of a point on the tread in the contact patch could be observed directly. A thick glass plate was used in place of the road surface, and a loaded tire was slowly rolled over it at a specified steer and camber angle while a video camera recorded motions in the contact patch of marked points on

the tire surface. Using image recognition software, the motion of each mark was record-
ed and the slip path plotted. This information was combined with data from a force trans-
ducer similar to those described earlier, and the values of slip energy were calculated.
Although the glass surface does not have the same characteristics as an actual road, this
approach gives a visual record of slip behavior with no restriction on the magnitude of
slip. Contact patch and footprint phenomena are fully described in chapter 7.

   The process of designing and building the special transducers required to measure the
surface and internal stresses, the tedious process of installing the transducers in tires, and
the careful handling required during testing, made testing a time-consuming and expen-
sive process. In addition, a transducer was a single use item and many were required to
obtain a complete picture of the stress pattern in a complete tire. As a result, after labora-
tory experiments were found to validate FEM results, tire designers tended to rely on FEM
calculations, rather than on experimental measurements .

Figure 6.8: Footprint pressure and motion transducer

7. Problems

Tire Description
Size: P235/75R15
Inflation Pressure   30 psi
Diameter   28.25 inch
Section Width   9.50 inch

Belt Cord Angle 22^0
End Count for Belt   18 epi (ends/inch)
Tread Rubber Thickness   0.60 inch
Belt Width   7.75 inch
Number of Body Plies   2
End count for Body Plies at Bead 28 epi
Bead Construction   5 x 5 (25 strands)
Rim Diameter   15 inch
Rim Width   6 inch
Tread Radius   42 inch

1. Calculate an approximation for the centerline belt cord tension in the tire described above, using only the first six lines of information.

2. Repeat the calculation using all of the information available for a more accurate approximation.

3. Estimate the contained air volume in the tire. Using this volume, calculate the energy stored in the air of the inflated tire.

4. By measurement, you determine the sidewall radius of curvature at mid-sidewall is 9.5 inch. Determine the cord tension in the sidewall cords. Using this value, estimate the bead tension due to the inflation loading.

8. References

1. Purdy, J. F., *Mathematics Underlying the Design of the Pneumatic Tire*, Hiney Printing Company, Akron, Ohio, 1963.

2. Richards,T., Sundaram, S. V., Brown, J.E., and R. L. Hohman, *Modal Analysis of Tires Relevant to Vehicle System Dynamics*, International Modal Analysis Conference III, Orlando, FL, January 28 – 31, 1985.

3. Rothert, H., and R. Gall, *On the Three Dimensional Computation of Steel Belted Radial Tires*, Tire Science and Technology TSTCA, Vol. 14, No. 2, Apr-Jun, 1986.

4. Faria, L., Bass, J., Oden, J.T., and E. Becker, *Three Dimensional Rolling Contact Model for a Reinforced Rubber Tire*, Tire Science and Technology TSTCA, Vol. 17, No. 3, Jul.-Sep., 1989.

5. Kennedy, R. and J. Padovan, *FEA of a Steady Rotating Tire Subjected to Point Load or Ground Contact*, Tire Science and Technology TSTCA, Vol. 15, No. 4, Oct-Dec., 1987.

6. Koishi, M., Kabe, K., and M. Shiratori, *Tire Cornering Simulation Using an Explicit Finite Element Analysis Code*, Tire Science and Technology TSTCA, Vol. 26, No. 2, Apr-Jun, 1997, pp. 109-119.

7. Kamoulakos, A. and B. G. Kao, *Transient Dynamics of a Tire Rolling over Small Obstacles — A Finite Element Approach with Pam-Shock*, Tire Science and Technology TSTCA, Vol. 22, No. 2, Apr-Jun, 1998 pp. 84-108.

8. Kern, W. F., *Strain Measurements on Tires by Means of Strain Gauges*, Revue Generale du Caoutchouc, Vol 36, October 1959.

9. Janssen, M. and J. D. Walter, *Stresses and Strains in Tires*, Akron Rubber Group, Fall Meeting, 1972.

10. Walter, J. D., *A Tirecord Tension Transducer*, Textile Research Journal, Vol 39, February 1969.

11. Walter, J.D. and G.L. Hall, *Cord Load Characteristics in Bias and Belted-Bias Tires*, Society of Automotive Engineers, 690522, 1969.

12. Clark, S. K. and R. N. Dodge, *Development of a Textile Cord Load Transducer*, ORA Report 01193-1-T, The University of Michigan, May 1968.

13. Walter, J.D., and R.K. Kiminecz, *Bead Contact Pressure Measurements at the Tire-Rim Interface*, Society of Automotive Engineers. 750458, 1975.

14. Howell, W., Tanner, S., & Vogler, W., *Static Footprint Local Forces, Areas, and Aspect Ratios for Three Type VII Aircraft Tires*, NASA Technical Paper #2983, Feb. 1991.

15. Lazeration, J., *An Investigation of the Slip of a Tire Tread*, Tire Science and Technology TSTCA, Vol. 25, No. 2, Apr-Jun, 1997, pp. 78-95.

Symbols

ρ_0, r_c — Centerline radius

θ_0 — Cord angle at the centerline,

measured from the circumferential direction

ρ, r — Radius to general point on carcass line

Δs — Element of length along carcass line

N_θ — Stress resultant in circumferential direction

N_ϕ — Stress resultant in meridional direction

α — Cord angle

ρ_m, r_w — Radius to the widest point on tire cross section

p — Inflation pressure

R — Radius of cylinder

T — Thickness of cylinder

σ — Stress in cylinder wall

ρ_θ — Radius of curvature in circumferential direction

ρ_ϕ — Radius of curvature in meridional direction

z — Axial distance to point on tire carcass line

t — Cord tension

t_h — Cord tension in belt cord

t — Cord tension in carcass cord

n_b — Number of cords / length — belt

n_p — Number of carcass ply layers

B_t — Bead tension

t_s — Ply cord tension

ϕ — Carcass tangent angle

ρ_b — Radius of bead

B — Total load in belt package

W — Energy stored in air contained in tire

p_1, p_2 — Pressure at conditions 1 & 2

V_1, V_2 — Volume of air at conditions 1 & 2

k — Adiabatic gas constant

Chapter 7
Contact Patch (Footprint) Phenomena

by M. G. Pottinger

Chapter 7
Contact Patch (Footprint) Phenomena
by M. G. Pottinger

1. Introduction

The tire has three boundary regions. One is the zone of contact with the road or test surface and the other two are the zones of contact between the tire bead areas and the rim. This chapter is concerned with the contact between the tire and a road or test surface.[1] The road surface is assumed to be dry and rigid, with limited texture unless otherwise noted. The term <u>footprint</u> is employed in place of the commonly-used alternative: <u>contact patch</u>. If a term is not defined in the text, the definition found in SAE J2047 [1][2] applies.

The study of the tire footprint is a very complex matter for several reasons.

The tire is a doubly-curved surface. It is curved both circumferentially and transversely. A doubly-curved surface is not a developable surface and cannot be made to conform to a flat or round surface simply by bending. Conformance requires that the tire structure be stretched and compressed as well as bent.

The tire is a relatively soft or flexible, pneumatically pre-stressed structure whose behavior depends on applied loads and operating conditions.

The friction of the road or test surface affects the deformation of the tire and, hence, the tire's footprint.[3]

In spite of these difficulties the obvious association between the tire footprint and other properties of the tire, including traction, tire/pavement interaction noise, ride over road irregularities, and wear, motivated engineers to study tire/road contact.

It is uncertain when the first studies of the tire footprint were conducted, but at least prints of the footprint area were commonly made by the early 1930s [2]. This work was preceded by mathematical studies of the contact of high-modulus elastic bodies from the time of Hertz [3], with practical applications to gears, rolling bearings, and contact between railroad wheels and rails. Certainly, contact studies related to the endurance of roads and rutting were well underway before the dawn of the twentieth century.

In the two editions of the book, "The Mechanics of the Pneumatic Tire", edited by Clark, footprint literature is reviewed up to 1981 [4,5]. In this chapter the discussion is primarily based on sources published since 1981. The earlier literature is discussed only when it provides the single or best source of information on a given subject.

This chapter primarily covers footprint physics and experimental techniques. Analytical techniques such as finite element analysis are mentioned as appropriate, but no attempt is made to discuss these techniques thoroughly. In order, we discuss the terminology used for describing the tire footprint, equipment and methodologies that have been used for studying the footprint, and footprint physics, followed by a few concluding remarks.

---

[1]The surface is called a road surface from this point onward.
[2]Numbers in [brackets] denote references at the end of the chapter.
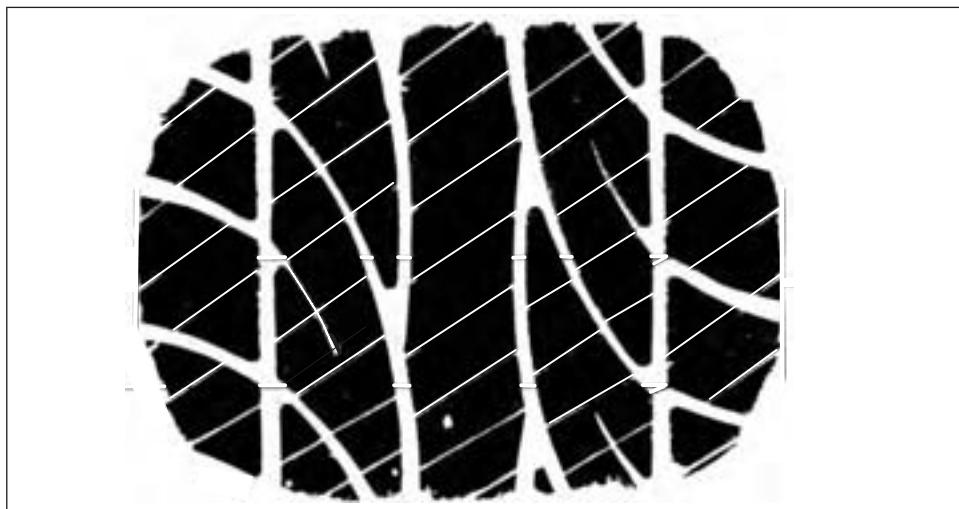
2. Describing the tire footprint

A general discussion of tire footprint mechanics or physics involves footprint geometry, tread pattern geometry, stresses, sliding displacements of the tread elements, and so on. Given the complexity of the situation different authors have chosen to adopt different viewpoints and ways of discussing the phenomena. The result can be confusion for an engineer reading several articles, because either the same phenomena is described differently, or the viewpoint and definitions used are not clearly stated. To avoid confusion, this section makes clear the geometric viewpoint adopted and the definitions used in this chapter. Further, whenever possible, figures taken from the literature have been transformed to fit the viewpoint and definitions used here. If it was not feasible to transform a figure, the descriptive parameters employed are provided along with the figure.

2.1 The basic viewpoint

In this chapter the footprint is viewed as if it were an ink impression, block printed, on top of the road, figure 7.1. This is consistent with the ink footprint images commonly used in the tire industry. The footprint is viewed either straight down, a plan view, as in figure 7.1, or from above and to the left or right rear, generating isometric images as shown later in this chapter.

Figure 7.1: Ink print of a tire footprint

2.2 The footprint axis system (FAS)
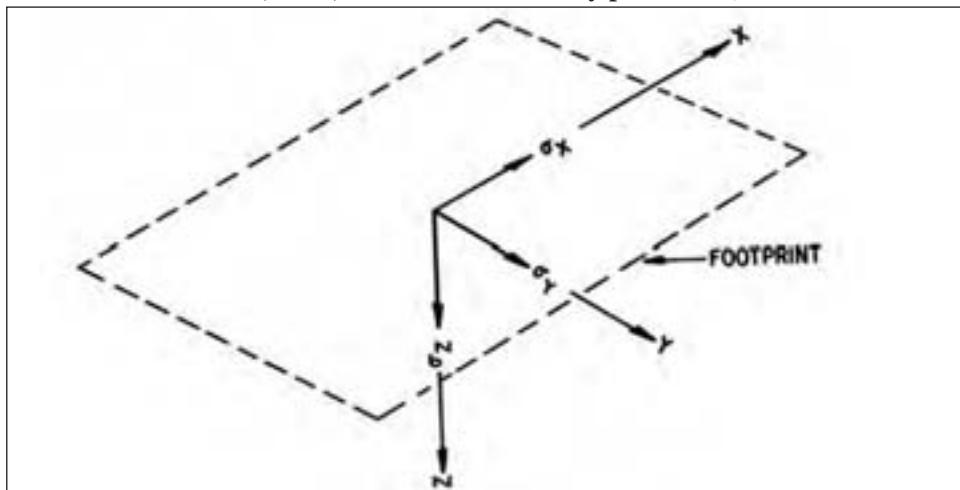
The tire footprint is described here in terms of an axis system based on, but not identical to, the SAE Tire Axis System, see Chapter 8. The Footprint Axis System (FAS) establishes a viewpoint and provides a coherent description of tire footprint behavior.[4] The differences between the two systems arise from the fact that instrumentation for measuring tire footprint behavior has a fixed orientation with respect to the road surface while instrumen-

---

[3]Plainly, a deformable road surface is going to affect the tire footprint. In the case of a wet surface, which is discussed later, water can alter the effective road surface topography preventing physical contact between the tire and road. This can completely alter the mechanics occurring in the tire footprint.

tation for measuring gross tire forces and moments has a wheel based orientation. Thus, it makes sense to discuss footprint behavior in terms of an axis system which is road surface fixed, but which can be readily related to the Tire Axis System.

The FAS, figure 7.2, is a right-handed, three axis, orthogonal Cartesian coordinate system with its origin at the contact center in the road plane. The road plane is the plane tangent to the road surface at the contact center. In experimental footprint studies it is the active plane for footprint sensing instrumentation. The contact center is the point in the road plane where the line defined by the wheel plane (the plane halfway between the rim flanges) to road plane intersection is cut by the projection of the spin axis onto the road plane. Thus, the contact center is defined by the wheel, not the tire[5], and is a common point for both the FAS and the SAE tire axis system. The FAS X-axis is in the road plane and is coincident with the tire's trajectory velocity. Positive X is in the direction of the tire contact center's velocity V over the road plane. The FAS Y-axis lies in the road plane perpendicular to the FAS X-axis. Positive Y is to the right when the system is viewed from the rear looking in the positive X-direction. The FAS Z-axis is defined by the cross product of + X into + Y. It is perpendicular to the road plane with its positive sense into the road plane.

Figure 7.2: Footprint axis system (reprinted from tire science and technology, vol. 20, no. 1, 1992 with Tire Society permission) [6]

Data in the FAS system may be transformed into data in the tire axis system or vice versa by a simple rotational transformation about the Z or Z' axes involving the sines and cosines of the slip angle, α.

2.3 Footprint stress definitions

Figure 7.2 shows the orientation σ_X, σ_Y, and σ_Z in the FAS. The indicated directions are the positive senses. In each case the stress is reported as the road acting on the tire. This is done for consistency with the SAE Tire Axis System and because the concern in tire/vehicle engineering is with the vehicle's path. As a consequence:

---

[4]The FAS is the author's suggestion to fill a gap in tire technology and has not so far been adopted by any standards organization.

[5]This avoids a definition in terms of the tire center of contact, which has no fixed location.

σ_X^+ pushes the tire forward (tending to accelerate the vehicle) and σ_X^- pushes the tire rearward (tending to cause deceleration). σ_X has both positive and negative values.

σ_Y^+ pushes the tire to the right and σ_Y^- pushes the tire to the left. σ_Y has both positive and negative values.
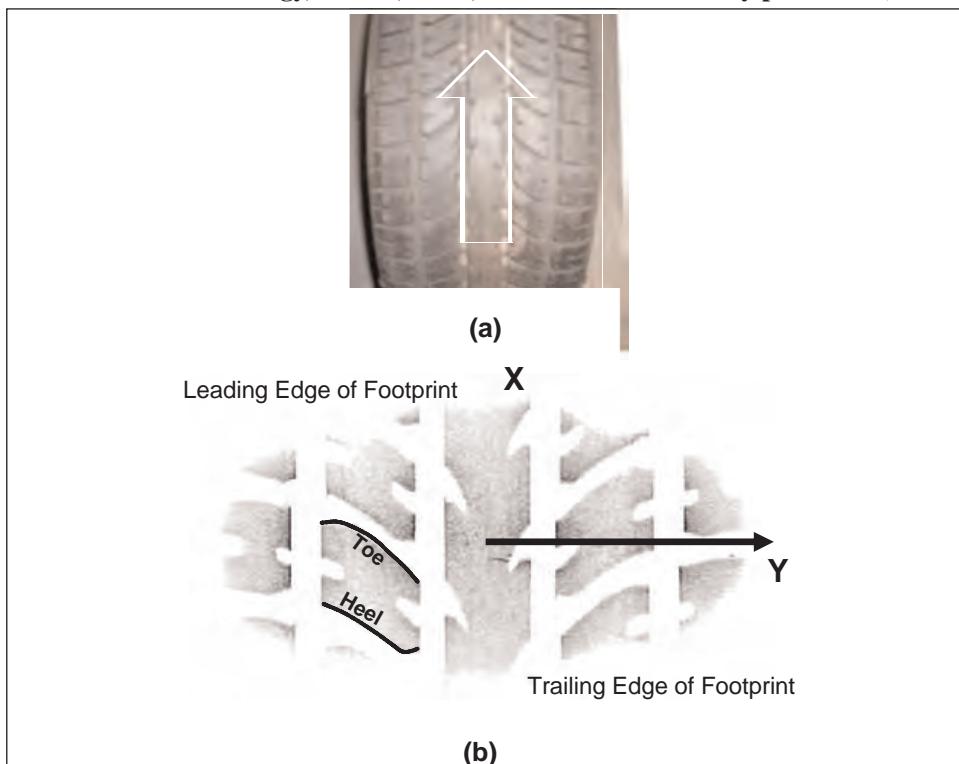
σ_Z^- supports the tire - it prevents the tire from sinking into the road. Thus σ_Z has only negative values.

2.4 Footprint geometry

Figure 7.3a shows a top view of a tire rolling toward the top of the page. Figure 7.3b is the resulting footprint image. The X and Y axes have been laid over the image and the edges of the footprint and tread elements have been designated. The edge of the footprint with the most positive X-value is referred to as the footprint leading edge. The edge with the most negative X-value is referred to as the footprint trailing edge. For blocks, elements generated by grooves cutting across the ribs, the first edge to enter contact, the block leading edge, is referred to as the heel. The last edge to enter contact, the Block Trailing Edge, is referred to as the toe. Note that the leading and trailing edges of the footprint and the blocks are reversed with respect to each other.

Ribs are counted from left to right along the Y-axis in order of increasing Y.
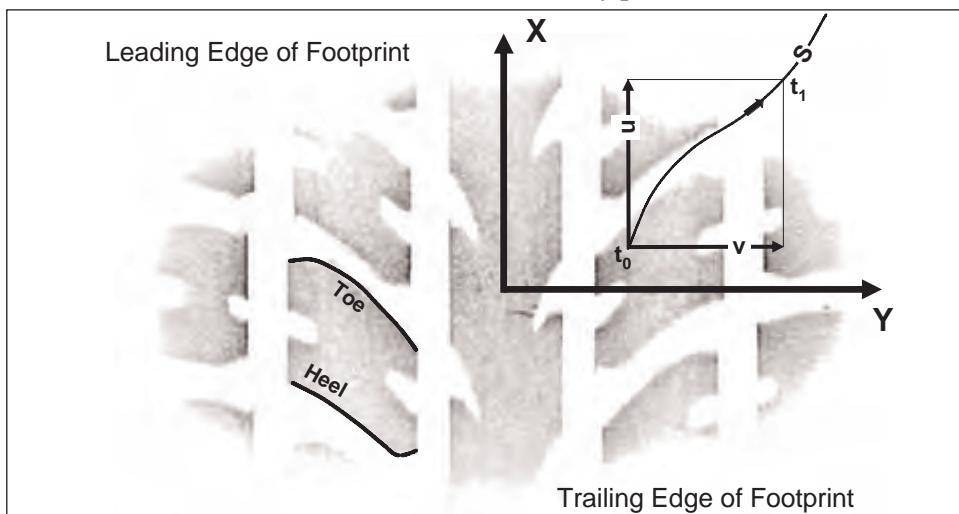
Figure 7.3: Positioning definitions for the footprint (based on a figure from Tire Science and Technology, Vol. 27, No. 3,   1999 with Tire Society permission) [7]

2.5 Footprint Displacements

Figure 7.4 shows the footprint image shown in figure 7.3b with addition of a graphic illustrating sliding displacements of points on the tread surface relative to the road. Two displacements are considered: u in the X-direction and v in the Y-direction. During contact, sliding displacement of a tread surface point is described by the difference between the instantaneous position of the point on the road surface and its position on the road surface at the time it first made contact. In figure 7.4 this is illustrated by a curved path S beginning at time t_0 showing u and v at a time t_1.

Figure 7.4: Definition of tread surface displacements relative to the road
(reprinted from Tire Science and Technology,
Vol. 27, No. 3,   1999 with Tire Society permission) [7]

3. Equipment and methodologies

This section is concerned with equipment and methods for studying the tire footprint and the mechanics of contact as the tire interacts with a road surface. Specific devices will be mentioned as representative of various technologies. Their mention should not be taken as a recommendation of these devices in comparison with similar ones available from other manufacturers.

For a discussion of the physics of the footprint see section 4 and its subsections.

3.1 Pure visualization

An imprint or picture of a tire footprint provides useful information: the gross size of the footprint (width and length), footprint shape (how the front and back of the footprint are curved), the amount of rubber actually in contact with the smooth printing surface (net contact area)[6], the amount of void area (the area of grooves, sipes, and so forth in the contact area), and, under the right circumstances, an idea of whether grooves are opening or closing in use.

Certain technologies, which will be discussed later in Section 3, provide data for normal stress, contact pressure, and slip displacement simultaneously with simple footprint visualization.

3.1.1 Ink block printing

For many centuries it has been common to produce pictures by carving a design on a wooden block, inking the block, and then pressing the block against a sheet of parchment or paper. Sometime early in the development of the tire, someone realized that if the surface of the tire were coated with ink, a paint, or other appropriate material, then an image of the tire as it sat statically on a smooth road could be produced by pressing the tire against a piece of heavy paper or cardboard. Figure 7.1 is an example of an ink block print. Figures 7.3 and 7.4 are prints made using carbon paper as the printing medium.

Making and measuring a good ink block print of a tire footprint takes skill: see ASTM F870 [8] for instructions. The method is usually only applied statically, because a rolling inked footprint does not contain information about the shape of the leading and trailing edges of the footprint. As discussed in section 4.1.1, static and rolling footprint shapes are not identical.
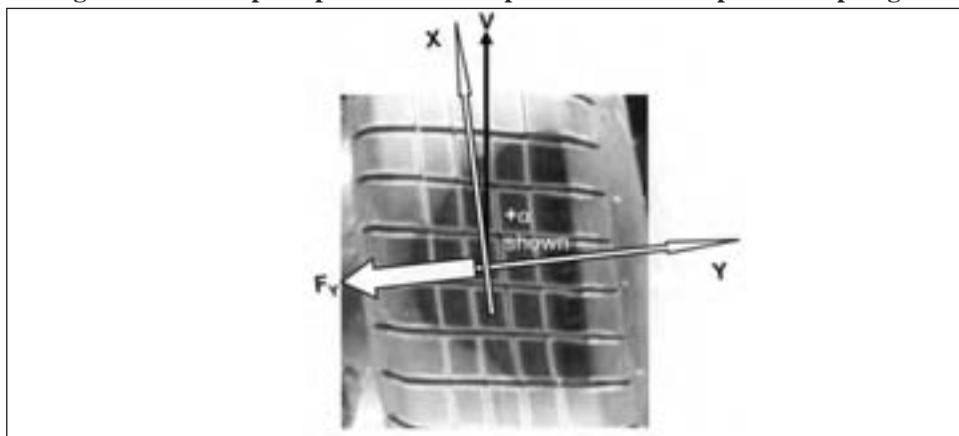
A variant of the ink block technique, in which a tire whose surface is coated with a release agent is statically loaded onto a surface covered with a sufficiently deep puddle of molding material, can yield information about changes in tread groove shape produced by loading as well as an image of the footprint surface.

3.1.2 Glass plate photography or video

Glass plate visualization is a way to study the tire footprint under dynamic as well as static conditions. Figure 7.5 is a photograph of a tire footprint taken while the tire operating at a slip angle was rolling at low speed.[7] The shape shown would not be available in static loading. In this picture, the image, which was taken from below, was flipped left to right so that the footprint itself appears as it would on the road surface in conformance with the viewpoint preference stated in section 2.1.

Sections 3.3.2 and 3.3.3 discuss methods in which modern computer-enhanced imaging can be used in conjunction with glass plate visualization to measure not only basic footprint shapes, but also to determine surface sliding or slip of the tread simultaneously.

Figure 7.5: Glass plate photo of the footprint of a tire at a positive slip angle
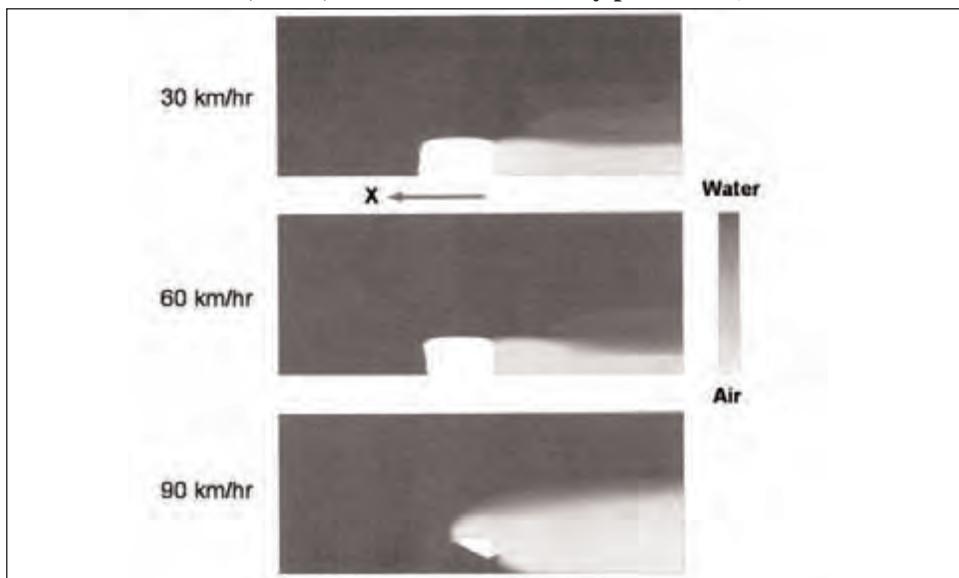
[6]For a surface with texture, like a real road surface, the actual area of tire/road contact is smaller because the tire's surface within the footprint cannot conform perfectly to road surface irregularities.

[7]The axes shown in Figure 7.5 are the SAE Tire Axes, as discussed in Chapter 8, not the FAS X and Y axes discussed in Section 7.1.2.

It is also possible to adapt glass plate photography to determine simultaneously both normal stress in the footprint and to image the footprint, see section 3.2.4.

Imaging of tire footprints operating at speed over flooded glass plates has long been important in hydroplaning studies [9]. Indeed, it is possible to apply shadow Moiré to ascertain the depth of water existing between various portions of the tread in the footprint and the surface of the glass plate. In recent years, combination of finite element methods with computational fluid dynamics has allowed the prediction of the contact area existing under wet conditions [10,11] as illustrated in figure 7.6.[8]

**Figure 7.6: Footprint shape for a tire operating on a
flooded pavement (reprinted from Tire Science and Technology,
Vol. 25, No. 4, 1997 with Tire Society permission) [10]**

3.2 Stress measurement techniques
Contact between the tire and road leads to a distribution of forces across the interface. Both a normal component and a shear component are generated at each point in the footprint. The precise nature of the distribution depends on the global forces and kinematic conditions existing at a given instant,[9] the tire's structure, and the tire-to-road friction. In a practical sense, it is best to discuss the force distribution in terms of the three components of stress defined in section 2.3 and shown diagrammatically in figure 7.2.

Footprint stress measurement techniques began with normal stress or pressure determination and have evolved, sometimes simultaneously, in two directions: determination of all three stress components, and ever finer dimensional resolution in an attempt to characterize what happens at the edges of tread elements and to avoid errors due to partial coverage of transducers.[10,11]

---

[8]Only the right half of the footprint is shown since symmetry could be used to reduce the amount of computation required.
[9]For a general discussion of the global forces and kinematic conditions existing during operation, see Chapter 8.

3.2.1 Pressure sensitive film

If an ink block print of the footprint is produced by interposing a sheet of soft carbon paper between the tire and the paper or cardboard on which the image is recorded, the test engineer will notice that the density of the image is variable. The image density is an indicator of the maximum pressure that exists in the footprint at a given location. With the invention of papers with encapsulated inks as a replacement for carbon paper sheets in business forms, it became possible to produce sheet materials that have a precise change in image density with applied pressure.

Fuji Photo Film used this observation and developed the first commercial product of this type, Prescale, which uses an encapsulated dye on a Mylar film. When this material is used to produce a static footprint image, the image density is proportional to the normal stress applied between the tire and the road. Using an appropriate densitometer and software, the maximum normal pressure can be determined at each point in the footprint with excellent resolution.

3.2.2 Individual force transducers
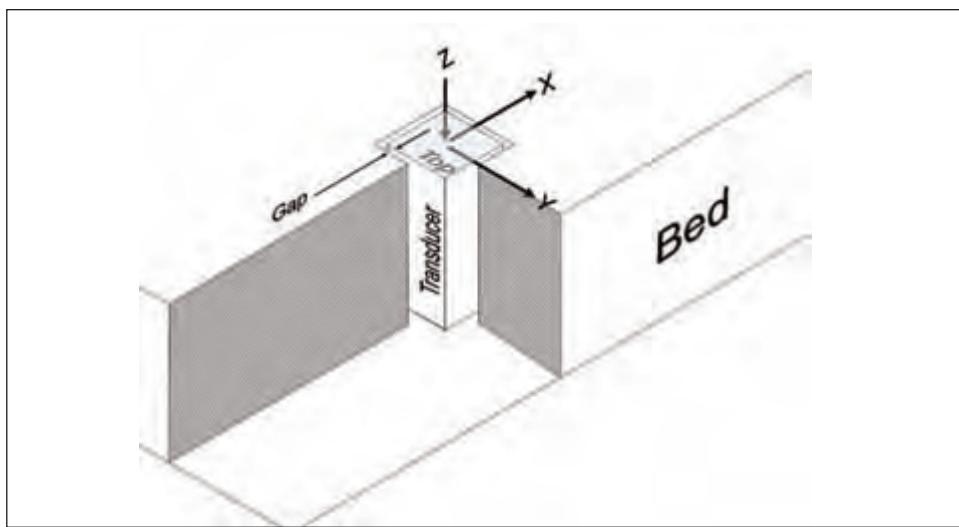
Miniature force transducers have been used to measure contact stresses for many years [12]. This is the only technology that allows determination of pressure plus the two shear stresses, using three-component force transducers.

Figure 7.7 is a schematic representation of a miniature force transducer installed in a test surface. Besides basic alignment of the sensitive directions with the FAS, there are three important installation requirements.

The transducer must be installed so that its top is flush with the plane of the test surface.

There must be a gap around the transducer to prevent grounding, i.e., a path for force transmission parallel to the transducer, leading to erroneous measurements.

**Figure 7.7: Schematic of a miniature force transducer
installed in the bed of a test machine**

[10]Partial coverage is discussed in detail in section 7.2.2.2.
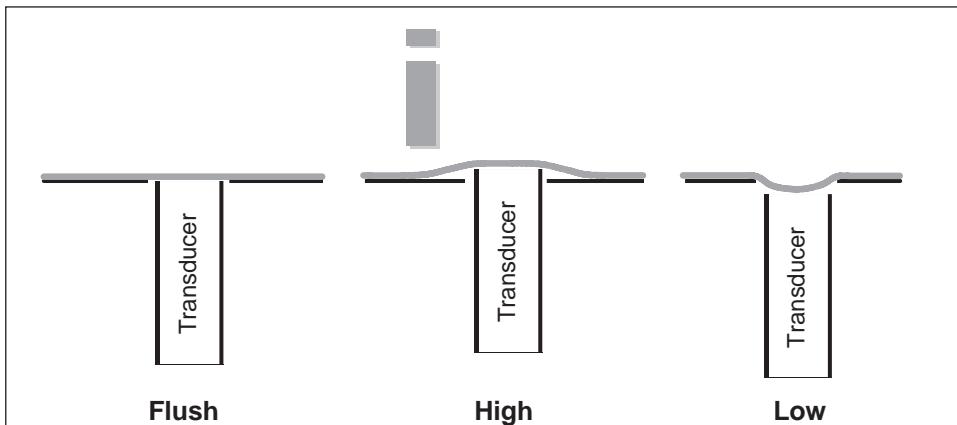
[11]The dimensional resolution problem can be regarded as an experimental analog to the problem of mesh refinement in Finite Element Analysis.

The gap must be small so that the stresses derived from the measured forces are given correctly by equation 7.1.

Figure 7.8 shows schematically the effect of a transducer installation that is not flush with the test surface. If the transducer is installed with its top flush with the test surface, the forces sensed are representative of those over the rest of the plane surface. However, if it is installed with the top above the road surface, it gives readings that are erroneously high, because it is supporting stress from a larger area than the top surface of the transducer. If it is installed with its top below the road surface, then the readings are erroneously low.[12]

The necessity for the gap, figure 7.7, has consequences with regard to cleanliness of the test facility. Particles that become lodged in the gap can short-circuit the force path. Thus, it is important to be able to clean the gap and avoid production or introduction of particles. Thus the best work is done with tires that have a clean surface[13] and when abra-

**Figure 7.8: Miniature force transducer
installation heights: correct and incorrect**

sion during the experiments does not produce particles.

The gap width must be reasonably small, a small fraction of a millimeter, because if it is large the question of how to deduce stress from the transducer force measurement becomes uncertain. Equation 7.1, which is commonly used, approximates the stress vector by dividing the force vector by the area of the transducer top. This implies that the transducer measures only the forces arising from that part of the tread that is in contact with its top.

$$\sigma = F/A_{Top} \tag{7.1}$$

Further, equation 7.1 yields three stresses which are assumed to be uniform on the

---
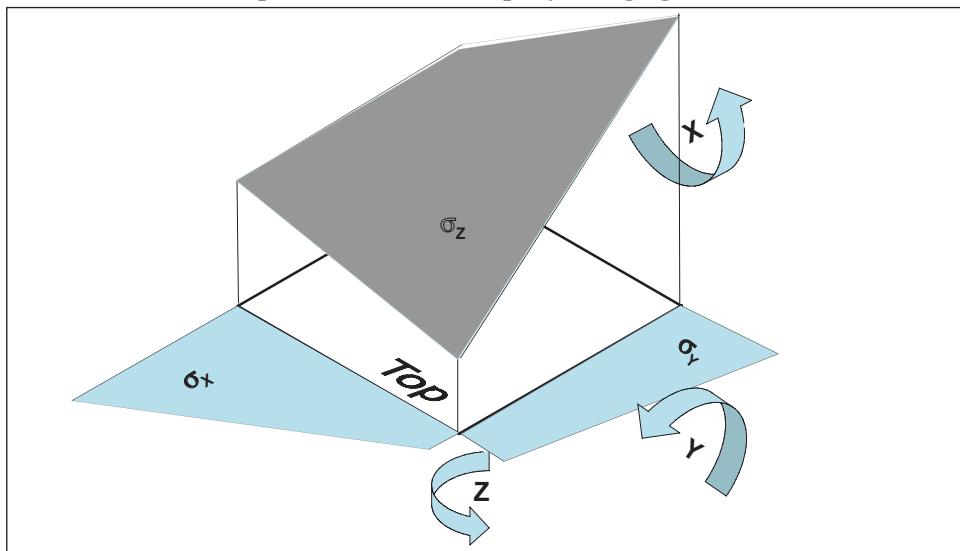
[12]An irregular tread surface can produce effects like those caused by incorrect installation of the transducer. Thus it is important to remove mold stubble and other local surface irregularities from new tires prior to testing. When testing worn tires, dirt adhering to the surface should be removed, but the surface irregularities due to wear are a real part of the sample and should not be removed.

[13]Particles are not the only troublesome form of surface contamination. Chemical contamination will change the surface friction. Thus, it is necessary to clean surfaces periodically with a solvent and to try to maintain a constant coating of diffusion products on the tire surface. For example, after surface cleaning, 8 to 10 passes of the tire may be necessary to approximately stabilize surface friction.

transducer top. Given that the contact stress field on a tire tread can change rapidly with distance over the tread surface, as will be seen in section 4, and that many tread elements are not large, the transducer top must be reasonably small if a reliable approximation to the stress field is going to be determined. Ideally, the transducer top should be vanishingly small, but in practice it is typically from one to five millimeters square or in diameter.

In regions of the footprint where the stresses are changing very rapidly, as illustrated in figure 7.9, appreciable moments can exist on the top of the transducer. The transducer should be designed so it rejects the effect of these moments, otherwise the resulting forces and, hence, stresses will be in error. It would be possible to use the moment information, if available, to generate couple stress components in the analysis, but this has not been done in systems designed to date.

Figure 7.9: Moments on a footprint transducer with a finite top surface area in a rapidly changing stress field
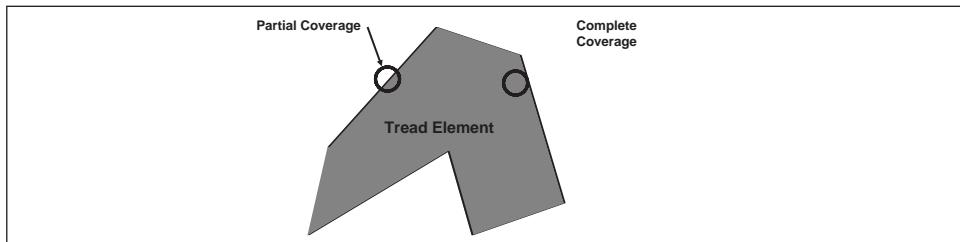
Another problem in three-axis transducers is the problem of cross-talk, an applied force in one direction that gives rise to not only the direct signal, but also to signals in one or both of the other measurement channels. This requires either a transducer design that thoroughly minimizes cross-talk, or a calibration and analysis procedure that corrects cross-talk. In section 4.3, a discussion is given of the calibration and analysis solution to this problem, couched in terms of the load cell system on a force and moment machine.

The assumption behind equation 7.1 can also be violated if the transducer top is only partially covered, figure 7.10. In this case the proper top area is not A, but rather some other unknown value. It is important to reject data from partial coverage.

In order to reject data from partially covered transducers, the position of the transducer with respect to the tire tread pattern must be known. The position can be determined in a number of ways, but the most practical one is to produce a footprint print image of the tire tread pattern at the test location on top of the transducer, or with the transducer at a known position with respect to the image location, as discussed in Reference 7. This requires longitudinal and lateral transducer indexing. Longitudinal indexing involves a combination of linearly encoding the transducer position along the FAS x-axis and angu-

larly encoding the tire's circumferential position, both synchronized to a mutual registration location, for example, the point where the FAS y-axis and the projection of the spindle center onto the road plane coincide. The lateral position of the transducer must be indexed so that it is known with respect to a known lateral position on the test surface, for example, the origin of the SAE Tire Axis System. This combination allows the coverage state of the transducer to be determined for all other positions of interest in the region of the tire under test. The result is an intelligent form of a data acquisition grid like the one superimposed on a footprint image in figure 7.11.
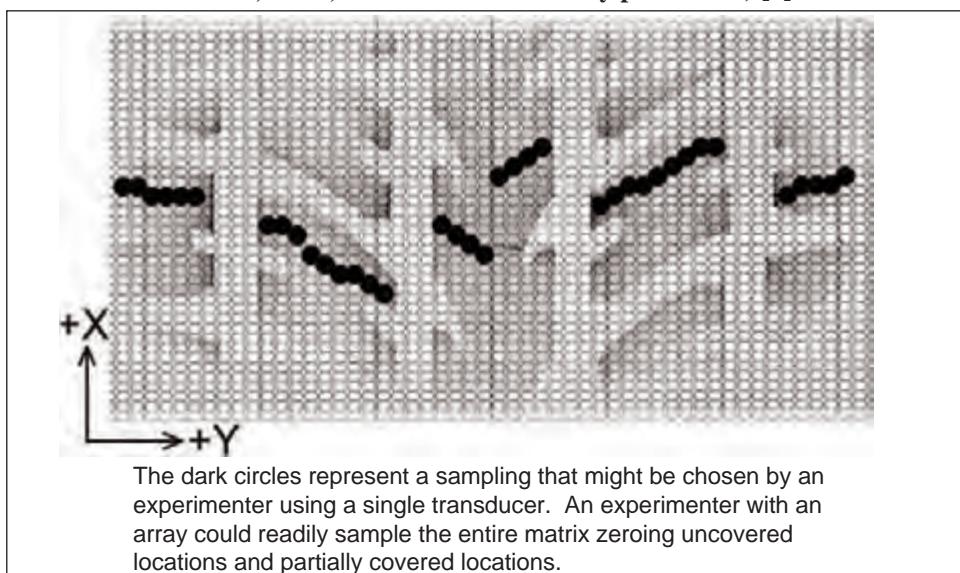
Figure 7.10: Partial coverage illustration

Obviously, testing at every point in the grid shown in figure 7.11 would be impossible within a reasonable period of time using a single transducer. Thus, there is a need to take data at multiple tread points every time the transducer system is within the footprint. This requires an array of transducers. Given the physical constraints on sizing and arranging transducers into an array, 3-D force transducer arrays have been used as line arrays.

Figure 7.11: Tread pattern with a superimposed data acquisition grid (reprinted from Tire Science and Technology, Vol. 27, No. 3,   1999 with Tire Society permission) [7]

The dark circles represent a sampling that might be chosen by an experimenter using a single transducer. An experimenter with an array could readily sample the entire matrix zeroing uncovered locations and partially covered locations.

One form of line array is a lateral or transverse line of transducers, as portrayed in figure 7.12.[14,15,16] Another form is a longitudinal or fore-aft line, shown schematically in figure 7.13. It is possible to apply either line array in a flat-surface (plank) test machine, figures 7.14 and 7.15, or curved-surface (roadwheel) test machine, figure 7.16, or in a real

road. However, in the literature the lateral line array has been applied most often in a low-speed plank type machine [7,15] or in a real road. The example shown in figure 7.12 is arranged in the test surface of the test machine as indicated in figure 7.17[7]. The longitudinal line has been most commonly applied in roadwheel machines. An example, taken from reference 16, is shown schematically in figure 7.18.

Figure 7.12: A lateral array of coaxial stress and displacement transducers (reprinted from Tire Science and Technology, Vol. 27, No. 3, 1999 with Tire Society permission) [7]
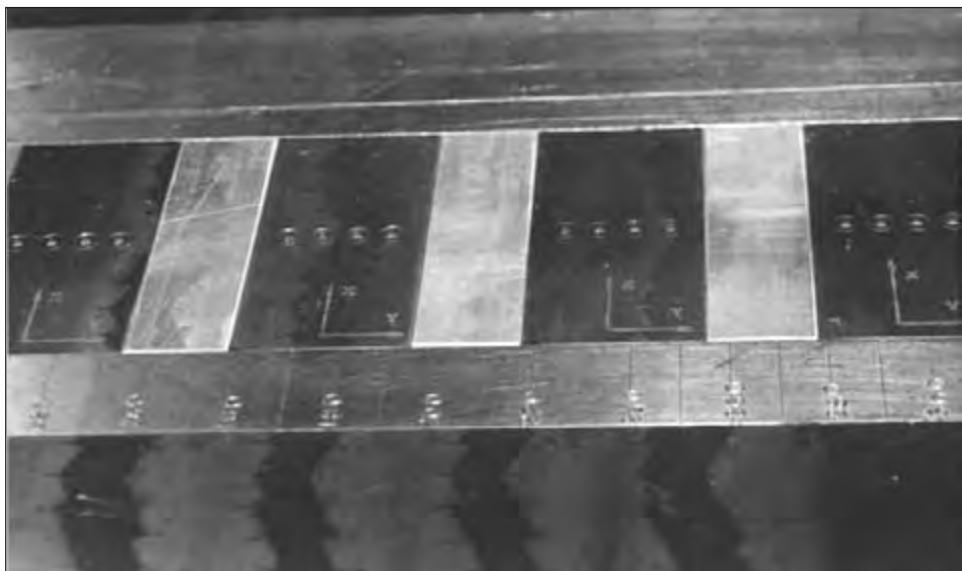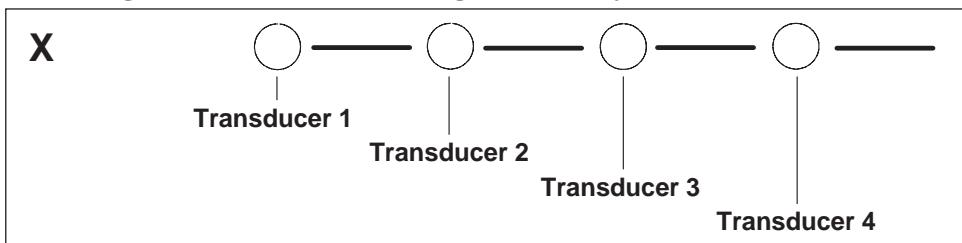
Figure 7.13: Schematic of a longitudinal array of stress transducers

---

[14]The specific transducer spacing shown in Figure 7.12 is a particular designer's concept. There are many other feasible spacings depending on the detailed mechanical design of the transducers and the array. Indeed, the patent [13] for the array shown in Figure 7.12 shows another possible transducer spacing, as does Figure 4 in Reference 15.

[15]The example is actually a combined stress and slip displacement transducer. It will be discussed in Section 7.2.6.1

[16]The first commercially produced line arrays appear to have been made by the Precision Measurement Company in the 1980s.

**Figure 7.14: A Stationary carriage, moving bed, flat-surface
machine now installed at Smithers Scientific Services, Inc.
(reprinted with permission from SAE 770870 © 1977 SAE International) [14]**

**Figure 7.15: A modern, moving carriage, stationary bed, flat-surface machine
manufactured by MTS Systems, Inc Bridgestone/Firestone Co.**

**Figure 7.16: An MTS 860 RoadWheel^{TM},
an example of a curved-surface test machine**

**Figure 7.17: Relationship of tire, machine bed, and transducers
during operation (reprinted from Tire Science and Technology,
Vol. 27, No. 3,   1999 with Tire Society permission) [7]**
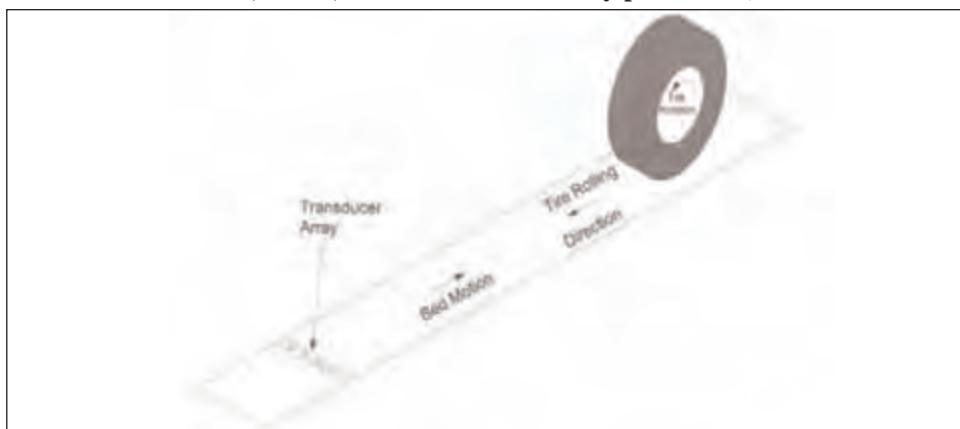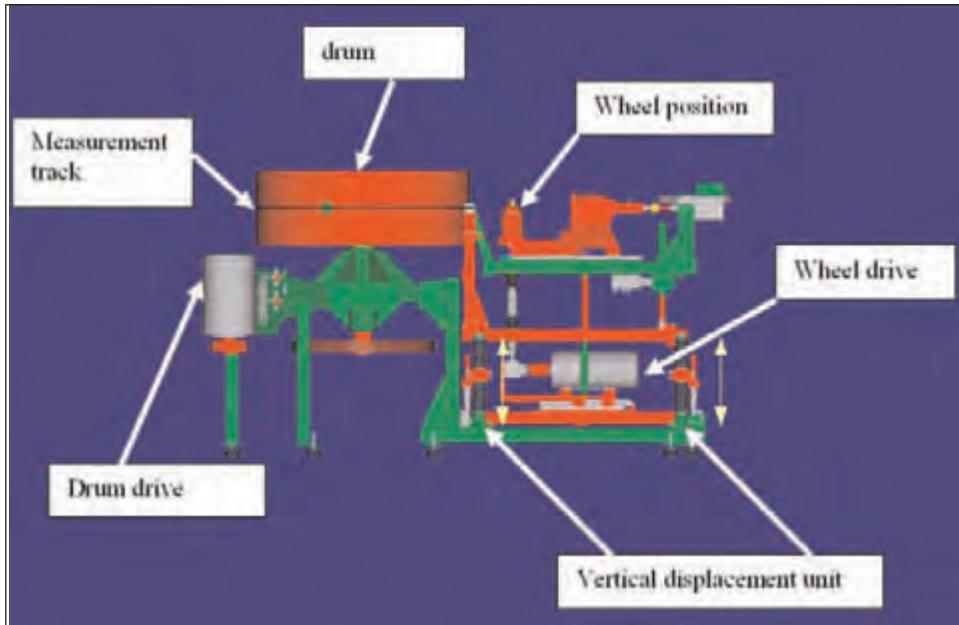
The efficient use of a lateral line array to map the tread surface, as indicated by the circles in figure 7.11, requires that the array have a carefully controlled lateral position, which can be adjusted from footprint pass to footprint pass. This is combined with circumferential position tracking/setting, discussed earlier in connection with rejecting data from partially covered transducers. The inability to precisely control and track their position makes experiments involving force transducer arrays in real road surfaces much less satisfactory than those conducted using testing machines.

The efficient use of a longitudinal array requires that the tire position also be carefully controlled and tracked, as noted above. Reference 16 provides an interesting solution to the problem of tire lateral position through precise stepwise change of tire position over the course of an experiment.

In the force transducer form of rolling footprint experiments engineers have historically made a tacit assumption that the force transducer is in contact with a given sample of the tread surface throughout contact. This tread surface sample is inherently thought of as a point on the tread surface. Thus, the results from a transducer are ascribed to a point. Indeed, it is common to say that the stresses were thus and so at that point during contact. In reality, slip during contact causes the portion of the tread sampled by a transducer to change throughout contact. If slip is small, this deviation from assumed behavior is not important. If slip becomes large enough, however, the simple concept no longer applies and the test engineer cannot decide which point on the tread is associated with the results. For that matter, with appreciable slip, partial coverage has a different definition from location to location throughout the footprint. The exact slip conditions at which these complex changes have to be taken into account depend on the physical size of the transducers among other things. For 5 mm diameter transducers, as used in Reference 13, the problem
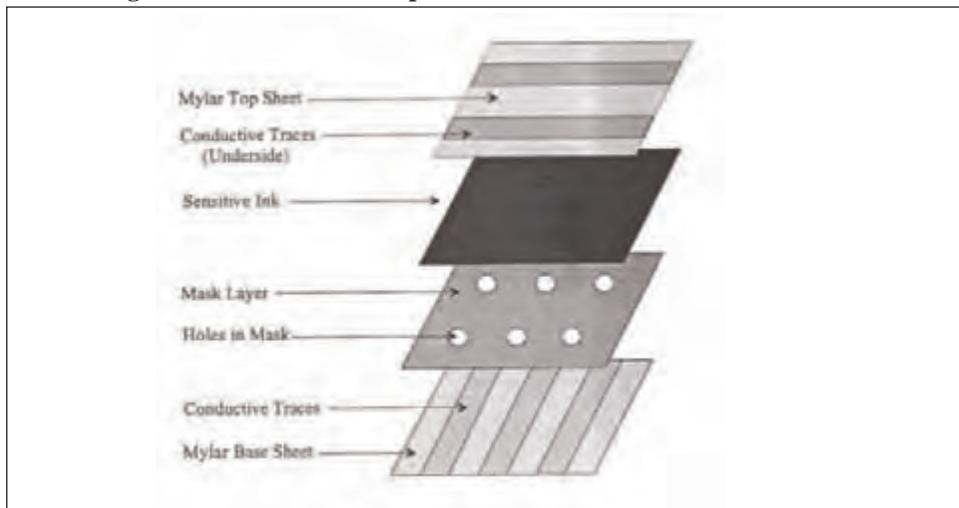
becomes severe at slips corresponding to a slip angle of just over 2 .

3.2.3 Normal stress (pressure) mats

It is possible to make measurements of normal stress or pressure over a large area using 1-D transducers employing printed circuit technology to generate an array of small force sensors. These can be resistive, capacitive, or piezoelectric. The basic concept came out of biomedical technology where there are many references to the technique.

Figure 7.19 is a schematic example of how a resistive array of this sort is constructed.

Figure 7.19: Resistive mat pressure transducer construction sketch

A grille of conductive, but force insensitive, leads is deposited on a flexible Mylar sheet. A second layer of Mylar acting as a mask is laminated over the sheet. An ink with pressure sensitive conductivity is deposited over the mask and the excess removed leaving an array of ink dots through the thickness of the mask. Finally, a second grille of leads running at right angles to the initial grille is bonded to the sandwich to form a flexible circuit card.

By rapidly querying the leads, one pair after another, the state of the sensitive element at each crossing point can be obtained, allowing production of a 2-D matrix of pressure measurements. It is possible with current technology to obtain pressure images under slow rolling conditions as shown in Section 4.1.1.[17]

At this time, mats have very limited durability under conditions of applied global shear such as those imposed by slip angle or torque. Thus, mats are basically limited to either static loading or straight-ahead free rolling.

3.2.4 Optical measurement of normal stress (pressure)
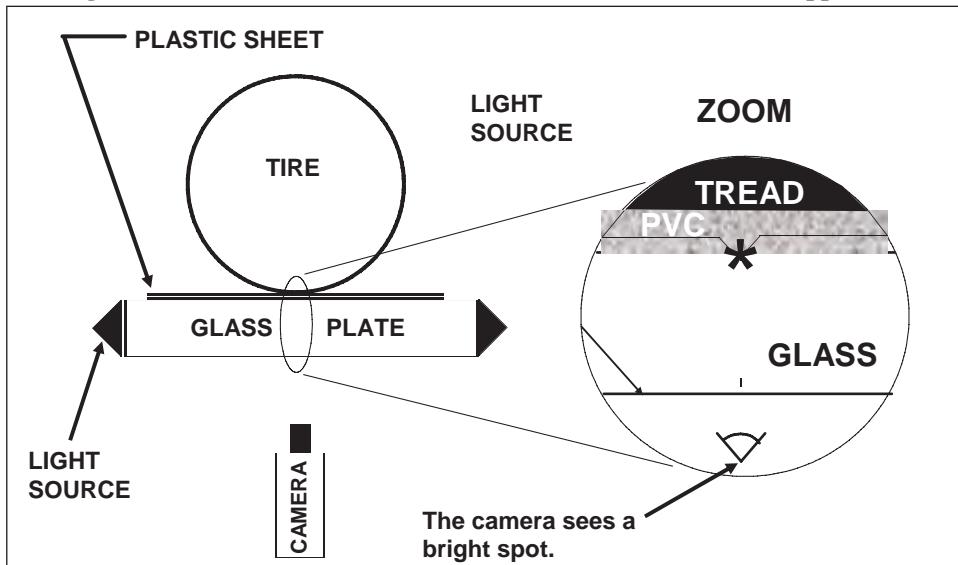
The most common method of obtaining pressure optically is referred to as Frustrated Total Internal Reflectance [18]. Light is shone into the edge of a glass plate at such an angle that the light is essentially totally reflected within the plate provided that nothing touches the surface of the plate and interferes with total reflection (except for the very limited leakage associated with the presence of an electrical disturbance in the air within a few wave-

---

[17]The pressure mat results in Section 7.3.1.1 were obtained using a Tekscan, Inc, resistive mat [17].

lengths of light of the glass surface). The angle at the glass/air interface exceeds the critical angle determined by Snell's law, see figure 7.20.

This situation can be changed if a third medium with a high optical density is brought

Figure 7.20: Schematic of a frustrated total internal reflectance apparatus
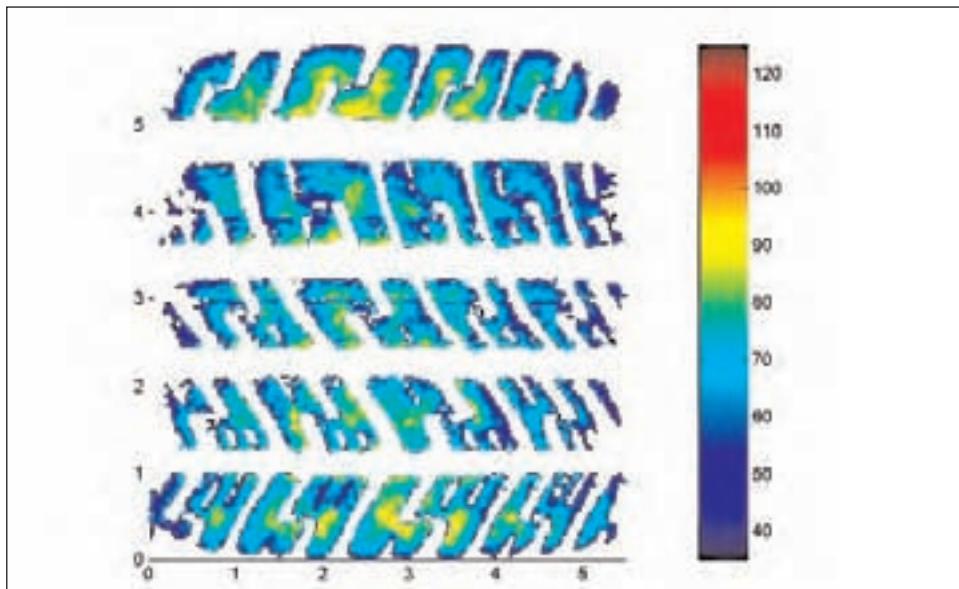
close to the interface. Light is then partially transmitted across the interface, the total internal reflectance is frustrated, and an illuminated spot appears in the field. In figure 7.20 a thin vinyl sheet with small dimples is introduced between the test tire and the glass.[18] The brightness of the illuminated spot at each dimple depends on the intimacy of contact at the dimple location, which depends on how firmly the sheet is pressed against the glass. Thus the field, interpreted in terms of brightness, is a measure of the applied pressure. Using a video camera and appropriate software, a pressure image like that in figure 7.21 can be produced. The method works statically or in slow free-rolling, but is not suitable for testing when the tire is subject to significant shearing forces such as those encountered in cornering or when spindle torque is applied.

A related procedure using absorption of light at a rubber/glass interface is described in reference 19. This method, which works with a matte rubber surface, does not require any intermediate sheet when used with a properly conditioned tire. Thus it will work in the presence of global shear if improved optics can be developed. It has been used only statically. A variant, based on enhanced optics, might offer results in rolling operation.

---

[18]Fortuitously, a very inexpensive textured vinyl table cloth with a tiny diamond pattern repeating at a small fraction of a millimeter is an adequate sheet.

**Figure 7.21: Example footprint pressure result obtained by
applying frustrated total internal reflectance**

3.3 Displacement measuring techniques

Slip of the tread surface across the road surface as defined in described in section 2.5 and shown schematically in figure 7.4 is associated with the generation of shear forces. These motions, which can be thought of as analogous to the motions of a sanding block over a wood surface, are associated with wear. They are not routinely measured. Three ways to determine these motions are discussed in this section.

3.3.1 Instrumented needles

Instrumented needles are the oldest slip displacement measuring technique in use. In this technique a very compliant and sharp needle instrumented to measure tip displacement passes through a small hole in the test surface, as shown schematically in figure 7.22. Assuming that the hole is not too large and that the vertical location of the needle tip with respect to the test surface is appropriate, it is possible to obtain a reasonable approximation of footprint slip displacements.[19]

It is immediately obvious that the geometric problems mentioned in section 3.2.2, which affect measurement of footprint stresses using miniature force transducers, are also a problem for needle measurements of slip displacements. However, if an adequate system is devised for mapping transducer results to positions on the tread surface, a needle system can also yield semi-automated results in a similar way.
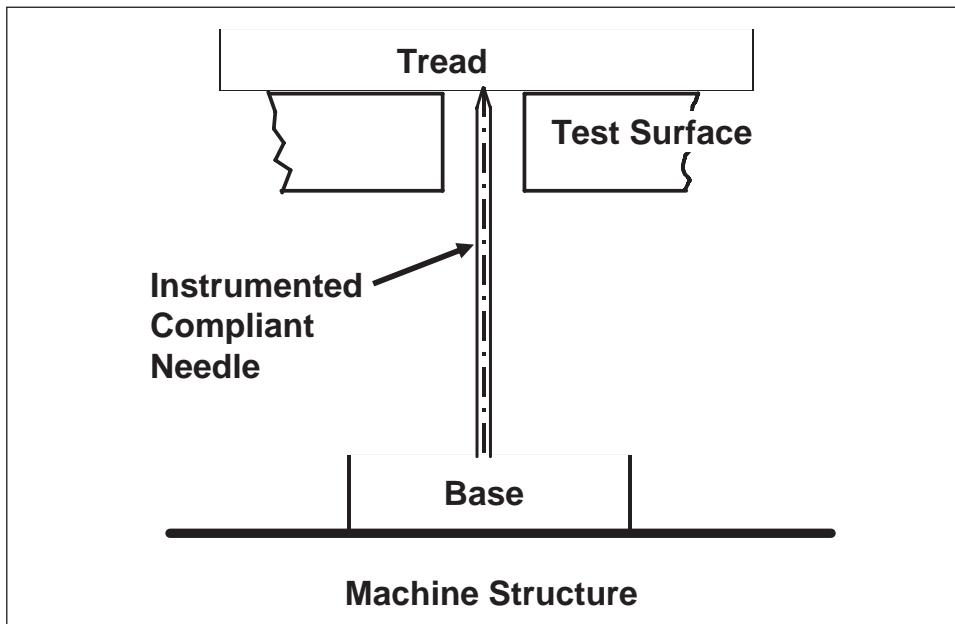
It is also immediately obvious that the largest displacements that can be measured using a needle type transducer are those which force the transducer into contact with the side of the hole. Consequently, the requirement that the hole around the needle be of small diameter limits the technique to small slip displacements. For example, when testing mod-

---

[19]Correlation with Moiré studies carried out on a smooth glass plate confirm that properly designed needle systems [7,13] can give reasonable slip displacement results.

ern radial passenger tires, the system described in reference 13 only works up to about 1.5 slip angle.

Needle type transducers adapt well as line arrays. Figure 7.12 shows the system used
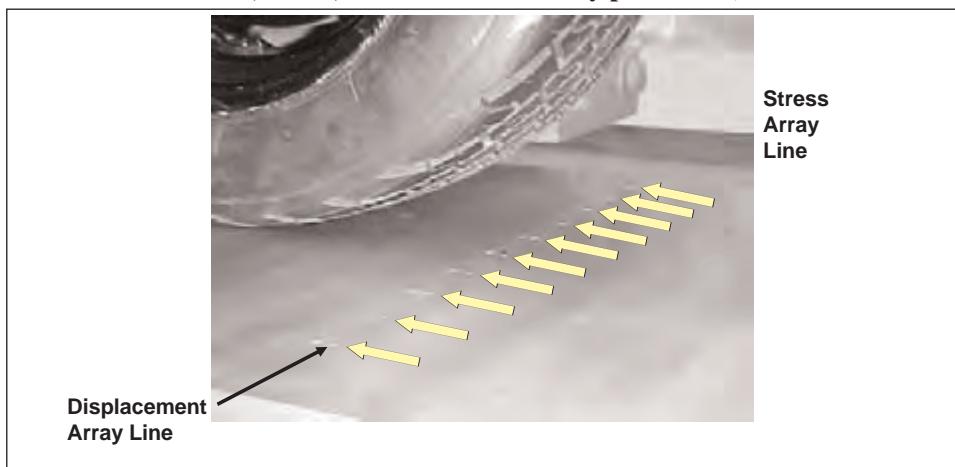
Figure 7.22: Schematic of a slip displacement needle apparatus

in reference 7. A line array of displacement transducers is mounted coaxially within a line array of force transducers. Figure 7.23 shows the system used in reference 15. In this system separate line arrays of stress and motion transducers are used. The coordinated use of stress and displacement transducer results is discussed in section 3.6.1.

To date, the displacement needle method has only been applied at low speeds due to trans-

Figure 7.23: An array produced by Precision Measurement Company
(reprinted from Tire Science and Technology,
Vol. 30, No. 2, 2002 with Tire Society permission) [15]
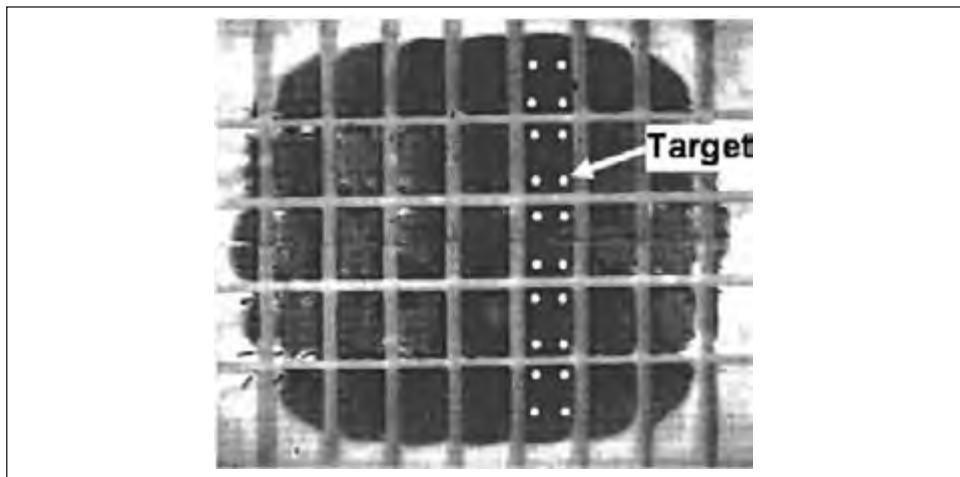
ducer dynamics. It would be possible to apply this method at appreciably higher speeds, if high-stiffness, low-mass, composite materials were applied in transducer fabrication.

3.3.2 Motion analysis video

Motion analysis technology, used in biomechanics to study human gait and sports-related questions, can be applied to the problem of slip displacements on a glass plate test surface. In this technology, small optically-contrasting or reflective targets are placed at points of interest on the test object and their position is tracked by computer analysis of successive video images. For a tire, white spots on the tread, as shown in figure 7.24 [20], are adequate targets for observing slip displacements over the surface of a glass plate.

The principal advantage of this method is that it will work under almost any slip con-

Figure 7.24: A tread surface prepared for a motion analysis study
(reprinted from Tire Science and Technology,
Vol. 25, No. 2, 1997 with Tire Society permission) [20]

dition. Thus, studies of behavior at high slip and inclination angles or under appreciable torque are possible. It does, however, require special tire preparation and the attention of a skilled operator.

Like the needle method it works best at modest rolling speeds. This is due to constraints on frame rates while maintaining good optical resolution.

3.3.3 Line scan analysis of edges

An automated optical method that tracks the slip displacement of the edges of tread blocks[20] is a feature of the machine shown schematically in figure 7.18 [21].[21] Glass plates are placed in the measuring track to allow optical access for the line scan camera arrangement shown diagrammatically in figure 7.25. In the figure, the camera can only see the laser line arising at the surface of the glass where the tread element contacts the road (point b). The camera cannot see the line where the laser shines on the tire groove

[20]Displacements internal to the tread blocks are not available using this method.

[21]The drum of this machine has no side plate on its top, thus, instrumentation can be easily mounted inside the drum.

(point a). At successive times the line scan camera sees a different image as the tread element slips across the window. This is illustrated in figure 7.26 where the evolution of the image from time 1 to time 2 to time 3 is illustrated. The rectangle surrounded with the heavy line in the figure is the block location at the indicated instant.

The example shown in this section is for slip displacement in one direction. To consid-

Figure 7.25: Line scan camera slip displacement measuring equipment schematic (reprinted from Tire Science and Technology, Vol. 32, No. 2, 2004 with Tire Society permission) [21]
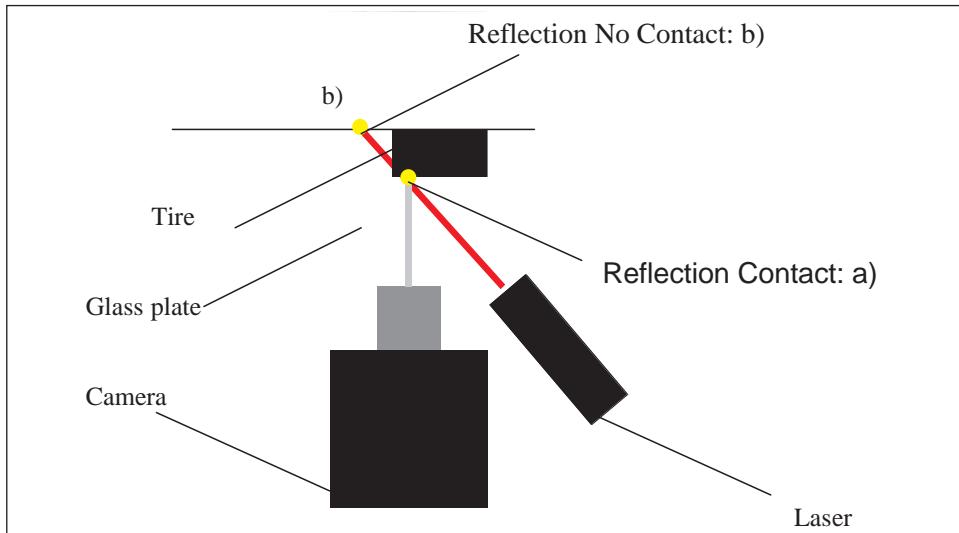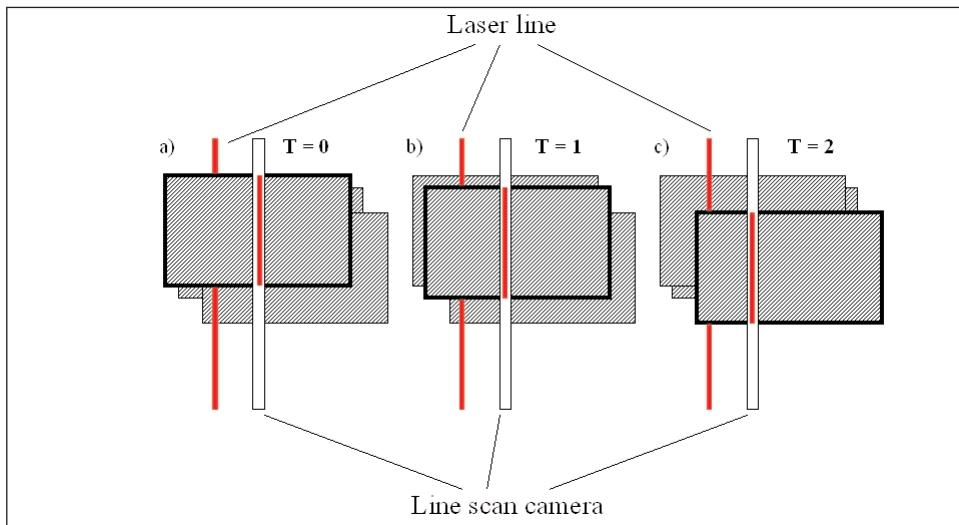
Figure 7.26: Evolution of the line scanned image (reprinted from Tire Science and Technology, Vol. 32, No. 2, 2004 with Tire Society permission) [21]

er displacement of the block edges in both directions, it is necessary to have two systems, one providing u-displacement and the other providing v-displacement. Again, tracking which point on the tread surface is associated with the data is very important.

This arrangement does not have severe dynamic limitations and functions in an automated way at reasonable test speeds up to 40 km/hr.
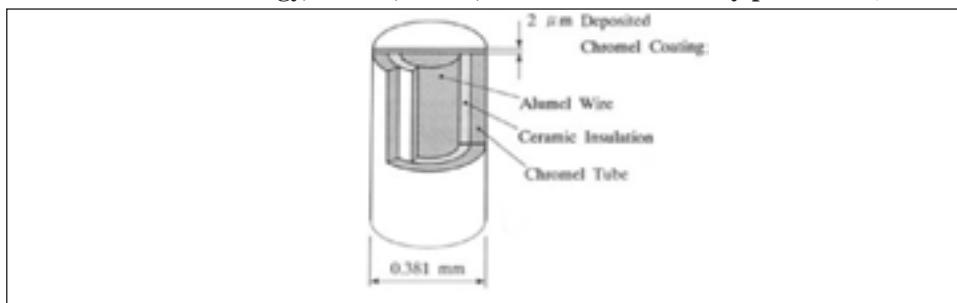
3.4 Temperature in the footprint
Tread temperature can be taken to refer to the surface temperature of the tread material, or within a fraction of a millimeter of the tread surface, or to the bulk temperature in the interior of the tread. In this section we are concerned with the tread surface temperature and in particular the change of that temperature as the tire passes through contact. The change in the surface temperature during a single pass through contact is a measure of energy dissipation due to slip, because tread compounds are reasonably good thermal insulators.[22] Indeed, the temperature change in the footprint might be regarded as a surrogate for the mechanical work dissipated in the footprint and, hence, as a possible predictor of uneven wear. This aspect is discussed in Section 3.7.2.

The abradability, stiffness, and coefficient of friction of the tread compound all depend on its temperature. Thus, wear resistance and vehicle handling also depend on the tire temperature in the footprint region, which, in turn, primarily reflects compound hysteresis and the magnitude of operational deformations. The bulk temperature is usually measured by use of some form of needle probe that is pushed into the tread.
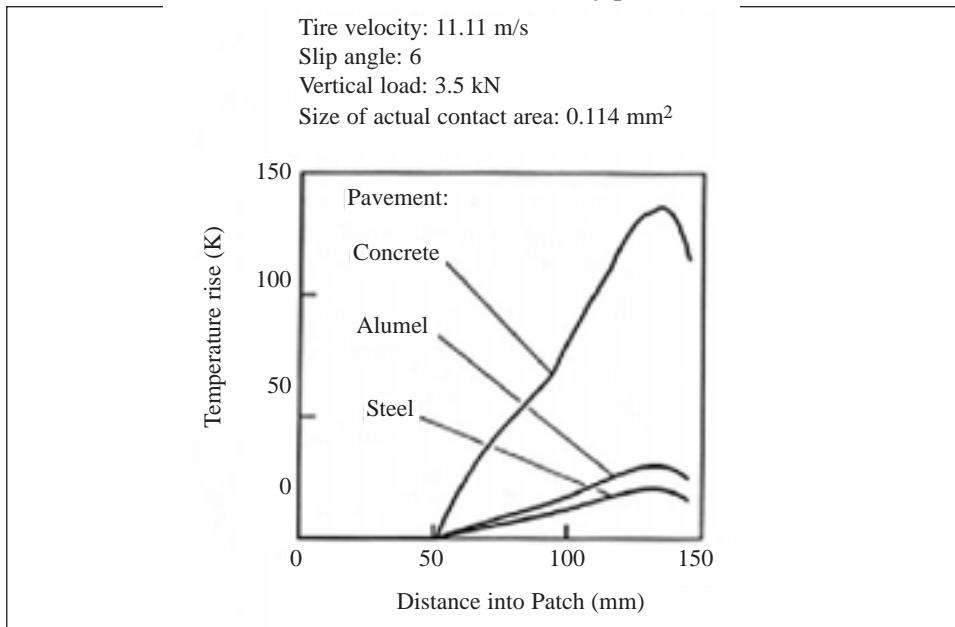
3.4.1 Thermocouples
Miniature thermocouples, figure 7.27, have been applied to measure the change in tread surface temperature during passage through the footprint [22]. In reference 22, the example data are for a 6 slip angle, which is a severe condition in terms of wear, and for a particular test surface texture which produces a contact area of about one-tenth of that measured on a smooth surface. Fujikawa and his associates [22] provide experimental data to support the use of a one-tenth factor. Whether this factor is precisely correct or not, the idea that the real tread contact area on a textured surface is less than that measured on a smooth surface is definitely correct. Figure 7.28 [22], based on computations known to correlate with experimental results, shows the effect of the thermal properties of the test surface on the tread surface temperature in the footprint. This is briefly discussed in footnote 22.

Figure 7.27: Schematic of coaxial thermocouple asperity (reprinted from Tire Science and Technology, Vol. 22, No. 1, 2004 with Tire Society permission) [22]

[22]Obviously, the effect of heat transfer with the test surface is important. If the test surface is highly conductive and not at a temperature reasonably near the mean tread surface temperature, the results of tread surface temperature studies will be markedly affected.

Figure 7.28: Effect of pavement thermal properties on computed temperature rise in tire contact (reprinted from Tire Science and Technology, Vol. 22, No. 1, 2004 with Tire Society permission) [22]

Tire velocity: 11.11 m/s
Slip angle: 6
Vertical load: 3.5 kN
Size of actual contact area: 0.114 mm^2
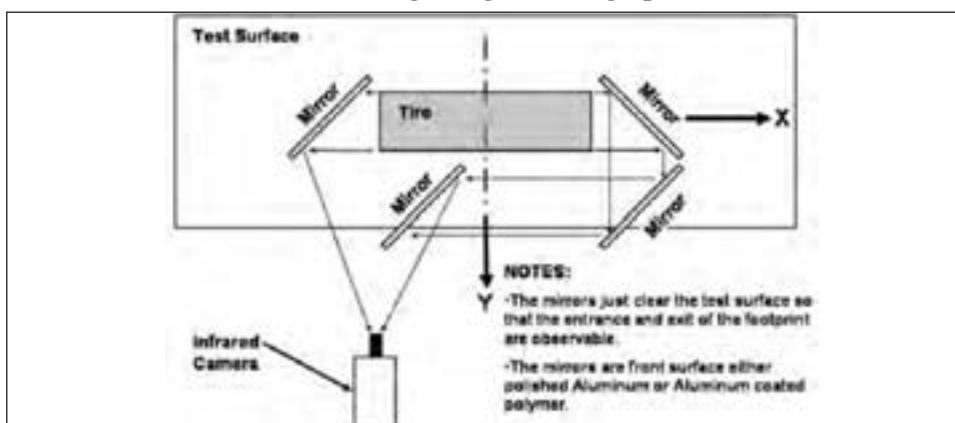
3.4.2 Infrared methods and thermography

 In an earlier study [23], Fujikawa and his associates used an infrared transparent window in an abrasive paper surface on a roadwheel to study temperature rise in the contact at various slip angles. The results were similar to those in Reference 22, but less severe.

   It is possible to apply thermography to measure the change in surface temperature between the front and rear of contact, using an arrangement like that shown in figure 7.29. In the case of roadwheel with an infrared transparent window in its surface, it should be possible to apply thermography to study the process within the footprint.

Figure 7.29: Schematic of setup for observing tire temperatures at the front and rear of contact using a single thermographic camera

Walters [24] observed, as noted at the outset of Section 3.4, that it is possible to attribute the temperature rise to the shear energy developed as the tire rolls through the footprint. It is necessary to start with the tire and an insulated test surface at the same temperature, and gather data for only a short period after rolling begins at a given set of test conditions. For example, one might test at a given load, slip angle and speed, from the start of rolling for a period of 90 seconds to two minutes, and then take data. The tire would then be removed from the test surface, allowed to cool, and test using the next set of conditions initiated after about 15 minutes or so. This procedure could be repeated as necessary to gain related data at many test conditions in a reasonably short period of time.

3.5 Tread topography measurement (worn surface characterization)

We stated at the beginning of this chapter that "the road surface is assumed to be a dry rigid surface with limited texture unless otherwise noted." In Section 3.2.2 we discussed the necessity of installing stress transducers in the plane of the test surface in order to produce valid and comparable engineering data over the footprint. Figure 7.8 is an illustration of why transducers need to be installed in the plane of the test surface.

When contact unevenness is due to the tire, it can have an important effect and must be considered in footprint studies. It is a potential cause of uneven wear, which is one of the the most serious wear problems.[23] Uneven wear causes the tread surface to lose the smoothly curving topography it had when new: different areas of the tread wear at different rates.

Because of the economic importance of uneven wear, the tire and automobile companies have developed equipment to quickly characterize the precise tread topography developed on worn tires. These measurements are very important to understanding contact geometry, footprint stresses, and slip displacements occurring in worn tires. Specific examples of the effects of uneven wear will appear scattered throughout Section 4.

3.5.1 Laser scanning

In the late 1980s work began on systems for mapping the topography of worn tires. Laser-triangulation based measurement systems have been used by a number of tire and automotive manufacturers since the early 1990's. Many of these systems were developed "in-house". However, a number of commercial systems have been marketed. Probably the first and best known of these is the CTWIST™ system developed by Bytewise Measurement Systems [25]. It is based on a licensing of Bridgestone/Firestone's (**C**ircumferential **T**read **W**ear **I**maging **S**ystem version **T**wo) [26]. Laser scanning gives very detailed topography and profiling as indicated in figure 7.30.

3.6 Characterizing tire usage for engineering purposes
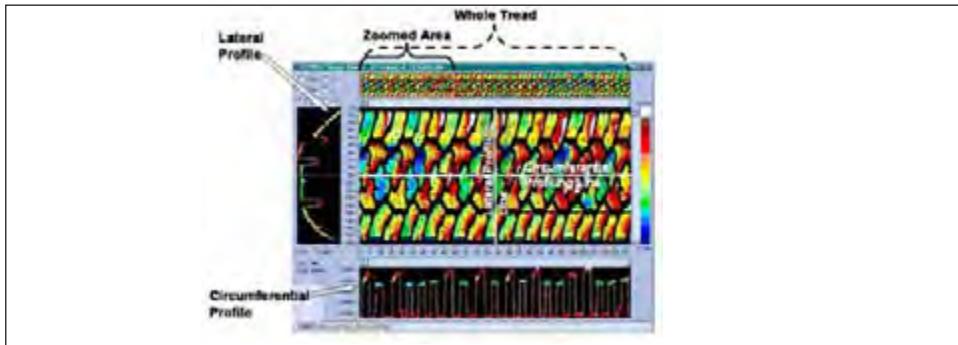
Tire behavior in the footprint is highly dependent on tire usage parameters of which the lateral and longitudinal forces are the most critical [27]. What happens in the footprint depends not only on the magnitudes of these forces, but also on how they are generated.

Equation 7.2, a widely accepted relationship, is discussed briefly in Reference 27 and noted in both References 24 and 27. It shows the tremendous sensitivity of overall tire

$$R = KF^n \tag{7.2}$$

---

[23]Today, almost all customer dissatisfaction with tire wear performance arises from uneven wear, which either produces unsatisfactory vibration and noise performance or leads to locally severe wear in an otherwise good tread.

Figure 7.30: Example of laser triangulation tread topographic data (reprinted)

Where: R = Wear Rate (mm/1000 km or other appropriate set of units)
F = Tire Shear Force
K = Constant (depends on tread compound and pavement)
n = Exponent between 2 and 4.

In most cases the exponent is between 2.0 and 2.5. For the road surfaces and small tires used by Walters [24] he quotes n = 2.3 for cornering and n = 2.0 for driving and braking.

wear rate to the magnitude of the shear force. Different drivers generate shear forces that can vary enough on a given course so that the wear rate varies by a factor of six [28]. Different courses can lead to wear variations by as much as a factor of 10 [28].

Reference 29 demonstrates that the exact way the forces are generated, the combination of slip and inclination angles existing due to suspension characteristics, has a dramatic influence on the uneven wear pattern developed even if the gross tire forces are nearly unchanged. Plainly, it is not appropriate to study footprint behavior under conditions that are unrelated to real operation. For example, straight free-rolling does not occur at zero slip and camber angles as noted in Chapter 8, Section 4.1.4.1. Therefore, a proper understanding of actual tire operating conditions is necessary if rolling footprint studies are going to be relevant.

$$R = KF^n \tag{7.2}$$

Where: R = Wear Rate (mm/1000 km or other appropriate set of units)
F = Tire Shear Force
K = Constant (depends on tread compound and pavement)
n = Exponent between 2 and 4.

In most cases the exponent is between 2.0 and 2.5. For the road surfaces and small tires used by Walters [24] he quotes n = 2.3 for cornering and n = 2.0 for driving and braking.
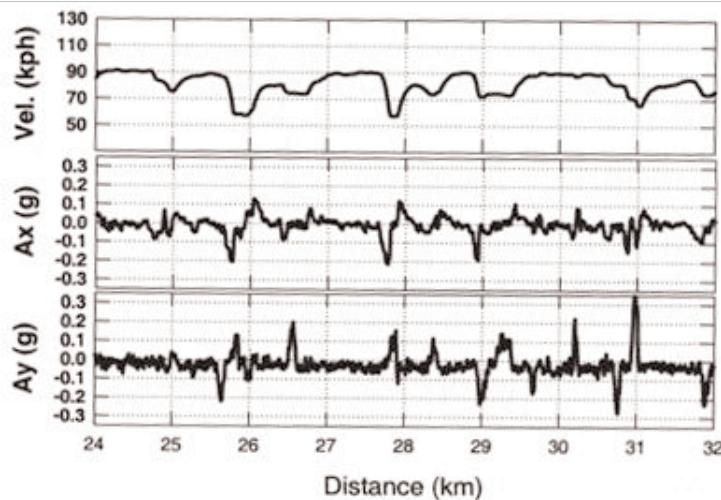
3.6.1 Characterizing tire usage

Stalnaker and Turner [30] provide an excellent discussion of characterizing tire usage, with a good list of references. This is a brief synopsis of their discussion.

The path of a vehicle over the road, its course, can be described in terms of its longitudinal acceleration (a_X), lateral acceleration (a_Y), normal acceleration (a_Z), and vehicle forward velocity (V_X). Figure 7.31 is an example of course description data for 8 km of the Uniform Tire Quality Grading Wear Course in Texas. The fact that an acceleration and

velocity description of a course-time history permits actual experimental replication of a test with reduced variance in the results was recognized in the 1970s [31] and formalized in a compact form in the 1980s [27].

Figure 7.31: Course description data for an 8 km sample of the UTQG wear course (reprinted from Tire Science and Technology, Vol. 30, No. 2, 2002 with Tire Society permission) [30]

Different vehicles, with different tires, operating according to the acceleration and velocity description of a course will develop different force and alignment details. Thus, it is necessary to extend the course description into a force description applicable to the individual tires operating on the test vehicle[24]: longitudinal force (F_X), lateral force (F_Y), inclination angle (g)[25], normal force (F_Z), and velocity (V_X), if footprint studies are to yield realistic results.

The force description can be determined experimentally, but in practice it is more efficient to derive the individual tire force description from the acceleration and velocity imposed by the course, by applying vehicle dynamics. This can be done by complex modeling [32] or by a blend of modeling and experiment [30].

The direct use of the force descriptions as time functions is briefly discussed in Section 4.3.3.

3.6.2 Route spectra
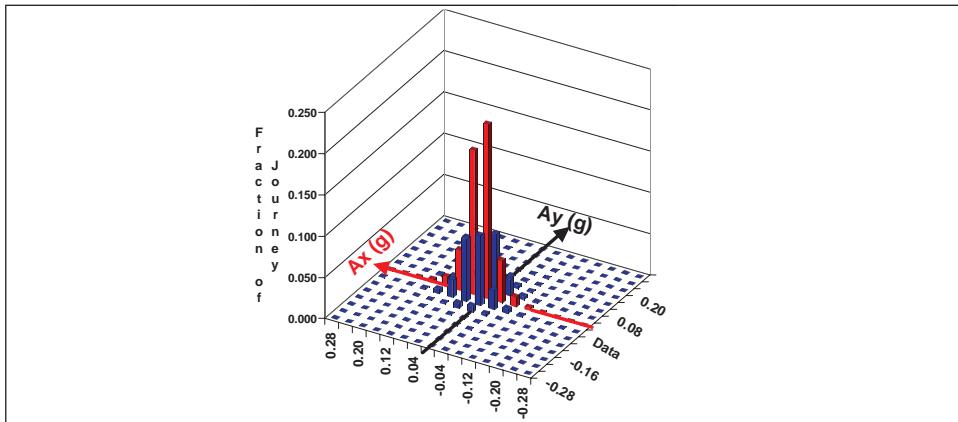
In a practical sense, the force versus time spectra are not useful for footprint studies due to the amount of time required for individual footprint experiments or simulations. To reduce the number of computer or physical experiments, the acceleration and course time description can be formulated as a probabilistic description like that illustrated in figure

---

[24]The operational conditions of a tire on a single vehicle depend on the position in which the tire is mounted. Front and rear are not the same. Left and right are not the same.

[25]Since lateral force is a nonlinear function of slip and inclination angles, it is necessary to allow the angles to be determined individually. See Chapter 8.

7.32. This approach has been applied in many publications such as [7], [15], [21], and [33]. Then, the force descriptions appropriate to each bin are computed.

Figure 7.32: Route spectra for a truck tire public road wear course

    The engineer conducting the footprint study must decide which of the bins to examine. If the intent is to produce a description, the route spectra can be used as discussed in Section 4.3.3.

3.7 Shear energy determination

It has long been accepted that the energy generated due to shear in the footprint is directly associated with wear (see the section by Schallamach and Grosch in Reference 5). Unfortunately, there is no way to determine shear energy directly. It is necessary to determine both the shear stresses (Section 3.2.2) and slip displacements (Section 3.3) at a sufficient number of representative points in the footprint and apply the following calculations [7].[26]

    Here, shear energy intensity denotes the total energy crossing the boundary between the tire and the road, arising from shear stresses and displacements at the interface, and reported on a per-unit area basis.[27] For each pass through contact, the path integral of Equation 7.3 can be computed at each location in the tread pattern-sampling grid where a point on the tire tread is located.

$$W_{ij} = \oint_S \overline{F}_{ij} \bullet d\overline{S}_{ij} \qquad \text{(Eq. 7.3)}$$

Where:

F_{ij} = Footprint force vector at point ij on the tread surface, a function of S.

i = Lateral position index with respect to the tread surface.

j = Circumferential position index with respect to the tread surface.

dS_{ij} = Differential footprint displacement vector (local motion/sliding).

S = Path of integration. Physically, the path of motion of a point ij on the tread relative

---

[26]In Finite Element Analysis the shear stresses and displacements should be computed so that the computation of energy can be easily added to the analysis.

[27]Energy also crosses the boundary in the footprint due to vertical deflection of the tire and heat transfer. These energy fluxes are not considered in this discussion.

to a fixed point on the road surface during contact, figure 7.4.

W_{ij} = Shear work at point ij.

Equation 7.4 is the differential form of Equation 7.3. In Equation 7.4 the footprint forces and differential displacement vectors at the points of the tread pattern-sampling grid have been decomposed into their X and Y components at a specific location on the tread.

$$dW_{ij} = \overline{Fx}_{ij} \cdot d\overline{u}_{ij} + \overline{Fy}_{ij} \cdot d\overline{v}_{ij} \quad \text{(Eq 7.4)}$$

Where:

dW_{ij} = Differential shear work at point ij.
Fx_{ij} = X component of the footprint force at point ij.
Fy_{ij} = Y component of the footprint force at point ij.
du_{ij} = X component of the differential displacement vector at point ij.
dv_{ij} = Y component of the differential displacement vector at point ij.

As the points on the tire tread follow path S through the footprint the differential shear work varies point-by-point. It can be approximated as indicated in Equation 7.5 for the transition from point k - 1 to point k on path S.[28]

$$dW_{ij,k} = 0.5[(Fx_{ij,k} + Fx_{ij,k-1})(u_{ij,k} - u_{ij,k-1})] + 0.5[(Fy_{ij,k} + Fy_{ij,k-1})(v_{ij,k} - v_{ij,k-1})] \quad \text{(Eq 7.5)}$$

Where:

k = The index of points along the integration path S. Data begins with k = 0, but the first k for which Equation 7.5 is defined is k = 1.

Shear work has a sign. At times the road will do work on the tread and at other times the tread will do work on the road. But from the standpoint of the tread material at the interface between the tire and road, the sign of shear work is not important. What is important is the total amount of shear energy that is generated at the interface per unit area of the tread surface during passage through contact. <u>This energy per unit area is the shear energy intensity.</u> Equation 7.5 can be rearranged to yield differential energy intensity by dividing the forces at the tread pattern-sampling points by the area of the transducer used to sense the shear forces and taking the absolute value. The result is Equation 7.6.

$$dI_{ij,k} = dIx_{ij,k} + dIy_{ij,k} \quad \text{(Eq 7.6)}$$

Where:
$dI_{ij,k}$ = Differential energy intensity for the kth step.

$$dIx_{ij,k} = |0.5[(Fx_{ij,k} + Fx_{ij,k-1})(u_{ij,k} - u_{ij,k-1})]/A| = |0.5[(\sigma x_{ij,k} + \sigma x_{ij,k-1})(u_{ij,k} - u_{ij,k-1})]|$$

$$dIy_{ij,k} = |0.5[(Fy_{ij,k} + Fy_{ij,k-1})(v_{ij,k} - v_{ij,k-1})]/A| = |0.5[(\sigma y_{ij,k} + \sigma y_{ij,k-1})(v_{ij,k} - v_{ij,k-1})]|$$

---

[28]More complex differential formulations could be used, but in practice, given data spacing, this has proven adequate.

A = The area associated with the forces.

σx = Longitudinal stress.

σy =Lateral stress.

Summing over k from one to n, equation 7.7, through the length of the footprint, generates the energy intensity at point ij applicable to passage of the tread through contact for the current operational condition. When this is done at all points of contact between the tread pattern-sampling grid and the tread, intensity maps are obtained like those in Section 4.3.

$$I_{ij} = Ix_{ij} + Iy_{ij} = \sum_{k=1}^{n} dIx_{ij,k} + \sum_{k=1}^{n} dIy_{ij,k} \qquad \text{(Eq 7.7)}$$

Where:

I_{ij} = Energy intensity at point ij.

Ix_{ij} = Energy intensity due to X stresses and displacements at point ij.

Iy_{ij} = Energy intensity due to Y stresses and displacements at point ij.

3.7.1 Combined arrays

In References 7 and 15 stress transducer data were combined with displacement needle data to provide the data required to compute I_{ij}. In reference 21 stress transducer data were combined with line scanning camera analysis to provide the data required to compute I_{ij}. In reference 33 stress and displacement results from finite element analysis were combined to compute I_{ij}. Section 4.3 discusses applications to the study of uneven wear.
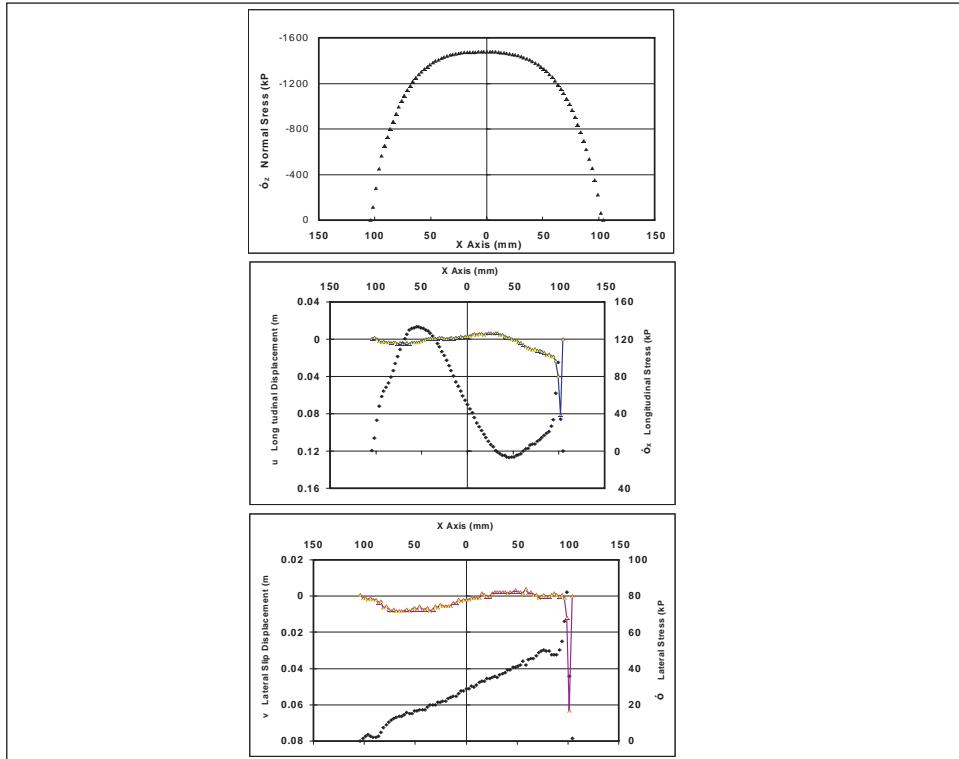
3.7.2 Temperature as a surrogate for shear energy

In section 3.4 we discussed the determination of temperature in the footprint. It was noted that tread surface temperature can be a surrogate for shear energy in the footprint as long as heat transfer does not significantly alter the tread surface temperature. Section 4.3.3 contains an example application.

4. Footprint physics

The footprint is a kinematically driven boundary. As noted at the outset of this chapter, the double curvature of the tire structure requires that the tire structure be stretched, compressed and bent to conform to the road surface. These forced displacements give rise to the footprint stress field. They are combined with the effect of the tire's pneumatically prestressed structure, the complex displacement field due to compression loading of nearly-incompressible treads cut into complex patterns, and the soft response of the tire structure to shearing displacements.

Figure 7.33 is an example of the stresses and slip displacements at a single point, with a truck tire rolling straight ahead. A similar set of data is found at every other point in the footprint. Each point is unique and experiences a unique set of operational conditions. Further, the precise data depends on the tire's structural design and architecture (shape, tread pattern, etc.). Thus, the presentation in this section is necessarily generic. In trying to use it, never forget that the footprint physics or mechanics applicable to a particular tire design and operational condition are unique.

Figure 7.33: Oscillograph images at a single point

4.1 The tire without tread pattern

Figure 7.34 shows typical free-rolling behavior for a smooth treaded example of an ordinary passenger tire constrained to operate at zero slip and inclination angles. All three stress components are shown.

A number of the effects evident in figure 7.34, and which are discussed in the next few paragraphs, are associated with the effect of the pneumatic prestress in the doubly curved tire as it is forced to conform with the road surface.[29] One effect is to relax the loads on the belt cords almost completely in the center of contact, figure 7.35. This causes the tire to pull inwards in contact, resulting in outwardly-directed footprint shear stresses, as sketched in figure 7.36.

The basic profile for the normal stress in a plane parallel to the X-Z plane is a trapezoid. In the case of figure 7.34 the top of the profile is almost flat. The center of pressure for normal stress in the footprint is slightly in front of the y-axis, and thus a positive rolling resistance moment exists. In a general sense, real tires show normal stress profiles on longitudinal planes through contact, ranging from trapezoidal to parabolic, dependent on the tire's design, construction, inflation pressure and load. The one in figure 7.33 lies somewhere between. figure 7.37 is an isometric plot of normal stress for a medium duty (TBR) truck tire. Obviously, a longitudinal section through these data is going to yield a parabolic profile.

---

[29]For a thorough outline of the effects, see the appendices to Reference 6.

For ordinary passenger tires, as in figure 7.34, it is typical to find the largest normal stress magnitudes on the shoulders with lower magnitudes in the crown.

Figure 7.34: Typical lateral, longitudinal, and normal stress isometrics for a passenger tire rolling at zero slip and inclination angles
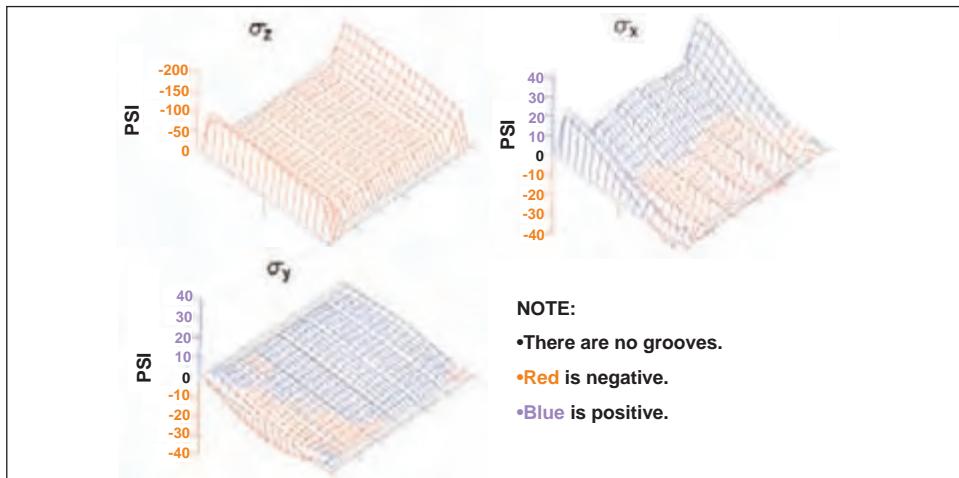
Figure 7.35: Cord loads for the tire used to produce the data presented in figure 7.34 (reprinted from Tire Science and Technology, Vol. 20, No. 1, 1992 with Tire Society permission) [6]
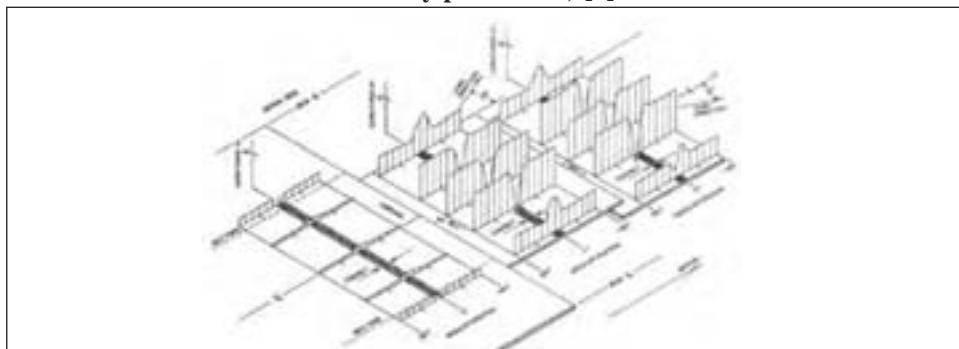
Figure 7.36: Radial tire footprint shear stresses conceptualized (reprinted from Tire Science and Technology, Vol. 20, No. 1, 1992 with Tire Society permission) [6]
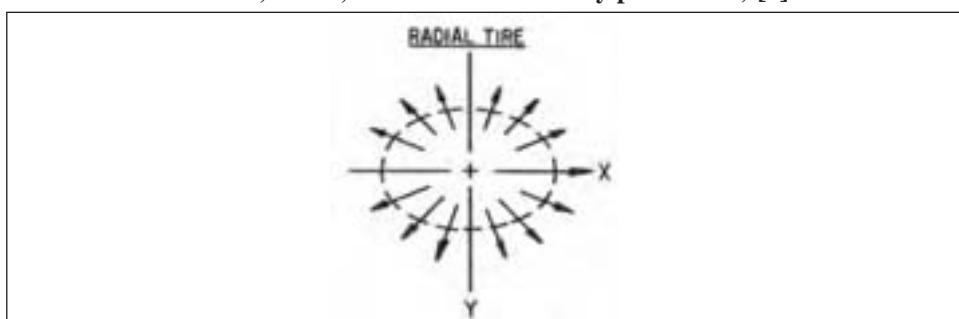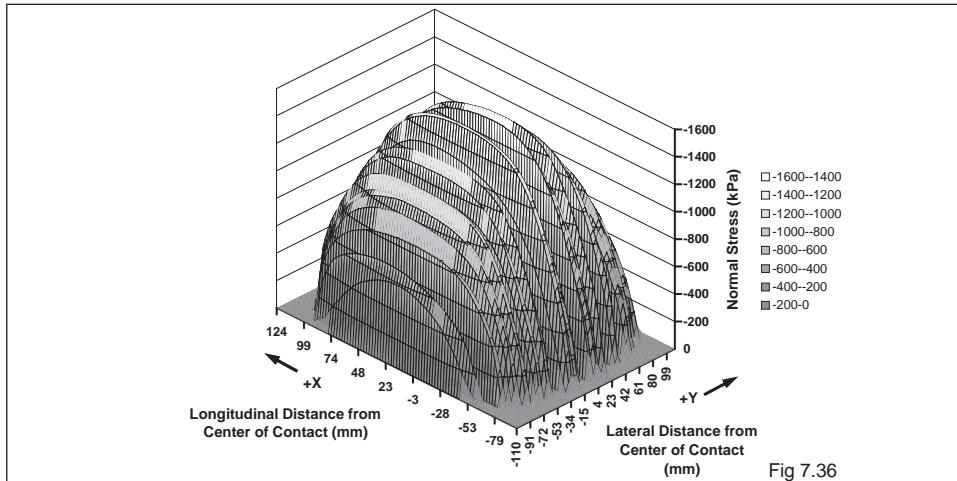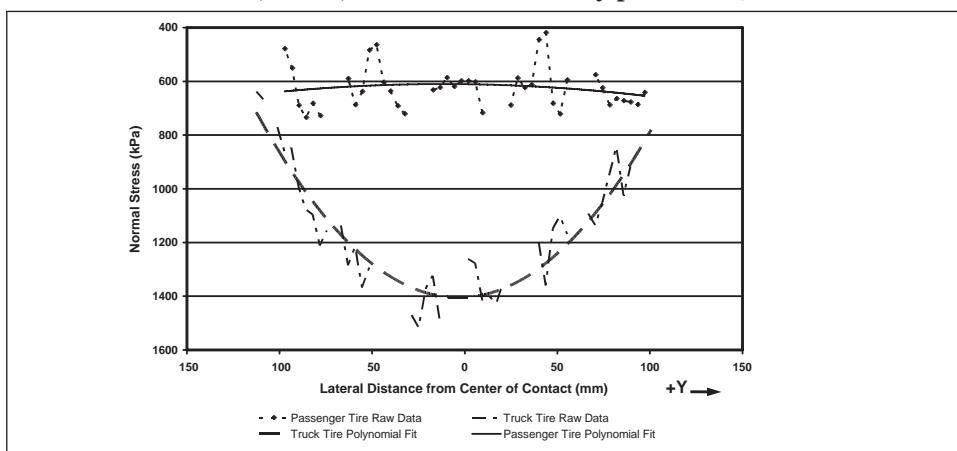
Figure 7.37: Normal stress isometric for a radial medium duty (TBR) truck tire rolling at zero slip and inclination angles (reprinted from Tire Science and Technology, Vol. 27, No. 3, 1999 with Tire Society permission) [7]

Thus, if the normal stress profile of an ordinary passenger tire is plotted in the Y-Z plane it has a bowl shape with the magnitudes on the shoulders representing the sides of the bowl and the magnitudes in the crown representing the bottom of the bowl. Figure 7.38 shows Y-Z plane normal stress profiles for a 50-Series Performance tire and a medium duty truck tire, both at typical service loads. The profiles in figure 7.38 are very different from the typical passenger profile. Why?

The 50-series tire is operating at about 60-percent of its load rating. The footprint, Figure 7.3, is not at all square, as is that one for the tire in figure 7.34. The pneumatic pre-strains in the belt cords have not been fully relieved, as was the case in figure 7.35.

Figure 7.38: Comparative normal stress on the Y-Z plane for a performance tire and a radial medium duty (TBR) truck tire rolling at zero slip and inclination angles (reprinted from Tire Science and Technology, Vol. 27, No. 3, 1999 with Tire Society permission) [7]

On the other hand, in the case of the medium duty truck tire, the inflation pressure is sufficiently high that very substantial pneumatic prestrains exist in the cords in the footprint during loading.

In figure 7.34, the longitudinal stress is positive at the front of the contact and negative at the rear. This is exactly what is expected based on figure 7.36, and is driven by the cord load changes portrayed in figure 7.35.

Another interesting feature can be noted in the longitudinal stress data. The longitudinal stress in the shoulders is more positive than in the crown. Now, by definition the slip ratio of the free-rolling tire is zero. For the longitudinal stress in the shoulder to be more positive than that in the crown, the shoulders must travel further than the crown during each tire revolution. This means that the shoulders have a larger effective rolling radius than the crown.[30] Looking at figure 7.35 this is expected since belt tension will affect belt length. The crown area of the belt, where pneumatic tension is reduced during transit of the footprint, will act as if it is shorter. This is a good example of kinematic forces and of the tire fighting with itself in the footprint region.
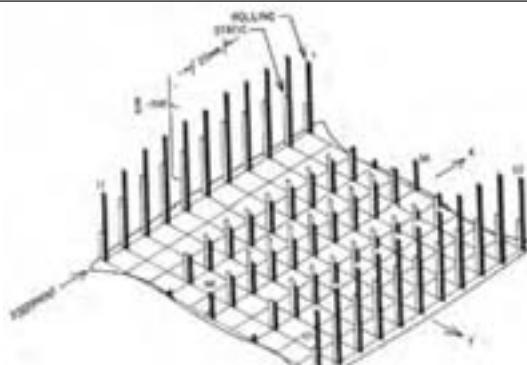
The lateral stresses in figure 7.34 also show the effect of cord load relaxation with the right shoulder showing positive stresses and the left shoulder showing negative stresses.[31] The outward shear direction is maintained. The very low level of a positive lateral stress bias is a result of plysteer.

4.1.1 Static vs. rolling

The discussion in Section 4.1 has so far dealt with a rolling tire. As is clear from the discussion in Section 3, the footprint is often characterized in static loading. This is a simple and useful procedure, but it can produce misleading results.

Figures 7.39, 7.40, and 7.41 show sparse isometric views of the change in a radial passenger tire's footprint stresses as it passes from statically loaded to straight-ahead free rolling.[32] They show that the change can be fairly dramatic.[33]

Figure 7.39: Isometric of footprint normal stresses of standard radial passenger tire loaded statically and in slow rolling (reprinted from Tire Science and Technology, Vol. 20, No. 1, 1992 with Tire Society permission) [6]


[30]The point whose data are shown in Figure 7.33 is on the shoulder, thus, its longitudinal stresses are also shifted positive.

[31]The lateral stresses in Figure 7.33 are also positive as would be expected since the example tread location is a right shoulder location.

[32]The footprint shape shown in Figure 7.39 applies to Figures 7.40 and 7.41 as well.

[33]A complete listing of the effects is found in the Appendices in Reference 6.

Figure 7.40: Isometric of footprint lateral stresses of standard radial passenger tire loaded statically and in slow rolling (reprinted from Tire Science and Technology, Vol. 20, No. 1, 1992 with Tire Society permission) [6]
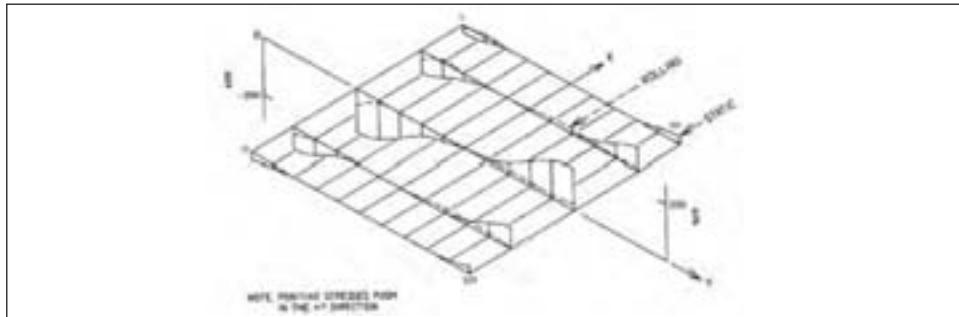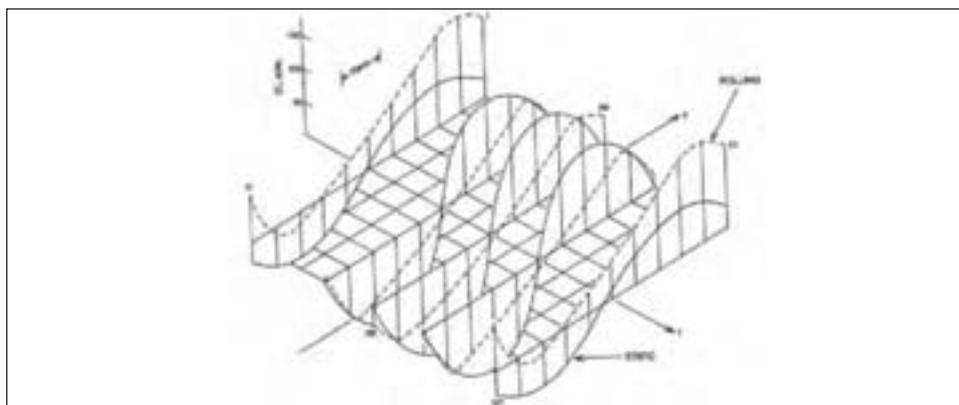
Figure 7.41: Isometric of footprint longitudinal stresses of standard radial passenger tire loaded statically and in slow rolling (reprinted from Tire Science and Technology, Vol. 20, No. 1,   1992 with Tire Society permission) [6]

The normal stresses in figure 7.39 are highest in magnitude in the shoulder and lowest in the crown, as seen in figure 7.34, regardless of whether the tire is stationary or rolling. The change is in relative magnitude. The difference from shoulders to crown is appreciably larger for the rolling tire. The normal stresses on the shoulder are higher in magnitude and the ones on the crown are lower. Basically, the shoulders are more heavily loaded and the crown is more lightly loaded during rolling.

The change in the normal stress pattern is associated with changes in lateral stress from static to rolling. As shown in figure 7.40, the outwardly-directed lateral stresses are greatly reduced in rolling. Fundamentally, the motion occurring in rolling frees the shoulders to move inward as a result of the relaxation of belt cord tension in the footprint, which is shown in figure 7.35 and was discussed earlier. Relatively, the shoulders move inward and roll under, while the crown tends to deform away from the road, reducing the magnitude of crown normal stress. An idealized sketch of the process is shown in figure 7.42.

Under static loading the longitudinal stress pattern in the contact region is symmetrical with respect to X, regardless of the Y position of the X - Z section examined. Rolling causes the shoulder stresses to become more positive and those in the crown region to become

more negative. This is due to the non-constant rolling radius effect noted in the discussion of longitudinal stress, based on data in figure 7.34.

Figure 7.42: Normal and lateral stress association schematic representative of the change from static loading to low speed straight free-rolling (reprinted from Tire Science and Technology, Vol. 20, No. 1, 1992 with Tire Society permission) [6]
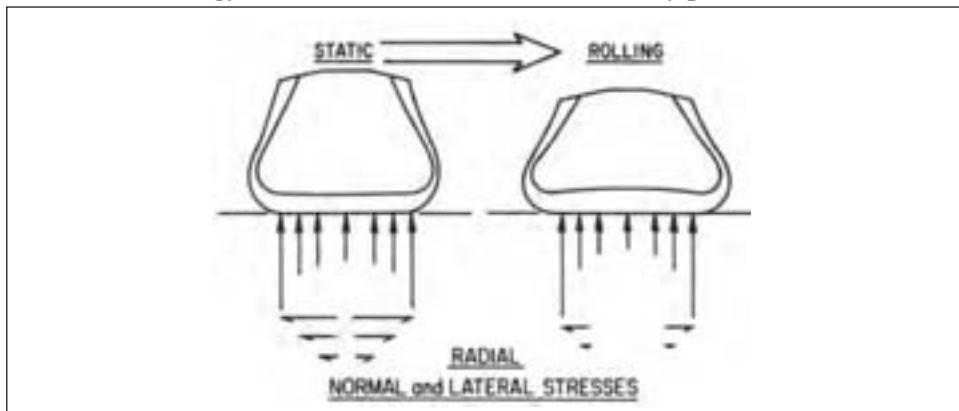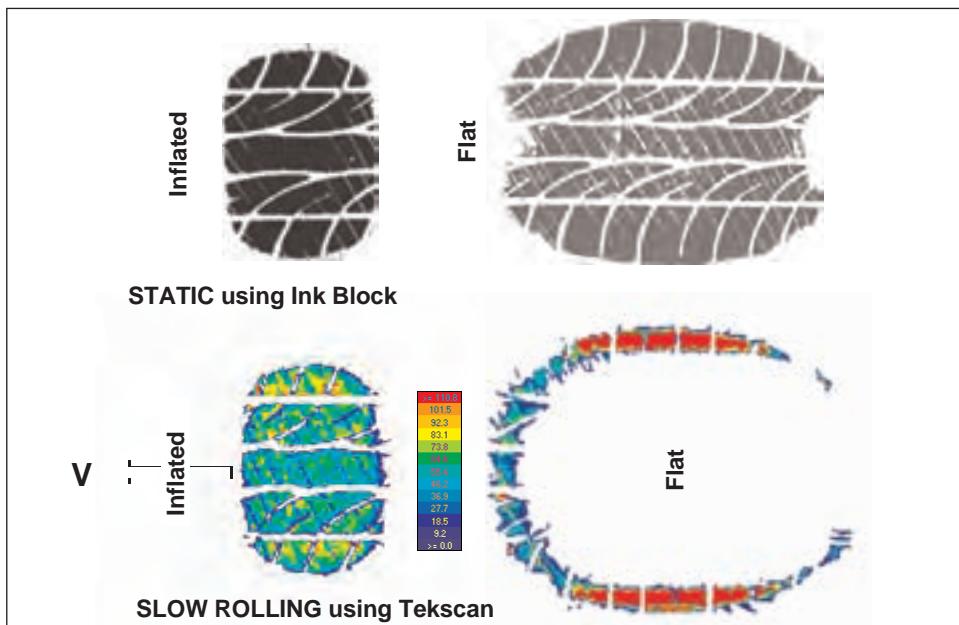
Figure 7.43 shows how the change from static to rolling can cause gross changes in the apparent footprint shape. In this case the tire actually buckled out of contact in much of the crown region when rolling.

Figure 7.43: Comparison of static (ink block) and slow rolling (pressure mat) footprints of a self-supporting tire (data courtesy of Smithers Scientific Services, Inc.)

4.1.2 Test surface curvature

Test surface curvature will affect the results, of course. Therefore, to the maximum extent possible, the results presented so far were obtained using a flat test surface. The effect of surface curvature increases as the curvature of the test surface approaches that of the tire, depending on the relative curvature of both test surface and tire.

Published data on the effect of curvature on footprint stresses and slip displacements are rare, although data on footprint-related tire performance does appear in the literature. That related to tire force and moment is reviewed in Section 8.5.1, leading to the conclusion that tests should be conducted on a flat surface if at all possible. Indoor wear data by Stalnaker and associates[34] indicated small differences when the radius of the tire was about 20 percent of the radius of the test surface.[34]

Laging and Rothert[35] performed finite element analysis of footprint behavior using a lightly loaded homogeneous (cast) tire. They concluded: "results from drum tests cannot be transformed directly into accurate results obtainable on a road, primarily because the contact area is not linearly related to contact pressures."
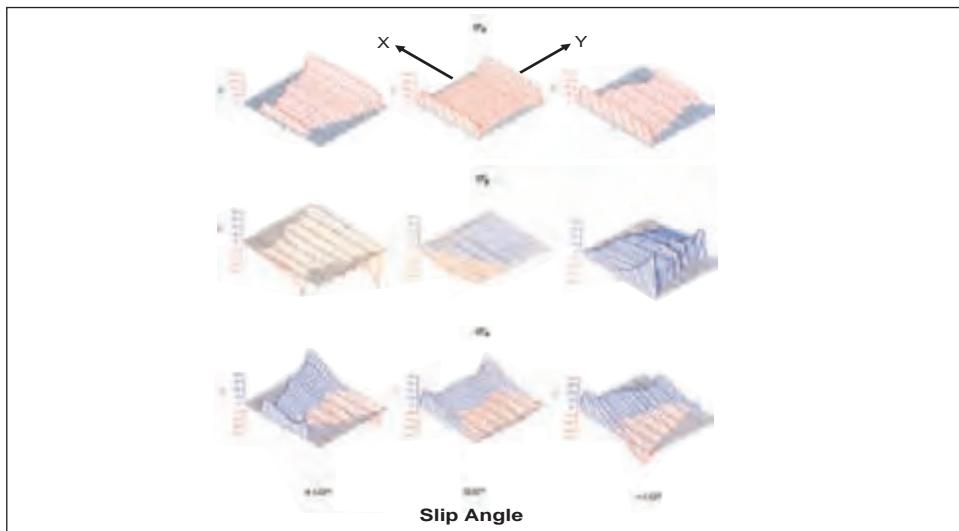
At present the effect of curvature is not well defined, and is an area worthy of further study.

4.1.3 Effect of operational parameters

Operational parameters significantly alter tire footprint stresses and slip displacements, thereby greatly affecting the overall forces and moments developed by the tire (see section 8.4).

As shown in figure 7.44, imposing a slip angle reshapes the footprint into a trapezoid in the road plane. A left turn leads to a long right shoulder and a short left shoulder, whereas a right turn leads to a long left shoulder and a short right shoulder. The long shoulder is exposed to a much higher magnitude of normal stress than the more lightly loaded short shoulder.

Figure 7.44: Effect of slip angle on the stress field of a smooth treaded tire
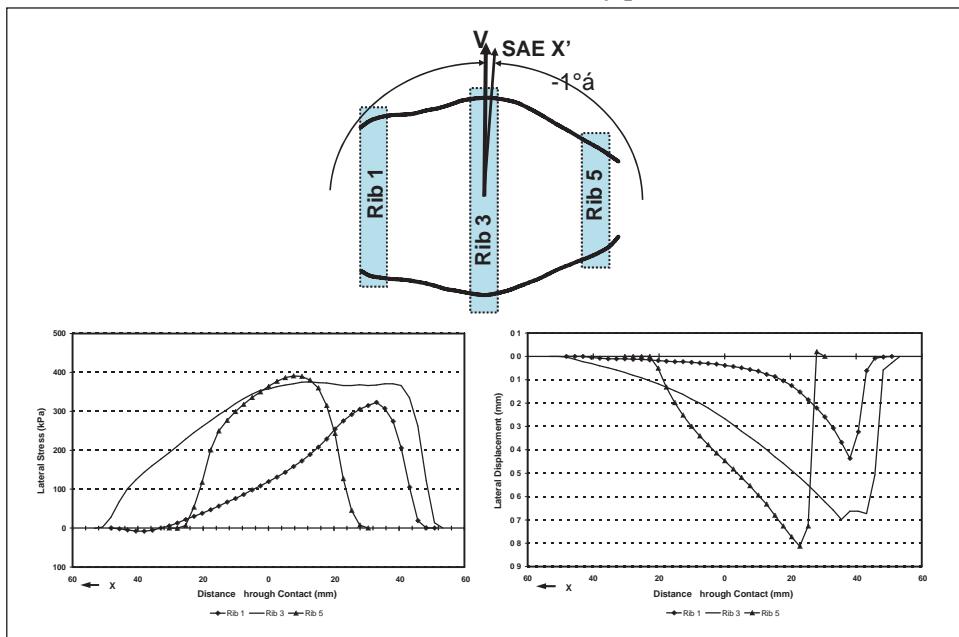
[34]It should be noted that existing flat surface machines are economically not feasible for studies of abrasive wear studies, because of first cost per test position and high maintenance costs. Thus, these tests have been routinely carried out on roadwheel machines.

[35]Its straight free-rolling footprint is shown in Figures 7.3 and 7.4.

The lateral stresses in turning are very much larger than for a tire rolling straight ahead. For a left turn, at a positive slip angle, the lateral stresses are essentially totally negative, and in the right turn they are essentially totally positive. The deformations discussed in section 8.4 are responsible for these lateral stresses. A careful look at the lateral stress fields in figure 7.44 reveals that the stress develops differently according to lateral position. Figure 7.45 gives a simplified view of the lateral stresses and associated slip displacements developed by the performance tire when turning right, at -1° slip angle.[35] Rib 1 (the left-most rib) is lengthened and subject to higher normal stresses. The lateral slip displacement occurs primarily in the rear of contact and the lateral stress distribution is definitely shifted to the rear. Rib 3, which is subject to a moderate level of normal stress reaches a maximum lateral stress at about halfway through contact and then the lateral stress ceases to grow (sliding is occurring) in spite of increasing slip displacement. Rib 5 is lightly loaded and its contact length is short. Again, sliding begins about halfway through contact. The basic lateral slip displacement field portrayed is in accord with that shown in reference 20.[36]

Figure 7.45: Rib by rib lateral stress and slip displacement for a cornering performance tire (reprinted from Tire Science and Technology, Vol. 27, No. 3,   1999 with Tire Society permission) [7]
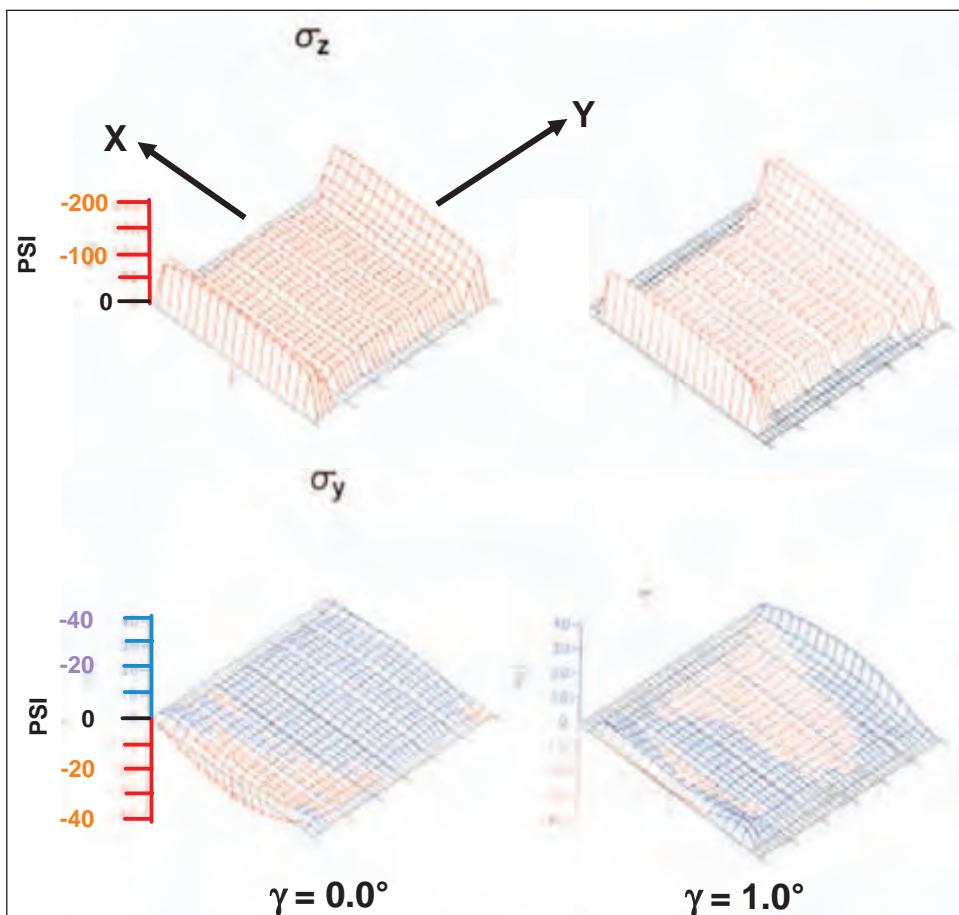
As shown in figure 7.44, longitudinal stress is warped by the effect on the cord loads of the slip angle induced deformation. The heavily loaded shoulder shows an exaggeration of the reduced rolling radius effect seen in the crown and discussed in the previous section. The lightly loaded shoulder shows an exaggeration of the increased rolling radius effect seen in the shoulder and discussed in the previous section.

---

[36]In reading Reference 20, take care about the meaning of terms and the senses shown in the diagrams, as they are not the same as those used in this chapter.

The data of figures 7.44 and 7.45 come from low slip angles. The distortion of the footprint increases as slip angle increases, as shown in figure 7.5. Thus, the general behavior observed should grow in magnitude with increasing slip angle.

Figure 7.46 shows that the effect of small inclination angles is much less that of small slip angles. This is expected, given the response of passenger tire forces and moments to inclination angle, section 8.4. The primary results are what would be expected when one shoulder is loaded more heavily and the load on the other is simultaneously reduced.

**Figure 7.46: Effect of inclination angle on
the stress field of a smooth treaded tire**

In all cases, the slip displacement due to an operational parameter has increased toward the rear of the footprint. The same is true in the case of torque application. Addition of braking slip to the free-rolling state leads to a change of the longitudinal stress seen at zero slip and inclination angle in figures 7.34 and 7.46, into the pattern seen in figure 7.47. This indicates that it is reasonable to assume as a first approximation that the effect of longitudinal slip is a linear change in stress from the front to rear of the footprint, as represented schematically in figure 7.48. Line 1 in figure 7.48 is the total component of longitudinal stress due to driving torque. Line 2 is the total component of longitudinal stress due to braking torque. Line 4 is the free-rolling longitudinal stress in the crown zone of the tire.

Adding lines 1 and 4 produces line 3, which gives a first approximation to the longitudinal stress in a driven tire. Adding lines 2 and 4 produces line 5, which gives a first approximation to the longitudinal stress in a braked tire.[37]

Figure 7.47: Longitudinal shear stresses for a braking smooth treaded tire [5]
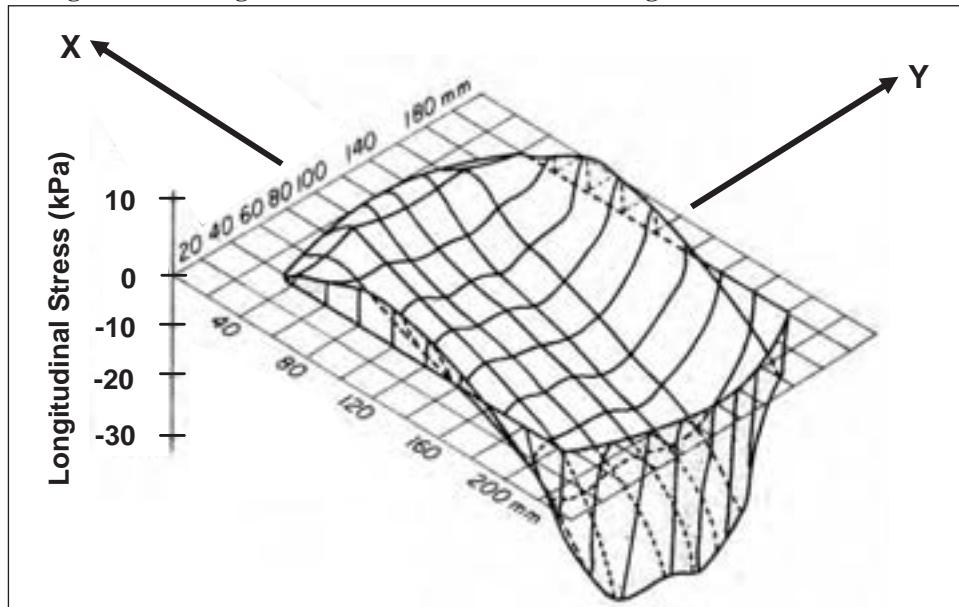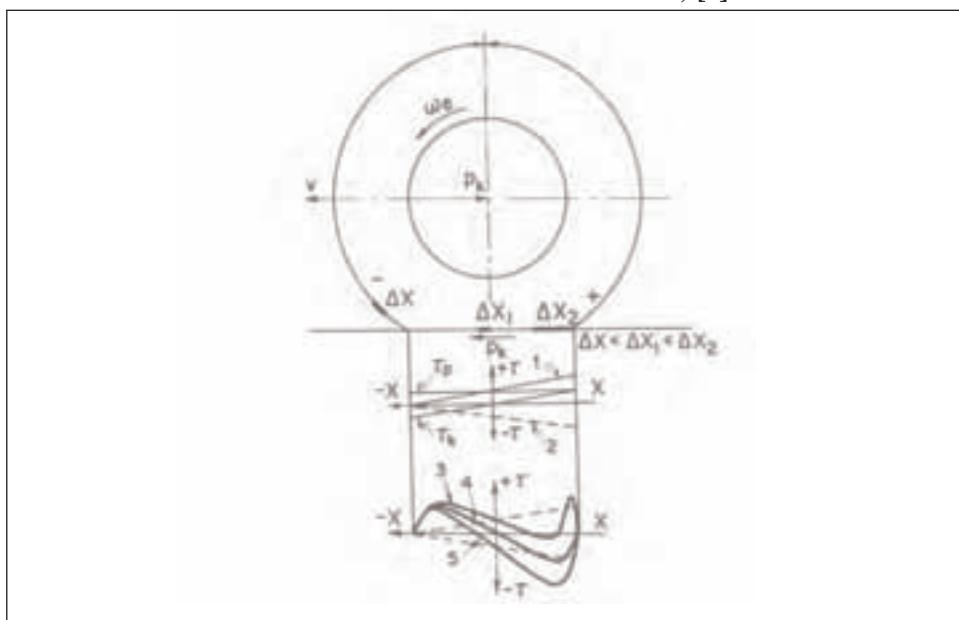
Figure 7.48: Rotation of a wheel (the distribution of longitudinal stress in the contact zone of driven and braked tire) [5]

---

[37]The discussion of deformation given in Reference 5 is not presented here as it is thought to be inadequate.

4.1.4 Relationship of footprint stresses and tire forces and moments
Equations 7.8 through 7.13 relate the tire forces and moments to the stress components. They allow direct checks of the accuracy of overall stress fields and answers to questions such as the most efficient patterns to use in uniformity grinding, a question of importance in Chapter 9.

$F_Z = \int \sigma_Z \, dxdy$ (Eq. 7.8)
$F_Y = \int \sigma_Y \, dxdy$ (Eq. 7.9)
$F_X = \int \sigma_X \, dxdy$ (Eq. 7.10)
$M_X = \int Y \cdot \sigma_Z \, dxdy$ (Eq. 7.11)
$M_Y = \int X \cdot \sigma_Z \, dxdy$ (Eq. 7.12)
$M_Z = \int (X \cdot \sigma_Y + Y \cdot \sigma_X) \, dxdy$ (Eq. 7.13)

Equation 7.13 makes a very important point. Aligning moment is a function of not only lateral stress, but also of longitudinal stress. It is common to think in terms of lateral stress only and in terms of pneumatic trail.[38] This is an incomplete model that can lead to misconceptions in the presence of inclination angle and applied torque.

4.2 Effect of tread pattern
To this point, the discussion has focused on a tire without a tread pattern although it was necessary to use data from some treaded tires to provide particular examples. The discussion now turns to the effect of the tread pattern, which is really the effect of cutting various grooves in the tread slab. It is always important to remember that the only reason that grooves exist in a tread is to aid traction in the presence of contaminants like water, snow, mud, ice, etc. If it weren't for road surface contaminants, a tread pattern would be unnecessary and no one would want to undertake the difficult task of obtaining even wear and quiet operation from a patterned tread. But a tread pattern is an engineering necessity for traction.

4.2.1 The solid tire as surrogate for a tread pattern
In a simple sense the ribs in the tread pattern on a pneumatic tire are like small solid tires fastened to a flexible rim. Thus, addition of the effects present in the footprint of a solid tire to the pneumatic effects inherent in the carcass gives a first approximation to the overall footprint behavior of a pneumatic tire.

It is important to note that the footprint shear stresses of a solid tire rolling straight ahead are governed by Poisson effects. Because rubber is virtually incompressible, it will contract laterally (Poisson contraction) under a longitudinal tensile deformation and it will bulge out sideways under a compression. Figure 7.49 shows the lateral stress field for a solid tire, both static and rolling. Note that the sense of the shears is reversed compared to that seen in the pneumatic tire, figure 7.40. The shear stresses are now directed inwards in response to slip displacements, and the slip displacements are directed outwards due to the predominance of the Poisson effect (bulging) as the tread compound is compressed. Notice also that rolling increases the stresses on the shoulders, exactly the reverse of what happened in the case of the pneumatic tire, figure 7.40.

---

[38]Pneumatic Trail is discussed in Section 8.2.1.

Figure 7.49: Isometric of lateral stresses in the footprint of a static and slow rolling solid tire (reprinted from Tire Science and Technology, Vol. 20, No. 1,   1992 with Tire Society permission) [6]
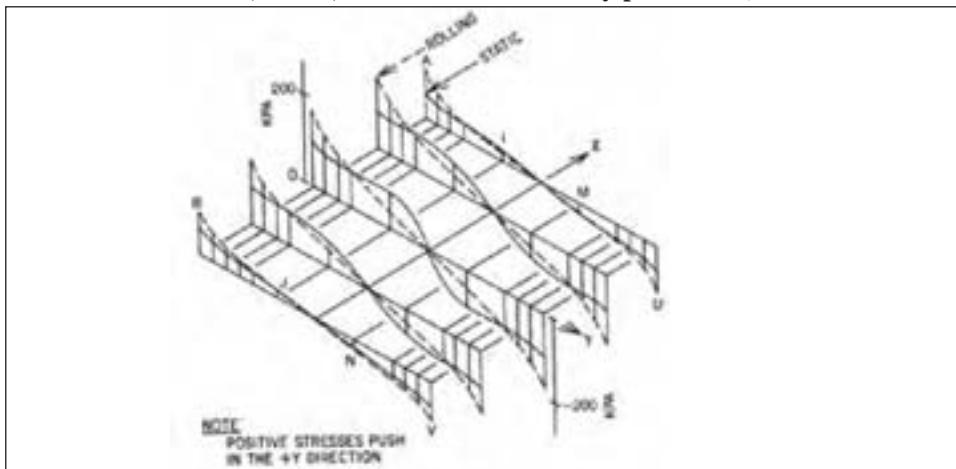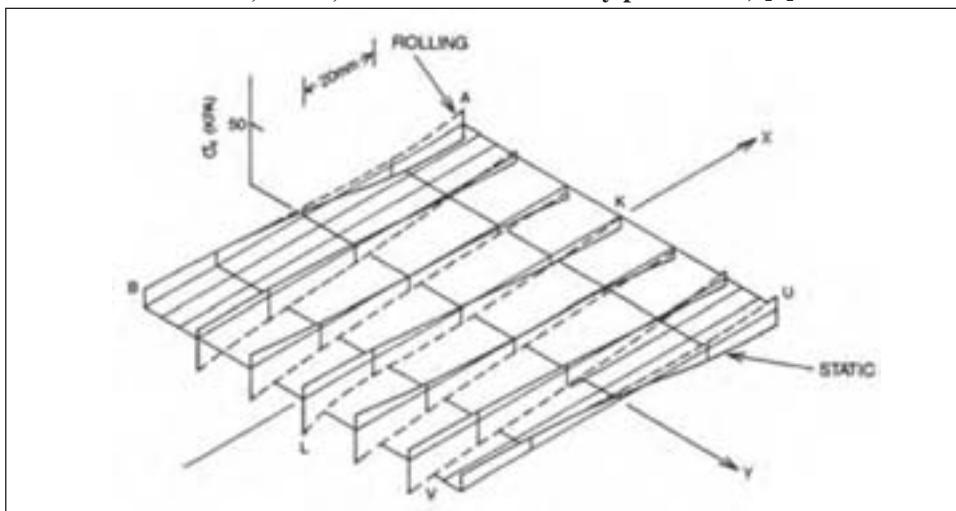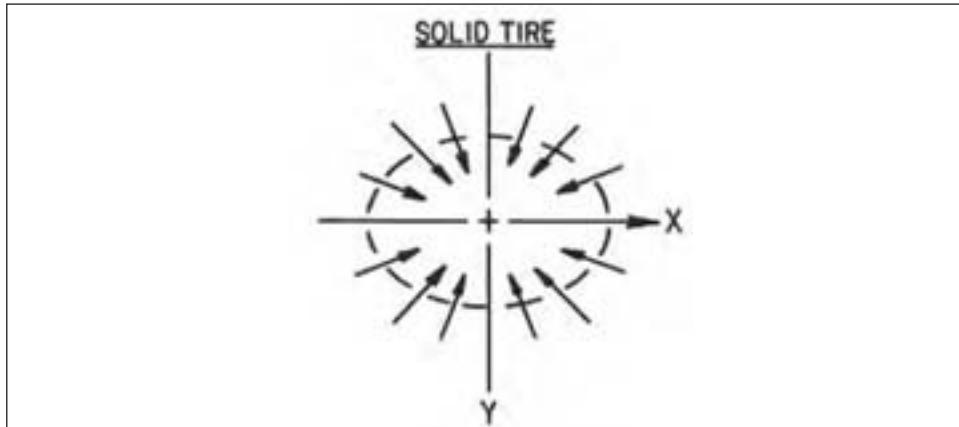

Figure 7.50 shows the longitudinal stress field for a solid tire, both static and rolling. Again, the sense of the stresses is reversed in comparison with that seen in the pneumatic tire, figure 7.41. But the rolling radius is larger on the shoulders and smaller in the crown, just as in the pneumatic case. The effect of rolling is very clear in the crown where negative shear stresses are absolutely dominant.

Figure 7.50: Isometric of longitudinal stresses in the footprint of a static and slow rolling solid tire (reprinted from Tire Science and Technology, Vol. 20, No. 1,   1992 with Tire Society permission) [6]

The result is a solid tire shear field like that in figure 7.51. Addition of this field to the global pneumatic field conceptually presented in figure 7.36 causes significant and complex changes.

Figure 7.51: Fundamental sense of shear stresses acting in the footprint of a solid tire (reprinted from Tire Science and Technology, Vol. 20, No. 1, 1992 with Tire Society permission) [6]
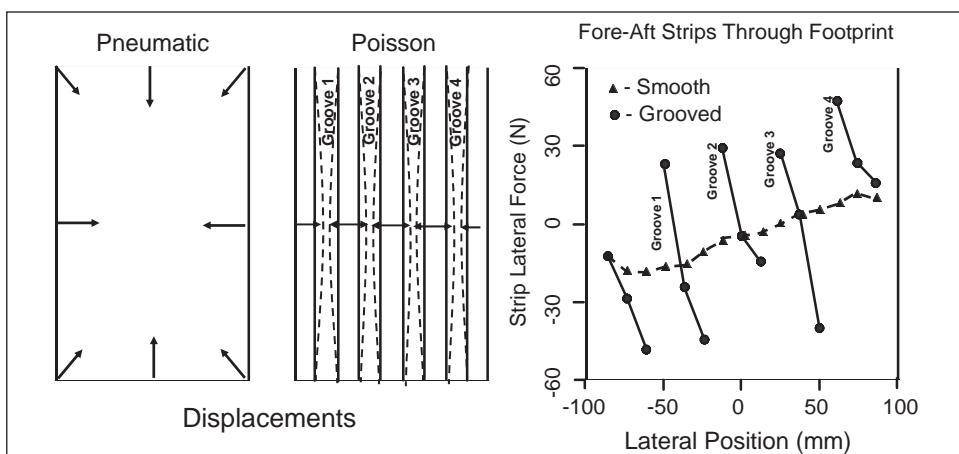
4.2.2 Deviations in footprint stresses and motions due to tread pattern

The effects of straight lateral and longitudinal grooves are discussed in this section. They are easily understood, based on the simple model of solid tread elements superimposed on a pneumatic structure. As grooves become complex in character the responses become complex, with the local Poisson effect changing direction with respect to the pneumatic field. Also, as slip angle, inclination angle, and torque are applied the tread elements bend in complex ways[36]. A full discussion of all possible interactions is beyond the scope of this chapter.

   Figure 7.52 shows the effect of adding longitudinal grooves to the smooth treaded tire used in the production of figures 7.34 and 7.44. The effect is expressed in terms of the lateral forces on footprint length strips having a width equal to that of the 3-axis stress transducers used in the experimental study. Without grooves, a smooth change occurs from negative forces on the left shoulder to positive forces on the right shoulder. This is exactly as expected due to the pneumatic effect, see figures 7.36 and 7.40. With grooves, there

Figure 7.52: Effect of longitudinal grooves on footprint forces

is a sharp change at each groove edge. The sense is exactly as expected based on figures 7.49 and 7.51. Consider groove 2 for example. The lateral force on the left edge is sharply negative compared to the value prior to having the groove cut. The right edge of the second rib is trying to slide into groove 2, inducing a leftward, negative, shear force. The effect on the right edge of groove 2 is the exact reverse, and this alteration continues across the tread.

Figures 7.53 and 7.54 show the rib/groove effect in terms of lateral stresses along the y-axis for a performance tire and a medium duty truck tire. The effect is the same regardless of tire type. However, it is worth noting that the underlying stress pattern in the truck tire does not show the effect of cord load reduction, as mentioned earlier in the discussion of figures 7.37 and 7.38. This is because the inflation preload of the cords in the truck tire is high enough to prevent a serious loss in cord load during contact deformation.

Figure 7.53: Effect of longitudinal grooves on the lateral stress field across the crown of a performance tire (reprinted from Tire Science and Technology, Vol. 27, No. 3, 1999 with Tire Society permission) [7]
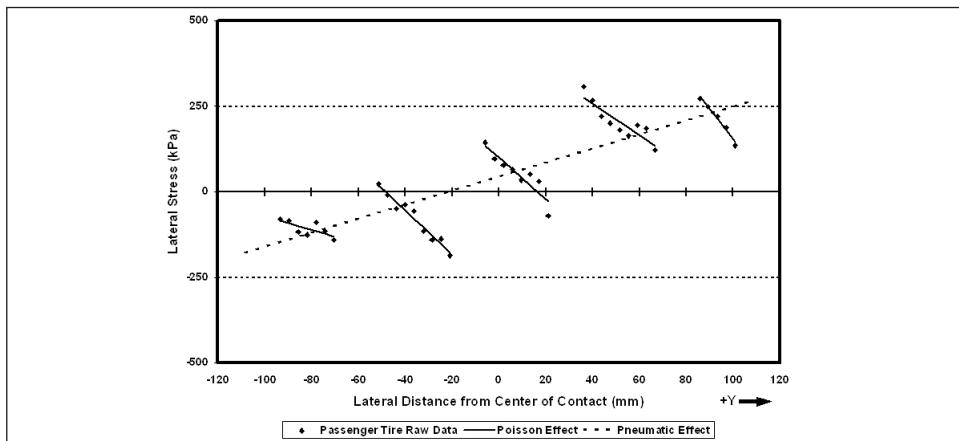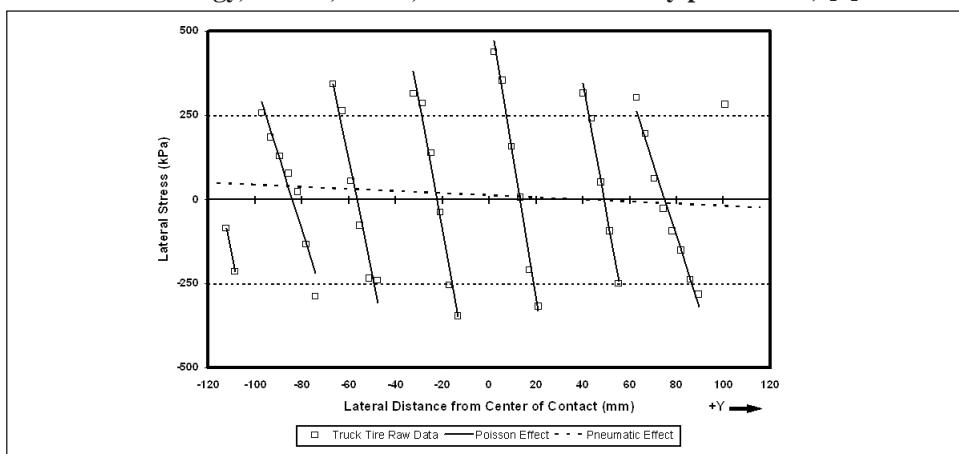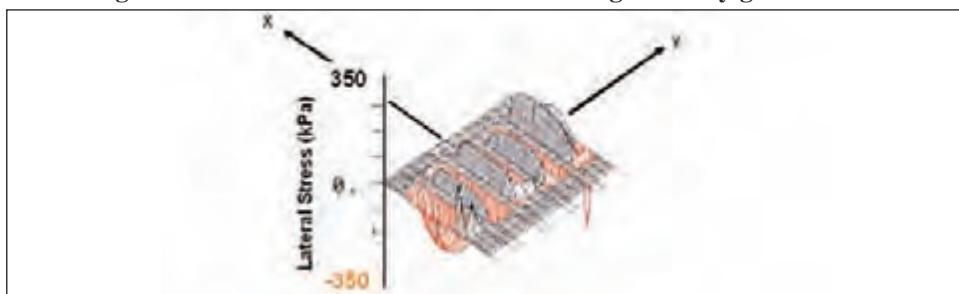
Figure 7.54: Effect of longitudinal grooves on the lateral stress field across the crown of a medium duty (TBR) truck tire (reprinted from Tire Science and Technology, Vol. 27, No. 3, 1999 with Tire Society permission) [7]

The total effect of longitudinal grooves is represented in figure 7.55.

Figure 7.55: Lateral stress isometric for a longitudinally grooved tire

Adding cross-cut grooves to the longitudinal groove pattern shown in figure 7.52 alters the longitudinal stress pattern as shown in figure 7.56. In this case the net force on a series of 5mm square areas along the leading edge of the blocks is positive while that on a series of 5mm square areas along the trailing edge of the blocks is negative. This is what would be expected based on Poisson bulging under compression.

Figure 7.56: Effect of lateral grooves on footprint forces
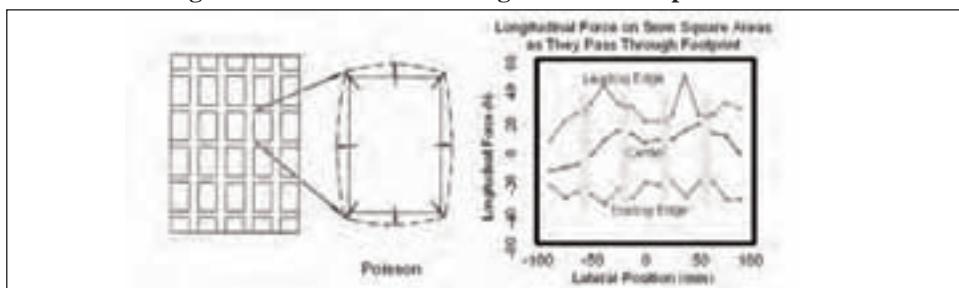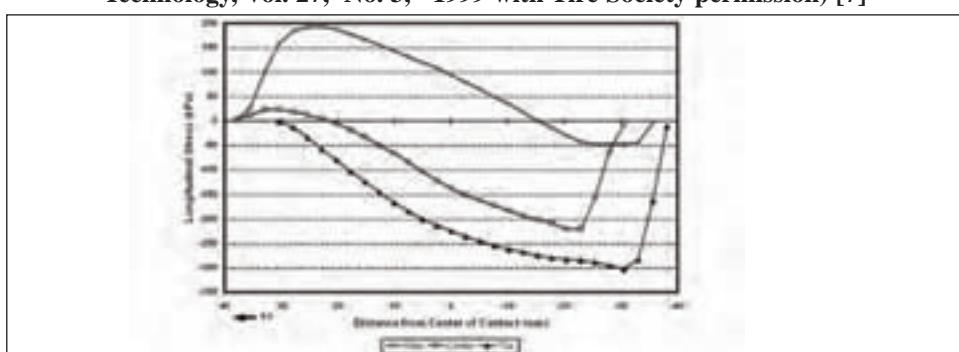
Figure 7.57 shows the effect of the edges of a lateral block element in the tread of a performance tire. The heel, i.e., the block leading edge, is subject to positive stresses as expected, and the toe, trailing edge, shows a definite negative bias, also as expected.

The Poisson effect in this case, when mixed with some braking, will produce heel /toe wear because the stresses on the toe are larger than on the heel. This is a common occurrence.

Figure 7.57: Effect of lateral grooves on the longitudinal stress field of a tread element in the crown of a performance tire (reprinted from Tire Science and Technology, Vol. 27, No. 3,   1999 with Tire Society permission) [7]

4.3 Shear energy and uneven wear

Shear energy intensity, I_{ij}, (J/m²/rev), was defined in section 3.7 along with equations to calculate it. Wear at the point (i,j) on the tread surface was expected to be proportional to the shear energy intensity at that point. Equation 7.14 expresses the wear at (i,j) for a given tire rotation, l, for a particular part of the route spectra m,n.

$$R_{ijlmn} = A\, I_{ijlmn} \qquad \text{(Eq. 7.14)}$$

Where:
A = Abradability (mm removed / (J/m²/rev))

R_{ijlmn} = Tread (mm) removed at point (i,j) in the lth revolution under the conditions existing in the $(m,n)^{th}$ route spectra bin.

Knowing the route spectra as represented in figure 7.32 it is possible to restate Equation 7.14 to represent the whole route, Equation 7.15.

$$R_{Tij} = A\, I_{Tij} = A\, l_T \left(\underset{mn}{\Sigma\Sigma}\, I_{ijmn}(l_{mn}/l_T) \right) \qquad \text{(Eq. 7.15)}$$

Where:

I_{Tij} = Route Intensity, Intensity indicative of the entire route (J/m²)

l_{mn}/I_T = The fraction of the route spectra represented by bin m,n.

l_{mn} = The number of revolutions in bin m,n.

l_T = Total number of tire revolutions.

R_{Tij} = Total Rubber Removed by driving the entire route (mm).

Obviously, a repeated course could be characterized by determining its route spectra then computing tread loss on the basis of the total operational distance.

Plainly, the ideal situation would be one in which I_{Tij} at every point (i,j) would be identical. In this case, R_{Tij} would be the same at every point and wear would be even. This is nearly impossible to achieve, but great effort goes into trying to achieve a reasonable approximation to this ideal state.

4.3.1 Operational and design effects on shear intensity

Shear energy intensity is very strongly affected by tire operational forces as is expected based on the fact that it is a result of shear stresses and slip displacements. It follows a power law, as one would expect based on equation 7.2 in section 3.6. Figure 7.58 illustrates how a slip angle of only + 1 produces changes by an order of magnitude in shear energy intensity and in expected wear for a performance tire.

Design effects can also be understood on the basis of shear energy intensity. Figure 7.59 portrays the shear energy intensity of a straight free-rolling medium duty truck tire. The overall intensity shows hotspots. Examining the X and Y intensities shows that the hotspots arise from different sources. I_X shows the effect of tie bars in ribs 2 and 4. I_Y shows the effect of shear along the longitudinal grooves. Plainly tread design effects are discernable in energy intensity measurements just as they are in real wear tests.

Figure 7.58: Slip angle and shear energy intensity (partially reprinted from Tire Science and Technology, Vol. 27, No. 3, 1999 with Tire Society permission) [7]
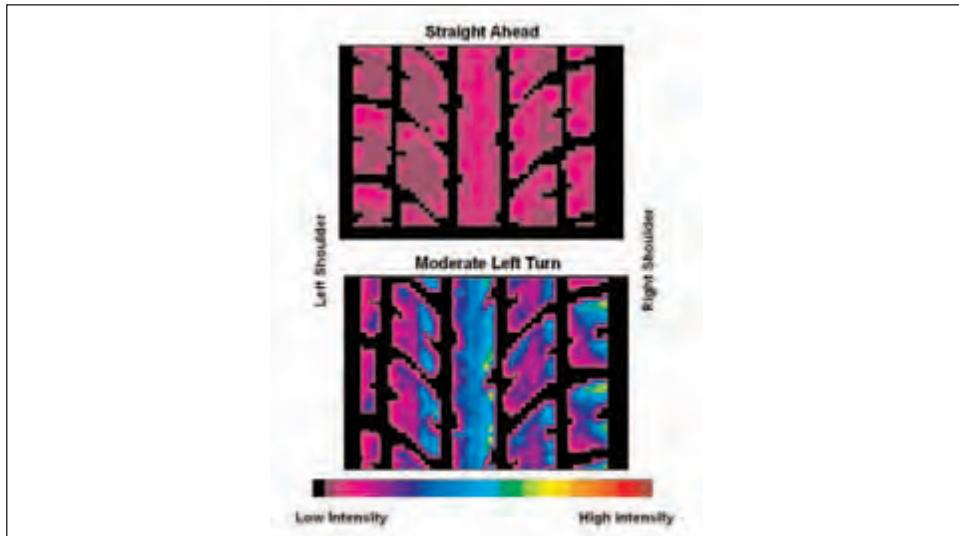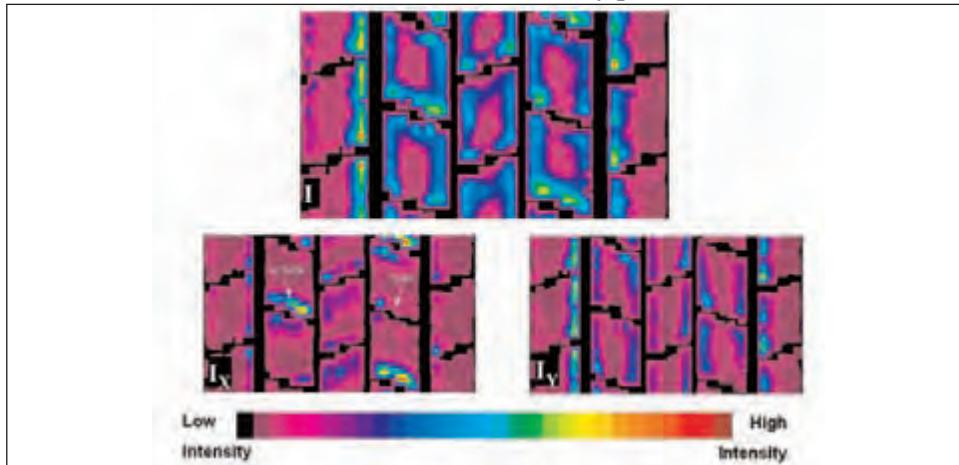

Figure 7.59: Tread pattern effects on shear energy intensity (partially reprinted from Tire Science and Technology, Vol. 27, No. 3, 1999 with Tire Society permission) [7]

4.3.2 Wear predictions based on shear energy intensity

The authors of references 7, 15, 21, and 33 have all tried to predict uneven wear based on shear energy intensity. Pottinger and McIntyre[7] introduced the concept as described in this chapter and it has been used by the other authors, but with only limited access to wear data and no access to abrasion data. Knisley[15], in figure 7.60 demonstrated a quite reasonable correlation between footprint shear energies and indoor wear experiments like those mentioned in section 4.3.4, without considering abradability. Koehne and Rieger [21] provide a number of correlation examples. Most interestingly, Zheng[33] obtained very reasonable predictions using an extensive multi-step finite element simulation of footprint

behavior, figure 7.61. Zheng simulated the entire wear process, including stepwise tread removal, using abradability based on over-the-road experiments. This is a comprehensive application of the concept expressed in equation 7.15.

Figure 7.60: Tire-by-tire agreement between wear rate and shear energy intensity (reprinted from Tire Science and Technology, Vol. 30, No. 2, 2002 with Tire Society permission) [15]
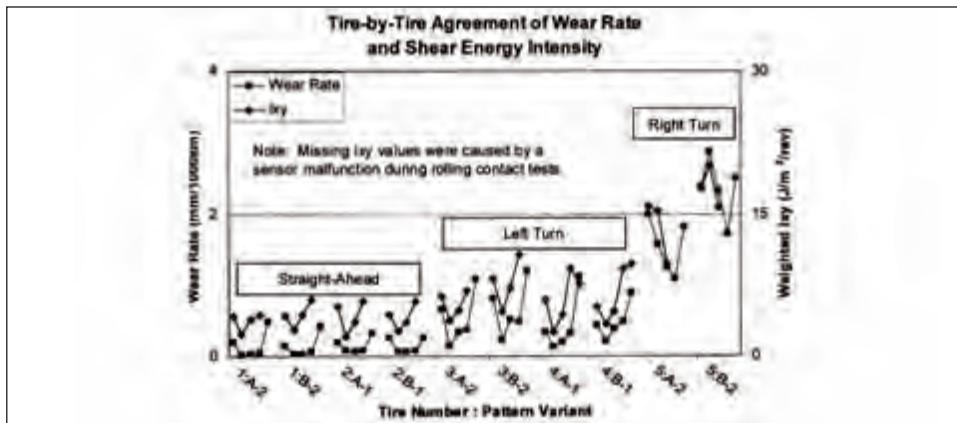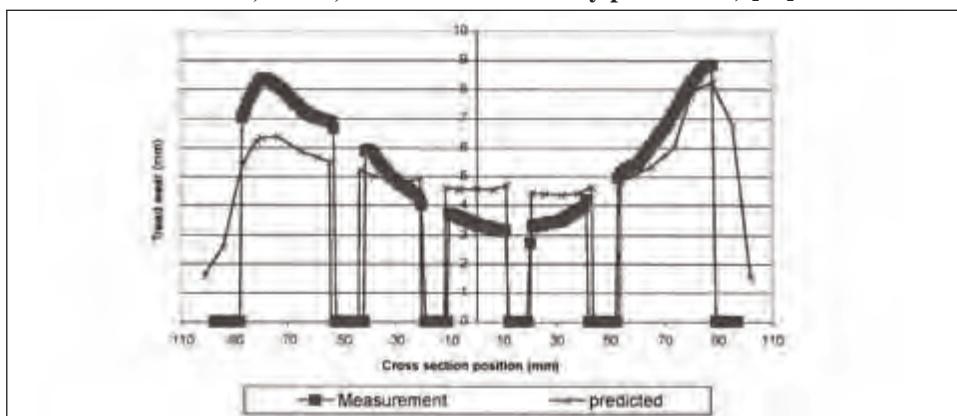
Figure 7.61: Cross section tread wear profiles for the right-front tire (reprinted from Tire Science and Technology, Vol. 31, No. 3, 2003 with Tire Society permission) [33]

4.3.3 Temperature as a surrogate for energy intensity

A discussion of temperature determination in the footprint was given in section 5.2. In section 5.2.2, Walters [24] observation that it is possible to use properly-obtained tread surface temperature as a surrogate for shear energy was mentioned. This has not been widely referred to, but Trivisonno demonstrated its feasibility in an oral presentation at the 1994 International Tire Engineering Conference. Differential surface temperatures on tread elements showed a good linear correlation with heel/toe wear, $r^2 > 0.9$.

4.3.4 Indoor laboratory simulations based on duplicating the energy history in an outdoor wear test

Over the last decade it has become common to use route characterizations of the type discussed in Section 3.6.1, to do indoor wear tests with machines like that portrayed in figure 7.16, equipped with dust applicators and collectors as portrayed in figure 7.62. The results give quite a reasonable simulation of outdoor wear results, figure 7.63 [32, 34].

Figure 7.62: Features of indoor wear test equipment (reprinted from Tire Science and Technology, Vol. 30, No. 2, 2002 with Tire Society permission) [30]
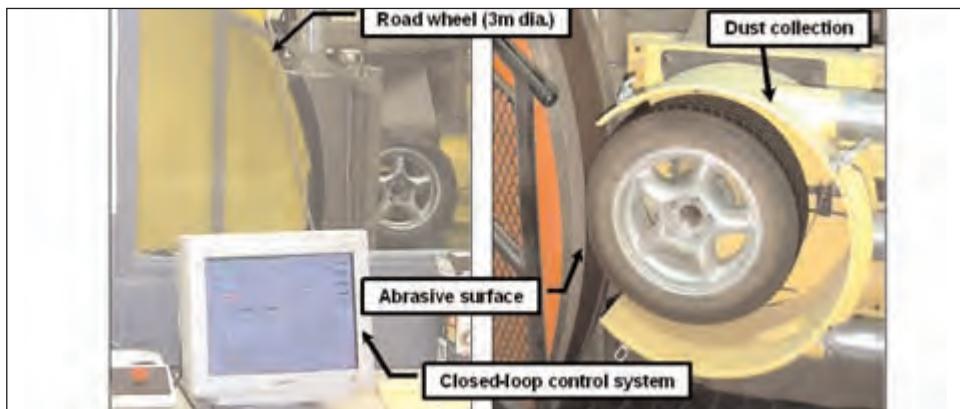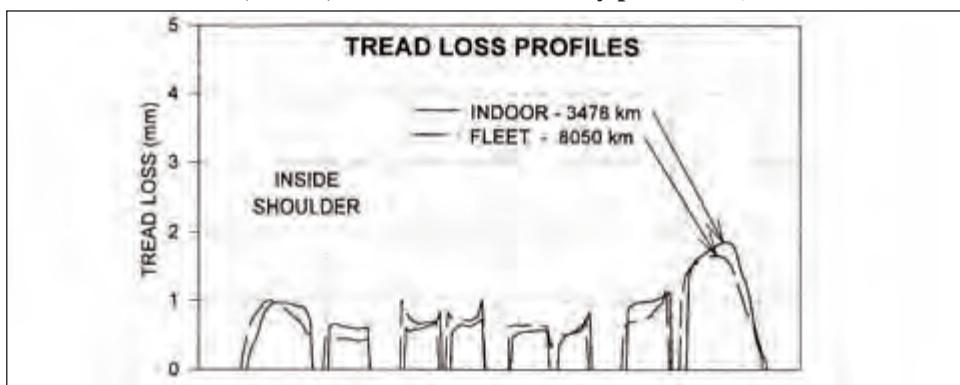
Figure 7.63: Comparison of fleet- and indoor-tested tread loss profiles for tire design A (reprinted from Tire Science and Technology, Vol. 24, No. 2,   2002 with Tire Society permission) [34]

5. Concluding Remarks
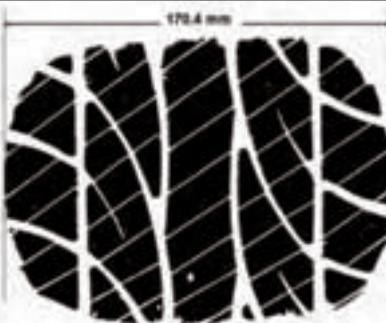
An orderly framework for discussing footprint behavior has been provided and the wide range of experimental methods that are used for analyzing footprint behavior has been described. Example results have been presented and the underlying physics and mechanics have been discussed. However, it should be obvious from the presentation that this subject is far from completely worked out - much remains to be elucidated. Although space limitations prevented the inclusion of many details of our present understanding of footprint behavior, it is hoped that the references provided will help the interested reader pursue the subject further.

6. References

1. "Tire Performance Terminology," Society of Automotive Engineers, SAE J2047, Warrendale, PA, 1998.

2. Michael, F., "Zur Frage der Abmessungen von Luftreifen für Flugzeuglaufräder," Jahrbuch 1932 der D. V. L., 3 p.17. Available in English Translation as NACA TM 689 (1932).

3. Hertz, H., "Gessammelte Werke," Vol. I, Leipzig, 1885.

4. "Mechanics of Pneumatic Tires," S. K. Clark Ed., Monograph 122, National Bureau of Standards, Washington, D.C., November 1971.

5. "Mechanics of Pneumatic Tires," S. K. Clark Ed., DOT HS 805 952, National Highway Traffic Safety Administration, Washington, D. C., August 1981.

6. Pottinger, M. G., "The Three-Dimensional Contact Patch Stress Field of Solid and Pneumatic Tires", *Tire Science and Technology*, TSTCA, Vol. 20, No. 1, January-March 1992, pp. 3-32.

7. Pottinger, M. G., "Effect of Suspension Alignment and Modest Cornering on the Footprint Behavior of Performance Tires and Heavy Duty Radial Tires," *Tire Science and Technology*, TSTCA, Vol. 27, No. 3, July – September 1999, pp. 128-160.

8. "Standard Practice for Tread Footprints of Passenger Car Tires Groove Area Fraction and Dimensional Measurements," F870-84, *Annual Book of ASTM Standards, Vol. 09.02*, ASTM, W. Conshohocken, PA, 2005.

9. Yeager, R. W., "Tire Hydroplaning: Testing, Analysis, and Design," *The Physics of Tire Traction*, D. F. Hays and A. L. Browne, Eds., Plenum Press, New York, N.Y., 1974.

10. Grogger, H., and Weiss, M., "Calculation of the Hydroplaning of a Deformable Smooth-Shaped and Longitudinally-Grooved Tire," *Tire Science and Technology*, TSTCA, Vol. 25, No. 4, October-December 1997, pp. 265-287.

11. Seta, E., Nakajima, Y., Kamegawa, T., and Ogawa, H., "Hydroplaning Analysis by FEM and FVM: Effect of Tire Rolling and Tire Pattern on Hydroplaning," *Tire Science and Technology*, TSTCA, Vol. 28, No. 3, July-September 2000, pp. 140-156.

12. Ginn, J. L., and Marlowe, R. L., "Road Contact Forces of Truck Tires as Measured in the Laboratory," Society of Automotive Engineers, SAE 670493, Warrendale, PA, 1967.

13. Pottinger, M. G., "Apparatus for Measuring Tire Tread Force and Motion," U. S. Patent No. 4,986,118.

14. Marshall, K. D., Phelps, R. L., Pottinger, M. G., and Pelz, W., "The Effect of Tire Break-In on Force and Moment Properties," Society of Automotive Engineers, SAE 770870, Warrendale, PA, 1977.

15. Knisley, S., "A Correlation Between Rolling Tire Contact Friction Energy and Indoor Tread Wear," Tire Science and Technology, TSTCA, Vol. 30, No. 2, April- June 2002, pp. 83-99.

16. Koehne, S. H., Matute, B., and Mundl, R., "Evaluation of Tire Tread and Body Interactions in the Contact Patch," Tire Science and Technology, TSTCA, Vol. 31, No. 3, July-September 2003, pp. 159-172.

17. Malacaria, C., "Making no Mark," *Tire Technology International*, June 2003, pp. 51.

18. Gentle, C. R., "Optical Mapping of Pressures in the Tyre Contact Patch," *Optics and Lasers in Engineering*, No. 4, 1983, pp. 167-176.

19. Sakai, E. H., "Measurement and Visualization of the Contact Pressure Distribution of Rubber Disks and Tires," *Tire Science and Technology*, TSTCA, Vol. 23, No.4, October-

December 1995, pp. 238-255.

20. Lazeration, J. J., "An Investigation of the Slip of a Tire Tread," *Tire Science and Technology*, TSTCA, Vol. 25, No. 2, April-June 1997, pp. 78-95.

21. Koehne, S. H. and Rieger, A., "Measurement of the Slip of Tread Blocks in the Contact Patch," *Tire Science and Technology*, TSTCA, Vol. 32, No. 2, April-June 2004, pp.69-80.

22. Fujikawa, T., Funazaki, A., and Yamazaki, S., "Tire Tread Temperatures in Actual Contact Areas," *Tire Science and Technology*, TSTCA, Vol. 22, No.1, January-March 1994, pp. 19-41.

23. Fujikawa, T., Funazaki, A., and Yamazaki, S., "Estimation of Tire Tread Temperature in Contact Patch," *JSAE Review*, Vol. 12, No. 1, January 1991, pp.44-49.

24. Walters, M. H., "Uneven Wear of Vehicle Tires," *Tire Science and Technology*, TSTCA, Vol. 21, No. 4, October-December 1993, pp. 202-219.

25. Harris, M., "Precision Tread Measurement,"

26. Sube, H. J., Fritschel, L. E., Siegfried, J. F., Dory, A. J., and Turner, J. L., "Method and Apparatus for Measuring Tire Parameters," U. S. Patent 5,245,867.

27. Veith, A. G., "The Driving Severity Number (DSN) – A Step Toward Quantifying Treadwear Conditions," *Tire Science and Technology*, TSTCA, Vol. 14, No. 3, July-September 1986, pp.129-159.

28. Le Maitrae, O., Sussner, M., and Zarak, C., "Evaluation of Tire Wear Performance," Society of Automotive Engineers, SAE 980256, Warrendale, PA.,1998.

29. Wright, C., Pritchett, G. L., Kuster, R. J., and Avouris, J. D., "Laboratory Tire Wear Simulation Derived from Computer Modeling of Suspension Dynamics," *Tire Science and Technology*, TSTCA, Vol. 19, No. 3, July-September 1991, pp.122-141.

30. Stalnaker, D. O., and Turner, J. L., Vehicle Course Characterization Process for Indoor Wear Simulation," *Tire Science and Technology*, TSTCA, Vol. 30, No. 2, April-June 2002, pp.100-121.

31. Chiesa, A., and Ghilardi, G., "Evaluation of Tire Abrasion in Terms of Driving Severity," Society of Automotive Engineers, SAE750459, Warrendale, PA., 1975.

32. Parekh, D., Whittle, B., Stalnaker, D., and Uhlir, E., "Laboratory Tire Wear Simulation Process Using ADAMS Vehicle Model," Society of Automotive Engineers, SAE 961001, Warrendale, PA., 1996.

33. Zheng, D., "Prediction of Tread Wear with FEM Steady State Rolling Contact Simulation," *Tire Science and Technology*, TSTCA, Vol. 31, No. 3, July-September 2002, pp.189-202.

34. Stalnaker, D., Turner, J., Parekh, D., Whittle, B., and Morton, R., "Indoor Simulation of Tire Wear: Some Case Studies," *Tire Science and Technology*, TSTCA, Vol. 24, No. 2, April-June 1996, pp. 94-118.

35. Laging, G., and Rothert, H., "Numerical Results of Tire-Test Drum Interaction," *Tire Science and Technology*, TSTCA, Vol. 14, No. 3, July-September 1986, pp. 160-175.

36. Okonieski, R. E., Moseley, D. J., and Cai, K. Y., "Simplified Approach to Calculating Geometric Stiffness Properties of Tread Pattern Elements," *Tire Science and Technology*, TSTCA, Vol. 31, No. 3, July-September 2003, pp. 132-158.

Problems

1. Figure 7.2 presents the Footprint Axis System. Figure 8.1 presents the SAE Tire Axis System. Derive the transformation from the FAS System to the SAE Tire Axis System.

2. Figure 7.1 presents an ink block plot of a footprint. The area enclosed by a line circumscribing the footprint periphery and touching image is referred to as the gross footprint area. The portion of the gross area that is printed in black is referred to as the net footprint area. The groove area is defined as the gross area minus the net area and the groove void fraction as the groove area divided by the net area times 100. Using the Problem 7.2 PowerPoint file as raw data, determine the gross footprint area, the net footprint area and the groove void fraction. *NOTE: For purposes of this problem all parts of the grooves have been assumed to be of equal depth and the tread thickness has been assumed to be equal to the groove depth.*

Problem 7.2:

3. Examining the half footprints shown in figure 7.6 it is obvious that the area in contact is shrinking with rising velocity. Given the concept that full hydroplaning will occur when the contact area is reduced to zero, at what speed should full hydroplaning occur?

4. Assuming that the footprint system in your laboratory is composed of transducers like that sketched in figure 7.7 with a 5 mm X 5 mm top and a 0.5 mm wide gap, compute the footprint stresses imposed on the tire when the transducer reports the following forces applied to it. What is the apparent coefficient of friction?

$F_X = 3$ N; $F_Y = -4$ N; $F_Z = 5$ N

5. Why is it important to reject data arising from partially covered footprint stress transducers? If the decision were to use data from partially covered transducers, what must be known besides the transducer loading in order to make the data valid?

6. What tare relationship must be known between a displacement needle transducer and applied normal stress in order to insure that the displacement data are accurate? *NOTE that this question that must be considered to insure that slight needle height discrepancies do not introduce errors. Surface lapping can take care of stress transducer height discrepancies.*

7. Assuming a footprint length of 10 cm, what would be the largest slip angle at which a

± 1.75 mm range displacement needle would likely be able to fully measure lateral displacement? Assume that the full lateral displacement occurs from beginning to the end of contact. Figure 8.3 provides a conceptual sketch of the expected displacement.

8. (Figure 7.33 data.XLS – worksheet, Osc Plot) is the data set used to draw figure 7.33. Cross plot s_X vs. u and s_Y vs. v. There are large changes in s_X and s_Y in the absence of appreciable changes in u and v. What feature of the tire's structure makes this possible?

Problem 8.5

Tire manufacturer	
Tire construction number	
Tire size	295/75R22.5
Tread pattern	
Load	6175 lbs.
Deflection	n/a
Inflation	125 psi
Rim width	8.25 in.
Slip angle	0 degrees
Chamber angle	0 degrees
Operator	CHP
Test date	3/10/1998
Comments	11 in data window
Slip factor	5
Torque value	0
Speed	3

9. The tire in figure 7.43 is a self-supporting tire. It will roll as much as 80 km at 80 km/hr when uninflated, before self-destructing. Given the situation portrayed in the flat rolling data, what would be your expectation with regard to wet road behavior?

10. (Figure 7.45 data.XLS – worksheet, lateral summary) is the data set used to draw figure 7.45. Turning to the Sz worksheet, add the normal stresses to the data in the Lateral Summary. What is the relationship of the stresses in each rib?

11. Using the data included for problem 10, how does the lateral intensity accumulate on Ribs 1, 3, and 5? What relative wear relationship would be expected if the tire continued to operate at a -1° slip angle, as it is in the example data?

12. If braking torque were applied to the tire portrayed in figure 7.56, what would be the expected worn block profile? What if driving torque had been applied instead?

Figure 7.33 Data
Test information
Sx
Sy
Sz
mx
my
Osc plot
Y plot
Sheet 5
X plot
Sigma Z plot
Sigma plot
Figure 10

Figure 7.45 Data
Test information
Sx
Chart 1
Sy
Sz
mx
Chart 2
my
Lateral summary
Figure 22a
Figure 22b

Chapter 8
Forces and Moments

by M. G. Pottinger

Chapter 8
Forces and Moments

by M. G. Pottinger

When pneumatic tires were first produced commercially, after John Boyd Dunlop invented them for the second time [1][1], they were viewed as vibration isolation devices with reduced rolling resistance. A bicyclist could readily perceive these characteristics. There was no immediate recognition that pneumatic tires had an improved ability to produce control forces.

The importance of the tire as the source of vehicle control forces was recognized when the automobile became the important tire market. Recognition began with the need for safety when braking. Understanding of the importance of lateral force came later.

Analytical vehicle dynamics began when tire force and moment data first became available. During the 1930s, R. D. Evans [2] of Goodyear and then A. W. Bull [3] of U. S. Rubber measured tire force and moment properties. Evans' work was on a smooth steel drum. Bull examined the question of testing on flat versus curved surfaces and was already concerned with test surface friction.

Maurice Olley, who can be viewed as the father of vehicle dynamics in the United States, noted the importance of this force and moment measurement work in a 1961 speech. Olley said, "With the introduction of independent front suspension… in this country and the first tire tests on smooth drums, by Goodyear in 1931 (by Cap Evans)…, the real study of the steering and handling of cars began."

World War II interrupted this early automotive progress and focused attention on other problems, particularly aircraft shimmy. This dynamic problem was of concern to all air forces, particularly the Luftwaffe, which held a meeting on shimmy at Stuttgart in 1941 [4]. Some of the first effective tire force and moment mathematical modeling was presented at that urgent meeting.

At the end of World War II, engineers expert in aeronautical stability theory began to apply modeling to the problem of automotive control and stability. William F. Milliken and Leonard Segel at the Cornell Aeronautical Laboratory, working under the sponsorship of General Motors, were leaders in this effort. Today, all tire and vehicle manufacturers apply modeling to the problem of vehicle control. The tire force and moment data requirements of vehicle modeling sparked the development of the current methods for determining, characterizing, and modeling tire force and moment behavior. These methods continue to evolve.

The data requirements of the existing virtual prototyping system for vehicle stability and handling design have largely been met by tire force and moment data developed on smooth road surfaces, without vertical undulations or bumps. Road-surface-excited tire vibration, which is discussed in chapter 9, has usually been treated as a separate subject. The split between subjects occurred because of the practical difficulty of solving the general problem.

In parallel with the major thrust to describe tire force and moment properties on a smooth dry road, substantial effort has been expended on the effects of contaminants such as water, snow, and ice. These effects have been studied extensively, along with the effects of pavement micro-texture and macro-texture, as noted in chapter 11.

---

[1]Numbers in [brackets] denote references at the end of the chapter.

This chapter treats tire force and moment behavior classically with an emphasis on dry road behavior. It then looks at modifications due to surface texture and surface contaminants.
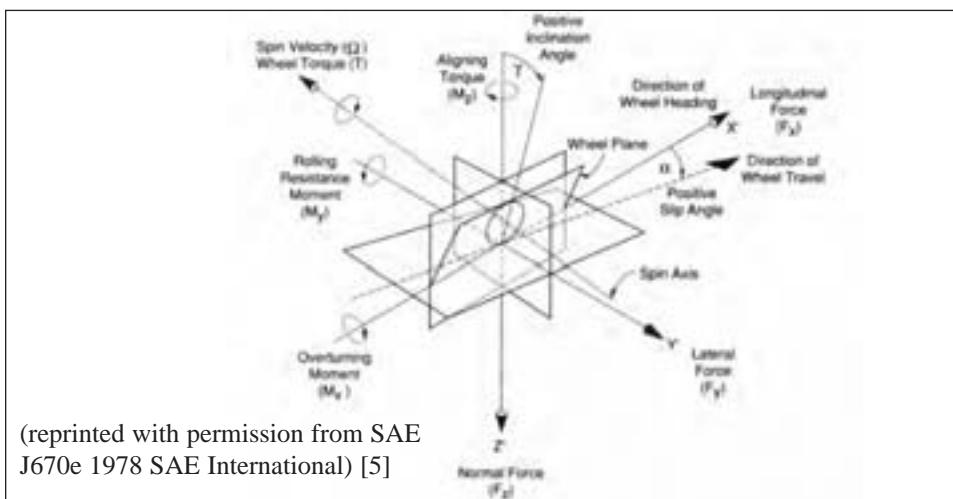
2. Describing tire forces and moments

Tire forces and moments are complex non-linear functions of the tire usage variables that are established by driver inputs and vehicle responses. On a laboratory test machine or an over-the-road testing device, the test conditions are established by the need to explore the expected range of usage. To allow communication, modeling, and use of the resultant data, a formal language has been developed for describing inputs to the tire and the force and moment responses developed by the tire. We will explore the SAE dialect of this language and then briefly show the ISO permutation. Both the SAE Tire Axis System and the ISO Wheel Axis System have their origins at the road since the source of tire forces and moments is at the road surface. In the following, the first mention of a term defined within a terminology document is capitalized to identify the fact that it is a universally defined term.

2.1 The SAE tire axis system

Figure 8.1 portrays the SAE Tire Axis System [5, 6]. The system is a right-handed, three-axis, orthogonal, Cartesian coordinate system with its origin at the Contact Center in the road plane. The road plane is the plane tangent to the road surface at the contact center. The contact center is the point in the road plane where the line defined by the intersection of the Wheel Plane (the plane halfway between the rim flanges) to road plane is cut by the projection of the Spin Axis onto the road plane. Thus, the contact center is defined by the wheel, not the tire. It is defined in terms of the wheel because the tire is flexible and the exact location of its center of contact at any given moment is indeterminate. The SAE X'-axis is along the line defined by intersection of the wheel plane with the road plane, the contact line. Positive X' is in the intended rolling direction for the tire. The SAE Y'-axis is along the projection of the spin axis onto the road plane. Positive Y' is to the right when the system is viewed from the rear looking in the positive X'direction. The SAE Z'-axis is defined by the cross product of +X' into +Y'. It is perpendicular to the road plane with its positive sense into the road plane.

Figure 8.1: Tire axis system

(reprinted with permission from SAE
J670e 1978 SAE International) [5]

2.2 Definition of the tire forces and moments

Since the precise effective location at which the road applies forces to the tire is unknown and the origin of the tire axis system is arbitrarily defined by the wheel and road geometry, three forces (F_X, F_Y, and F_Z) and three moments (M_X, M_Y, and M_Z) are required to define the road's action upon the tire.[2]

Each of the three forces acts along its associated axis in the tire coordinate system. For example, F_X acts along X'.[3] The positive direction for each force is the same as the positive direction for its associated axis as indicated in figure 1. The three forces are defined as follows.

Longitudinal force, F_X, is the force of the road on the tire along the X'-axis. It accelerates or decelerates the vehicle dependent on whether the tire is driven or braked. If F_X is positive, the tire is driven, and F_X is called driving force. If F_X is negative, the tire is braked, and F_X is called braking force.[4]

Lateral Force, F_Y, is the force of the road on the tire along the Y'-axis. It forces the vehicle to move to the left or right dependent on whether the tire is steered and/or cambered to the left or right.[5]

Normal force, F_Z, is the force of the road on the tire along the Z'-axis. It is the contact force between the road and tire. By definition, it is negative.

Each of the three moments acts about its associated axis in the tire axis system. For example, M_X acts about X'. The right hand rule applies. The positive sense for each moment is clockwise about the positive branch of its associated axis when looking away from the tire axis system origin along the positive branch of the axis. This is shown in figure 1. The three moments are defined as follows.

Overturning moment, M_X, is the moment about the X'-axis. It accounts for the effect of left-to-right displacement of the point of action of the normal force with respect to the contact center. M_X influences camber behavior.

Rolling resistance moment, M_Y, is the moment about the Y'-axis. It accounts for the fore-aft displacement of the point of action of normal force with respect to the contact center. M_Y is somewhat misnamed, as it has little to do with rolling resistance, see chapter 12.

Aligning moment, M_Z, is the moment about the Z'-axis. It accounts for the point of action of the shear forces, F_X and F_Y, within the road plane.

The tire and wheel are also subjected to moments due to gyroscopic and angular accelerations that occur during dynamic operation. These will be mentioned as appropriate, but are not a major concern in most force and moment studies.

2.3 Tire usage variables or inputs that lead to development of tire forces and moments

In use, tires generate the forces and moments we have just defined. Tire force generation

---

[2]The reason for describing the forces and moments in terms of the road's action on the tire is that these are the forces that move the vehicle and the engineer's interest is in vehicle behavior.

[3]Complete mathematical correctness would say the F_X [5] should be $F_{X'}$ [6]. While this correction was made in Reference 6, common usage has continued to follow Reference 5. The author has chosen common usage in this chapter.

[4]If the tire is mounted on a steered axle, F_X has a moment about the Kingpin Axis [5] and can cause lateral movement of the automobile by steering the tires. Also, F_X can steer the vehicle by modulating lateral force. This is discussed in Section 8.4.3. These steering effects can usually be considered secondary in normal driving.

[5]Obviously, if F_X can modulate F_Y as noted in footnote 4, F_Y can modulate F_X. Thus, cornering affects the ability to accelerate or decelerate a vehicle. This is discussed in Section 8.4.3.

comes about kinematically in response to a number of usage variables, and inputs such as pressure and driving speed. The effects of these parameters are considered in Section 8.5. The usage variables are defined in this section.

Tire load, which is characterized in terms of Normal Force (F_Z), is the most important tire usage variable. It largely determines the tire structural deformations. Normal force is a crucial player in the generation of frictional forces and, hence, in this whole discussion. R_l, Loaded Radius, is the distance from the spin axis to the contact center in the wheel plane. This is an important geometric variable in tire force and moment studies. It is dependent on normal force and the tire's structure.

A tire generates lateral force in response to two principal angular variables shown in figure 8.1.

Slip angle, α, is measured from the X′-axis to the direction of wheel travel, trajectory velocity, V_T. V_T, the velocity of the contact center across the road, lies in the road plane. α is positive clockwise around the positive branch of the Z′-axis. A positive slip angle is associated with a left turn.

Inclination angle, γ, measures the tilt or camber of the wheel plane with respect to the Z′-axis. Inclination angle is measured from the Z′-axis to the wheel plane within the Y′-Z′ plane. It is positive clockwise around the positive branch of the X′-axis. The top of a tire showing a positive inclination angle is moved to the right with respect to its contact center, as seen from the rear.

Tire engineers use inclination angle instead of camber angle to maintain sign consistency at all tire positions on a vehicle. Inclination angle is positive when the top of a tire leans to the right. Camber angle is defined as positive, if the tire is leaning outward on a vehicle. Thus, on the right side of a vehicle camber angle is equal to inclination angle, but on the left side of a vehicle camber angle is the negative of inclination angle.

If the path followed by the tire has very large curvature, i.e., very small turning radius, the path curvature itself measurably affects lateral force and aligning torque generation. For automotive and truck tires, path curvature at normal operating speeds is small and is ignored. However, in the case of motorcycle weave, path curvature should be considered.

Longitudinal force generation depends on angular velocity about the spin axis and in particular on the relationship of the instantaneous angular velocity to the angular velocity existing when the tire is free-rolling in a straight line.[6] The moment or torque that is applied from the axle to the tire is what determines the tire angular velocity. Thus, the torque applied about the spin axis is also important in the generation of longitudinal force. Spin angular velocity, Ω, is the angular velocity of the tire about the spin axis.

Slip ratio, SR, equation 8.1, characterizes spin angular velocity at a given time relative to the spin angular velocity of the straight free-rolling tire, Ω_0. When Ω is greater than Ω_0, SR > 0, the tire generates a driving force. When Ω is less than Ω_0, SR<0, the tire generates a braking force.[7]

$$SR = (\Omega - \Omega_0)/\Omega_0 \qquad (8.1)$$

Wheel torque, T, is the external moment applied to the tire about the spin axis, see figure 8.1. T causes the tire to operate in either a driven or braked state. When T is greater than zero, it is called Driving Torque. When T is less than zero, it is called braking torque.

---
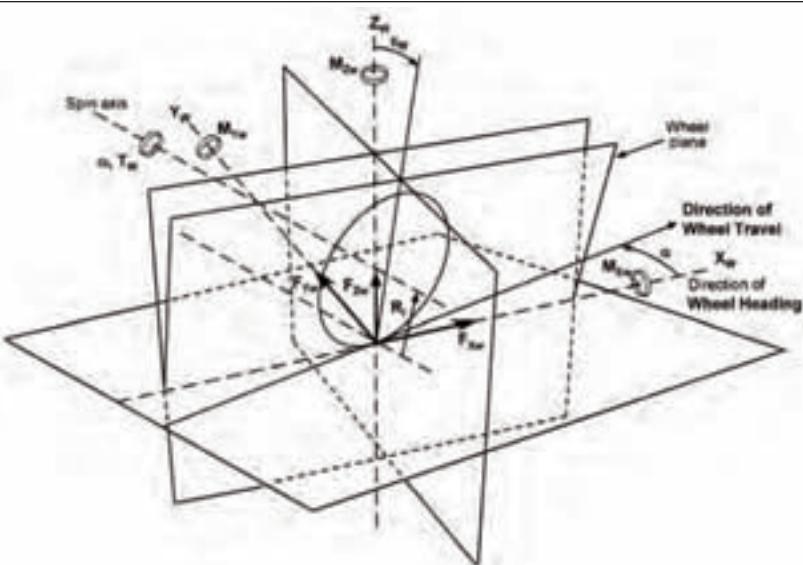
[6]A free-rolling tire is subject only to tire rolling resistance and bearing drag.

[7]The definition given above is the common definition. There are other definitions sometimes used in the literature because they lend themselves to particular mathematical formulations [7].

2.4 The ISO wheel axis system
Figure 8.2 portrays the ISO Wheel Axis System [6]. This system has the same function in ISO 8855 that the tire axis system has in SAE J670e. Some of the elements forming the wheel axis system have slightly different names and symbols than they have in the tire axis system. In a practical sense, the wheel axis system represents a 180° rotation of the tire axis system about the X′-axis (or X_W-axis in ISO terms) resulting in positive Z_W being upward and positive Y_W being to the left. In the wheel axis system, a positive slip angle is associated with a right turn. Again, a positive inclination angle moves the top of the tire to the right with respect to the contact center when viewing the tire from behind looking in the positive X_W direction.

Figure 8.2: Wheel axis system

(Reprinted with permission from SAE J2047   1998 SAE International) [6]

3. Tire deformation responses to individual usage variables
These are simple descriptions of the tire deformations or kinematic responses that produce tire forces and moments. The ones described are for pure inputs. In some cases, more elaborate examples are provided in chapter 7.

*3.1 Response to pure slip angle*
Imagine that the tire belt and tread band have been simplified to a string representing the centerline of the tread, the equatorial line running around the tire's crown. Further imagine that the string is supported by an elastic foundation that supports the string away from the wheel radially and will return the string to the center with respect to the wheel plane if the string is deflected laterally and released. Further, imagine that the string's surface has small blocks of a high friction material like tire tread rubber attached at successive points along its length.
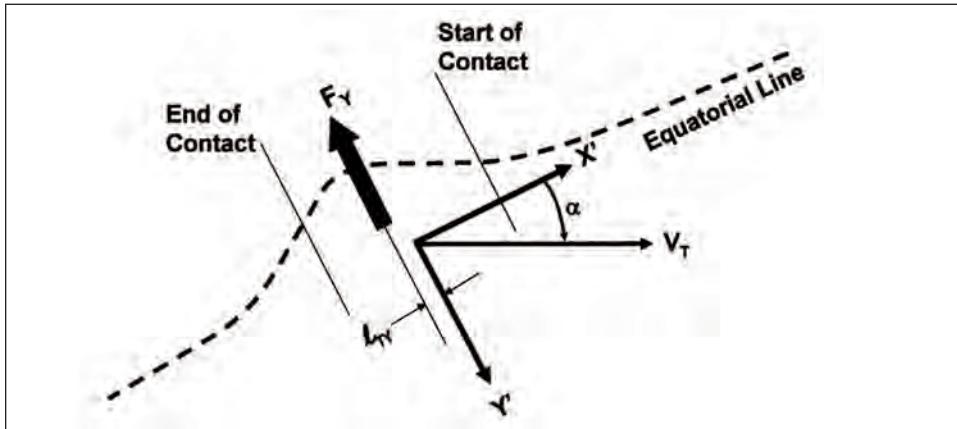
    Let's now look down on top of the road surface and trace the path of the string repre-

senting the tread centerline. This will be done as the simplified tire is rolled against the road with a positive slip angle, yaw angle, existing between the trace of the wheel plane on the road surface and the local velocity vector of the contact center, the trajectory vector. This left turn situation is portrayed in figure 8.3 where the string is referred to as the equatorial line.

When a block on the surface of the string first touches the road it tends to adhere to the

Figure 8.3: String tire at a slip angle in contact with the road

road surface. Then, as the tire rolls forward the block moves further into the contact patch, initially following the direction of the trajectory velocity. This induces frictional forces between the block and the road because the string's elastic foundation is trying to return the string to the wheel plane. At some point in its path through contact the block can no longer provide the friction needed to perfectly follow the path of the trajectory velocity and it begins to slide over the road surface. Given long enough, or really a large enough rolling distance for the situation to equilibrate, the string takes up a configuration like that represented in figure 8.3.

The integral of the lateral stresses, lateral force, is negative for a positive slip angle and has a line of action located behind the center of contact for slip angles that occur in ordinary driving. Thus, the lateral force has a moment, aligning moment, about the Z'-axis, which tends to return the tire to its unsteered state. The distance from the contact center to the line of action of lateral force is called the pneumatic trail, l_{TY}. The example illustrates that aligning moment is inherently positive for a small positive slip angle, which is what we encounter in normal driving.

Assuming that the normal stresses act on the line of the string, then it is plain that their integral, normal force, has a positive moment, overturning moment, about the X'-axis.[8]

Real tires have treads of finite width, and belt packages. The tread and belt package, which is a ring, also has bending stiffness. Thus, if the package is deformed laterally, as in the string model, simple continuity considerations force it to twist out of the road plane. This causes the footprint to go from a roughly symmetric shape laterally, as shown in figure 8.4, into a trapezoidal shape like that in figure 8.5. The heavily loaded, long side of the footprint lies on the more forward lateral edge of the footprint. In the example case,

---

[8]In this discussion sidewall compliance effects are assumed to have been accounted for in the characteristics of the elastic foundation supporting the string.

positive slip angle – left turn, the long edge is the right edge. This tends to cause the normal force to lie to the right of the X′-axis, induce a negative overturning moment.

Figure 8.4: Glass plate photo of footprint shape for a straight free-rolling tire
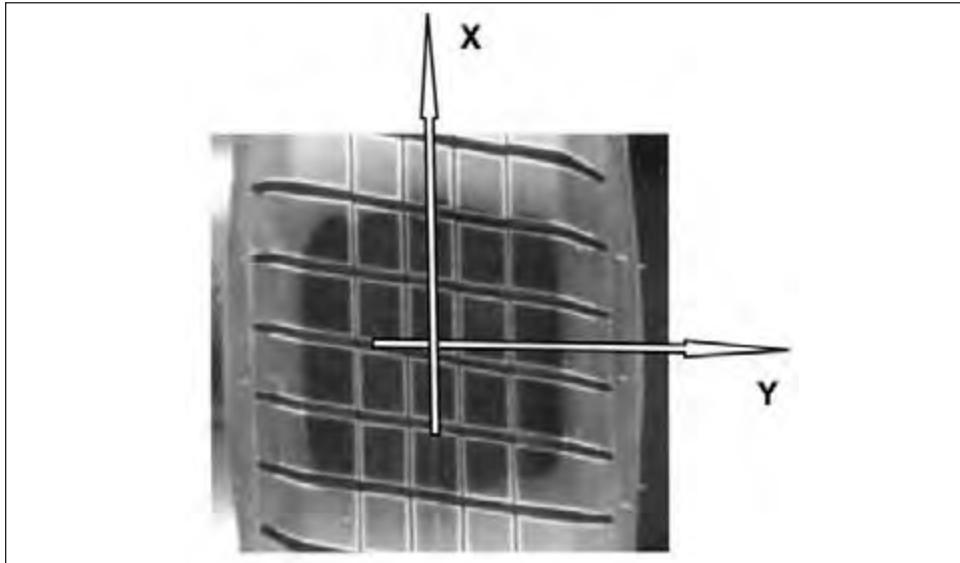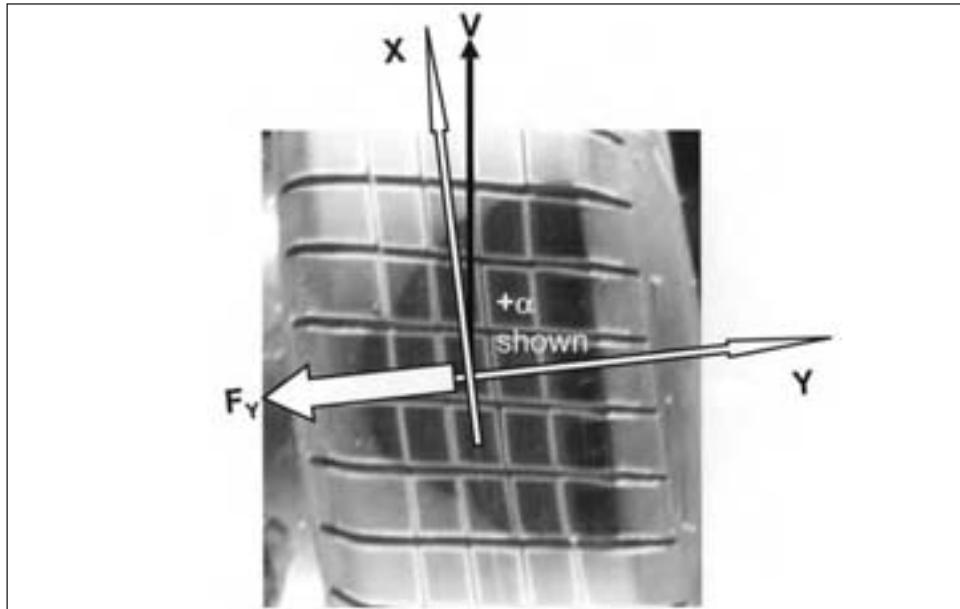

Figure 8.5: Glass plate photo of footprint shape at a positive slip angle

Considering that there are two mechanisms driving the development of overturning moment, each with a different relationship to slip angle, overturning moment can be either positive or negative dependent on the tire's design, on load, and on which mechanism predominates under a given operating condition.

Fortunately, the mechanics for lateral force and aligning moment are only modulated by out-of-plane twisting, not changed completely. Thus, the string model presents a simple conceptual model for them.
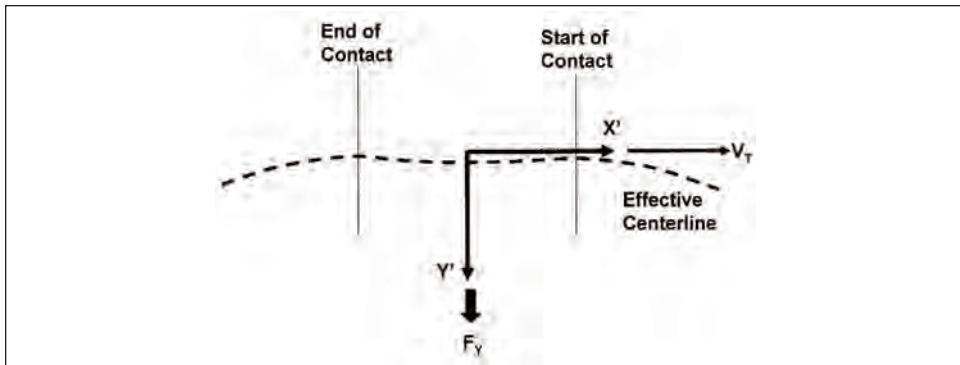
3.2 Response to inclination angle

The discussion just presented for conceptualizing response to slip angle is broadly accepted. The one that will now be given for conceptualizing response to inclination angle is less universally accepted.
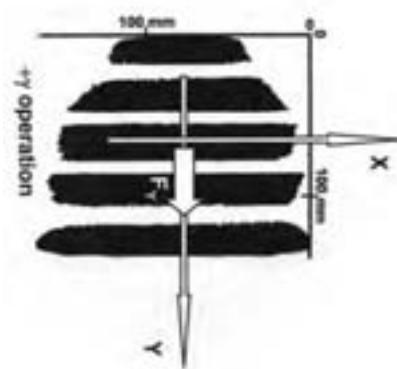
The explanation begins with the effective tread centerline then considers general out-of-plane twisting effects associated with tread band width and bending stiffnesses. The case of positive inclination angle will be examined.

Figure 8.6 illustrates that the effective line is pushed away from the wheel plane by the geometric change when the surface of the inclined tire goes from round to flat on coming into contact with the road surface. The resulting deflection is symmetric with respect to the contact center, in principle, rather than growing throughout the footprint as is the case for slip angle. Thus, the magnitude of inclination-induced lateral forces are expected to be smaller than those induced by slip angle. Furthermore, if the blocks never slide, the line of action of the lateral force would be approximately coincident with the Y′-axis and the aligning moment would be inherently zero. This deformation pattern produces a positive lateral force because of a positive inclination angle.

Figure 8.6: String tire at an inclination angle in contact with the road

In the case of a real tire, the approximately symmetric straight free-rolling footprint as shown in figure 8.4 is again distorted into a trapezoidal shape due to inclination angle, figure 8.7. The lateral deformation of a longitudinal slice through contact becomes more severe as the slice's location moves from the lightly loaded shoulder toward the heavily loaded shoulder. Due to the ideally symmetric character of the lateral stresses, sliding, if it occurs, will be in front of the contact center. This will cause the lateral force resultant to lie in front of the center of contact. Hence, one would expect a positive aligning moment to be associated with positive inclination angle. Furthermore, the local rolling radius of each longitudinal slice is inherently smaller as the slice's location moves from the lightly loaded to the heavily loaded shoulder. At some lateral location the local slice's rolling radius would be the same as the tire's rolling radius. To the left of this section, the tread surface would be driven, and to its right, it would be braked. The resultant differential longitudinal stress distribution would also produce a positive aligning moment component in response to a positive inclination angle.

Figure 8.7: Footprint shape at a positive inclination angle
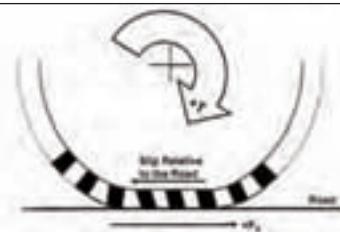
3.3 Response to spindle torque

The effect of spindle torque is to either increase the angular velocity of the tire with respect to its free-rolling angular velocity, driving, or to decrease it, braking.

Imagine a tire rolling along the road at its straight free-rolling angular velocity. In this state, the tire will act as if it were subject to very light braking, and a small net negative longitudinal force will exist because of tire rolling resistance, chapter 12, and bearing drag at the spindle. The tire will be operating at zero longitudinal slip as defined by Eq. 8.1. The tread elements will, in net, have a slight forward motion relative to the road as they pass through contact.

Now assume that a positive spindle torque is applied. The torque will raise the tire's angular velocity inducing a positive longitudinal slip, the tread elements will deform due to the speed differential between the tire surface and the road until the friction limit is reached at which point the tread elements will slide. This is illustrated in figure 8.8. The road will oppose this relative sliding motion and a net positive longitudinal force will be exerted by the road. The vehicle will accelerate in response to the positive spindle torque.

Application of a braking torque reverses the process as a negative longitudinal slip is developed. The tread elements move forward in net with respect to the local road surface. A negative longitudinal force develops in response to the negative spindle torque decelerating the vehicle.

Figure 8.8: Simplified tire subject to driving torque

## 4. Determining force and moment properties
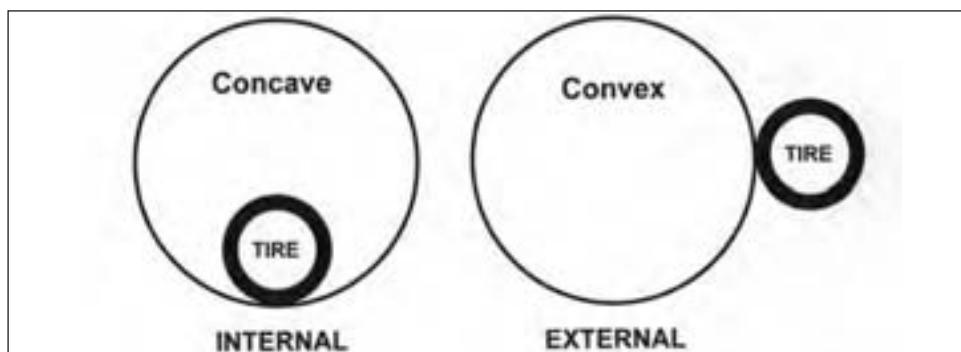
As noted in the introduction to this chapter, the measurement of tire force and moment properties was the crucial step that opened the path to vehicle dynamics. Making some of these measurements has become relatively routine, but some of them have seldom been made, and almost always complaints are expressed about the cost of these measurements, performed with special test machines.

Force and moment machines consist of three basic parts: a road or roadway, tire manipulator, and force sensors. Given these basics, the form of the machine can be quite variable. Both indoor and outdoor (over-the-road) machines exist, but neither of them fully meet the needs for design purposes; so good engineering practice makes use of both types of machine, recognizing the advantages and disadvantages of each.

4.1 The road or roadway

In the real world, road out-of-plane curvature is small. In common terms, real roads are flat. However, when a laboratory machine is built, there are three options for the roadway configuration: round – concave, round – convex, and flat. Round – concave, internal, and round – convex, external are illustrated in figure 8.9.

Figure 8.9: Round - concave, internal, and round - convex, external, roadways
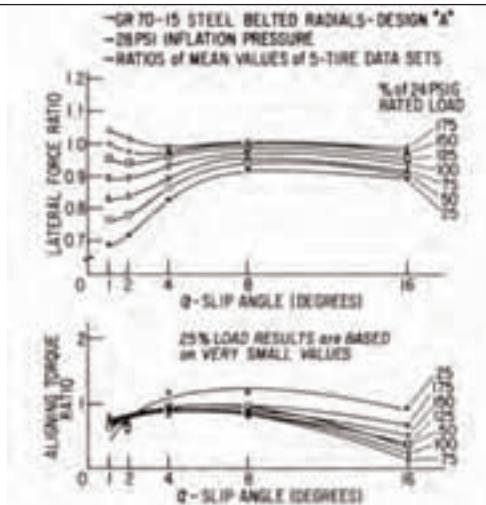
Roadway curvature causes complex deviations of the tire force and moment properties from the ones existing on a flat surface. Figures 8.10 and 8.11 [8] show ratios of force and moment results from an external drum and a flat surface. These ratios are results from the drum divided by results from the flat surface with both sets of data being taken at the same test conditions. They were obtained on the TIRF machine at the Tire Research Facility, part of the General Dynamics Company facility in Buffalo, New York. [9] That machine has the unique characteristic of allowing measurements to be made on both a drum and a flat surface using the same measuring head.

Unfortunately, the relationship between results on curved and flat surfaces is not only complex, but depends on the tire diameter with respect to the diameter of the test surface and on the individual tire construction. No simple rule of thumb exists for converting force and moment data taken on a curved surface to data taken on a flat surface.
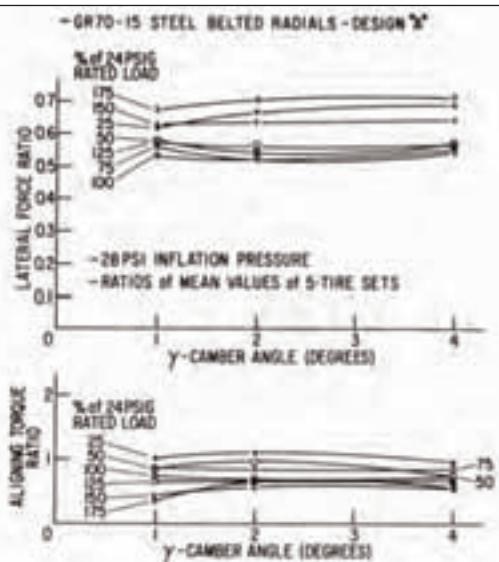
[9]The Tire Research Facility was originally associated with CALSPAN and in 2004 is owned by General Dynamics.

**Figure 8.10: TIRF 1.7m (67 in.) roadwheel / TIRF Flat belt - slip angle**

(Reprinted with permission from SAE 760029 1976 SAE International) [8]

Figure 8.11: TIRF 1.7m (67 in.) roadwheel / TIRF flat belt - inclination angle data

(Reprinted with permission from SAE 760029   1976 SAE International) [8]

If there is such a problem converting data from round to flat, why would anyone use a round test surface? Historically, round surfaces were used for studying tire endurance and high speed performance at the time that Evans [2] and Bull [3] began to study tire force and moment properties. They began with what existed. Further, though it is easy to create a low speed flat surface machine using either a slowly moving table like that in a large milling machine or by moving the tire manipulator over a stationary table; creating a high-

speed flat-surface test machine is not easy. Such machines are much more complex and expensive than drum machines, and not as durable. Internal drum machines allow the ready introduction of real pavement surfaces, and adding water or ice. In the end, however, the high-speed flat-surface test machine has become the preferred device for determining dry surface forces and moments. It typically consists of a steel belt running between two drums with a flat surface in the central contact zone maintained by using a special bearing under the belt, figure 8.12. A major machine control task is to retain the lateral position of the steel belt in the presence of lateral force. This is a dynamic process requiring a belt tracking system. Practically speaking, the TIRF Machine (where the belt is supported by a hydrostatic air bearing) [9], figure 8.13, was the first truly viable high-speed flat-surface machine. The MTS Flat-Trac® (where the belt is supported by hydrodynamic water bearing) [10, 11, 12], figure 8.14, came later. It is the most commonly used test machine in commercial service. [10]

**Figure 8.12: Sketch of a steel belt roadway layout**
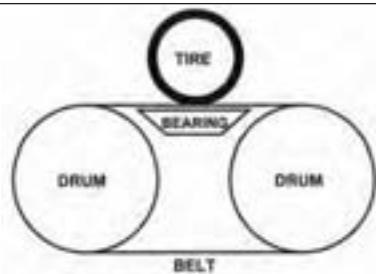
Figure 8.13: The TIRF machine

(Reprinted with permission from SAE 730582 1973 SAE International) [9] The photograph is personal.

---
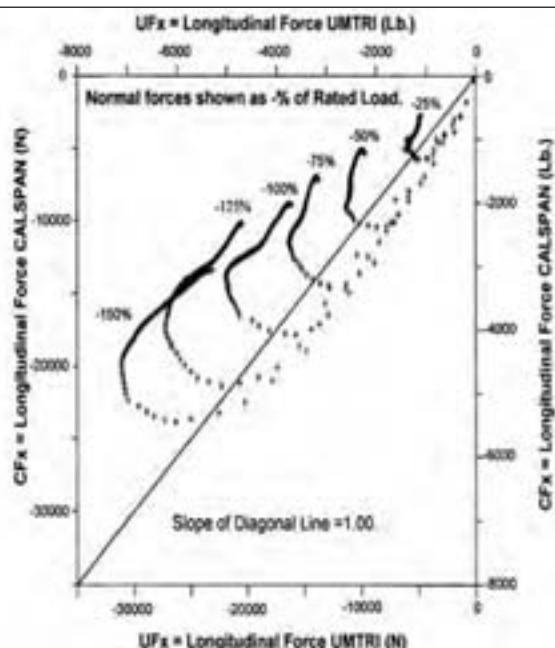
[10]Since the introduction of the Flat-Trac®, it has passed through a number of models and in 2004 exists in a light truck size.

Figure 8.14: The flat-trac I machine, the original Flat-Trac

(Reprinted with permission from SAE 800245 1980 SAE International) [10] The photograph is personal.

Figure 8.15: Correlation between an indoor surface and cross-brushed concrete

(Reprinted from Rubber World Magazine 1996 with Rubber World permission) [13]

Ignoring the question of surface contaminants like water, snow, ice, mud, etc., it is still not easy to deal with the question of surface friction. Indoors, the common practice is to coat the belt with sandpaper[11]. Sandpaper surfaces are believed to be both more realistic than smooth steel and to give relatively stable friction.[12] Does the friction of sandpaper correlate with that of a real road? Often, not as well as would be desired. Figure 8.15 from Reference 13 gives an example of the inherent problem. In this case, the indoor surface on the TIRF machine was a 120-grit previous-generation THREE-M-ITE ® with a cloth backing. The outdoor surface used by UMTRI (University of Michigan Transportation Research Institute) was a cross-brushed concrete. Figure 8.15 shows the relationship between the data. It is not a single val-ued function relating forces on one surface to forces on the other. A true function exists only at low slip ratios where one set of data is linearly related to the other. It is plain that the two machines measured considerably different values even where the force data were functional-ly related. Some will say that there is a simple solution: test over-the-road on a real surface. The question is which real road surface? And when?. Whitehurst and Neuhardt [14] showed that real road surfaces vary in friction from day-to-day, season-to-season, and year-to-year. Surface friction is a thorny issue that demands further work.

4.2 Tire manipulators

To allow precise application of tire forces and moments in response to usage variables, it is necessary to have a tire manipulator to support the tire, load it, apply precise yaw and/or incli-nation angles, and appropriate spindle torques. The tire manipulator is often called a carriage.

The manipulator frame and mechanisms must be quite rigid in order to provide a good base for measurements, not confounded by machine resonances or undesirable deflec-tions. Assuming adequate rigidity, the ability to conduct dynamic measurements is dependent on the actuators provided and the masses which must be moved. By way of example, the Flat-Trac III®, an update of the machine described in Reference 11, is avail-able with a variety of hydraulic pumps and actuators. One particular example allows steer-ing angle changes at rates up to 25°/sec. The steer tube, the load cell, and the load cell attachment bracket (strong arm) are moved around the steer tube axis. The same machine only allows inclination to occur at 1°/sec, since the whole A-frame assembly, a much larg-er inertia, must be moved around an axis tangent to the road surface.

There are many possible mechanisms that can form a satisfactory manipulator pack-age. Each has advantages for particular circumstances, but no single design is so superior that it has rendered all other possibilities obsolete.

4.3 Force sensors

Force and moment machines incorporate various numbers and arrangements of load cells to provide data. It is possible to have these load cells as fixed, non-rotating, parts of the machine or to utilize a spinning—wheel load cell package. For dedicated force and moment machines it is common practice to use the more accurate and convenient fixed arrangements. Spinning wheel load cell systems are ideal for on-vehicle measurements since they can be employed without reconstructing the suspension system. Fixed systems are discussed in this section.

---

[11]An example of such a surface current in 2004 is THREE-M-ITE   a product of 3M.

[12]To insure relative frictional stability, a statistical process control procedure must be applied to the abrasive surface or experiments defining wear along with usage tracking must be applied.

Figure 8.16: Unitary measuring head from a flat-trac II

(Reprinted from Tire Science and Technology, Vol. 20, No. 2, 1992 with Tire Society permission) [11]

Fixed systems may be configured with either unitary or distributed measuring heads. Unitary heads gather all the load cells into a compact arrangement directly supporting the spindle bearings, figure 8.16. A typical arrangement has a spindle supported by two bearings, one thrust and one free-floating. This arrangement allows direct determination of F_X, F_Y, F_Z, M_X, and M_Z. Distributed heads have the load cells strategically placed over a considerable volume of space perhaps even surrounding the frames that form the tire manipulator as in the flat surface tire dynamics machine [15]. In either case, the geometric arrangement of the cells is carefully defined so that the load cell outputs can be transformed into the forces and moments defined in Section 8.1.2. For unitary heads it is also necessary to measure R_l and γ in order to account for the geometry so that the results can be reported in terms of the tire or wheel axis systems.

Today, the unitary head is the common arrangement due to its compactness and high stiffness resulting in a potential high-frequency response. When used in a free-rolling condition, one end of the spindle supports the tire and the other end is unconstrained with respect to rotation. If braking is the only desired torque input, a brake rotor can be installed on the end of the spindle shaft opposite to the tire. However, there is one drawback to using a brake; it is difficult to control the slip ratio after the peak braking force is reached. If both braking and driving torque are desired, it is common to place a coupling between the end of the spindle shaft opposite to the tire and a hydraulic motor. The slip rate control problem is non-trivial, but reasonable control can be achieved using a torque motor.

Load cell systems not only measure forces in the design direction of a given load cell, but also measure a small amount of the force applied in other directions. For example, no matter how well a measuring head is designed and constructed; applying a normal force will cause small readings in the F_X, F_Y, etc. load cells. These small but spurious components can be eliminated from linear systems through a calibration procedure that allows computation of an interaction matrix. This matrix describes the output of all force and moment channels arising from each separately-applied force or moment so that the interactions can be taken into account. Several SAE J-Documents, of which reference 16 is an

example, consider the use of interaction matrices within their discussions.

Finally, the reader is reminded that the original analog signals from the load cells of any force and moment machine must be subjected to proper anti-aliasing filters, if good quality data are to be taken. This is assumed here, and not discussed further.

Table 8.1: Advantages and disadvantages of indoor force and moment machines

Advantages
Reproducible road surface (see footnote 7.)
Controlled environment - no weather generated delays
Most precise control of usage variables (α, γ, F_Z, SR)
Good dynamic response possible
Can readily run tests that would endanger drivers

Disadvantages
Does not use a real road surface
Does not use real weather conditions

**Table 8.2: Advantages and disadvantages
of over-the-road force and moment machines**

Advantages
Real road surfaces
Real weather conditions

Disadvantages
Low tire testing rate (tires tested per unit time)
Less precise control of usage cariables (α, γ, F_Z, SR)
Some tests endanger operators
Reduce dynamic responses
Real weather conditions[13]
Real road surfaces[14]

4.4 Advantages and disadvantages of indoor and over-the-road testers
Tables 8.1 and 8.2 summarize the advantages and disadvantages of indoor and over-the-road force and moment test machines in simple terms. Careful thought about the material in section 8.3 will show why the statements in each table are as they are. You will also note that there may be both good and bad aspects.

5. General data characteristics
To this point, the discussion has provided fundamental background information. We now turn to the general characteristics of tire data that is obtained in response to the various usage variables. These data were measured on machines generally like those described in section 8.3. Each aspect discussed begins with the relevant pure usage inputs and then

---

[13]The weather may not permit testing.

[14]The road surface may not be in the expected condition.

moves to the case of combined inputs. The example results are expressed in the SAE Tire Axis System. One or two problems provide an understanding of how the same data appear when expressed in the ISO Wheel Axis System.

The example results shown should not be considered correct in detail for every tire. Further, the magnitude of responses for various tire specifications[15] can be quite different one from another.

5.1 Free-rolling cornering

Free-rolling cornering is the tire state that exists when a tire is negotiating a bend without being subject to either driving or braking forces. This can occur in response to a slip angle only, in response to an inclination angle only, or as is usually the case in response to slip and inclination angles acting simultaneously. There is also a special case of considerable economic interest in which the tire's self generated lateral forces and aligning moments can cause a vehicle that was intended to travel in a straight line to deviate into a large radius bend, as if it were subject to small steer inputs. This last case, pull-force, is a persistent nuisance for drivers.

5.1.1 Steady state response to slip angle alone

In this case, the loaded tire is steered only. This generates a slip angle, α, and, hence, forces and moments. The usual intent is to acquire steady state data. For this purpose, it is typical to determine the data for free-rolling cornering by either of two methods. The first method (an incremental test) increases α incrementally and then increments the normal force, F_Z, to create a net of points, or test conditions. The second (a sweep test) increases F_Z incrementally and then sweeps (ramps) α from a small negative value to a positive value, to a negative value, and then to a small positive value to create an array of data. There are other possibilities, but they are not discussed in this chapter.

In the case of the incremental test, both slip angle and normal force have fixed values at each test point or condition. The tire is given ample rolling distance at each point after α and F_Z reach their set points to allow equilibration before data are acquired. This settling period, usually two tire revolutions, is typically followed by data acquisition over two tire revolutions at 32 to 64 fixed circumferential locations around the tire. The data are averaged to suppress tire non-uniformity, chapter 9. This test method is typically applied at low speeds, but can be applied at highway speeds. The problem with the incremental method at highway speeds is substantial tread wear if the testing net is extensive.

The sweep test method is suitable at highway speeds as it reduces associated wear. However, to acquire data representative of steady state operation, careful attention must be paid to the relation between distance traveled per unit time and the steering (slip angle) ramp rate. Section 8.4.1.2 discusses response to dynamic steering providing a view of the limitations of a sweep test as a source of steady state data.

Which forces and moments are of concern vary somewhat depending on the slip angle magnitudes. Lateral force is always the primary concern. Aligning moment is the secondary concern at low and modest slip angles up to six or eight degrees. At large slip angles, over 15°, overturning moment is the secondary concern. Loaded radius is an important geometric variable measured simultaneously with the forces and moments.

---

[15]A tire specification is a unique design expressed in terms of mold profile, tread pattern, compounding, cord characteristics, details of the tire composite lay-up, etc.

Lateral force as a function of slip angle, figure 8.17, is approximately reflected with respect to the point at which $F_Y = 0$, reference 17. As shown in figure 8.17, lateral force is not typically zero at the point that $\alpha = 0$.[16] This is an important characteristic of tire behavior related to on-center behavior and is discussed in section 8.4.1.4.1.

A negative lateral force is associated with a positive slip angle and a positive lateral force is associated with a negative slip angle. In the normal driving range the slope of lateral force as a function of slip angle is negative.

The absolute value of slope of the lateral force curve at zero slip angle is commonly

Figure 8.17: Lateral force at a single normal force as a function of slip angle
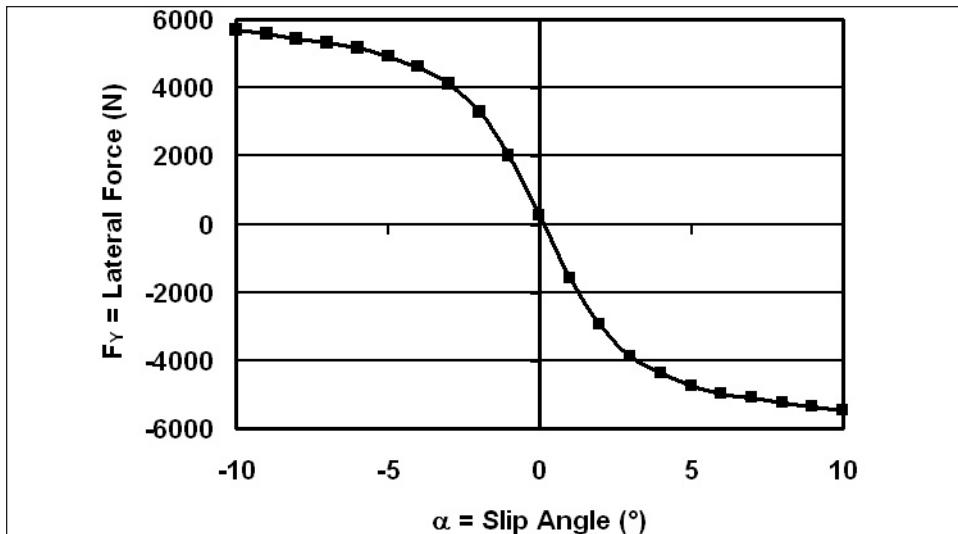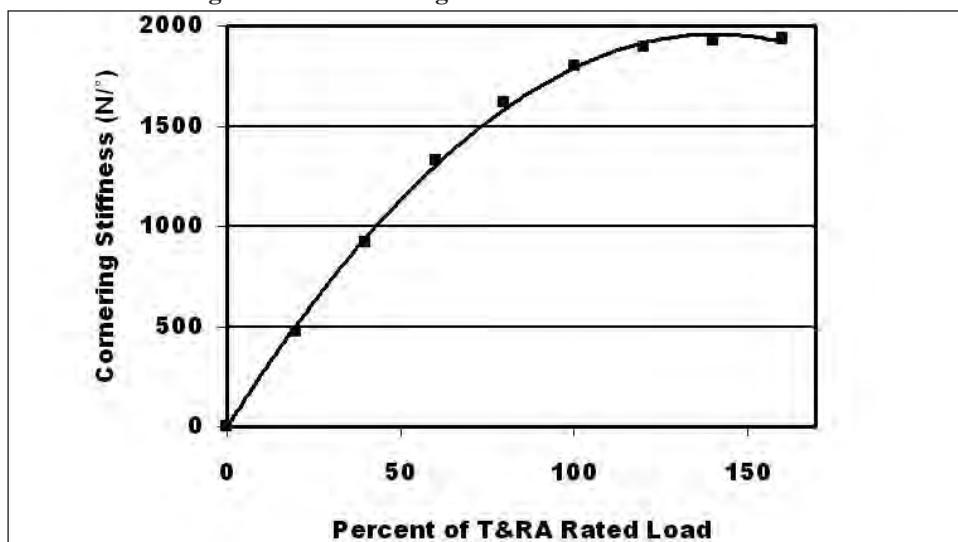
Figure 8.18: Cornering stiffness as a function of load
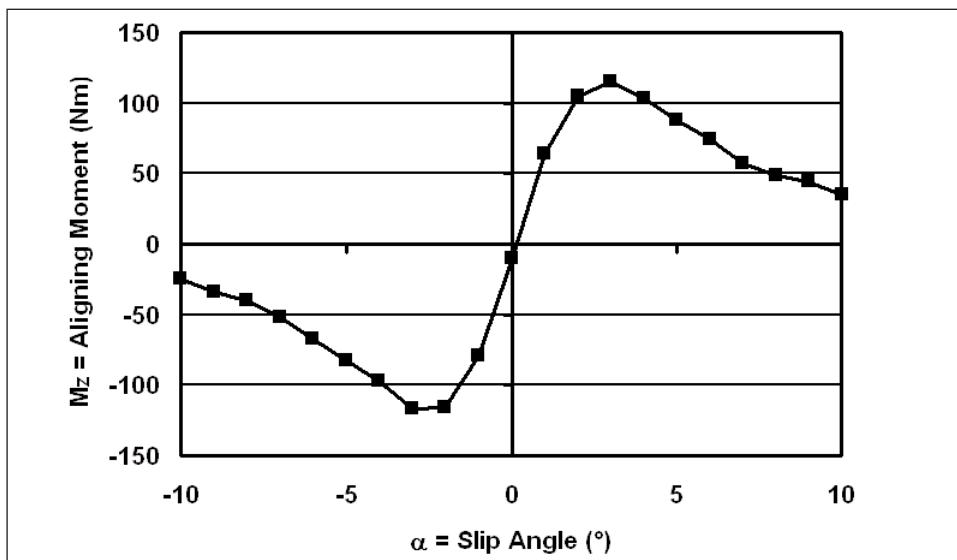
[16]It is possible to design such that FY = 0 when   = 0, but this has a cost and has only been done as an R&D exercise [18, 19].

called the Cornering Stiffness [6]. This is a very important parameter in determining the linear range behavior of vehicles, the area in which most driving is done. Cornering stiffness depends on load (normal force), figure 8.18. It typically increases up to some fraction of the tire rated load [6] then gradually falls off in magnitude as load continues to increase. The data in figure 8.18 extend only to the peak of cornering stiffness with load. Where the cornering stiffness peaks depends on the tire design. For good handling, it is desirable that the peak occurs at or above tire rated load, as it does for the example tire. This produces a positive value of load sensitivity [20, 21], which is the slope of the lateral force curve from 80 percent of tire rated load to 100 percent of tire rated load.

The increase in lateral force with slip angle is a complex non-linear function. The magnitude of F_Y eventually peaks and then declines in a similar way to that for a tire subject to longitudinal braking. Think back to section 8.2.1 and the deformation of the string tire, figure 8.3. As slip angle becomes large, more and more of the available contact area is involved in sliding, thus, a maximum or peak amount of lateral force will be generated at some slip angle. Beyond the slip angle associated with the peak, increasing sliding systematically decreases the lateral force.

Aligning moment as a function of slip angle, figure 8.19, is also approximately symmetrical with respect to the point at which $M_Z = 0$, reference 17. However, in this case, the slope in the normal driving range is positive. As shown in figure 8.19, the aligning moment is not typically zero at the point when $\alpha = 0$ [17] nor is it typically zero at the slip angle for which the lateral force is zero. This is an important characteristic of tire behavior related to on-center behavior and is discussed in section 8.5.1.4.1.

Figure 8.19: Aligning moment at a single normal force as a function of slip angle

The absolute value of the slope of the aligning moment curve at zero slip angle is commonly called the aligning stiffness [6]. This is an important parameter in determining the linear range understeer behavior of vehicles, chapter 14. Note that the aligning stiffness

---

[17]It is possible to design for a particular value of MZ when   = 0. Though this is a complicating detail, the required design modifications are made to insure proper on-center vehicle performance [18, 22].

depends on the load (normal force).
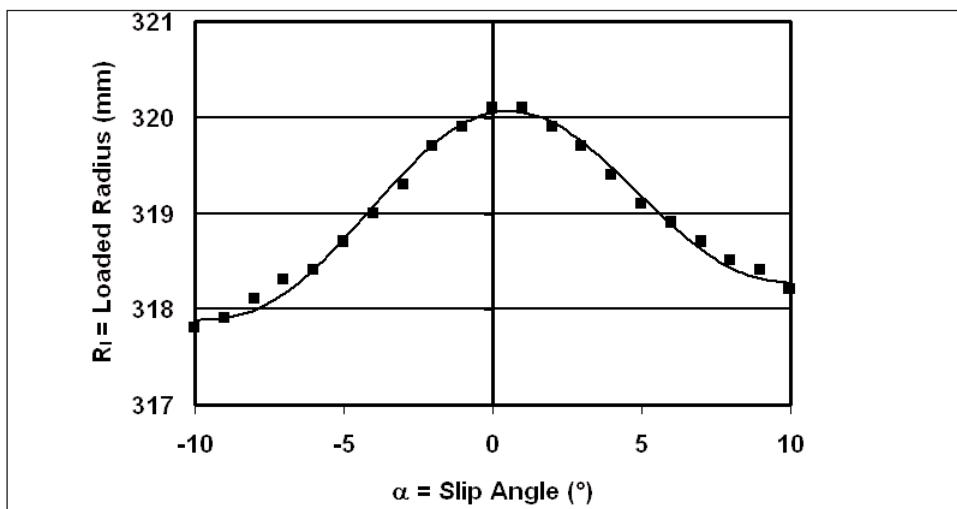
The dependence of aligning moment on slip angle is a complex non-linear function. The magnitude of M_Z peaks at a few degrees slip angle and then declines. Think back to section 8.2.1 and the deformation of the string tire, figure 8.3. As the slip angle becomes large the location of the lateral force resultant moves closer to the origin of the SAE Tire Axis System and can even move slightly ahead of the origin at very large slip angles. This shift of the resultant leads to the complex shape of the aligning moment curve.

Because two mechanisms give rise to the overturning moment, it is not feasible to give a general description of its dependence on slip angle. Examples of the possibilities are presented below.

Loaded radius responds to slip angle by developing an approximately bell-shaped curve representative of softening, figure 8.20.

To this point, the data illustrated are for a single normal force.

Figure 8.20: Loaded radius at a single normal force as a function of slip angle

As noted above, lateral force has the basic form illustrated in figure 8.17. A change in load produces detailed adjustment in the shape of the F_Y data, figure 8.21. The cornering stiffness generally increases with load as was illustrated in figure 8.18, but the rate of increase declines as load increases. The peak of the lateral force curve occurs at higher and higher slip angles as the normal force increases. However, if a pseudo coefficient of friction is computed by dividing the peak value of F_Y at each load by the load itself, one discovers that the frictional capability of the tire declines with increasing load. Thus, high performance vehicles on a dry road will exhibit their maximum cornering ability using large tires operating at relatively light loads.

In a practical sense, the initial region for lateral force up to the slip angle associated with the peak in F_Y is the range where a driver can maintain vehicle control. The probability of loss of control in cornering becomes higher as the operating slip angle approaches the angle associated with the peak lateral force for the normal load, F_Z. In general, lowering the tire aspect ratio causes the lateral force data and data for the other forces and moments to exhibit higher initial slopes and a more abrupt transition from the initial slopes to the behavior at high slip angles. Thus, the width of the transition zone between

well controlled behavior and a possible loss of control is smaller in terms of slip angle for lower aspect ratio tires.

For higher aspect ratio passenger tires like the one that provided the data in figures 8.21, 8.22, 8.24, and 8.25, the overturning moment, figure 8.22, is basically generated by a lateral shifting of the tire contact patch, which can be approximately modeled by the deformation of a string on an elastic foundation, section 8.2.1, figure 8.3. The trend in M_X with slip angle has a positive slope.

Figure 8.21: Lateral force vs. slip angle and load for a 75 aspect ratio tire
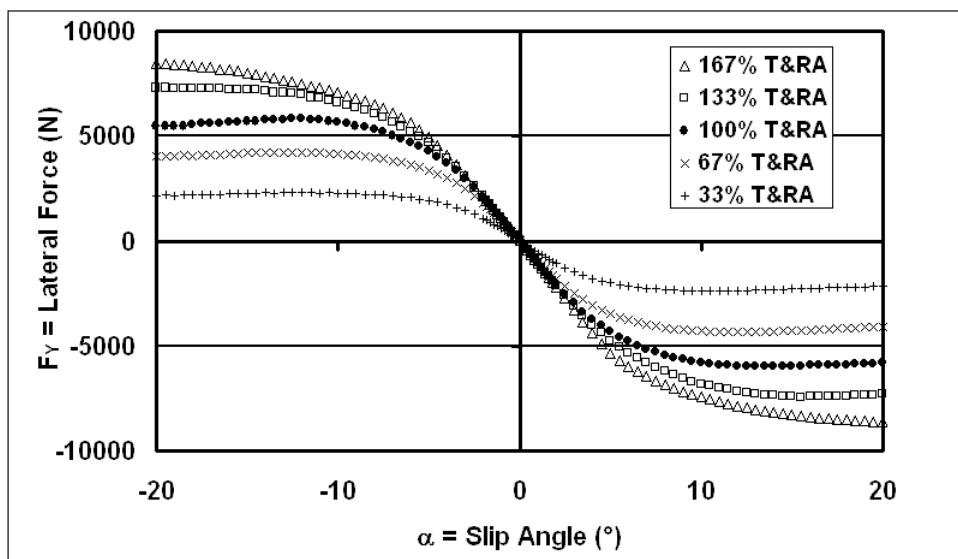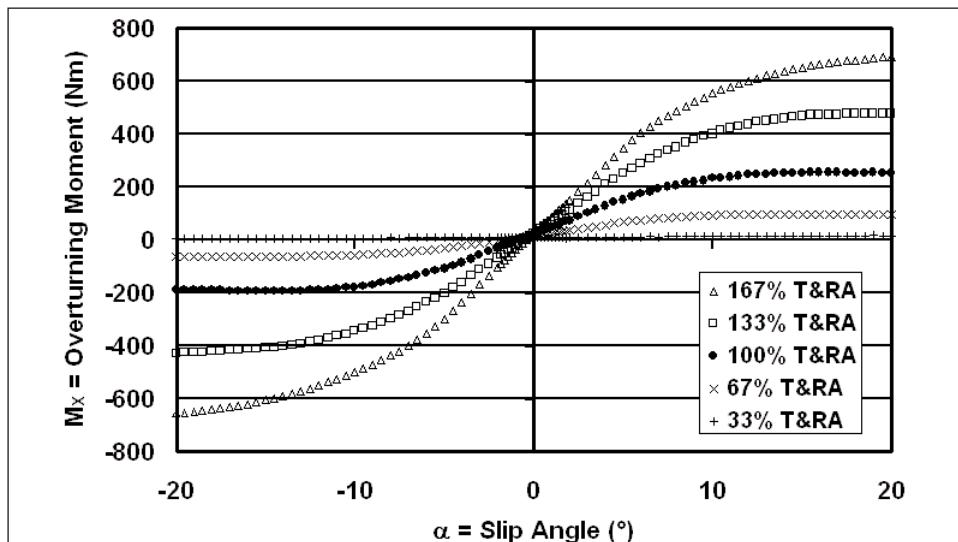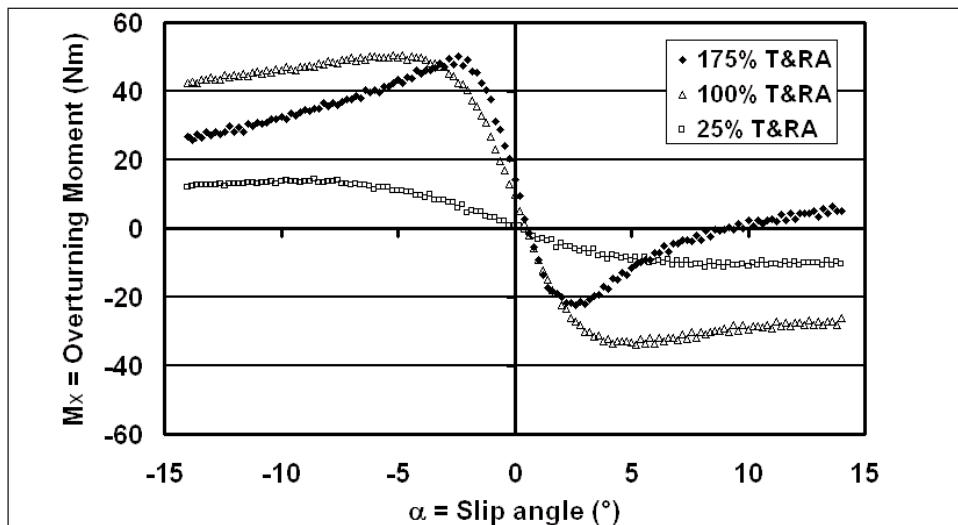
Figure 8.22: Overturning moment vs. slip angle and load for a 75 aspect ratio tire

The situation for a low aspect ratio tire like that used to obtain the data shown in figure 8.23 is different. The out-of-plane twisting that causes the footprint shape to become trapezoidal, see figure 8.5, becomes the predominant effect. The result is a basically negative trend of M_X with increasing slip angle. As load increases, the lateral displacement of the contact patch, as shown in figure 8.3, also becomes a significant source of overturning moment. This is seen at the rated load and above in figure 8.23.
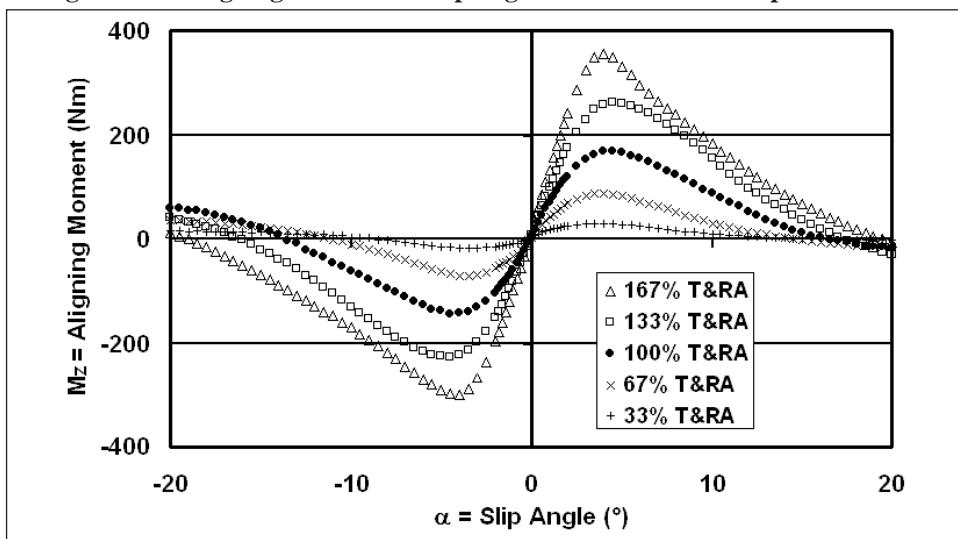
Figure 8.23: Overturning moment vs. slip angle and load for a 45 aspect ratio tire

Typically, results for M_X can be very complex. Depending on the tire aspect ratio and inflation pressure, almost any relationship can be found to hold.
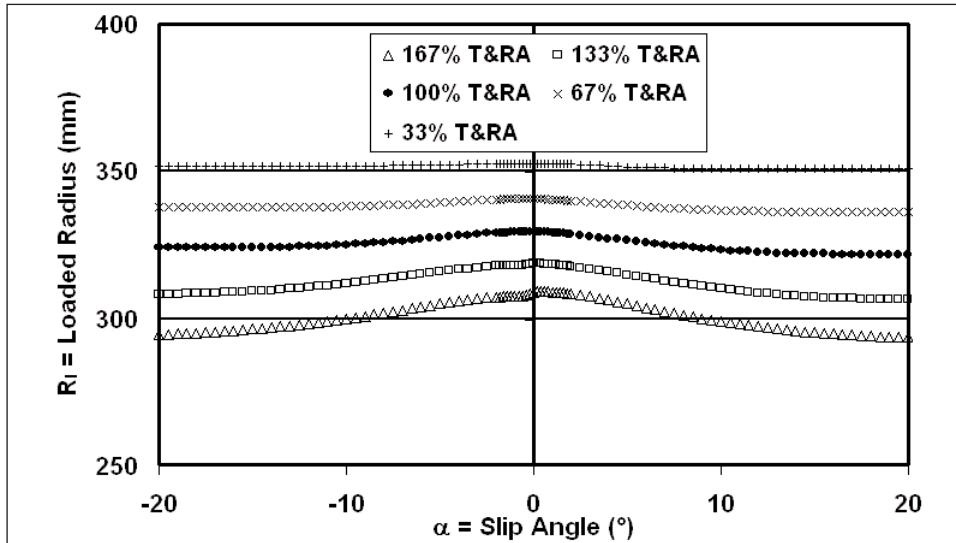
Like lateral force, curves of aligning moment versus slip angle retain the same characteristic shape as load changes, figure 8.24, but change in amplitude.

Figure 8.24: Aligning moment vs. slip angle and load for a 75 aspect ratio tire

Curves of loaded radius versus slip angle are bell-shaped, and the shape becomes more pronounced as load increases, figure 8.25.

Figure 8.25: Loaded radius vs. slip angle and load for a 75 aspect ratio tire

The data in all figures representing pure slip angle behavior have been shown as a function of both positive and negative slip angles. Sometimes when there is no interest in the offsets near zero shown in figures 8.17 and 8.19, engineers will compute "mirrored" data using the method illustrated in Eq. 8.2.[18]
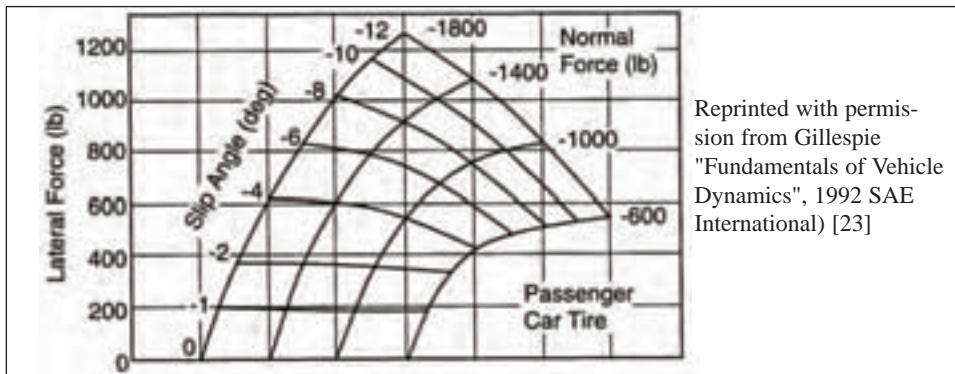
$$f(\alpha) = (f(\alpha^+) - f(\alpha^-))/2 \qquad (8.2)[19]$$

Data obtained in this way are used to produce carpet plots like the one in figure 8.26, where both slip angle and normal force are shown as negative numbers. Carpet plots are produced by plotting both normal force and slip angle on the horizontal axis. For each successively higher slip angle, the origin of the normal force axis is moved to the right. The result overlays a group of F_Y vs. F_Z graphs for single slip angles, one on top of the other, where the origins have been moved to the right by an amount proportional to the slip angle. The loads at each slip angle are then connected. The constant slip angle - variable load curves together with the constant load - variable slip angle curves form a comprehensive data set.

---

[18]Reference 17 provides a detailed discussion of different ways to look at slip angle only data.

[19] + signifies positive slip angle.   - signifies negative slip angle.
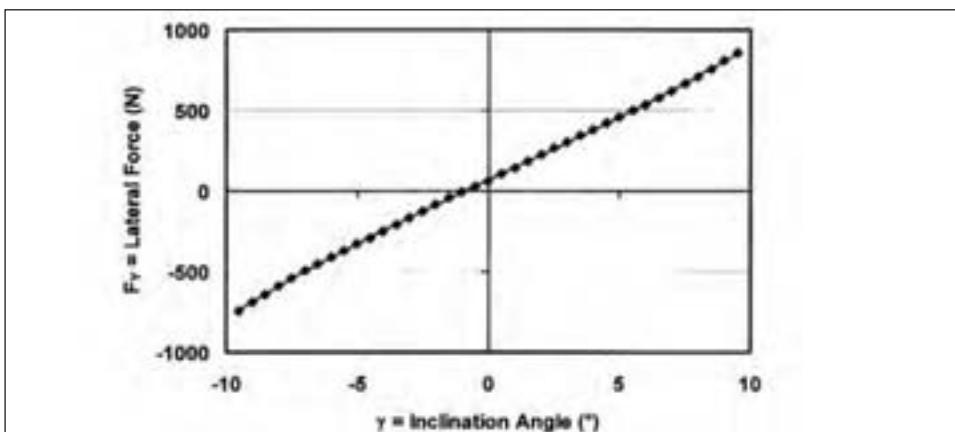
Figure 8.26: Lateral force carpet plot ((ISBN 1-56091-199-1)

Reprinted with permission from Gillespie "Fundamentals of Vehicle Dynamics", 1992 SAE International) [23]

5.1.2 Steady state response to inclination angle alone

The steady state response to changes in inclination angle does not vary in character with increasing load. Thus, results for a single load are adequate to understand the basic function. Results presented in figures 8.27 – 8.30 are in response to changes in inclination angle only (the slip angle was set to zero). They are typical for a radial passenger tire with a normal tread profile, though the precise magnitude of the responses will vary with tire size, aspect ratio, etc. Results for a motorcycle tire would be quite different because of its very different profile.

Figure 8.27: Lateral force at a single normal force as a function of inclination angle

The response of lateral force to inclination angle, figure 8.27, is much weaker than the response to slip angle, figure 8.17. The inclination stiffness, the inclination equivalent to cornering stiffness, is 10 percent or less of the cornering stiffness in terms of force per degree. In the example case used here, the inclination stiffness is less than 5 percent of the cornering stiffness. Note that the slope of lateral force with inclination is positive; a positive change in inclination angle is associated with a positive change in lateral force. This is the reverse of the situation with slip angle where a negative lateral force is associated with a positive slip angle. As expected, the lateral force at zero inclination angle is not zero, due to pull forces. One of the pull forces (plysteer) is associated with a structurally induced self-steering and the other (conicity) is associated with a structurally induced self-

Figure 8.28: Overturning moment at a single normal force as a function of inclination angle
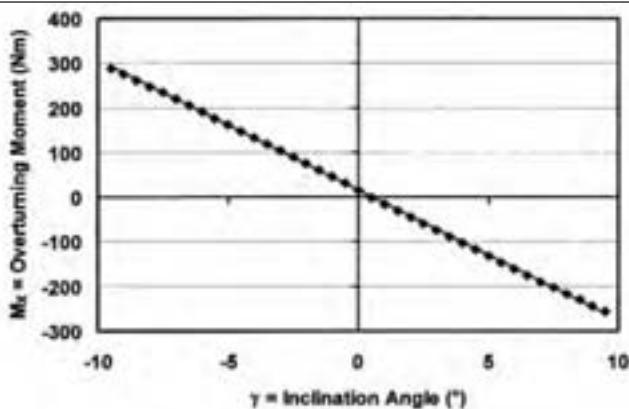

Figure 8.29: Aligning moment at a single normal force as a function of inclination angle
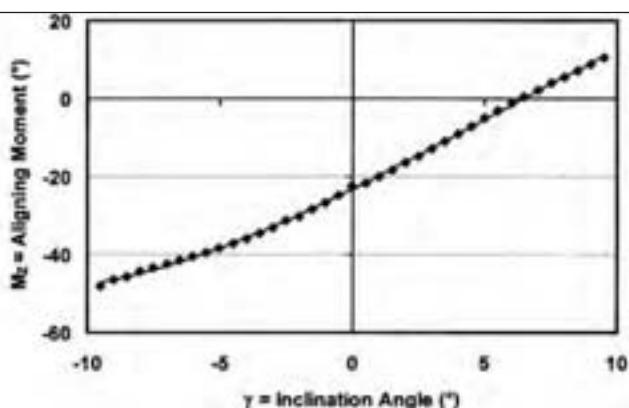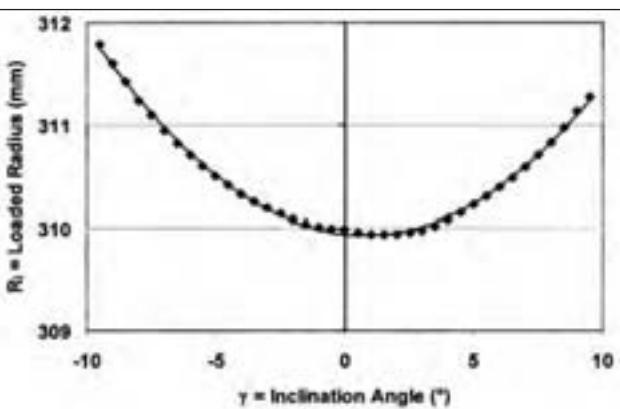

Figure 8.30: Loaded radius at a single normal force as a function of inclination angle

inclination. These are discussed in section 8.4.1.4.

For inclination, a negative overturning moment is associated with a positive inclination angle as shown in figure 8.28. Basically, the trapezoidal reshaping of the footprint, figure 8.7, leads to the line of action of normal force moving off-center in the direction toward which the tire is inclined. In the case of the tire used to provide the example inclination data, the rated resultant of normal force moves off-center about 4mm for every degree of inclination angle. An offset at zero inclination is also noted in M_X.
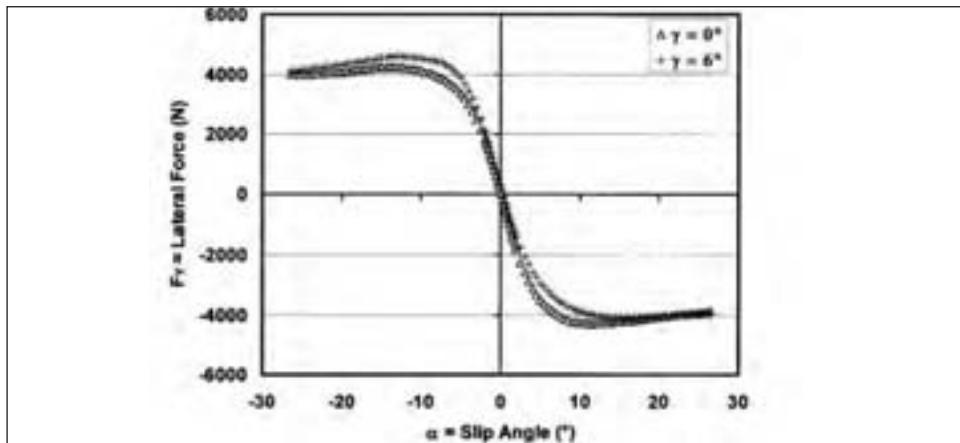
The aligning moment has a positive slope with inclination angle, figure 8.29, just as it has an initial positive slope with slip angle, figure 8.19. However, the mechanisms of generation are very different as pointed out in sections 8.2.1 and 8.2.2. Here, the offset at zero inclination is a major factor due to the weak generation of aligning moment in response to inclination angle.

Interestingly, loaded radius increases with increasing inclination angle, figure 8.30, rather than decreasing as is the case for slip angle, figure 8.20.

5.1.3 Steady state response to combined slip and inclination angles

The basic effect produced by combining inclination and slip angles can be understood functionally from data at a single load. The examples in figures 8.31 -8.34 are based on data for a 75-series tire operating at 80 per cent of its rated load. The precise degree of warping of the slip angle behavior by the simultaneous presence of an inclination angle will depend on the tire specification (size, aspect ratio, structural details, etc.) and application details such as load and inflation pressure. The warping increases as inclination angle increases.

Figure 8.31: Effect of inclination angle on lateral force as a function of slip angle

In the examples, the tire is inclined positively, such that the lateral force generated by inclination is positively directed. Thus, the inclination-generated lateral force adds to the lateral force generated by a negative slip angle in the Tire Axis System, see section 8.2.1. If the tire is inclined at a negative angle, it is evident that the reverse applies.
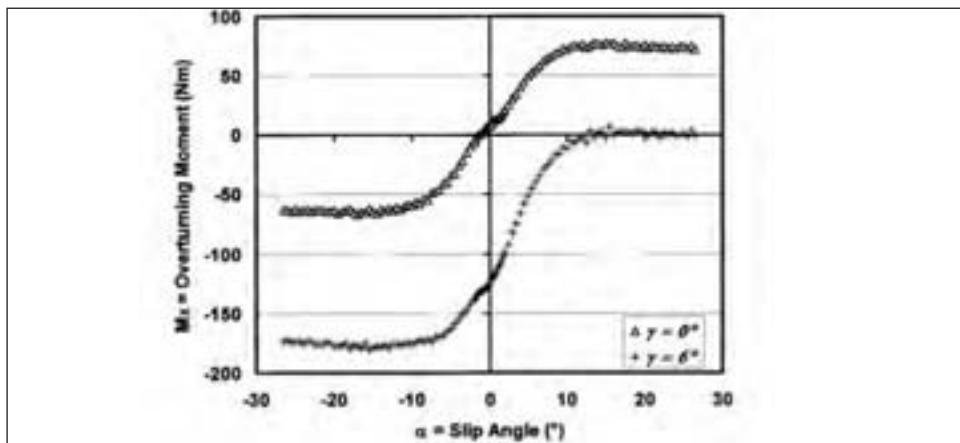
The lateral force, figure 8.31, shows three characteristics that are due to the asymmetric behavior that occurs in the presence of combined slip and inclination angles. Note that as slip angle becomes quite large, inclination angle does not have much effect on the magnitude of the lateral force. This is because the tire is operating beyond the peak of the fric-

tion curve in lateral slip. It is moving closer and closer to full lateral sliding as the slip angle continues to increase.

Inclination angle offsets the data in the vicinity of zero slip angle, as is shown in figure 8.27. This apparent simple addition of the effects of slip and inclination angles first noted by Evans [2], is only valid at low slip and inclination angles. As noted below, behavior at higher angles is more complex.
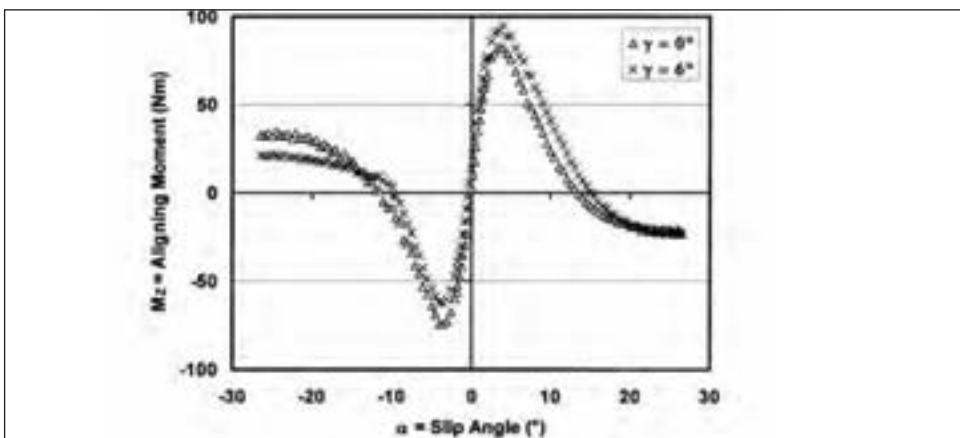
When the lateral forces due to slip angle and inclination angle have the same sense and act in the same direction, the peak lateral force is higher and sharper than in the case of slip angle only. When the inclination angle is positive, this occurs for a negative slip angle. Both lateral forces are then positive, to the right.

Figure 8.32: Effect of inclination angle on
overturning moment as a function of slip angle

When the lateral forces due to slip angle and inclination angle have opposite senses, the peak in lateral force is lower and broader than in the case of slip angle only. When the inclination angle is positive, this occurs for a positive slip angle. The lateral force due to the inclination angle is positive, to the right, but the lateral force due to the slip angle is negative, to the left.

Figure 8.33: Effect of inclination angle on aligning moment as a function of slip angle

Overturning moment, figure 8.32, is offset negatively, as would be expected for a positive inclination angle on the basis of the results for inclination alone, shown in figure 8.28. It is important to note that the offset is larger when the direction of lateral forces induced by the slip angle and the inclination angle are the same, and the offset is smaller when they are in opposite directions.
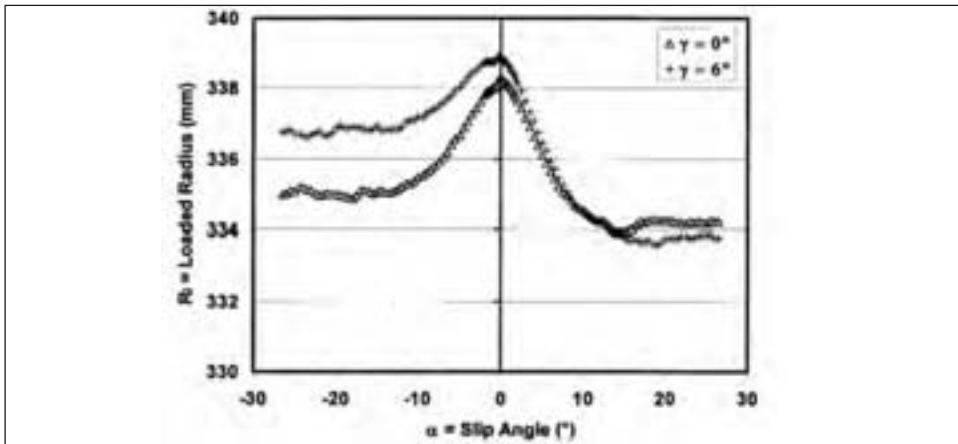
Aligning moment, figure 8.33, is warped into asymmetry, much as is the case for lateral force, except that in this case the direction of the aligning moments is important.

When the aligning moments have different directions, the magnitude of the aligning moment is reduced in comparison with that for a pure slip angle. This occurs when inclination angle is positive and slip angle is negative.

When the aligning moments are in the same direction, the magnitude of the aligning moment is increased with respect to that observed in the case of pure slip angle. In the example, this occurs when the inclination angle and the slip angle are both positive.

Figure 8.30 showed that the vertical stiffness of the tire increases with increasing inclination angle. This appears in the combined case, figure 8.34, with the effect being augmented when the components of lateral force due to inclination and slip angles act in the same direction. The lateral distortions of the tire carcass then reinforce each other.

Figure 8.34: Effect of inclination angle on loaded radius as a function of slip angle

5.1.4 Special cases of steady state free-rolling and cornering

There are several special cases of free-rolling and cornering at small slip and inclination angles that are significant. Two are considered in some detail: tire-induced steering pull, and groove wander. A third, denoted nibbling, is the force and moment behavior of tires negotiating an edges that runs almost parallel to the direction of motion. It received attention when bias and belted-bias tires were common [24], but is much less important for radial tires. Nibbling is not discussed in detail here.
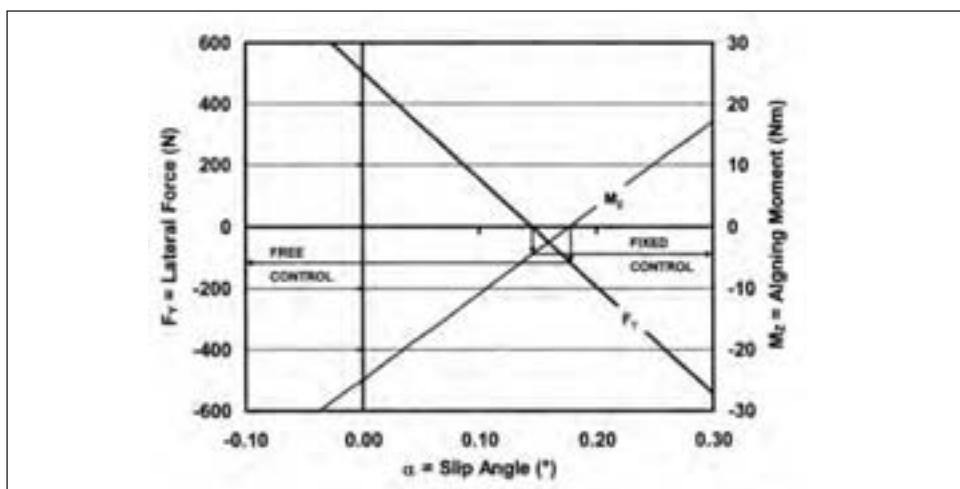
5.1.4.1 Tire induced steering pull

In section 8.4.1.1 the fact that lateral force and aligning torque do not typically become zero at zero slip angle was mentioned. Figure 8.35 shows lateral force and aligning moment data at low slip angle for a typical pair of tires on the front axle of a car. They are not both zero at the same slip angle. Why is this important?

Assume that the driver releases the steering wheel when going straight ahead. The car

enters free-control (see [5]) and the aligning moment will become zero, i.e., self-steering, but typically the lateral force is not zero. The front of the vehicle will be pushed to the side and a yaw moment will be imposed on the car. In this case the car will only travel straight along a straight road if the driver exerts an aligning torque to maintain zero lateral force on the front of the car to maintain direction (see [5]). The driver is aware that the car is not tracking properly and becomes fatigued by the process of simply driving straight ahead. If the driver is inattentive or ceases to maintain trim, the car may change lanes, cross the centerline of the road, or drift off the road altogether. Also, the driver will bring his car in for wheel alignment service which will continue to be unsatisfactory as long as the properties of the tires are unsatisfactory, as discussed later in this section.

**Figure 8.35: Small slip angle lateral force and
aligning torque exerted on the front axle of a car**

The first authors to demonstrate that tire-induced steering pull had its source in the facts mentioned in the last paragraph were Gough *et al.* in 1961 [25]. Unfortunately, their discussion was not as clear as it might have been. Topping [26] gave a clearer explanation in 1975. He showed that tire-induced steering pull was a direct result of the presence of residual lateral force on the front axle when the steering wheel was allowed to seek its free position. Topping showed that the rear axle could basically be ignored as a source of tire-induced vehicle pull, but is a source of vehicle side-slip, denoted dog-tracking, when traveling straight. The conclusion that the rear axle did not contribute to the tire-induced pull problem was based on experiments and simple, but unpublished, analysis. In 2000, Lee [27] published a model equivalent to the one used by Topping.

There are two features of tires that give rise to a residual lateral force.[20] The first is generally termed conicity. Conicity is usually the result of the tire belt being applied slightly off-center, as a result of manufacturing variance. This constrains the rolling radius on the side of the tire toward which the belt is shifted to be slightly smaller than the rolling radius on the other side of the tire. At the belt level, where rolling radius is determined, the tire acts as if it had a conical cross-section, and develops lateral force and aligning

---

[20]Residual lateral force is the free control expression of tire pull. In fixed control, the case where the driver is maintaining trim, tire-induced pull expresses itself as a residual aligning moment (torque).

torque as if it was cambered toward the more constrained side of the tire. The distribution of conicity values for a group of tires is very flat, as shown schematically in figure 8.36. The mean value is near zero, but may not be precisely zero due to asymmetries in the manufacturing process. Other effects are termed plysteer. Plysteer arises when the tire structure is anisotropic, causing the tread band to undergo in-plane shear when it is forced to become flat in the footprint [18], figure 8.37. Additional in-plane shearing occurs due to the change in belt tension in the contact zone, and causes footprint curvature and a plysteer residual aligning moment or torque. Pottinger [28] has discussed these effects in detail. Plysteer effects are due to tire design.[21] The distribution of values is narrow, as shown schematically in figure 8.36, centered on the design value, which can have a considerable range as illustrated in figure 8.38. Indeed, the research used in producing figure 8.38 could have yielded a target plysteer anywhere in the range from –370 N to + 370 N with an associated residual aligning torque from –11 Nm to +11 Nm.[22]

**Figure 8.36: Schematic of distribution of conicity and plysteer**

(Reprinted with Permission from SAE 760731   1976 SAE International) [18]
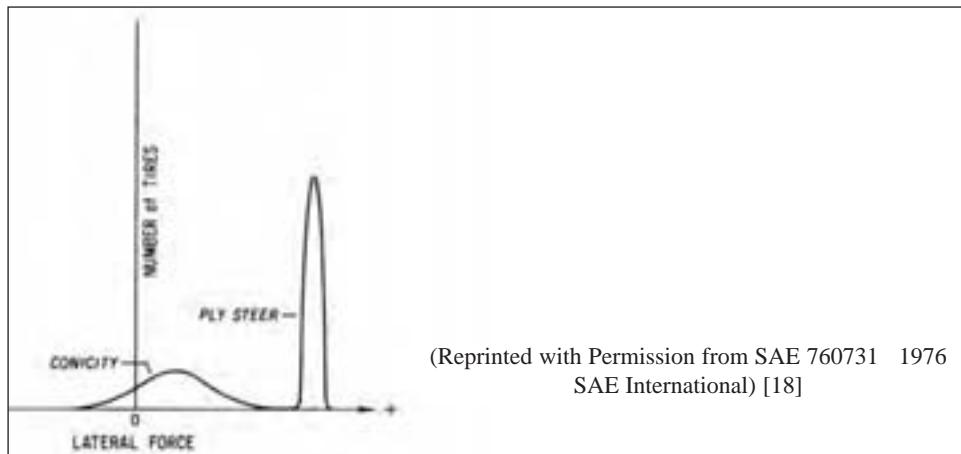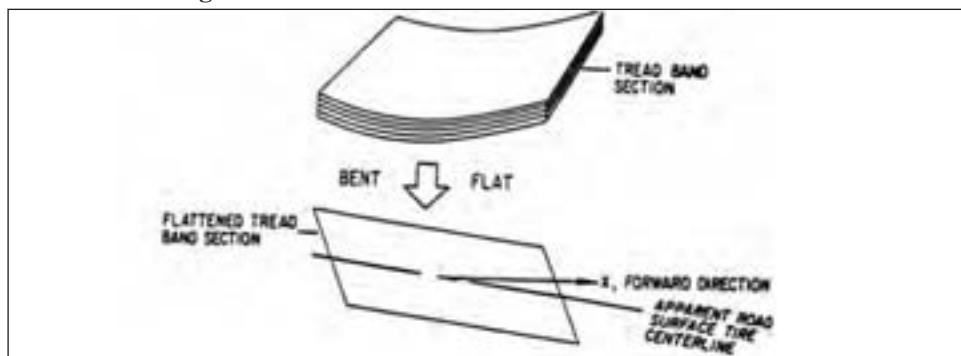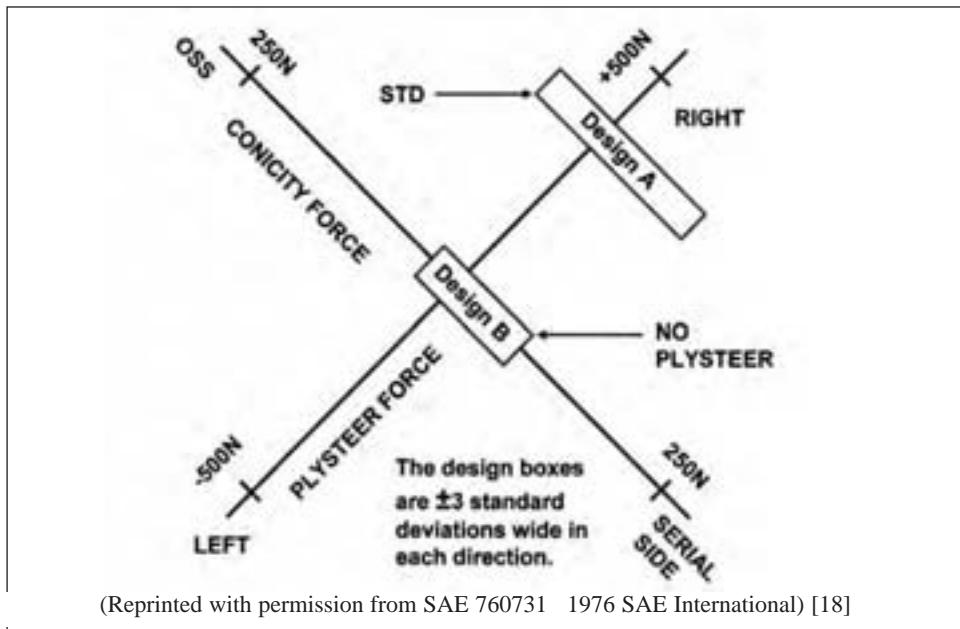
Figure 8.37: Deformation of the tread band when bent

---

[21][18], [19], and [22] present basics on designing to eliminate or modify plysteer components.

[22]Note that practical considerations would not have allowed the full range of values indicated to be present in production tires.

Figure 8.38: Plysteer design illustration

(Reprinted with permission from SAE 760731   1976 SAE International) [18]

The importance of conicity and plysteer effects has led to an SAE recommended practice covering their determination [29].

As pointed out in reference 28 and in Yamazaki *et al.* [30], the resulting steering pull depends on tire properties, suspension alignment, and road crown. The consequence for the tire industry is that automobile manufacturers set limits on components of pull force for their tire suppliers. These limits make tire-induced pull effects manageable from the standpoint of the automobile manufacturers. All restrict conicity to a narrow band about zero so that they can ignore its effects. The situation with regard to plysteer residual aligning torque (moment) is more complex and less satisfactory. Each OEM establishes an allowable band of values for residual aligning moment or torque, depending on their own design philosophy. Some automobile manufacturers use tire plysteer residual aligning torque (PRAT) to counteract road crown. Thus, their tire specifications require that tires supplied to them have particular values of plysteer residual aligning torque. Other automobile manufacturers demand zero PRAT, within a narrow tolerance, and counteract road crown effects solely through the suspension alignment. This can lead to vexing differences in tire design that tire manufacturers must introduce in nominally identical tires in order to meet the requirements of different automobile manufacturers. These differences are not obvious to tire stores or purchasers. The result can be pull problems when OE tires are replaced because the available tires in the aftermarket may not match the properties specified by the car manufacturer. The car may not travel straight without driver input, even when the suspension is aligned in accordance with OEM specifications.
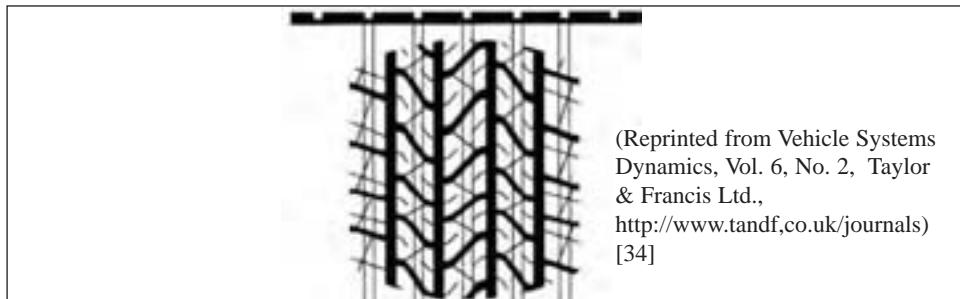
5.1.4.2   Groove wander
Maintaining good wet traction requires that water on the road surface be expelled from under tire tread elements and that the boundary layer remaining after the gross water layer

is expelled be broken so that intimate contact is achieved between the tire tread and the road. Expelling the gross water layer depends on having both an appreciable groove volume in the tire tread and having voids present on the road surface, termed macro-texture.

Often the road surface macro-texture will be worn away over time leaving a road surface with a low void content. In this situation the chance of a wet traction accident is significantly increased, particularly at high speeds when the lack of drainage contributes to hydroplaning during a heavy rainfall. To counter this problem, highway departments treat

Figure 8.39: Tire contact overlaid over rain grooves

(Reprinted from Vehicle Systems Dynamics, Vol. 6, No. 2, Taylor & Francis Ltd., http://www.tandf,co.uk/journals) [34]

pavements lacking adequate drainage by introducing regularly-spaced rain grooves into the pavement using diamond saws. The grooves are cut parallel to the direction of travel in order to avoid a major increase in tire-road interaction noise. The result is that the tire tread now interacts with a road tread pattern as shown schematically in figure 8.39.

The rain grooves greatly reduce wet traction accidents; see the introduction to reference 31. Unfortunately, the interaction of the two patterns gives rise to a feeling of instability called "groove wander" or more colloquially, "LA wiggle."[23] The car feels as if it is oscillating to and fro laterally. It makes the driver nervous, and can lead to steering mistakes. The magnitude of groove wander is an indicator of quality to the driver and hence a concern to the tire manufacturer. It is also something the OEM vehicle manufacturer does not want his customer to feel when driving a new car.

Tarpinian and Culp [31] observed that the number of coincidences between the tire tread pattern spacing and the rain groove spacing correlated with the driver's subjective rating of groove wander. Their model assumes that the edges of tread elements become interlocked with rain grooves until the increasing lateral stress associated with normal lateral motion of the vehicle causes a sudden release, giving an impulsive effect. Figure 8.40 illustrates the interaction concept. The same basic idea of tread/road groove interaction was applied to motorcycle tires by Doi and Ikeda [32], but without taking coincidences into account. It works acceptably for tires with longitudinal grooves, but doesn't work well for block patterns, curvilinear patterns, or zigzag tread patterns [33, 34]. Thus, until a few years ago, tire companies had to depend on road tests to design treads to minimize groove wander.

As reported by Peters [33], an indoor test designed to replace road testing led to the suggestion by test engineers at Smithers Scientific Services[24] that the real source of groove wander was simple modulation of the lateral stress field in the footprint of the

---
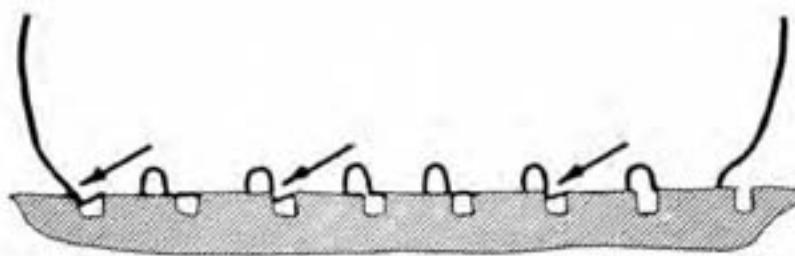
[23]A similar sensation exists when driving on a bridge deck surfaced with a steel grating.

[24]M. Pottinger and J. McIntyre.

rolling tire because small lateral movements made the stress field oscillate in a repeatable fashion each time the lateral motion of the car took it across a groove spacing. Peters applied finite element analysis to the stress field for tires with a variety of tread patterns and predicted that the lateral force waveform would look like the one portrayed in figure 8.41. This waveform is quite similar to the one obtained from the indoor experiments.
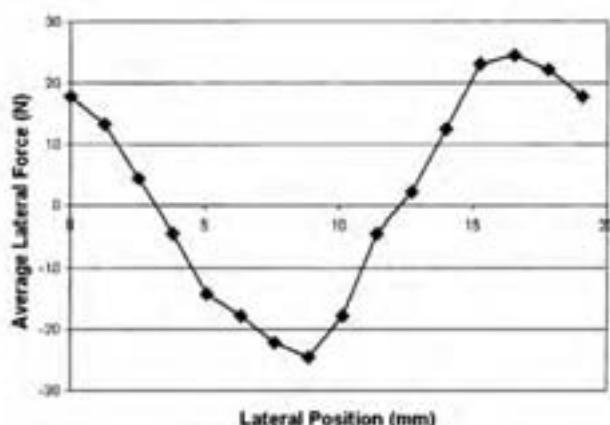
Recently, Nakajima [34], applied the same concept used in Peter's work and obtained an excellent correlation to subjective ratings by drivers, figure 8.42. This figure shows subjective ratings of groove wander by the test driver as a function of the computed pea to-peak amplitude of the lateral force waveform resulting from tire interaction with longitudinal grooving in the pavement.

**Figure 8.40: Illustration of coincidence concept
of tread pattern to rain groove interaction**
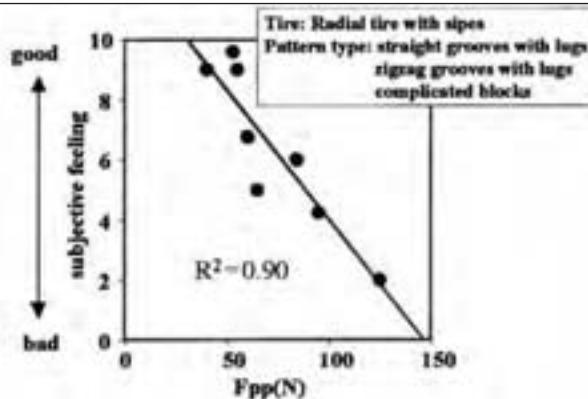
(Reprinted from Tire Science and Technology, Vol. 29, No. 4, 2001 with Tire Society permission) [33]

Figure 8.41: Example tread pattern to rain groove interaction lateral force waveform

(Reprinted from Tire Science and Technology, Vol. 29, No. 4,   2001 with Tire Society permission) [33]

Figure 8.42: Correlation of driver subjective opinion of groove wander to the amplitude of the tread pattern to rain groove interaction lateral force waveform

(Reprinted from Vehicle Systems Dynamics, Vol. 6, No. 2, Taylor & Francis Ltd., http://www.tandf,co.uk/journals) [34]

5.2 Straight-line driving or braking

To this point, the discussion has been confined to free-rolling cornering for which the generation of lateral force, aligning moment, and overturning moment is a response to slip and inclination angles, except for the special case of groove wander.

This section focuses on the response of a tire at zero slip and inclination angles to the imposition of wheel torque, T. The slip ratio, SR, as defined in equation 8.1, is the usage or input variable. The longitudinal force, F_X, is the output. F_Z is seen as a parameter affecting the magnitude of the F_X (SR) results.

Discussion in this section will be confined to operation on a dry surface. A few comments on responses to contaminated surfaces are found in section 8.5.7. For those interested, chapter 11 contains a thorough discussion of friction as it affects traction.

Braking experiments are the most common way to characterize a tire's response to longitudinal slip. These experiments are most often performed outdoors using instrumented vehicles or special trailers. They are less commonly performed indoors on specially equipped force and moment machines like an MTS Flat-Trac III®.

Figure 8.43 is a single load example of data from a braking experiment.

A pure driving experiment yields data similar in character, but different in detail from that obtained in a braking experiment on the same tire. These differences are discussed later.

Figure 8.43 illustrates the general curve shape for F_X (SR) and highlights three parameters commonly used to describe he response of tires to slip ratio.

Longitudinal stiffness is the initial slope of the response. It is ideally evaluated at SR = zero. If the experiment is strictly a braking test, the initial slope is referred to as Braking Stiffness. In a driving experiment, it is referred to as Driving Stiffness. The magnitude of the initial stiffness is independent of the type of experiment.

Peak longitudinal force is the maximum value of F_X during the experiment. It typically occurs at a modest value of slip ratio. The exact location of the peak and characteristic shape of the curve in the vicinity of the peak depends on the test surface and tire design features (aspect ratio, tread compound, tread design, belt stiffness, etc.). Further, as will

be seen in the discussion of figure 8.44, the peak in driving is not usually equal to the peak in braking.

**Figure 8.43: A typical longitudinal force response to braking torque application**
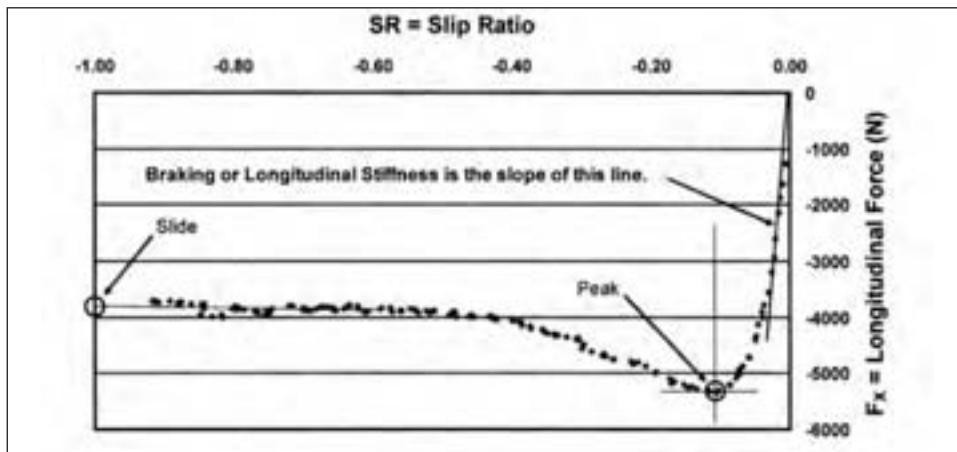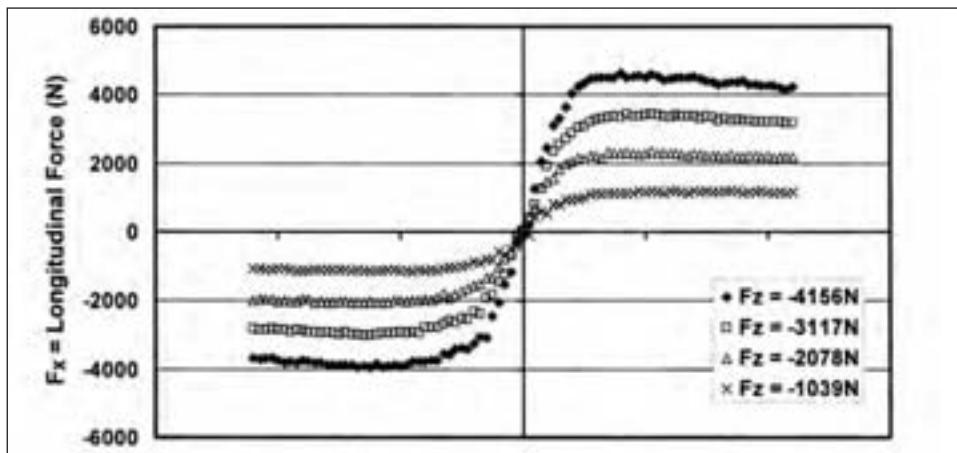
Figure 8.44: Driving and braking longitudinal forces compared

Slide longitudinal force is the value of F_X that occurs when the slip ratio in braking becomes -1.00 (the wheel is locked). When wheel spin occurs in driving, SR can exceed 1.00. Examples of cases where spin occurs are the launch of a dragster or when excess driving torque is applied on a slick surface. In this particular example case, $F_{X\,SLIDE}$ was obtained by extrapolation of the end of the response curve.[25]

Figure 8.44 illustrates F_X (SR) over a range of slip ratios encompassing both driving and braking. It shows the response asymmetries just mentioned.

The magnitudes of the driving and braking data are not the same. For example, at the highest load the magnitude of the peak longitudinal force in driving is over 4500N whereas the magnitude of the peak longitudinal force in braking does not quite reach 4000N.

---

[25]In the example case the experiment was terminated before slide in order to prevent tire flat-spotting which will lead to vibrations that can cause test load control problems.
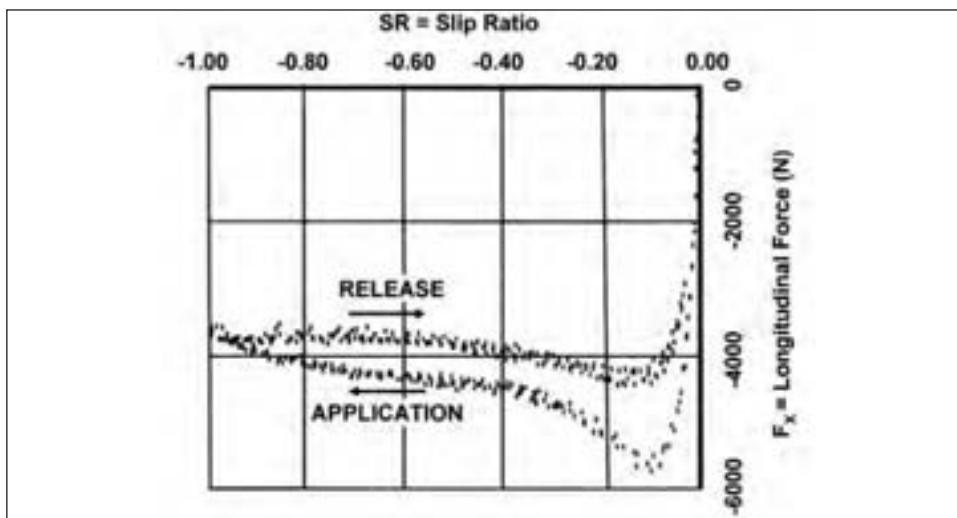
The location of the peaks is also different. The driving peak occurs at a lower slip ratio than the braking peak.

In general, as noted a few paragraphs back, the driving and braking longitudinal force curves are generically similar, but have different values of the descriptive parameters. The braking response surface is warped differently than the driving response surface because of these parametric differences which arise from footprint stress distributions that do not mirror each other as the tire changes from braking to driving, see chapter 7.

The rate at which slip ratio is applied affects the response obtained. Application of torque and release of torque, the two sides of a half triangular wave that can be imposed using test machines equipped with controlled-rate hydraulic systems, do not typically lead to the same F_X (SR) response curve. This effect, which appears to be thermally induced, is separate from the tire dynamics and relaxation effects noted in section 8.4.4. Figure 8.45 [11] is an illustration of this effect. As the slip ratio ramp rate is reduced, the total experiment becomes longer, and the difference increases between the longitudinal force curves for application and release. Also, if the tread is severely overheated, the surface will become tacky and the apparent coefficient of friction will change because of altered adhesion, see chapter 11. Wear during testing should also be monitored in order to avoid data which are, unknowingly, dependent on the wear state.

Always bear in mind the importance of test surface friction. As illustrated in figure 8.15 and discussed in Section 8.3.1, even different dry surfaces can give quite different results.

**Figure 8.45: Longitudinal force in response to both
braking torque application and release**

8.4.2.1 Torque steer
Differential longitudinal forces acting on the two sides of a car or light truck traveling in a straight line apply a yaw moment to the vehicle. The result is a lateral response to longitudinal force[26].

---

[26]Longitudinal force in straight ahead operation is usually thought of as producing only vehicle acceleration or deceleration.

In the design of vehicles, particularly with front wheel drive, considerable engineering effort is expended to insure against inadvertent introduction of yaw moments or steering system inputs due to longitudinal forces occurring during acceleration or deceleration. Anti-lock braking systems and traction control systems help in limiting yaw moments due to variable friction across the roadway. Stability control systems deliberately induce a stabilizing yaw moment by inducing a desirable longitudinal force differential.

In straight line operation there are effects due to differences between the tires mounted on an axle, particularly on the drive axle of front wheel drive cars, that can contribute to undesirable yaw moments. These effects are lumped together under the name torque steer [28].[27] If a torque steer problem arises, the engineer should check three potential tire sources of force differences: rolling radius, torsional spring rate, and inconsistent frictional properties. The most common source is a side-to-side rolling radius difference. If the difference in rolling radius between the left and right tires is too small to cause the car's differential to function, but still significant, the vehicle will follow a radius defined by the rolling radius difference. On a straight road, relatively minor differences can be significant.

5.3 Combined cornering, braking, and driving

Real vehicle operation involves cornering (slip angles and inclination angles) combined with driving and braking (torque application). Cornering plus some simultaneous torque application occurs during most driving. Since the tire has only a limited ability to produce frictional force, the resultant shear force cannot simply be the vector sum of the free-rolling lateral force at a given slip angle and the un-steered longitudinal force at a given longitudinal slip. Rather, the tire produces a combination of lateral force and longitudinal force that apportions the total shear force available in a manner dependent on the tire's design. The total shear force is a function of the magnitude of the shear vector, s, and its angular orientation with respect to the tire axis system. The shear vector is a non-dimensional representation of shear derived from the velocity triangle existing at the origin of the tire axis system, as illustrated in figure 8.46 drawn from Schuring et al. [35].

The shear vector representation in figure 8.46 is referred to as the slip circle.[28] The shear vector has the components noted in Eqs. 8.3 – 8.6.

$$s_X = (SR) \cos\alpha \qquad\qquad (8.3)$$
$$s_Y = (SR) \sin\alpha \qquad\qquad (8.4)$$
$$s = ((s_X)^2 + (s_Y)^2)^{0.5} \qquad\qquad (8.5)$$
$$\tan\beta = (F_Y/F_X) = (-\tan\alpha)/(SR) \qquad\qquad (8.6)$$

The shear force, $F(s,\beta)$, is a function of the magnitude of the shear vector and its orientation. $F(s,\beta)$ appears in figure 8.46 as a non-circular arc.[29] Bearing this in mind and working with small slip angle data such that s_X is approximately equal to slip ratio yields the combined cases usually considered. Inclusion of inclination angle in the mix causes further complications which will be discussed briefly when figure 8.52 is considered.

---

[27]Always remember that the car design itself may contribute to or be the torque steer problem. Some vehicle design sources are described in Reference 28, which also outlines a road test procedure to distinguish between the various sources of tire induced vehicle pull.

[28]The version shown in Figure 8.46 is the all slip angle version. It is a modification of the figure shown in reference 35 to include the form of Eqs. 8.3 - 8.6, which appear in an Appendix to the Reference 35.

[29]$F(s,\beta)$ is usually assumed to be an ellipse, but as pointed out in the discussion associated with Figure 8.52, this is not always a valid assumption.

At least three ways are conventionally employed for functionally or graphically visualizing combined data. The first, figure 8.47, represents lateral force, F_Y, at a fixed slip angle as a function of slip ratio. Longitudinal force, F_X, for driving is also included in figure 8.47 to illustrate a point discussed in the next paragraph. The second way, figure 8.48, represents lateral force at fixed slip angles as a function of longitudinal force. This representation is the one that is mainly used in this section. The third, figure 8.49, represents

Figure 8.46: Slip Circle

$\beta = 0°$: straight-line driving
$\beta = 90°$: free-rolling cornering to right
$\beta = 180°$: straight-line braking
$\beta = 270°$: free-rolling cornering to left

(Reprinted with Permission from SAE 960180 1996 SAE International) [35]
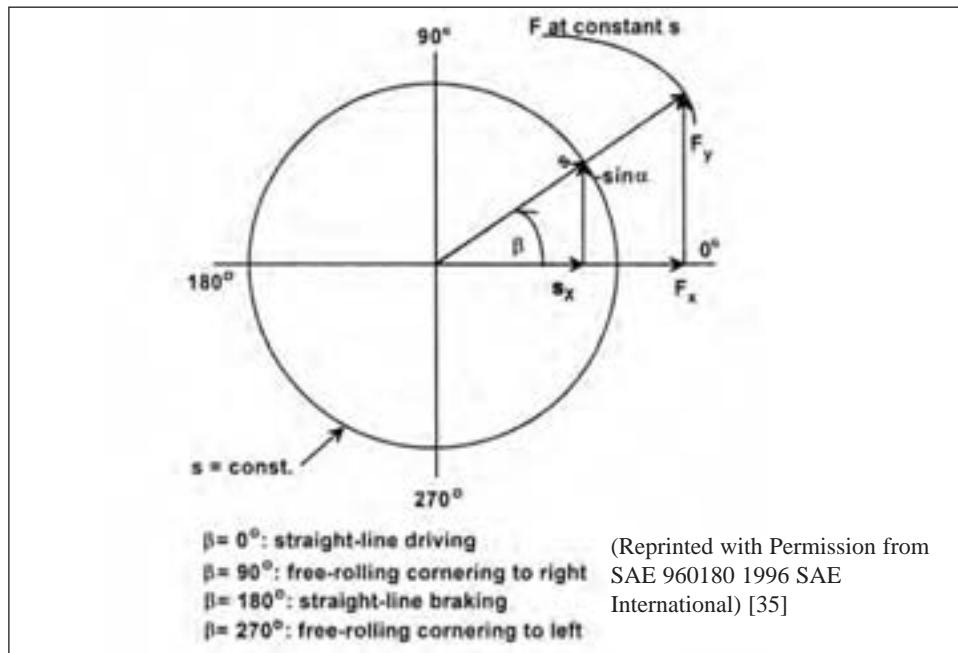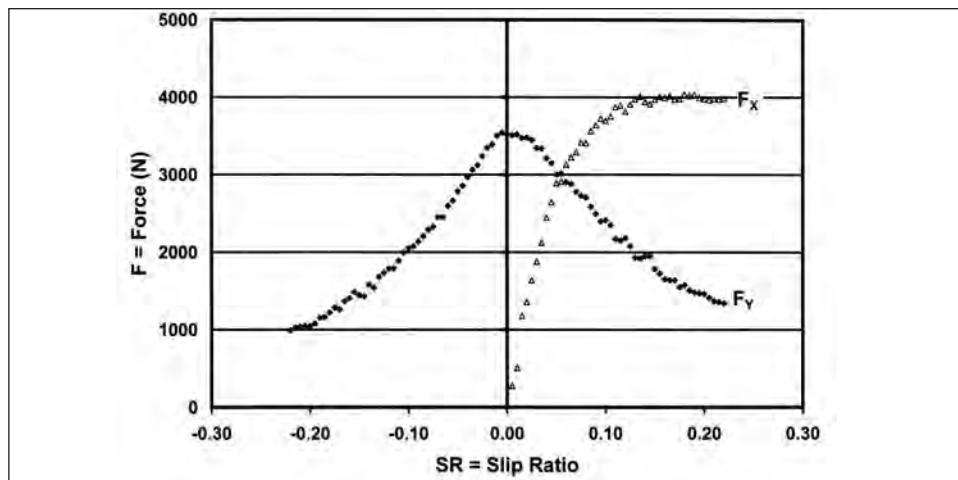
Figure 8.47: Lateral force at 4° slip angle and driving longitudinal force as a function of slip ratio
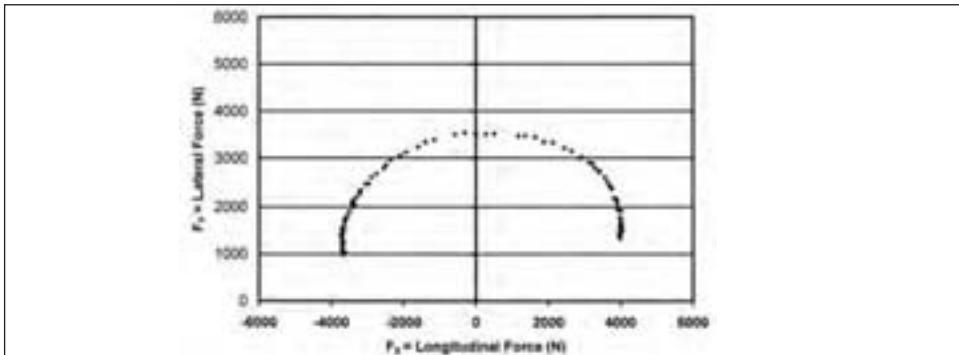
longitudinal force as a function of slip ratio at fixed slip angles.

Lateral force at a fixed slip angle falls off as slip ratio increases forming a bell shaped curve, figure 8.47. Examination of the associated longitudinal force makes it very clear that antilock or stability control systems are going to help lateral stability best under conditions where the demand for lateral force is not already approaching the limit of the available force when torque is added. In the example, appreciable reductions of available lateral force occur at even modest slip ratios.
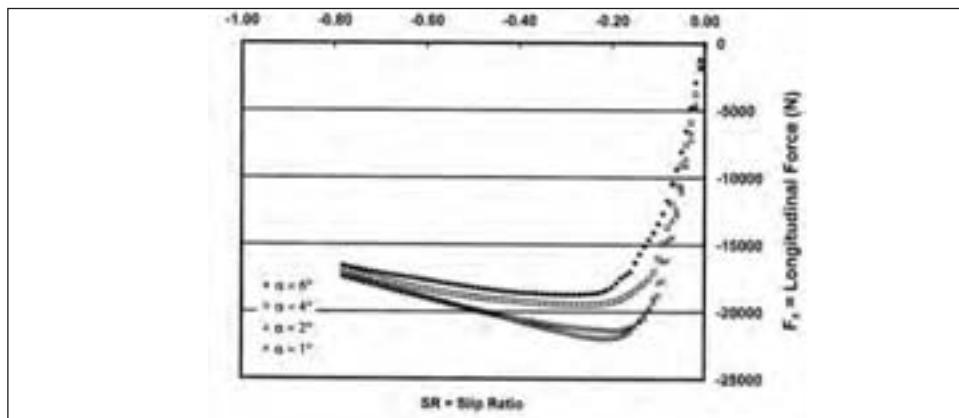
Lateral force at a fixed slip angle, as a function of longitudinal force, reaches a maximum and then curves back on itself, figure 8.48. This returning curve, shown strongly in figure 8.50, occurs because of the existence of the longitudinal force peak and slide phenomena discussed in section 8.4.2. Again, it is plain that application of considerable torque when the lateral force demand is high will produce an appreciable change in the lateral behavior of a vehicle.

**Figure 8.48: Lateral force at 4° slip angle as a function of longitudinal force**
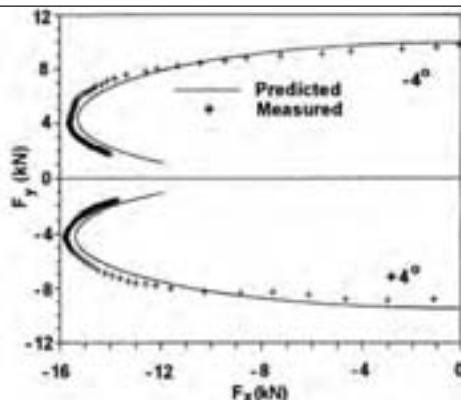
The effect of combined slip on longitudinal force is to make the peak longitudinal force occur at lower and lower magnitudes and at ever higher slip ratios, figure 8.49.[30] Unfortunately, actual data, like these, do not always perfectly match the ideal as represented in figure 2.18 in reference 7. Although the expected trend is generally present, at low

Figure 8.49: Longitudinal force as a function of braking slip ratio at fixed slip angles
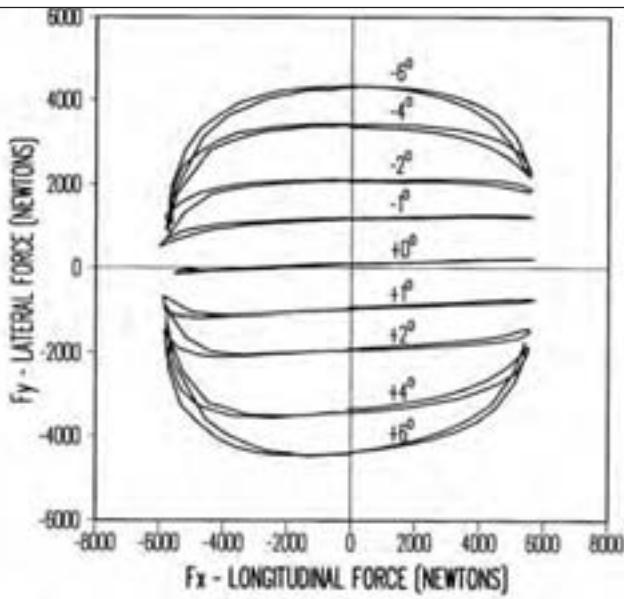
[30]The data are the average of tests of four tires and show some of the difficulties that can occur in experimentally characterizing real force and moment data. These data were developed in the course of preparing Reference 37.

Figure 8.50: Illustration of the return of the FY(FZ) curves at high slip ratios

(Reprinted with permission from SAE 960180 1996 SAE International) [35]

slip angles the behavior is often not in good accord.

If the results from cycles of torque application and release at numerous slip angles are plotted together, as in figure 8.51 drawn from reference 36, it is evident that the shape of $F(s,\beta)$ changes with slip angle. Also, as shown by Pottinger *et al* [37] the shape of the response depends on normal force. Thus, many diagrams like figure 8.51 are needed to represent the combined response in actual operation. Also, as noted in Reference 36, there

Figure 8.51: Lateral force as a function of slip angle and longitudinal force

(Clemson Tire Conference 1990) [36]

are fine asymmetrical details in the response shown in figure 8.51.

If the F_Y versus F_X relationship at a given slip magnitude is plotted for a symmetrical tire, where only the slip angle is the source of lateral force, the resultant curve is referred

to as a friction ellipse. Unfortunately, camber and tire asymmetry considerably complicate the situation. Figure 8.52 is an example of what can happen. In this case the tire is directional and is operating at a positive inclination angle as well as at both positive and negative slip angles. The resulting diagram is quite asymmetrical. The pure cornering modes: right, $\beta = 90°$, and left, $\beta = 270°$, have different magnitudes. Pure driving, $\beta = 0°$, and pure braking, $\beta = 180°$, are different. Further, figure 8.53, which gives the magnitude of the forces in each mode of operation for the same example as that of figure 8.52, indicates that the asymmetrical shape would vary strongly with slip magnitude. From the standpoint of modeling, it is fortunate that $F(s,\beta)$ basically degenerates into a circle as slip, s,

**Figure 8.52: Lateral force vs. longitudinal force at
one slip level, s, for a P205/60HR13 directional tire**

(Reprinted with permission from SAE 960180   1996 SAE International) [35]
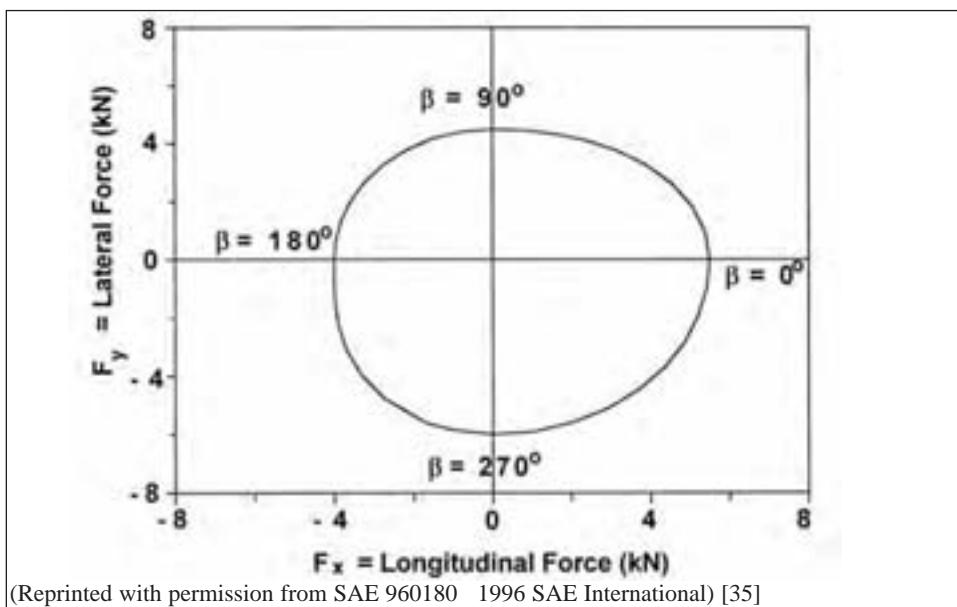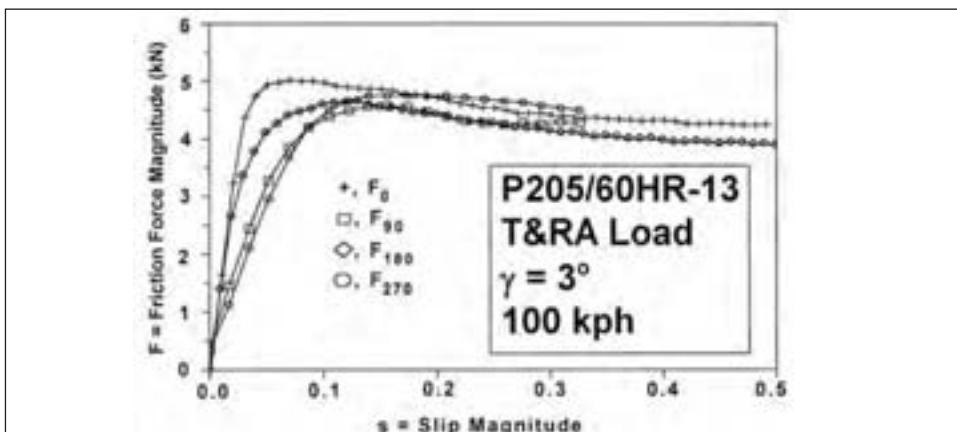
**Figure 8.53: Friction force, F, vs. slip magnitude, s, for a
P205/60HR13 tire at 3° inclination angle and T&RA load**

approaches 1.00.

   Aligning moment as a function of cornering and driving or braking is a more difficult problem mathematically than lateral force. M_Z versus F_X, figure 8.54, is just not a simple function. This is because anything that affects the lateral location of the resultant longitudinal force vector is going to affect the aligning moment. Inclination can have enormous effects on M_Z in the presence of torque. This is illustrated in figure 8.55, where the inclination angle is minus three degrees. Indeed, in the case of pure inclination combined with longitudinal force the resulting diagram (unpublished) bears a striking resemblance to a line drawing of the petals of a Spider Chrysanthemum blossom.

   As noted by Pottinger [36], overturning moment is also not an orderly function of longitudinal force.

**Figure 8.54: Aligning moment as a function of slip angle and longitudinal force**

(Clemson Tire conference 1990) [36]
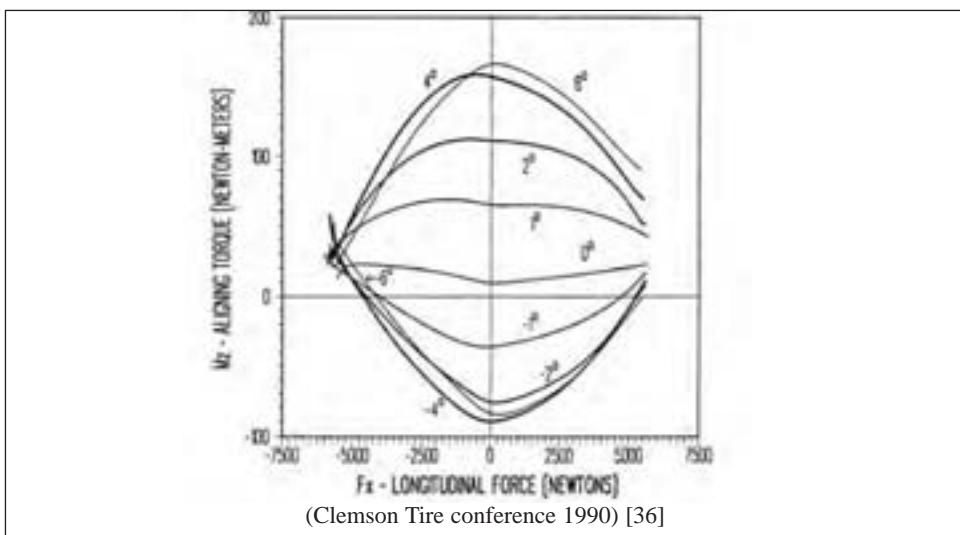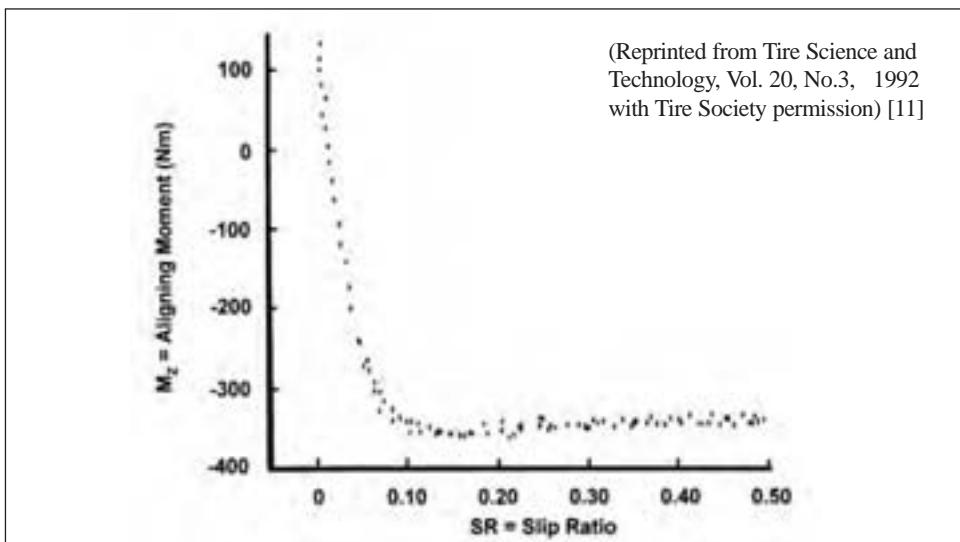
Figure 8.55: Aligning torque as a function of slip ratio

(Reprinted from Tire Science and Technology, Vol. 20, No.3, 1992 with Tire Society permission) [11]

5.4 Transient effects

To this point, we have considered data acquired for rates of application of the usage variable (α, γ, T) that are too small to make tire dynamics a major consideration. Data acquired under these conditions are commonly referred to as steady state data. Steady state data are completely adequate descriptions of tire behavior for many automotive design functions. However, they are not completely adequate to describe tire forces and moments in certain dynamic or transient situations, such as shimmy, where the tire's dynamic response is of paramount importance, or in violent transients, such as pre-rollover maneuvers, where the tire's phase lag behavior becomes important. This section is a very modest introduction to dynamic behavior of tires. If a thorough theoretical discussion of the topic is important, the reader should consult Pacejka [38].[31]

Rapid imposition of tire usage variables (α, γ, T) will result in a time-varying tire force and moment response due to the flexible nature of the tire structure. Figures 8.3 and 8.6 conceptually illustrate the complex deformations that must occur in order for a tire to generate steady state forces and moments. These complex deformations do not occur instantly.

It is common to characterize the tire dynamic response experimentally using a unit step or a sinusoidal sweep. Recently, response to a pulse has also been used [39].

5.4.1 Relaxation length and response to a unit step

To a first approximation, the dynamic responses at handling frequencies can be characterized in terms of response to a step input by an equation of the form of Eq. 8.7. This accounts for first order lag effects, but does not account for second order effects, which occur as tire modes begin to have a perceptible effect.

$$F = A (1 - e^{-Bt}) \qquad (8.7)$$

　　　　Where:
　　　　A = the steady state value of F.
　　　　B = a constant with the form $1/\tau$.[32]
　　　　F = a particular force or moment.
　　　　t = time.

Assuming a constant test velocity, v, equation 8.7 can be restated in terms of distance rolled.

$$F = A (1 - e^{-(X/l)x}) \qquad (8.8)$$

　　　　Where:
　　　　l = $v\tau$ is relaxation length.[33]
　　　　x = vt

The value of relaxation length is different for the different inputs, for example, a torque input will produce a different result than a slip angle input. These differences are because

---

[31]This book summarizes a professional lifetime's experience on tire transient effects and tire force and moment modeling.
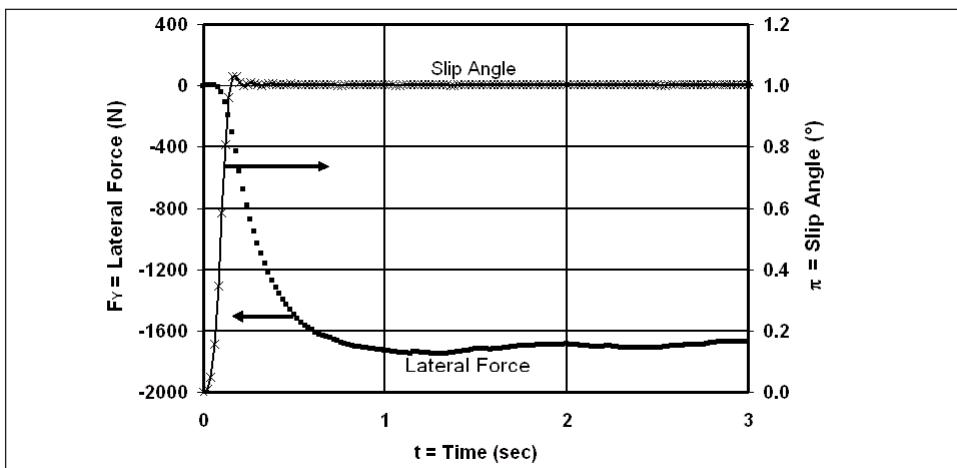
[32] τ is the length of time require for e-Bt to change from 1 to 1/e.

[33]In the context of this discussion, relaxation length is defined as the distance a tire subject to a step input in slip angle, load, torque, or other usage variable must roll in order to reach 63.2 percent of the steady state value that the force and moment in question will attain as a result of the step input in the pertinent usage variable.   In certain cases, for example, step slip angle, there is a corresponding physical definition as noted in Reference 6.

the relevant deformations are not the same. The value of the relaxation length also varies with testing parameters such as load and with tire design features.
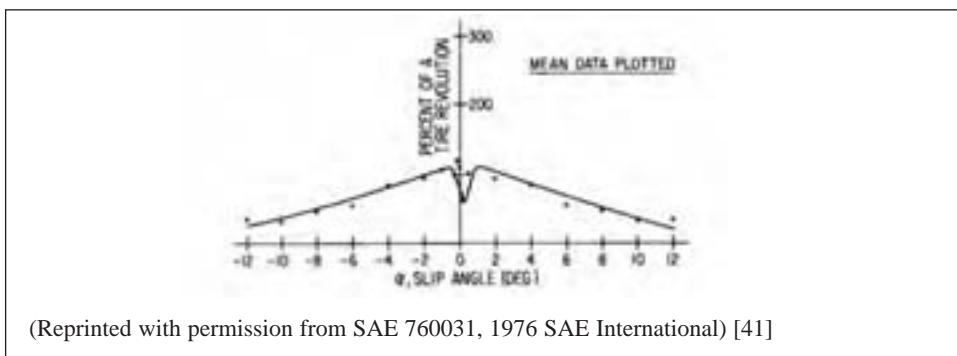
Relaxation effects with respect to slip angle have been studied with considerable thoroughness over many years. Figure 8.56 is a sample response. In this case, the step was imposed by rapidly imposing a fixed slip angle on a slowly rolling tire. Data were taken after a period of steady state rolling sufficient to characterize the pull force and uniformity signals produced by the tire, which were then subtracted to produce the data plotted in figure 8.56. It is also common to simulate a step steering response by loading a non-moving tire onto a plank type roadway and then to start the roadway to generate an equivalent to a step steer response [40].

Figure 8.56: Example data from a relaxation length experiment (uniformity and pull force removed in data processing)

It is important to note that lateral relaxation length in response to slip angle is dependent on slip angle magnitude [41], figure 8.57. Darnell, Mousseau, and Hulbert [42] provide force development curves at various slip angles and loads.

Figure 8.57: Distance from the start of motion to equilibration at steady state for radial tires

(Reprinted with permission from SAE 760031, 1976 SAE International) [41]

Relaxation in transient inclination response has been studied much less than in the case of relaxation due to imposed steer. Higuchi and Pacejka [40] provide results from both

experimentation and modeling. An experimental complication in this case is that the only practical way to simulate a step, given existing equipment limitations, is some form of static preloading followed by rolling from the preloaded condition. Preloading at an inclination induces a static lateral force response, which is not the same as the normal response to inclination. The result is that it is necessary to assume that the relaxation length represented in the change from the static response to the normal rolling response is indeed the correct relaxation length for inclination.

Relaxation length during torque application is important to the designers of anti-lock braking systems. Extensive information does not exist. The literature [38, 43, 44] indicates that the relaxation length in braking is appreciably less than in the case of cornering and grows shorter as the applied longitudinal force becomes closer to producing a completely locked condition. In the step to a locked wheel case the behavior of the tire, excluding stick-slip oscillations, would be very like the behavior observed in a static longitudinal spring rate test.

5.4.2 Response to sinusoidal steer
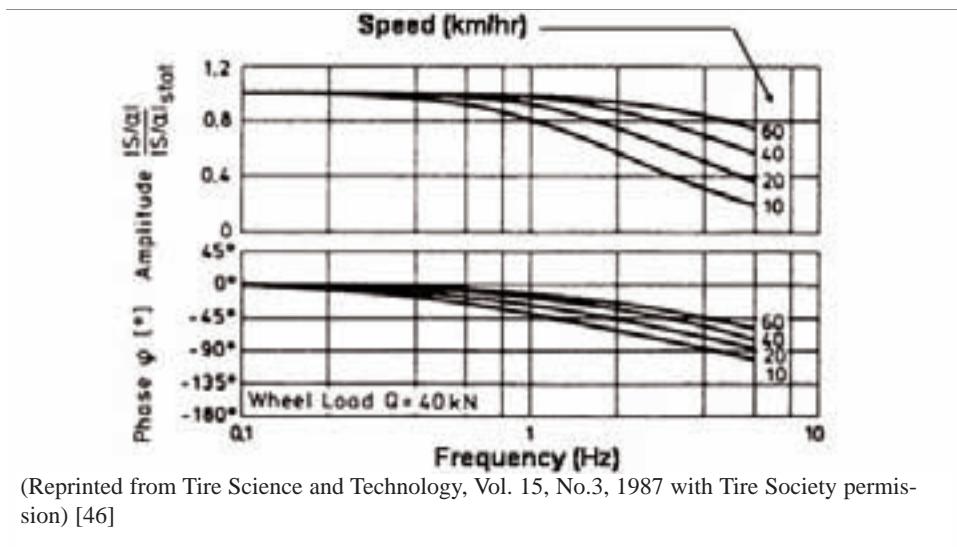
Sinusoidal steering input is the classical way to study the dynamic force and moment characteristics of tires [45]. It began with the study of shimmy in aircraft [4] and permits consideration of behavior over a broad frequency range accounting for second order effects.

Imposition of a sinusoidal slip angle excitation to the tire leads to a sinusoidal force and moment response which lags the excitation, Eqs. 8.9 and 8.10. If any of the resulting forces or moments is cross plotted with slip angle, the result is a loop, which is elliptical in the case of lateral force [45]. The phase lag and amplitude of the tire's response are dependent on frequency, ω, and test velocity [46], figure 8.58.

$$\alpha = \alpha_0 \sin \omega t \qquad (8.9)$$

$$F = F_{amp} \sin (\omega t + \phi) \qquad (8.10)$$

**Figure 8.58: Frequency response of lateral force for a 15R22.5 tire at 850 kPa inflation**
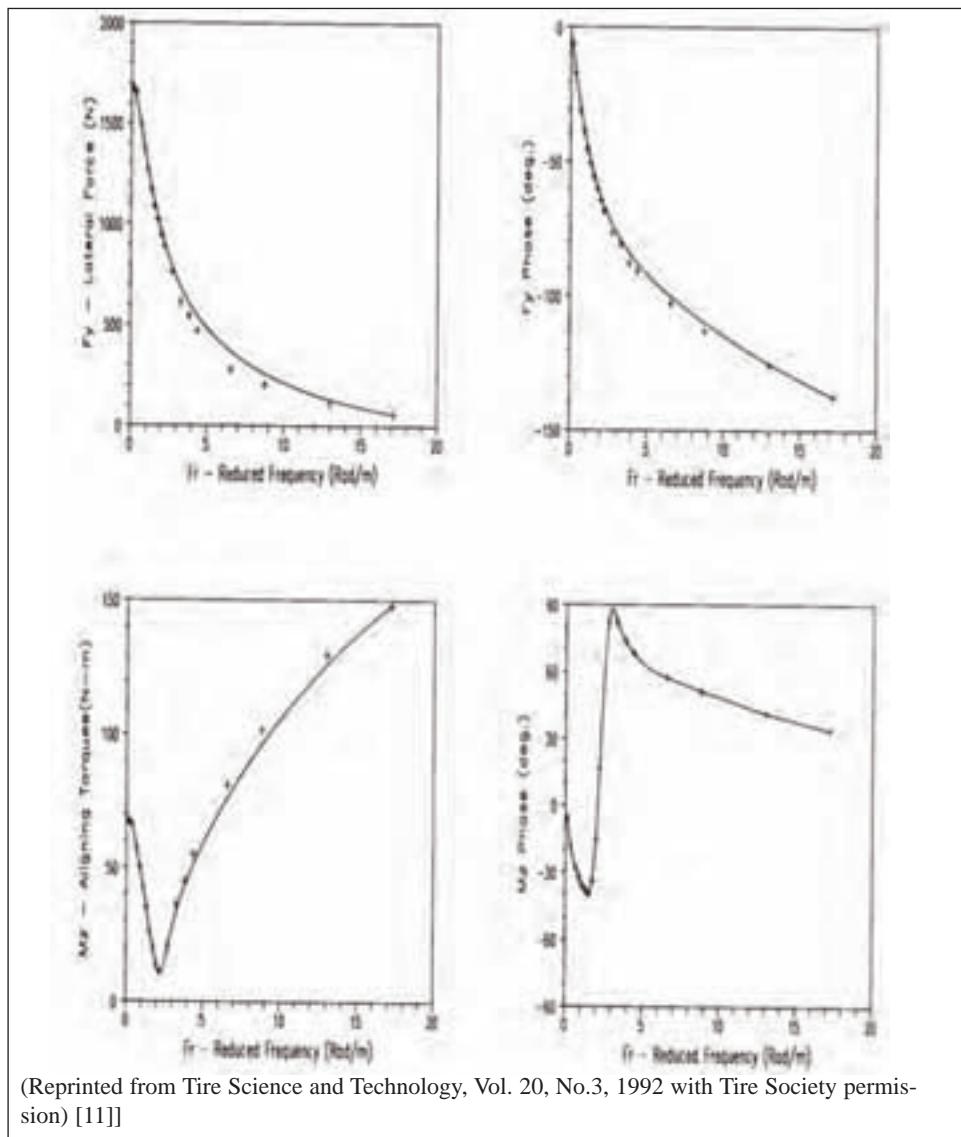
(Reprinted from Tire Science and Technology, Vol. 15, No.3, 1987 with Tire Society permission) [46]

Fortunately, to an excellent approximation, the responses at different speeds for a given tire specification reduce to a single curve when the data are viewed in terms of path frequency, ω_p, defined in equation 8.11. Path frequency is employed to transform Eqs. 8.9 and 8.10 into equations involving distance traveled by substitution of the relationship:

$$\omega_p = \omega/v \qquad (8.11)$$

This ability to express the results in terms of path frequencies, i.e., radians steered per meter of travel, allows the data to be exhibited as in figure 8.59. These data illustrate the complexity of the actual response as path frequency increases, especially for aligning moment.

Figure 8.59: Sinusoidal steer
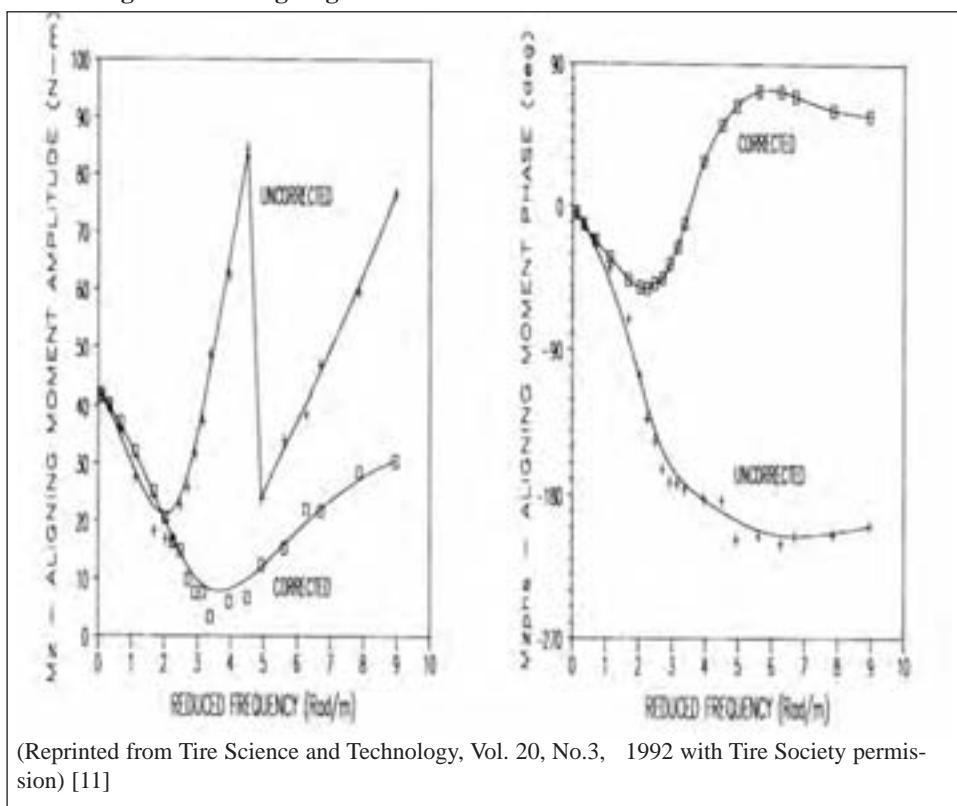
(Reprinted from Tire Science and Technology, Vol. 20, No.3, 1992 with Tire Society permission) [11]]

5.4.3 Inertial and gyroscopic effects

To this point, the discussion of dynamic responses has dealt with force and moment responses generated at the tire footprint. In real operation, inertial and gyroscopic effects are also generated as the tire is subjected to dynamic slip angles, inclination angles, and so forth. These effects must be accounted for by measurements when tires are applied on vehicles. Figure 8.60 gives an example of what was directly sensed at the spindle and what the actual or corrected tire structural response was after subtracting the effects of rigid body accelerations that existed during the test.[34] If the overturning moment data for the same test were plotted, it would be immediately evident that a gyroscopic effect was observed that had little to do with tire deformation.

Figure 8.60: Aligning moment corrected and uncorrected for inertia

(Reprinted from Tire Science and Technology, Vol. 20, No.3,   1992 with Tire Society permission) [11]

5.4.4 Brief comments on the significance of transient effects

As noted at the outset of section 8.4.4 many vehicle design studies do not require transient data. Certainly, shimmy studies always require transient data. In terms of handling, transients are most significant at lower speeds, because higher path frequencies are produced at a given rate of steering, or under circumstances where very high steering rates occur due to a severe emergency, or where low speeds and high steering rates are combined.

---

[34]Under dynamic conditions, it is always well to remember that most force measuring devices are to some degree also accelerometers.

As observed by Schuring [45], transients are important for limit handling, primarily in terms of the effect on phase lag, not in terms of amplitude effects. For example, consider a violent maneuver and a vehicle with a 20:1 steering ratio. The upper end of human performance is reached when about 800 degrees per second is applied at the steering wheel. This would produce 40 degrees per second at the road, or about 0.7 radians per second. Assuming a 100 km/hr speed, the path frequency would be approximately 0.025, which would have little effect on lateral force magnitude, but would yield a measurable phase shift or lag. The lag effect could be accounted for with the relaxation length model as noted in Section 8.4.4.1. Thus, the amount of detail inherent in sinusoidal excitation data is not really necessary for handling studies. Certainly more important than the pure lateral effect would be the combination of tire lateral dynamics with load variation effects occurring during the vehicle maneuver.

Schroeder and Chung [47] demonstrated that the effect of the relaxation length associated with slip angle on transient handling at modest lateral accelerations is discernable, but not nearly as important as the effect of cornering stiffness under normal driving conditions.

6. Testing and environmental parameters affecting the magnitude and character of forces and moments

The unfortunate truth about tire forces and moments is that a tire specification or, for that matter, an individual tire does not have a single well-defined set of force and moment characteristics. What a test tire or specification has, according to the test data, is the set of characteristics consistent with the tire construction and pre-test history, as demonstrated by the precise test protocol used. This uncertainty in characteristics arises from the changing chemical and viscoelastic properties of tire materials combined with the effects of wear.

To get data capable of answering relevant design questions, it is mandatory to give careful consideration to the items discussed in this section on test planning. The standardized tire force and moment testing protocols used by different companies have usually been developed to consider as many of the items as possible, and involve definite decisions as to what to do about them. The goal is to always produce data representative of usage in the relevant vehicle operational state or states.

6.1 Test surface curvature

Test surface curvature has already been considered in section 8.3.1 where the question of roadway curvature for test machines was discussed. Figures 8.10 and 8.11 demonstrate the complex relationships that exist between data taken on a curved surface and on a flat surface. As noted, the only practical solution is to employ a flat surface roadway when doing force and moment testing. Laging and Rothert [48] demonstrated that a curved surface produces complex alterations in the footprint stress field. It is probable that these alterations are responsible for lack of correlation between force and moment measurements on round and flat surfaces.
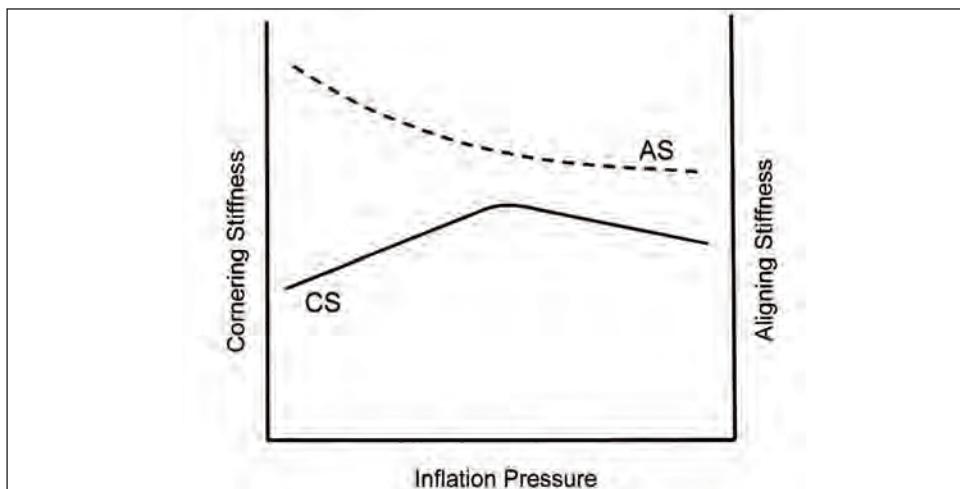
6.2 Inflation pressure

Increasing inflation pressure stiffens the tire structure. Often, people believe that the cornering stiffness simply goes up with inflation pressure, but this is not true. The cornering stiffness will peak with increasing inflation pressure and then fall off as the pressure is

increased further.

Increasing inflation reduces the size of the footprint, and thus the amount of tread rubber in contact with the road. At some point, the reduction in cornering stiffness due to a lower area of contact outweighs the increase in carcass stiffness due to increased pressure and the cornering stiffness begins to fall. A reduction of aligning torque is associated with an increase in inflation pressure because the shorter footprint also reduces pneumatic trail, section 8.2.1. Figure 8.61 is a schematic representation of the phenomena just described.

Figure 8.61: Aligning moment corrected and uncorrected for inertia

Additionally, increasing unit loading on the tread rubber reduces friction as shown by Ervin and associates [49]. Thus, if the inflation pressure is adequate to prevent buckling under the expected lateral and longitudinal forces, increasing the inflation pressure will likely lead to lower apparent friction.

6.3 Test speed

Speed effects exist on both dry and contaminated surfaces, for example, wet surfaces. This section deals with the situation on a dry surface. Section 8.5.8 will briefly mention effects observed on a contaminated surface. Chapter 11 considers the case of wet surfaces in some detail.

As test speed rises, the tire stiffens structurally. The result is an increase in cornering and aligning stiffnesses, figure 8.62. It is expected that a similar characteristic increase will occur in longitudinal stiffness. This will cause the lateral and longitudinal forces to peak at lower slip angles or slip ratios.

The magnitude of the peak longitudinal force in braking on a dry surface is almost independent of test speed, figure 8.63. Thus, the peak amplitude of lateral force is also not likely to change much with speed for modest changes in the peak location, as for ordinary road speeds on a dry surface.

The slide longitudinal force is entirely different, figure 8.64. It has a strong inverse dependence on test speed on a dry road. Thus, the decreasing (back) slope of both the lateral force and longitudinal force will become steeper as speed rises.

**Figure 8.62: Effect of test speed on lateral force
and aligning torque due to slip angle**

(Reprinted with permission
from SAE 760029 1976 SAE
International) [8]
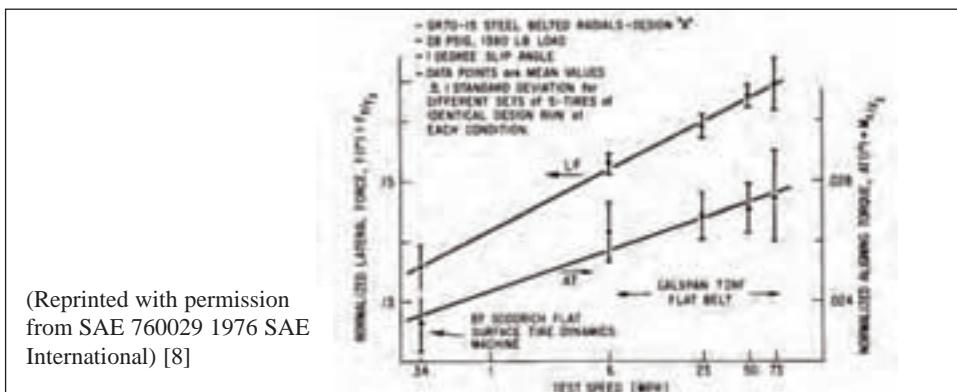
Figure 8.63: |FXpeak| vs. water depth and speed for a new tire

(Reprinted with permission from SAE 962153 1996 SAE International) [50]
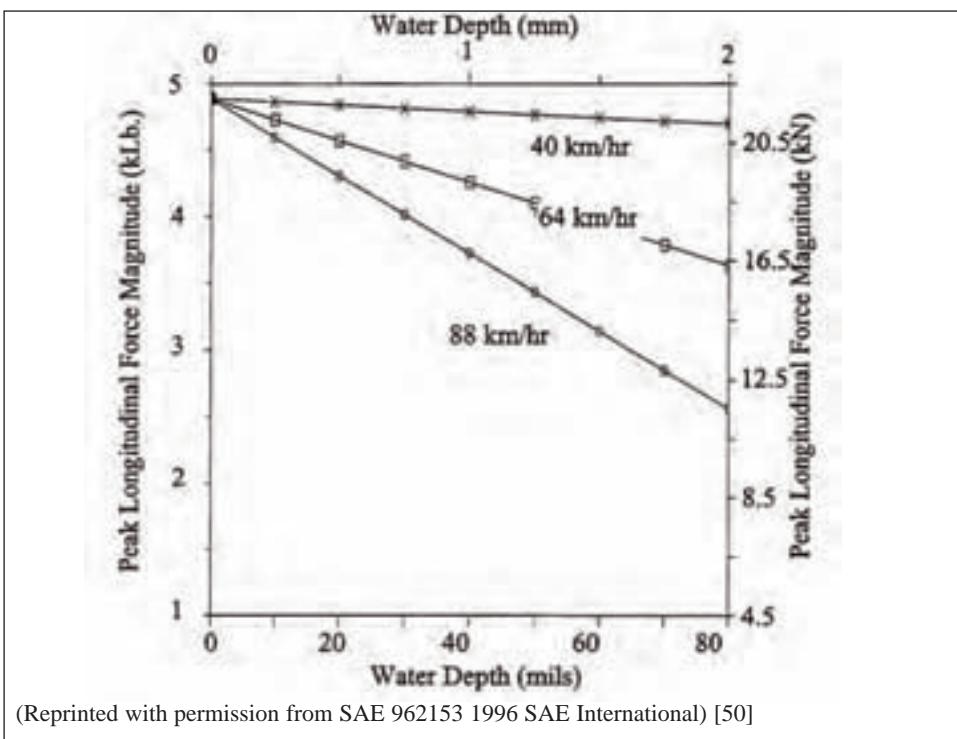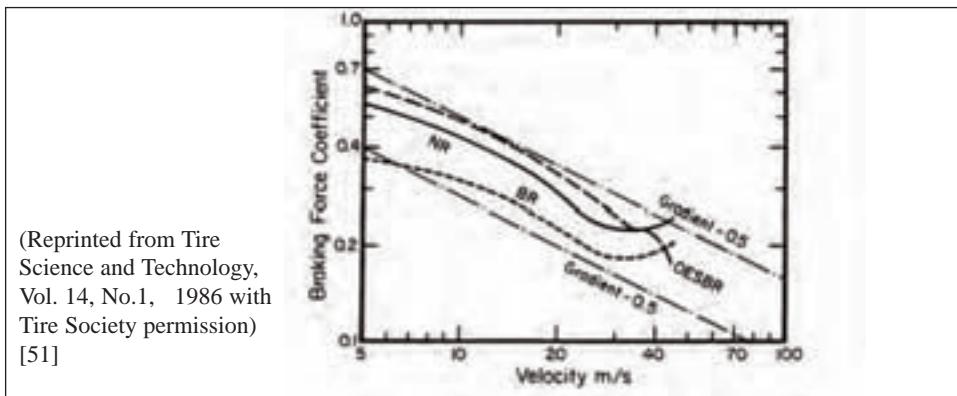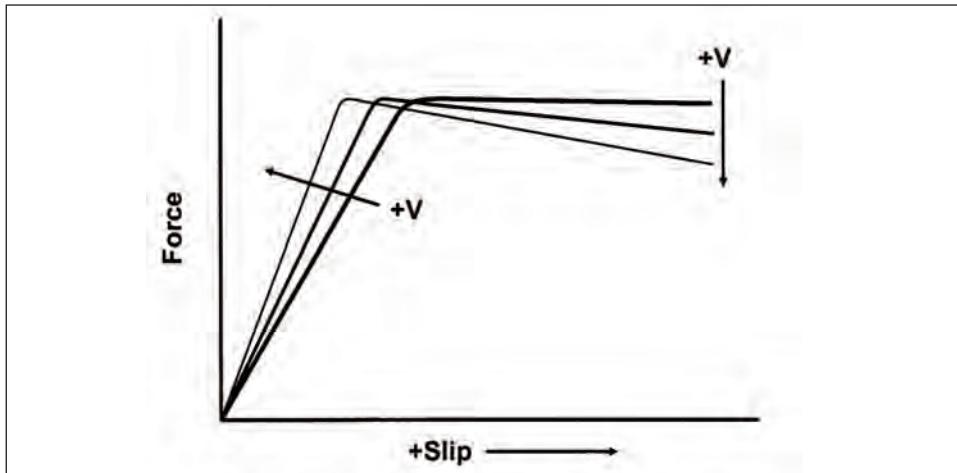
**Figure 8.64: The braking coefficients on eight pavement textures for
three cap compounds as a function of sliding velocity**

(Reprinted from Tire
Science and Technology,
Vol. 14, No.1,   1986 with
Tire Society permission)
[51]

The changes just discussed will warp tire lateral and longitudinal force performance
with speed to generate a sharper peak as sketched in figure 8.65. It is evident that the con-
sequence of warping the tire's response for the pure slip cases, which are the axes in the
slip circle, figure 8.46, will be to change the shape of the friction ellipse as speed rises.
Thus, the combined behavior is speed dependent.

Figure 8.65: Expected warping of either lateral or longitudinal force with speed

6.4 Tire aging

Tire force and moment properties change with time, even when nothing is apparently
going on: the tire is just sitting on the shelf. This is due to the additional crosslinking of
rubber with time. The result, as shown by Pottinger and Marshall [52][35], is a steady
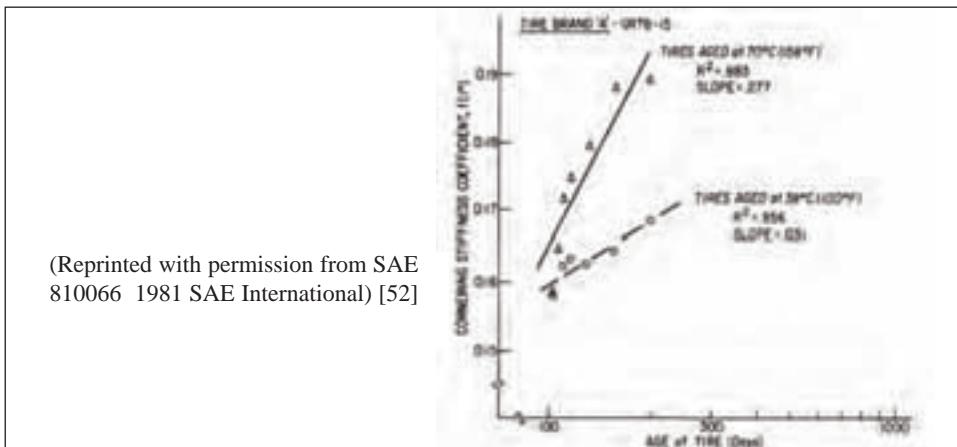
[35]The discussion in this reference is extensive and includes the actual aging changes in the tire compound stiff-
nesses, a discussion of aging in service, and a never-explained observation that two different aging mechanisms
are discernable from the force and moment data.

increase of cornering and aligning stiffnesses with the age of the tire. Using cornering stiffness as an example, the changes can be appreciable, see figure 8.66, and the rate of change is strongly dependent on storage temperature. Eq. 8.12 shows how the rates of change at different temperatures are related, for temperatures below about 70°C (158°F).

$$RATE_{@T2} = RATE_{@T1} \bullet 2^{\,0.1(T2-T1)} \qquad (8.12)$$
T = Temperature in °C

Figure 8.66: Effect of temperature on tire aging

(Reprinted with permission from SAE 810066 1981 SAE International) [52]

In a practical sense, whenever tire forces and moments are compared for different tire specifications or even for different samples drawn from the same tire specification, it is important to know the age of each sample and how each one has been stored prior to testing. Samples drawn from the same tire specification, but stored under different conditions can yield very different force and moment properties. And old samples are not the same as new ones. "Control" tires change just due to storage times and conditions. Machine correlations can be rendered invalid by aging effects. The rule is: be careful and never ignore aging.

6.5 Tire wear and exercise state
As a tire wears and is subjected to forces and moments that deform (exercise) its structure, the tire's force and moment properties change. The structural changes can occur quickly so that the tire may exhibit properties that only apply for a few moments.

Marshall *et al* [53] conducted tests in which tires were rolled for a known distance at a known slip angle, a process referred to as break-in, and then the cornering and aligning stiffnesses were tracked over a period of days. Figure 8.67 portrays the break-in matrix employed in Reference 53.

Though wear was not large, break-in was performed on both a sandpaper surface, noted as the common indoor test surface in section 8.3.1, and on a smooth steel surface. This determined if the changes observed were due to the removal of a skim coat from the tread surface or due to cyclical strain of the tire materials during the experiment. Cornering stiffness and aligning stiffness results were similar.

Break-in at higher slip angles produced a reduction in tire cornering stiffness followed by a viscoelastic recovery over time, figure 8.68. The magnitude of the cornering stiffness

reduction was dependent on distance and slip angle magnitude, i.e., lateral force level, as illustrated in figure 8.69. It appears that after traveling some distance at a given slip angle the cornering stiffness stabilizes, and ceases to change. Interestingly, operation at a slip angle of one degree did not appear to induce a break-in. Thus, there must be a threshold strain level for the break-in effect.

Figure 8.67: Matrix experiment to determine the effect of slip angle, load, and distance rolled on break-in

(Reprinted with permission from SAE 810066 1981 SAE International) [52]
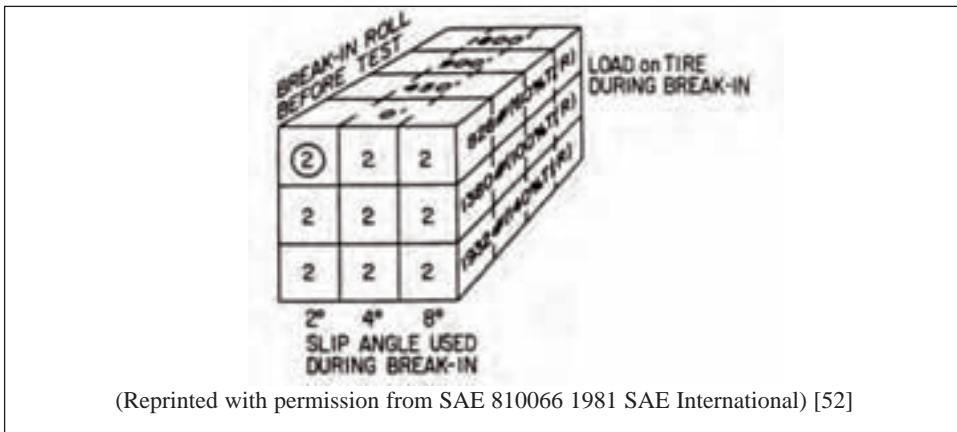
Figure 8.68: Effect of tire break-in; viscoelastic recovery vs. time for cornering stiffness coefficient - 24 tire sample

(Reprinted with permission from SAE 770870   1977 SAE International) [53]
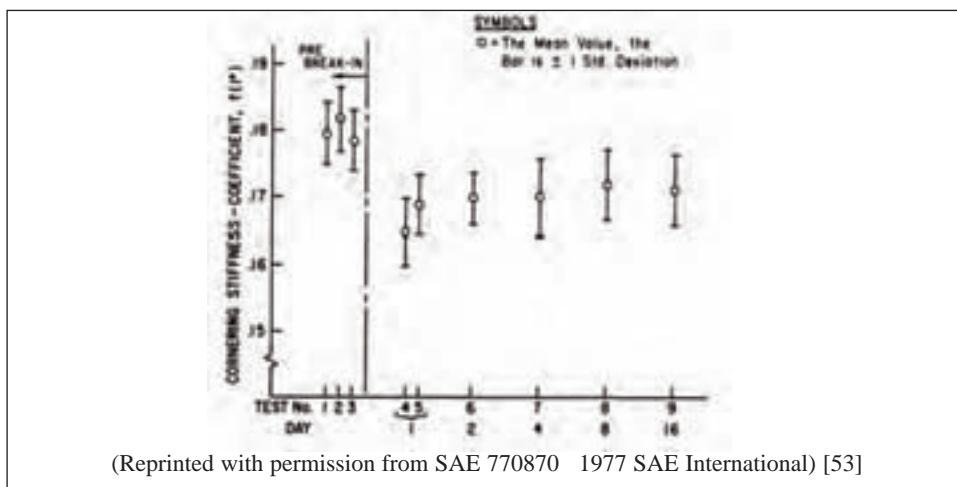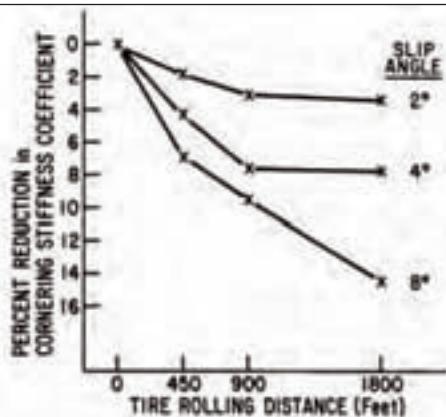
Figure 8.69: Reduction in cornering stiffness coefficient, following a break-in at various slip angles and rolling distances

(Reprinted with permission from SAE 770870   1977 SAE International) [53]

The break-in effect did not depend on removal of a skim coat by wear. Thus, the source of the break-in effect is internal to a tire's structure.

The reduction in cornering stiffness was independent of the tread depth so the source of the break-in effect is within the carcass and belt package, not in the tread.

The implication of these results is that strain cycling of the tire carcass, induced by applying a pure slip angle, will alter a tire's force and moment properties by a magnitude that is dependent on the slip angle, applied normal force, distance traveled, and time since the end of operation at a higher slip angle. Practically, this means two things.

A force and moment test protocol should be designed so as to expose a tire to approximately the same strain state an engineer would expect to occur on the vehicle.

In a real emergency maneuver, tire forces and moments will change throughout the actual maneuver.[36]

Wear itself leads to increased cornering stiffness.[37] This is due to the effect on tread element shear stiffness of tread element height or groove depth [54]. The effect is most marked in tires with appreciable tread depth, like snow tires or truck tires. By way of example, the change from a 15 mm tread depth to a 3.75 mm tread depth as a 295/75R22.5 steer axle tire wore down by 75 percent increased its cornering stiffness by 48 percent [50]. In the case of blocky tread patterns, wear will also increase longitudinal stiffness as the tread depth is reduced.

6.6 Ambient temperature

Temperature affects both tire tread frictional properties and tire stiffness. Racing tire engi-

---
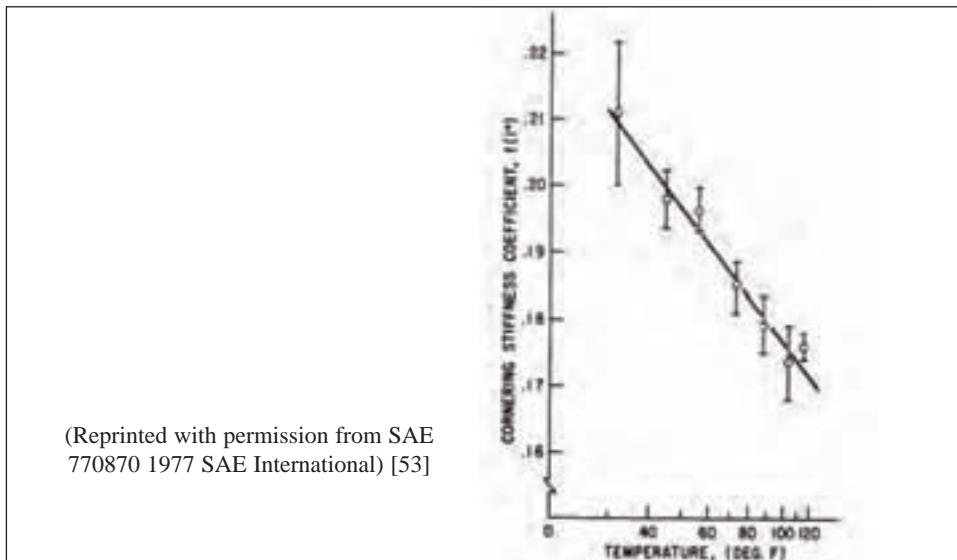
[36]In the latter part of Reference 52, a limited experiment tracing small samples of tires over thousands of kilometers of highway use indicates that normal driving does not lead to appreciable changes in tire lateral forces from those which exist in new not-broken-in tires. Apparently, aging, break-in, and wear combined to produce compensating effects. Thus, a sudden exposure to high slip angles will lead to changing force and moment properties in a real, one-time only, emergency maneuver.

[37]Racing tire engineers minimize tread depth to achieve the maximum possible cornering stiffness.

neers are very concerned with tread temperatures because special racing compounds vary strongly in adhesion depending on tread temperature. Chapter 11 considers both the adhesion and viscoelastic components of friction.

The stiffness of the tire structure declines as its temperature increases primarily because of a decrease in the stiffness of the compounds that form the matrices of the tire composites. To a first approximation, for normal environmental conditions the temperature of a tire increases by a given temperature increment for a defined operational state regardless of the tire's cold temperature. Figure 8.70 shows that cornering stiffness decreases with the logarithm of the tire's cold temperature for a tire soaked at a constant temperature and then tested. Viewing the soaked results as being the effect of varying the ambient temperature, we can deduce the effect of variations in ambient temperature on force and moment data. It is clearly important to maintain good control of ambient temperature during force and moment testing.

Figure 8.70: Cornering stiffness coefficient vs. logarithmic temperature

(Reprinted with permission from SAE 770870 1977 SAE International) [53]

6.7 Test surface

Section 8.3.1 dealt with the road or roadway as a part of the force and moment measuring system. The focus was on dry, uncontaminated, surfaces. As mentioned there, indoor roadways are typically coated with sandpaper and the correlation between the indoor surface and an outdoor surface may not be at all satisfactory. A correlation between a 120 grit THREE-M-ITE® surface and a brushed concrete surface was provided as an example in figure 8.15.
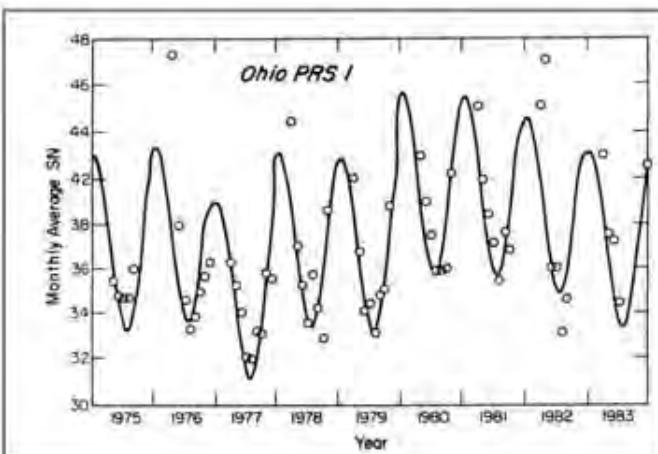
The frictional characteristics of both indoor and outdoor surfaces change as the surface micro-texture changes with wear.[38] Table 8.3, drawn from Reference 56, shows how much frictional variance can occur on a sandpaper surface as the sandpaper varies from lot-to-lot and in the absence of an aggressive process control protocol.

---

[38]Micro-texture is the small sharp texture that feels rough on sandpaper [55].

Table 8.3: Control tire in braking tests[39]

Statistic	Coefficient of friction at 80% braking slip
Minimum	0.49
Mean	0.57
Maxium	0.64
Standard deviation	0.05

In the case of an outdoor surface the micro-texture is also a function of weathering. It is this variation in micro-texture that is responsible for the day-to-day, season-to-season, and year-to-year variance of pavement frictional properties illustrated in figure 8.71. In the figure, drawn from Whitehurst and Neuhardt [14], the variation in pavement frictional properties is expressed in terms of Skid Number using ASTM Test Method E274.

Figure 8.71: Example of friction change for an outdoor test surface

(Reprinted with permission from STP 929   1986 ASTM International) [14]

The question of the effect of surface contamination (water, snow, and ice) is covered thoroughly in chapter 11 from the standpoint of friction. In general the effect of contaminates is to grossly alter tire force and moment properties.

The figures in reference 50, of which figure 8.63 is an example, illustrate characteristic tire responses to water depth, test speed, tread depth, and load. Typically, force levels in the wet decline with respect to those measured in the dry as:

- Tread depth declines due to wear[40],
- Water depth increases,
- Speed increases,

and

- Load decreases.
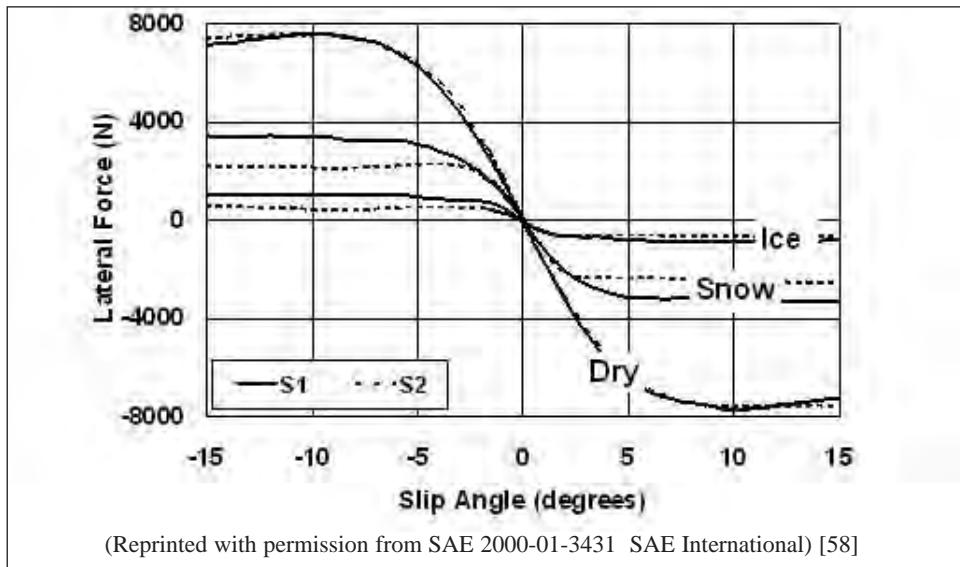
Effectively the force and moment response surfaces become warped.

---

[39]These data were acquired over a limited period in the autumns of 1996 and 1997.
[40]Interestingly, Williams and Evans [57] have shown that tread wear unevenness decreases tire performance on a wet pavement.

Warping of all features of the tire forces and moments, both stiffnesses and friction levels, on contaminated surfaces is illustrated in figure 8.72, which compares behavior on a dry road, a snow covered surface, and ice. Plainly, using a simple scaling factor to account for surface differences is not an adequate representation of real data.

Figure 8.72: Lateral force dry, on snow, and on ice for two tire specifications

(Reprinted with permission from SAE 2000-01-3431 SAE International) [58]

In planning a test program it is obviously crucial to test on a surface that is appropriate for the vehicle design problem under consideration. Correct test parameters together with the correct amount and type of contaminants must be used.

Tire companies have long studied the problem of surfaces and how to generate relevant responses. Recently, Finite Element Analysis has been combined with computational fluid dynamics to provide increased insight into tire-to-surface interactions in the presence of surface contaminants [59, 60, 61, 62].

7. Modeling tire forces and moments

To make use of force and moment data in vehicle design, tire characterizations must be put into mathematical terms, that is, as models. At present (2004), there are two practical limitations that affect the use of tire models as part of a vehicle model. First, a tire model must not consume so many computer resources that the vehicle model does not run at a reasonable speed. This means that the tire model cannot be too complex. Moreover, it must become simpler as the requirement for operational speed increases, for example, in using real-time models for hardware-in-the-loop-testing. Second, a model must not require major engineering input so that the effects of different tire designs can be compared and evaluated on vehicle models for a rational cost.

There are three basic ways to model force and moment behavior: from purely structural considerations (finite element analysis), using lumped parameters (structurally based), or empirically (or semi-empirically) by fitting a relationship ("curve") to experimental data. Generally, FEA models are not satisfactory as substructure elements of vehicle models because they do not meet the criteria stated in the previous paragraph. Lumped param-

eter models can be used as substructure elements, but that requires determining some structurally-related parameters. Empirical models with prudent insertion of some lumped parameter aspects (making them semi-empirical) are the current models of choice for evaluating tire forces and moments in vehicle modeling.

7.1 Pure structural (FEA)

At this time, finite element models are useful for refining and understanding the effects of tire design on forces and moments. Examples of the power of this method were given for wet traction and hydroplaning in section 8.5.7. References 63, 64, and 65 include examples of applying the method to other force and moment topics. FEA is also used currently to predict the values of the parameters in lumped-parameter models that yield tire forces and moments.
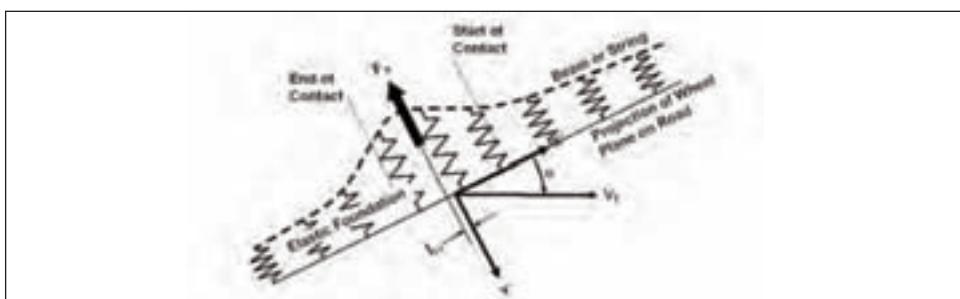
Vehicle modelers and others with an interest in forces and moments, but who are not themselves tire structural modelers, will find the current technical literature to be the best way of following the continuing progress in using finite element modeling to calculate tire forces and moments.

7.2 Lumped parameter

Lumped parameter models are simplified structural models that may or may not be physically realistic representations of the tire structure. They contain structural elements that can produce realistic simulations of tire force and moment behavior, if the parameters are assigned appropriate values. But these models are not all-purpose. Each works best to simulate some particular feature or features of the tire's behavior. Historically, the values of the parameters have been chosen on the basis of experiments. Today, in some cases, the values of the parameters can be assigned based on finite element simulations of the tire structure. Lumped parameter models can be compact enough to employ in vehicle models.[41]

Lumped parameter models began with an assumption of an infinitely-long transversely-flexible structural member, supported by an elastic foundation, figure 8.73, with a finite footprint zone.

Figure 8.73: Beam or string on an elastic foundation model
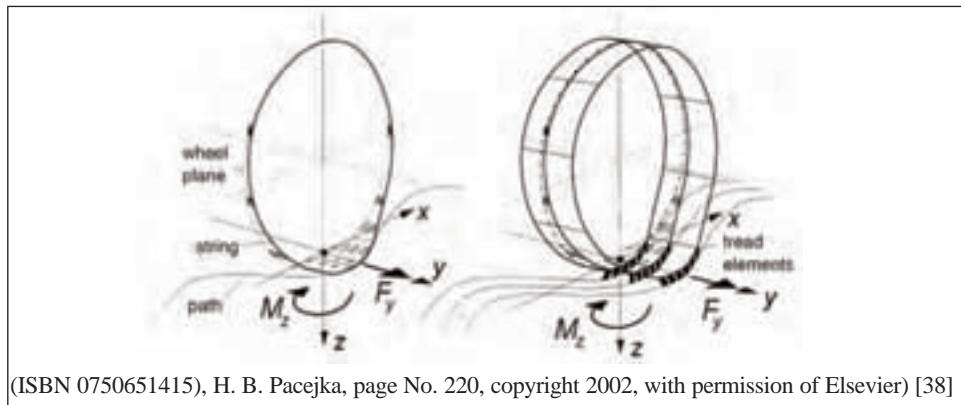
This approach began with the work of von Shlippe and Dietrich [66] where the infinitely long transverse element was a string. Later von Shlippe and Dietrich [67, 68] included the effect of contact width by representing the tire by two parallel strings. Over

---

[41]The emphasis in this chapter is on forces and moments. Lumped parameter models are widely used in studying dynamics in the wheel plane for purposes of ride, and impact with road irregularities. They are also important in trying to deal simultaneously with ride factors, and forces and moments.

the years the string on an elastic foundation approach has been elaborated to include multiple parallel strings and an elastic tread, figure 8.74. Chapter 5 of Pacejka [38] discusses string models in great detail with a particular emphasis on transients.

Figure 8.74: Tire model with single-stretched string and model extended with more parallel strings provided with tread elements with longitudinal flexibility from "tyre and vehicle mechanics"

(ISBN 0750651415), H. B. Pacejka, page No. 220, copyright 2002, with permission of Elsevier) [38]

Gough [69, 70] replaced the string with a composite beam, a more appropriate structure to represent a radial tire. This concept led to a number of design insights about forces and moments. Sakai [71] used the beam on the elastic foundation concept, but with the beam formed into a hoop. Then to simplify the situation, he assumed that the beam was rigid laterally, but could bend in the tire-wheel plane, to establish the footprint. The flexibility of the tread was used to generate longitudinal and lateral forces along with the relevant moments.

Carrying the idea of a flexible tread to its logical conclusion, one can simply allow the tread to possess all of the required flexibilities. The carcass can be considered rigid. This generates the so-called brush model, figure 8.75. It is capable of simulating pure and combined slip forces and moments, given the right selection of properties for the bristles. However, simulation of transient effects requires a flexible carcass so that it is now common to attach a brush tread to a flexible carcass. A large number of authors have used versions of the brush model. Again, Pacejka [38] contains extensive discussions.

### 7.3 Empirical (semi-empirical)
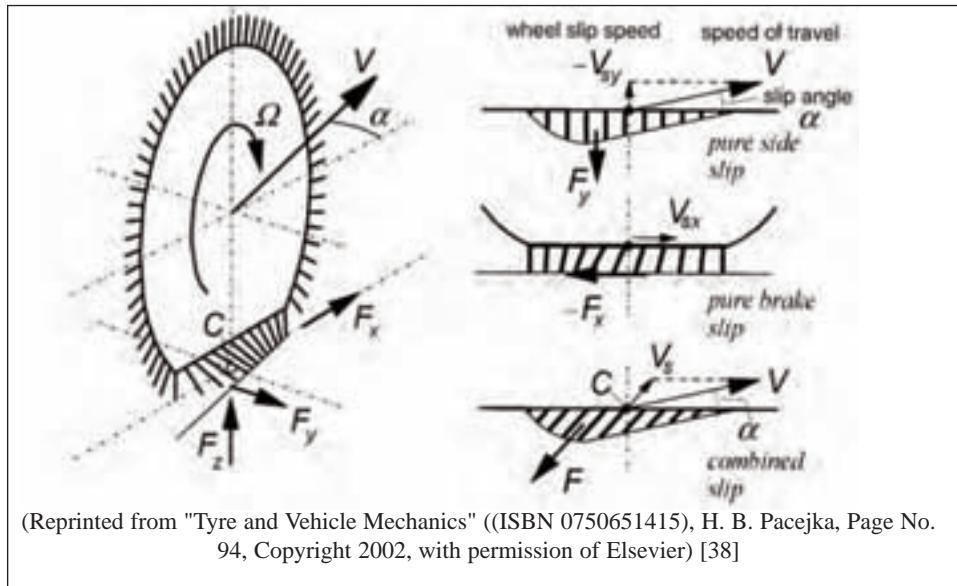
Empirical models began as curve fits. That is the way tire force and moment data is most commonly used in vehicle modeling. In order to deal efficiently with combined operations, such as simultaneous driving or braking, and cornering or transients, certain elements from lumped-parameter models have been incorporated into empirical models in recent years. Thus, various initially-empirical models might now be regarded as semi-empirical models.

It is now possible to process experimental data from predefined tests through a prepared set of computer routines and quickly obtain coefficients for a "standardized" model that is incorporated within vehicle simulation software.[42] Thus, with minimal trouble,

---

[42]The precise form of the "standardized" models in use often varies from corporation to corporation and from one software package to another, even though they often share a common origin, because the engineers and programmers who devised the particular version had divergent ideas in detail.

vehicle dynamicists who use commercial software like DELFT TYRE^{TM} can concentrate on vehicle simulation without being intimately concerned with understanding tire structural behavior or becoming an expert on tire data.[43]

Figure 8.75: The brush tire model

(Reprinted from "Tyre and Vehicle Mechanics" ((ISBN 0750651415), H. B. Pacejka, Page No. 94, Copyright 2002, with permission of Elsevier) [38]

In this section, we focus on modeling where, by one method or another, the parameters in the model can be related to actual tire behaviors like cornering stiffness, peak coefficient of friction, etc. Neural network modeling is not considered because it gives no insight on how to deal with what-if questions. For example, a vehicle dynamicist may wish to know what happens if the tire has the cornering stiffness increased by 10 percent. This is an appropriate question that a tire modeling routine should be able to answer.

Perhaps the simplest way to deal with empirical data is to apply interpolation to tables of tire force and moment values. This has been done in the past and can be done efficiently today for simple cases where the forces and moments are functions of two, or at most three, tire usage variables. However, interpolation quickly becomes an unwieldy procedure in the face of combined operations and transients, where large amounts of experimental data are required. Simple interpolation has therefore become relatively uncommon.

Pure polynomial fits can work well for a limited range of tire data and for data confined to restricted operational ranges. Polynomials can be made useful for fitting data accurately over a wide range if used in structured sets. For example, it is possible to divide the total data range into small sections, then fit each section by a power series, and provide good continuity at the section joints [72]. Another way to ensure continuity and tight fits is to apply spline techniques [73]. For the case of pure slip angle and normal force, regionalized bi-cubic spline models work effectively over the normal range of operating slip angles. But regionalized fitting methods can lead to large numbers of coefficients and

---

[43]Given that the subjects of tire modeling and tire properties are not yet completely understood, development of force and moment testing and modeling technology is continuing to take place.

do not permit ready answers to what-if questions.

One approach to reducing the number of coefficients is data normalization before fitting, and thus collapsing the data set to a minimum number of relationships. Radt and Glemming [74] provide a thorough exploration of this technique. Unfortunately, normalization doesn't work quite well enough to meet the needs of many vehicle dynamicists.

Today, the most common empirical or semi-empirical models are derived from the "Magic Formula", equation 8.13, introduced in a 1987 paper by Bakker, Nyborg, and Pacejka [75].

$$y = D \sin [C \arctan \{(B \bullet x - E (B \bullet x - \arctan (B \bullet x)))\}] \qquad (8.13)$$

This curve possesses certain symmetry characteristics, equation 8.14.
$$y(x) = -y(-x) \qquad (8.14)$$

If two transforms are applied (equations 8.15 and 8.16), the location of the center point of the curve (x = y = 0) can be defined in terms of real physical variables X and Y. As shown in figure 8.76, the curve then has a form commonly seen in tire data.

$$x = X + S_h \qquad (8.15)$$
$$Y(X) = y(x) + S_v \qquad (8.16)$$

Where, for example: $X = \alpha$ or SR
$Y = F_X, F_Y,$ or M_Z

Six important properties of the "Magic Formula" are noted in a subsequent paper by Bakker, Pacejka, and Lidner [76]. The two that seem most important are: a) the formula can match the experimentally observed characteristics of lateral force, aligning torque, and longitudinal force quite well and b) the coefficients can be related to actual physical tire data in a recognizable way.
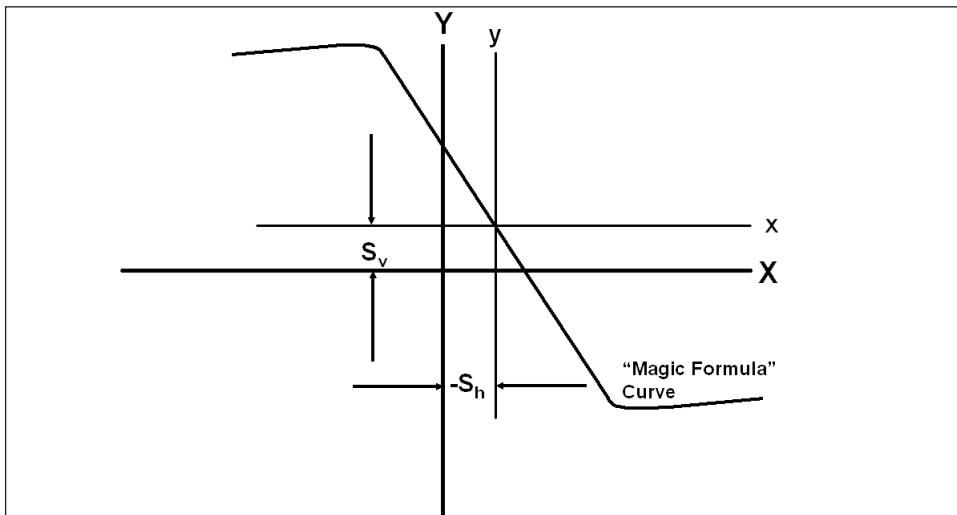
The discussion in Schuring, Pelz, and Pottinger [77] is very helpful for understanding the mathematical features of the "Magic Formula" and sheds light on both the interpretation of the coefficients B, C, D, E, S_h and S_v and the consequences of the values chosen for C and E. [In that paper, S_h and S_v are denoted S_x and S_y respectively, and the x to X transformation formula is expressed in a slightly different way.]

S_v and S_h simply locate the center point of the Magic Formula curve with respect to the origin when the traditional representation of tire data is used. For example, in the case of lateral force S_v and S_h arise from plysteer and conicity, Section 8.4.1.4.1.

$B \bullet C \bullet D$ is the initial slope of the curve. In practice, this product is the cornering stiffness, aligning stiffness, or longitudinal stiffness depending on which force or moment is being modeled.

B and D are size factors. D can be estimated from the maximum value of y when the curve has a definite peak. The fact that y cannot exceed D leads immediately to this relationship.

C and E are shape factors. Graphic examples of the effect of various choices for the values of C and E are given in Reference 77. For E < 1, the region in which "Magic Formula" curves are shaped like typical force and moment curves, the value of C controls the initial slope, final level, extreme values and passage through zero (where y goes from plus to minus or vice versa). For typical curves 1 < C < 4 and indeed in almost all cases 1 < C < 3.

Figure 8.76: "Magic formula" schematic

Following the methods outlined in reference 78 all the "Magic Formula" constants can be determined from tire force and moment characteristics. The resultant individual fits as functions of only lateral or only longitudinal slip angles are quite good, figure 8.77 through 8.81.
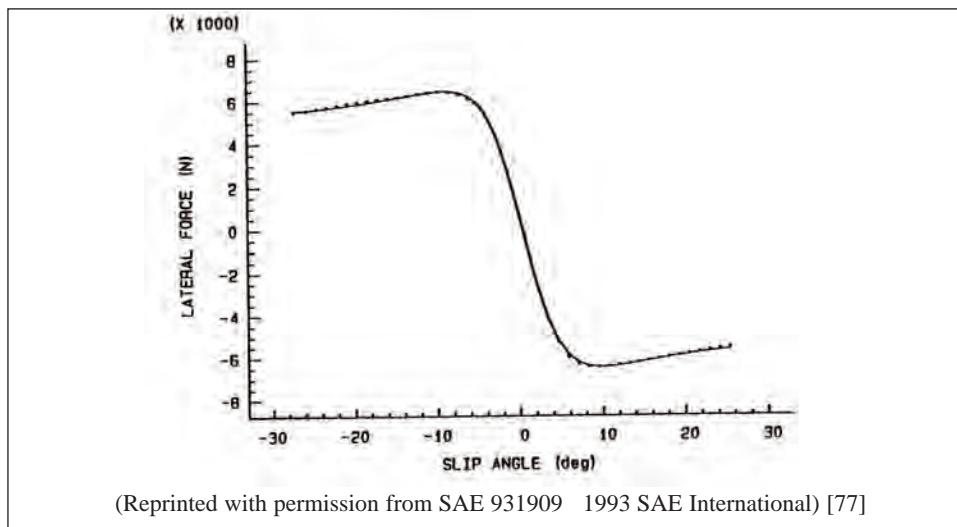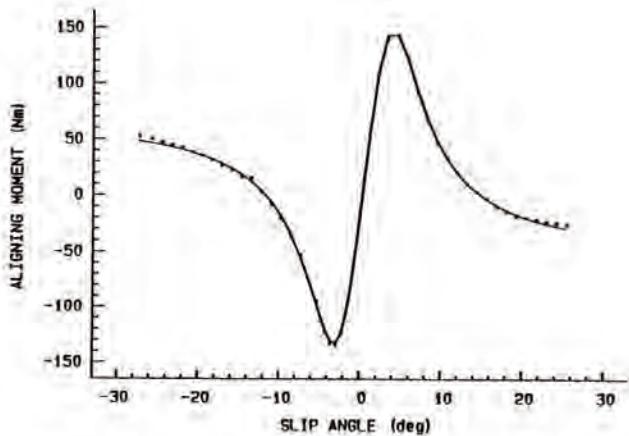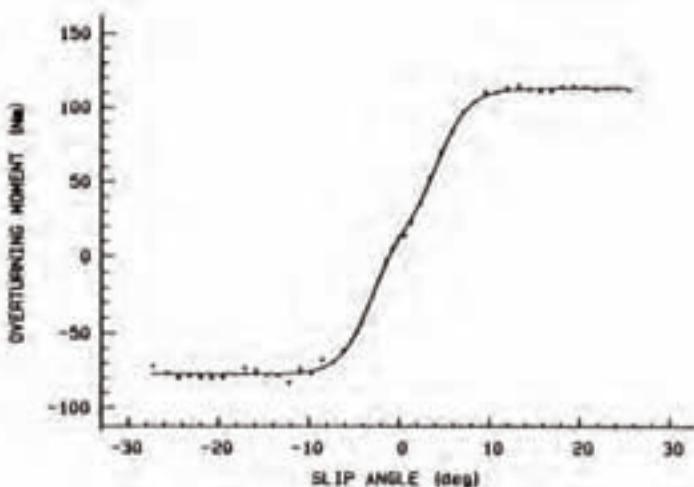
Figure 8.77: Lateral force vs. slip angle at one load

(Reprinted with permission from SAE 931909   1993 SAE International) [77]

Figure 8.78: Aligning moment vs. slip angle at one load
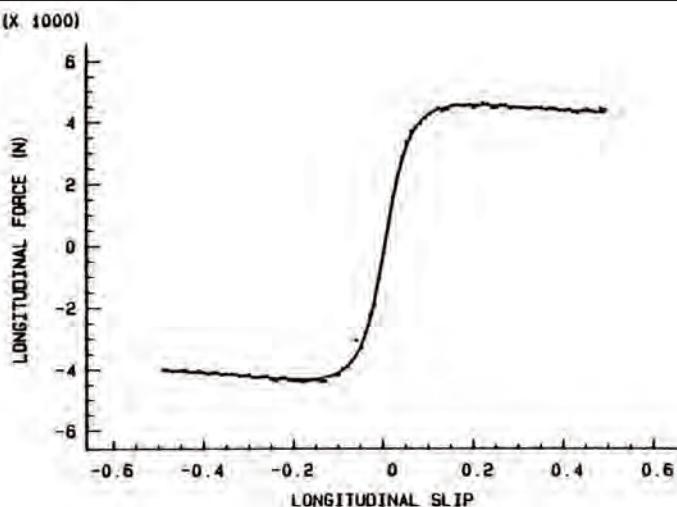

(Reprinted with Permission from SAE 931909   1993 SAE International) [77]
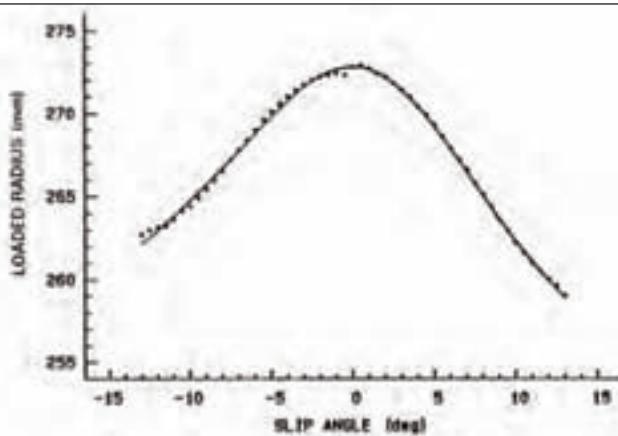
Figure 8.79: Overturning moment vs. slip angle at one load

(Reprinted with permission from SAE 931909   1993 SAE International) [77]

**Figure 8.80: Longitudinal force vs. longitudinal slip at one load**

(Reprinted with permission from SAE 931909 1993 SAE International) [77]

**Figure 8.81: Loaded radius vs. slip angle at one load
in the presence of inclination angle**
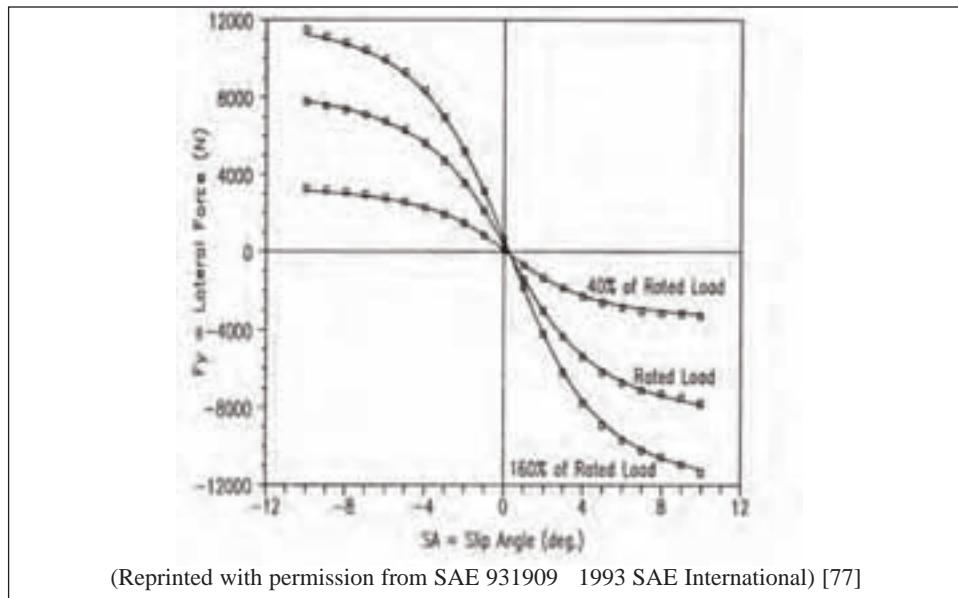
(Reprinted with permission from SAE 931909 1993 SAE International) [77]

It is necessary to express the "Magic Formula" constants B, C, D, etc., as functions of normal force and inclination angle in order to produce generalized models that represent F_X, F_Y, M_Z, etc. over the range of usage. This problem is dealt with in references 75 and 76. Although these papers are from the same research group, it is clear that the form of the functions was evolving, and they have continued to evolve, becoming increasingly complex, as noted in chapter 4 of reference 38.

Different modelers have used different functions to represent the constants in their implementations of the "Magic Formula". Actually, any set of functions that will repre-

sent B, C, D, etc., adequately is acceptable. Figures 8.82 and 8.83 were drawn from an implementation that used simple polynomials in two variables as representations.
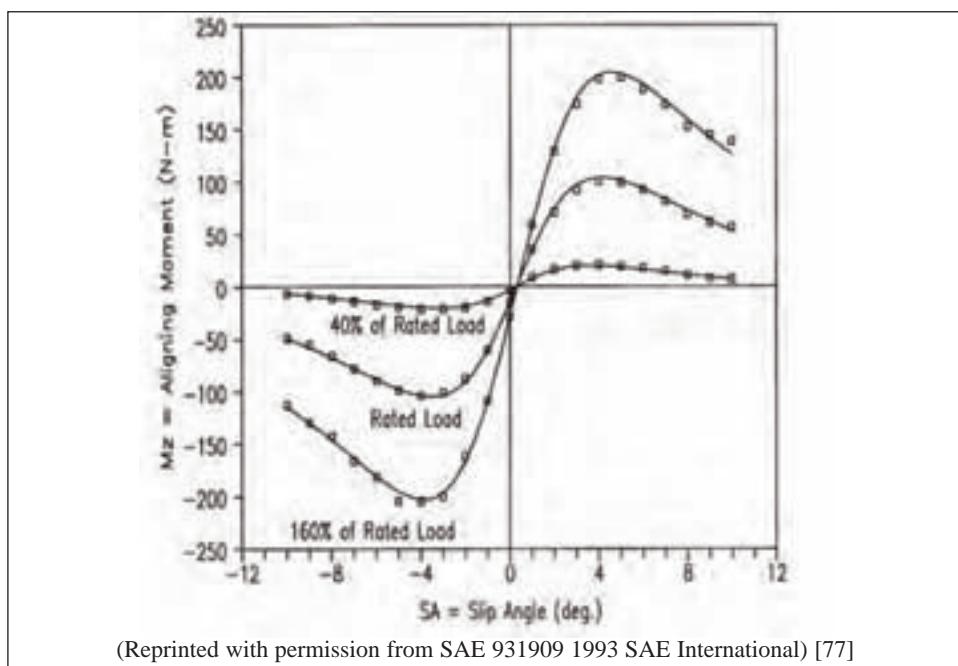
Figure 8.82: Lateral force at three loads

(Reprinted with permission from SAE 931909   1993 SAE International) [77]

Figure 8.83: Aligning moment at three loads

(Reprinted with permission from SAE 931909 1993 SAE International) [77]

It is worth mentioning that the asymmetry induced by inclination, see figures 8.31 through 8.34, renders the raw curves unfit for "Magic Formula" modeling. This problem can be dealt with by making E dependent on the sign of the base usage variable. In this case, E at positive slip angle takes one value and E at negative slip angle takes another. Basically, two curves are derived by splitting the original curve into two pieces at its center point and treating each piece as one-half of a complete and symmetrical "Magic Formula". It is just an application of the relationship given in Eq. 8.14.

7.4 Accounting for combined slip
The problem of combined driving, braking, and cornering is handled in a number of ways. One method employs a cosine version of the "Magic Formula" due to Bayle, Forissier, and Lafon [79] to develop weighting functions which when multiplied by the pure slip functions produce the interaction effects. This approach requires actual combined data as well as data for pure cornering and longitudinal slip.

Another approach, [35], does not require actual combined data and gives reasonable, though not perfect predictions, as shown in figure 8.50. It is easily implemented.

A third method, recently published by Svendenius and Gafvert [80], employs a brush model to handle the problem of combining data. Reference 80 treats adhesion and sliding separately, and should be superior to [35] on these grounds. However, it may not be readily implemented.

There are other approaches. The interested reader is advised to follow further developments in the literature as this is not a completely settled issue.

7.5 The special problem of modeling down to zero speed
The definitions of slip angle and longitudinal slip presented throughout this chapter work very well at normal road speeds. However, at speeds essentially equal to zero, which occur at vehicle start up or just before stopping, these definitions become inapplicable for numerical reasons as velocity goes to zero. Also, there are differences in the mechanics of force generation at a stop and the mechanics that exists in normal road speed operation. These questions are quite important in the operation of models developed for driving simulators where cars start from a stop and return to a complete stop. The work of Bernard and Clover [81] is of great utility when considering models that must deal with zero speed.

8. Concluding remarks
The discussion in this chapter has covered a very broad range of tire force and moment behavior and effects. The literature reviewed suggests that research and development is still needed in these areas of tire mechanics.

Tire force and moment modeling needs improvement with respect to clarity, overall standardization, and economic efficiency. At this time, the complexity of models often makes them the domain of specialists. Thus, the engineering value potentially present is not realized because use by the broader community is inhibited. A drive for standardization could eliminate considerable duplication of effort. Also, it is rather rare to see a discussion of the economic merits of a modeling approach, including the data acquisition needs and the engineering man-hours required for routine use.

Where to get certain tire test data is a vexing question. The ability to acquire force and moment data is limited for larger tires, light truck sizes and above. The existing infrastructure for testing these tires is definitely inadequate.

Representing operation on the "right" or "proper" surface remains a problem. Routine conversion of data taken under convenient frictional conditions to make them representative of realistic frictional conditions is not a common practice.

It is hoped that future reviews of this nature will be able to state that some of the problems described above have been laid to rest.

9. References

1. Dunlop, J. B., "An Improvement in Tyres of Wheels for Bicycles, Tricycles, and Other Road Cars," Provisional Specification, 20 July 1888.

2. Evans, R. D., "Properties of Tires Affecting Riding, Steering, and Handling," Society of Automotive Engineers, SAE Transactions, Vol. 30, February 1935,   pp. 41-49.

3. Bull, A. W., "Tire Behavior in Steering," Society of Automotive Engineers, SAE Transactions, Vol. 45, No. 2, 1939, pp. 344-350.

4. "Papers on Shimmy and Rolling Behavior of Landing Gears Presented at Stuttgart Conference Oct. 16-17, 1941," NACA Technical Memorandum 1365, W a s h i n g t o n , August 1954.

5. "Vehicle Dynamics Terminology," Society of Automotive Engineers, SAE J670e, Warrendale, PA, 1978.

6. "Tire Performance Terminology," Society of Automotive Engineers, SAE J2047, Warrendale, PA, 1998.

7. Milliken, W. F. and Milliken, D. L., "Race Car Vehicle Dynamics," Society of Automotive Engineers, SAE J670e, Warrendale, PA, 1995, pp. 39-40.

8. Pottinger, M. G., Marshall, K. D., and Arnold, G. A., "Effects of Test Speed and Surface Curvature on Cornering Properties of Tires," Society of Automotive Engineers, SAE 760029, Warrendale, PA, 1976.

9. Bird, K. D., and Martin, J. F., "The CALSPAN Tire Research Facility: Design, Development, and Initial Test Results," Society of Automotive Engineers, SAE 730582, Warrendale, PA, 1973.

10. Langer, W. J., and Potts, G. R., "Development of a Flat Surface Tire Testing Machine," Society of Automotive Engineers, SAE 800245, Warrendale, PA, 1980.

11. Pottinger, M. G., "The Flat-Trac II® Machine, the State-of-the-Art in Tire Force and Moment Measurements," Tire Science and Technology, TSTCA, Vol. 20, No. 3, July-September 1992, pp. 132-153.

12. Jenniges, R. L., Zenk, J. E., and Maki, A. E., "A New System for Force and Moment Testing of Light Truck Tires," Society of Automotive Engineers, SAE 2003-01-1272, Warrendale, PA, 2003.

13. Pottinger, M. G., Tapia, G. A., Winkler, C. B., and Pelz, W., "A Straight-Line Braking Test for Truck Tires," *Rubber World*, September 1996, pp. 29–36.

14. Whitehurst, E. A. and Neuhardt, J. B., "Time-History Performance of Reference Surfaces," *The Tire Pavement Interface*, *ASTM STP 929*, M. G. Pottinger and T. J. Yager, Eds., American Society for Testing Materials, W. Conshohocken, PA, pp. 61-71.

15. Ginn, J. L., and Marlowe, R. L., "Road Contact Forces of Truck Tires as Measured in the Laboratory," Society of Automotive Engineers, SAE 670493, Warrendale, PA, 1967.

16. "Combined Cornering and Braking Test for Truck and Bus Tires," Society of Automotive Engineers, SAE J2675, Warrendale, PA, 2004.

17. Pottinger, M. G., & Fairlie, A. M., "Characteristics of Tire Force and Moment Data," *Tire Science and Technology*, TSTCA, Vol. 17, No. 1, January-March 1989, pp. 15-51.

18. Pottinger, M. G., "Plysteer in Radial Carcass Tires," Society of Automotive Engineers, SAE 760731, Warrendale, PA, 1976.

19. Kabe, K., and Morikawa, T., "A New Tire Construction Which Reduces Plysteer," *Tire Science and Technology*, TSTCA, Vol. 19, No. 1, January-March 1991, pp. 37-65.

20. Nordeen, D. L., "Analysis of Tire Lateral Forces and Interpretation of Experimental Tire Data," Society of Automotive Engineers, SAE 670173, Warrendale, PA, 1967.

21. Nordeen, D. L., "Application of Tire Characterizing Functions to Tire Development," Society of Automotive Engineers, SAE 680409, Warrendale, PA, 1968.

22. Matjya, F. E., "Steering Pull and Residual Aligning Torque," *Tire Science and Technology*, TSTCA, Vol. 15, No. 3, July-September 1987, pp. 207-240.

23. Gillespie, T. D., "Fundamentals of Vehicle Dynamics," Society of Automotive Engineers, Warrendale, PA, 1992, pp. 351.

24. Marshall, K. D., Pottinger, M. G., and Gibson, G. E., "Nibbling – the Force and Moment Behavior of Tires Over Edges," *International Rubber Conference*, Brighton, England, May 1972.

25. Gough, V. F., Barson, C. W., Gough, S. W., and Bennett, W. D., "Tire Uniformity Grading Machine," Society of Automotive Engineers, SAE 322A, Warrendale, PA, 1961.

26. Topping, R. W., "Tire Induced Steering Pull," Society of Automotive Engineers, SAE 750406, Warrendale, PA, 1975.

27. Lee, J-H., "Analysis of Tire Effect on the Simulation of Vehicle Straight Line Motion," *Vehicle Systems Dynamics*, Vol. 33, No. 6, Swets & Zeitlinger, Lisse,   The Netherlands, June, 2000, pp. 373-390.

28. Pottinger, M. G., "Tire/Vehicle Pull: An Introduction Emphasizing Plysteer Effects," *Tire Science and Technology*, TSTCA, Vol. 18, No. 3, July-September 1990, pp. 170-190.

29. "Residual Aligning Moment Test," Society of Automotive Engineers, SAE J1988, Warrendale, PA, 1994.

30. Yamazaki, S., Fujikawa, T., Suzuki, T., and Yamaguchi, I, "Influence of Wheel Alignment and Tire Characteristics on Vehicle Drift," *Tire Science and T e c h n o l o g y*, TSTCA, Vol. 26, No. 3, July-September 1998, pp. 186 -205.

31. Tarpinian, H. D. and Culp, E. H., "The Effect of Pavement Grooves on the Ride of Passenger Cars – The Role of Tires," Society of Automotive Engineers, SAE 770869, Warrendale, PA, 1977.

32. Doi, T. and Ikeda, K., "Effect of Tire Tread Pattern Design on Groove Wander of Motorcycles," *Tire Science and Technology*, TSTCA, Vol. 13, No. 3, July-September 1985, pp. 147 -153.

33. Peters, J. M., "Application of the Lateral Stress Theory for Groove Wander Prediction Using Finite Element Analysis," *Tire Science and Technology*, TSTCA, Vol. 29, No. 4, October-December 2001, pp. 244 -257.

34. Nakajima, Y., "Prediction of Rain Groove Wandering," *Vehicle Systems Dynamics*, Vol. 40, No. 6, Swets & Zeitlinger, Lisse, The Netherlands, 2003, pp. 401-418.

35. Schuring, D. J., Pelz, W., and Pottinger, M. G., "A Model for Combined Tire Cornering and Braking Forces," Society of Automotive Engineers, SAE 960180, Warrendale, PA, 1996.

36. Pottinger, M. G., "Tire Force and Moment in the Torqued State an Application of the

Flat-Trac II ® Tire Testing Machine," Clemson Tire Conference, Greenville,   S.   C., October 1990.

37. Pottinger, M. G., Pelz, W., Tapia, G. A., and Winkler, C. B., "A Combined Cornering and Barking Test for Heavy Duty Truck Tires," *Road Transport Technology – 4*, Ann Arbor, MI, June 1995, pp. 583-592.

38. Pacejka, H. B., "Tyre and Vehicle Dynamics," Butterworth-Heinmann, Oxford, UK, 2002.

39. Lee, S., Heydinger, G. J., Chrstos, J. P., and Guenther, D. A., "Modeling of Dynamic Characteristics of Tire Output Responses to Concurrent Inputs," ASME, "Advanced Automotive Technologies - 1995" - DSC-Vol. 56, DE-Vol. 86, pp. 91 - 98, 1995 ASME Winter Annual Meeting, November 1995.

40. Higuchi, A. and Pacejka, H. B., "The Relaxation Length Concept at Large Wheel Slip and Camber," *Vehicle Systems Dynamics*, Supplement to Vol. 27, Swets & Zeitlinger, Lisse, The Netherlands, 1996, pp. 50-64.

41. Phelps, R. L., Pelz, W., Pottinger, M.G., and Marshall, K. D., "The Mathematical Characteristics of Steady State, Low Slip Angle Force and Moment Data," Society of Automotive Engineers, SAE 760031, Warrendale, PA, 1976.

42. Darnell L., Mousseau, R., and Hulbert, G., "Analysis of Tire Force and Moment Response During Side Slip Using an Efficient Finite Element Model," *Tire Science and Technology*, TSTCA, Vol. 30, No. 2, April-June 2002, pp. 66-82.

43. Zegelaar, P. W. A., and Pacejka, H. B., "Dynamic Tyre Responses to Brake Torque Variations," *Vehicle Systems Dynamics*, Supplement to Vol. 27, Swets & Zeitlinger, Lisse, The Netherlands, 1996, pp. 65-79.

44. Fancher, P., Bernard, J., Clover, C., and Winkler, C., "Representing Truck Tire Characteristics in Simulations of Braking and Braking-in-a-Turn Maneuvers," *Vehicle Systems Dynamics*, Supplement to Vol. 27, Swets & Zeitlinger, Lisse, The Netherlands, 1996, pp. 207-220.

45. Schuring, D. J., "Dynamic Response of Tires," *Tire Science and Technology*, TSTCA, Vol. 4, No. 2, 1976, pp. 115-145.

46. Weber, R., and Munster, M., "Transient Properties of Truck Tires on Real Road Surfaces," *Tire Science and Technology*, TSTCA, Vol. 15, No. 3, July-September 1987, pp. 188-197.

47. Schroder, C., and Chung, S., "Influence of Tire Characteristic Properties on the Vehicle Lateral Transient Response," *Tire Science and Technology*, TSTCA, Vol. 23, No. 2, April-June 1995, pp. 72-95.

48. Laging, G., and Rothert, H., "Numerical Results of Tire–Test Drum Interaction," TSTCA, Vol. 14, No. 3, July-September 1986, pp. 160-175.

49. Ervin, R., McAdam, C., Fancher, University of Michigan Highway Safety Research Institute, Report PF-75-3.

50. Pottinger, M. G., Pelz, W., Pottinger, D. M., and Winkler, C. B., "Truck Tire Wet Traction: Effects of Water Depth, Speed, Tread Depth, Inflation, and Load," Society of Automotive Engineers, SAE 962153, Warrendale,   PA, 1996.

51. Ettles, C. M. McC., "A Quantitative Theory for the Computation of Tire Friction Under Severe Conditions of Sliding," *Tire Science and Technology*, TSTCA, Vol. 14, No. 1, January-March 1986, pp. 44-72.

52. Pottinger, M. G. and Marshall, K. D., "The Effect of Tire Aging on Force and Moment

Properties of Radial Tires," Society of Automotive Engineers, SAE 810066, Warrendale, PA, 1981.

53. Marshall, K. D., Phelps, R. L., Pottinger, M. G., and Pelz, W., "The Effect of Tire Break-In on Force and Moment Properties," Society of Automotive Engineers, SAE 770870, Warrendale, PA, 1977.

54. Akasaka, T., Kabe., K., Koishi, M., and Kuwashima, M., "Analysis of the Contact Deformation of Tread Blocks," *Tire Science and Technology*, TSTCA, Vol. 20, No. 4, October-December 1992, pp. 230-253.

55. Bond, R., Lees, G., and Williams, A. R., "An Approach Towards the Understanding and Design of the Pavement's Textural Characteristics Required for Optimum Performance of the Tire," *The Physics of Tire Traction; Theory and Experiment*, D. F. Hays and A. L. Browne, Eds., Plenum Press, New York – London, 1974, pp. 339-360.

56. Pottinger, M. G., Pelz, W., Winkler, C. B., Pottinger, D. M., and Tapia, G. A., "Force and Moment Properties of a Small Sample of Tire Specifications: Drive, Steer, and Trailer with Evolution from New to Naturally Worn-Out to Retreaded Considered," Society of Automotive Engineers, SAE 982748, Warrendale, PA, 1998.

57. Williams, A. R. and Evans, M. S., "Influence of Tread Wear Irregularity on Wet Friction Performance of Tires," *Frictional Interaction of Tire and Pavement, ASTM STP 793*, W. E. Meyer and J. D. Walter, Eds., American Society of Testing and Materials, 1983, pp. 41-64.

58. Pottinger, M. G., McIntyre, J. E. III, Kempainen, A. J., and Pelz, W., "Truck Tire Force and Moment in Cornering-Braking-Driving on Ice, Snow, and Dry Surfaces", Society of Automotive Engineers, SAE 2000-01-3431, Warrendale, P A, 2000.

59. Grogger, H., and Weiss, M., "Calculation of the Three-dimensional Free Surface Flow Around an Automobile Tire," *Tire Science and Technology*, TSTCA, Vol. 24, No. 1, January-March 1996, pp. 39-49.

60. Grogger, H., and Weiss, M., "Calculation of the Hydroplaning of a Deformable Smooth-Shaped and Longitudinally-Grooved Tire," *Tire Science and Technology*, TSTCA, Vol. 25, No. 4, October-December, 1997, pp. 265-287.

61. Seta, E., Nakajima, Y., Kamegawa, T., and Ogawa, H., "Hydroplaning Analysis by FEM and FVM: Effect of Tire Rolling and Tire Pattern on Hydroplaning," *Tire Science and Technology*, TSTCA, Vol. 28, No. 3, July-September, 2000, pp. 140-156.

62. Okano, T., and Koishi, M., "A New Computational Procedure to Predict Transient Hydroplaning of a Tire," *Tire Science and Technology*, TSTCA, Vol. 29, No. 1, January-March, 2001, pp. 2-22.

63. Darnell, I., Mousseau, R., and Hulbert, G., "Analysis of Tire Force and Moment Response During Side Slip Using an Efficient Finite Element Model," *Tire Science and Technology*, TSTCA, Vol. 30, No. 2, April – June 2002, pp. 66-82.

64. Ohishi, K., Suita, H., and Ishihara, K., "The Finite Element Approach to Predict the Plysteer Residual Cornering Force of Tires", *Tire Science and Technology*, TSTCA, Vol. 30, No. 2, April – June 2002, pp. 122-133.

65. Rao, K., Kumar, R., and Bohara, P., "Transient Finite Element Analysis of Tire Dynamic Behavior", *Tire Science and Technology*, TSTCA, Vol. 31, No. 2, April – June 2003, pp. 104-127.

66. Schlippe, B. von and Dietrich, R., "Das Flattern eines Bepneuten Rades," *Papers on*

Shimmy and Rolling Behavior of Landing Gears Presented at Stuttgart Conference Oct. 16-17, 1941, NACA Technical Memorandum 1365, Washington, August 1954. ""

67. Schlippe, B. von and Dietrich, R., "Zur Mechanik des Luftreifens, " Zentrale fur Wissensvhaftliches Berichtwesen, Berlin-Adlershof, 1942.

68. Schlippe, B. von and Dietrich, R., "Das Flattern eines mit Luftreifen versehenen Rades," *Jahrbuch der Deutsche Luftfahrforschung*, 1943.

69. Gough, V. E., "Nondestructive Estimation of Resistance of Tire Construction to Tread Wear," Society of Automotive Engineers, SAE 667A, Warrendale, PA, 1963.

70. Gough, V. E., *Kautschuk and Gummi*, Vol. 20, p469, 1967.

71. Sakai, H., "Study on Cornering Properties of Tires and Vehicles," *Tire Science and Technology*, TSTCA, Vol. 18, No. 3, July – August 1990, pp. 136-169.

72. Sitchin, A., "Acquisition of Transient Tire Force and Moment Data for Dynamic Vehicle Handling Simulations," Society of Automotive Engineers, SAE 831790, Warrendale, PA, 1983.

73. DeBoor, C., "Bicubic Spline Interpolation," *J. Mathematics & Physics*, Vol. 41, 1962, pp. 212-218.

74. Radt, H. S., and Glemming, D. A., "Normalization of Tire Force and Moment Data," *Tire Science and Technology*, TSTCA, Vol. 21, No. 2, April – June 1993, pp. 91-119.

75. Bakker, E., Nyborg, L., and Pacejka, H.B., "Tyre Modeling for Use in Vehicle Dynamics Studies," Society of Automotive Engineers, SAE 870432,   Warrendale, PA, 1987.

76. Bakker, E., Pacejka, H. B., and Lidner, L., "A New Tire Model with an Application in Vehicle Dynamics Studies," Society of Automotive Engineers, SAE 890087, Warrendale, PA, 1989.

77. Schuring, D. J., Pelz, W., and Pottinger, M. G., "The BNPS Model – An Automated Implementation of the 'Magic Formula' Concept," Society of Automotive Engineers, SAE 931909, Warrendale, PA, 1993.

78. Schuring, D. J., Pelz, W., and Pottinger, M. G., "The Paper-Tire Concept: A Way to Optimize Tire Force and Moment Properties," Society of Automotive Engineers, SAE 970557, Warrendale, PA, 1997.

79. Bayle, P., Forissier, J. F., and Lafon, S., "A New Tyre Model for Vehicle Dynamics Simulations," *Automotive Technology International*, 1993, pp. 193-198.

80. Svendenius, J., and Gafvert, M., "A Brush-Model Based Semi-Empirical Tire-Model for Combined Slips," Society of Automotive Engineers, SAE 2004-01-1064, Warrendale, PA, 2004.

81. Bernard, J. E., and Clover, C. L., "Tire Modeling for Low-Speed and High-Speed Calculations," Society of Automotive Engineers, SAE 950311, Warrendale, PA, 1995.

10. Problems

1. Define the transformation matrices required to convert data from the SAE Tire Axis System to the ISO Wheel Axis System.

2. What is the sense of the aligning moment and lateral force associated with a positive inclination angle in the ISO Wheel Axis System?

3. Due to the width of the tire to be tested and clearance problems with respect to the load cell system, a special adapter was manufactured to move the test wheel plane off-center with respect to the design wheel plane location for the force and moment machine. The assembly wheel plane is now 5 cm outboard (Y′+) of the location that the machine's programming assumes to be the origin of the Tire Axis System. Derive the equations that properly express the data in the actual SAE Tire Axis System using the machine reported data as input. Be sure to assume that inclination angle is present. Review the definition of the origin of the Tire Axis System given in Section 8.1.1 before beginning this problem.

4. Transform the F_Y and M_Z data used to generate figures 8.17 and 8.19 from the SAE Tire Axis System to the ISO Wheel Axis System. These data are for a constant F_Z. The data are in the problem 4 data set.

Problem 4: Data set

SA (deg)	Fy (N)	Mz (Nm)
-10	5689	-25
-9	5602	-34
-8	5440	-40
-7	5306	-52
-6	5155	-67
-5	4917	-83
-4	4595	-97
-3	4124	-117
-2	3275	-116
-1	2006	-79
0	242	-10
1	-1588	64
2	-2966	105
3	-3893	115
4	-4397	103
5	-4744	88
6	-5000	74
7	-5101	57
8	-5248	49
9	-5357	44
10	-5455	35

5. Sketch revised versions of figures 8.31 - 8.34 showing the expected effect of a negative inclination angle.

6. Beginning with reference 29 as a guide, determine the plysteer, conicity, plysteer residual aligning moment, conicity residual aligning moment, and plysteer   residual   lateral force for the data in the problem 6 data set. For the sake of simplicity assume that linear models of $F_Y(\alpha)$ and $M_Z(\alpha)$ are adequate. F_Z is a constant.

Problem 6: Data set

Right rotation (operation as if on right side of car.)

SA	Fy	Mz
Deg	N	N-m
-1.00	1897	-74.7
-0.80	1601	-64.3
-0.60	1275	-52.5
-0.40	968	-40.8
-0.20	637	-27.6
0.00	268	-13.0
0.20	-83	1.1
0.40	-436	15.3
0.60	-784	29.2
0.80	-1121	42.4
1.00	-1425	54.5

Left rotation (operation as if on right side of car.)

SA	Fy	Mz
Deg	N	N-m
-1.00	1897	-73.9
-0.80	1522	-60.5
-0.60	1242	-50.3
-0.40	949	-39.4
-0.20	590	-25.6
0.00	238	-11.9
0.20	-109	1.9
0.40	-456	16.1
0.60	-792	29.9
0.80	-1132	43.9
1.00	-1408	55.0

7. Under appreciable torque a particular differential is known to not function until the difference in angular velocity between the left and right front tires reaches 0.265 percent of the angular velocity of the larger tire. As an engineer at a company that is considering using the differential design in question, you are asked to estimate the potential magnitude of the lateral movement for a new car design with a 1520 mm track width. You decide to characterize the problem in terms of how far the vehicle must travel forward in order to move 3.66 m laterally on a dead level road. Further, you decide the characterization will assume the smaller tire is on the right side of the front axle. Based on data in your company's files, the larger tire probably produces 470 revs/km, thus it is logical to consider the smaller tire in the worst case would produce 471.25 revs/km. How far forward does a worst-case equipped car roll under torque before it moves 3.66 m laterally?

8. Based on a qualitative examination of figures 8.47 through 8.51, what is your expectation of the change in effectiveness of anti-lock braking as a means of avoiding lateral instability due to braking as cornering severity, slip angle, increases?

9. Based on the problem 9 data set, estimate the relaxation length associated with figure 8.56. The data provided are with the uniformity removed. NOTE: If uniformity were present, the data would be appreciably more difficult to analyze. Uniformity is discussed in chapter 9.

Problem 9: Data set

Time sec	Distance rolled (m)	Fy N
0.00	0.000	-3
0.02	0.038	-2
0.04	0.076	2
0.06	0.114	1
0.08	0.152	-15
0.10	0.190	-44
0.12	0.228	-107
0.14	0.266	-196
0.16	0.304	-307
0.18	0.341	-433
0.20	0.379	-559
0.22	0.417	-677
0.24	0.455	-782
0.26	0.493	-874
0.28	0.531	-955
0.30	0.569	-1030
0.32	0.607	-1100
0.34	0.645	-1164
0.36	0.683	-1221
0.38	0.721	-1272
0.40	0.759	-1319
0.42	0.797	-1361
0.44	0.835	-1396
0.46	0.873	-1428
0.48	0.911	-1461
0.50	0.948	-1495
0.52	0.986	-1526
0.54	1.024	-1549
0.56	1.062	-1566
0.58	1.100	-1580
0.60	1.138	-1596
0.62	1.176	-1613
0.64	1.214	-1627
0.66	1.525	-1637
0.68	1.290	-1642
0.70	1.328	-1648
0.72	1.366	-1657
0.74	1.404	-1669
0.76	1.442	-1679

Problem 9: Data set (continued)

Time	Distance rolled	Fy
sec	(m)	N
0.78	1.480	-1687
0.80	1.518	-1692
0.82	1.556	-1698
0.84	1.593	-1703
0.86	1.631	-1709
0.88	1.669	-1711
0.90	1.707	-1714
0.92	1.745	-1716
0.94	1.783	-1719
0.96	1.821	-1724
0.98	1.859	-1727
1.00	1.897	-1730
1.02	1.935	-1732
1.04	1.973	-1737
1.06	2.011	-1741
1.08	2.049	-1743
1.10	2.087	-1745
1.12	2.125	-1747
1.14	2.163	-1749
1.16	2.200	-1741
1.18	2.238	-1741
1.20	2.276	-1742
1.22	2.314	-1745
1.24	2.352	-1747
1.26	2.390	-1748
1.28	2.428	-1750
1.30	2.466	-1753
1.32	2.504	-1753
1.34	2.542	-1750
1.36	2.580	-1747
1.38	2.618	-1744
1.40	2.656	-1741
1.42	2.694	-1737
1.44	2.732	-1733
1.46	2.770	-1730
1.48	2.808	-1725
1.50	2.845	-1721
1.52	2.883	-1717
1.54	2.921	-1718
1.56	2.959	-1721
1.58	2.997	-1723
1.60	3.035	-1722
1.62	3.073	-1719
1.64	3.111	-1716
1.66	3.149	-1713
1.68	3.187	-1710
1.70	3.225	-1708
1.72	3.263	-1704

10. If you were the driver of a car that was going to be operated over a large speed range, what are the handling implications inherent in concepts expressed within figure 8.65? Give special consideration to how the vehicle will behave in the vicinity of the peak lateral force.

11. A sample of tires stored in an air conditioned warehouse is split into two sub-samples. One sub-sample remains in the original warehouse; the other is shipped to a warehouse without air conditioning located in a southwestern state. On average the air-conditioned warehouse is maintained at 24°C for the next 150 days whereas the average temperature in the desert warehouse is 42°C. When the sample was split, the cornering stiffness coefficient was 0.175. After the 150 days of differential storage, what would you expect the two cornering stiffness coefficients to be?

12. Test drivers are given four sets of tires. They are told that the interest is in low acceleration, ordinary driving maneuvers so the tires are not to be "broken-in". The tires are really the same except for pretreatment. One set is not broken-in, the second has been broken-in at 2° slip angle, the third has been broken-in at 4° slip angle, and the fourth at 8° slip angle, but are marked as if they were different constructions. Given that low lateral acceleration behavior is proportional to cornering stiffness, how would you expect the drivers to rank the "constructions"? Also, given that the drivers would consider a 5 percent change as significant, which "constructions" would they consider to be significantly different?

13. Handling tests are performed on several different days over a period of weeks, but someone did not keep the control data so the raw results and the ambient temperature on the test days are all the data you have. The ambient temperatures are 13°C, 22°, and 29°. You have to decide how a control tire would probably have ranked on the three days in question. Assume that the cornering stiffness coefficient of the control is 0.175 at 22°C. Further, would the drivers have judged significant differences to exist between control tire results from the different days based on the 5 percent rule expressed in problem 12?

14. A vehicle is driven on a dry road, a snowy road, and an icy road. Assuming figure 8.72 represents the tires, what differences in perceived behavior will occur based on the changes in tire force and moment properties with surface?

Chapter 9
Tire Noise and Vibration

by K. D. Marshall

Chapter 9
Tire Noise and Vibration
by K. D. Marshall

Introduction

The tire is a complex dynamic system. When it vibrates it can generate noise and vibration signals observers may find objectionable. These problems are typically referred to as "ride disturbances," and over the years many tactile (feel) and acoustic (hearing) ride disturbances have been identified, figure 9.1 [1][1]. The definitions of these terms, and several others, are provided in the Glossary and closely follow the SAE Standards [2]. As figure 9.1 shows, both the road and the tire may be the source of ride disturbances, and these problems can occur over the frequency range of near zero to several thousand Hertz (cycles per second).

**Figure 9.1: Noise and vibration ride disturbances [1]**
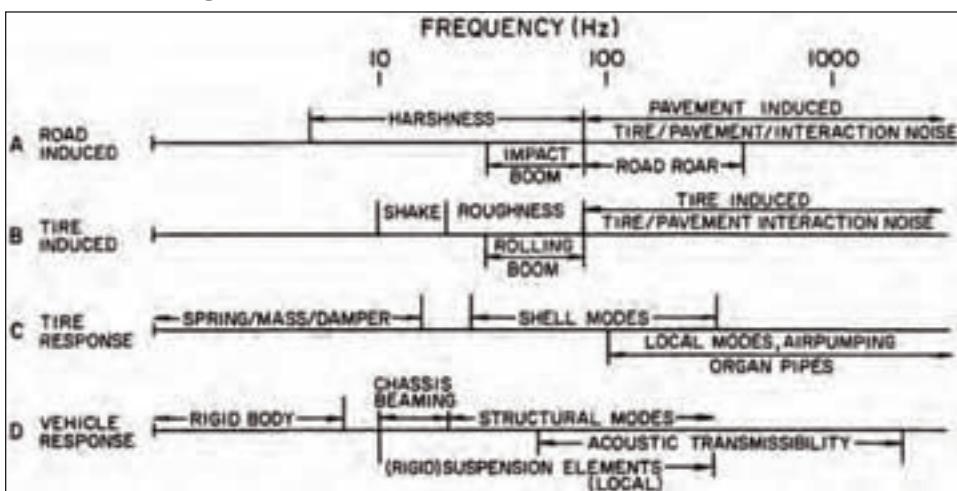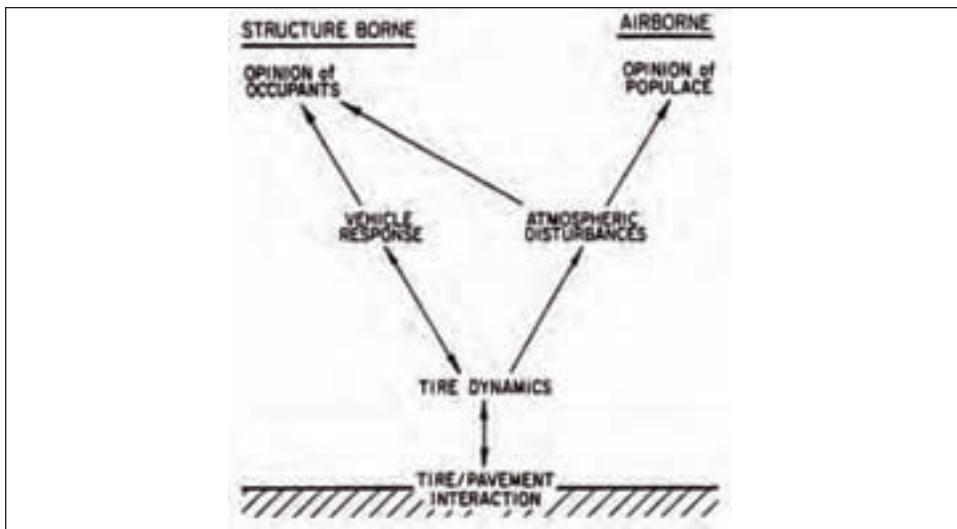
Figure 9.2 illustrates the relationship between the road, the tire, the vehicle and the observer. Ride disturbances can be excited by the road or from mechanisms internal to the tire. The ride disturbances can propagate either through the air (airborne noise) or through the structure of the tire and the vehicle (structural borne vibrations). Airborne noise can travel away from tire and arrive at the location of observers near a passing vehicle. This is often referred to as Passby Noise. Airborne noise can also enter the vehicle by passing though openings in the body or by acoustically coupling with the vehicle and re-radiated inside the vehicle by panel vibrations. The structure borne vibrations travel through the tire, the suspension and other components of the vehicle, and appear inside the vehicle as either tactile or acoustic signals. Finally, the tire and the vehicle can exhibit individual and joint characteristics that can amplify and/or attenuate the noise and vibration signals.

The emphasis of this chapter is on what the tire or vehicle engineer needs to know

---

[1]Numbers in [brackets] denote references at the end of the Chapter.

about tire noise and vibration. However, it is impossible to comprehend why certain aspects of tire performance are important without some consideration of how the tire and the vehicle interact, and how human beings respond to noise and vibration disturbances.

Figure 9.2: Airborne and structure borne transmission paths [1]

Throughout this chapter we will provide references to the topic being discussed. These references are not exhaustive, however. They are merely a roadmap to what can be found in the literature.

1. Tire vibrations

Like many dynamic systems, the behavior of a tire is dependent on the operating conditions. At low frequency a tire can be approximated by lumped parameters and a single, linear second-order system. At higher frequencies the tire behaves like a continuum of linear second-order systems, although some non-linearities can appear at times.

1.1 Low frequency behavior

At low frequency, which is often assumed to be less than 20 Hertz, a tire behaves like a spring-mass-damper. There is, however, an important distinction between a tire and a conventional second order system. A tire can rotate, and this introduces some important differences.

The spring rate of a tire is typically measured by performing a load-deflection test, often with the tire operating at low speed and a preload. Figure 9.3 shows the spring rate behavior for a stationary and rotating tire. There is a significant difference between the two test conditions. The rolling tire has a relatively constant spring rate whereas the   stationary tire spring rate changes considerably as the amplitude of the wheel hub motion increases. This type of behavior also extends to the damping properties of a tire. The percent critical damping of a tire can be determined from the log decrement of a freely bouncing tire[2]. Figure 9.4 illustrates how the percent critical damping of a tire changes with operating speed. Eventually the critical damping ratio typically stabilizes at a value of 1 to 2 percent.

---

[2]Several other techniques also exist, and they are discussed in any good vibration text.

**Figure 9.3: Spring rate for an oscillating tire [3]**
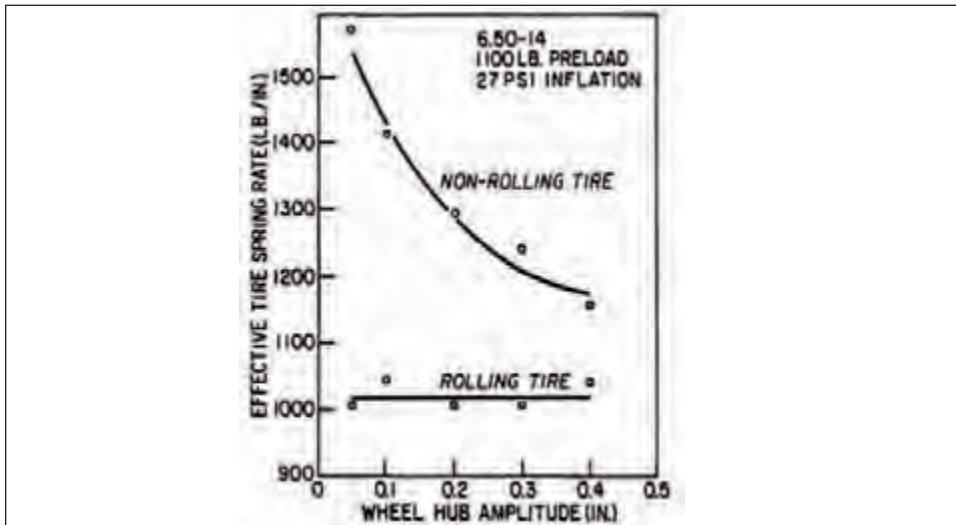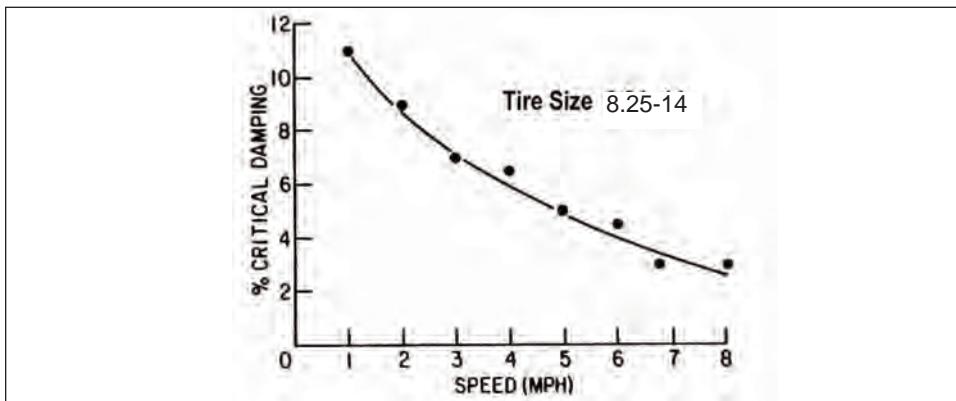
Figure 9.4: Percent critical damping vs. speed [4]

Most investigators believe these changes in spring rate and damping are the result of the tire footprint constraint being relaxed as the tire begins to rotate. The spring rate and damping of a tire are also generally piecewise linear about any given set of operating conditions.

Figure 9.5 illustrates the effect of various testing conditions and tire materials on the rolling spring rate of a radial tire. The spring rate demonstrates a slight increase with load and speed, a large increase with inflation pressure, and is unchanged for many carcass/belt combinations. Table 9.1 provides additional spring rate data in the vertical, lateral and longitudinal directions, and about the steering axis of the tire.

Figure 9.5: Effect of load, speed, belt material and inflation pressure changes on radial tire vertical spring rate behavior, V = 80.5 km/h [5]
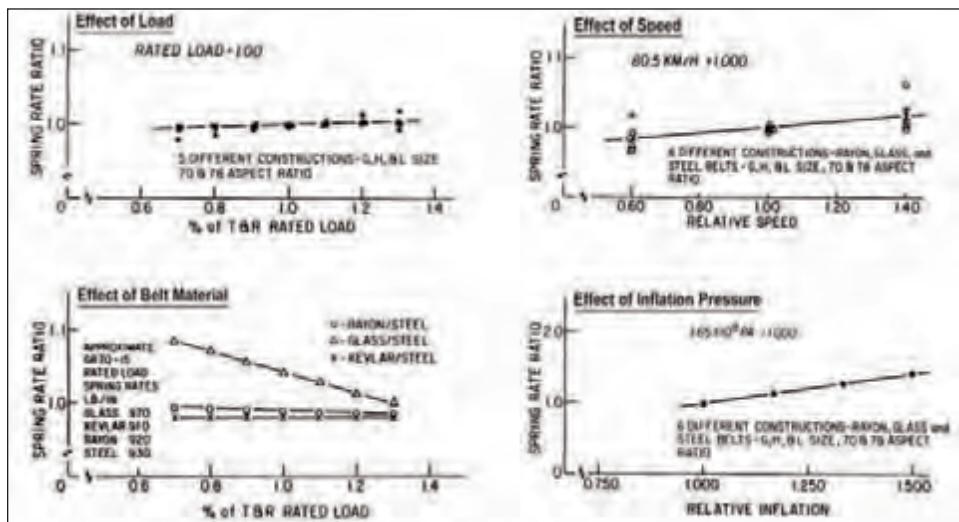

Table 9.1: Example tire spring rates

	P245/70R15 [6]		6.50-16 [7]	
Pressure (kPa)	179.3	220.6	320.0	320.0
Load (N)	3300	4000	5200	5200
Velocity (km/h)	0.0	0.0	0.0	10.0
Kx (kN/m)	163.2	188.1	312.0	220.0
Ky (kN/m)	127.1	147.4	-	-
Kz (kN/m)	193.1	232.0	245.0	210.0
Kmz (N-m/deg.)	61.8	67.8	-	-

1.2 Tire vibrations

Above approximately 20 Hertz, the quasi-steady state conditions discussed above no longer apply. Since a tire is essentially a pressurized shell, it will exhibit a continuum of vibrational modes over a wide range of frequencies. The vibrational modes will also be directionally sensitive. A free tire is axisymmetric in the plane perpendicular to the axis of rotation[3]. That is, the vertical direction (SAE z-axis, or "normal" or "radial" direction) and the longitudinal direction (SAE x-axis, or "circumferential" or "fore/aft" direction) will exhibit identical sets of vibrational modes, but the modes will be rotated with respect to each other by 90 degrees. The lateral direction (SAE y-axis) will possess a completely different set of vibrational modes.

There can also be torsional modes about each of the linear axes. The free rotational modes about the x and z axes will be identical and rotated by 90 degrees, and will differ

---
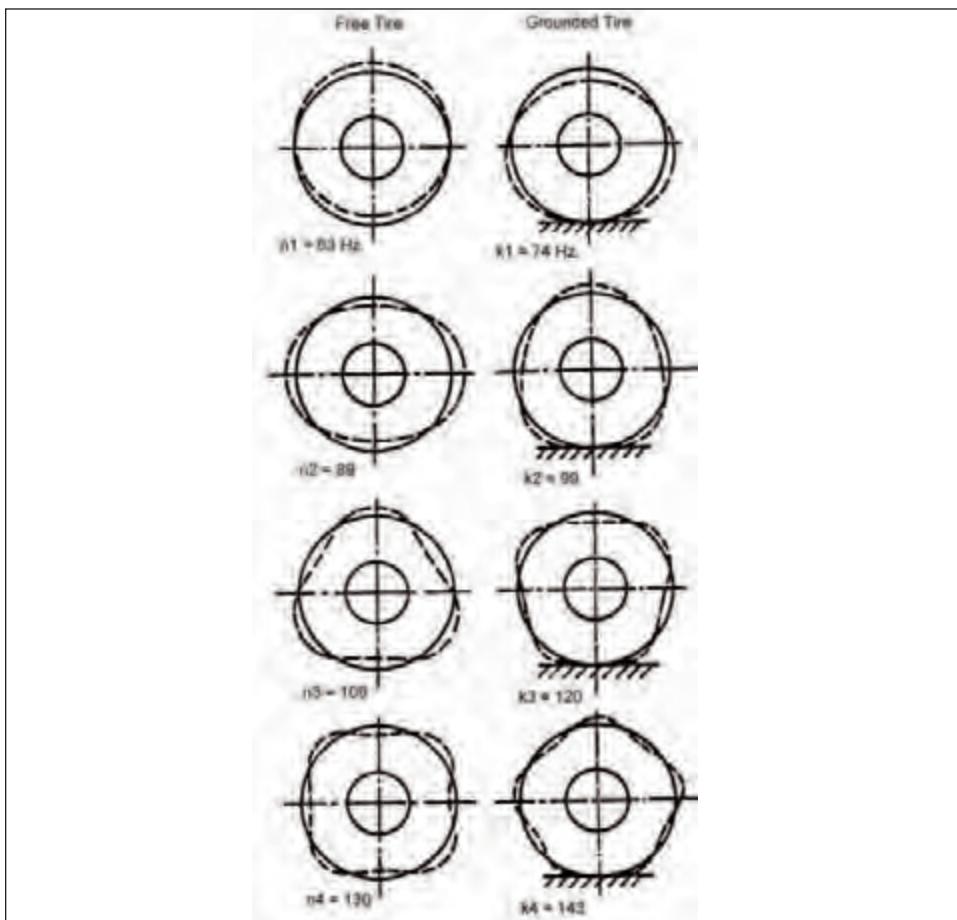
[3]The term "free tire" implies that the tire is suspended above the ground using rubber bands or by some other soft supporting method that does not affect the vibrational motion of the tire. The low frequency "bouncing" of the tire on the rubber bands is not considered a vibrational mode of the tire.

from the rotational modes about the y-axis.

The vibrational motion of the tire has been measured by a number of investigators. One set of data for a FR70-14 tire was provided by G. Potts, et al. figure 9.6. On the left side of the figure are the first four modes of vibration in the vertical direction. An equivalent set of vibrational modes would exist in the longitudinal direction. For this test the wheel was rigidly clamped and the tread was not in contact with the ground. The solid line is the undeflected shape of the tire and the dashed line is the deformed motion of the tire (greatly amplified here for the sake of clarity). The deformed motion is often called the "mode shape" of the tire.

On the right side of figure 9.6 are the comparable vertical modes when the tire was loaded against the ground.

Figure 9.6: Vibrational modes of a FR70-14 tire, pinned wheel [8]

The nomenclature identifies the mode shape number and the resonant frequency. For example, "n1=63 Hz" indicates that the first vertical mode of vibration has a frequency of 63 Hertz. As the mode number increases the deformed shape of the tire becomes increasingly complex, and the number of nodal points for any mode of vibration is equal to twice the mode number. That is, the 3rd mode of vibration has 6 nodal points. Although only
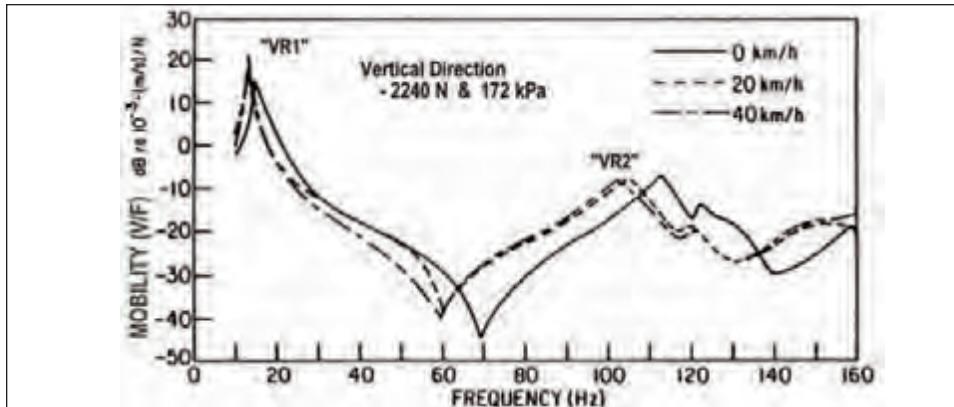
four modes of vibration are shown in figure 9.6, in reality there is no limit to the numbers of modes of vibration that can exist in any direction.

Investigators have also considered the vibrational behavior of a tire for a variety of different boundary and operating conditions, Table 9.2 [9]. In this experiment the wheel was free to move in all three axial directions, or in six directions if one considers the torsional modes. Earlier it was mentioned that the tire was axisymmetric in the plane of the tire, but this is not the case once the tire is in contact with the ground. The modal frequencies in the vertical and longitudinal directions are significantly different. Table 9.2 also shows that an increase in inflation pressure generally causes an increase in the resonant frequency, the tire load has a relative minor effect on the resonant frequencies, and an increase in speed from 0 to 8 km/h lowers the resonant frequencies. It should be mentioned, however, that the speed effect is limited to low speeds. Increasing the speed above 20 km/h has little effect on the resonant frequencies. This can be seen in figure 9.7.

**Table 9.2: Effect of operating conditions on
the resonant frequencies of a P205-70R14 tire. [9]**
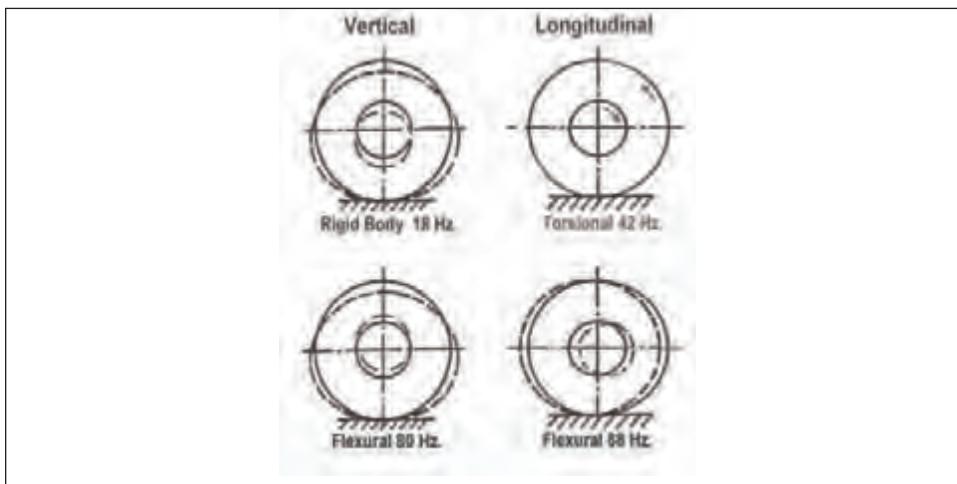
Mode	Control (0 kph, 4890 N) (207 kPa)	Inflation change (0 kph, 4890N) (240 kPa)		Rolling tire (8 kph, 4890 N) (207 kPa)		Load change (0 kph, 3900 N) (207 kPa)	
	Frequency Hz	Frequency Hz	Diff %	Frequency Hz	Diff %	Frequency Hz	Diff %
First fore/Aft	5.5	5.4	-2%	5.3	-4%	4.8	-13%
Second fore/Aft	46	48	+4%	42	-9%	46	0%
Third fore/Aft	90	91	+1%	88	-2%	94	+4%
First vertical	19	20	+5%	18	-5%	18	-5%
Second vertical	84	86	+2%	80	-5%	84	0%
First lateral	9.6	9.5	-1%	9.4	-2%	8.3	-14%
Second lateral	35	36	+3%	33	-6%	33	-6%
Third lateral	57	59	+4%	54	-5%	57	0%
Forth lateral	74	76	+3%	70	-5%	74	0%
First steer	20	19	-5%	19	-5%	18	-10%
Second steer	80	83	+4%	77	-4%	80	0%

Figure 9.7: Driving point mobility for a 165R13 tire [10]

Four of the lower order modes in the vertical and longitudinal directions deserve special mention, figure 9.8 [11] and Table 9.2. As will be seen later, these modes have a critical effect on the ride performance of the tire/vehicle system. The lowest mode in the vertical direction is essentially a rigid body motion of the tire/wheel assembly at 18 Hertz. In this case the tire and wheel move as a single unit and deflect the carcass of the tire in the vicinity of the tire footprint. The longitudinal mode at 42 Hertz is a torsional mode where the wheel rotates clockwise and the tread rotates counterclockwise (or vice versa).

Figure 9.8: Lower order vibrational modes, 8 km/h, table 2 [11]

The next higher vertical and longitudinal modes, 80 and 88 Hertz, respectively, are flexural modes where there is an out-of-phase motion between the tire and the wheel. For convenience these vertical and longitudinal modes will be designated as VR1, VR2, LR1 and LR2. Note that VR1 and VR2 are prominently visible in figure 9.7.

In relative terms, for ride performance the higher order vertical and longitudinal modes are usually less important (3rd mode and above). This is principally because the amount of rim motion becomes progressively smaller at the higher order modes. In fact, the even-order modes exhibit no wheel motion whatsoever for a free tire, whereas the odd-order modes demonstrate a small amount of wheel motion, and will thus have some effect on the ride performance of the tire.

There are a number of construction and operational factors that can influence the resonant frequencies of the tire. Some of the more important effects are shown in Table 9.3.

Table 9.3: Factors that can increase radial direction resonances in radial ply tires [12]

Factors	Effective change
Increase inflation pressure	0.5 to 1.5 hertz for 1 psi increase
Increase modulus of body ply cord	2.0 hertz increase for 10% increase
Increase ply end count	1.0 to 1.5 hertz increase for 10% increase
Increase ply compound modulus	0.7 to 1.2 hertz increase for 50% increase
Increase belt angle	0.1 to 0.4 hertz increase for 10% increase
Increase belt end count	0.8 to 1.8 hertz increase for 10% increase

2. Internally excited noise and vibration disturbances

This section will discuss four internal factors that can excite tire noise and vibrations; tire imbalance, tire uniformity, tread pattern design and tire cavity resonance.

2.1 Tire imbalance

The result of a non-symmetrical distribution of the mass in the tire, wheel or other rotating component of the suspension system is Tire Imbalance. Imbalance can be either "static" or "dynamic."

Static, or in-plane, imbalance is confined to the wheel plane of the tire. It generates a periodic force variation at the axle in the vertical and longitudinal directions. Common tire sources of static imbalance are large splices, multiple splices near the same circumferential location around the tire, or mass variations in other rotational components. A non-symmetrical axis of rotation can also cause a static imbalance. The magnitude of the imbalance force is given by the following equation.

$F=mr\omega^2$ (1)

where $F =$ the imbalance force,
              $m =$ the imbalance mass,
              $r =$ effective radius,
              $\omega =$ rotational speed (radians/second) $= 2\pi f$
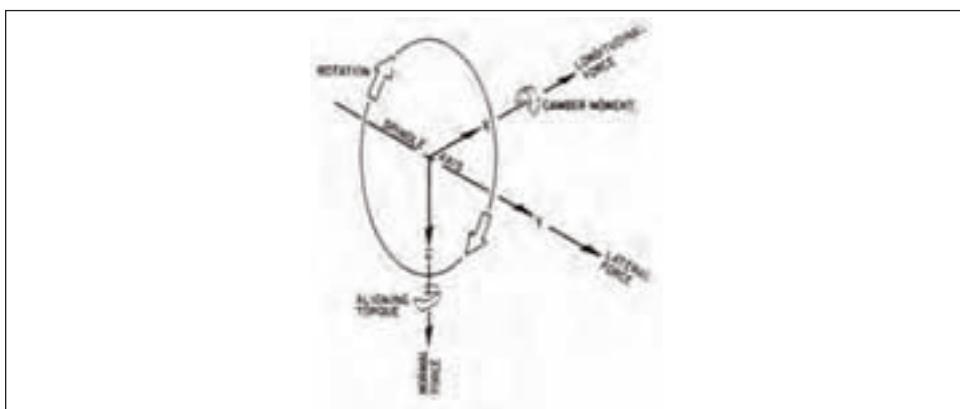
Dynamic, or out-of-plane, imbalance results from a non-symmetric mass distribution along the axis of rotation. This produces an overturning moment variation about the longitudinal axis and an aligning moment variation about the vertical axis. Dynamic imbalance can cause a vibration of the vehicle steering system, so it is particularly important for a tire mounted on the steered axle.

2.2 Tire non-uniformities

Tire nonuniformities refer to material or manufacturing anomalies that can generate varying forces and moments at the axle of the tire/wheel assembly, figure 9.9.[4] Tire nonuniformity forces and moments have traditionally been measured in one of two ways, low-speed factory machines or high-speed research machines.

Figure 9.9: Force and moments at tire/wheel spindle [1]

4Similar factors in the other rotating components can also be a problem, but will not be discussed here.

2.2.1 Factory type machine
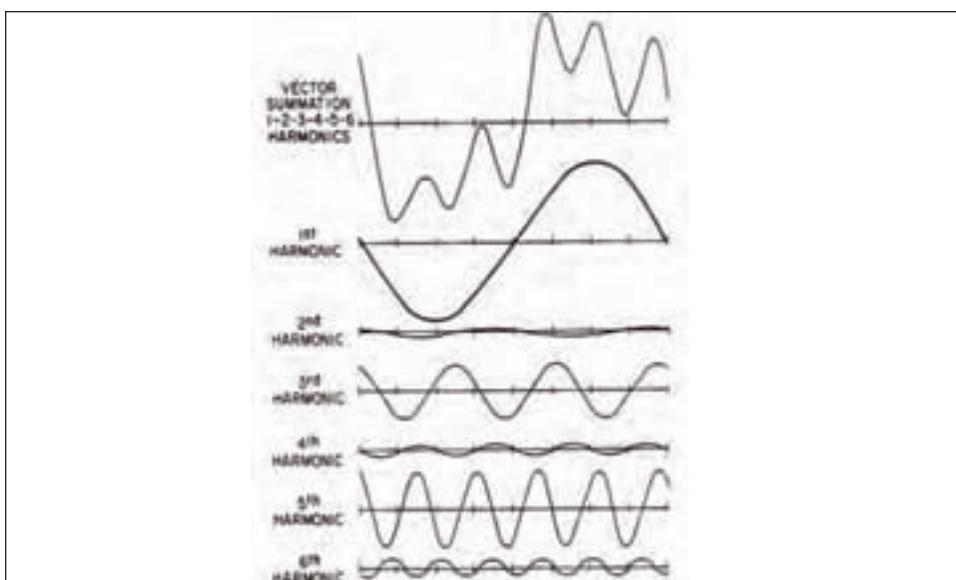
This machine consists of a wheel to mount and inflate the tire and a small steel drum (usually 33" diameter) against which the tire is loaded. The machine is operated at one (1) rps and the vertical and lateral force variations are measured at the axle of the drum. Since the operating speed of the machine is very low the resonances of the tire are not excited and the measured data are the force variations that occur at the contact patch of the tire. This type of machine may also have a grinding stone to correct the tire force variations (discussed later in this section).

2.2.2 High speed uniformity machine

This type of machine can operate at realistic road speeds, and the experimental measurements made at the tire/wheel axle include the effect of tire resonances. Usually the three force variations are measured, but some machines also record one or more of the moment variations. Since the dynamic behavior of the tire is being measured, these machines must be carefully designed to insure that machine resonances do not contaminate the measured data. Because of the complexity and high cost of this type of machine they are normally found in the research laboratories rather than in the manufacturing plants, but some exceptions do exist.

   The force and moment variations will repeat for each rotation of the tire, and are thus periodic with respect to the physical location on the tire. Figure 9.10 illustrates what the radial force variation might look like at low speed. The top curve is the composite or overall radial force variation signal. By performing a Fourier analysis it is possible to decompose the composite signal and reveal the individual harmonics, or the orders of vibration. The first six harmonics are illustrated in figure 9.10. The harmonics usually receive greater attention than the composite force variation. This is because it is usually easier to correlate an internal tire anomaly with one or more of the harmonics rather than with the composite waveform, and thereby correct the problem.

**Figure 9.10: Radial force variations for one tire revolution [1]**

If the rotational rate of the tire is known, it is possible to determine the frequency of any harmonic order at any test speed by using the following formula.

$$f = N \ x \ RPS \qquad (2)$$
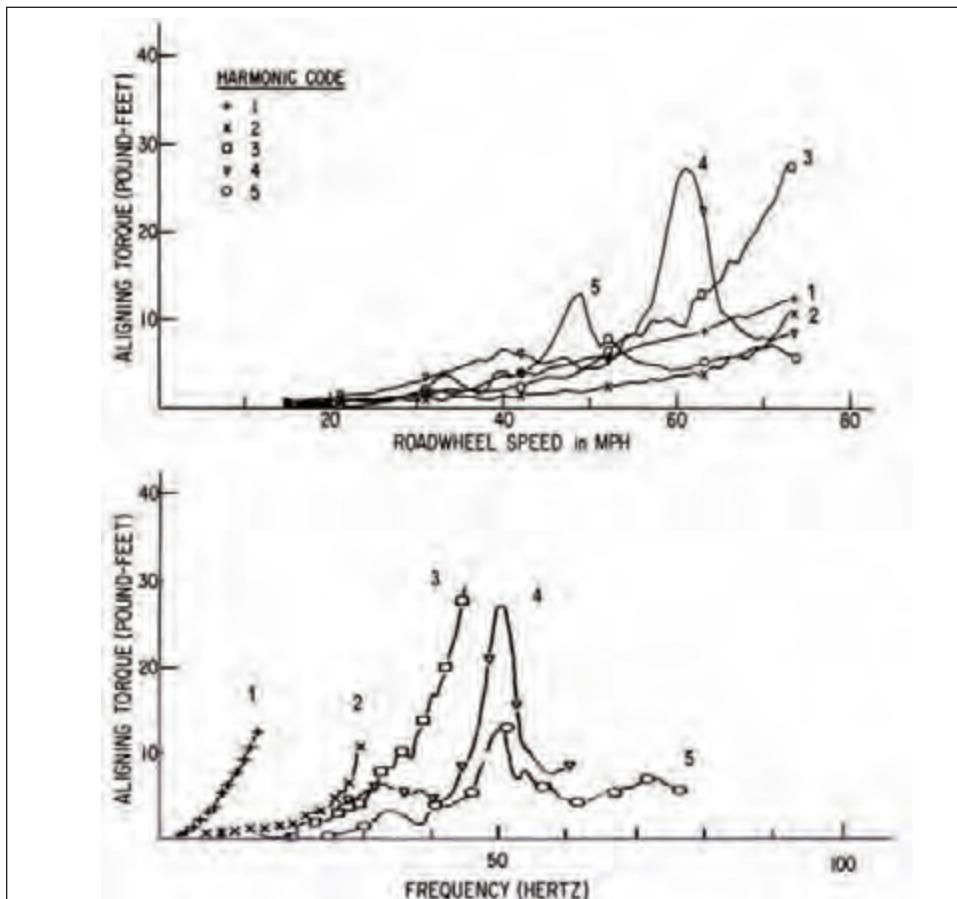
where f = frequency (Hertz)
          N = harmonic order
          RPS = revolutions per second of the tire

Since the rotational speed of a passenger tire is approximately 1 revolution for every 5 mph of test speed, at 50 mph the frequency of 1st harmonic of radial force variation (RH1) will be approximately 10 Hertz, the 2nd harmonic, 20 Hertz, etc. As the speed of the tire increases, the frequencies of the harmonic orders will also increase. At some point the frequency of a harmonic will coincide with and excite a resonant frequency of the tire, and the level of the force variation will increase dramatically. Figure 9.11 illustrates how an aligning moment resonance of a HR70-15 tire can be excited by a number of different harmonics. Note that each harmonic order increases in amplitude until it excites the tire resonance at a certain speed. At the resonance speed the force variation will exhibit a peak value, after which the force variation value will decrease as speed further increases.

**Figure 9.11: Aligning moment resonance, HR70-14 tire [13]**
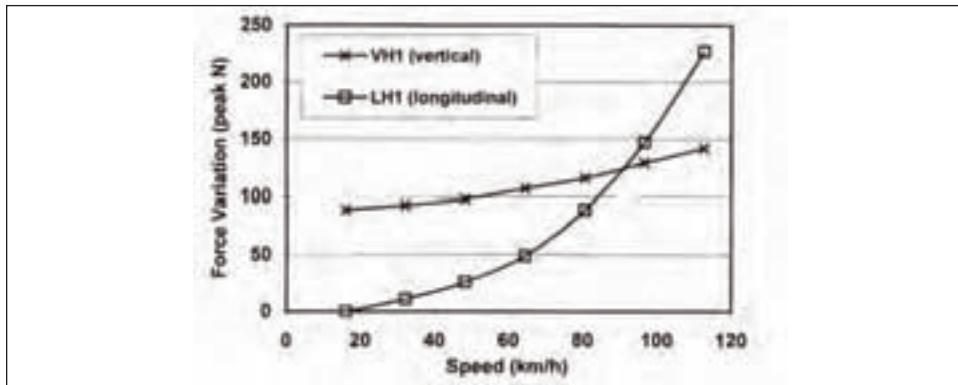
Any force and moment variation can potentially cause a ride disturbance, but experience has shown the radial (vertical) and longitudinal (fore/aft, or drag) directions are the most important contributors [13]. In addition, the aligning moment resonance shown in figure 9.11 can cause a torsional vibrational disturbance of the steering system of the vehicle.

Figure 9.12 shows the normal trend for the 1st harmonics of radial and longitudinal force variation as a function of speed. Typically RH1 will show a gradual increase with test speed, whereas LH1 is very small at low speed and increases dramatically as the speed increases. The behavior of LH1 was explained by Walker [14]. Equation 3 shows that the longitudinal force variation is proportional to the radial runout of the tire and the square of the velocity.

$$F \propto v^2 \Delta R [\mathrm{K}] \qquad (3)$$

where ΔR = radial runout
              v = velocity
              K = constant

Figure 9.12: Representative radial and longitudinal non-uniformity force variations

There are a number of potential causes of tire nonuniformities, many of which have been reported in the literature. There is also a general tendency for certain material or construction anomalies to preferentially affect either the radial or longitudinal force variation. Anomalies that affect mass variation around the tire are very important to radial force variation, and anomalies that affect stiffness or runout variation are more important to longitudinal force variation. Table 9.4 provides a comparison of a number of potential sources of force variation.
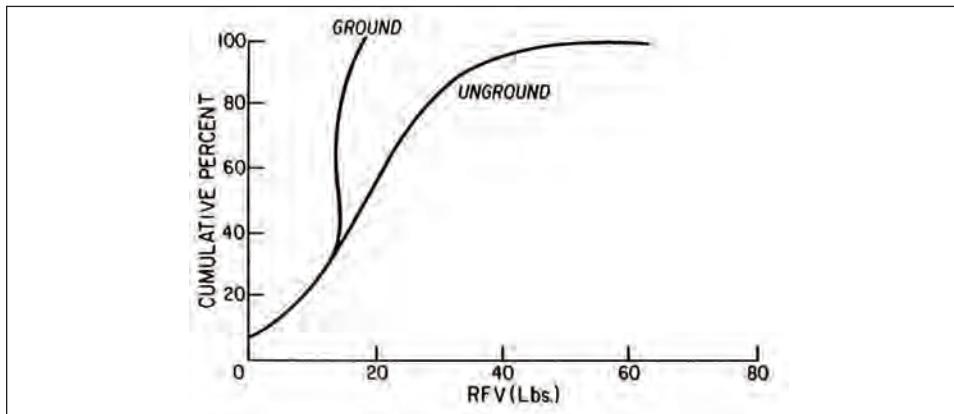
Table 9.4: Sources of tire nonuniformity force variation

| Source type	Radial FV	Longitudinal FV
Heavy or light splices	**	*
Spread or bunched cords	**	*
Tread thickness variation	**	*
Non-symmetric bead setting	*	**
Building drum irregularities	*	**
Mold irregularities	*	**
Carcass run-out	*	**
* = some effect ** = significant effect		
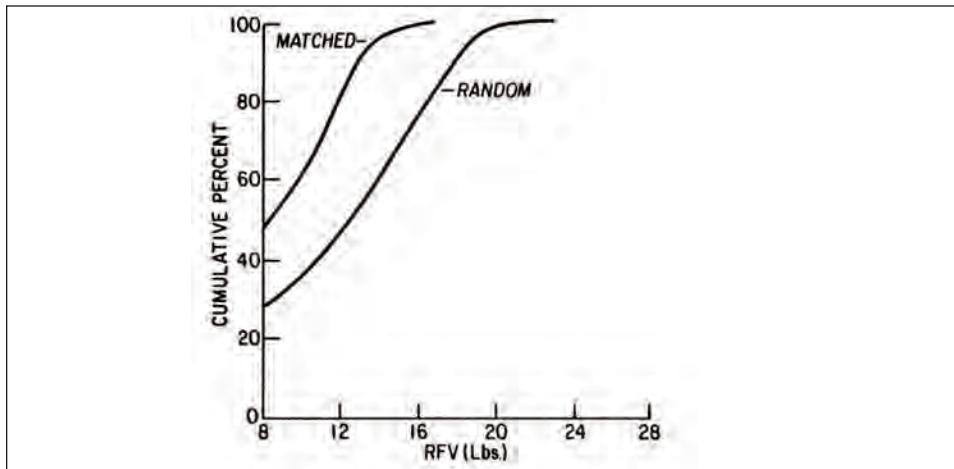
For many years tires have been "ground" on the factory uniformity machines to reduce radial force variations [15]. This process is generally most effective for the 1st harmonic of radial force, which is critical to improving a ride problem that will be discussed later. Grinding is accomplished by removing a small amount of rubber from the shoulder of the tire, or across the entire tread surface, at the high point of the RH1 term. Figure 9.13 shows that grinding can have a beneficial effect on the radial force variation of the tire. In recent years, however, grinding has lost favor and become less acceptable to automotive manufacturers and tire consumers.

Figure 9.13: Effect of tread grinding on radial first harmonic force variation [15]

Match mounting is another technique that has been used to minimize RH1. Match mounting is usually applied at the end of the vehicle assembly line where the tires and the wheels come together, figure 9.14 [16]. In this process the tire and wheel are positioned such that the high point of RH1 for the tire is aligned with the low point of the 1st harmonic of the bead-seat runout of the wheel. This process minimizes the overall 1st harmonic of radial force variation for the tire/wheel assembly.

Figure 9.14: Effect of match mounting on radial first harmonic force variation [16]

2.3 Tire noise and tread design

Sound is the result of pressure variations traveling through the air. If the pressure variations are detected by the human ear they may result in audible sound. For a pressure wave to be audible, the frequency and amplitude of the pressure variations must meet certain requirements. The frequency of the pressure variations must be between 20 and 20,000 Hertz, and the amplitude of the pressure wave must be sufficiently large to be detected. The measurement unit for Sound Pressure Level (SPL) is the decibel (dB). The decibel is defined as,

SPL (dB) = 20 log (A/A$_{ref}$)   (4)

where A = the amplitude of the measured pressure variation,

A$_{ref}$ = the reference sound pressure = 0.00002 (Newton / meter^2).

If the amplitude of a pressure variation doubles, the SPL will increase by 6 dB. If the pressure amplitude increases by a factor of 10, the SPL will increase by 20 dB. It is important to remember that SPL is a logarithmic quantity and SPL values cannot be directly added. For example, suppose SPL1 = 92 dB and SPL2 = 94 dB. If SPL was a linear quantity the total SPL would be 186 dB. But since SPL is logarithmic the total SPL is found from the following equation.

$$SPL_{Total} = 10 \text{ x log} \sum_{i=1}^{n} \left[10^{SPL1/10} + 10^{SPL2/10} + \bullet\bullet\bullet + 10^{SPLn/10} \right] \qquad (5)$$

$$SPL_{Total} = 10 \text{ x log} \left[10^{(92/10)} + 10^{(94/10)} \right] = 96.12 \; dB$$

There are a number of potential sources of tire noise. Several of these sources are discussed below [1, 17, 18, 19].

2.3.1 Aerodynamic noise

Aerodynamic noise is caused by air turbulence due to the translation and rotation of the tire as it travels down the highway. Studies have shown that at low speed this is a secondary noise source, but at speeds above 100 km/h aerodynamics can contribute significant noise signals.

2.3.2 Air pumping

When the tread of a tire rolls into contact the void areas in the tread pattern compress and air is forced out of the voids. When the tread elements leave contact the voids expand and air rushes back in. This repetitive compression and expansion of the tread voids is known as "air pumping" and it can cause significant tire noise. If the tread blocks vibrate, as they do at the exit from contact, the pressure wave will oscillate and approximate a decaying exponential sinusoid.

2.3.3 Cavity resonances

It is possible for "standing waves" to develop inside the tire air cavity. This can be an important source of tire noise and is discussed in section 2.4.

2.3.4 Organ pipes

Grooves in the tread that are substantially straight can act as organ pipes and generate narrow frequency peaks that are independent of operating speed. For a tire traveling on a smooth road, longitudinal grooves can increase the noise level by about 3 dB.

2.3.5 Stick/slip noise

Stick/Slip noise can occur in the footprint of the tire when contact stresses cause the tread elements to slide in the lateral and longitudinal directions. Normally this occurs near the exit from contact, where it also affects the tread block vibrations. Adhesive noise occurs above approximately 2000 Hertz and is normally a secondary noise source. However, stick/slip noise can become very noticeable if a tire is subjected to significant driving or braking torque or cornering forces.

2.3.6 Tread block impacts and vibrations

At the entrance to contact the tread blocks impact against the road surface, and at the exit from contact the tread blocks release from the road surface and vibrate (stick/snap). Both of these actions can provide significant forces to the tire that can excite tread and carcass resonances and generate tire noise.

    Tire noise generation mechanisms have been extensively studied for many years, and the issue of whether tread/carcass vibrations or air pumping is the most important cause of tire noise has been widely debated. It is unlikely this debate will end any time soon, but there is general agreement about certain factors.

1. Tread/sidewall vibrations are the dominant source of tire noise at frequencies below about 1000 Hertz, and belt/carcass resonances are believed to cause a wide noise peak between 700 and 1000 Hertz.
2. Air pumping is the dominant noise mechanism above 2,000 Hertz.
3. Between 1000 and 2000 Hertz, tire resonances and air pumping are both important noise sources.
4. The tread design of the tire plays an important role as an excitation source of tire noise.
5. The leading and trailing edges of contact are the most important noise source locations, with the sidewall being about 10 dB less important.
6. Test speed has a major influence on tire noise. Passenger car tire noise increases at a rate of approximately 40 log V, and truck tire noise increases at a rate between 30 log V and 40 log V.
7. Truck tires are typically 3-5 dB noisier than passenger tires, principally due to the larger loads they carry.
8. Among a class of tire, such as passenger tires, tire to tire differences are generally in the range of 4-6 dB.

The degree of acceptability of the sound presented to the passengers in a vehicle, or near a passing vehicle, is the result of both the amplitude and the spectral content of the noise signal. The best tread patterns are those which minimize the overall amplitude of the noise, spread the noise energy over as wide a frequency range as possible, and avoid narrow frequency peaks that will cause the tire to be viewed as tonal. One of the fundamental ways to control tire noise is by the design of the tread. There are a number of factors involved in tread pitch design of a tire.

a. The total number of pitches around a tire
b. The size of the pitch lengths
c. The pitch ratio (the relative size of the different pitch lengths)
d. The sequence of pitches around the tire
e. The number of pitches of each size
f. The circumference of the tire

Figure 9.15(a) shows a conceptual half-tire representation of a pitch length (or pitch
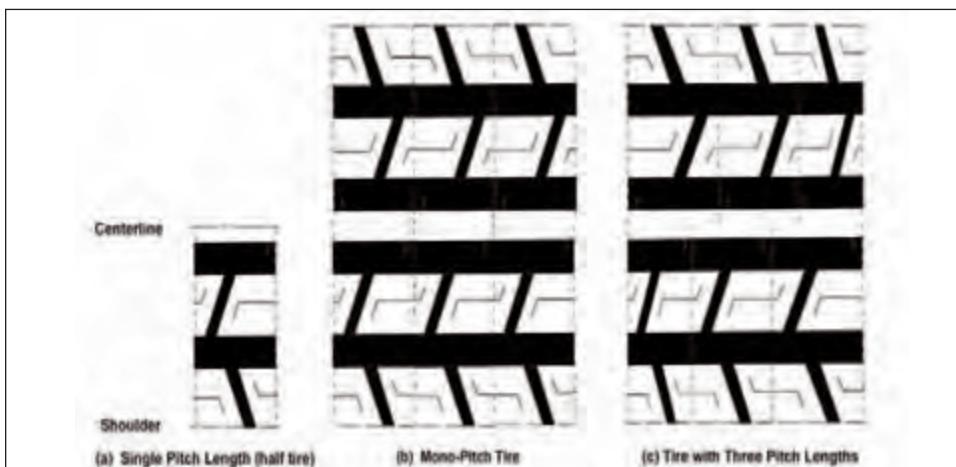
segment) where the black areas designate the grooves in the tread. The pitch length is the fundamental design unit of the tread pattern. If the same pitch length was repeated around the circumference of the tire the result would be a Mono-Pitch design, figure 9.15(b). Mono-pitch treads are still found in off-the-road, farm service and a few other types of tires, but they are never used in highway passenger tires. The reason is the frequency spectrum of a mono-pitch design is principally confined to the rotational order of the tire and its harmonics. That is, if the tire has 56 equal pitch lengths around the circumference, the frequency spectra would exhibit a 56th order and probably the 112th, the 168nd, etc. Tread designs that exhibit this type of "peaky" spectrum will result in a tonal sound that is very disturbing to the observer.

To avoid tonality, tires are normally designed using a number of different pitch lengths around the circumference, often three or more, and a carefully designed pitch sequence. figure 9.15(c) illustrates a situation where the fundamental pitch length has been modified to accommodate three pitch lengths of different sizes. In this case the scaled sizes of the pitch lengths are 0.80, 1.00 and 1.20 units. Since the largest pitch length is 50% greater than the smallest pitch length, the pitch ratio of the tire would be 1.50. Note also that the pitch sequence is different on the left and right sides of the tire. Although there are aesthetic and practical limits on what is possible in a real tire, techniques that have proven useful in spreading out the noise energy over a wide frequency band are listed below.

a. Use as many different pitch lengths as possible
b. Use as large a pitch ratio as possible, but avoid ratios of integers such as 3/2, 4/3, etc.
c. Use as many pitches as possible around the tire
d. Use a randomized pitch sequence around the tire
e. Use a different pitch sequence on the left and right side of the tire

The first detailed analysis of pitch sequence theory was provided by Varterasian [20]. In this classic study he discussed the importance of utilizing "mechanical frequency modulation" to eliminate tonal situations. This technique is analogous to electrical frequency modulation where a modulating signal is used to transfer energy from a dominant frequency peak into its sidebands, thereby making the peak amplitude and its sidebands nearly equivalent and smoothing out the spectra. It should be noted that this technique flattens the spectrum but the total energy contained in the spectrum is normally not reduced.

Figure 9.15: Tread design pitch length examples

(a) Single Pitch Length (half tire)   (b) Mono-Pitch Tire   (c) Tire with Three Pitch Lengths

Over the years a number of U. S. Patents have been issued to tire companies that cover a variety of pitch sequence design methods. Most of the approaches use some variation of an up-down methodology where the pitch sequence sinusoidally increases and then decreases one or more times around the tire. There are, however, a couple of exceptions. Williams [21] revealed a technique where three pitch lengths are used, but in a significant percentage of the time the smallest pitch length is immediately followed by the largest pitch length, or vice versa. This produces a much less sinusoidal translation between the pitch lengths. In a related vein, Bandel [22] patented a technique that utilizes numerical methods to generate random sequences of at most three pitch lengths, and preferably only two pitch lengths.

Figure 9.16 illustrates that a properly designed tread design can markedly improve the noise performance of a tire [22]. The curve labeled "poor randomization" is a very tonal tire with large frequency peaks. The "optimized randomization" tire has spread out the noise energy and greatly lowered the distinct frequency peaks.

Pitch sequencing is not the only technique that is useful in improving tire noise. Shown in Table 9.5 are a number of "design rules" that have proven useful. However, it is important to remember that, depending on the design of the tire and the intended market, some of these suggestions may not be feasible because they may negatively affect other desirable tire properties such as wet traction, handling, power loss, etc.

Figure 9.16: Effect of randomizing pitch sequence [19, revised Fig 10.29]
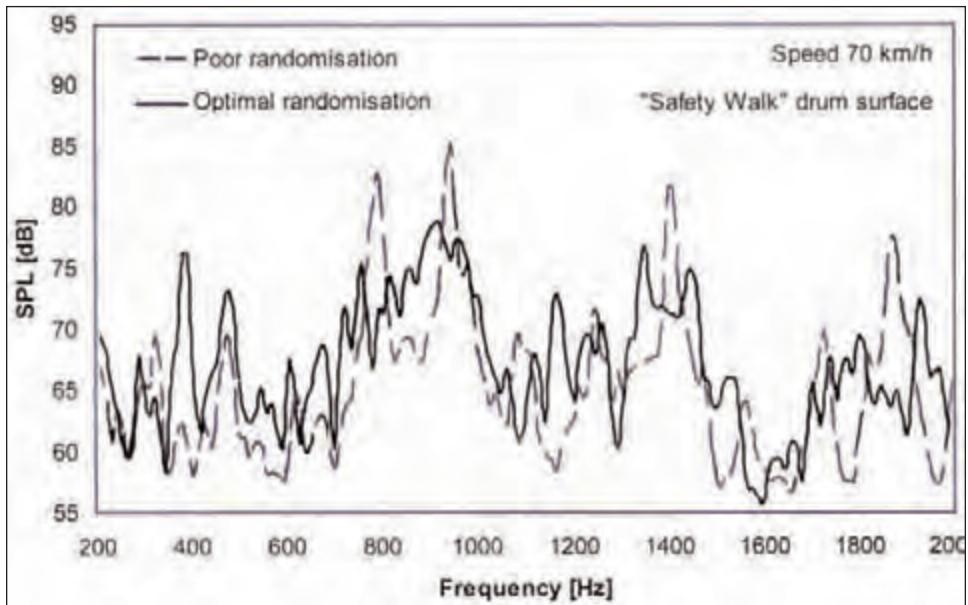
Table 9.5: Methods of reducing tire noise and smoothing the spectral content*

Technique	Reasoning
1. Use narrower, less deep grooves.	Smaller transverse grooves produce less vibration and pump less air.
2. Smaller blocks are generally preferrable to large blocks.	Reduces tread impact excitation.
3. Angle the lateral grooves in the circumferential direction.	Provides a smoother load transition from one element to the next, and lower vibrational impacts at the entrance to contact and a more gradual air release at the exit from contact.
4. Grooves should be well ventilated.	Avoids enclosed pockets of air, and minimizes the number of partially closed grooves that might resonate.
5. Randomize/Optimize the Tread Design and Pitch Sequence. Stagger the lateral grooves so multiple grooves do not intersect the leading or trailing edge of contact at the same time, and the shape of the grooves should not match the shape of the leading and trailing edges of contact.	Insures that large excitations do not occur at discrete places around the tire, and maintains a fairly constant amount of void area intercepted by the edges of contact around the tire.
The pitch sequence on the left side of the tire should be different than that on the right side of tire. This is often called "phasing" or "offset."	Further randomizes the pitch sequence.
Use a high Pitch Ratio, but avoid integer ratios such as 3/2. 4/3, etc.	Generally aids in spreading the noise energy, but integer ratios can cause harmonic orders that are independent of pitch sequencing.
Use as many different pitch lengths as possible.	Helps smoothes out the energy spectrum.
A larger number of pitches is generally better than a smaller number of pitches.	Reduces the block size and the resulting tread impacts.
The Fourier analysis of the pitch sequence should avoid a 1st harmonic and should contain 2nd, 3rd and 4th harmonics with approximately the same amplitude.	Generally helps smooth the frequency spectrum.
6. Reducing the modulus of the tread or sidewall generally reduces the noise level.	Soften impacts of tread elements with the road.
7. Decreasing the load on the tire or increasing the inflation pressure often reduces the noise level.	It is usually beneficial to have a smaller amount of the tread in contact with the road, and hence fewer active noise sources.

* It is important to remember that many of these suggestions can affect other tire properties, such as wet traction, handling, power loss, etc.

2.4 Tire cavity resonances

The internal air cavity of the tire is capable of supporting the development of standing waves. These standing waves will occur at a number of harmonically related frequencies, starting in the range of 200 to 250 Hertz for passenger tires. The standing waves can interact with the wheel and transmit vibrational energy through the suspension and be re-radiated as acoustic disturbances in the passenger compartment. This problem has received considerable study by tire and vehicle engineers, and it is an important consideration when optimizing the ride performance of a tire/vehicle system [23, 24]. The fundamental frequency of the cavity resonance for an axisymmetric (unloaded) tire can be found from the following equation.

$c = \lambda f$ (6)

where,
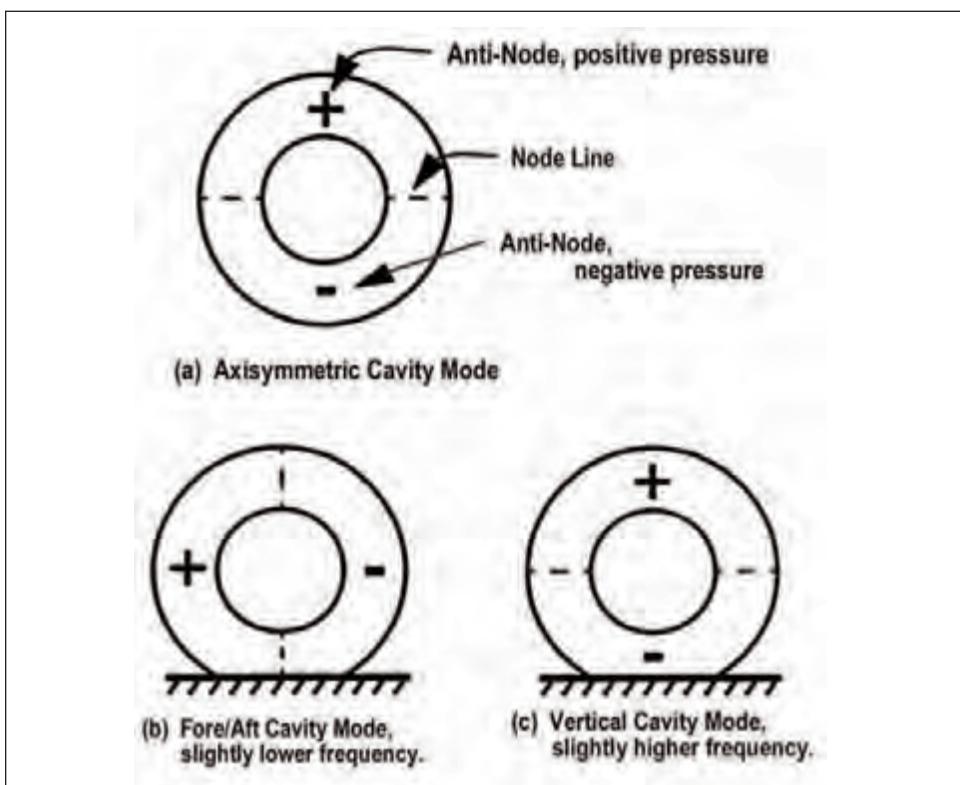
c = speed of sound (343 m/sec for dry air at 20° C)

λ = *w*ave length (meters, at mid point of the tire cavity cross-section)

f = frequency (hertz)

Figure 9.17(a) shows that the fundamental cavity mode for an axisymmetrical (free) tire exhibits a single acoustic wavelength around the tire. There is one maximum and one minimum pressure point on opposite sides of the tire. Nodal points are located midway between the high and low pressure points. When the tire is loaded, the footprint introduces a perturbation and the axisymmetric mode splits into two modes. The longitudinal mode occurs at a slightly lower frequency than the vertical mode, figure 9.17(b).

Figure 9.17: Tire cavity resonances [23]

(a) Axisymmetric Cavity Mode

(b) Fore/Aft Cavity Mode, slightly lower frequency.

(c) Vertical Cavity Mode, slightly higher frequency.

Sakata [24] reported that the tire can exhibit higher order modes that are harmonically related to the fundamental modes, but only the first vertical and longitudinal modes will interact with the wheel and transfer energy to the vehicle. Investigators have also found that these cavity modes are fairly independent of inflation pressure, tire load and tire aspect ratio.

Scavuzzo, et al. [23] reported that the cavity modes can also couple with a bending mode of the wheel. The bending of the wheel disk (see figure 9.18) will result in the wheel rotating about the longitudinal axis and this, in turn, will produce a vertical force on the vehicle spindle. This structural/acoustic coupling will augment the energy transfer to the vehicle by the tire cavity modes and produce a higher noise level in the vehicle. Figure 9.19 illustrates the sound pressure level inside a vehicle. In the upper graph, the 78 dB SPL peak in the vicinity of 230 Hertz is the result of the interaction of the tire cavity and the wheel resonance. The middle chart shows that if the tire is filled with helium the large SPL peak is reduced to 54 dB, or a change of about 24 dB. This is because the speed of sound is much higher in helium than it is in air and the tire cavity modes are shifted upwards and away from wheel resonance. The bottom chart shows that if an aluminum wheel is used in place of the steel wheel, the SPL peak is reduced to about 66 dB. This occurs because the aluminum wheel resonance is significantly higher than the steel wheel, and the structural/acoustic coupling of the cavity/wheel resonances is virtually eliminated.

**Figure 9.18: Structural wheel resonance,
which couples with the acoustic cavity modes [23]**
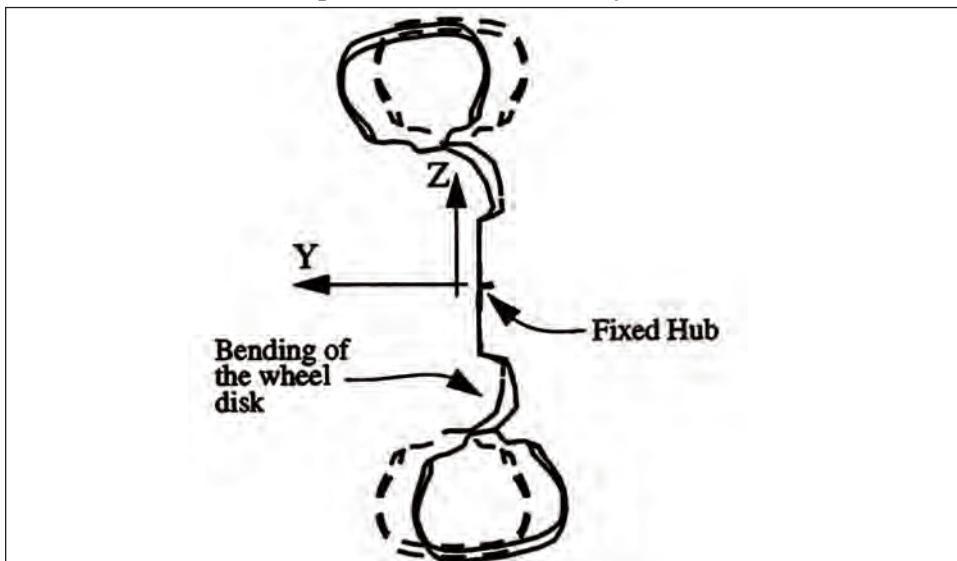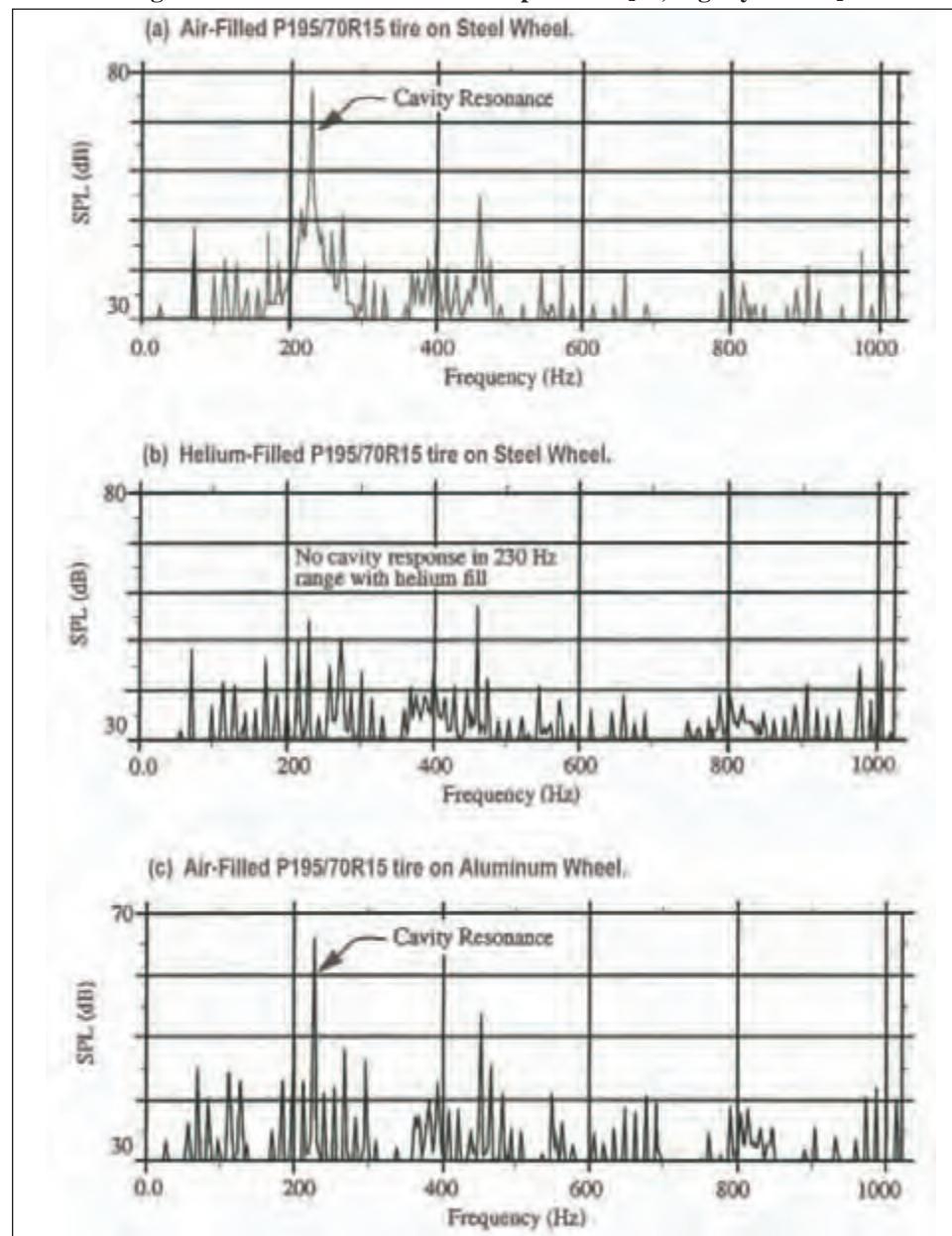
Figure 9.19: Vehicle interior noise spectrum [23, slightly altered]

(a) Air-Filled P195/70R15 tire on Steel Wheel.

Cavity Resonance

(b) Helium-Filled P195/70R15 tire on Steel Wheel.

No cavity response in 230 Hz range with helium fill

(c) Air-Filled P195/70R15 tire on Aluminum Wheel.

Cavity Resonance

3. Externally excited noise and vibration disturbances

There are several types of road inputs that can excite the tire and cause noise and vibration disturbances in a vehicle. These inputs are discussed in this section.

3.1 Pavement characteristics

Highway characteristics are essentially random inputs that range from potholes and tar

strips to the fine surface texture of the pavement. The pavement's characteristics of interest are changes in the elevation of the pavement as the vehicle traverses the road. The elevation changes are normally classified according to wavelength.

    a. Undulations   – wavelength greater than 50 cm
    b. Road Roughness   – wavelengths between 10 cm and 50cm
    c. Macrotexture   – wavelength between 0.5 mm and 10 cm
    d. Microtexture   – wavelengths less than 0.5 mm

    The temporal frequency of the vibrations created by a vehicle traveling along the road is given by the following equation.

    $f_t = V/\lambda = Vk$

$$\tag{7}$$
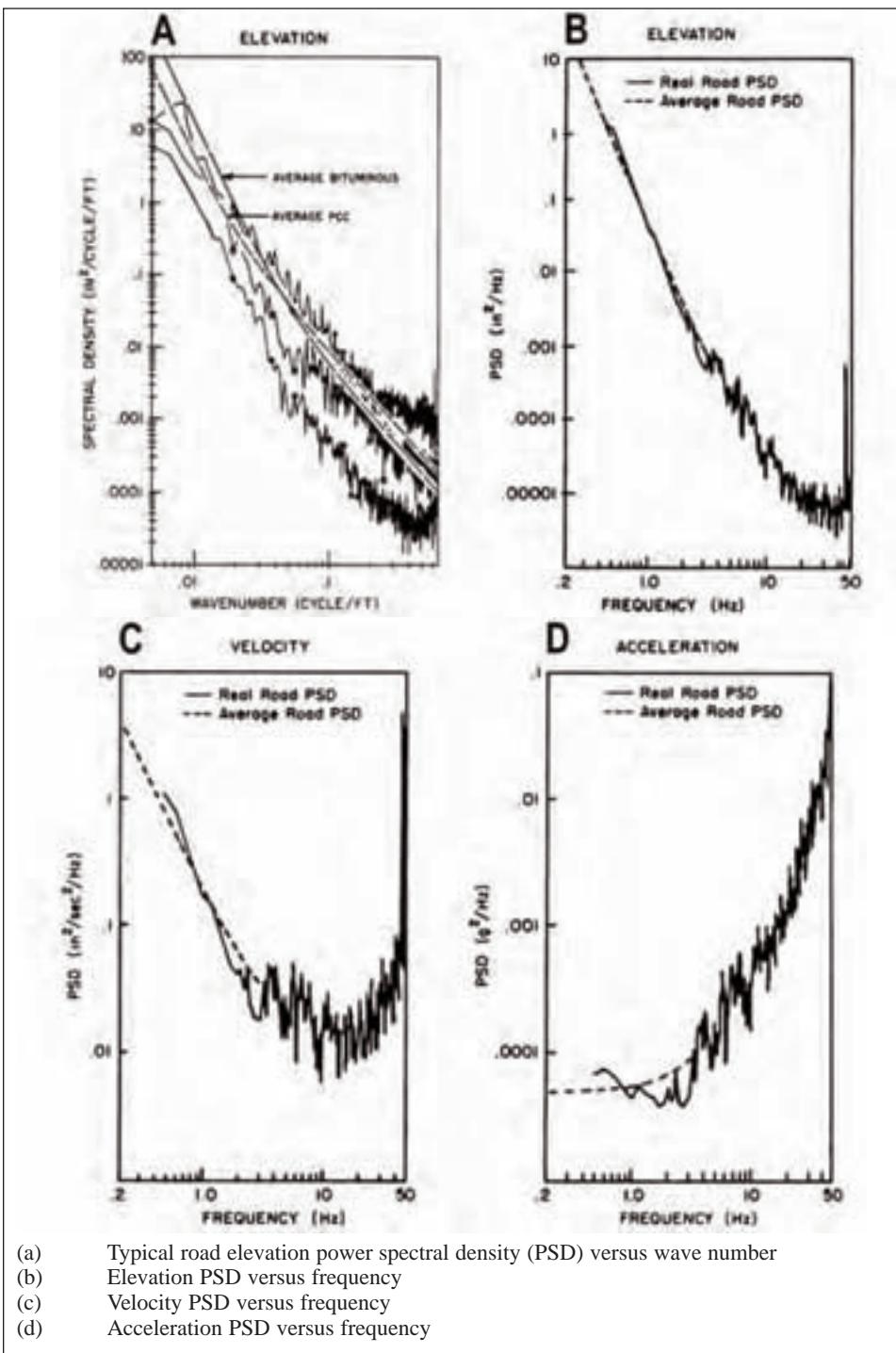
where f_t = temporal frequency (cycles per second)
                       V = vehicle velocity (m/sec)
                       λ = wavelength (m/cycle)
                       k = wave number (cycles/m)

    Suppose a vehicle is traveling at 27.8 m/s (100 km/h) and the tire encounters a sinusoidal pavement undulation with a wavelength of 1.39 m. In this case the tire will experience a vibrational input of 20.0 Hertz. Since tactile inputs as low as 1.0 Hertz and acoustic inputs as high as 20,000 Hertz are of interest, highway characteristics that fall into groups 'b' and 'c' can impact the ride quality of a vehicle.

    Although every highway is different, highway engineers have measured hundreds of roads over the years and it is possible to define an "average" road. figure 9.20(a) shows some representative highway elevation curves, the "average" for Portland Cement Concrete roads (PCC), and PCC overlaid with a smooth asphalt coating (Bituminous). Road irregularities with a long wavelength are on the left side of the chart and those with a short wavelength are on the right. The amplitude measurement is power spectrum density, a convenient statistical measure of pavement roughness.

    Assuming a vehicle is traveling on the road at 80 km/h, figure 9.20(b) shows the displacement input to the tire, and by differentiation the velocity (9.20(c)) and acceleration (9.20(d)) inputs to the tire. Elevation (displacement) inputs are large at low frequencies and acceleration inputs are large at high frequencies.

**Figure 9.20: Tire pavement characteristics, for a vehicle
traveling at 80 km/h, for real and average roads [25]**

(a)   Typical road elevation power spectral density (PSD) versus wave number
(b)   Elevation PSD versus frequency
(c)   Velocity PSD versus frequency
(d)   Acceleration PSD versus frequency
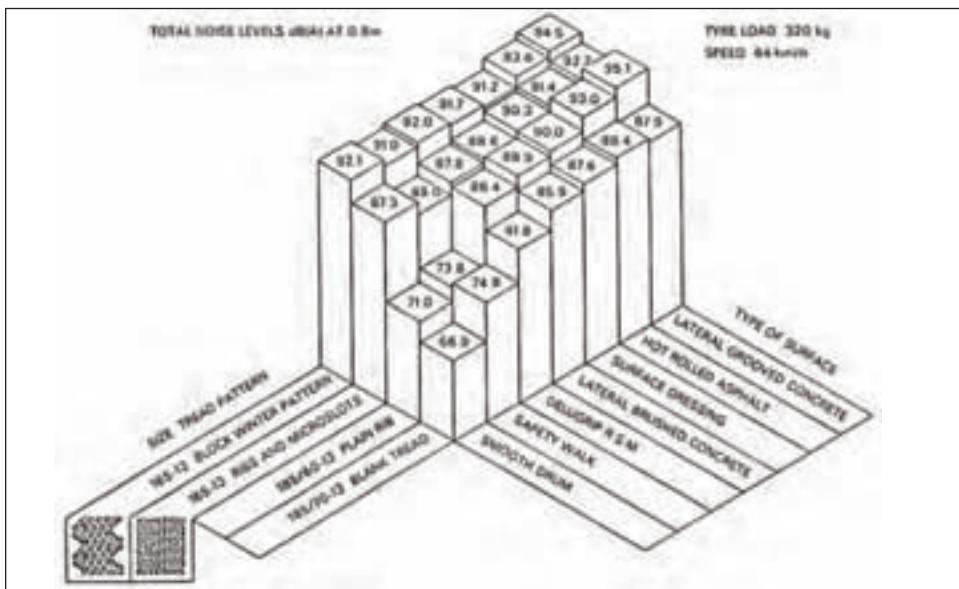
3.2 Tire/pavement interaction noise

The texture of the highway has a significant influence on the noise generated by a tire. Walker [26], Sandberg and Ejsmont [19] and many others have studied the manner in which various types of tread patterns interact with the surface texture of the road. Figure 9.21 shows the results from indoor drum testing of radial tires running on different replicated pavement textures [26]. The "blank tire" has no tread pattern whereas the "plain rib" is a blank tire with straight, circumferential ribs. The other two patterns are straight ribs with serrations and an aggressive block pattern (winter type tire). The surfaces include a Smooth Steel Drum, Safety Walk® (a 3M sandpaper type material, generally considered to be smooth), Delugrip® (an asphalt-like surface patented by Dunlop), Lateral Brushed Concrete (relatively smooth concrete, brush marks about 1 mm deep, 3 to 10 mm apart), Surface Dressed Asphalt (typical smooth highway construction, chip size less than 10 mm), Hot Rolled Asphalt (rough surface, chip size 19mm or larger), and Lateral Grooved Concrete (very rough surface, lateral grooves 10mm wide, 30-50mm apart).

   The reader will notice that the different types of tread patterns do not all react the same way when going from one surface to another. At the risk of overly simplifying the situation we will examine a few of the more extreme cases, the blank and the block tires running on the Safety Walk (SW) and the Hot Rolled Asphalt (HRA) surfaces.

Figure 9.21: Tire pavement interaction noise [26]

3.1.1 Blank tire on SW surface (smooth surface) – 74.8 dB(A)

This is usually a very quiet tire/road noise combination. The primary noise source is tread and carcass vibrations at the entry and exit from contact. These emphasize the lower frequencies, 800 to 1000 Hertz and below, and some organ pipe noise.

3.1.2 Blank pattern on HRA surface (rough surface) – 88.4 dB(A)

The rough highway surface impacts the tire and generates significantly higher levels of tire noise, particularly at the lower frequencies. It is possible that the air trapped in the

replicated surface also contributes to the tire noise. The increase in tire noise is 13.6 dB(A).

3.1.3 Block pattern on SW surface – 91.0 dB(A)
There is a very significant increase in noise level compared to the rib tire on the SW. The smooth surface seals around the tread grooves and highlights the air pumping mechanism at the higher frequencies, 1000 Hertz and above. The impacts of the blocks at the entrance to contact and stick-slip block vibration at the exit from contact are also significant contributors.

3.1.4 Block pattern on HRA surface – 93.6 dB(A)
The rough surface of the road eliminates some of the air pumping from the tread pattern (the air "escapes" through the road texture), but the impact of the coarse surface of the road with the tire more than overcomes the reduction in air pumping. The increase in tire noise as compared to the block tire on the SW is 2.6 dB(A).
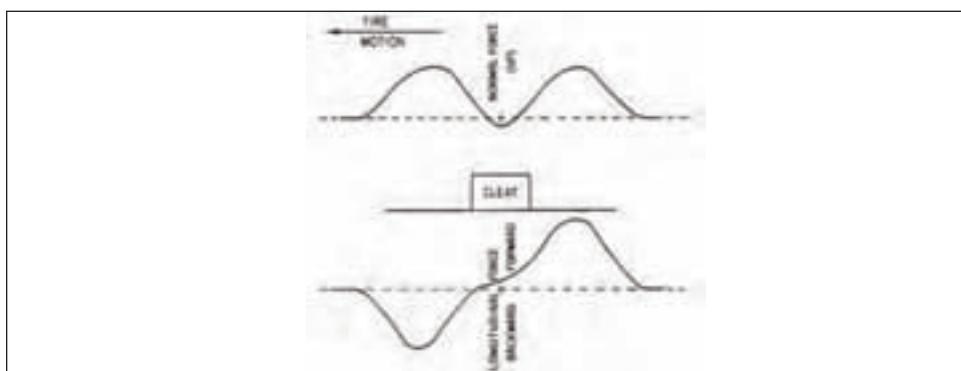
It is important not to lose sight of the fact that the comments above are not fully reflective of reality. The various mechanisms that influence how the tire and the road interact to produce tire/pavement interaction noise are very complicated. The reader may wish to consult Sandberg and Ejsmont [19] for additional and more detailed information. This is an excellent reference on tire noise.

3.2 Tire envelopment
When a tire encounters a road input with a wavelength greater than the length of the tire footprint, the tire can be treated as a spring/mass/damper excited by a point follower. When the road excitation is shorter than the tire footprint, such as a tar strip, the local stiffness of the tire shell comes into play and tire envelopment becomes important. The term "envelopment" refers to the ability of a tire to absorb or dampen a transient input from the road, thereby minimizing the amount of energy transferred to the vehicle. Tire envelopment was originally studied at low rolling speeds, and figure 9.22 shows a tire encountering a short bump at very low speed. For this type of situation the characteristics of the force signals are dependent on the size and shape of the bump and the operating conditions. The magnitudes of the forces are linearly dependent on the inflation pressure and non-linearly related to the height of the bump. The response to an upward bump (tar strip) normally differs from the response to a downward bump (chuck hole).
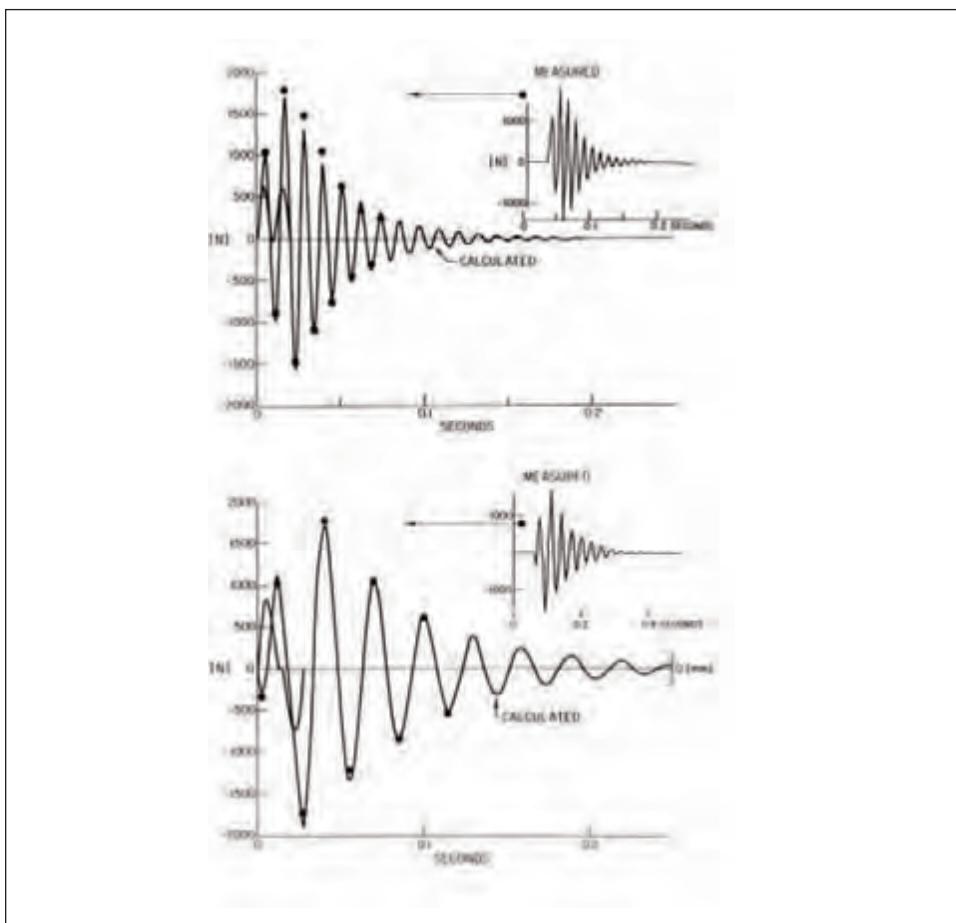
Figure 9.22: Typical tire enveloping forces from a small cleat at low speed [27]

Barone [28] extended envelopment studies to highway speeds and found that the input forces excite vibrational signals that correspond to the resonant modes of the tire in the vertical and longitudinal directions. The frequency ranges were 80-100 Hertz and 30-50 Hertz, respectively. The envelopment process and the resulting forces at the axle are therefore extremely important to the ride performance of the vehicle in the frequency range of 20 to 100 Hertz.

Bandel and Monguzzi [29] developed a semi-empirical approach to the envelopment process that modeled the in-plane motion of the tire as second-order systems in the vertical and longitudinal directions. The envelopment of the bump was treated as a low speed process where a "basic curve" was determined by the size and shape of the bump. The basic curve and its mirror-image were offset by an amount that depended on the deflection of the bump, and the two curves were added together to determine the input from the road. The predicted forces at the tire/vehicle axle in the vertical and horizontal directions correlated very well with the measured results, figure 9.23. This tire model was designed to serve as a "black box" that could be interfaced with vehicle models and solved with minimal computational effort.

Figure 9.23: Measured and calculated cleat forces [29]

Mancuso et al. [30] proposed a methodology that extended the Bandel model and eliminated the need to provide experimental tire data, thus allowing "virtual" testing of the tire during the design process. They used a 3D FEA model of the tire and extracted a mathematical-physical model of the tire that could be interfaced with vehicle models to model the in-plane ride performance from dc to 100 Hertz. The tire contact information, including envelopment, is determined from a separate FEA model of the tread pattern of the tire.

Efforts are also underway by investigators to extend the frequency range of the analysis for tire durability modeling. Tire durability requires modeling the response of the tire as it undergoes severe impacts and other extreme conditions that might stress the tire and/or suspension to the point of failure [31]. FEA and multi-body system models are being used to investigate time domain transient results as the tire encounters very large obstacles.
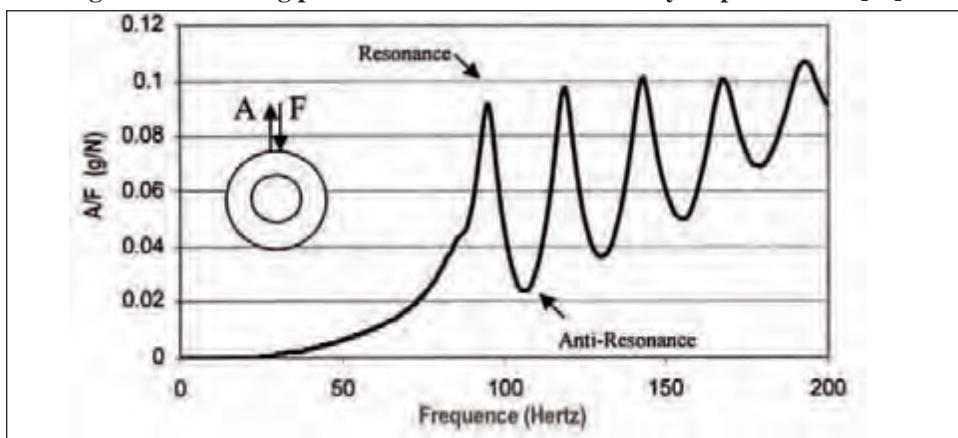
4. Tire modeling

Numerous techniques have been used over the years to model the vibrational behavior of tires. A few of these approaches are discussed in this section.

4.1 Modal analysis

Modal Analysis can be defined as "describing the dynamic behavior of a structure in terms of its modes of vibration." The experimental results presented in Section 1 are often gathered by using experimental modal analysis. Typically a force is applied at some location on the tire and the motion of the tire is measured at a number of different locations. If the excitation force is a short pulse, which can be provided by an instrumented impact hammer, all the modes of vibration of the tire will be excited at the same instant. After the data is analyzed the results can be plotted as Frequency Response Function (FRF), figure 9.24. In this instance the response acceleration has been divided by the input force and plotted versus frequency. Each peak in the curve indicates a mode of vibration of the tire, or a "resonance." Each resonance has a unique modal frequency, mass, damping and mode shape (the pattern of deformation). The frequency, mass and damping are global properties over the whole tire. The mode shape is a local property, since some points may move a great deal while other points may move very little.

Figure 9.24: Driving point FRF for a P225/60R15 freely suspended tire [32]

The benefit of using a modal representation to model the tire is a very small number of parameters can accurately describe the vibrational behavior of the tire. All one needs are the modal frequencies, masses and damping values and the mode shapes at the locations of interest, which are usually the tire footprint and the tire/wheel spindle. The disadvantage of modal analysis is that data must be gathered for every tire and all operating conditions of interest. This can be very time consuming. There is no direct way to determine the modal properties from the design parameters of the tire such as the belt angle, carcass, compound modulus, etc.
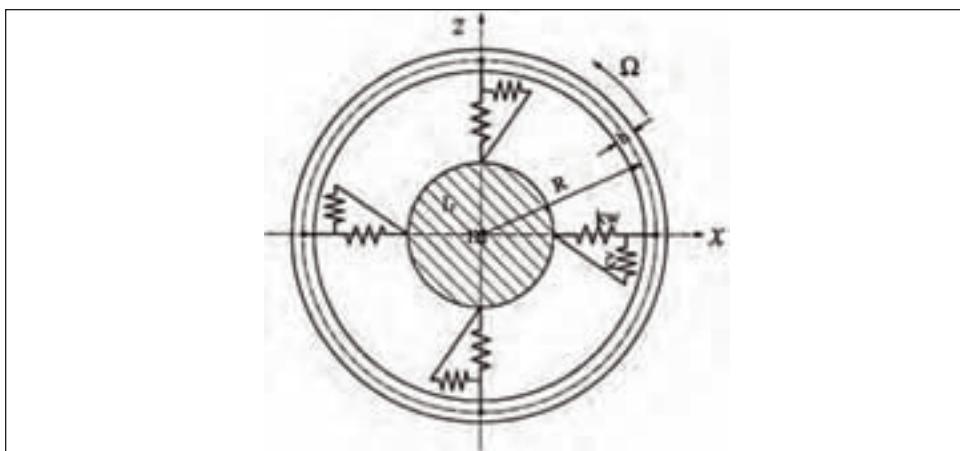
Finally, it has previously been noted that the boundary conditions at the ground and the wheel have an important effect on the vibrational behavior of the tire. W. Soedel [33] reported that the "preferred" or "baseline" set of experimental (or analytical) modal properties should be obtained for a free, axisymmetric tire. That is, a tire should be measured without the imposition of any constraints at the tire/wheel spindle or the ground plane. The reason for this is constraints can be easily added to the axisymmetric data to obtain the non-axisymmetric results. However, removing constraints from non-axisymmetric data to obtain the axisymmetric results is a more difficult process and requires knowledge of the forces of constraint.

4.2 Ring on an elastic foundation

The "classical" approach to modeling a tire is to use a flexible ring (or beam or shell) mounted on a set of springs. The stiffness and flexibility of the tread ring accounts for the higher frequency vibrational behavior of the tire, whereas the non-flexural motion of the tread ring displacing the elastic foundation accounts for the low frequency behavior of the tire.

A good example of the current state of knowledge for this type of model formulation can be found in Gong [34]. Figure 9.25 shows the basic tire model, which consists of a circular elastic ring representing the tread-band of the tire (tread, belts, undertread, liner, carcass, and other components), and radial and circumferential springs representing the tire sidewall and inflation pressure of the tire. The wheel is represented by a rigid mass with three degrees of freedom, linear in-plane motions in the vertical and longitudinal directions and a rotational degree of freedom about the spin axis.

Figure 9.25: Ring on an elastic foundation tire model [34]

The equations of motion are developed using Hamilton's principle and the assumption that the tread ring is inextensible in the circumferential direction. A solution is sought by assuming the deflected motion of the ring can be expanded as a complex Fourier series. This is essentially a modal extraction procedure, and the solution to the characteristic equation of the system is the modal properties of the tire. Since the model is developed without any constraints being imposed, it is possible to utilize this type of model to predict the vibrational behavior of the tire and the transmission of vibrational energy from the ground to the vehicle.

There are certain limitations to this type of model. First, there is not a provision to account for the vibration of the tire in the lateral direction. Second, since the stiffness of the ring and the sidewall are lumped together it is not possible to easily incorporate tire design changes into the model without performing additional calculations.

4.3 Finite element analysis and boundary element methods

The de facto "gold standard" in tire modeling at the present time is Finite Element Analysis (FEA). There are many advantages to the FEA approach, but probably the most important is that the actual design variables of the tire are explicitly considered in the model. For example, if the belt of the tire is altered during the design phase, the geometry and material properties used in the FEA model will be changed and the predicted performance of the tire will be updated to reflect these changes. FEA tire model predictions are typically accurate through approximately 300 Hertz.

The FEA modeling process is not without some significant costs. Aside from the time and expense of developing the FEA model, there can be large investments in computer run-times to solve the model. This is particularly the case when four FEA tire models are linked together with a FEA model of the vehicle to predict the system performance.

With regard to noise and vibration problems, however, there is a saving grace. W. Soedel suggested that once a tire is inflated and loaded it can be viewed as a linear shell and analyzed by conventional modal expansion methods [33]. Only the tire inflation and loading step require dealing with significant geometric and material non-linearities. The eigenvalue extractor present in virtually every FEA code can be used to identify the modal properties of the tire, and these properties can then be incorporating into various types of tire/vehicle models.
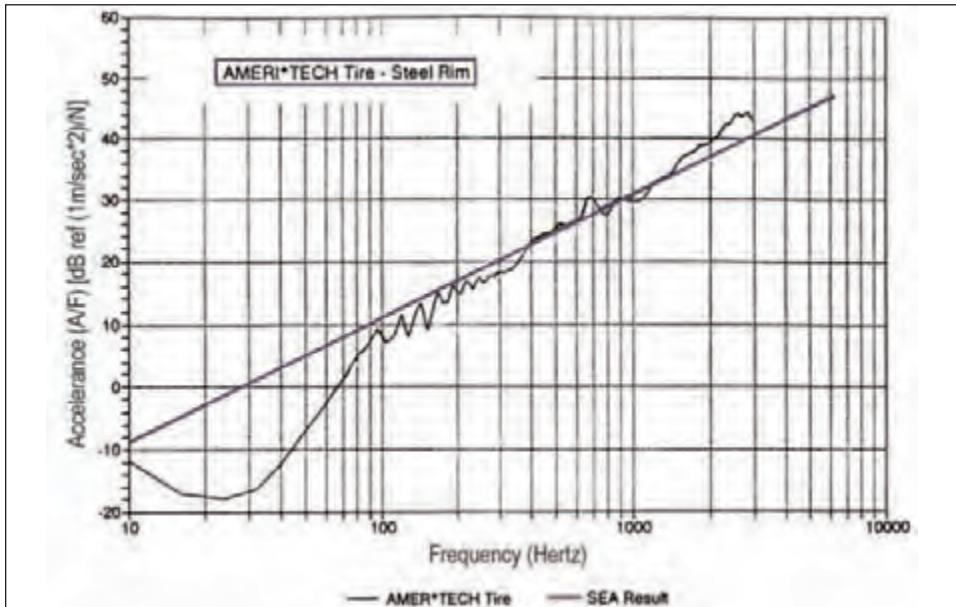
Boundary Element Methods (BEM) can also make use the modal properties from the FEA analysis of the tire. BEA can predict the acoustic radiation of a tire from knowledge of the geometry and the surface velocity of the tire. The tire geometry is readily identifiable, and the modal properties can be used to determine the velocity at any point on the surface of the tire. The intensity of the radiated sound can thus be determined and tracked while design changes are made to the tire.

4.4 Statistical energy analysis (SEA)

FEA and BEA are extremely useful modeling approaches through approximately 300 Hertz. Above this point, however, the number of vibrational modes becomes very large and the size of the FEA model is correspondingly large and difficult to solve. Figure 9.26 shows the input acceleration/force at the tread of a tire. Above 250 Hertz the individual modes become hard to discern, but the slope of the response curve continues to increases by about 6 dB per octave. SEA is applied to dynamic systems where it becomes impractical to evaluate each mode separately, but modeling the response of the system at higher

frequencies is desired. SEA is a statistical tool that allows the average response of a system to be estimated by grouping the vibrational modes into subsystems that are represented by idealized components such as plates, beams, acoustic cavities, etc. As figure 9.26 shows, SEA provides a good estimate of the system response through several thousand Hertz.

Figure 9.26: Accelerance for tire on steel wheel using a SEA model [after 35]

4.5 Other tire models
Aside from the models discussed above, there are a large number of other specialized and general purpose tire noise and vibration models, including models that predict the effect of pavement characteristics on tire noise. The reader may wish to consult Sandberg and Ejsmont and the references listed therein [19].

5.   Tire/vehicle systems
In the previous sections various aspects of tire noise and vibration behavior were discussed. How the tire and the vehicle behave as a dynamic system will be considered in this section.

5.1 Rigid body motions (0.5 to 5 hertz)
In this frequency range the tire/vehicle system behaves as a group of masses connected together by springs and dampers, figure 9.27. The principal rigid body displacements of the Sprung Mass are bouncing in the z-direction, pitching about the y-axis and roll about the x-axis. These motions normally occur at low speeds, have a vibrational frequency in the range of 1 to 3 Hertz, and are damped by the shock absorbers after a short period of time. The most common excitation source is pavement irregularities with fairly long wavelengths. Tire non-uniformity force variations in the vertical direction can also be an excitation source. At each corner of the vehicle it is possible to define a quantity known

as the "ride rate," which is the effective spring rate of the suspension and the tire

    $RR = (KtKs)/(Kt+Ks)$,   (8)

where *Kt and Ks* are the spring rates of the tire and suspension respectively. The undamped resonant frequency of the "quarter car model" is given by,

$$f = 0.159\sqrt{RR/M} \qquad (9)$$

    where   M = ¼ of the total sprung mass.
The damped resonant frequency is given by,
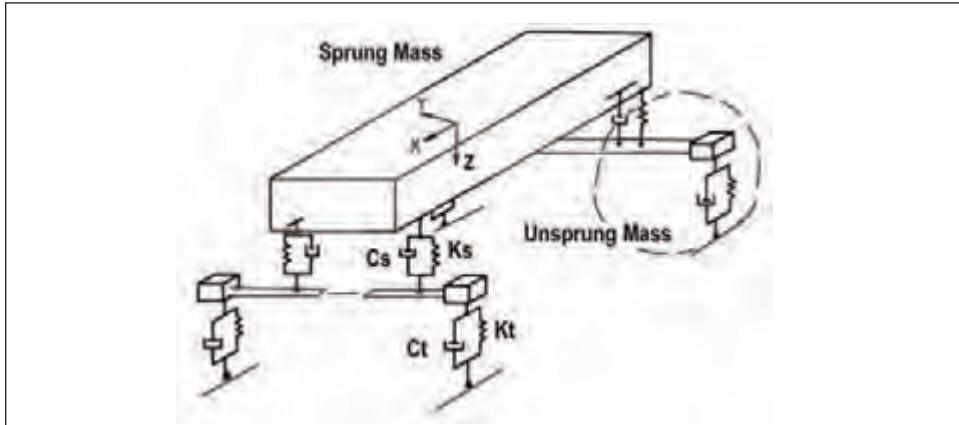
$$f_d = f\sqrt{1-\varsigma^2} \qquad (10)$$

    where ς is the critical damping ratio.

For good ride performance this frequency should be as low as possible, preferably less than 1.5 Hertz. The critical damping ratio of the suspension is typically between 0.2 and 0.4 (20 to 40 percent of critical damping). [25]

Figure 9.27: Simplified tire/vehicle system [after 36]

The other three rigid body motions of the vehicle body are longitudinal and lateral translations (x & y axes) and yaw about the z-axis. These motions generally occur in the frequency range of 3-5 Hertz and are usually less important than the vertical bounce and pitch and roll motions.

5.2 Wheel hop resonance (5 to 20 hertz)
Wheel Hop Resonance is a situation where the unsprung mass acts as like a rigid body and excites a vertical resonance of the suspension. The wheel hop mode is labeled as "VR1" in figure 9.7. The tire stiffness and the vehicle spring form a composite spring, and the tire damping and the shock absorber contribute the damping term. The undamped Wheel Hop resonant frequency can be found from the following equation.

$$f = 0.159\sqrt{(Kt+Ks)/M_u} \qquad (10)$$

    where M_u = unsprung mass
    Most modern passenger vehicles have an unsprung mass in the range of 40 to 50 kg

---

[5]A hemi-anechoic test room has a hard floor but absorptive material is attached to the other five surfaces.

and a Wheel Hop resonance between 10 and 20 Hertz. The damping ratio is between 0.2 and 0.4. [25]

Tire uniformity is the most important excitation source for wheel hop, although under some circumstances road undulations may excite this mode of vibration. The prime contributor is the first harmonic of radial force variation (RH1) and the critical driving speed is 80 km/h and above. When the wheel hop resonance is excited the ride disturbance is typically referred to as "Shake." Historically, Shake has been the leading cause of ride adjustments for tire manufacturers. Shake can be controlled in two ways.
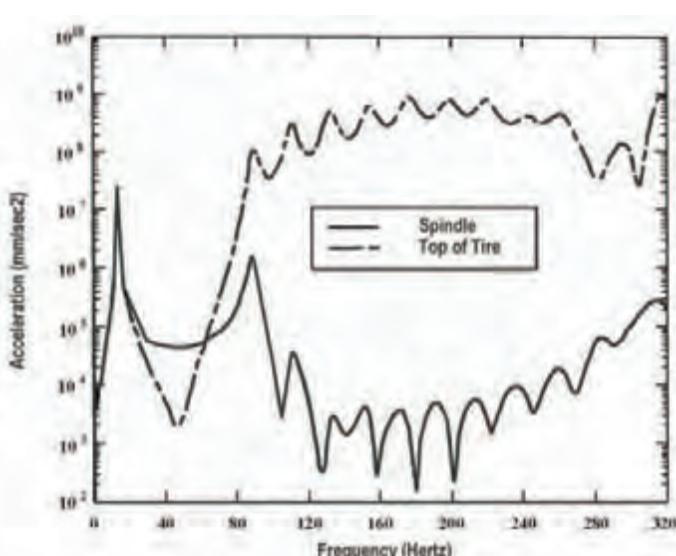
RH1 should be small throughout the operating speed range. The required force level depends on the sensitivity of the vehicle and the tolerance level of the observer.

Shift the Wheel Hop resonance upward as much as possible. There are two reasons for doing this. First, to insure that the speed at which wheel hop is most strongly excited is above the normal driving speed range. Second, the human body is less sensitive to a 20 Hertz vibration than to a 10 Hertz vibration, so a higher wheel hop frequency is less disturbing to an observer (also see Section 6 and figure 9.32).

5.3 Suspension resonances (20 to 300 hertz)
There are a number of ride disturbances that fall within this frequency range. Investigators have found that structural-borne disturbances dominate up to about 300 Hertz, and airborne disturbances dominate above that point. At the lower frequencies the vehicle has numerous structural and suspension resonances that can be excited by forces created by, or transmitted through, the tire. As the frequency increases the responsiveness of these resonances gradually diminish until the airborne disturbances become dominant. An equally important factor is that the strongest tire/wheel resonances in the vertical and longitudinal directions are found below 120 Hertz, figure 9.28. Above 120 Hertz the tire resonances are much less responsive, usually by at least an order of magnitude. In this figure the vertical resonances (VR1 and VR2) resonances are seen to occur at about 10 Hertz and 90 Hertz. A similar situation exists in the longitudinal direction, except the first mode of vibration usually occurs between 30 and 50 Hertz and the second between 80 and 110 Hertz (the LR1 and LR2 longitudinal modes are not shown).
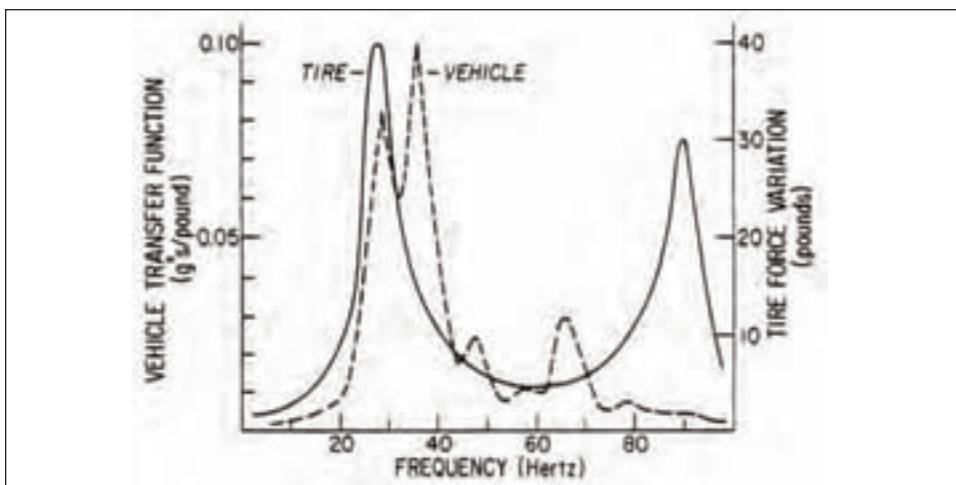
Figure 9.28: Road roughness at spindle and top of tire [after 37]

5.3.1 Tire roughness (25-50 hertz)

Tire Roughness is a tactile disturbance that occurs on a smooth road at highway speeds, but gives the impression of driving on a coarse surface. It is normally caused by the 2nd or 3rd harmonic of uniformity longitudinal force variation exciting the longitudinal resonance of the tire/wheel suspension (LR1). This, in turn, excites a resonance of the steering wheel, floorpan or some other component of the vehicle. Figure 9.29 shows the tire/vehicle longitudinal resonance (solid line) and the steering column resonances in the vehicle (dotted line). Tire Roughness can also cause acoustic disturbances inside the passenger compartment.

Figure 9.29: Tire longitudinal force and vehicle response at steering wheel

5.3.2 Harshness (25 to 50 hertz)

This is a tactile disturbance that is caused by a tire encountering a pavement discontinuity such as a tar strip. The vertical and longitudinal resonances (VR2, LR1 and LR2) of the tire/vehicle system respond to these impulsive forces which, in turn, excite the steering wheel, floorpan and other components of the vehicle. Impact Boom can also occur if the forces excite vehicle panel vibrations (also see Boom below).

5.3.3 Road roughness (or road roar, 25 to 300 hertz)

This is an acoustic disturbance that results from a tire operating on a coarse surface. Vibrational energy is structurally transmitted into the passenger compartment and re-radiated as acoustic noise by vibrating panels. At normal driving speeds this is often an extremely important ride disturbance. Detailed computer modeling to decouple the tire from the vehicle, the application of damping materials to the suspension and vehicle components, and the use of absorptive materials inside the passenger compartment have all proven effective in reducing the noise level. At the low end of the frequency range Road Roughness can also tactically excite the steering wheel or floor pan and gives the impression of Tire Roughness. Between 200 and 300 Hertz, the Tire Cavity Modes can also become excited and augment other acoustic disturbances.
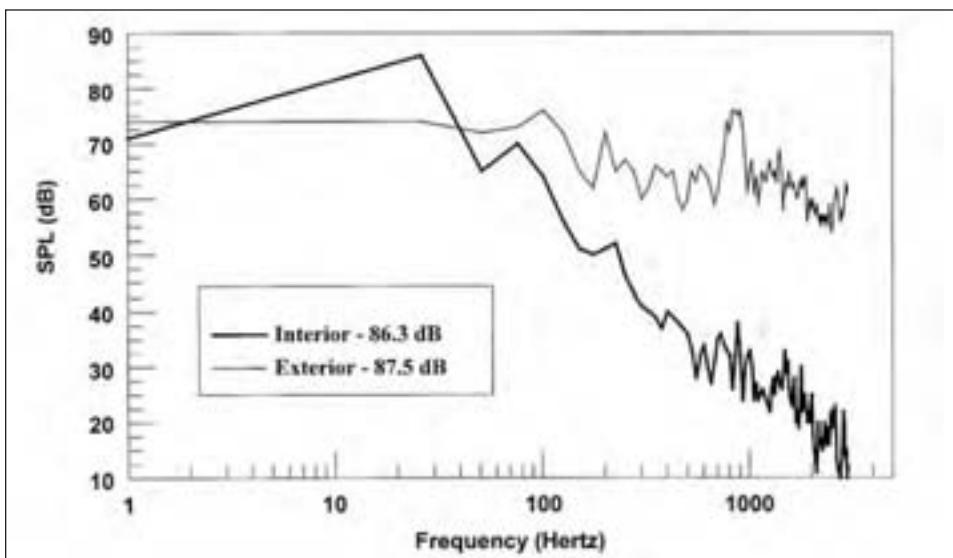
5.3.4 Boom
Like most enclosed spaces, it is possible for the passenger compartment of a vehicle to support the development of standing waves. There are a number of causes of boom including Road Roughness, tire uniformity (4th or 5th harmonics of radial and longitudinal force variation), and rotational inputs from the engine and driveline. The frequency range is generally between 30 and 100 Hertz. FEA techniques are often used to address this problem.

5.4 Airborne disturbances (300 hertz and higher)
Above 300 Hertz, the primary disturbances are caused by airborne noise signals radiating from the tire. Figure 9.30 illustrates the result of noise measurement performed in a hemi-anechoic test chamber.[5] The left front wheel of the vehicle was operating on a floor-mounted dynamometer at 100 km/h. The thin line is the SPL recorded 1 meter to the side of the tire, and the heavy line is the SPL measured inside the vehicle at the location of the drivers head. A comparison of these curves illustrates several important aspects of the tire/vehicle system. First, at very low frequencies the Interior SPL is larger than the Exterior SPL, albeit at only a single spectral line. This is an example of a structural borne disturbance (RH1) exciting the wheel hop resonance. The passengers would "feel" rather than "hear" this disturbance. Second, as the frequency increases the exterior noise signals are attenuated by the body of the vehicle due to the "mass law." The mass law is a semi-empirical relationship that states for every doubling of frequency or the surface mass of a single panel, the noise signal will be attenuated by 6 dB. A vehicle body is not a single panel so the SPL change is only approximately the predicted values, but the concept is a useful approximation when considering airborne noise disturbances.

Figure 9.30: Noise levels at 100 km/h, full size sedan [39]

---

[5] A hemi-anechoic test room has a hard floor but absorptive material is attached to the other five surfaces.
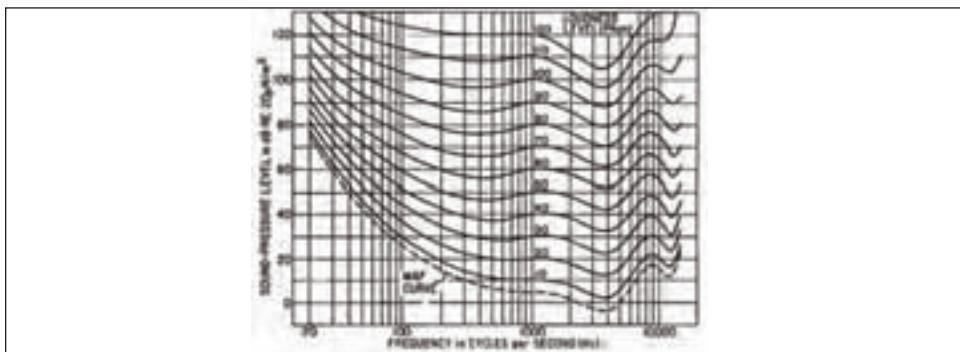
6. Human response to noise & vibration disturbances

This section will consider how human subjects respond to tactile and acoustic disturbances.

6.1 Human response to acoustic signals.

Psychoacoustics is the study of how subjects respond to acoustic signals. In the 1950s Robinson and Dadson re-determined a series of free-field equal loudness contours for pure tones presented to observers, figure 9.31. The dashed line labeled "MAF" is the minimum audible field, or the threshold of hearing for a person with excellent hearing. All points along any given curve have the same level of subjective loudness in a free field.[6] For example, a 70 dB tone at 1000 Hertz has the same perceived loudness as an 80 dB tone at 75 Hertz. These curves incorporate two aspects of human hearing, the physiological process of *how* we hear and the psychological response to *what* we are hearing. Note that individuals are most sensitive to acoustic signals in the frequency range of 3000 to 4000 Hertz.

Figure 9.31: Free-field equal loudness contours for pure tones [40]
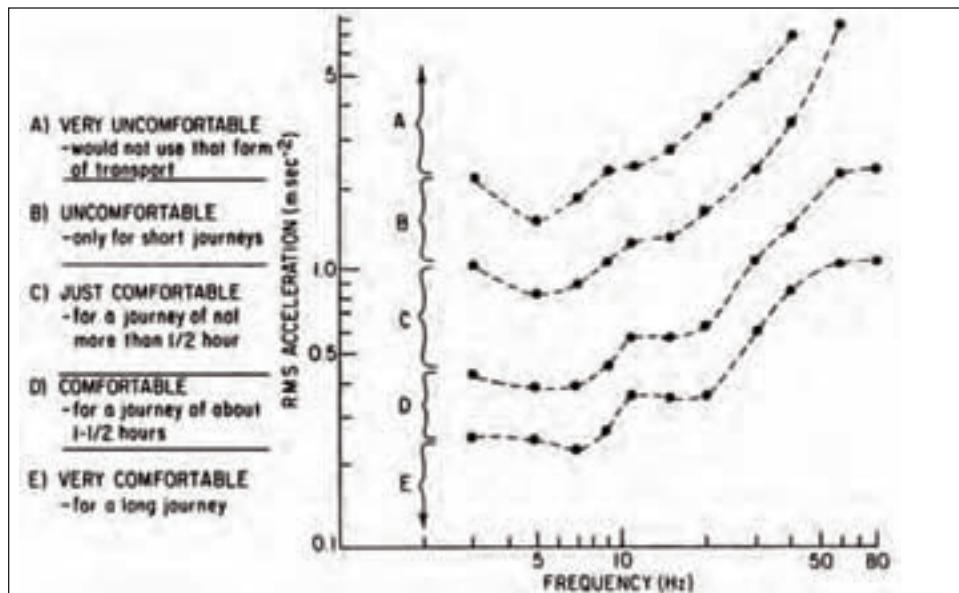
It is occasionally suggested that dB units are used in acoustic measurements because people "listen logarithmically." This is not the case. The real reason is that the human ear can respond to pressure variations over a range of 10 million to one — a truly remarkable engineering feat — and using dB units simply makes the numbers easier to deal with.

6.2 Response to tactile disturbances

The study of the response of the human body to tactile vibrations follows those for acoustic studies, but the results are considerably different. Figure 9.32 shows the vertical equal sensitivity contours for a seated passenger in a vehicle. A seated individual is most sensitive to tactile inputs in the frequency range of 4-8 Hertz, and the sensitivity decreases with increasing frequency. Similar curves are found for vibrational inputs to the hands and the feet. The phrases on the left side of the graph describe the level of comfort as a function of vertical acceleration level. Consider, for example, the lowest curve and the descriptive quantity "very comfortable." Assume that the vertical acceleration values are recorded over the frequency range from 3 to 80 Hertz (rms - m/sec^2). If each and every acceleration data point lies on or below the dashed curve, then the ride will be Very Comfortable for a long journey.

---

[6]The laymen's definition of a free field is an observer sitting in an open field without any nearby reflecting surfaces.

Figure 9.32: Equal comfort zones for seated passengers, vertical excitation [41]

6.3 Combined noise and vibration disturbances
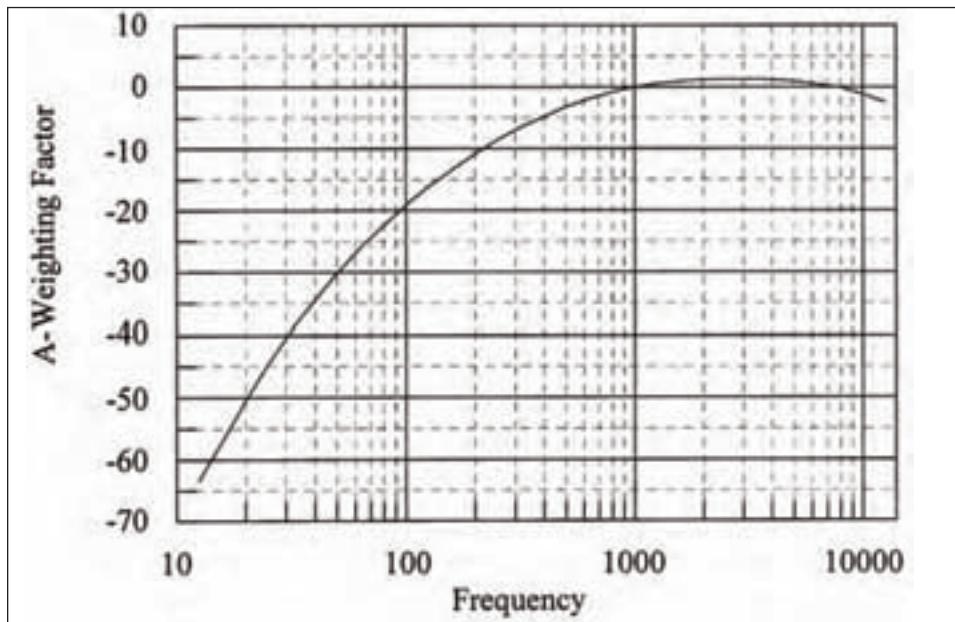
An extensive study of the combined effects of acoustic and tactile disturbances on observers was performed at NASA by Leatherwood, et al. [42]. Ride Comfort was evaluated by considering random or sinusoidal tactile inputs for five axes of motion (three linear motions and two rotational motions) plus factors to account for the presence of noise. The results were presented as a single number that expressed the total discomfort experienced by the observers. As one might expect, the combined effect of noise plus vibration was more disturbing than either noise or the vibration experienced alone.

6.4 Ride / sound metrics

For many years investigators have used equal sensitivity data to derive Ride or Sound Metrics. The Metrics are then correlated with the subjective response of the observers to provide quantitative predictive tools of the ride environment.

The literature is replete with Metrics, and, although it is not normally thought of as such, the A-Weighting curve is by far the most widely used Sound Metric, figure 9.33. The A-weighting curve is calculated by essentially inverting the 40 phon Loudness Level curve in figure 9.31, thus incorporating the combined effect of the physiological and the psychological aspects of hearing. The weighting process is accomplished by subtracting the A-weighting values from measured SPL dB data on a frequency by frequency basis, thus obtaining SPL dB(A) values. The overall SPL dB(A) value can be found from equation 5. This procedure can also be performed for data that is presented in one-third octave band terms, table 9.6.

In either case, the lower frequencies are considerably attenuated, the mid-range frequencies between 1,000 and 6,300 Hertz are amplified, and frequencies above 6,300 Hertz are attenuated.

Figure 9.33: A-weighting curve

Table 9.6: A-weighting factors for one-third octave bands

Frequency	A-weighting	Frequency	A-weighting	Frequency	A-weighting
25	-44.7	200	-10.9	1,600	1.0
31.5	-39.4	250	-8.6	2,000	1.2
40	-34.6	315	-6.6	2,500	1.3
50	-30.2	400	-4.8	3,150	1.2
63	-26.2	500	-3.2	4,000	1.0
80	-22.5	630	-1.9	5,000	0.5
100	-19.1	800	-0.8	6,300	-0.1
120	-16.1	1,000	0.0	8,000	-1.1
160	-13.4	1,250	0.6	10,000	-2.5

6.5 Monaural & binaural measurements

Monaural means a single microphone is used to make a measurement, whereas binaural means using a pair of microphones separated by the distance between a person's ears. Monaural measurements made outdoors in a free field, such as vehicle pass-by studies, generally correlate quite well with subjective response. This is because in an open field the sound from a passing vehicle is presented to the listener from more or less a single direction at any instant of time, so the SPL at the observer's ears is essentially the same for either ear.

The situation is very different inside a vehicle. In this case sound sources can be located at a number of different positions, and the presence of a human body will also diffract (alter) the sound field. The result is the acoustic signals at the left and right ears of the

observer can be very different in both amplitude and phase. This is called an interaural difference, and binaural measurements are required to account for these effects.

6.6 Ride and sound quality analyzers

Beginning in the late 1980s, a number of manufacturers began marketing Sound Quality analyzers. Typically these devices consist of a binaural manikin (artificial head with microphones in the ear canals and a half-torso), a digital recording device (often DAT tape), computer software to process the recorded signals, and methods of presenting the stored or processed results to listeners.

In the late 1980s, automotive engineers were principally interested in reducing the SPL inside a vehicle. This effort was very successful, but eventually a point was reached where additional SPL reductions could be accomplished only by adding thicker sound deadening materials, using heavier metal panels, or utilizing other techniques that added mass and/or cost to the vehicle.

In the 1990s, a more market driven approach was adopted and this became known as "Sound Quality" engineering. The goal changed from merely reducing the SPL level to understanding what type of sound the customer desired. For example, although it might be possible to design a car door that would close almost without a sound, most vehicle owners prefer a door that closes with a solid "thump." A new set of Sound or Ride Metrics also appeared, such as "sharpness" (a large amount of high frequency energy in the noise signal), "muffled" (a large amount of low frequency energy), "roughness" (amplitude modulations of the time domain waveform), "tonality" (a few or several prominent frequency peaks), "annoying" sounds that don't greatly add to the overall noise level but are nonetheless disturbing (wind noise, whining small motors, rattles, squeaks, etc.) and other issues.

The current approach to noise control is: (1) binaural recordings made of the existing environment, (2) test subjects audition the recordings and assign subjective ratings, (3) the data is processed to obtain objective (quantitative) ratings, (4) the objective and subjective ratings are correlated to identify what the user wants, and, (5) "cutting metal" to cost effectively delivery the desired performance in the vehicle.

References

1. Pottinger, M. G. and Yeager, T. J., Ed., *The Tire/Pavement Interface,* American Society for Testing and Materials, STP 929, Baltimore, MD, 1986.
2. *Vehicle Dynamics Terminology* , Society of Automotive Engineers, SAE J670E, 1976.
3. Rasmussen, R. E. and Cortese, A. D., "Dynamic Spring Rate Performance of Rolling Tires," Society of Automotive Engineers, SAE 680408, 1968.
4. Melvin, J. W., Klein, R. G. and Marshall, K. D., B. F. Goodrich file data, 1968.
5. Pottinger, M. G., Thomas, R. A. and Naghshineh, K., "Stiffness Properties of Agricultural Tires," *International Conference on Soil Dynamics,* Auburn, AL, June, 1985.
6. Marshall, K. D., Ohio Dynamics, Inc., unpublished file data, 1997.
7. Jianmin, G., Gall, R. and Zuomin, W. "Dynamic Damping and Stiffness Characteristics of Rolling Tires," *Tire Science and Technology,* TSTCA, Vol.29, No. 4, Oct-Dec, 1997.
8. Potts, G. R., Bell, C. A., Charek, L.T. and Roy, T.K., "Tire Vibrations," *Tire Science and Technology,* TSTCA, Vol. 5 No. 4, Nov. 1977.
9. Scavuzzo, R.W., Richards, T. R. and Charek, L. T., "Tire Vibration Modes and Effects

on Vehicle Ride Quality," *Tire Science and Technology,* TSTCA, *Vol. 21, No. 1, Jan-March, 1993.*

10. Mills, B. and Dunn, J. W., "The Mechanical Mobility of Rolling Tires," *Vibration and Noise in Motor Vehicles,* Institute of Mechanical Engineers, London, England, pp 90-101, 1972.

11. Richards, T. R., Charek, L. T. and Scavuzzo, R. W., "The Effect of Spindle and Patch Boundary Conditions on Tire Vibration Modes," Society of Automotive Engineers, SAE 860243, 1986.

12. Kung, L. E., "Radial Vibrations of Pneumatic Radial Tires," Society of Automotive Engineers, SAE 900759, 1990.

13. Marshall, K. D., Wik, T. R., Miller, R. F. and Iden, R. W., "Tire Roughness – Which Tire Nonuniformities are Responsible," Society of Automotive Engineers, SAE 740066, Detroit, MI, 1974.

14. Walker, J. C. and Reeves, N. H., "Uniformity of Tire at Operating Speeds," American Society for Testing and Materials Committee F-9, Symposium on Tire Uniformity and Vibrations, Akron, OH, November, 1973.

15. Nedley, Q. L. and Gearig, D. M., "Radial Improvements in Tire and Wheel Manufacture – Their Effects upon Radial Force Variation of the Assembly," Society of Automotive Engineers, SAE 700089, Detroit, MI, 1970.

16. Hofelt, C., Jr., "Uniformity Control of Cured Tries," Society of Automotive Engineers, SAE 690076, 1969.

17. Hayden, R. E., "Roadside Noise from the Interaction of a Rolling Tire and the Road Surface," Technical paper presented at the 81st meeting of the Acoustical Society of America, Washington, D. C., April, 1971.

18. Plotkin, K. Fuller, W. and Montroll, M., "Identification of Tire Noise Generation Mechanisms Using a Roadwheel Facility," *Proceedings –International Tire Noise Conference,* Stockholm, Sweden, August, 1979.

19. Sandberg, U. and Ejsmont, J. A., "Tyre/Road Noise Reference Book," Informex, SE-59040, Kisa, Sweden, 2002.

20. Varterasian, J. H., "Quieting Noise Mathematically – Its Application to Snow Tires," Society of Automotive Engineers, SAE 690520, Detroit, MI, 1969.

21. Williams, T. A., "Multiple Pitch Sequence Optimization," *U.S. Patent Document 5,309,965* (1994) The General Tire and Rubber Company, May 10, 1994.

22. Bandel, P. *et al.,*"Low Noise Sequence of Tread elements for Vehicle Tire and Related Generation Method," *U.S. Patent Document 5,371,685* (1994) The Pirelli Tire Company, December 6, 1994.

23. Scavuzzo, R. W., Charek, L. T., Sandy, P. M. and Shteinhauz, G. G., "Influence of Wheel Resonance on Tire Cavity Noise," Society of Automotive Engineers, SAE 940533, Detroit, MI, 1994.

24. Sakata, T., Morimura, H. and Ide, H., "Effects of Tire Cavity Resonance on Vehicle Road Noise," *Tire Science and Technology,* TSTCA, Vol. 18, No. 2, April-June, 1990, pp 68-79.

25. Gillespie, T. D., *Fundamentals of Vehicle Dynamics,* Society of Automotive Engineers, Warrendale, PA, 1992.

26. Walker, J. C., "The Reduction of Noise Generated by Tyre/Road interaction," The German Rubber Conference, Wiesbaden, Germany, June, 1993.

27. Julien, M. A. and Paulsen, J. F., "The Absorptive Power of the Pneumatic Tire,

Experimental Method of Measurement and Definition," IV Intl. Technical Conference on Automobiles, Madrid, Spain, 1952.

28. Barone, M. R., "Impact Vibrations of Rolling Tires," Society of Automotive Engineers, SAE 770612, 1977.

29. Bandel, P. and Monguzzi, C., "Simulation Model of the Dynamic Behavior of a Tire Running Over and Obstacle," *Tire Science and Technology,* TSTCA, Vol. 16, No. 2, April-June, 1988, pp 62-77

30. Mancuso, F., Sangalli, R., Cheli, F., Ciarlariello, G. and Braghin, F., "A Mathematical-physical 3D Tire Model for Handling/Comfort Optimization on a Vehicle: Comparison with Experimental Results," *Tire Science and Technology,* TSTCA, Vol. 28, No. 4, October-December, 2000, pp 210-232.

31. Haney, R., Crolia, D. and Hauke, M., "Tire Modeling for Misuse Situations," Society of Automotive Engineers, SAE 2001-01-0748, 2001.

32. Marshall, K. D., Ohio Dynamics, Inc., file data, 1997.

33. Soedel, W. and Prasad, M.G., "Calculation of Natural Frequencies and Modes of Tries in Road Contact by Utilizing Eigenvalues of the Axisymmetric Non-Contacting Tire," Journal of Sound and Vibration, Vol. 70(4), 1980, pp 573-584.

34. Gong, S., "A Study of In-Plane Dynamics of Tires," Delft University of Technology, MS Thesis, 1993.

35. Lee, J.J., Pham, H.Q. and Moore, J.A., "Structure-Borne Vibration Transmission in a Tire and Wheel Assembly," *Tire Science and Technology,* TSTCA, Vol. 26, No. 3, July-September, 1998, pp 173-185.

36. Healey, A. J., Nathman, E. and Smith, C. C., "An Analytical and Experimental Study of Automobile Dynamics with Random Roadway Inputs," Journal of Dynamic Systems Measurement and Control, Trans ASME, December, 1977.

37. Yu, H. J. and Aboutorabi, H., "Dynamics of Tire, Wheel and Suspension Assembly," *Tire Science and Technology,* TSTCA, Vol. 29, No. 2, April-June, 2001, pp 66-78.

38. Marshall, K. D. and St.John, N.W., "Roughness in Steel Belted Radial Tires – Measurement and Analysis," Society of Automotive Engineers, SAE 750456, Detroit, MI, 1975.

39. Marshall, K. D., Ohio Dynamics, Inc., unpublished file data, 1994.

40. Robinson, D. W. and Dadson, R. S., "A Re-determination of the Equal Loudness Relations for Pure Tones," British Journal of Applied Physics, Vol. 7, 1956, pp. 166-181.

41. Smith, C. C. and McGee, D. Y., "The Prediction of Passenger Riding Comfort from Acceleration Data," ASME paper 77-WA/Aut-6, American Society of Mechanical Engineers, New York, 1977.

42. Leatherwood, J. D., Dempsey, T. K. and Clevenson, S. A., "A Design Tool for Estimating Passenger Ride Discomfort within Complex Ride Environments," Human Factors, Vol. 22, No. 3, 1980, pp 291-312.

Glossary

Acoustic:
Boom
A high intensity vibration (25 – 100 Hz.) perceived audibly and characterized as a sensation of pressure by the ear.

Noise
Unwanted sound is typically referred to as noise.

Road roar
A high intensity vibration (100 – 300 Hz.) perceived audibly and excited by the pavement texture such as pebbly surfaces.

Thump
A periodic vibration and/or audible sound generated by the tire and producing a pounding sensation which is synchronous with wheel rotation.

Tire/pavement interaction noise
Airborne sound that is created by the excitation of the rolling tire by the road surface.

Tactile:
Harshness
Vibrations (15 to 100 Hz.) perceived tactily and/or audibly, produced by the interaction of the tire and road irregularities.

Tire roughness
Vibration (15 to 100 Hz.) perceived tactily and/or audibly, generated by a rolling non-uniform tire on a smooth road, and producing the sensation of driving on a coarse surface.

Shake
The intermediate frequency (5-25 Hz.) vibration of the sprung mass as a flexible body, generated by the first harmonic of radial (normal) force variation.

General:
Nodal point
A nodal point is a location on a vibrating structure where the amplitude of motion for some particular mode of vibration is equal to zero. Other vibrational modes may or may not exhibit zero motion at the same location.

Sprung mass
Sprung mass is all the mass that is supported by the suspension of the vehicle, including the mass of a portion of the suspension itself.

Unsprung mass
Unsprung mass is the mass of the tire and the wheel plus the portion of the mass of the suspension that is not part of the Sprung Mass.

Questions and problems

1. What are the frequency ranges for tactile and acoustic ride disturbances?
     a. Tactile 1 – 60 Hertz,   Acoustic dc – 10000 Hertz.
     b. Tactile 20 – 300 Hertz, Acoustic dc – 10000 Hertz.
     c. Tactile 1 – 300 Hertz,   Acoustic 20 – 20000 Hertz.
     d. Tactile 20 – 300 Hertz, Acoustic 20 – 20000 Hertz.
     Answer: c

2. What are representative values for a passenger tire spring and percent critical damping?
     a. Spring rate 600 kN/m,   Damping 1.5 percent.
     b. Spring rate 200 kN/m,   Damping 1.5 percent.
     c. Spring rate 600 kN/m,   Damping 5.0 percent.
     d. Spring rate 200 kN/m,   Damping 5.0 percent.
     Answer: b

3. What are the most important vibrational frequency ranges for a loaded passenger tire?
     a. Vertical 10 to 25 Hertz and 60 to 120 Hertz,
        Longitudinal 30 to 50 Hertz and 60 to 120 Hertz.
     b. Vertical dc to 10 Hertz and 60 to 120 Hertz,
        Longitudinal 10 to 30 Hertz and 60 to 120 Hertz
     c. Vertical dc to 10 Hertz and 20 to 80 Hertz,
        Longitudinal 10 to 30 Hertz and 20 to 80 Hertz
     d. Vertical 10 to 25 Hertz and 20 to 80 Hertz,
        Longitudinal 30 to 50 Hertz and 20 to 80 Hertz
     Answer: a

4. Assume a passenger vehicle has a boom frequency of 42 Hertz. What is the speed of the vehicle when the 3rd, 4th and 5th harmonics of force variation excite the peak value of this ride disturbance? Assume the tire rotational rate is 1 rps per 5 mph.
Answer: 3rd harmonic = (42 Hz / 3rd) x (5 mph)   = 70.0 mph
          4th harmonic = (42/4) x (5)   = 52.5 mph
          5th harmonic = (42/5) x (5)   = 42.0 mph

5. What are important causes of radial and longitudinal force variation?
Answer: Radial; anything that affects mass variation.
Longitudinal; anything that affects tire runout or spring rate variation.

6. What are the most important causes of tire noise?
Answer:
a. Tread/Sidewall vibrations due to block impacts/vibration (frequencies less than 1000 Hertz).
b. Air pumping from the tread pattern (frequencies higher than 2000 Hertz).
c. Both 'a' and 'b' are important between 1000 and 2000 Hertz.

7. What are three key factors to producing acceptable tire noise?
Lowering the overall sound pressure level.
Spreading out and flatten the frequency spectrum.
Insuring there are no large, discrete frequency peaks.

8. Which of the following would NOT be effective in reducing tire noise?
a. Randomize the pitch sequence.
b. Use larger tread blocks.
c. Angle the transverse grooves in the circumferential direction.
d. Use narrower and less deep grooves.
Answer: b.

9. Rank the following tire/road interaction noise combinations from quietest to loudness.
Rough road, blank pattern.
Smooth road, block pattern.
Rough road, block pattern.
Smooth road, blank pattern.
Answer: d, a, b, c

10. What is the preferred method of performing tire vibration tests?
a. Pinned wheel, free footprint.
b. Free Wheel, fixed footprint.
c. Pinned wheel, fixed footprint.
d. Free wheel, free footprint.
Answer: d

11. What is the damped suspension frequency for a ¼ car model for a vehicle with a mass of 1,400 kg, and tire and suspension spring rates of 200 kN/m and 30 kN/m, respectively. Assume the weight distribution is 50/50 front/rear, and the damping ratio is 0.25.
Answer: Ride Rate = (30 x 200)/230 = 26.1 kN/m
¼ Mass = .25(1400) = 350 kg
$f = .159 (26,100/350)^{0.5} = 1.37$ Hertz
$f_d = 1.37 (1 - .25^2)^{0.5} = 1.33$ Hertz

12. If the unsprung mass of the suspension in problem 11 is 50 kg, what is the undamped wheel hop resonance?
Answer: $f = .159 (30000+20000/50)^{1/2} = 10.8$ Hertz

13. Assume a noise signal is composed of two 1/3 octave bands of acoustic energy; B_{400} = 63 dB and B_{630} = 60 dB. What is the overall sound pressure level?
Answer: SPL = $10 \log (10^{63/10} + 10^{60/10}) = 64.76$ dB

14. What is the A-weighted sound pressure level for the noise signal in problem 13?
Answer: B_{400} (A) = 63 - 4.8 = 58.2 dB(A)
        B_{630} (A) = 60 – 1.9 = 58.1 dB(A)
                SPL = $10 \log (10^{5.82} + 10^{5.81}) = 61.16$ dB(A)

Chapter 10
Waves in Rotating Tires

by D.M. Turner

Chapter 10
Waves in Rotating Tires

by D. M. Turner

1. Introduction

This chapter describes the phenomenon of "standing waves" observed in tires at high speeds, causing increased energy consumption and overheating. A simple theoretical treatment is proposed that accounts for the main features in bias-ply tires: the existence of a critical speed C at which the waves first appear, and the increase in energy consumption at speeds above C. The theory is then modified to apply to radial tires and more complex tire constructions.

In the 1950s in Europe there was intense competition between motorcycle manufacturers in Grand Prix Racing. At least four tire manufacturers were also competing. The 500cc bikes were achieving speeds of over 150 mph and occasionally a tyre lost its tread. Tests on drum dynamometers showed that at speeds above 70 to 80 mph there was a steep increase of power consumption with increasing speed. Close examination of the tyre profile as it parted from the surface of the drum showed the presence of a wave. Gardner and Worswick [1] carried out an experimental investigation and found that the angle of tire cords relative to the circumference of the tire (crown angle) was a vital factor - the lower the angle the higher is the speed at which the wave effects arise. Hysteresis in the rubber causes the wave to be heavily damped so that it extends for only a short distance round the tire. This implies that there will be no reflection of the waves in the circumferential direction.

Figure 10.1: Standing wave in a tire

Tire: 205/55R16 91V
Load = 525 kg
Initial Pressure = 2.2 bar (0.22 MPa)
Drum Radius = 2 m
Test Speed = 320 km/h

To some extent the waves are analogous to the wake behind a ship. These appear to travel through the water at a phase velocity that is the same as that of the ship. However the energy of the wave travels at a lower velocity, the group velocity, and consequently energy is carried away at a rate proportional to the difference between the two velocities.
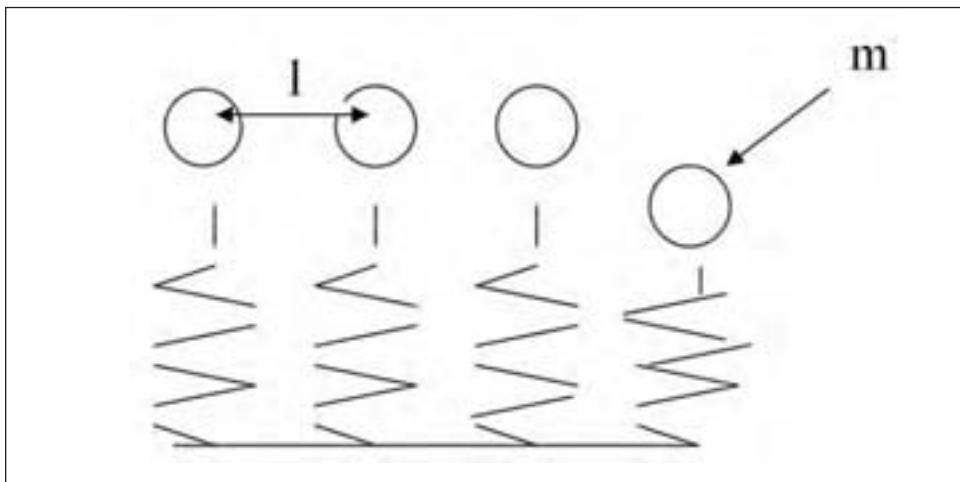
2. Wave mechanics

A tire is remarkably complex in its structure and geometry. A model embracing too many of the features becomes over-complicated and the basic understanding is lost. Here we consider three basic cases of wake formation in a wheel/tire, selected to demonstrate the principles that are involved.

2.1 Sprung mass sections

The simplest case for the formation of a wake is a wheel with a line of independent masses, each supported by a spring as illustrated in figure 10.2.

Figure 10.2: Diagram of a spring-mass system.

In figure 10.2 m represents the mass of a tire segment and l is the pitch length. The linear density is given by $\rho = m / l$. We imagine that the spring-mass system is arranged radially around a wheel of radius R that is compressed afgainst a flat surface so that an angle ϕ is subtended between the center and the end of the contact patch. V_t is the velocity of the tire. The vertical component of the velocity of the tire as it leaves the contact patch is $V_t \sin f$ but as ϕ is generally small, replacing $\sin \phi$ by ϕ is a satisfactory approximation for present purposes.

Thus tire segments leave the ground at a vertical velocity of ϕV_t with energy $\frac{1}{2} m (\phi V_t)^2$. All of this energy is eventually dissipated by damping processes in the tire. The rate of energy loss is $\frac{1}{2} m (\phi V_t)^2 V_t / l = \frac{1}{2} \rho \phi^2 V_t^3$.

If E is the elastic constant of each spring, the resonant frequency of each mass will be $F = \sqrt{(E / m)}$ and the wavelength will be $\lambda = V_t / F$. Note that this model does not predict a critical velocity that must be reached before waves can be seen or before they contribute to the power consumption.

2.2 Tensioned string

The next case to consider is the effect of interconnecting the segments with a string carrying a tension T. The velocity of a wave travelling in the string is $C = \sqrt{(T/\rho)}$. As before, rotation of the wheel takes energy away from the edge of the contact patch at a velocity V_t but the tension will cause the energy to flow back to the contact patch at a velocity C relative to the wheel. Thus the net velocity of flow of energy will be $V_t - C$ and the rate of energy loss will now be $\frac{1}{2} \rho (\phi V_t)^2 (_t - C)$. This model illustrates the effect of the critical velocity C.

Following many previous authors, Chatterjee, Cusumano and Zolock [2] used a combination of the above two models to explain the behavior of a small balloon tire for a large scale model aircraft. The model included damping and elasticity in the radial direction, and damping and shear stiffness between successive mass elements. Shear stiffness acts in a similar way to tension. The inclusion of the radial springs provides a restoring force to the elements to bring them back to their original position. However in pneumatic tires such a restoring force is provided by the lateral tension anchored by the two beads. Thus an appropriate model has to operate in a plane rather than being confined to the centre line.

2.3 Diagonal waves

"Diagonal waves" is the mechanism for waves travelling in ducts such as electromagnetic waves in a wave guide. A pair of plane waves progresses down the wave guide at an angle according to the frequency and the width of the wave guide.

This mechanism was proposed by Turner [3] to describe the propagation of a wave along a uniform flexible tensioned membrane bounded by two rigid longitudinal X and transverse Y directions. The velocity of propagation of a plane wave along the membrane is $C = \sqrt{(T/\rho)}$. T has dimensions of force per unit length and ρ of mass per unit area.

If two plane waves are transmitted simultaneously at an angle θ to the X axis there will be a symmetrical succession of peaks and troughs travelling along the centre of the membrane.

Figure 10.1 in fact exhibits clearly a fundamental wave where the whole of the tire section alternately moves outwards or inwards relative to the equilibrium position. **Figure 10.3** illustrates the formation of a fundamental wave by two intersecting plane waves with the red lines representing crests and the blue lines representing troughs. The wave fronts advance in a direction perpendicular to the wave front, i.e. from point O to point Q and from point S to P.

At the bead, where there can be no displacement, a crest is reflected as a trough and a trough as a crest. Where the crests intersect on the centre line at O and P there are peaks. Similarly an intersection of troughs creates a depression. The colored contours illustrate the effect in three dimensions.

Figure 10.3
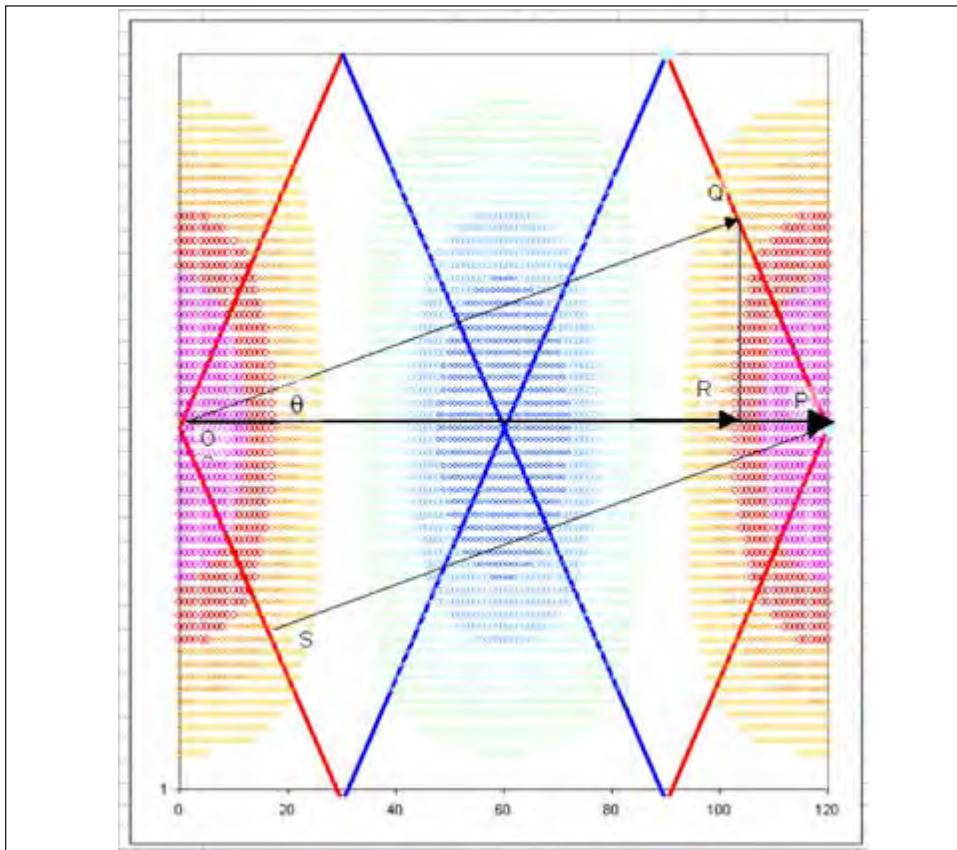
Figure 10.3: The Y axis is in the vertical direction and the X axis is horizontal. A   single cycle is illustrated and further cycles would occur along the X axis. It is seen that the displacements are greatest at the centre line and zero at the beads.

In one cycle the distance travelled by the wave front at velocity C is OQ. The distance between peaks on the centre line is the wavelength $\lambda = OP$. The phase velocity V_p is the velocity of propagation of the peak in the X direction:

$V_p = (OP/OQ) C = C /\cos \theta$. Therefore $\cos \theta = C/ V_p$.

The group velocity V_g is the velocity of flow of energy in the direction of the X axis: $V_g = (OR/OQ) C = C \cos \theta$. The wavelength $\lambda = OP = 4 B \tan \theta$, where $\tan \theta = \sqrt{((1 - \cos^2\theta)/\cos^2\theta)}$. Thus $\lambda = 4B\, V_p /C\sqrt{(1 - C^2/ V_p{}^2)}$.

So far the diaphragm has been considered to be static. However the waves are observed to be stationary *relative to the axis of the tire*. This can only happen if the velocity of the tire V_t is the same as the phase velocity V_p but in the opposite direction. This means that that wave is actually travelling through the tire towards the contact point with the road. This is illustrated in Figure 10.4.

Figure 10.4
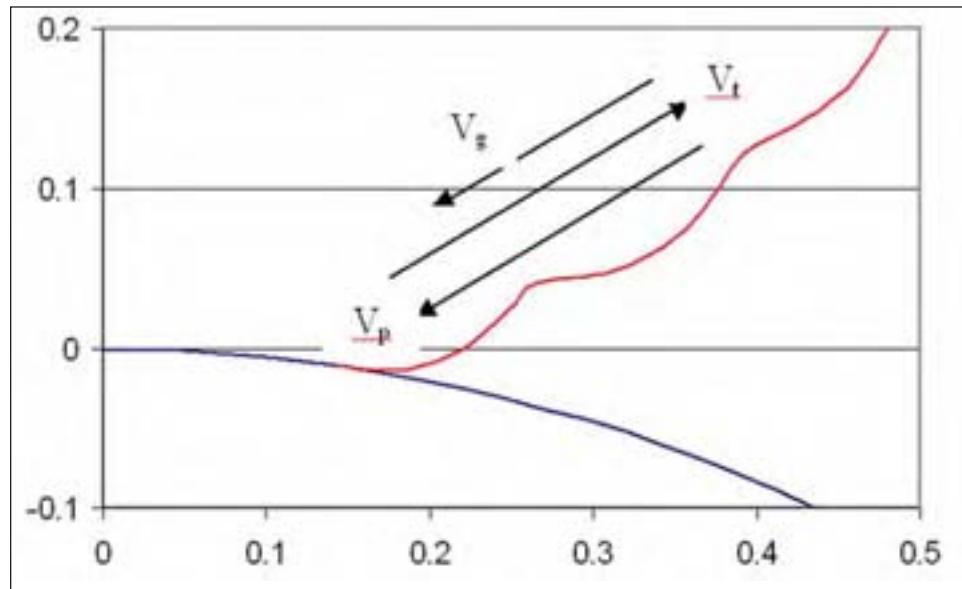
Figure 10.4: The path of the center line of the tire running on a drum at a velocity V_t that exceeds the critical velocity C for wave formation. The wave is travelling at velocity V_p where V_p is equal to the tire velocity V_t but in the opposite direction.

The speed of flow of energy away from the contact area is V_t - V_g, where V_t - $V_g = V_t - V_t \cos^2\theta = V_t (1 - C^2/V_t{}^2)$. The energy per unit length of a single diagonal wave is $\frac{1}{2} B \rho ((\phi V_t)^2$. The power consumption of a pair of waves is thus $2 (V_t - V_g) \frac{1}{2} B \rho ((\phi V_t)^2 = \phi^2 \rho B V_t (V_t{}^2 - C^2)$. Note that there is no power consumption due to the waves until the velocity of the tire V_t exceeds the critical velocity C.

3. Cross-ply tires.

A tensioned diaphragm of uniform density is a reasonable simplification for a light treaded racing motorcycle tire. The inflation pressure and the radius of curvature prevailing in the cross-section determine the lateral tension. However it is the circumferential tension that controls the critical velocity.

3.1 Cord tensions and centrifugal force

T_c and T_t are the circumferential and transverse tensions in a crossply tire. At the crown the angle of the cord to the centre line is θ. Then $T_c = T_t / \tan^2 \theta$. Also at the crown, $P = T_c / R_c + T_t / R_t$, where $T_c = P R_c /(1 + \tan^2 \theta R_c / R_t)$
and $T_t = P R_t /(1 + R_t /(R_c \tan^2 \theta)$.

The critical velocities in the two directions are $C_c = \sqrt(T_c /\rho)$ and $C_t = \sqrt(T_t /\rho)$.

This difference will cause anisotropy in the propagation of diagonal waves (not considered in the earlier treatment [3]. The main effect will be equivalent to a proportional increase in the value of the distance B from the centre line to the bead and consequently   in the wavelength.

At the crown the pressure is supplemented by centrifugal force $\rho\, V_t^2 / R$ acting radially. Then $T_c/R_c + T_t/R_t = P + \rho\, V_t^2/R_c$, where

$\quad T_c = (P\, R_c + \rho\, V_t^2)\, /(1 + \tan^2 \theta\, R_c/R_t)$.

Thus to maximise the tension T_c, R_t must be large. This is the case in the crown of wide-section low-profile tires.

Chapter 10.4 refers to networking of the cords and shows how the equilibrium shape of the casing depends on the crown angle. The lower the crown angle the squatter the equilibrium shape. Motorcycles using tires with low crown angles, inflation pressures of around 30 psi and light nylon casings won all of the Grand Prix races in the late 1950's. Thus a tire that is moulded in a squat shape with a low crown angle can be very effective. Standard 80 series low profile cross-ply tires were used very successfully for Formula Ford Racing in Europe in the 1960's. Tires for Indianapolis car and F1 racing continued the trend for low aspect ratios.

In radial tires with low profiles and very low belt angles virtually all of the centrifugal force will be contained by the circumferential tension. The additional contribution to T_c is: $T_{circ} / R_c = \rho V_t^2/ R_c$. Then $C = \surd(T_{circ} /\rho)= V_t$. Thus centrifugal force should always prevent waves from forming in radial tires. However, waves are observed near the belt edges (see figure 10.1) as discussed in section 5. Centrifugal force also reduces the angle of deflection ϕ in accordance with an effective increase in pressure.

3.2 Drum radius

The energy of the wave is controlled by the rate of separation of the tire from the road surface: $\phi\, V_t$. The drum curvature enhances ϕ by a factor of $[1 + (R_c/R_d)]$. This factor will apply directly to the amplitude of the wave and the square of this factor to the power consumption. In the case of the motorcycle tire on a drum the power was increased by a factor of 1.89. Thus to match drum results to road results the load should be reduced by $1/ \surd1.89$.

3.3 Power consumption of motorcycle tires

The 1954 paper [3] showed calculated and measured power consumptions for a racing motorcycle tire run at four different loads with tire pressures chosen to give similar values of contact length.

	Load	Pressure	Critical velocity
	lbs	psi	mph
A	230	10	50
B	280	15	59
C	330	20	68
D	380	25	77

The results are shown in figure 10.5.
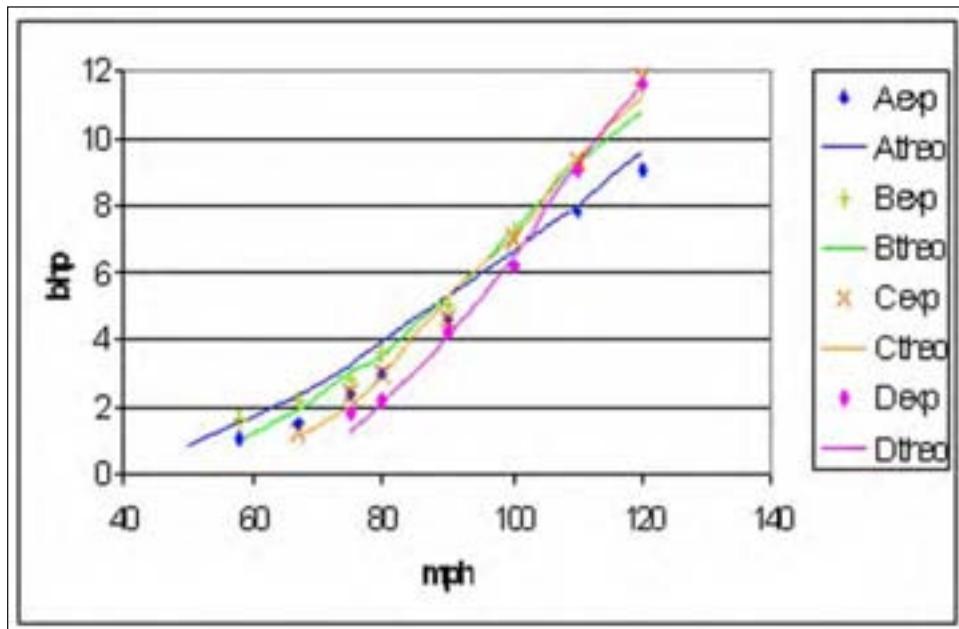
Figure 10.4

Figure 10.5: Measured (exp) and theoretical power consumptions for a 3.50-18 motorcycle racing tire [3]. An amount of 0.018 bhp per mph has been added to the theoretical power consumption as an allowance for non-wave contributions.

The motorcycle tire with a relatively light tread, a well rounded section and a low overall tire to wheel diameter ratio gives the best chance of obtaining a good match between experiment and predictions from the simple model. The present results show at least a satisfactory first approximation. A comparison between the different loading conditions is more valid. The tire with the lowest pressure has the lowest critical velocity but it also benefits most from the contribution of the centrifugal force.

4. Time domain modelling.
Akasaka [4] showed that it is necessary to ascribe different values for density and cord tension to bands across the section of the tire. He was able to make better predictions for car tires in this way but the mathematics is extremely complex and time consuming. Since then there have been similar attempts using FEA.

In recent years fantastic processing power has become available in PC's. Solutions are found by repeatedly running a program thousands of times using small time steps. With small enough steps and appropriate damping the solution converges. Such a program has been developed for waves in tires. The tire is divided up into a number of circumferential bands from the centre line of the tread to the rigid bead, each band with its own value of mass per unit area and circumferential tension. Each band is then divided up into segments, connected with its neighbours by either lateral tension or circumferential tension. Some shear stiffness may exist and this can be included by enhancing the lateral tension.

The input to the model is the radial velocity in the tire just as it leaves contact with the ground. This will vary according to the length of the contact patch and consequently ϕ.

Bands beyond the contact patch have zero input.

Parameters for the program at the current stage of development are as follows:

x is the number of the segment in the circumferential direction, starting from the edge of the contact patch.
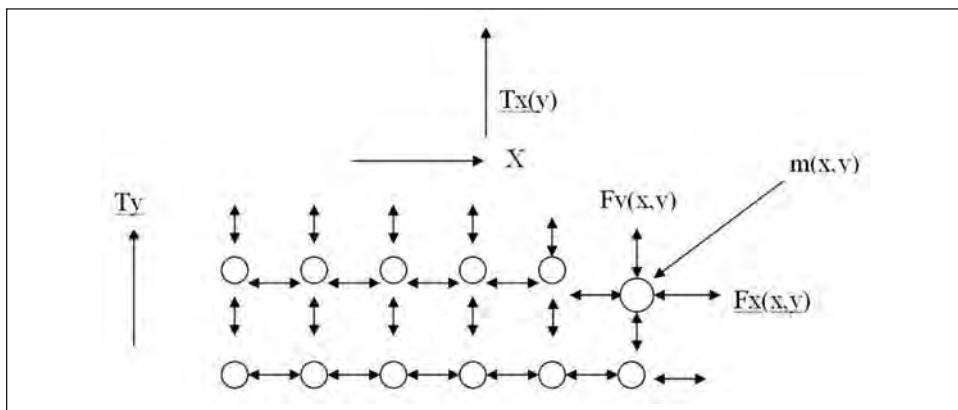
y is the number in the transverse direction, starting from the center line.

		Units
Lx = length of segment in circumferential direction		m
Ly = length of segment in transverse direction		m
e(y)= mass per unit area		kg/m^2
M(y) = ρ(y) Lx Ly = mass of a segment		kg
Tx(y) = circumferential tension		N/m
Ty = Lateral tension		N/m
Sx = Tx(y) Ly /Lx = elasticity in the circumferential direction		N/m
Sy = Ty Lx /Ly = elasticity in the transverse direction		N/m
ηx = viscous constant in the circumferential direction		Nsec/m
ηy = viscous constant in the transverse direction		Nsec/m

The last four constants relate to the forces acting on an individual segment. The viscosity constants are empirical and are chosen so that the distance the wave extends round the tire is in accord with observations.

Where there is an array (y), values for the parameter can change according to the transverse position. The derived parameters minimise the number of repeated calculations. The time step is set so that the results are stable and further reductions in the time step do not affect the result. Typically there will be 100 x steps, 10 y steps and 2000 time steps, which take only a few minutes to run on a PC.

Figure 10.6: Mass and tension network for the time domain model

Fx(x,y)and Fy(x,y) are two of the four forces acting on the segment of mass m(x,y). Fx(x-1,y) and Fy(x,y- 1) are the other two. Z(x,y) is the displacement and V(x,y) is the velocity of the segment (x,y) perpendicular to the plane of the casing.

Fx(x,y) = (Z(x+1,y) - Z(x,y)) Sx + (V(x+1,y) - V(x,y)) hx

Fy(x,y) = (Z(x,y+1) - Z(x,y)) Sy(x) + (V(x,y+1) - V(x,y))hy

$$V(x,y) = V(x,y) + ((Fx(x,y) - Fx(x-1,y) + Fy(x,y) - Fy(x,y-1))/M(y)) \, dt$$
$$Z(x,y) = Z(x,y) + V(x,y) \, dt$$
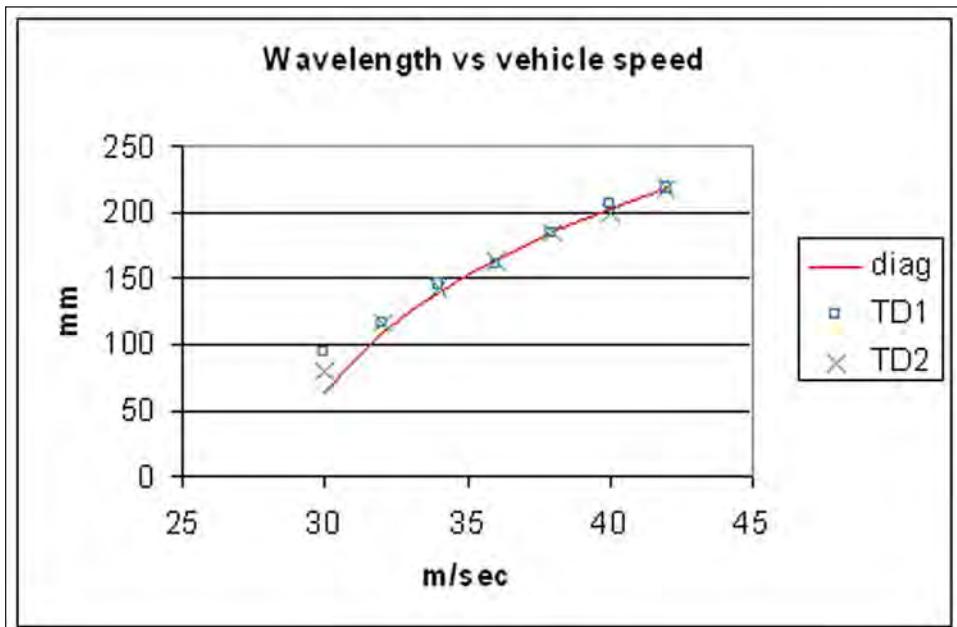
The segments are moved on by Lx when the incremental time dt is greater than the segment length divided by the velocity of the tire. Boundary conditions are set so that when x = 1 the velocities are those of the tire leaving the road (or drum) and so that there are minimal reflections at the far end. There are no forces across the centre line and no displacements at the bead.

Figure 10.7 shows a comparison of the wavelength versus velocity calculated using the diagonal wave theory and the time domain model. The agreement is exact except at the slowest vehicle velocity where the wave is highly damped and the wavelength is a little longer for the time domain model. The diagonal model had no provision for damping and the time domain model needs damping to contain the wave within the observed distance round the tire. The second time domain result, where the damping is half that of the first, illustrates that the damping is the likely factor affecting the difference in results at low velocities.

Figure 10.7. "Diag" represents results obtained by the theory. TD1 and TD2 are results from the time domain model with two different levels of damping.

Both the diagonal model and the time domain model assume that the casing lies flat in a plane. Photographs for bias-ply tires show the peaks and troughs extending from bead to bead that are consistent with a flat diaphragm. This might not have been expected for a deflected toroidal tire where the radial distance from the axis to the crown is reduced and the maximum cross-section is increased. This issue will be considered further for radial tires.

Figure 10.7

5. Radial tires

The time domain model allows the question of waves in radial tires to be tackled. In general, tires with fabric belts and folded edges or steel belted tires with cord fabric overlapping the belt do not exhibit waves. However a radial tire with a steel belt can exhibit waves that are confined to the belt edges. The photograph in Figure 1 of a 205/55R16 tire running on a drum at 320 km/h illustrates such a case. If the upper steel ply terminates before the lower steel ply at each side the tread will not be fully supported by the belt. Consequently the circumferential tension for this band will be reduced. There is no circumferential tension due to the cords in the sidewall but the shear stiffness of the sidewall rubber provides some interconnection in that direction.

The program was used to calculate vertical displacements of the 13 mm wide bands of another tire. The densities of the bands are as follows:
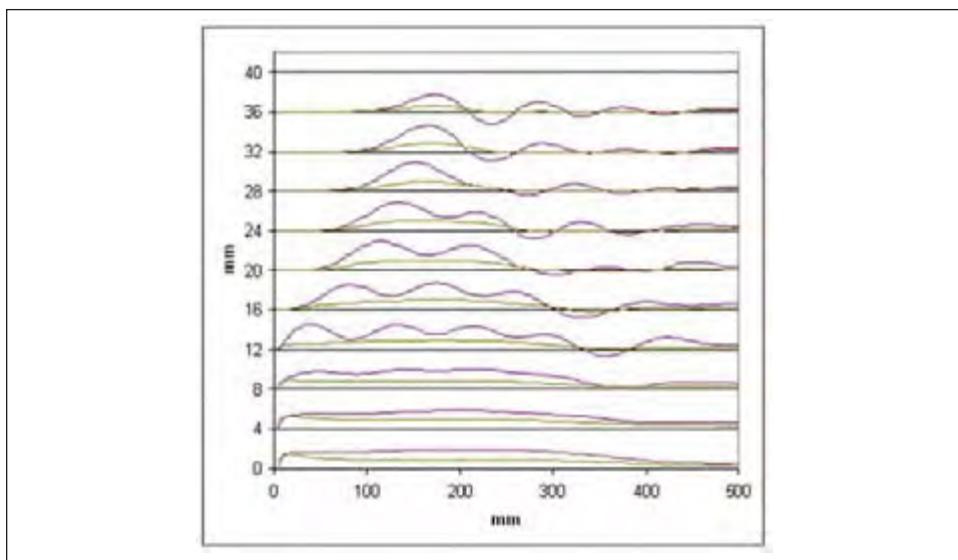
Tread	20.2	kg/m^2
Belt edge	16.5 – 11.8	kg/m^2
Sidewall	5.9	kg/m^2

The circumferential tension and relevant velocities are as follows:

Tire velocity		Circumferential tension	Critical velocity	CV (shoulder)
m/sec	kph	kN/m	m/sec	m/sec
45	162	85	65.3	35.7
5	180	94.8	68.8	37.7
55	198	105.3	72.6	39.7

Figure 8. Displacements for the tire on a drum at 50m/sec with 4 mm added progressively to the displacements for each subsequent band starting at the centre line (0) and closest to the bead (36). The green line denotes the case where the tread is fully supported by the belt. The red line is the case where the tread edge (band at 12 mm) is not fully supported and the tension in the circumferential direction is reduced by a factor of 0.3.

Figure 10.8
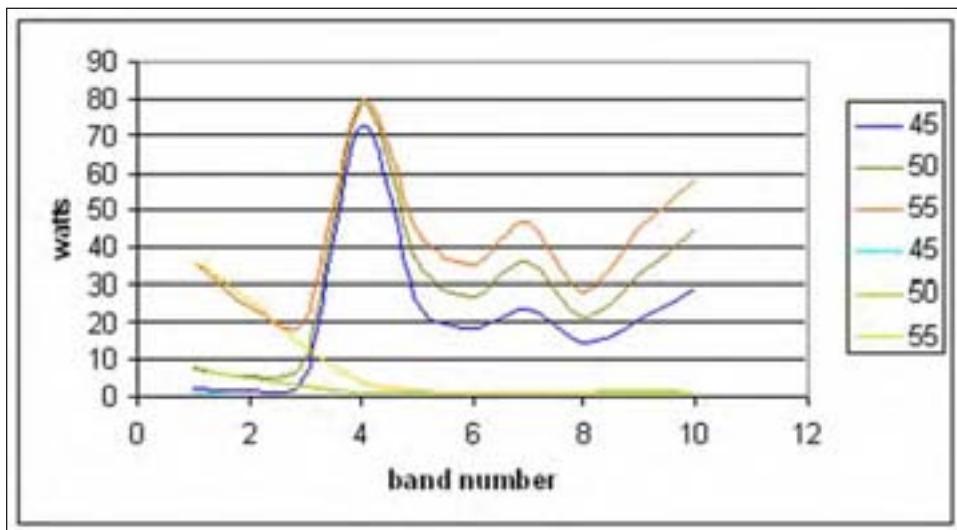
The tread edge wave is a diagonal wave. On one side a reflection is caused by the highly tensioned tread area. On the other side there will be a partial reflection due to the impedance mismatch at the interface with the sidewall and a full reflection at the bead. The wavelength of the sidewall wave differs from the tread edge wave and although initiated by the latter it will have its own regime. At present the sidewall tensions and stiffnesses to be employed are only guesses. Fitting the results to some substantial experimental data is necessary to carry the modeling further.

The energy consumed by the wave can be calculated by multiplying the force due to viscous damping by the relative velocity at each face of a segment and summing along the length for each band. Figure 9 shows the result of this operation for the case illustrated in figure 10.8.

Figure 10.9: Rate of consumption of energy in watts predicted by the time domain model for a 155/80 R13 tire on a drum at 45, 50 and 55m/sec. The dark colours are for an unsupported tread edge and the light colours for a fully supported edge.

Figure 10.9

6. Discussion

There is an indication of a second wave affecting the tread bands. It is estimated that the wavelength is about 800 mm giving a frequency of 63 Hz at a speed of 50m/sec, while the frequency at the tread edge is in the region of 550 Hz. Runs on the model over a range of speeds suggest that the frequency of the former may be constant indicating that the mechanism is of a mass, i.e. the tread and belt as a single band, supported on a spring, i.e. the sidewall, as described in section 2.2. The model covers this case but it should be noted that the spring rate due to the cord tension in the sidewall needs to be that when the sidewall is curved rather than a plane.

Concern has been expressed that the load on the tire will reduce the circumferential tension. Rough calculations on high speed tires which have low loads, high inflation pressures and high centrifugal forces indicate that they should not lose more than 10% of the tension. Dedicated numerical or FE programs are needed to provide accurate results

7. Conclusions

A proper study of standing waves in tires requires an approach that considers the tire as a surface. The mechanical properties will vary very considerably from the tread centre line to the bead. Thus a numerical approach is required. It has been shown that a model using extremely simple concepts and mathematics will cope automatically with some quite complex physics. There is considerable scope for further development of the model in response to needs arising from the operation of tires at high speeds.

It is unfortunate that the term "standing wave" has been accepted for this phenomenon. The wave is in fact a travelling wave, progressing with a phase velocity equal and opposite to that of the tire perimeter. A standing wave would only be formed if there were a reflection of the travelling wave at the far end of its path. No waves have been reported that have travelled completely around the tire and thus the resonance that causes a standing wave has not been encountered.

References
1. E. R. Gardner and T. Worswick, Trans. Instn. Rubb. Industr. **27**, 127 (1951).
2. A. Chatterjee, J. P. Cusumano and J. D. Zolock, J. Sound Vibration **227** (5), 1049-1081 (1999).
3. D. M. Turner, Proc. 3rd. Internatl. Rubber Conf., London, 1954, pp. 735-748.
4. T. Akazaka and K. Yamagishi, Trans. Jap. Soc. Aerospace Sci. **11** (18), 12-22 (1968).

Chapter 11
Rubber Friction and Tire Traction

by K. A. Grosch

Chapter 11
Rubber Friction and Tire Traction
by K. A. Grosch

Introduction

Tire traction describes the force transmitted between tire and road under all circumstances. It is a prerequisite for controlled steering, acceleration and braking of self-propelled vehicles. It finds its upper limit in the frictional force when total sliding occurs. Two aspects have therefore to be considered: The mechanics of force transmission of elastic wheels under limited slip and rubber friction.

1. Rubber friction
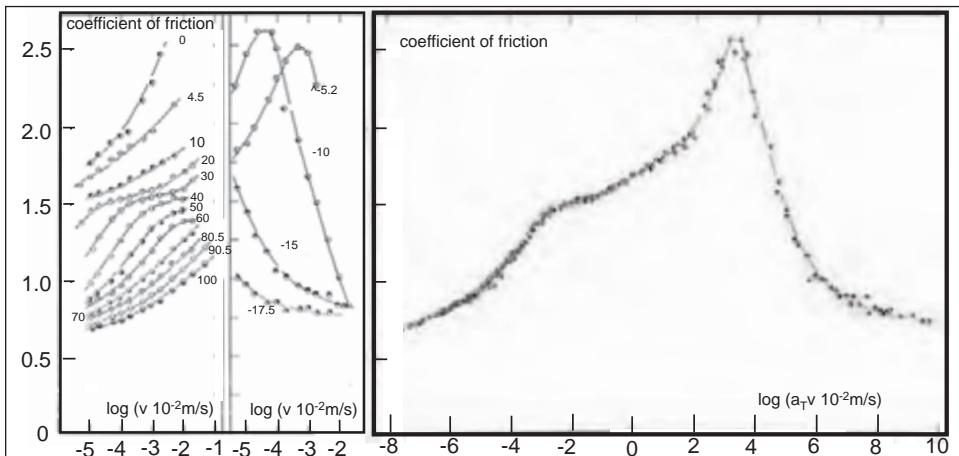
Some aspects of rubber friction are dealt with in the chapter on tire wear and abrasion. Since traction is rigorously associated with friction it is necessary to discuss the important aspects that bear on tire traction in more detail. Rubber friction differs from friction between hard solids in that it depends on the load and strongly on speed and temperature, while in hard solids it is virtually independent of these parameters [1]. The load dependence is discussed in connection with abrasion in Chapter 13, where it is shown that although the effect of load is important for soft rubbers on smooth surfaces [2,3] it is not so important for tire compounds on roads which are always sufficiently rough for the load dependence to be small [4,5]. The temperature and speed dependence of friction, however, have such a large impact on tire traction that they require a much more detailed treatment than is given in Chapter 13.

1.1 Temperature and speed dependence of rubber friction.

Rubber friction is dominated by the visco-elastic properties of the rubber. The most striking manifestation is that an equivalence exists between the effects of temperature and speed. Williams, Landel and Ferry demonstrated that this equivalence for visco-elastic properties could be described by a universal function, the famous WLF transformation equation [6]. Conceived originally for describing the viscosity of liquids [7] and later applied to the dynamic modulus of gum rubber compounds [7], tearing energy [8] and strength [9] the author has shown that it can be applied to rubber friction for both gum and filled rubber compounds [10, 11]. Generally the transform is carried out by measuring the friction coefficient over a logarithmic range of speeds, with the highest speed low enough for temperature rises in the contact patch to be negligible. The experiments are then repeated for a range of temperatures (see figure 11.1, left). If the data are plotted as function of log speed the curves for different temperatures are seen to be segments of a single, so called "master curve". This curve is obtained by horizontal displacements (shift factors) to the curve for a convenient reference temperature, as shown in figure 11.1(right) for an ABR gum compound sliding on a silicon carbide 180 track. Stable friction values are obtained as long as the slope of the curve of friction coefficient vs. log $a_T v$ (where log a_T is the shift factor) is positive. Once it turns negative, stick-slip sets in. The friction coefficient rises until a maximum value is reached and then snaps back to a very low value. The rate of increase and hence the frequency of stick-slip depends on the stiffness of the

measuring equipment, the sliding speed and the magnitude of the friction coefficient. The highest attainable friction coefficient during stick-slip is taken as representative of polymer friction in order to establish the decreasing branch of the master curve.

Figure 11.1: Experimental friction data (left) as function of log speed at different of temperatures and master curve (right) of an ABR gum compound on a clean dry silicon carbide 180 track surface referred to room temperature [from ref 11].

The corresponding log a_T curve is then superposed on the WLF function by vertical and horizontal shifts. Figure 11.2 shows the WLF equation with experimental points obtained from friction measurements for four different gum rubber compounds. From the difference between the reference temperature and the zero value of the WLF equation the Standard Reference Temperature is obtained. This is approximately $T_g + 50^O$C, where T_g is the glass transition temperature of the elastomer. Table 11.1 compares the actual standard reference temperatures obtained from friction measurements with values of $T_g + 50$ ^{O}C. The deviation for the friction experiments is generally less than 5°C. Hence the master curve can also be constructed using the WLF equation with a Standard Reference Temperature of $T_s = T_g + 50$ to calculate the required shift factors. This may not be quite as accurate as the actual shifting procedure but is much less tedious and generally leads to very good results.

Figure 11.2: Shift factors fitted to the WLF equation of four different gum compounds on a silicon carbide 180 track [from ref 11].
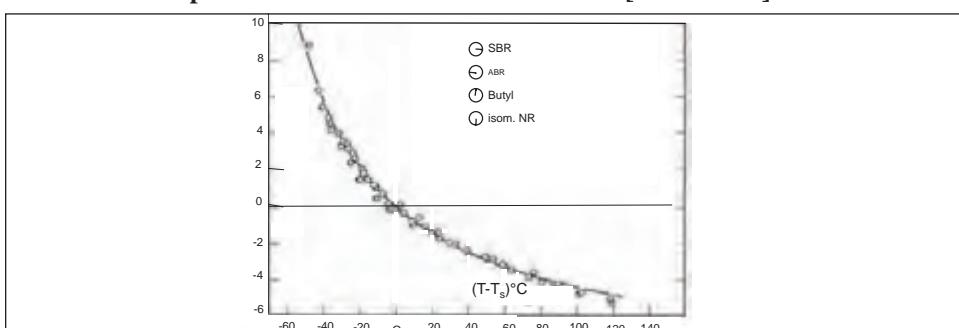
Table 11.1: Comparison of standard reference temperatures obtained by fitting the shift function (shift factors vs. T - To) to the WLF equation with values for Tg + 50 [from ref 11]; shear modulus measured with a torsion pendulum*.

Comp.	Polymer	Parts of black	T_s from friction measurements on			T_s from shear modulus*)	T_g+50
			silicon carbide 180 clean	silicon carbide 180 dusted	glass		
A	SBR	0	+8	+8	0	3	5.4
		50	+9				
B	ABR	0	+33	+33	+30		
		20	+33	+31	+24		+28.6
		50	+35				
C	Butyl	0	-21	-25	-20		-21.6
		50	-20				-30
D	NR	0		-20		-21	-21
		50					
E	isom NR(40%)	0					
		50	-21	-25	-20	-21	-21

Master curves of the friction coefficient have been obtained for a wide range of rubber compounds on different types of track and for dry and wet surfaces. The technique would undoubtedly also function for sliding on ice. However, because ice is generally close to its melting point it displays special properties that influence the friction of rubber in contact with it. In addition the temperature in the contact area cannot rise above 0°C.

The shape of the master curve and its position on the log a_Tv axis depends both on the rubber compound and on the structure of the track surface. If it can be obtained, it contains all the friction information for a rubber on a particular surface. Slight deviations have been observed recently for complex tire tread compounds. These will be discussed towards the end of this chapter.
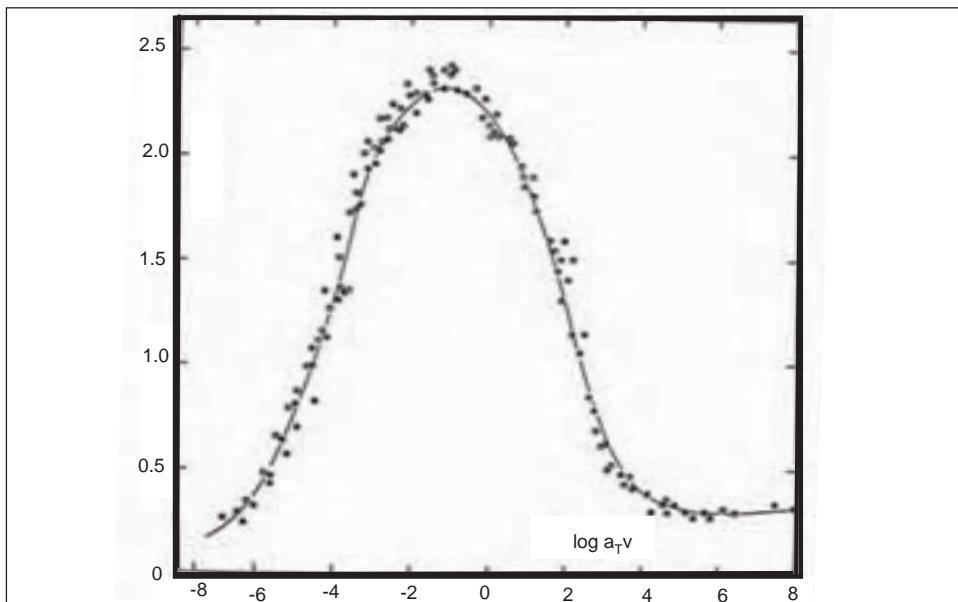
1.1.1 The master curve on smooth and rough surfaces.
On dry, clean polished glass the friction master curve for gum rubbers rises from very small values at low values of log a_Tv to a maximum, which may reach a friction coefficient of more than 3, and then falls at high log a_Tv to values which are normally associated with hard materials, about 0.3, as shown for an ABR gum compound in figure 11.3. If the position of the maximum on the log a_Tv axis for different gum rubbers is compared with that of the maximum in a curve of log E″ vs. log a_Tf, where f is the deformation frequency, a constant length l of molecular dimensions (6×10^{-9} m) is obtained, indicating that the friction arises from molecular adhesion. Schallamach explained the behavior in terms of a relaxation process, considering both the making and breaking of adhesion bonds as activated dynamic processes [12]. The correspondence between the positions of maximum friction and the maximum in log E″ arises not because the visco-elastic quantity E″ itself is important but because the maximum in E″ represents the maximum in the relaxation spectrum of the rubber. Exactly the same length l would have been obtained if the first derivative of the real part of the dynamic modulus E′ had been used for the comparison.

On comparing figure 11.3 with figure 11.1 it will be noticed that at low values of log a_Tv the friction coefficient is much higher on the rough silicon carbide track than on the smooth surface. It appears to pass through a maximum, or rather a hump, at approximate-

ly the same log $a_T v$ position as for the same compound on glass. However, it then rises further to reach a maximum similar in height to that on the glass surface but at a much higher value of log $a_T v$. If the rough track is dusted with a fine powder, preferably magnesium oxide, the hump disappears but the larger maximum remains virtually unchanged, at the same height and in the same position as on the clean surface. The presence of fine powder has impaired the molecular adhesion between rubber and track. This is confirmed if the friction of a dusted sample is measured on glass. In this case the friction coefficient remains low at a value of about 0.2 for all temperatures and speeds.

Figure 11.3: Master curve of the friction coefficient of an ABR gum compound on smooth clean dry glass, referred to room temperature. [from ref 10]
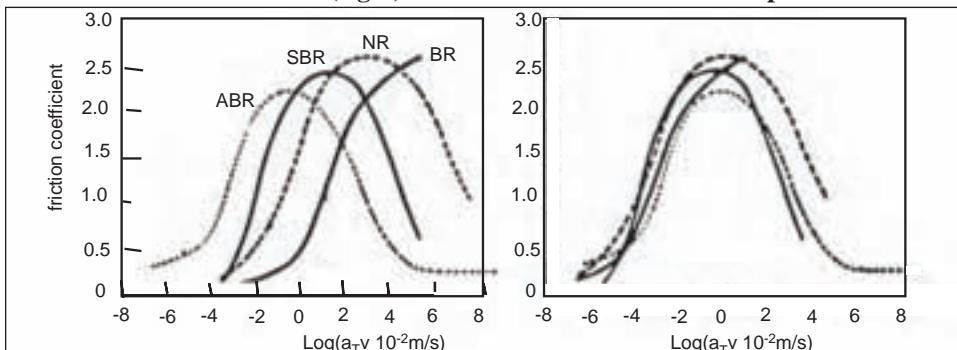
The value of log $a_T v$ at which friction is a maximum for sliding on silicon carbide bears a constant relation to the frequency of the maximum loss angle of the material, indicating that this friction process is based on a classic cyclic hysteresis loss mechanism. The constant length of 5×10^{-4} m that relates sliding speed and deformation frequency is consistent with the spacing of the track asperities. A number of authors have published theoretical treatments of this mechanism of friction due to deformational hysteresis [13, 14, 15]. It is important to bear in mind that adhesion also plays a major role. Purely vertical deformations lead to friction values that are much too small [16]. The fact that friction on a dusted track is still high at very low log $a_T v$ values, a range where the adhesion is also low, suggests that quite a small adhesion component is sufficient to produce large local tangential stresses in the rubber at the contact points with track asperities, as is also borne out by the occurrence of abrasion. This is discussed in more detail in Chapter 13. These tangential deformations cause elastic energy to be stored that cannot be returned to the rubber on release and is therefore dissipated as heat, akin to an adiabatic process in thermo-dynamics, leading to the high friction observed in the region of low log $a_T v$ values where hysteretic and adhesion losses are low.

1.1.2   The polymer effect on the master curve.

The friction master curves for gum rubbers all have a similar shape on smooth surfaces and exhibit a single maximum of about the same height. They differ essentially in their position on the log $a_T v$ axis. If the curves are referred to a constant reference temperature, say 20°C, the position of the maximum moves further towards lower log $a_T v$ values the higher the glass transition temperature of the elastomer. If they are referred to their standard reference temperatures or to the glass transition temperature the maxima occur at almost the same log $a_T v$, as shown in figure 11.4. Hence the principal difference in friction behavior on smooth surfaces stems from the difference in their glass transition temperatures.

Figure 11.4: The position of different gum rubbers on the log $a_T v$ axis (left) referred to 20°C and (right) to their standard reference temperatures.

The adhesion and deformation mechanisms of friction are related to the relaxation spectrum and loss factor, respectively. Thus the shape of the friction master curve on rough surfaces depends on the difference between the position of maximum loss modulus and maximum loss factor. The smaller this difference is, the broader the friction master curve on rough surfaces. For smooth surfaces the following relation holds for all polymers between log $a_T v$ for maximum friction and log $a_T f$ for maximum loss modulus
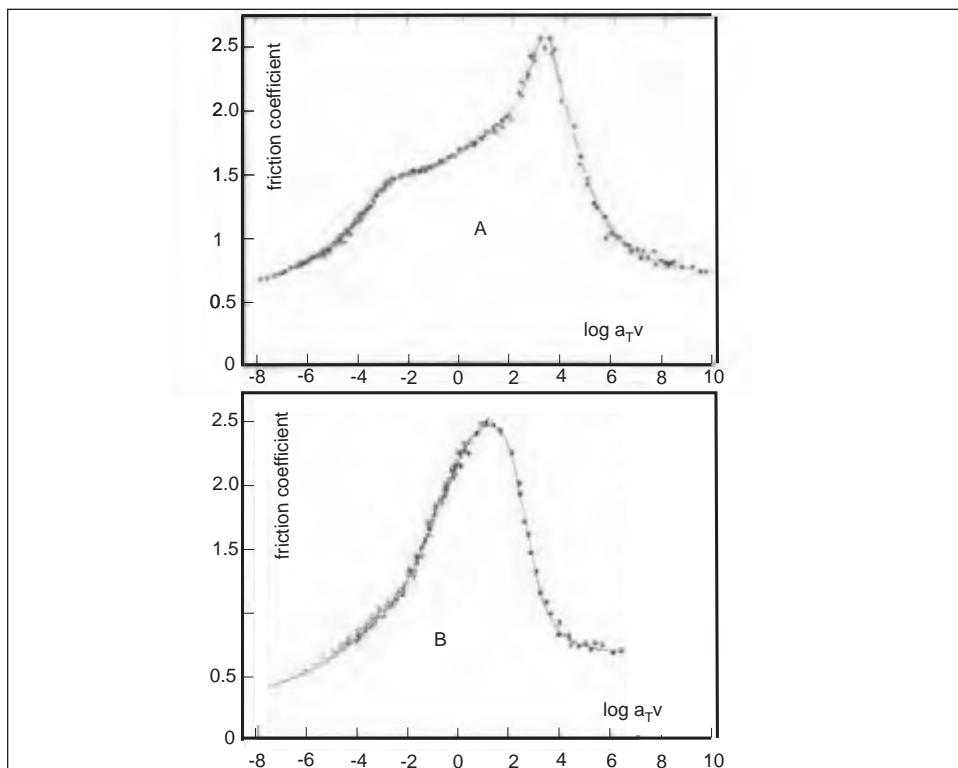
$$\left[\log(a_T v)\right]_{smooth} - \left[\log(a_T f)\right]_{E''} = -9.22 \qquad [1a]$$

For the rough surfaces the following relation holds:

$$\left[\log(a_T v)\right]_{rough} - \left[\log(a_T f)\right]_{\tan\delta} = -3.8 \qquad [1b]$$

From this it follows that, if the difference between the two log frequencies of the dynamic properties is small, the difference between the two log speeds of the friction master curve must be large, which is indeed the case. For ABR, for example, the difference between the two log frequencies is small and hence the difference between the two log speeds of maximum adhesion friction and deformation friction is large. For butyl rubber exactly the opposite is true and the difference between adhesion and deformation friction is so small that it cannot be distinguished. The shape of these two master curves are compared in figure 11.5 where results are shown for a gum ABR and butyl rubber sliding on a silicon carbide 180 track.

Figure 11.5: Comparison of the master curves of an ABR gum compound (upper) with a Butyl gum compound (lower) both on 180 clean silicon carbide.

1.1.3 Effect of filler and oil extension on the shape of the master curve.

The unfilled compounds used above to demonstrate the influence of polymer and track surfaces are too soft to be used in tires. Tire compounds invariably contain a considerable amount of filler, predominantly carbon black but increasingly also silica. Addition of filler does not affect the WLF speed - temperature equivalence but changes the shape of the friction master curve considerably.

Figure 11.6 shows the master curves for an ABR compound (a) unfilled, (b) filled with 20 parts of carbon black per hundred of rubber by weight (pphr) and (c) with 50 pphr of carbon black, sliding on smooth glass and on a dusted and a clean silicon carbide track. On glass the curves for gum and filled rubbers have a similar shape, the single maximum, however, is reduced progressively as the filler content is increased. It also shifts slightly towards lower speeds. On the two rough tracks the deformation friction maximum also decreases with increasing amount of black. On the clean rough track the deformation peak has decreased to the same level as the vestiges of the adhesion maximum so that a broad plateau appears between the maxima for the adhesion and deformation friction components maxima when 50 parts of black have been added.

On the dusted track the adhesion friction component is clearly lower for all three compounds when comparing the results with the master curves obtained on a clean track

The friction plateau observed for the compounds filled with 50 parts of black (which

is typical for tire tread compounds) is found for most elastomers, as shown in figure 11.7. The width of the plateau depends on the difference between the frequencies of maximum loss modulus and loss factor as explained above. If this difference is small, the plateau is broad; if the difference is large, the plateau becomes narrow. For butyl it is non-existent and only a single distinct maximum is displayed.

Figure 11.6: Master curves on smooth, wavy glass, on a silicon carbide track dusted with magnesium oxide and on a clean silicon carbide track of three ABR compounds: unfilled, filled with 20 pphr carbon black and 50 pphr respectively [from ref 11].
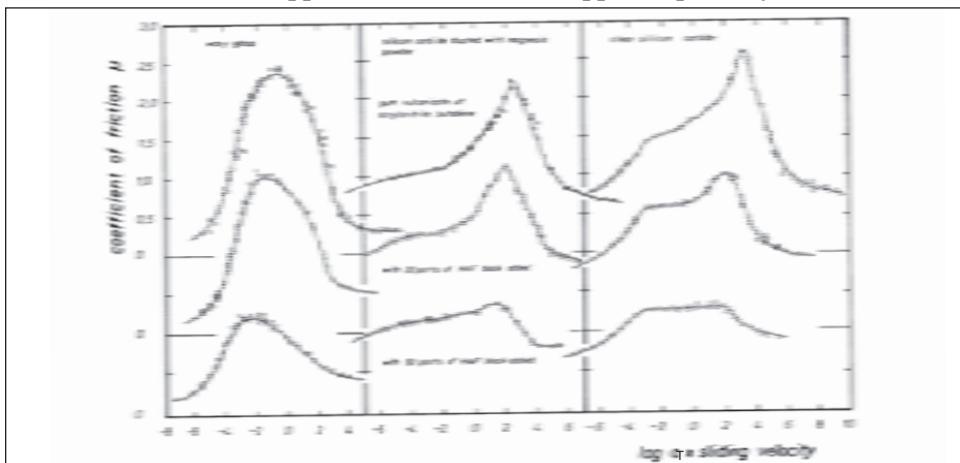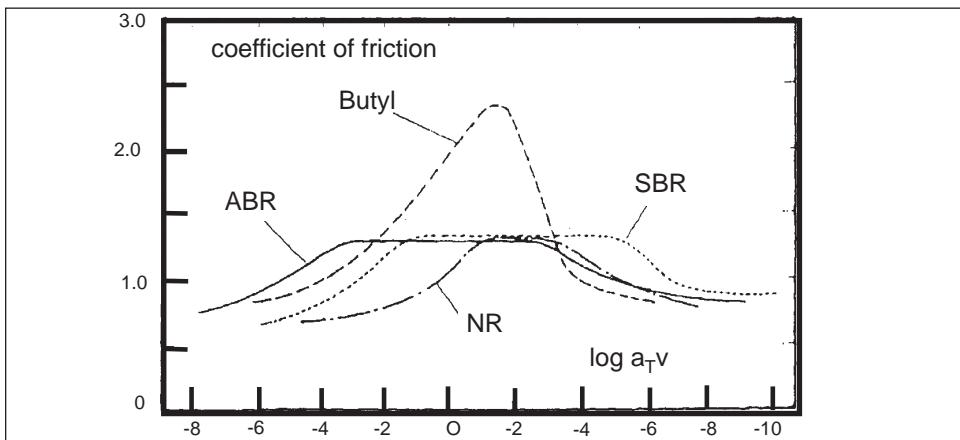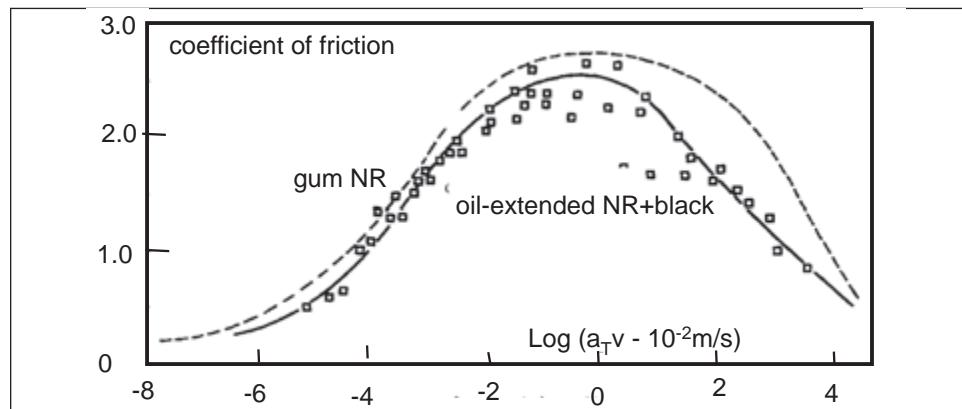
Figure 11.7: Master curves of different types of polymer all filled with 50 parts of carbon black referred to 20 °C (from ref 10]

If oil is added to the compound during mixing and the carbon black level is adjusted to maintain the same hardness, the master curve on glass displays a maximum that is only a little lower than for the gum rubber, as shown in figure 11.8 for an oil-extended black filled NR. The dotted line indicates the master curve of the gum rubber. It is a general experience in compounding tire treads that incorporating oil with raised black levels to maintain the same hardness causes the friction coefficient to be increased significantly.

Figure 11.8: Master curve of a black-filled, oil-extended NR tire tread compound on smooth glass. Also shown is the master curve of unfilled NR (dotted line) [from ref 5]

1.2 The friction master curve on wet tracks

If friction coefficients are measured on wet, rough surfaces at different water temperatures over a range of logarithmically-spaced speeds, keeping the highest speed low, the data can be assembled into a master curve as before. This is shown in figure 11.9 where results are plotted for an unfilled ABR compound of the same formulation as used previously on dry silicon carbide tracks. In the present case sliding took place on an Alumina 180 grindstone surface lubricated with distilled water and water with 5% detergent added, respectively. Comparison with the friction master curve obtained on the dry track shows that the same features are displayed when distilled water is used [17]. Friction reaches a peak at the same value of log $a_T v$ and the adhesion hump is also clearly visible. However, if detergent is added to the water, this hump disappears. A similar effect was observed when dry tracks were dusted with magnesia. Roberts [18] has shown that when a rubber sphere approaches a wet glass plate the water tends to aggregate into globules in the contact area leaving regions that are virtually dry as shown in the photograph of figure 11.10 (left) where measurements of the height of the water globules are also shown. In contrast, if a detergent was added to the water a very thin uniform film was maintained over the whole contact area up to very high pressures (figure 11.10, right). Friction on wet tracks appears therefore to be similar to dry friction but at a lower level. Because the real contact area is reduced by the presence of the water globules the frictional force is reduced accordingly, the water globules carrying some of the normal load. The total friction is then due to adhesion in the dry regions where deformation friction is enhanced by tangential stresses set up in the rubber as well as by normal deformation. Even in the presence of the detergent and hence presumably in the absence of dry regions, friction is still very much higher than would be expected solely from energy losses in normal compressive deformations so that tangential stresses must also be present in the contact area. The thickness of the continuous film is so small – Roberts's measurements indicate a thickness of about 1.5×10^{-8} m – that some form of molecular adhesion must still be present. Only the visco-elastic contribution of the rubber has been impaired, as when powder is applied to a dry track. Figure 11.11 demonstrates this similarity between dry and wet friction by comparing directly the master curves of the ABR gum rubber on (a) dry glass, (b) dry clean silicon carbide, (c)

dry silicon carbide dusted with magnesium oxide powder (d) an alumina track wetted with distilled water and (e) wetted with water + 5% detergent.

**Figure 11.9: Friction master curve of an ABR gum
compound on an Alumina 180 wet surface: (a) wetted
with distilled water and (b) with 5% detergent added to the water [from ref. 17]**
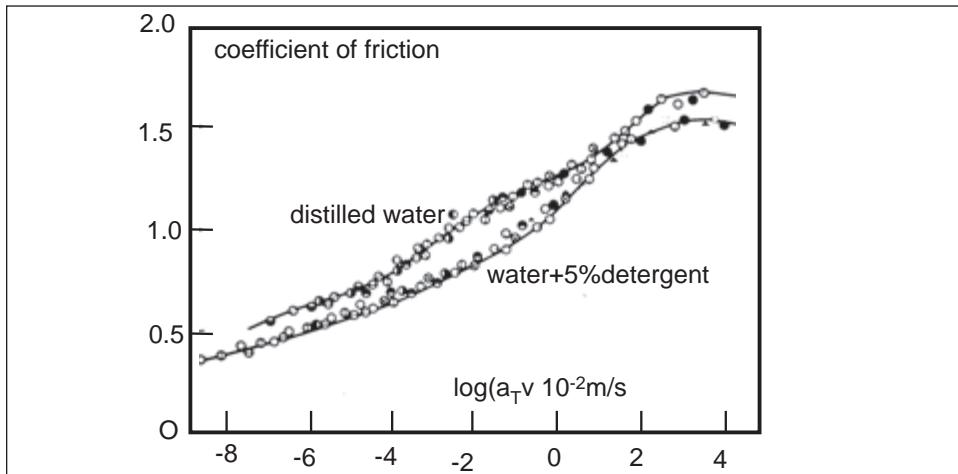

**Figure 11.10: Interference fringes and the corresponding
contour diagrams for contact of a rubber sphere and a
glass plate when (left) wetted with distilled water and (right) with added
detergent. The distilled water collects into globules leaving virtually dry
regions while a thin continuous film forms when detergent is added [from ref. 18]**
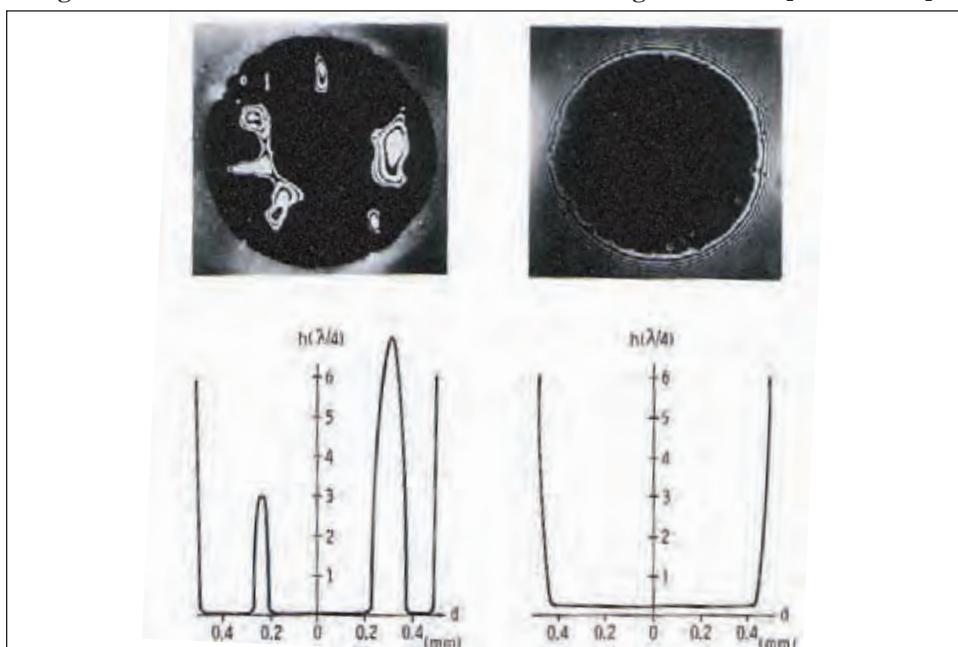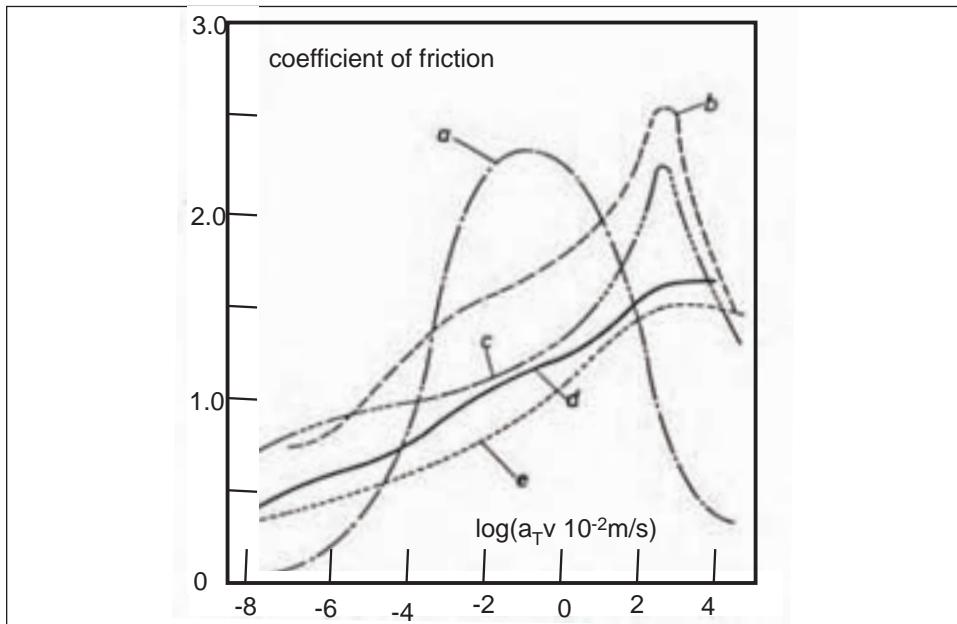
Figure 11.11: Friction master curves of ABR gum rubber on (a) dry glass, (b) dry clean silicon carbide 180, (c) dry silicon carbide dusted with magnesium oxide powder (d) Alumina 180 wetted with distilled water and (e) wetted with water + 5% detergent.

1.3 Water lubrication effects on rubber friction

There are two effects that reduce friction between rubber and a wet surface. One is classical lubrication as in the case of shafts rotating in bearings lubricated with oils and greases, i.e. with liquids having a high viscosity. In this case, lubrication is intentional. In rubber friction on wet surfaces, on the other hand, efforts are made to reduce lubrication. Fortunately water has a low viscosity.

The other effect of the presence of water is due to its inertia. When tires roll or slide on a wet road the water has to be displaced – squeezed – out of the contact area against its own inertia. This is required both when a tire rolls freely as well as when partial or total sliding occurs.

Consider first lubrication in sliding: If a rectangular hard slab slides over a hard, flat and wet surface at a velocity v and if it can rotate freely around an axis parallel to its plane and normal to the sliding direction then a wedge-shaped film of water forms between the two hard surfaces separating them through the normal pressure generated by the velocity gradient between the front and the rear of the tilted plate in the sliding direction. This is the basis of sliding lubrication. For a detailed treatment consult reference [19]. The minimum film thickness at the end of the slider is given by
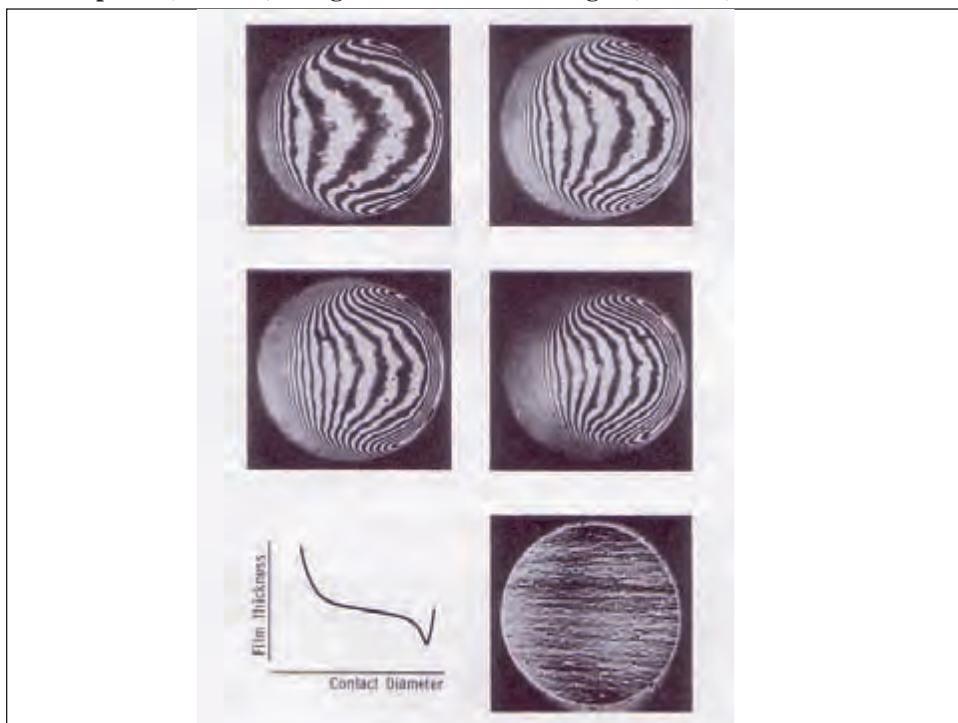
$h = \text{const.} \ (a^2 b \eta v/L)^{1/2}$ [2]

where a and b are the dimensions of the slab in and vertical to the sliding direction respectively, η is the viscosity of water, v is the sliding speed and L is the load acting on the slab. Of particular interest here is the case when a soft rubber slides over a hard smooth surface. In this case a wedge shaped film forms even when the bodies slide nominally par-

allel to each other, because the rubber will deform under the hydrodynamic pressure. Roberts [18] has demonstrated this convincingly by letting a rubber sphere slide over a smooth glass surface lubricated with a silicon oil film. His results are shown in figure 11.12. The Newtonian fringes represent lines of equal height; the central contour line is shown at the bottom left. For the case of a rubber cylinder sliding on a flat hard surface, the average film thickness is given by Archard and Kirk [20] as
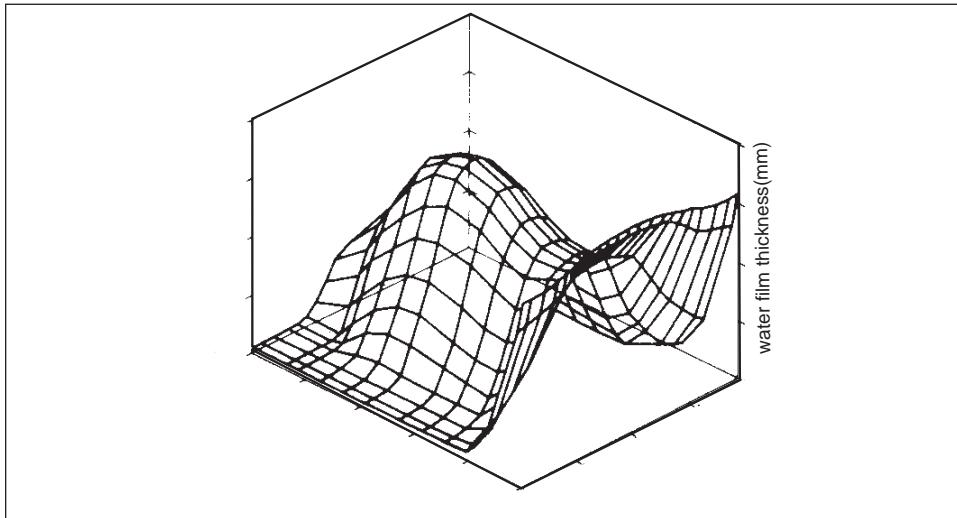
$$h = 0.9\left[\frac{\eta\, vR}{E}\right]^{1/2} \qquad [3]$$

Figure 11.12: Newton's fringes used to measure the film thickness and deformation of a rubber sphere sliding at different speeds over a smooth glass plate lubricated with silicon oil. The graph at bottom left shows the center contour line of the rubber sphere (ordinate) along the center contact length (abscissa) [from ref.18]

where R is the radius of the rubber cylinder and E is the modulus of the rubber. From dimensional considerations a similar relation should also hold when a hard solid sphere slides on a soft rubber surface. A typical water film thickness map under a smooth tire sliding over a wet hard surface is shown in figure 11.13 [21].

Figure 11.13: Water film thickness in the contact area of a smooth tire sliding over a hard surface; v = 68 km/h; inflation pressure = 1.3 bar [from ref 21]

Assuming that the frictional force F will be proportional to the effective dry area of contact A_d

$$F = const \cdot A_d \qquad [4]$$

and assuming that the roughness of the hard surface - micro or otherwise – can be represented by spheres of radius r, and that the average thickness h of the lubricating film at the sliding velocity v is smaller than r, the dry contact area penetrating through the film is

$$A_d = n\pi r^2 \left(1 - \frac{h}{r}\right) \qquad [5]$$

where n is the number of spheres in the contact area. Using equation 2 for the film thickness, the friction coefficient m can be written as

$$\mu = \frac{F}{L} = \frac{const}{L}\left[1 - \left(\frac{a^2 b \eta v}{L r^2}\right)^{1/2}\right] \qquad [6]$$

or with equation 3

$$\mu = \frac{F}{L} = \frac{const}{L}\left[1 - 0.9\left(\frac{R \eta v}{E r^2}\right)^{1/2}\right] \qquad [7]$$

The speed dependence follows then in the form
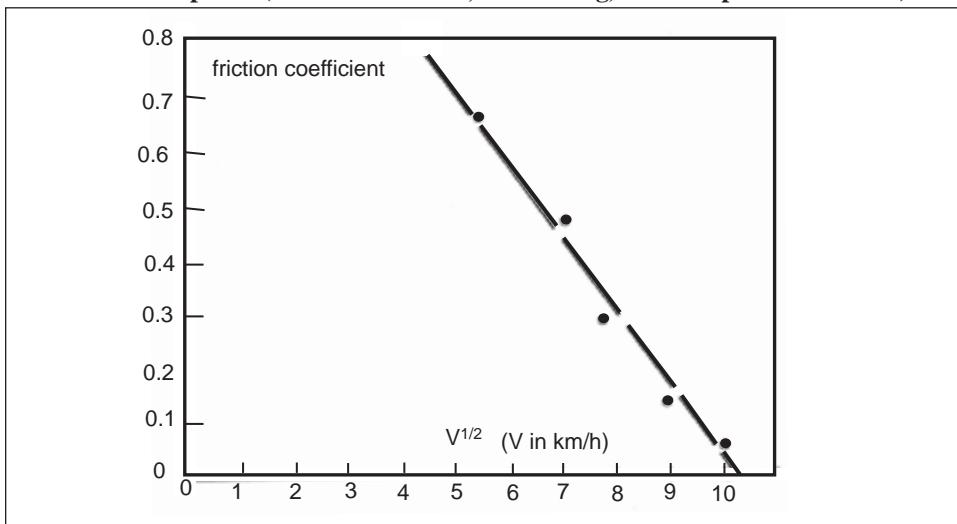
$$\mu = \mu_d\left[1 - \left(\frac{v}{v_{crit}}\right)^{1/2}\right] \qquad [8]$$

where μ_d is the coefficient of friction on a dry track and v_{crit} is the speed at which the friction coefficient becomes zero, i.e. when perfect lubrication is achieved. The value of v_{crit} depends on which model is used to calculate it. And, in practice, the friction does not

become zero. A small frictional force remains because of the resistance to displacing the bulge of excess water that is created in front of the tire or sample. Also, of course, the model simplifies the road surface structure. In reality the road surface contains particles of different size and shape having different contact radii and different height. In addition the asperities themselves often have a micro roughness. [22-25].
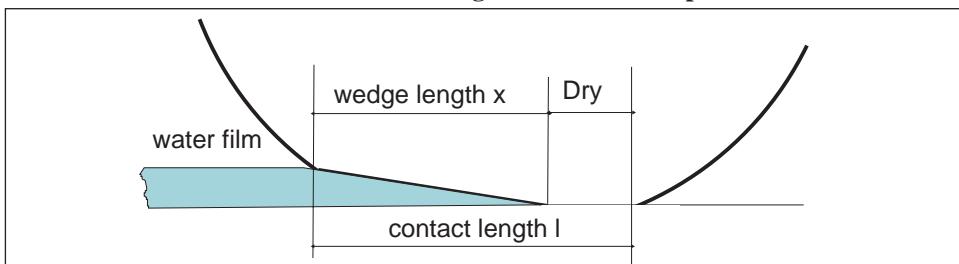
The theoretical considerations outlined above suggest that in lubricated sliding the friction coefficient should decrease with the square root of the speed. Practically all friction measurements on wet tracks in the speed range where hydro-dynamic lubrication occurs are in the form of tire skid measurements. They will be discussed in greater detail in section 2.2. Only one instance will be discussed here. Figure 11.14 shows the results of a braking test for a smooth tire on wet finely-structured concrete. The friction coefficient was measured as function of the speed after the wheels had been locked. Plotting the data as a function of the square root of the speed results in a straight line graph with an extrapolated value of the abscissa at zero friction coefficient of 10.2, corresponding to a critical speed of 104 km/h. The intercept at zero gives a dry friction coefficient of 1.35, which is very close to what would be expected from laboratory measurements of tread compounds on rough surfaces. The critical speed can be related to the roughness of the track. Using equation 2 with a = 0.12 m, b = 0.15 m, L = 3500 N, v_{crit} = 28.9 m/s and η = 1.01×10^{-3} N.s/m^2, the radius of the track asperities is obtained as r = 0.13 mm. If the calculation is based on equation 3, using R = 0.31 m as the radius of the tire, E = 24 N/mm^2 and the viscosity as given above, the asperity radius r is obtained as r = 0.21 mm. Although the two values differ by almost a factor of 2, both are close to reality. In any case equation 6 successfully describes water lubrication between rubber and a rough track using two measurable quantities: the dry friction coefficient and a critical speed at which the friction becomes zero, two very useful quantities to judge the wet traction behavior of tires on a particular road surface. Notice that in this model the water film thickness does not enter directly into the calculations – it appears indirectly in the critical sliding speed.

**Figure 11.14: Locked wheel braking coefficients of a tire with a
smooth tread on a wet polished concrete track as a function of the square
root of the speed. (Tire size 175 R 14, load 350 kg, inflation pressure 1.9 bar)**

Consider now the effect of the inertia of the water. This plays no part in laboratory experiments with test samples but it always manifests itself in tire use. It will be discussed here to complete the discussion of models that predict the effect of water on friction. The inertia effect is associated with aquaplaning. It has been discussed extensively by R. W. Yeager [26]. In aquaplaning the thickness of the water film is greater than the height of the asperities and water has to be squeezed out of the contact area. As a point on the rubber surface moves through the contact area it sinks through the water film until it makes contact with the tips of the asperities at a distance x along the contact patch (see figure 11.15). This length x is proportional to the sink time t_a which is itself a function of the water height above the asperities and to the speed v_f of the vehicle

Figure 11.15: Sketch of a water wedge forming in the front part of the contact area of a tire rolling on a wet road with a water film thickness rising above the road asperities.

$x = v_f t_a$ [9]

With increasing speed the point at which dry contact is made moves further along the contact patch reducing thereby the extent of dry contact and hence the friction. When the speed is so high or the sink time is so long that even at the end of the contact patch (of length l) the water cannot be removed, then all frictional contact is lost and with it the steering and braking/accelerating capability of the vehicle.

The first experimental and theoretical attempts to describe this phenomenon were made by Saal [27]. A number of other authors have described experimental procedures and other theoretical models [28,29]. The very brief and simple approach to be presented here is based on Barthelt's theory [30]. Under a given set of conditions determined by road surface structure, state and design of the tire, in particular the tread pattern, and the water level on the road, let the length of the dry contact region be l - x. Part of the load on the tire, proportional to x, will be carried by the water film and will not contribute to the frictional force required to drive, brake or steer the tire. The frictional force F_W will then be given by

$F_W = \mu_{dry} R_d$ [10]

where R_d is the reaction force of the "dry" contact area. This can be deduced from the wedge length x and contact length l as

$$R_d = \frac{l-x}{l} \cdot L \quad [11]$$

where L is the normal load on the tire.

Aquaplaning occurs when the water film length becomes equal to the contact length l

where

$$1 = v_{aq} t_c \quad [12]$$

Combining these equations leads to

$$\mu = \mu_o \left(1 - \frac{v_f}{v_{aq}}\right), \quad [13]$$

where v_{aq} is the critical speed at which contact is lost. This depends on the road surface conditions including the height of the water level above the road asperities and tire properties such as tread pattern design and the condition of the tire, primarily the available void volume of the tire tread.

Using the Barthelt model and neglecting secondary terms like the influence of water outside the contact area, the aquaplaning speed v_{aq} can be written as

$$v_{aq} = f(\text{tire}) \cdot g(\text{road}) \quad [14]$$

The tire function is given by

$$f(\text{tire}) = \sqrt{\frac{12 p_m}{\rho} \frac{l_m}{b_m}} \quad [15]$$

where p_m is the mean ground pressure which is about equal to the inflation pressure of the tire, ρ is the density of the water, l_m and b_m are the contact length and width respectively.

The function f is itself a characteristic speed of the tire. For a smooth passenger tire of width 205 mm and an inflation pressure of 2.5 bar, the contact width and length are both about 0.18 m. Hence the characteristic speed in this case is 55 m/s, i.e. 198 km/h.

The road function is characterized by two heights, h_r which is a measure of the structure of the road surface and h_o, which is the water film thickness above the height h_r

$$g(\text{road}) = (1n(k_s))^{-1} \quad [16]$$

with

$$k_s = \left\{ \frac{h_o}{h_r} + \sqrt{\left[\frac{h_o}{h_r}\right]^2 - 1} \right\} \quad [17]$$

Note that equation 17 is valid only for films of water with thickness $h_o > h_r$. If $h_r = 0.5$ mm and $h_o = 2.0$ mm, corresponding to quite a large film thickness on a relatively smooth surface, then g(road) = 0.48 and the aquaplaning speed for the smooth tire would be 96 km/h. With a tread pattern, the contact width is reduced to the rib width and the aquaplaning speed increases dramatically, provided the water level is such that the void volume of the tread pattern is not completely filled.
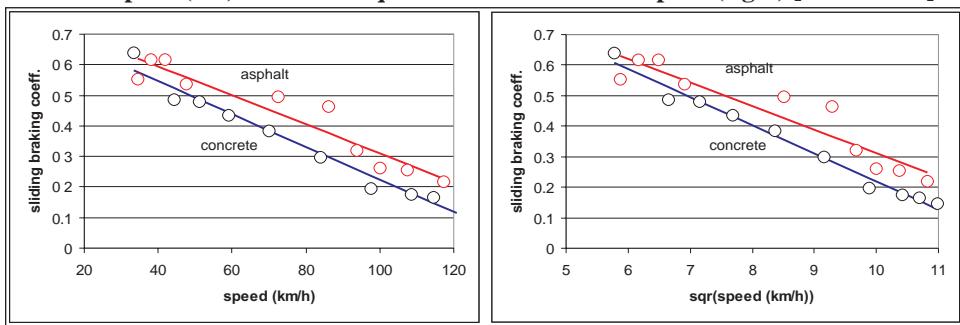
The sink time of equation [12] is made up of two additive terms. One acts until the voids of the tire have been filled with water and the second term is that for a smooth tire to which the tread pattern degenerates when the voids are filled. During free rolling the available frictional force is determined by the forward and the aquaplaning speed. If forces are transmitted, sliding lubrication sets in and the friction coefficient, modified by sliding lubrication, limits the maximum force transmission further. The factor μ_o of equation [13] contains the temperature and speed dependence of the friction coefficient and the effect due to sliding lubrication. Which of the two lubrication contributions dominates depends on the external conditions. If the water level is small, sliding lubrication is the

most important contributing factor. Inertial resistance to displacement of the water becomes important only if the water level is above the tips of the asperities and then it depends on the tread pattern.

Experimentally, the aquaplaning speed can only be determined during free rolling. It becomes apparent when the forward speed and circumferential speed of the free rolling tire become different.

Braking tests on wet tracks of proving grounds occasionally show a linear decrease in braking ability with increasing speed [31,32], suggesting that it is dominated by inertia effects instead of sliding lubrication. However, if speed is plotted on a square root scale an equally good linear fit is obtained as shown in figure 11.16. Hence, it is not always possible to distinguish between the two factors in equation [8] and equation [13], which of course includes equation [8].

Figure 11.16: Sliding braking coefficients on wet concrete and asphalt as function of vehicle speed (left) and of the square root of the vehicle speed (right) [from ref 31]

1.4 Friction on ice.

To establish a master curve on ice is difficult because the ice surface, being not far removed from its melting point, reacts very sensitively to pressure, speed and temperature changes. Roberts [33] has shown that small additions of different salts change the ice properties at the surface dramatically, as shown in figure 11.17. This may well be a major reason for the generally observed large variability of winter tests on ice carried out in the open air. Figure 11.18 shows the friction coefficient of an NR gum compound on a smooth ice track as a function of the track surface temperature for three different speeds. Near the melting point of ice the friction is low. Obviously, some melting in the contact area has lubricated the track. In addition the shear strength of the ice is low so that some shearing of the ice may also take place. The friction coefficient rises sharply as the track temperature is decreased reaching similar values as on a smooth dry track. The actual values depend on the speed; the higher the speed the lower the maximum friction coefficient. The drop in friction at –25°C at the lowest speed is probably not due to compound properties - it may be due to a slight thaw formed on the track.

Figure 11.17: Frictional properties of ice when small amounts of different salts are added to the water before freezing [from ref 33]
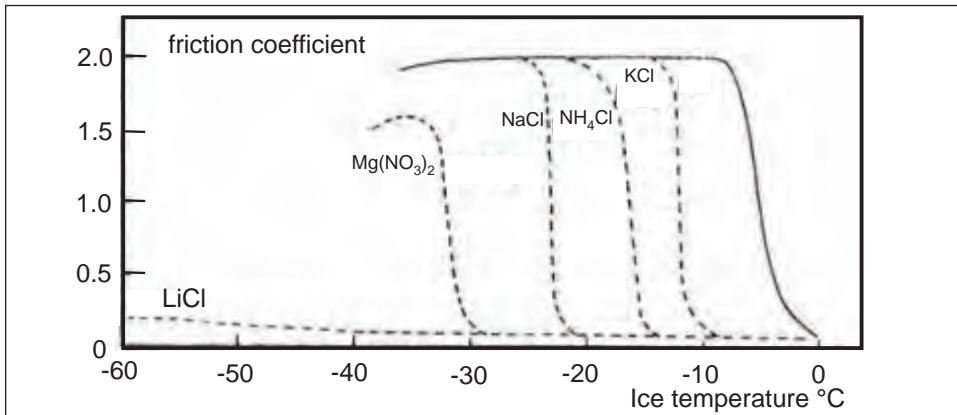

Figure 11.18: Friction coefficient of an NR gum compound as a function of the ice temperature at three different speeds [from ref 34]
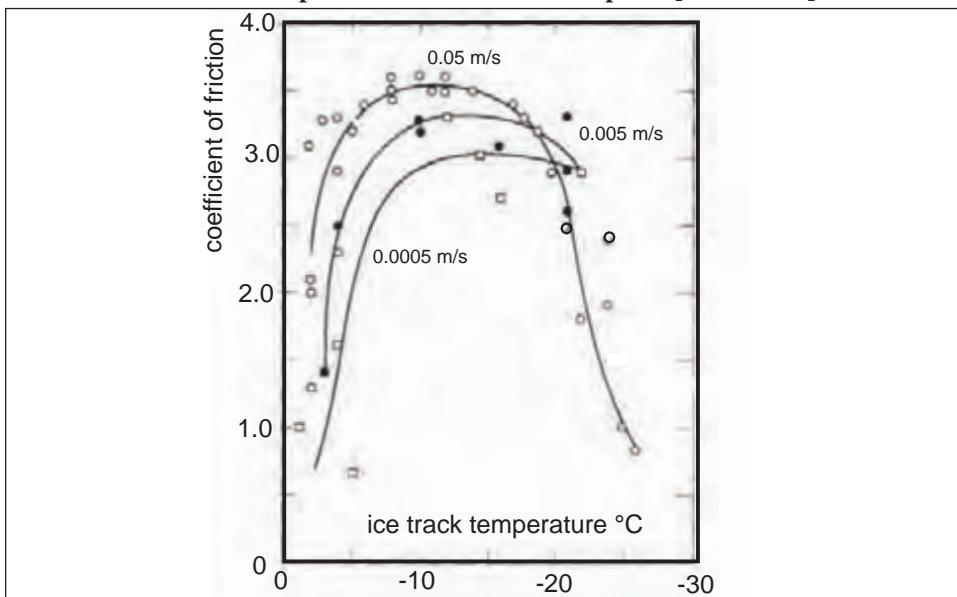

Figure 11.19 shows the friction coefficient as a function of the ice track temperature for four different gum elastomers sliding at a constant speed [34]. NR displays a broad maximum as already seen above. The friction coefficient of the SBR compound rises only over a small temperature range and begins to drop already at an ice temperature of –5°C. The friction coefficient of BR on the other hand rises with decreasing ice temperature over the whole experimental range, while that of the ABR compound remains very low. The major difference between these elastomers is their glass transition temperature. The visco-elastic nature of the friction behavior on ice becomes apparent if the above data are plot-ted as a function of log $a_T v$. For each polymer only part of its friction master curve is pro-duced because of the single speed and the limited temperature range. However because of

their different glass transition temperatures they occupy different ranges on the log $a_T v$ axis. If all four master curve segments are plotted as a function of log $a_T v$ on one graph, they form the shape of a single master curve with a single maximum which has the same position as on glass, as shown in figure 11.20 (compare with figure 11.4, right). This shows clearly that the friction process on ice is the same as on smooth glass. A peak for deformational friction is absent demonstrating clearly that the friction on ice is due to adhesion.

Figure 11.19: Friction coefficient of four different gum compounds having different glass transition temperatures as a function of the ice track temperature at a constant sliding speed of 5 mm/s [from ref 34]
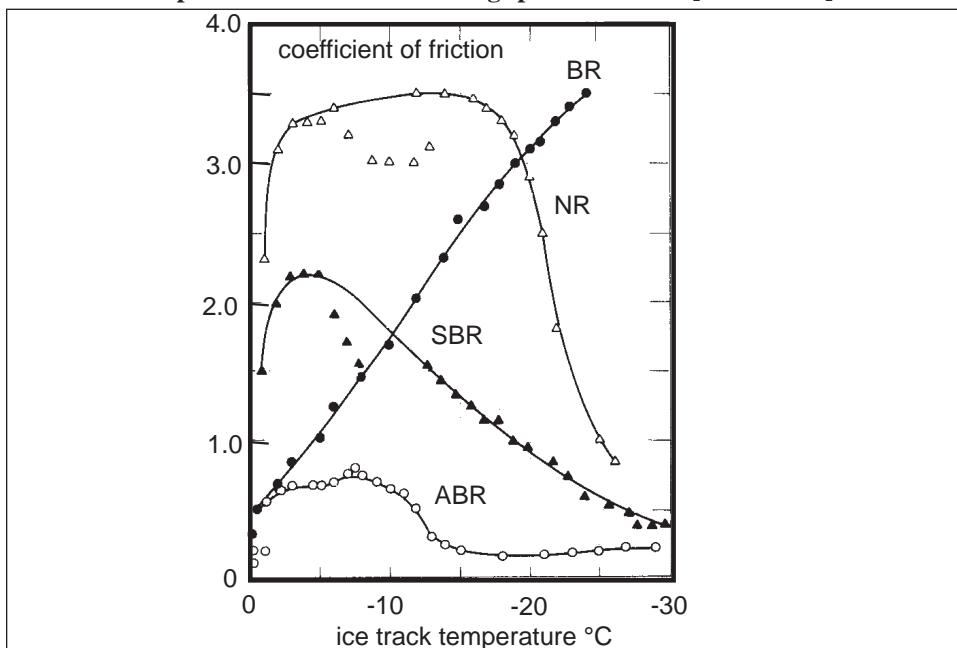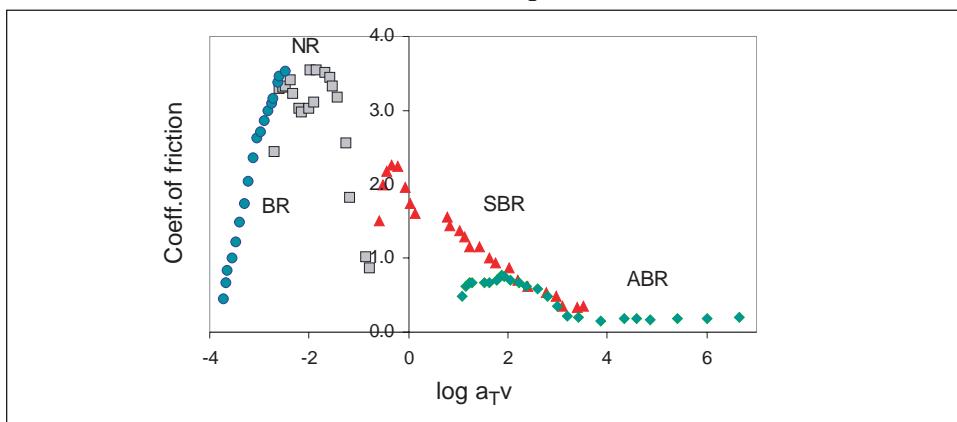
Figure 11.20: Friction coefficients of the four unfilled compounds of figure 19 plotted vs. log $a_T v$ [data from ref 34]

Friction coefficients were measured recently on the ice track disk of an LAT 100 traction and abrasion tester, comparing several compounds at different ice surface temperatures, right up to – 4.5 °C, a temperature which is of great practical importance for winter conditions in many northern countries with a moderate winter climate [35]. Table 11.2 shows a summary of the results at this critical ice surface temperature. A is a Standard 100 OSBR summer tire compound, B is an NR + N234 carbon black traditional winter compound with a low glass transition temperature and C is a 70 BR/30 SBR blend + N375, i.e., a modern black filled winter tread also with a low glass transition temperature. D has the same polymer composition but is filled with silica with silane coupling. The difference between the two black filled compounds with low glass transition temperatures and the summer compound is striking. Addition of silica improves the performance still further. Because of the closeness to the melting point of the ice at – 4.5°C the absolute values of the friction coefficient are very low, a dangerous situation in any case, so that the advantage conferred by a superior tread compound is even more important.

Table 11.2: Friction coefficients and relative rating at an ice track temperature of - 4.5°C and a sliding speed of 0.6 km/h for four tire tread compounds of different composition: A: OESBR + N375 black, B: NR+N220 black, C: 70 BR/30 SBR + N375 black, D: 70 BR/30 SBR + silica

Compound	Measurement				average	rating
	1	2	3	4		
A	0.0528	0.0770	0.0642	0.0718	0.0665	54.7
B	0.1208	0.1279	0.1188	0.1182	0.1214	100.0
C	0.1390	0.1360	0.1370	0.1364	0.1371	112.9
D	0.1402	0.1375	0.1479	0.1566	0.1455	119.8

1.5 A model for rubber friction on ice

The basic assumption is that the friction coefficient on ice can be expressed as the product of three functions [35]

$$\mu = f_{ice}(\varphi) \cdot g_{lub}(v, \mu d) . \mu_d(v, \varphi) \quad [18]$$

where f_{ice} represents the ice properties and is a function of the ice temperature φ, and g_{lub} describes the influence of lubrication. Finally, μ_d is the friction master curve for a dry track surface. As shown in figure 11.20, the shape and position of this curve are those for adhesional friction.

The function f_{ice} is determined by two boundary conditions. First, at zero temperature the function is zero if sufficient ice is present that no ground contact is made, implying that the ice/water mixture has no shear resistance. Second, at a particular temperature the full strength of the ice is reached and the ice surface behaves like a normal hard surface. This temperature can be determined by experiment. It lies between –10 and –15 °C. At this temperature the function f_{ice} = 1 and its slope is zero. A function that fulfills these conditions is the integral of the normal distribution function, normalized to give 1 when a given temperature is reached

$$f_{ice} = \frac{1}{norm} \int_{\varphi}^{\varphi} \left[\frac{-(\varphi - \varphi_m)^2}{2\sigma^2} \right] d\varphi \quad [19]$$

where

$$\text{norm} = \int_0^{\varphi_{hard}} \left[\frac{-(\varphi - \varphi_m)^2}{2\sigma^2} \right] dt \qquad [20]$$

In these equations, φ is the ice surface temperature, φ_{hard} is the temperature at which it is assumed that the ice has reached its full strength (from a friction point of view), and σ is the width of the normal distribution function. To cover the complete area the integration of the norm should go from $-\infty$ to $+\infty$. However, since a range of 6σ covers 99.9 %, this is taken as giving sufficient accuracy to the integration. Hence the integration covers the range from -3σ at 0°C to 6σ at φ_{hard} with $\varphi_m = \varphi_{hard}/2$.

Frictional heating in the contact area melts some ice, forming a thin water film. The function g_{lub} defines the state of lubrication through this melting.

$$g_{lub} = \left[1 - \frac{h}{h_{crit}} \right] \qquad [21]$$

where h is the water film thickness and h_{crit} is the water film thickness when contact is completely lost. For this to happen, enough water has to be melted to fill all voids of the two contacting surfaces. The water film thickness is obtained from power consumption in the contact area

$$F \cdot v = b_w \cdot h \cdot v \cdot \rho \cdot \{c_h(0-\varphi) + M_h\} \qquad [22]$$

where F is the frictional force, φ is the contact temperature, v is the sliding speed, b_w is the contact width, which is generally the block or groove width of the tire tread pattern, h is the film thickness, ρ is the water density, c_h is the specific heat of ice, and M_h is the latent heat of melting. The frictional force F can be written as

$$F = \mu \cdot p \cdot b_w \cdot l_{bl} \qquad [23]$$

where p is the ground pressure, taken to be equal to the inflation pressure, and l_{bl} is the contact length. Combining these two equations and estimating the melted film thickness it is easily seen that it is only a few nanometers thick. Zero temperature is reached very quickly as the friction coefficient rises with decreasing ice temperature. The high latent heat of melting is responsible for the fact that only a very thin film of melted water can form.

On the other hand, even for rather smooth surfaces of ice and rubber, the surface roughness is at least two orders of magnitude larger than the melted film thickness. Hence melted ice water plays no significant role in braking on ice at any speed once the ice temperature is a few degrees below its melting point. Thus the critical water film thickness does not need to be known accurately.

Combining the above equations leads to

$$g_{lub} = \left(1 - \frac{\mu p l_c}{\rho \left(c_w (0 - \varphi) + M_h \right) h_{crit}} \right) \qquad [24]$$

Writing

$$k_2 = \frac{p \cdot l_c}{h_{crit} \cdot \rho \cdot \{c_h (0 - \varphi) + M_h\}} \qquad [25]$$

and
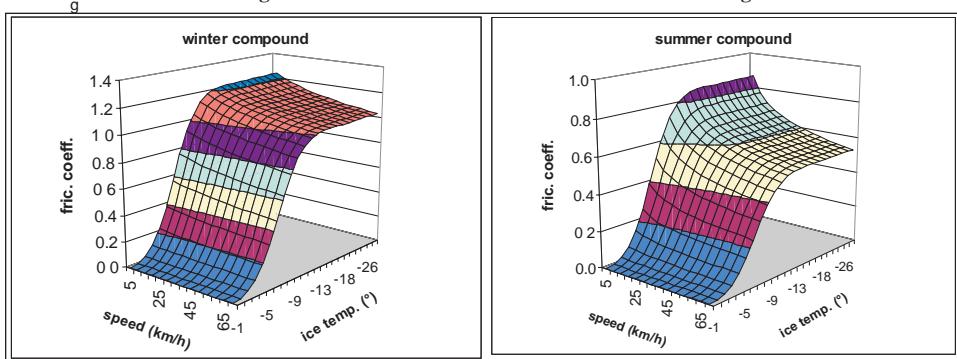
$g_{lub} = (1 - k_2\mu)$ [26]

the friction coefficient becomes

$$\mu = \frac{\mu_d \cdot f_{ice}}{1 + k_2 \cdot \mu_d \cdot f_{ice}}$$ [27]

Figure 11.21 shows the friction coefficient of two model tread compounds as function of the ice temperature and the sliding speed. Both have the same shape of the master curve, a normal distribution function to represent the friction master curve on a smooth surface, but they have different glass transition temperatures, - 68°C for the winter tread and – 46°C for the summer compound. As expected the friction coefficient is very low around 0°C and rises to a maximum near the point where the ice reaches its full hardness. Once friction has reached a value high enough to create sufficient heat to bring the contact temperature to zero, melting of the ice sets in and keeps the temperature at zero. Hence the friction coefficient is virtually independent of the ice temperature, but drops with increasing speed because of the increasing value of log a_Tv.

Figure 11.21: Friction coefficient of two tread compounds (master curve simulated by a normal distribution function with the following parameters: $\mu_{min} = 0.2$, $\mu_{max} = 1.45$, $\log(a_Tv)\mu_{max} = -1.5, \sigma = 2$), as a function of sliding speed and ice surface temperature φ, with $\varphi hard = -15°C$. The only difference between the compounds is their glass transition temperature: For the winter compound $T_g = -68°C$ and for the summer compound $T_g = -46°C$

The rating of these two model compounds is shown in Figure 11.22 as a function of the ice track temperature and speed. Clearly, the winter tread compound has a much higher rating over the whole range of variables, in particular when the ice temperature is very close to its melting point. This is important since the absolute value of the friction coefficient is very low in this region. These conclusions are in good agreement with the results of laboratory experiments shown in Table 11.2.

The reason for this behavior is the high values of log a_Tv which occur because the ice temperature cannot rise above zero. This is demonstrated in Figure 11.23 which shows the model master curve and the operating log a_Tv values for the dry friction coefficient of the two compounds. Because they are on the right-hand branch of the curve the compound with the higher glass transition temperature also has higher log a_Tv values and hence a lower friction coefficient. A broader treatment of this is given in section 3.3 below.

**Figure 11.22: Relative rating of two model tread compounds
with polymers of different glass transition temperature, Tg = - 46°C
representing a summer compound and Tg = - 68°C for the winter
compound. Master curve parameters as for Figure 11.21.**
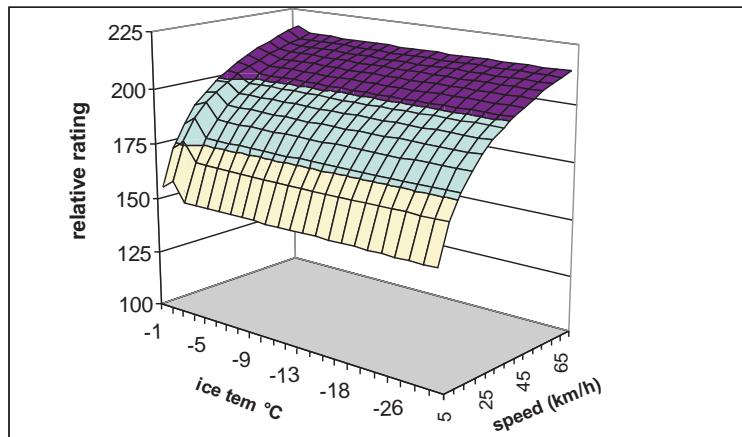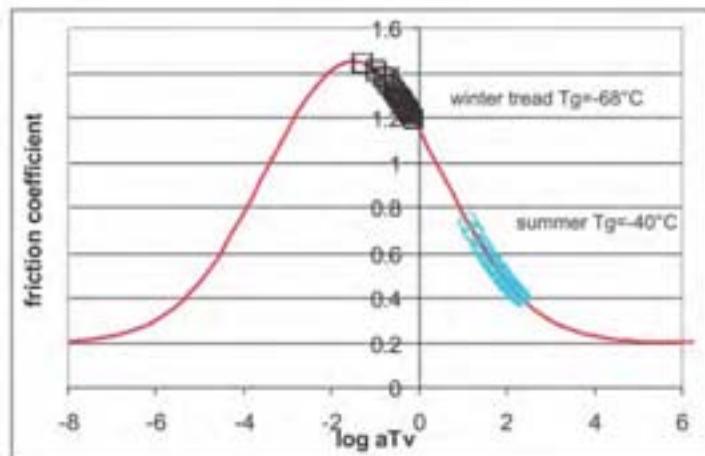

**Figure 11.23: Model friction master curve for a smooth surface represented by a
normal distribution function as for figure 11.21, showing the experimental ranges of
the friction simulation for the winter and summer tire tread compounds.**

2. Use of slipping wheels to determine the friction properties of rubber compounds

2.1 Slip and load dependence of the side force.

In Chapter 13 it is shown that the relation between side force and slip angle can be described by two parameters: the cornering stiffness of the wheel and the friction coefficient of the compound. Moreover, the stiffness dominates the side force at small slip

angles while the coefficient of friction determines the side force at large slip angles. (The same conclusions hold for longitudinal slip.) These results were obtained using a simple model of a tire - the so-called "brush" model proposed by Schallamach and Turner [reference 25 of Chapter 13] - in which the tire is treated as a large number of independent radial elements ("bristles") that deform elastically under side and/or longitudinal forces. A fuller account is given in Section 3.1.2 of Chapter 13. Although it is extremely simple, the model describes the main features of slipping tires remarkably well. Figure 11.24 shows a curve of the side force coefficient vs. slip angle for two different friction coefficients calculated using the brush model with the same stiffness and applied load. It is seen that above 10° the influence of the friction coefficient is clearly apparent. This offers a very useful practical method to evaluate traction properties of rubber compounds in the laboratory. In this case, too, it is convenient to describe the data by means of the side force coefficient, defined in the usual way as the ratio of the side force to the normal load. This coefficient depends on the load. The side force is shown in Figure 11.25 for four different tread compounds at a constant slip angle and speed. The lines drawn through the experimental points represent the curve obtained with the brush model of slipping wheels with the two parameters, friction coefficient and cornering stiffness, adjusted to give the highest linear correlation coefficient between the calculated and measured values [36]. These best-fit parameters are shown in Table 11.3 for measurements of the four compounds on three different surfaces. A possible load dependence of the friction coefficient was taken into consideration, using a power function, but in all cases the power index n was either zero or very close to it. It is clear that the load dependence of the side force coefficient is entirely due to the properties of the slipping wheel and not due to a load dependence of the friction coefficient. Also, while there is some variation of the cornering stiffness, it appears to be random. The ranking of the friction coefficient of the four compounds, however, is very clear and independent of the type of surface. The discrimination between compounds increases as the surfaces become blunter. This is particularly true for the SBR and 3,4 IR compounds. Finally the friction coefficients are lower the smoother the surface, indicating that water lubrication is more effective on blunter surfaces, as expected.

**Figure 11.24: Calculated side force coefficients as a function
of the slip angle for friction coefficients of 1.2, and 0.9, using the
brush wheel model with a cornering stiffness of 400 N.**
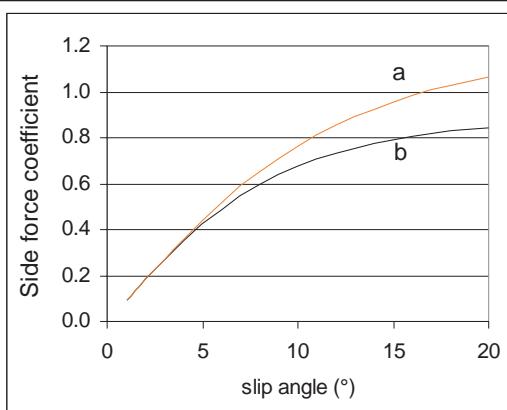
Figure 11.25: Side force as a function of load at a constant slip angle of 13° and a speed of 0.06 km/h on a wet, blunt alumina 180 surface for four tread compounds based on four different polymers, all filled with N 234 black. Full lines were determined with the brush model
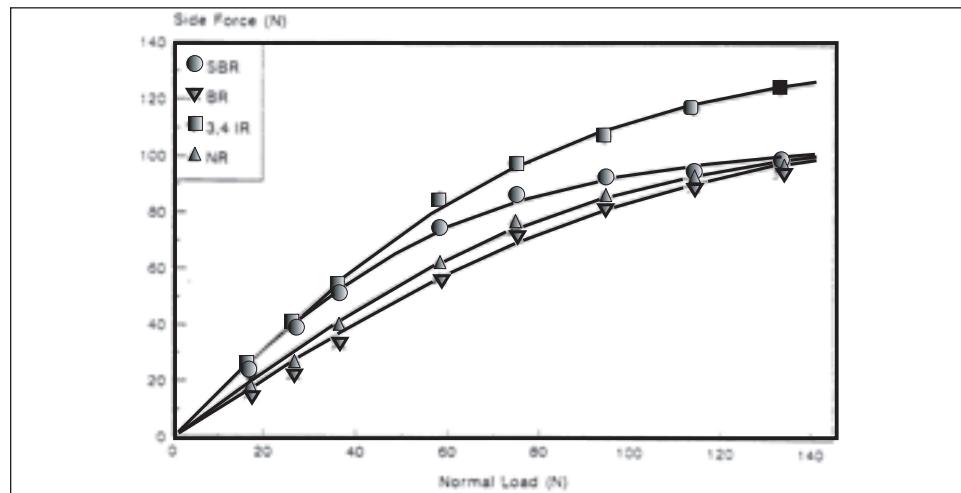

Table11.3: The parameters for the curves of Figure 25: cornering stiffness Ks, friction coefficient μo, power index n to allow for a possible load dependence of the friction coefficient, and correlation coefficient r between the calculated values using the brush model and measured values

Slip angle: 13.1°
Speed: 0.15 m/s

Compound based on	Ks (N/rad)	μo	n	r
Surface: 180 sharp wet				
OE-SBR	413	1.735	0	0.997
BR	448	1.133	0	0.996
3,4 IR	549	1.736	0	0.998
NR	408	1.39	0	0.995
Surface: 180 blunt wet				
OE-SBR	418	1.562	0	0.998
BR	474	1.039	0	0.996
3,4 IR	548	1.58	0	0.999
NR	447	1.18	0	0.998
Surface: ground glass wet				
OE-SBR	427	0.803	-0.01	0.997
BR	402	0.56	-0.01	0.997
3,4 IR	502	0.925	0	0.997
NR	377	0.671	0	0.997

2.2 Speed and temperature dependence of the side force coefficient

Figure 11.26 shows the side force coefficient as a function of log speed for different temperatures at a constant load and slip angle for a tire tread compound based on 3,4 cis-poly-isoprene, a polymer with a high glass transition temperature. The data were obtained on the flat side of a wet blunt alumina 180 grindstone using the LAT 100 abrasion and traction tester [36]. The temperature was regulated by the temperature of the water that was pumped onto the track in a closed circuit. In Figure 11.27 the data have been transformed into a master curve, not by empirical shifting of the data, but by using shifts calculated from the WLF equation using a standard reference temperature $T_s = T_g+50$. It is seen that a single curve results and shows all the features discussed above for the friction coefficient on dry and wet tracks. For dry friction a plateau between the adhesion and deformation friction components would be expected for this type of black filled compound. For the side force measurements there is still a deformation peak discernable, but also a clear change in curvature at the position of the adhesion maximum expected on dry smooth surfaces. Also shown in Figure 11.27 is the master curve for the friction coefficient for the same compound on the same surface. In this case the adhesion friction is more distinct and the deformation friction less so, forming a plateau as for dry friction of this type of compound. The maximum of the deformation friction occurs at a lower speed than the maximum side force coefficient. This is largely due to the fact that the forward speed was used for the transformation of the side force coefficient, about 0.7 decade higher than the slip speed, which in turn is approximately equal to the sliding speed of the friction coefficient. Figure 11.28 shows the master curves of the side force coefficients for the 3,4 IR tread and the SBR tread compound used for the load dependence experiments of Figure 11.25. Because of the much lower glass transition temperature of the SBR, the decrease of the side force coefficient at high log $a_T v$ values falls outside the experimental range. The figure demonstrates how misleading spot measurements can be. Two measurements carried out at two different water temperatures under otherwise the same conditions give totally different results, reversing the ranking of the compounds, an experience that is encountered frequently in practical tests of tire traction.

**Figure 11.26: Side force coefficient of a 3,4 IR tread compound
as a function of log (speed) at different water temperatures on a
wet alumina 180 surface, with blunted tips [from ref 36]**
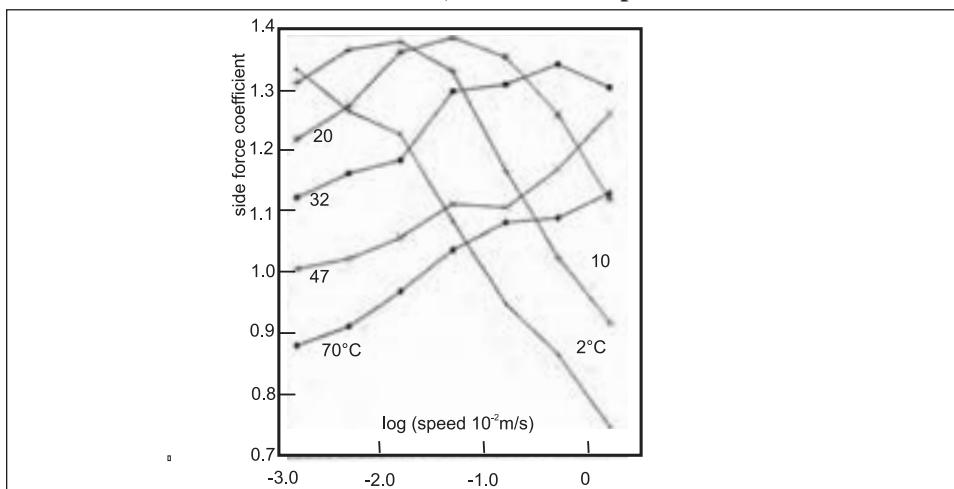
Figure 11.27: The data of figure 26 plotted as function of log a_Tv with the standard reference temperature taken to be Ts = Tg + 50°C. Also shown is the friction master curve for the same compound on the same surface.
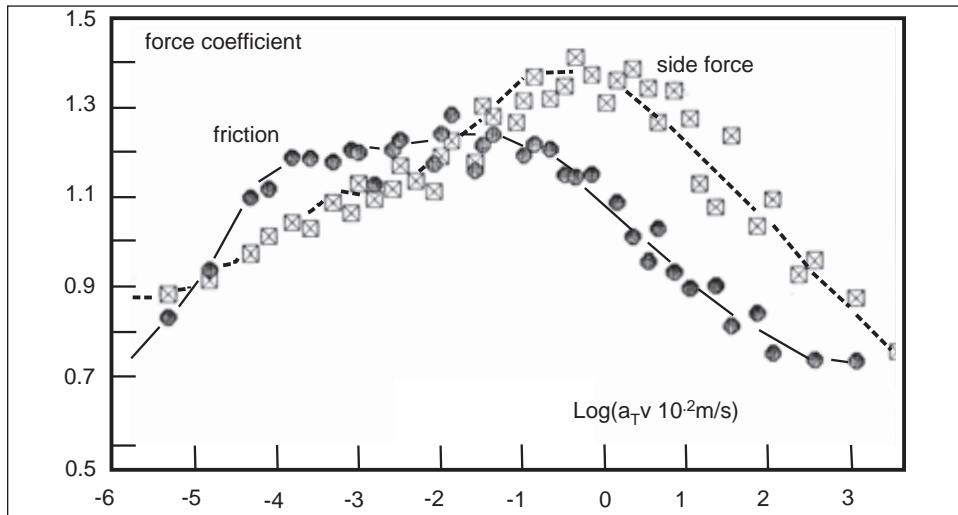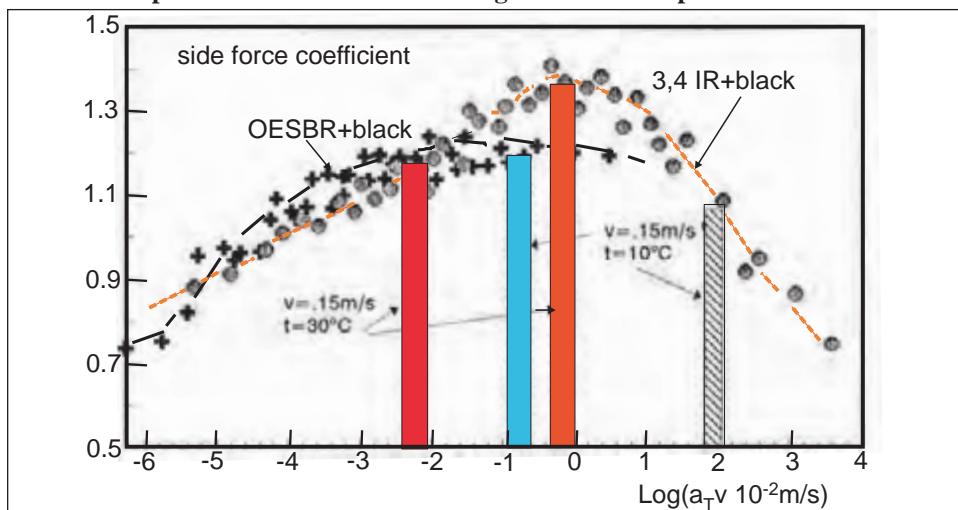

Figure 11.28: Master curve of the side force coefficient of two tread compounds with different glass transition temperatures on wet alumina 180: 3,4 IR (Tg = - 21°C) and OESBR (Tg = - 46°C) [from ref 36]. Two spot measurements at different water temperatures show that the ranking of the two compounds reverses.

2.3 Traction properties of tread compounds at higher speeds.

In order to establish master curves of friction or side force coefficients, the speeds have to be kept low in order to avoid significant temperature rises in the contact area. Temperature rises will also affect lubrication if the experiments are carried out on wet tracks. Generally, however, it is necessary to allow higher speeds in order to study the

influence of temperature rises and lubrication effects in the contact area. These effects profoundly influence the traction capabilities of tires. In the chapter on abrasion and tire wear, it is shown that the temperature rise in the contact area can be considerable as the sliding speed is increased and this influences abrasion by oxidation and thermal degradation. Friction is primarily influenced because the temperature rise affects the operating range on the log $a_T v$ axis of the master curve.

In order to calculate the relevant log $a_T v$ values a relation is required between the temperature rise in the contact area and the sliding speed. Carslaw and Jaeger [38] have dealt in detail with the problem of moving heat sources over plane surfaces of semi-infinite bodies. They predict that the maximum temperature rise, occurring for rubber near the end of the contact area, is given by the following relation:

$$\Delta t = Q \sqrt{\frac{2 l_r}{\pi \rho c K v_s}} \qquad [28]$$

where Q is the heat generated per unit area and per unit time, l_r is the contact length of the heat source, ρ is the density, c the specific heat and K its heat conductivity. In this case it is assumed that all the heat flows into the rubber. If the heat is produced by friction, part of it will flow into the rubber and the other part will flow into the track surface. Assuming a large heat capacity for both and neglecting heat losses to the sides, the amount of heat flowing into the rubber is given by

$$\psi = \frac{q_r}{Q} = \frac{\sqrt{\kappa_r}/K_r}{\sqrt{\kappa_r}/K_r + \sqrt{\kappa_t}/K_t} \qquad [29]$$

where the subscripts t and r stand for track and rubber respectively, k is the heat diffusivity, and q_r is the amount of heat which flows into the rubber per unit area and time. The temperature rise near the end of the slider will then become

$$\Delta t = \psi_r \mu p \sqrt{\frac{2 l_r v_s}{\pi \rho c K_r}} \qquad [30]$$

This relation can be simplified to
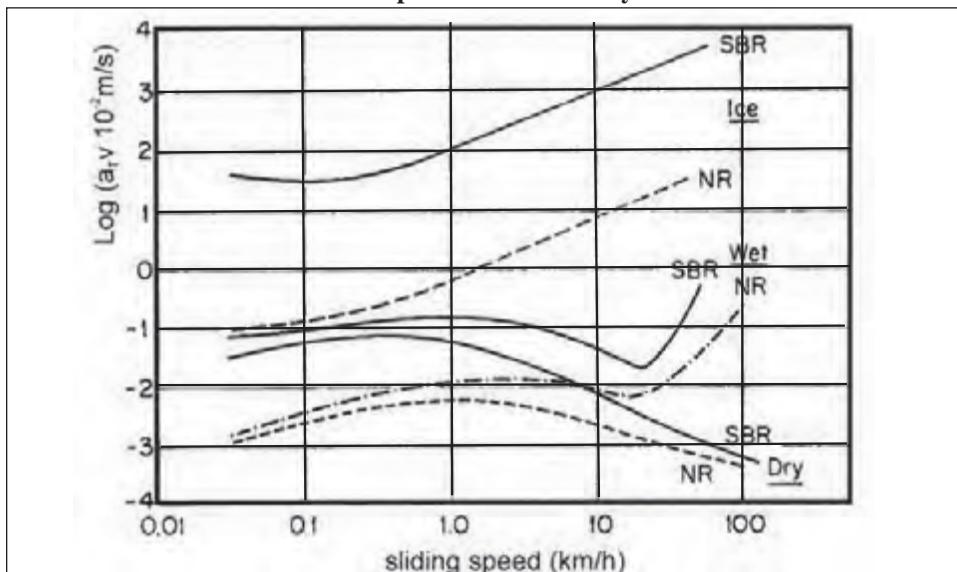
$$\Delta t = \xi_c \mu p \cdot \sqrt{v_s} \qquad [31]$$

where the constant ξ_c contains the constants listed above. Unfortunately, it is hardly ever possible to deduce ξ_c from this formula. The value has to be determined by experiment. For practical road traction tests on wet surfaces a method will be described in section 5.7.

If the temperature is a function of speed, then the factor log a_T is also a function of speed, changing the operating point on the master curve. Log $a_T v$ increases with speed and decreases with increasing temperature. At very low speeds log v wins, but as the speed increases the influence of log a_T becomes larger, eventually overtaking log v and the term log $a_T v$ passes through a maximum. Figure 11.29 shows log $a_T v$ values as a function of the sliding speed for an NR and an SBR tread compound under different track surface conditions at a constant ambient temperature. To obtain these curves the constant ξ_c had to be estimated. For dry track conditions this was derived from figure 11.36 of the chapter on abrasion and tire wear. For wet conditions its value cannot exceed 100°C and was reduced accordingly. For icy conditions the value cannot exceed the melting point of ice. In each

case the range of log $a_T v$ values obtainable is limited. On dry and wet surfaces log $a_T v$ goes through a maximum. In addition, on wet surfaces lubrication leads to a decrease of the temperature at high speeds so that the log $a_T v$ values rise again. And because of the temperature limit of 0°C on ice, the curve rises continuously.
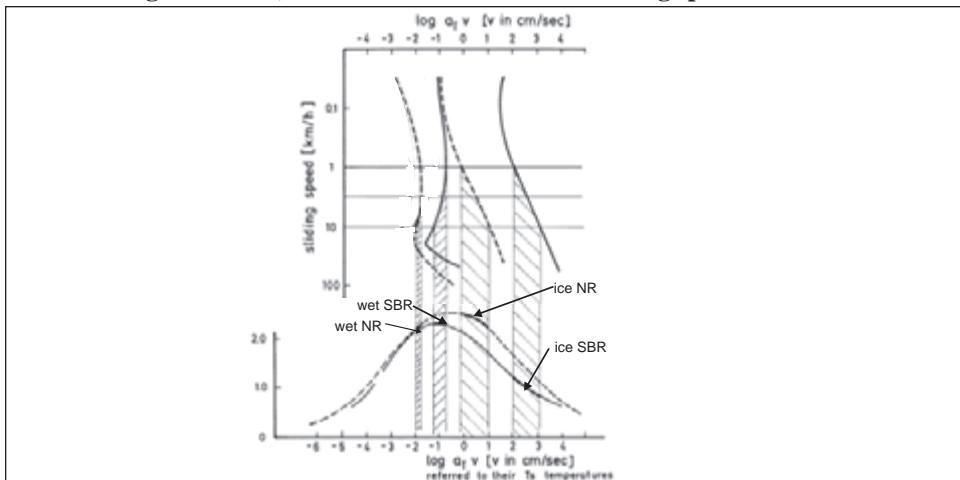
Figure 11.29: Log $a_T v$ values as a function of speed for an
NR and an SBR compound on wet and icy track surfaces.

The range of log $a_T v$ values obtainable in practical tire tests is therefore limited to about 2 decades and only a small part of the master curve is covered. However this portion depends strongly on the ambient conditions.
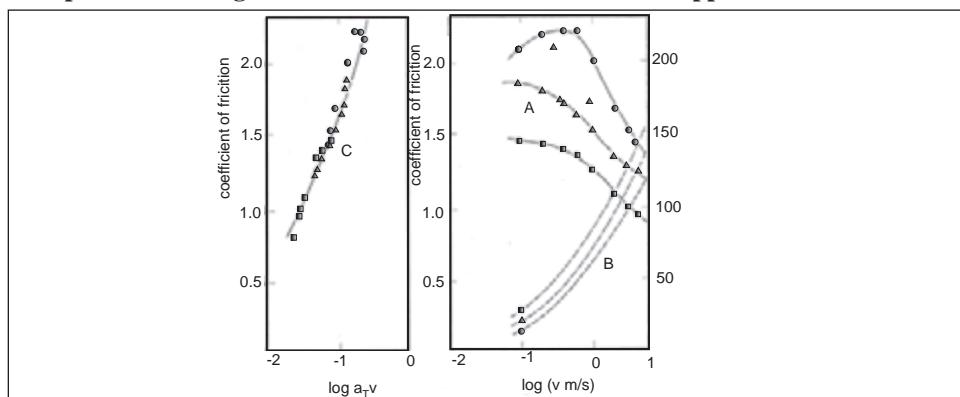
Because of the different glass transition temperatures for different polymers the operative values of log $a_T v$ also differ considerably for different compounds since they are determined by the difference between the contact temperature and the standard reference temperature T_s, or more fundamentally, the glass transition temperature T_g. Figure 11.30 indicates the relevant regions of log $a_T v$ for sliding speeds between 1 and 10 km/h (corresponding to about 10 to 100 km/h forward speed with ABS braking) on the two master curves for unfilled NR and SBR compounds sliding on glass (see upper part of the diagram) under wet and icy environmental conditions respectively. On wet surfaces the SBR compound is better than the NR compound because the operative log $a_T v$ range is on the rising part of the master curve. On ice it is on the decreasing branch, and the ranking is reversed, as already remarked when discussing rubber friction on ice. This is the reason for using separate sets of tires for winter and summer.

Figure 11.30: The log a_{Tv} speed function of the previous figure is combined with the friction master curves for an NR and an SBR gum compound on glass showing the limited range of friction values (and their position on the log a_{Tv} axis for different testing conditions) that are obtained when the sliding speed is increased.

The maximum in the log a_Tv curve also produces a maximum in the curve relating friction to speed. But this has nothing to do with the maximum in the friction master curve. On dry or wet surfaces the operating points lie generally on the rising part of the master curve for friction. Thus, the maximum friction is determined by the maximum value of log a_Tv. This is demonstrated in figure 11.31 which shows friction measurements on an unfilled NR compound with a slider which had a thermo-couple embedded in it. Both friction and the corresponding contact temperature were measured, allowing transformation of the data into a friction vs. (log a_Tv) curve. The three experimental curves were obtained under different loads producing different temperature rises. It is seen that a single rising curve results from the transformation. The load dependence is revealed in this case as a disguised temperature effect.
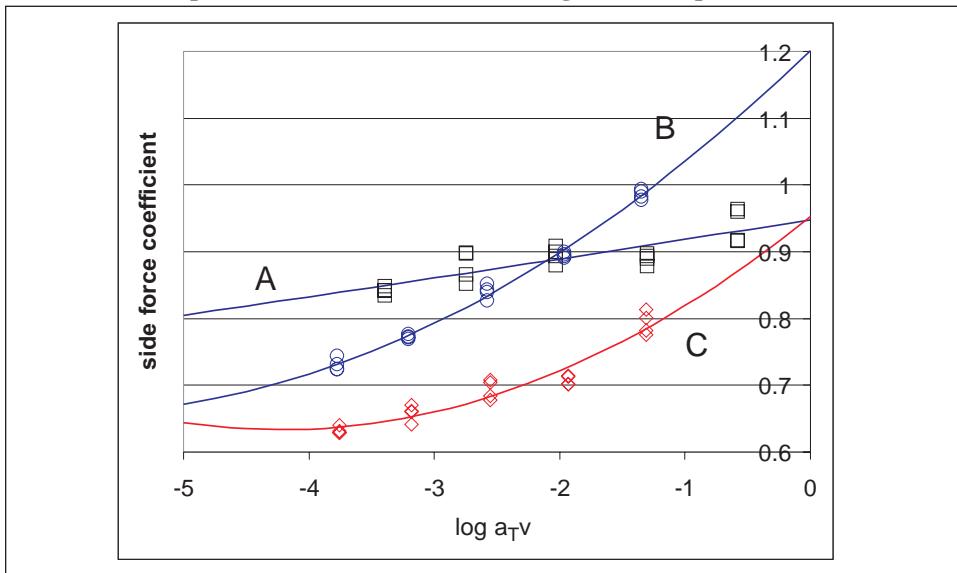
Figure 11.31: Coefficient of friction (A) and temperature rise (B) in the contact area between an NR gum compound and a thermo-couple slider as a function of speed at different loads. Also shown are the data plotted against log a_Tv (C), indicating a rising portion of a single master curve which absorbs also the apparent load effect.

2.4 The friction/side force master curve over a reduced range of log a_Tv values

Since only a limited region of the master curve is relevant for a particular environmental con-
dition, for routine practical compound development a limited number of experimental points
are often sufficient. Figure 11.32 shows a comparison of three tread compounds over a range
of log a_Tv obtained using five temperatures at a constant speed. A quadratic curve was fitted
to the data by the least squares method to represent the portion of the master curve.
Compound A is a classic summer OESBR black filled compound, compound B is a blend of
solution SBR and BR with a silica filler and silane coupling. It is seen that compound B is
better than the standard compound A at high values of log a_Tv and worse at low ones. This
corresponds to practical experience. With modern ABS braking systems contact temperatures
are kept low, particularly on wet surfaces, so that the values of log a_Tv are relatively high.
The silica filled compound is then superior to the standard black filled one. With locked wheel
braking the contact temperatures are high and the log a_Tv values are low: the ranking of the
braking performance of these two compounds is then reversed. Compound C is a classical
winter tread compound which is poorer over the whole experimental range of log a_Tv values.
It would show its merits at temperatures below zero.

**Figure 11.32: Side force coefficient at a constant load, slip angle and speed as a func-
tion of log a_Tv obtained by using five different temperatures as measuring points and
assuming that the WLF transformation applies. To obtain a continuous curve a quad-
ratic equation was fitted to the data using the least squares method**

*2.5 Effect of the temperature rise and lubrication on the side force coefficient as a func-
tion of slip angle on wet tracks*

The temperature rise in the contact area also influences the side force coefficient during
partial sliding. The brush model assumes a constant friction coefficient. However, the slip
speed v_s will affect the temperature in the contact area and hence the effective speed a_Tv_s
and thus the friction coefficient. This also affects the relation between side force and slip

at a constant forward speed v_f.

The slip speed v_s is a function of the slip angle θ

$v_s = v_f \sin \theta$ [32]

The temperature in the contact area is

$$t = \xi_c F \sin \theta \sqrt{v_f \sin \theta} + t_a \qquad [33]$$
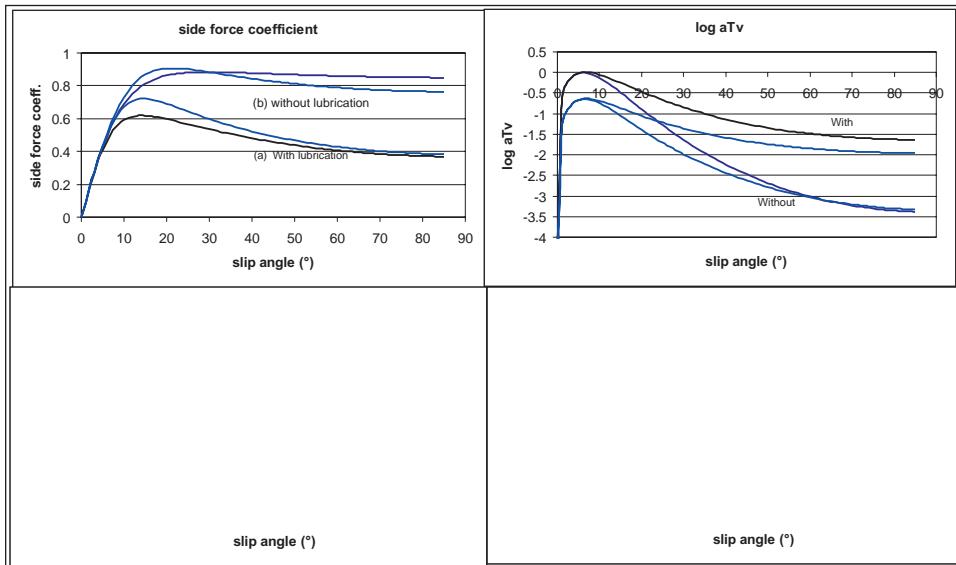
where ξ_c is a constant, $F \sin \theta$ is the energy dissipated by the slipping wheel, and t_a is the ambient temperature. To obtain the appropriate side force coefficient from the friction master curve for the relevant compound the log $a_T v$ value is calculated for the above temperature and slip speed using the WLF equation. The side force F is then calculated using the brush model with the relevant friction coefficient μ. If the friction master curve for the compound is available the friction coefficient can be assigned for the calculated values of log $a_T v$. If only a limited number of points are available, a curve has to be fitted to them and the appropriate friction coefficient is read from that. Usually a quadratic equation is sufficient as seen from Figure 11.32. In general the operative values of the friction coefficient are on the left branch of the master curve. As the temperature in the contact area rises, the log $a_T v$ value drops and the friction coefficient, and with it the side force, decrease with increasing slip angle.

In addition to the influences of temperature and speed on the log $a_T v$ values, the friction coefficient is reduced on wet tracks as the sliding speed increases because of the increasing hydrodynamic lift. For a constant forward speed the hydrodynamic lift increases with the slip angle in cornering and with the circumferential slip when braking or accelerating. The side force coefficient can be calculated using the brush model with a friction coefficient modified by the temperature rise in the contact area and by water lubrication as described by equation [8], but replacing the speed v by the slip speed $v_f \sin \theta$

$$\mu = \mu_d \left[1 - \left(\frac{v_f \sin \theta}{v_{crit}} \right)^{1/2} \right] \qquad [33]$$

An example is shown in Figure 11.33 using the master curves of Figure 11.32 for compounds A and B. Also shown is the calculated contact temperature, the values of log $a_T v$ obtained from the temperatures and sliding speeds and the rating of compound B relative to A. In all cases the curves were obtained for a friction coefficient (a) without considering the effect of water lubrication and (b) taking it into account, using the same temperature calibration constant for both cases. The reduction of the friction coefficient through water lubrication leads also to lower temperatures in the contact area. The higher temperature dependence of compound B results in a cross-over at higher slip angles as is already apparent from the master curve of Figure 11.32. This is a general experience in tire tests. In fact compound B has primarily been developed for use in conjunction with the ABS braking system which limits the slip to about 10%, a range in which this compound is clearly superior to the standard black filled OESBR both on dry and lubricated tracks.

Figure 11.33: Side force coefficient as a function of slip angle (upper left), calculated by using the data from figure 32 for compounds A and B, the brush model and a variable friction coefficient taking into account temperature rises and lubrication effects on wet tracks. Curves were constructed allowing temperature rises without lubrication effects and with a hydrodynamic lift due to water lubrication. Also shown are the operating log aTv values (top right) the calculated temperature rises (bottom left) and the rating of compound B relative to A (bottom right)

3. Tire traction
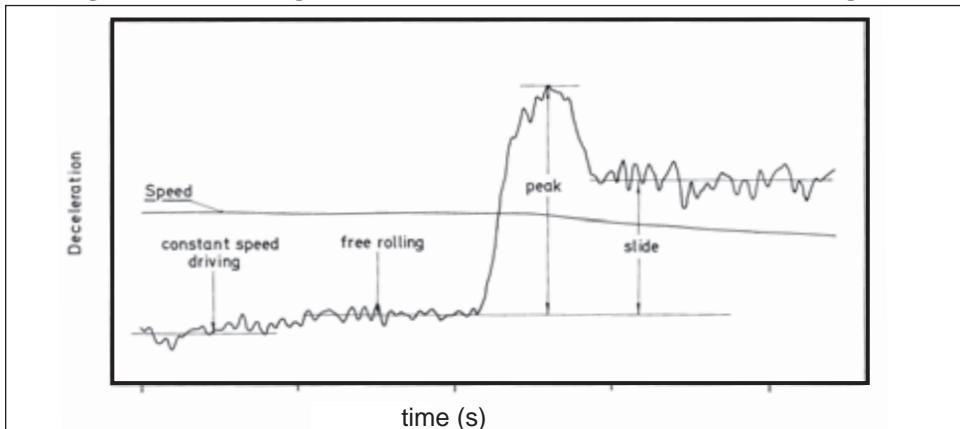
3.1 Braking test procedures

In a typical braking test deceleration of the test car is measured over a short time starting from a set initial speed. A wide range of speeds can be covered. The rear brakes are disconnected so that the side forces on the rear wheels keep the vehicle stable up to the highest approach speeds. Because the drop in speed is small during the time of braking the speed dependence of the braking coefficient can be obtained over a wide range. A typical deceleration time diagram for a locked wheel braking test is shown in Figure 11.34. The speed is also recorded. Before the brakes are applied the vehicle is allowed to roll freely for approximately one second to establish a base line. The deceleration increases as the brakes are applied, passes through a maximum, and then levels off at a lower value that remains approximately constant with time, provided that the time interval of braking is short so that the decrease in speed is small. To obtain the actual braking coefficient from the measured deceleration, two corrections due to load transfer during braking have to be applied: (a) the normal reaction on the front wheels increases and (b) the vehicle tilts forward, decreasing the measured deceleration in the absence of an inertia platform. Both effects are vehicle dependent but can be obtained from the vehicle data. The actual braking coefficient b_c can be written as

$$b_c = \frac{F}{R} = c_1 b'(1 - c_2 b')$$ [34]

where F is the frictional force, R is the normal reaction on the front wheels of the testing vehicle, c_1 and c_2 are constants depending on the testing vehicle and b' is the measured braking coefficient.

Figure 11.34: Braking deceleration time record for a short-time braking test

The abrupt drop from the peak to the sliding value of the braking force is associated with spontaneous locking of the wheels that occurs because of the negative force-slip relation, which itself is due to the rising temperature and increasing lubrication, as shown in Figure 11.32.

The sliding value of the braking coefficient is not always constant. Often it rises with the time of braking, as shown in Figure 11.35. This is expected from decreasing lubrication and falling temperature in the contact area as the speed decreases. However, if experiments are carried out with different initial speeds and the instantaneous speed is also recorded, as shown in the time records above, a single curve of the sliding coefficient should be obtained over a wide range of instantaneous speeds, independent of changes with time during the test. But this is often not the case, as shown in Figure 11.36 where the slide coefficient is shown as a function of tire speed on a wet asphalt track. The different symbols refer to different initial speeds. The tire which has skidded for a long time has a higher slide coefficient than the one that has skidded for only a short time, both compared at the same instantaneous speed. Thus conditions in the contact area change not only

Figure 11.35: Braking deceleration time record for a short-time braking test on wet asphalt at a lower initial speed showing a sliding coefficient rising with time
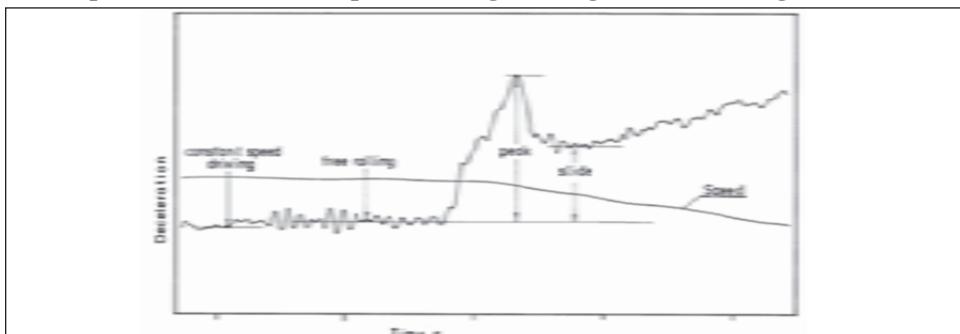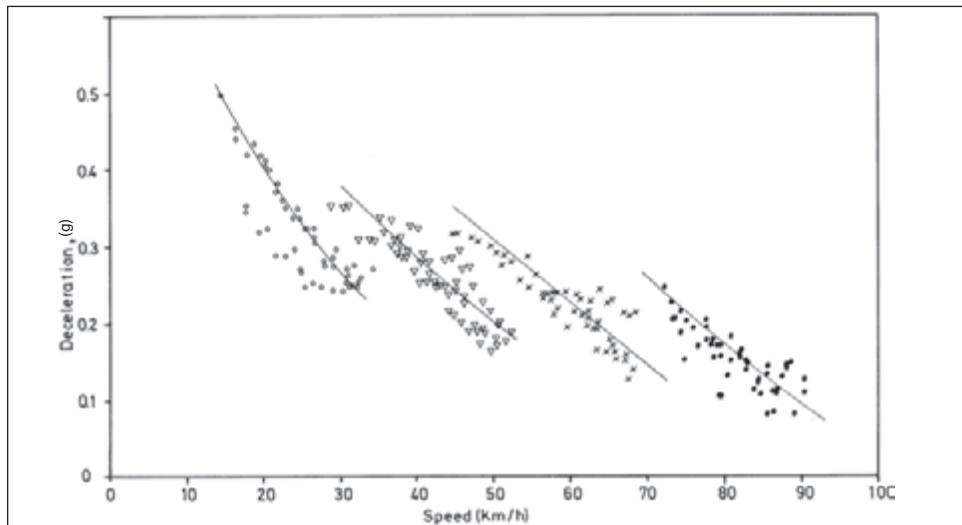
Figure 11.36: Slide value of the braking coefficient as a function of instantaneous speed for different approach speeds (different symbols)

with speed but also with time. There is no obvious explanation for this. The tire surface in contact with the track appears to be modified during braking, most likely by abrasion, perhaps even through some thermal degradation, thereby influencing the friction coefficient. For example, NR tread compounds tend to become sticky in friction experiments on wet tracks at quite moderately elevated water temperatures, showing an increase in friction at log $a_T v$ values where it would not be expected on visco-elastic grounds.

In a second type of braking experiment a trailer is pulled by a car and the tow bar pull is measured while the brakes of the trailer wheels are applied. Either one or two wheeled trailers are used. In both case there are a number of disadvantages over the car skid test. The tow bar pull measures the force acting between car and trailer and any acceleration or deceleration of the car during the experiment causes an error. This can be overcome to some extent by allowing the car to roll freely during the experiment and determining its own rolling resistance in a separate experiment. The range of speeds that can be covered is also much smaller since it is difficult to maintain the trailer in a stable condition at higher speeds. In this case, too, load transfer occurs, but in the opposite sense - the normal reaction to the tire load is reduced and transferred to the connecting pin of the tow bar. The formula for the braking coefficient is then given by

$$b_c = c_1 b'(1 + c_2 b') \qquad [35]$$

where the constants c_1 and c_2 are obtained from force transducer calibration and trailer dimensions. b' is the apparent friction coefficient - the frictional force divided by the normal load on the tires.
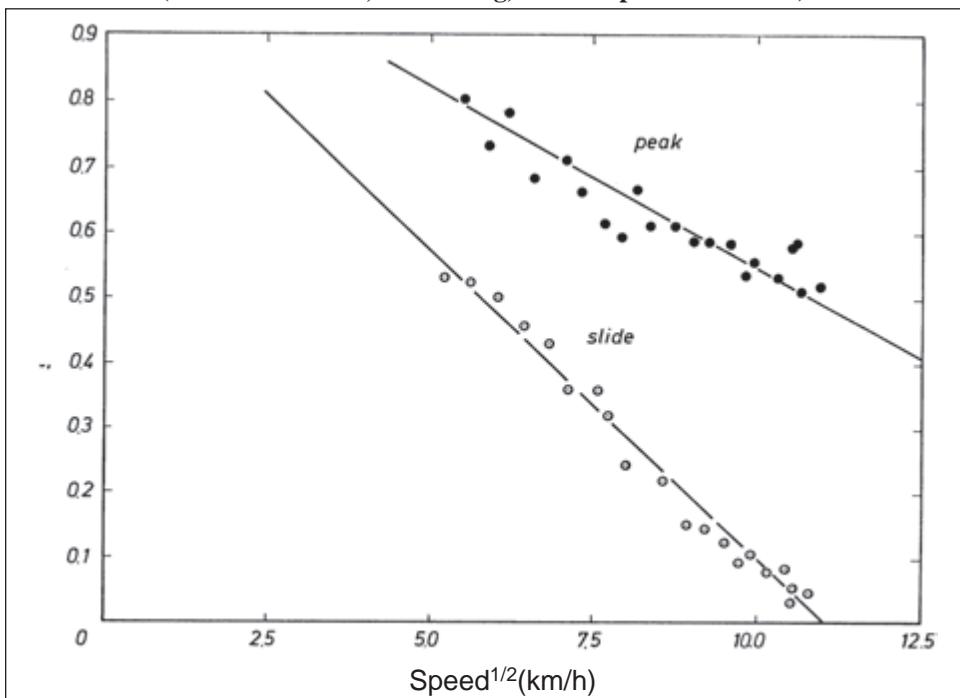
In recent times the simple measurement of stopping distance has become popular because it is less sensitive to variations in road surface structure and also, in many cases, to slight variations in water depth. This method, however, produces only a single reading. Some indication of the effect of speed can be obtained by using different initial speeds. More sophisticated equipment uses measuring hubs either on one wheel of a testing vehicle or on a fifth wheel mounted on a large mobile testing platform. In most cases five com-

ponents can be measured: three forces and two moments. Simpler versions can still measure the three force components. Both measurements can be made under controlled longitudinal slip and cornering.

3.2 Speed dependence of peak and slide braking coefficients.
Plotting peak and slide values of the braking force coefficient b_c as functions of the square root of the initial speed yields straight line graphs as shown in Figure 11.37. If a distinct time dependence was present, the minimum slide value was used. Since this always occurs at approximately the same time after the brakes are applied, a possible time effect is minimized. In these tests the temperature in the contact area increases with increasing sliding speed as described above. As the operative values of log $a_T v$ lie generally on the

Figure 11.37: Peak and slide braking coefficients as a function of the (initial speed)$_{1/2}$ at the beginning of braking on wet fine concrete. (Tire size 175 R 14, load 350 kg, inflation pressure 1.9 bar)

rising branch of the friction master curve, the braking coefficient decreases with increasing contact temperature. In addition, the braking coefficient drops because the water lubrication effect increases with increasing sliding speed. There is not sufficient information available to separate the two effects which both work in the same direction. The fact that straight line graphs are obtained when plotting the data in this way suggests that the water lubrication effect dominates.

    From the two straight-line graphs for the peak and slide values (the latter is also shown in Figure 11.14) two parameters can be deduced. The "dry" braking coefficient at zero speed is nearly the same for both: 1.045 for the slide value and 1.085 for the peak brak-

ing coefficient. From the intercepts on the square root of speed axis, the critical sliding speeds v_c are 118 and 388 km/h respectively. Writing equation [8] as

$$b_c = b_{cd}\left[1-\left(\frac{s_l v_f}{v_c}\right)^{1/2}\right] \qquad [36]$$
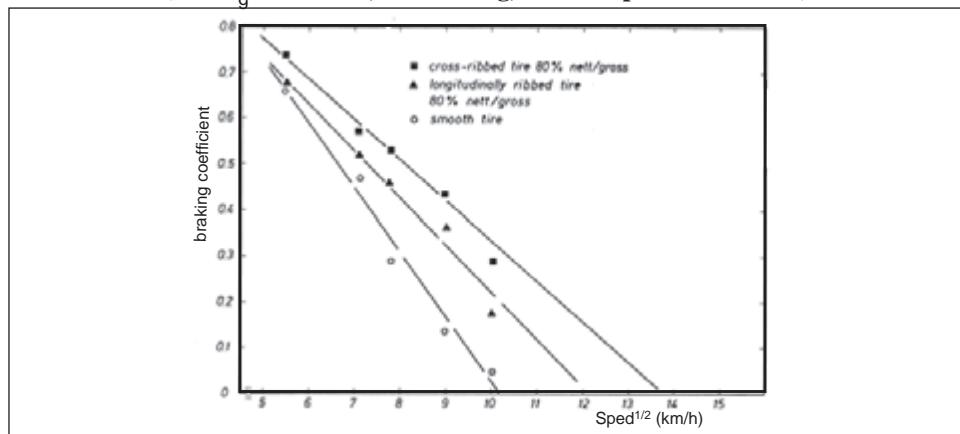
where b_{cd} is the braking coefficient at zero speed, s_l is the slip, ($s_l = 1$ in sliding), and v_f is the vehicle speed at the time of measurement. The ratio of $[v_c]_{slide}$ to $[v_c]_{peak}$ should give the slip s_l. The value of 0.3 is somewhat larger than the value expected from direct measurements, about 0.2.

3.2.1 Role of the tread pattern

The sole purpose of a tire tread pattern is to increase safety in driving on wet, snowy and icy roads, and on muddy and other slippery off-road surfaces. The greatest disadvantage of a tread pattern is the noise it creates. Figure 11.38 compares locked-wheel braking coefficients for two basic tread patterns and for a smooth tire. Again, straight line graphs are obtained if the braking coefficients are plotted versus $(speed)^{1/2}$. At zero speed the three lines almost coincide, indicating that the "dry" braking coefficients are the same. From values of the intercept on the abscissa, the critical speeds are seen to increase from smooth to longitudinal ribs to the cross ribbed tire pattern, emphasizing the greater importance of a short contact length in the sliding direction than at right angles to it, as indicated above in equation [6] for sliding lubrication. On the other hand, for water levels higher than the asperities the inertial effect of the water becomes important as discussed above. As long as there is some contact, water cannot flow out of the contact region towards the rear and flow towards the front is limited to the maximum possible flow speed

$$v_f = \sqrt{\frac{2p_m}{\rho}} \qquad [36]$$

Figure 11.38: Slide values of the braking coefficient as a function of $(speed)_{1/2}$ for a radial ply tire on wet concrete, comparing two basic patterns with a smooth tire. (Tire size 175 R 14, load 350 kg, inflation pressure 1.9 bar)

where p_m is the mean ground pressure, which is about the same as the inflation pressure, and ρ is the density of water. For a normal passenger car this flow speed is about 80 km/h.
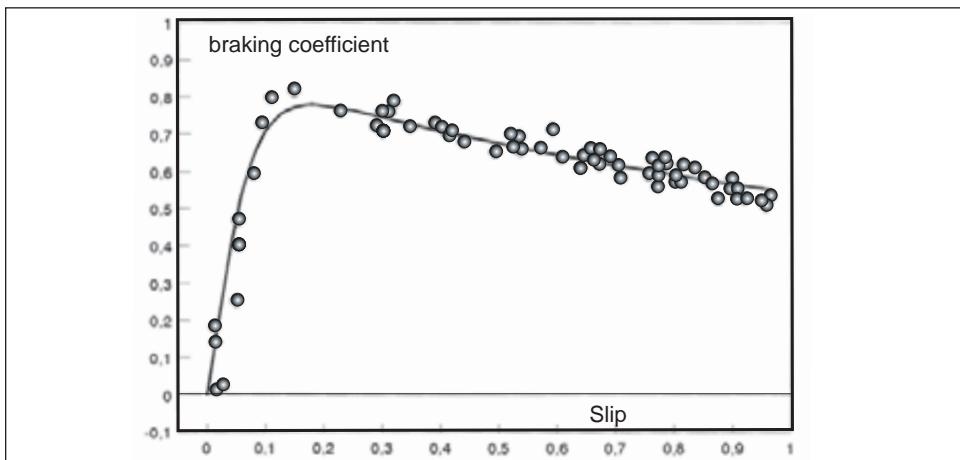
Water is mainly removed towards the sides. Hence longitudinal ribs with short lateral channels are required to provide short drainage distances towards the sides and thus to increase the critical aquaplaning speed of the tire. To optimize the removal of water, diagonal ribbing and directional tread patterns are employed. A modern high performance tire can no longer be mounted in either direction on the rim. Attention has to be paid to mounting the correct side-wall towards the outside in order to achieve maximum water drainage. Diagonal ribbing also helps to reduce tire noise. Pattern design has become very sophisticated, to combine maximum safety with the lowest noise level.

3.3 Braking under controlled slip
3.3.1 The braking force slip curve under controlled slip
In order to avoid locking of the brakes when the braking force exceeds its maximum value, cars are now generally fitted with an anti-locking braking system (ABS). The brakes are released for a short time when the slip exceeds a set value and are then applied again immediately. This ensures that the braking force stays near its maximum. In this way not only shorter stopping distances are achieved but also the car can be steered during braking, helping the driver to avoid possible collisions. Figure 11.39 shows the braking coefficient as a function of the circumferential slip at a constant vehicle speed, load and zero slip angle. Obtaining such data requires highly sophisticated testing equipment

Figure 11.39: Braking force coefficient as a function of slip at zero slip angle on wet asphalt at a constant speed of 30 mph, obtained with the Mobile Traction Laboratory of NHTSA. The curve was fitted using the brush model and a variable friction coefficient taking account of temperature and lubrication effects.

as indicated above. The data presented here were obtained with the NHTSA Mobile Traction Laboratory (MTL). The curve was fitted to the data using the brush wheel model and a variable friction coefficient as defined in equation [8]. Regression coefficients between calculated and measured values were used to find the best-fit parameters.

Theoretically, it is possible to take into account separately the temperature and speed dependence of the friction coefficient μ_d. However, because they tend to be additive, both effects are included in the power index and μ_d appears as a constant. It is seen that the braking coefficient decreases steadily with increasing slip. The abrupt drop between peak and slide values in the time record of a braking test is due to the negative slope of the curve relating braking coefficient to slip.

3.3.2 The relation between braking force and slip for composite slip on wet roads
The force-slip relation when both cornering and longitudinal acceleration/braking forces are acting on a tire simultaneously was discussed under abrasive tire wear for the brush model with a constant friction coefficient (see chapter 13). With the MTL it was possible to establish braking force curves under a set slip angle as shown in Figure 11.40. It is seen that the side force coefficient decreases as the braking force increases. The reason is that the total friction force is limited to a maximum value of μL, where L is the normal load. The brush model describes this behavior very well as seen by the curves that have been fitted to the data using the model with a friction coefficient which takes into account the lubrication effect as a function of the slip speed. Figure 11.41 shows calculated curves for different set slip angles using the brush model and a variable friction coefficient.

These data can also be plotted with the side force coefficient portrayed as a function of the braking/acceleration coefficient, producing a semi-ellipse for a constant friction coefficient. For a variable friction coefficient these ellipses turn inward at high braking forces, indicating that the braking coefficient decreases, as shown in Figure 11.42. Similarly, the maximum side force coefficient decreases for large slip angles.

Figure 11.40: Braking and side force coefficients as a function of the longitudinal slip for a set slip angle of 8° on wet asphalt at a constant speed of 30 mph, obtained with the Mobile Traction Laboratory of NHTSA. The curves were fitted using the brush model for composite slip with a variable friction coefficient.
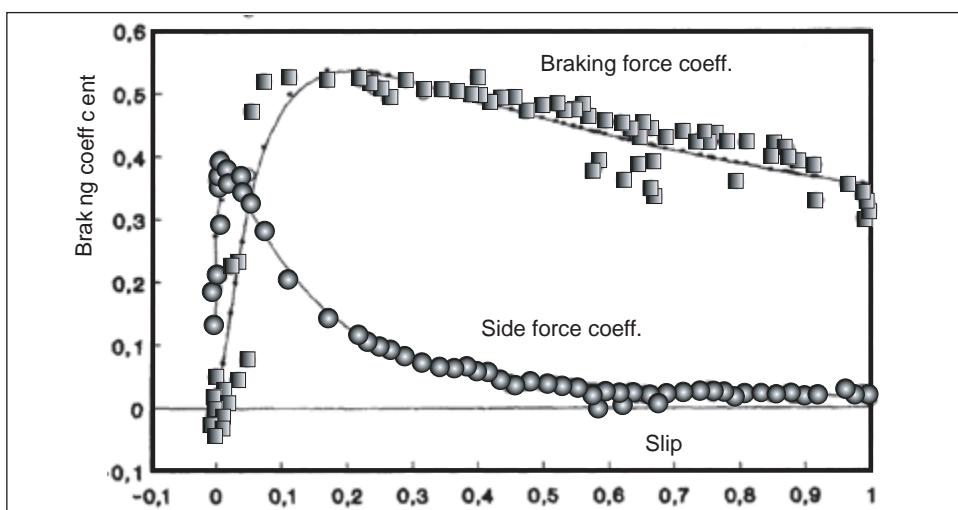
Figure 11.41: Braking coefficient as a function of slip for different slip angles, calculated with the brush tire model and a variable friction coefficient.
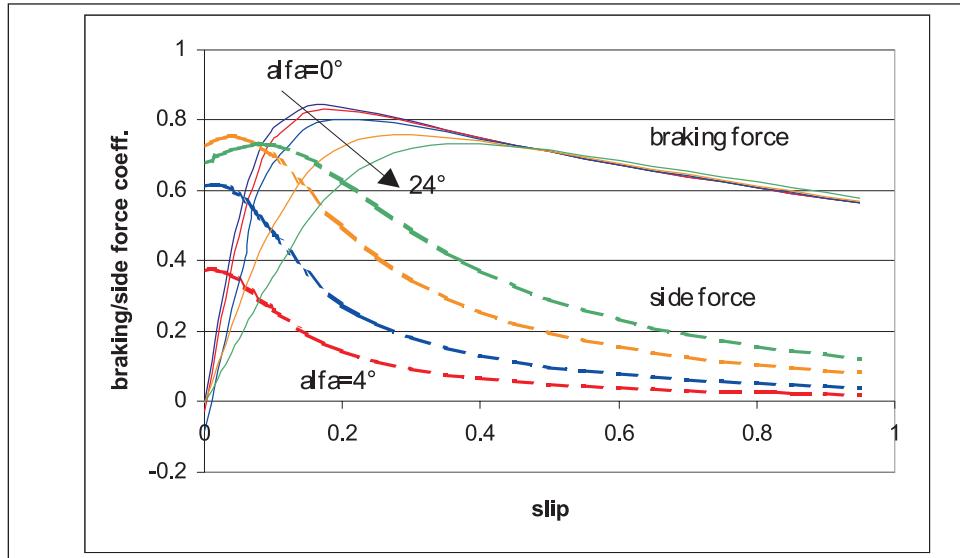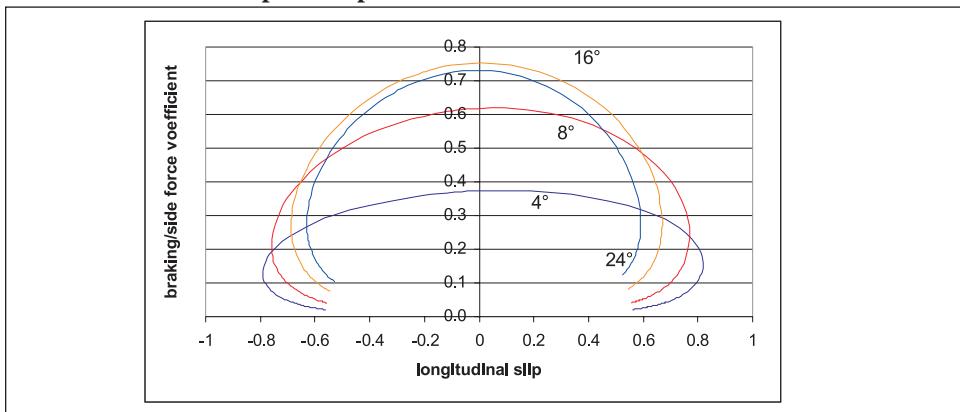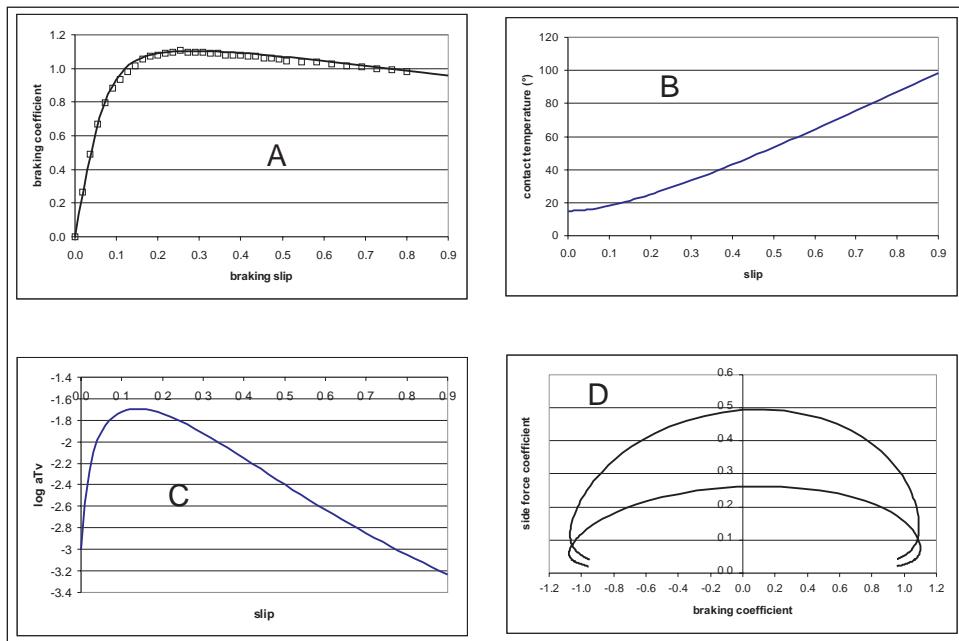

Figure 11.42: Side force coefficient as a function of the acceleration/braking coefficient for different set slip angles. Model curves using the brush model for composite slip and a variable friction coefficient.

Segel [39] obtained similar graphs on dry tracks again using traction equipment that could measure all of the force components and moments under controlled slip at set slip angles. At zero slip angle (and at all other slip angle settings) the braking force coefficient increased with increasing slip and passed through a shallow maximum at about 20% slip as shown in Figure 11.43 A. The experimental points have been taken from one of Segel's curves (Figure 11.7 of his chapter). They agree with the hypothesis that the friction coefficient decreases with increasing temperature brought about by increasing slip speed. The solid line was drawn using the brush model and a temperature and speed dependent friction coefficient. The temperature rise in the contact area required to obtain the curve fit is

shown in Figure 11.43 B and the resulting log a_Tv values are shown in Figure 11.43 C. The friction coefficient was calculated using a model master curve represented by a normal distribution function with parameters given in Figure 23 and with T_g = - 46°C. Finally, with the above data, the side force coefficient was plotted vs. the braking coefficient for two slip angles of 4 and 8°. The turn-in at high braking force coefficients is due to the increasing temperature in the contact area. These curves agree with the corresponding curves that Segel shows in Figure 11.17 of reference 39.

Figure 11.43: Braking force coefficient as a function of slip (A). The marked points are from figure 7 of Segel's paper [ref 39]. The line was obtained from the brush model with a variable friction coefficient and taking into account temperature rise with increasing slip. Also shown: the contact temperature rise (B) and log a_Tv as a function of slip. D shows the side force vs. braking force coefficient for set slip angles of 4° and 8° (compare with fig. 17 of ref 39)

4. Correlation between road test data and laboratory measurements on wet tracks

4.1 Laboratory measurements.

Laboratory measurements are primarily concerned with tread compound traction properties. Effects of tread pattern and other tire parameters such as cornering and longitudinal slip stiffness still require tests of tires on large in-door machines or at the proving ground. The basis of comparison between laboratory and road tests are use of similar log a_Tv values and similar track surface structures and conditions. As discussed in Section 3.1, side force measurements at constant slip angle and load over a suitable range of speeds and temperatures form a very good basis for comparison with road data.

The following laboratory surfaces have given high correlations with a wide range of road test data:

Alumina of several grades of coarseness and sharpness

Ground glass

Stainless steel with finely cut grooves.

Because of the limited range of log $a_T v$ values, a range of temperatures between 1 and 50°C and a sliding speed range of three decades from 2 km/h downward is sufficient to cover most of the slip speeds and log $a_T v$ values encountered in the contact area. Most of the laboratory evaluations are carried out on wet surfaces, where the water provides the required temperatures. In order to obtain the best correlation between road test ratings at one testing condition and laboratory ratings over a given range of log $a_T v$ it is useful to fit a simple mathematical function to the experimental points of the master curve. As already pointed out, a quadratic equation usually gives good results. A more sophisticated approach, that is better when minimum and maximum values of the master curve are to be included, is to use the normal distribution function but this is rarely necessary. Figure

Figure 11.44: Side force coefficient of compound A (an OE-SBR black filled tire tread compound) on wet blunt alumina 180 as a function of log $a_T v$ obtained at three speeds and five temperatures (open squares) with a quadratic equation fitted to the data (black solid line). The red marked points were obtained at one speed for five temperatures with the dotted red line the best-fit quadratic equation, showing the risk of extrapolating from a limited set of data.
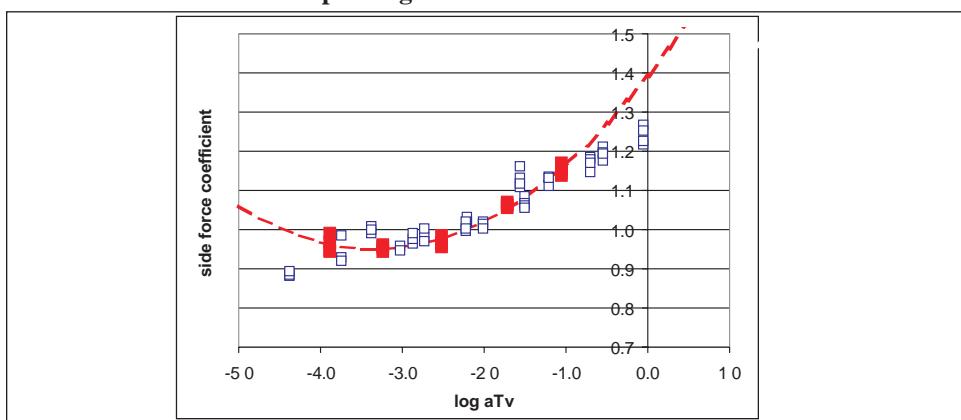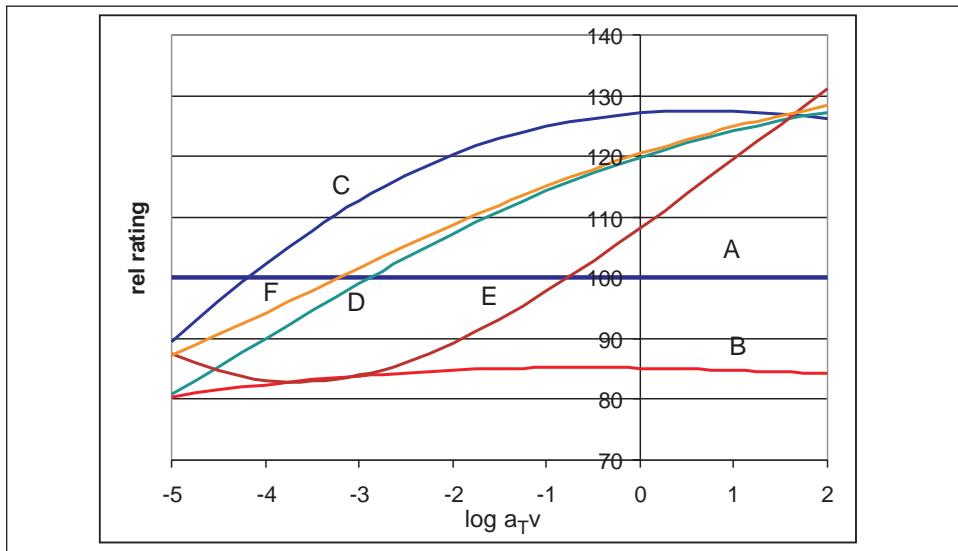

Table 11.4: Parameters for fitting a quadratic equation to the side force coefficients as a function of log $a_T v$ for six tread compounds on wet, blunt alumina 180 at different speeds and temperatures.

| Compound | Parameter of quadratic equation | | | Correlation coefficient |
	a	b1	b2	r
A	1.262	0.136	0.013	0.962
B	1.074	0.113	0.009	0.961
C	1.604	0.188	0.006	0.976
D	1.513	0.226	0.014	0.992
E	1.365	0.288	0.035	0.942
F	1.520	0.226	0.016	0.969

Figure 11.45: Ratings of the six compounds of table IV as a function of log $a_T v$ using compound A as reference
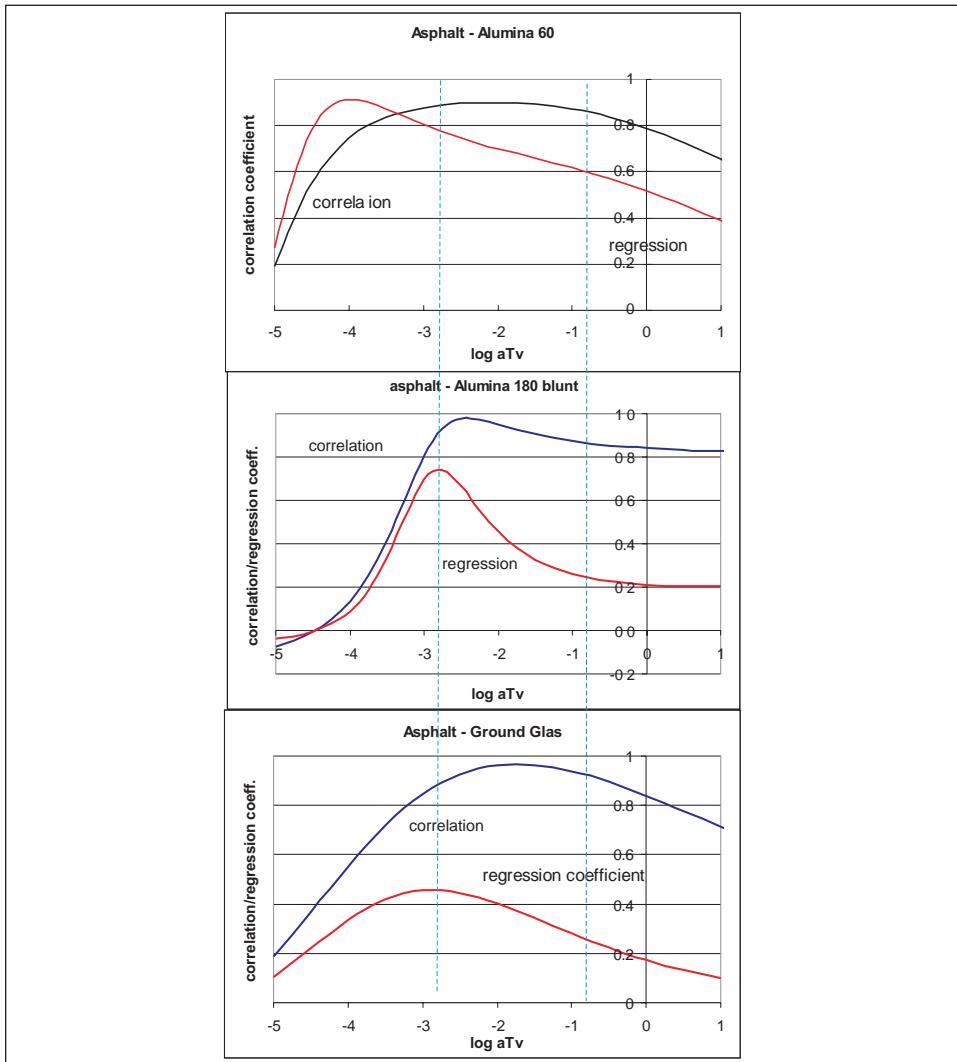

11.44 shows data for an OE-SBR black-filled passenger tire tread compound, obtained at different temperatures and speeds (black open squares and solid black line) and transformed into a master curve using the WLF equation, fitted with a quadratic function using the least-squares method. Table 11.4 shows the coefficients of such a function, together with the correlation coefficients, applied to six tire tread compounds for which road test results were also available. Figure 11.45 shows the compound ratings referred to compound A obtained from the fitted quadratic functions. It appears that most of the other compounds show improvements of ratings in relation to the control only over part of the experimental range.

4.2. Comparison of laboratory measurements with road test ratings.
In order to obtain a quantitative assessment of the correlation between road tests and laboratory tests, the road test ratings are compared with the laboratory ratings as a function of the log $a_T v$ values by calculating the linear regression line and correlation coefficient over a range of log $a_T v$ values. The resulting functions for the regression line and correlation coefficient are shown in Figure 11.46. The road test ratings were obtained on wet asphalt from braking distance measurements at speeds between 90 and 10 km/h. The laboratory measurements were carried out with an LAT 100 traction and abrasion tester on three wet surfaces: alumina 60, a coarse abrasive surface; alumina 180 blunt, a finer surface which was additionally blunted by skimming off the tips of the asperities; and a glass disk which had been dulled by grinding its surface with alumina 120 powder. It is seen that a good correlation exists over a range of about two decades for all three laboratory surfaces indicating that the road surface structure does not have to be matched closely in order to obtain a high correlation. The regression coefficients, however, vary considerably with the type of surface used both in the laboratory tests, as well as on the road surface. They are a measure of the discrimination between the two measurements that are being

Figure 11.46: Correlation and regression coefficients between road test ratings obtained on an asphalt track and laboratory ratings obtained on three different laboratory surfaces as a function of log $a_T v$

compared. In the present case the laboratory rating was used as the independent variable and the road rating as the dependent one. This means that the discrimination of the laboratory measurement is higher than that of the road if the regression coefficient is smaller than 1, and the reverse is true if it is larger than 1. It is seen that the regression coefficient becomes smaller the blunter and finer the surface. On the other hand, the repeatability of the laboratory measurements is higher the sharper the surface, being often better than 1% while on the very blunt ground glass it is about 3 - 5%. The finer surfaces are useful for screening compounds in the early stages of development because of their high discriminating power despite their greater variability.

4.3 Road test correlation with side force measurements at a constant speed, load and slip angle

Since the range of the master curve values of log a_Tv needed for a high correlation between road test ratings and laboratory measurements is only about two to three decades it may be sufficient to limit the experiments to a small number of temperatures at a constant speed. This saves a considerable amount of time in the early stages of compound development. To interpolate and extrapolate the curve to some extent, again a square-law relation is fitted to the curve relating side force coefficient to log a_Tv. In Figure 11.44 the red points are such measurements taken at five different temperatures at a constant speed of 0.6 km/h. The dotted red line is the square relation obtained by the least squares method based on the five measured points. It is seen that good agreement is obtained within the experimental range but that extrapolation in both directions leads to considerable deviations from the curve obtained from a wider range of measurements. It is important to be always conscious of this risk.

   If road test ratings are available the same procedure can be followed.

4.4 Road test correlation between laboratory side force measurements at a single test condition.

The high correlation obtained over a range of log a_Tv values suggests that a high correlation may also be obtained at a single temperature and speed test condition if this condition is chosen with reasonable care. Figure 11.47 shows such a correlation obtained with 10 different tire tread compounds [37]. The road test ratings were obtained from the times it took to negotiate a wet slalom test track between two electronic measuring gates. The laboratory tests were carried out on wet ground glass at a water temperature of 2°C and a speed of 0.6 km/h. The road test rating times were converted into force-based ratings using the argument that the time taken is a measure of the maximum cornering capability of the tread compound.

   If the slalom course is described by a sine function the acceleration of a mass traveling along the sinusoidal path is given by

$$\frac{d^2y}{dt^2} = -\sin x \cdot \left(\frac{dx}{dt}\right)^2 = -v_f^2 \cdot \sin x \qquad [37]$$

where v_f is the forward speed of the mass. The maximum acceleration is given by the maximum cornering force that can be sustained without complete sliding

$$F_{max} = \frac{\mu_p}{g} W \qquad [38]$$

where μ_p is the peak friction coefficient on a wet track and W is the weight. Since this coefficient is proportional to (maximum speed)^2 the rating is given by

$$R = \frac{F_{exp}}{F_{contr.}} \cdot 100 = \frac{t_{control}^2}{t_{exp}^2} 100 \qquad [39]$$

where t_{exp} is the time taken to negotiate the course.

   It is seen that a very high correlation is obtained between road test ratings and laboratory measurements for the ten compounds with a very much larger discrimination for the

laboratory ratings than for the road test results.

Figure 11.47: Correlation between a slalom test on asphalt and laboratory ratings obtained under a single test condition on ground glass. Slip angle 13.5°, water temperature 1.4°C, load 76 N, speed 0.6 km/h [from ref 37]
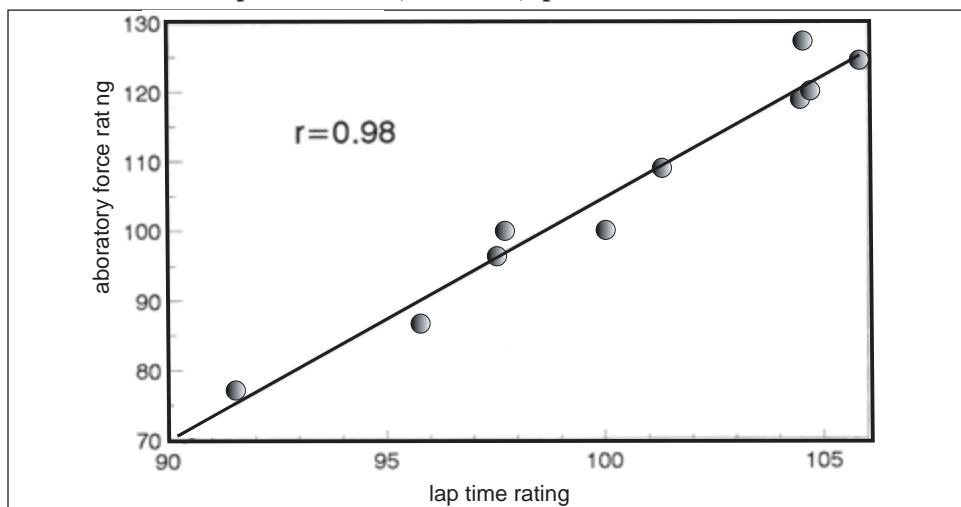

Figure 11.48: Correlation between road test ratings supplied by different tire manufacturers and average laboratory ratings on a wet, blunt alumina 180 surface from a testing program using a range of temperatures and speeds.
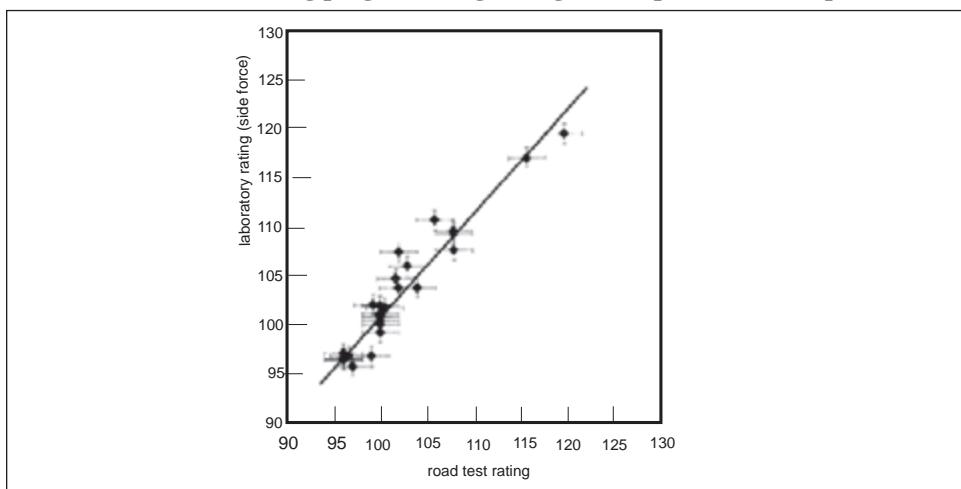
Figure 11.48 shows laboratory ratings that were obtained from the average values of tests on an LAT 100 tester at Degussa in cooperation with several tire companies who used different road test evaluation methods for determining the wet traction properties of the same compounds [40, 41]. In this case, too, a high correlation is obtained between road and laboratory test results. Such screening tests give obviously only limited information, as discussed above. It is known that traction performance often depends critically on the test conditions and a more extensive laboratory testing program will reveal regions of better and worse traction performance.

4.5 The influence of the track surface structure on the correlation between laboratory and road test ratings.

Considerable efforts have been expended to find the best possible laboratory surface for evaluating the traction of tread compounds. The simplest way would be to bring road surfaces into the laboratory. This is not possible for two reasons. First, there are no well-defined road surfaces. Although they are primarily made up of either concrete or asphalt, they differ drastically in coarseness and sharpness. Second, none of them is durable enough to withstand continuous use in the laboratory.

In the present context, with the emphasis on wet friction, only surfaces with some roughness are considered. Grindstones of different grain size have been used but also glass surfaces either dulled chemically or mechanically and in one case stainless steel with fine interlacing groves.

Table 11.5: Correlation (upper right) and regression coefficients (lower left) obtained with a single test condition using six different laboratory surfaces and road test ratings obtained with one testing condition on three different proving ground surfaces. Laboratory test condition: side force measurements at 13° slip angle, 76 N load, and 2°C water temperature. Road test condition: stopping distance from 90 km/h to 10 km/h, ABS braking, ambient temperature 5°C.

	Al 60 sharp	Al400 sharp	Al400 blunt	Al180 blunt	Ground glass	Stle. steel finely lathed	Concrete	Asphalt-1	Asphalt-2
Al 60		0.860	0.999	0.946	0.965	0.954	0.968	0.991	0.986
Al 400 sharp	0.999		0.859	0.951	0.850	0.961	0.962	0.951	0.993
Al 400 blunt	1.077	1.075		0.953	0.853	0.870	0.968	0.980	0.941
Al 180 blunt	0.884	0.959	1.116		0.967	0.877	0.884	0.970	0.942
Ground glass	2.362	1.946	2.106	2.772		0.993	0.896	0.864	0.970
St. steel	0.965	2.380	2.016	2.189	2.881		0.954	0.876	0.908
Concrete	0.374	0.377	0.928	0.792	0.866	1.071		0.943	0.922
Asphalt-1	0.879	0.326	0.340	0.824	0.687	0.751	0.939		0.921
Asphalt-2	0.732	0.654	0.240	0.243	0.613	0.536	0.587	0.681	

Experiments with the six different compounds referred to above on six laboratory surfaces of widely differing sharpness and coarseness and tire test ratings on three different road surfaces showed that a good correlation existed in all cases when the surfaces were

compared with each other at a single, carefully chosen testing condition, as shown in Table 11.5. The correlation coefficients are given in the upper right and the regression coefficients in the lower left part. If the coefficient is larger than 1, then the surface listed in the left column is more discriminating than the surface listed in the corresponding row.

The results in this table confirm again that the surface structure is not a major variable when considering friction and traction under a limited range of testing conditions on wet surfaces.

4.6 Data evaluation treating speed and temperature as independent variables.

Up to this point, all comparisons were based on the speed-temperature equivalence given in the WLF equation. There is a good reason for doing this. Even if deviations from the WLF equation did occur, there is overwhelming evidence that temperature and speed are not independent of each other. An interrelation between speed and temperature is obviously dominating the behavior. The WLF transform is therefore a good starting point. A very broad body of data exists which conforms closely to this transformation within the accuracy of careful measurements of friction or side force. Occasionally, however, deviations are observed. Usually the speed dependence at a given temperature is less pronounced than would be expected from the WLF transformation. One explanation could be that lubrication plays a part, despite the low speeds used in the experiments. Since, however, the phenomenon appears also to be associated with specific compounds, a reason could be that modern compounds are often blends of different polymers, and the glass transition temperatures are not well defined. Also the influence of modern filler systems, particular silica with silane coupling, may contribute to such deviations. Carbon black generally does not influence the transformation but only affects the magnitude of the friction coefficient. This may not be true for silica because of the different coupling interaction with the polymer. At present there are insufficient data available to test these hypotheses.

A correlation with road test ratings can often be improved if an independent term in log v is added to the transformation variable log a_Tv. The friction or side force coefficient can then be written as

$$fc = a + b_1 \cdot [\log(a_T v)] + b_2 \cdot \{\log(a_T v)\}^2 + b_3 \cdot \log(v) \qquad [40]$$

using again a square relation to represent the master curve.

A full data set over a range of temperatures and speeds is necessary to determine the

**Figure 11.49: Side force coefficient as a function of log a_Tv
and log v for compound A and compound C of table IV.**
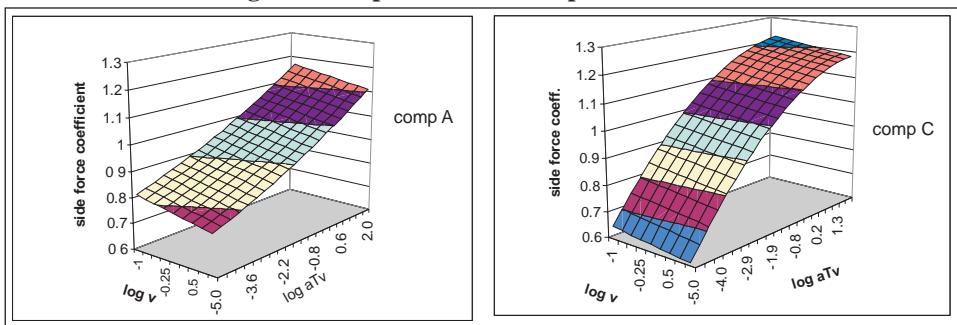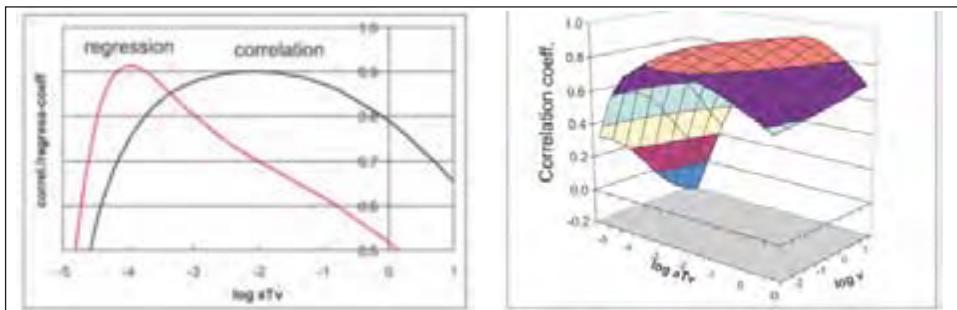
Figure 11.50: Correlation coefficient between road test ratings on a wet concrete track and laboratory measurements on a wet blunt alumina 180 disk. Upper part as a function of log $a_T v$ and lower part as a function of log $a_T v$ and log v.

four constants by the least-squares method. The results have to be presented as a table or as a three dimensional graph. As an example, the side force coefficients are shown in Figure 11.49 for compounds A and C of Table 11.4. It is seen that the major variation is due to the log $a_T v$ terms and only a small part is due to the additional log v term. The correlation with road test ratings of the six compounds of Table 11.4 is shown in Figure 11.50, comparing the results using log $a_T v$ only (upper part) and the extended version with the added log v term (lower part). Both laboratory data sets were obtained on wet blunt alumina 180. The road test ratings were obtained on a concrete track from stopping distance measurements for speeds between 90 and 10 km/h using ABS braking. It appears that the point of highest correlation shifts slightly with the speed and is also improved.

If the WLF transform is not obeyed rigorously, a more empirical analysis is possible, treating temperature and speed as separate variables. The temperature dependence can be described by a square law, and the speed dependence by a linear relation between the friction or side force coefficient and log (speed). The addition of an interaction term, i.e. a dependence of friction or side force on both temperature and speed, would amount to recognizing some kind of equivalence between them, i.e. invoking a treatment similar to the WLF equation described above.

Figure 11.51 shows the side force coefficient (upper part) of compound C of Table 11.4 and its rating (lower part) relative to compound A as a function of temperature and log (speed). The side force coefficient depends on temperature and log (speed). Indeed, the rating of compound C relative to A depends on temperature so strongly that a reversal in ranking occurs. The dependence on speed, however, is small. Figure 11.52 compares the correlation coefficient between a road test on wet concrete and laboratory side force measurements for the six compounds of Table 11.4 on blunt, wet alumina 180 (a) with a log $(a_T v)$ - log v evaluation and (b) with a temperature - log v evaluation. It appears that the correlation coefficient for the temperature - log v evaluation depends strongly on both temperature and speed, i.e. on the laboratory testing condition, while in the log $(a_T v)$ - log v evaluation the correlation depends on log $(a_T v)$ but not on log v. Both methods: log $a_T v$ - log v and temperature - log v give equivalent results and similar correlations with road test data and both are slightly more precise than the evaluation based on log $(a_T v$ alone). Clearly, the direct temperature-log v evaluation is easier to handle and probably also more easily understood in routine evaluation and comparison of compounds. The log $(a_T v)$

Figure 11.51: Side force coefficient of compound C of table IV and its rating relative to compound A as a function of temperature and log v.
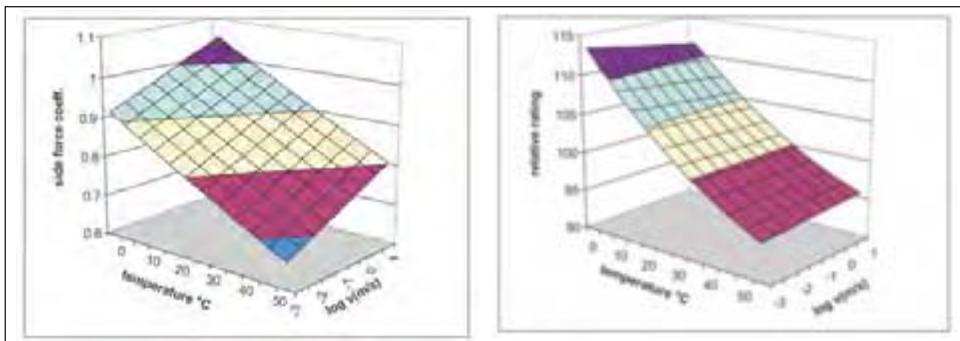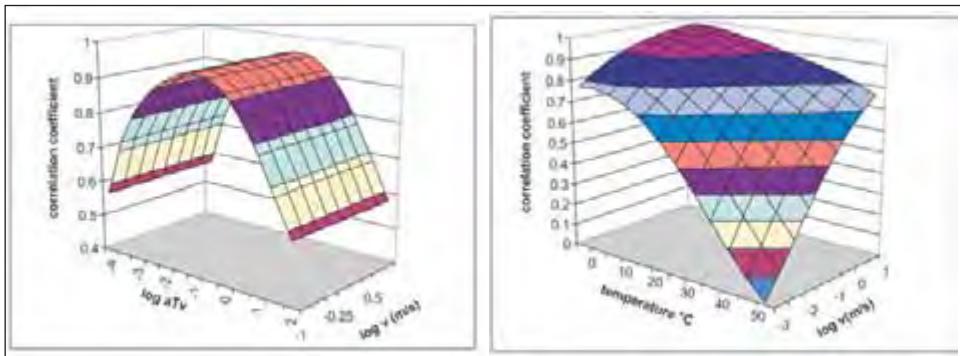

Figure 11.52: Comparison of the correlation coefficients between laboratory side force measurements with the six compounds of table IV on wet, blunt alumina 180 and a concrete road test track. Left, as a function of log aTv and log v and, right, as a function of temperature and log v.

method, however, has a clear physical interpretation and if deviations from the master curves are observed repeatedly then it would be worthwhile to spent some research effort to identify the cause. In particular, if deviations are compound-specific, it may be very useful and of practical benefit to understand their origin.

4.7 Correlation between road test ratings and simulated road tests using laboratory measurements.

It was pointed out above that when practical traction tests are to be simulated using laboratory data the heat transfer constant and hence the operating temperature in the contact area cannot be determined explicitly. However, if road test ratings are available they can be used to determine this constant.

For this purpose a road test simulation program is necessary using the test conditions under which the actual road test ratings were obtained and a set of laboratory measurements to determine the parameters with which laboratory ratings can be calculated for a range of log (a_Tv) and log v values.

Starting with the initial vehicle speed, the braking slip condition and an initial value for the constant ξ_c, a temperature in the contact area and hence a value of log a_Tv and a provi-

sional value of the braking coefficient for the first compound is obtained. Because the braking coefficient is employed in the temperature rise equation an iteration process is required to find the actual temperature, the log a_Tv value and the corresponding braking coefficient.

For braking distance measurements the distance and speed attained after a small time interval are then calculated. This procedure is repeated and the incremental distances are added up until the final (set) speed is reached, giving the total braking distance. The whole procedure is repeated for all compounds in the testing program. From the braking distances ratings are calculated for all compounds relative to the chosen reference tire. A linear regression equation and correlation coefficient between these ratings and road test ratings are obtained. The procedure is then repeated with different ξ_c values until the highest correlation coefficient is reached.

Such an evaluation is shown in Table 11.6, which lists the road test conditions, the road test ratings for the six compounds on wet concrete and ratings calculated from laboratory data of side force coefficients at five temperatures and four logarithmically-spaced speeds on wet alumina 60. It is seen that a high correlation is achieved using a heat transfer constant of 0.79. This is not a universal constant, however; it depends strongly on the type of braking test, in particular whether it is ABS or locked-wheel braking, and also on road conditions such as surface structure and water level and ambient temperature.

Table 11.6: Comparison of a road test simulation using laboratory data obtained on wet alumina 60 with six compounds (parameters from table IV) with a road test on wet concrete to give the calibration constant of the contact temperature rise with the highest correlation

road surface	test conditions:		statistic:	
	unitial speed	90 km/h	**calibaration factor**	**0.79**
	final speed	10 km/h	ordinate intercept	5.4
concrete	Critical speed for		regression coeff.	0.937
	sliding lubrication	150 km/h	**correlation coeff**	**0.957**
	Aquaplanuing speed	400 km/h		
	ambient temperature	5 °C		
	inflation pressure	2.5 bar		

calc. ratings	exp. ratings
100.0	100.0
80.1	80.9
113.1	107.9
102.0	106.8
86.1	83.4
95.6	93.4

Conclusions

The visco-elastic properties of an elastomer have been shown to play a dominating role in the friction of tire tread compounds. Two processes contribute to the total friction: adhe-

sion and internal energy losses though cyclic deformation. Both are strongly influenced by visco-elasticity. Adhesion is an activated process akin to the cohesion of liquids. This is demonstrated by the applicability of the WLF speed-temperature equivalence. Moreover, the conversion constant between the speed of maximum friction and the time of the maximum in the relaxation spectrum of the polymer coincides with the frequency of the maximum loss modulus or the maximum of the first derivative of the real part of the modulus. On optically smooth surfaces this molecular adhesion process is the dominating factor in elastomer friction. On rough surfaces a cyclic local deformation process causes internal energy losses. In this case the conversion constant is a length directly linked to the asperity spacing of the track. But adhesion also plays a major role on rough tracks. Purely normal deformation contributes only a very limited fraction of the total friction. Tangential stresses are required to account for the high friction on rough surfaces and these are made possible by the presence of adhesion. Even a small adhesion component, as for contaminated rubber surfaces, produces large tangential stresses in the rubber. Indeed, friction on rough surfaces is not only due to internal cyclic energy losses, but rather the total energy stored through the presence of tangential stresses is lost. The process can be likened to an adiabatic thermodynamic cycle.

This basic rubber friction process is present on all surfaces, dry, wet or icy, being modified only by the external conditions. On wet surfaces this is primarily water lubrication which is itself influenced by the water depth, roughness of the road surface and the state of the tire tread pattern. For given conditions the lubrication depends on the slip speed between tire and road and modifies the dry friction coefficient. An additional effect is produced by the inertia of the water that must be removed from the contact area. The lubrication effect becomes operative only when forces are transmitted between tire and road. This occurs also during free rolling but at considerably higher speeds if sufficient tread pattern is available to allow good water drainage from the contact area.

The low friction on ice near its melting point is mainly due to the properties of the ice. A special winter tread compound is required because the contact temperature cannot exceed 0°C. Because of the large latent heat of melting, the film of water produced through heat generated in the contact area is so thin that it does not affect the friction coefficient significantly. Hence high friction coefficients on ice are possible at temperatures below about –10°C. The limitation is set by the compound properties, expressed through its glass transition temperature.

The friction master curve of a polymer on a particular surface contains practically all of the frictional information. However, recent experiments suggest that there may be small deviations from this, particularly for modern blends where the glass transition temperature is not well defined. There are also possibly effects due to use of new filler systems that may affect rubber friction separately from the visco-elastic relation to some extent. This could become an interesting area of research since every possibility of increasing friction on the road without simultaneously raising the internal friction and hence the rolling resistance of the tire is of great practical value.

Basically, a road traction test differs from a laboratory test only in that the temperature in the contact area is allowed to rise and is not really measurable, while in the laboratory the speed is kept so low that the temperature rise may usually be neglected. The different surface structures of the road and laboratory test surfaces appear to play a minor role. This is not surprising since at a given speed the coarseness of a track (the average spacing of the asperities) influences the friction only on a logarithmic scale. Also the observed

dependence of the friction coefficient on load for soft rubber compounds on smooth surfaces disappears for harder black or silica filled tread compounds on rough surfaces.

A good correlation between road tests and laboratory measurements is usually obtained only over a limited range of the master variable log (a_Tv). Comparisons of the friction coefficients of different compounds over a wider range of log (a_Tv) values with road test ratings identify the useful range and give a detailed picture of its capabilities in practical tire use. Further developments of compounds can be limited to laboratory assessments over a limited range of log (a_Tv), i.e. of temperatures and speeds with a strong assurance that the road performance will reflect the laboratory findings. Winter compounds are still best developed on an ice track because this is the easiest way to produce the necessary low temperature range.

Since modern compounds are highly sophisticated compositions of polymer types and fillers, a detailed understanding of the exact shape of a master curve, its relation to the WLF transform, and possible deviations from it, still requires further research.

References

1. F. B. Bowden and A. D. Tabor (1954), Friction and Lubrication of Solids, Oxford University Press (London)

2. P. Thirion, Gen. Caout. **23**, (1946), 101

3. A. Schallamach, Proc. Phys. Soc. **B65**, (1952), 657

4. A. Schallamach, Wear **1**,(1958) 384

5. K. A. Grosch, Rubber Chem. Technol. Rubber Reviews, **69**, (1996), 3

6. M. L. Williams, R. F. Landel, and J. D. Ferry, J. Am. Chem. Soc **77** (1955) 3701

7. See literature on visco-elasticity, for example J. D. Ferry (1961) The Visco-elastic Properties of Polymers

8. L.Mullins, Trans I.R.I., **35**, (1959), 213

9. T. L. Smith, J. Polym. Sci. **32**, (1958), 99

10. K. A. Grosch, Proc. Royal Soc. **A 274** (1963) 21

11. K. A. Grosch, Ph.D. Thesis "Sliding Friction and Abrasion of Rubbers", University of London, 1963

12. A. Schallamach, Wear **6** (1963) 375

13. F. A. Greenwood and D. Tabor, Proc. Phys. Soc **71** (1958), 989.

14. F. A. Greenwood and J. B. P Williams, Proc. Roy. Soc, **A 295** (1966), 300

15. M. Klüppel, A. Müller, A. Le Gal and G. Heinrich ACS, Rubber Division Meeting San Francisco, Spring 2003

16. H. Rieger, Dissertation TH Munich 1968

17. K. A. Grosch, The Speed and Temperature Dependence of Rubber Friction and its Bearing on the Skid Resistance of Tires, in "The Physics of Tire Traction, Theory and Experiment", ed. by D. L. Hayes and A. L. Browne, Plenum Press New York, 1974, 143

18. A. D. Roberts, Lubrication studies of smooth rubber contacts, in "The Physics of Tire Traction, Theory and Experiment", ed. by D. L. Hayes and A. L. Browne, Plenum Press New York, 1974, 143

19. A. G. M. Mitchell, "Viscosity and Lubrication, The Mechanical Properties of Fluids", Blackie and Sons Ltd, London, 1944

20. T. Kirk and T. F. Archard, Proc. Roy. Soc: London, **261**, (196), 532

21. A. L. Browne, Tire Sci. Technol. **3,** No. 1 (1975) 6

22. K. A. Grosch, Kautschuk und Gummi, Kunststoffe, **49**, Nr. 6 (1996), 132

23. G. Heinrich, ACS Rubber Division Spring Meeting Montreal 1996

24. B. Persson, Surface Science, **401,** (1998) 445

25. M. Klüppel, G. Heinrich, ACS Rubber Division Meeting Spring 1999, paper 43

26. R. B. Yeager, Tire Hydroplaning,.Testing, Analysis and Design, in "The Physics of Tire Traction, Theory and Experiment", ed. by D. L. Hayes and A. L. Browne, Plenum Press New York-London 1974, 143

27. R. N. J. Saal, J. Soc. Chem. Ind., **55,** (1936), 3

28. A. L. Browne, Tire Sci. Technol. **1**, (1977)

29. W. B. Horne and U.T. Joyner, SAE report **870 C** (1965)

30. H. Barthelt, Automobil Technische Zeitung, **10,** (1973), 368

31. G. Maycock, Proc. Inst. Mech Eng. **80,** 2A (1965-66), 122; Rubber Chem. Technol. **41,** (1968) 780

32. K. A. Grosch and G. Maycock, Trans I.R.I., **43**, (1966), 280; Rubber Chem. Techn.**41**,(1968) 477

33. A. D. Roberts and J. D. Lane, J. Phys. D, **16** (1983) 275

34. W. Gnörich and K. A. Grosch, J. I R I., **6** (1972) 192

35. K. A. Grosch, to be published

36. K. A. Grosch Kautschuk, Gummi, Kunststoffe, **6** (1996),432

37. K. A. Grosch, International Tire Technology Conference, RAPRA Technology Ltd London (1998)

38. H. S. Carslaw and J. C. Jaeger, Oxford University Press (1959), p. 279

39. I. Segel, Tire Traction on Dry, Uncontaminated Surfaces, in "The Physics of Tire Traction, Theory and Experiment", ed. by D. L. Hayes and A. L. Browne, Plenum Press New York-London 1974, 65

40. M. Heinz; Conference on Time Dependent Materials 2000; 17-20 Sept. 2000, Erlangen, Germany

41. K. A. Grosch and M. Heinz; International Rubber Conference 2000; Helsinki, Finland

Chapter 12
Rolling Resistance

by T. J. LaClair

Chapter 12
Rolling Resistance

by T. J. LaClair

1. Introduction

When a tire rolls on the road, mechanical energy is converted to heat as a result of the phenomenon referred to as rolling resistance. Effectively, the tire consumes a portion of the power transmitted to the wheels, thus leaving less energy available for moving the vehicle forward. Rolling resistance therefore plays an important part in increasing vehicle fuel consumption.

Since the oil embargo in 1973, there has been increasing pressure to reduce fuel consumption. The Corporate Average Fuel Economy (CAFE) program was established by the United States federal government as part of the Energy Policy and Conservation Act of 1975. The CAFE standards were mandated in an effort to minimize the country's dependence on foreign oil. The regulations require each automobile manufacturer to achieve an annual sales-weighted average fuel economy that meets or exceeds the specified CAFE standards. Otherwise, the manufacturer is subject to fines, which are currently set at $5.50 per vehicle sold for each 0.1 mpg by which the average fuel economy is below the standard. Separate standards exist for passenger cars and light trucks, and the average fuel economies are calculated separately for the two categories of vehicles.

Vehicle manufacturers have therefore continued to push tire manufacturers for reductions in rolling resistance. While the CAFE standards have forced tire manufacturers to focus heavily on tires for new vehicles, it is likely in the future that they will also be required to provide replacement tires with low rolling resistance. The State of California recently passed legislation that will require replacement tires to have a level of rolling resistance that is, on average, equivalent to or better than original-equipment tires [1], and the U.S. Senate is also proposing to establish tire efficiency standards and labeling for replacement tires. The pressure for attaining improvements in rolling resistance is likely to continue.

This chapter is intended to provide the reader with an introduction to the subject of tire rolling resistance. The following topics are discussed: physical causes and effects of rolling resistance, design and use factors that impact rolling resistance, prediction and measurement methods and test standards, and the effect that rolling resistance has on vehicle fuel consumption. While the author has attempted to provide a comprehensive account, the technical literature should be reviewed for details on specific topics that are covered only briefly here. Several thorough reviews exist [2-4], and these should serve as excellent starting points for more detailed studies.

1.1 Definition of rolling resistance

Most people are familiar with the phenomenon of rolling resistance from first hand experience. When riding a bicycle or pushing a wheelbarrow with under-inflated tires, one notices that a fair amount of effort is required to keep it moving, even at a relatively slow speed. The reason for this is, of course, that the resistance to rolling increases with reduced tire pressure. Most people will immediately realize the cause and inflate the tires to a higher pressure. (It is rather ironic that people do not usually reach the same conclusion about

their car tires - that additional energy is needed to drive with under-inflated tires - probably because cars have sufficient power so that the reduction in performance is not so obvious.)

Rolling resistance is the effort required to keep a given tire rolling. Its magnitude depends on the tire used, the nature of the surface on which it rolls, and the operating conditions — inflation pressure, load and speed. Rolling resistance has historically been treated as a force opposing the direction of travel, like a frictional force. While the force concept is appropriate for a free-rolling tire on a flat surface, it proves unsatisfactory in other cases. A more general concept is in terms of the *energy* consumed by a rolling tire. Although several authors [5-8] recognized the importance of energy consumption, the concept of rolling resistance as a retarding force has persisted for many years. Schuring [9] provided the following definition of rolling resistance as a loss in mechanical energy:

"Rolling [resistance] is the mechanical energy converted into heat by a tire moving for a unit distance on the roadway."

He proposed the term "rolling loss" instead of "rolling resistance" so that the long-standing idea of a force would be avoided. Although the term "rolling loss" has been used regularly since then, at present the generally accepted term, and that appearing in current test standards (for example the SAE J1269 rolling resistance standard) is "rolling resistance," which is also used throughout this chapter [10].

Schuring pointed out that although rolling resistance — defined as energy per unit distance — has the same units as force (J/m = N), it is a scalar quantity with no direction associated with it. This distinction is important, once we understand the causes of rolling resistance, and the idea of rolling resistance as a retarding force should be disregarded. Even though the normal symbol used to denote rolling resistance is F_R, it is emphasized that, in many instances, the value of F_R is calculated from operating and geometrical parameters – it does not correspond to an actual physical force. Rolling resistance includes mechanical energy losses due to aerodynamic drag associated with rolling, friction between the tire and road and between the tire and rim, and energy losses taking place within the structure of the tire. Bearing losses at the tire spindle, however, are excluded, since they result in a reduction in the energy transmitted to the tire.

Schuring defined rolling resistance as "mechanical energy converted into heat." For any device where the output (generation) or transmission of mechanical energy is a primary concern — as for the automobile and, ultimately, the tire — thermodynamics becomes a useful tool for evaluating losses in mechanical energy (work). Detailed discussion of this view is postponed until Section 2.6, but it is appropriate at this point to mention the importance of heat with respect to rolling resistance. Thermodynamics tells us that energy transfer across system boundaries takes only two forms, work and heat transfer. As a result of energy transfer, the internal energy often changes within a system, resulting in changes in temperature. In a tire, much of the energy conversion occurs internally, resulting in heat dissipation within the volume of tire, causing its temperature to increase. This heat dissipation is a result of mechanical hysteresis of the materials in the tire. Additionally, friction between the tire and road, and between the tire and rim, causes heat to be generated, and the aerodynamic drag between the tire and surrounding air leads to thermal energy generation as a result of the dissipative action of the air's viscosity. Thus, all of the mechanical energy losses associated with the rolling tire are, indeed, converted into heat.

Holt and Wormeley [5] presented an analysis of the energy losses associated with a rolling tire (although they considered the energy loss to be different from the rolling resistance). They evaluated the power losses for tires using a test apparatus consisting of a tire driven by an electric motor (i.e., operating under torque) rolling against a test drum that was connected to an electrical generator, which provided a braking force to maintain the tire at a constant speed for a given torque input. They performed an energy balance resulting in the following expression:

$$P_{tire}=P_{in}-P_{out} \hspace{4cm} (1.1)$$

The term P_{tire} denotes the rate of energy converted to heat by the tire, while P_{in} and P_{out} are the input and output mechanical energies, which were directly measured through the electrical power input and output from the motor and generator, respectively. Schuring noted that the energy balance approach, as applied in this specific case, is entirely general and claimed that it could be used in any rolling situation to determine the rolling resistance. Equation 1.1 applies to steady-state operating conditions and can be easily modified, as shown in section 2.6, for transient conditions.

During a time interval, dt, the tire travels a distance ds = v dt with respect to the surface on which it rolls. The road speed, v, is the speed at which the road or test surface moves relative to the tire, whether the tire physically moves, as in the case of a vehicle driving on the road, or the tire rolls in place, as on a test wheel or flat track machine that moves under the tire. The mechanical energy loss of the tire during the interval dt is given by

$$\delta W_{tire}=F_R ds=F_R v dt, \hspace{3cm} (1.2)$$

where F_R is the rolling resistance. Since power, in general, is given by force times velocity, the rolling resistance can be calculated from the input and output powers, as

$$F_R=(P_{in}-P_{out})/v. \hspace{3cm} (1.3)$$
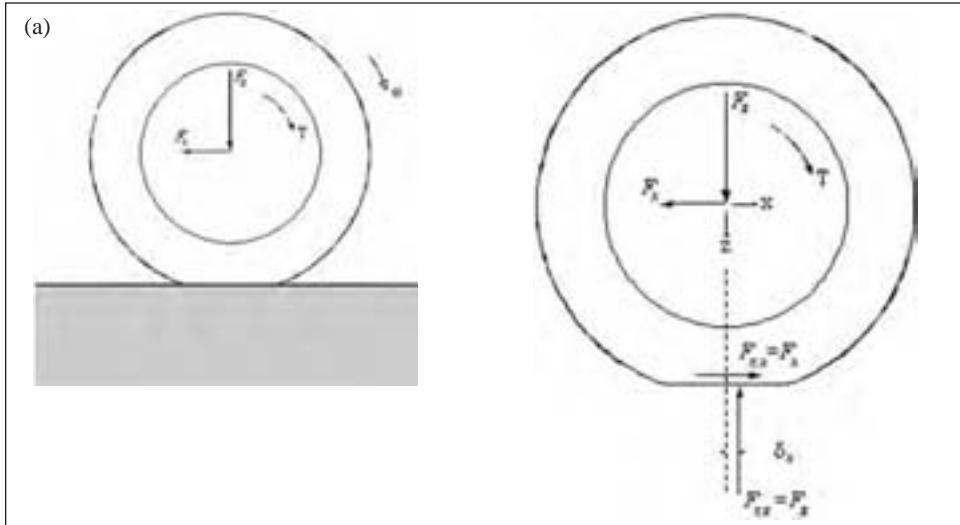
Schuring regarded this equation as the most general expression for calculating rolling resistance. Note that $P_{in}-P_{out}$ is the *net* mechanical power input to the tire, denoted $\dot{W}$ in standard thermodynamic terms.

1.2 Rolling resistance relations for rolling under various conditions

Using Eq. 1.3, the rolling resistance can be determined for any steady operating condition of a tire. As an example, consider the case of a tire rolling with zero camber and slip angles on a flat surface while operating under an applied torque, T. Figure 12.1 (a) shows the applied forces and torque acting on the rolling tire, while figure 12.1 (b) is the free-body diagram for the tire with all reactive forces included. Note that the vertical reaction force at the ground is not aligned with the centerline of the tire in the general case, as illustrated in figure 12.1 (b), as can be shown by applying a moment balance about the center of the wheel. This force does not affect the power, however, since the load is perpendicular to the direction of travel. The power input due to the torque is Tw, while that due to the force $F_{r,x}$ is $-F_{r,x}v = -F_x v$. (Note that if the coordinate system is defined with the origin attached to the wheel axle, as in the figure, the force at the spindle does not contribute to the net power, since the spindle velocity is zero in this reference frame.) Therefore, the

net input power applied to the tire is $(T\omega - F_X v)$, where ω is the angular velocity of the

Figure 12.1: (a) Tire rolling under applied torque on a flat surface.
(b) Free-body diagram of the tire.

wheel. The rolling resistance in this case is therefore obtained from Eq. 1.3 as

$$F_R = T\frac{\omega}{v} - F_x.$$ (1.4)

It is seen that in the case of a free-rolling tire ($\omega = 0$) the rolling resistance is equal in magnitude to the force F_x opposing the motion of the tire. However, in the general situation this is clearly not the case.

The rolling resistance for other operating conditions can similarly be determined by application of Eq. 1.3. Table 12.1 provides formulas for the calculation of rolling resistance for steady operating conditions on either a flat surface or a cylindrical drum for different combinations of camber, slip angle and torque, as derived by Schuring [9]. The rolling resistance is calculated from the various forces and moments acting on the tire, as given by the equation

$$F_R = AT + BF_x + CF_y + DM_x + EM_z.$$ (1.5)

In Eq. 1.5, F_y is the lateral force, M_x is the overturning moment, and M_z is the aligning torque, as defined in the SAE standard terminology [10].
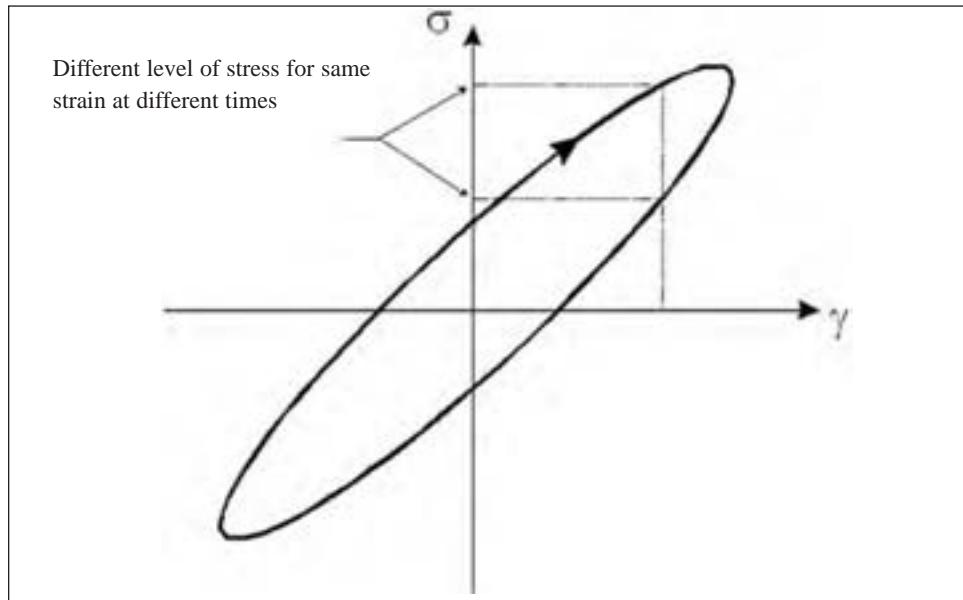
**Table 12.1: Rolling resistance on a test drum and flat surface,
with applied slip angle, camber angle, and torque**

| Test surface	Condition	A	B	C	D	E
	General	$\omega/v+\cos\alpha/(R\cos\gamma)$	$-(\cos\alpha+R_1\cos\alpha/(R\cos\gamma))$	$-\sin\alpha$	$-\sin\alpha/R$	$-\cos\alpha\sin\gamma/(R\cos\gamma)$
Roadwheel	$\gamma=0$	$\omega/v+\cos\alpha/R$	$-(\cos\alpha+R_1\cos\alpha/R)$	$-\sin\alpha$	$-\sin\alpha/R$	0
(surface with con-	$\alpha=\gamma=0$	$\omega/v+1/R$	$-(1+R_1/R)$	0	0	0
stant radius, R)	$T=\gamma=0$	0	$-(\cos\alpha+R_1\cos\alpha/R)$	$-\sin\alpha$	$-\sin\alpha/R$	0
	$T=\alpha=\gamma=0$	0	$-(1+R_1/R)$	0	0	0
	General	ω/v	$-\cos\alpha$	$-\sin\alpha$	0	0
Flat surface	$\gamma=0$	ω/v	$-\cos\alpha$	$-\sin\alpha$	0	0
	$\alpha=\gamma=0$	ω/v	-1	0	0	0
	$T=\gamma=0$	0	$-\cos\alpha$	$-\sin\alpha$	0	0
	$T=\alpha=\gamma=0$	0	-1	0	0	0

Rolling resistance calculated as $F_R=AT+BF_x+CF_y+DM_x+EM_z$; α= slip angle, γ = camber angle, T= tire spindle torque, ω= tire angular velocity, v = road speed, R_1 = tire loaded radius, R = test drum radius.

1.3 Hysteresis and viscoelasticity
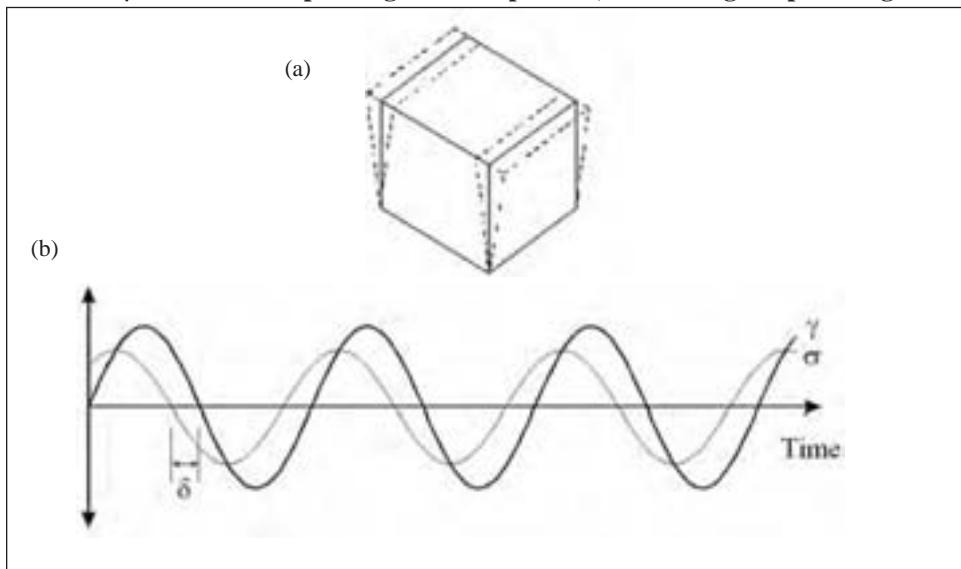
In section 1.1, it was mentioned that rolling resistance is largely a result of energy dissipation within the volume of the tire. In fact, hysteretic losses account for about 80-95% of the total rolling resistance, and most research efforts related to reducing rolling resistance have focused on this aspect. The dissipation occurs as a result of the viscoelastic behavior of tire materials as they are cyclically deformed during rolling. The local rate of dissipation, expressed on a per unit volume basis, is referred to as the "volumetric heat generation rate" in the context of heat transfer, which is discussed in section 2.7 with respect to predicting the temperature of a rolling tire using Finite Element Analysis (FEA).

A brief definition of hysteresis is in order here. A basic stress – strain cycle for sinusoidal oscillation of an elastomeric block is shown in figure 12.2. Although, we consider rubber to be an elastic material, with stress proportional to strain, there is also a component of stress that depends on the strain rate, as for a viscous material, and thus it changes sign when the strain reverses. As a result, rubber dissipates energy. Viscoelastic behavior and modeling of material properties is discussed in Chapter 2, and several texts are devoted to this topic [11-13].

Figure 12.2: A typical hysteresis cycle for sinusoidal loading of an elastomer.

Consider a simple example - a homogeneous rubber sample subjected to pure shear deformations, as shown in figure 12.3(a). If a sinusoidal shear strain, given by

$$\gamma(t) = \gamma_0 \sin\omega t, \hspace{3cm} (1.6)$$

Figure 12.3: (a) A rubber sample subjected to pure shear. (b) Imposed sinusoidal strain γ and the corresponding stress response σ, illustrating the phase lag δ.

is applied to the sample, it is found that the stress response is also sinusoidal. However, the stress exhibits a phase lag relative to the input shear strain:

$$\sigma(t) = \sigma_0 \cos(\omega t + \delta). \tag{1.7}$$

The strain input and stress output are plotted as a function of time in figure 12.3(b), and the stress and strain cross-plotted over a cycle give the hysteresis loop shown in Fig 1-2. Eq. 1.7 can be expressed in the form

$$\sigma(t) = \gamma_0(G'\sin\omega t + G''\cos\omega t) = \sigma_{st} + \sigma_1, \tag{1.8}$$

where the constants G' and G'' are defined as the elastic shear storage and loss moduli, respectively, and σ_{st} and σ_l are the corresponding storage and loss contributions to the total stress. It is easily shown that the ratio G''/G' is related to the phase lag δ, as

$$\frac{G''}{G'} = \tan \delta, \tag{1.9}$$

and the term $\tan \delta$ is referred to as the loss tangent.

It should be noted that the properties G' and G'', and hence $\tan \delta$, are strongly dependent on the frequency of oscillation and the temperature of the material, see Chapter 2. To illustrate the dependence on strain rate, Eq. 1.8 can be written in the form

$$\sigma(t) = \left(G'\gamma(t) + \frac{G''}{\omega}\dot{\gamma}(t) \right), \tag{1.10}$$

where $\gamma(t) = w\gamma_0\cos\omega t$ is the strain rate. During each period of oscillation, the net work input per unit volume of the material can be calculated as

$$w = \oint \sigma\, d\gamma = \int_{t=0}^{2\pi/\omega} \sigma(t)\,\dot{\gamma}(t)\,dt, \tag{1.11}$$

Calculation of the integral after substituting and the relation for from Eq. 1.8 into Eq. 1.11, yields

$$w = \pi\gamma_0^2\, G''. \tag{1.12}$$

Over a complete cycle, the energy that is stored elastically is fully recovered, but the energy associated with G'' is simply converted to heat in the sample. G'' is termed the "loss modulus" since all of the mechanical energy loss is associated with it. Although the above analysis is based on an imposed strain, similar results are obtained for an imposed stress or other modes of operation. In short, any deformation of a polymer results in energy dissipation as a result of viscoelasticity. It is precisely the viscoelastic behavior of rubber that makes it ideal in tires for damping vibrations and absorbing large shocks, and it is also responsible for the tire's grip. However, although viscoelasticity of rubber provides the tire with some of its most desirable — and critical — qualities, it is also the cause of the energy dissipation that comprises a major part of rolling resistance.

2. Physics of rolling resistance

Rolling resistance is simply the manifestation of all of the energy losses associated with the rolling of a tire under load. Since most of the energy is dissipated through hysteretic losses as the materials of the tire are deformed, it is important to understand the various deformations that take place during rolling. This section deals with the physical aspects of rolling resistance and the mechanics of rolling. Additionally, a general modeling methodology using Finite Element Analysis (FEA) for the prediction of rolling resistance and tire temperature is presented based on a generalized viscoelastic theory.

2.1 Basic deformations

As a tire rolls, it is subjected to repeated deformation leading to energy dissipation. Each material point of a loaded tire undergoes a deformation cycle as the tire completes a revolution. Such repeated deformation occurs throughout the tire as it conforms to the road surface, especially in the vicinity of the contact patch.

Tire flattening in the contact patch causes three main kinds of deformation: bending of the crown, the sidewalls and the bead area; compression of the tread; and shearing of the tread and sidewalls. For radial tires, the energy dissipation is distributed as follows (typical values): crown: 70 %, sidewalls: 15 %, bead area: 15 %.

2.1.1 Deformations in the crown

A tire in contact with the road develops a flat contact patch, flattening the tire crown both longitudinally and transversely as shown in figure 12.4. As the crown enters the contact patch, its circumferential curvature is modified due to the longitudinal bending, as illustrated in figure 12.5. Before making ground contact, the crown first bends, resulting in a smaller radius of curvature than in the undeformed tire. In the contact patch itself the crown flattens and the radius of curvature becomes infinite. At the exit of contact, a region with low radius of curvature exists, essentially identical to that at the entrance region. Finally, beyond the contact region the crown returns to its initial shape. Thus, both the minimum and the maximum curvature of the crown occur in the region around the contact patch,. Relative to the unloaded inflated shape of the tire, bending occurs in opposite directions within this relatively small region. In fact, most of the hysteretic energy dissipation in the tire occurs within this zone (through which all material of the tire passes during rolling).

**Figure 12.4: (a) Longitudinal and
(b) transverse bending of the tire in the contact patch.**
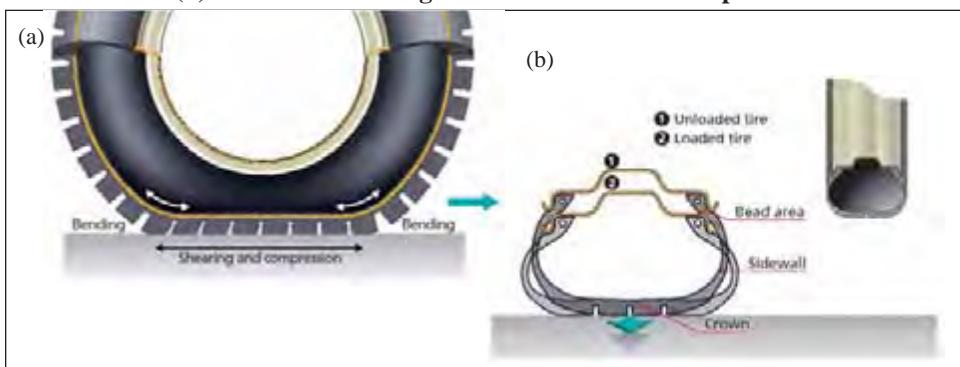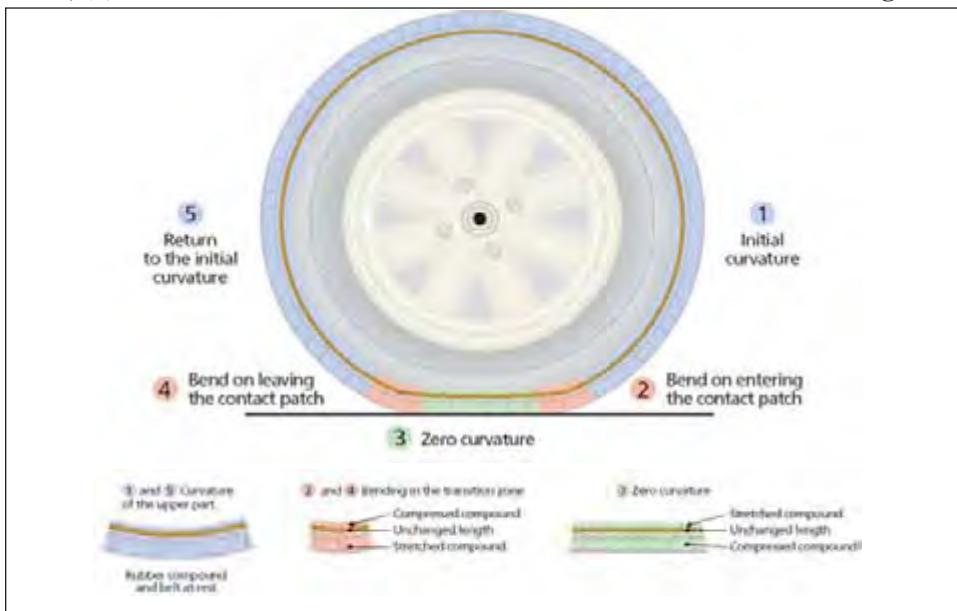
Figure 12.5: Longitudinal bending of the crown: (a) overall deformations of the tire, (b) deformations at different circumferential locations in the crown region.

The tire crown can be likened to a three-layered composite structure where the central layer is the belt with reinforcing cords that make it both inextensible and incompressible and the two outer layers – the tread and the liner – are soft visco-elastic materials. When the crown bends, the outside layer (tread) is stretched and the inside layer (liner) is compressed. Conversely, when it flattens, the outside layer is compressed and the inside layer stretched. Similar compression/stretching phenomena occur across the width of the crown due to transverse bending. Such repeated deformation leads to energy dissipation and contributes substantially to the rolling resistance.

Compression of the tread also occurs in the contact patch due to the load that the tire carries. Typical compression strain levels are around 5% for passenger car tires and 14% for truck tires. The actual level depends on the local stress, which in turn is dependent on inflation pressure and load. In the contact region of the tire, the normal forces resulting from the load must be balanced locally by the force generated by the tire's internal pressure, hence the vertical stresses at the carcass are effectively limited by the tire pressure. As a result, the contact patch length adjusts in order to carry the load and the mean stress and strain levels of the tread are nearly independent of the load itself. When a higher load is applied the longer contact patch results in a longer period of compression for each material point passing through the contact patch but the transient portion of the stress-strain cycle is similar. Since the energy dissipated by hysteresis is determined by the integral

$$\int \sigma \, d\varepsilon,$$

adding a period in which the strain remains constant in the contact patch will not result in additional energy loss. This suggests that the energy dissipation might be unchanged in the case of a higher applied load, resulting in a reduced coefficient of rolling resistance, which is simply the ratio of rolling resistance to applied load. However, the increased flat-

tening in the longer contact patch and additional bending of the sidewall tend to counter-act this effect, and the rolling resistance coefficient in fact tends to remain nearly constant with load.

The void ratio of the tread design and the tread block size have an important effect on the compressive stress and strain in the tread blocks. If the tread design employs a large void ratio, the stresses in the tread must be larger in order to transmit the same load to the carcass. The average pressure over the contact patch (the total area of the road surface below the tire surface including the area of voids) is close to that of the tire pressure, i.e. around 2 bars for a passenger car tire and 8 bars for a truck tire. However, the tread pattern includes grooves and other features, i.e. voids, which make up about 30% of the tread for most tires. Only the other 70% is in contact with the road surface. The pressure exerted on the tread blocks in the contact patch ($P_{contact}$) depends on the void ratio (*Void*) and tire inflation pressure (P_{tire}) in the following manner:

$$P_{contact} = P_{tire}/(1-Void) \qquad\qquad (2.1)$$
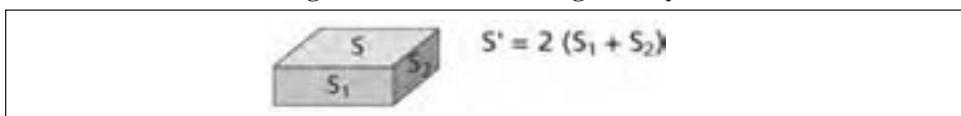
Equation 2.1 indicates that the average pressure exerted on tread blocks in contact with the road surface is about 45 % higher for a typical value of the void ratio, i.e. about 3 bars for a passenger car tire and 11 bars for a truck tire.

When a tread block is compressed vertically it expands sideways because rubber compounds are essentially incompressible in volume. Thus, the compression stiffness of a tread block increases as the compression strain is increased. The effect depends on the ratio of height to width. A short, wide block increases in compression stiffness more than a tall, narrow block. The compression strain may be estimated using a formula such as the following:

$$\varepsilon_{compression} = 0.33\left(1-e^{\frac{\sigma}{M_{10}\,F}}\right), \qquad\qquad (2.2)$$

where σ is the pressure, M_{10} is the tensile stress measured at 10 % strain, and F is the aspect ratio, equal to S/S′, where S and S′ are defined in figure 12.6.
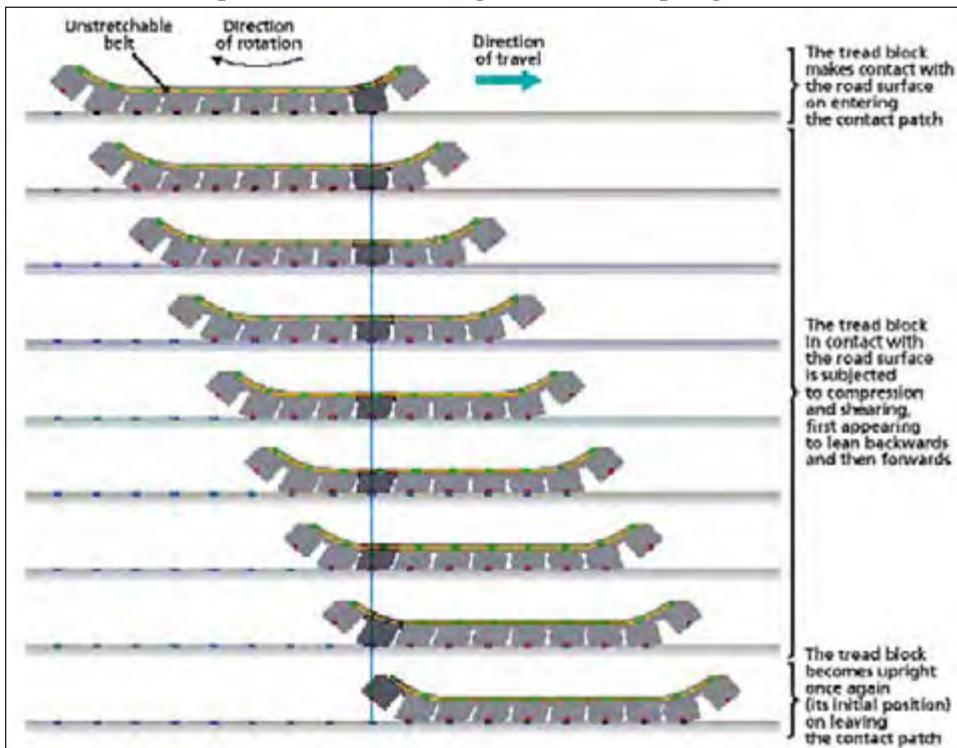
Figure 12.6: Tread block geometry.

In addition to bending and compression strains that occur in the crown of the tire, shear stresses and strains are also generated due to driving and braking stresses that occur as a natural consequence of the rolling process. When a tread block enters the contact patch, because the tire is round, the block does not make contact with the road surface vertically but at an angle, as illustrated in figure 12.7. At this instant, it appears to lean backwards. Since the tire belt is largely inextensible (because of the cords) but the tread block is deformable, the tread block's progression is dictated by the belt. In the absence of slippage between the road surface and tread (good grip on a dry road), the angle of the tread block is determined by the relative position between its point of impact on the road sur-

face (blue dot in figure 12.7) and its point of attachment to the belt (green dot). To "keep up" with the belt as it approaches the center of the contact patch, the tread block gradually becomes upright again. Finally, the shearing force exerted on it just before leaving the contact patch makes it appear to lean forwards.

Figure 12.7: Movement of a tread block through the contact patch for a -free-rolling tire with no slip angle.

Shear stresses are also generated in the lateral direction within the contact patch as a result of the lateral bending of the crown; force coupling interactions in the tread construction, which is orthotropic; and as a result of the transmission of forces through the tread that are generated as a result of interactions during bending of the belt plies, which are laid at opposing angles and thus form an orthotropic composite structure. While it is beyond the scope of the current chapter to discuss the mechanics of stresses within the contact patch in detail, it should be clear that these stresses and strains will affect the rolling resistance. It is fortunate that a minimization of these stresses is generally desirable for most aspects of tire performance; hence it is desirable to optimize the crown profile both to minimize these stresses and simultaneously to reduce the rolling resistance.

### 2.1.2 Deformations in the sidewall and bead regions
While the crown of the tire is responsible for the major part of the total energy dissipation, the sidewall and bead regions of the tire, combined, account typically for an additional 30%. This contribution can be influenced by the tire design, particularly in the bead
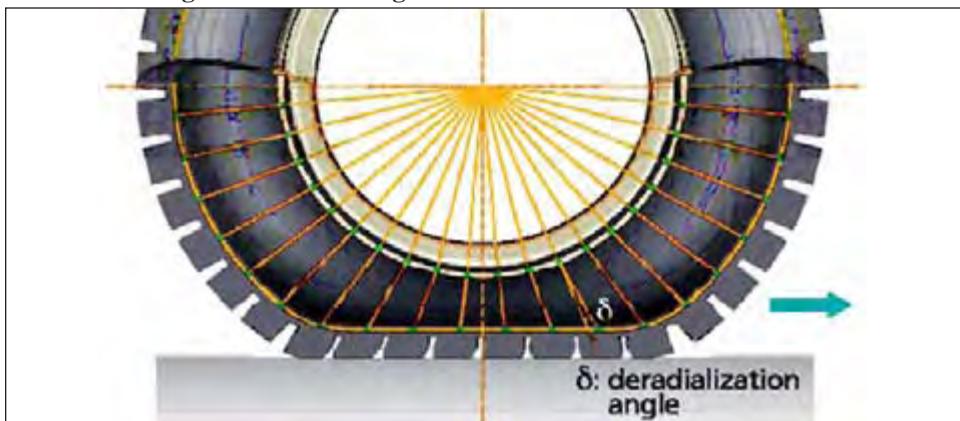
region. Hence it is important to understand the primary deformations that take place in the bead and sidewall regions.

For both the bead and sidewall, flexure of the region directly above the ground contact area is significant. Loading of the tire and accompanying flattening of the contact patch force the lower sidewall and bead to bulge and flex as shown in figure 12.4(a). Flexure in this region results in compressive and tensile stresses in the inner and outer regions of the bending zone, in a similar manner to that discussed above for the crown of the tire. In the sidewall the cord or cords typically define the neutral bending axis. Flexure therefore results primarily in tension of the rubber material on the outer surface of the tire and compression of the inner liner. Out of the contact region, in the upper half of the tire the cords in the sidewall support the applied load and the sidewall region will straighten somewhat relative to the unloaded shape of the tire. This can cause bending stresses in the tire opposite to those occurring in the lower region, although the bending resulting from this "counter-deflection" is less significant than that occurring above the contact patch. The flexing of the sidewall and the cyclically varying compressive and tensile stresses and strains as each point travels through the contact region is responsible for most of the energy dissipation in the sidewall.

Another deformation in the sidewall and bead region that contributes to the rolling resistance is termed deradialization. As a result of the inextensibility of the belt plies, when the crown of the tire flattens as it enters the contact patch, the position of the body plies in the crown region deviates from its initially radial position in the unloaded tire, as shown in figure 12.8. This deradialization extends through the sidewall and into the bead region. As a result, the rubber surrounding the cords of the body plies is stretched and sheared, causing energy dissipation. Note that, while it may be possible to limit deradialization in some regions, the deformation is inherent in the operation of the radial tire, and hence cannot be completely eliminated.

Figure 12.8: Shearing of sidewalls due to deradialization.

During acceleration and braking, and to overcome the drag forces acting on a vehicle during steady state operation, a torque must be applied to the wheel. This torque is transmitted through the tire to generate a force at the road surface. When torque is applied, the bead and sidewall regions transfer the forces from the rim to the crown by means of r-θ shearing of the materials present. This generates torsional shearing in the materials and

also results in deradialization of the body plies, although in a different manner than that resulting from tire loading. It should be pointed out that steady state shearing of the sidewall would not result in energy dissipation if the shear levels were constant around the tire, but instead simply shift the operating point to a different shear level. Of course, the shear strains due to any applied torque are superimposed on the circumferentially varying shear strains present in the sidewall due to rolling.

As discussed above, many of the deformations that take place in the sidewall also occur in the bead region of the tire to some degree. Additionally in the bead, however, at boundaries between materials of significantly different stiffness, shearing of the softer material can be important and the associated energy dissipation may contribute significantly to the rolling resistance. Of particular importance is the shearing of the rubber in the calendered body ply. In the direction of the textile cord, the body ply provides a high stiffness that resists extension. Hence, any flexing of the tire in a direction that attempts to extend the ply cords will instead cause the surrounding material to shear. The relatively high modulus of the bead filler results in a similar effect, although the stiffness of the rubber material is less than that of the cords, so the effect is reduced somewhat. Additionally, the bead filler is typically sandwiched between the inner and outer wraps of the body ply and is thus itself forced to shear under the stresses imposed by the tire bending. In general, designs that permit the bead to flex more easily, thereby minimizing the stresses in the bead, tend to result in a lower contribution to the rolling resistance. The contributions of the various stresses and strains, however, must be evaluated carefully using analytical methods, for example Finite Element Analysis (FEA), which will be discussed in section 2.7.
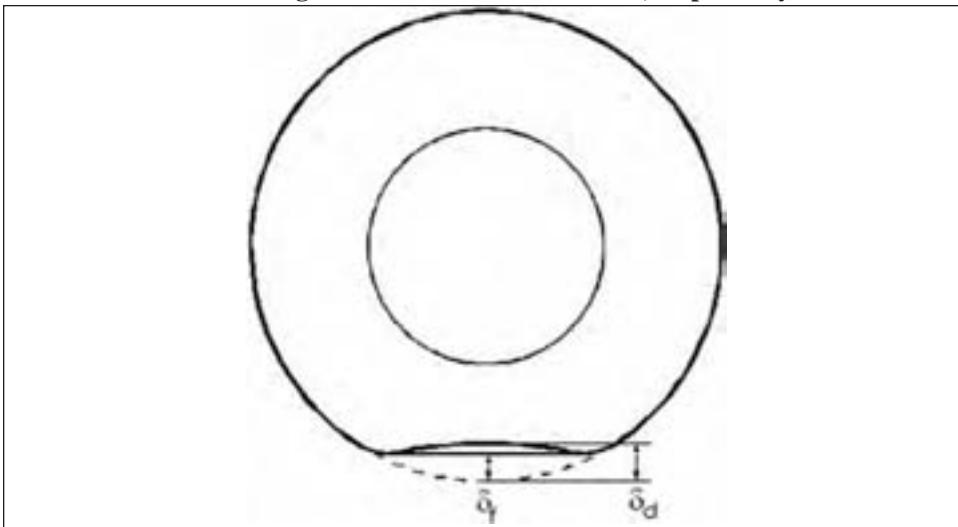
2.1.3 Effects of surface curvature

While it is certainly preferable to evaluate tire rolling resistance using test conditions that closely match actual use conditions, it is the nearly universal practice in the tire and automotive industries to carry out rolling resistance tests on cylindrical drums. Measurement of tire rolling resistance is discussed in Section 3, but the effect of using a drum is addressed here since the fundamental difference is in the deformations of a tire rolling on a flat or curved surface.

Because the crown area must now conform to the shape of the drum, the deformations are higher than those occurring on a flat surface, as shown in figure 12.9. The greater degree of bending of the crown results in larger bending stresses throughout the thickness and additionally, the shear stresses between the belt plies will tend to be larger. The maximum deflection of the tire is also larger when loading a tire on a drum at identical load and inflation pressure. A more subtle difference between the two cases is that the pressure in the contact patch is higher than that corresponding to the internal pressure of the tire when operating on a curved surface since, according to membrane theory, a component of the circumferential stress acts in a direction tangent to the entry and exit of contact. This additional stress can result in a contact pressure that is 10-25% higher (based on FEA predictions) for rolling on a 1.7 m diameter drum as compared to a flat surface. This increased contact pressure also causes the length of the contact patch to be shorter on a road wheel than on a flat surface, and the tangential stresses in the contact patch are modified as well.

The increased deflections for rolling on a drum also cause an increased amplitude of standing waves, and perhaps in an earlier onset of standing waves (see Chapter 10). Since

Figure 12.9: Comparison of tire deformations. δ_f and δ_d are the total deflections when rolling on a flat surface and a drum, respectively.

the presence of standing waves, which are discussed in more detail in Section 2.2.2, results in significant stress-strain cycling of the crown of the tire, the energy dissipated increases substantially. This increased amplitude of waves on a drum can significantly impact the rolling resistance at high speeds, even at speeds below the point at which standing waves are visible.

The effects due to surface curvature discussed above primarily affect the crown region of the tire. While the bending of the sidewall and bead will also be different when rolling on surfaces of different curvature, the differences in energy dissipation in these regions tends to be smaller and the relative contribution to the total rolling resistance from these areas of the tire is usually reduced. In conclusion, the contribution from the crown of a tire to its rolling resistance is typically amplified during road wheel testing, while improvements in the sidewall and the bead area may be masked somewhat.

Frequently, when only road wheel data is available and a flat surface value is desired, a correction is made using an expression developed by Clark [14]:

$$F_{Rd}=F_{Rf}(1+r/R)^{1/2}, \qquad\qquad (2.3)$$

where $F_{R,d}$ is the rolling resistance measured on a drum of radius R, $F_{R,f}$ is the rolling resistance on a flat surface, and r is the tire radius. This equation was based on a number of simplifications and assumptions related to the tire deflection and stresses in various regions in the tire. While the theoretical model does not encompass all of the curvature effects influencing rolling resistance, the result has gained wide acceptance and is frequently used to estimate rolling resistance on a flat surface.

2.1.4 Surface roughness

Measurements show that tire rolling resistance increases in proportion to the macroroughness of the road surface. It is generally believed that this increase is due primarily to changes in indentation of tread blocks, but increased friction due to scrubbing on the

road surface has also been suggested as a possible mechanism. Surface roughness has been found to increase rolling resistance more significantly in tires with high-hysteresis tread compounds, suggesting that deformational hysteresis is the cause of the observed differences in rolling resistance. Although deformations due to surface asperities are relatively small compared to the bulk deformations of loading, the local stresses may be large. Additionally, the high deformation frequency causes the hysteretic losses to be increased (see section 2.5).

Among typical road surfaces, the rolling resistance may vary by up to about 10%, but considerably higher values have been reported in some cases [15]. Descornet [16] measured energy losses due to surface variations while pulling an instrumented trailer and reported that larger scale unevenness in road surfaces can result in even greater energy losses. This may be a result of losses due to suspension interactions with the road surface and not a true rolling resistance effect, however.

For rolling resistance measurements, an 80-grit surface is specified in the SAE rolling resistance test standards (Safety Walk and 3M-ite for the SAE J1269 and J2452 standards, respectively) and is permitted in the ISO standard. The grit surface is intended to mimic a road surface and has been reported to increase tire rolling resistance by 2-11% compared to a smooth steel surface. Luchini [17] found that rolling resistance measurements were more reproducible when a smooth steel roadwheel was coated with a grit surface, and the effect of the age of the test surface, if any, was small [18].

2.2 Effects of operating conditions

Vehicles operate under a range of environmental conditions and tires are subjected to varying load, pressure, speed, applied torque, and steer inputs. The effects of these conditions on rolling resistance, many of which can be deduced from the basic deformations discussed in the previous section, are now examined in detail. Additionally, an empirical model used to capture the load, pressure and speed dependency is presented.
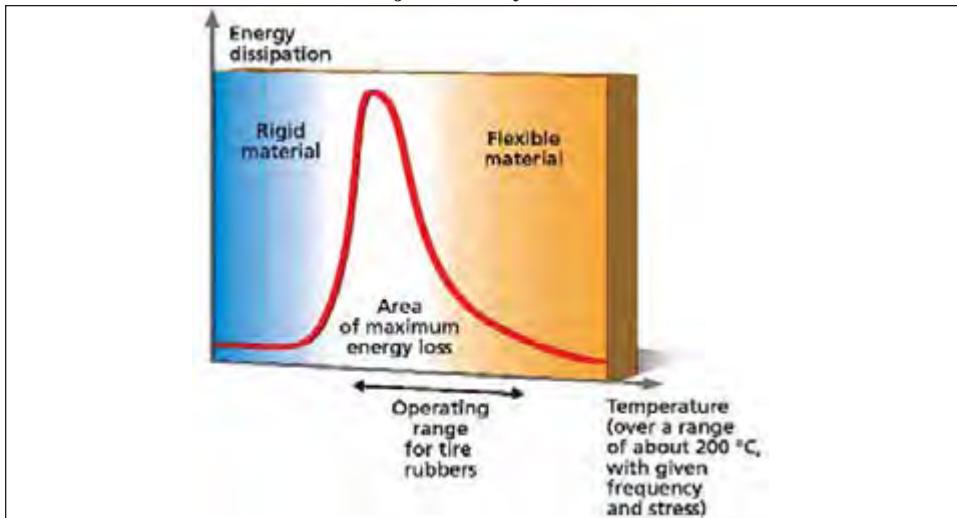
2.2.1 Temperature effect

Typically, the internal temperature of a tire fitted to a standard passenger car lies between 20 and 90°C, depending on the type of tire, the way the car is driven and the ambient temperature. Naturally, the higher the ambient temperature, the higher the tire temperature. Within this normal temperature range, the amount of energy dissipated by the rubber components in the tire when subjected to repeated deformation decreases as temperature increases, as shown in figure 12.10. In addition to this material effect, an increased temperature causes the inflation pressure to rise due to thermal expansion of air in the tire (if it is not directly controlled). The increased pressure increases the tire stiffness and deformations are reduced somewhat. Rolling resistance is therefore lower when ambient temperature is high. The variation in rolling resistance as a function of temperature is not linear. However, between 10 and 40°C, an increase of 1°C corresponds to a reduction in rolling resistance of about 0.6% under normal road operation. Rolling resistance measurements are frequently adjusted to a reference temperature based on this dependence:

$$F_{RR_{ref}} = F_{RR_{meas}} [1 + k(T_{amb} - T_{ref})], \tag{2.4}$$

where $k = 0.006$ °C^{-1}. Other values of k are sometimes used, but its value is typically in the range of 0.005 to 0.008 °C^{-1}.

**Figure 12.10: Effect of temperature on energy dissipation by
elastomers subjected to cyclical deformation.**



2.2.2 Load, pressure and speed effects
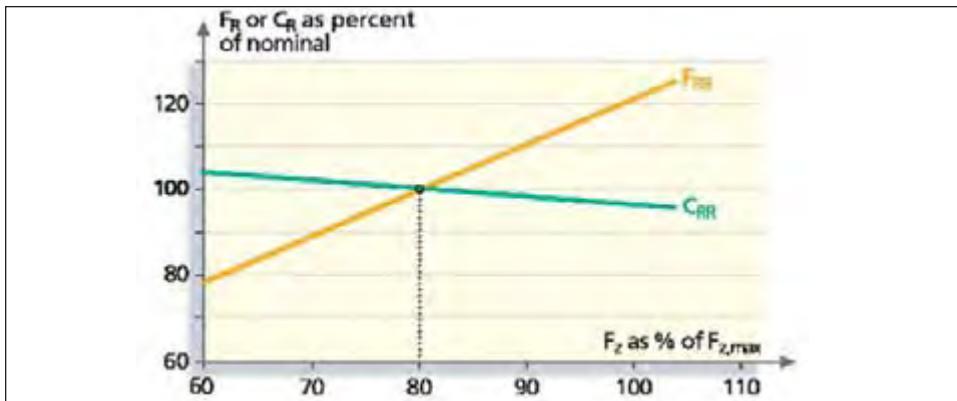
It is found that rolling resistance increases nearly proportionally to the applied load due to the increased levels of bending and shearing that take place. As a result, it is convenient to define a coefficient of rolling resistance, defined by

$$C_R = F_R / F_z, \tag{2.5}$$

where F_z is the vertical load applied to the tire. While the coefficient is a number, without units, it is frequently expressed either as a percentage or by using units of kilogram force for the rolling resistance (a kilogram-force = 9.81 N) and metric tons for the load (1 ton-force = 1000 kgf). The resultant unit is kg/t, stated as "kg's per ton". Thus a coefficient C_R of 0.008 may also be expressed as 0.8% or 8 kg/t. A typical range of C_R for modern passenger car tires is 7-12 kg/t and for heavy truck tires it is 5-7 kg/t. The lower values for truck tires are a result of their higher stiffness, due to increased operating pressures and the use of a steel cord carcass.

Although the load effect on tire rolling resistance is approximately linear, the increase in energy dissipation that accompanies an increased load causes the temperature of the tire to rise. This results in a lower hysteretic loss coefficient for the elastomer materials, and as a result the coefficient of rolling resistance often decreases somewhat with increasing load, as shown in figure 12.11.
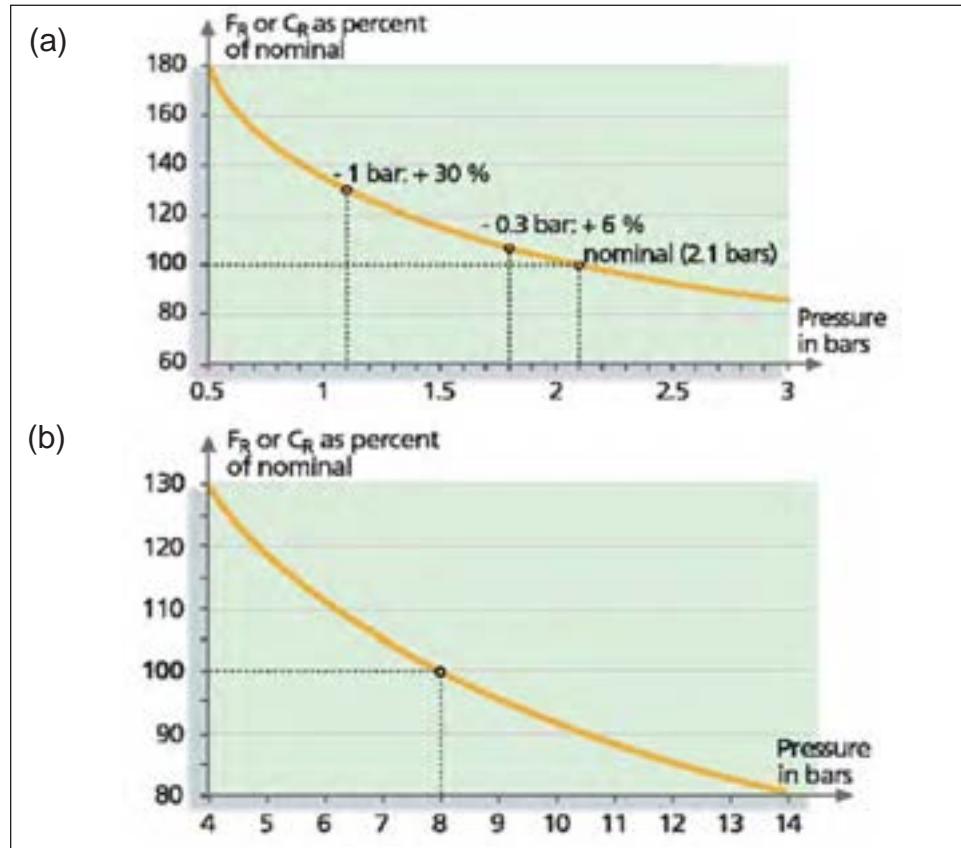
Figure 12.11: Effect of load on rolling resistance for passenger car tires.
Rolling resistance plotted as a percentage of that measured at 80% of
the tire's maximum load capacity.

A reduction in pressure affects the global deformations of the tire in a manner similar to that of an increased load. The increased bending and shear stresses result in a larger rolling resistance. However, in some cases the reduction of compressive stresses in the tread can offset the bending deformations to such an extent that a pressure reduction has little effect on the rolling resistance, and in some instances the rolling resistance may even decrease. Truck tires having a block structure in the tread pattern are most likely to exhibit this effect, since the tread blocks tend to deform more under compression than in a rib sculpture. For solid ribbed tread patterns, the added stiffness provided by the incompressibility of rubber reduces the compressive strains due to load in the tread, as was discussed in section 2.1.1. This reduces the contribution to the tire's rolling resistance resulting from compression. Due to the same effect, some of the stresses associated with bending may actually be higher in the case of a solid ribbed tire, which tends to increase the rolling resistance when the pressure decreases. For passenger car tires, the inflation pressure is not usually high enough for compression to be a significant source of the total energy dissipation. Figure 12.12 shows the typical effect of pressure on rolling resistance for both passenger car tires and truck tires.
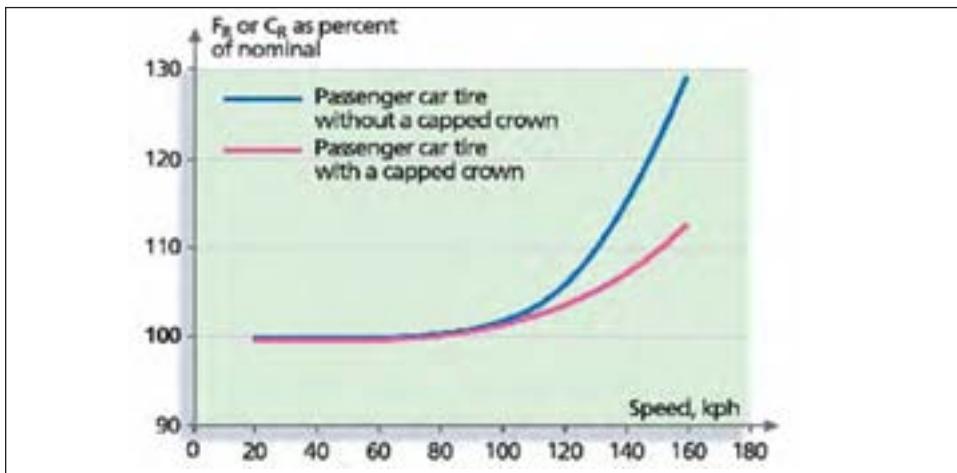
With increased speed, several effects influence the tire rolling resistance. In general, rolling resistance increases as a result of centrifugal forces and, at higher speeds, the formation of standing waves. Also, increased speed causes the frequency of deformation to increase, which tends to increase the loss tangent, $\tan \delta$, of the rubber materials. On the other hand, the higher heat generation rate,q , causes the tire temperature to rise and the increased temperature causes $\tan \delta$, and therefore the rolling resistance, to decrease, as discussed in section 2.2.1. The combined influence of these effects is typically an increase in rolling resistance with speed, but there are some cases where the rolling resistance may decrease as a result of the temperature dependence of $\tan \delta$ or due to tire construction. While changing the load or pressure by a given percentage results in differences in rolling resistance that are of the same order of magnitude as the parameter change, the variation in rolling resistance with speed is generally much smaller, at least for speeds below that at which standing waves begin to form.

Figure 12.12: Effect of tire pressure on rolling resistance for (a) passenger car tires and (b) truck tires. Rolling resistance plotted as a percentage of that measured at the nominal pressure condition.

On a flat surface at speeds below 120 kph, standing wave formation is not typically observed and the increase in rolling resistance is fairly small. Nonetheless, this speed range is of particular interest in the United States, where legal speed limits are everywhere below 75 mph (121 kph). Centrifugal forces cause the tire's radius to increase in the upper region opposite ground contact, while the deformations associated with flattening of the contact patch remain nearly constant at various speeds. The result is that the relative displacements through each revolution are larger at higher speed, resulting in higher energy dissipation for each cycle. In tires with a nylon cap, particularly tires with H speed rating or above, the added crown reinforcement tends to minimize the effects of centrifugation and the change in rolling resistance with speed tends to be reduced. Figure 12.13 shows the typical effect of speed on rolling resistance for two passenger car tires, both with and without a nylon cap ply. In some instances the rolling resistance may even decrease with increasing speed due to the improved centrifugation performance.

**Figure 12.13: Effect of speed on rolling resistance. Rolling resistance
plotted as a percentage of that measured at 80 kph.**

Because of the influence of temperature on rolling resistance, the degree to which a tire is allowed to reach thermal equilibrium at a given speed plays an important role in the speed dependence. When a passenger car tire begins rolling at a steady speed, it takes more than 30 minutes to reach a fully steady-state operating temperature. If the rolling resistance is measured for a tire immediately following a speed increase, a higher value will be observed than if the measurement is made after allowing the tire to achieve a constant temperature. If the variation of rolling resistance due to speed is not very large, the temperature effect can even reverse the direction of the sensitivity between stabilized measurements and those made immediately after changing test conditions, i.e. the rolling resistance may increase with speed for non-stabilized measurements but decrease with speed for measurements in which the tire is at thermal equilibrium. Except in highway driving, a tire rarely operates for extended periods of time at a constant speed, hence defining an appropriate measurement depends on the objective of the test. For making comparisons of rolling resistance among different tires, however, it is generally accepted that rolling resistance measurements should be made after allowing the temperature to stabilize at a given speed. This approach is incorporated into all of the major test standards for rolling resistance measurements made at a single speed.

The formation of standing waves causes rolling resistance to increase very rapidly. Even before they can be observed visually, the rolling resistance begins to increase at an accelerated rate, which may be an indication of the onset of standing waves. As described in Chapter 10, standing waves occur as a result of the large momentum of deformed portions of the tire exiting the contact region at high speed. This momentum carries the deformed contact region, including both the crown and sidewall, through the exit of contact and beyond the normal deformation path in the tire; i.e. the tire cannot recover from the deformation imposed by ground contact to its equilibrium loaded shape at high speed [19]. Beyond the contact region, the over - deformed elements of the tire are acted upon by forces which attempt to restore the tire to its equilibrium loaded shape. This interaction of the momentum and restoring forces results in a circumferentially traveling vibratory motion of each element of the tire. Although each element experiences an oscillatory

motion during its trajectory about the axis of rotation of the tire, when viewed from a fixed location adjacent to the rolling tire the deformation path is stationary relative to the contact patch, which is where the standing waves are initiated.

It should be apparent that the large strain cycles associated with the standing wave phenomenon will cause significant energy dissipation due to hysteresis. Ultimately, hysteresis dampens the standing waves and prevents them from continuing around the full circumference of the tire. Increasing the tire's speed provides greater momentum and kinetic energy to the tire, which is converted to vibrational energy in the standing waves and subsequently to rolling resistance. Therefore, the rolling resistance continues to increase with increasing speed as a result of the standing wave phenomenon.

To characterize the rolling resistance of a tire, it is important to determine the effects of load, pressure and speed, including interactions between them. Empirically, it has been found that these effects can be correlated quite well using various mathematical relations when taken independently. Schuring [2] includes an excellent review of correlations that have been used in the past. The SAE J1269 measurement standard calls for a regression fit of the following form:

$$F_R = F_z(A_0 + A_1 F_z + A_2/P) \text{ for passenger car tires} \qquad (2.6)$$
$$F_R = A_0 + A_1 F_z + A_2/P + A_3 F_z/P + A_4 F_z/P^2 \text{ for light truck tires}$$

This is based on measurements conducted at a single speed of 80 kph since speed has a minor influence, as discussed above. However, it is desirable to use a more refined model that includes the speed effect since evaluations for a specific application will frequently consider only a single operating load and pressure combination. A single speed data point clearly does not provide a complete picture in this case. A simple quadratic form incorporating interactions between the effects is
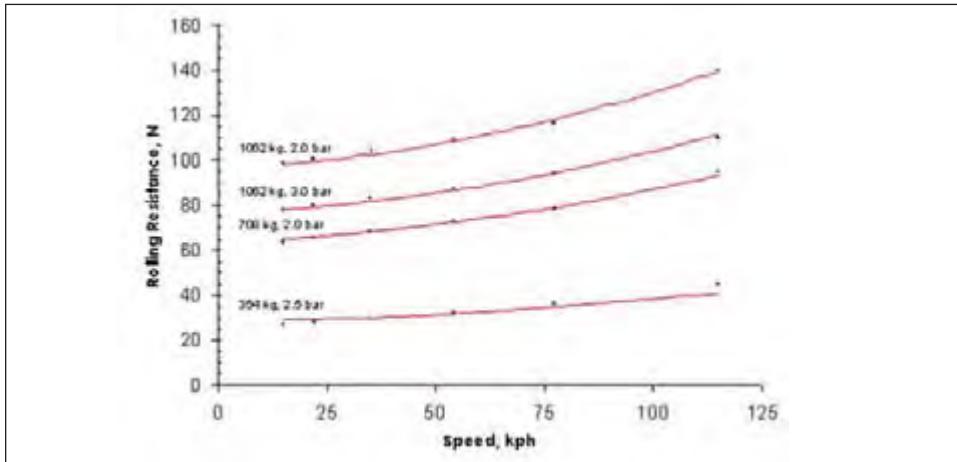
$$F_R = a_0 + a_1/P + a_2 F_z + a_3 v + a_{11}/P^2 + a_{22} F_z^2 + a_{33} v^2$$
$$+ a_{12} F_z/P + a_{23} F_z v + a_{13} v/P \qquad (2.7)$$

The reciprocal pressure is used since the rolling resistance is approximately hyperbolic when plotted against pressure. Although this form can provide a good correlation for a suitably large set of data, it provides little insight into the functional dependencies. A more recent method is provided in the SAE J2452 standard for passenger car and light truck tires. In this test standard, discussed in more detail in section 3.2, rolling resistance is measured at several load/pressure combinations during a simulated coastdown. Data are then regressed to obtain coefficients for the relation

$$F_R = P^\alpha F_z^\beta (a + bv + cv^2) \qquad (2.8)$$

This form was proposed by Grover [20] after evaluating a variety of functional forms, and it fits data quite well for a broad range of tire designs and load, pressure and speed combinations. Values of α are typically in the range of -0.3 to -0.5, and for β, the value is close to unity. A typical plot of rolling resistance measurements from the SAE J2452 standard and the curve fit to the data is presented in figure 12.14. The functional form given by Eq. 2.8 is quite flexible and can be used to represent data obtained by measurements other than the simulated coastdown, provided that sufficient data is available to perform the regression.

Figure 12.14: Measured rolling resistance data for a P265/75R16 tire following the SAE J2452 test standard, along with curves showing the regression to the form $F_R = P^\alpha F_Z^B (a + bv + cv^2)$.
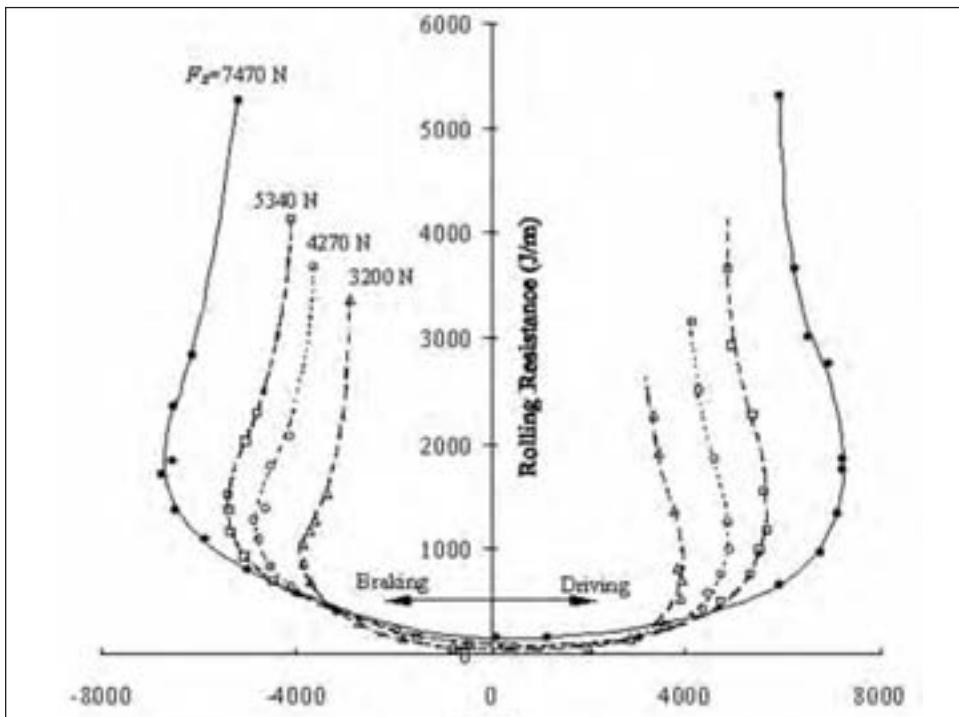

Equation 2.8 shows that rolling resistance is rather strongly dependent on inflation pressure. While load and speed are largely fixed for a given vehicle and application, tire pressure is easily adjusted by the user. When a tire is under-inflated, its rolling resistance increases by a factor of, on average, about $(P/P_0)^{-0.4}$, where P_0 is the specified inflation pressure. Since fairly substantial under-inflation is rather common in the United States, there is an opportunity to improve the average level of rolling resistance even without changing tire designs. In a study conducted by NHTSA [21], it was discovered that 27% of passenger cars and 32% of light trucks operating with P-metric tires had at least one tire under-inflated by at least 8 psi (0.55 bar), and more than 10% of vehicles had at least one tire under-inflated by more than 10 psi (0.69 bar). These pressure levels represent, on average, under-inflation by more than 25%, with a corresponding rolling resistance increase, relative to proper inflation, of about 12%.

2.2.3 Effect of applied torque
Driving or braking torque applied to a tire directly affects the shearing stresses and strains and can have a large impact on rolling resistance. Figure 2-12 shows rolling resistance as a function of longitudinal force for a passenger car tire. As the magnitude of torque applied (driving or braking) increases, the rolling resistance gradually increases up to a point at which slippage at the road surface becomes significant and the rolling resistance then increases very rapidly. This rapid increase occurs as the maximum torque that the tire can transmit is approached. At low to moderate levels of torque, shearing of the tread and sidewall are the primary contributors to rolling resistance. At large torque, however, the hysteretic contribution does not increase beyond a maximum level and much of the energy loss is then due purely to frictional dissipation at the contact surface. Beyond the maximum torque, the wheel begins to spin or is fully locked (braking), and the torque transmitted to the ground actually decreases, although the rolling resistance continues to increase as the slip ratio increases.

Figure 12.15: Rolling resistance as a function of longitudinal force (driving/braking torque) for various vertical loads (Adapted from Schuring [22]).

Schuring [22] evaluated the torque effect and claimed that the minimum rolling resistance does not occur under freely rolling conditions, but rather under a small driving torque. As shown in section 1.2, the rolling resistance for a tire rolling under an applied torque is given by

$$F_R = (T\omega/v) - F_x, \qquad\qquad (2.9)$$

where T is the torque, ω is the angular velocity of the rotating wheel and v the speed of travel. Under free-rolling conditions, the torque is zero and the value of F_x is negative, i.e. the force acting on the tire in the contact patch opposes the forward motion. When a positive torque is applied, this force becomes less negative and eventually becomes positive, so that the rolling resistance is reduced by the force F_x acting on the contact patch. If F_x increases more quickly than the term $T\omega/v$, then rolling resistance will decrease. Based on the relationships for the slip ratio — which is directly related to ω/v — and the longitudinal force as a function of the applied torque, Schuring showed that indeed there is a minimum of the rolling resistance at positive torque for the tires he considered. He argued that the physical mechanism responsible for this surprising result is that a small positive torque may reduce slippage losses occurring during free rolling more than it increases hysteretic dissipation in the tire. In his comprehensive review, Schuring [2] comments that in some cases a minimum in rolling resistance is observed under braking conditions, and this has been observed also by Bäumler [23]. It may be that some factor of tire design dictates the

relative rates of increase of the terms $T\omega/v$ and F_x, and thus determines the torque level at which the rolling resistance is a minimum.

2.2.4 Slip angle effect

The effect of slip angle on tire rolling resistance has significant consequences for fuel economy, not because of steering inputs made by the driver, but rather as a result of toe angle. Generation of a lateral force, when needed, is fundamental to steering but, because large steering inputs are typically applied only during a small proportion of vehicle operation, reduced rolling resistance during steering has low priority. On the other hand, toe angle influences rolling resistance during all phases of operation. This section is primarily directed to making vehicle designers aware of the effect of their decisions regarding toe angle may have on rolling resistance.

For a free rolling tire, with no camber input, the rolling resistance is given by

$$F_R=-[F_x(1+R_l/R)\cos\alpha+(F_y+M_x/R)\sin\alpha], \tag{2.10}$$

where R_l and R are the dynamic loaded radius of the tire and the surface radius of curvature, respectively, and M_x is the so-called overturning moment, which is the moment acting in the contact patch about the direction of travel. On a flat surface, this reduces to

$$F_R=-(F_x\cos\alpha+F_y\sin\alpha). \tag{2.11}$$

Since the slip angles for both toe and steering are generally quite small, typically less than $3°$, the value of $\cos\alpha$ is close to unity and $\sin\alpha\cong\alpha$. The value of F_x does not change significantly with slip angle, and the lateral force, F_y, is approximately a linear function of slip angle, so

$$F_y=C_\alpha\alpha, \tag{2.12}$$

where C_α is the cornering stiffness. Substituting these simplifications into Eq. 2.11, the rolling resistance at small slip angles reduces to

$$F_R=F_x+C_\alpha\alpha^2=F_{R0}+C_\alpha\alpha^2 \tag{2.13}$$

where F_{R0} is the rolling resistance without a slip angle applied. It should be noted that the cornering stiffness is roughly proportional to the applied load, hence the coefficient of rolling resistance is largely independent of load for normal operating conditions.

Taking as an example a 225/60R16 tire with a rolling resistance of 47 N at a load of 620 kg, inflation pressure 2.2 bars and speed of 80 kph, the cornering stiffness is about 1.5 kN/deg (86 N/mrad). For a total toe angle of $0.3°$ ($0.15°$/tire), the rolling resistance increases by about 0.6 N, or 1.3%, while at $1.0°$ of total toe ($0.5°$/tire), the increase is 6.5 N, or about 14%. Clearly, if the vehicle is configured with a significant toe angle, the resulting increase in rolling resistance can quickly counteract any improvements made in tire design. This result also indicates the importance of precise tire alignment during rolling resistance measurements.

2.2.5 Transient effects

Although rolling resistance testing in the laboratory typically focuses on stabilized measurements, steady levels of rolling resistance are not encountered during normal driving. Thus, a single value of rolling resistance is not appropriate. Non-steady speeds on the road and the resulting variations in the tire temperature cause the rolling resistance to vary.

Schuring et al. [24] reported that rolling resistance depends not only on the instantaneous operating conditions of load, pressure and speed but also on the temperature of the tire, which is a function of the history of the operating conditions. The temperature at each location in the tire affects the local energy dissipation as a result of changes in material properties, causing thermally-induced changes in rolling resistance. The temperature field in the tire varies in a rather complex way, however, and modeling of the transient temperature variations everywhere in the tire would be a laborious and time-consuming effort, prone to inaccuracies. A much simpler approach was presented by Mars and Luchini [25] that results in reasonable predictions of the transient behavior of the rolling resistance and requires only a characterization of the steady state behavior of rolling resistance.

Their model is based on the observations of Schuring et al. [24], that the transient rolling resistance can be determined from the stabilized value for the instantaneous operating conditions of load, pressure and speed if a correction is made for changes in the tire temperature. In short, the model applies a temperature correction similar to that in Eq. 2.4 to account for the difference between the rolling resistance at the stabilized temperature and that occurring at the actual, transiently varying temperature. Both temperatures are determined from an energy balance for the tire using a lumped capacitance thermal model that incorporates the effects of heat generation in the tire (due to rolling resistance) and convective heat transfer from the tire, and in the transient case includes thermal energy storage in the tire. The result of the model is a first order differential equation for the temperature,

$$m c_p \frac{dT}{dt} = \left[h_0 A \left(\frac{v}{v_0} \right)^p + k v F_R^* \right] (T_\infty - T) + v F_R^* + k \frac{v_0^p}{h_0 A} v^{2-p} \left(F_R^* \right)^2 , \qquad (2.14)$$

where m is the tire mass, c_p (1300 J/kg-K) is an average specific heat for the tire, h_0 (100 W/m²-K) is the convection coefficient corresponding to a reference speed v_0 (80 kph), A is the tire surface area, p (0.5) is an exponent characterizing the heat transfer coefficient as a function of speed (a power law in velocity, $h = h_0(v/v_0)^P$, is frequently used for convective heat transfer correlations), T_∞ is the ambient temperature, F_R^* is the stabilized rolling resistance corresponding to the instantaneous speed condition, and k (0.0061 /°C) is the temperature sensitivity of rolling resistance. The temperature calculation must be solved numerically for a given velocity cycle. Subsequently the rolling resistance is calculated from the following:

$$F_R(t) = F_R^* \left[1 + k \left(F_R^* \frac{v_0^p}{h_0 A} v^{1-p} + T_\infty - T(t) \right) \right] . \qquad (2.15)$$
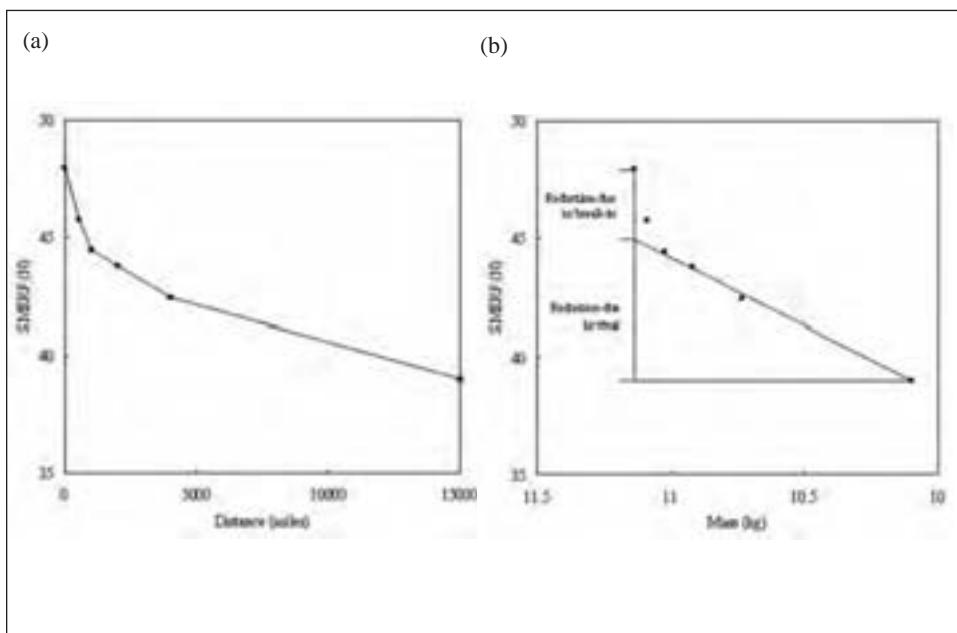
Mars and Luchini used the values given in parentheses above for the parameters of the model and found quite good agreement with experimental measurements. Due to the model's simplicity, it is quite valuable for prediction purposes.

2.3 Changes in rolling resistance throughout tire life

Although most measurements of rolling resistance are made when a tire is new, it is of interest to know what happens during its normal service life. Rubber continues to vulcanize and other chemical changes occur associated with aging and oxidation. Removal of tread rubber due to normal wear also has an impact on the rolling resistance. There are three relatively distinct periods of change in rolling resistance during a tire's life. Rolling resistance decreases during an initial break-in period due to stabilization of the tire materials after fabrication. During this initial period, weak bonds in the rubber may break and the material softens and stabilizes. Typical decreases of 2-5% in rolling resistance are expected during the initial break-in. A break-in period of 60 minutes at 80 kph is found to be generally sufficient for passenger car tires both to complete the initial break-in of the tire and achieve thermal stabilization.

The most rapid changes in rolling resistance occur in initial break-in period. Slower changes take place after that, due to material relaxation effects and changes in crown profile. Figure 12.16(a) shows the rolling resistance evolution for a P215/65R16 tire that was operated during normal driving for 15,000-miles with all tires on the vehicle remaining in the same position. Both tire mass and rolling resistance measurements were made at intervals to determine the effect of the mileage and wear on rolling resistance. During the first 1000 miles, which is an extension of the initial break-in period, material properties of the rubber and cords continue to evolve somewhat. Although mass loss during this period is not very significant, the effects of cord accommodation, rounding of features in the tread pattern, stress relaxation, and compression set of the tread rubber result in changes to the crown profile. These shape changes will vary depending on the vehicle, driver behavior, road surface, and other factors. Therefore, the duration of this period of evolution is like-

Figure 12.16: Rolling resistance as a function of (a) distance and (b) mass for a 215/65R15 tire run on-vehicle for 15,000 miles.

ly to be quite variable. Tire rotation (to different positions on the vehicle) will result in the crown profile changing to a different shape. As a result, this phase may be repeated, at least in part, following each rotation. It should be noted that artificially induced changes in the crown profile (buffing) can have a positive or negative impact on rolling resistance, and in some cases, changes to the profile may increase rolling resistance even when the tire mass decreases [26].

Continued operation after the crown profile and the material properties are essentially fully stabilized results in the rate of decrease of the rolling resistance reaching an approximately constant value that continues throughout the remainder of the tire tread life (assuming that tires are not rotated). The rolling resistance is plotted against the tire mass in figure 12.16(b): it is clear that mass reduction is the main cause of continued reduction in rolling resistance during this stage of tire life.

2.4 Effects of tire design parameters on rolling resistance

Ideally, one would like to determine the role of each design factor on the tire's performance so that an analysis could be conducted to optimize all aspects of the tire's function. Unfortunately, there are many interactions among design parameters, and such a methodology is not practical. For example, if the tread width of the tire is reduced, the mass will typically decrease as well, and the path that the carcass plies follow will need to be adjusted if the crown curvature remains constant. If the mold width and diameter remain constant, the body ply is typically shorter, which will result in a change in the inflated tire dimension as well. Usually, there would also be a reduction in the width of the belts of the tire.

Despite these difficulties, the roles of several design parameters are quite clear and their impact on rolling resistance is generally consistent. These can be confidently applied when reductions in rolling resistance are sought. The effects of the tire mass, crown shape, the use of a cap ply, and dimensional influences are discussed below. Additionally, in the next section the effects of materials are discussed.

Beyond materials, perhaps the single most important factor in tire design impacting rolling resistance is the mass. Since the deformation of rubber throughout the tire is the primary source for all energy dissipation responsible for rolling resistance, removal of rubber material will reduce the rolling resistance. Tread depth and width are two key design parameters that affect the tire mass, and both parameters have an important effect on rolling resistance. As noted in the previous section, rolling resistance decreases nearly linearly with tread wear. The total reduction in rolling resistance between new and fully worn tires may exceed 20%. A reduction of tread depth in the initial design will reduce the tire rolling resistance from the start in a manner similar to that observed in the stabilized tread loss period of the tire life. It has been observed that reductions in the shoulder tend to have a larger impact on the rolling resistance than in other regions of the tread, probably because stresses and strains in this region are more significant.

Similar to tread depth, reductions in the tread width can be used to remove mass, thus reducing the rolling resistance. Care should be taken, however, to ensure that the tread width does not decrease to a point at which the stresses in different regions of the tread become very non-uniform or excessive. Excessive loading of the shoulder portion of the crown can occur if the tread width is excessively reduced, which will have adverse effects on rolling resistance in addition to other performance aspects of the tire. Of course, the wear life of the tire will also decrease when tread rubber is eliminated from the tire.

Reduction of mass from other parts of the tire also improves rolling resistance, but tends to be less effective than crown modifications. Nonetheless, it is worthwhile for rolling resistance, not to mention cost, to remove as much mass as possible from a tire if the additional rubber is not necessary for a specific function.

The curvature of the crown has an important effect on the stresses generated in the contact patch during rolling, and also on stresses in the belts. Although a flatter crown (decreased curvature) is not always better, this is generally the case. It results in reduced lateral bending since achieving good contact with the road requires less flattening of the summit. Lateral stresses in the contact patch are also reduced, so that shear stresses in the tread are generally lower. However, the tire shoulders can be excessively loaded if the crown radius becomes too large. This causes the stress levels there, and thus the energy dissipation, to increase. Additionally, if the carcass shape in the meridional plane remains the same, a flatter crown will result in an increased thickness of tread in the shoulder regions of the tire. In this case the mass effect may counteract any reductions in energy dissipation obtained through flattening, and the rolling resistance may increase as a result.

The addition of a nylon cap ply tends to increase the rolling resistance by several percent, and this difference can be even larger if the tire that was not initially designed for use with a cap ply. Although a nylon cap helps reduce rolling resistance at high speeds, as discussed in section 2.2.2, this is not the case at more typical operating speeds. Below about 120 kph the rolling resistance is larger when a nylon cap is present due to several effects. First, adding the cap ply simply adds mass to the tire. Second, the added rubber and the cords dissipate energy. Although energy loss in the cords is not as significant as that in a similar volume of rubber, it may contribute up to 2% to the rolling resistance due to hysteretic energy dissipation as the cords are cyclically stretched and relaxed. Additionally, the cap ply stiffens the crown region circumferentially, which influences the stresses both in the contact patch and the belts, and it restricts growth in the shoulders when the tire is inflated thus making the crown profile more round than in a tire without a cap ply. These effects require that the tire design be adjusted when a cap ply is used. Otherwise, the rolling resistance may be impacted negatively.

Various studies have been conducted on the effects of tire size (see Schuring [2] for a rather detailed review). The results have been quite mixed, probably because of interactions among the many variables of tire design. One parameter that appears to have a clear effect is the tire outer diameter: a larger diameter tends to reduce the coefficient of rolling resistance. Pillai and Fielding-Russell [27] found that the coefficient of rolling resistance is approximately proportional to the outer diameter raised to the -1/3 power,

$$F_k = \frac{k}{OD^{1/3}}$$
(2.16)
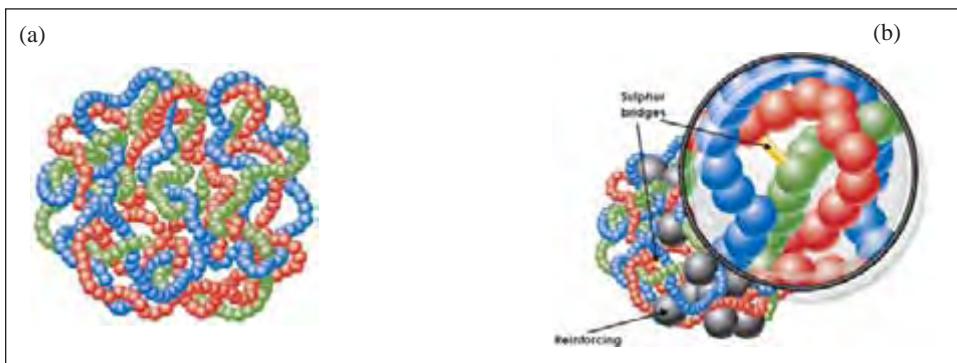
for tires of similar construction. This relationship holds for a wide range of tire sizes within the same tire line, using the same construction and materials. Pillai and Fielding-Russell used this relation to predict the effect of aspect ratio using different combinations of other dimensional variables. They considered section height, section width and seat diameter, which were interrelated with the tire outer diameter to predict their effects using Eq. 2.16.

2.5 Basics of rubber compounding for low rolling resistance
The materials used in a tire can have a profound impact on the rolling resistance. The

placement of an appropriate material in each location of the tire is critical for the overall performance. The purpose of this section is to provide an overview of some issues in rubber compounding that have a significant impact on energy dissipation and hence on the tire's rolling resistance. Additionally, compounding approaches are discussed that reduce energy dissipation while still maintaining satisfactory wear and grip performance. A detailed description of rubber compounding is given elsewhere [see, for example, references 28 and 29].

Figure 12.17: Elastomer molecular structure: (a) Pure polymers, and (b) reinforced polymer structure, showing sulfur bridges that form following vulcanization.

2.5.1 A brief description of rubber compounding

Since about 70% of the energy dissipation is derived from the crown region of the tire, primary emphasis for rolling resistance considerations must be focused on the materials present in the crown, and due to the large mass of the tread rubber, this is generally the compound where the most attention is focused.

The actual energy loss due to the deformation of rubber compounds originates primarily from the polymers they contain, amplified by the presence of reinforcing fillers. To reduce energy dissipation, we can therefore either select less hysteretic polymers or improve the bonding of rubber to reinforcing filler particles. However, it is difficult to implement these solutions without compromising tire performance, especially tread grip and resistance to wear.
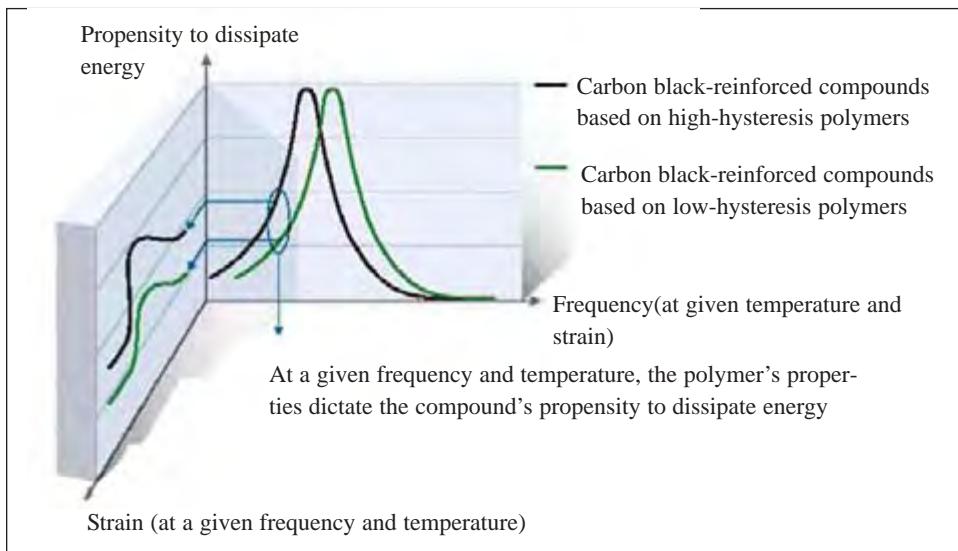
2.5.2 Effect of the polymer system on hysteresis

The hysteresis that increases rolling resistance, and is undesirable, is also responsible for the desirable feature of a tire's grip on the road. The two properties must therefore be considered together. The surface deformations responsible for grip occur at high frequencies, between 10^5 and 10^{10} Hz, whereas the structural deformations responsible for rolling resistance occur at the frequency of rolling wheel, that is, about 15 times a second for a car traveling at 100 km/h, or generally in a frequency range of 10-150 Hz.

The hysteretic properties of a polymer depend on temperature and the frequency and magnitude of the applied deformation, as described in Chapter 2. Although grip and rolling resistance are generated at different frequencies, the energy dissipation processes in these two domains are closely related; thus a low-hysteresis polymer has potentially

low traction. Changing the polymer used in a tire will just cause a shift in the hysteretic properties, both for rolling resistance and grip. Figure 12.18 illustrates the effect of the choice of polymer on the dependence of hysteresis on temperature and strain magnitude. New approaches to resolving the dilemma involve changing the bonding of reinforcing fillers within the rubber compound.

**Figure 12.18: Effect of the polymers used in a rubber compound on its propensity to dissipate energy.**

Propensity to dissipate energy

— Carbon black-reinforced compounds based on high-hysteresis polymers

— Carbon black-reinforced compounds based on low-hysteresis polymers

Frequency(at given temperature and strain)

At a given frequency and temperature, the polymer's properties dictate the compound's propensity to dissipate energy

Strain (at a given frequency and temperature)

2.5.3 Impact of filler system on compound hysteresis

With carbon black, the polymer chains are adsorbed on the surface of each particle. When the rubber compound is deformed, the polymer chains may become desorbed and the material then becomes softer. Simultaneously, energy is lost. The decrease in modulus and increase in energy dissipation (Payne Effect, see Chapter 2) occurs progressively as the strain amplitude is increased. It is also greater when the filler concentration is increased, as shown in figure 12.19.

Several possibilities for minimizing this effect are depicted in figure 12.20. The first two options involve reducing the filler content. However, it is found empirically that the wear resistance (abrasion resistance and tear resistance) is optimal when the volume fraction of reinforcing fillers is about 20-25%. We therefore cannot greatly reduce the percentage of filler used without compromising overall tire performance.

The bonding of polymer to filler particles can be improved in two ways. The first is to increase the mixing time. The second is to bond the polymer molecules to the filler aggregates using specific functional groups attached to the polymer chains. For carbon black the functional group used is an amine, and for silica it is a silanol. However, it is difficult to use functionalized polymers because the compound becomes more viscous and harder to process. To summarize, the difficulty lies not in the design of low rolling resistance compounds, but in their use in tire manufacture.

Figure 12.19: Effect of filler aggregate spacing on non-linearity.

2.5.4 Special features of silica

Unlike carbon black, silica is not adsorbed well by hydrocarbon polymers and silane coupling reagents are required to obtain good bonding. These reagents contain a chemical group capable of bonding to the surface of a silica particle during mixing and another group containing sulfur that reacts with the polymer during curing. This bonding process results in lower energy dissipation at low deformations and the conflict between wear resistance and low rolling resistance disappears. However, use of silica and silane requires modifying the mixing process so as to control the compound temperature accurately. The temperature must be high enough to allow the silica and silane to react, but not so high as to induce a premature reaction between the sulfur group and polymer molecules.

In summary, obtaining a tire with low rolling resistance requires not only use of specific compounds but also a specific mixing process.

2.6 Rolling resistance and the first law of thermodynamics

Our basic definition of rolling resistance relates mechanical energy and heat, which are both fundamental to thermodynamics. This section considers consequences of the first law of thermodynamics with respect to rolling resistance and the tire temperature.

The first law of thermodynamics, written as a rate equation for a closed system, can be stated mathematically as follows [30]:
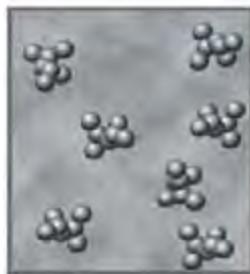
$$\dot{W} + \dot{Q} = \frac{dE}{dt},$$ (2.17)

In this equation, $\dot{W}$ is the rate of work input (power) into the system, $\dot{Q}$ is the rate of heat transfer to the system, and dE/dt is the rate of change of the total energy of the system. Equation 2.17 states simply that the combined power inputs (and/or outputs in the case of negative values of $\dot{W}$ or $\dot{Q}$) due to work and heat transfer, into a closed system, result in

Figure 12.20: Filler strategies to reduce energy dissipation.

Method 1 - Reducing the volume fraction of reinforcing filler (while keeping aggregate size unchanges)

Rubber compound 1

Rubber compound 2

Material with a large percentage of filler: carbon black aggregates are close to each other
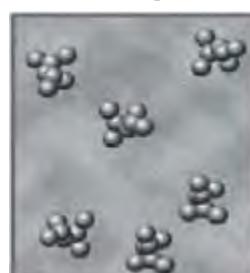
Less filler: the aggregates are further apart.

Method 2 - Increasing the size of filler aggregates (while keeping the filler volume fraction unchanged)

Rubber compound 1

Rubber compound 2

Materials reinforced with small carbon black aggregates: filler aggregates are close to each other.
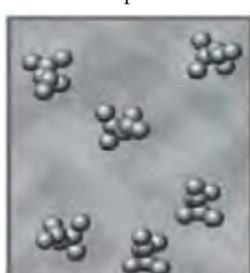
Material reinforced with larger carbon black aggregates: filler aggregates are further apart on average

Method 3 - Homogenizing the distribution of reinforcing filler

Rubber compound 1

Rubber compound 2

Uneven distribution of filler: aggregates may be close to each other.

Even distribution of filler: aggregates are further apart on the whole.

an equivalent rate of increase of the energy of the system.

   Consider the thermodynamic system of a tire rolling on flat ground or on a drum. The power input, W, is the net mechanical power acting upon the tire, whether the tire is driven, braked, or free rolling. The heat transfer rate is simply the net rate of thermal energy input (or removal) as a result of temperature differences between the tire and its surroundings. The total energy for the tire includes the kinetic energy, which is a function of the road speed, and the internal energy, U, which is related to the temperature of the tire.

2.6.1 First law considerations for transient speed operation

If we consider only steady (fixed) operating conditions (but still allow for temperature changes in the tire), the rate of change of the energy, dE/dt, is simply dU/dt. However, with variations in the speed, the kinetic energy also changes, and the first law takes the form

$$\dot{W} + \dot{Q} = \frac{dU}{dt} + \frac{d}{dt}(KE),$$ (2.18)

where *KE* is the kinetic energy of the tire, including rotational and translational forms. If the kinetic energy increases during a transient, Eq. 2.18 requires that additional power be supplied to the tire, and this must be in the form of mechanical power for a traditional tire. Therefore, this portion of the mechanical energy input is not converted to heat, and, in fact, it can be converted back into mechanical energy. Based on the definition of rolling resistance, then, this term does not contribute to the rolling resistance. Similarly, a negative rate of change of kinetic energy does not directly affect the heat-related terms, Q and dU/dt, hence it does not reduce the rolling resistance. Under transient speed conditions, it is possible to have a net power *output* from a tire simply by decelerating the tire sufficiently quickly. If the rolling resistance were defined strictly in terms of the net work or power input to the tire, then with a sufficiently negative rate of kinetic energy change, the rolling resistance would itself become negative, which is undesirable since it is not consistent with the concept of mechanical energy consumption, or a conversion of mechanical energy to heat. This of course still does take place, through material hysteresis, when the tire is rapidly decelerated. Therefore, for transient speed operations, the mathematical description of the rolling resistance must be modified to account for mechanical energy inputs, or outputs, into the system that do not result in an increase in thermal energy. Instead of relying on the net mechanical power input for the general formulation, as was done for the constant speed case in Eq. 1.3, it is appropriate to define the rolling resistance directly in terms of changes in the thermal energy of the tire, as follows:

$$F_R = \left(\frac{dU}{dt} - \dot{Q}\right) / v \, .$$ (2.19)

For the case discussed above, this reduces to the desired result of a reduction of the net power input by the rate of change of kinetic energy of the system,

$$F_R = \left(\dot{W} - \frac{d(KE)}{dt}\right) / v \, .$$ (2.20)

It should be noted that other changes in operating conditions may affect other aspects of the total energy of the system in Eq. 2.17. For example, transient changes in load will modify the stored elastic energy of the tire. Equation 2.19 generalizes Eq. 1.3, and allows

the rolling resistance to be determined in cases where operating conditions are transiently varying.

2.6.2 Influence of rolling resistance on tire temperature

Rolling resistance has a very direct impact on the tire's operating temperature. This fact has been discussed briefly in previous sections, but it warrants a more complete discussion. Since rolling resistance is predominantly the consequence of hysteretic power dissipation throughout the volume of the tire, the tire's internal energy, and hence its temperature, must increase when the tire begins to roll and power is dissipated internally. This is a direct consequence of the first law of thermodynamics, which is an expression of the conservation of energy. We now consider the effect of rolling resistance on the tire's temperature, including transient effects when a tire first begins to roll.

Equation 2.19 can be re-written as

$$F_g v = \frac{dU}{dt} - \dot{Q} , \tag{2.21}$$

which is valid at any instant in time. Consider what happens to the tire as it begins to roll. A positive velocity and rolling resistance are attained but there is no heat transfer since heat transfer cannot occur without a difference in temperature. Equation 2.21 thus requires that the internal energy increases, which results in the tire temperature beginning to rise. As the temperature increases, heat is transferred from the tire to the environment, and the heat transfer rate becomes more and more significant as the tire temperature rises. Based on Eq. 2.21, this results in a reduction in the rate of increase of the internal energy of the tire. After some period of time, the tire temperature increases to a point at which the heat transfer rate exactly balances the rolling resistance and a steady state condition results. At this point, the rate of change of internal energy becomes zero and thermal equilibrium again exists between the tire and its surroundings. This is the condition described as "thermally stabilized". It is apparent, therefore, that under the conditions described above the energy dissipation rate due to the rolling resistance initially contributes entirely to a rise in the tire's internal energy (when there is no heat transfer from the tire) and later is redistributed so that all of this energy is removed through heat transfer, with intermediate distributions of the energy between these endpoints.

Due to transient variations in speed and other operating conditions, it is also possible that the tire temperature can be above the thermally stabilized temperature corresponding to the instantaneous operating speed. In this situation, the heat transfer rate from the tire will exceed the power input due to the rolling resistance, and the rate of internal energy change, and hence the tire's temperature, must decrease. Alternatively, if ambient temperatures increase, the tire temperature may be below the ambient temperature and heat transfer will occur from the environment to the tire instead of in the other direction. These scenarios show that it is possible to have several combinations of positive or negative values of heat transfer and internal energy changes for the tire, depending on the history of operating conditions and, ultimately, the current state of the tire and ambient conditions.

In most situations an increase in rolling resistance will be accompanied by a rise in tire temperature. If two tires of similar size and construction but with different values of rolling resistance operate under the same conditions, the tire with the higher rolling resistance will generally experience higher temperatures. However, that the heat transfer from

the tire to its environment is a function of the tire's *boundary* temperature. For the same level of rolling resistance, two tires can have different internal stabilized temperatures if the heat transfer inside the two tires is not similar. For example, a tire with a thicker crown region but identical rolling resistance will reach higher internal temperatures since the added thickness results in a larger thermal resistance. Additionally, one should note that the heat transfer rate appearing in Eq. 2.21 is a net heat transfer rate for the complete tire. Different distributions of temperature may exist for two tires with the same total heat transfer rate if the boundary conditions are not identical, for example in tires with very different tread patterns, or even as a result of sidewall lettering [31]. These features can influence air flow patterns over the tire, which may alter the local convective heat transfer coefficient and result in differing heat transfer efficiencies among different tires. In addition to these effects, different temperature distributions will occur when different regions of the tire contribute to the rolling resistance in differing proportions. If one tire has a very hysteretic bead region but uses an efficient tread compound, for example, the temperature distribution will be quite different than for a tire employing a more hysteretic tread and a low hysteresis bead filler.

As mentioned in previous sections, and as shown in Eq. 2.21, the power input from rolling resistance is not simply the rolling resistance itself, but the product of rolling resistance and speed. This is an important point that affects the tire temperature at high speeds. As the speed is increased the tire temperature continues to rise, although not typically in direct proportion to the speed. Since heat transfer coefficients, and thus the heat transfer rate, usually increase with speed, the increase in temperature with speed tends to be sub-linear if rolling resistance remains relatively constant. As discussed in section 2.2.2, at speeds above 120 kph, the rolling resistance can increase quite rapidly, and the temperature can rise sharply as a result.

2.7 Modeling of rolling resistance and temperature using finite element analysis (FEA)
Several approaches have been taken for prediction of tire rolling resistance, with various degrees of complexity. Schuring [2] and Schuring and Futamura [4] provide excellent reviews of different models developed over the years for predicting rolling resistance. Many early models considered specific effects of operational and/or design variables, and were successful for providing physical insight into some of the mechanisms responsible for rolling resistance. However, the development of many of these models, often purely empirical or semi-empirical in nature, frequently required that significant quantities of experimental data be used to derive the model parameters, and the applicability was often limited to tires of a specific construction, tread pattern, size, etc.

Computer simulation is a powerful tool that has become standard practice in tire design. With the availability of fast desktop computers and workstation clusters, tire modeling is now primarily based on numerical simulations using well-established methods. Finite element analysis (FEA), in particular, has gained widespread acceptance due to its flexibility, the level of development and availability of both commercial and proprietary software, and the level of detail and precision that FEA modeling can provide. Complete three-dimensional tire models used for loaded analyses frequently contain more than 100,000 degrees of freedom, and very detailed models can easily grow to be an order of magnitude larger. Typical simulations can be run in a period of a few hours or less, to evaluate the effects of specific design changes on tire performance and to make comparisons

between several designs in order to optimize the design. Furthermore, very detailed inves-
tigations of tire physics are possible by interpreting FEA-predicted stresses and strains
along with other calculated physical quantities at precise locations in the tire.

The starting point for FEA modeling of tires is a mathematical formulation of the
physics of tire behavior, consisting of the differential equations governing the physical
phenomena to be studied, appropriate boundary and initial conditions for the particular
problem, and material behavior laws. The tire geometry is first subdivided, or discretized,
into sub-domains, or elements. An approximate solution for the dependent variables is
then calculated simultaneously for each of the elements of the model. The solution proce-
dure in FEA consists of a minimization of weighted residuals for the differential equations
resulting from the approximating functions [32,33]. This process is complicated by many
factors in tire modeling, including non-linearities due to material behavior and large
deformations, discontinuities in material properties with large differences in stiffness
(metal, textiles, rubber), the dependence of properties on previous history, difficulties in
determining pre-strains and stresses of the tire prior to inflation, and complex boundary
conditions associated with tire rolling. Many assumptions and approximations, along with
other auxiliary data are necessary to specify a rolling tire problem sufficiently and solve
it completely, and the details of FEA methodologies employed by tire manufacturers are
generally proprietary as a result.

For standard tire mechanical analyses, the FEA procedure is typically applied in a
sequence of mechanical simulations employing non-linear elastic material models to esti-
mate the complete field of deformations for an inflated and loaded tire. The calculated
deformations are subsequently used to determine local stresses, strains, and reactive
forces. For calculating rolling resistance, various methods can be employed. It is not prac-
tical to routinely solve a complete viscoelastic model of a three-dimensional tire [34].
However, the deformation field obtained from a standard elastic analysis of a loaded,
rolling tire may be used to calculate heat generation rates (dissipated energy) in the tire
using an independent viscoelastic model on an element by element basis. The heat gener-
ation rates can subsequently be applied to the elements in a thermal model for tempera-
ture prediction and the sum of all of the energy losses represents the tire rolling loss. This
approach has been referred to as "semicoupled" or a "one-way coupling" of the mechan-
ical, viscoelastic and thermal solutions. A more direct coupling that better represents the
physics of the material behavior is through the use of a true viscoelastic model [35,36].
Although a purely elastic analysis neglects the dynamic variations of stiffness that result
from the viscoelastic behavior of the rubber, the deformation results are similar to those
obtained in a viscoelastic simulation, and the basic physics of the hysteretic contribution
to rolling resistance can be captured in subsequent analysis with this approach.
Furthermore, through iteration, converged thermo-mechanical results can be obtained. A
typical semi-coupled thermo-mechanical analysis procedure is depicted in the flow chart
of figure 12.21. The details of such a modeling approach are discussed in greater detail
below.

2.7.1 Hyperelastic material property modeling

For many materials, normal use results in only small levels of strain and the behavior of
the material under mechanical deformation is linear. In such cases, the classical linear the-
ory of elasticity, valid for infinitesimal strains, predicts the response of the material under

imposed loads and deformations. Rubber, on the other hand, is frequently used in situations where large levels of strain are imposed, and the linear theory breaks down. A more general theory is necessary to account for the non-linear mechanical behavior. For calculating the stress and strain relationship of any elastic material, it is convenient to use a strain energy function (see Chapter 2). The elastic properties of rubber are frequently modeled assuming incompressibility, and in this case the strain energy function reduces to a function of just two measures of strain,
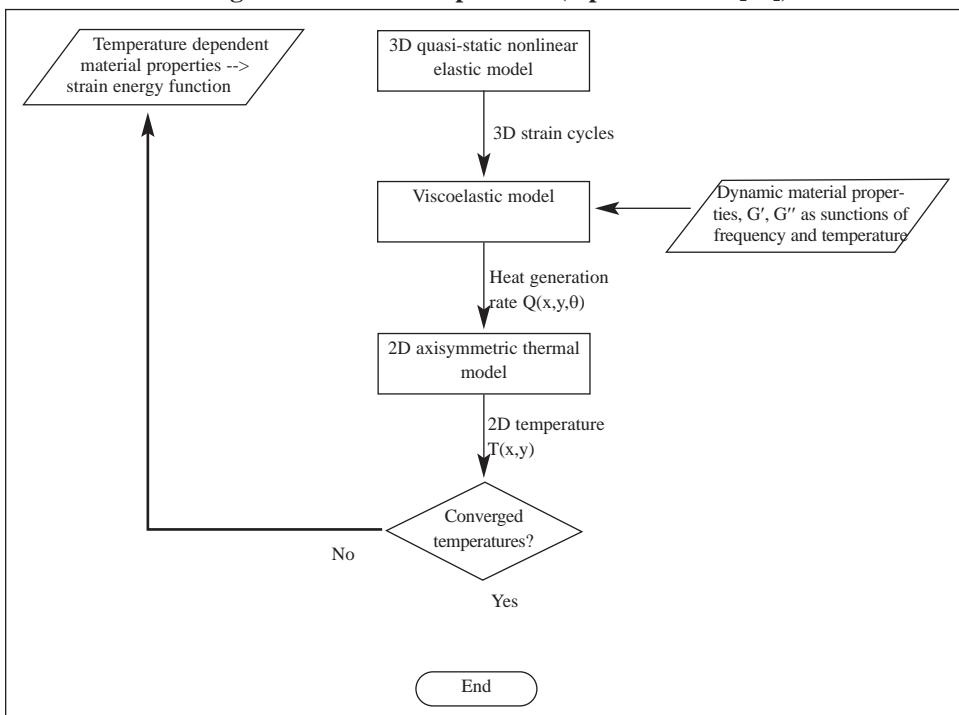
$$W = f(I_1, I_2). \qquad (2.23)$$

where I_1 and I_2 are the strain invariants defined in Chapter 2, Section 2.1. Among material models, the Mooney-Rivlin model is frequently cited. Their strain energy function is

$$W = C_{10}(I_1 - 3) + C_{01}(I_2 - 3). \qquad (2.24)$$

It results in a linear relationship between stress and strain in the case of simple shear [39] and hence it cannot capture non-linearities observed in shear experiments at high strains. Furthermore, the Mooney-Rivlin equation does not provide a satisfactory prediction of rubber behavior under compression [40]. In general, a strain energy function that includes more terms in the strain invariants is necessary to describe adequately the stress-strain relations of rubbery materials.

Figure 12.21: Flowchart of a typical FEA procedure for calculating tire rolling resistance and temperature (reprinted from [37]).

2.7.2 Details of the viscoelastic and thermal calculations

With appropriate elastic material properties and the tire geometry completely defined, the load, pressure and contact surface boundary conditions must be specified, and the FEA analysis of the tire is then performed to obtain the deformation field in the tire. Frequently, the FEA model is based on a quasi-static loading on the desired surface (e.g. flat or curved), which may be modeled as frictionless. Alternatively, frictional contact or rolling of the tire on the ground may be simulated using appropriate boundary conditions and constraints. Additionally, momentum effects can be handled by including centrifugal forces.

With the three-dimensional deformation field for the tire calculated from the elastic model, the material energy losses (heat sources) are next determined by employing a viscoelastic material model based on dynamic property measurements. The viscoelastic stress-strain behavior is frequently modeled using either a Maxwell or Kelvin-Voigt formulation [11], and the stress is calculated for each element in the tire — including the purely elastic stress σ_{st} and dissipative stress σ_l, i.e. the components corresponding to the storage modulus and the loss modulus, respectively (see Chapter 2 and section 1.3 in this chapter for a discussion of the viscoelastic behavior of rubber materials). The dynamic material properties are typically characterized at several temperature and strain amplitude levels, and a temperature-frequency equivalence, such as the Williams-Landel-Ferry (WLF) model, is employed to calculate the material properties at other frequencies.

The energy associated with the storage modulus is recovered during a complete cycle. The energy dissipation rate per unit volume is thus generated only by the loss modulus

$$\dot{q} = \sigma_l \frac{d\gamma}{dt} \ . \tag{2.25}$$

The FEA simulation represents the tire relative to a reference frame attached to, but not rotating with, the axle of the tire. However, the nodes and elements of the model do not move to simulate the rolling of the tire. Instead, one can consider that the material points of the rolling tire pass through each point in the stationary finite element model but follow the path determined by the calculated deformation field. Stated in the terms of continuum mechanics, the loaded tire analysis used for FEA is based on an Eulerian formulation of rolling. Since Eq. 2.25 applies to each *material* point in the tire, the derivative is actually the substantial derivative,

$$\frac{D\gamma}{Dt} = \frac{\partial \gamma}{\partial t} + \bar{v} \cdot \nabla \gamma \ . \tag{2.26}$$

The position of each material point of the tire can be determined, at a time *t*, by applying a rotation about the axle of the wheel (due to the rotational velocity) and subsequently adding the deformation calculated in the FEA model at the corresponding position. Mathematically, the position of a material point can be expressed as

$$\bar{X}(r, \theta, z, t) = \left(\bar{X}_0 + \bar{u} \right) \Big|_{(r, \theta + \omega t, z)} = \bar{X}_0(r, \theta + \omega t, z) + \bar{u}(r, \theta + \omega t, z) \ . \tag{2.27}$$

In Eq. 2.27, represents the reference configuration of the tire, which also corresponds to the undeformed finite element geometry. The vector function gives the initial position of a material point whose coordinates are given by (*r*, *θ*, *z*), and it is convenient to use an
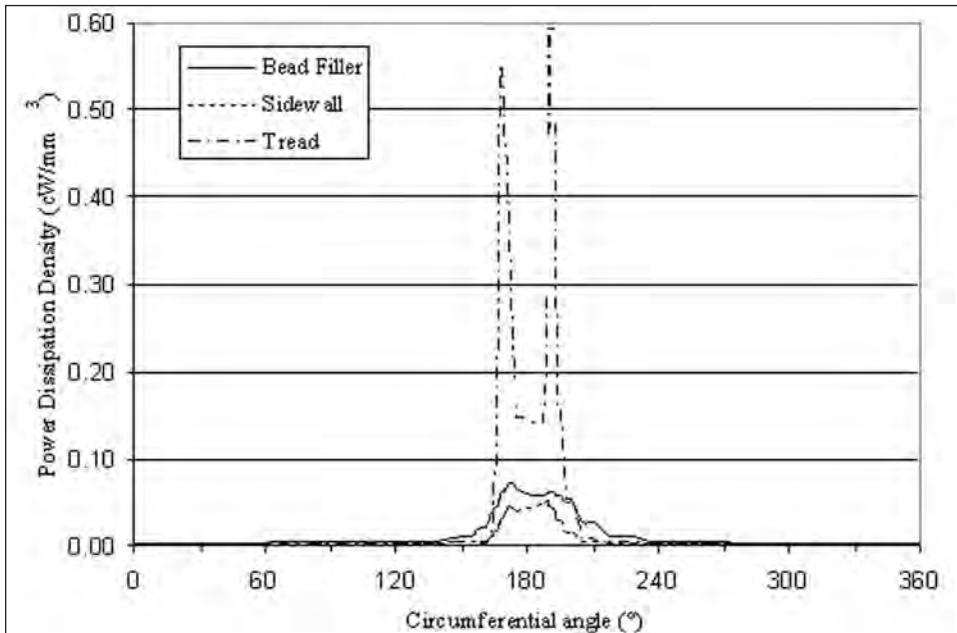
identity mapping. The velocity vector is then determined by direct calculation from these relations, and the strain rate is calculated from Eq. 2.26, where the strain gradient in each element is calculated from the displacement field. From this, the energy dissipation is calculated from Eq. 2.25. The sum of the energy dissipation for all elements in the tire for one revolution, divided by the distance that the tire travels in one revolution, is the rolling resistance, while the local heat dissipation rate, calculated on a unit volume basis, is the internal "heat source" term, q, that appears in the heat transfer equation, which for steady state conditions, is

$$k \nabla^2 T(r, \theta, z) + \dot{q}(r, \theta, z) = 0, \qquad (2.28)$$

where k is the thermal conductivity and T is the temperature.

In order to simplify the thermal analysis, the hysteretic energy loss may be averaged over one tire revolution to obtain an average heat source to be applied at each meridional position in the tire. Then, to obtain the equilibrium temperature of the tire, steady state heat transfer calculations may be performed using only the two-dimensional axisymmetric cross-section of the tire with circumferentially averaged heat transfer boundary conditions applied at all of the tire boundaries. Thermal boundary conditions include the effects of convection with air both inside and outside the tire, conduction to the rim and to the ground surface, and radiation to the environment and within the cavity of the tire [41,42]. The two dimensional heat transfer approximation is justified since for rolling speeds of interest, the rate of diffusion of heat within the tire is much slower than the rate of variation in either the internal heat generation or the heat transfer at the tire boundaries. Essentially, the tire temperature distribution does not respond quickly enough to the high frequency variations in heat sources and boundary conditions to have a significant impact on the temperature at different locations circumferentially around the tire, and the actual temperature distribution is very nearly two-dimensional. However, there is a thin region near the surface of the tire within the contact patch where temperature variations in the circumferential direction may be significant, depending on the way heat transfer is distributed between convection with the air and conduction to the ground. Typically, however, these surface temperature variations are not of much interest. On the other hand, variations in hysteresis circumferentially around the tire can be useful to consider, even if they are not used for temperature calculations. An evaluation of the differences can provide insight into different design options for minimizing the rolling resistance. Figure 12.22 shows the circumferentially varying energy dissipation for several positions in a light truck tire.

Figure 12.22: Density of dissipated power as a function of circumferential position for several components of a LT245/75R16 tire operating at 80 kph, 5 bars, 1170 kg on a flat surface.

3. Laboratory testing of tire rolling resistance

In a typical laboratory measurement of rolling resistance, the tire is held against a test drum (roadwheel) by an actuating cylinder aligned with the center of the drum, as shown in figure 12.23. A motor coupled to the drum makes it rotate, thus driving the tire through friction at the contact patch. The tire's rolling resistance has a braking effect on the drum's rotation, which is then measured using some combination of forces, torques, speeds, accelerations, etc. The rolling resistance is then calculated from the measured quantities.
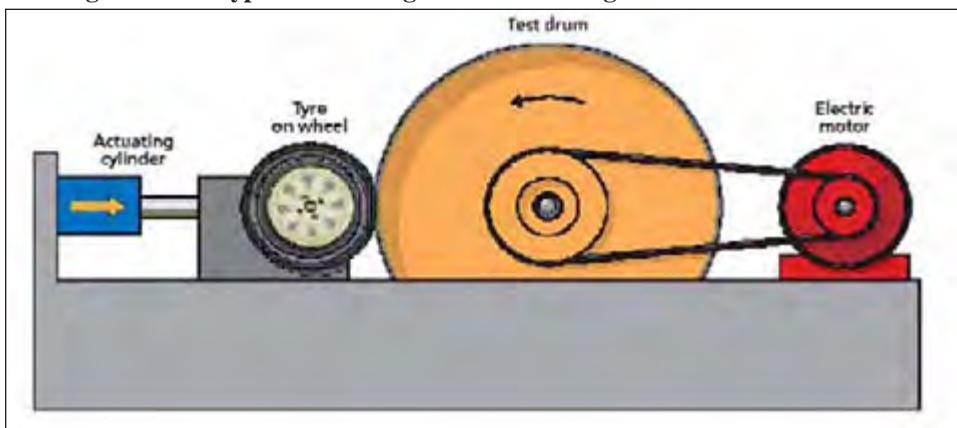
Accepted methods and best practices have been incorporated into test standards to help provide consistency to measurements made by different organizations. The test standards define measurement conditions, based on the tire's load and pressure capacity, that are representative of typical applications. SAE (the Society of Automotive Engineers) and ISO (the International Organization for Standardization) have formalized test procedures and conditions. Their standards are used extensively in the tire and automotive industries for measuring rolling resistance, both at the specified conditions and at operating conditions other than those defined by the test standards. This section focuses primarily on the measurement methods and test standards for passenger car and light truck tires.

3.1 Test measurement methods

Four measurement methods are in common use and are prescribed in test standards [43-46], although not all of the methods are advocated in every standard. These methods are applicable to freely rolling tires operating at zero camber and slip angle. They may still be applicable for other operating modes, but the calculation of the rolling resistance is often different when conditions change, and additional quantities may be necessary in some

cases. The methods described in the test standards include the following: measurement of the resistive force at the tire spindle while rolling at constant speed (spindle force method), measurement of the resistive torque on the drum hub at constant speed (torque method), measurement of the electrical power used by the motor to keep the drum rotating at a constant speed (power method), and measurement of deceleration when the driving force at the drum is discontinued (deceleration method). Each of these methods is described in more detail below.

Figure 12.23: Typical test configuration for rolling resistance measurements.

3.1.1 Aerodynamic drag measurement

In laboratory measurements, the aerodynamic drag typically accounts for about 1-15% of the rolling resistance, depending on the particular test condition. It is quite common to subtract the aerodynamic losses from the measured rolling measurement to deduce the hysteretic losses in the tire. In fact, all of the SAE and ISO rolling resistance standards specify that energy losses due to aerodynamic drag may be subtracted from rolling resistance measurements. In some measurement methods, it is always subtracted while in others this is only an option. When it is subtracted from the measured rolling resistance, the hysteretic losses are given by

$$F_h = F_R - F_{aero} = F_R - \tau_{aero}/R_t, \qquad (3.1)$$

where $F_{aero} = \tau_{aero}/R_t$ is the energy loss per distance traveled due to aerodynamic drag. The hysteretic loss, , itself is often referred to as "rolling resistance", even in the test standards, and hence it is important to ascertain whether it includes aerodynamic drag or not when reviewing test data.

This confusion about including or removing aerodynamic drag has arisen due to several factors. One important reason is that the magnitude of the aerodynamic drag on the tire when operating on a vehicle can be very different than in laboratory measurements made on a drum. In the former case, there is a net velocity of the vehicle, accompanied by a bulk flow of air over the tire. This results in a greater overall air speed than for rolling on a drum, where the only air flow is that resulting from the tire's rotation. Also, air flow

around the tires is quite variable among different vehicles, depending on wheel well sizing, height of the vehicle above the ground, etc., so that the total aerodynamic drag depends on the vehicle design. As a result of the inability to include aero drag that is fully representative of actual use, it has been decided that rolling resistance measurements should simply not include the aerodynamic drag at all, i.e. it should be subtracted from the rolling resistance measurement.

In addition, there is a practical limitation to the measurement itself for some of the test methods. They include techniques to remove systematic (bias) errors associated with machine offset and parasitic losses due to bearing losses, aerodynamic drag of the road wheel, etc. from the rolling resistance measurement. In order to do this, a reference measurement that includes the parasitic losses must be made and subtracted from the test measurement. In several test methods, such a measurement can be made only while including the effect of aerodynamic drag on the tire. Friction between the tire and roadwheel is also subtracted in many of the measurement methods in common use.

It should be noted that in adjusting for parasitic losses, the bearing losses are usually assumed to be independent of load. If the bearing loss is characterized as a function of load (as specified by the bearing supplier, for example), this effect can be taken into account in the rolling resistance calculation. However, with modern, low friction bearings, the bearing loss is a rather small percentage of the total losses measured in rolling resistance measurements. Thus, compensating for load rarely has a significant effect. For normal speed operations, the ratios between hysteretic, aerodynamic and bearing losses are approximately on the order 100:10:1, although the ratios depend significantly on the load, pressure and speed conditions. Figure 12.24 compares hysteretic, aerodynamic and spindle bearing losses for a typical rolling resistance measurement. In this figure, the bearing loss was calculated based on the manufacturer-supplied bearing properties and the aerodynamic component was measured from a skim measurement (see below) reduced by the calculated bearing friction component.

3.1.2 Spindle force method
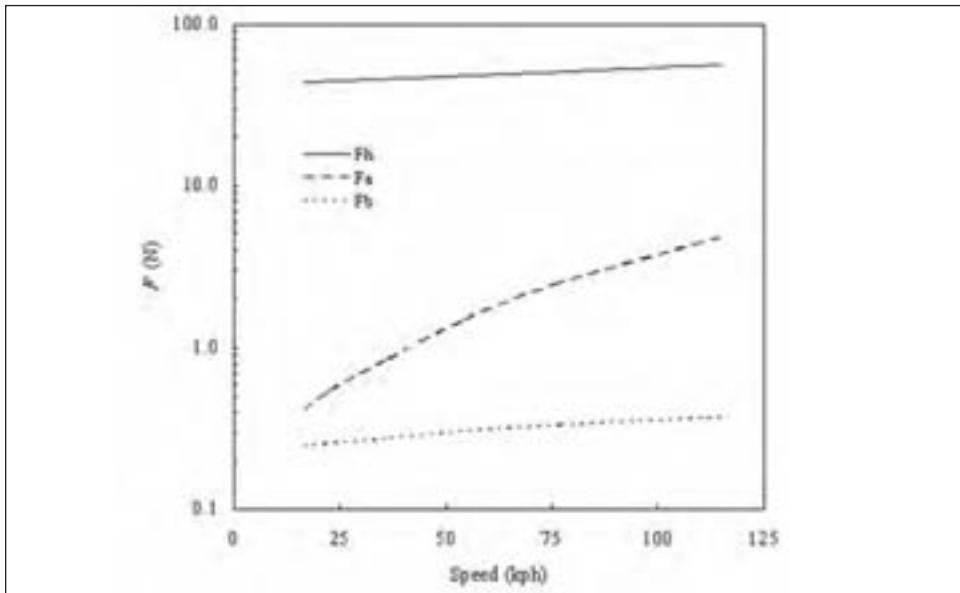
In the spindle force method, when the tire load is applied horizontally, as illustrated in figure 12.23, the center of the wheel is fitted with a vertical force sensor to measure the longitudinal force acting at the spindle. A horizontal force sensor is also typically used for measurement and control of the applied load F_z. The rolling resistance is then calculated as

$$F_R = -F_x(1 + R_l/R_d) \qquad\qquad (3.2)$$

where F_x is the measured spindle force, R_l is the dynamic loaded radius of the tire (the distance, along the line connecting the centers of the roadwheel and tire spindle, from the center of the spindle to the surface of the test drum) and R_d is the radius of the test drum. The negative sign for F_x is based on the fact that the force opposes the direction of travel of the wheel, which is taken as the positive direction.

For the spindle force method, a measurement of aerodynamic drag on the tire — referred to as the "skim measurement" — is made by repeating the spindle force measurement while a very light load is applied to the tire. The load should be large enough for the tire to remain in contact with the test drum at the test speed, but small enough that hys-

Figure 12.24: Comparison of the magnitude of hysteretic, aerodynamic, and bearing losses for rolling resistance measurement of a 225/70R16 tire at 580 kg, 2.6 bar.

teretic dissipation in the tire is negligible. For passenger car tires, a load of about 100 N is sufficient. It is assumed that the aerodynamic drag acting on the tire during the skim measurement is equal to that during the loaded tire measurement. For the spindle force method, the standards specify that F_x should be replaced by the difference F_x-F_{x0} in the calculation appearing in Eq. 3.2, where F_{x0} is the skim measurement.

The primary advantage of the spindle force method is that the only significant potential source of error is the spindle bearing loss. Bearing losses in the roadwheel have no effect on the calculated rolling resistance. However, load misalignment and interactions between load and spindle force can result in significant errors. These effects should be quantified and either removed or compensated for in the measurements [47].

3.1.3 Torque method
In the torque method, the center of the test drum is fitted with a torque sensor that measures the torque generated as a result of rolling resistance. Based on a moment balance, the torque τ_d is given by

$$\tau_d = -F_x(R_d+R_l),\tag{3.3}$$

where F_x is the spindle force. Therefore, from Eq. 3.2, the rolling resistance is

$$F_R = \tau_d/R_d\tag{3.4}$$

As in the case of the spindle force method, a skim force measurement is made, and the torque from the skim measurement is subtracted from that in the fully loaded condition. The standards also permit a machine offset reading instead of a skim measurement. In this case the torque is measured at the measurement speed with no tire contacting the drum.

This provides a measure of the bearing and aerodynamic losses of the roadwheel alone. It should be noted that if the machine offset method of parasitic loss subtraction is used, then the calculated rolling resistance includes the aerodynamic drag in addition to hysteretic losses in the tire.

The main advantage of the torque method is that it is a nearly direct measurement. Only the net torque applied to the road wheel must be measured to obtain the rolling resistance. However, the measurement includes frictional losses in the spindle bearing in addition to the roadwheel bearing and aerodynamic losses. These can be effectively removed by applying the parasitic loss correction. It is important that the speed is held constant. Otherwise, the torque measurement can include large errors associated with transient accelerations of the roadwheel. Such errors can be minimized by averaging the measured torque over a suitable time period.

3.1.4 Power method
To keep the test drum running at a constant speed, the electric motor must provide the power (P) needed to compensate for the power dissipated in rolling resistance, $F_R v$. This power is measured with a wattmeter. The rolling resistance is then calculated as

$$F_R = P/v. \tag{3.5}$$

The standards specify that either a skim measurement or machine offset reading, as in the spindle force or torque methods, should be performed to account for parasitic losses. As in the previous methods, the measured power in the parasitic loss measurement is subtracted from that measured under the specified test condition before calculating the rolling resistance.

The power method is extremely simple since force and torque transducers are not needed to determine the rolling resistance. However, this method does not account for electrical losses in the motor or other transmission losses. A careful calibration of the motor is necessary to ensure accurate results, and it may be necessary to determine motor efficiency as a function of speed and power output. In addition, special controls may be needed to prevent power fluctuations.

3.1.5 The deceleration method
In the measurement methods discussed above, rolling resistance measurements are made while the roadwheel drives the tire at constant speed under steady state conditions. In the deceleration method, also referred to as the coastdown method, the motor drive for the roadwheel is disconnected and the rolling resistance is determined based on measured rates of deceleration. The deceleration method is only described in the ISO rolling resistance standards, and the discussion that follows is a summary of the specifications for the method as defined there. It was at one point also part of the SAE standard, but it was discontinued there because it was deemed to be less sensitive to tire differences and to give less precise results than other methods [17].

The tire and test drum system is initially accelerated to a speed slightly above the measurement speed. The motor is then uncoupled from the rest of the system, which is allowed to slow down under the action of all the dissipative forces acting on the system. In order to measure the parasitic losses acting on the roadwheel and tire system, separate coast-

down periods are necessary. The measurement consists of two distinct periods, during which three separate decelerations are measured. Following the break-in and warm-up periods, the first step is to measure the deceleration of the test drum against which the tire is being held ($\dot{\omega}_d$) while the tire and drum roll together at the same speed. (Although the term $\dot{\omega}_d$ is referred to as a deceleration, its value is negative, following normal convention for a change in angular velocity, as are other $\dot{\omega}$ terms discussed below.) The deceleration is measured when the speed of the tire and roadwheel pass through the test speed. The angular deceleration $\dot{\omega}_{tire}$ of the tire is calculated based on the ratio of the drum and tire radii.

In the second step, the tire and drum are brought back to a speed slightly above the measurement speed. The tire is then moved away from the test drum, and the deceleration of the unloaded tire $\dot{\omega}_{tire,u}$, due to tire spindle friction and aerodynamic drag, is measured while the tire slows through the measurement speed. Simultaneously, the deceleration is measured of the unloaded test drum alone, $\dot{\omega}_{d,u}$, as the result of aerodynamic and bearing frictional losses acting on it. This step is analogous to the skim measurement in the other test methods, although it should be noted that in this method, there is no contact friction present in this step. (It is possible that leaving out contact friction in the measurement of parasitic losses is the reason for differences observed between the results of deceleration and other test methods. If this is so, then the deceleration method should be a better measure of rolling resistance, i.e. more representative of road operations, since road friction is included.)

As is standard, the assumption is made that the parasitic losses acting in each component of the system are identical in the loaded and unloaded cases. Appropriate substitutions are made to calculate the rolling resistance. From angular momentum considerations, the rolling resistance is calculated as

$$F_R = \frac{I_d}{R_d}\left(\dot{\omega}_d - \dot{\omega}_{d,u}\right) + \frac{I_t}{R_r}\left(\frac{R_d}{R_r}\dot{\omega}_d - \dot{\omega}_{t,u}\right), \tag{3.6}$$

where R_r is the rolling radius of the tire, I_d and I_t are the moments of inertia for the drum and tire, respectively, and the other variables are as previously defined.

The main advantage of this method is its relative simplicity. Only the tire deceleration needs to be measured, along with the moments of inertia. Also, since the motor does not drive the roadwheel during the measurements, errors due to transients in the speed controller that can occur in the other test methods are absent. If the deceleration of the tire is calculated as a finite difference in velocity or from a measurement of the slope of the velocity - time curve, it is important to make precise measurements of velocity and to consider the variability and smoothness of the test data to obtain accurate results.

3.2 Comparison of rolling resistance test standards

Table 12.2 provides a summary comparison of the standards for rolling resistance measurements for passenger car and light truck tires that are in common use in the U.S. (SAE J1269 and SAE J2452) and in the rest of the world (ISO 8767). The SAE J1269 standard also pertains to highway truck and bus tires. The ISO 8767 [45] standard applies to passenger car tires, while ISO 9948 [46] applies to truck and bus tire measurements. At the time of writing, it is hoped to establish a single ISO standard for passenger car, truck and bus, and motorcycle tires.

The different rolling resistance standards are very similar in terms of the methods of measurement, but the test conditions and equipment, warm-up times, etc. for each standard are somewhat different. The main differences between the ISO 8767 and SAE J1269 standards are the measurement conditions, but they both consist, essentially, of stabilized rolling resistance measurement(s) at a single speed of 80 kph. The SAE J1269 standard expressly includes measurements at several different load and pressure combinations to characterize the rolling resistance sensitivity to these effects, while the ISO 8767 standard specifies that only one standard test condition be measured (other operating conditions are optional).

The SAE J2452 standard is unique in that the speed dependence of rolling resistance is measured during a simulated coastdown from 115 to 15 kph at multiple load and pressure conditions. An example of the measurement cycle for one load and pressure condition is shown in figure 12.25. The specified set of load, pressure and speed test conditions provides a complete characterization of the rolling resistance with respect to these parameters. The resulting data are fitted to the following empirical model

$$F_R = P^\alpha F_z^\beta \left(a + bv + cv^2 \right) \tag{2.8}$$

which was discussed somewhat in section 2.2.2. This approach was developed largely in response to changes in test methods for vehicle emissions and fuel economy in North America. Vehicles are tested on a dynamometer, with load forces based on vehicle coastdown tests performed over the same 115 to 15 kph range [48,49]. Vehicle manufacturers are only required to test a portion of their fleets; the remaining fuel economy values can be calculated based on modeling. Since the rolling resistance of tires is one of the inputs to these models, the speed dependence of rolling resistance is a required input.

With rolling resistance data available for different speeds, vehicle fuel economy can be modeled for different use scenarios. Additionally, the average rolling resistance corresponding to a particular drive cycle can be calculated using Eq. 2.8. This procedure is described in the SAE J2452 standard, in which the mean equivalent rolling force (MERF) is defined as

$$\text{MERF} = \frac{\int_{t_0}^{t_1} F_R(v(t))dt}{\int_{t_0}^{t_1} dt} = \frac{\int_{t_0}^{t_1} P^\alpha F_z^\beta \left(a + bv + cv^2 \right) dt}{\int_{t_0}^{t_1} dt}, \tag{3.7}$$

where the integration is performed for velocities corresponding to the desired drive cycle (The term denotes a function of velocity at time t, not a product.) The form of the rolling resistance regression given in Eq. 2.8 is convenient for calculating the MERF since the pressure and load terms are constant with respect to the integration. Therefore, Eq. 3.7 simplifies to

$$\text{MERF} = P^\alpha F_z^\beta \left(a + C_1 b + C_2 c \right), \tag{3.8}$$

where C_1, and C_2 are the average values of the velocity and square of velocity over the given drive cycle, respectively. These terms only need to be calculated once for each drive

cycle. The MERF depends on the specific load and pressure conditions, but a standard mean equivalent rolling force, SMERF, is defined for a standard reference load and pressure test condition, which is defined in the test standard. The SMERF is intended to serve as a single measure of rolling resistance for quantitative comparisons between tires. The combined EPA urban and highway drive cycles are normally used to calculate MERF and SMERF values.

**Table 12.2: Summary of Rolling Resistance Testing Standards
for Passenger/Light Truck (LT) Tires**

	SAE J1269 [1,2] November 1979	SAE J2452 [1,3] June 1999	ISO 8767 [1] August 1992
Effective Date of standard			
Test methods	Force, torque or power method	Force or torque method	Force, torque, power or deceleration method
Test wheel diameter	No specification given. Standard states that the most common test wheel is 1.708 m diameter.	Minimum diameter of 1.219 m (48 in).	1.5 to 3.0 m diameter.
Test wheel (drum) surface	Medium-coarse (80 grit) surface. A surface conditioning procedure is required to ensure consistent results.	80 grit textured surface. A surface conditioning procedure is required to ensure consistent results.	Smooth steel surface is normal, but an 80 grit textured surface is permitted.
Test rims	Normal rim for testing is the design rim for the tire, although other approved rims may be used.	Normal rim for testing is the measuring rim for the particular dimension, although other approved rims may be used.	Standard measuring rim, or, if not available, the next wider rim.
Test conditions	Equilibrium (thermally stabilized) rolling resistance measured at several test conditions: A single test speed of 80 kph is used.	An array of speed/load/pressure conditions are tested during a stepwise coastdown (not equilibrium conditions) from 115 to 15 kph.	Equilibrium (thermally stabilized) rolling resistance measured at several test conditions:

**Table 12.2: Summary of Rolling Resistance Testing Standards
for Passenger/Light Truck (LT) Tires (continued)**

	SAE J1269 [1,2]	SAE J2452 [1,3]	ISO 8767 [1]
	For passenger car tires, the standard test conditions include four load/pressure conditions with loads of 50 and 90% of the max load, and pressures ranging from 50 kPa below to 70 kPa above the base pressure. For LT tires, there are 5 test conditions. Load ranges from 40 to 100% of max load and pressure ranges 30 to 110% of the base pressure. (Base pressure is the pressure corresponding to the max. load for the tire.) Standard recommends that capped pressure be used for the first measurement with subsequent measurements made under regulated pressure. Test speed for all measurements is 80 kph.	Rolling resistance is measured at six different speeds for each load/pressure combination during simulated coastdown. For passenger tires, a separate coastdown is made at four load/pressure combinations, with loads ranging 30-90% of the max. load, and pressures 40 kPa below to 60 kPa above the base pressure. For LT tires, the coast-down measurements are performed at five load/pressure conditions, with load ranging 20-100% of the max. load and pressure 50-110% of the max pressure. Regulated pressure.	Either a single speed or multiple speed measurement can be made. Standard specifies 80 kph for a single speed measurement, and, 50, 90 and 120 kph for multiple speeds. Load: 80% of max load capacity of the tire. Other load/pressure combinations are suggested if it is desired to obtain sensitivities to these effects. Inflation pressure: the pressure corresponding to max load reduced by 30 kPa. Capped pressure.
Test cell temperature	Held between 20 and 28°C. Rolling resistance values must be corrected to an ambient reference temperature of 24°C.	Held between 20 and 28°C. Measurements corrected to ambient reference temperature of 24°C.	Must be between 20 and 30°C. Measurement corrected to 25°C if made at different temperature.

**Table 12.2: Summary of Rolling Resistance Testing Standards
for Passenger/Light Truck (LT) Tires (continued)**

	SAE J1269 [1,2]	SAE J2452 [1,3]	ISO 8767 [1]
Break-in/warm-up	Break-in accomplished by operating the tire at the first load/pressure condition for a period of 1 hour at 80 kph, followed by a cool down period of at least 2 hours to achieve thermal equilibrium at the test temperature. A warm-up at 80 kph for the first test condition is required: 30 minutes for passenger car tires; 60 minutes for LT tires. Subsequent conditions require a warm-up of 10 min for passenger car tires and 15 minutes for LT tires.	Same as SAE J1269, with a separate warm-up for each load/pressure condition. The standard also allows the first 30 minutes of operation of the tire (during the warm-up) to be considered sufficient for break-in.	A minimum 1 hour break-in at a min speed of 80 kph is required at the test load/pressure conditions. Following the break-in, the tires must be permitted to equilibrate to the cell temperature before performing a warm-up of the tire to achieve stabilized steady-state conditions (minimum of 30 minutes required for first data point, followed by 10 minutes for subsequent load/pressure conditions or 20 minutes for subsequent speed measurements.)

Notes:
1. All standards call for a measurement of parasitic losses to determine the tire aerodynamic drag and zero-load losses of the test apparatus, and the aerodynamic drag is subtracted from the rolling resistance, so that only hysteretic losses are included.
2. For SAE J1269, the data are regressed to the following form for passenger car tires (Eq. 2.6):

$$F_R = F_z \left(A_0 + A_1 F_z + \frac{A_2}{P} \right),$$

and for light truck tires to the following form:

$$F_R = A_0 + A_1 F_z + \frac{A_2}{P} + A_3 \frac{F_z}{P} + A_4 \frac{F_z}{P^2}.$$

3. The SAE J2452 standard specifies that rolling resistance data will be regressed to provide a relation of the following form (Eq. 2.8):

$$F_R = P^\alpha F_z^\beta \left(a + bv + cv^2 \right)$$

In addition, the Standard Mean Effective Rolling Force (SMERF) is typically reported, which is defined by

$$MERF = \frac{\int_{t_i}^{t_f} P^\alpha F_z^\beta \left(a + bv + cv^2 \right) dt}{\int_{t_i}^{t_f} dt}$$
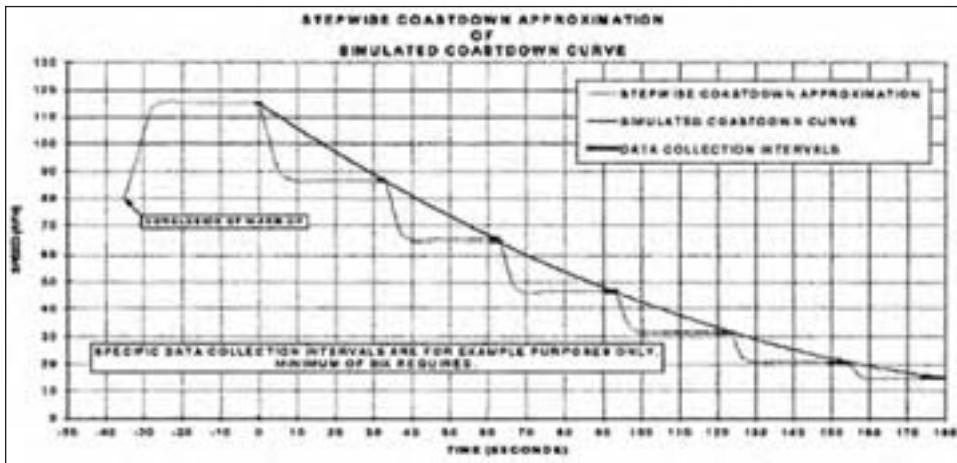
where the velocity profile in the integration typically corresponds to the EPA combined Urban and Highway cycle.
4. Temperature corrections are made using Eq. 2.4,

$$F_{R,T_{ref}} = F_{R,T_{amb}} [1 + k(T_{amb} - T_{ref})],$$

with k=0.006 °C[-1] for the SAE standards and k=0.01 °C[-1] for the ISO 8767 standard.

**Figure 12.25: Simulated coastdown prescribed for the
SAE J2452 standard (reprinted from [44])**

4. Impact of tire rolling resistance on vehicle fuel efficiency

This section investigates the contribution that rolling resistance has to vehicle fuel consumption, and discusses various methods that can be applied to predict the improvement in fuel economy that may be expected from reduced rolling resistance. A reduction in rolling resistance means that less torque needs to be provided to the wheels and the power needed to drive at the same speed therefore decreases. But inefficiencies in the vehicle engine and drive train result in a larger total energy expenditure than that transferred to the tires. Therefore, more fuel is saved than just the amount from a reduction in rolling resistance. Additionally, accessories, such as the air conditioner, alternator, etc. require a portion of the engine power output. Figure 12.26 shows a breakdown of where the energy provided by the fuel is used [50].

4.1 Simple analysis of the effect of rolling resistance on fuel consumption

We begin with some basic considerations of vehicle fuel consumption. While the analysis is too simplistic to represent a generic drive cycle with any vehicle accurately, the resulting relation captures the first-order effect of rolling resistance on fuel economy and provides some insight into other relationships between them.

A value of drivetrain efficiency can be used to describe the energy consumption for a specified drive cycle [51,52]. The total engine energy output may be expressed as

$$E_{engine} = \frac{E_{tract}}{\varepsilon} + P_{acc} \, T \,, \tag{4.1}$$

where E_{tract} is the total tractive energy delivered over the drive cycle, ε is the drivetrain efficiency, P_{acc} is the average accessory power requirement, and T is the total time of travel.

The fuel consumed by the engine is directly proportional to the thermal energy E_{fuel} released through combustion of the fuel. E_{fuel} is the product of the average fuel consumption per distance traveled, F_c, the distance traveled over the drive cycle, D, and the lower volumetric heating value of the fuel, H_0:

$E_{fuel}=F_cDH_0.$ (4.2)

The purpose of the engine is to generate mechanical power, but the thermal to mechanical energy conversion is limited by the engine's thermal efficiency, and frictional losses within the engine cause the power output to be further reduced. The total mechanical energy output from the engine can be related to the fuel energy by the following relation [51]:
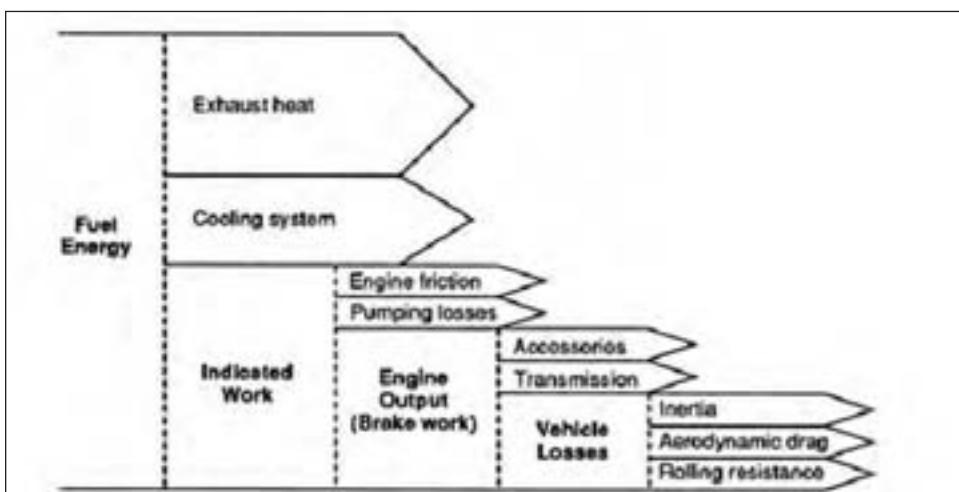
$E_{fuel}=aN+E_{engine}/\eta.$ (4.3)

In Eq. 4.3, a is a frictional loss coefficient, N is the number of revolutions of the engine over the drive cycle, η is an engine thermal efficiency, and E_{engine} is the total mechanical energy output by the engine over the drive cycle. Ross and An [53] showed that this equation works quite well for engine operations that are typical of normal driving conditions, specifically for power levels that are below two-thirds of the power generated at wide-open throttle. They evaluated the parameters a and $b=1/\eta$ for a wide array of engines and found that the values were quite consistent. By combining Eqs. 4.1 through 4.3, we obtain an equation relating the fuel consumption of the vehicle over a drive cycle to the required tractive energy input,

$$F_c = \left(aN + \frac{E_{tract}}{\varepsilon\eta} + \frac{P_{acc}T}{\eta}\right) / (DH_0)$$ (4.4)

The tractive energy E_{tract} is the total mechanical energy provided to the drive wheels to overcome all of the forces opposing the vehicle's motion during a specific drive cycle. These forces include aerodynamic drag, gravitational forces (when the vehicle is climbing a slope), inertial forces, and of course, the force required to overcome the rolling resistance of all of the tires on the vehicle. The tractive energy is therefore given by

Figure 12.26: Use (and loss) of fuel energy in a vehicle. The size of the arrow for each term is intended to indicate the relative proportion of the total fuel energy consumed. (Reprinted from [50]).

$$E_{tract} = E_{aero} + E_{grav} + E_{inertia} + E_{tire}. \qquad (4.5)$$

Each of the terms E_{aero}, E_{grav}, and $E_{inertia}$ is calculated by integrating the corresponding force over the distance traveled during the drive cycle. It can be shown that these forces, and the rolling resistance, do not contribute to the total tractive energy during periods of braking for standard vehicles that do not use regenerative braking, but this generally has a rather small impact on the fuel consumption for most drive cycles and is not included in the current analysis for simplicity.

Substitution of Eq. 4.5 into Eq. 4.4, along with the basic definition of rolling resistance (energy dissipated per unit distance traveled), provides the functional dependence of fuel consumption on rolling resistance as

$$F_c = \left(\frac{E_{aero} + E_{grav} + E_{inertia} + F_{R,tot}D}{\varepsilon \eta} + aN + \frac{P_{ac}T}{\eta} \right) / (DH_a) \qquad (4.6)$$

where $F_{R,tot}$ is the sum of the average rolling resistance over the drive cycle for all tires on the vehicle. The appropriate average is that calculated by integrating over the drive cycle with respect to the distance traveled, which can also be written as a time integral through a change of the integration variable:

$$F_{R,avg} = \frac{1}{D} \int_{path}^{0} F_R \, ds = \frac{1}{D} \int_{t=0}^{t_f} F_R(v(t)) \cdot v \, dt$$

$$. \qquad (4.7)$$

This is similar, but not equivalent, to the mean equivalent rolling force (MERF) that is specified in the SAE J2452 rolling resistance standard. ($F_{R,avg}$ can be calculated from the coefficients determined from the J2452 standards, however, in a manner similar to that described in section 3.2.)

Equation 4.6 can be used to obtain an estimate of the fraction of total vehicle fuel consumption attributable to rolling resistance for a drive cycle. Without evaluating the contributions of the other loss terms, this is calculated from a measured fuel consumption rate by

$$\frac{F_{c,tire}}{F_c} = \frac{F_{R,tot}}{\eta \varepsilon H_a F_c} = \frac{C_R W_{vehicle}}{\eta \varepsilon H_a F_c} , \qquad (4.8)$$

where $F_{c,tire}$ is the consumption per unit distance due to the tires. Values for representative vehicle classes, based on typical values of the various parameters, are presented in Table 12.3.

We now consider the effect of a variation in rolling resistance for the drive cycle, and assume that the other loss terms do not change when rolling resistance is modified. Based on Eq. 4.6, the variation of the energy consumption per distance traveled based on a change in tire rolling resistance is given by

$$\Delta F_c = \frac{\Delta F_{R,tot}}{\eta \varepsilon H_a} = \frac{\Delta C_R W_{vehicle}}{\eta \varepsilon H_a} , \qquad (4.9)$$

where $W_{vehicle} = m_{vehicle} \, g$ is the weight of the vehicle. The second equality in Eq. 4.9 assumes that the coefficient of rolling resistance for all tires on the vehicle is uniformly decreased by ΔC_R. Since the engine thermal efficiency η and drivetrain efficiency ε are

both less than unity, this relation shows that a reduction in rolling resistance results in an amplified fuel energy savings. As mentioned above, the value of the thermal efficiency is rather consistent among modern engines, and an average value of 0.408 is used. The value of ε is taken as 0.90. With a value of H_0=32 kJ/cm^3 for gasoline, Eq. 4.9 predicts that for every 1 kg/ton reduction in the coefficient of rolling resistance, the gasoline consumption rate decreases by 0.835 cm^3/km for each metric ton of vehicle weight. The general trend that fuel efficiency varies linearly with changes in rolling resistance for a given vehicle and drive cycle has been confirmed by numerous measurements of fuel economy, as shown in figure 12.27. The precise ratio of $\Delta F_C/\Delta F_R$, of course, is somewhat variable, but measured values are relatively well predicted by this simple approximation. It is interesting that the impact of rolling resistance on the fuel consumption is largely independent of the vehicle on which tires operate, except for the effect of the vehicle weight, since rolling
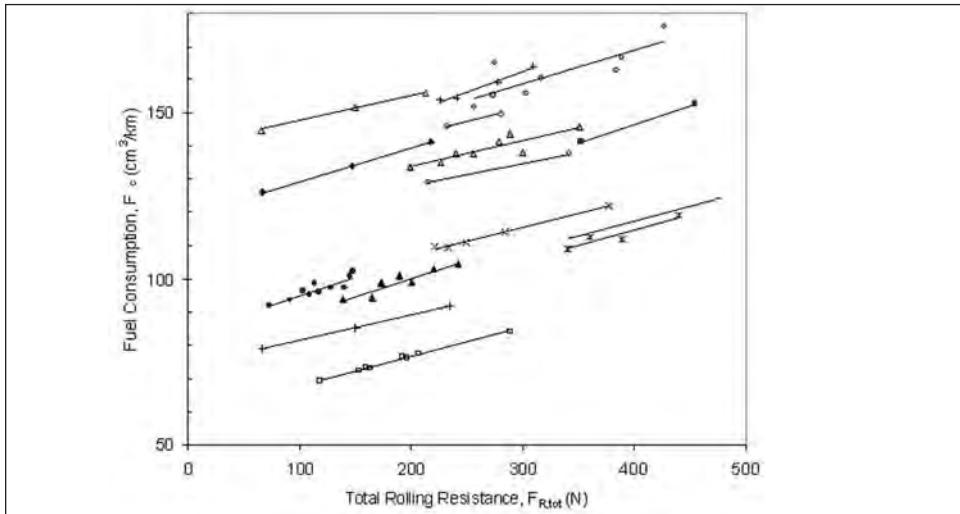
Table 12.3: Representative values of fuel economy, vehicle weight, and ratio of tire contribution to total fuel consumption by vehicle class. Fuel economy (FE) and fuel consumption are representative values based on the EPA combined urban/highway drive cycles. Values of Fc,tire/Fc are based on a CR range of 7-11 kg/ton.

Vehicle class	FE, mpg/F_c, L/km	Vehicle weight, lbs.	Calculated $F_{c,tire}/F_c$
Compact	33/0.071	2800	0.105-0.165
Midsize sedan	25/0.094	3500	0.099-0.155
Large sedan	22/0.107	4200	0.104-0.164
Small SUV	20/0.117	3500	0.079-0.125
Large SUV	17/0.138	5300	0.102-0.160
Minivan	22/0.107	4500	0.112-0.176
Small pickup	18/0.130	4100	0.084-0.132
Large pickup	15/0.156	6000	0.102-0.161

resistance is proportional to the load.

It should be noted that the overall drivetrain efficiency, ε, is somewhat dependent on the drive cycle considered, and this can also clearly vary from vehicle to vehicle. In addition to the limitations previously discussed, the basic model presented above cannot capture coupled effects of various drivetrain components, including different operating modes during changes to the power requirements. As an example, a reduction in the power output requirements from the engine as a result of a rolling resistance reduction may result in a change in the gear selection for an automatic transmission over some speed range, due to the engine efficiency characteristics and the programming of the controllers for the vehicle. This change in operating condition may result in a relatively less fuel-efficient operating condition than predicted by Eq. 4.9. To accurately predict the fuel consumption of a vehicle over a drive cycle, and the relative contribution of the various losses, a more detailed engine map of the vehicle should be used that includes the rate of fuel consumption defined as a function of power and engine speed over all operating ranges. Additionally, characterizations of the components in the drivetrain can be used to provide accurate predictions of their losses, and more detailed modeling of the tire rolling resistance, including its speed dependence, should be used. In recent years, several software packages have been designed to simulate vehicle performance, including fuel economy, using detailed vehicle characterization data, drive cycle definitions and even patterns of driver behavior. Such modeling is useful for evaluating the impact of changes to vehicle

Figure 12.27: Fuel consumption as a function of rolling resistance for several vehicles and drive cycles (adapted from [2,4]).

components on fuel economy.

We now discuss the impact that a global reduction in rolling resistance can have on fuel consumption. It was calculated above that a one kg/ton improvement in rolling resistance (about 10-12% of current average values for passenger cars) results in a fuel savings of about 0.835 cm^3/km traveled per ton of vehicle mass. If the average vehicle mass is assumed (conservatively) to be 1600 kg (3520 lbs.), then the estimated fuel consumption savings possible nationwide by a reduction in the coefficient of rolling resistance of 1 kg/ton is 1.5 billion gallons of gasoline per year. This figure is based on year 2000 data from the Federal Highway Administration (FHWA) of 2.7 trillion vehicle miles traveled (VMT) annually in the U.S. Since the significantly higher mass of trucks results in even larger energy consumption associated with the tires, the total potential savings due to the same level of improvement in rolling resistance is even larger when all vehicles are considered.

4.2 Relationship between rolling resistance and fuel economy

In the United States, fuel economy — expressed in miles per gallon (mpg) — is used to evaluate and compare vehicle performance instead of fuel consumption per distance traveled. This section considers the sensitivity of fuel economy to changes in rolling resistance. Relations based on the analysis of the previous section are presented to better understand and interpret such data.

For fuel economy predictions, Schuring [54] introduced the concept of the return factor, which is defined as the ratio of the percentage improvement in fuel economy to a percentage reduction in rolling resistance,

$$R = \frac{\Delta FE / FE}{-\Delta F_R / F_R},$$

(4.10)

where *FE* is the fuel economy. This has frequently been stated as a ratio in the form of

1:x, indicating that a 1% improvement in fuel economy requires x% improvement in rolling resistance, however a simple fraction (e.g. 0.1) may avoid confusion. Since fuel economy and fuel consumption per distance traveled are reciprocals of each other, it is easily shown that for small variations the percentage change of the two are equivalent but opposite in sign, i.e. . Schuring and Futamara provided a normal range of the return factor as 0.08 to 0.20 for passenger vehicles, and state that for fully loaded heavy trucks an appropriate value is about 0.33. With these values, it is quite straightforward to calculate the fuel economy or fuel consumption change resulting from a rolling resistance improvement.

The fuel economy is related to rolling resistance through the fuel consumption per distance traveled, F_c, which can be written as the sum of the tire contribution and other losses. If the fuel economy is written as a function of the fuel consumption per distance traveled,

$$FE = F_c^{-1} = (F_{c,tire} + F_{c, other})^{-1}, \qquad (4.11)$$

It is assumed, further, that the consumption per distance traveled associated with other losses is not affected by changes in the rolling resistance. The relative rate of change of fuel economy due to a relative change in the tire contribution is then obtained by taking a differential in Eq. 4.11. The result can be written as

$$\frac{d(FE)}{FE} = -\frac{dF_{c,tire}}{F_{c,tire} + F_{c,other}} = -\frac{dF_{c,tire}}{F_{c,tire}}\left(\frac{F_{c,tire}}{F_c}\right) = -\frac{dF_R}{F_R}\left(\frac{F_{c,tire}}{F_c}\right) \qquad (4.12)$$

where the last equality is based on the definition of $F_{c,tire}$ from the previous section. Also, it is again assumed that the thermal efficiency η and drivetrain efficiency ε do not change with rolling resistance. Eq. 4.12 can be rewritten in the same form as Eq. 4.10, yielding the return factor

$$R \approx \frac{F_{c,tire}}{F_c}, \qquad (4.13)$$

Values of the ratio of the tire contribution to the total fuel consumption rate over a drive cycle were provided in Table 12.3. More accurate values are easily calculated from Eq. 4.8 if both the rolling resistance of the tires on the vehicle and the actual fuel economy are known. Of course, the values of η and ε are also necessary for a detailed calculation, so estimates can only be expected to be accurate within, roughly, 10-20% in the absence of specific information regarding these parameters. Nonetheless, a comparison of the $F_{c,tire}/F_c$ values in Table 12.3 to the typical ranges provides support for this approach.

References
1.State of California, Assembly Bill No. 844, 2003.
2.Schuring, D.J., 1980, "The Rolling Loss of Pneumatic Tires," *Rubber Chemistry and Technology*, v. 53(3), 600-727.
3.Clark, S.K, 1983, "A Brief History of Tire Rolling Resistance," in *Tire Rolling Resistance*, Rubber Division Symposia Vol. 1, Edited by D.J. Schuring, Rubber Division, American Chemical Society, Akron, Ohio.

4. Schuring, D.J. and Futamura, S., 1990, "Rolling Loss of Pneumatic Highway Tires in the Eighties," *Rubber Chemistry and Technology*, v. 63(3), 315-367.

5. Holt, W.L. and Wormeley, P.L., 1922, "Power Losses in Automobile Tires," Technologic Papers of the Bureau of Standards, v. 16, 451-461.

6. Gough, V.E., 1958, "Tire-to-Ground Contact Stresses," *Wear*, v. 2, 107-126

7. Petrushov, V., "On Some Correctives to Coulomb's Law as Applied to Rolling of an Automobile Tire," Proc. NAMI, 1969.

8. Crum, W.B., 1975 "Road and Dynamometer Tire Power Dissipation," SAE Paper 750955, SAE International, Warrendale, PA.

9. Schuring, D.J., 1977, "A New Look at the Definition of Tire Rolling Loss," *Tire Rolling Losses and Fuel Economy—an R&D Planning Workshop*, SAE Conf. Proc. P-74, 31-37.

10. SAE Recommended Practice, 1975, Vehicle Dynamics Terminology, SAE J670D, SAE International, Warrendale, PA.

11. Ferry, J.D., 1980, *Viscoelastic Properties of Polymers*, 3rd edition, Wiley, New York.

12. Young, R.J. and Lovell, P.A., 1991, *Introduction to Polymers* (2nd Edition), Chapman and Hall, New York.

13. Aklonis, J.J. and MacKnight, W.J., 1983, *Introduction to Polymer Viscoelasticity* (2nd Edition), John Wiley and Sons, New York.

14. Clark, S.K., 1976, "Rolling Resistance Forces in Pneumatic Tires," U.S. Dept. of Transportation, TSC Rep. No. DOT-TSC-76-1.

15. Deraad, L.W., 1978, "The Influence of Road Surface Texture on Tire Rolling Resistance," SAE Paper 780257, SAE International, Warrendale, PA.

16. Descornet, G., 1990, "Road-Surface Influence on Tire Rolling Resistance," in *Surface Characteristics of Roadways: International Research and Technologies*, ASTM STP 1031, Ed. by W.E. Meyer and J. Rechert, American Society for Testing and Materials, Philadelphia, 401-415.

17. Luchini, J.R., 1983, "Rolling Resistance Test Methods," *Tire Rolling Resistance*, Rubber Division Symposia Vol. 1, Edited by D.J. Schuring, Rubber Division, American Chemical Society, Akron, Ohio.

18. Fuller, D.L., Hall, G.L., Conant, F.S., 1984, "Effect of Testing Conditions on Rolling Resistance of Automobile Tires," SAE Paper 840068, SAE International, Warrendale, PA.

19. Wong, J.Y., 1993, *Theory of Ground Vehicles*, Chapter 1, 2nd edition, John Wiley and Sons, New York.

20. Grover, P.S., 1998, "Modeling of Rolling Resistance Test Data," SAE Paper #980251, SAE International, Warrendale, PA.

21. Thiriez, K. and Bondy, N., 2001, NHTSA'S Tire Pressure Special Study, February 2001," US DOT/National Highway Traffic Safety Administration, Paper Number 256.

22. Schuring, D.J., 1976, "Energy Loss of Pneumatic Tires Under Freely Rolling, Braking, and Driving Conditions," *Tire Science and Technology*, TSTCA, v. 4(1), 3-15.

23. Bäumler, M., 1987, "Development and application of a measurement procedure for investigating the power loss of passenger car tires," Ph.D. Thesis, University of Karlsruhe.

24. Schuring, D.J., Siegfried, J.F. and Hall, G.L., 1985, "Transient Speed and Temperature Effects on Rolling Loss of Passenger Car Tires," SAE Paper #850463, SAE International, Warrendale, PA.

25. Mars, W.V. and Luchini, J.R., 1999, "An Analytical Model for the Transient Rolling Resistance Behavior of Tires," *Tire Science and Technology*, TSTCA, v. 27(3), 161-175.

26. Luchini, J.R., Motil, M.M. and Mars, W.V., 2001, "Tread Depth Effects on Tire Rolling Resistance," *Tire Science and Technology*, TSTCA, v. 29(3), 134-154.

27. Pillai, P.S. and Fielding-Russell, G. S., 1991, "Effect of Aspect Ratio on Tire Rolling Resistance," *Rubber Chemistry and Technology*, v. 64(4), 641-647.

28. Mark, J.E., Erman, B., and Eirich, F.R. (Eds.), 1994, *Science and Technology of Rubber*, 2nd edition, Academic Press, San Diego.

29. Barlow, F.W., 1993, *Rubber Compounding: Principles, Materials, and Techniques*, 2nd edition, Marcel-Dekker, New York.

30. Wark, K., 1988, *Thermodynamics*, 5th Edition, McGraw-Hill, New York.

31. Oswald, L.J. and Browne, A.L., 1981, "The Airflow Field Around An Operating Tire and Its Effect on Tire Power Loss," SAE Technical Paper 810166, SAE International, Warrendale, PA.

32. Reddy, J.N., 1993, *The Finite Element Method*, 2nd Edition, McGraw-Hill, New York.

33. Stasa, F.L., 1995, *Applied Finite Element Analysis for Engineers*, Oxford University Press.

34. Ebbott, T.G., Hohman, R.L., Jeusette, J.-P., Kerghman, V., 1999, "Tire Temperature and Rolling Resistance Prediction with Finite Element Analysis," *Tire Science and Technology*, TSTCA, v. 27(1), 2-21.

35. LeTallec, P. and Rahier, C., 1994, "Numerical Models of Steady Rolling for Non-linear Viscoelastic Structures in Finite Deformations," Int. J. Numer. Meth. Eng., v. 37, 1159-1186.

36. Becker, A., Dorsch V., Kaliske M., and Rothert H., 1998, "Material model for simulation of the hysteretic behaviour of filled rubber for rolling tyres," *Tire Science and Technology*; v. 26(3), 132-48.

37. Hall, D.E. and Moreland, J.C., 2001, "Fundamentals of Rolling Resistance," *Rubber Chemistry and Technology*, v. 74(3), 525-539.

38. Rivlin, R.S., 1956, "Large Elastic Deformations," in *Rheology: Theory and Applications*, Vol.1, Ed. by F.R. Eirich, Academic Press, New York, Chapter 10.

39. Yeoh, O.H., 1993, "Some Forms of the Strain Energy Function for Rubber," *Rubber Chemistry and Technology*, v. 64, 754-771.

40. Erman, B. and Mark, J.E., 1994, "The Molecular Basis of Rubberlike Elasticity," in *Science and Technology of Rubber*, 2nd edition, Edited by J.E. Mark, B. Erman, and F.R. Eirich, Academic Press, San Diego, Chapter 4.

41. Dehnert, J. and Volk, H., 1991, "An Approach to Predict Temperature Distributions in Rolling Tires Using Finite Element Methods," presented at the 10th meeting of the Tire Society, Akron, Ohio.

42. Browne, A.L. and Arambages, A., 1981, SAE Technical Paper 810163, SAE International, Warrendale, PA.

43. SAE Surface Vehicle Recommended Practice, 1979, "Rolling Resistance Measurement Procedure for Passenger Car, Light Truck, and Highway Truck and Bus Tires," SAE J1269, SAE International, Warrendale, PA.

44. SAE Surface Vehicle Recommended Practice, 1999, "Stepwise Coastdown Methodology for Measuring Tire Rolling Resistance," SAE J2452, SAE International, Warrendale, PA.

45. ISO International Standard, 1992, "Passenger Car Tyres—Methods of Measuring Rolling Resistance," ISO 8767, ISO, Geneva.

46. ISO International Standard, 1992, "Truck and Bus Tyres—Methods of Measuring Rolling Resistance," ISO 9948, ISO, Geneva.

47. SAE Surface Vehicle Recommended Practice, 1979, "Measurement of Passenger Car, Light Truck, and Highway Truck and Bus Tire Rolling Resistance," SAE J1270, SAE International, Warrendale, PA.

48. SAE Recommended Practice, 1996, "Road Load Measurement Using Onboard Anemometry andCoastdown Techniques," SAE J2263, SAE International, Warrendale, PA.

49. SAE Recommended Practice, 1995, "Chassis Dynamometer Simulation of Road Load Using Coastdown Techniques," SAE J2264, SAE International, Warrendale, PA.

50. National Research Council, 1992, *Automotive Fuel Economy: How Far Should We Go?,* National Academy Press, Washington, D.C.

51. An, F. and Ross, M., 1993, "A Model of Fuel Economy and Driving Patterns," SAE Paper #930328, SAE International, Warrendale, PA.

52. Adler, U., Bauer, H., Bazlen, W., Dinkler, F., Herwerth, M. (Eds.), 1986, *Bosch Automotive Handbook*, 2nd Edition, Robert Bosch GmbH, Stuttgart.

53. Ross, M. and An, F., 1993, "The Use of Fuel by Spark Ignition Engines," SAE Paper #930329. SAE International, Warrendale, PA.

54. Schuring, D.J., 1988, "Tire Rolling Loss—An Overview," Presented at the Seventh Annual Meeting and Conference on Tire Science and Technology, Akron, Ohio.

Chapter 13
Rubber Abrasion and Tire Wear
by K. A. Grosch

Chapter 13
Rubber Abrasion and Tire Wear

by K. A. Grosch

1. Introduction

Abrasion or wear occurs whenever two bodies slide against each other under friction. Material is transferred from one body to the other and this process can go in both directions. Wear is therefore associated with friction. Friction is present in every aspect of life and indeed life would not be possible without it. Although it is a dissipative process in which mechanical energy is turned into heat, high friction is often useful, and even essential, and the resulting wear has to be tolerated. Research tries to find ways to retain high friction while minimizing wear.

   High friction is required when forces must be transmitted across two surfaces in contact. The most common case is whenever human beings or animals want to walk or run. The case that concerns us here is the movement of self-propelled vehicles, i.e., automobiles, under controlled conditions over road surfaces of all kinds. In all these cases some wear occurs: both surfaces lose some material.

   This chapter deals with the forces that are transmitted between tire and road and the wear of the tire that occurs and affects its useful life. Although the main emphasis is on wear, some remarks are included on rubber friction since abrasion and tire wear is closely associated with friction.

   First, the factors will be considered which govern the abrasion of rubber in controlled laboratory experiments, then the major contributing factors to tire wear will be discussed and a link established between laboratory abrasion and tire wear.

2. Sliding abrasion

2.1 The load dependence of friction

The frictional force is a function of the load, the force that acts normal to the contact surfaces and presses the two bodies together. For friction between two hard bodies the frictional force is generally proportional to the load and can therefore be written as follows

$$F = \mu \cdot \text{load} \qquad [1]$$

where F is the frictional force and μ is the friction coefficient, which is independent of the load. For rubber this is not always the case. For soft rubbers on smooth surfaces the friction coefficient decreases with increasing load. Assuming that the frictional force is proportional to the real area of contact A [1,2,3], which is usually much smaller than the apparent one, and that the rubber asperities are much larger than those of the hard smooth contact surface and may be represented by hemispheres, the real area of contact increases with the load as follows:
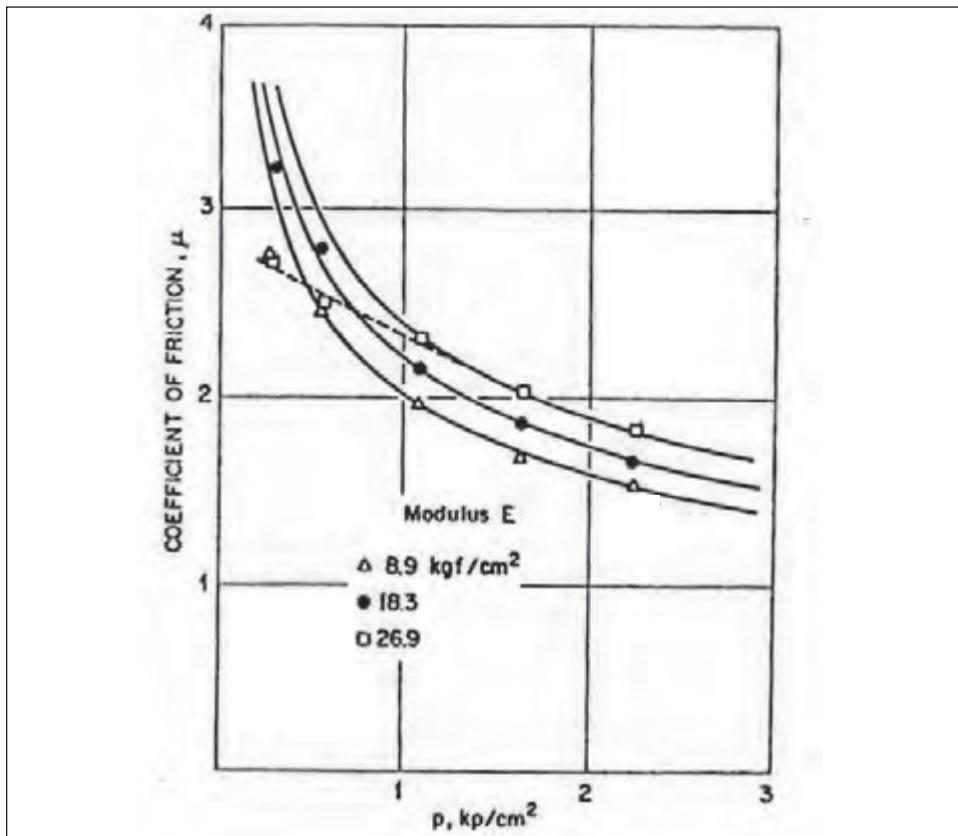
$$A = A_o \cdot \left\{ \frac{L}{L_o} \right\}^{\frac{2}{3}} \qquad [2]$$

where A_o and L_o are reference values of the real contact area and load. This leads to the following relation for the friction coefficient

$$\mu = \mu_o \cdot \left\{ \frac{L}{L_o} \right\}^{\left(-\frac{1}{3}\right)} \qquad\qquad [3]$$

Figure 13.1 shows the friction coefficient as function of pressure for three unfilled natural rubber compounds with different elastic moduli [3].

Figure 13.1: Friction coefficient as function of pressure for three NR unfilled compounds of different moduli on a smooth surface [from ref. 3]

Schallamach has shown that the exponent in Equation 3 changes to –1/9 if both surfaces have hemi-spherical asperities [4]. The author has carried out extensive experiments with different tread compounds on tracks of different asperity shape and coarseness and has found that for these hard tread compounds the exponent of the friction coefficient ranged between - 0.1 to + 0.1 but was in many cases very small so that the load dependence may be neglected [5]. In figure 13.2 and table 13.1 the friction coefficients and values of the exponent at a load of 100 N are given for several elastomer compounds sliding under various surface conditions.

Figure 13.2: Friction coefficient of different tread compounds as function of load on a blunt wet alumina 180 surface. Speed 0.015 m/s. [from ref. 5]
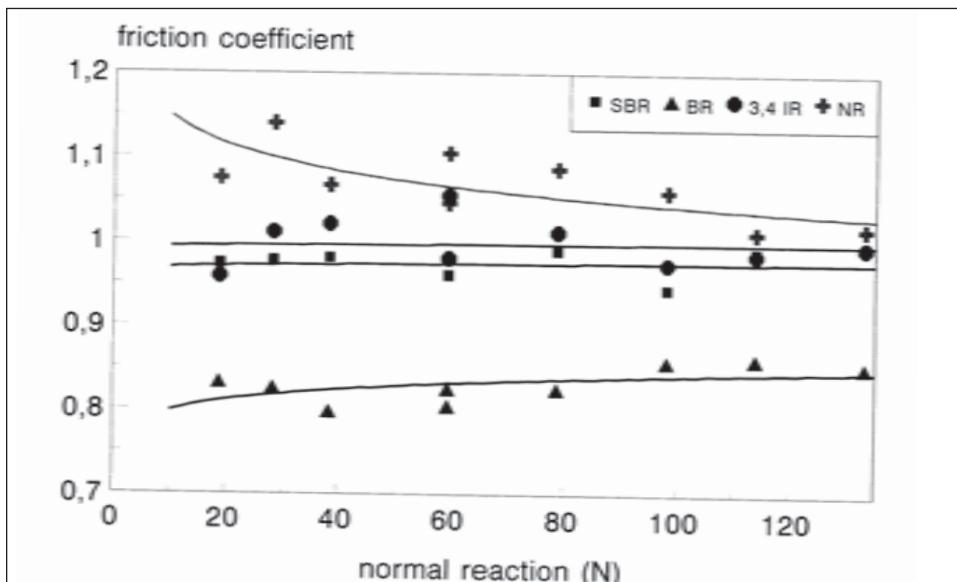
Table 13.1: Parameter of the friction load relationship under different surface conditions

Compound	Ground glass dry		Ground glass wet		Corundum 180 Sharp wet		Corundum 180 Blunt wet	
	μ_o	n	μ_o	n	μ_o	n	μ_o	n
BR	1.080	0.111	0.613	0.098	0.815	-0.096	0.841	0.023
NR	1.519	0.049	0.775	-0.009	1.041	-0.097	1.042	-0.042
SBR	0.956	0.086	0.660	-0.033	1.043	-0.103	0.975	0.003
3.4 IR	0.803	0.080	0.844	0.038	1.180	-0.054	0.998	0.002

mean over all rubber compounds and conditions: 0.004

2.2 Pressure dependence of sliding abrasion

An abrasion experiment is carried out by sliding a rubber sample for a given distance. The volume loss is determined by some suitable method, usually by measuring the difference in weight before and after sliding. It is generally assumed that the abraded volume is proportional to the distance covered, which is reasonable if the sharpness of the track remains constant. Hence the abraded volume is always referred to unit sliding distance. This basic quantity depends on the pressure between the sliding surfaces, the temperature, sliding speed, and topography such as sharpness and coarseness of the asperities of the track.

In contrast to the frictional force, the resulting abrasion is generally a non-linear function of the pressure p

$$abr = abr_{ref} \cdot \left\{ \frac{p}{p_o} \right\}^n \qquad [4]$$

with a positive exponent n, greater than 1. For a constant apparent area of contact, a similar relation results for the load dependence. The reference abrasion loss Abr_{ref} at the reference pressure p_o and the exponent n depend both on the type of track and the rubber compound. If the abrasion is referred to the amount of frictional energy dissipated in sliding, usually referred to as the abradability of the rubber compound, then the exponent would vary if the friction coefficient depended on the load and would remain the same if it did not.

   If the track is smooth the abrasive loss may be so small that it eludes normal measurement, although the frictional force may be very high, while on rough sharp surfaces the abrasive loss may be pronounced even at a moderate frictional force. It follows that stress concentrations in the contact area enhance the abrasion process for similar external forces. Figure 13.3 shows the abrasion loss of a BR tread compound on four surfaces of different sharpness, as a function of the pressure using logarithmic scales for both axes. The straight-line graphs differed both for their reference loss as well as for their exponent n [6]. The smallest value for n was obtained for abrasion on the flat side of a silicon carbide grinding wheel. The others were for a tarmac road surface and two concrete floor surfaces. Note that n was always significantly greater than 1. It is generally observed that the index becomes larger the blunter the abrading surface. On very sharp tracks, on the other hand, the index n may be reduced to 1, as shown in figure 13.4 [7].

Figure 13.3: Abrasion loss as function of pressure for a BR tread compound on four different abrasive surfaces. [from ref. 6]
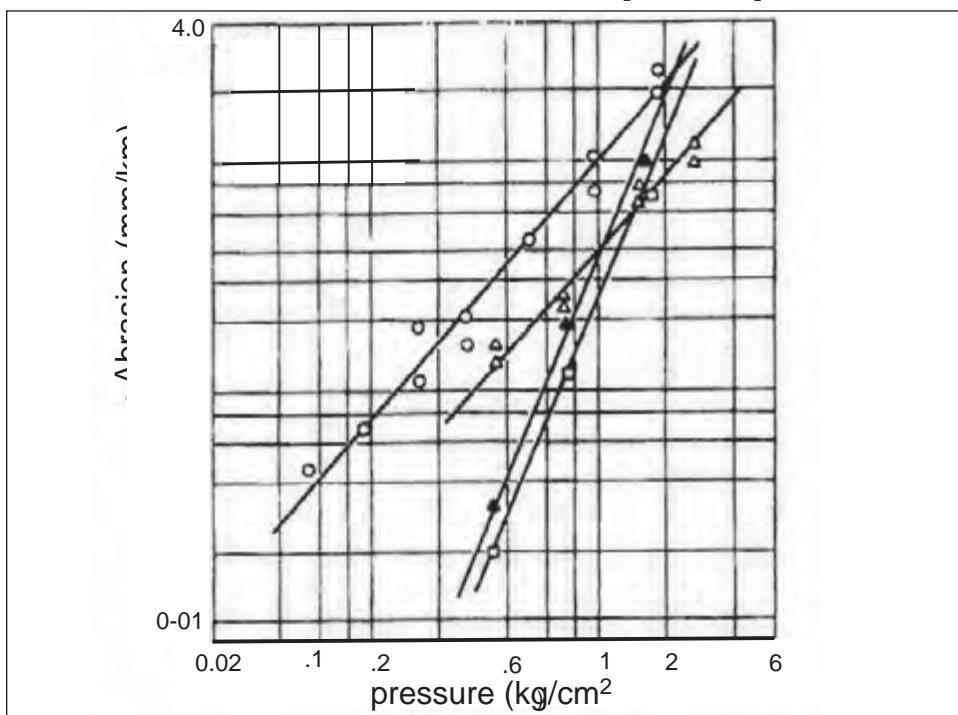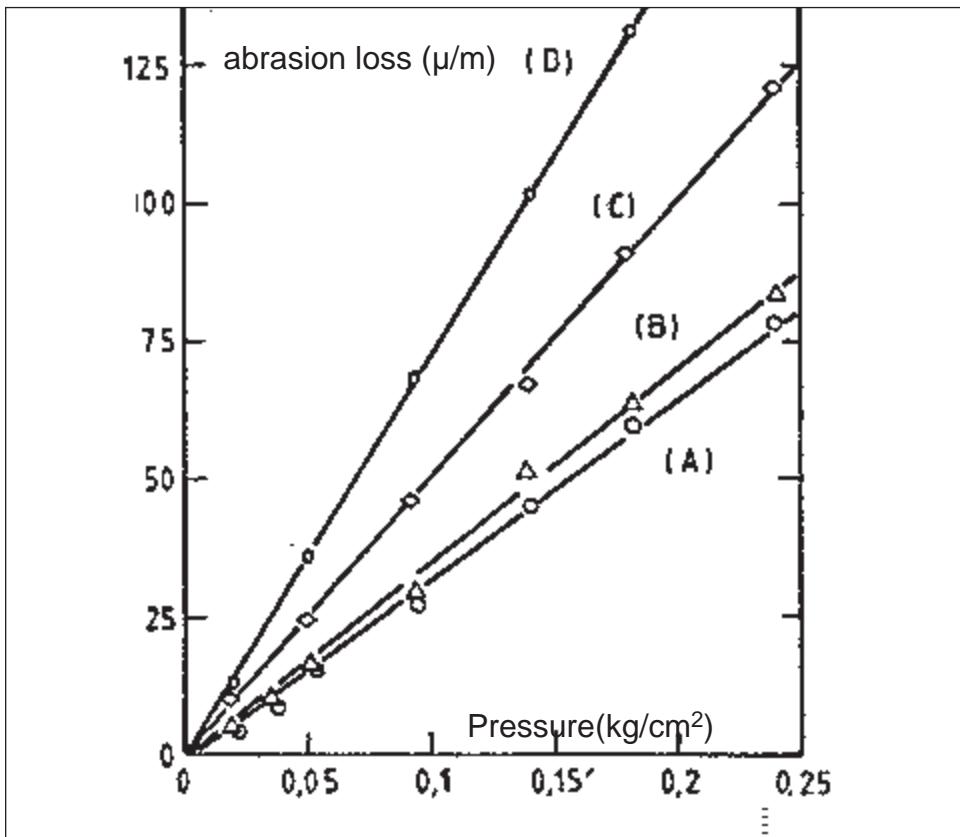
**Figure 13.4: Abrasion loss as function of pressure for four different compounds
[from ref .7] A, SBR+50 HAF black; B, NR +50 HAF black;
C, NR+50 thermal black; D, NR+50 activated CaCO$_3$**

2.3 *The dependence of abrasion on energy consumption in the contact area.*
A more basic approach is to consider not the dependence of the abrasion loss on pressure but on the energy dissipation W caused by the frictional force F. For sliding experiments this is

$W = F \cdot s$ [5]

where s is the distance covered. Hence the energy dissipation W per unit distance becomes equal to the frictional force. On very sharp tracks the abrasion loss is nearly proportional to the frictional force; more generally, however, it is a power function of the energy dissipation, whereby the exponent depends both on the sharpness of the track and on the rubber compound in question. When referred to the energy dissipation, the abrasion loss is generally called the abradability of the rubber compound on the track on which it was measured.
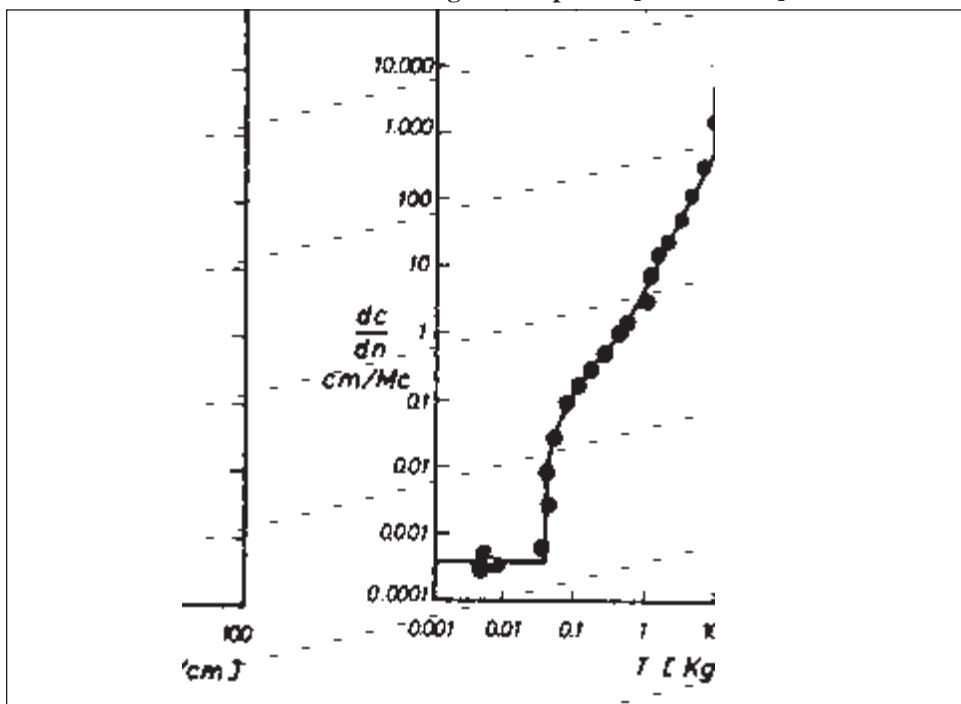
This behavior is similar to the cut growth and fatigue behavior of rubber compounds. The rate of the growth of a cut is a function of the tearing energy [8,9] which itself is pro-

portional to the stored elastic energy density in the test piece. The exact value depends on the geometry of the test piece.

2.4 The relation between rate of cut growth and tearing energy
Since this relation appears to be the basis of the abrasion process it is necessary to study its characteristic shape. Figure 13.5 shows the relation for an unfilled natural rubber compound [10,11]. It can be divided into four regions.

Figure 13.5: Rate of cut growth dc/dn as function of tearing energy
T for a natural rubber gum compound [from ref. 10]

Below a limiting tearing energy T_o there is no mechanical tearing. Cut growth is then due to attack of ozone, which cleaves elastomer molecules. The rate of growth of cracks due to ozone is independent of the tearing energy and depends only on the ozone concentration.

Above T_o there is a small region for which the cut growth rate dc/dn is proportional to the tearing energy T

$$\frac{dc}{dn} = A_{cr} \cdot \{T - T_o\} \qquad [6]$$
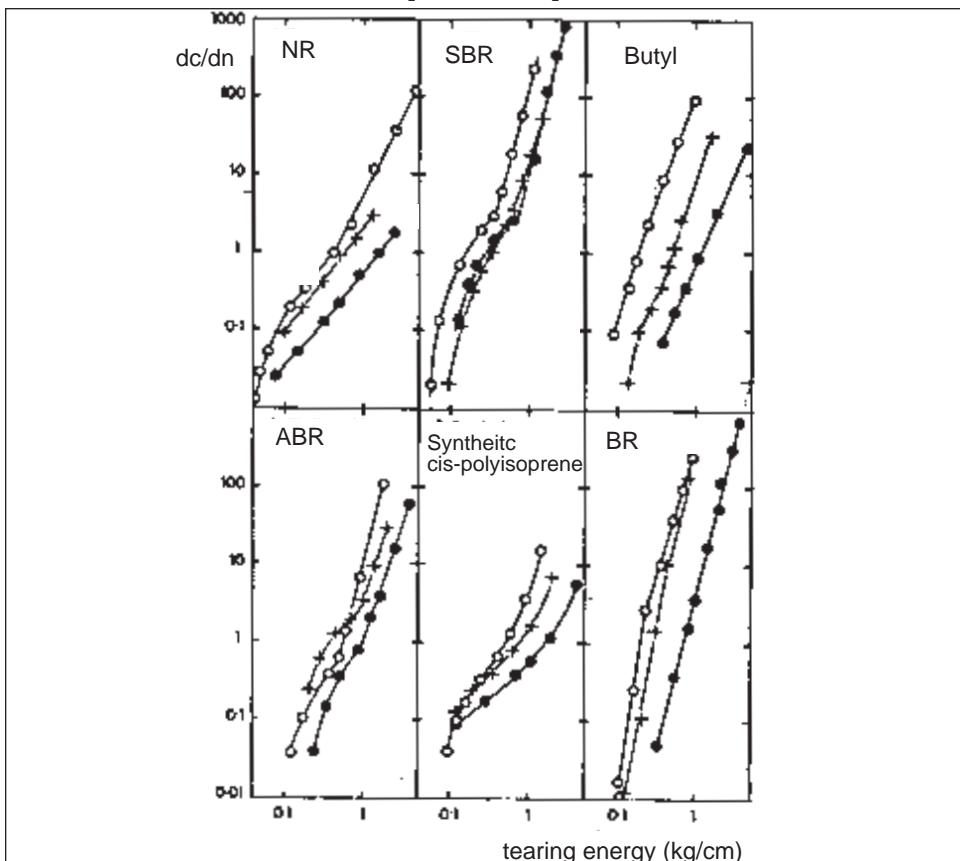
where A_{cr} is a material property that is influenced by temperature and oxygen.
In a third region, the cut growth rate can be described by a power law

$$\frac{dc}{dn} = B_{cr} T^{\beta} \qquad [7]$$

In this region the growth rate constant B_{cr} is also influenced by temperature and the presence of oxygen. The exponent β depends primarily on the polymer.

When the tearing energy approaches a critical value T_c the rate of cut growth becomes suddenly very large, and spontaneous rupture occurs. The critical tearing energy T_c is proportional to the energy density at break. Figure 13.6 shows the cut growth rate for six polymers as gum rubbers and filled with two levels of reinforcing carbon black [10]. They can all be represented by a power function over a considerable range of tearing energies. Note that addition of carbon black filler reduces the rate of cut growth but has only a small effect on the exponent.
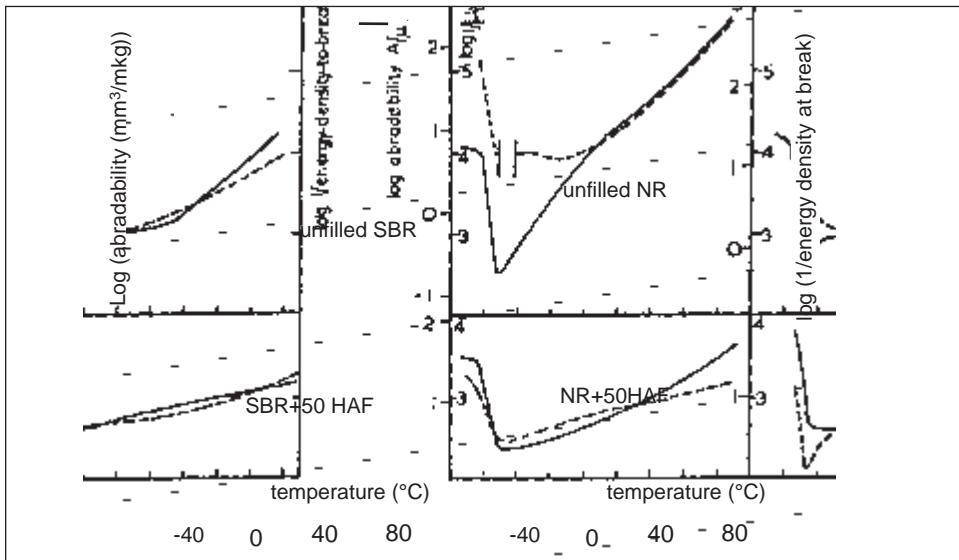
Figure 13.6: Rate of cut growth for six different rubbers ( ) gum rubber, (+) loaded with 20 pphr reinforcing black and (") with 50 pphr reinforcing black. [from ref. 10]

Generally it appears that abrasion occurs mainly in the third region, except when the abrasive track is very sharp. In this case the number of cycles to detach a small piece of rubber becomes small and the rate of abrasion is proportional to the reciprocal of the energy density at break of the rubber compound. This becomes apparent when the temperature dependence of sliding abrasion on a sharp silicon carbide track is compared with that of the inverse of the energy density at break [12]. Both curves look very similar as shown in

figure 13.7. In order to superpose the two curves, the rate of extension employed in measuring the energy density at break had to be about 100/sec for a sliding speed of 10 mm/s. The difference between the origins of the two ordinate scales represents the log of the coefficient in the relation between abrasion resistance, defined by the energy required to remove unit volume of rubber (J/mm^3) and the energy density at break in the same units.

Figure 13.7: Abrasion loss per unit energy (abradability)(---) as function of temperature for four different compounds on a silicon carbide track at a speed of 1 cm/s together with energy density measurements(-) at an extension rate of 10^2/s [from ref. 12]

$$k = \frac{A_{resis\tan ce}}{U_{break}} \qquad [8]$$

where $A_{resistance}$ is the inverse of the abradability, defined as the abrasion loss per unit energy and U_{break} is the energy density at break. The value of k is about 2000, indicating that the energy required to remove unit volume of rubber, even by a sharp abrasive track, is used quite inefficiently. It is sufficient to break 2000 times the amount of rubber that is actually abraded away.
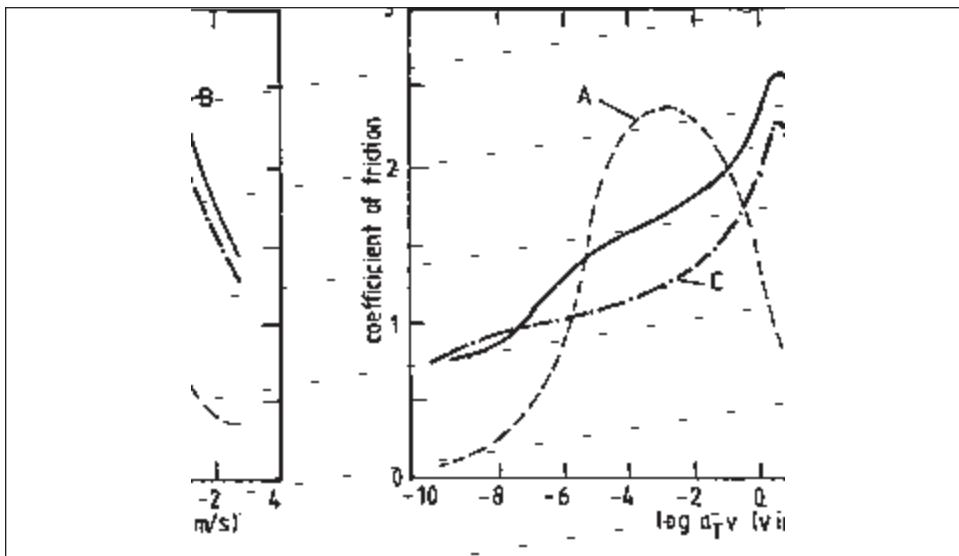
2.5 The temperature dependence of sliding abrasion
2.5.1 Temperature and speed dependence of rubber friction
Unlike hard solids, the friction of rubber depends strongly on temperature and speed because rubber friction is dominated by the visco-elastic properties of the compound. The strongest possible evidence of this is given by the fact that the effects of temperature and speed are inter-related. The friction coefficient can be expressed as a function of the combined variable log $a_T v$ where a_T is given by the WLF rate-temperature equivalence equation [see Chapter 2]. Friction measurements are carried out at different temperatures over a range of speeds where the highest speed is selected to be sufficiently low that no signif-

icant temperature rise occurs in the contact area. Multiplying the experimental sliding speed by the factor a_T of the WLF equation and plotting the friction coefficient as a function of log $a_T v$, a single continuous curve results from measurements at various temperatures and speeds. This so-called master curve describes the frictional properties of the compound on the track surface completely. Figure 13.8 shows the master curves of an ABR gum rubber on polished glass (A), on a clean silicone carbide track (B) and on the same track lightly covered with magnesium oxide powder (C) [14]. On glass the friction is very low at low values of log $a_T v$, then rises to a maximum and falls again at high log $a_T v$ values. On a silicon carbide track, the friction at low values of log $a_T v$ is considerably higher than on glass. It also rises with increasing log $a_T v$ and reaches a small plateau at the point of maximum friction on glass. For further increase of log $a_T v$, however, it does not fall but increases further to a sharp peak at values of $a_T v$ several decades above that for maximum friction on glass. Beyond that point the friction coefficient falls rapidly to values expected for hard solids.

Figure 13.8: Master curve of the friction coefficient as function of log $a_T v$ for an ABR gum compound on polished glass (A), clean (B) and dusted (C) silicon carbide respectively [from ref. 14]. Dust used: MgO powder

When powder is present at the interface, the curve on silicon carbide still shows a maximum at the same position as on the clean track, but the hump has disappeared. If powder is used with a smooth glass track, the friction coefficient remains very low over the whole range of log $a_T v$, indicating that the hump on clean silicon carbide is due to the same friction process as occurs on clean glass.

It is useful to compare the speed of maximum friction with the frequency dependence of visco-elastic properties for different polymers. It turns out that there is a direct proportionality between the speed for maximum friction on smooth glass and the frequency of maximum loss modulus E''. The factor relating them is a distance: $\lambda = 6 \times 10^{-9}$ m, which is of molecular dimensions and is the same for all elastomers examined. The fact that it is

associated with the maximum of the loss modulus suggests that friction on such smooth surfaces is a molecular relaxation process since the loss modulus curve is a rough approximation of the relaxation spectrum of the material. Indeed, an identical length could also be derived from the first derivative $d(\log E')/d(\log f)$ of the real part of the modulus, which gives an improved approximation to the relaxation spectrum.

Schallamach has developed a theory based on this assumption, which predicts the essential features of the observed curve [15]. Because it is based on a single relaxation time the predicted dependence on $\log a_T v$ is narrower than the experimentally-observed one. Its greatest shortcoming, however, is that it predicts zero friction both at very small and at large values of $\log a_T v$; i.e. it does not incorporate a "static" friction coefficient.

Thus, on smooth surfaces friction is due to an adhesion relaxation process. On such tracks there is also no measurable material transfer, i.e. no abrasion loss.

For friction on the rough silicon carbide track the speed of maximum friction is related to the frequency of the maximum loss factor and the associated length is 1.5×10^{-4} m, which is close to the spacing of abrasive particles on the track. It is thus obvious that this type of friction is associated with energy losses under a cyclic deformation. However, these losses are not only due to the deformation caused by the normal load, they are reinforced through tangential stresses produced by adhesion and magnified by the shape of the abrasive particles. Schallamach has demonstrated in a two-dimensional transparent model [16], shown in figure 13.9, how stresses are distributed in rubber due to indentation by a wedge under a normal force and when, in addition, a frictional force is applied. The results agree closely with the calculated stress distribution due to a line force acting at an angle to the surface of a semi-infinite solid (figure 13.10) [17]. Figure 13.11 (upper) shows the elastic stored energy of two line forces acting at an angle a to the surface of the semi-infinite body simultaneously and figure 13.11 (lower) shows the horizontal stress component. As expected, both energy and stress show strong peaks at the points of contact. The stress is compressive in front of the contact, i.e. the friction component pushes. At the end of the first contact the stress is strongly tensile, decreasing rapidly away from the contact and it becomes again compressive at a point midway between the two contacts. If more contact points are considered, this pattern is repeated. The stress is also limited to a small range of depths. If the distance between the two contact points is 1 mm then at a depth of 0.04 mm the horizontal stress component has dropped to about 20% of that at 0.01 mm depth. The stress at the surface itself cannot be calculated because a point has an infinitesimally-small contact area and hence the stress becomes infinitely large. In reality, the force due to an asperity with a small but finite tip radius produces a small but well-defined contact area, particularly between a hard asperity and a soft rubber compound, and keeps the contact stress finite. Nevertheless, the smaller the contact radius, the higher are the stresses at the contact point. The contact radius defines the sharpness of the wedge and in a three-dimensional case the sharpness of an asperity.

The stored energy between the line forces does not become zero and a tensile stress acts at the end of the line forces and a compressive stress at the front. At each pass the energy peaks at the contact points causing crack growth to start from small surface flaws. This is the mechanical contribution to the abrasion process. In any case a large amount of *elastic* stored energy is lost and turned into heat. This is not a hysteretic process in the normally-understood sense of energy lost in a cyclic process. It is a thermodynamic process in which rubber is extended and energy is stored but it cannot be retrieved on retraction

and is therefore turned into heat. This is the reason for the high friction observed at low values of log a_Tv in sliding on silicon carbide, figure 13.8.

Generally the stresses are not large enough to tear the rubber away in one pass but repeated passes over a rough surface will detach particles. This process is aided by the temperature rise that occurs under normal wear conditions and causes thermal and oxidative degradation of the rubber. Since the energy is stored in a very small depth and the heat conductivity of rubber is low, the temperature rise within a small surface layer may become quite high, promoting both modes of degradation.

Figure 13.9: Two-dimensional stress pattern in a transparent rubber block under a line force [from ref. 16]
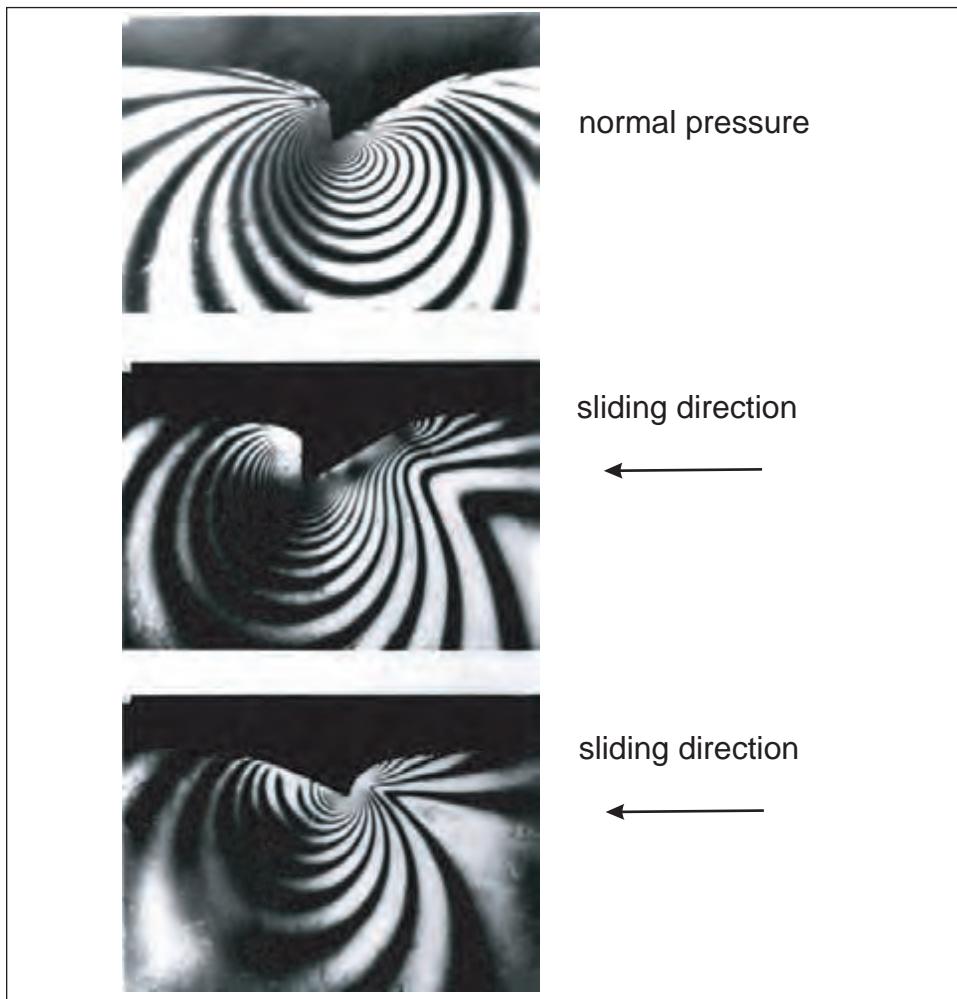
Figure 13.10: Calculated lines of equal stress for a line force made up of normal load and frictional force acting on the surface of a semi-infinite body.
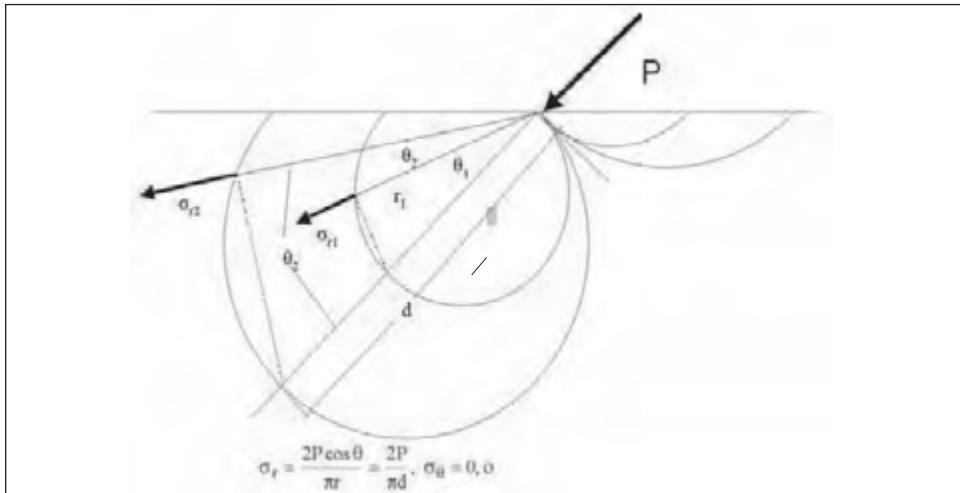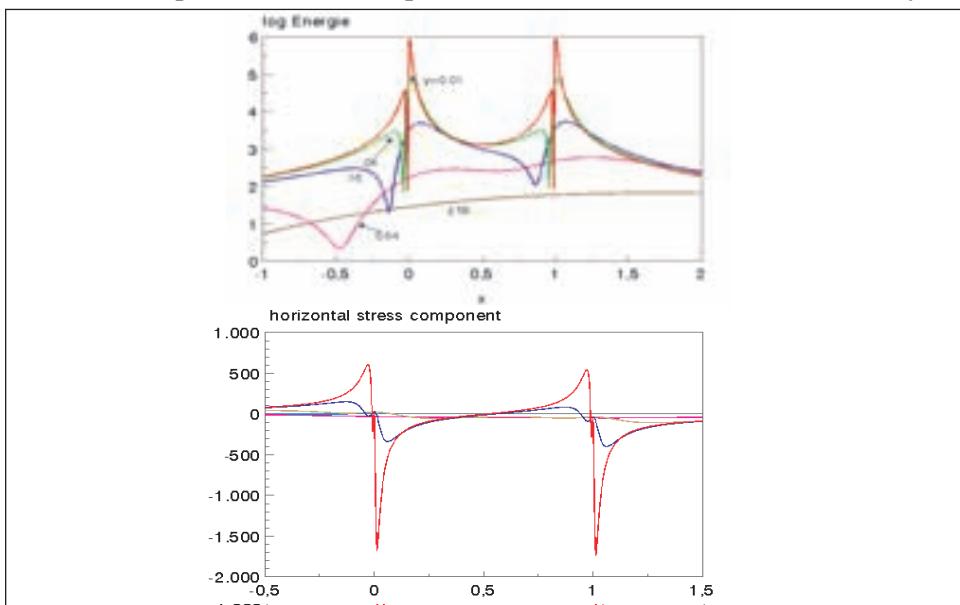
Figure 13.11: Calculated stored elastic energy and the horizontal stress component due to two line forces at an angle to the plane of the rubber surface and a fixed distance x apart for different depths from the surface of a semi-infinite body.
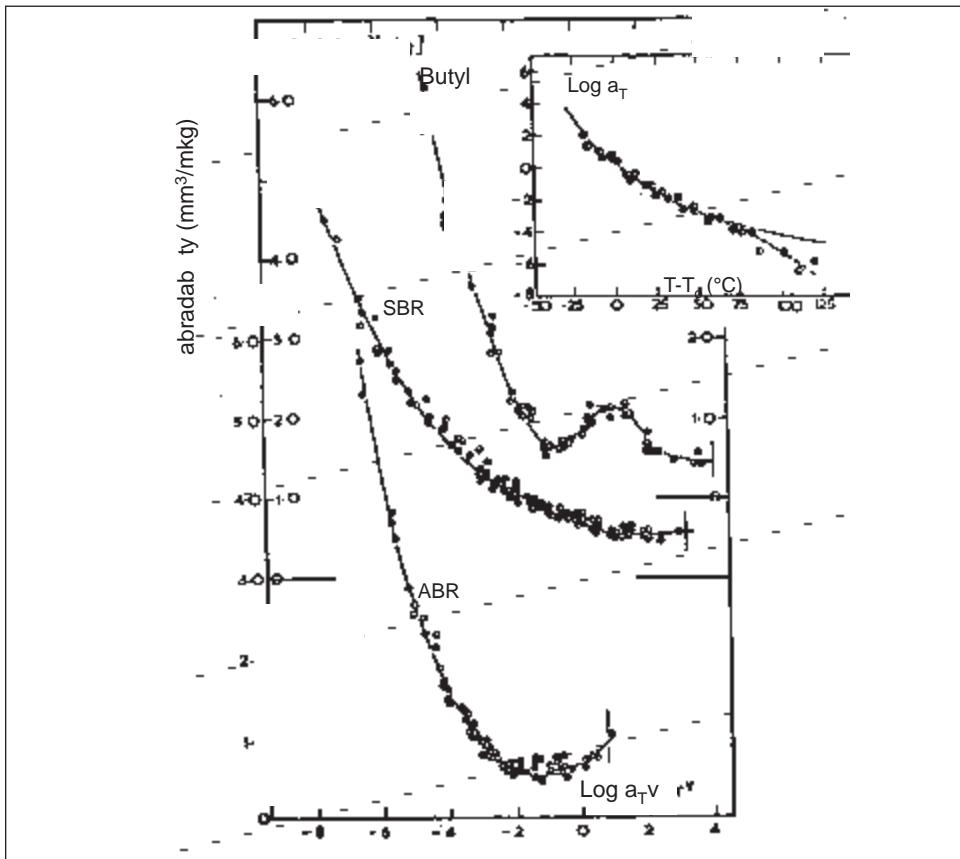
2.5.2 Temperature and speed dependence of sliding abrasion

For simple unfilled, non-crystallizing rubber compounds the temperature and speed dependence of sliding abrasion on sharp tracks is dominated by the visco-elastic nature of the rubber, provided that the sliding speed is so low that temperature rises due to friction are small. Combining the two variables using the WLF transformation results in single
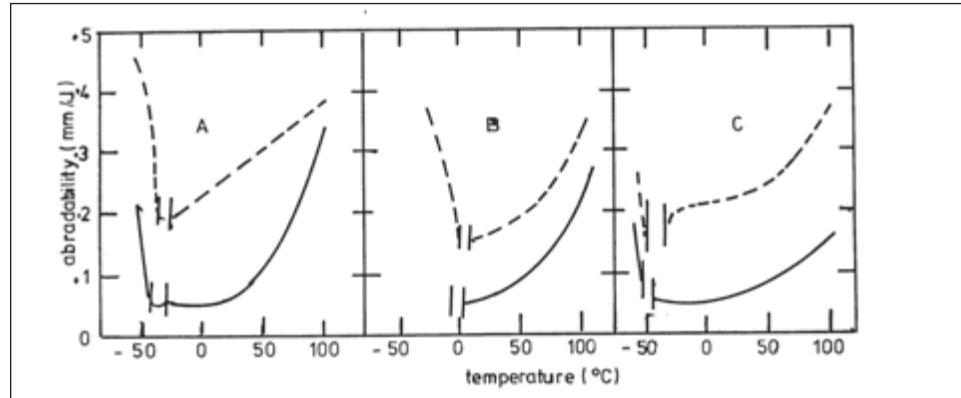
"master" curves as shown in figure 13.12 [12]. The abrasion loss decreases with decreasing temperature reaching a minimum value. At lower temperatures, it begins to rise sharply. This is accompanied by a drastic change in appearance of the abraded surface, as discussed in the next section. It appears that the lowest abrasion loss occurs when the rubber has a maximum extensibility. This also corresponds to the highest energy density at break, as already discussed in section 2.3

Figure 13.12: Sliding abradability as function of the variable log $a_T v$ for four non-crystallizing rubber compounds on dusted silicon carbide 180

The WLF transform only works well for abrasion of non-crystallizing gum rubbers. For tire tread compounds the temperature dependence is smaller. However, in this case, too, the abrasion loss, measured at a constant speed, reaches a minimum at a particular temperature as shown in figure 13.7. A surprising result is that tread compounds have a much higher abrasion loss than the corresponding unfilled compounds, as shown in figure 13.13 where the rate of abrasion is plotted as a function of temperature for three elastomers: (A) SBR, (B) ABR and (C) NR. The solid lines are for the unfilled compounds and the dotted ones are for the same elastomers filled with 50 parts of HAF black. The reason for the differences becomes apparent on examining the appearance of the abraded surfaces.
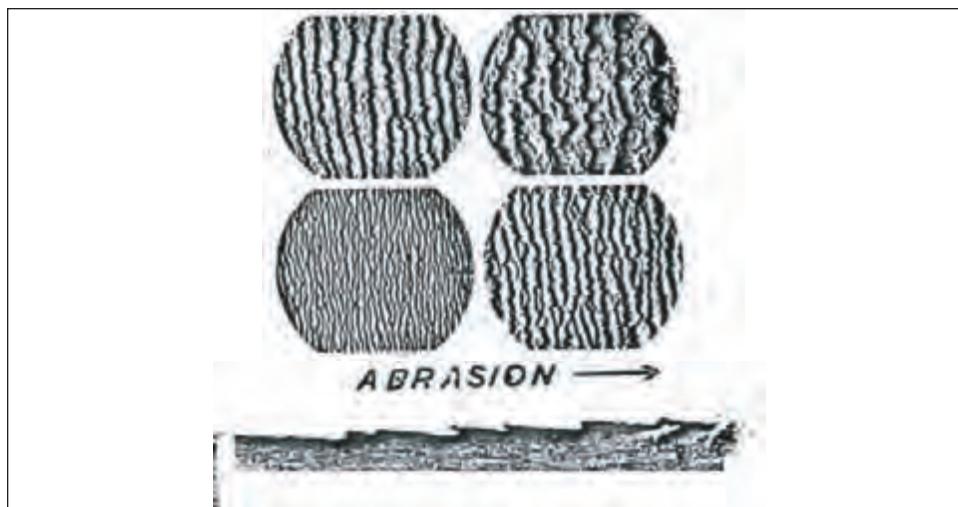
**Figure 13.13: Sliding abrasion of three different tread compounds as function of temperature at a sliding speed of 0.01 m/s (a) SBR, (b) ABR, (c) NR
---- tread compound,   - gum compound**

2.5.3 The appearance of abraded rubber surfaces

At normal temperatures the surface of a rubber sample that has been subjected to sliding abrasion has a characteristic ridge pattern, the direction of the ridges being normal to the sliding direction (see figure 13.14a). This is generally termed an abrasion, or Schallamach, pattern [18]. A cross-sectional view reveals that the ridges are undercut, the tips pointing against the abrasion direction (figure 13.14b). During sliding, an asperity of the track bends the tip over and stretches it until the adhesion force can no longer hold it and the ridge snaps back. However, as the tip extends, the stress at the bottom of the ridge rises and a crack can grow there by tearing to a limited extent. After a number of passes of an asperity across the surface the ridge tip has become so undermined that part of it tears
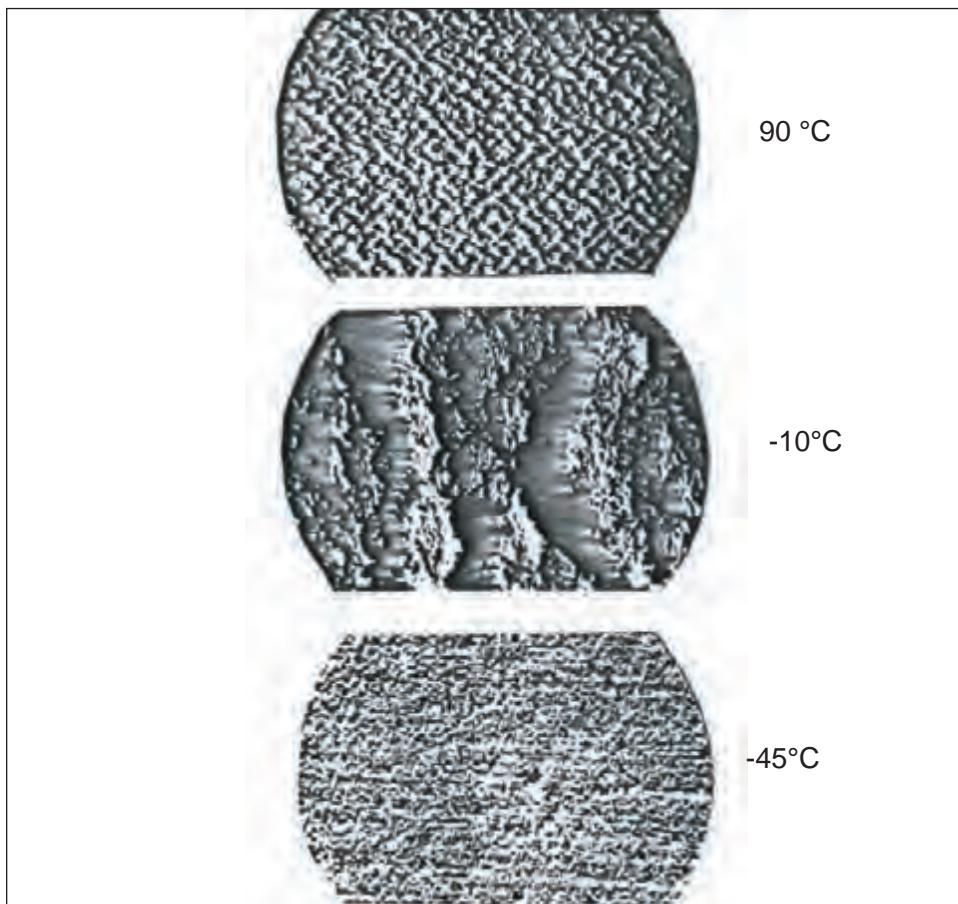
Figure 13.14: Abrasion pattern: (a) appearance for different rubbers under different testing conditions (b) cross section through abraded samples.

away. Thus, during sliding abrasion the pattern moves slowly in the direction of abrasion.

This abrasion mechanism prevails for soft rubbers with high extensibility. In fact, the higher the extensibility, the coarser the abrasion pattern becomes, as seen in figure 13.15 which was obtained during the abrasion - temperature experiments described above. Although the samples were rotated through 90° at regular intervals in order to suppress their formation, abrasion patterns were formed. However, because of the frequent rotation of the sample they appear as nipples rather than ridges at low values of log $a_T v$ (high temperatures, low sliding speeds) as shown in the upper photograph of figure 13.15. As the minimum rate of abrasion is approached, very pronounced ridges formed despite the rotation (middle photo of figure 13.15) and the rate of abrasion increased forming a small hump in the abrasion vs. log $a_T v$ curves (figure 13.12 above). At still higher values of log $a_T v$, scoring marks appeared (lower photo, figure 13.15). The rubber now acts like a hard solid, in this case like a glassy plastic. However, because of the high rate of extension both in the abrasion process and also in the energy to break experiments, this change occurs well before the conventional glass transition temperature is reached. The rate of abrasion increases drastically, as seen in figure 13.12, in accordance with the decreasing
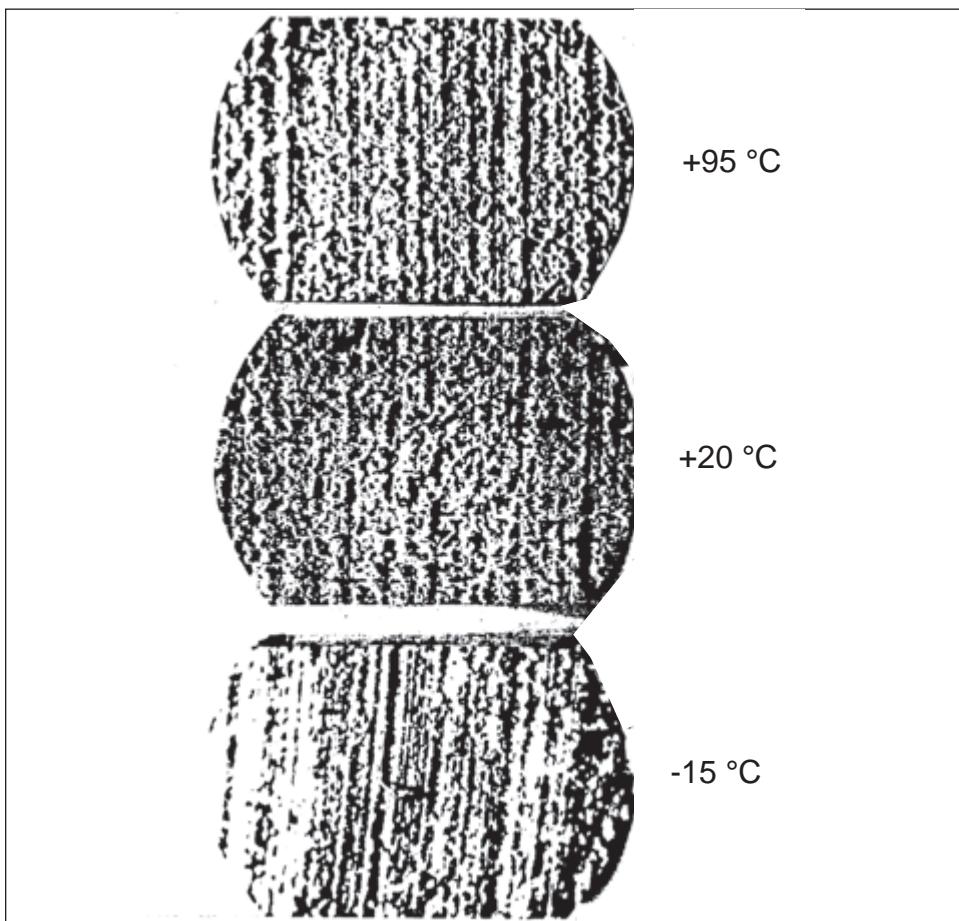
Figure 13.15: Abrasion pattern of ABR gum rubber from the sliding abrasion experiment at different temperatures

energy density at break.

Tire tread compounds are filled with highly reinforcing carbon black. This means above all that the compound is harder. Their extensibility, however, is lower than that of the unfilled compound and accordingly the abrasion pattern is much more closely spaced and less pronounced. In many cases scoring marks are present at the same time as an abrasion pattern at all temperatures, as shown in figure 13.16. The abrasion loss is then higher for the black filled compound than for the corresponding unfilled compound, as shown in figure 13.13. Veith has interpreted the presence of scoring marks in black-filled compounds as evidence that they have regions of plastic behavior [17].

Figure 13.16: Abrasion surface appearance of an NR black filled tire tread compound for sliding abrasion at different temperatures

+95 °C

+20 °C

-15 °C

2.6 Abrasion by a razor blade

Champ, Southern and Thomas [21] devised a simple abrasion experiment, measuring the weight loss caused by a razor blade pressed against, and scraping across, a rubber surface. They used as test samples Akron abrader test wheels made from soft unfilled non-crystalliz-

ing rubber compounds. Under their abrasion conditions strong abrasion patterns developed.
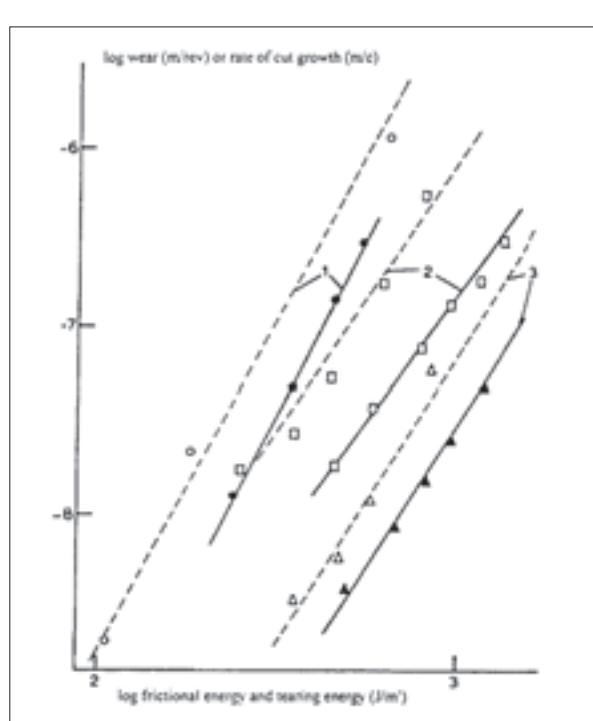
If the increase in the crack length at the base of an abrasion pattern ridge is dc the increase in abrasion depth per pass, i.e. per cycle, is dc.sin β where β is the angle between the cut growth direction and the surface of the sample. Assuming that crack growth in abrasion resembles crack growth in a trouser test piece the tearing energy is given by

$$T = F/b \cdot (1 + \cos \beta) \qquad [9]$$

where b is the width of the sample wheel and F is the tangential force on the blade. By using different loads, different tearing energies are produced. The rate of crack growth can be measured independently as a function of the tearing energy.

Figure 13.17 shows the results of their experiments for three unfilled compounds. The solid lines represent the amount of abrasion per cycle and the dashed lines the rate of cut growth. The agreement between the two measurements is very satisfactory. However, cut growth rates of rubber compounds depend on the applied tear energy by a power law, with the exponent α of tear energy being 2 to 4, depending on the elastomer and compound. Whilst the agreement between the cut growth rates and the rate of abrasion was good for the non-crystallizing elastomers, with α about 3, it was unsatisfactory for unfilled natural rubber, which shows good resistance to crack growth by fatigue (α about 2) but poor resistance to abrasion (α about 3). Strain-induced crystallization reduces the rate of crack
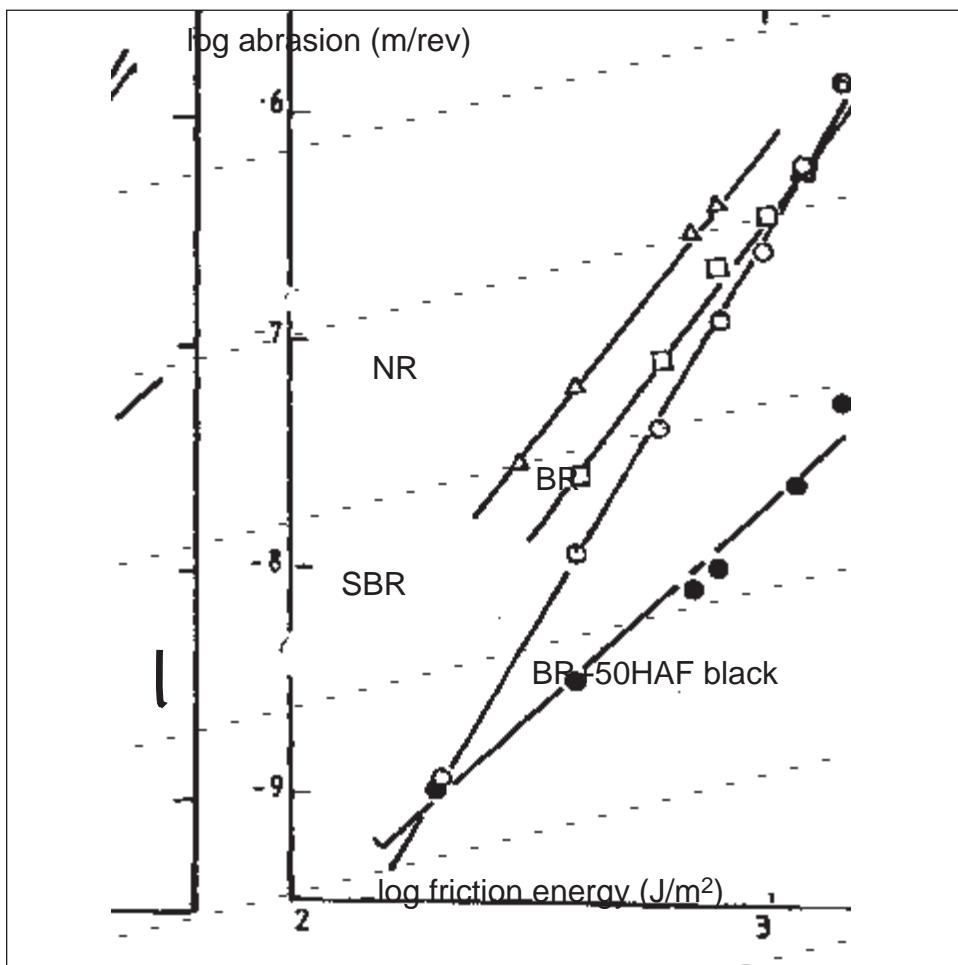
Figure 13.17: Log abrasion loss by a blade (solid lines) and log cut growth rate (dashed lines) of non-crystallizing rubber compounds as function of log frictional and log tearing energy respectively. 1, isomerized NR; 2, SBR; 3, ABR [from ref. 21]

growth significantly but in the abrasion experiment it appears to have less effect.

Pulford and Gent [22] have extended these experiments. They obtained straight-line graphs on plotting log abrasion against log frictional energy dissipation, as shown in figure 13.18. The slopes of the lines were compared to those obtained from cut growth experiments. For the black-filled BR compound the slope was much smaller than for cut growth, whilst for the unfilled compound it was similar (compare with figure 13.6 above).

Figure 13.18: Log abrasion by a blade as function of log frictional energy for three unfilled and a black filled rubber [from ref. 22]
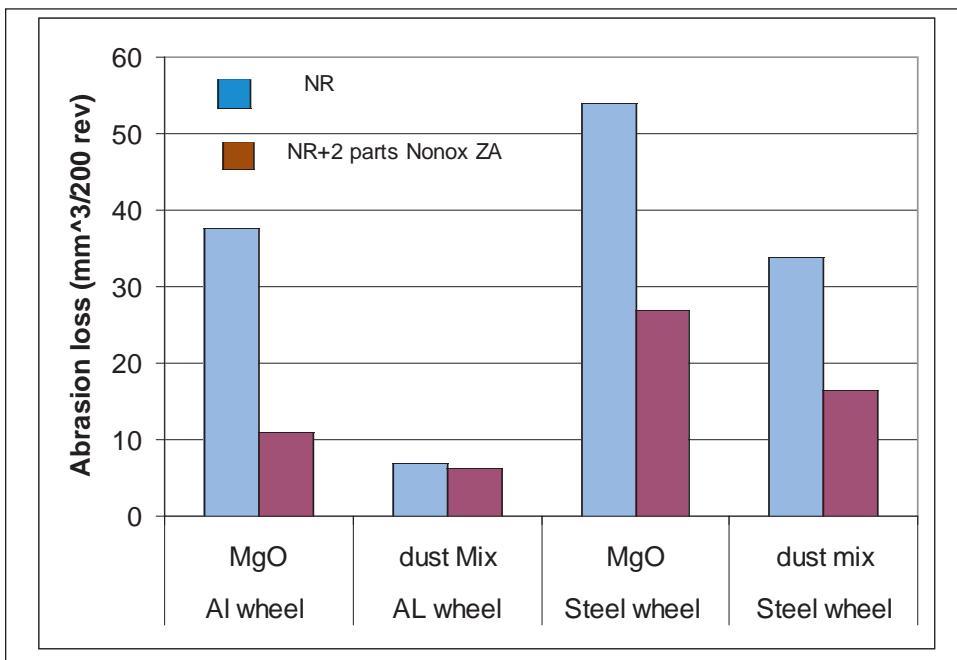
2.7 The effect of smearing and abrasion in an inert atmosphere.
One of the most obvious features of laboratory abrasion measurements, associated with chemical effects, is so-called smearing. Abrasion debris tends to collect in rolls of abraded rubber. The rolls are often quite large and consist of many very small rubber particles that have been degraded both thermally and by oxidation. The rolls are sticky and adhere to the rubber surface, protecting it from further abrasion. As a result, the rate of abrasion

drops and abrasion may stop altogether. In road wear this phenomenon is only observed under extreme conditions like car racing. Normally there is sufficient dust on the road to be adsorbed by the debris and cause the rolls to disintegrate or not to form at all. Hence, a suitable powder is often applied to the track in laboratory abrasion experiments in order to absorb the smeary abrasion debris that would otherwise falsify the abrasion results. Magnesium oxide has proved to be one of the most effective agents for absorbing abrasion debris and thus preventing smearing. Schallamach carried out experiments on blunt abrasive tracks using MgO and a mixture of Fuller's earth and alumina powder [23]. The results are shown in figure 13.19 for two blunt surfaces, one of knurled aluminum, and the other of knurled steel. Aluminum produces a lower abrasion loss than steel. On both surfaces, however, the rate of abrasion was much higher when MgO was used as an absorbing powder than with the mixture of Fuller's earth and alumina. The two compounds examined were an NR compound without antioxidant and one with 2 parts of Nonox ZA. There is a very clear difference between the two compounds indicating that oxygen plays

Figure 13.19: Abrasion of two NR tread compounds, one unprotected, the other with 2 parts Nonox ZA on a knurled aluminum and a knurled steel surface in the presence of (a) Magnesium oxide powder and (b) a dust mix of Fuller's earth and alumina powder. [deduced from ref. 23]
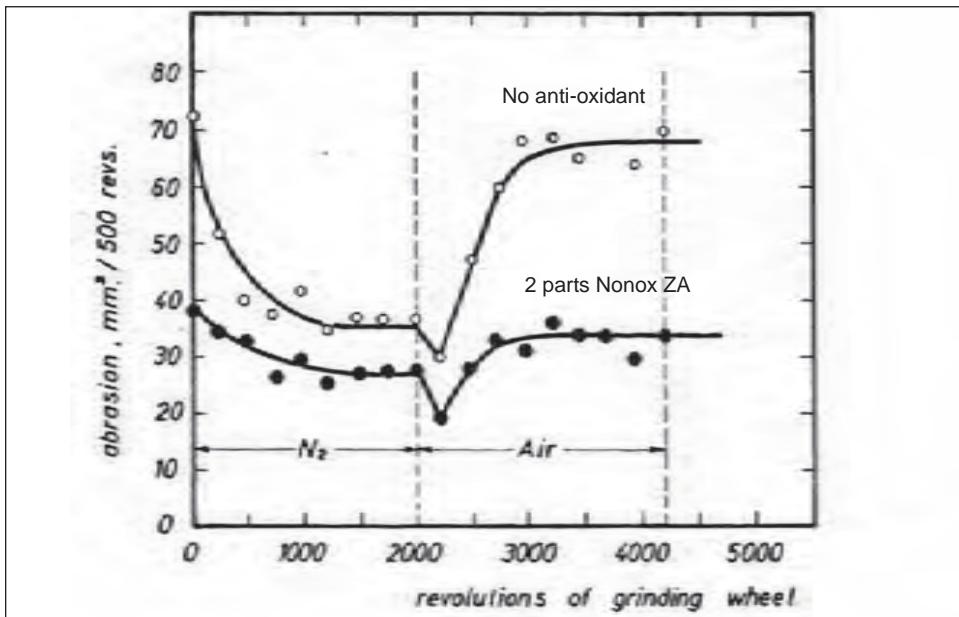
an important role.

Abrasion experiments in nitrogen, first carried out in Russia [24], showed that abrasion in practically all cases was higher in air than in nitrogen (with the interesting exception of butyl rubber), and the effect was larger with blunt abrasives than with sharp ones. Figure 13.20 is an abrasion time record that Schallamach obtained on an Akron grinding wheel when switching from air to nitrogen and back again. A mixture of alumina powder and

Fuller's earth was fed into the nip between the sample wheel and the abrasive wheel to counteract smearing. The sample was first run in air until a constant rate of abrasion had been reached. On introducing nitrogen the abrasion loss dropped rapidly and significantly more so for the unprotected compound. After air was re-introduced the rate of abrasion rose again to approximately the former value. Each time the atmosphere was changed it took a few readings before a steady state was reached, indicating that a certain time was

Figure 13.20: Time record of the abrasion loss on a standard Akron grinding wheel in nitrogen and in air of an NR tread compound (a) unprotected and (b) protected with an antioxidant [from ref.23]
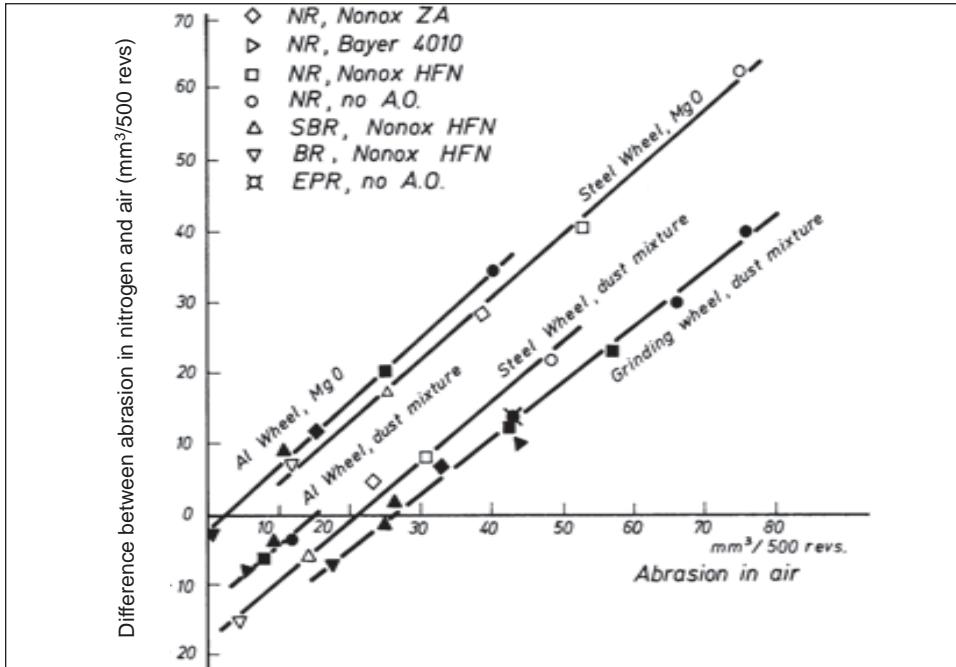
needed before the effect of oxygen on the surface layer was complete.

In figure 13.21 the difference between abrasion in air and in nitrogen is plotted as a function of the abrasion in air for different compounds abraded on several surfaces of different sharpness and using either magnesium oxide or a mixture of Fuller's earth and alumina powder as agents to counteract smearing. Introducing the powder has two opposing effects on the abrasion loss, but to differing degrees in air and in nitrogen. It prevents smearing and helps in this way to increase the abrasion loss. On the other hand it can lubricate the track and protect the rubber from abrasion. Thus if smearing is small in air and the lubrication effect is significant, abrasion in nitrogen may be greater than in air. MgO powder produced very large differences between abrasion in air and nitrogen when the losses in air were high i.e. when the oxygen-induced smearing effect was large (unprotected NR) suggesting it is highly effective in eliminating smearing. If the compound was well protected by antioxidant, the rate of abrasion in air was similar to that in nitrogen, suggesting that the effect of lubrication was also small. Thus MgO can be seen to be a very effective agent to eliminate smearing without interfering in the abrasion process itself. On the other hand the mixture of powders produced less abrasion in air and in some cases for

well-protected compounds the rate of abrasion was higher in nitrogen than in air. If it is assumed that the lubrication effect is about the same in both air and nitrogen, then clearly the mixture of powders is not very effective in preventing smearing.

Figure 13.21: Difference between abrasion in air and nitrogen as function of abrasion in air for different compounds in the presence of either MgO or a mixture of Fuller's earth and alumina [from ref. 23]

Gent and Pulford [55] noticed that black-filled compounds tend to smear more than unfilled ones, especially for NR, SBR and EPR, while BR and TPPR showed no smearing at all. Instead, the latter elastomers produced abrasion debris that was dry and powdery. This was also the case for NR in nitrogen or in vacuum, showing clearly that oxidation is a major cause of smearing in air. But thermal degradation may also play a role since it is known that BR, for instance, has a very high decomposition temperature (> 500 °C) so that smearing would be expected to be less than for NR which has a much lower thermal decomposition temperature (about 260°C). Gent and Pulford suggested that there are three chemical contributions to the abrasion and smearing process: thermal degradation due to local frictional heating, oxidation which is also aided by the raised temperatures, and formation of free radicals in the rupture process which then also participate in oxidation reactions. In all experiments BR has the smallest smearing effect, i.e. it has the highest resistance to thermal and oxidative degradation. It is suggested that this is the reason for its well-known high resistance to abrasion, rather than any special strength properties.

2.8 A brief summary of the basic factors contributing to abrasion
The different experimental results described above show that abrasion is essentially a cut-

growth phenomena starting from small flaws in the rubber matrix. Cut growth, in turn, is governed by the tearing energy available and hence it is not surprising that rubber abrasion depends above all on the frictional energy supplied. Since the cut growth process is influenced by the presence of oxygen, abrasion is also affected by the surrounding atmosphere.

In addition, dissipation of frictional energy is likely to raise the temperature in the contact area, increasing the rate of oxidation and/or thermal decomposition and at the same time weakening the resistance of the rubber to cut growth, thus further increasing the rate of abrasion. Hence abrasion is not purely a physical phenomenon but is strongly influenced by chemical processes that depend on the chemical structure of the polymer and any protective agents added to the compound. The cut growth process and the associated loss of material by abrasion depend on the sharpness of the abrasive surface. This also influences the oxidation. Blunt surfaces produce less abrasion per unit distance so that oxygen has more opportunity to react. The coarseness of an abrasive is less important. Its influence is limited to an interaction between asperity spacing and sliding speed, and the frequency dependence of the visco-elastic properties of the rubber compound.

3 Abrasion under limited slip

3.1 Forces on slipping wheels

The speed and direction of a self-propelled vehicle are controlled by the forces between tire and road. These forces have an upper limit set by the friction coefficient. Once the ratio between tangential traction and normal pressure exceeds this limit, local sliding occurs. It is important to remember that sliding friction has no preferred direction; once sliding sets in over the whole contact area, directional control is lost. This is the case when the wheels are locked: the vehicle then continues to move in the direction in which its center of mass was moving when the wheels became locked. At first sight this would appear to be the case whenever the circumferential speed of the tire differs from its forward speed, and would indeed be the case if the wheel and track were infinitely stiff. For all elastic wheels, however, the possibility exists that, through deformation of the wheel, only a part of the contact area slides and the remainder maintains contact by adhesion and thus enables a controlled change of direction to take place as well as longitudinal acceleration and braking. Because of the elastic nature of the contact between tire and track, the circumferential speed differs from the forward speed of the wheel whenever a force is acting on the wheel.

3.1.1 Simple slip

The difference between the circumferential and the traveling velocities is specified by the slip s_l which is a vectorial quantity defined as

$$\bar{s}_l = \frac{\vec{v}_f - \vec{v}_c}{|v_c|} \qquad [9]$$

where v_f is the traveling (forward) velocity and v_c is the circumferential velocity of the wheel. The difference between v_f and v_c is called the slip velocity v_s. When the forward velocity makes an angle θ with the plane of the wheel the slip becomes

$$s_l = \sin\theta \qquad [9a]$$

For circumferential slip

$$s_l = 1 - \frac{v_c}{v_f} \qquad [9b]$$

For braking, $v_f > v_c$, s is positive with a maximum value of 1. For acceleration, $v_f < v_c$, s is negative and becomes infinite when the forward speed v_c is zero, i.e. when the driven wheel spins.

Slip can be considered as the ratio of energy that is turned into heat by friction against the road surface to the kinetic energy stored in the mass carried by the wheel. When the wheels are locked, this ratio becomes 1. Under normal braking conditions the slip is smaller than 1 and the kinetic energy of motion is mainly dissipated as heat in the brakes. During cornering also, energy is lost and the forward speed is smaller than the circumferential speed. When accelerating, energy is supplied to increase the forward speed. Hence the negative sign of the slip. If the vehicle cannot gain any kinetic energy because the wheel spins, then the slip becomes infinite.

3.1.2 The relation between the force acting on the wheel and simple slip
When forces are transmitted, slip occurs because the wheel is being deformed. The relation between force and slip is one of the most important laws in tire mechanics, because it influences the all-important properties of traction, durability and – important in the present context – tire wear. (This is not only true for tires but for all forces transmitted by adhesional friction).

Even for a homogeneous elastic wheel the distortion is complex and requires sophisticated methods to arrive at a precise relation between force and slip. For tires this is even more difficult because of their complex internal structure. Nevertheless, even the simplest model produces answers that are reasonably close to reality in describing the force - slip relation in terms of measurable quantities. This model, called the brush model – or often the Schallamach model [25] when it is associated with tire wear and abrasion – is based on the following assumptions:

The wheel consists of a large number of equally-spaced deformable elements, like the fibers of a brush. They project radially outwards and carry the compressive load. Under lateral forces they deform sideways in accordance with a linear elastic relation:

$$f = k_f \cdot y \qquad\qquad [10]$$

where f is the lateral force applied to an element, y is the lateral deformation and k_f is the spring constant of the element. This assumption of linear elasticity has the consequence that no distortion of the wheel occurs outside the contact area.

Consider first the case of cornering, when the wheel runs at a slip angle. Lateral distortion of the wheel creates a force normal to the plane of the wheel referred to as side force or cornering force. In tires it serves to steer the vehicle.

The load on the wheel creates a contact area of finite length a caused by compression of the air within the inflated tire. Note that lateral distortion of the wheel caused by the load is ignored, whereas solid rubber wheels would bulge out. Thus, the above relation for lateral force is really a shear relation. The fibers are assumed to have high compressive stiffness and low shear stiffness, which in fact is a good approximation for rubber.

Within the contact region, as the distance x from the point of contact increases, the lateral deflection increases proportionally. For unit area, the stiffness k is given by $k = n\,k_f$ where n is the number of fibers per unit area. Hence the distorting stress t is given by $t = k\,x\,\tan\theta$. This condition is maintained until a limiting stress, set by the available friction,

is reached. If it is assumed that the pressure distribution along the x-axis is elliptical and the friction coefficient is a constant, sliding occurs along the curve f(μp). A diagrammatic view of this is given in figure 13.22. The total side force is proportional to the area under the curve. A similar diagram is also obtained for the braking or accelerating force, except that in these cases the force acts in the plane of the wheel instead of sideways. The force-slip relation for the brush model is given by

$$S, B, A = \frac{\mu L}{\pi}\left[q + \sin^{-1} q\right] \qquad [11a]$$

where S, B, A stand for either the side-force, braking-force, or accelerating force. μ is the friction coefficient and the function q is given by

$$q = \frac{2c}{1 + c^2} \qquad [11b]$$

where c depends on the type of force considered. For a side force

$$c = \frac{\pi}{8} \cdot \frac{k_s a^2}{\mu L} \cdot \tan\theta \qquad [11c]$$

where L is the applied load, a is the length of the contact area and k_s is the stiffness normal to the plane of the wheel, μ is the friction coefficient and θ is the slip angle, the angle which the plane of the wheel makes with the forward velocity of the wheel.
At small slip angles the force - slip angle relation reduces to

$$S = \frac{k_s a^2}{2} \cdot \theta \qquad [11\ d]$$

This means that at small slip angles the force is independent of load (except for the dependence of the length a of the contact patch on load) and independent of friction coefficient. The slope of the relation between side force and slip angle, termed the cornering stiffness K_s of the wheel, is given by

$$K_s = \frac{k_s a^2}{2} \qquad [11e]$$

Thus, K_s is a measurable quantity.
Similarly for circumferential slip

$$c = \frac{\pi}{8} \cdot \frac{ka^2}{\mu L} \cdot \frac{s_1}{1 - s_1} \qquad [12]$$

which, at small slip s, becomes

$$B, A = \frac{k_c a^2}{2} \cdot s_1 \qquad [12a]$$

where B is the braking force and A is the accelerating force. In this case the slope of the curve at zero slip is given by

$$K_c = \frac{k_c a^2}{2} \qquad [12b]$$

where K_c is the circumferential slip stiffness of the wheel. Note that K_c has a different value from the cornering stiffness, but can also be measured directly.

$F/\mu L$ is plotted as a function of the quantity c in Figure 13.23, together with the adhesion(A) and sliding (B) contributions, making up the total force. Up to a value of c of about 0.82, the adhesion region dominates. At larger values the sliding region becomes more and more important. At large values of c, i.e. at a high stiffness or large slip, or at low friction coefficient or low load L, the force F tends asymptotically to μL.

Figure 13.22: Diagrammatic view of the contact area for the brush wheel model under cornering.
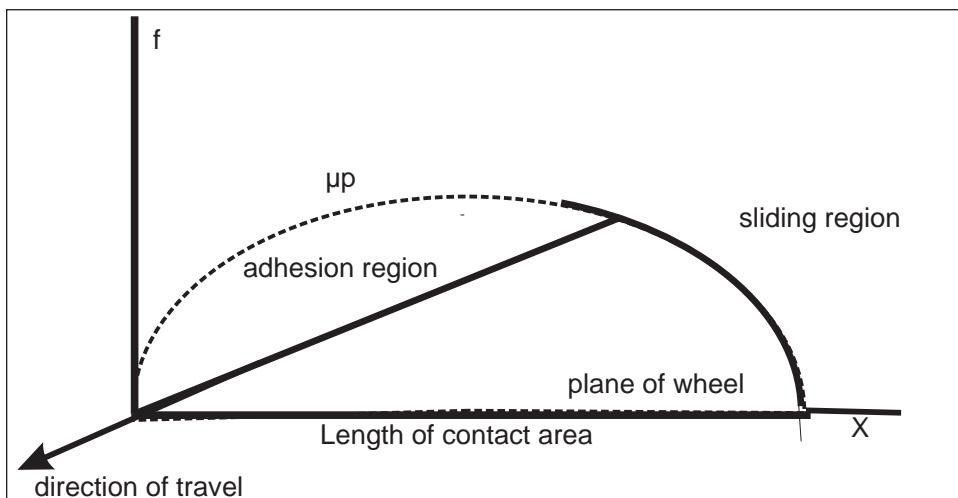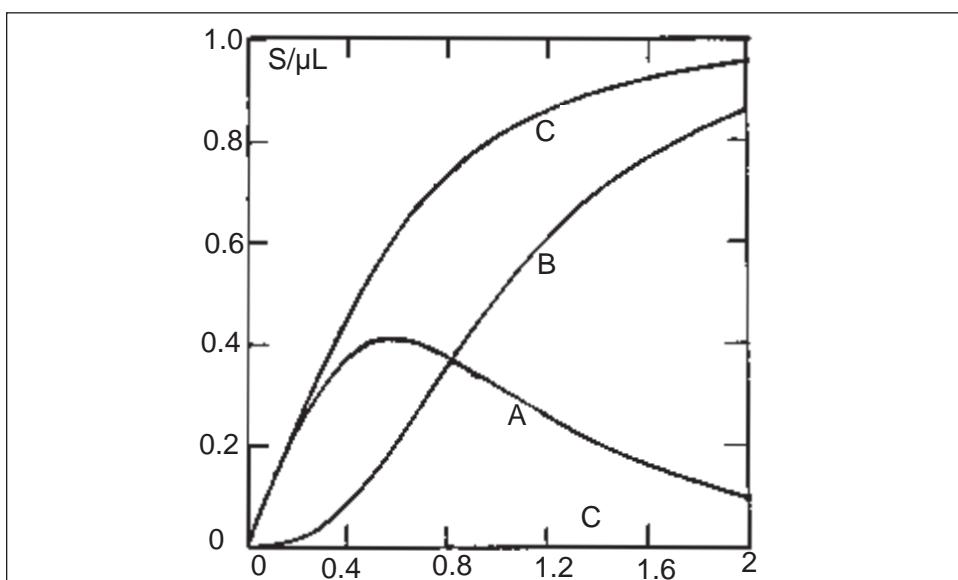
Figure 13.23: Side force coefficient (dimensionless quantity S/μL) as function of the parameter c (Equation 11c) showing the two components due to adhesion and sliding

3.1.3 Self-aligning torque of a cornering wheel according to the brush model
Because the point of action of the side force is not identical with the center of the contact area of the wheel, a torque appears. For moderate slip angles the side force acts behind the center of the contact area. Thus, the torque acts in such a way as to reduce the slip angle. The brush model gives the following relation

$$T = \frac{2}{3}\mu aLq \qquad [13a]$$
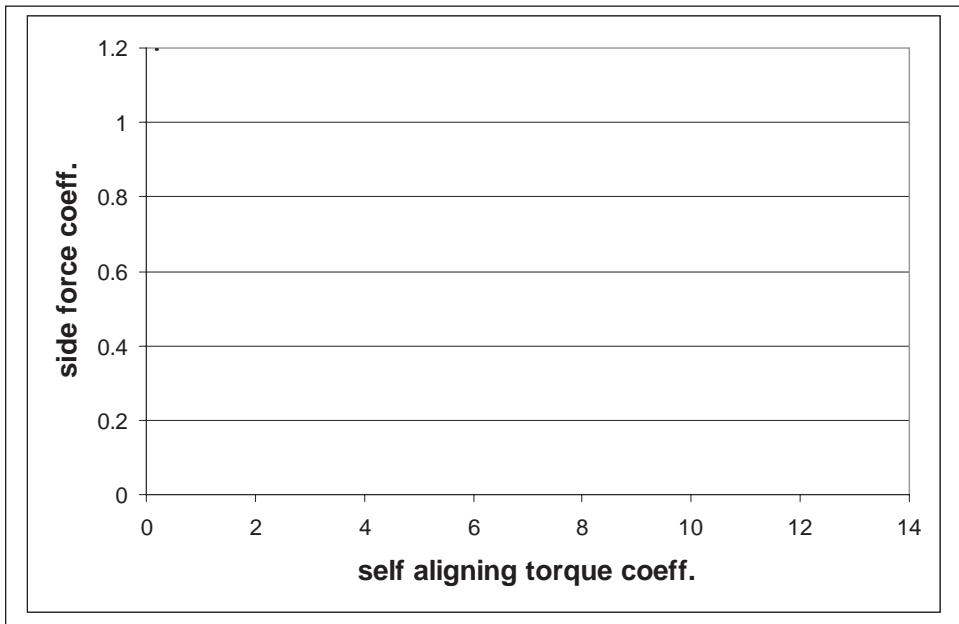
where q is given by equation [11b] and a is the length of the contact area.
At small slip angles the self-aligning torque becomes

$$T = \frac{1}{12}k_s a^3\theta = \frac{1}{6}K_s a\theta \qquad [13b]$$

Thus, the self-aligning torque is proportional to the cornering stiffness, the length of the contact area and the slip angle. It is an important aid to the steering control of a vehicle. A car driver controls the direction of his vehicle as much by sight as by the force on the steering wheel supplied by the self-aligning torque. As long as the side force is proportional to the self-aligning torque the driver feels safe and in control (see figure 13.24). At large slip angles, however, the torque decreases with further increase of side force, misleading the driver. This becomes particularly important when the friction coefficient is low, as is the case on wet roads and even more so on snow and ice.
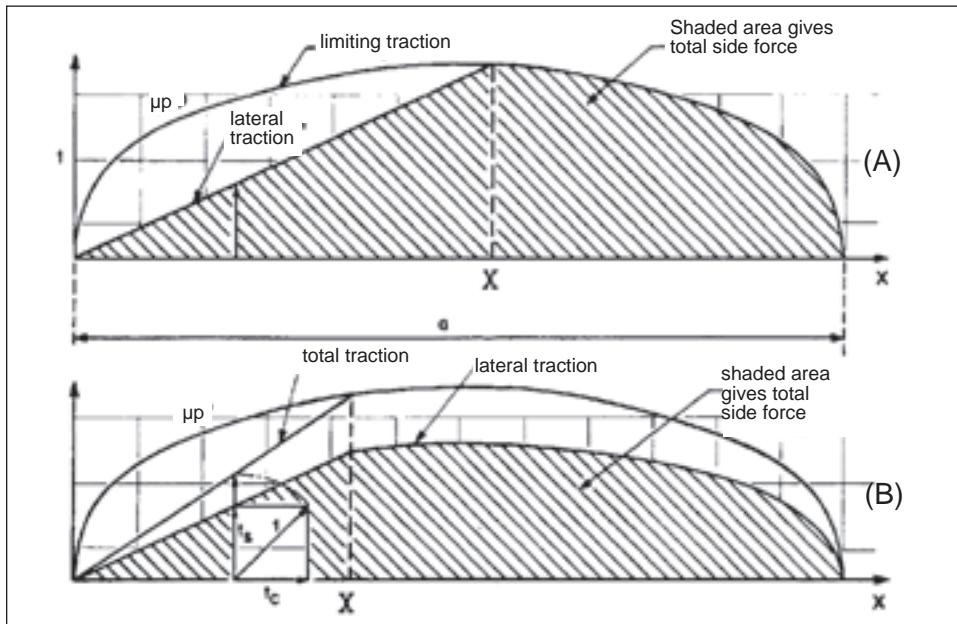
**Figure 13.24: Side force coefficient (S/µL) as a function of
the self-aligning torque coefficient (T/aµL)**

3.1.4 Force - slip relation for composite slip

The brush model can also be used when both lateral slip and in-the-wheel-plane slip components act simultaneously. The limiting force is still determined by the friction coefficient and pressure. The total traction at a point x in the contact area is the vector sum of the two components. This determines the point at which sliding begins and hence the circumferential contribution is the total force less the side force contribution. This is shown diagrammatically in figure 13.25. [7]

Figure 13.25: Diagrammatic view of the combined side- and braking/accelerating force function for the brush wheel model [from ref. 7]

The side force becomes

$$S = \frac{\mu L}{\pi} \cdot \frac{K_s \sin\theta}{\sqrt{(K_s^2 \sin^2\theta + K_c^2 s^2)}} \{\theta_{com} + \sin^{-1} q_{com}\}$$
[14a]

where K_s and K_c are the cornering stiffness and the circumferential slip stiffness respectively and

$$q_{com} = \frac{2\sigma}{1+\sigma^2} \quad \text{and} \quad \sigma = \frac{\pi}{4\mu L} \cdot \frac{\sqrt{(K_s^2 \sin^2\theta + K_c^2 s_{co}^2)}}{\cos\theta - s_{co}}$$

with $s_{co} = 1 - s_l$

The braking and acceleration forces are obtained from

$$B = A = \frac{K_c s_{co}}{K_s \sin\theta} \cdot S$$
[14b]

The model is also capable of explaining the self- aligning torque that occurs during cor-

nering of a braking or accelerating wheel, but this is not of concern when considering abrasion. Abrasion is to be expected whenever energy is being dissipated in the contact area of slipping wheels. The general expression for the energy dissipation W is

$$W = \text{force x slip}$$

For cornering this is given by

$$W_s = S \cdot \sin \theta \qquad [15a]$$

and for circumferential slip

$$W_c = B \cdot s_1 \qquad [15b]$$

The total energy loss in a slipping wheel under composite slip is then the sum of these two components.

3.1.5 Experimental verification of the model

Figure 13.26 shows experimental values for the side force for a bias-ply tire as a function of the variable c for different loads [25, data from 26]. The solid line is the force - slip relation for the brush model. In order to compare the data with the predictions of the theory, the cornering stiffness and the friction coefficient had to be determined. For this, Schallamach calculated the theoretical relation between S/L and tan q. By plotting the values on logarithmic scales, vertical and horizontal shifts brought the calculated curve into coincidence with experimental measurements and thus he obtained values for the friction coefficient and the cornering stiffness.

Figure 13.26: Side force coefficient as function of c (equation [11c]) for a bias tire for different loads. The solid line is from the brush model [ref. 25, data from ref. 26]
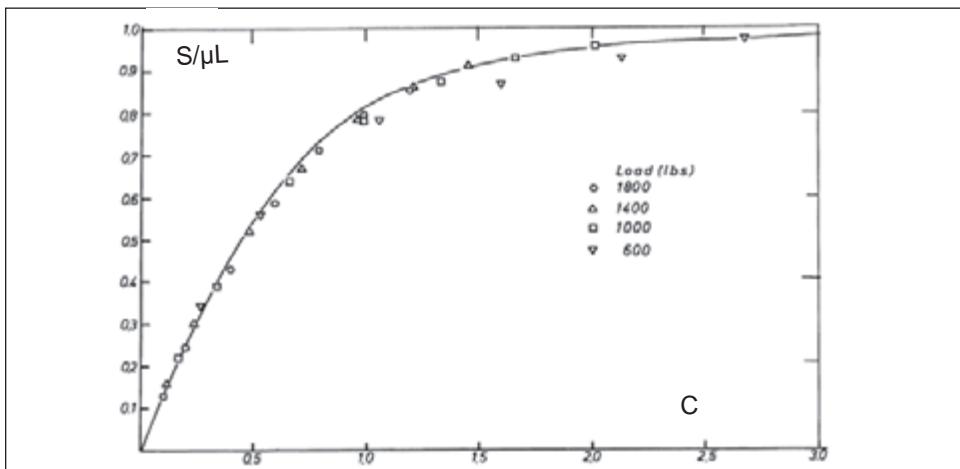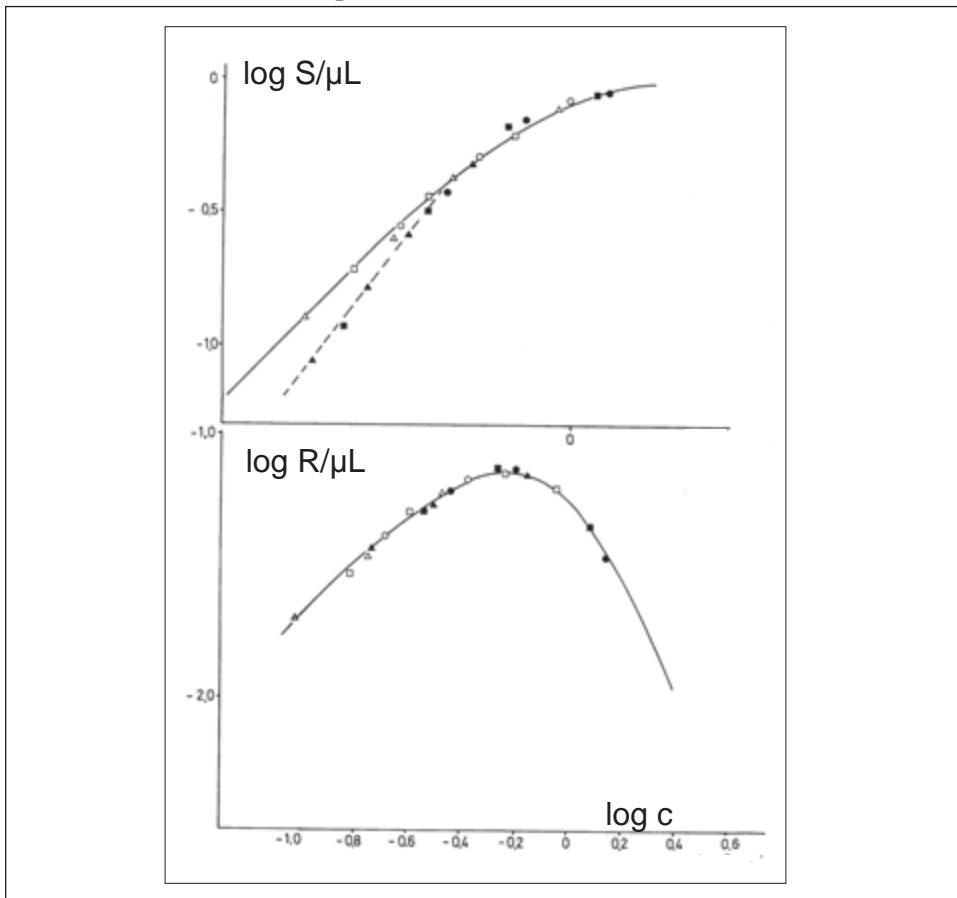
Figure 13.27 shows results for a radial ply tire, obtained using a trailer equipped with a force-measuring hub. Different load and slip angle settings were used on two different wet road surfaces to give different friction coefficients. The self-aligning torque is also shown. At low friction coefficients the experimental data for the side force deviate from the model, but otherwise the agreement is very satisfactory.

Figure 13.27: Side force coefficient and self aligning torque of a radial ply tire 175 R14 on two wet road surfaces of different friction coefficient, at three slip angles and loads as a function of the parameter c (equation [11c]) all on log scales. The solid lines correspond to the brush model [from ref. 7]

Finally, side force measurements were carried out at different slip angles on a laboratory abrasion tester at constant load and speed. The results are shown in figure 13.28. The cornering stiffness and friction coefficient were obtained by a curve fitting method using a computer program. Since the sample runs on the flat side of a circular disk, the side force is not exactly zero when the slip angle is zero. The program also determined the deviation from zero. The calculated curve agreed excellently with the data.

A similar diagram was obtained for different loads as shown in figure 13.29. In this case the friction coefficient depended on the load according to the relation

$$\mu = \mu_o \left[\frac{L}{L_o} \right]^{-0.1} \qquad\qquad [16]$$

After adjusting for this effect, all data could be fitted to the tire model curve. Thus, good agreement is reached in all cases with the simple brush model. It is very useful for describing the relation between force and slip using measurable properties of the tire: cor-

nering stiffness, longitudinal slip stiffness, and friction coefficient. But, as it stands, it is of little use to the tire construction engineer since it does not predict the important quantities: tire stiffnesses and friction coefficient.

Figure 13.28: Side force coefficient S/L as function of slip angle at a constant load for a tire tread compound measured in the laboratory on an LAT 100 abrasion tester. Surface: alumina 60. Speed: 6 km/h. Load: 75 N
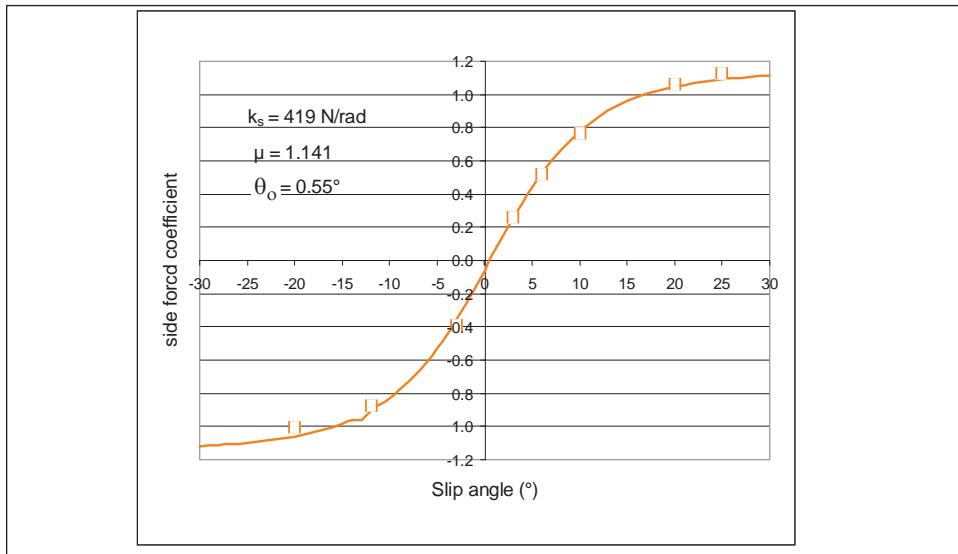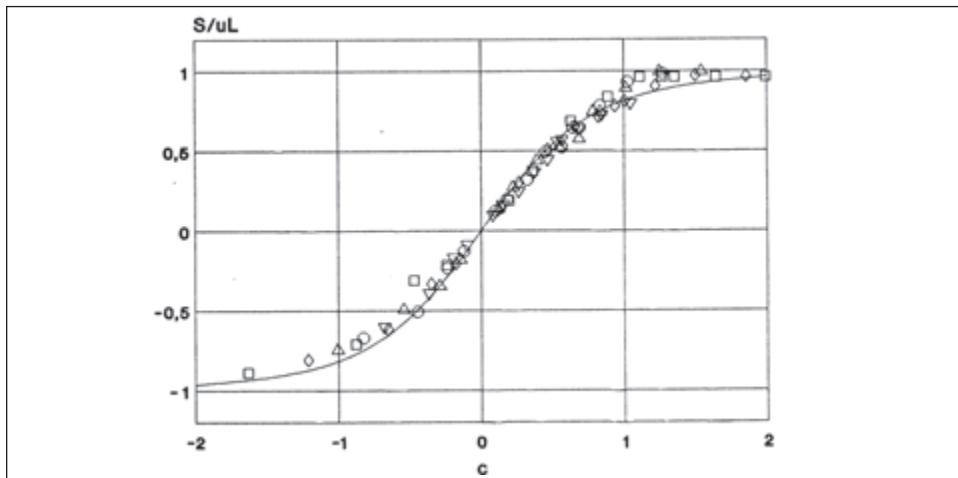
Figure 13.29: Side force coefficient S/L as a function of slip angle for different loads. To fit the brush model relation the friction coefficient was adjusted for load dependence using $\mu = \mu' L^{-0.1}$. Surface: Alumina 180. Speed: 2 km/h.

3.2 Abrasion as a function of slip and load

Abrasion under limited slip used to be, and to some extent still is, measured either with the standard Akron abrader or the Lambourn abrader. In the Akron abrader the sample wheel runs under a given slip angle against the abrasive surface of an alumina grindstone. Speed and load are fixed; the side force is not measured.
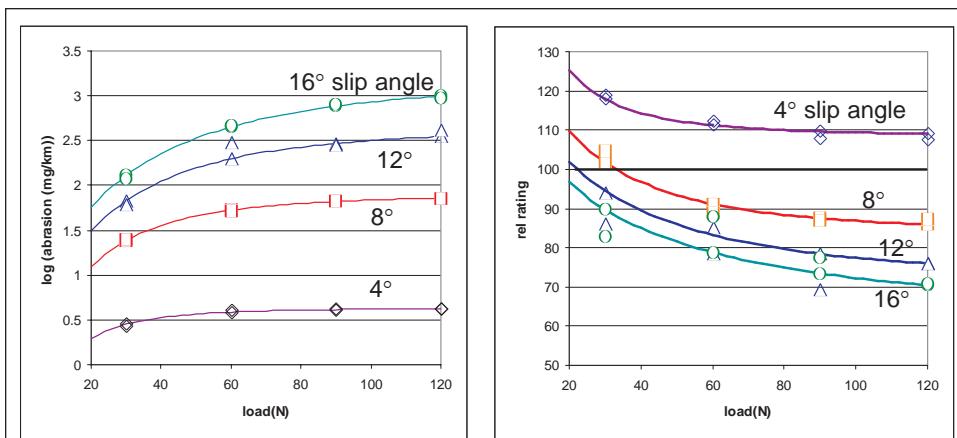
The author [28, 29] developed an extension of the Akron abrader principle by incorporating the following features:

- measuring the side force
- varying the slip angle over a wide range from – 40° to + 40°
- permitting a speed range from 2 km/h to 100 km/h, although the maximum speed is not usually required for abrasion measurements except perhaps for research purposes
- providing a continuous range of loads from 10 to 150 N
- employing abrasive surfaces of different grain size and sharpness
- allowing measurements at elevated surface temperatures between the dew point and 70°C.

The advantage of such a test arrangement is the very wide range of speeds and severities (load and slip angle) that can be covered, as well as the possibility of using a considerable range of abrasive surfaces. The instrument is now available commercially as a fully automatic device (except for mounting the sample), with multiple testing stations, and it also permits making friction measurements on wet and icy surfaces. Most of the following data were obtained using this instrument.

Figure 13.30 shows the abrasion loss of an OE-SBR tread compound as function of load for different slip angles on a sharp alumina 60 surface. Because of the wide range of abrasion rates they are plotted on a log scale. It is seen that at small slip angles the dependence on load is small – it becomes more pronounced as the slip angle is increased. This is expected from the brush model. At small slip angles the side force is largely independent of the load and hence it is expected that the abrasion loss will also be constant.
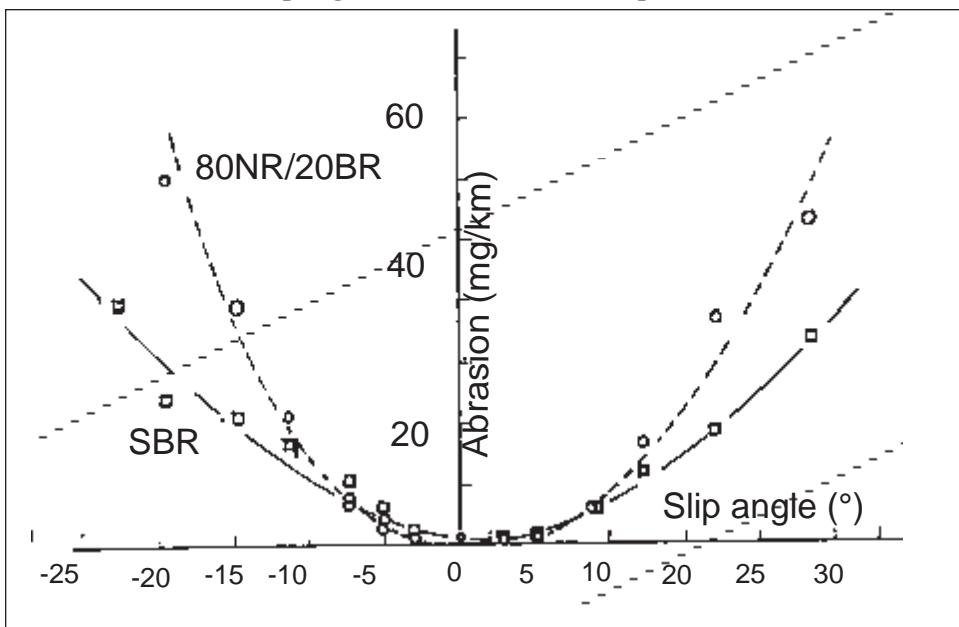
Figure 13.30: Log(abrasion) of an OESBR and an NR tire tread compound as a function of load at different slip angles at a speed of 19.2 km/h. Left: Abrasion loss of the OESBR compound as a function of load. Right: Wear resistance rating of NR relative to OESBR as a function of load for different slip angles.

   Also shown is the relative rating between an OE-SBR compound and an NR + carbon black tire tread compound. At the smallest slip angle the rating of the NR compound is better than the OE-SBR compound but the rating of the NR compound decreased with increasing load. As the slip angle is increased the ratings are reversed.

   Figure 13.31 shows the abrasion loss as a function of slip angle for an OE-SBR tread compound and an 80NR/20 BR compound, measured at constant load. Clearly the abrasion depends very strongly on the slip condition. Careful examination of the graph shows that the abrasion loss for the NR/BR blend is higher at large slip angles but it becomes lower at low slip angles. This is more apparent when the data are plotted on log scales, see figure 13.32. Straight-line graphs are obtained with slightly different slopes for the NR compound and the SBR compound. Plotting the relative rating of the NR compound with respect to the OE-SBR compound as a function of log slip angle shows that the small difference between the slopes is, in fact, highly significant when considering the relative rating, i.e. in a practical comparison of the two compounds.
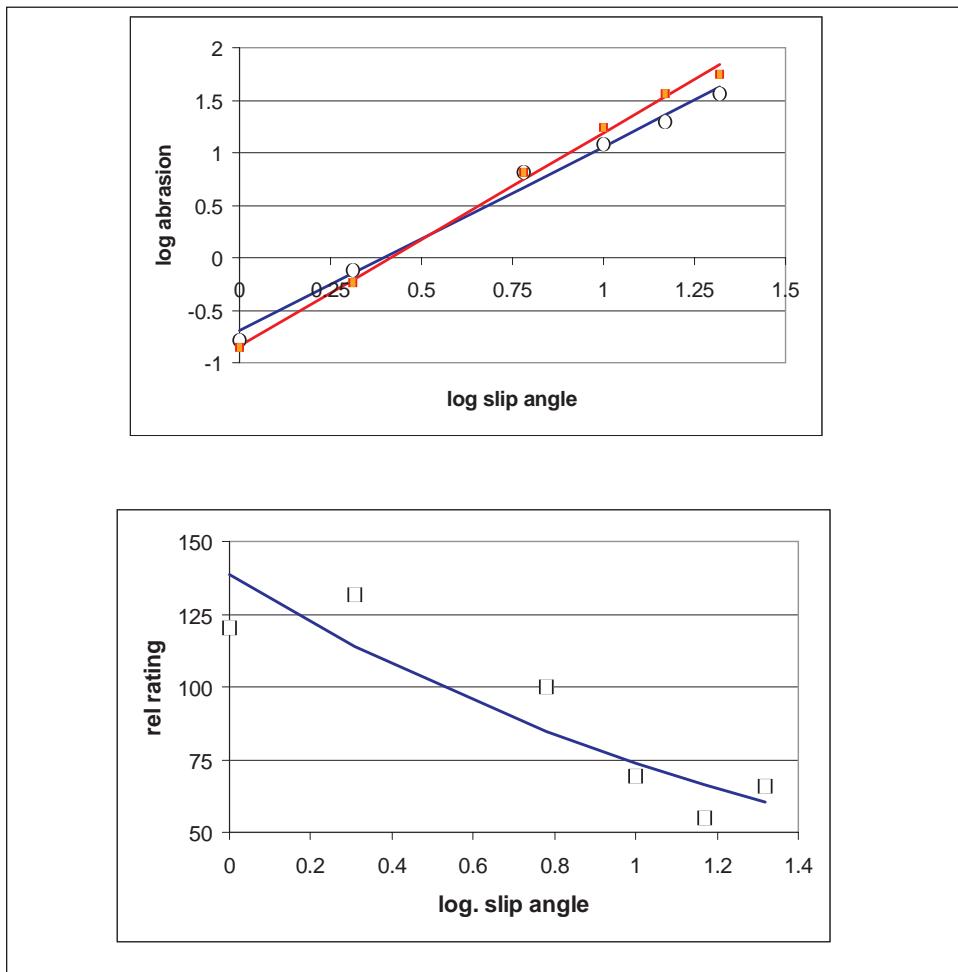
Figure 13.31: Abrasion of OESBR and an 80 NR/20 BR blend tire compound as a function of slip angle at a load of 76 N and a speed of 19.2 km/h

   Both load and slip angle can be combined if the abrasion is treated as a function of the energy dissipated, as already discussed in some detail in the section on sliding abrasion. If the side force is measured and the slip angle is known the data can be evaluated directly as a function of energy. A comparison is shown in figure 13.33 between NR and SBR abraded against a sharp alumina 60 and a blunted alumina 180 surface [30]. Again, straight line graphs are obtained if the two variables are plotted on logarithmic scales. The lines are seen to cross over at low energy levels for both compounds and for both abrading surfaces. The slopes of the lines and the intercepts (the average absolute abrasion loss) differ considerably for the two surfaces. Moreover, the slopes are larger than 1, indicat-

ing that the process is more related to a fatigue failure by crack growth than to a direct tearing process. This is particularly so for the blunt surface. Although the abrasion loss is distinctly lower on the blunt surface at low energies, the slopes of the lines are much higher and the lines eventually cross so that the abrasion losses at high energies are higher on the blunt surface.
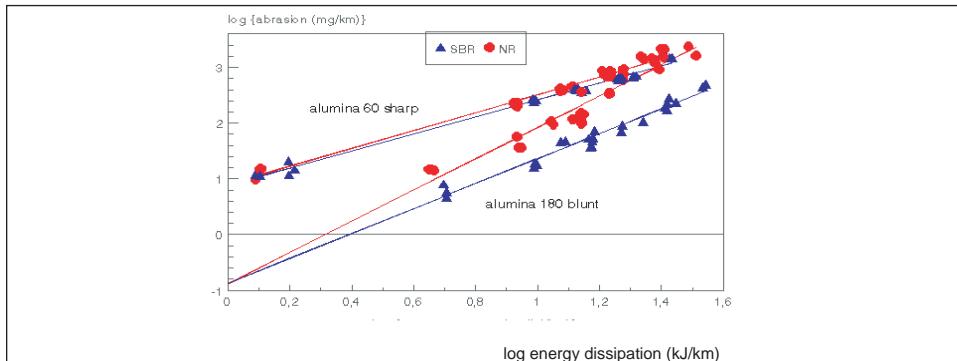
Figure 13.32: The abrasion data of figure 31 plotted on logarithmic scales and the rating of the NR/BR blend relative to OESBR as a function of log slip angle

The difference in the slopes for NR and SBR is also larger on the blunt surface than on the sharp one. In fact, this difference is much larger than would be expected from observations of tire wear, suggesting that road surfaces are not blunt but act rather like a sharp abrading surface.

Figure 13.33: Log (abrasion) for two tread compounds NR + black and SBR + black on two surfaces of different sharpness: alumina 60 and alumina 180 (blunt) as a function of log (energy dissipation) [from ref. 31]

3.3 Effect of speed on the abrasion of slipping wheels

If experiments are carried out as a function of energy dissipation (slip angle and/or load) at different speeds and the data plotted on log scales, straight-line graphs are obtained again, but they have different slopes [5] (figure 13.34). This is not easily explained if abrasion is assumed to be a purely mechanical cut growth process. We conclude that, in general, abrasion is a function of several variables acting simultaneously. As energy dissipation in the contact area increases, the surface temperature will rise since a considerable portion of the input energy is turned into heat. This effect is also a function of speed. The rubber surface may change as a result of heating, and the dynamic strength of rubber is a function of temperature. Abrasion will be affected, possibly through changes in cut growth resistance. Figure 13.35 shows the abrasion losses of three tire tread compounds as functions of speed, plotted on logarithmic scales [31]. Although the effects are much smaller than that of the energy dissipated, and hence the scatter is larger, clear differences are seen between the compounds. Empirically, the data are consistent with a straight-line dependence. Because the effects are small a large number of measurements would be needed to demonstrate any significant deviation from linearity.

Figure 13.34: Log (abrasion) as a function of log (energy dissipation) for a commercial tire tread compound at three different speeds. Surface: alumina 60
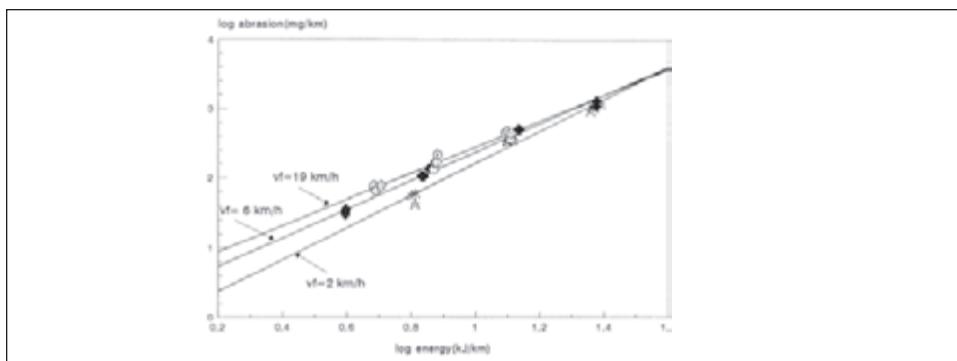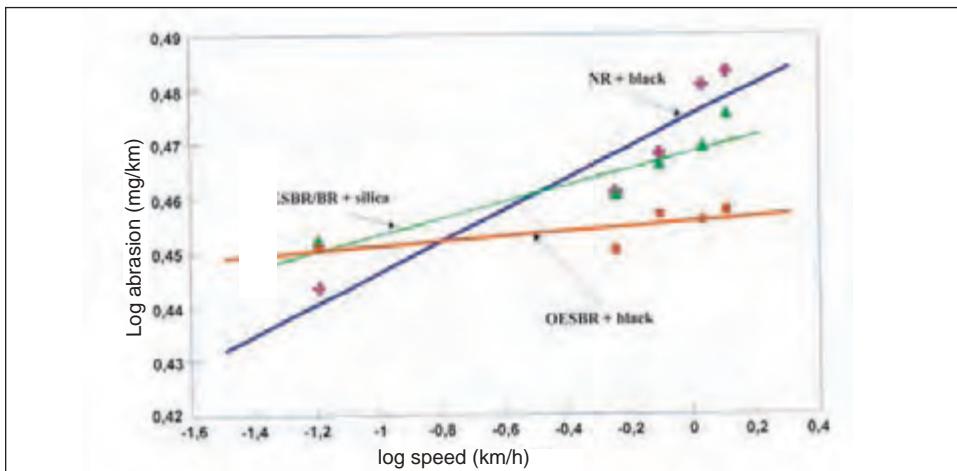
Figure 13.35: Log (abrasion) as a function of log (speed) for three different tire tread compounds [from ref. 31]. Load: 76 N. Slip angle: 14.6°. Surface: alumina 60

Abrasion rises with increasing speed but the slope of the line is considerably different for the three compounds. The SBR compound has the smallest dependence on speed and the NR compound the largest. This is most easily explained if it is assumed that the temperature in the contact area rises with speed and that both speed and temperature together er influence the abrasion. In this temperature range it would be expected that the rate of abrasion rises with increasing temperature, from considerations of both loss in strength and thermo-oxidative degradation, whilst it would be expected to fall with increasing speed if the temperature could be kept constant, because of viscoelastic strengthening. Clearly the thermo-oxidative effect outweighs the viscoelastic effect. This is in accord with the finding that the effect of speed is much smaller for SBR than for NR. The SBR/BR blend filled with silica lies between the two. However, the present author does not know of any measurements of the thermal and oxidative resistance and the visco-elastic properties for this type of compound, for comparison with abrasion rates.

3.4 Temperature in the contact area of a tire

Few experiments have been carried out to determine the temperature rise in the contact area between rubber and a hard slider. Schallamach rubbed a thermo-couple over a rubber pad at different loads and measured considerable rises in temperature. The author used a thick rubber strip glued to a tire-testing drum with a thermo-couple embedded in a small spherical slider to which different loads could be applied. Figure 13.36 shows the temperature rise in the contact area as a function of speed [32]. It is seen that the temperature rises rapidly with increasing speed, reaching values of over 300 °C. The curves can be described exactly by a simple relation

$$Temperature - rise = const \cdot \sqrt{v_s} \qquad\qquad [17]$$

where v_s is the sliding speed. The constant contains the strength and dimensions of the heat source and the thermal conductivity [33]. Note that the rubber does not burn, although its ignition temperature has been exceeded. This is because the temperature

decreases rapidly as soon as it leaves the contact area. Because the heat conductivity of rubber is low the temperature also decreases rapidly with increasing depth.

Figure 13.36: Temperature rise in the contact area of a small steel indentor as a function of speed. (a) Cone, tip radius 1 mm (b) Sphere, 11 mm dia. Load on both: 2.5 N.
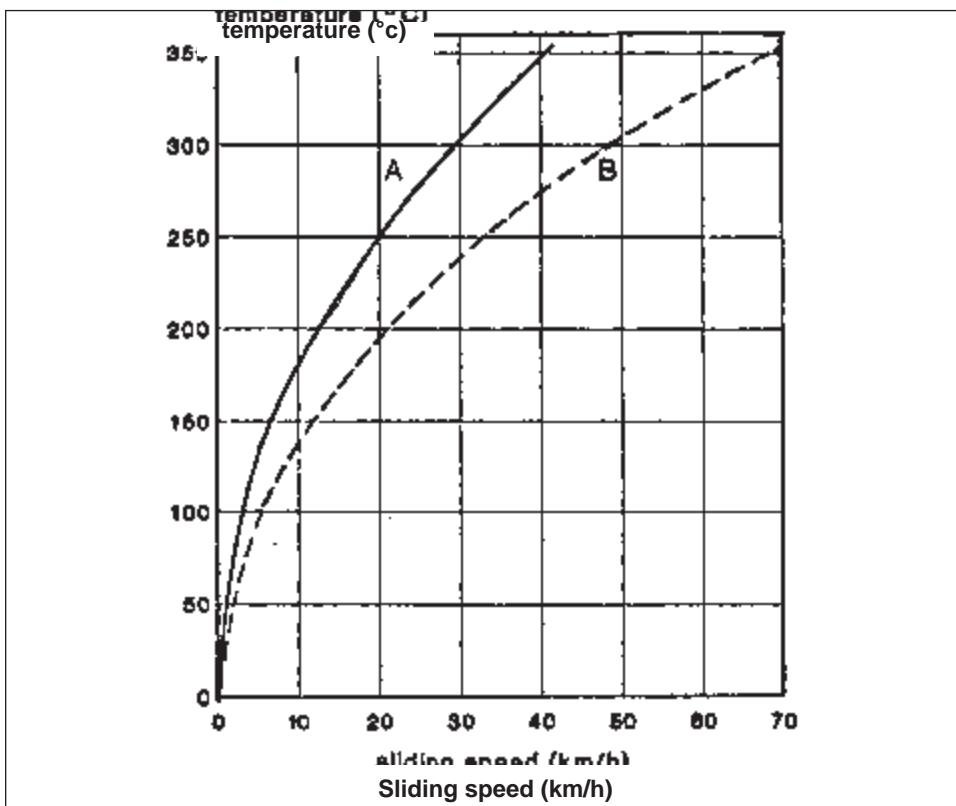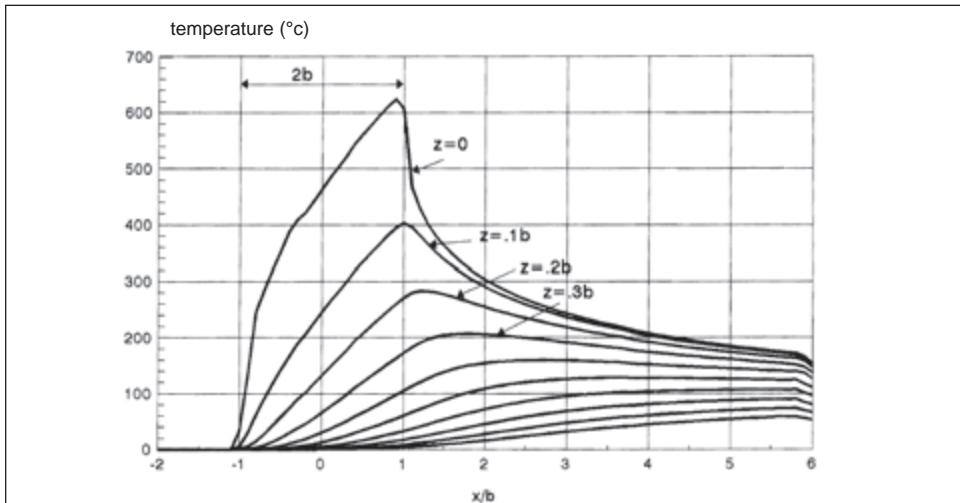
Figure 13.37 shows a theoretical calculation of the temperature rise of a rectangular pad sliding under a constant load and speed over a semi-infinite rubber block [33]. The figure shows the temperature profile along the pad in the sliding direction. Heat losses towards the sides have been neglected. The maximum temperature occurs near the rear of the pad and decays rapidly after the pad has passed. The temperature in the interface is, of course, the same for the slider and the rubber surface. It is determined by the heat conductivities of the two materials and their specific heat capacities. Roberts [34] measured the decay of the surface temperature after a slider had passed over it. This agreed well with the theoretical calculations. There can therefore be no doubt that a considerable temperature rise occurs in the contact area between a sliding rubber sample and an abrasive track. Thus the abrasion process must be considered as a form of mechanical-oxidative crack growth at elevated temperatures. These considerations explain why a crossover may occur between rates of abrasion on sharp and blunt surfaces, which could not be accounted for if abrasion was due purely to crack growth at a constant temperature.

On rough surfaces the contact time between an asperity and the rubber is generally very short and hence the temperature rise is small. However, since the next asperity arrives before the temperature rise has died away the temperature continues to rise.

**Figure 13.37: Theoretical temperature rise in the contact area of a
pad sliding over a semi-infinite solid at different depths from the surface.
Width (2b) = 2mm; speed = 3 m/s; pressure = 2 Mpa; μ=1.
Heat conductivity: 0.15 W/m/°K. Heat diffusivity: 10^{-4} m^2/s**

3.5 Combining the energy dependence and speed dependence of abrasion
Since plots of abrasion rate against both sliding energy and sliding speed give straight-line graphs when the variables are plotted on logarithmic scales these quantities may be summed. However, in order to allow for the fact that the slope of the plot of log abrasion vs. log energy depends on speed, and vice versa, a further term must be included. The simplest way is to introduce the product of the two variables log (speed) and log (energy), giving the following equation:

$$[\log(A)] = a + b_1[\log(W)] + b_2[\log(v)] + b_3[\log(W) \cdot \log(v)] \qquad [18]$$

where A is the abrasion volume loss per km, W is the energy dissipation per km and v is the forward speed of the abrasive disk in the contact area relative to the sample wheel.

In order to determine the coefficients of this equation, at least four different testing conditions are required: two energy levels, given by two combinations of slip angle and load, and two speeds. The slip can be circumferential instead of at a slip angle – the important point is that the resulting slip force is measured in order to obtain a measure of the energy dissipation. In practice more test conditions are useful, say three energy and three speed levels and for each condition repeat measurements are advisable because abrasion is always subject to variation. The four coefficients are then calculated from the abrasion results using the statistical method of least square deviations from the mean [31, 35]. Table 13.2 shows the coefficients obtained in this way for four passenger tire tread com-

pounds. The coefficient a gives the expected abrasion loss at an energy dissipation of 1 kJ/km and a speed of 1 km/h. The coefficient b_1 is the power index for the abrasion-energy relation at constant speed and temperature. It is positive and larger than 1 for all compounds indicating that a cut-growth process is dominant. However, it is smaller than would be expected purely from cut-growth results but larger than from simple tearing. The coefficient b_2 is related to the abrasion-speed relation at constant energy and temperature. It is negative, showing that at a constant temperature the rate of abrasion would decrease with increasing speed, emphasizing the visco-elastic nature of abrasion resistance. The coefficient b_3 is positive and can be taken as the effect of temperature due to both energy and speed.

Table 13.2: Coefficients of the abrasion equation [18] for four passenger tire tread compounds together with the correlation coefficient between calculated and measured data.
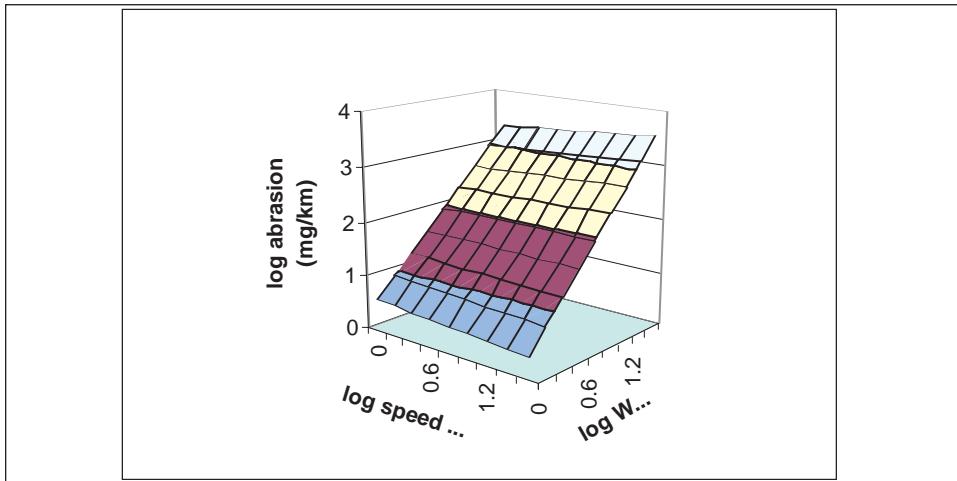
		Coefficients			Correlation
Compound	a	b1	b2	b3	r
OESBR	0.683	1.640	-0.339	0.223	0.994
pol blend+silica l	0.583	1.706	-0.115	0.152	0.996
pol blend+ silica ll	0.908	1.502	-0.465	0.388	0.994
NR+black	0.690	1.636	-0.345	0.871	0.995

These coefficients can be used to calculate the best estimate of abrasion loss over a wide range of energy and speed levels on the particular surface on which they were obtained. Figure 13.38 shows a program of testing conditions designed to cover a wide field of severities. The range suggested for log energy and log speed, from 0 to 1.6 respectively, has proved to be very useful. To fill it, some extrapolation from actual data is required, which has to be carried out with some care. To extend the experimental conditions down to the left upper corner of the table is not practicable because under these very mild conditions a long time would be required to obtain a measurable abrasion loss and the results would be rather variable as environmental fluctuations become important. The four conditions at the corners of the test scheme are mandatory. Two further conditions at moderate speed and energy are desirable because they support the mildest condition, which takes the longest time and is subject to the largest variations. A complete program using nine conditions gives very reliable results.

Figure 13.38: Proposed testing scheme for evaluating the coefficient of the abrasion equation [18]

					speed (km/h				
energy	log	1.00	1.58	2 51	3.98	6.31	10.00	15.85	25.12	39.81
(kJ/km)	energy	0	0.2	0.4	0.6	0.8	1	1.2	1,4	1.6
1.00	0									
1.58	0.2									
2.51	0.4									
3.98	0.6									
6.31	0.8									
10.00	1									
15.85	1.2									
25.12	1.4									
39.81	1.6									

Abrasion loss as log(abrasion) vs. log(energy) and log(speed) is best presented either in tabular form, figure 13.38, or as a three dimensional graph [30], as shown in figure 13.39. Notice that the rate of abrasion between the mildest condition (upper left) and the most severe condition (lower right) differs by a factor of about 1000.

Figure 13.39: Log abrasion as a function of log (energy) and log (speed) for a tire tread compound.
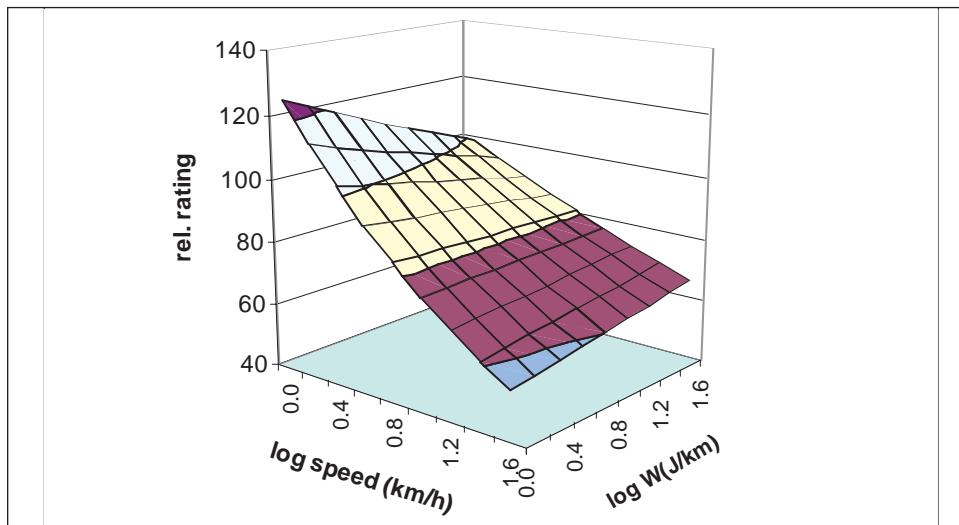
More important for practical use is the relative rating of an experimental compound with respect to a standard reference compound, usually a well-proven compound for which a substantial set of road data are available. The relative rating is defined as

$$\text{rel. rating} = \frac{\text{abrasion of standard compound}}{\text{abrasion of experimental comp.}} \cdot 100 \qquad [19]$$

Note that there is no single rating because the value depends on the severity of the test. In fact, reversals in ranking occur. An example is shown in figure 13.40 as a three dimensional diagram. This compound (Compound 2 of table 13.2 compared to Compound 1) is better than the control at low speeds and low energies. In this case the presentation of the ratings in a table is more useful because it gives a detailed quantitative view of the behavior of each compound. Table 13.3 shows the ratings for Compound 2 and Compound 4 for which the abrasion coefficients are listed in table 13.2, using Compound 1 as the reference. Both compounds show reversals in ranking with changes in severity. This agrees closely with road wear experience. The upper compound (Compound 2) is better at low energies and speeds than the reference and is known to be better under driving conditions typical for the USA, i.e. under speed restrictions and on long straight roads that lead to low and moderate rates of abrasion. Under European traffic conditions this type of compound is appreciated for its high wet grip but it is also known to be somewhat inferior in wear resistance compared to the reference.

**Figure 13.40: Rating of compound 2 relative to compound 1 of table 13.2
as a function of log (energy) and log (speed)**

The NR compound is known to be better under low temperature conditions than the control but worse under high temperature conditions. Chemically, NR has the lowest thermal stability of the elastomers used for tread compounds in tire technology and it has therefore the highest temperature dependence of abrasion and wear. Thus, it is generally accepted that NR has better wear resistance in a moderate climate than, for instance, SBR but is much worse in hot climates. This will be thoroughly documented below under tire wear.

In table 13.3, NR was better whenever the sample surface temperature was near room temperature, i.e. at low speeds for all energies and at low energies for all speeds. When both energy and speed were raised the sample surface temperature rose considerably and the rating of the NR decreased correspondingly.

**Table 13.3a: Ratings of compound 2 relative to compound 1 of
table 13.2 as a function of log (energy) and log (speed)**

SBR/BR+SI vs. OESBR black									
log energy					log speed (km/h)				
	0.0	0.2	0.4	0.6	0.8	1.0	1.2	1.4	1.6
0.0		113.6	102.4	92.4	83.3	75.2	67.8	61.2	55.2
0.2	122.1	110.9	100.7	91.4	83.0	75.3	68.4	62.1	56.4
0.4	118.5	108.3	98.9	90.4	82.6	75.5	69.0	63.1	57.6
0.6	114.9	105.7	97.2	89.4	82.3	75.7	69.6	64.0	58.9
0.8	111.5	103.2	95.6	88.5	81.9	75.9	70.2	65.0	60.2
1.0	108.1	100.8	93.9	87.5	81.6	76.0	70.9	66.0	61.5
1.2	104.9	98.4	92.3	86.6	81.2	76.2	71.5	67.1	62.9
1.4	101.8	96.1	90.7	85.7	80.9	76.4	72.1	68.1	64.3
1.6	98.7	93.8	89.2	84.8	80.6	76.6	72.8	69.2	65.7

**Table 13.3b: Ratings of compound 4 relative to compound 1 of table 13.2
as a function of log (energy) and log (speed) (continued)**

NR+ black vs. OESBR+black

log energy					log speed (km/h)				
	0.0	0.2	0.4	0.6	0.8	1.0	1.2	1.4	1.6
0.0	**113.2**	**113.6**	**113.9**	**114.2**	**114.5**	**114.8**	**115.1**	**115.5**	**115.8**
0.2	**113.4**	**111.2**	**109.0**	**106.8**	**104.7**	**102.6**	**100.6**	98.6	96.6
0.4	**113.7**	**108.9**	**104.3**	99.9	95.7	91.7	87.9	84.2	80.6
0.6	**113.9**	**106.6**	99.8	93.5	87.5	82.0	76.7	71.9	67.3
0.8	**114.1**	**104.4**	95.6	87.5	80.0	73.2	67.0	61.4	56.2
1.0	**114.3**	**102.2**	91.5	81.8	73.2	65.5	58.6	52.4	46.9
1.2	**114.5**	**100.1**	87.5	76.5	66.9	58.5	51.2	44.7	39.1
1.4	**114.7**	98.0	83.8	71.6	61.2	52.3	44.7	38.2	32.6
1.6	**114.9**	96.0	80.2	67.0	55.9	46.7	39.0	32.6	27.2

A further example is shown in table 13.4. This gives the laboratory rating as a function of log energy and log speed for four passenger tire tread compounds for which road test ratings were available. They are shown on the left of each table. For compound 1, practically all the laboratory ratings were less than 100 and in the tire road test the compound was also distinctly poorer than the control. Compound 3 was slightly better than the control but the ratings were higher under some conditions and lower under others. Hence, it is not certain whether the compound is better in general, under a variety of service conditions. On the other hand, compound 4 was much better than the control under most testing conditions and this is reflected in the high road test rating. Note that the compound developer gets a much broader view of the wear potential of a compound with this, admittedly more time consuming, laboratory abrasion method than with a single point test result.

The cells marked in red in the laboratory abrasion table show by inspection only two testing conditions for which a high correlation exists between road ratings and a single laboratory abrasion test condition (speed, slip and load). It would have been very difficult to pick one of these laboratory test conditions without any background knowledge. Moreover they are only applicable to the particular road test; if the road test conditions change, then the relevant laboratory test conditions also change.

By using regression analysis between the road test ratings and the ratings obtained for any one cell, i.e. for any particular testing condition, the correlation coefficient, the regression coefficient and the intercept of a linear regression equation can be calculated for each cell, i.e. for each laboratory condition.

This is shown in table 13.5 for the data of table 13.4. If the criterion is used that the regression coefficient should be nearly 1 and the intercept nearly zero, besides a high correlation coefficient, the two best testing conditions differ slightly from those obtained by inspection. The range over which the correlation coefficient is high is quite large, but for a perfect 1:1 correlation it is very limited.

Similar data were also obtained for truck tire compounds during an extensive sur-

Table 13.4: Relative ratings of four passenger commercial tire tread compounds for which road test ratings were available as functions of log (energy) and log (speed)

road test rating		laboratory evaluation								
		compound 1								
					log vf					
	log W	0	0.2	0.4	0.6	0.8	1	1.2	1.4	1.6
	0	51.8	57.5	63.8	70.7	78.5	87.1	96.7	107.3	119.0
	0.2	58.9	63.2	67.9	73.0	78.4	84.3	90.6	97.3	104.6
	0.4	66.9	69.6	72.4	75.4	78.4	81.6	84.9	88.3	91.9
87	0.6	76.0	76.6	77.2	77.8	78.3	78.9	79.5	80.1	80.7
	0.8	86.4	84.3	82.3	80.3	78.3	76.4	74.5	72.7	70.9
	1	98.3	92.8	87.7	82.8	78.2	73.9	69.8	66.0	62.3
	1.2	111.7	102.2	93.5	85.5	78.2	71.5	65.4	59.9	54.8
	1.4	127.0	112.5	99.6	88.2	78.1	69.2	61.3	54.3	48.1
	1.6	144.3	123.8	106.2	91.1	78.1	67.0	57.5	49.3	42.3
100		compound 2 = control =100								
		compound 3								
					log v					
	log W	0	0.2	0.4	0.6	0.8	1	1.2	1.4	1.6
	0	91.9	105.0	120.1	137.3	157.0	179.5	205.2	234.7	268.3
	0.2	97.9	106.7	116.3	126.7	138.1	150.4	163.9	178.6	194.6
	0.4	104.4	108.4	112.6	116.9	121.4	126.1	130.9	135.9	141.1
107	0.6	111.3	110.2	109.0	107.9	106.8	105.6	104.5	103.5	102.4
	0.8	118.7	111.9	105.6	99.5	93.9	88.5	83.5	78.7	74.2
	1	126.6	113.7	102.2	91.9	82.6	74.2	66.7	59.9	53.9
	1.2	134.9	115.6	99.0	84.8	72.6	62.2	53.2	45.6	39.1
	1.4	143.9	117.4	95.8	78.2	63.8	52.1	42.5	34.7	28.3
	1.6	153.4	119.3	92.8	72.2	56.1	43.7	34.0	26.4	20.5
		compound 4								
					log v					
	log W	0	0.2	0.4	0.6	0.8	1	1.2	1.4	1.6
	0	68.1	88.0	113.7	147.0	190.0	245.5	317.3	410.1	530.0
	0.2	75.1	92.5	114.0	140.4	172.8	212.9	262.2	322.8	397.6
	0.4	82.9	97.3	114.2	134.0	157.3	184.6	216.6	254.2	298.3
170	0.6	91.5	102.3	114.4	127.9	143.1	160.0	178.9	200.1	223.8
	0.8	101.0	107.6	114.6	122.2	130.2	138.7	147.8	157.5	167.9
	1	111.4	113.1	114.9	116.6	118.4	120.3	122.1	124.0	125.9
	1.2	122.9	118.9	115.1	111.4	107.8	104.3	100.9	97.6	94.5
	1.4	135.6	125.1	115.3	106.3	98.0	90.4	83.4	76.9	70.9
	1.6	149.7	131.5	115.5	101.5	89.2	78.4	68.9	60.5	53.2

vey by the European Union of the durability and wear of re-treaded tires. An abrasion program carried out with three compounds using different polymer blends with the same carbon black gave a high correlation with road test ratings on driven axles for different use at high energy levels. Two such correlations are shown in figure 13.41. For seven compounds containing different types of filler with the same polymer formulation (80 SBR/20 NR) the correlation between road wear and laboratory ratings was narrower as shown in figure 13.42. Notice that the regression coefficient was only about 0.5. This means that the laboratory experiments were twice as discriminating between compounds as the road wear data.

The laboratory data were obtained on an alumina abrasive track. The question arises as to the degree to which this surface corresponds to real road surfaces.

Table 13.5: Correlation, regression coefficient, and intercept of linear relations between the road test ratings from table 13.4 and the laboratory ratings obtained for each cell.

	log U	0.2	0.4	0.6	log v 0.8	1	1.2	1.4	1.6
correlation coefficent	0.2	0.283	0.623	0.824	0.911	0.949	0.968	0.673	0.978
	0.4	0.354	0.678	0.866	0.947	0.978	0.990	0.993	0.993
	0.6	0.444	0.746	0.906	0.970	0.983	0.999	0.998	0.996
	0.8	0.564	0.829	0.935	0.961	0.962	0.965	0.954	0.951
	1	0.898	0.925	0.923	0.877	0.839	0.812	0.793	0.782
	1.2	0.778	0.988	0.830	0.693	0.607	0.548	0.505	0.473
	1.4	0.717	0.916	0.635	0.447	0.338	0.267	0.213	0.169
	1.6	0.563	0.877	0.395	0.215	0.114	0.048	0.000	-0.037
		0.2	0.4	0.6	0.8	1	1.2	1.4	1.6
regression coefficient	0.2	0.55	1.03	1.02	0.81	0.60	0.45	0.34	0.26
	0.4	0.78	1.30	1.28	1.04	0.80	0.62	0.48	0.38
	0.6	1.13	1.68	1.62	1.32	1.06	0.85	0.69	0.56
	0.8	1.72	2.25	2.02	1.53	1.33	1.09	0.91	0.78
	1	2.52	3.07	2.38	1.77	1.36	1.14	0.97	0.86
	1.2	3.04	3.94	2.41	1.51	1.08	0.83	0.68	0.59
	1.4	2.51	3.92	1.88	0.96	0.58	0.39	0.28	0.20
	1.6	1.55	2.60	1.08	0.42	0.18	0.07	0.00	-0.04
	log U	0.2	0.4	0.6	log vf 0.8	1	1.2	1.4	1.6
ordinate intercept	0.2	67	13	4	17	33	46	57	64
	0.4	43	-13	-20	-3	17	33	46	56
	0.6	6	-52	-51	-28	-2	19	33	45
	0.8	-57	-110	-87	-46	17	8	23	35
	1	-148	-194	-116	-52	-11	14	31	42
	1.2	-216	-286	-114	-20	25	49	64	74
	1.4	-170	-287	-59	35	71	88	97	103
	1.6	-88	-153	17	82	103	112	116	118

Figure 13.41: Correlation coefficient between road test ratings of three truck tire compounds on re-treaded tires at two different axles and laboratory ratings as functions of log (energy) and log (speed).
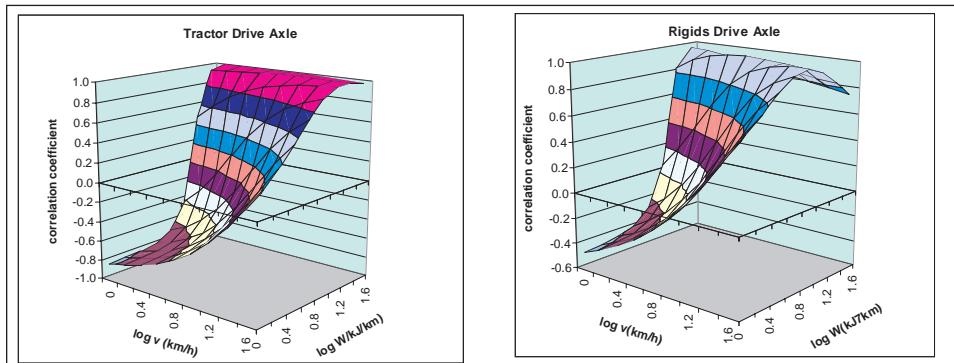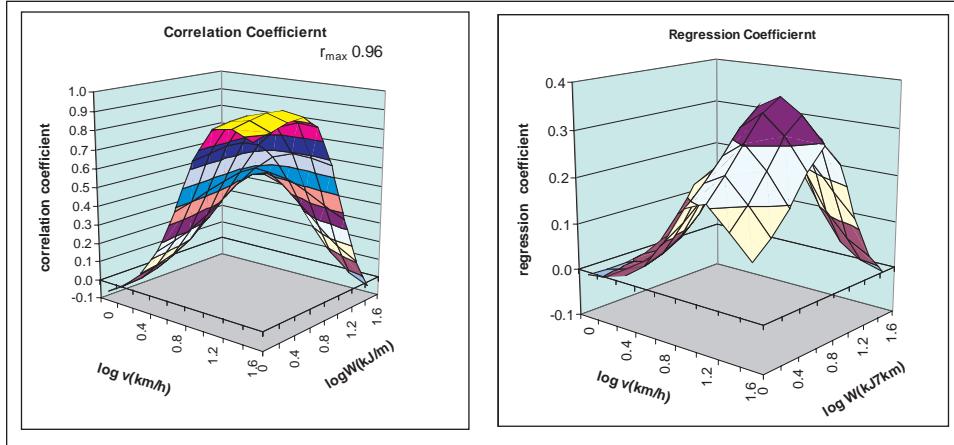
Figure 13.42: Correlation and regression coefficients between road test ratings of seven truck tire compounds based on 80SBR/20NR but differing in type and amount of filler and laboratory abrasion ratings obtained on LAT 100 testing equipment.

4. Tire wear

4.1 Tire wear under controlled slip conditions

One of the simplest instruments to measure actual tire wear under controlled load and slip is a towed two-wheeled trailer with its wheels set at a given slip angle. Both wheels must have tires mounted of the same construction, tread pattern and compound, so that the tires run at the same slip angle. A trailer of this type was employed in abrasion studies by Schallamach [34]. The rate of wear as a function of slip angle is shown in figure 13.43 for three different black filled tire tread compounds. Plotting wear and slip angle on log scales produces straight line graphs indicating that the wear loss can be described by a power law, in agreement with the model described previously. The straight-line graphs cross, indicating reversals in ranking. The NR and SBR compounds cross at a low slip angle. With a blend of 50 NR/50 BR the crossing point shifts to higher slip angles. All tires developed a characteristic Schallamach abrasion pattern. The most important variable, however, was the tire surface temperature. It increased dramatically with increasing slip angle.

If the rating of NR relative to SBR is plotted as function of the tire surface temperature, as shown in figure 13.44, a clear relation is seen to hold with NR better at low tire surface temperatures, but worsening rapidly as the temperature rises. The tire surface temperature may also be affected by environmental conditions. Wear measurements with tires set at a constant slip angle but with changing ambient temperature produced a larger temperature dependence of the wear rate for NR than for SBR, as shown in figure 13.45. The straight-line graphs showed a crossover at a surface temperature of about 48 °C. Such temperatures are also produced in ordinary tire wear. Measurements on the trailer tires themselves, where the slip angles were much smaller, gave much lower wear rates, as expected, but the relative wear rating of NR to SBR corresponded to that expected from the measured tire surface temperature, see figure 13.44 (open circles). The shift of the crossover point towards higher slip angles (i.e. higher surface temperatures) for a NR/BR blend indicates that this blend has a higher thermal stability.

All these observations are qualitatively in agreement with the laboratory investigations described above. They underline the important role that temperature plays in the wear process. Although temperature affects the dynamic properties of rubber its main effect is to accelerate the thermal oxidative processes that occur in abrasion and wear, and lower the resistance of compounds to them.

Figure 13.43: Log (tire wear) as a function of log (slip angle) for three tire tread compounds. Results obtained with the MRPRA trailer
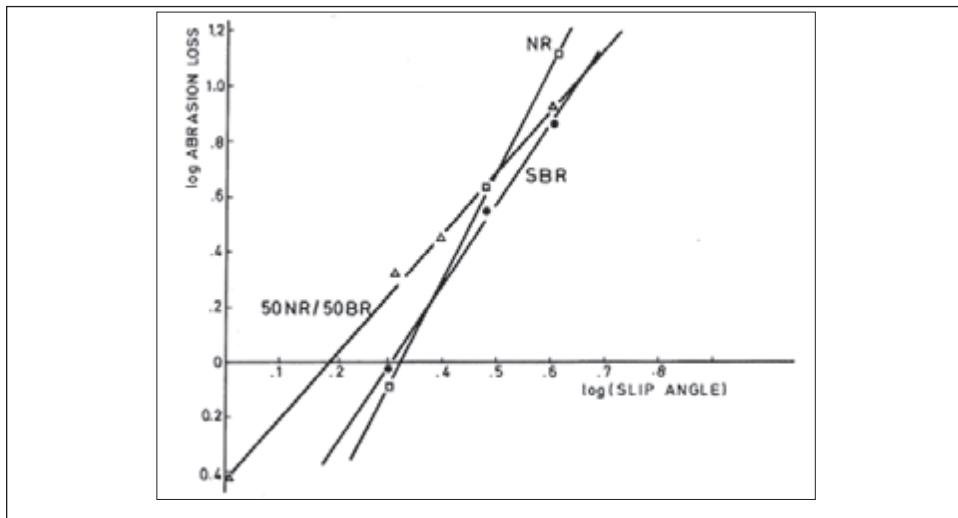
Figure 13.44: Relative compound rating as a function of the tire surface temperature. Data for three compounds obtained with the MRPRA test trailer and including data from the towing vehicle
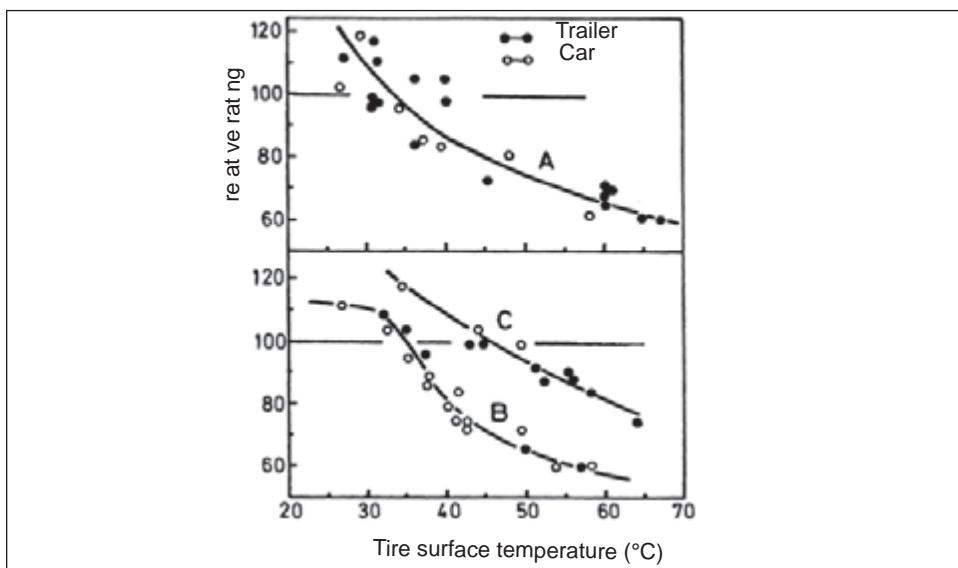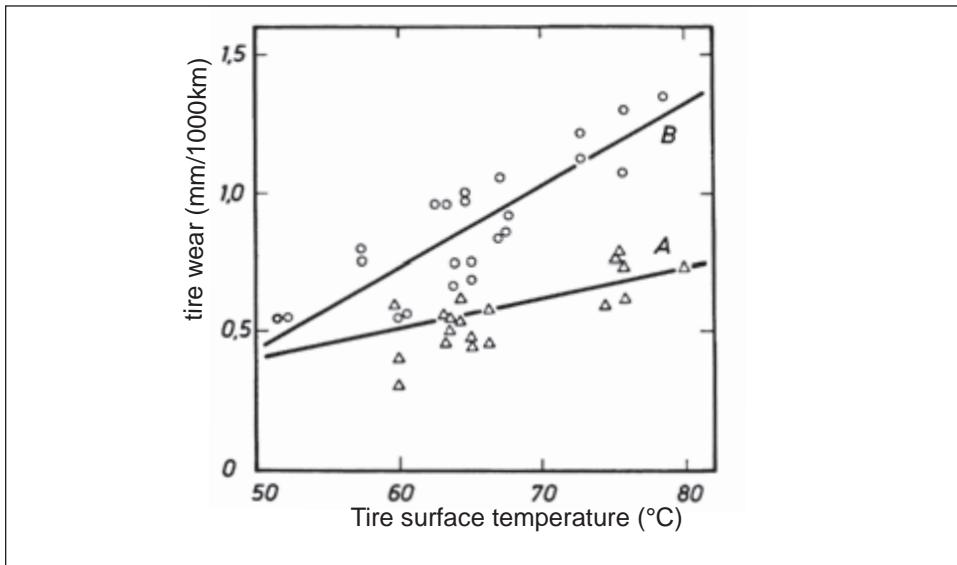
Figure 13.45: Abrasion of an NR and an SBR tread compound as a function of the tire surface temperature.   Meaasurements made at a constant slip angle using the MRPRA test trailer

4.2 Conditions affecting tire wear in road tests and normal usage.

4.2.1 Influence of the road surface

Consider first a test car that is driven for an eight-hour shift over a prescribed route with a length of about 600 km. The route could be selected to have special features like predominantly interstate highway (motorway, turnpike or freeway) or passing through windy and hilly country. In any case there will inevitably be a number of changes of road surface resulting in the need to characterize the average road surface structure, i.e. the sharpness and coarseness of the road surface, that are likely to have a significant influence on the abrasion loss. The average structure may be different for different test routes but the difference between the two averages are already likely to be smaller than the differences encountered along each route separately. Moreover, the average of a test route is likely to reflect the average of a whole geographical region. Differences between the average road surfaces in highly developed countries are likely to be small while larger differences exist between such countries and less developed ones. But even the structures of a chosen test route vary with the season. It is well known that road surfaces in areas of moderate climate are much sharper in winter than in summer. Even over much shorter periods the sharpness often changes drastically as a result of weather conditions.

Since wear results are generally obtained over a span of time they are inevitably averages. This is not too serious if the ranking of test compounds is not strongly influenced by the road surface structure and in particular by the changes that occur. Nevertheless it is obvious that repeatability is limited and as the few examples taken from laboratory experiments have shown, reversals in ranking are rather the rule than the exception. Hence a single road test result can have only limited validity.

4.2.2 Tire construction influences
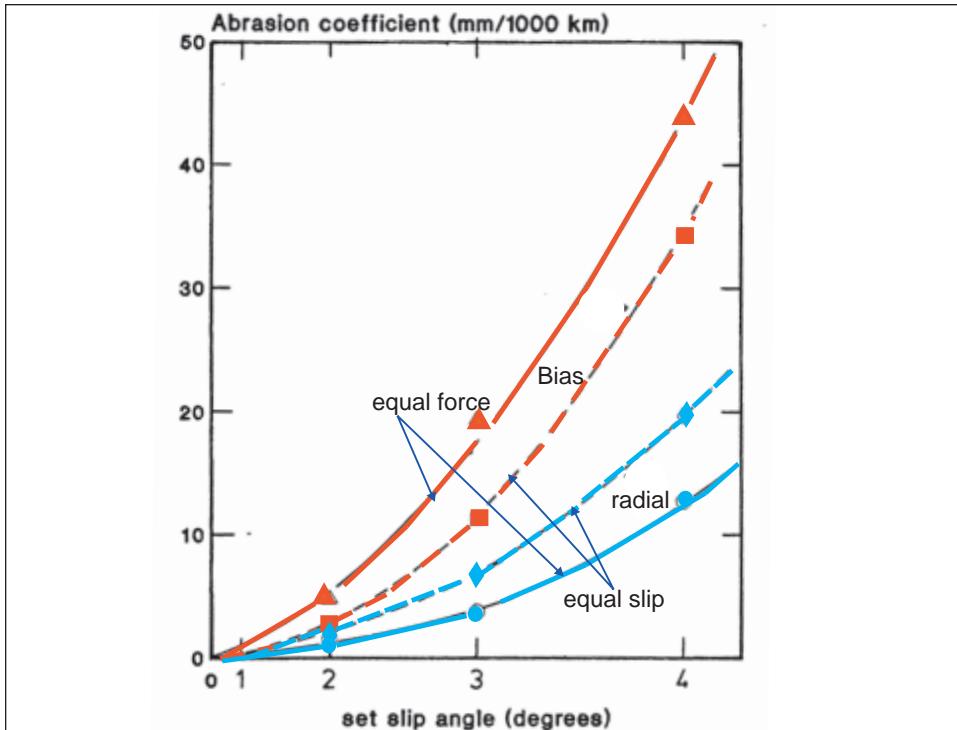
Road wear is force controlled. This is a fundamental difference between slip-controlled laboratory abrasion test machines, or wear tests with a trailer as described above, and real driving conditions. In force-controlled events the abrasion loss is inversely proportional to the stiffness of the tire while under slip control abrasion is proportional to the tire stiffness (see equations [11] and [12]).

   The effect can be seen in figure 13.46, which shows results obtained with the two wheeled trailer discussed above. Tire group A was a re-treaded bias-ply tire, and group B a commercial steel-belted radial ply tire. When one tire of each group was mounted on the axle of the trailer set for equal slip angles, the direction of the tow bar adjusted itself in such a way that the tires ran under the same side force; the slip angle of the stiffer tire was reduced and that of the softer (bias-ply) tire was increased. Hence a considerable difference in wear occurred for the two groups. If two tires of the same group were mounted on the trailer it ran under the set slip angle for both groups. The stiffer tires then wore more than under the previous condition and the softer tires wore less, whereas generally in tire tests a stiffer tire construction reduces tread wear. [Note that a stiffer construction includes the effect of carcass and belt, height to width ratio, and also the tread pattern and the stiffness of the tread compound.]

   A valid road test on different tires requires that two identical vehicles be used, each

**Figure 13.46: Rate of wear of a retread bias tire
compared with that of a commercial radial ply tire.**
(a) With one tire of each type mounted on a trailer axle (equal force comparison).
(b) With two similar tires mounted on the trailer axle (equal slip)
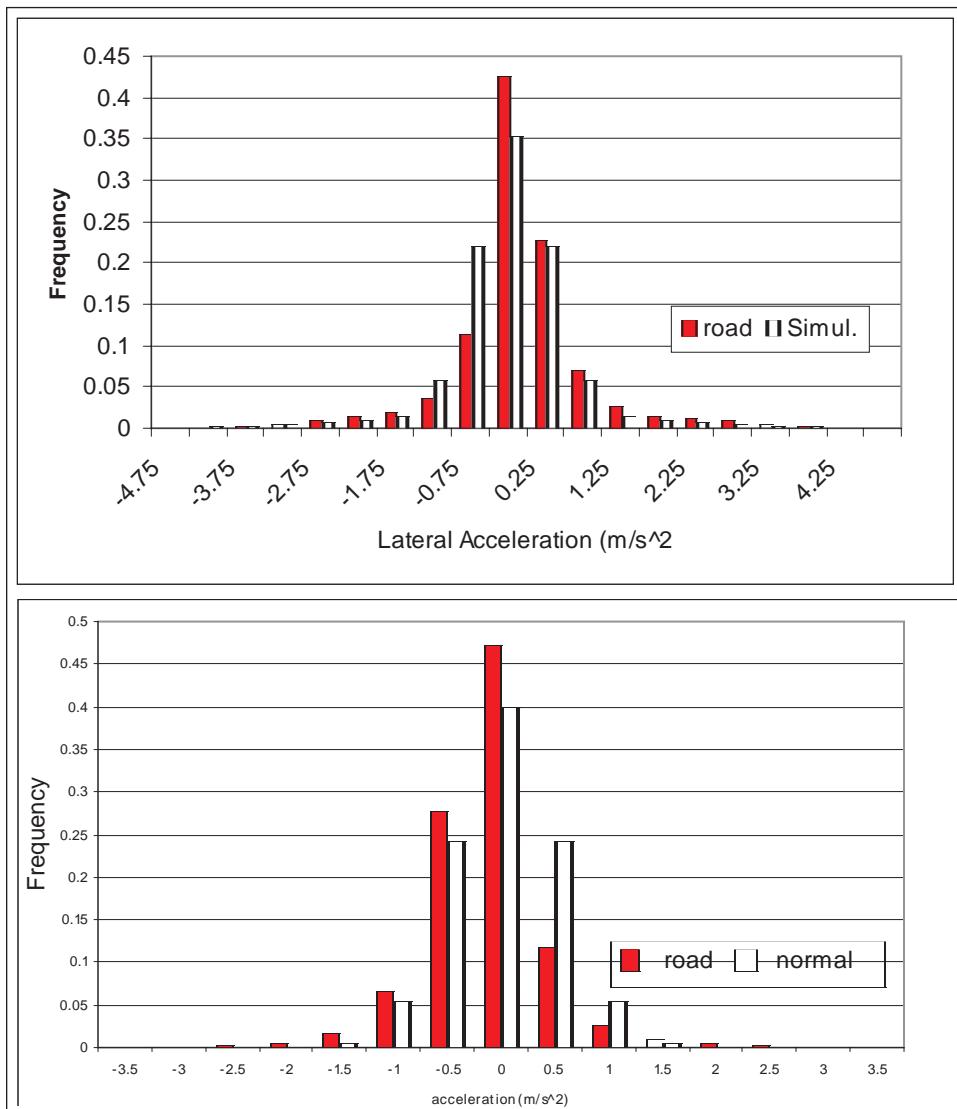
equipped with a test group of four identical tires. If this is not possible, at least one axle must have identical tires. Otherwise an average slip angle will be set up that brings into balance the side forces acting on the axle. This force will be larger for the stiffer tire than would be required if both tires had the same stiffness and it will be smaller for the softer tire. Hence the wear result is falsified with an advantage being conferred on the softer tire. The same argument holds for multi-section tires.
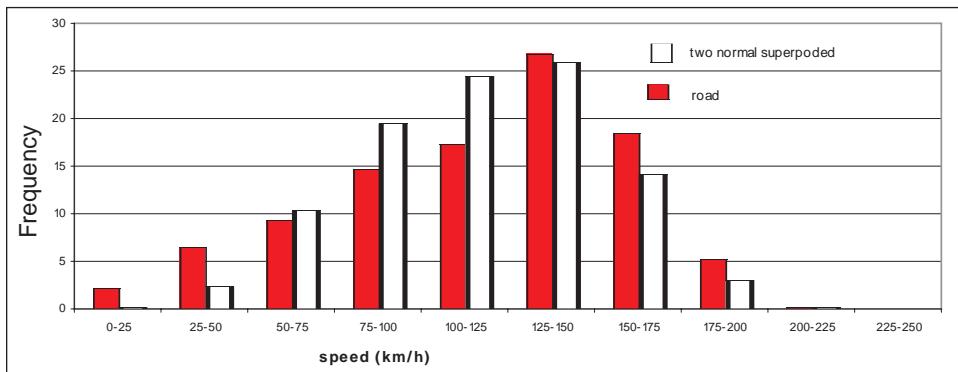
4.2.3 Driving influences

The forces acting on a car are due to cornering, acceleration and braking, wind pressure, and rolling resistance. In order to obtain a quantitative estimate of their effects, the route is divided into small sections over which it may be assumed that the force and speed conditions are constant. Consider first the cornering acceleration component. Curves will differ in radius and the speeds with which they are negotiated. The decisive aspect for wear is the centripetal acceleration that a curve requires. These accelerations can be measured. They are likely to follow a statistical distribution function symmetrical around zero. Figure 13.47a shows the measured cornering force distribution obtained in a controlled road test for a passenger car tire. Also shown is a normal distribution adjusted for its width to fit the data. It is obvious that the real distribution is very similar to a normal one. The same holds for the fore and aft acceleration, as seen in figure 13.47b. The force due to wind resistance is a function of the speed and the vehicle dimensions. The rolling resistance is due to the tires and the vehicle. Both are primarily functions of the load. In controlled road tests the load is usually kept constant, but the speed is varied. Figure 13.48 shows a speed distribution obtained on a controlled road test measured over 600 km. Two superposed normal distribution functions gave good agreement with the data. For the general user the load is also not constant and it can be represented by an appropriate distribution function.

Figure 13.47: Measured distribution of (a) cornering and (b) fore and aft accelerations in a controlled road wear test for passenger car tires.

Figure 13.48: Speed distribution in a controlled road test for passenger car tires.
Also shown is a distribution made up of two super-posed normal ones
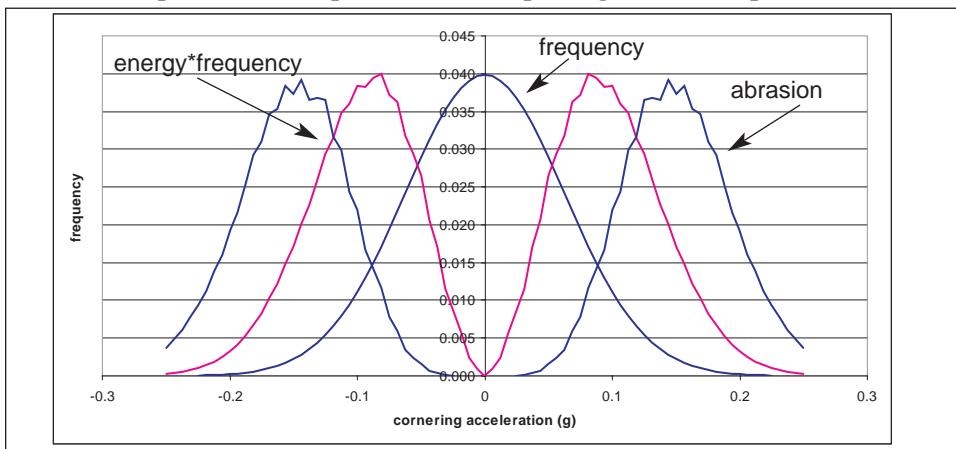
4.3 Road wear test simulation.

Using distribution functions for accelerations, speeds and loads, it is possible to calculate the resulting tire slip for a large number of driving events with the help of the brush tire model, each event being defined by a cornering acceleration, a longitudinal acceleration (speed-up or braking), the mass of the vehicle determined by the load and weight of the vehicle and the forces needed to overcome the wind and rolling resistance of tires and vehicle. All these are assumed to be constant for a short distance, hence the energy dissipation in the contact area due to the resulting slip can be calculated. Using the laboratory abrasion equation [18] the volume loss for each event is obtained. With distribution functions describing the frequency of their occurrence the volume loss over the entire route is obtained.

4.3.1 Force distributions

It has already been shown that real measured distribution functions can be represented satisfactorily by normal distributions. Hence, in a simulation program it is convenient to use such functions in the absence of real functions. Normal distributions around zero are used for the acceleration components. Their width is defined by 3 times their standard deviation, which includes 99.9% of all events. They are a major indication of the severity of the driving style. Figure 13.49 shows a normal distribution of the cornering acceleration, the resulting energy dissipation multiplied by the frequency of occurrence and the abrasion multiplied by the frequency, using a laboratory abrasion equation [18] with data obtained for a test compound on the LAT 100 abrasion tester. The energy and abrasion curves were normalized so that their heights correspond approximately to that of the distribution function. The curves are shown as continuous functions for clarity. In a practical simulation program a limited number of steps would have to be used.
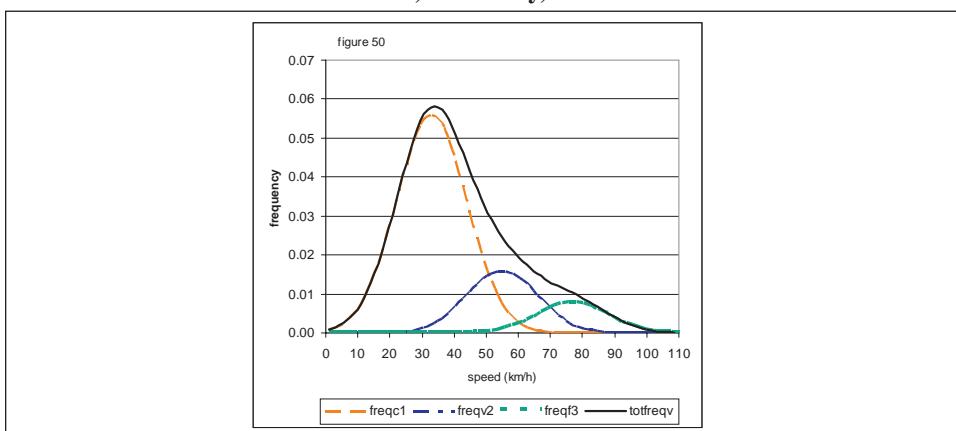
Figure 13.49: Theoretical acceleration (force) distribution function in a computer simulation, the resulting energy dissipation multiplied by the frequency of occurrence, and the expected abrasion loss, using equation 18 with parameters for a passenger tread compound.

4.3.2 Speed and load distributions

For the speed and load distributions, three superposed normal distributions around three fixed mean values are used, corresponding to the speed in town, country, and motorway (turnpike or freeway) traffic. A maximum speed fixes the total width of the curve from zero to the maximum. This corresponds to 10σ, where σ stands for the standard deviation of the three superposed distributions. The three mean values are fixed at 3, 5 and 7σ. Their heights can be varied according to the frequency with which the three distributions occur, with their sum adding up to 1. A similar distribution is also used to describe the different load conditions using low, medium and high loads. Figure 13.50 gives an example of such a triple distribution function.

Figure 13.50: Theoretical triple distributions as used in a computer simulation for speed and load distributions. Height ratios: town, 0.7; country, 0.2; motorway, 0.1

With the assumption that the frequencies of the different distributions determine one event, the frequency of each event is defined by the product of the individual frequencies. Having calculated the force for a particular event the slip is calculated using the brush model and hence the energy dissipation is obtained.

The forces are different for a driven and a non-driven axle and accordingly different abrasion rates will result. The load transfer that occurs during cornering averages out and is therefore not included. With the tire data, i.e. dimensions, tread width, net/gross area ratio for the tread pattern, and tread depth, expected tire lives are calculated under the above specified conditions. This approach is highly empirical (although supported by some distribution measurements). It has the merit that, with an existing set of laboratory abrasion data, a large number of road test simulations with different boundary conditions can be run in a very short time and their effect on tire life and compound rating can be estimated.

4.3.3 Results of road test simulation calculations

Table 13.6 gives a list of the boundary conditions that define a tire wear test simulation and in fact also an actual road test. The road surface used is the laboratory surface on which the abrasion data for the simulation were obtained. There is as yet no adequate definition of a road surface and even if there were one, it would be of little use since road surface structures change frequently as pointed out above.

**Table 13.6: Boundary conditions necessary to define
a wear test for a passenger tire road test**
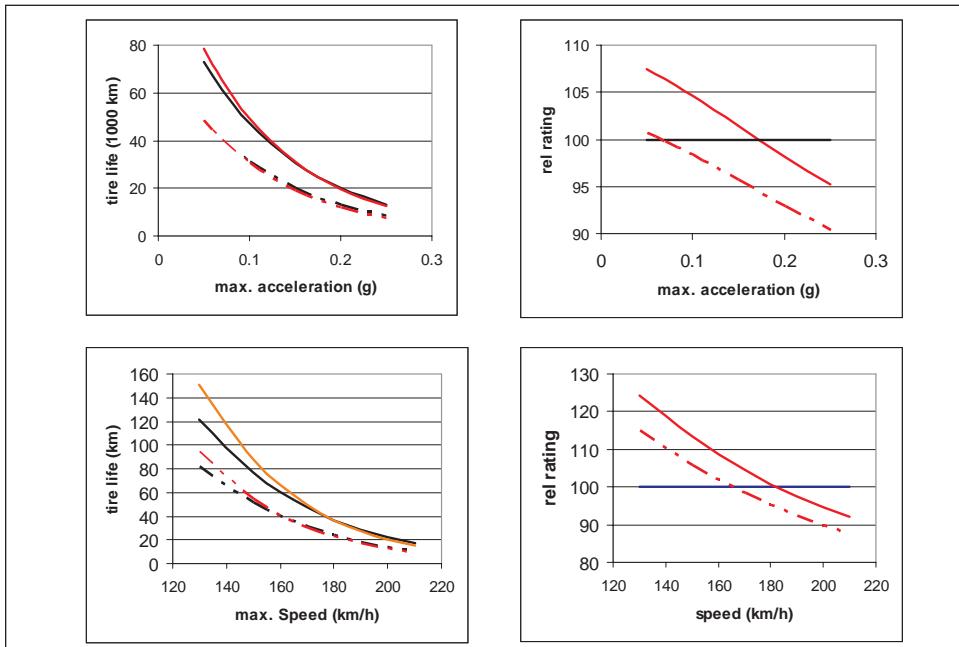
tire size:	205/ 65R 15			
Laboratory surface	alumina 60			
	tire construction:		tread pattern	
tire	kso(N/rad)=	60000	pattern width/tire width	0.78
parameter	kco(N/sl)=	120000	Net/gros =	0.7
	friction coefficient =	1.1	cross-section ratio =	0.65
			pattern depth (mm) =	8
vehicle	rol. resistance coef.=	0.01		
parameter	cw=	0.3		
	Proj vehicle cross-sect	2.5		
	max. corn accel.(g)=	0.15	smallest tire load(N)=	3200
driving	max longitudinal accel.	0.15	largest tire load(N)=	4900
parameter	max vehicle speed(km	170		
		low	med.	high
	3-load distr. ratio=	0.2	0.5	0.3
	3-speed distr. ratios.=	0.2	0.3	0.5

The tire construction influences the stiffness for both cornering and longitudinal slip. This includes the tire carcass, breaker construction, inflation pressure, and tread pattern design. However, since the two stiffness components can be measured, knowledge of the construction details is not necessary. The vehicle geometry influences tire wear through the air resistance it creates and through the load distribution between front and rear axle. The driving parameters are determined by the maximum values of their distribution functions and in case of load and speed by the ratios between low, medium and high loads and town, country road and highway traffic speeds, respectively. The tread pattern influences tire life through its effect on the abraded rubber volume.

Figure 13.51 shows the major influences on tire life. The most important are clearly the

driving style, determined by accelerations and maximum speed, and the tire construction as determined by the cornering and longitudinal slip stiffnesses. The figure compares two representative modern passenger tire tread compounds: an OE-SBR black filled compound and a solution SBR/BR blend filled with silica. The two upper graphs show the influence on tire life of the relevant distribution functions of the maximum acceleration components at a constant maximum speed. It is clear that tire life decreases rapidly with increasing severity. The solid lines refer to the cornering stiffness components of table 13.5 while for the dotted lines the stiffness components have been reduced by a factor of 0.75, keeping all other values the same. This reduces the tire life considerably. However, not only are the tire lives affected but the relative ratings of the two compounds are also changed. At low accelerations the OE-SBR/BR blend + silica is better than the OE-SBR black compound but the rating reverses with increasing acceleration. The same is observed if the maximum speed of the speed distribution function is varied and the acceleration is kept constant. As the speed is increased the tire life is drastically reduced and the rating of the silica compound reverses with respect to the OE-SBR black compound.

Figure 13.51: Major contributions to wear in a road test simulation

4.3.4 Influence of the shear stiffness of the tire tread compound
Principally the simulation compares tires under equal force conditions. It calculates the resulting energy dissipation and slip speed. Using the abrasion equation [18] the abrasion volume loss is obtained. Generally the program uses one cornering and one longitudinal slip stiffness, usually that for the control tire for all groups. This leads to correct predictions as long as the tire construction and tread pattern and the shear modulus of the tread are the same. This is usually the case for the construction and tread. In most cases dif-

ferences between the moduli of different tread compounds are also small and hence the results are reasonably correct. But ideally the cornering and longitudinal slip stiffnesses should be measured. If this is not possible the two stiffness components ought to be corrected for differences in shear modulus of the tread.

Considering the tire as a composite short beam under shear the following correction may be applied to the basic stiffness of the control

$$K_x = K_o \frac{\rho(1+\varphi)}{(1+\varphi\rho)} \qquad [20]$$

where K_o is the slip stiffness component of the control tire, φ is the ratio between the tread and carcass stiffness and ρ is the ratio of stiffness of the experimental tread to that of the control. The latter quantity can be estimated from the side force coefficients obtained during abrasion experiments at a small slip angle and a high speed. They reflect directly the compound stiffness and since the dimensions of test wheels are the same, the same ratio holds for the shear modulus.

For a balanced construction the ratio φ should be 1. If this is assumed to be the case the correction becomes

$$K_x = K_o \frac{2\rho}{(1+\rho)} \qquad [20a]$$

if $\varphi<1$ then the correction is larger, approaching ρ in the extreme case. If φ is larger than 1 the correction becomes smaller than given by equation [20a], so that K_x approaches K_o. If multi-section tires or experimental and control tires are mounted on the same axle, as is often the case for tests with truck tires on commercial fleets, the inverse of the above relation should be applied because the tires are now running under an imposed common slip.

5. Correlation between laboratory road test simulation and road wear test results

5.1 Correlation with a set of passenger car tires

It has already been shown how a correlation between road test ratings and laboratory abrasion can be obtained over a range of energies and speeds. Usually a good correlation, with a high correlation coefficient and a regression coefficient near 1, is obtained only over a limited range. This can be taken a step further by comparing road test ratings with a simulated laboratory test rating. This reduces the comparison again to a single number, a result usually desired by managers and compounders. However, the number is now based on the range of boundary conditions defined by the road test. This means that the appropriate road test conditions must be selected. Since today it is an easy matter for tire and vehicle manufacturers to carry out the required measurements, a representative set of boundary conditions and a comprehensive set of laboratory abrasion data could save an enormous amount of compound development time [37].

For the available road test data, such information was not available. However because a road test simulation takes only a very short time and reasonable conditions are not hard to guess, good correlations can be shown to exist between laboratory road test simulations and actual abrasion road test ratings without exact knowledge of the boundary conditions.

Table 13.7 shows three road test simulations of increasing severity by raising the maximum-acceleration components in three steps. The remainder of the boundary conditions were only loosely known and were therefore guessed at. The calculated ratings are compared with the

road test ratings. A very good correlation is achieved at a maximum acceleration for both components of 0.35g. This corresponds to a hard driving style, but one which is common for tire test drivers. The calculated tire lives are accordingly short, in agreement with this style of driving, and seem quite realistic.

Table 13.7: Correlation between road test ratings and laboratory road test simulations for a group of four passenger tires, discussed above for their laboratory abrasion and correlation to road test ratings

Tire size	205/ 60R 15				
Laboratory surface:		Alumina 180			
cornering stiffness (N/rad)		45000	tire cross-section ratio		0.6
circumf. slip stiffness (N/slip)		90000	net/gros of pattern		0.7
frction coefficient		1	pattern width/ tire width		0.76
tire load (N)		4500	pattern depth (mm)		8
rolling resistance (N)		45			
cw coefficient		0.3			
maximum speed (km/h)		170			
max cornering acceleration (g)		0.2			
max fore and aft acceleration (g)		0.2			

compound	Vol/km	km/mm	tire life (km)	Rating	Rating fr, road
1	12.2	17563	112404	**80**	87
2	9.8	21929	140348	**100**	100
3	10.9	19617	125549	**89**	107
4	5.4	39566	253224	**180**	170

max cornering acceleration (g)		0.3			
max fore and aft acceleration (g)		0.3			

1	49.0	4386	28072	**86**	87
2	42.0	5120	32766	**100**	100
3	41.1	5231	33477	**102**	107
4	25.5	8439	54008	**165**	170

max cornering acceleration (g)		0.35			
max fore and aft acceleration (g)		0.35			

1	83.7	2566	16420	**88**	87
2	73.9	2906	18600	**100**	100
3	69.7	3080	19711	**106**	107
4	46.0	4671	29896	**161**	170

5.2 Correlation with truck tire road test ratings

Table 13.8 shows the ratings of a laboratory wear simulation and the average road test ratings obtained for the three re-tread truck tire compounds used in a European Commission project to improve retread tire quality (see figures 13.39 and 13.40). Because either multi-section tires were mounted on all vehicles or two groups were mounted on the same axle, in each case the comparison occurred under equal slip conditions rather than equal force. The stiffness of each compound was estimated from the measured side force coefficients obtained during abrasion experiments at the smallest slip angle and highest speed. The simulations were carried out correcting the stiffness of the tires for differences in shear modulus of the compounds according to equation [20] with $\varphi=0.3$: (a) for equal force, (b) for equal energy (this assumes the same stiffness for all compounds) and (c) for equal slip conditions. In the latter case the inverse of equation [20] is used.

Table 13.8: Boundary conditions for a road test simulation using laboratory abrasion data to achieve a correlation with average road test ratings for three truck tire re-tread compounds mounted on the axles of several trucks, either as multi-section tires or as whole tires but with two groups on the same axle together with the simulation and actual ratings when compared (a) under equal force (b) under equal energy (assumes the same slip stiffness for all groups and (c) under equal slip conditions
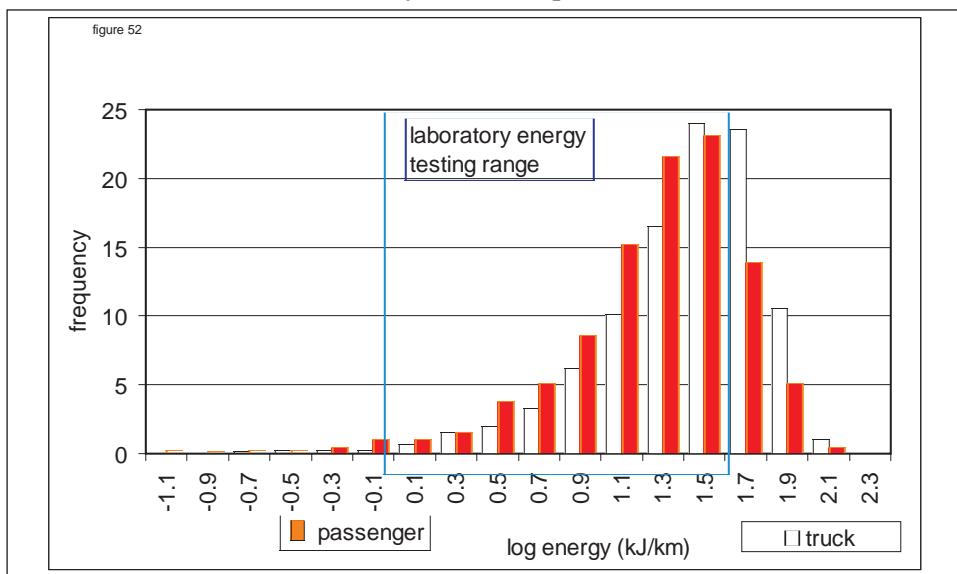
tire size:	275/ 80R 22.5						
Laboratory surfac		alumina 120					
	tire construction:			**tread pattern**			
tire	kso(N/rad)=		175000	pattern width/tire width =		0.82	
parameter	kco(N/sl)=		325000	Net/gros =		0.72	
	friction coefficient =		1.1	cross-section ratio =		0.8	
				pattern depth (mm) =		16	
vehicle	rol. resistance coef.=		0.01				
parameter	cw=		0.9				
	Proj vehicle cross-sect.(m^?		5				
	max. corn accel.(g)=		0.15	smallest tire load(N)=		13500	
driving	max longitudinal accel.(g)=		0.15	largest tire load(N)=		27500	
parameter	max vehicle speed(km/h)=		80				
			low	med.	high		
	3-load distr. ratio=		0.25	0.3	0.45		
	3-speed distr. ratios.=		0.3	0.4	0.3		
	comp.	Vol/km	km/mm	tire life(km)	Rating	average road rating	correlation coefficient
equal force	1	298.9	1726	24853	**100.0**	100	
	2	287.7	1793	25818	**103.9**	118	0.34
	3	217.5	2372	34154	**137.4**	113	
equal energy	1	298.9	1726	24853	**100.0**	100	
	2	275.5	1873	26967	**108.5**	118	0.648
	3	246.2	2095	30167	**121.4**	113	
equal slip	1	298.9	1726	24853	**100.0**	100	
	2	260.5	1980	28516	**114.7**	118	0.977
	3	277.6	1859	26764	**107.7**	113	

Since no data apart from a description of the general use of the truck (mostly short distance haulage) and the axle position on which the tires were mounted were available, again reasonable assumptions had to be made on maximum accelerations and speeds as well as load distributions. They are listed in table 13.8 together with the three comparisons. The boundary conditions chosen are reasonable for the kind of application under which the tires operated and the achieved mileages agree well with those obtained from the simulation. It is seen that good agreement is only reached if equal slip conditions are assumed, with a correlation coefficient of 0.977.

5.3 Energy consumption and slip speeds in road wear.
The road test simulation program also lists the energy consumption and slip speeds that occur for each event in the simulation. These quantities can be presented in the form of frequency distributions. The two energy distributions for a typical passenger tire and a truck tire simulation are shown in figure 13.52. Notice that they are almost identical for passenger and truck tires, although the boundary conditions are very different. The reason is twofold. First, the truck tires are much stiffer and hence the resulting slip angle for the same force is much smaller. Second, accelerations for truck tires are distinctly lower than for cars. Apart from engine power/kg mass being much lower (7 to 10 kW/ tonne for trucks compared to about 70 kW/ tonne for passenger cars), high levels of acceleration could well cause damage to the goods carried.

Figure 13.52: Energy distributions in a typical passenger car and truck tire road test simulation. Also shown is the range of energies used in laboratory abrasion experiments.

In addition, the laboratory range of energies, marked by the blue box, is also close to the range of energies in practical tire use. The reason for this is that much larger slip angles are used but at much smaller forces. A similar situation exists for the slip speeds. They are lower for trucks than for passenger tires but both are within the range of slip

speed used in the laboratory abrasion tests.

Hence the extrapolation between a laboratory abrasion test and tire wear in general use is much smaller than would be expected at first sight. It is therefore not surprising that the laboratory test procedure, which admittedly is much more complex than a single point reading, gives a close correlation for ratings and indeed also for mileages.

6. Conclusions

During the last fifty years our understanding of the very complex phenomena of abrasion and tire wear has progressed steadily. This chapter has traced the main strands of the story. Some details may still be missing but the main points are now clear. Starting from the underlying basic mechanisms, knowledge of the wear of tires has progressed so far that it is possible to predict compound ratings from laboratory experiments with sufficient accuracy that tire tread compounds can be developed with confidence without the necessity of tire road testing.

Basically abrasion is a cut growth process. This process is understood to be governed by the tearing energy as defined by Rivlin and Thomas 50 years ago. Schallamach was the first to conceive of abrasion as a function of energy dissipated in the contact area of rubber and track. Basic experiments have demonstrated that the relation between cut growth and tearing energy on the one hand and the relation between abrasion and energy consumption on the other are closely connected. A power law relation between rate of abrasion and energy consumption is now firmly established and holds over a wide range of energies. The power index and constant depend on both the compound and the abrasive track. The primary effect of the track is due to its sharpness rather than its coarseness. This influences both the level of abrasion as well as the value of the power index in the relation between abrasion and sliding energy.

Both processes, abrasion and cut-growth, are not purely physical phenomenon because chemical processes, primarily oxidation and thermal decomposition, play an important role. Indeed, in abrasion they can become dominant; for example, highly-degraded rubber is a sticky material, pulled off the tire by adhesion to the road. It is important to recognize that energy consumed in abrasion raises the temperature at the interface between rubber and track and thereby modifies the abrasion process. Because the temperature in the contact patch is a function of the power consumption, it depends also on the sliding speed. The physical and the chemical processes are so significant that they lead to different behavior of compounds under different service conditions: reversals in ranking of compounds for abrasion resistance are common. It is therefore in principle not possible to design a single laboratory abrasion test that can reflect the practical experience of service conditions. A range of energies and speeds are a minimum requirement. Computer simulation of road test conditions has shown that both these quantities can be applied in laboratory experiments to cover the same ranges that occur in service, increasing the likelihood of producing compound ratings that accurately reflect practical experience.

The question of the influence of the road surface on tire wear cannot be answered unequivocally because of the large effect on their abrasive power of different compositions, state of use and effect of weather. Road surfaces are also not durable enough for laboratory use. Hence reliance has to be placed on the correlation between laboratory results on a laboratory abrasive surface and road test experience. Alumina of different grain size (but primarily 60) has proved to be the most useful. Even so its sharpness

changes with use and test disks have only a limited useful life.

The link between laboratory abrasion test methods and road tests is now well established so that further research can concentrate on elucidating the basic underlying processes. For example, the interaction between filler systems and elastomers is continually changing through introduction of both new polymers and new fillers. But now the link does not need to extend from basic experiments to road testing of actual tires. It can be limited to some well-defined laboratory abrasion tests supplemented by measurements of the basic physical properties of the compound.

References
1. F. B. Bowden and D. A. Tabor (1954), "Friction and Lubrication of Solids", Oxford University Press, London, 1954
2. P. Thirion, Rev. Gen. Caout. **23**, (1946), 101
3. A. Schallamach, Proc. Phys. Soc. **B65**, (1952), 657
4. A. Schallamach, Wear **1** (1958) 384
5. K. A. Grosch, Rubber Chem. Technol. Rubber Reviews, **69** (1996) 495
6. K. A. Grosch and A. Schallamach, Kautschuk, Gummi und Kunstst. **22**, (1969) 288
7. A. Schallamach and K.A. Grosch, "The Mechanics of Pneumatic Tires" ed. S. K. Clark, US Dept of Transportation, National Highway Traffic Safety Administration, Washington DC 20950, Chap. 6, p. 408
8. R. S. Rivlin and A. G. Thomas, J. Polymer Sci. **10** (1953) 291
9. A. G. Thomas, J. Appl. Polymer Sci. **3** (1960) 168
10. G. J. Lake and P. B. Lindley, Rubber J. **146 (10)** (1964) 10.
11. P. B. Lindley and A.G. Thomas, 4th Rubber Technology Conference London, 1962
12. K. A. Grosch and A. Schallamach, Trans. IRI **41** (1965) T 80; Rubber Chem. Technol. **39** (1966) 287
13. M. L. Williams, R. F. Landel, and J. D. Ferry, J. Am. Chem. Soc. **77** (1955) 3701
14. K. A. Grosch, Proc. Roy. Soc. **A 274** (1963) 21
15. A. Schallamach, Wear **6** (1963) 375
16. A. Schallmach, Wear **13** (1969) 13
17. S. P Timoshenko and J. N. Goodier, "Theory of Elasticity", McGraw-Hill International Book Co., 19th ed., 1983.
18. A. Schallamach, Trans. Inst. Rubb. Ind. **28** (1952) 256
19. K. A. Grosch and A. Schallamach, Trans. I.R.I, **41,** T80; Rubber Chem. Technol. **30** (1966) 287
20. A. Veith, Polymer Test. **7** (1987) 177
21. D. H. Champ, E. Southern, and A. G. Thomas, "Advances in Polymer Friction and Wear", ed. by L. H. Lee, Plenum, New York (1974) p. 134
22. A. N. Gent and C. T. R. Pulford, J. Appl. Polymer. Sci. **28** (1983) 943
23. A. Schallamach, J. Appl. Polymer Sci. **12** (1968) 281
24. G. J. Brodskii, Sakhuoskii, M.M. Reznikovskii and V. F. Estratov, Soviet Rubber Technol. **19** (1960) B. 22
25. A. Schallamach and D. Turner, Wear **3** (1960) 1
26. D. L. Nordeen and A. D. Cortese, Trans. S.A.E. **72** (1964) 325
27. K. A. Grosch, Conference Proc. IRC Kobe (1995), p.155
28. K. A. Grosch, Kautschuk Gummi und Kunststoffe **49** No. 6 (1998) 432

29. K. A. Grosch, Conference Proc. Tyre Technol., London (1998) 14.6T1

30. K. A. Grosch and M. Heinz, Proc. IRC 2000, Helsinki (2000) paper 48

31. K. A. Grosch, H. Moneypenny and I. H. Wallace, IRC 2001 Birmingham (2001), IOM Communications, 307

32. K. A. Grosch, "The Speed and Temperature Dependence of Rubber Friction and its Bearing on the Skid Resistance of Tires" in "The Physics of Tire Traction" ed. by D.F. Hays and A. L. Browne, Plenum Press, 1974

33. H.S. Carslaw and J. C. Jaeger, Oxford University Press (1959), p. 279

34. A.D. Roberts, J. Nat. Rubb. Res. **2**, No. 4 (1987) 255

35. K. A. Grosch, ACS Rubber Div Meeting, Fall 2001, Cleveland, OH, Paper 48, pp 33,012

36. K. A. Grosch and A. Schallamach, Wear **4**, (1961), 356

37. D. O. Stalnaker and J. L.Turner, Tire Sci. Technol. **30**, No.2 (2002) 100

Chapter 14
Tire Properties That Affect Vehicle Steady-State Handling Behavior

by Joseph D. Walter

Chapter 14
Tire Properties That Affect Vehicle Steady-State Handling Behavior

by Joseph D. Walter

14.1 Introduction

Tires generate the control forces – characterized as driving and braking in the longitudinal direction and cornering in the lateral direction – that affect and effect vehicle motion in general and vehicle handling in particular. Handling is one of the important subjects of vehicle dynamics along with ride and straight line tractive performance. Vehicle response to steering wheel inputs (i.e., handling) is governed principally by cornering forces generated at the tire-road interface. For some vehicle classes cornering forces can also act as a fulcrum if tire-road friction is sufficiently large precipitating vehicle rollover.

In the present chapter, we make a variety of simplifying assumptions that allow us to focus solely on the influence of tires in controlling vehicle motion in a turn which allows for an understanding of handling and rollover in elementary terms. It will be shown that handling is strongly influenced by the understeer behavior of a vehicle, which quantitatively is dominated by differences in the cornering stiffnesses of the front and rear tires. On the other hand, the rollover propensity of a road car is governed principally by vehicle geometry with tires being of secondary influence.

Detailed derivations of the equations used herein and further discussion of vehicle dynamics can be found in the texts of Wong[1], Gillespie[2] and Pacejka[3].

14.2 Steering Geometry

To understand the response of an automobile in a turn, it is instructive to first analyze some simplified steering geometries. We initially consider low speed turns for which lateral accelerations (and therefore inertial forces) are negligible. In this case, tires operate at essentially zero slip angle with only steer angle present at the front tire-wheel assembly.
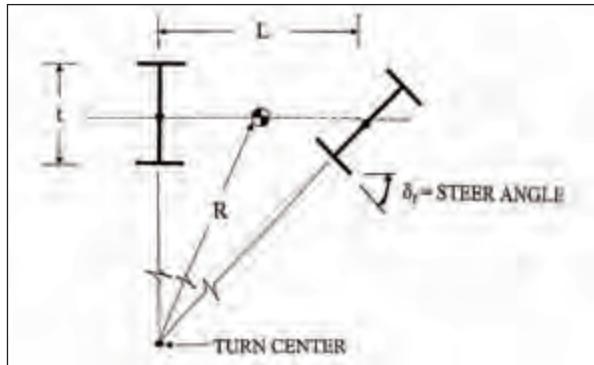
In a steered vehicle, it is desirable to have all four wheels roll about a common turn center to minimize scrub or lateral sliding in the tire footprint. Excessive scrub results in increased tire wear and steering effort on the part of the driver. The simplest kinematics to illustrate the concept of a common turn center for a two-axle vehicle is afforded in the case of wagon steer[1] (Figure 14.1). Here it is theoretically possible to achieve rolling without lateral slip of the tires by having the two front wheels remain parallel to one another while pivoting about a vertical (yaw) axis through a steer angle, δ_f, which

---

[1] The terminology "wagon steer" is also used to describe the steering of articulated, tracked vehicles (Wong [1], p. 425).

controls the turn radius R for a given wheel base L. When R >> L, which is the usual case, we can assume

$$\delta_f = L/R \qquad\qquad (1)$$
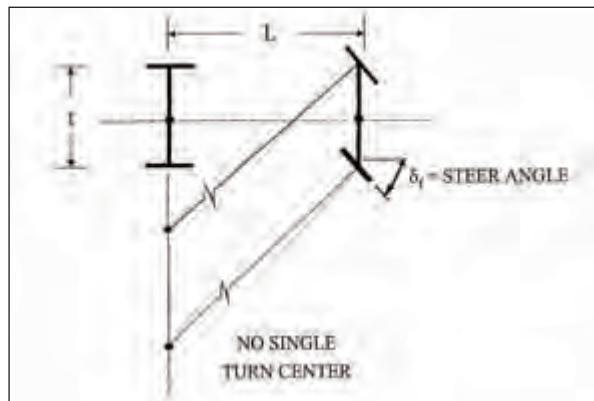
Figure 14.1: Wagon steering geometry

The steer angle is nominally the angle between the wheel plane and the longitudinal axis of the vehicle. It is apparent that as steer angle increases, the turn radius decreases for a vehicle of given wheelbase. It is, of course, not feasible to have a solid front axle pivoting as shown on a road car.

However, if the front axle remains parallel to the rear axle in a low speed turn with the front tires remaining parallel to each other as they pivot vertically, the yawing motion of the front axle is eliminated. Figure 14.2 illustrates this concept for so-called parallel steering geometry. But the motion described occurs at the expense of a non-common turn center with concomitant tire scrub.

Figure 14.2: Parallel steering geometry

The Ackermann steering geometry shown in Figure 14.3 eliminates the problems of both wagon and parallel steer. For this lay-out, the front axle remains parallel to the rear axle for a vehicle in a turn while the wheels rotate individually about vertical pins (known

as king-pins) relative to the front axle.[2] The concept is illustrated for a simple co-planar steering mechanism; sub-axles AL and BR about which the wheels rotate are part of the steering knuckles CAL and DBR, respectively. These knuckles are connected to the front axle by king-pins at A and B which allow pivoting motion. The two steering knuckles in turn are connected to the tie rod CD at C and D. Because the tie rod is shorter than the distance between the king-pins, the inside wheel will turn through a greater steer angle δ_i than the angle δ_o of the outside wheel. The steering gear transmits the driver's steering wheel motion to the front axle steering mechanism. This ingenious arrangement, dating from the era of horse-drawn carriages in the early 1800s, allows the front axle to remain parallel to the rear axle with each tire-wheel assembly rolling about a common turn center.
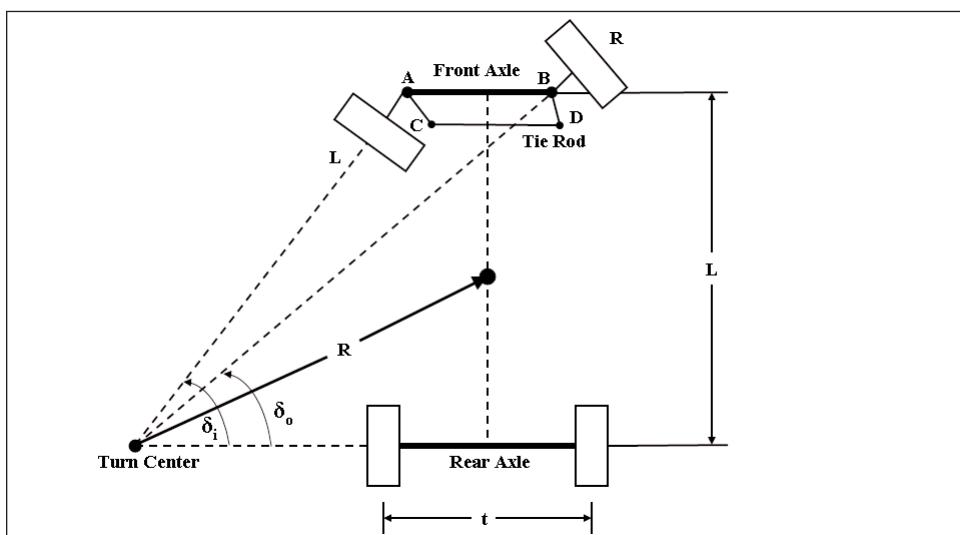
There are two distinct equations that can be obtained from the Ackermann steering concept:

$$\cot\delta_o - \cot\delta_i = t/L \tag{2}$$

and

$$(\delta_i+\delta_o)/2 = \delta_f \doteq L/R \tag{3}$$

Figure 14.3: Ackermann steering geometry

Equation 2, based solely on geometry, establishes the relationship between the steer angles δ_i and δ_o with vehicle wheel base L and track t that minimizes tire scrub. Equation 3 defines an average front steer angle δ_f that forms the basis of subsequent analysis (Section 14.3) used to describe the steady state handling characteristics of an automobile. However, Equation 3 needs to be extended to include laterally compliant tires – i.e., tires operating at a slip angle – in order to quantify the concept of understeer.

---

[2]While present day automobiles are generally produced with independent front and rear suspensions, "axle" is used in the text and shown in Figures 14.1-14.3 for conceptual purposes.

14.3 Understeer and Oversteer

In this section, the relation between cornering force and slip angle is explained, and equations describing the influence of tires on vehicle behavior in steady state (non-time varying) cornering are developed. Handling behavior is based on motion on a circular path at constant vehicle speed. Nonetheless, Newton's 2nd Law applied in the plane of motion perpendicular to the path radius can be used to predict important aspects of handling performance without considering the transient (time dependent) response or moment of inertia properties of the vehicle and its tires. This approach greatly simplifies analysis in that algebraic rather than differential equations of motion can be employed to understand the basics of the directional behavior of front-steer, four wheel, on-road vehicles.

When a vehicle negotiates a curve at other than low speeds, the centrifugal force acting through the mass center of the car tends to produce either slide-out or possibly rollover at the adhesion limit of the tires on the road. We consider vehicle behavior prior to slide-out or rollover where the centrifugal force is equilibrated by the cornering forces generated at the tire-road interface.
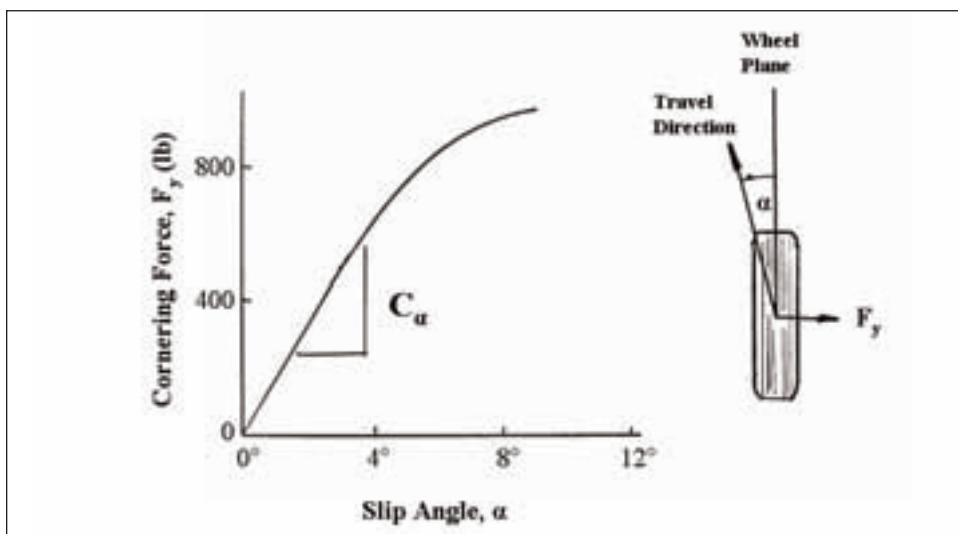
The cornering forces in turn produce slip angles in the flexible tires which vary generally as shown in Figure 14.4 where:

$$F_y = \text{cornering force}[3]$$
$$\alpha = \text{slip angle}$$
$$C_\alpha = \text{cornering stiffness (initial slope of curve)}$$

Figure 14.4: Representative trend of tire cornering force vs. slip angle

---

[3] In the SAE coordinate system, the coordinate "y" denotes the lateral direction; other lateral forces acting on a tire include camber thrust, ply steer and conicity - but these are generally smaller in magnitude than cornering forces. (See Chapter 8).

Note that the force F_y remains perpendicular to the wheel plane in a cornering maneuver and is considered to be zero when slip angle α is zero. The travel direction is coincident with the direction of the velocity vector of the tire-wheel assembly.

In the normal range of use parameters, the cornering stiffness C_α increases with increasing wheel load, inflation pressure, rim width, tread wear, and other factors, and is markedly influenced by tire cross-sectional geometry and internal construction features. Surprisingly, C_α is relatively insensitive to vehicle velocity (at normal highway speeds) and tread compounding ingredients (with the latter becoming important at higher slip angles where the "F_y vs. α" relationship becomes non-linear). The complete set and nature of tire force and moment properties, and especially cornering force, is discussed in Chapter 8.

The units of cornering stiffness are commonly reported as lb/deg or N/radian. Cornering stiffness is occasionally and mistakenly referred to as cornering power. Cornering stiffness divided by wheel load is known as the cornering coefficient. The cornering coefficient is sometimes cited as normalized lateral force. Note that as wheel load increases, the cornering stiffness of a tire increases while the cornering coefficient decreases (i.e., lateral force builds-up more slowly in magnitude than wheel load). Values of the load and pressure dependent cornering stiffness may range from a low of 100 lb/deg for a slightly underinflated bias ply passenger car tire to magnitudes in excess of 400 lb/deg for a radial performance tire.
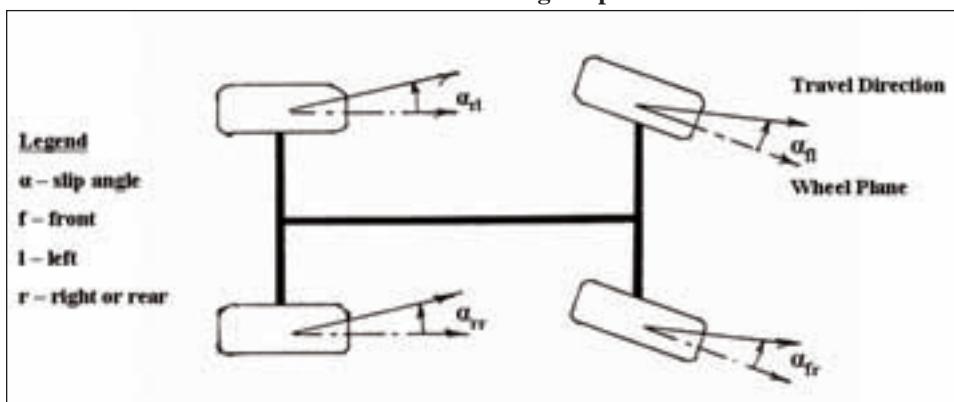
For purposes of this analysis, we consider only the linear tire regime for which

$$F_y = C_\alpha \alpha \tag{4}$$

The cornering force-slip angle curve for most passenger car tires can be considered to remain linear to approximately four degrees of slip angle (which is generally about 0.3g's of lateral acceleration).
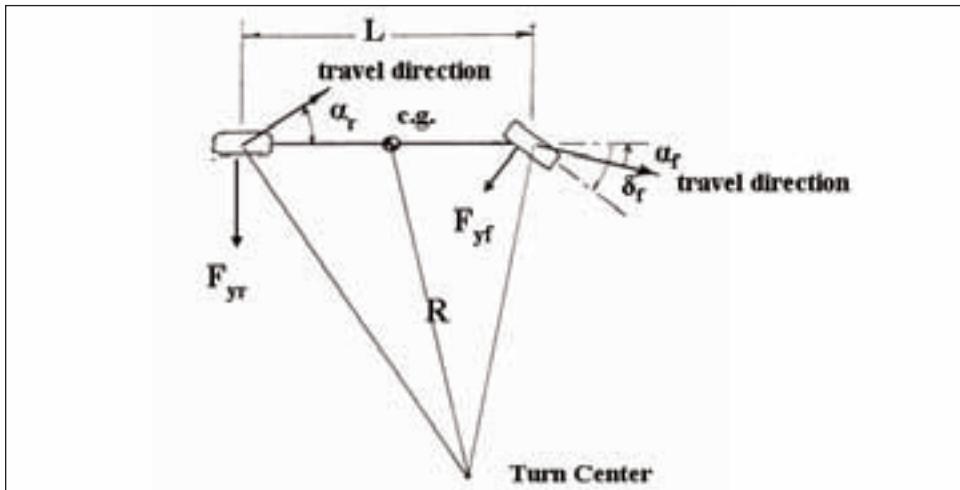
Note, however, for a vehicle in a turn with four nominally identical tires, that slip angles will vary left-to-right as well as front-to-rear depending on the level of lateral load transfer and front/rear axle loads (Figure 14.5). Knowing the tire cornering characteristics, vehicle geometry, and operational conditions allows each of the four slip angles to be estimated for a given level of lateral acceleration.

Figure 14.5: Variation of tire slip angles (left-to-right and front-to-rear) for a vehicle turning at speed

For purposes of subsequent analysis, left and right tire cornering stiffnesses are combined at the front and rear axles, respectively, to produce the so-called "bicycle model" as shown schematically in Figure 14.6. Note that the forward vehicle velocity (travel direction) at any point is perpendicular to the turn radius at that point and, again, cornering forces front and rear are perpendicular to the wheel plane. Slip angles are measured between the wheel plane and the velocity vector. The turn center is located at the intersection of line segments perpendicular to the velocity vectors at the front and rear tire-wheel assemblies. With the turn radius much larger than the wheel base we can reasonably assume small differences in the inside and outside steer angles and represent the average angle $(\delta_i + \delta_o)/2$ as δ_f – the front wheel steer angle.

Figure 14.6: Bicycle model

Note that on a cornering vehicle, steer angle is not equal to tire slip angle while in the laboratory environment of the tire test dynamometer the two angles are identical. Also observe that slip angles on the rear tires of a vehicle also produce forces needed to maneuver – just as the front tires – but produce such lateral forces without the benefit of a rear steer angle.[4]

From Figure 14.6 the following geometrical relation can be obtained

$$\delta_f = L/R + (\alpha_f - \alpha_r) \tag{5}$$

which is just the Ackermann equation extended to include slip angles at the front and rear of the vehicle. In some earlier automotive engineering publications, the slip angles δ_f and δ_r are descriptively referred to as drift angles and steer angle δ_f as Chapter 14. Tire Properties That Affect Vehicle Steady-State Handling Behavior angle.

By equilibrating tire cornering forces with the lateral inertial force acting through the vehicle center of gravity, Equation 5 can be recast as

[4]Vehicles with four-wheel steer are discussed by Gillespie [2].

$$\delta_f = \frac{L}{R} + \left(\frac{W_f}{2C_{\alpha f}} - \frac{W_r}{2C_{\alpha r}} \right) \frac{v^2}{gR} \tag{6}$$

where linear tire properties have been employed (Equation 4), and

W_f, W_r = load on front and rear axles,

$C_{\alpha f}$, $C_{\alpha r}$ = cornering stiffness of individual front and rear tires,

with other terms as previously defined. The local value of acceleration due to gravity is denoted by "g" and the vehicle forward velocity by v.

The expression in parentheses in Equation 6 is often denoted by the symbol K_{us} and is referred to as the understeer coefficient by Wong [1] due to vehicle weight distribution and tires – i.e.,

$$K_{us} = \frac{W_f}{2C_{\alpha f}} - \frac{W_r}{2C_{\alpha r}} \tag{7}$$

Note that the understeer coefficient as defined by Equation 7 is dimensionless but is often expressed in degrees rather than radians. Each term on the right hand side of this equation – with dimensions of load divided by cornering stiffness – is often referred to as cornering compliance.

Equations 5 and 6 can now be re-written in the forms:

$$\delta_f = \frac{L}{R} + \frac{K_{us}v^2}{gR} \tag{8}$$

or

$$\delta_f = L/R + K_{us}(a_y/g) \tag{9}$$

where a_y is the steady state lateral acceleration.

The understeer coefficient defined by Equation 7 depends solely on front and rear static axle loads and tire cornering stiffnesses. While the cornering stiffness is dependent on many construction variables controlled by the tire manufacturer, it is also dependent on many factors under the direct or indirect control of the driver – especially inflation pressure. In fact, the easiest way to alter the understeer characteristics of an automobile is to change the tire pressure.

Note that the coefficient K_{us} can be positive, negative or zero. If positive, the vehicle is said to be understeering with controllable driving behavior; if negative, the vehicle is said to be oversteering tending to handle in a counter-intuitive manner. An oversteering vehicle is generally not safe at highway speeds in the hands of an average driver. Alternately, we may state that the driving sensation felt in an understeering car is one of stability and predictability; the sensation felt in an oversteering car is one of instability and a constant need for correction during normal highway driving. When K_{us} is zero, which is equivalent to slip angles being equal at the front and rear, the steer angle δ_f required to turn a corner reduces to the low speed Ackermann equation – i.e., $\delta_f = L/R$.

Modifying the front and rear static axle loads in Equation 7 to accommodate longitudinal load transfer due to braking or accelerating, or to account for aerodynamic lift or down force, is inappropriate. However, the load transfer that occurs, e.g., to the front axle while backing off the throttle upon entering a curve increases the cornering stiffness of the front tires (due to the increased load) and reduces same in the rear. This action shifts the handling balance of the vehicle toward oversteer. Further, if longitudinal forces are present due to braking or driving, the ability of the tire to generate lateral (cornering) forces is diminished and the cornering stiffness of the tire, C_α, is accordingly reduced.

From analysis or measurement, Equations 8 and 9, are often plotted to graphically explain the condition of understeer, oversteer and neutral steer. Steer angle (δ_f) is plotted schematically as a function of vehicle velocity (v) in Figure 14.7 and as a function of lateral acceleration (a_y/g) in Figure 14.8 for constant radius turns. As shown in these figures, the steer angle δ_f increases as velocity and acceleration increase for understeering vehicles; for oversteering vehicles, the steer angle decreases for the same conditions. Also, understeering vehicles may tend to oversteer at higher lateral accelerations (dotted line shown in Figure 14.8).

Figure 14.7: Relation between steer angle and vehicle velocity (equation 14.8)
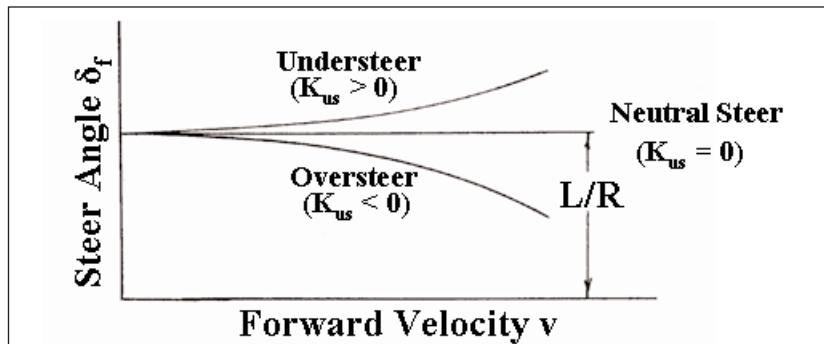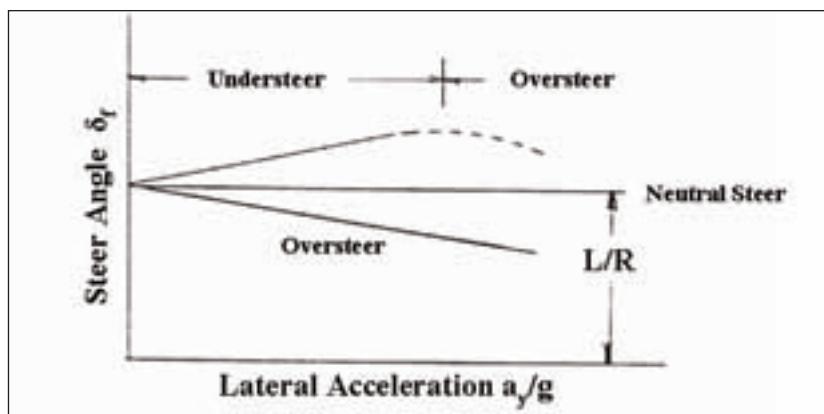
Figure 14.8: Relation between steer angle and lateral acceleration (equation 14.9)

Measurements of tire cornering stiffness in a controlled laboratory test environment coupled with knowledge of vehicle static weight distribution are not enough, however, to quantify the understeer/oversteer characteristics of an automobile on the highway using Equation 7 alone. Either additional calculations are required for which data are not readily available (some of which are given in Gillespie [2]), or vehicle on-road measurements can be conducted. An expression, useful in conjunction with on-road testing, can be obtained by taking the derivative of δ_f in Equation 9 with respect to a_y – i.e.,

$$d\delta_f/da_y = K \qquad\qquad\qquad (10)$$

where $K = K_{us}/g$ defines the on-road understeer/oversteer gradient (with units of degrees/g or radians/g).

One of the standard tests for determination of understeer is usually carried out on a skid pad of constant radius at different fixed vehicle speeds. Surprisingly little in the way of instrumentation is required to quantify such tests. In the simplest case, vehicle forward velocity, lateral acceleration, and steering wheel angle are measured. The steer angle δ_f can be computed from the steering wheel angle divided by the steering gear ratio; more sophisticated instrumentation can be employed to measure δ_f directly at the tire-wheel assembly. For more advanced dynamic analyses, yaw rate as well as roll angle (as a function of time) can be obtained. Procedures are described in SAE Recommended Practice J266[4].

There are many factors present in on-road tests that can influence the cornering forces developed in a turn including tire camber angle, lateral load transfer, suspension compliance, etc. These will affect the directional behavior of a vehicle; importantly, these effects are captured during testing – though not explicitly stated in Equation 7. These additional factors generally act to shift the control balance to more understeer. The importance, then, of Equation 7 (not containing these factors) lies in the fact that it indicates the change in the directional response of a vehicle which can occur in-service due to changes in tire cornering characteristics due to, e.g., air loss, tread wear or throttle-off conditions.

Vehicles for highway use are designed to be understeering (2 deg/g or greater) so that driver inputs to the steering wheel required to follow a desired path follow naturally – i.e., the motion expected and produced by the vehicle is in-phase with clockwise or counterclockwise rotation of the steering wheel. The amount of understeer designed into a vehicle depends on the manufacturer's perception of customer requirements and skills. Thus, a vehicle designed with a modest level of understeer may experience oversteer in some circumstances during highway service due to changes in tire cornering characteristics or axle loadings. Operating beyond the linear tire range at steady state lateral accelerations in excess of 0.3g's may also change the balance of an understeering automobile to oversteer (*cf.* Figure 14.8).

A range of understeer gradients (all positive) for a variety of vehicles is given in Table 14.1 taken from measurements made by the National Highway Traffic Safety Administration [NHTSA].

Table 14.1: Representative understeer gradients measured on various vehicles [5]

Vehicle	Class	Understeer gradient (deg/g)
1998 Chevrolet Astro	Minivan	6.13
1998 Chevrolet Lumina	Full-size car	5.49
1997 Ford Ranger	Small pickup truck	4.59
1998 Dodge Neon	Small car	3.59
1998 Ford Explorer	Sport utility vehicle (SUV)	2.89

The five vehicles included in Table 14.1 (out of 12 that were tested) were selected for their wide range of measured understeer. Also, reported by Garrott, et al. [5] are a variety of metrics useful to vehicle dynamicists for steady-state and transient simulation studies but not required herein.

It may be helpful at this point to summarize some of the known properties of tires that influence cornering stiffness C_α – and, consequently, vehicle handling. For example, the cornering stiffness of a radial passenger car tire can be increased during the design stage of development by, among other things:

a) lowering aspect ratio;
b) increasing belt width;
c) stiffening the bead turn-up region;
d) reducing tread depth;
e) reducing tread void volume.

These changes may reduce the ride quality of the tire and in some cases (e.g., increasing belt width) may adversely impact long-term durability. Further, the cornering stiffness of an existing tire on a given vehicle may be increased by:

a) increasing inflation pressure;
b) increasing tire load;
c) increasing rim width;
d) increasing camber angle;
e) removing tread rubber.

To increase the understeer behavior of an existing tire-vehicle system:

a) increase rear tire pressures;
b) increase front axle load;
c) place higher C_α tires on rear.

The only exception to item c) immediately preceding is when only two new tires are purchased with two partially worn tires of the same type staying on the vehicle. The new (full tread depth) tires with better traction should be placed on the rear for wet road driving conditions.

Qualitative example

Consider the effect of rapid air loss due to foreign object penetration in one of the front tires on the change in the steady state directional behavior of an automobile. Since the cornering stiffness of the tires on the front axle is reduced, the understeer coefficient K_{us}

(Equation 7) becomes more positive. While the driver may experience a pull in the steering wheel (in the direction of the deflated tire), vehicle response will tend to be more sluggish, but predictable.

On the other hand, for the loss of air in one of the rear tires, the vehicle will be less understeering – and even perhaps oversteering – depending on the total amount of understeer present in the vehicle at the time of air loss. If the vehicle becomes oversteering, its handling behavior is unstable.

One of the limitations of the "bicycle model" is that lateral load transfer and vehicle roll effects cannot be accommodated in the analysis. It is known from on-road tests or more advanced models than the reduction in the understeer coefficient (or gradient) due to a rear tire disablement is position sensitive depending on the turning motion of the vehicle. If the outside rear tire (left or right depending on the turn direction) is disabled, oversteer is more likely to occur. The effect is exacerbated in vehicles with a solid rear axle.

Quantitative example
Consider an automobile with the following characteristics:
    Weight = 4200 lb
    Wheel Base = 110 in
    Distance to c.g. =50 in (from front axle)

that is equipped with two radial tires (C_α=300 lb/deg) and two bias tires (C_α=200 lb/deg) per axle.

For the case of bias tires at the front and radial tires at the rear:

$$K_{us} = \frac{W_f}{2C_{\alpha f}} - \frac{W_r}{2C_{\alpha r}} = \frac{2290}{(2)200} - \frac{1910}{(2)300} = 5.73° - 3.18° = +2.54° \ (0.0443 \text{ rad}).$$

This tire fitment tends to shift the control balance of the automobile to more understeer.

For the case of radial tires front and bias tires rear:

$$K_{us} = \frac{W_f}{2C_{\alpha f}} - \frac{W_r}{2C_{\alpha r}} = \frac{2290}{(2)300} - \frac{1910}{(2)200} = 3.82° - 4.75° = -0.93° \ (-0.0162 \text{ rad}),$$

and the vehicle becomes less understeering – and perhaps oversteering.

While it is not recommended to mix tire constructions on the same vehicle, if for some reason this needs to be done, radials should be placed on the rear axle with bias tires on the front.

It may be useful to end this discussion of vehicle oversteer and understeer by listing the assumptions used in developing the algebraic equations employed herein:
    a) constant vehicle velocity;
    b) path of constant curvature;
    c) turn radius much larger than wheel base of vehicle;
    d) tire cornering forces vary linearly with slip angle;
    e) bicycle model.

These assumptions are far removed from vehicle behavior in cornering maneuvers at lateral accelerations in excess of 0.3-0.4 g's, but the equations developed offer useful insights into the handling behavior in the linear domain where the vast majority on-road driving occurs.

Although the understeer coefficient was derived for the case of a vehicle in a turn, it can be shown that it also applies to vehicle response in straight-ahead driving. For example, oversteering vehicles have a critical speed at which forward motion is unstable [1].
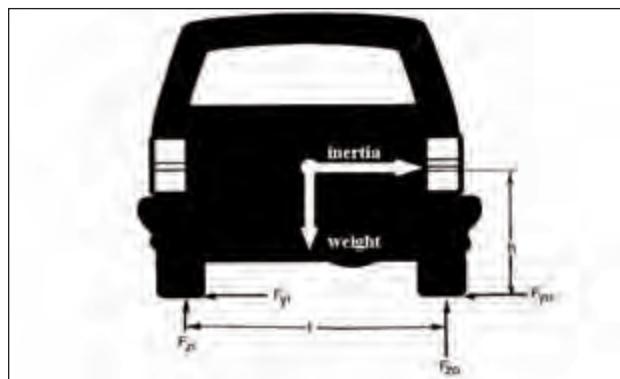
Non-linear, steady state, tire behavior and its influence on vehicle directional control is discussed in detail by Pacejka [3]. References to transient vehicle handling behavior can be found in Wong [1] and Gillespie [2]. On-road tests allow one to evaluate non-linear tire characteristics and transient vehicle behavior where elementary theories of 'dynamic understeer" have yet to be developed. Complex computer models are often employed to analyze the limit behavior and skid recovery of complete tire-vehicle systems in non-steady state conditions.

14.4 Rollover

If lateral forces produce a sufficiently large roll moment about the c.g. of a vehicle, it will rollover about a longitudinal axis. When the lateral forces are due to cornering during highway maneuvers, the rollover event is termed "untripped;" if the lateral forces arise due to a roadway obstruction (such as a curb or soft shoulder on the edge of the highway), the rollover is referred to as "tripped." The majority of rollover accidents involve a tripping mechanism – i.e., impact or engagement with an obstacle – but we consider only the simpler case of untripped rollover because the results obtained correlate well with rollover accident statistics whether the event is tripped or untripped [6].

Figure 14.9 shows the forces acting on a roll plane of a vehicle in a steady state turn with a reversed inertia vector directed away from the turn center. There is no recognition of front and rear axles or of a compliant suspension in this rigid body, planar analysis. As velocity is increased or turn radius is decreased, lateral load transfer occurs; that is, the normal load F_{zi} on the inside tires decreases while the normal load F_{zo} on the outside tires increases. The accompanying tire cornering forces behave in a similar manner. If the coefficient of friction between tire and road is sufficiently large, the cornering forces on the front and rear outside tires act as a pivot axis about which the inertial (centrifugal) force tends to rotate the vehicle in the roll plane away from the turn center. In other words, steering left into a turn causes the vehicle to roll to the right, and vice-versa.

Figure 14.9: Forces acting on a vehicle in a turn prior to rollover

At the instant of incipient inside tire lift-off, $F_{zi} = 0$, and (roll) moment equilibrium requires that

$$a_y/g = t/2h \tag{11}$$

where t is the track width of the vehicle and h is the height of its center of gravity (c.g.), the other terms being previously defined. Equation 11 is termed the rollover threshold by vehicle dynamicists or the static stability factor (SSF) by NHTSA. The terms are used synonymously herein. Equation 11 predicts the lateral acceleration level (g's) necessary to cause inside tire lift-off prior to possible vehicle rollover. It involves only two parameters related to vehicle geometry (track width and c.g. height) and no tire properties. Static stability factors predicted from this simple mechanics model range from 0.4 for heavy trucks to 1.7 for sports cars [2]. The lower the SSF, the greater is the propensity for rollover to occur – i.e., vehicles having higher values of SSF are safer, *ceteris paribus*.

The same free body diagram (Figure 14.9) can be used to show that

$$a_y/g = \mu$$

where μ is the coefficient of friction between the tire and road surface . Thus, high μ surfaces are required to effect untripped rollover while low μ surfaces promote lateral sliding of the vehicle.

Representative values of the static stability factor or rollover threshold for various vehicles are given in Table 14.2.

Table 14.2: Representative SSFs predicted for various vehicles [5]

Vehicle	Class	SSF
1998 Chevrolet Astro	Minivan	1.12
1998 Chevrolet Lumina	Full-size car	1.34
1997 Ford Ranger	Small pickup truck	1.07
1998 Dodge Neon	Small car	1.44
1998 Ford Explorer	Sport utility vehicle	1.06

The understeer gradients for these same vehicles are given in Table 14.1. It is apparent that vans, pickup trucks and SUVs (so-called light trucks for fuel economy rating purposes) have lower rollover thresholds than passenger cars principally due to their higher centers of gravity. The problem is exacerbated in light trucks as passengers, cargo, and/or luggage are added because the vehicle c.g. tends to move upward and rearward with added weight. Both of these movements have a potentially destabilizing effect on stability: the upward movement of the c.g. decreases the rollover threshold (Equation 11) and its rearward movement decreases the understeer coefficient (Equation 7).

Since this elementary, quasi-static[5] model lacks a suspension and does not consider time-dependent steering inputs, it overpredicts the lateral g's necessary to produce rollover in controlled experiments. Stability factors (static and dynamic) predicted from a

[5]The term quasi-static and steady-state are used synonymously.

variety of more complex models incorporating a generalized vehicle suspension and time varying steering inputs are given in Table 14.3 for a generic small car having an SSF of 1.25. Although there is a large reduction in the stability factors when dynamic steering inputs are considered, the ability of the advanced models to properly discriminate among the differing rollover levels obtained from measurements made on vehicles of a given class (such as SUVs) is no better than that given by the rollover threshold or SSF defined by Equation 11. Further, it is again appropriate to point out that tire properties do not appear explicitly in either the elementary or more complex models – though the compliance of tires subjected to a vehicle roll moment, not a big effect in any case, could be accounted for in the suspension parameters used in the more advanced models. Those interested in those issues from a vehicle dynamics perspective should consult the chapter references, namely [2 and 7].

Table 14.3: Prediction of small car rollover propensies from various models
[7, p. 342]

Time Dependence	Vehicle Suspension	Static or Dynamic Stability Factor
Quasi-static	No	1.25[6]
Quasi-static	Yes	1.19
Step-steer Input	Yes	0.92
Sinusoidal Steer	Yes	0.80

While tire properties do not appear explicitly in any of the rollover equations, some implicit factors are present. For example:

a) slight changes in inflation pressure produce very small changes in vehicle c.g. height and possibly tire-road friction coefficient and cannot be effectively employed to greatly change the rollover propensity of a given vehicle;

b) large reductions in inflation pressure (~ 25%) will tend to reduce the cornering force available for untripped rollover as well as the cornering stiffness of the tire (affecting understeer behavior); however, such large pressure reductions adversely impact tire durability, rolling resistance, hydroplaning and high speed behavior.

c) as tires wear, the c.g. height of the vehicle is slightly lowered, thereby marginally increasing the SSF;

d) in wet weather driving, the road surface friction coefficient is reduced, thereby increasing the chance of vehicle slide-out rather than an untripped rollover in driving maneuvers. Tripped rollovers, however, remain a possibility if the sliding vehicle encounters an obstacle;

e) by installing wheels with negative offset[7] on front and rear axles, vehicle track width

---

[6] SSF predicted from Equation 11.

[7] Offset is the horizontal distance from the mid-point of the wheel rim to the wheel disk. It may be positive, negative or zero.

is increased thereby increasing SSF markedly;

f) by designing a vehicle to accommodate tires of smaller overall diameter, the c.g. height is lowered and SSF is increased; this approach would seem to be impractical because of performance, ground clearance and marketing issues.

The appeal and utility of the simple approach used herein to develop Equation 11 lies in the demonstrated correlation of SSF with accident statistics [6]. These statistics, based on more than 200,000 instances of rollover, show that such events increase appreciably when the SSF falls below 1.20. Gillespie [2, p.329] shows similar trends based on much older data. Thus, SSF continues to be the best, and easiest to implement, predictor of catastrophic vehicle rollover.

Fortunately, the static stability factor for the most rollover prone class of vehicles sold in the U.S. market (SUVs) has been increasing – especially since the year 2000. The sales weighted average SSF trends for different vehicle classes are shown in Table 14.4.

Table 14.4: Sales-weighted average SSF trends for different vehicle classes [8]

	Model Year					
Vehicle Class	1980	1985	1990	1995	2000	2003
Passenger Cars	1.36	1.36	1.37	1.41	1.42	1.41
Minivans	N/A	1.11	1.16	1.19	1.24	1.24
Pickup Trucks	N/A	1.18	1.17	1.18	1.18	1.18
Sport Utility Vehicles	1.07	1.08	1.07	1.09	1.11	1.17
Full Size Vans	N/A	1.09	1.09	1.11	1.12	1.12

The positive trend for some of the more recent production vehicles is partially due to changes in geometry (t/2h ratio), and the rising penetration of advanced electronic vehicle systems that preferentially control driving and braking forces on all four tires of an automobile which reduces the development of potentially de-stabilizing yawing motions.[8] As electronic stability control (ESC) systems are increasingly being offered to purchasers of new cars, it is expected that rollover thresholds, as predicted by Equation 11 supplemented by a government mandated dynamic on-road test sensitive to the presence (or lack thereof) of ESC, should continue to show evolutionary improvements over time.

14.5 Concluding Remarks

This chapter has narrowly focused on the role of tires in contributing to possible loss of vehicle control through oversteer or rollover. While the equations employed are elementary, tires are shown to strongly influence vehicle handling but have little effect on rollover, *per se*, unless some unforeseen action shifts the control balance away from understeer leading to a potential accident. The interested reader should refer to references cited herein for deeper insights into these and other aspects of vehicle dynamics.

---

[8]Large yaw and roll motions occur prior to vehicle rollover; 3-D models incorporating both yaw and roll response are discussed by Gillespie [2].

References

1. J.Y. Wong, *Theory of Ground Vehicles*, Third Edition, Wiley, New York, 2001.
2. T.D. Gillespie, *Fundamentals of Vehicles Dynamics*, Society of Automotive Engineers, Warrendale, PA, 1992.
3. H.B. Pacejka, *Tyre and Vehicle Dynamics*, Butterworth-Heinemann, Oxford, 2002.
4. SAE Recommended Practice J266, Steady-State Directional Control Test Procedures for Passenger Cars and Light Trucks, Society of Automotive Engineers, Warrendale, PA, 1996.
5. W.R. Garrott, et al., Experimental Examination of Selected Maneuvers That May Induce On- Road Untripped, Light Vehicle Rollover. Phase 2 of NHTSA's 1997-1998 Vehicle Rollover Research Program, National Highway Traffic Safety Administration, DOT HS 808 977, East Liberty, OH, 1999.
6. *Rating System for Rollover Resistance, An Assessment*, Transportation Research Board Special Report 265, National Academy Press, Washington D.C., 2002.
7. R. Stone and J.K. Ball, *Automotive Engineering Fundamentals*, Society of Automotive Engineers, Warrendale, PA, 2004.
8. M.C. Walz, Trends in the Static Stability Factor of Passenger Cars, Light Trucks, and Vans, National Highway Traffic Safety Administration, DOT HS 809 868, Washington D.C., 2005.

Test Questions

1. On-road tests show that a sports car designed for responsive handling has a measured understeer gradient of 1.1 deg/g. It weighs 3200 lb with the driver and has a 55/45 static split in front-to- rear axle weight distribution. The wheel base is 103 in. and the cornering stiffness of the tires varies with load as shown:

Tire Load (lb)	Cornering Stiffness (lb/deg)
450	180
675	230
900	260
1125	280

   a) Quantify and discuss the changes in vehicle directional control that can occur if a tire puncture happens in a front vs. a rear position.
   b) If 400 lb of "cargo" are placed in the vehicle with the resultant of the added weight acting over the rear axle, compare and contrast quantitatively the expected handling behavior vs. the original unladen condition (with four inflated tires).
   c) Determine the steer angle required to negotiate:
       - a 300 ft radius curve at 50 mph;
       - a 1000 ft radius curve at 100 mph.

2. Derive an equation for the rollover threshold for a vehicle traveling around a superelevated curved highway with a transverse slope angle? Discuss the implicit role that tire properties may have, if any, on the results.

Chapter 15
Introduction to Tire Safety, Durability and Failure Analysis
by J.D. Gardner and B.J. Queiser

Chapter 15
Introduction to Tire Safety, Durability and Failure Analysis
by J.D. Gardner and B.J. Queiser

1. Introduction
Over time, as science, engineering, and manufacturing technology have advanced, tires have offered an increasingly higher degree of utility, reliability, and value. However, tires can become damaged, or when pushed beyond their limits, they will fail. Pneumatic tires have always had a certain failure rate, and for this reason, vehicles have typically carried spare tires—in the early days, more than one. Over time, failure rates have decreased, but not vanished.

Tires are subjected to a wide variety of use and operating conditions, depending on the vehicles they are attached to, the use and maintenance habits of their operators, the environment in which they operate, and random events that can inflict damage or affect their operation. While great strides have been made in design and manufacturing, with rare exception, it is what a tire experiences or is exposed to in the field that determines whether it will fail in service.

Still more complicated is the issue of safety. Tire failure during operation, for instance on a highway at speeds safe for conditions, is the precursor to an inconvenience, i.e. pulling over and applying the spare, or, it is the first in a series of events that may lead to loss of control, and in some cases an accident. However, the vast majority of the time tire disablements do not result in an accident [1].

Performing a failure analysis on a tire is a scientific process that begins with an understanding of the product, including its materials, mechanics, and operational characteristics. These items are evaluated as evidence that tells a story through testing, inspection, and evaluation.

The goal of this chapter is to outline elements of tire safety, basic mechanics and factors pertinent to tire durability, including common tire failure modes and analysis. These subjects can be very broad, thus it is not practical to deal with all of them. The tire photographs and examples shown in this chapter are intended to illustrate the concepts being addressed and do not include all of the possible variants that can occur in testing or result from use in the field.

2. Tire safety
2.1 Definition
The issue of tire safety is more complex than assessing the mere occurrence of a tire failure; because a tire has failed does not necessarily mean that it was unsafe. If that were true, all tires could be deemed unsafe because all tires can be made to fail under some conditions. Tire safety is usually part of a complex relationship involving the tire itself, human beings, a vehicle or service equipment, and other external elements. There are two primary areas of tire safety that pertain to failure:

· Tire servicing and maintenance
· On-vehicle, in-service conditions

In the first case, potential harm or injury is associated with mounting and demounting tires, performing maintenance on wheels and rims, and in making repairs. In the second case, the definition of tire safety is essentially the same as that for vehicle safety. Tires are part of a system that has the function to transport humans and goods as quickly, comfortably, efficiently, and ecologically sound as possible, without causing an unreasonable risk of harm or injury [2]. Tire safety in this context includes proper tire selection for the vehicle (including load, inflation, speed, and other performance parameters); proper tire design for durability and resistance to failure; and a dependency on the end-user for care and maintenance.

2.2 Tire Servicing/maintenance safety

Typical tire servicing safety issues involve mounting/demounting and maintenance/repair. Some of the potential situations that may result in serious injury or death include the following:

· Tire/Wheel Mismatch—The wheel is too large or too small for the tire bead diameter. During inflation, in an attempt to seat the beads, the tire could burst or de-bead if the inflation pressure exceeds safe levels.
· Bead Hang-Up—The tire is not properly fitted to the wheel or one of the components is out of tolerance or inadequately lubricated. If excessive inflation is applied to seat the bead(s), the tire could burst or de-bead.
· Improper Rim Parts/Assembly—Mismatched, damaged/deteriorated multipiece rim components, or incomplete assembly. During inflation, or subsequently, the rim assembly could burst apart.
· Ether—Use of a volatile gas to assist in seating beads and inflation can cause an explosion of the tire.
· "Zipper" Rupture—During handling or inspection of a pressurized tire with suspected damage, fatigued ply cords may break one after another until a rupture occurs, typically in the upper sidewall, with explosive force and instantaneous air loss.
· Welding—Repair of a wheel component by welding, brazing, or otherwise heating while a tire is mounted and inflated to it can cause excessive pressure to build up within the tire and result in an explosion.

Tire and wheel servicing should be done only by specially trained persons using proper, prescribed procedures and equipment. For instance, the tires and wheels themselves are designed to facilitate the process of mounting/demounting; tires have strong, but flexible, beads, and wheels for passenger cars and light trucks are typically a single -piece, drop-center design [3]. In addition, warnings, recommendations, and step-by-step procedures are outlined by the Rubber Manufacturers Association (RMA) and the Occupational Safety and Health Administration (OSHA) [4 - 9].
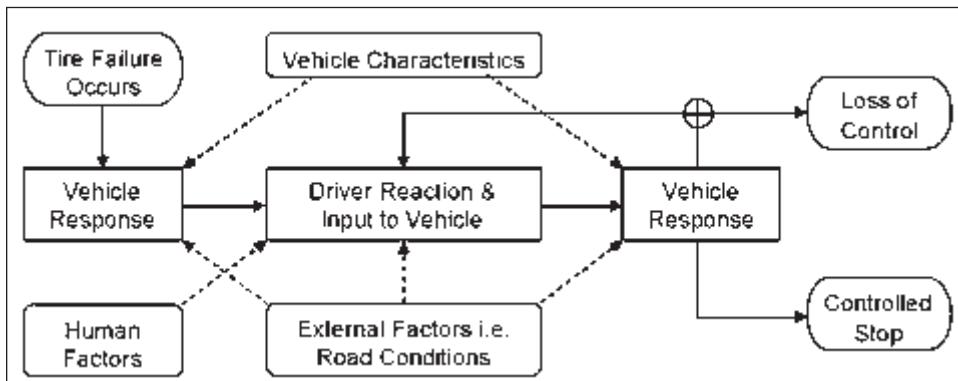
2.3 On-vehicle, in-service tire safety

When a tire fails in service, the safety aspects are far more complex than the servicing issues outlined previously. Additional variables are involved, such as different vehicles, different drivers, and different operating conditions. These variables combine to influence

the ultimate result of a tire failure. A flow chart of the occurrences and influences is shown in Figure 15.1.

Whether a tire failure in service is a safety issue depends upon numerous factors. Therefore, assessing tire safety in this context can be difficult.

Figure 15.1: Processes/influences following in-service tire failure [1, 10]

2.4 Crash data perspective
Nearly 3 trillion (3,000,000,000,000) vehicle miles were traveled and 6.3 million crashes were reported in the United States for 2003. While the trend in the number of crashes during the previous 15 years was essentially flat, the number of miles traveled each year steadily increased. The resulting crash rate, therefore, steadily declined, and the vehicle occupant crash fatality rate for 2003, the data most currently available at the time of writing, was at an all time low since record keeping began in the mid-1970's [11].

Data trends that began in the 1990's indicate a shift of fatalities from passenger cars to sport-utility vehicles (SUVs) and other light trucks, which correlates with an increase in popularity of these vehicles. However, the data indicates that increasing light truck fatalities, particularly those for SUVs, have been offsetting fatality reductions credited to increased seat belt use, reduced drunk driving, increased use of child restraints, and the proliferation of airbags [11 - 13].

2.5 Tire failures and crash causation
In 2003, nearly 300,000,000 new passenger and light truck tires were shipped [14] to supply the U.S. fleet of about 230,000,000 registered vehicles [11]. For myriad reasons, tires fail in use every day. For instance, in 2002, AAA responded to 2,400,000 "flat tire" service calls [15].

However, in-service tire failures result in a crash, presumably from loss of vehicle control, only a fraction of the time, from 0.06% [1] to about 0.50% [16] of overall occurrences. These statistics indicate that very few accidents are caused by tire failures. In fact, the mere inclusion of a readily-accessible spare tire as a vehicle component indicates that it can be applied when needed, i.e. at the side of the road after pulling over.

2.6 Warranty and adjustment data
Historically, the tire industry and the National Highway Traffic Safety Administration

(NHTSA) have relied upon warranty or adjustment data as a measurement of tire performance and customer satisfaction in the field. An adjustment refers to the credit a customer receives at a retail outlet when a tire is exchanged under the terms of a warranty, or for goodwill. Therefore, the data may include adjustments made on tires that are not under warranty or for conditions not covered by a warranty, simply to maintain or foster customer satisfaction.

Adjustment data is prolific enough to provide statistical significance. It streams in continually to the tire manufacturer where it is coded to identify the reason for the adjustment, which can be for a variety of reasons, including durability, ride, comfort, and cosmetics. By compiling and monitoring the data, a tire manufacturer can identify product performance and/or customer satisfaction trends. This feedback can be used to implement countermeasures on a timely basis, to enhance business relationships, and for future product development. Because of its commercial value, tire manufacturers keep adjustment data confidential.

There is no standard within the tire industry or government regarding the evaluation of adjustment statistics; for instance, there is no level which automatically triggers attention. In addition, adjustment data for one tire may not necessarily be meaningfully compared with data for other tires. For instance, performance trends that are apparent from a review of data for a large, conglomerate population of tires may not apply to a particular tire because of differences in such parameters as design or application. Essentially, to evaluate the performance of a particular tire, it is necessary to examine that tire's unique performance history.

2.7 Personal injury and property damage claim/lawsuit data

Additional information is received by tire manufacturers in the form of personal injury and property damage claims or lawsuits that may allege harm from a tire failure. While there is no industry definition for a claim, for purposes here, a claim is a request for compensation made directly to a tire manufacturer for alleged property damage or personal injury (or both) incurred from a tire failure. A tire company may have a standard policy or procedure to handle these claims. A lawsuit involves a legal complaint against the tire manufacturer filed in a civil court. Similar to claims, lawsuits pertaining to alleged tire failures usually involve property damage or personal injury (or both).

Property damage claims, typically the greatest portion of the data, are usually made for the costs of repairing minor sheet metal or paint damage and/or replacing a damaged wheel as a result of a tire failure. Personal injury claims are typically made for medical and/or compensatory expenses associated with bodily harm incurred in an accident after a tire failure. Lawsuits involve similar issues, however, usually to a greater degree, particularly in situations where an accident has resulted in serious injuries or death.

Tire companies take these matters very seriously for a variety of reasons. Inspections of the tire(s) are undertaken by company personnel, and often independent consultants. Accident investigations/reconstructions, depositions, and requests for documents/records may also be completed. It is in the best interest of the tire manufacturer to determine the validity of the allegations and the cause of the tire failure.

Claims and lawsuit data differs from adjustment data in numerous ways. For instance, it is not generally as voluminous; therefore, its statistical significance is limited. As well, the data is not as timely as that of adjustments. Lawsuits, in particular, are typically not filed soon after an incident and the tire(s) in question may not be made available for

inspection for months, even years. In some cases alleging tire failure, the tire may no longer be available, or may not be provided for inspection, making it practically impossible to determine the cause of the alleged failure.

Another fundamental difference between a claim/lawsuit and an adjustment is that an adjustment related to tire durability is commonly made before the tire has sustained a complete failure. This is accomplished through routine inspection of tires by the consumer or tire service professional or because of other warning signs, such as loss of inflation, vibration, and irregular wear. Almost all claims and lawsuits could have been an adjustment if the tire was removed from the vehicle sooner. Failed tire adjustments are also examples of a failure that does not result in an accident, contrary to some allegations involving claims and lawsuits.

2.8 Early warning data systems

The adjustment, claims, and lawsuit data may be monitored concurrently with "early warning" database and analysis systems. By monitoring trends related to safety, such as accidents, the tire manufacturer may be able to identify product performance that is not meeting expectations or other potential issues. Resulting actions may be to more closely monitor a specific product or application, issue a technical service bulletin or consumer advisory, or initiate a replacement campaign or recall.

2.9 Consumer recommendations

While it is not practical to list all of the relevant tire safety warnings and recommendations here, the following basic advice is often repeated:

· Check tire inflation monthly and before long trips or when carrying extra load. Use a pressure gauge, since radial tires can be deceptively low on pressure even if they pass a quick visual check. Follow the vehicle manufacturer's recommendations for inflation as indicated on the vehicle tire placard or vehicle owner's manual.

· Properly load the vehicle and tires. Do not exceed tire load capacity and follow vehicle manufacturer's recommendations as indicated on the vehicle tire placard or owner's manual.

· Routinely rotate and evaluate tires for tread wear and damage or unusual conditions, such as bumps, bulges, cracks, worn areas, etc.

· Tires must be properly repaired—an improper repair can be inadequate and can contribute to an eventual tire failure.

Information may be found at tire retail outlets and on-line, at www.rma.org (Rubber Manufacturers Association), www.nhtsa.gov (National Highway Traffic Safety Administration), and tire manufacturer websites.

3 Fundamentals of tire durability

3.1 The nature of tire durability

Tires are the vehicle component which transfers forces and moments to the vehicle in response to driver and vehicle dynamics directives, the least of which being to carry the load of the vehicle and occupants. In addition, tires can be exposed to a plethora of road (and off-road) surfaces, environments, operating conditions, maintenance habits, and damaging events.

For purposes of this chapter, the term "durability" refers to the structural integrity of

the tire in service. The rate of wear of tread rubber may constitute a durability parameter in some cases, but it is not addressed here.

Tire engineers and chemists optimize the tire structure for performance factors relating to traction, wear, ride comfort, handling, durability, rolling resistance, and more. Cost or economy is a factor as well. Within the limits of science and engineering, certain parameters may conflict with one another, or require engineering trade-offs. For this reason, the marketplace contains a wide range of tire products designed with different operating and performance parameters in mind, such as those necessary for off-road versus highway, high speed use. From a durability perspective, the tire is designed to provide a balance of desired attributes, while relying on the end-user for basic care and maintenance.

Because a tire has failed does not necessarily mean that there was anything deficient in its design or manufacture. Structural failure of a tire can occur at virtually any point in its expected lifetime, whether it is brand new with full tread depth, or nearly worn out after years of use. Any tire can fail. The objective is to design a product that meets internal company, industry, and government standards, and performs according to the consumer's needs until the tire is worn out and replaced. However, as previously noted, external factors such as severe service conditions or damaging events can affect the tire's ability to endure and shorten or end its service life.

3.2 First principles of tire durability

Fatigue is a common cause of failure of a steel belted radial tire in use. Within the tire structure, fatigue occurs through a process of progressive fracturing from excessive stress and strain during cyclic loading [17]. As a viscoelastic material, contributing factors to the strength of rubber include temperature and rate of loading [18]. Additional influences include damage inflicted upon the tire structure from breakage, tearing, puncturing, contamination, and intra-carcass pressurization. Damage to the tire may accelerate the fatigue process or cause an immediate failure.

3.3 Deflection

The most basic factor that affects tire durability performance is the vertical deflection. Using the simple model shown in Figure 15.2, when a tire is bearing a load P the deflection d is the difference between the unloaded radius r_o and the loaded distance r_L between the wheel center and the ground:

$$d = r_o - r_L$$

Considering the pressurized tire as a vertical spring, and applying Hooke's Law:

$$P = K\,d$$

where the vertical stiffness, K, is primarily attributable to the internal inflation pressure. (It should be noted that the precise load/deflection behavior is more complex than this model; see chapter 5.)   The work W done in compressing a linear spring is

$$W = \tfrac{1}{2}\,K\,d^2$$

As the deflection increases, more work energy is imparted to the tire, whether from situations involving a decrease in K (such as from reduced inflation pressure) or an increase

in load. As the tire rolls, a mechanical energy loss mechanism manifests itself through the generation of heat [19 - 21]; see chapters 2, 11 and 12. As the tire deflection and/or load increases, the energy loss increases as well, as shown in Figure 15.3 for a steel belted radial tire.

Figure 15.2: Unloaded and loaded tires
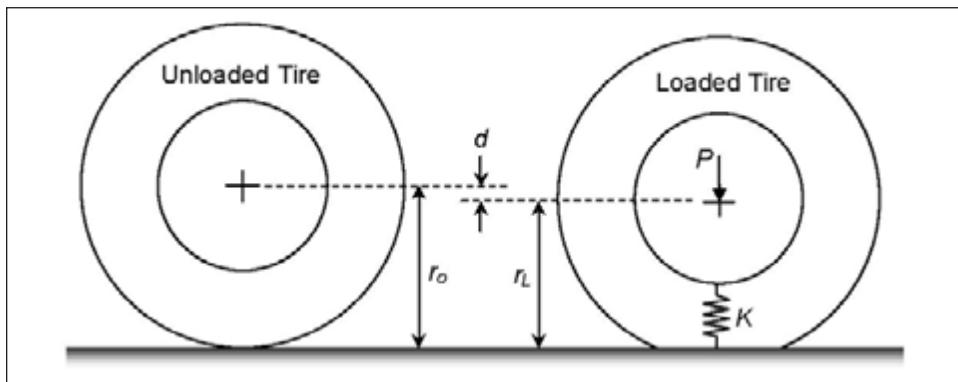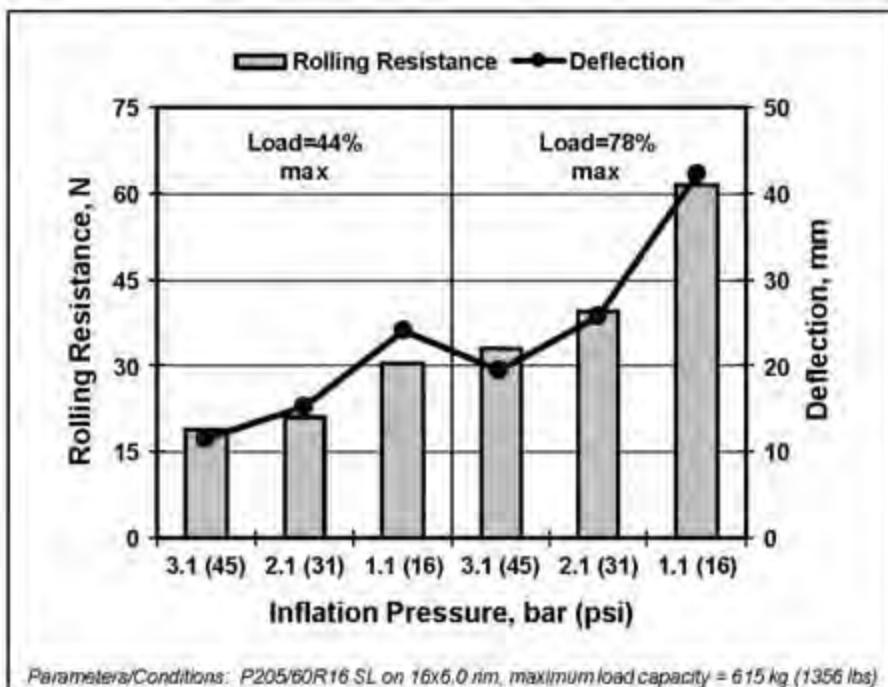
Figure 15.3: Rolling resistance and deflection of a passenger tire

The effect of the tire deflection can be seen by observing the size, shape, and pressure of the contact patch—also known as footprint—of a tire on a flat surface, as shown in Figure 15.4. The length of the footprint in the circumferential direction increases with an

increase in load or a decrease in inflation pressure, which is correlated to the amount of deflection (chapter 5).

In Figure 15.4, note that the footprints at the lowest inflation pressure, particularly at the highest load, indicate a tendency of the tread to lose contact pressure in the outer shoulder groove locations; essentially due to a buckling of the tread and belt structure; see chapter 7 for further details.

Of interest to tire durability is the strain energy density in the location between the belt edges in the shoulder areas of the tire. The interlaminar strains developed in the belt package are due to bending and stretching of the tread area that occurs during the deflection process. These strains are concentrated at the belt edges [22]. The fundamental mechanics of stress and strain development are now evaluated using finite element analysis (FEA) techniques. One such example is shown in Figure 15.5, where a solid element cyclic strain energy density (SED) plot is given for a P215/55R18 standard load (SL) tire.

Figure 15.4: Flat surface contact conditions of a passenger tire
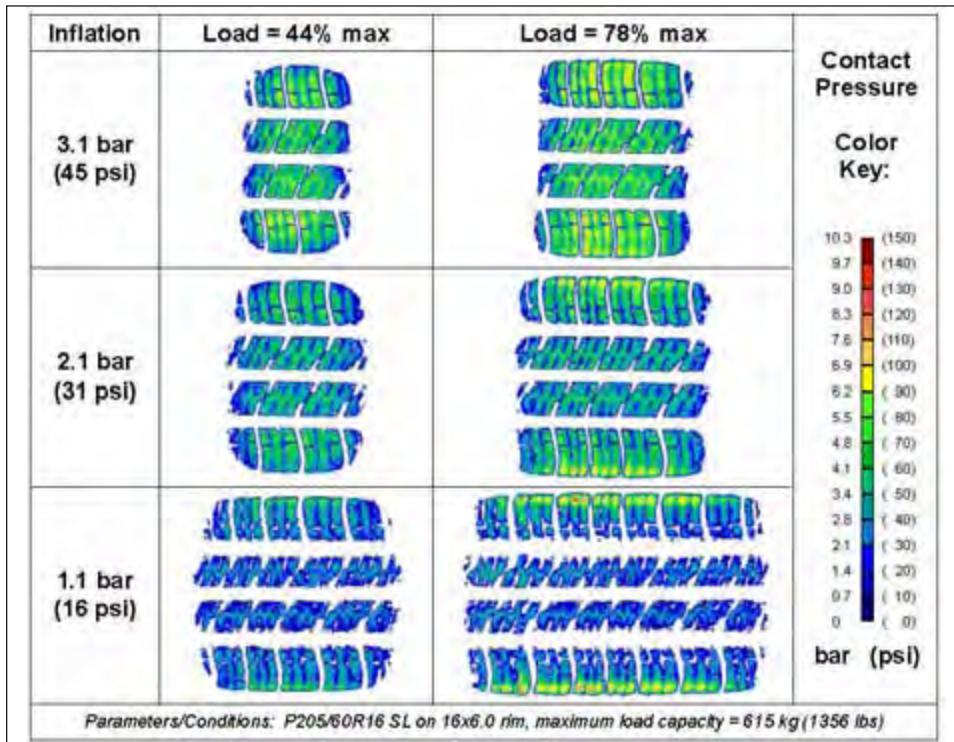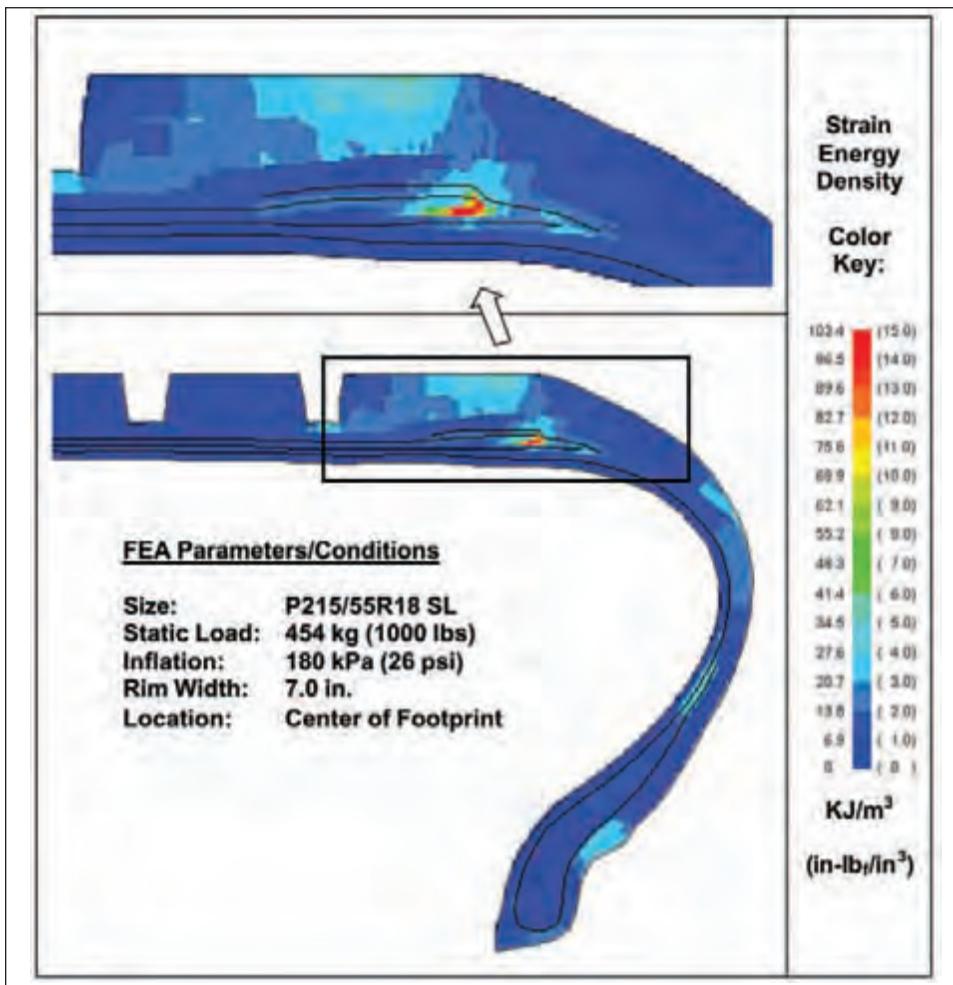
Figure 15.5: Example of FEA solid element cyclic strain energy density

3.4 Heat

As previously mentioned, tires develop heat as they are operated. As a tire is cyclically deflected, it reaches thermal equilibrium in terms of its internal component temperatures, and in terms of the contained air temperature within the tire cavity. Changing operating conditions and physical changes to the tire structure itself can change the state of equilibrium.

Elevated and extended heat generation is a primary factor in the breakdown of a tire. Increased heat decreases rubber tear resistance which promotes crack initiation and propagation [18]; see chapter 2. Permanent degradation of material properties from exposure to elevated temperatures occurs as well, depending on the exposure history.

The shoulder areas of a radial tire are generally the highest in heat generation. Figure 15.6 illustrates the increasing temperatures that develop in the shoulder area when a tire is operated with increasing deflection. Rubber deterioration (reversion) from excessive heat build-up results in a decrease in tensile strength and a general softening. This break-

down from heat is an additive effect that can drive the temperature higher still. Ultimately, a component or portion of the tire can reach a critical temperature range where the deterioration of the rubber can cause detachment from the tire of pieces or whole sections of the tread.   Reverted rubber has a porous appearance, such as the pieces of reverted tread rubber shown in Figure 15.7. Other components may melt, such as the polyester body cord shown in Figure 15.8.

Figure 15.6: Thermographic images of a tire operated with decreasing inflation [23]
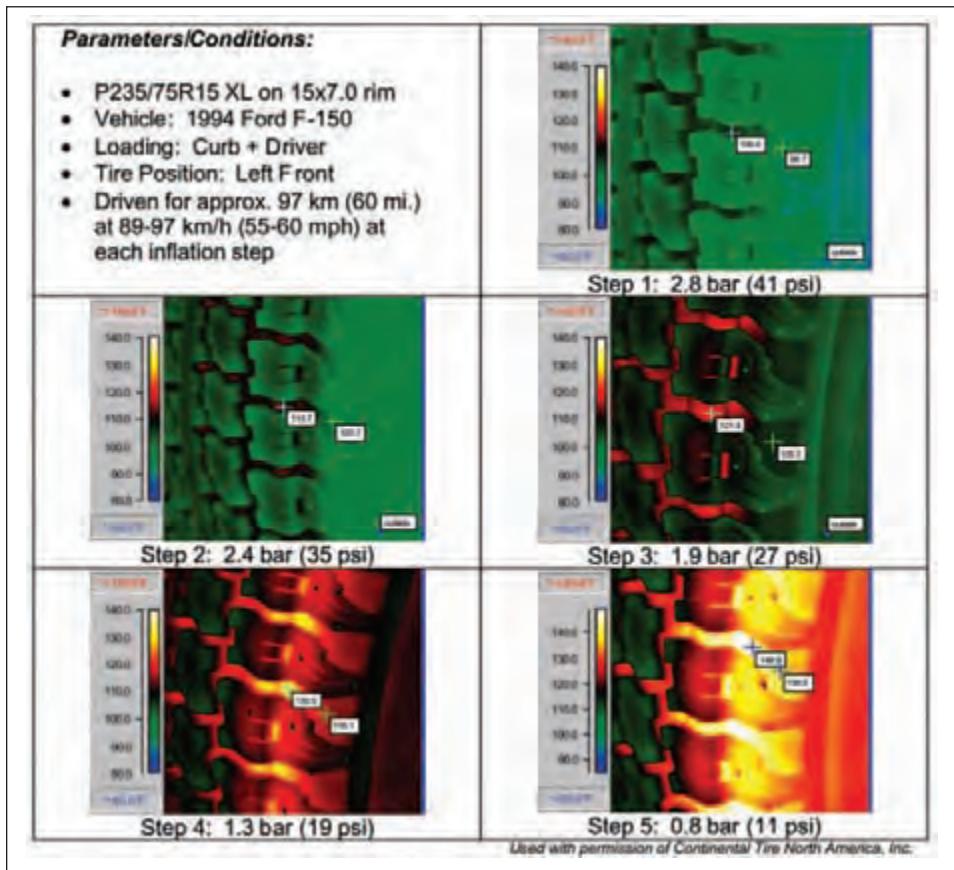
Figure 15.7: Examples of reverted tread rubber

Figure 15.8: Melted polyester cord (lower sidewall)

3.5 Speed
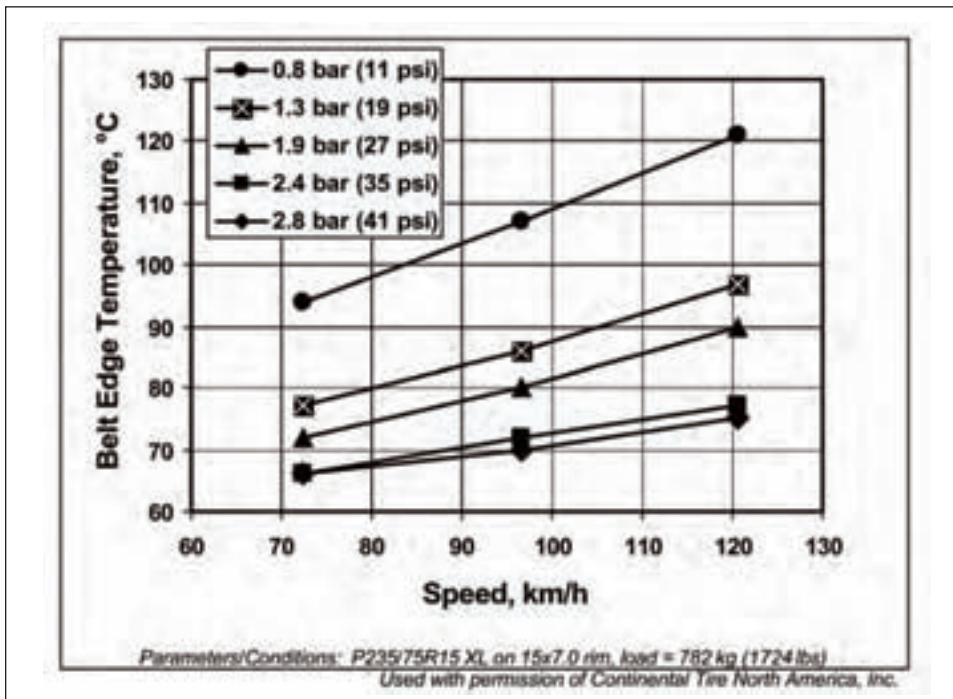
Changing the speed of tire rotation affects the centrifugal force and frequency of the deflection cycle. Corresponding changes in the stresses and strains developed in the tire components affect the tire's heat build-up characteristics. Additional deflections occur from "standing waves", treated in chapter 10. This phenomenon depends upon the size, construction, stiffness, and especially the rotational speed of the tire.

The fundamental effect of speed is its influence on the frequency of cyclic deformation. With each rotation, a given radial section of the tire undergoes a stress-strain cycle as it passes through the contact patch. Increasing the cyclic frequency increases the heat that develops, and hence affects the performance of the tire as a whole, particularly parameters that relate to durability.

The centrifugal force acting on a body is directly proportional to the mass, the distance from the axis of rotation, and the square of the angular speed of rotation. For a tire, the tread and belt structure is located the greatest distance from the center of rotation and comprises a substantial portion of the tire mass. It is thus evident that centrifugal force can affect the tread area, particularly the shoulders, which are concurrently undergoing a stress/strain cycle with each rotation.

Testing has verified that increasing speed causes an increase in tire temperature, particularly in the shoulder area [23, 24]. In Figure 15.9, results are shown for a tire tested at speeds up to 120 km/h (75 mph) with numerous inflation pressure settings at constant load. The results indicate a near-linear relationship between speed and temperature, with increasing slope as the inflation pressure was decreased.

Figure 15.9: Belt edge temperature of a tire operated with increasing speed at various inflation pressures
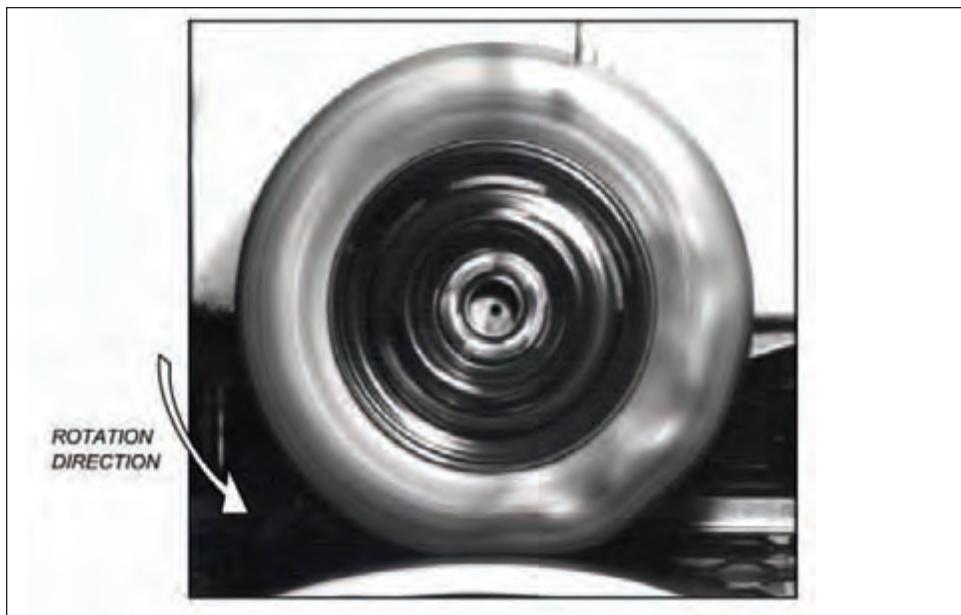
Combating the effects of centrifugal force may be accomplished in various ways. Other than reducing tire size or mass, which may not be practical, a common design solution is the use of a circumferential reinforcement in the tread area. The tire industry typically refers to this feature in a tire construction as a cap ply, strip, or layer, which may be a single or multiple component. It is typically placed beneath the surface of the tread around the steel belts, often at the shoulders. In essence, these components act to restrict the growth of the tire that results from the effects of centrifugal force during high speed operation. Generally, for passenger car tires, the speeds at which these design features are particularly necessary are usually greater than 180 km/h (112 mph). However, light truck tires, or tires with heavy tread lugs, for instance, may require reinforcement at lower speeds.

For a tire with certain construction and stiffness parameters, the standing wave phenomenon emerges at a specific rotational speed; see chapter 10. Essentially, a standing wave forms when the tire tread and sidewalls do not recover from the effects of one deflection before re-engaging with the contact surface and initiating another deflection cycle. Figure 15.10 exemplifies this wave deformation in a tire operating at relatively high speed; note the rippling of the sidewall and tread that is initiated at the contact patch and extends nearly 180° around the tire. Standing waves are particularly destructive due to additional stress, strain, and heat generation. Increasing the stiffness of the tire and reinforcing the tread region, such as through the use of cap ply materials, effectively shifts the onset of standing wave generation to higher speeds.

Note that design changes to counter the effects of centrifugal force and standing waves do not alter the frequency of cyclic deformation and do not usually influence the stress/strain durability performance of a tire performing at typical highway speeds or lower. Therefore, addressing tire durability performance in one range of speeds may not meet the preferred tire design methodology and engineering parameters in another speed range.

Figure 15.10: Standing wave deformation

ROTATION
DIRECTION

3.6 Lateral force / turning
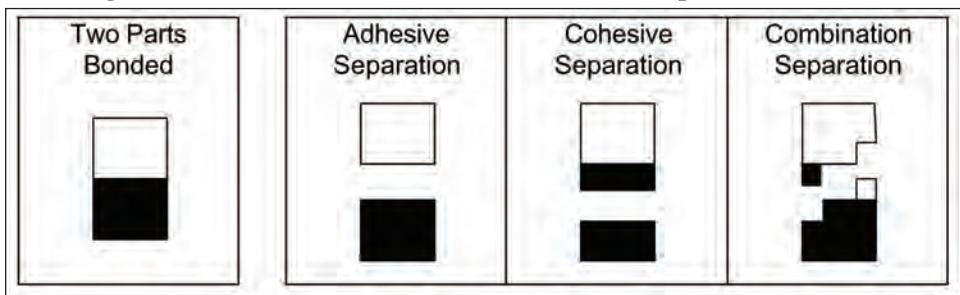
Beyond the scope of this chapter, but addressed in chapters 4 and 8, is the contribution to tire stress and strain through the simple matter of turning or applying a lateral force to a deflected tire, as on the steering axle of a vehicle. Particularly relevant are the contortions of the tread and belt plies through the contact patch during turning, not only in creating additional stress and strain, but also in contributing additional heat from increased hysteresis and tread abrasion. Variables affecting the magnitude of this effect include the duration and rate of turning and the slip angle history through the turn.

3.7 Tire structural failures

With a sufficiently high applied stress or strain, every material is subject to failure.   In use, tire materials are subjected to the effects of fatigue, wear, heat, corrosion, and other external damage. The magnitude and frequency of externally applied forces and moments can ultimately cause rubber to fatigue and tear or cause steel and polyester cords to rupture. The process of tire structural failure can progress slowly, or be essentially immediate; it depends upon the structure itself, the magnitude and rate of imparted energy, and external conditions such as temperature.

When a tire is cured, the separate tire layers and components do not mix or become homogeneous. Rather, during the vulcanization process, the materials chemically bond to one another. Fracture and crack propagation can occur between the materials at their interface, within an individual material, or along a failure surface that is a combination of both, as shown schematically in Figure 15.11.

Figure 15.11: Adhesive, cohesive and combination separation fractures

Cracking of rubber can begin at or near an interface with a tire cord, as in the case of the polyester cord shown in Figure 15.12. Such cracking may progress around the cord itself, creating a condition known as socketing. Continued crack growth can result in smaller cracks meeting one another and progressing further. Figure 15.13 shows a typical separation between the steel belt edges. Fracture of cords or filaments can lead to structural weakness that causes a whole-tire rupture or leads to more slowly developing internal ply separation, depending on the extent of the damage. Tensile fracture of a steel cord filament is shown in Figure 15.14.

Figure 15.12: Incipient cracking adjacent to polyester cord
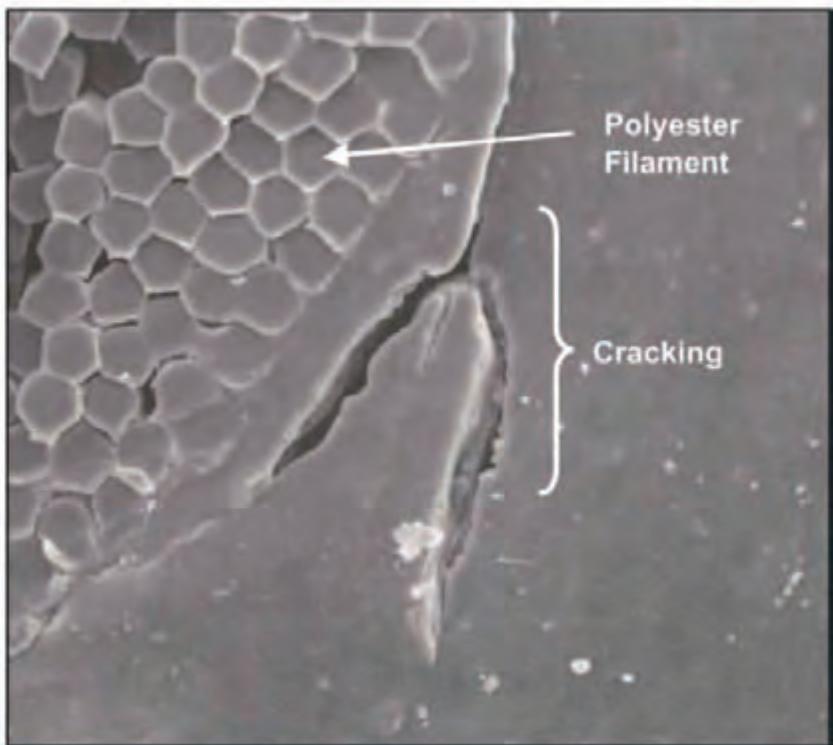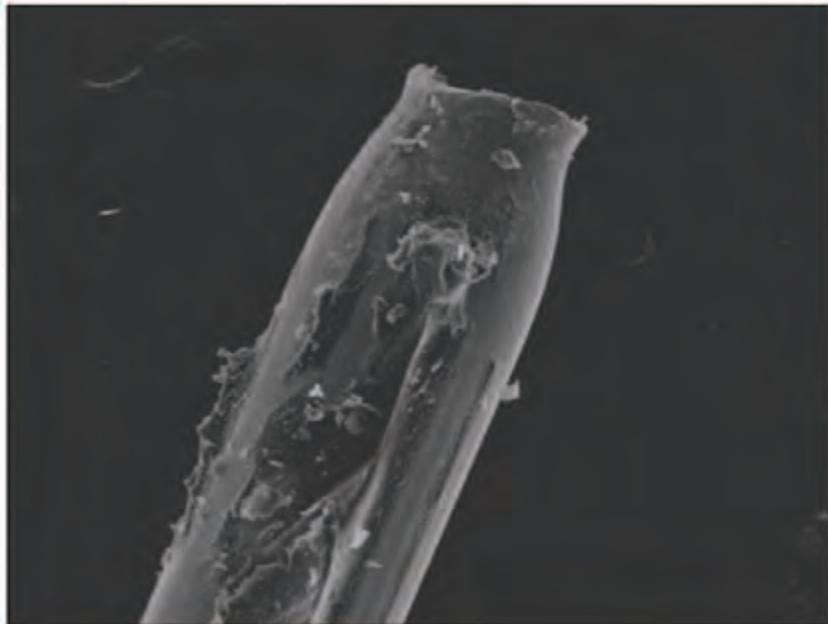
Figure 15.13: Cracking between steel belt edges

Figure 15.14: Tensile fracture of steel cord filament

4. Fundamental tire failures and analysis

4.1 Common in-service tire failure modes

In-service tire failures, although increasingly rare, occur in one of three common modes: a run low, sidewall flex break; a belt and/or tread detachment; and a rapid loss of air through a break in the tire.

4.2 Run low / flex break

If a tire is run in a grossly overdeflected condition at highway speeds, at or near flat condition, it is severely flexed in the upper sidewall and tread shoulder regions. Flex fatigue and extreme heat build up in these areas of the tire, and even melting of polyester radial body cords as in Figure 15.15, ultimately result in circumferential breakage of one or both sidewalls from the entire tread structure. It is common for these failures to arise from continued loss in inflation pressure during operation.

Figure 15.15: Broken, heat-fused polyester body cords, upper sidewall

4.3 Tread/belt detachment

If a tire is operated with a propagating separation in the tread region, the separation can progress to a level that results in one or more stabilizer plies (i.e. steel belts) and/or the tread rubber to be torn from the remainder of the tire body, as in Figure 15.16. Incipient separations grow circumferentially around and laterally across the tire before reaching a threshold that results in the detachment. These failures commonly occur at highway speeds when the centrifugal force is sufficiently high.

Figure 15.16: Exemplar tire after tread/belt detachment

4.4 Rapid air loss

When a cut or break occurs in a tire, the air within the cavity will escape through the open-ing. Obviously, the rate of air loss depends on the size of the hole. Rapid air loss, or sud-den deflation, occurs when the size of the opening is substantial, i.e. greater than 6.4 mm (0.25 inch), as in Figure 15.17. This failure mode is sometimes referred to as a "blow out."

Figure 15.17: Upper sidewall break through to cavity

4.5 Common causes of in-service tire failures
Since it is not practical to address here all of the possible conditions and causes of failure, this section presents the types of tire failure causations that occur most frequently.

4.6 Overdeflection
As noted previously, the deflection of a tire is a dominant parameter in tire performance because it determines stress, strain, and heat generation. When a tire is designed and tested for a rated load and inflation pressure, it has a specific deflection and will perform satisfactorily at that deflection within a reasonable tolerance. Overdeflection is defined as a deflection that is greater than that intended for the rated load and inflation pressure. Overdeflection occurs when the load is excessively high, or the inflation pressure is too low, or when a combination of load and inflation pressure creates an excessively high deflection. A moderate degree of overdeflection, depending on speed and other operating parameters, can initiate and propagate steel belt edge separation and tread/belt detachments. Severe, gross overdeflection, generally at nearly flat-tire conditions, commonly causes sidewall flex break failures.

If overdeflection occurs for a short period of time, the tire failure itself may be the only evidence of overdeflection. If the overdeflection occurs over a longer period of time, it can be evidenced by conditions such as rim grooving [23], balance weight impressions, and/or tread wear patterns.

4.7 Intracarcass pressurization
Since the advent of tubeless tires in the 1950's, intracarcass pressurization has existed. A tubeless tire is a pressurized air container. The pressure inside the cavity is higher than atmospheric pressure, hence there is a tendency for the air molecules to migrate out from

the air cavity to the atmosphere. First, they must pass through the innerliner which is specifically formulated to resist air permeation, typically through the use of halogenated butyl rubber. Any air molecules that pass through the innerliner then continue through the remainder of the tire until they eventually reach the atmosphere. The overall rate of air permeation through the tire depends on many factors. Loss in inflation pressure is generally 1-2 psi per month for steel belted radial passenger and light truck tires.

During the process of air permeation a pressure gradient exists within the tire structure. Over time, this pressure gradient attempts to reach equilibrium. If the interior of the tire is breached by a puncture, impact, tear to the bead, etc., pressurized air within the tire cavity can pass directly into the tire structure. This creates two problems. First, the air brings moisture and excess oxygen into the tire structure, which can break down chemical bonds and consequently the adhesion/cohesion of internal components. Secondly, since the tire cavity pressure is higher than the equilibrium gradient pressure within the tire structure, the pressurized air will tend to force the structural components of the tire apart, particularly at high stress/strain areas of the tire such as the belt edges. These two conditions can lead to or aggravate separations, including in some cases tread/belt detachment.

4.8 Cuts and punctures

Cuts and punctures usually refer to tire damage by relatively sharp objects that penetrate into the tire or through the tire into the tire cavity. Some cuts and punctures are from objects that may also be considered an impact or road hazard injury, the resulting damage from which is addressed in a subsequent section.

Cuts and punctures that are small, at the time they enter the tire, cause an opening in the tire that extends partially or completely through the tire. The damage to the tire is localized and does not initially affect the structure of the tire beyond the immediate area. Obviously, the primary concern with a puncture through to the tire cavity is the loss in inflation pressure that inevitably occurs, if not immediately. If the hole does not penetrate into the cavity, the potential for, and manner of, any tire failure depends on the location and size of the hole and whether moisture or other contamination can enter into the tire structure through the opening. If the hole is large or in a high stress/strain area, such as the steel belt edge or upper sidewall, the hole can grow in size to a point where a rupture of the tire occurs. For tread penetrations, contact pressure between the tire and road can drive moisture and other contaminates further into the tread and belt structure—i.e. along the steel cords— causing corrosion and an adhesion failure separation, ultimately failing in a manner such as tread/belt detachment.

If the hole penetrates into the tire cavity, the tire must be discarded unless it meets the criteria for puncture repair set by the tire manufacturer or RMA [25, 26]. If a repair is performed against recommendations and the tire is returned to service, it is likely that the repair will be inadequate or fail, as discussed in the following section.

When a tire is operated with an unrepaired cut/puncture that extends into the cavity, the tire is likely to fail as a result of underinflation, intracarcass pressurization, or a combination of these. Underinflation occurs statically and/or dynamically when the puncturing object comes out of the tire or it does not completely seal the hole allowing air to escape to the atmosphere. As previously addressed, intracarcass pressurization occurs when the hole is not sealed within the tire cavity, i.e. at the innerliner, but is sealed or partially sealed from the atmosphere. In this situation, air is forced into the tire structure causing a pressurization of the tire carcass itself, leading to separation and failure.

4.9 Improper repair

Improper repairs typically fall into two categories: repairs that were made after the tire was excessively damaged in service and repairs that were performed against tire manufacturer or industry recommendations. If a repair is not done in a timely manner, the tire can be damaged through continued use in an underinflated condition and/or from air migrating into the structure around the object causing intracarcass pressurization. In this situation, no matter how well the puncture repair is made, internal separation or other structural damage cannot be repaired and may certainly progress until the tire fails in service. Thus, careful inspection of the tire for externally apparent signs of damage to the tire structure, including an examination of the cavity/innerliner, is required prior to performing a repair.

Once a tire has been determined to be suitable for repair, if proper procedures and repair materials are not utilized, the tire is more likely to fail after returning to service. For instance, current industry recommendations stipulate that passenger and light truck tire repairs should only be made if they are in the central portion of the tread region of the tire, excluding the shoulder ribs. In addition, the puncture hole should be no greater than 6.4 mm (0.25 inch) in diameter [25]. If the hole is larger, it is likely that structural damage has occurred that weakens the tire or that even after the hole is filled, moisture or other contamination will enter into the tread and belt structure causing the adhesion to break down. If structural damage, such as broken steel cords, is large enough, the tire is likely to rupture at the repair location as in Figure 15.18(a/b).

A puncture hole must be filled with a plug material and sealed with a patch on the innerliner surface. Without a patch, as in Figure 15.19(a), air can migrate into the tire structure causing intracarcass pressurization. If the hole is not filled, as in Figure 15.19(b), moisture or other contaminants can migrate into the tread and belt structure from the external environment and cause a breakdown of adhesion.

Even when the proper materials are used, if repair procedures are not followed properly, the tire can be damaged further and lead to a failure. For example, in Figure 15.20, excessive buffing of the innerliner has exposed the polyester body cords; this condition permits air to migrate into the tire structure causing intracarcass pressurization.
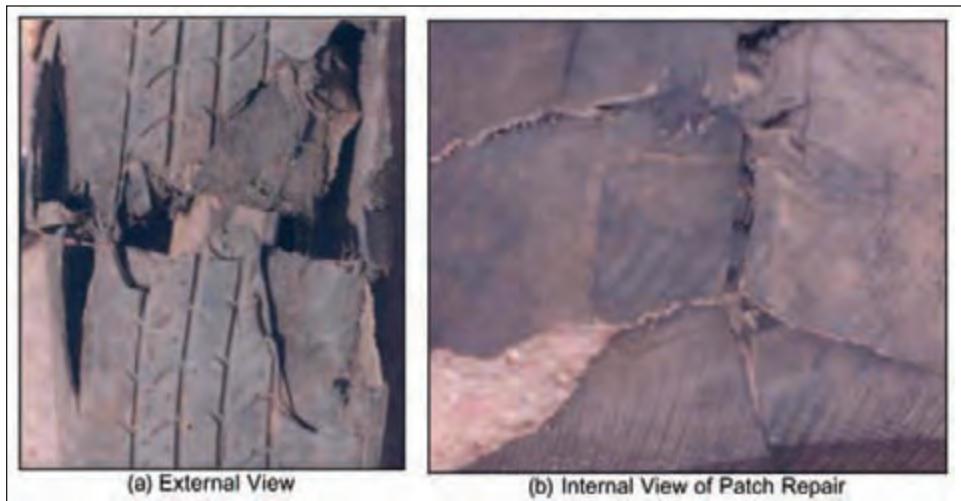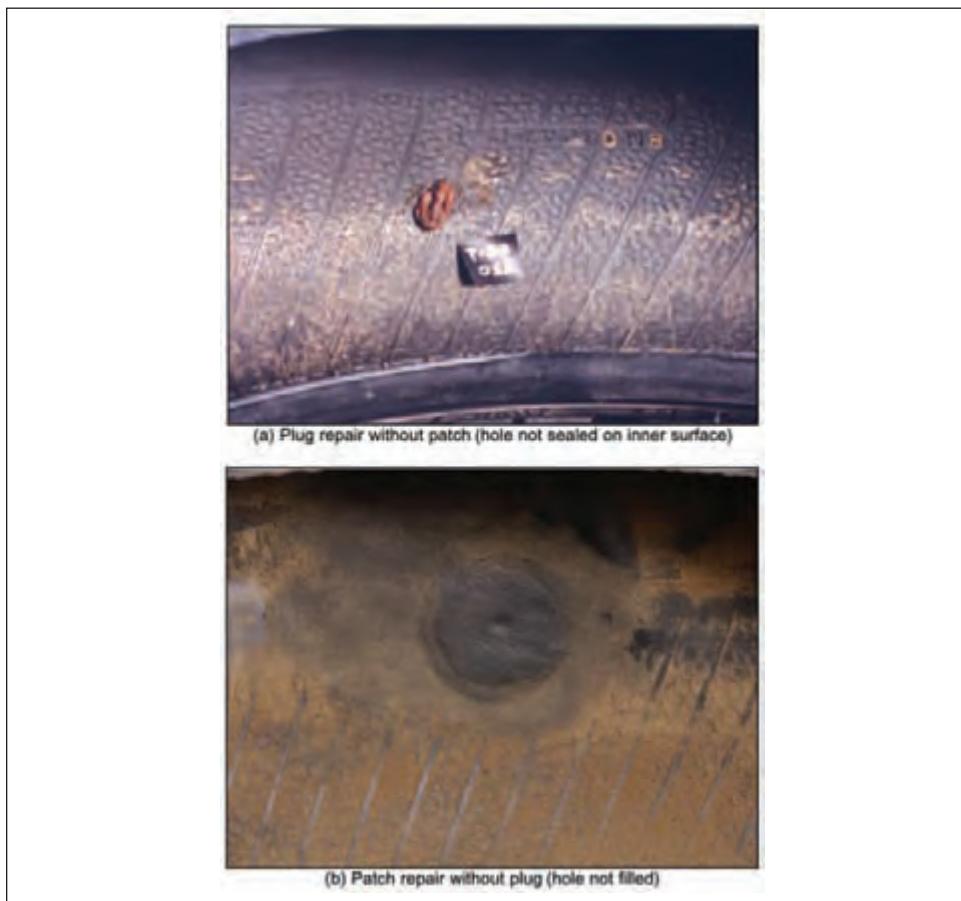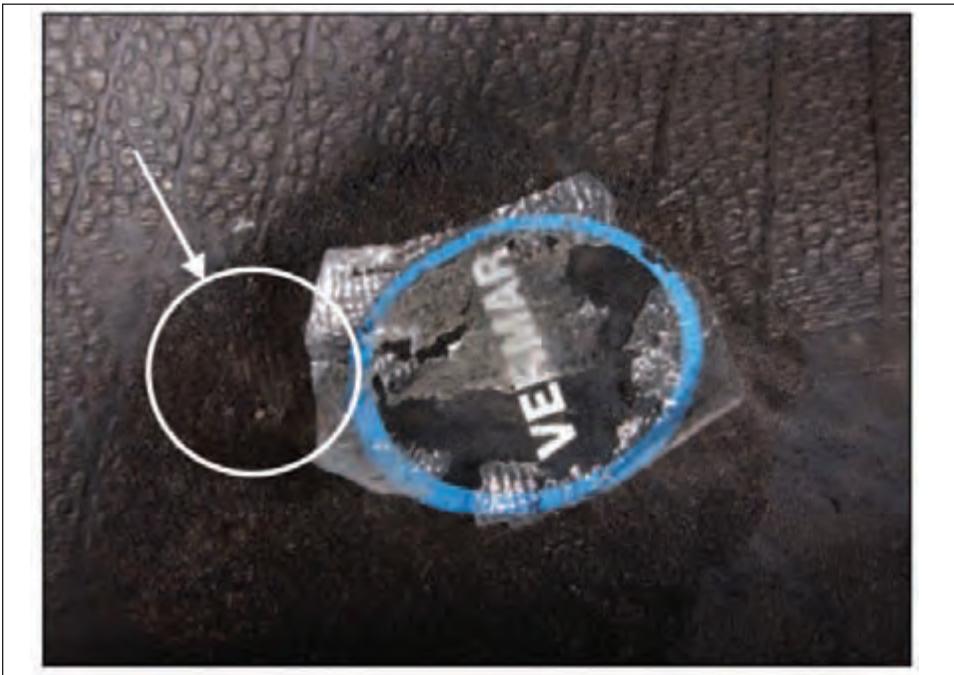
Figure 15.18: Excessive puncture damage with rupture at repair location

(a) External View

(b) Internal View of Patch Repair

Figure 15.19: Examples of improper puncture repair

(a) Plug repair without patch (hole not sealed on inner surface)

(b) Patch repair without plug (hole not filled)

Figure 15.20: Excessive buffing has exsposed polyester cords

4.10 Impact / road hazard

Tire impacts, or road hazard injuries, are one of the most common initiators of tire failures [27]. They occur when a tire operating in service encounters an object or irregularity in the roadway. Despite the improvements in highway design and maintenance over the years, studies have found that debris clutters highways throughout the United States [28]. In addition, deterioration of the roads and highways themselves present obstacles that tires can hit while in service. A resulting road hazard-related tire failure can occur immediately, or hundreds or thousands of miles after the impact. When a tire strikes a relatively small object such as a nail, the tire is likely to be punctured, as previously addressed. When the object is larger, what happens to the tire depends on several factors:

· The size and shape of the object.

· The texture and sharpness of the object.

· The orientation of the object and tire; where and at what angle the object impacts the tire.

· The inflation pressure in the tire and the load on the tire.

· The rate at which the object deforms the tire.

· The degree of damage that occurs to the tire structure during the impact and how that damage propagates or grows over time if the tire remains in service.

From an engineering point of view, impact damage is simply the result of energy imparted to the tire. One must therefore understand how the structural elements of a tire are loaded and how that loading changes when the tire attempts to absorb the energy of an impact.

The body cords, belt cords, beads and any other reinforcing materials in the tire are under tension due to the inflation pressure [29]. When a tire is loaded and deflected, cor-

nering and other loads are superimposed on the inflation loads [30]. When a tire encounters an object or irregularity in the roadway such as a pothole, rock, or other debris, the part of the tire (i.e. tread, sidewall) that comes in contact with the object attempts to take the shape of the object by deforming around it. Hence, the initial orientation of the reinforcing cords and rubber must change to accommodate or envelope the object. Moving a reinforcing cord relative to its rubber matrix has been studied in the laboratory by pulling cords (steel, polyester, etc.) out of rubber pads or other configurations. The results of such testing depend on the rate and degree of strain applied to the cord and its surrounding rubber material. At lower strains, the cord rubber matrix changes shape and no damage occurs. At higher strain levels , the cord or the rubber matrix fractures. For a group of cords, a combination can occur. Figure 15.21 shows the results of a steel cord pull test from a rubber block matrix; in this case the cord fractured.

Figure 15.21: Steel cord tensile pull test, resulting in cord fracture
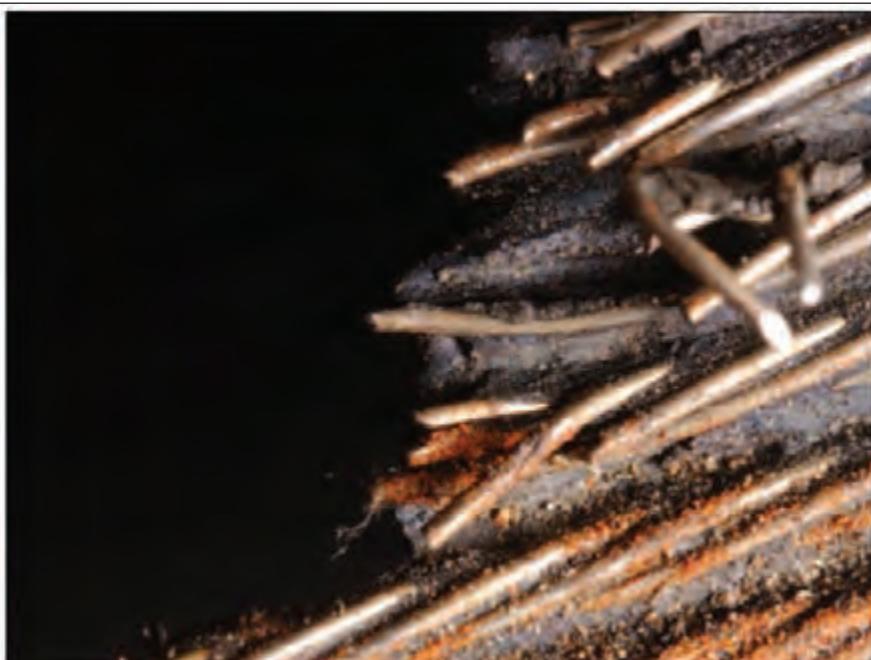
The same phenomenon can occur in a tire during an impact [31]. The additional stress/strain loading imparted by an impact is different for different cords within the same tire. Thus, after an impact injury, a unique damage pattern will exist in the tire. In some cases the damage pattern will be so extensive that a hole will be present and an immediate loss of air will result, as in Figure 15.17. In other cases, the tire will be damaged internally, but capable of continued operation until it fails sometime after the impact.

If, when, and how the tire fails depends on the initial damage pattern and the type and severity of the subsequent operation. The failure modes can be as diverse as the damage pattern. They can be localized to the impact area or spread circumferentially around the tire. If the impact causes a tear between the belts, broken cords, or a combination of these, the damage can propagate and result in a tread/belt separation or detachment.

In some cases, an opening or radial split of the tire cavity, particularly the innerliner, will occur at the time of the impact. Over time, air will migrate through the split into the tire causing intracarcass pressurization (previously addressed). The tire can subsequently fail from a tread/belt detachment or other related failure mode.

Rarely is the object that the tire impacted available for inspection or the cord loading and orientation at the time of the impact known. Impact failures are analyzed by examining any damage the impact caused, such as rubber tears, fractured steel cord as in Figure 15.22, broken body ply cords, radial splits, propagation patterns, surface damage to the tire, and wheel deformations.

Figure 15.22: Broken steel cords of a stabilizer (steel belt) ply

4.11 Tire defects

The word "defect" has different meanings to different people depending on the context. For example, a police officer investigating an accident might refer to a worn out tire or an impacted tire as a "defective " tire, even though the tire was designed and manufactured flawlessly. Lawyers and judges attach a legal meaning to the word "defect." Hence, care should be used when using the word so that the intent is clear. Modifiers in front of the word such as "manufacturing" will make the meaning clearer. In some cases, engineers use words such as "anomaly" to avoid confusion.

A tire design defect usually refers to a defect that occurs in a tire during the design and development phase of the tire. In other words, the tire was manufactured in compliance with the specification and allowable manufacturing tolerances, but still has a defect. A tire manufacturing defect usually refers to a defect that occurs during the manufacturing process. In other words, the tire was properly designed and developed, but during production it deviated from the design specification and/or allowable manufacturing tolerance.

Design and manufacturing defects generally fall into two categories: those that affect the performance of the tire and those that affect other things such as the appearance of the tire. The categories that affect the performance of the tire include those that are safety related and those that are not. Missing or misplaced components, improper vulcanization, and foreign material are examples of manufacturing defects. However, whether a defect such as a misplaced component is a performance or safety related issue depends on where and how the components are misplaced.

Because the major tire manufacturers have been in business for decades and have extensive research, design, development, manufacturing, and quality control activities and procedures—and employ thousands of specially trained scientists, engineers, and production personnel—design and manufacturing defects in tires are extremely rare. Because of this, defects tend to be one-of-a-kind occurrences and are typically evaluated accordingly.

4.12 Bead breakage / mounting accidents

Mounting accidents are rare, but occasionally occur when safe mounting procedures are not followed. An accident of this nature typically happens when a tire bead ruptures during the initial inflation process to seat the beads on a rim. Safety procedures in effect to prevent injury are designed to prevent a bead from breaking in the first place, and to protect a person in the event that a bead does break.

Typical passenger and light truck tire beads are constructed of one or more strands of bronze plated steel wire formed into a hoop called the bead bundle. When the tire is operating in service, the bead bundle is fully seated on the rim and all the wires in the bead bundle are ideally carrying an equal share of the load. Thus, the total strength of the bead bundle is equal to the sum of the strength of the individual bead wires.

During the mounting process of a tire on a drop center rim, the beads must move from the drop center of the rim to the bead seats of the rim. This process is called bead seating and is accomplished through increasing inflation pressure, which pushes the beads onto the bead seat area of the rim. If this process is impeded because of a lack of centering, improper lubrication, a corroded rim, an improper diameter rim for the tire, etc., the bead can become "hung up" and fail to seat properly. In this situation, the circular bead bundle will attempt to straighten (chord) in the location of obstruction. Because the length of a chord is different from the segment of the circle that includes the wires within the bundle, the individual wires will attempt to assume different lengths. As this occurs, the loading on the wires will vary and the strength of the bundle is lowered to the strength of the strand of wire with the highest load. If that wire breaks because the inflation pressure is excessive, the load shifts to the next wire, and so on, until the entire bundle ruptures. When the bundle ruptures, the bead goes over the flange and a person may be injured if they are in the trajectory of the tire/wheel assembly.

In the proper mounting of a passenger or light truck tire, the pressure should never exceed 40 psi to seat a bead. If this rule is followed, the bead will not break even if the tire is in a "hung up" condition. During the bead seating process, the operator should stand clear of the trajectory of the tire/wheel assembly by using a clip-on inflation chuck and an in-line inflation gauge with the tire in a safety cage or secured to the mounting machine. In addition, the components must be matched properly (i.e. 16" tire mounted to a 16" rim), and be clean and free of corrosion, and the beads must be well lubricated and centered before an attempt is made to seat them [6 - 8].

References

1. Baker, J.S. and McIlraith, G.D., Tire Disablements and Accidents on High-Speed Roads, Highway Research Record, Number 272, Highway Research Board, Washington, DC, 1969.

2. Seiffert, U. and Wech, L., Automotive Safety Handbook, SAE International, Warrendale, PA, 2003.

3. Burton, W.E., The Story of Beads and Tires, McGraw-Hill Book Company, Inc., New York, 1954.

4. Care and Service of Automobile and Light Truck Tires Including Recreational Vehicle Applications, Publication RMA ALT 9/95, Rubber Manufacturers Association, Washington, DC, 1995.

5. Care and Service of Truck and Light Truck Tires Including Tires for Buses, Trailers and Other Applications, Publication HTM-2-98, Rubber Manufacturers Association, Washington, DC, 1998.

6. Demounting and Mounting Procedures for Automobile and Light Truck (LT) Tires That Are Used on Single-Piece Rims, Wall Chart DMPAT-7/95, Rubber Manufacturers Association, Washington, DC, 1995.

7. Demounting and Mounting Procedures for Truck/Bus Tires, Wall Chart TTMP-7/95, Rubber Manufacturers Association, Washington, DC, 1995.

8. Multipiece Rim Matching Chart, Wall Chart RMC-7/93, Rubber Manufacturers Association, Washington, DC, 1993.

9. Warning Zipper Rupture, Wall Chart RMA Z295, Rubber Manufacturers Association, Washington, DC, 1995.

10. Ranney, T.A., Heydinger, G., Watson, G., Salaani, K., Mazzae, E.N., and Grygier, P., Investigation of Driver Reactions to Tread Separation Scenarios in the National Advanced Driving Simulator (NADS), DOT HS 809 523, U.S. Department of Transportation, Washington, DC, 2003.

11. Traffic Safety Facts 2003, DOT HS 809 775, U.S. Department of Transportation, Washington, DC, 2005.

12. Shankar, U. and Longthorne, A., Analysis of FARS and Exposure Data Between 1982 and 2002; Why Are We Not Seeing Reduction in Highway Fatalities?, U.S. Department of Transportation, Washington, DC., 2004.

13. Characteristics of Fatal Rollover Crashes, DOT HS 809 438, U.S. Department of Transportation, Washington, DC, 2002.

14. US Tire Industry Facts, Rubber Manufacturers Association, Washington, DC, 2004.

15. Nashworthy, M., "Car Care Month: Tire Technology is on a Roll," AAA Today, Vol. 22, No. 5, September/October 2003, p. 10.

16. "Federal Motor Vehicle Safety Standards; Tires; Final Rule; 49 CFR Part 571, Docket No. NHTSA-03-15400, RIN 2127-AI54," Federal Register, Vol. 68, No. 123, June 26, 2003, pp. 38115-38152.

17. Williams, J.G., Fracture Mechanics of Polymers, Ellis Horwood Limited, Chichester, 1984.

18. Gent, A.N., "Strength of Elastomers," Science and Technology of Rubber, Second Edition, ed. by Mark, J.E., Erman, B., and Eirich, F.R., Academic Press, San Diego, 1994, pp. 471-512.

19. Gehman, S.D, "Rubber Structure and Properties," Mechanics of Pneumatic Tires, ed. by Clark, S.K., DOT HS 805 952, U.S. Department of Transportation, Washington, DC, 1981, pp. 1-36.

20. Rolling Resistance Measurement Procedure for Passenger Car, Light Truck, and Highway Truck and Bus Tires, SAE J1269 Surface Vehicle Recommended Practice, Society of Automotive Engineers, Inc., Warrendale, 2000.

21. Measurement of Passenger Car, Light Truck, and Highway Truck and Bus Tire Rolling Resistance, SAE J1270 Surface Vehicle Recommended Practice, Society of Automotive Engineers, Inc., Warrendale, 2000.

22. Walter, J.D. and Clark, S.K., "Cord Reinforced Rubber," Mechanics of Pneumatic Tires, ed. by Clark, S.K., DOT HS 805 952, U.S. Department of Transportation, Washington, DC, 1981, pp. 123-202.

23. Grant, J.L. Rim Line Grooves as an Indicator of Underinflated or Overloaded Tire Operation in Radial Tires, Paper 45, Presented at the International Tire Exhibition and Conference, Akron, Ohio, September 21-23, 2004.

24. Song, T.S., Lee, J.W., and Yu, H.J. Rolling Resistance of Tires—An Analysis of Heat Generation, SAE Technical Paper 980255, Society of Automotive Engineers, Inc., Warrendale, 1998.

25. Puncture Repair Procedures for Passenger and Light Truck Tires, Wall Chart PRP-PLTT-1004, Rubber Manufacturers Association, Washington, DC, 2004.

26. Puncture Repair Procedures for Truck/Bus Tires, Wall Chart PRP-TBT-1004, Rubber Manufacturers Association, Washington, DC, 2004.

27. Herzlich, H.J., The Effect of Snaked Belt Anomalies on Tire Durability, Paper 15C, Presented at the International Tire Exhibition and Conference, Akron, Ohio, September 12-14, 2000.

28. Forbes, G. and Robinson, J., The Safety Impact of Vehicle-Related Road Debris, AAA Foundation for Traffic Safety, Washingto n, D.C., June 2004.

29. French, R.W. and Gardner, J.D., The Distribution of the Inflation Forces on the Structural Members of a Radial Tire, SAE Technical Paper 820814, Society of Automotive Engineers, Inc., Warrendale, 1982.

30. Walter, J.D., "Cord Force Measurements in Radial Tires," Paper No. 71-RP-A, Journal of Engineering for Industry, American Society of Mechanical Engineers, New York, May 1972, pp. 678-682.

31. Bolden, G.C., Smith, J.M., and Flood, T.R., "Impact Simulations II," (Pending Publication), 2005.

Chapter 16
Non-Destructive Tests and Inspections
by J.A. Popio and T. M. Dodson

Chapter 16
Non-Destructive Tests and Inspections
by J.A. Popio and T. M. Dodson

1. Overview

In 1985 Trivisonno published a technical review of nondestructive evaluation (NDE) techniques used on tires.[1] He reviewed radiography, in particular x-ray; and optical methods including holography and shearography; ultrasound; infrared; and electrical methods such as eddy current. The same methods are used today. Although some NDE equipment has become commercially available, the techniques and procedures often remain proprietary and confidential.

In this section, we review some current techniques and the underlying fundamental principles, and refer to commercially available equipment if it is available.

2. Introduction

Pneumatic tires are complex structures manufactured from many different materials using complex processes in an attempt to meet various performance requirements. Often a tire development or quality engineer would like to answer the question: "How did I do?" Or an automotive engineer may want to know "How do these tires compare internally?" without actually destroying the structure or tire. These questions and the desire to make consistent and reproducible products have promoted the use of non-destructive evaluation (NDE) of tires. Four commonly-used NDE techniques are X-ray, shearography, ultrasound, and eddy current analysis. They aid in evaluating the internal structure of the tire without modifying or changing it. For example, the following conditions or areas of the tire may be studied and analyzed[2]:
- Foreign material in the "green" or uncured tire
- Rust or corrosion of the steel belt
- Sidewall blisters
- Abnormal cord spacing or cord diameter
- Crossed and/or broken body ply cords
- Cord separation
- Steel belt placement (wandering, snaking, scalloping, necking, flaring)
- Loose wires
- Open and heavy splices
- Voids and porosity
- Bead concentricity
- Component thicknesses

3. X-ray examination

X-ray examination of tires started in the 1950s.[3] It is particularly useful when there are gross differences in the density of components, as in tires, and the technique has been widely adopted for nondestructive evaluation. Cost savings can be realized through early identification of tires that do not meet specified construction details or component placement. This allows timely corrections to be made during the production cycle, and reduces

the possibility of customer dissatisfaction.[4]

   Figure 16.1 shows an x-ray beam passing through a tire specimen and reaching a detector.[5] The detector can be radiographic film or paper, or as in this case a direct-view fluoroscopic screen with image intensification. Radiation entering the specimen is absorbed at varying rates depending on the density of components and the existence of a discontinuity. The resultant image is an x-ray shadow of the interior[6], termed a radiograph, that provides information about the internal structure. However, some error exists due to the conical nature of the x-ray beam. Figure 16.2 shows projection or measurement error.[7] Some x-ray techniques correct these errors digitally, others use specified gauge lengths in the field of view, or special panoramic x-ray tubes. Figure 16.3 is a comparison of images from a panoramic tube and from a more conventional x-ray source.[8]

Figure 16.1: Typical X-ray setup.
X-rays pass from the center of the tire to the detector.

Figure 16.2: Measurement error caused by the conical shape of the x-ray beam.
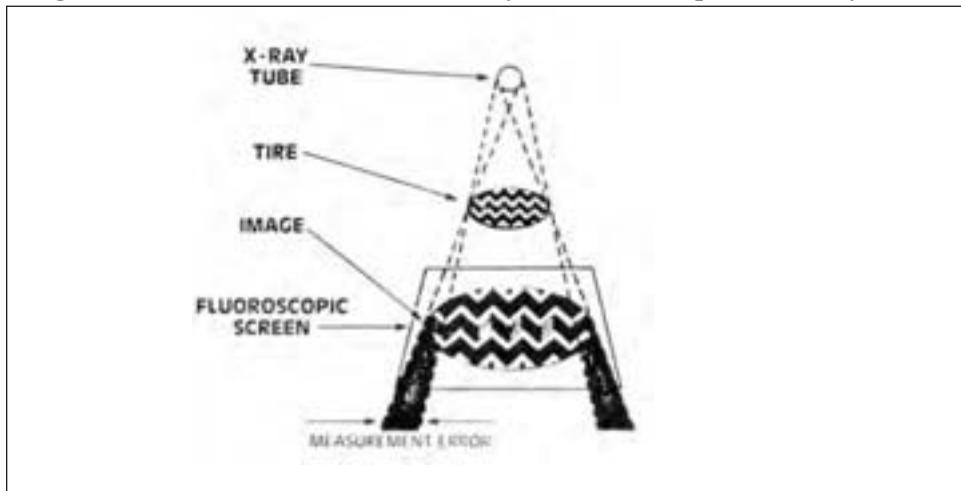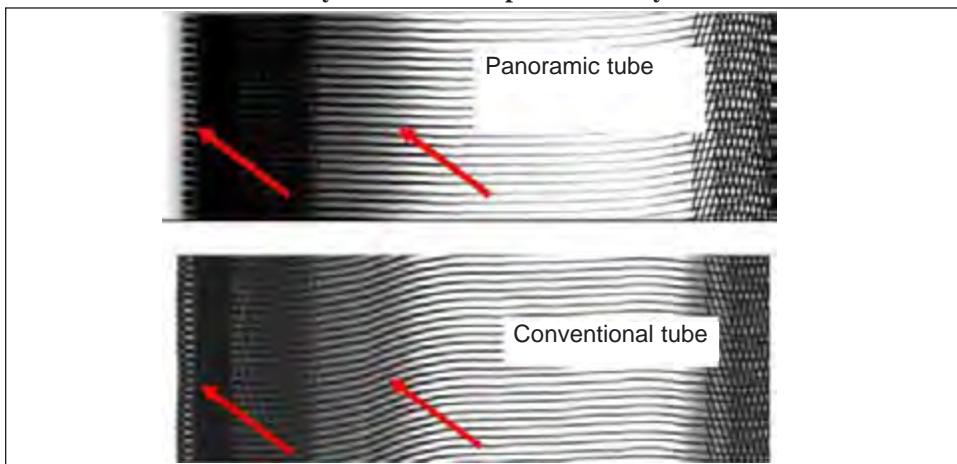
**Figure 16.3: Another measurement error
caused by the conical shape of the x-ray beam.**

X-ray methods are most helpful in studying steel components or other materials that have significantly higher density than rubber compounds. For example, broken, missing, loose or overlapping steel belt cords can readily be detected. Belt placement, belt step, foreign material, and significant corrosion of the steel belt filaments may also be detected. Figure 16.4 shows a variation in belt step. The long white lines directed up and to the right at an oblique angle are from one set of steel belts and the lines directed up and to the left are from another steel belt package. The overlap is not symmetric about the centerline of the tire. Figure 16.5 shows a white object, a stone that is embedded in the tread of the tire. Figure 16.6 shows another piece of foreign material, in this case a nail. Figure 16.7 shows variation in steel cord spacing, and Figure 16.8 shows a loose wire filament.

**Figure 16.4: Variation in the belt step. One belt package is offset from
the other, whereas the belt step should have been symmetrical.**
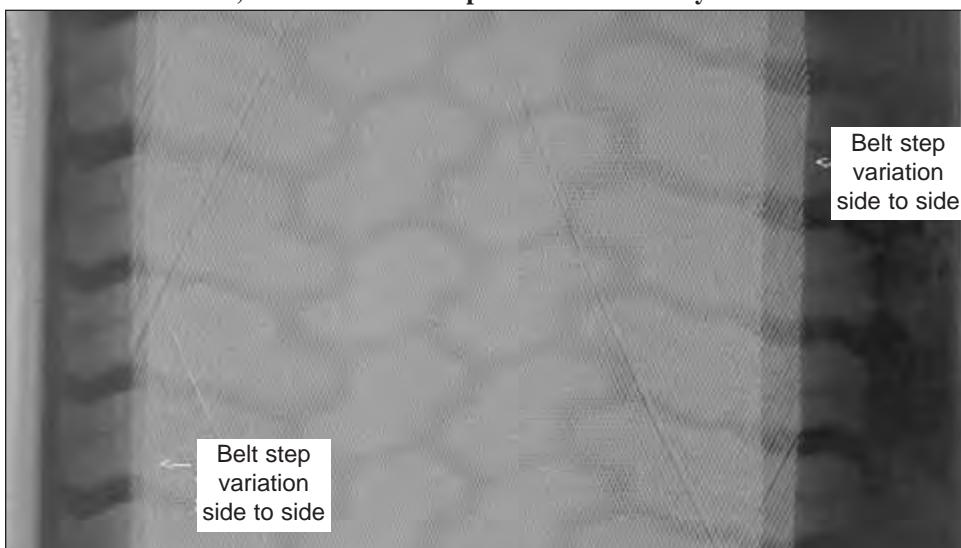
Figure 16.5: A small stone found in the tread of a tire.

Figure 16.6: A nail embedded in the tread of a tire.
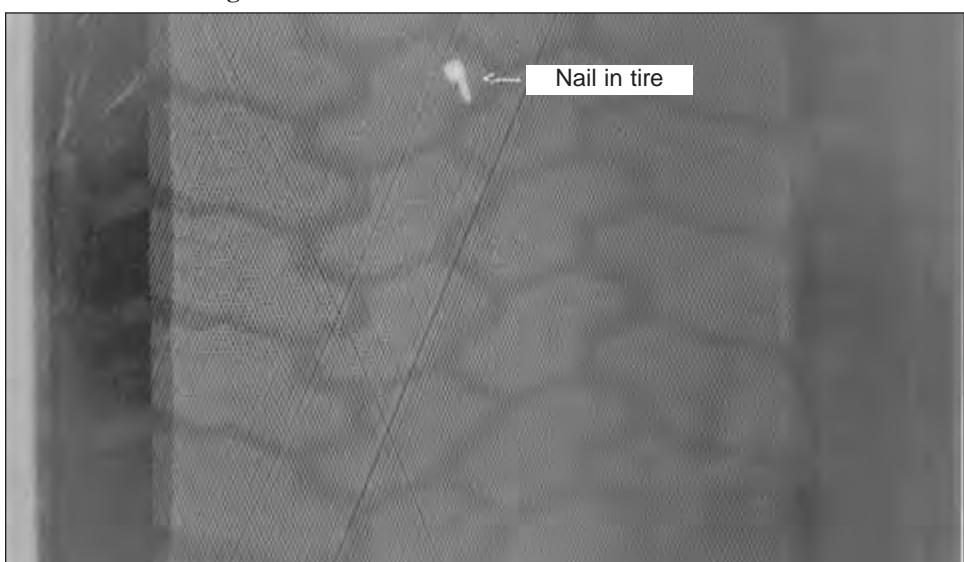
Figure 16.7: A gap detected in the steel belt that runs up and to the right.
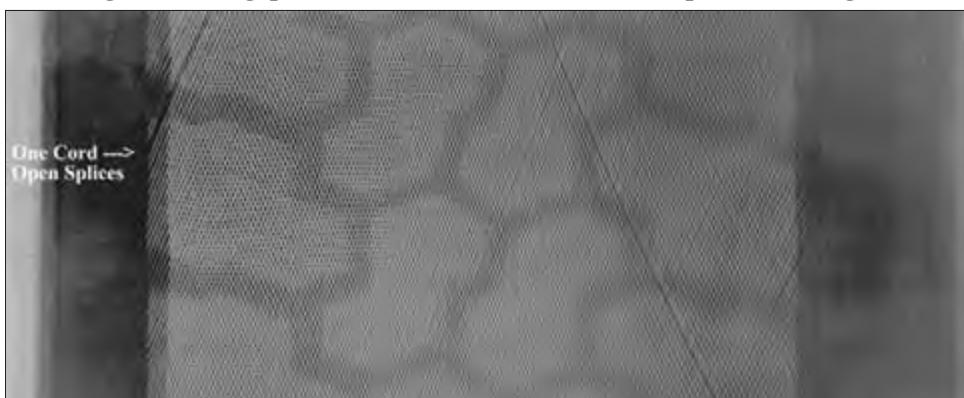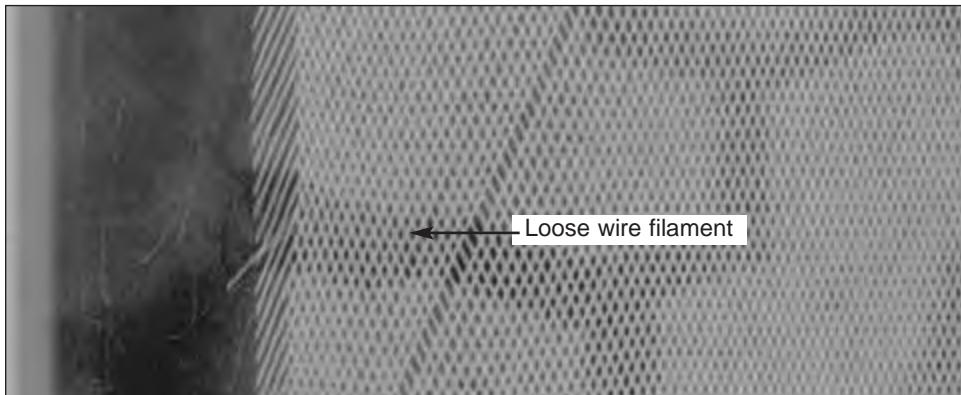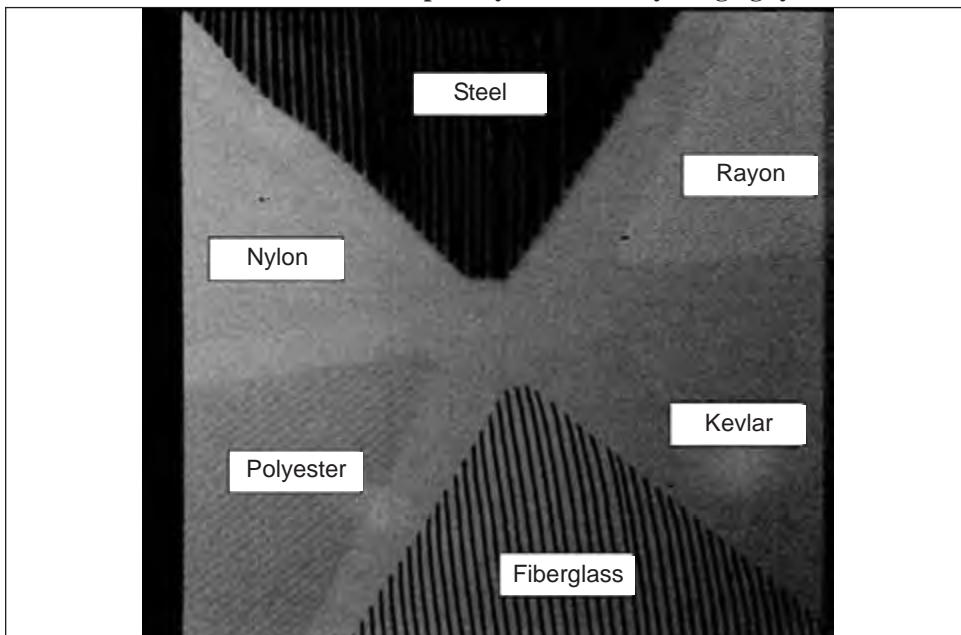
Figure 16.8: A loose wire from the steel belt package.

Broken bead wires, body ply cord condition, spacing, and turn up heights are easily detected. However it is more difficult to evaluate the condition of non-steel reinforcement due to the similarity in densities of polyester, rayon, nylon, and rubber. The capability of X-ray equipment to distinguish between these similar densities is commonly evaluated using the ASTM F1035 standard.[9] Figure 16.9 shows an image of the standard "Rubber – Cord Pie Disk".[10] This disk has six different types of reinforcing materials embedded in it: steel, nylon, polyester, fiberglass, Kevlar and rayon. The image shows the density differences between these materials and the relative clarity and ease with which they can be observed.

Figure 16.9: An X-ray image of the ASTM rubber - Cord pie disk that is used to examine the discernment capability of a tire x-ray imaging system.

Another application of x-rays is to evaluate bead fitment. Tangential x-rays are used to study the relative placement or fitment of the bead grommet and the bead seat relative to the wheel flange. Bead fitment is important when evaluating tire uniformity for improving vehicle ride quality. Figure 16.10 shows a schematic of a tangential x-ray device.[11] The x-ray beam passes longitudinally through the tire and wheel, and the image is collected on the other side. Figure 16.11 shows the resulting radiograph. In this case a gap can be seen between the tire bead and the rim flange.

X-ray analysis is the most firmly established and widely used of all of NDE techniques, with different techniques being used in development and production.

Figure 16.10: The tangential x-ray technique.
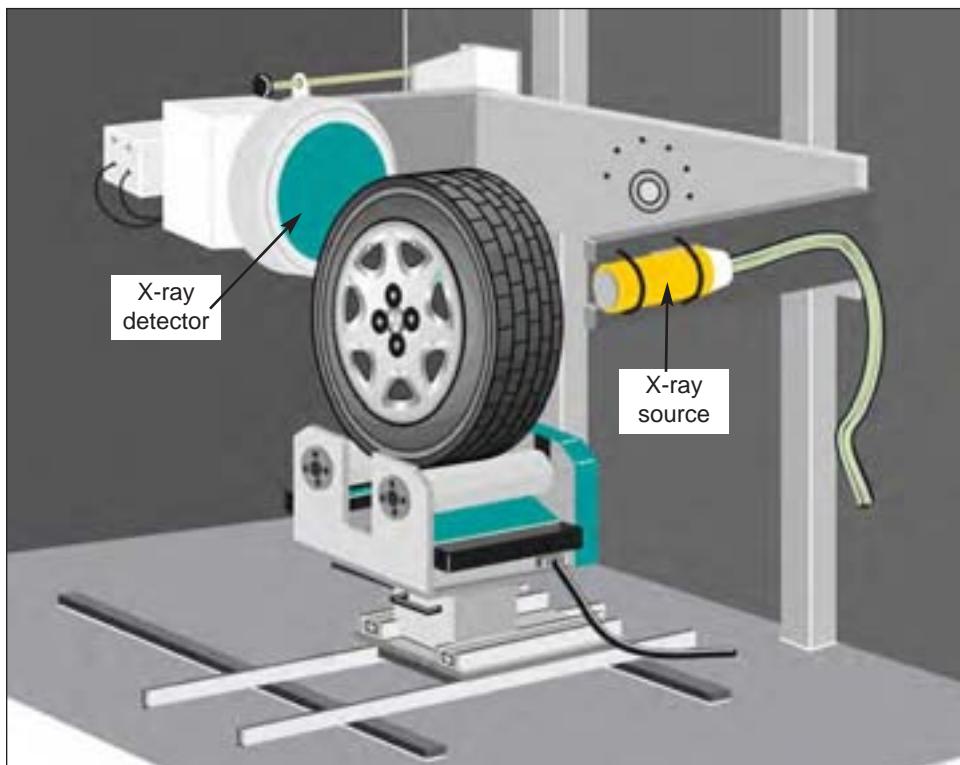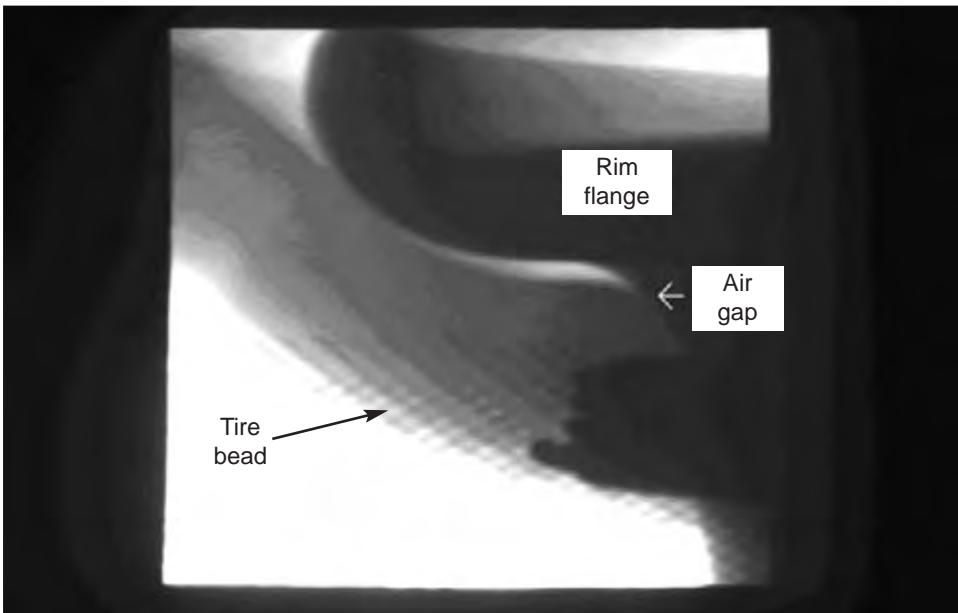
Figure 16.11: Result of a tangential x-ray observation.
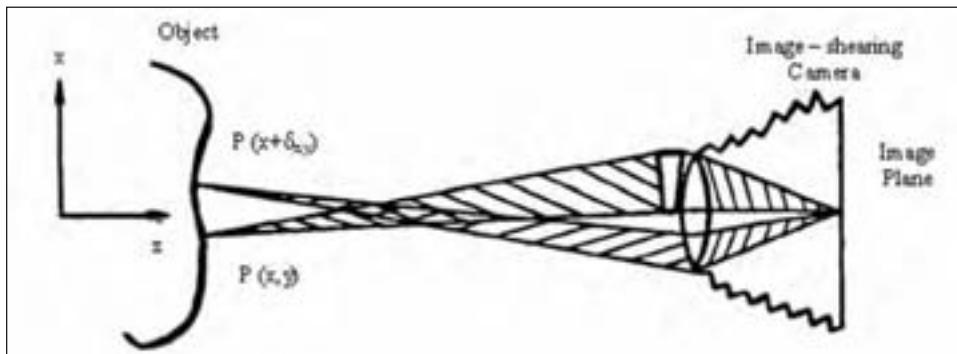
4. Shearography

Shearography is an interferometric method that permits full-field observation of surface strains in tires.[12]   Holography, another interferometric method, is also used. The difference between the two is that shearography measures displacement gradients directly while holography measures actual displacements. It has been shown that it is easier to correlate voids with variations in displacement gradient rather than in actual displacements.[13] As a result, shearography is now more popular. It can detect internal voids when corresponding surface displacements can be excited. Voids in belts and sidewalls, corrosion damage of steel cables, blisters between components, broken belts and cord socketing may all be observed with this technique.

The basic shearography method entails illuminating the tire surface with a single stable-frequency light source. Laser light is the preferred choice. A baseline photograph is then taken using a Shearography camera This camera is equipped with a shearing device, i.e., a thin glass angle prism (shear crystal) located at the iris plane of the lens and covering one-half of the lens aperture.[14]   The prism allows the light rays from each point P_0 (x,y) to be mapped into two points P_1' and P_2' in the image plane. Thus, the shearing camera brings light rays scattered from one point on the object surface to meet rays scattered from a neighboring point in the image plane.[15] As a result the rays interfere with each other, causing a random speckle pattern. Figure 16.12 shows two points on the object:

$P(x,y)$ and $P(x + d_{x,y}, y)$.[16]

Figure 16.12: Rays from two neighboring points brought to meet in the image plane.
Figure adapted from Rubber Chem. & Tech Vol. 54.

After the speckle pattern is obtained, the tire is stressed or deformed by applying a vacuum, vibration, heat, mechanical force or microwave energy. (It is usual to use a vacuum.) Another photograph is taken of the tire in the deformed state. If there is a relative displacement of the points P(x,y) and P(x + $d_{x,y}$, y), different from that elsewhere due to the presence of a void or other anomaly, then a change will be observed in the speckle pattern.

The shearography software compares the baseline photograph to the stressed photograph, producing a fringe pattern. The fringe pattern is described by the following equation[17]

$$I = 4a^2 \left[1 + \cos(\phi + \Delta/2) \cdot \cos(\Delta/2) \right]$$,

where *I* is the intensity distribution, *a* is the amplitude of illumination, ϕ is a random phase angle and Δ is the phase angle related to the relative displacements. Providing the camera and the illumination lie on the z-axis[18],

$$\Delta = \frac{4\pi}{\lambda} \left[W(x + \delta_{x,y}) - W(x, y) \right]$$,

where W is the displacement component in the z-direction, λ is the wavelength of the illuminating light, ϕx is the separation between two neighboring points that is a function of the shear crystal angle α and the distance, D_0 from the lens to the object

$$\delta_x = D_o(\mu - 1)\alpha$$,

where μ is the refractive index of the shear crystal. Rewriting the equation for Δ yields

$$\Delta = \frac{4\pi}{\lambda} \left[\frac{W(x + \delta x, y) - W(x, y)}{\delta x} \right] \delta x$$.

For small dx,

$$\Delta \approx \frac{4\pi}{\lambda} \left(\frac{\partial W}{\partial x} \right) \delta x$$;

therefore the fringes are lines of constant strain.

Shearography can detect relative motion at the surface of the tire as a result of external excitation; however, it cannot reveal what the motion is due to. Figure 16.13

shows the crown image of a section of a tire. The image has been digitally processed and the anomalies show up as elliptical fringes. They appear to be at the belt edges, but it is not clear whether they are between the belts, below the belts, or elsewhere. Figure 16.14 is another processed image, but only of the sidewall. It shows some anomalies around the turn-up area of the bead. Figure 16.15 shows other anomalies on the sidewall of a tire. To determine exactly what they are due to would require dissection of the tire. The last example, Figure 16.16, shows an unknown anomaly in the crown area of the tire.

Shearography is a good tool for quality control in manufacturing and it can also be used to track degradation of the tire in durability testing. However, interpretation of the shearogram is often difficult: a skilled operator is needed.[19] A shearogram or hologram taken on a new or used tire without a baseline or without subsequent shearograms taken after additional fatigue cycles provides very limited information about the condition of the tire and its durability.

Figure 16.13: A processed shearogram of the crown area of a tire. The image is taken from the inside of the tire. Anomalies are indicated in the belt edge area.
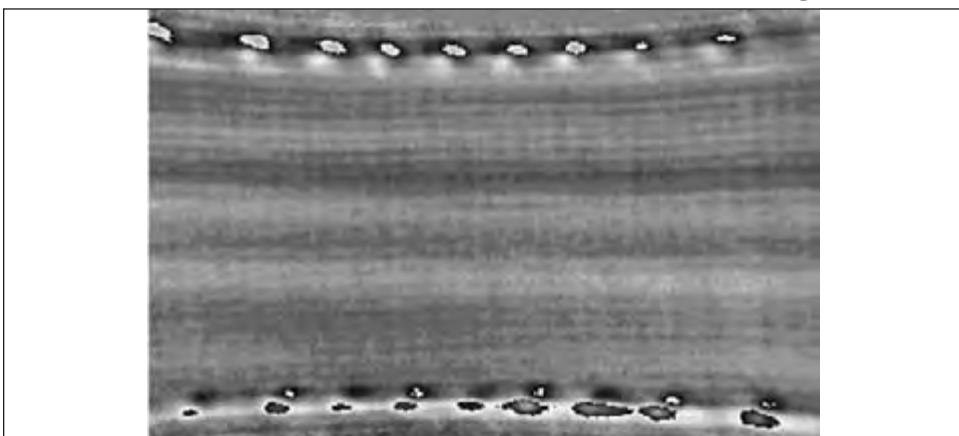
Figure 16.14: A processed shearogram of part of a tire sidewall. The image is taken from outside the tire. Potential anomalies are revealed at the turn up of the sidewall.
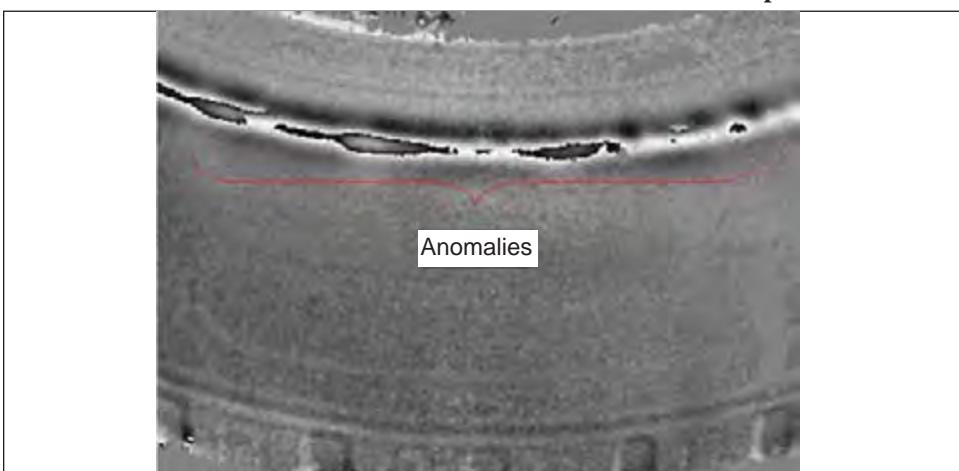
Figure 16.15: A processed shearogram of part of a tire sidewall. The image is taken from outside the tire and shows two defects.
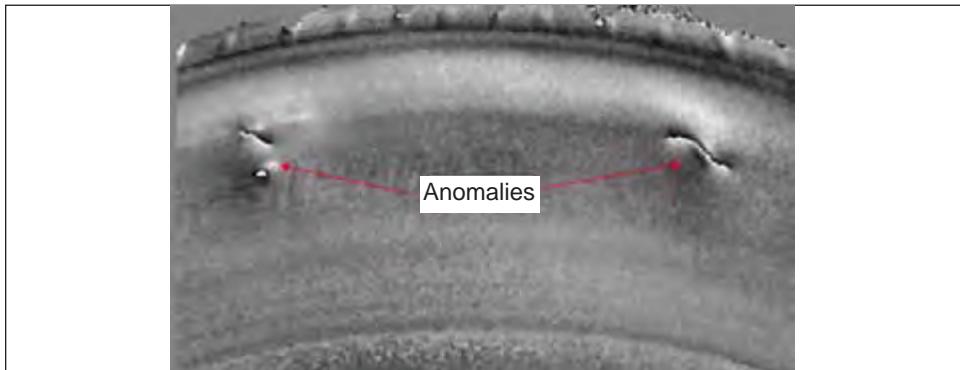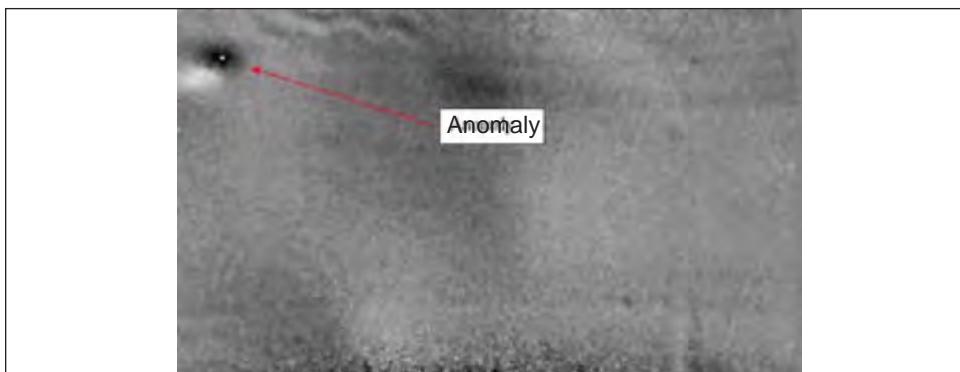
Figure 16.16: A processed shearogram of part of the crown of a tire. The image is taken from inside the tire and indicates an anomalous feature in the crown.

5. Ultrasound

Another nondestructive method is ultrasound. Although it is not widely used in the tire industry as a whole, it is regularly used by tire retreaders, and they have developed proprietary equipment and techniques. Some ultrasonic equipment is available commercially. Ultrasonic inspections are effective in evaluating abnormal cord spacing, belt anomalies, abnormal splices, and changes in wall thickness.

Ultrasound consists of sound waves that propagate through a medium, but the frequencies used, 1 to 10 MHz, are much higher than those in the audible range, 30 Hz to 20 kHz. The velocity V is given by

$$V = f\lambda$$

where f is the frequency and λ is the wavelength. For longitudinal waves, the particle displacement is in the direction of wave propagation, but in solids there are also shear waves, with particle displacement normal to the direction of wave travel, and elastic surface waves can also occur, known as Rayleigh waves.[20]

The velocity of a longitudinal compression wave is given by

$$V_c = \left(\frac{K_a}{\rho}\right)^{1/2},$$

where K_a is the elastic coefficient for adiabatic volume changes and ρ is the density. Alternatively,

$$V_c = \left(\frac{E(1-v)}{(1+v)(1-2v)\rho}\right)^{1/2},$$

where E is the modulus of elasticity and n is Poisson's ratio. The velocity of shear waves within a solid are given by[21]

$$V_s = \left(\frac{G}{\rho}\right)^{1/2},$$

where G is the modulus of rigidity of the material. The velocity of Rayleigh waves in a solid is about 90% of that of a shear wave, and is given by[22]

$$\frac{V_r}{V_s} = \frac{0.87 + 1.12v}{(1+v)}.$$

In order to generate and detect sound waves, it is usual to use piezoelectric transducers. They are typically coupled acoustically to the tire surface using a gel coupling agent or similar material. Exciting the generating transducer with either a step voltage or a continuous wave impulse launches the sound wave, which travels through the test material and is either reflected off the far side or is received by another transducer at that point.[23]

Ultrasound may be used to determine the position of ply cords or the wall thickness of a tire. Using a sensor on the outer surface of the tire, the sound wave is reflected by either the steel or body ply, or by the inner surface.

6. Eddy currents

Eddy current technology is based on electromagnetic induction. When an AC current passes through a coil of wire placed in proximity to a conductive material, it produces a magnetic field and secondary, or eddy, currents within the material.[24] The interaction between the two currents is known as impedance. A change in impedance indicates a discontinuity in the material or a change in thickness. Although eddy currents are used extensively in the metals industry for detecting discontinuities and changes in coating thickness, no details of its application in the tire industry could be found in the literature.

Nevertheless, a tire causes a known change in the magnetic field. The inductive reactance versus the effective resistance is seen in Figure 16.17. Placing a tire in the magnetic field and rotating it about the y-axis allows an investigator, in this case a tire retreader, to observe changes in impedance Z, given by

$$Z = \sqrt{(X_L^2 + R^2)},$$

where $X_L = \omega L$, L is the inductance of the coil and $\omega = 2\pi f$, where f is the frequency of the alternating current. This information along with the phase angle Θ between the voltage and current

$$\Theta = \sin^{-1}\left(\frac{X_L}{Z}\right)$$

are acquired using analog electronics, and calibrated to provide distances that correlate with the tread thickness. Figure 16.18 shows a typical setup.[25]

Figure 16.17: Inductive resistance from an AC current applied to a coil. Figure adapted from Hocking: "Eddy Current NDT".
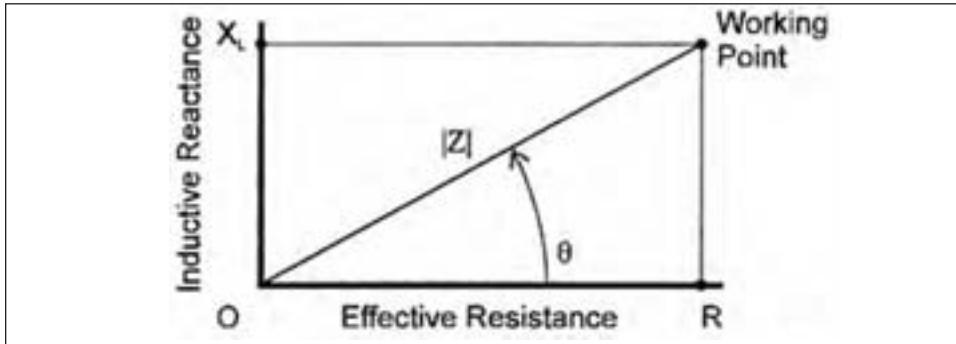
Figure 16.18: Eddy current measurement applied to a tire to evaluate retread thickness.

7. Summary

Nondestructive evaluation methods provide tire engineers with insight into the internal structure of a tire without actually destroying it. X-ray methods have been mainly used, and appear to be the most well-developed nondestructive technique. Shearography, ultrasound and eddy currents provide other information. All of the methods require much skill, training and experience to interpret the data.

   Application of nondestructive evaluation to tires will probably continue to increase. Improved equipment and computer technologies have allowed some techniques to be automated and hold significant promise for more broad-based application. However, actual destructive analysis of tires will continue to be necessary in critical cases.

References

1. Trivisonno, N.M., Rubber Chemistry and Technology, "Non-Destructive Evaluation of Tires", Vol. 58, 1985.

2. Bartel, Jill. P. 3.

3. J.M.Forney, "Proceedings of the Second Symposium on Nondestructive Testing of Tires", P. E. J. Vogle, Ed., Sponsored by the Army Materials and Mechanics Research Center, Watertown, MA, 1974, P. 13.

4. Neuhaus, T. G., ibid.

5. YXLON International, Modular Tire Inspection System Presentation, December 2003.

6. Raj. P., Reference 5, P. 55.

7. Neuhaus, T.G., "Review of Tire X-ray Systems 1982", Akron Rubber Group Technical Symposium, Akron, OH, April 22, 1982.

8. YXLON International, Modular Tire Inspection System Presentation, December 2003.

9. ASTM Standard Practice F1035, "Use of Rubber – Cord Pie Disk to Demonstrate the Discernment Capability of a Tire X-ray Imaging System.

10. (See reference 12).

11. Schematic is courtesy of YXLON Internation, Akron, OH USA

12. Y.Y. Hung, R.M. Grant, "Sherography: A New Optical Method for Nondestructive Evaluation of Tires", Rubber Chem. Vol. 54, P. 1042.

13. Ibid., P. 1044.

14. Ibid., P. 1045.

15. Ibid., P. 1046.

16. Y.Y. Hung, R.M. Grant, "Sherography: A New Optical Method for Nondestructive Evaluation of Tires", Rubber Chem. Vol. 54, P. 1046.

17. Y.Y. Hung and C.L. Liang, Applied Optics 18, (7) 1046 (1979).

18. Ibid.

19. Department of Transportation, NHTSA, FMVSS 49 CFR Part 517, Vol. 68, No. 123, Thursday, June 26, 2003, Rules and Regulations, P. 38143.

20. Hull, B., Vernon, J., Reference 4, P. 57.

21. Hull, B., Vernon, J., Reference 4, P 58.

22. Hull, B., Vernon, J., Reference 4, P. 58.

23. Nelligan, T. J., "An Introduction to Ultrasonic Material Analysis", Panametrics-NDT.

24. Hull, B., Vernon, J., Reference 4, P. 33.

25. Kaman Instrumentation Corporation, Measuring Systems Group, Colorado Springs, Colorado, USA, Application Handbook, P. 72.

Chapter 17
Tire Standards and Specifications
by Joseph D. Walter

Chapter 17
Tire Standards and Specifications
by Joseph D. Walter

17.1 Tires and highway safety

Pneumatic tires have certainly evolved a great deal during the past 100 years from low mileage, low speed products reinforced with cross woven fabric to today's relatively high mileage, high speed radial ply constructions. Since the driver controls the acceleration, braking and steering of the automobile through the tires, tires obviously play a key role in the safe operation of any passenger vehicle. Unexpected air loss due to a puncture leading to loss of vehicle control remains an important issue for highway safety. In fact, the first fatal automobile accident on pneumatic tires that is well documented occurred near London in 1899 and was due to tire failure occasioned by hard braking during downhill travel [1].

Each year, more than a million people worldwide are fatally injured in automobile accidents with the number of highway deaths exceeding 40,000 in the U.S. on an annual basis. While fatality trends in the U.S. are down (Table 17.1), the fact remains that over three million Americans have been killed on roadways since the advent of the motor car.

Today, tires are estimated to be the proximate cause of about one percent of automo-

Table 17.1: U.S. highway fatality trends

Year	Highway Fatalities	Rate per 100,000 Population	Rate per 100,000 Vehicles	Rate per 100 Million VMT[1]
1970	52,627	25.67	47.31	4.74
1980	51,091	22.48	34.39	3.35
1990	44,599	17.88	24.20	2.08
2000	41,945	14.87	19.33	1.53

bile related deaths – i.e., about 400-500 fatalities per year.[2] There are a variety of reasons why tires can be involved in loss of vehicle control leading to an accident, including failure due to puncture, underinflation, excessive speed, overloading or insufficient tread depth to stop a vehicle in a timely fashion on a slippery road surface. The precise number of highway fatalities due to tire related causes is not well documented but can only be inferred from accident reports issued by various police jurisdictions.

A variety of technologies have been developed to reduce or eliminate air loss as a cause of tire disablement including self-sealing or sealant tires, run-flat tires, and airless tires. Each approach involves trade-offs and compromises with vehicle weight, fuel economy,

---

[1]Vehicle Miles Travelled

[2]The National Accident Sampling System (Crashworthiness Data) estimates 535 fatalities
(2001) while NHTSA estimates 414 (2002).

ride comfort and cost.

Other countermeasures are being considered or are in place to address other aspects of tire safety. The underinflation problem is serious enough that it is being addressed at the federal level through the issuance of a standard[3] requiring tire pressure monitoring systems (TPMS) to be installed on all new light duty vehicles (below 10,000 lb. gross weight). The proposed phase-in schedule would require manufacturers to certify that 20% of their 2006 model year vehicles comply with the TPMS requirements, 70% of 2007 vehicles, and 100% of 2008 vehicles. Underinflated tires not only are more likely to fail in service due to heat build-up and the accompanying elevated temperatures (Chapter 15), they also hydroplane on water covered highways at a lower speed than tires inflated to their recommended pressure (Chapter 11). Further, the critical speed for the onset of traveling waves – which can quickly produce tire failure – is also lowered at reduced inflation pressure (Chapter 10).

A major reason, then, for government regulation of tires is an attempt to promote highway safety as a matter of public policy. These regulations, so-called Federal Motor Vehicle Safety Standards (FMVSS), have been in existence since the 1960s and are discussed in Section 17.2.

The tread depth issue is currently addressed in different ways by each of the 50 states and the District of Columbia (DC) as shown in Table 17.2 [2].

Table 17.2: Legal minimum tread depths (light duty vehicles)

2/32 in	1/32 in	No requirement
43 states and DC	CA and ID	AR, ND, WV, NM and SC

Note that most state laws require a minimum tread depth of 2/32 in. Federal law only requires that passenger car tires incorporate tread wear indicators during manufacture that become exposed when tread depth is less than this amount. The corresponding European (ECE) requirement for minimum tread depth is the equivalent of 2/32 in – i.e., 1.6 mm.

Most new passenger car tires are produced with tread depths in the range of 9/32-13/32 of an inch depending on tire size and application and are considered worn out when minimum tread depth is reached. As tread depth is reduced due to tire wear, reductions in driving and braking forces occur in wet, snow and muddy conditions compared to dry road performance. The critical speed for the on-set of hydroplaning on rain covered highways is similarly lowered with increasing tire wear due to the reduced drainage capacity of the grooves, sipes(kerfs), and slots in the tread design (Chapter 11).

In addition to the federal standards and state laws, there are a variety of industry sanctioned regulations pre-dating the governmental standards that must be met before tires can be sold and safely used on the highway. These industry sanctioned specifications address features such as tire load carrying capacity, tire dimensions, and interchangeability of tires and wheels. These voluntary standards have been in existence almost from the advent of

[3]Federal Motor Vehicle Safety Standard 138.

the pneumatic tire. Some aspects of these industry standards are safety related and are discussed in Section 17.3.

Finally, there are further government requirements intended to provide useful consumer information to the end user regarding the treadwear, traction and temperature resistance capabilities of passenger car tires and are known as Uniform Tire Quality Grade (UTQG) labeling standards. The traction (wet road surface) and temperature resistance (surrogate for high speed capability) grades are inherently safety related; the treadwear index is not usually considered as a safety related measure of tire performance but tires with tread designs and compounds having excellent wet grip, *ceteris paribus*, tend to compromise wear and vice-versa, tread compounds formulated to deliver high mileage tend to sacrifice wet skid resistance. Thus, even the treadwear grade, in some way, is often an indirect measure of safety with respect to wet weather driving. The UTQG labeling system is discussed in Section 17.4.

Thus, the specifications and standards that are covered in this chapter:

   a) indicate that minimum safety levels regarding, *inter alia*, high speed
      performance and durability of the tire have been met;
   b) assure interchangeability on a given vehicle of tires (and wheels) produced by
      different manufacturers for tires having the same designation molded, stamped,
      or otherwise imprinted on the sidewall;
   c) provide somewhat useful information to the user regarding treadwear, traction
      and temperature resistance capabilities of the tire.

None of the industry or government regulations specify the kind of material to be used in either tires or wheels. That choice is determined by the manufacturer.

17.2 Federal motor vehicle safety standards

Government requirements for tires were rigorously established in the U.S. in 1967 based on the Congressional Safety Act of 1966 and became mandatory for all passenger car tires manufactured after January 1, 1968. Shortly after this period(1970), Congress created the National Highway Traffic Safety Administration (NHTSA) under the U.S. Department of Transportation (DOT) to implement the provisions of the Act.

The resulting government regulations, known as Federal Motor Vehicle Safety Standards (FMVSS), specified tire dimensions and laboratory test requirements for bead unseating resistance, strength, endurance, and high speed performance. The regulations further defined tire load ratings and sidewall labeling requirements and also required that tires incorporate tread wear indicators. These federal regulations were issued and known as FMVSS 109. Many of the test requirements adopted by the government were based on existing industry standards.

Following Congressional passage of the TREAD[4] Act of 2000, NHTSA issued an updated standard (FMVSS 139) to be effective June 2007 which increases the severity of the endurance and high speed tests and added a low pressure endurance requirement. The

---

[4]Transportation Recall Enhancement Accountability and Documentation.

TREAD Act was responsible for the first major revisions to federal tire safety regulations since originally issued when bias ply tires were the norm. An additional revision to FMVSS 139 is anticipated as NHTSA is actively developing a test to assess the effect of aging on tire performance. Bias ply tires are exempt from the provisions of FMVSS 139 and remain subject to the older regulations (FMVSS 109). The tire manufacturers certify that their products meet the minimum federal safety levels with compliance sampling conducted by the government.

Current government safety standards applicable to passenger car tires are published in the Code of Federal Regulations (CFR), Title 49 (Transportations), Part 571 (FMVSS). The relevant portions of Part 571 are discussed in the remainder of this section.

Bead unseating

Underinflated tires in service may experience temporary or permanent bead dislodgement from the rim – especially due to curb impact or hard cornering where, in the latter case, appreciable lateral forces may be generated. Low aspect ratio tires (45 series and below) are especially vulnerable to unseating since the circumferential restraining force generated by the inflation pressure needed to maintain bead contact with the rim is considerably reduced as tire section height is decreased.

The bead unseating test is a laboratory measure of the ability of the tire to maintain an air tight seal at the tire-rim interface when subjected to a lateral force applied directly to the tire sidewall. The non-rotating tire-wheel assembly is positioned horizontally in a holding fixture and a contacting anvil applies the lateral force quasi-statically – i.e., 2 in/min. The tire is inflated to the maximum pressure allowed (normally 35 psi). Specific details related to anvil geometry and test fixture configuration for different size tires and wheels are described in the standard.

The bead unseating force must equal or exceed the values shown in Table 17.3 depending on the section width of the tire.

Table 17.3: Bead unseating force requirements

Tire section width	Bead Unseating Force
Less than 6 in	1500 lb
Equal to or greater than 6 in but less than 8 in	2000 lb
Equal to or greater than 8 in	2500 lb

It should be noted that, compared to the load and inflation conditions of this test, passenger car tires on a vehicle in highway service:

  a) experience shock loads at the sidewall due to curb impact as well as cyclic dynamic loads in the contact patch;

  b) are normally inflated to pressures less than that required in the laboratory test.

Plunger strength

When FMVSS 109 was first developed, the structural robustness of the tread region of the bias tires in use at the time tended to correlate directly with the number of plies in the tire

and the cord spacing in each ply. More strength, load carrying capacity and tread impact resistance could be achieved by adding more plies and using more densely packed cords in each ply. The so-called plunger test was a measure of this strength and resistance to road hazards.

To conduct this test, an inflated but otherwise unloaded tire is held fixed; a ¾ inch diameter cylindrical steel shaft (the plunger) with a hemispherical head is forced into a tread rib on or near the tire center line at a travel rate of 2 in/min.

The minimum value of plunger energy needed to meet the strength requirement (which ranges from 1950-5200 in-lb – calculated as one-half the product of plunger force times distance traveled) varies with tire section width and permissible inflation pressure. Generally, radial passenger car tires contain a minimum of three plies in the tread region (two belt plies and at least one radial body ply) and rarely fail to achieve the minimum value of plunger energy necessary to meet the test requirements. This test is especially moot for steel belted tires featuring nylon cap or overlay plies added to the belt region to achieve high speed ratings. Also, very low aspect ratio tires tend to limit plunger travel which can cause the tire tread region to come in contact with the rim (i.e., "bottom out") before the requisite level of calculated energy is achieved unless plunger force is allowed to build up against the rigid surface of the rim without further plunger travel.

Tire Endurance

Mass market radial passenger car tires are normally designed to deliver about 40,000 miles of tread wear in the U.S. This mileage represents approximately 30 million revolutions of the tire under a wide spectrum of driving and environmental conditions – and occurs on average over a three year period. The tire endurance test is meant to assess the durability of the tire in a relatively short period of time under controlled laboratory conditions. Tire load, speed, inflation pressure and ambient temperature can be used in various combinations to control the test severity.

The tire to be checked is run continuously on a curved road wheel or drum at constant speed with increasing loads per the schedule shown in Table 17.4.

Table 17.4: Endurance test parameters

Ambient Temperature	38° C (100° F)
Roadwheel Diameter	1.708 m (67.23 in)
Inflation Pressure	180 kPa (26 psi)
Speed	120 km/h (75 mph)
Load Steps[5]	4 hr @ 85% load
	6 hr @ 90% load
	24 hr @100% load

Test duration is 34 hours with a total distance traveled of 4,080 km (2550 miles) or

[5]The percentages are applied to the maximum load rating marked on the tire sidewall.

approximately two million tire revolutions. To successfully complete this test, the tire can not show any evidence of component failure or experience any air loss. In contrast to highway use, no cornering or camber angles are imposed on the tire during the test.

High speed performance

Radial passenger car tires are available in a variety of speed ratings normally from "Q" (99 mph) to "Y" (186 mph), even though posted speed limits on the U.S. interstate highway system are mostly in the range of 55-75 mph. These speed ratings are discussed in detail in Section 17.3. The government high speed performance test is meant to assess the capability of the tire in an intermediate speed range from 85 to 100 mph.

The tire to be checked is run at a fixed load and 0° camber and slip angles at increasing speeds per the schedule given the Table 17.5.

Table 17.5: High speed test parameters

Ambient Temperature	38° C (100° F)
Roadwheel Diameter	1.708 m (67.23 in)
Inflation Pressure	220 kPa (32 psi)
Load[5]	85%
Speed Steps	30 min. @ 140 km/h
	30 min. @ 150 km/h
	30 min. @ 160 km/h

Again, there can be no evidence of component failure or air loss at the completion of the test.

Low pressure test

Industry and government surveys generally indicate that about one in four passenger car tires operate in a seriously underinflated condition – a problem that is being partially addressed in the future by FMVSS 138 requiring tire pressure monitoring systems on new vehicles.

NHTSA initially proposed and solicited commentary on two alternative low pressure tire tests in their Notice of Proposed Rulemaking (NPRM) issued in advance of the FMVSS 139 final rule: an endurance version and a high speed version. The government adopted the endurance version as being more representative of actual service conditions. The tire to be evaluated for the low pressure test must have first successfully completed the 34 hour endurance test – and then the same tire is further tested at reduced inflation pressure per the schedule given in Table 17.6.

Table 17.6: Low pressure test parameters

Ambient Temperature	38° C (100 ° F)
Roadwheel Diameter	1.708 m (67.23 in)
Inflation Pressure	140 kPa (20 psi)
Speed	120 km/h (75 mph)
Load[5]	100%

[5]ibid.

Test duration is 90 minutes. Again, there can be no evidence of component failure or air loss at the completion of the test. For example, a tire that remains fully inflated at the end of the test but suffers a tread "chunk-out" (the loss of one or more tread elements) fails the test. This is an issue for many winter tires.

Tire aging

Oxygen and ozone are the primary agents responsible for the aging and weathering of rubber as well as the degradation of the bond at the many thousand cord-rubber interfaces in tires; contributing factors are heat, light, humidity and mechanical factors (stress and strain) arising during highway service. Even unvulcanized rubber can be adversely affected by these conditions during tire manufacturing operations. Aging of rubber is addressed in Chapter 2.

In any case, the factors causing aging, alone or in combination with one another, are responsible for the loss of physical properties of the constituent components of the tire and may control its useful life.

Two long term trends have exacerbated the tire aging problem:

a) the number of years tires remain in service has increased considerably due to the high mileage attained by many current products;

b) weight reductions achieved by employing thinner sidewalls, etc., have tended to produce cooler running tires, albeit a small effect, allowing for reduced levels of anti-oxidants and anti-ozidants.

Thus, NHTSA has indicated that a laboratory tire aging standard will be included at a future date in FMVSS 139. This could be as simple as an "expiration date" molded on the tire sidewall after which use would be prohibited; or it could be as complicated as a laboratory roadwheel test involving the multiplicity of conditions previously mentioned involving chemical, mechanical and thermal factors.

The development of a meaningful accelerated aging test that will accurately predict long term tire performance subject to the vagaries of customer use in different geographical regions remains a formidable challenge.

17.3 Tire and wheel specifications and issues

Tire specifications

The tire sidewall is a veritable advertising billboard containing much useful information – albeit difficult to read – that is mostly ignored by the motoring public. Perhaps the most important inscription molded on the tire sidewall is that giving tire size, aspect ratio, construction and wheel diameter immediately followed by the service description (which specifies load carrying capability and speed rating). The tire dimensions and service description are principally under the purview of three major non-governmental organizations:

a) the Tire and Rim Association (TRA) in the U.S.;

b) the European Tyre and Rim Technical Organization (ETRTO);

c) the Japan Automobile Tire Manufacturers' Association (JATMA).

As an example of a typical sidewall inscription, consider a passenger car tire for a mid-size sport sedan; its size and service description would appear, e.g., as P215/55R16 91H. This nomenclature is deciphered as follows:

P	Passenger car tire
215	Nominal section width in millimeters
55	Aspect ratio
R	Radial construction
16	Rim diameter in inches
91	Load index
H	Speed symbol

The service description, comprised of the load index "91" and the speed symbol "H," is written in code. The load index is an assigned number varying from 0 to 279 which for U.S. passenger car tire sizes (so-called P-metric or P-type[6]) ranges mostly from 80 to 109 as listed in Table 17.7.

Table 17.7: Load index (LI) range for passenger car tires

LI	kg	lb	LI	kg	lb	LI	kg	lb
80	450	992	90	600	1323	100	800	1764
81	462	1019	91	615	1356	101	825	1819
82	475	1047	92	630	1389	102	850	1874
83	487	1074	93	650	1433	103	875	1929
84	500	1103	94	670	1477	104	900	1985
85	515	1136	95	690	1521	105	925	2040
86	530	1169	96	710	1566	106	950	2095
87	545	1201	97	730	1610	107	975	2150
88	560	1235	98	750	1654	108	1000	2205
89	580	1279	99	775	1709	109	1030	2277

For the example P215/55R16 91H tire, the "91" indicates a load carrying capacity of 615 kg or 1356 lb at the maximum rated inflation pressure of 35 psi.

Tires are designed to operate over a restricted range of inflation pressures with a corresponding range of loads. There is a minimum pressure below which tires should not be operated due to the damaging effects of heat build-up since the internal temperature of tire components varies inversely with pressure. One of the most important responsibilities of TRA and similar international organizations is the establishment of tire load/inflation relationships. The load carrying capacity of a passenger car tire is based on a semi-empirical formula containing tire section width, rim diameter and the square root of inflation pressure (see Chapter 5).

For the P215/55R16 91H tire previously considered, the tire load limits at various cold inflation pressures are given by TRA as follow:

---

[6] The European or Euro-metric designation eliminates the letter "P" and the comparable sidewall inscription would appear as: 215/55R16 91H.

Inflation pressure	26	29	32	35	psi
	180	200	220	240	kPa
Load limits	1179	1246	1312	1356	lb
	535	565	595	615	kg

The overall tire dimensions and approved rim widths are also specified by TRA. For the example tire on a measuring rim width of 7.00 in, the design section width is 226 mm (8.90 in); the overall diameter is 642 mm (25.28 in); and rim widths approved for use in highway service are 6, 6½, 7 and 7½ inches.

The speed rating of a tire indicates the maximum speed at which it can safely carry a given load at a specified inflation pressure. The speed symbol, denoted in code by a letter of the alphabet, is the second part of the service description (following the load index). For most passenger car tires, speed ratings normally vary from "Q" (applicable to many winter tires) to "Y" (reserved for high performance sport cars) as shown in Table 17.8.

For the example P215/55R16 91H tire, the "H" indicates a speed capability of 210 km/h (130 mph) if the tire is inflated to its maximum allowable pressure (35 psi) at a load equal to or less than the maximum allowed (1356 lb). In 2004, TRA adopted an additional inflation adjustment (increase) based on the maximum speed capability of the vehicle. This makes the proper selection of both the tire size and specified inflation to ensure no overloading a more complex task for the vehicle manufacturer.

Table 17.8: Speed symbols, maximum speeds and typical applications

Speed symbol	Maximum speed		Typical application
	km/h	mph	
Q	160	99	Winter Tires
R	170	106	LT-Metric Tires[7]
S	180	112	Entry Level Cars
T	190	118	Sedans/Vans
U	200	124	-
H	210	130	Sport Sedans
V	240	149	Sport Sedans
W	270	168	High performance cars
Y	300	186	High performance cars

The speed rating system evolved in Europe with the commercial development of radial tires in the 1950s and was originally comprised of three symbols:

S designating standard tire;

H designating high speed tire;

V designating very high speed tire.

As tire manufacturers made more speed rated tires for an increasingly complex car population, the category was expanded to cover earthmover and agricultural tires at the

[7]LT = Light Truck

lower end of the alphabet and to high performance luxury sedans and sports cars at the upper end. U.S. tire manufacturers voluntarily adopted the load index and speed rating symbols in the 1990s to be in conformity with European practice. The load index and speed rating, along with the tire size, are important safety factors when purchasing replacement tires for automobiles.

Wheel issues

The tightness of the fit at the tire-rim interface on a given wheel is controlled by the tire design in the bead region and is governed principally by:

a) the bead winding diameter relative to the wheel diameter;
b) the stiffness of tire components between the bead and the rim;
c) the bead seat taper angle.

Thus, the interchangeability of tires and wheels presents important design challenges to the tire development engineer. Importantly, interchangeability assures that a tire manufactured in one country can be fit to a wheel made in another country when placed in service on a vehicle produced in yet a third country.

Tubeless passenger car tires are designed to have an interference fit with the rim so that an air-tight seal exists at the tire-rim interface and to prevent circumferential slip of the inflated tire on the wheel due to braking or driving torque. Another important aspect of specifying tire dimensions is to assure the conformity or uniformity of fitment of the tire bead region to the rim. Rim contours are specified by TRA, ETRTO and JATMA along with other wheel dimensions. These other dimensions, rim width, wheel diameter, and offset[8] are important parameters, in conjunction with the tire, that influence vehicle ride and handling.

17.4 Uniform tire quality grade labeling

Additional federal tire labeling and test requirements were mandated in 1975 that were meant to provide relevant information to the end user as an aid in assessing mileage, wet braking and heat dissipating properties of tires. Grade requirements were established for wear, traction and temperature resistance, respectively. These requirements – the Uniform Tire Quality Grading (UTQG) system – apply to passenger car tires with the exception of winter tires and temporary spares. The grades must be indicated on the tire sidewall. Interestingly, the wear test is conducted using vehicles on public roads, the traction test on skid pads using a towed trailer, and the temperature test is run in a controlled laboratory environment. Federal rules allow manufacturers to "derate" tires (i.e., lower the grade) for the tread wear, traction and temperature resistance which may be done for either technical or marketing purposes.

UTQG standards along with test details are contained in the Code of Federal Regulations (CFR), Title 49 (Transportation), Part 575 (Consumer Information Regulations), Section 104 (cited in the literature as 49 CFR 575.104).

---

[8]Offset is the horizontal distance from the mid-point of the wheel rim to the wheel disk.

Treadwear

UTQG tread wear grades for radial passenger car tires typically range from 100 to over 600 in 20 point increments. Higher numbers indicate better resistance to wear. The grades are based on tests conducted under controlled conditions on a government pre-scribed 400 mile course comprised of public roads in the vicinity of San Angelo, Texas. A group of not more than four test vehicles travels the course in a convoy so that all tires experience similar conditions. The same procedure is followed for a set of control or course monitoring tires (CMTs). Tread depths of candidate tires and CMTs are measured every 800 miles. The vehicles travel a total distance of 7,200 miles with the first 800 miles used as a "break-in" period (i.e., no tread depths are measured). After the comple-tion of both tests, wear rates are compared and the candidate tires are assigned a UTQG tread wear grade by the manufacturer.

The wear grades are only meant to be a relative (and not absolute) indication of tread wear performance since the tire wear rates experienced by the driver of a given vehicle will depend on road surface abrasiveness, weather conditions, driving habits, wheel align-ment, and other factors addressed in Chapter 13.

Traction

The UTQG traction grade is a measure of the ability of the candidate tire to stop on wet concrete and asphalt surfaces in a straight-ahead, locked-wheel braking test from 40 mph. Grades of AA, A, B, and C are assigned depending on the following deceleration levels (reported as traction coefficients[9]) experienced by the tire:

Traction grade	Traction coefficient	
	Asphalt	Concrete
AA	above 0.54	above 0.38
A	above 0.47	above 0.35
B	above 0.38	above 0.26
C	0.38 or less	0.26 or less

Measurements are made using an instrumented towed trailer.

The traction grade assigned may not be an accurate prediction of wet road acceleration, cornering or hydroplaning performance. It is only a measure of sliding (locked wheel) friction so the coefficients as reported can not be used to predict stopping distances of vehicles equipped with anti-lock braking systems (ABS). Further, at highway driving speeds on rain covered roadways, tire tread designs play a dominant role in evacuating water from the contact patch – a factor not well accounted for in this test. Rubber friction and tire traction, including the subject of hydroplaning, are addressed in Chapter 11.

---

[9] The so-called traction coefficient is actually a braking and not a driving coefficient of friction as the word traction might imply.

Temperature resistance

The UTQG temperature grade is based on the sustained speed a tire can achieve without failure. This speed is considered to be a measure of the ability of the tire to dissipate internal heat build-up; that is, speed is a surrogate for temperature. Temperature resistance ratings are determined by testing candidate tires on an indoor road wheel (as used in FMVSS109 and 139) under controlled laboratory conditions. Successive 30 minute runs are made in 5 mph increments starting at 75 mph and continuing until the tire fails or is removed at the highest speed with no failure. Temperature grades, based on the speeds achieved without failure, are assigned per the following schedule:

Temperature Grade	Speed (mph)
A	over 115
B	between 100 to 115
C	between 85 to100

Every tire sold in the U.S. must be capable of meeting a minimum rating of "C" in contrast to the treadwear and traction grades where absolute minimums are not prescribed. Note that any tire that meets the FMVSS 139 high speed test requirement will, by default, achieve at least the minimum "C" rating for temperature.

17.5 List of Initializations and Acronyms

ABS .... Anti-lock Braking System
CFR .... Code of Federal Regulations
CMT .... Course Monitoring Tire
DOT .... Department of Transportation
ECE .... Economic Communities of Europe
ETRTO .... European Tire and Rim Technical Organization
FMVSS .... Federal Motor Vehicle Safety Standard
JATMA .... Japan Automobile Tire Manufacturers Association
LI .... Load Index
LT .... Light Truck
NHTSA .... National Highway Traffic Safety Administration
NPRM .... Notice of Proposed Rule Making
TPMS .... Tire Pressure Monitoring System
TRA .... Tire and Rim Association
TREAD .... Transportation Recall Enhancement Accountability and Documentation
UTQG .... Uniform Tire Quality Grading

Bibliography

- Code of Federal Regulations, Title 49, Transportation:
- U.S. Government Printing Office, Washington D.C., issued annually.
       a) Federal Motor Vehicle Safety Standards
               i) 49 CFR 571.109 (FMVSS 109)
               ii) 49 CFR 571.139 (FMVSS 139)
       b) Consumer Information Regulations
               i) 49 CFR 575.104 (UTQG)

- *The Tire Tech Guide*, Bennett Garfield, Boca Raton, Florida, issued annually.

- Traffic Safety Facts, A Compilation of Motor Vehicle Crash Data from the Fatality Analysis Reporting System and the General Estimate System, National Highway Traffic Safety Administration, DOT HS 809 620, Washington D.C., issued annually.

- Year Book of the Tire and Rim Association, TRA, Copley, Ohio, issued annually.

References

1. L. Evans, *Traffic Safety*, Science Serving Society, Bloomfield Hills, Michigan, 2004.
2. W. Blythe and D.E. Seguin, Legal Minimum Tread Depth for Passenger Car Tires in the U.S.A., Paper submitted for publication, 2005.

Test Questions

True   False

____   ____   The number of estimated highway fatalities attributed to tires each year is about 4,000-5,000 in the U.S.

____   ____   It is a violation of federal law to use worn out tires (tread depth less than 2/32 in) on rain covered highways.

____   ____   The Uniform Tire Quality Grade (UTGQ) labeling standards are the principal federal regulations governing tire safety.

____   ____   Speed rated tires may be driven at their maximum rated speeds at inflation pressures between 26 – 35 psi.

____   ____   The load limits specified for a given tire increase with decreasing inflation pressure.

____   ____   Load and inflation pressure limits on a given size tire are controlled directly by the National Highway Traffic Safety Administration (NHTSA).

____   ____   The plunger test is a laboratory measure of the ability of a tire to maintain an air-tight seal at the tire-rim interface.

____   ____   The endurance, high-speed, and low pressure tests prescribed in FMVSS 139 are all conducted on previously untested tires.

____   ____   The UTGQ tread wear grade can be used by consumers to predict tire mileage on a given vehicle.

____   ____   The service description on the tire sidewall, comprised of the load index and speed rating, is mandated by federal law.

Chapter 18
Tire Materials: Recovery and Re-use
by A. I. Isayev and J. S. Oh

Chapter 18
Tire Materials: Recovery and Re-use
by A. I. Isayev and J. S. Oh

1. Introduction

Manufacturing of pneumatic tires and other rubber products involves vulcanization, leading to a three-dimensional chemical network. This makes the direct reprocessing and recycling of used tires and waste rubber impossible. Therefore, the environmental problems caused by used tires and other waste rubber products have become serious in recent years. In fact, Goodyear, who invented the sulfur vulcanization process more than 150 years ago, was also the first to initiate efforts to recycle cured rubber wastes through a grinding method.

A large number of tires are scrapped each year. According to a recent survey by the Scrap Tire Management Council of the Rubber Manufacturers Association, approximately 281 million scrap tires were generated in the United States alone in 2001. The market for scrap tires consumed about 77.6% of that total while the rest was added to an existing stockpile of an estimated 300 million scrap tires located around the USA (www.rma.org/scrap_tires/scrap_tire_markets/facts_and_figures/). These stockpiled tires create serious fire dangers and provide a breeding ground for rodents, snakes, mosquitoes, and other pests causing health hazards and environmental problems.

The major use of scrap tires in the U.S. is to generate so-called tire-derived energy by burning them. However, burning tires may contribute to air pollution. About 53% of the consumed scrap tires were burnt in 2001, and only 19% of the total consumed amount were turned into ground tire rubber (GRT), the initial material for tire rubber recycling processes.

Waste tires, being made of high quality rubber, represent a large potential source of raw material for the rubber industry. The main reasons for the low scale of current rubber recycling are: more stringent requirements for high quality of rubber articles; the substitution of raw rubber by other materials, for example by plastics in some cases; rising cost of producing reclaim rubber from tires and rubber waste due to more stringent regulations for environmental protection; comparatively high labor requirements for producing reclaim; and, as a result of all this, the high cost of reclaimed rubber [1]. However, the increasing trend to restrict landfills is inducing a the search for economical and environmentally sound methods of recycling discarded tires and waste rubber. Recent aggressive policies of the automotive industry are aimed to increase the usage of recycled plastic and rubber materials. This is an example of the growing industrial demand for such technologies.

The main objective of this chapter is to provide an up-to-date account of recycling of used tires and waste rubber, including existing methods and emerging technologies of grinding, reclaiming and devulcanization, and also the possibility for utilizing recycled rubber in products. Devulcanization is a process in which scrap rubber or vulcanized waste product is converted using mechanical, thermal or chemical energy into a state in which it can be mixed, processed and vulcanized again. Strictly speaking, devulcanization of sulfur-cured rubber consists of cleaving, totally or partially, the sulfide crosslinks formed during the initial vulcanization [2]. However, in the present context, it is defined

as a process that causes breakup of the chemical network and/or the macromolecular chains.

A number of methods have been applied to tire rubber recycling and waste rubber utilization [1-5]. These methods include retreading, reclaiming, grinding, pulverization, microwave and ultrasonic processes, pyrolysis and incineration. Processes for utilization of recycled rubber are also being developed to manufacture rubber products and thermoplastic/rubber blends and to use ground rubber to modify asphalt and cement.

2. Retreading of tires

Retreading is one way of recycling. Also it saves energy. It takes about 83 liters of oil to manufacture one new truck tire whereas a retread tire requires only about 26 liters. The cost of a retread tire can be from 30-50 % less than a new tire [3, 6]. Approximately 24.2 million retreaded tires were sold in North America in 2001, with sales totaling more than $2 billion. Mostly medium and heavy duty truck tires, off-the-road vehicles, and aircraft tires were retreaded [6]. However, high labor costs and tougher safety regulations may hurt the retreading business [3].

3. Recovery of tire materials

3.1 Reclaiming technology

Reclaiming is a procedure in which vulcanized rubber waste is converted, using mechanical and thermal energy and chemicals, into a state in which it can be mixed, processed and vulcanized again. The principle of the process is devulcanization.

Generally, ground rubber scrap is used as the feedstock. Warner [2], Adhikari et al. [4] and Isayev [5] have presented reviews of various methods of devulcanization.

The pan process, digester process (either wet or dry), and mechanical or reclaimator process are currently the common processes used for reclaiming.

The digester process [1, 2, 4, 5] uses a steam vessel equipped with a paddle agitator for continuous stirring of the crumb rubber while steam is being applied. The wet process may use caustic soda and water mixed with the rubber crumb while the dry process uses steam only. Various reclaiming oils may also be added. The dry digester has the advantage of causing less pollution and was adopted after the Clean Air and Water Act was enacted.

A mechanical or reclaimator process [2, 4, 5] has been used for the continuous reclaiming of whole tire scrap. Fine rubber crumb (typically 30 mesh) mixed with various reclaiming oils is subjected to high temperature with intense mechanical working in a modified extruder.

Scrap rubber containing natural and synthetic rubbers can be reclaimed by a digester process using reclaiming oil having a molecular weight between 200 and 1000 and consisting of benzene, alkyl benzene and alkylate indanes.

Recently, a new technology for the devulcanization of sulfur cured scrap elastomers was reported by STI-K America using a proprietary material termed "Delink". In this process 100 parts of 40 mesh or finer crumb is mixed with 2 to 6 parts of Delink reactant in an open two-roll mixing mill. Furthermore, a simple process for reclaiming rubber with a vegetable product that is a renewable resource material (RRM) was developed in India. The major constituent of RRM is diallyl disulfide. Other constituents are other disulfides, monosulfides, polysulfides and thiol compounds.

It is known that sulphur-vulcanized NR can be completely recycled at 200-225°C by

diphenyldisulphide. Recently, the efficacy of other disulphides as recycling agents for NR and EPDM vulcanizates were reported. While complete devulcanization was observed for sulphur-cured NR at 200°C, a decrease of crosslink density by 90% was found when EPDM sulphur vulcanizates were heated to 275°C with diphenyldisulphide in a closed mold for 2 hours. EPDM cured by peroxide showed a decrease in crosslink density of about 40% under the same conditions.

Another chemical method was recently proposed by Goodyear Tire and Rubber Company. It is based on the use of 2-butanol as a devulcanizing agent for sulfur-cured rubber at high temperature and pressure. It is claimed that the molecular weight of the rubber is retained and its microstructure is not significantly altered during the devulcanization process. However, the process is slow and requires separating the devulcanized rubber from the solvent.

Rubber can also be devulcanized by means of inorganic compounds. Discarded tires and tire factory waste were devulcanized by desulfurization of rubber vulcanizate crumb (10~30 mesh) suspended in a solvent such as toluene, naphtha, benzene, or cyclohexane in presence of sodium. The alkali metal cleaves mono-, di-, and polysulfidic crosslinks of the swollen and suspended rubber crumb at around 300°C in the absence of oxygen. However, this process may not be economical because it involves swelling of the vulcanized rubber crumb in an organic solvent where the metallic sodium can reach the sulfidic crosslink sites. Also, use of a solvent may increase pollution and be hazardous. A technology was also proposed to reclaim powdered rubbers using an iron oxide/phenyl hydrazine based catalyst with copper (I) chloride-tributyl amine.

Depending on the specification of the finished products, fillers may be added to the devulcanized material before further processing. The devulcanized rubber mix is then strained and refined before being powdered, baled, sheeted or extruded into the finished form.

A possible method for devulcanizing the vulcanized network uses chemical agents that attack the C-S or S-S bonds. However, this process is slow and creates further problems in removing solvents. Additional waste is generated in the form of sludge.

3.2 Surface treatment

This technology, proposed by Goodyear Tire and Rubber Company, uses a solvent to treat (devulcanize) the surface of rubber crumb particles of sizes from about 20 to 325 mesh. The process is carried out at temperatures between 150°C to 300°C at a pressure of at least 3.4 MPa in the presence of an alcohol or ketone solvent. 2-butanol exhibited the best ability to devulcanize sulfur-cured SBR rubber. The process takes about 20 min. Reported data were obtained by treating small amounts of rubber crumb in a gas chromatography column. A suitable solvent should have a critical temperature in the range 200°C to 350°C. It is claimed that preferential breakage of S-S and C-S bonds takes place with little breakage of the main chains.

The rubber crumb obtained was vulcanized as prepared and also in blends with virgin rubber. The vulcanizates exhibited good retention of mechanical properties in blends with virgin rubber. However, the process has only been tested on a laboratory scale.

3.3 Grinding and pulverization technology

Use of waste rubber in the vulcanized state most often requires reduction of particle size

and/or increase of surface area, for example by grinding. Presently, three methods are used: ambient grinding, cryogenic grinding and wet-ambient grinding. Vulcanized scrap rubber is first reduced to 2 inch by 2 inch or 1 inch by 1 inch chips. Then a magnetic separator and a fiber separator (cyclone) remove steel and polyester fragments. The chips can then be further reduced using ambient grinding or cryogenic grinding.

Another method for obtaining fine-mesh rubber is by cooling scrap tires in liquid nitrogen below their glass transition temperature and then pulverizing the brittle material in a hammer mill. But for inexpensive rubbers such as tire rubbers, the process is probably not economical because of the large amount of liquid nitrogen or other cryogenic liquids needed to freeze the rubber. However, little or no heat is generated in the process. This results in less degradation of the rubber. In addition, almost all fiber or steel is liberated from the rubber, resulting in a high yield of usable product.

Because of the high cost of cryogenic size reduction, chopping and grinding is often used instead. The vulcanized rubber is sheared and ground into small particles using a conventional high-powered rubber mill, set at close nip. With this relatively inexpensive method it is common to produce 10 to 30 mesh material and relatively large crumb. Multiple grinds can be used to further reduce the particle size. Ambient grinding produces an irregularly-shaped particle with many small hair-like appendages that attach to the virgin rubber matrix producing an intimate well-bonded mixture. The lower particle limit for the process is 40 mesh. The process, however, generates a significant amount of heat that can degrade the rubber and if not cooled properly first, cause combustion on storage.

Other recycling processes include mechanical and thermo-mechanical methods, which only comminute the rubber and similar to the above mentioned processes do not devulcanize it. A process using a wet grinding method to achieve a crumb fineness of approximately 200 mesh has been reported. When this product, which had a high surface-to-mass ratio, was then devulcanized, no chemicals and only minimal heating and mechanical processing were required. Wet or solution process grinding may yield the smallest particle size, ranging from 400 to 500 mesh, allowing good processing and producing relatively smooth extrudates and calendered sheets.

Pulverization techniques for rubber are also being developed based on the process originally proposed for plastics [7]. Polymer powder is produced using a twin-screw extruder which imposes compression and shear on the polymer at temperatures that depend on the polymer. Pulverization of rubber waste by solid-state shear extrusion is also proposed [8]. The obtained rubber particles were fluffy and exhibited a unique elongated shape.

Recently, pulverization of rubbers in a single screw extruder has been carried out, producing particles varied in size from 40 to 1700 μm [9]. A schematic diagram is shown in Figures 18.1a and 18.1b. As indicated in figure 18.1a, the extruder consists of three zones: feeding (Zone 1), compression (Zone 2) and pulverization (Zone 3). The screw is square-pitched with the compression zone having a uniform taper to create a compression ratio of 5. The water-cooling channel is located in the barrel in order to remove heat generated by pulverization. Experiments showed that a significant amount of heat is generated by friction, leading to partial degradation of the rubber. The rubber granules are fed into the hopper of the extruder and conveyed into the compression zone. They emerge from the pulverization zone as a powder with a small particle size. Surface oxidation of the particles and agglomeration of a fraction of them may take place. The particles exhibit irregular shapes with rough surfaces and a porous structure. Their crosslink density and gel frac-

tion are reduced in comparison with the initial rubber granules. This indicates that partial devulcanization has occurred. Due to this, the particles can be molded into products by applying high temperature and high pressure for a period of at least one hour. Table 18.1 shows the dependence of the elongation at break, tensile strength and crosslink density of compression-molded slabs of the original rubber compound and slabs prepared from pulverized particles of size in the range 250 to 425 , obtained from discarded by-products of natural rubber (SMR-20) vulcanizates. The approximate composition of the rubber compound was about 54 wt % of SMR-20, 27 wt % carbon black (SRF), 11 wt % aromatic oil and 8 wt % vulcanizing ingredients. Molding temperature and pressure were 157°C and 5.11 MPa, respectively. Slab F1, produced without adding sulfur curatives, exhibited the best strength properties of slabs obtained from the rubber powder. In this sample, oil, vulcanization residues and soluble materials were removed by toluene extraction. According to the authors, this led to enhanced particle bonding and improved strength properties. On the other hand, slabs F2 and F3, produced by adding sulfur curatives to the particles, showed inferior strength properties due to less particle bonding. Furthermore, slabs F1, F2 and F3 showed inferior strength to the original slab indicating that compression molding of the rubber particles did not achieve the properties of the original vulcanizate.

Figure 18.1: Schematic diagram of the single screw extruder for pulverization of rubbers (a) and geometry of the screw channel with variable depth (b) [from Rubber Chem. Technol., 73, 340-555, 2000].
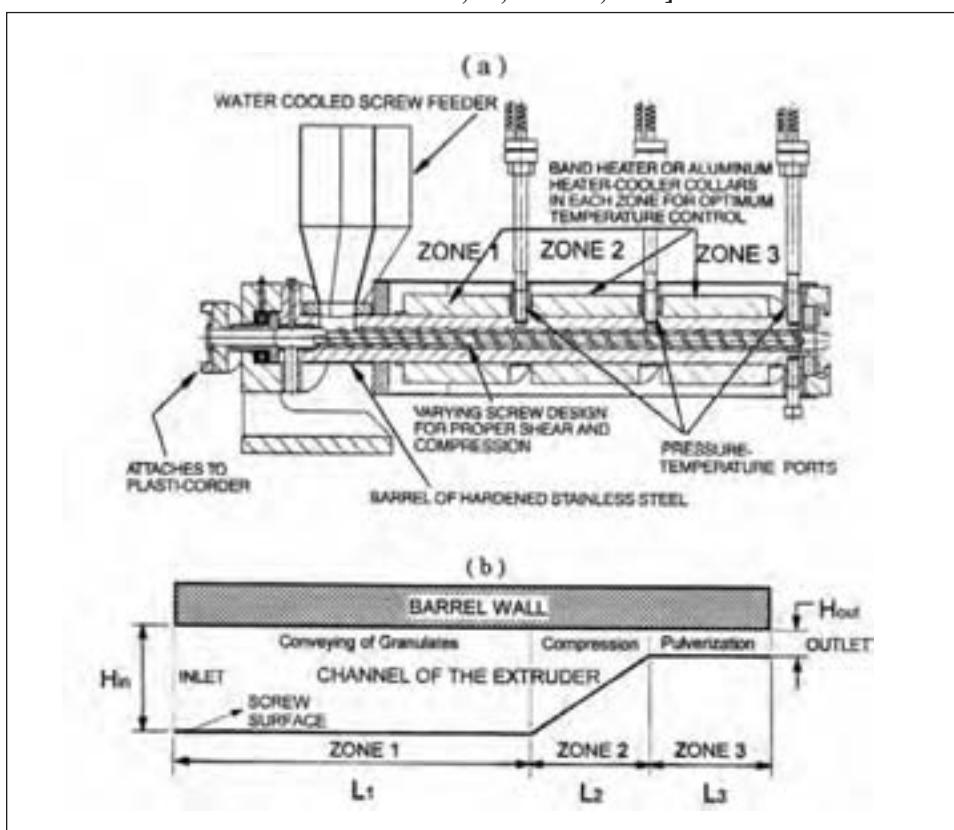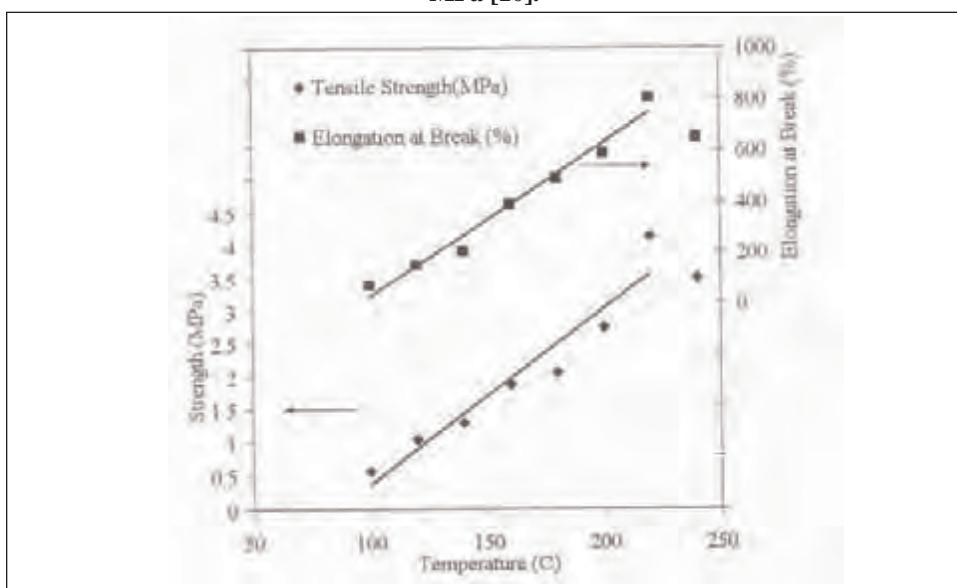
Table 18.1: Properties of slabs of pulverized rubber waste [9]

	Revulcanizing system		ε_b(%)	σ_b(MPa)	ν(mol/m^3)
Slab code	Sulfur (phr)	TBBS (phr)			
F1	-	-	360	10.3	50.4
F2	1.0	0.5	350	7.0	73.9
F3	1.0	-	320	8.2	69.5
Original	-	-	470	16.5	66.9

Particles obtained by other grinding processes can also be compression molded into slabs by means of high-pressure and high-temperature sintering [10]. Rubber particles based on several elastomers, and obtained by various grinding methods, were compression molded into slabs with and without addition of various acids and chemicals. The effects of time, pressure and temperature on the mechanical properties of sintered slabs was studied. Figure 18.2 shows the effect of molding temperature on mechanical properties of a NR/SBR slab compression molded from 80 mesh particles for 1 hour at 8.5 MPa [10]. It clearly shows the importance of the molding temperature. Below approximately 80°C, the process was unsuccessful. The highest tensile strength, about 4 MPa, was achieved with a reasonably high breaking elongation (about 800%). The mechanism of consolidation of particles in this process is the creation of radicals that react with other radicals across the particle interface and thus create chemical bonds. The authors explained the inferior properties of sintered NR rubber particle slabs in comparison to the original as due to the presence of voids. Less energy is required to generate voids in the sintered slabs and this does not allow strain-induced crystallization to be achieved.

Figure 18.2: Effect of molding temperature on the mechanical properties of NR/SBR slabs compression molded from particles of 80 mesh for 1 hour at a pressure of 8.5 MPa [10].

3.4 Devulcanization technology

3.4.1. Microwave method

Microwave technology has been proposed by Goodyear Tire and Rubber Company to devulcanize waste rubber. This process applies heat quickly and uniformly to waste rubber. A controlled amount of microwave energy is applied to devulcanize a sulfur vulcanized elastomer containing polar groups or components, to a state in which it can be compounded and revulcanized to produce useful products, such as hoses, requiring significant physical properties. On the basis of relative bond energies, it was deduced that scission of the sulfur-sulfur and sulfur-carbon crosslinks was preferred to scission of carbon-carbon bonds in the rubber molecule. However, the material must be polar enough to develop the heat necessary for devulcanization. This method is a batch process and requires relatively expensive equipment.

Recently, thermogravimetry was employed to study the changes occurring in rubber vulcanizates during devulcanization by microwave treatment. The degree of degradation of the polymer chains was measured to establish the best conditions for devulcanization.

3.4.2 Ultrasonic method

Numerous publications are devoted to the study of the effect of ultrasound on fluids, polymer solutions [11] and on polymer melts during extrusion [12].
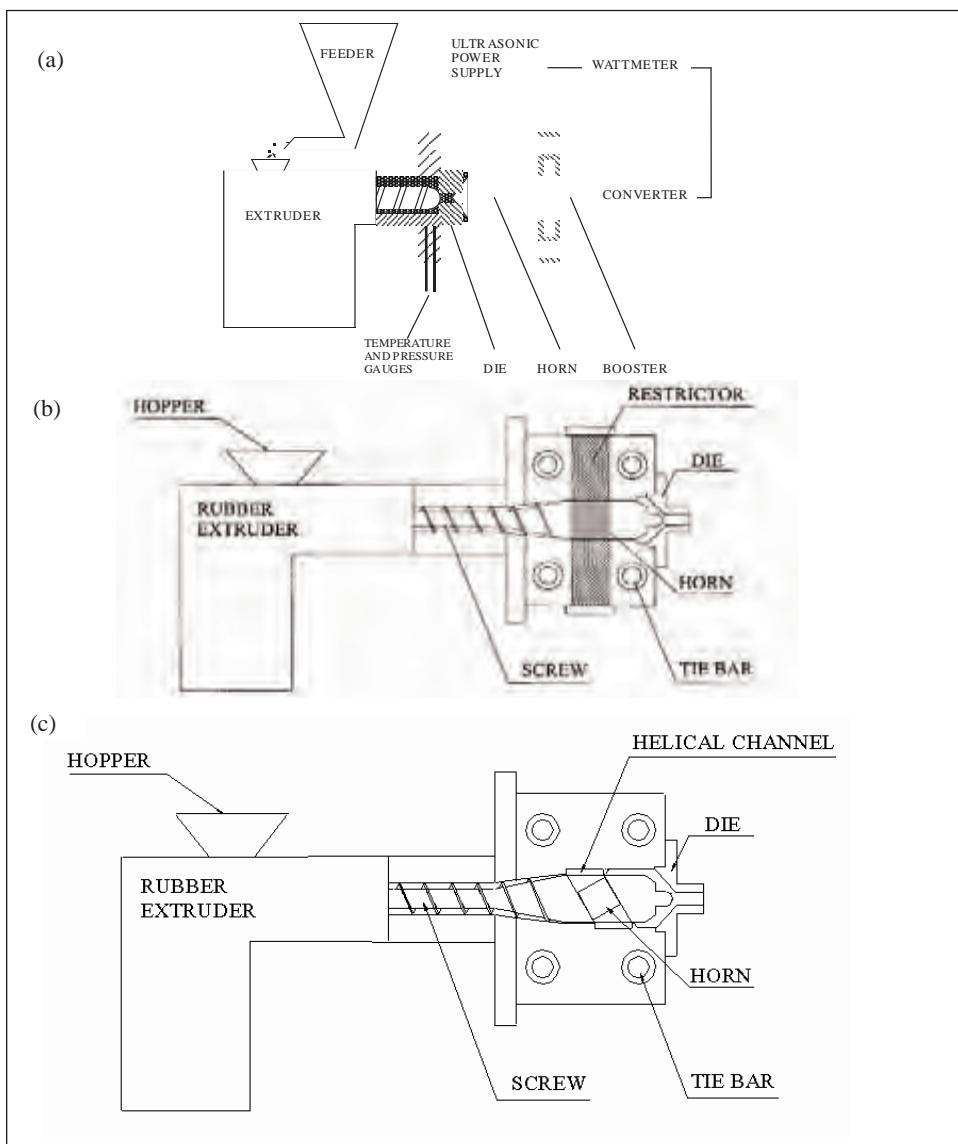
The application of ultrasonic waves to devulcanize rubber is an attractive proposition. However, earlier studies indicated that rubber is vulcanized by ultrasound rather than devulcanized. Devulcanization was first discussed by Yokohama Tire and Rubber Company as a batch process using 50 kHz ultrasonic waves for twenty minutes. The process was claimed to break down carbon-sulfur bonds and sulfur-sulfur bonds, but not carbon-carbon bonds. The properties of the revulcanized rubber were found to be very similar to those of the original vulcanizates.

A novel continuous process has been developed by Isayev and coworkers for devulcanizing rubber as a suitable way to recycle used tires and waste rubbers [2-5]. This technology is based on the use of the high-power ultrasound. Ultrasonic waves of certain levels, in the presence of pressure and heat, can quickly break up the three-dimensional network of crosslinked rubber. The process is fast, simple, efficient, and free from added solvents and chemicals. Devulcanization occurs in times of the order of a second and may lead to preferential breakage of sulfidic crosslinks. The process is also suitable for decrosslinking peroxide-cured rubbers and plastics. A schematic diagram of the various reactors suitable to carry out this process is shown in Figure 18.3. Initially, the so-called coaxial devulcanization reactor (Figure 18.3a) was developed. It consists of a single screw rubber extruder and an ultrasonic cone-shaped die attachment. The die plate and the horn are water-cooled. The shredded rubber is fed into the extruder at a controlled rate. An ultrasonic power supply, an acoustic converter, booster and a cone-tipped horn are used. The unit is mounted onto the extruder flange. The horn vibrates longitudinally at a frequency of 20 kHz and at a chosen amplitude. The convex tip of the horn matches the concave surface of the die, so that the clearance between the horn and the die is uniform at a controlled gap. Rubber flows through the gap and becomes devulcanized under the action of the ultrasonic waves, that propagate perpendicular to the flow direction.

Later, barrel (Figure 18.3b) and grooved barrel (Figure 18.3c) ultrasonic reactors were developed. In the barrel reactor, two ultrasonic water-cooled horns of rectangular cross

sections were inserted into the barrel through two ports. Two bronze restrictors were placed in the barrel. These restrictors forced the rubber to flow through the gap created between the rotating screw and the tip of the horn. In the devulcanization section, the larger diameter provided a converging flow of the rubber to the devulcanization zone. This feature may enhance the devulcanization process. In the grooved barrel ultrasonic reactor, the barrel surface has two helical channels (grooved barrel). Rubber flows through the channels and passes through the gap between the rotating shaft and the tip of the horns where devulcanization takes place.

Figure 18.3: Schematic diagram of coaxial reactors for devulcanization of rubbers.
(a) original (b) barrel reactor (c) grooved barrel reactor.

A prototype machine for ultrasonic devulcanization has been developed. Retreaded truck tires containing 15 wt% and 30 wt% of ultrasonically devulcanized carbon-black-filled SBR passed the preliminary dynamic endurance test.

Extensive studies on the ultrasonic devulcanization of rubber and some preliminary studies on decrosslinking plastics have been carried out. The devulcanized rubber is soft, and can be processed, shaped and revulcanized in much the same way as virgin rubber. The technology has been applied to many materials: a ground tire rubber (GRT), unfilled and filled NR, guayule rubber, unfilled and filled SBR, unfilled butadiene rubber (BR), unfilled and filled silicone rubber, unfilled and filled EPDM roofing membranes, unfilled and filled polyurethane, a fluoroelastomer, ethylene vinyl acetate foam and crosslinked polyethylene. After revulcanization, the rubber samples exhibited good mechanical properties, which in some cases are comparable to those of virgin vulcanizates.

The effect of processing parameters such as pressure, power consumption, die gap, temperature, flow rate and ultrasonic amplitude have been studied and also the effect of the reactor design.   Structural changes occur in various rubbers on devulcanization, and affect the rheological properties, the curing kinetics and the mechanical properties of revulcanized rubbers. Figure 18.4 shows the entrance pressure of the devulcanization zone for GRT vs. amplitude of ultrasound, at a flow rate of 0.63 g/s with a gap of 2 mm. The entrance pressure was substantially reduced as the amplitude of ultrasound was increased because of devulcanization taking place as the GRT particles entered the devulcanization zone. The barrel reactor showed a higher pressure in the devulcanization zone than the coaxial reactor and the grooved barrel reactor showed the lowest pressure. However, at an ultrasound amplitude of 10 μm, the entrance pressure for the coaxial and barrel reactors was almost the same. The highest flow rate achieved in the barrel and grooved barrel reactors was 6.3 g/s. A devulcanized sample from the coaxial reactor could not be obtained at this flow rate due to an overload of the ultrasonic generator. Furthermore, in the grooved barrel reactor, the gap size had to be increased to 3.5 mm and the ultrasonic amplitude had to be decreased to 6 μm to avoid overloading the ultrasound unit. At high flow rates, the barrel reactor had a lower entrance pressure at the devulcanization zone than the other reactors.   Note that in the barrel and grooved barrel reactors, rubber in the devulcanization zone was subjected to pressure and drag flow while in the coaxial reactor there was only a pressure flow.

A comparison of stress-strain behavior of vulcanizates prepared from devulcanized GRT produced by the three reactors at the maximum flow rate is shown in Figure 17.5. The sample from the barrel reactor showed a tensile strength of 8.7 MPa, elongation at break of 217 % and modulus at 100% elongation of 2.6 MPa.   The revulcanized sample obtained from the grooved barrel reactor shows a tensile strength of 8.3 MPa, elongation at break of 184 % and modulus at 100% elongation of 3.3 MPa. These properties meet the higher level specification for tire reclaim [1].

It is thought that ultrasonic devulcanization is based on cavitation. In this case, acoustic cavitation occurs in a solid, in contrast to cavitation that occurs in liquids subjected to rapidly alternating pressures of high amplitude. Any bubble present in the liquid will thus expand and contract alternately. The bubble can also collapse suddenly during compression, resulting in almost instantaneous release of a comparatively large amount of energy, that depends on the acoustic pressure amplitude and, hence, the acoustic intensity.

Figure 18.4: The entrance pressure for GRT of devulcanization zone of different reactors vs ultrasonic amplitude at a flow rate of 0.63 g/s, and vs flow rate at an amplitude of 10 μm. Gap = 2 mm.
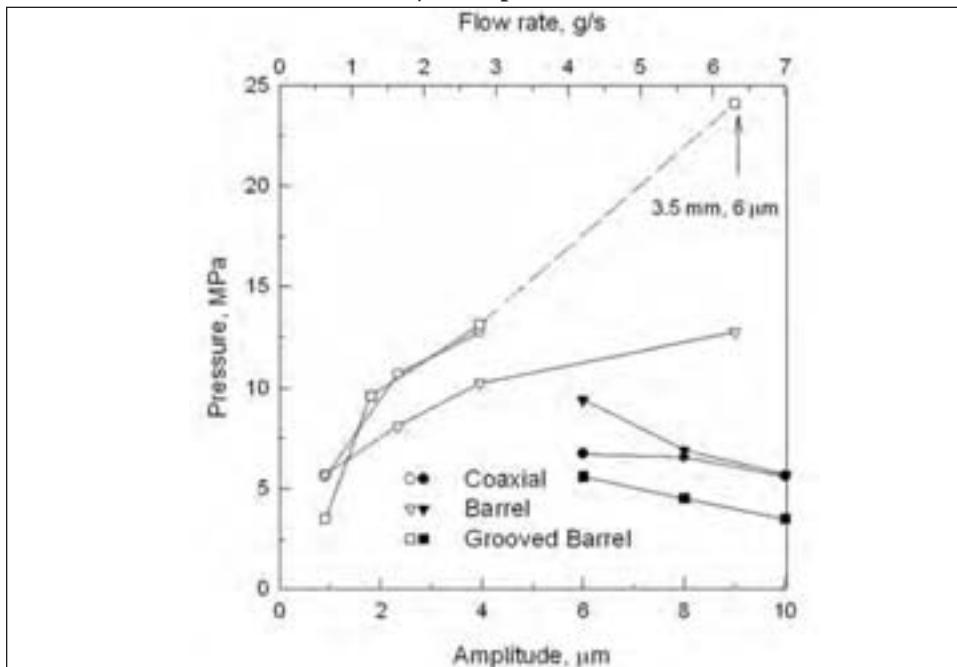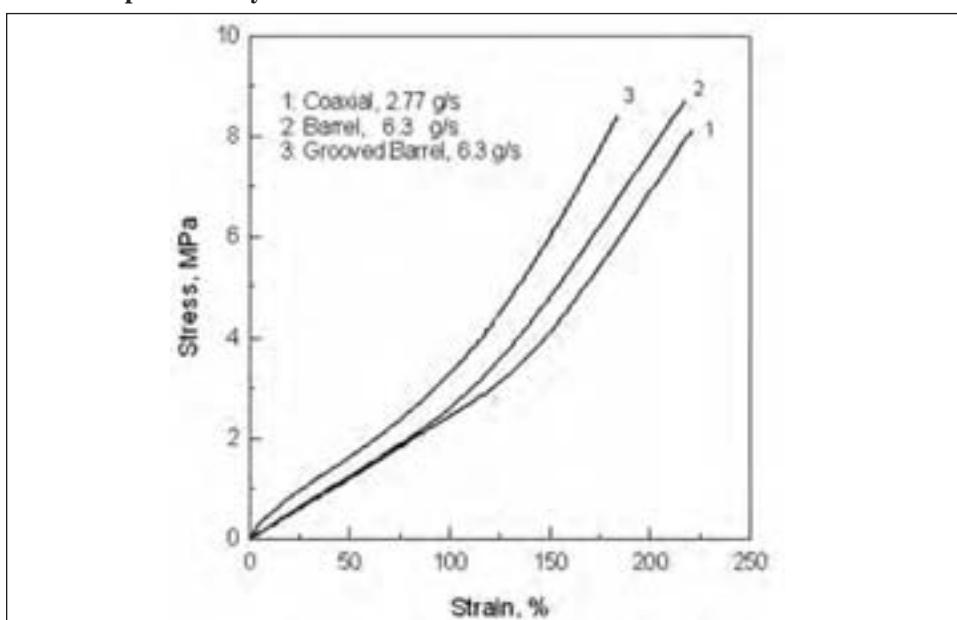
Figure 18.5: Stress-strain curves of vulcanizates prepared from devulcanized GRT produced by the three reactors at the maximum flow rate shown.

Cavitation can also occur in bubble-free liquids when the acoustic pressure amplitude exceeds the hydrostatic pressure acting on the liquid. In the tensile half of the pressure cycle, voids are formed at weak points in the structure of the liquid. These voids grow in size and collapse in the same way as gas-filled bubbles.

In the case of polymer solutions, irradiation by ultrasound waves produces cavitation, and the formation and collapse of bubbles plays an important role in causing scission of the macromolecules. In solid elastomers, intrinsic microvoids are thought to be responsible for cavitation when the material is subjected to a sudden hydrostatic tension, or a sudden depressurization.

Studies of ultrasonically treated rubber show that the breakup of chemical crosslinks is accompanied by partial degradation of the rubber molecules. But the mechanism of devulcanization is not well understood, unlike the degradation of long-chain polymers in solutions. In particular, the way in which ultrasonic energy is converted into chemical energy is not clear. The proposed models of devulcanization [13, 14] are based upon breakdown of the rubber network caused by cavitation created by high-intensity ultrasonic waves in the presence of pressure and heat.

Under some devulcanization conditions, the tensile strength of unfilled revulcanized SBR was found to be much higher than that of the original vulcanizate with the elongation at break being practically unchanged. Figure 18.6 shows the stress-strain curves of unfilled virgin vulcanizates and revulcanized SBR obtained from rubber devulcanized at various ultrasonic amplitudes, A. The devulcanized samples were made with the coaxial ultrasonic reactor depicted in Figure 18.3 (a) at a barrel temperature of 120°C, a screw speed of 20 rpm, and a flow rate of 0.63 g/s. The improvement in mechanical properties is attributed to the presence of a bimodal network in the revulcanized rubber. Superior properties of revulcanized rubber were also observed in unfilled EPDM and silicone rubbers. Unfilled revulcanized NR rubber also showed good properties, with the elongation at break remaining similar to that of the original vulcanizate, but the ultimate strength was reduced to about 70 % of the original. Interestingly, revulcanized NR showed the characteristic strain-induced crystallization of NR, as indicated in Figure 18.7 by the upturn in the stress-strain curves for both the original and the revulcanized material.

It is of interest to establish what role a filler plays in the devulcanization process. Figure 18.8 shows stress-strain curves for vulcanizates of virgin and devulcanized NR containing 35 phr of carbon black. The original vulcanizates were cured using 5 phr ZnO, 1 phr stearic acid, 1 phr CBS, 2 phr sulfur. The revulcanization recipe contained 2.5 phr ZnO, 0.5 phr stearic acid, 0.5 CBS and 2 phr sulfur. The mechanical properties of revulcanized rubbers typically deteriorate depending on the devulcanization conditions. This is evident in Figure 18.8. It is thought that ultrasonic devulcanization causes a partial deactivation of filler due to breakup of macromolecular chains attached to the surface of carbon black. When devulcanized rubber was blended with virgin rubber, the vulcanizates showed significantly improved properties. Also, vulcanizates containing fresh carbon black exhibited better properties. However, revulcanized samples prepared from EPDM roofing membrane material containing carbon black and a significant amount of oil showed mechanical properties similar to or better than the original rubber. Possibly, the oil prevents deactivation of the filler during devulcanization.

Figure 18.6: Stress-strain curves of unfilled virgin vulcanizates and revulcanized SBR obtained from rubbers devulcanized in a coaxial reactor at various ultrasonic amplitudes.
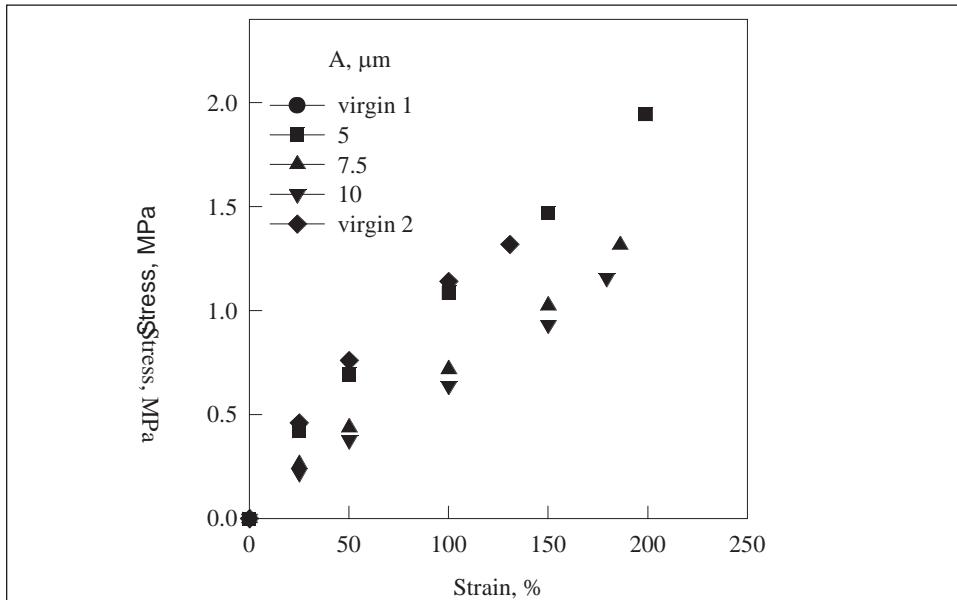
Figure 18.7: Stress-strain curves for unfilled NR vulcanizates prepared from NR devulcanized in a coaxial reactor at various flow rates and amplitudes with a gap of 2.54 mm and a barrel temperature of 120°C.
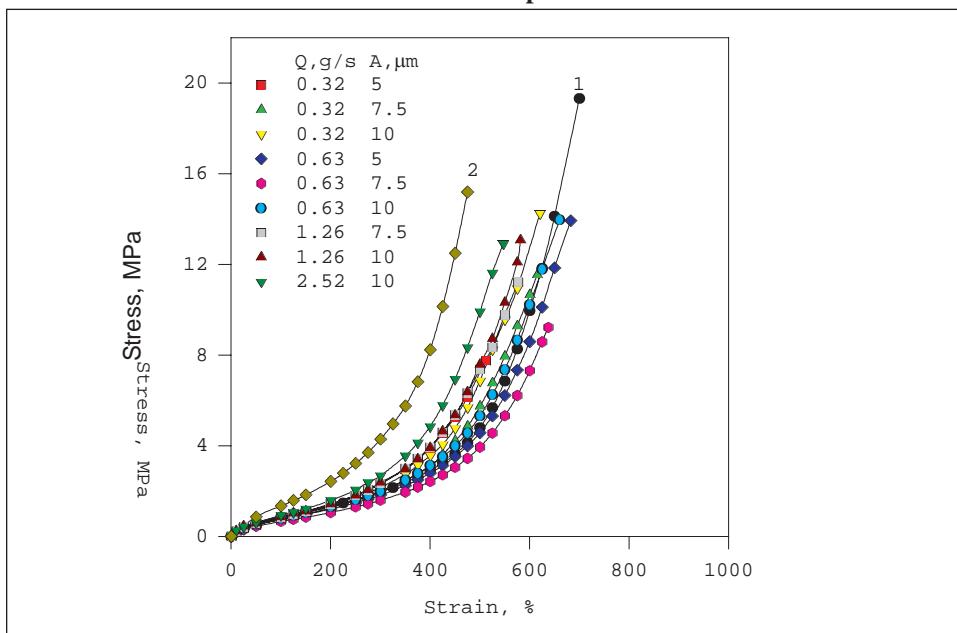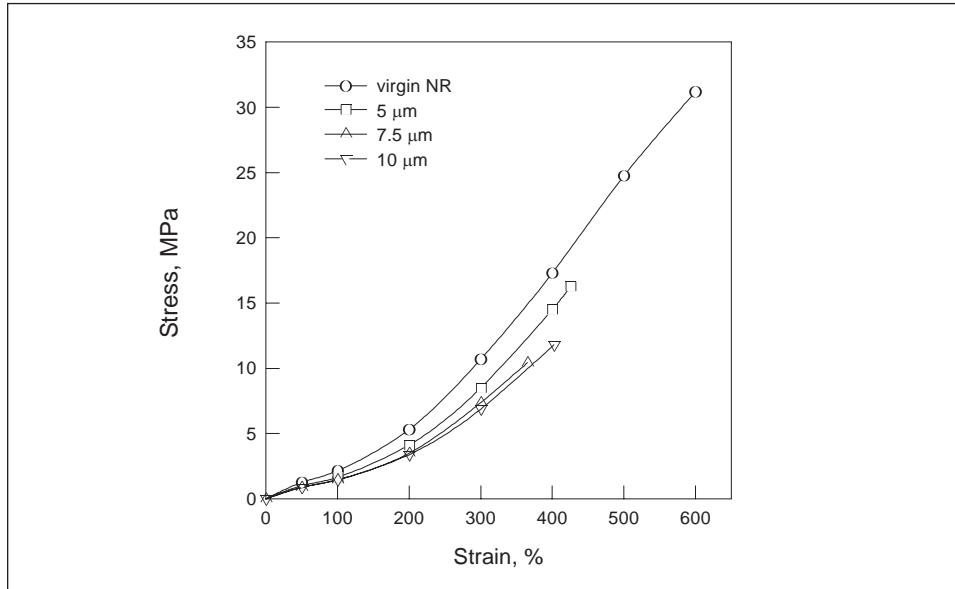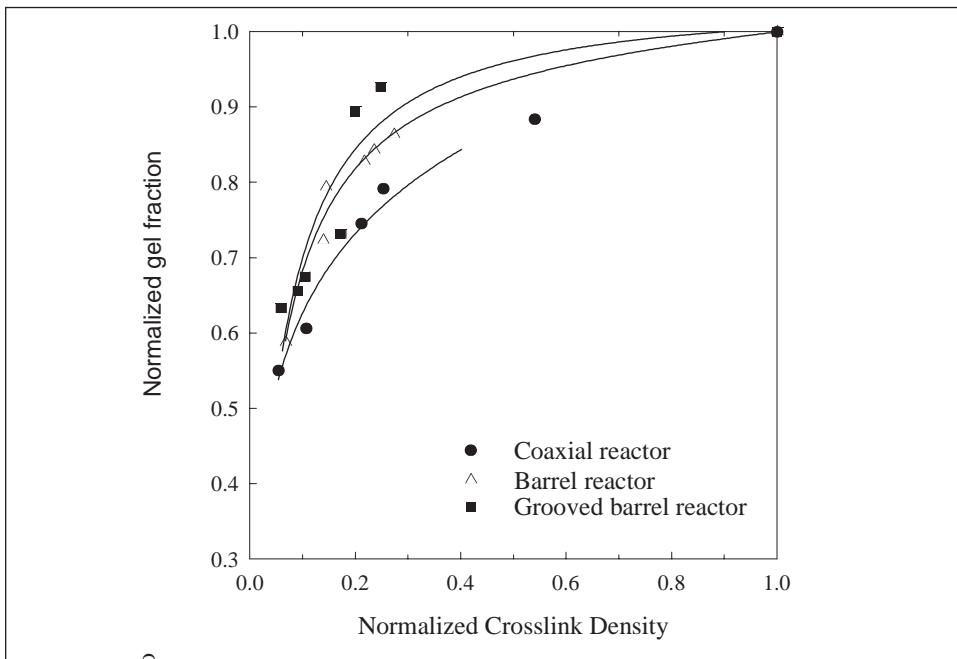
Figure 18.8: Stress-strain curves for 35 phr carbon black filled virgin NR and revulcanized NR devulcanized in a coaxial reactor at a flow rate of 0.63 g/s and various ultrasonic amplitudes. Gap = 2.54 mm, barrel temperature = 120°C.

Ultrasonic devulcanization also alters the kinetics of revulcanization. For SBR the induction period was shorter or absent. This was also the case for other unfilled and carbon black filled rubbers, such as GRT, SBR, NR, EPDM and BR cured by sulfur-containing curative systems, but not for silicone rubber cured by peroxide. The decrease or disappearance of the induction period for sulfur-cured rubbers is attributed to a crosslinking reaction between rubber molecules chemically modified in the course of devulcanization and unmodified rubber molecules. Note that approximately 85% of the accelerator remained in the devulcanized SBR rubber.

Ultrasonically devulcanized rubber consists of sol and gel fractions, where the gel portion is typically soft and has a lower crosslink density than the original vulcanizate. Crosslink density and the gel fraction were found to be correlated by a master curve that is unique to the particular elastomer. Figure 18.9 shows the normalized gel fraction as a function of the normalized crosslink density for devulcanized GRT, obtained from three different reactors. The dependence of gel fraction on crosslink density was described by a single curve, independent of processing conditions. The curve for the barrel and grooved barrel reactors was shifted toward lower crosslink density indicating a higher efficiency of devulcanization, possibly due to an additional shearing effect.

**Figure 18.9: Normalized gel fraction vs. normalized crosslink density for GRT devul-
canized under various conditions using coaxial, barrel and grooved barrel reactors.**

4. Use of recovered tire rubber

4.1 General remarks

There are certain technical limitations to devulcanization. Vulcanization is, in fact, not
truly fully reversible and partial devulcanization usually results in a degradation of phys-
ical properties. This may limit the amount of substitution in high-tech applications such
as passenger tires. But it can provide the compounder of less stringent products with an
excellent low-cost rubber that can be used as the prime elastomer or at very high substi-
tution levels. According to the available literature, reclaim cannot be used for tread com-
pounds in tires because it decreases their resistance to wear. However, it is not known
whether this applies to rubber devulcanized without addition of chemicals. Considerable
amounts of reclaim are used for carcasses of bias ply tires made from NR compounds, but
for carcasses of radial tires no reclaim is added. On the other hand, reclaim is added to
compounds for bead wires and it may also be added to sidewalls.

A number of applications for GRT outside the rubber industry have been proposed,
including its use as a filler in asphalt for highway construction and as a rubberized surface
for sport facilities. Ground scrap rubber can be used as a filler in plastic compounds.
However, the compatibility with the matrix and the size of the filler, as well as the discon-
tinuity at the interface between the two phases should be considered. Rubber products
containing ground rubber have low tensile properties due to insufficient bonding between
the ground rubber and the virgin matrix. However, this bonding can be improved by addi-
tion of devulcanized rubber.

4.2 Use in new tires

Many different types of rubber and carbon black reinforcement are used in tire components. Thus, GRT is a blend of various rubbers and carbon blacks. Accordingly, in using GRT powder and devulcanized GRT in new tire manufacturing many factors should be considered. Evidently, scrap tire powder can be used as a filler for virgin rubbers and devulcanized GRT can be used in blends with virgin rubbers. This market consumed approximately 50 million pounds of scrap tire rubber in 2001.

Until recently, it was generally understood that only a few percent of ground rubber can be used in new tires. The Scrap Tire Management Council reports that five percent of recycled tire rubber is used in an original equipment tire for the Ford Windstar. Although no other information on the amount of devulcanized rubber used in new tires is available in the open literature, a possibility exists for the use of up to 10 weight % of recycled tire rubber in new tire compounds [3]. Recently, it was reported that actual road tests of truck tires containing 10 wt % of devulcanized rubber in the tread exhibited wear behavior almost equal to that for the standard tire made with new rubber [15]. The amount of recycled rubber used in tires is growing but it is likely that service results will not be available for a number of years.

4.3 Rubber/recycled tire rubber blend

Rubber particles from scrap tires can be incorporated into virgin rubber as a filler. The effect of GRT particles of different sizes incorporated in a NR compound on its mechanical properties was reported [16]. Table 18.2 shows the tensile strength, elongation at break and tear strength before and after aging for a virgin NR vulcanizate and NR vulcanizates containing 30 phr of GRT particles of various sizes: 650-450, 300-215, 205-160 and 150-100. The curing recipe contained 6 phr ZnO, 0.5 phr stearic acid, 3.5 phr sulfur and 0.5 phr MBT. Incorporation of GRT decreased the physical properties of the vulcanizate, with the effect being larger for large particles. However, the vulcanizate containing GRT exhibited better retention of properties upon aging. It was noted that smaller particles contain less rubber but a higher amount of fillers and metals.

Recycled tire rubber in the form of large crumb particles is also used for making prepackaged pour-in-place surfacing products. GRT is combined with pre-mixed polyurethane to produce a soft, pliable energy-absorbing rubber surface for playground and other recreational surfaces and is intended for placing over compacted gravel, concrete or asphalt.

Table 18.2: Properties of GRT filled NR vulcanizates [16]

Properties	Control		A		B		C		D	
	Before aging	After aging	Before aging	After aging	Before aging	After aging	Before aging	After aging	Before aging	After aging
Tensile strength (MPa)*	14.0	8.8 (63)	2.2	1.6 (71)	4.2	2.5 (60)	7.3	3.3 (45)	8.0	2.5 (31)
Elongation at break (%)*	1175	770 (66)	430	230 (53)	620	360 (58)	780	410 (53)	860	400 (47)
Tear strength (kN/m)*	28.2	20.3 (72)	12.4	9.7 (78)	18.5	10.6 (57)	23.8	11.5 (48)	21.2	9.7 (46)
Sol%	2.1	2.2	5.8	6.4	5.2	6.2	4.9	6.0	4.3	6.6
% increase in sol (%) after aging	---	4.8	---	10.3	---	19.2	---	22.4	---	53.5

* Values in parentheses show the % retention of properties after aging at 100°C for 36 h.

4.4 Thermoplastic/recycled tire rubber blend

The technology of polymer blending has emerged as a useful tool in tailoring polymers to the needs of the end users. An exciting development is the introduction of thermoplastic elastomers (TPEs) based on plastic/rubber blends. These materials are becoming increasingly important because of their elastomeric properties, easy processability, and low cost.

Blending of waste rubber with thermoplastics is important from the point of view of both disposal of waste and reduction in product cost. More attention has been focused on compounding ground tire rubber (GRT) with thermoplastics which can be subsequently re-melted and shaped into a wide range of molded and extruded products. Generally, adhesion between the GRT and polymer matrix and size of the GRT particles are the two major factors controlling the mechanical properties of such composites. Also, dynamic vulcanization techniques can be used to improve the properties of the blends of ultrasonically devulcanized GRT and thermoplastics [17]. Dynamic vulcanization is the process of vulcanizing the elastomer during its mixing with the molten plastic.

It was reported that the GRT has a detrimental effect on most of the physical properties of these composites, the extent of deterioration increasing with the amount and size of the GRT. There have been several attempts to improve the adhesion between the GRT and polymer matrix.

The effects of various compatibilizers in promoting the adhesion of polyethylene (PE) in blends with GRT were studied, using a melt blending process where each component was first treated with compatibilizers of similar structure before the actual blending was carried out. Among the various compatibilizers, epoxydized natural rubber, ethylene-co-acrylic acid copolymer and ethylene-co-glycidyl methacrylate polymer were found to be effective in improving the impact properties of PE/GRT composites. It was also reported that use of smaller GRT particles results in a small increase in the impact property of the composite and has a greater influence on the melt processability. The percent improve-

ment in the impact energy for linear low density polyethylene (LLDPE) composites was greater than that for the corresponding high density polyethylene (HDPE) composites. It was also suggested that the low polarity and/or low crystallinity of the matrix polymer appeared to favor compatibility with GRT.

Modification of the surface of GRT particles has been studied to improve the compatibility of GRT and polymer. Surface modification can be carried out by chemical treatments, for example, chromic acid etching, thermal oxidation or by mechanical means. Maleic anhydride-grafted and chlorinated GRT improved the physical properties of GRT/EPDM/acrylated high-density polyethylene and GRT/polyvinyl chloride blends. It was found that surface treatment of ground rubber with a mixture of unsaturated curable polymer and a curing agent could also improve the performance of the blends. The effect of cryogenically ground rubber (CGR, approximately 250 µm) from old tires on some mechanical properties of an unsaturated polyester resin was investigated. Composites made from silane-treated ground rubber showed better mechanical properties than a composite made from untreated CGR. However, the particle size of the ground rubber was apparently too large to produce a toughening effect.

High-energy treatments including plasma, corona discharge and electron-beam radiation were used to modify the surface of GRT. Oxidation of the surface, such as occurs in plasma, and autoclaving in an oxygen atmosphere were shown to improve adhesion between GRT and polyamide. An epoxy resin compounded with tire rubber particles modified by plasma surface treatment was also studied. An improvement in mechanical properties of the resulting material over those containing the untreated rubber was observed. The effects of corona discharge treatment of GRT on the impact property of a thermoplastic composite containing GRT were investigated. X-ray photoelectron spectroscopy analysis showed that the treatment increased the amount of oxygen-containing groups on the rubber surface. For some composites it has been found that treated GRT marginally improved the impact property. However, prolonged times of treatment and higher power inputs for corona discharge reduced the impact strength.

A phenolic resin cure system and maleic anhydride grafted polypropylene (PP) compatibilizer significantly improved the mechanical properties of a blend of PP and ultrasonically devulcanized GRT, prepared by dynamic vulcanization. Also, improvement in processing efficiency and better properties of PP/GRT blends were achieved when ultrasonic treatment was carried out during extrusion in a more efficient reactor [17]. Mechanical properties of PP/GRT, PP/devulcanized GRT (DGRT) and PP/revulcanized GRT (RGRT), mixed in a 40/60 proportion, are shown in Table 18.3. The tensile strength, Young's modulus and elongation at break of the blend prepared in this way are higher than those obtained earlier. Also, properties of PP/RGRT at 10µm are higher than those of PP/GRT. Evidently, the ultrasonic treatment of PP/GRT blends led to increased compatibilization between the plastic and rubber phases. This was attributed to mechanochemical reactions induced by ultrasound. In addition, ultrasonically devulcanized GRT was blended with HDPE using a Brabender internal mixer and a twin-screw extruder. These blends were dynamically vulcanized in the mixers. Also, HDPE and GRT blends mixed in a twin-screw extruder were then passed through an ultrasonic devulcanization extruder and subsequently dynamically vulcanized by means of an internal mixer and twin-screw extruder. The blends mixed by using the twin-screw extruder prior to devulcanization were found to have better tensile properties and impact strength than any other blends.

Table 18.3: Mechanical properties of PP/GRT, PP/DGRT and PP/RGRT blends [17]

Blend		Tensile strength MPa	Young's modulus, MPa	Elongation at break, %
PP/GRT		6.7	116	16.6
PP/DGRT	2 horns, 5μm	6.6	98	21.5
	2 horns, 7.5μm	6.5	100	20.6
	2 horns, 10μm	5.15	102	7.6
	1 horn, 5μm	6.9	110	19.3
	1 horn, 7.5μm	6.6	104	17.4
	1 horn, 10μm	7.0	116	21.0
	earlier work	5.2	108	20.7
PP/RGRT	2 horns, 5μm	6.7	109	13.2
	2 horns, 7.5μm	6.7	110	13.3
	2 horns, 10μm	5.9	111	7.0
	1 horn, 5μm	6.4	110	11.8
	1 horn, 7.5μm	6.6	110	13.3
	1 horn, 10μm	7.2	122	14.8
	earlier work	6.7	110	18.0

Novel blends of GRT and recycled HDPE from used milk containers have been studied. Effects of GRT particle size and concentration on mechanical and rheological properties were determined. The blend systems were optimized by using a soft rubber-plastic binder produced from a mixture of HDPE and EPDM, wherein EPDM is dynamically vulcanized during its mixing with the HDPE. It was concluded that the softening of the HDPE binder provides compositions of improved ultimate mechanical properties.

4.5 Concrete modified by tire rubber
Production of rubber-filled concrete compositions is a possible area for a further expansion of GRT usage [18]. The advantages are increased resistance to cracking, freeze-thaw, acid rain and impact, absorption of shock waves and reduced heat conductivity. However, the compressive and flexural strength is reduced. The effect of the size of rubber particles on the compressive strength is unclear. The results are contradictory. Some tests showed a lower compressive strength of concrete upon adding coarse rubber particles and an increase on adding fine particles. Other tests showed opposite results. This contradiction is possibly due to differences in rubber source, geometry of particles and the way that particles were prepared.

The influence of the shape of rubber particles on mechanical properties, workability and chemical stability of rubber-filled cement was studied [18]. A composite containing shredded rubber was able to bridge cracks and prevent catastrophic failure of the specimen, while a composite containing granular rubber particles was unable to bridge cracks. A pull-out test indicated poor interfacial bonding between the granular rubber particles and the matrix. In fact, many studies in this area show that the interface between rubber and cement is weak. Some improvement has been achieved by washing the particles with water, a mixture of water and carbon tetrachloride, or a latex mixture leading to enhanced

adhesion. Several surface modifications are also proposed including treatment of rubber with sulfuric acid and nitric acid to chemically oxidize the rubber and introduce polar groups. Contrary to expectation, treatment with nitric acid led to a decrease of the strength of the composite. On the other hand, treatment with sulfuric acid improved the adhesion of rubber to concrete. Using a combination of chemical and surface probing techniques it was shown that the hydrophilicity of the rubber surface is greatly improved by acid or base treatment. Typically, the rubber surface is hydrophobic because rubber usually contains zinc stearate that diffuses to the surface. By acid treatment the zinc stearate can be hydrolyzed to stearic acid. Treating the rubber with base, the zinc ions are converted into sodium ions creating the soluble sodium stearate.

It was also found that addition of rubber particles to mortar led to a decrease in compressive and flexural strength. However, treatment of the particles before mixing with a bifunctional silane-coupling agent, such as gamma mercapto trimethoxy silane, improved the interface and led to increased ductility. This research should be expanded to include the effects of the type of coupling agent on the adhesion and the fracture behavior of rubber-filled cement paste, mortar and concrete, used in highway pavement overlays, sidewalks, medians, and sound barriers.

4.6 Asphalt modified by tire rubber

Asphalt can be blended with tire rubber to modify its properties. This remains the largest single market for ground rubber. In 2001, an estimated 220 million pounds, or approximately 12 million tires were used in the United States, mostly, in California, Arizona, and Florida. However, other states are beginning to recognize the benefits of the modified asphalt. It was reported that the asphalt industry can absorb up to 40% of scrap tires.

Adding scrap tire rubber to asphalt has advantages in the performance and longevity of roads. The ductility, crack resistance, skid resistance and noise reduction are improved. But the use of rubber-modified asphalt increases the cost of road construction by about 50% [19] and the requirement for hot mixing may possibly cause toxic emissions.

Two processes are used in preparing the rubberized asphalt, called dry and wet process. For both processes the GRT particle size ranges from 6.35 mm to 40 mesh. In the wet process, asphalt is blended with GRT particles and then added into the hot mix. In the dry process, GRT is mixed with aggregate and the resulting mix is blended with asphalt.

Blending GRT with asphalt has been carried out for quite some time. The composition of the GRT may include different rubbers which, because they are crosslinked, are mostly immiscible in bitumen. The blends show an improvement in basic asphalt properties as well as some rubber-like characteristics.

Blending of GRT with asphalt began in the 1960s by McDonald who developed and patented a patching material consisted of 25 wt % rubber scrap and asphalt blended at 375°F for 20 minutes. Macdonald expanded his work to applying it to actual road pavement test sections as a seal coat. In 1968, Sahmaro Petroleum and Asphalt applied a blend of GRT and asphalt as a binder for hot premix, a mixture of stone aggregate, sand and the tire-asphalt binder, premixed in a batch or drum type mixer. This material is then applied as a carpet on top of the road by means of a paving machine, followed by a steel roller for compacting the material. Thereafter, many variations of the basic hot premix process described above with a blend of GRT and asphalt as the binder have been proposed. Most of them involve replacing stone aggregate with GRT. However, this method does not truly

modify the asphalt binder. Thus, the blending process of GRT and asphalt before preparing a mixture is most efficient in improving properties. Typical use levels range from 15 to 30 wt %.

A limited amount of work has been done on characterizing blends of GRT and asphalt. Blends are typically mixed at temperatures of 300 to 400°C for a period of 0.5 to 2 hours. The mix increases in viscosity and has the consistency of a slurry with discernable rubber particles spread throughout. At room temperature the resulting composition is a tough rubbery-elastic material. The mixing period is often referred to as reaction or digestion time. The elastic quality of the blend is attributed to undissolved rubber particles acting as an elastic component within asphalt, which is modified by the fraction of the rubber particles that have dissolved. Longer mixing times, 2 hours, compared to 0.5 or 1 hour, significantly improve elastic recovery and reduce the amount of solid rubber in the mixture. The addition of GRT at 10, 20 and 30 wt % levels significantly increases the softening point and strain recovery of asphalt, with a viscosity increase of similar magnitude for all three blends.

Rheological properties are affected by asphalt composition, particle size and amount of dissolved rubber, and temperature. By controlling these variables binders with improved resistance to cracking and rutting can be produced. Finally, scrap tires, used as a crumb rubber modifier for asphalt, improve paving performance and safety and are an excellent and cost effective material for highway pavements.

4.7 Use of tire crumb in soil
Tire crumb can improve soils by resisting compaction. The improved resiliency of the turf is not a direct consequence of the elastic nature of rubber but rather the result of increased aeration. Crumb rubber was found to significantly reduce soil hardness, soil shear strength, and water content.

4.8 Products made from recovered tire rubber
Compounds containing devulcanized or ground tire rubbers can be utilized to make a variety of rubber products, for example, shoe soles and heels, tubes, conveyor belts, rubber moldings, automobile floor mats, mud flaps, livestock stall mattresses, playground and track surfacings, railroad track crossings, lower layers of floor coverings, various molded and extruded profiles, sealing plates, battery boxes and other hard rubber goods. Since tire rubbers are typically black, they therefore cannot be used for light and colored compounds unless additional measures have been taken to change the color. Obviously, for every such use the recycled tire rubber must undergo extensive testing.

5. Pyrolysis and incineration of tires
5.1 Recovery of hydrocarbon liquids and carbon black
One particular method for recycling used tires is pyrolysis [20]. Pyrolysis is the thermal decomposition of rubbers in the absence of air and oxygen to produce oils and gases for reuse by the petrochemical industry. Carbon black and other solids remaining after pyrolysis can be utilized as fillers. Pyrolysis is typically carried out in boilers, autoclaves, rotary kilns, screw conveyors and fluidized beds. Also, hydrogenation has been performed using a tubing bomb reactor. Research on tire rubber pyrolysis to recover hydrocarbon liquid and carbon black was quite extensive in the 1960s and 1970s and led to plant construc-

tion. However, these attempts proved to be economically unsuccessful due to the low price of crude oil at that time. Also, pyrolysis plants are thought to produce toxic waste as a byproduct of operation. However, significant research has been carried out recently and various new pyrolysis processes have been developed. Despite this progress, pyrolysis of scrap tires is still performed on a quite limited scale, mainly due to the absence of a large market for oil and carbon black produced in this way.

5.2 Tire-derived fuel

Tire rubber can be used for its energy value, by incineration. This use is advocated by a number of the major tire and rubber companies and also by utility companies. Scrap tires are used in kilns for manufacturing Portland cement. This reduces the amount of coal consumed by up to 25 %. Scrap tires are also burnt to generate energy. 115 million scrap tires were consumed for fuel in the United States in 2001. However, valuable rubber materials are lost in this way. It should be noted that 60,000 BTU of energy is consumed to make one pound of synthetic tire rubber. In contrast, the caloric value recovered by burning is only 13,000 to16,000 BTU per pound of rubber which is not much higher than that obtained by burning much cheaper coal. Moreover, burning tires for energy may contribute to atmospheric pollution [21].

6. Concluding Remarks

Waste tires are an important problem of international significance. This chapter describes some routes available to solve this problem. Many technologies are being developed. Among them, in addition to the well-known grinding techniques, are continuous pulverization methods based on single or twin-screw extruders that may serve as a possible means of supplying rubber powder as a feedstock for various present and future devulcanization and recycling technologies. These include reclaiming, surface treatment, ultrasonic devulcanization and utilization of rubber particles for making composites with other materials. Ultrasonic technology is considered a promising method to produce devulcanized rubber suitable for making products from 100% recycled rubber and for adding to virgin rubber, virgin and recycled plastics, asphalt, concrete and cement. High-output equipment is needed to make the process economically acceptable. Clearly, there is a need for better understanding of various recycling processes. Development of the science of rubber recycling, novel processes for recycling, and novel materials using recycled rubber, would significantly reduce energy consumption and reduce the problem of disposing of scrap tires and rubber waste.

References

1. Makarov, V. M., and Drozdovski, V. F., 1991, Reprocessing of Tyres and Rubber Wastes, Ellis Horwood, New York.
2. Warner, W. C., 1994, Rubber Chem. Technol, 67, 559-566.
3. Myhre, M., and MacKillop, D. A., 2002, Rubber Chem. Technol., 75, 429-474.
4. Adhikari, B., De, D., and Maiti, S., 2000, Prog. Polym. Sci., 25, 909-948.

5. Isayev, A. I., 2001, in "Rubber Technologist's Handbook", ed. by White, J. R., and De, S. K., RAPRA, Shawbury, UK, Ch. 15, pp. 511-547.

6. 2002 Fact Sheet, Tire Retread Information Bureau.

7. Enikolopian, N. S., 1985, Pure Appl. Chem., 57, 1707-1711.

8. Khait, K., and Torkelson, J. M., 1999, Polym. Plast. Technol. Eng., 38, 445-457.

9. Bilgili, E., Dybek, A., Arastoopour, H., and Bernstein, B., 2003, J. Elast. Plastics, 35, 235-256.

10. Morin, J. E., Williams, D. E., and Farris R. J., 2002, Rubber Chem. Technol., 75, 955-968.

11. Price, G. J., 1990, in Advances in Sonochemistry, ed. by Mason, T. J.,1, 231-287.

12. Isayev, A. I., Wong, C., and Zeng, X., 1990, Adv. Polym. Technol., 10(1), 31-45.

13. Kasner, A. I., and Meinecke, E. A., 1996, Rubber Chem. Technol., 69, 424-443.

14. Yashin, V. V. and Isayev, A. I., 2000, Rubber Chem Technol., 73, 325-339.

15. Fukumori, K., Matsushita, M., Okamoto, H., Sato, N., Suzuki Y. and Takeuchi, K., 2002, JSAE Review, 23, 259-264.

16. Naskar, A. K., Pramanik, P. K., Mukhopadhyay, R., De, S. K., and Bhowmick, A. K., 2000, Rubber Chem. Technol., 73, 902-911.

17. Oh, J. S., and Isayev, A. I., 2002, Rubber Chem. Tech., 75, 617-625.

18. Raghavan, D., Huynh, H., and Ferraris, C. F., 1998, J. Mater. Sci., 33, 1745-1752.

19. McQuillen Jr., J. L., Takallou, H. B., Hicks, R. G., and Esch, D., 1988, ASCE J. Transport. Eng., 114, 259-277.

20. Kaminsky, W., and Sinn, H., 1996, in Book "Recycling and Recovery of Plastics", ed. by Brandrup, J., Bittner, M. , Michaeli, W., and Menges, G., Hanser Publishers, Munich, Chapter 5.3.1, pp. 434-443.

21. Mastral, A. M., Callen, M. S., Murillo, R., and Garcia, T., 1999, Environ. Sci. Technol., 33, 4155-4158.

Index

DOT HS 810 561
February 2006

U.S. Department
of Transportation

**National Highway
Traffic Safety
Administration**